Transactions of the ASME®

Transactions of the ASME, Journal of Engineering for Gas Turbines and Power (ISSN 0742-4795) is published quarterly (Jan., April, July, Oct.) by The American Society of Mechanical Engineers, Three Park Avenue, New York, NY 10016. Periodicals postage paid at New York, NY and additional mailing offices. POSTMASTER: Send address changes to Transactions of the ASME, Journal of Engineering for Gas Turbines and Power, c/o THE AMERICAN SOCIETY OF MECHANICAL ENGINEERS, 22 Law Drive, Box 2300, Fairfield, NJ 07007-2300.
CHANGES OF ADDRESS must be received at Society headquarters seven weeks before they are to be effective. Please send old label and new address.
STATEMENT from By-Laws. The Society shall not be responsible for statements or opinions advanced in papers or ... printed in its publications (B7.1, par. 3).

INDEXED by Applied Mechanics Reviews and Engineering Information, Inc. Canadian Goods & Services Tax Registration #126148048

Journal of Engineering for Gas Turbines and Power

Published Quarterly by The American Society of Mechanical Engineers

VOLUME 125 • NUMBER 1 • JANUARY 2003

TECHNICAL PAPERS

(Contents continued on inside back cover)

This journal is printed on acid-free paper, which exceeds the ANSI Z39.48-1992 specification for permanence of paper and library materials. ♾™
♻ 85% recycled content, including 10% post-consumer fibers.

(**Contents continued**)

Journal of Engineering for Gas Turbines and Power **JANUARY 2003**

Volume 125, Number 1

Journal of Engineering for Gas Turbines and Power **JANUARY 2003**

Volume 125, Number 1

Development of Low NO_x Combustion Technology in Medium-Btu Fueled 1300°C-Class Gas Turbine Combustor in an Integrated Coal Gasification Combined Cycle

T. Hasegawa
e-mail: takeharu@criepi.denken.or.jp

T. Hisamatsu

Y. Katsuki

M. Sato

Central Research Institute of Electric Power Industry,
2-6-1 Nagasaka, Yokosuka-shi,
Kanagawa-ken 240-0196, Japan

H. Koizumi

A. Hayashi

N. Kobayashi

Hitachi Ltd.,
832-2 Horiguchi Hitachinaka-shi,
Ibaragi-ken 312-0034, Japan

The development of integrated coal gasification combined cycle (IGCC) systems ensures higher thermal efficiency and environmentally sound options for supplying future coal utilizing power generation needs. The Japanese government and electric power industries in Japan promoted research and development of an IGCC system using an air-blown entrained-flow coal gasifier. On the other hand, Europe and the United States are now developing the oxygen-blown IGCC demonstration plants. Gasified coal fuel produced in an oxygen-blown entrained-flow coal gasifier, has a calorific value of 8–13 MJ/m^3 which is only 1/5–1/3 that of natural gas. However, the flame temperature of medium-Btu gasified coal fuel is higher than that of natural gas and so NO_x production from nitrogen fixation is expected to increase significantly. In the oxygen-blown IGCC, a surplus nitrogen produced in the air-separation unit (ASU) is premixed with gasified coal fuel (medium-Btu fuel) and injected into the combustor, to reduce thermal-NO_x production and to recover the power used for the ASU. In this case, the power to compress nitrogen increases. Low NO_x emission technology which is capable of decreasing the power to compress nitrogen is a significant advance in gas turbine development with an oxygen-blown IGCC system. Analyses confirmed that the thermal efficiency of the plant improved by approximately 0.3% (absolute) by means of nitrogen direct injection into the combustor, compared with a case where nitrogen is premixed with gasified coal fuel before injection into the combustor. In this study, based on the fundamental test results using a small diffusion burner and a model combustor, we designed the combustor in which the nitrogen injection nozzles arranged on the burner were combined with the lean combustion technique for low-NO_x emission. In this way, we could reduce the high-temperature region, where originated the thermal-NO_x production, near the burner positively. And then, a combustor with a swirling nitrogen injection function used for a gas turbine, was designed and constructed, and its performance was evaluated under pressurized conditions of actual operations using a simulated gasified coal fuel. From the combustion test results, the thermal-NO_x emission decreased under 11 ppm (corrected at 16% O_2), combustion efficiency was higher than 99.9% at any gas turbine load. Moreover, there was different effects of pressure on thermal-NO_x emission in medium-Btu fuel fired combustor from the case of a natural gas fired combustor. [DOI: 10.1115/1.1496772]

Introduction

IGCC is considered one of the most important systems for future coal utilization technology in power generation systems, and is being promoted by Japan, the United States, and Europe. In Japan, the government and electric power companies have been undertaking experimental research for a 200T/D pilot plant project ([1]), from 1986 to 1996. The Central Research Institute of Electric Power Industry (CRIEPI) has developed an air-blown pressurized two-stage entrained-flow coal gasifier ([2]), a hot gas cleaning system ([3]), 150 MW, 1573 K-class ([4]) and 1773 K (1500°C)-class gas turbine combustor technologies for low-Btu fuel ([5,6]). Furthermore, the government and electric power companies have started feasibility studies at a demonstration IGCC plant from 1996.

Other studies concerning the IGCC system and gas turbine combustor using the oxygen-blown gasified coal fuel include: The Cool Water Coal Gasification Project ([7]), the flagship demonstration plant of IGCC; the Shell process (SGCP) ([8]) in Buggenum as the first commercial plant, which started test operation in 1994 with commercial operation was expected from 1998; the Wabash River coal gasification repowering plant ([9]) in the United States, in operations since 1995; and the Texaco process at the Tampa power station ([10]), in commercial operation since 1996. Furthermore, the diversification of fuels used for the electric power industry, such as biomass, poor quality coal and residual oil, are also the most significant issues for gas turbine development in IGCC: The development of biomass-fueled gasification received considerable attention in the United States in the early 1980s ([11]) and the prospects for commercialization technology

Contributed by the International Gas Turbine Institute (IGTI) of THE AMERICAN SOCIETY OF MECHANICAL ENGINEERS for publication in the ASME JOURNAL OF ENGINEERING FOR GAS TURBINES AND POWER. Paper presented at the International Gas Turbine and Aeroengine Congress and Exhibition, Munich, Germany, May 8–11, 2000; Paper 2000-GT-028. Manuscript received by IGTI, Nov. 1999; final revision received by ASME Headquarters, Feb. 2000. Associate Editor: D. R. Ballal.

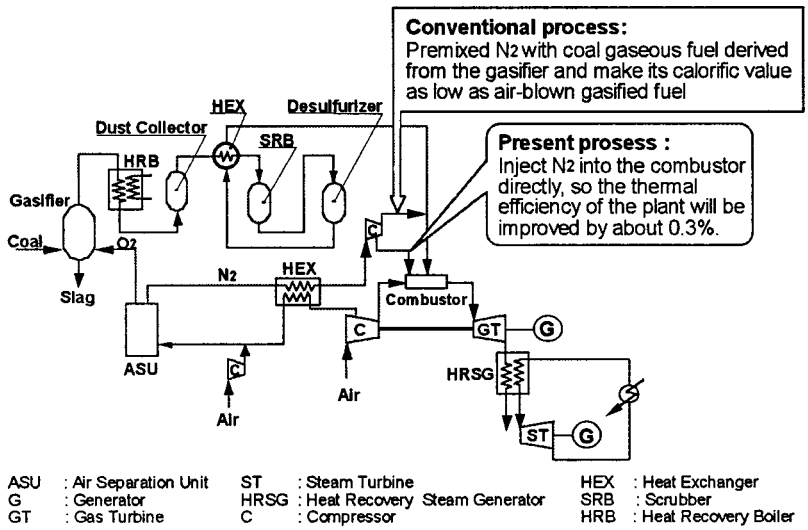

Fig. 1 Schematic diagram of an HYCOL-type oxygen-blown IGCC system

appear considerably improved at present ([12]). Our research institute has started researching the gasification technology of orimulsion fuel ([13]). All of the systems which used oxygen as an oxydizer were assumed to adopt the wet-type syngas cleaning system. Moreover, in almost all systems, NO_x emission is controlled and gas turbine output is increased by premixing the surplus nitrogen, produced from the oxygen production unit, with a gaseous fuel. From the viewpoint of both expensive running costs and initial costs of removing the NO_x in exhaust gas derived from the gas turbine system, the electric power industry aimes for low-NO_x combustion technology that promises higher efficiency and environmentally sound options.

According to the research into low-NO_x combustion technology using medium-Btu gaseous fuel, other studies include White et al. [14] studies on the rich-lean combustor for low and medium-Btu gaseous fuels and Dobbeling et al. [15] studies on low-NO_x combustion technology which quickly mixed fuel with air using the ABB double cone burner (called EV burner). (Since the burning velocity of medium-Btu fuel is about six times greater than conventional natural gas, a lean premixed combustion for low NO_x emission has so far been difficult to adopt); Dobbeling et al. [16] studies on the premixed combustion technology of medium-Btu gaseous fuel in a small burner for low NO_x emission; Cook et al. [17] studies on the effective method of returning nitrogen to the cycle, where nitrogen is injected from the head end of the combustor for NO_x control; Zanello and Tasselli [18] studies on the effects of steam content in the medium-Btu gaseous fuel on combustion characteristics; Hasegawa et al. [19] studies on low-NO_x combustion technology using surplus nitrogen injected from the burner.

This paper will propose a low- NO_x combustion technology for medium-Btu gasified fuel and provide useful engineering guidelines for the research and development of a gas turbine combustor using nitrogen injection technology at the swirler of the combustor for NO_x and CO emission control.

Description of the Oxygen-Blown IGCC System

Characteristics of the Oxygen-Blown IGCC System. In the oxygen-blown IGCC system, nitrogen in large quantities is produced in the air separation unit. In almost all of the systems, gasified coal fuels, premixed with the rest of the nitrogen not used to feed coal into the gasifier, etc., are injected into the combustor to increase electric power and to decrease NO_x emissions from the gas turbine.

In this paper, we propose a HYCOL-type system ([20]), shown in Fig. 1, in which coal is fed into the gasifier with some nitrogen and the rest of nitrogen is directly injected into the gas turbine combustor. This system is based on the practical gasification of coal using an oxygen-blown entrained-flow gasifier at elevated pressure and temperature; the use of aqueous scrubbing to clean a fuel gas; a reheated double high-pressure steam system; and, the development of 1573 K (1300°C)-class (combustor-outlet gas temperature is about 1700 K) gas turbines, which have the potential to significantly increase the efficiency of the IGCC system in excess of 43% (higher heating value basis). Furthermore, it is necessary to return a large quantity of nitrogen produced from the air-separation unit (as much as the fuel flow rate), to the cycle from the standpoint of recovering power for oxygen production. Basically, the flow rate of the surplus nitrogen produced in the air-separation unit is almost proportional to the fuel flow rate at any gas turbine load, and all surplus nitrogen should be effectively injected into a gas turbine combustor prior to a turbine, while surplus nitrogen fluctuates little in proportion to changes in the gas turbine load.

Characteristics of Oxygen-Blown Gasified Fuel. The typical compositions of medium-Btu gasified fuel produced in oxygen-blown gasifiers are shown in Table 1 ([21]). Each gasified fuel produced some raw materials with CO and H_2 as the main combustible components, and a small percent of CH_4. Calorific values varied widely (5.2–13.0 MJ/m^3), from about one-eighth to one-third of natural gas, with raw materials and gasifier types. For example, a gasified fuel derived from biomass contained 30–40 percent steam in the fuel.

Figure 2 shows the adiabatic flame temperature of fuels which were (1) medium-Btu fuels, with fuel calorific values (HHV) of 12.7, 10.5, 8.4, 6.3 MJ/m^3 without nitrogen; (2) medium-Btu fuel blended with surplus nitrogen, or low-Btu fuel of 4.2, 2.5 MJ/m^3 (HHV); and (3) methane. Calculations of flame temperature were done with a CO-H_2 mixture (CO/H_2 molar ratio of 1.4:1) under any condition, and the fuel calorific value was adjusted with nitrogen. When the fuel calorific value was 8.4 MJ/m^3 or higher, the maximum flame temperature of the medium-Btu fuel without nitrogen was about 400 K higher than that of the nitrogen-blended fuel. That is, the flame temperature of medium-Btu gasified fuel, produced in an oxygen-blown gasifier, was higher than high-calorie gases such as natural gas which consisted methane for the main part, while the medium-Btu fuel had a calorific value as low as one fifth of methane. NO_x emission was expected to increase

Table 1 Typical compositions derived from the oxygen-blown gasifiers

Fuel	Coal				Biomass	Heavy residue	Orimulsion™
Gasifier type	Fixed	Entrained			Entrained	Entrained	Entrained
Fuel feed	Dry	Dry		Slurry			
Developer	BGL	Shell	HYCOL	Texaco		Texaco	CRIEPI
Composition							
CO	56.4%	65.2-67.8%	63.3%	40.9%	21.9-23.1%	51.7%	43.5%
H_2	25.6%	28.8-31.0%	26.3%	29.9%	12.5-22.4%	43.1%	42.2%
CH_4	6.6%	0.01-0.03%	0.3%	0.1%	2.2%	0.2%	0.4%
CO_2	2.8%	1.0- 2.8%	6.1%	9.5%	20.7-18.6%	3.2%	11.8%
H_2O	-(a)	-(b)	0.4%	12.3%	40.9-31.5%	-(b)	-(b)
NH_3	-(a)	100- 600ppm	-(c)	-(c)	0- 200ppm	-(a)	-(c)
H_2S+COS	20ppm	0.14- 1.1%	-(c)	-(c)	0.285-1.132%	1.6%	1.35%
Others(N_2)	8.6%	-(a)	8.6%	7.3%	1.800-1.048%	0.2%	0.75%
CO/H_2 mole ratio	2.2	2.1- 2.4	2.4	1.4	1.0-1.8	1.2	1.0
HHV[MJ/m^3]	13.0	12.2-12.5	11.5	9.0	5.2-6.6	12.1	11.0

(a): Faulty description, (b): Dry base, (c): Unknown

more when burning medium-Btu fuel than with nitrogen-blended fuel, or low-Btu fuel ([22]). We intended to inject surplus nitrogen directly into higher temperature regions from the burner and to effectively decrease NO_x emissions produced from these regions.

Testing the Combustor

Subjects of the Medium-Btu Fueled Combustor. As mentioned above, if the surplus nitrogen was premixed with fuel produced from the oxygen-blown gasifier, the fuel calorific value decreased as low as a low-Btu fuel derived from an air-blown gasifier. Therefore, the combustion air of medium-Btu gasified fuel for any combustion temperature decreased as the flow rate of nitrogen injection into the combustor increased. Figure 3 shows the relation between the nitrogen injection flow rate into the gas turbine combustor and air distribution using medium-Btu gasified coal fuel. The average gas temperature of the combustor outlet was set at 1700 K. To calculate air distribution, the overall amount of air was assumed to be 100%. The amount of air for complete combustion in a real combustor was first calculated at 1.4 times theoretical air ($\phi = 0.71$). The remainder was considered cooling air for the combustion liner and diluting air. According to Fig. 3, as the ratio of nitrogen flow over fuel flow (N_2/Fuel) increases, the ratio of cooling and diluting air decreases slightly, and flexibility of combustor design is minimized. Since the N_2/Fuel was 0.9 kg/kg in the HYCOL system considered in the present study, the ratio of cooling and diluting air to total air was around 40%. To summarize these characteristics, it can be said that the design of a gas turbine combustor, utilizing direct injection of nitrogen into a combustor, should consider the following issues for an oxygen-blown IGCC:

(1) Low NO_x-emission technology. It is necessary to restrain NO_x production from nitrogen fixation using nitrogen injection into the combustor, not by blending nitrogen with gasified fuel.

(2) Combustion stability. It is necessary to tailor the nitrogen injection so as to avoid destabilizing the flame of medium-Btu fuel.

(3) Cooling technology. It is necessary to maintain the combustor wall under a heat resistant temperature with less amount of air, in the cases where the surplus nitrogen is supplied into the combustor and the combustor design is intended for a low NO_x and stable combustion.

Figure 4 presents characteristics of the designed, medium-Btu fueled 1573 K (1300°C)-class combustor based on the above considerations. The main design concept for the tested combustor in the present study was to secure stable combustion of medium-Btu fuel with nitrogen injection in a wide range of turn-down operations, low NO_x emissions and enough cooling air for the combustion liner. The overall length of the combustion liner is 650 mm and the inside diameter is 230 mm.

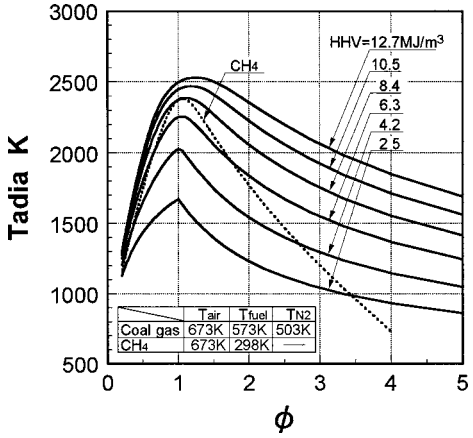

Fig. 2 Relationship between equivalence ratio and adiabatic flame temperature for gasified coal fuels and CH_4

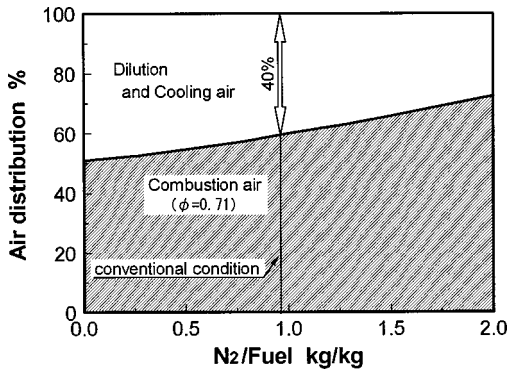

Fig. 3 Air distribution design of a medium-Btu fueled gas turbine combustor with nitrogen injection

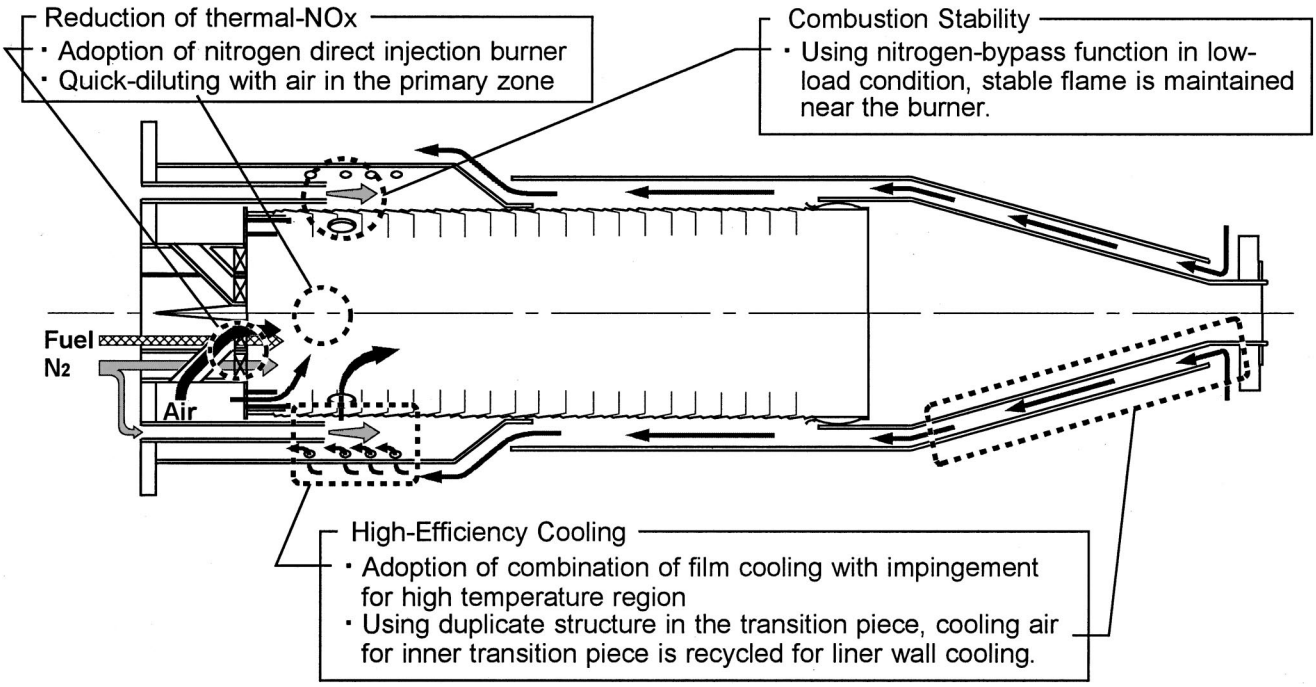

Fig. 4 Design concept of a medium-Btu fueled gas turbine combustor

Reduction of NO_x and CO Emission, and Stable Combustion. To restrict thermal NO_x production originating from nitrogen fixation and CO emissions, we designed the burner with nitrogen injection, based on combustion tests previously conducted using a small diffusion burner ([23]).

Figure 5 presents an example of the test results, under atmospheric pressure condition, which indicate the influence of the primary-equivalence ratio on NO_x emission characteristics in two-staged combustion for comparing three cases: (1) a fuel calorific value (HHV) of 12.7 MJ/m^3, without nitrogen injection; (2) a fuel calorific value of 12.7 MJ/m^3, where nitrogen is blended with the combustion air from the burner; (3) a fuel blended with nitrogen of the same quantity as case (2), or low-Btu fuel of 5.1 MJ/m^3. From Fig. 5, we know that nitrogen blended with fuel or air injected from the burner has a great influence over decreasing NO_x emissions from nitrogen fixation.

Figure 6 shows the CO emission characteristics under the same conditions as Fig. 5. According to CO emissions, we know that CO emission concentration reached a maximum value at the primary-equivalence ratio of 1.2 and decreased as the primary-equivalence ratio increased, in every case. Furthermore, in the case where nitrogen blended with air was injected into the combustor, CO emissions decreased as low as medium-Btu gasified fuel not blended with nitrogen, while CO emissions significantly increased when fuel was blended with nitrogen. That is, in the medium-Btu fuel combustion with nitrogen injection, all of the surplus nitrogen should be injected into the primary combustion zone to reduce the thermal-NO_X emission and should not be blended with fuel, or the primary zone should be fuel-lean condition for a low NO_X and stable combustion in a wide range of turn-down operations.

Figure 7 shows the combustion gas temperature distribution in the both cases of no nitrogen injection and of nitrogen injection of 1.0 kg/kg N_2/Fuel from the burner under atmospheric pressure condition, using a model combustor ([24]). In tests, allowing for the heat resisting performance of thermocouples, the combustor-

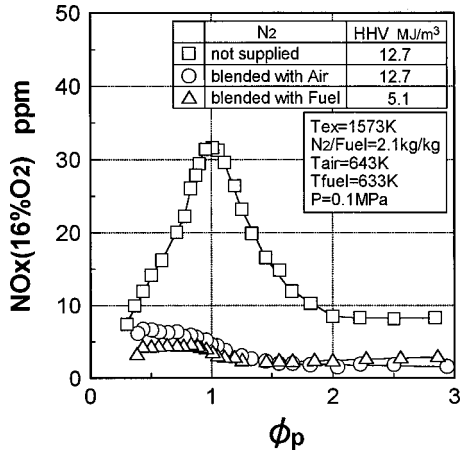

Fig. 5 Effect of nitrogen injection on NO_X emission characteristics in two-staged combustion, using a small diffusion burner

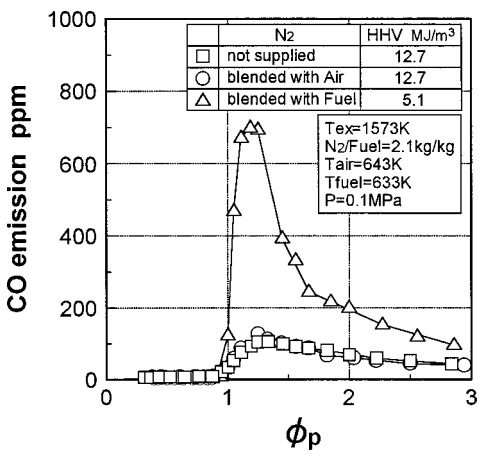

Fig. 6 Effect of nitrogen injection on CO emission characteristics in two-staged combustion, using a small diffusion burner

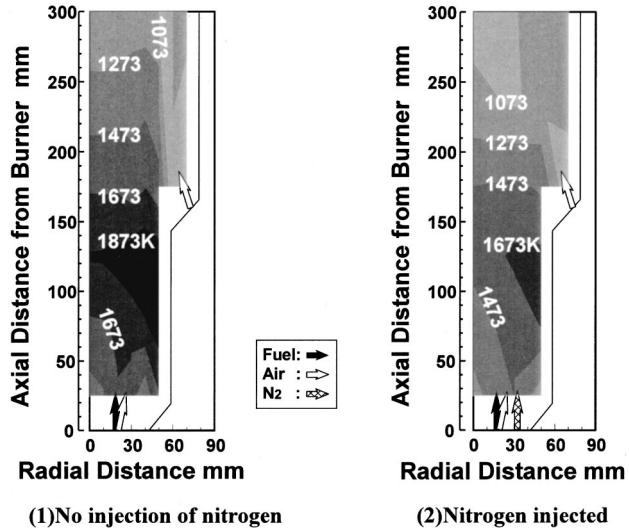

Fig. 7 Effect of nitrogen injection on combustion gas temperature distribution, using a model combustor

outlet gas temperature is set at 1373 K. From Fig. 7, we know that nitrogen injection from the burner has a great influence over decreasing hot regions by around 200 K in this test conditions. So, in the way of nitrogen injection, NO_X production from nitrogen fixation in the hot regions was restrained one-fifth that of the case no nitrogen injection, shown in Fig. 8 which indicates the NO_X production distribution in a model combustor under the same conditions as Fig. 7.

Based on these results, we arranged the nitrogen injection intakes in the burner and adopted the lean primary combustion for a low NO_X and stable combustion. The nitrogen injected directly into a combustor has the effect of decreasing power to compress nitrogen higher than the pressure of fuel or air, which is needed for even blending. In this way, from the system analysis, the thermal efficiency of the plant improved by 0.3% (absolute), compared with a case where nitrogen was premixed with gasified coal fuel before injection into the combustor. Furthermore, it is possible to control the mixing of fuel, air, and nitrogen positively by way of nitrogen being injected separately into the combustor. The fuel, the combustion air, and the nitrogen from the burner are

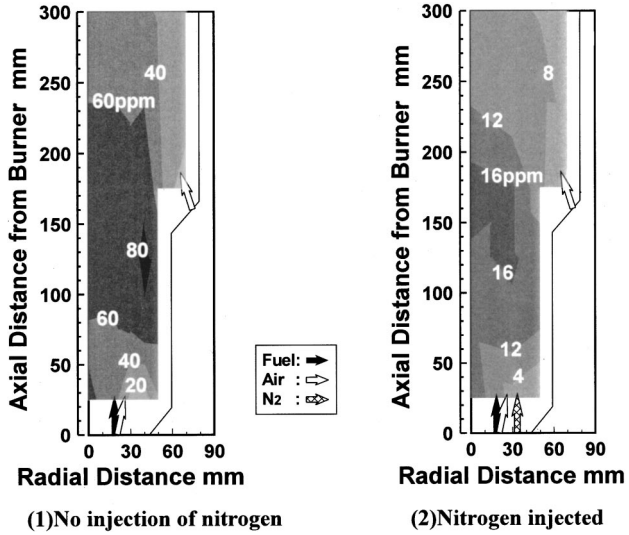

Fig. 8 Effect of nitrogen injection on NO_X production distribution, using a model combustor

Table 2 Typical composition of the supplied fuel

Composition	CO	30.4 %
	H_2	27.5 %
	CH_4	6.8 %
	CO_2	35.3 %
	H_2O	-
	N_2	0.0 %
HHV	10.1 MJ/m^3 (2400 kcal/m^3)	
LHV	9.2 MJ/m^3 (2210 kcal/m^3)	

separately injected into the combustor through a swirler, to dilute the flame of medium-Btu fuel with nitrogen directly. And we intended to quench the flame as soon as possible, both by sticking the combustion air injection tubes out of the liner dome and by arranging the secondary combustion air holes on the upstream side of the combustion liner. This new technique causes a decrease in flame temperature in the primary combustion zone which produces NO_X from nitrogen fixation, NO_X production near the burner are controlled, just as in the case of fuel blended with nitrogen. Design of the combustor was intended for the medium-Btu fuel, the nitrogen injection function was combined with the lean combustion technique for a low NO_X combustion based on the results of combustion tests using a diffusion burner and a model combustor. By setting the primary-combustion zone to fuel-lean state under the rated load condition, the NO_X emission decrease, and by bypassing nitrogen to premix with the combustion air under partial load conditions, a stable flame can be maintained in a wide range of turn-down operations.

Cooling of the Combustor Liner Wall. In order to compensate for a declined cooling-air ratio associated with a surplus nitrogen injection into a gas turbine combustor and lean primary combustion, the tested combustor is equipped with a dual-structure transition piece so that the cooling air in the transition piece can be recycled to cool down the combustor liner wall. The cooling air flowing into the transition piece cools the interior wall by an convection method, and moves to the combustor liner on the upstream side. For the primary-combustion zone where temperatures are expected to be especially high, the dual-cooling structure was employed, in which the cooling air was impinged from the air flow guide sleeve to the combustion liner and used as film cooling air for the combustion liner. For the secondary-combustion zone the film-cooling method was used.

Table 2 shows the standard properties of the supplied fuel in tests. As for tests, the higher heating value of the supplied fuel was set at 10.1 MJ/m^3, a $(CO+CH_4)/H_2$ molar ratio at 1.4. A part of surplus nitrogen produced from the air-separation unit was used to feed coal or char into the gasifier and the flow rate of the rest was about 0.9 times the fuel flow in the actual process. Since the density of the supplied fuel is higher than that of the gasified coal fuel and temperature of supplied nitrogen is lower in the case of the test conditions than in the actual operations, we also investigate the combustor performance in the case of 0.3 kg/kg N_2/Fuel ratio, in which firing temperature of the burner outlet corresponds to the case of actual operations. Rated load conditions in the combustion tests are summarized in Table 3. The combustor-outlet gas

Table 3 Standard test condition

T_{air}	:	643 K
T_{fuel}	:	473 K
T_{N_2}	:	333 K
N_2/Fuel	:	0.30 kg/kg
T_{ex}	:	1700 K
P	:	1.4 MPa
I_c	:	2.2×10^2 W/(m^3·Pa)

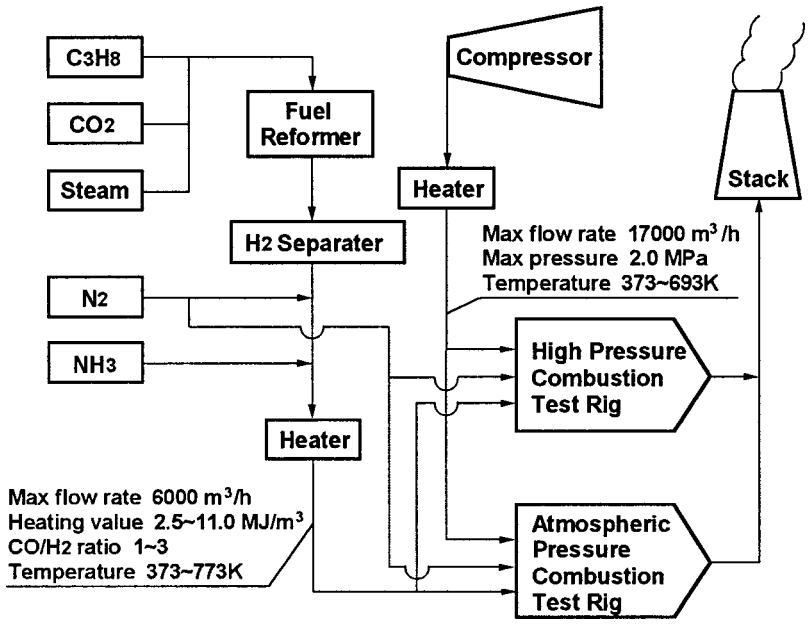

Fig. 9 Schematic diagram of experimental facility

temperature is 1700 K and the combustion intensity in the combustor at the design point is 2.2×10^2 W/($m^3\cdot$Pa).

Test Facilities and Test Method

Test Facilities. The schematic diagram of the test facilities is shown in Fig. 9. The raw fuel obtained by mixing CO_2 and steam with gaseous propane was decomposed to CO and H_2 inside the fuel reforming device. A hydrogen separation membrane was used to adjust the CO/H_2 molar ratio. N_2 was added to adjust the fuel calorific value to the given calorie, then coal derived simulated gases were produced.

This facility had one more nitrogen supply line, by which nitrogen was directly injected into the combustor. Air provided to the combustor was pressurized to 2.0 MPa by using a four-stage centrifugal compressor. Both fuel and air were supplied to the gas turbine combustor after being heated separately with a preheater to a given temperature.

The combustion testing area had two test rigs, each of which were capable of performing full-scale atmospheric pressure combustion tests for a few hundreds MW-class multican-type combustor as well as half-scale high-pressure combustion tests, or full-scale high-pressure one for around a 100 MW-class multican-type combustor. Figure 10 shows a cross-sectional view of the combustor test rig under pressurized conditions. After passing through the transition piece, the exhaust gas from the combustor was introduced into the measuring section where gas components and temperatures were measured. The components of the combustion gas

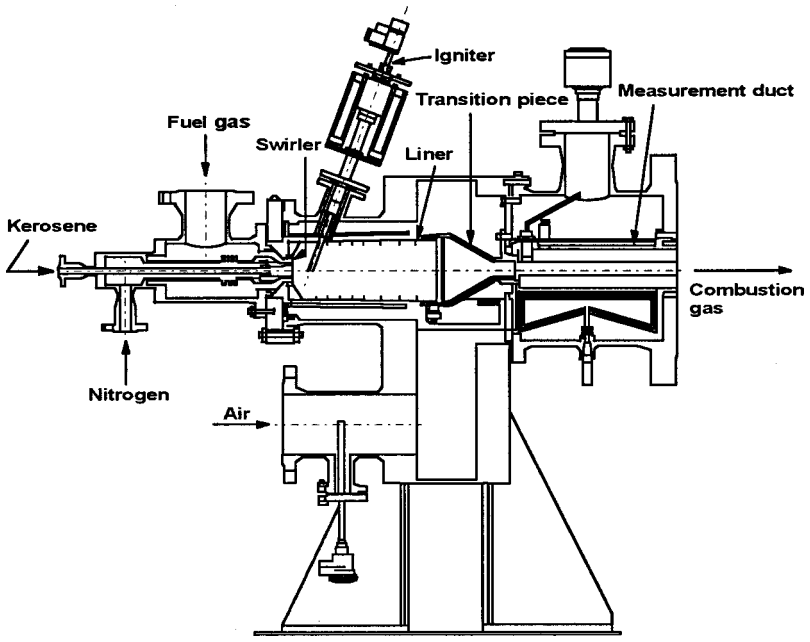

Fig. 10 Combustion test rig

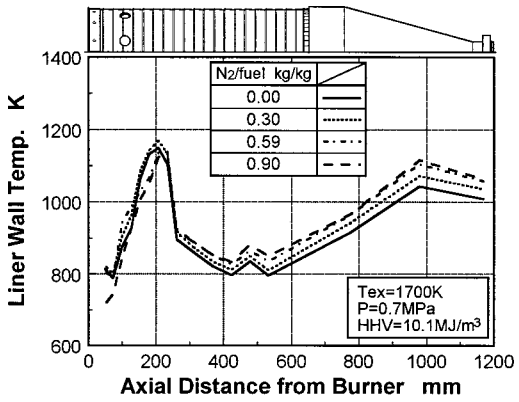

Fig. 11 Combustor wall temperature distribution using the nitrogen injection flow rate from the burner as a parameter

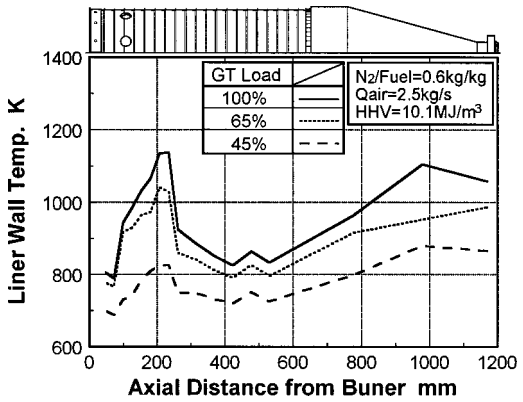

Fig. 12 Effect of the gas turbine load on the combustor wall temperature distribution

were analyzed by an automatic gas analyzer. After that, the gas temperature was lowered through a quenching pot, using a water spray injection system.

Combustion tests were conducted on a full-scale combustor for a 100 MW-class gas turbine under high pressure conditions.

Measurement System. Sample gases were taken from the exit of the combustor through water-cooled stainless steel probes located on the centerline of a height-wise cross section of the measuring duct. The sample lines of stainless steel were thermally insulated with heat tape to maintain the sampling system above the dew point of the exhaust gas. The gas samples taken were from an average of sampling points on the center-line of the measuring duct and continuously introduced into an emission console which measured: CO and CO_2 by infrared analyses, NO and NO_X by chemilluminescence analyses, O_2 by paramagnetic analysis, and hydrocarbons by flame ionization. The medium-Btu simulated fuel were sampled from the fuel gas supply line at the inlet of combustor and CO, H_2, CH_4, H_2O, CO_2, and N_2 were determined by gas chromatography. Heating values of the simulated gaseous fuel were monitored by a calorimeter and calculated from analytical data of gas components obtained from gas chromatography.

The temperatures of the combustor liner walls were measured by 40 sheathed type-K thermocouples with a diameter of 1 mm sticked on the liner wall with a stainless foil welding. The temperature distributions of the combustor exit gas were measured with an array of three pyrometers, each of which consists of five type-R thermocouples.

Test Results and Discussion

Thermal Characteristics of the Combustor Liner Wall The supplying conditions of surplus nitrogen varied depending upon the operation conditions in IGCC and gas turbine. Figure 11 shows the effects of nitrogen injection from the burner on the temperature distribution of the combustor liner wall. As the flow ratio of nitrogen injection over fuel (N_2/Fuel) was varied, the fuel flow rate was changed to maintain the air flow rate at a constant value of 2.5 kg/s and the outlet-gas temperature at 1700 K. In tests, the higher heating value of fuel is set at a constant 10.1 MJ/m^3. The liner-wall temperature around the secondary-air inlet section declines by 100 K and the liner temperature on the downstream side rises by 100 K with the increase in nitrogen injection, or variation of the overall temperature is maintained less than 100 K at any nitrogen injection. That is, it is surmised that the flame near the burner was maintained at any N_2/Fuel ratio and stable combustion was maintained, while the adiabatic flame temperature of the nitrogen-blended fuel decreased about 200 K with the rise in the nitrogen injection of N_2/Fuel ratio from 0.0 kg/kg to 0.9 kg/kg under the condition of the same equivalence ratio.

Figure 12 shows the temperature distributions of the combustor liner wall, when the gas turbine load changes. As the gas turbine load was varied, the fuel flow rate was changed to maintain the air flow rate at a constant value of 2.5 kg/s and the N_2/Fuel ratio at 0.6 kg/kg. Even when the gas turbine load rose to the rated load of 100%, the liner-wall temperature remained almost always under 1123 K, which is lower than the allowable heat resistant temperature, while the liner-wall temperature almost uniformly increased with the rise in the gas turbine load. Furthermore, it is not shown here that the overall temperature of the liner wall shows significantly lower level down to the conditions equivalent to no load of gas turbine.

Emission Characteristics. We carried out researches into the effects of the combustor-outlet gas temperature, the nitrogen injection, combustion intensity, combustion pressure, and gas turbine load on the combustion characteristics. Figure 13 shows the correlation between the combustor-outlet gas temperature and the emission characteristics of NO_X from nitrogen fixation with nitrogen flow rate of N_2/Fuel as a parameter, when the air flow rate was set and maintained at 3.5 kg/s. In tests, as the combustor-outlet gas temperature, which is equivalent to the gas turbine load condition, was changed, the pressure conditions were adjusted to the corresponding values at the each partial load condition on the basis where the pressure in the combustor is set to lower level of 1.0 MPa at the equivalent, rated load. At any N_2/Fuel ratio, the NO_X emission increased exponentially with the rise in the outlet-gas temperature. Furthermore, the NO_X emission decreased with the rise in the N_2/Fuel ratio comparing with the same outlet-gas

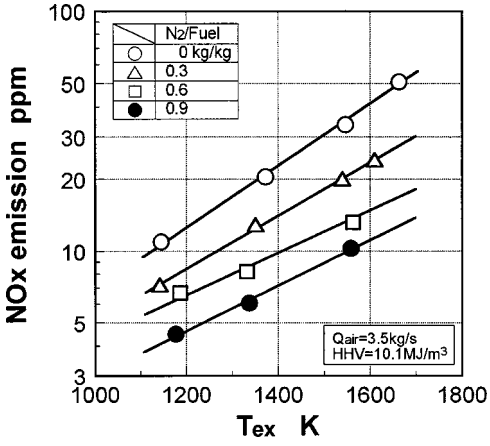

Fig. 13 Effect of the combustor outlet gas temperature on NO_X emission characteristics

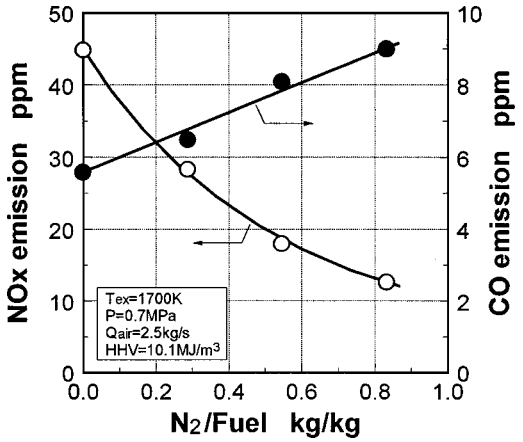

Fig. 14 Effect of the nitrogen injection flow rate from the burner on combustion emission characteristics

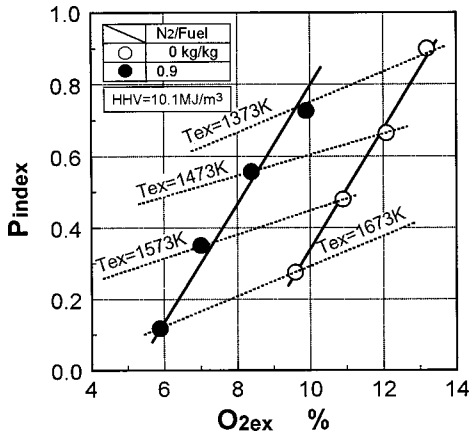

Fig. 16 Dependence of NO_X emission characteristics on the pressure in the combustor

temperature. Because the nitrogen injection effectively lowered the flame temperature in the primary combustion zone in which a high temperature region was expected, as mentioned in Fig. 7, we consider that the NO_X production from nitrogen fixation was suppressed.

Nitrogen injection into the combustor resulted in the rise of the equivalence ratio by which the outlet gas temperature of the combustor was adjusted to 1700 K. We observed the emission characteristics when the nitrogen injection flow rate to the combustor changed. Figure 14 shows the relationship between nitrogen injection and the emission characteristics of both NO_X from nitrogen fixation and CO, where air flow rate was set at 2.5 kg/s, where the pressure was set at 0.7 MPa and where the combustor-outlet gas temperature was maintained at 1700 K.

NO_X emission concentration decreased in inverse proportion to the flow rate of nitrogen injection, N_2/Fuel ratio, into the combustor. However, it is different from NO_X emission characteristics that CO emissions gradually increased as the N_2/Fuel ratio increased. This is because the equivalence ratio, which adjusted the combustor-outlet gas temperature to 1700 K, was raised and the temperature in the primary-combustion zone decreased as nitrogen injection from the burner increased, as shown in Fig. 7.

Figure 15 shows the effect of the combustion intensity on the emission characteristics of both NO_X from nitrogen fixation and CO with the combustor-outlet gas temperature as a parameter, where N_2/Fuel ratio was set at 0.3 kg/kg. In tests, as the combustion intensity was varied, the pressure in the combustor was changed to maintain the fuel, air, and nitrogen flow rates at constant values, on the basis where the equivalent, rated pressure was set to lower level of 1.0 MPa and the pressure conditions were adjusted to the corresponding values at the each combustor-outlet gas temperature of partial load condition. At any outlet-gas temperature, NO_X emission gradually decreased with the rise in the combustion intensity. On the other hand, CO emission characteristics vary according to the outlet-gas temperature. That is, under the condition of 1173 K outlet-gas temperature or lower, CO emission sharply increased with the rise in the combustion intensity, while CO is little emitted under the higher temperature conditions over 1373 K. The tested combustor showed the same tendencies as the conventional ones, where the increase in the combustion intensity is attributable to both the decrease in NO_X emission and the increase in CO emission, due to a decrease in the residence time of the combustion gas in the combustor.

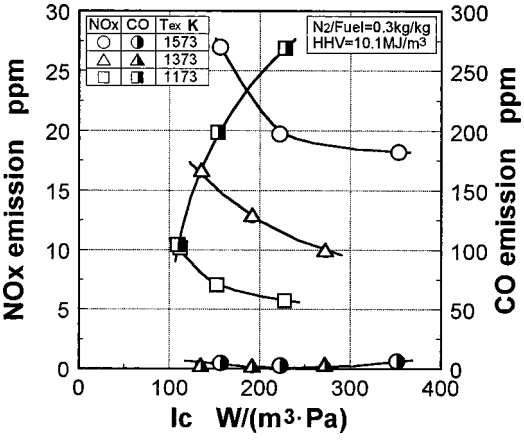

Fig. 15 Effect of the combustion intensity in the combustor on combustion emission characteristics

In order to estimate the combustion characteristics of the designed combustor under high-pressure conditions, Fig. 16 shows the effects of pressure on the NO_X emission characteristics in the both cases of nitrogen injection of 0.9 kg/kg N_2/Fuel ratio and of no nitrogen injection. The horizontal axis indicates the oxygen concentration in the combustor exhaust, O_{2ex}, and the vertical axis indicates the pressure index of NO_X emission, P_{index} which designates the ratio between the logarithm of the ratio of NO_X emissions at two pressure conditions in the combustor and logarithm of the pressure ratio, as shown by the following equation:

$$P_{\text{index}} = \frac{\text{Ln}([\text{NO}_X]_2/[\text{NO}_X]_1)}{\text{Ln}(\text{P}_2/\text{P}_1)}$$

where the subscripts 1 and 2 designate the emission and the pressure in the combustor at the respective conditions. In tests, the combustion pressure or the combustor-outlet gas temperature were changed, under the conditions where the average sectional flow velocity of the exhaust gas was adjusted to be kept constant.

At any N_2/Fuel ratio, the pressure index, P_{index}, rises in direct proportion to the increase in the oxygen concentration in the exhaust gas. That is, in the case of no nitrogen injection, P_{index} indicates higher value of 0.9 at around 13% oxygen concentration in the exhaust gas, while P_{index} shows the lower value of 0.27 at around 10% oxygen concentration in the exhaust gas.

As an example of the effect that pressure exerts on the level of the NO_X emission from the nitrogen fixation in the gas turbine combustor using hydrocarbon fuels, it is known that the pressure to the power of 1.5 is nearly proportional to the speed at which the Zel'dovich NO is produced (i.e., $d[\text{NO}]/dt \propto P^{1.5}$) and that the NO_X emission mole fraction varies with pressure to the 0.5 power ([25]). Actually, Sawyer et al. [26] had corrected NO_X emission data from variety of engines with varying pressure ratios and re-

sulted in that NO_X emission varies with pressure to the approximately the 0.5 power at any temperature. Besides, Blazowski et al. [27] suggested that NO_X emission varied directly with pressure to the power of 0.63 and Davis et al. [28] resulted that the effect of pressure is to the 0.29 power. However, in the case of the tested combustor used simulated gasified-coal fuel under consideration, the pressure index of NO_X emission from nitrogen fixation, P_{index}, varied in accordance with the oxygen concentration in the exhaust, O_{2ex}.

That is, NO_X emission is controlled by the following modified Zel'dovich NO mechanism

$$N_2 + O \Leftrightarrow NO + N \quad (1)$$

$$N + O_2 \Leftrightarrow NO + O \quad (2)$$

$$N + OH \Leftrightarrow NO + H \quad (3)$$

in the high-temperature condition, mainly reaction 1, and strongly affected by the flame temperature. When the equivalence ratio is declined, oxygen concentration in the exhaust gas, O_{2ex} increases and the combustor outlet-gas temperature declines. With the decrease in the combustion temperature, Zel'dovich NO formation is controlled and prompt NO formation become relatively important. So, in case of the fuel contained hydrocarbons, HCN is produced in the fuel-rich region by the following reactions:

$$CH + N_2 \Leftrightarrow HCN + N \quad (4)$$

$$CH_2 + N_2 \Leftrightarrow HCN + NH. \quad (5)$$

Some HCN is oxidized into NO by reactions 6 and 7, and the rest is decomposed into N radical by the following reactions.

$$HCN + OH \Leftrightarrow CN + H_2O \quad (6)$$

$$CN + O_2 \Leftrightarrow CO + NO \quad (7)$$

$$CN + O \Leftrightarrow CO + N. \quad (8)$$

And some NH radical produced by the reaction 5 is decomposed into N radical by the reaction 9, and the rest is decomposed into N_2 by the reaction 10. This N radical produced by the reactions 4, 8, and 9, is oxidized into NO by the reactions 2 and 3.

$$NH + OH \Leftrightarrow N + H_2O \quad (9)$$

$$NO + NH \Leftrightarrow N_2 + OH \quad (10)$$

The simulated gasified coal fuel contains both hydrogen as a main combustible component, which produces Zel'dovich NO and shows in the strong dependence on the flame temperature, and 7% CH_4 produces prompt NO mainly in the fuel-rich lower-temperature region. And also, as shown above chain reactions, the interdependence between Zel'dovich NO and prompt NO is necessary to be taken into account. That is, in the simulated gasified coal fuel, it is surmised that dependence of NO_X emission on the pressure is different from that of hydrocarbon fuels.

Furthermore, in the case of same oxygen concentration in the exhaust gas, combustor-outlet gas temperature declines and the P_{index} rises sharply, when nitrogen of 0.9 kg/kg N_2/Fuel ratio is injected into the combustor. On the other hand, comparing the cases of the same outlet-gas temperature, nitrogen injection of 0.9 kg/kg N_2/Fuel ratio shifts the P_{index} on the lower O_{2ex} side and the P_{index} declines by 0.15. From the view point of the NO_X formation, it is known that the NO_X emission is affected by the super equilibrium O-atom. By injecting nitrogen into the high-temperature zone, the decrease of O_{2ex} or oxygen partial pressure in the flame of the same combustion temperature results that the super equilibrium O-atom decreases significantly and NO_X emission decreases. So, in the case of the same outlet-gas temperature, it is surmised that the NO_X production rate increases with the rise in the oxygen partial pressure.

Figure 17 shows the relationship between the gas turbine load and the combustion emission characteristics, under the condition

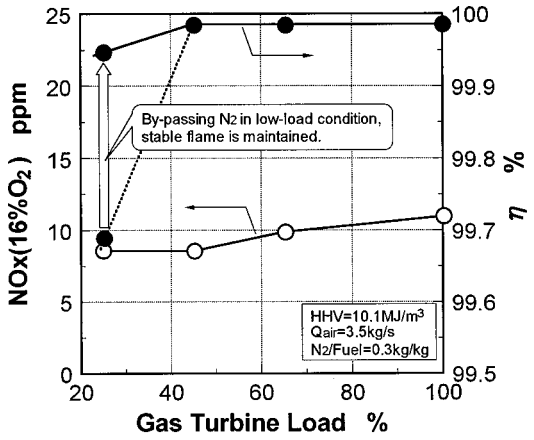

Fig. 17 Effect of the gas turbine load on combustion emission characteristics

where the pressure in the combustor is set to lower level of 1.0 MPa at the equivalent, rated load. When the gas turbine load was 25% or higher, which is the single fuel firing of gasified coal fuel, the NO_X emission was reduced as low as 11 ppm (corrected at 16% O_2), while the NO_X emission tends to increase slightly with the rise in the gas turbine load. Considering the effects of pressure as shown in Fig. 16 and of nitrogen injection as shown in Fig. 14, it could be said that NO_X emission was surmised as low as 12 ppm (corrected at 16% O_2) at any gas turbine load.

On the other hand, combustion efficiency shows around 100% in the case where the gas turbine load was 25% or higher, by bypassing nitrogen to premix with the combustion air at low load conditions. Since CO emission tends to decrease with the rise in pressure, we can expect that combustion efficiency is around 100% under real application conditions of the medium-Btu fueled gas turbine.

From these results, it appears that direct injection of nitrogen will sufficiently allow low NO_X emission levels and the IGCC system will be able to achieve the full performance benefits of this concept.

Conclusions

Based on the combustion tests results using a small diffusion burner and a model combustor, a combustor with a suitable nitrogen injection nozzle for an oxygen-blown IGCC, was designed, constructed, and tested under gas turbine operational conditions. Tests results are summarized as follows:

(1) The direct nitrogen injection technique has the effect of decreasing NO_X emissions from nitrogen fixation, NO_X emission is surmised to decrease as low as 12 ppm (corrected at 16% O_2) at any gas turbine load. On the other hand, combustion efficiency is maintained around 100% at any gas turbine load condition, by bypassing nitrogen into the combustion air at low load conditions.

(2) NO_X emission of the medium-Btu fuel increases in accordance with the pressure, and the pressure index of NO_X emission (P_{index}) declines in both cases where the oxygen concentration of exhaust gas (O_{2ex}) decreases and where the nitrogen is injected into the combustor.

Acknowledgments

The authors wish to express their appreciation to the many people who have contributed to this investigation. In testing this combustor, we received helpful support from K. Kawashima and Y. Kousaka (Central Research Institute of Electric Power Industry), Y. Baba, S. Negishi, and H. Fukui (Techno Service Corp.).

Nomenclature

HHV = higher heating value of the fuel, MJ/m^3
LHV = lower heating value of the fuel, MJ/m^3
I_c = combustion intensity in the combustor, $W/(m^3 \cdot Pa)$
H_f = lower heating value of the fuel supplied to the combustor
H_{ex} = lower heating value of the unburned fuel in the exhaust gas
N_2/Fuel = nitrogen by the fuel supply ratio, kg/kg
$NO_x(16\%O_2)$ = NO_x emission corrected at 16% oxygen, ppm
P = pressure in the combustor, MPa
P_{index} = pressure index of NO_x emission
= $\mathrm{Ln}([NO_x]_2/[NO_x]_1)/\mathrm{Ln}(P_2/P_1)$ subscripts 1 and 2 designate the respective conditions
Q_{air} = air flow rate, kg/s
T_{adia} = adiabatic flame temperature, K
T_{air} = air inlet temperature, K
T_{ex} = combustor outlet gas temperature, K
T_{fuel} = fuel inlet temperature, K
T_{N_2} = nitrogen inlet temperature, K
η = combustion efficiency, %
= $(1-H_{ex}/H)_f \times 100$, %
ϕ = equivalence ratio (inverse way of air/fuel ratio)
ϕ_{ex} = equivalence ratio at combustor outlet
ϕ_p = equivalence ratio in the primary combustion zone

References

[1] Ichikawa, K., 1996, "R&D of an IGCC System by the 200T/D Pilot Plant at Nakoso," 8th DOE-METC/ANRE-NEDO Joint Technical Meeting on Surface Coal Gasification.

[2] Kurimura, M., Hara, S., Inumaru, J., Ashizawa, M., Ichikawa, K., and Kajitani, S., 1995, "A Study of Gasification Reactivity of Air-Blown Entrained Flow Coal Gasifier," *Proc. 8th. Int. Conference on Coal Science*, **1**, Elsevier Science B.V., Amsterdam, pp. 563–566.

[3] Nakayama, T., Ito, S., Matsuda, H., Shirai, H., Kobayashi, M., Tanaka, T., and Ishikawa, H., 1990, "Development of Fixed-Bed Type Hot Gas Cleanup Technologies for Integrated Coal Gasification Combined Cycle Power Generation," Central Research Institute of Electric Power Industry Report No. EW89015.

[4] Nakata, T., Sato, M., Ninomiya, T., Yoshine, T., and Yamada, M., 1993, "Effect of Pressure on Combustion Characteristics in LBG-Fueled 1300°C-class Gas Turbine," ASME Paper No. 93-GT-121.

[5] Nakata, T., Sato, M., Ninomiya, T., and Hasegawa, T., 1994, "A Study on Low NO_X Combustion in LBG-Fueled 1500°C-Class Gas Turbine," ASME Paper No. 94-GT-218.

[6] Hasegawa, T., Sato, M., and Ninomiya, T., 1997, "Effect of Pressure on Emission Characteristics in LBG-Fueled 1500°C-Class Gas Turbine," ASME Paper No. 97-GT-277.

[7] Savelli, J. F., and Touchton, G. I., 1985, "Development of a Gas Turbine Combustion System for Medium-Btu Fuel," ASME Paper No. 85-GT-98.

[8] Bush, W. V., Baker, D. C., and Tijm, P. J. A., 1991, "Shell Coal Gasification Plant (SCGP-1) Environmental Performance Results," EPRI Interim Report No. GS-7397, Project 2695-1.

[9] Roll, M. W., 1995, "The Construction, Startup and Operation of the Repowered Wabash River Coal Gasification Project," *Proc. 12th. Annual Int. Pittsburgh Coal Conference*, University of Pittsburgh, Pittsburgh, PA, pp. 72–77.

[10] Jenkins, S. D., 1995, "Tampa Electric Company's Polk Power Station IGCC Project," *Proc. 12th. Annual Int. Pittsburgh Coal Conference*, University of Pittsburgh, Pittsburgh, PA, p. 79.

[11] Kelleher, E. G., 1985, "Gasification of Kraft Black Liquor and Use of the Products in Combined Cycle Cogeneration, Phase 2 Final Report," DOE/CS/40341-T5, prepared by Champion International Co. for U.S. Department of Energy, Washington, DC.

[12] Consonni, S., Larson, E. D., and Berglin, N., 1997, "Black Liquor-Gasifier/Gas Turbine Cogeneration," ASME Paper No. 97-GT-273.

[13] Ashizawa, M., Takahashi, T., Taki, M., Mori, K., Kanehira, S., and Takeno, K., 1996, "A Study on Orimulsion Gasification Technology," *Proc. 9th International Conference & Exhibition for the Power Generating Industries*, **8**, PennWell Corp. and PennEnergy, Houston, TX, pp. 235–243.

[14] White, D. J., Kubasco, A. J., LeCren, R. T., and Notardonato, J. J., 1983, "Combustion Characteristics of Hydrogen-Carbon Monoxide Based Gaseous Fuels," ASME Paper No. 83-GT-142.

[15] Dobbeling, K., Knopfel, H. P., Polifke, W., Winkler, D., Steinbach, C., and Sattelmayer, T., 1994, "Low NO_X Premixed Combustion of MBtu Fuels Using the ABB Double Cone Burner (EV burner)," ASME Paper No. 94-GT-394.

[16] Dobbeling, K., Eroglu, A., Winkler, D., Sattelmayer, T., and Keppel, W., 1996, "Low NO_X Premixed Combustion of MBtu Fuels in a Research Burner," ASME Paper No. 96-GT-126.

[17] Cook, C. S., Corman, J. C., and Todd, D. M., 1994, "System Evaluation and LBtu Fuel Combustion Studies for IGCC Power Generation," ASME Paper No. 94-GT-366.

[18] Zanello, P., and Tasselli, A., 1996, "Gas Turbine Firing Medium-Btu Gas From Gasification Plant," ASME Paper No. 96-GT-8.

[19] Hasegawa, T., Hisamatsu, T., Katsuki, Y., Sato, M., Yamada, M., Onoda, A., and Utsunomiya, M., 1998, "A Study of Low-NO_X Combustion in Medium-Btu Fueled 1300°C-Class Gas Turbine Combustor in IGCC," ASME Paper No. 98-GT-331.

[20] Ueda, T., Kida, E., Nakaya, Z., Shikata, T., Koyama, S., and Takagi, M., 1995, "Design of the HYCOL Gasifier," *Proc. Int. Conference Power Engineering-'95*, The Chinese Society of Power Engineering, Shanghai, China, pp. 242–247.

[21] Hasegawa, T., Hisamatsu, T., Katsuki, Y., Sato, M., Iwai, Y., Onoda, A., and Utsunomiya, M., 1999, "A Development of Low NO_X Combustion in Medium-Btu Fueled 1300°C-Class Gas Turbine Combustor in IGCC," *Proc. Int. Gas Turbine Congress 1999 Kobe*, The Gas Turbine Society of Japan, **2**, pp. 783–791.

[22] Hasegawa, T., and Sato, M., 1997, "Study on NO_X Emission Characteristics of Medium-Btu Coal Gasified Fuel," Trans. Jpn. Soc. Mech. Eng., **63**(613), pp. 3123–3130 (in Japanese).

[23] Hasegawa, T., Katsuki, Y., Hisamatsu, T., and Sato, M., 1996, "Effect of the Oxygen Concentration in the Air on Emission Characteristics in Coal-Derived Gaseous Fuel," *Proc. the 34th Japanese Symposium on Combustion*, Combustion Society of Japan, Osaka, pp. 597–599 (in Japanese).

[24] Hayashi, A., Koizumi, H., Kobayashi, N., Hasegawa, T., Hisamatsu, T., Katsuki, Y., and Sato, M., 1998, "Combustion Characteristics of Gas Turbine Combustor for Medium-Btu Fuels," *Proc. 13th Fall Annual Conference of The Gas Turbine Society of Japan*, Gas Turbine Society of Japan, Tokyo, pp. 125–130 (in Japanese).

[25] Fenimore, C. P., 1971, "Formation of Nitric Oxide in Premixed Hydrocarbon Flames," *Proc. 13th Symp. (Int.) on Combustion*, The Combustion Institute, Pittsburgh, PA, pp. 373–379.

[26] Sawyer, R. F., Cernansky, N. P., and Oppenheim, A. K., 1973, "Factors Controlling Pollutant Emissions from Gas Turbine Engines," *Atmospheric Pollution by Aircraft Engines*, AGARD CPP-125, (22) pp. 1–13.

[27] Blazowski, W. S., Walch, D. E., and Mach, K. D., 1973, "Prediction of Aircraft Gas Turbine NO_X Emission Dependence on Engine Operating Parameters and Ambient Conditions," AIAA Paper No. 73–1275.

[28] Davis, L. B., Murad, R. J., and Wilhelm, C. F., 1973, "Emission and Control of NO_X in Industrial Gas Turbine Combustors: Experimental Results," 66th Annual AIChE Meeting, Nov. 11–15.

Influence of the Combustor Aerodynamics on Combustion Instabilities From Equivalence Ratio Fluctuations

T. Sattelmayer
Lehrstuhl A für Thermodynamik,
Technische Universität München,
Boltzmannstraße 15,
D-85748 Garching, Germany

Gas turbine combustors are often susceptible to self-excited oscillations, which lead to unacceptable levels of pressure, velocity, and heat release fluctuations. Although instabilities can occur in systems with locally constant equivalence ratio, it is very important to take into account the influence of equivalence ratio fluctuations, which are generated in the fuel air mixer in the unstable case. These fluctuations are convected into the flame and lead to an additional mechanism for the generation of heat release fluctuations. Moreover, entropy waves are produced in the flame, which travel through the combustor and generate additional pressure waves during the acceleration of the flow at the combustor exit. To date, available theories use the physically unrealistic assumption that the equivalence ratio waves as well as the entropy waves are convected downstream without any spatial dispersion due to the combustor aerodynamics. An analytical approach is presented, which allows us to take the spatial dispersion into consideration. For that purpose, the response of the burner and the combustor to an equivalence ratio impulse or an entropy impulse is calculated using the Laplace transformation and a more general transfer function for harmonic waves is derived. The obtained expression has three parameters, which represent the influence of the burner or the combustor aerodynamics, respectively. This equation can be used in numerical codes, which represent the combustion system through a network of acoustic multiports, if the equivalence ratio and the entropy are added to the vector of variables considered. The parameters required for the dynamic combustor model can be deduced from a detailed CFD analysis of the combustor flow in case of the application of the theory to a particular combustor design. As an example, a simple model combustor is used to demonstrate the application of the theory. It is highlighted how the spatial dispersion of the equivalence ratio and entropy fluctuations can be included in the stability analysis. The calculated examples reveal that the influence of both variables on the generation of instabilities is highly overpredicted if the spatial dispersion is not taken into account. Furthermore, it can be deduced from the study that burner and combustor designs with a wide range of convective time scales have advantages with respect to the stability of the combustor. [DOI: 10.1115/1.1365159]

Introduction

The driver for noise and pulsations in gas turbine combustors is the fluctuating heat release of the reacting mixture in the primary zone. For the purpose of modeling, it is useful to split the combustor into the supply, which incorporates also the burners or injectors, and the combustor with the nozzle guide vanes at the exit (Fig. 1). Both parts are interconnected via the flame and in most cases via bypass air ports for mixing and cooling purposes. Even if fluctuations of the equivalence ratio are not taken into account, four different physical phenomena can contribute to the noise spectrum. Flame turbulence produces first of all a background noise level. In addition, this turbulent broad band driving mechanism can be considerably amplified at the eigenfrequencies of the combustion system to produce distinct pulsation peaks. It is well known that in particular in swirling flows natural coherent structures can occur, which can force oscillations at fixed Strouhal numbers. Although both driving mechanisms are governed from the character of the nonreacting cold flow and are essentially independent from the acoustic feedback, the acoustic properties of the combustor and the supply determine the noise spectrum. Forced coherent flow structures represent the third class of driving mechanisms. They appear if flow instabilities respond to the triggering by a velocity perturbation with subsequent phase locking. The forth driving mechanism is the classical mode of self-excitation. In this case, instabilities can grow without any influence of flow turbulence or flow periodicity.

Many of the instability investigations on premixed flames published in the literature used external premixing of fuel and air or assumed at least that the influence of equivalence ratio fluctuations can be neglected. However, in technical combustors the fuel air mixer is a part of the mixture supply. Moreover, since it is very often located near a velocity antinode, combustor pulsations produce a fluctuating mixture strength, if the impedance of the fuel inlet $Z_{\mathrm{inj,fuel}}$ is not identical to the impedance of the air side $Z_{\mathrm{inj,air}}$. The equivalence ratio pattern generated at the injector travels downstream with the flow and is dispersed by the velocity and turbulence field in the burner. Subsequently, the heat release rate of the flame is modulated and the acoustic velocity downstream of the flame is altered accordingly. As the equivalence ratio fluctuations lead to fluctuations of the entropy in the flue gas, the wave propagation in the hot gases is no longer isentropic. This problem can be overcome if entropy waves are introduced in addition to the (isentropic) acoustic waves (Keller [1]). The dispersion of the entropy waves during convection due to the combustor aerody-

Contributed by the International Gas Turbine Institute (GTI) of THE AMERICAN SOCIETY OF MECHANICAL ENGINEERS for publication in the ASME JOURNAL OF ENGINEERING FOR GAS TURBINES AND POWER. Paper presented at the International Gas Turbine and Aeroengine Congress and Exhibition, Munich, Germany, May 8–11, 2000; Paper 2000-GT-082. Manuscript received by IGTI Oct. 1999; final revision received by ASME Headquarters Oct. 2000. Associate Editor: D. Wisler.

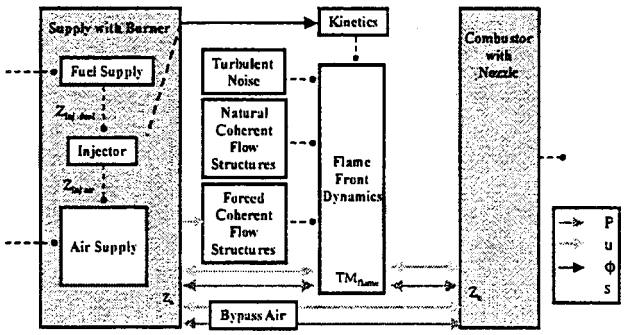

Fig. 1 Driving mechanisms for combustion instabilities

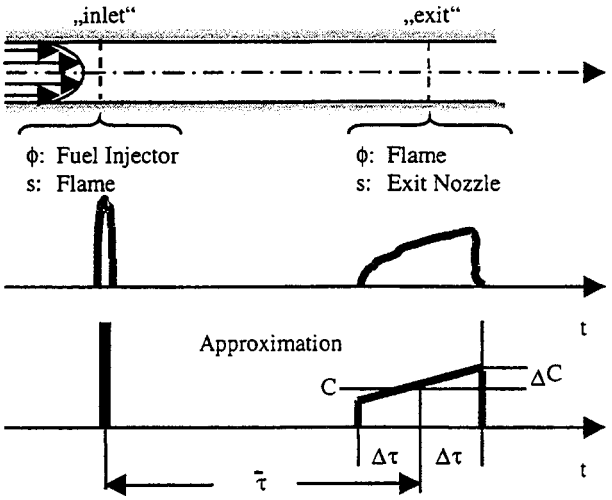

Fig. 2 Convection of a scalar field in a tube

namics is similar in nature to the processes which govern the convection of the equivalence ratio waves. The feedback of the entropy waves occurs at the combustor exit. When the flow is accelerated to high Mach numbers by the inlet guide vanes, the entropy waves lead to pressure waves and the combustor exit impedance is altered accordingly.

In the past, the role of equivalence ratio fluctuations and entropy fluctuations (Hubbard and Dowling [2] and Polifke et al. [3]) has been studied under the simplifying assumption that the shape of the wave does not undergo any change during convection and that an average flow velocity exists, which describes the propagation process properly. This is equivalent with the assumption of block profiles in the burner as well the combustor and neglects the influence of the detailed velocity field including recirculation zones, of boundary layers and also of turbulent diffusion during convection. At least for flows with high complexity, the simple approach is highly questionable, since all three effects contribute to the spatial dispersion of the waves and reduce the driving potential for instabilities. To date, the fundamental differences of the propagation characteristics of acoustic waves and equivalence ratio/entropy waves have not been considered in sufficient detail. It appears that the available theories are influenced by a kind of thermoacoustic paradigm: Waves which are convected with the flow are treated similar to acoustic waves, although only the latter exhibit a one-dimensional propagation characteristic in slender confinements. It is highly desirable to develop an improved procedure, which is compatible with currently employed stability analysis methods, in order to represent the impact of convected waves on the system stability appropriately.

Spatial Dispersion of Equivalence Ratio and Entropy Fluctuations

The most widely used method for the investigation of the combustion stability is the approach to split a complex system into a network of small elements, which can be described analytically. These elements are essentially one-dimensional, although modifications can be made to include circumferential or transverse modes. Due to the one-dimensionality of the acoustic field in the elements, it is of great interest to develop a tool, which reduces the two- or three-dimensional convection of equivalence ratio and entropy waves to one dimension. The derivation must satisfy the restriction that the stability of the system in the frequency domain must be calculated using one common network of elements for the acoustic part and the equivalence ratio as well as entropy waves.

The elements of such a network which convect the waves are tubes, diffusers, and nozzles. Since the two latter can be represented in principle by a set of tubes and area changes, the convection in tubular elements is the basis of the model to be developed. For that reason, the flow in a tube of an arbitrary cross sectional shape but with constant area is considered (Fig. 2).

The scalar ψ is a property of the flow field and represents the equivalence ratio or the entropy. To date, it us usually assumed, that the cross sectional average of the scalar ψ at the exit can be linked to the scalar at the inlet by means of a delay time τ and that no further modifications of the scalar must be taken into account:

$$\Psi_{\text{exit}}(t) = \Psi_{\text{inlet}}(t-\overline{\tau}). \tag{1}$$

After Fourier transformation we obtain in the frequency domain

$$\frac{\tilde{\Psi}_{\text{exit}}(i\omega)}{\tilde{\Psi}_{\text{inlet}}(i\omega)} = e^{-i\omega\overline{\tau}}. \tag{2}$$

In order to derive an expression for less stringent assumptions, it is now assumed, that an impulse δ is imposed on the scalar ψ at the inlet uniformly across the inlet area. It has to be expected, that the response at the tube exit, which is obtained after the integration over the exit cross section will depend strongly on the fluid mechanics in the tube. The impulse is generally not preserved. The distribution found at the exit is formally a probability density function of the delay time in the tube.

For a given burner or combustor geometry, the required pdf can be calculated in principle on the basis of a detailed CFD analysis of the turbulent flow field. At least for the combustion of gaseous fuel, simpler procedures such as the particle tracking in a calculated or measured flow field provide results with sufficient quality. For the burners investigated within the study, a relatively simple form of the pdf was found to be sufficient. Figure 3 shows the radial distribution of the residence time and the pdf, which was derived from this data for an experimental dual fuel bumer as an example. For the calculation of the pdf, the radial distribution of the mass flux density, which is proportional to the local velocity and the radius must be taken into account. The calculated distribution can be approximated by a trapezoid. The most important parameter for the description of the dispersion of the impulse due to the tube aerodynamics is the width of the trapezoid at the exit, $2\,\Delta\tau$ (see Fig. 2). In the model, the height of the trapezoid is allowed to vary linearly with time in order to obtain greater flexibility. This second degree of freedom was found to have only very minor influence on the results of the stability analysis. For that reason, it is possible to replace the trapezoid with a simple rectangle without major loss of accuracy.

In order to derive the one-dimensional transfer function of the tube with respect to the scalar Ψ we use some standard relationships of control theory. The scalar at the exit can be linked to the scalar at the inlet by means of Green's function

$$\Psi_{\text{exit}}(t) = \int_0^t g(\tau)\Psi_{\text{inlet}}(t-\tau)\,d\tau. \tag{3}$$

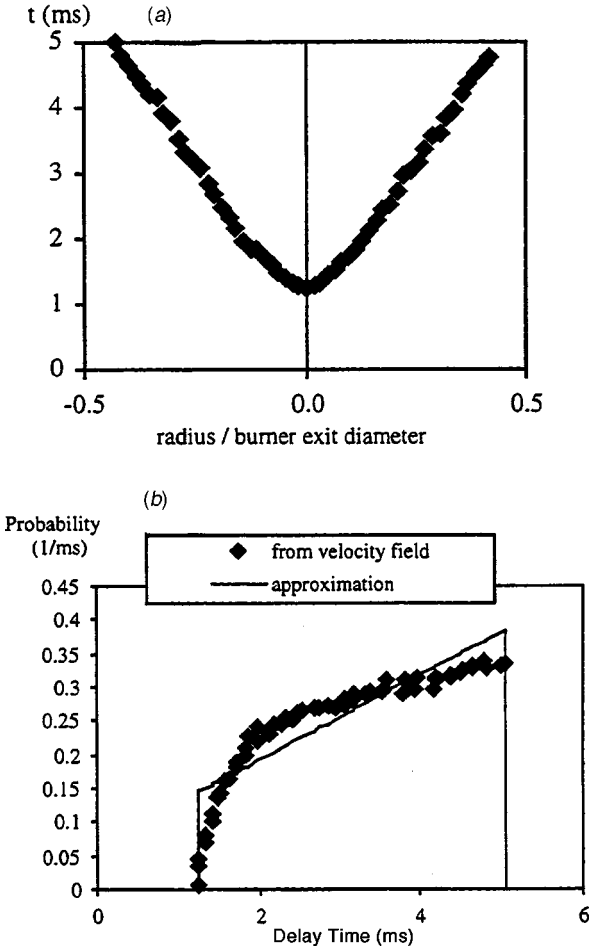

Fig. 3 Distribution of the residence time in a premix burner. (*a*) Radial distribution, (*b*) probability density distribution.

The scalar at the exit can be calculated by integration, if Green's function $g(\tau)$ is known. After Laplace transformation, the following expression is obtained:

$$\Psi_{\text{exit}}(s) = G(s)\Psi_{\text{inlet}}(s). \tag{4}$$

For the special case of $\Psi_{\text{inlet}}(t) = \delta(t)$ the Laplace transformation delivers $\Psi_{\text{inlet}}(s) = 1$. As a consequence, the scalar at the exit is identical to the transfer function of the tube

$$\Psi_{\text{exit}}(s) = G(s). \tag{5}$$

If the response of the tube exit to the impulse at the inlet is specified analytically in the time domain, the transfer function is obtained by Laplace transformation of $\Psi_{\text{exit}}(t)$ in analytical form. The guidelines for the construction of the impulse response mentioned above lead to the following expression (see Fig. 2):

$$\Psi_{\text{exit}}(t) = C\left(1 + \frac{\Delta C}{C}(t - \overline{\tau})\right) \quad \overline{\tau} - \Delta\tau < t < \overline{\tau} + \Delta\tau. \tag{6}$$

The continuity for the scalar quantity requires that

$$\int_{-\infty}^{\infty} \delta(t)dt = 1 = \int_{-\infty}^{\infty} \Psi_{\text{exit}}(t)dt = C2\Delta\tau. \tag{7}$$

After C has been replaced by $\Delta\tau$, the following form is obtained:

$$\Psi_{\text{exit}}(t) = \frac{1}{2\Delta\tau}\left(1 + \frac{\Delta C}{C}(t - \overline{\tau})\right) \quad \overline{\tau} - \Delta\tau < t < \overline{\tau} + \Delta\tau. \tag{8}$$

The Laplace transformation of this expression yields

$$\Psi_{\text{exit}}(s) = \frac{1}{2\Delta\tau s^2}\left\{ e^{-s(\overline{\tau}-\Delta\tau)}\left(\frac{\Delta C}{C} + s - \frac{\Delta C}{C}\Delta\tau s\right) - e^{-s(\overline{\tau}+\Delta\tau)}\left(\frac{\Delta C}{C} + s + \frac{\Delta C}{C}\Delta\tau s\right)\right\}. \tag{9}$$

Since only harmonic waves are of interest in the framework of the stability analysis, the independent variable s of the Laplace transformation can be replaced by $i\omega$ of the Fourier transformation and the following final result for the dispersion of the scalar Ψ in the tube is obtained:

$$\frac{\tilde{\Psi}_{\text{exit}}(i\omega)}{\tilde{\Psi}_{\text{inlet}}(i\omega)} = \frac{1}{2\Delta\tau(i\omega)^2} e^{-i\omega\overline{\tau}}\left\{ e^{i\omega\Delta\tau}\left(\frac{\Delta C}{C} + i\omega - \frac{\Delta C}{C}\Delta\tau i\omega\right) - e^{-i\omega\Delta\tau}\left(\frac{\Delta C}{C} + i\omega + \frac{\Delta C}{C}\Delta\tau i\omega\right)\right\}. \tag{10}$$

The equation describes the dispersion of the scalar in the tube as a function of the minimum and maximum delay time, which are expressed indirectly through $\overline{\tau}$ and $\Delta\tau$ and a measure $\Delta C/C$ for the slope of the probability density function in between these two times. It was mentioned earlier, that the parameter $\Delta C/C$ has a weak effect on the result of the stability analysis. The reason for this finding lies in the low sensitivity of Eq. (10) to $\Delta C/C$. It can be concluded from this result that Eq. (10) can also be used as an approximation for residence time distributions, which cannot be fitted by Eq. (8) with the same level of accuracy as shown in Fig. 3.

The subsequent analysis is based on the special case of $\Delta C/C = 0$, since all effects of interest can be demonstrated without a systematic variation of $\Delta C/C$ is being made. Figure 4 shows the gain predicted from Eq. (10) as a function of the pulsation frequency. In the upper part (*a*) an average delay time $\overline{\tau} = 3$ ms is selected, in order to simulate the dispersion of the equivalence ratio waves in the mixing tube of an utility gas turbine premix bumer. A higher average delay time of $\overline{\tau} = 30$ ms was chosen in the lower part of the figure (*b*). This much larger value is realistic for the dispersion of the entropy waves in the combustor (typical residence time in large utility gas turbine combustors).

In the case with no dispersion of the waves ($\Delta\tau/\overline{\tau} = 0$), there is no damping of the convected wave in the mixing tube and the combustor, respectively. It can be assumed, that the range of delay times in gas turbine premix burners and combustors falls into the interval $0.1 < \Delta\tau/\overline{\tau} < 0.5$. Figure 4(*a*) reveals that for this range only moderate damping of the equivalence ratio wave in the mixing tube can be expected for frequencies in the range below 250 Hz, which is usually susceptible to instability. Longer mixing tubes (longer average delay time) have a higher potential for wave attenuation, if the aerodynamics is designed for a wide range of residence time. The results for the convection of the entropy waves in the combustor are of completely different nature. According to Fig. 4(*b*) a high degree of damping can be achieved for the same interval of $\Delta\tau/\overline{\tau}$, because the average residence time is one order of magnitude higher. From these findings the conclusion can be drawn that from the viewpoint of stability it is desirable to design the burner as well as the combustor flow for a wide range of residence times. Moreover, it is obvious that a strong damping of entropy waves generated in the flame occurs in the combustor even for small values of $\Delta\tau/\overline{\tau}$. In light of this fact, the assumption that the waves travel down-stream without any dispersion, which is often made when combustion instabilities are investigated theoretically, cannot be justified. In the past, it was proposed to model flames with a wide longitudinal heat release distribution with one single "characteristic" delay time (e.g., Lieuwen et al. [4]). Equation (10) and Fig. 4 show clearly that the effect of dispersion cannot realistically represented by a similar approach.

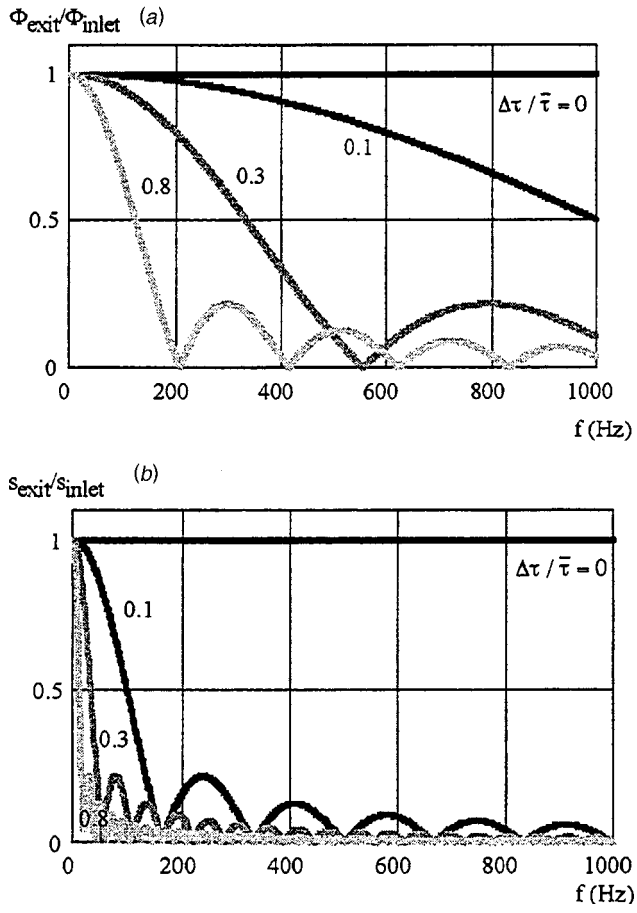

Fig. 4 Wave damping. (*a*) Equivalence ratio wave in a premix burner, (*b*) entropy wave in a combustor.

Model Combustor

In order to demonstrate the effect of the attenuation of the convected waves, the simple model combustor depicted in Fig. 5 was selected. Somewhat unrealistic for a real gas turbine combustor, proper plenum conditions are assumed upstream. The fuel injector has a high stiffness against pressure perturbations and the mixer is placed at the inlet of the burner, which is represented by a mixing tube of constant cross section. The flame sits somewhat downstream of the area change in the combustor. At the combustor end, the exhaust gas is accelerated to a high velocity in a compact nozzle.

At the bumer inlet $\tilde{p}_1 = 0$ is used as the boundary condition. A Mach number correction for the reflection coefficient at the inlet is used (Davies [5]), which models the acoustic losses. An equivalence ratio fluctuation

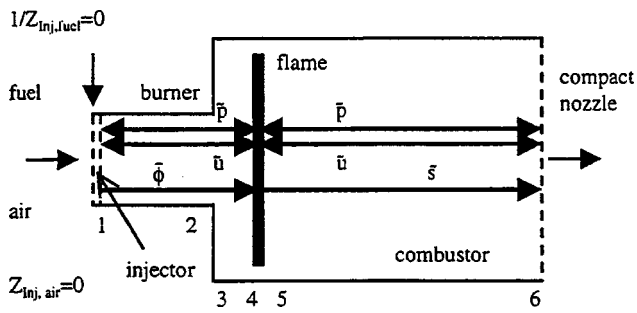

Fig. 5 Model combustor

$$\tilde{\phi}_1 = -\frac{\overline{\phi}_1}{\overline{u}_1}\tilde{u}_1 \tag{11}$$

is produced, if the air velocity pulsates. The convection of these waves is modeled using Eq. (10) with $\tilde{\Psi}_{\text{exit}}(i\omega) = \tilde{\phi}_4(i\omega)$ and $\tilde{\Psi}_{\text{inlet}}(i\omega) = \tilde{\phi}_1(i\omega)$. Fluctuations of the heat release rate have two sources; the first being the velocity fluctuations upstream of the flame. This part can be modeled by means of a transfer function for externally premixed systems. Many of these transfer functions of very different form and character have been proposed in the past (Deucker [6], Fleifil et al. [7], Ohtsuka et al. [8], Peracchio and Proscia [9]). In the framework of the current study, the following equation was used, which was derived from the work of Lenz [10] and Dowling [11]:

$$\tilde{u}_{5,\phi_4=\text{const}} = \tilde{u}_4\left(1+\left(\frac{\overline{p}_u}{\overline{p}_d}-1\right)\frac{e^{-i\omega\tau_{\text{fl}}}}{1+2D\dfrac{\omega}{\omega_0}-\left(\dfrac{\omega}{\omega_0}\right)^2}\right). \tag{12}$$

The reason for this choice was the high flexibility of a three parameter equation. The gain can be influenced by ω_0, even a forced coherent flow structure can be modeled to some extent, if the damping coefficient D is properly selected, and the delay time τ_{fl} allows a simple modification of the phase loss. The second source for heat release fluctuations are the equivalence ratio waves, which are convected into the flame. If no velocity fluctuation upstream of the flame exists, Eq. (13) can be derived from the conservation laws after linearization:

$$\tilde{u}_{5,u_4=\text{const}} = \tilde{\phi}_4 \cdot \frac{\overline{u}_5}{\overline{\phi}_4}\left(\frac{\overline{\rho}_u}{\overline{\rho}_d}-1\right). \tag{13}$$

No dynamic term must included in this equation if it assumed that the residence time distribution calculated (Fig. 3) represents the true radial time history from the points of injection of the fuel down to the points where the flame front is reached. In this case, it can be assumed that the combustion will take place instantaneously without further dynamics. A certain weakness of this assumption is that cases with excessive longitudinal oscillation of the heat release are not very well represented. Nevertheless, the assumption is acceptable for well stabilized flames with high swirl. In these cases, temporal relative changes of the total residence times distribution are usually small.

Both effects can be superimposed in the linear case, since each effect on its own leads to a fluctuation of the acoustic velocity downstream of the flame:

$$\overline{u}_5 = \overline{u}_{5,u_4=\text{const}} + \overline{u}_{5,\phi_4=\text{const}}. \tag{14}$$

Equation (14) is valid even for nonlinear systems after they have been linearized. If present, the coupling appears in the second and the higher order terms, which are truncated.

For the pressure coupling across the flame, the commonly used relationship is applied:

$$\tilde{p}_5 = \tilde{p}_4. \tag{15}$$

Apart from the equivalence ratio waves, entropy fluctuations also generate acoustic velocity downstream of the flame, which can be calculated from the first and second law of thermodynamics:

$$ds = \frac{dh - v\,dp}{T}. \tag{16}$$

For $v\,dp = 0$ the following relationship can be derived:

$$\tilde{s}_5 = c_p\frac{\tilde{T}_5}{\overline{T}_5} = \frac{c_p\left(1-\dfrac{\overline{\rho}_5}{\overline{\rho}_4}\right)}{\overline{\phi}_4}\tilde{\phi}_4. \tag{17}$$

Once again, Eq. (10) is used for the modeling of the wave attenuation during convection with $\tilde{\Psi}_{\text{exit}}(i\omega) = \tilde{s}_6(i\omega)$ and $\tilde{\Psi}_{\text{inlet}}(i\omega)$

$=\tilde{s}_5(i\omega)$. The choked nozzle at the combustor exit is calculated using a relationship taken from the literature (Marble and Candel [12]):

$$\tilde{u}_6=\frac{M_6}{2}\left(\frac{\kappa-1}{\rho_6 c_6}\tilde{p}_6+\frac{c_6}{c_p}\tilde{s}_6\right). \tag{18}$$

Commonly applied relationships for the modeling of the area change are employed

$$\tilde{p}_4=\tilde{p}_3, \tag{19}$$

$$\tilde{u}_4=\frac{A_3}{A_4}\tilde{u}_3. \tag{20}$$

The propagation of u and p in the three tubular segments of the combustor (mixing tube, cold and hot part of the flame tube) can be derived from the Riemann invariants for the forward and backward propagating waves:

$$\tilde{u}_{2,4,6}=\frac{\tilde{u}_{1,3,5}}{2}(e^{-ik_f L}+e^{ik_b L})+\frac{\tilde{p}_{1,3,5}}{2\bar{c}_{1,3,5}\bar{\rho}_{1,3,5}}(e^{-ik_f L}-e^{ik_b L}), \tag{22}$$

$$\frac{\tilde{p}_{2,4,6}}{\bar{c}_{2,4,6}\bar{\rho}_{2,4,6}}=\frac{\bar{u}_{1,3,5}}{2}(e^{-ik_f L}-e^{ik_b L})+\frac{\tilde{p}_{1,3,5}}{2\bar{c}_{1,3,5}\bar{\rho}_{1,3,5}}(e^{-ik_f L}+e^{ik_b L}). \tag{23}$$

In the calculations, the influence of a convective bulk flow velocity on the wave numbers is taken into consideration.

As a result, a system of 16 linear equations is obtained. The vector of variables consists of the six acoustic pressures and velocities and the equivalence ratio and entropy wave fluctuations at two axial positions.

Analysis of the Supply

Since the stability analysis of the system presented in the next section of the paper does not necessarily lead to a full detailed physical understanding of the causes of instability, it is useful to investigate in addition the mixing tube (1→2) as well as the supply with the flame (1→5) first. For that purpose, only the upstream part of the system is considered. It is assumed that cross section 1 represents an acoustically open end and that a velocity fluctuation is present at that location.

Mixing tube (1→2): The purpose of the investigation of the mixing tube isolated from the system is to calculate the fluctuation of the thermal power at the burner exit. Since at the fuel inlet $1/Z_{\text{inj,fuel}}=0$ is assumed, the fuel flow rate is constant in cross section 1 and the thermal power does not fluctuate. As a consequence, the fluctuation of the fuel flow rate at cross section 2 results entirely from the velocity and the equivalence ratio fluctuations in the mixing tube.

In Fig. 6, three cases are compared with each other for a mixing tube length of 0.3 m. The dispersion of the equivalence ratio waves (see Eqs. (8) and (10)) is not taken into account ($\Delta\tau/\bar{\tau}=0$). If only the acoustic part is considered, the fluctuation at cross section 2 is in phase and drops with increasing frequencies until a minimum is reached. At higher frequencies, the amplitude recovers again in the antiphase domain. The equivalence ratio exhibits a constant gain and a phase loss, which increases linearly with frequency. Although the mixing tube alone is a rather simple system, the influence of the frequency on the gain is quite complex, if both effects are considered simultaneously. At very low frequencies, the fuel flow at the bumer exit plane is constant, although the equivalence ratio and the acoustic velocity pulsate. Both effects compensate each other. At higher frequencies, the phase difference is dominated by the convection of the equivalence ratio waves. This finding is very important in the frame-work of the stability analysis presented below, since it can be concluded directly that the two models (with and without equivalence ratio fluctuations) will exhibit completely different stability characteristics. Due to the difference in phase shift, however, it cannot be stated, that a high fluctuation intensity (in particular in the frequency range between 100 and 250 Hz, which often is unstable in utility gas turbines) automatically will lead to stability problems. The check, whether stabilization or destabilization will occur due to the equivalence ratio fluctuations requires the stability analysis of the entire system, which will be presented below.

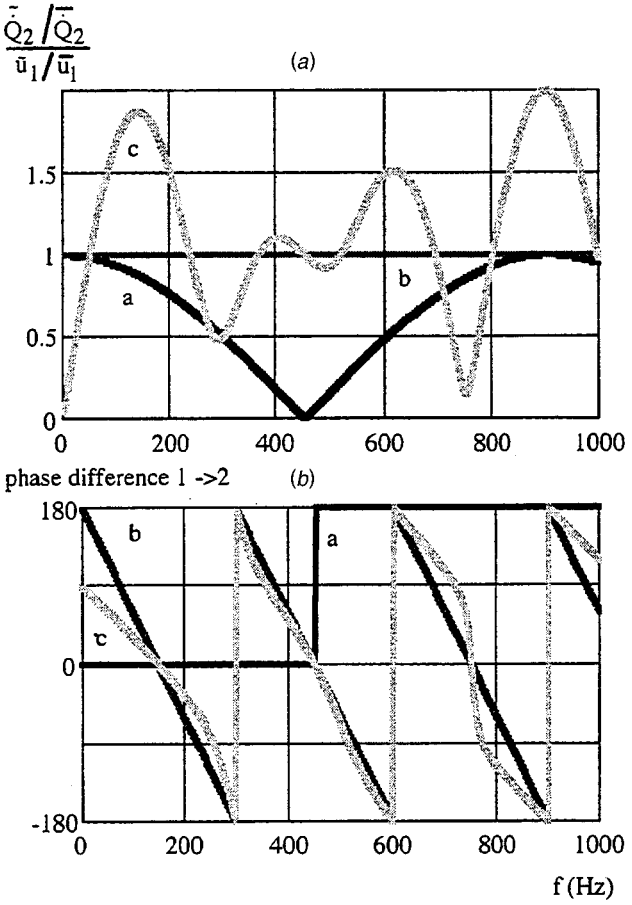

Fig. 6 Fluctuations of the thermal power at the burner exit. (a) Acoustics, no equivalence ratio fluctuations, (b) no acoustics, equivalence ratio fluctuations, and (c) acoustics and equivalence ratio fluctuations.

The length of the mixing section has a strong influence on the frequency band with high amplification factors. In Fig. 7 the results for three lengths are presented (acoustics and equivalence ratio fluctuations without dispersion). A very short mixing zone is required for amplification factors below 1 in the frequency range of 100 to 250 Hz. From Fig. 4(*a*), a strong effect of the dispersion of the equivalence ratio waves on the thermal power fluctuation at the bumer exit can only be expected at high frequencies. In Fig. 8 the dispersion parameter $\Delta\tau/\bar{\tau}$ was varied for a mixing section length of 0.3 m. It is shown, that a peak in the low frequency domain cannot be avoided even for high $\Delta\tau/\bar{\tau}$. For the cases with a strong dispersion, the acoustics dominates at higher frequencies and the solution approaches case (*a*) in Fig. 6.

Supply and flame (1→5): If the supply side with the flame is investigated separately from the hot part of the combustor with the nozzle at the exit, the ratio of the acoustic velocities $\tilde{u}_5/\tilde{u}_1$ (see Fig. 5) can be calculated and the contribution of the equivalence ratio waves to the velocity fluctuations downstream of the flame can be quantified. In order to obtain a clearer picture which is not influenced by the effects of the flame dynamics, the dynamic term

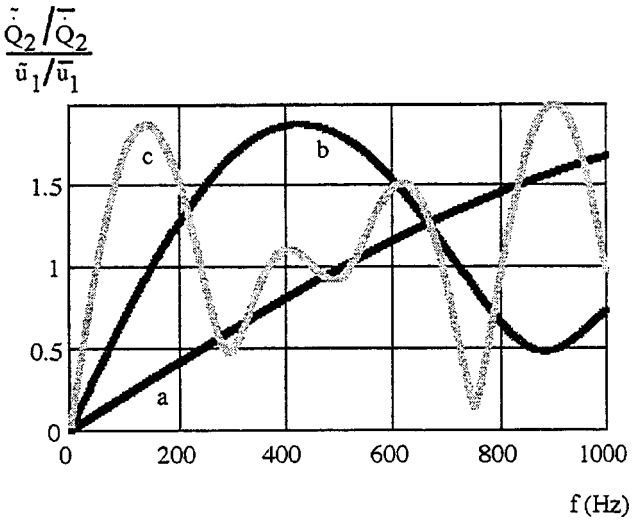

Fig. 7 Fluctuations of the thermal power at the burner exit: (a) $L_{1\to2}=0.03$ m, (b) $L_{1\to2}=0.1$ m, (c) $L_{1\to2}=0.3$ m

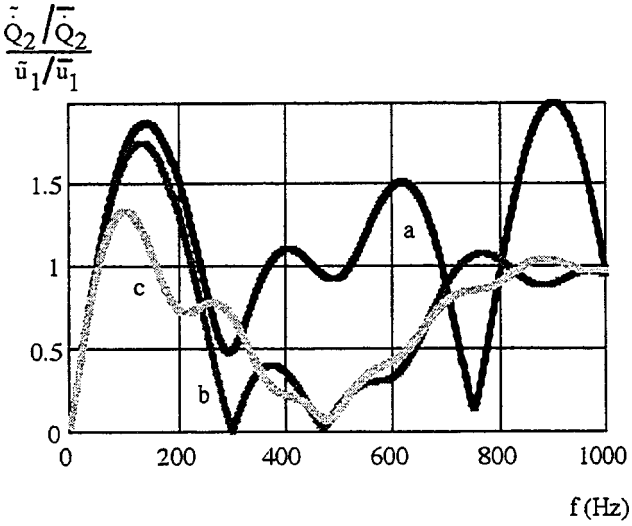

Fig. 8 Fluctuations of the thermal power at the burner exit: (a) $\Delta\pi/\bar{\tau}=0$ (b) $\Delta\pi/\bar{\tau}=0.3$, (c) $\Delta\pi/\bar{\tau}=0.8$

of the flame transfer function (12) was set to one ($\tau_{fl}=0$ and $\omega_0\to\infty$) in Fig. 9. As a result, the velocity ratio $\tilde{u}_{5,\phi_4=\text{const}}/\tilde{u}_4$ is proportional to the ratio of the mean densities. It can be seen from the results without dispersion presented in Fig. 9, that the equivalence ratio fluctuations alter the behavior of the acoustic system at low frequencies completely, whereas at high frequencies a kind of modulation of the gain calculated on the basis of pure acoustics is observed. With respect to the stability of the combustion system, it is in addition important to notice (not shown), that the phase relationship is completely different in the cases (a) and (c).

If the wave dispersion is considered (Fig. 10), the ''modulation'' vanishes and the acoustic solution is approached for higher frequencies. The same does not apply for frequencies below approx. 250 Hz, where the phase is also dominated by the convection of the equivalence ratio fluctuations. With respect to the amplitude ratio, the effects remain qualitatively unchanged when the flame dynamics is considered (Fig. 11). However, the phase relationship is altered due to the flame dynamics (not shown).

The investigations of the mixing tube as well as the supply with flame clearly show that the incorporation of equivalence ratio fluctuations alter the behavior of the system substantially. The

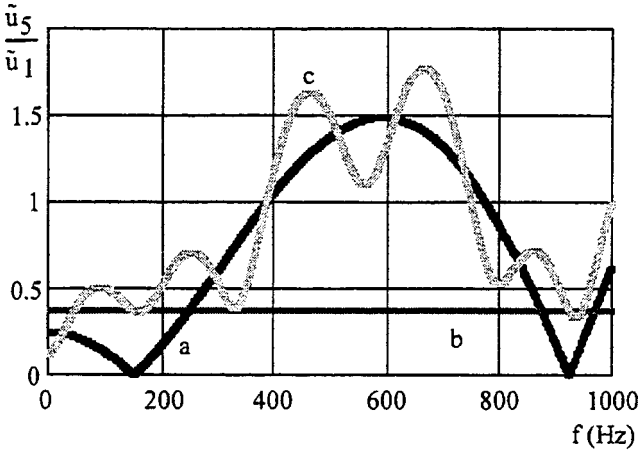

Fig. 9 Fluctuations of the acoustic velocity downstream of the flame: (a) acoustics, no equivalence ratio fluctuations, (b) no acoustics, equivalence ratio fluctuations, (c) acoustics and equivalence ratio fluctuation

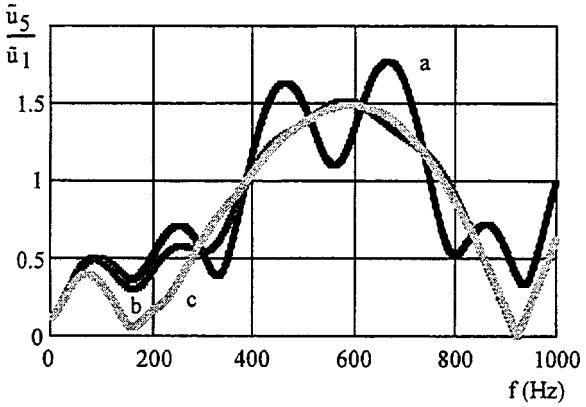

Fig. 10 Fluctuations of the acoustic velocity downstream of the flame: (a) $\Delta\pi/\bar{\tau}=0$, (b) $\Delta\pi/\bar{\tau}=0.3$, (c) $\Delta\pi/\bar{\tau}=0.8$

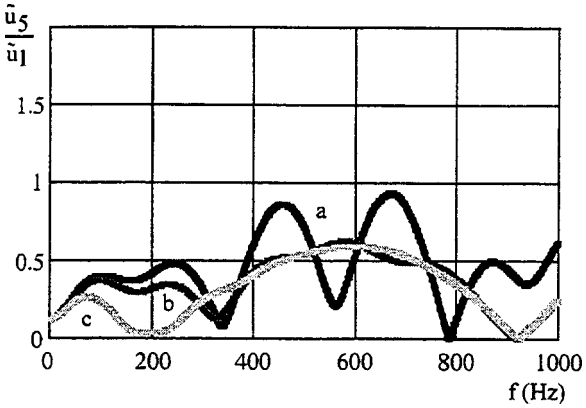

Fig. 11 Fluctuations of the acoustic velocity downstream of the flame (flame dynamics included): (a) $\Delta\pi/\bar{\tau}=0$, (b) $\Delta\pi/\bar{\tau}=0.3$, (c) $\Delta\pi/\bar{\tau}=0.8$

same applies to the dispersion of the equivalence ratio waves in the mixing tube. Due to their influence on the phase relationships, however, statements to what extent the stability of the system is influenced cannot be made directly. For the purpose of checking the system stability, a classical stability analysis of the model combustor in Fig. 5 was made.

Stability Analysis

Solving the set of 16 equations for the entire (unforced) system yields the complex eigenfrequencies of the combustor. The imaginary part determines the stability (>0 stable, <0 unstable) and the real part characterizes the frequency of the damped or amplified oscillation. In Figs. 12–14 the results of the stability analysis are summarized. The amplitude ratio of two successive cycles of the pulsation is plotted on the vertical axis versus the (real part) of the eigenfrequencies. For amplitude ratios >1 the pulsation is unstable (growing). For values smaller than 1 the pulsation decays and vanishes.

In Fig. 12, the effect of the equivalence ratio fluctuations on the stability is shown. The acoustic system has four eigenfrequencies below 1000 Hz, if the equivalence ratio fluctuations are not taken into account. The parameters of the flame model were chosen such that all eigenfrequencies are stable. The lowest value is near the eigenfrequency of the Helmholtz mode approximation.

If the equivalence ratio fluctuations are added to the system, the number of eigenfrequencies increases considerably due to the phase shift of the convective equivalence ratio transport. For the case without dispersion ($\Delta\tau/\bar{\tau}=0$), most of them are stable but three highly unstable frequencies are found also. Interestingly, the system stability is strongly improved at low frequencies, although the amplitude gain of the supply with flame increases (see Fig. 9, cases (a) and (c)). The reason for the improvement of the stability as well as the increase of the lowest eigenfrequency can be attributed to the change in phase difference of the supply with flame if the equivalence ratio fluctuations are added. This result cannot be generalized. It is possible, that a destabilising effect appears, if the parameters are chosen accordingly.

The dispersion of the equivalence ratio wave must be considered in order to draw a more realistic picture. Two cases for $\Delta\tau/\bar{\tau}=0.3$ and $\Delta\tau/\bar{\tau}=0.8$ are displayed in Fig. 12. It is evident that in these cases the system stability is not massively deteriorated in comparison to the acoustic case, as it is when dispersion is not taken into account. It becomes obvious that a realistic description of the dispersion of the equivalence ratio waves is mandatory for the proper characterization of the system stability.

The influence of the entropy fluctuations on the stability is shown in Fig. 13. In order to provide strong driving for the wave generation in the flame front, no dispersion of the equivalence ratio waves is assumed. The case without entropy waves is identical to the most unstable case in Fig. 12. The number of eigenfrequencies for the cases with entropy waves increases strongly due to the excessive phase loss during the wave convection. The most interesting result of the calculation is that the highly unstable frequencies are not substantially altered by the entropy waves without as well as with entropy wave dispersion. All other frequencies are stable. At low frequencies, the system stability is deteriorated if dispersion is not taken into account, but the stabil-

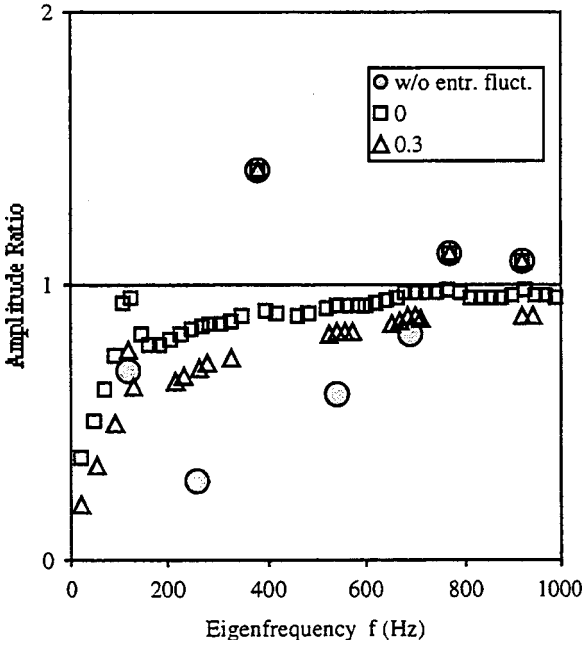

Fig. 13 Influence of the entropy fluctuations ($\Delta\tau/\bar{\tau}$) on the stability of the model combustor (*w/o* dispersion of the equivalence ratio waves)

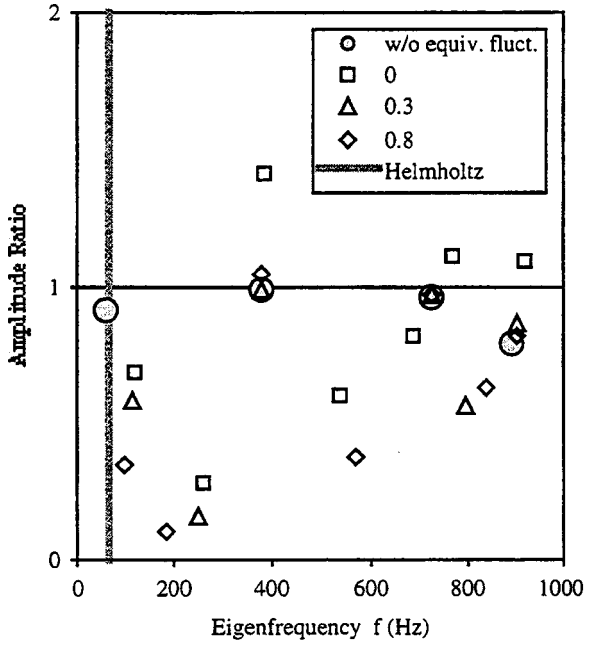

Fig. 12 Influence of the equivalence ratio fluctuations ($\Delta\tau/\bar{\tau}$) on the stability of the model combustor

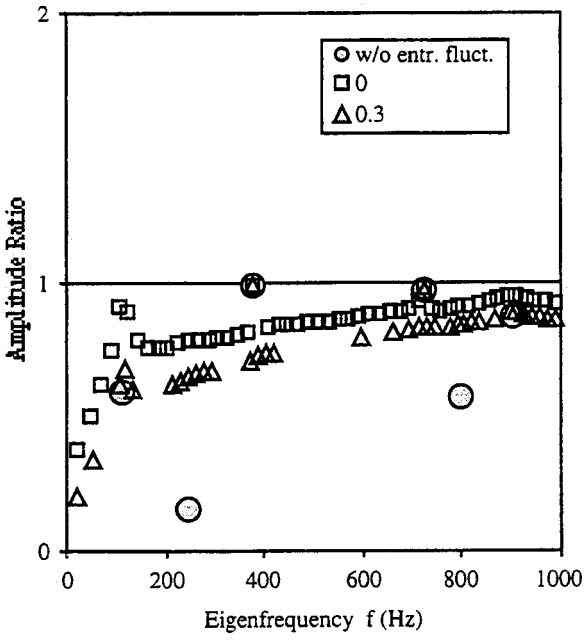

Fig. 14 Influence of the entropy fluctuations ($\Delta\tau/\bar{\tau}$) on the stability of the model combustor (with dispersion of the equivalence ratio waves)

ity limit of the system is not reached in the present case. With dispersion, no considerable deterioration of the system stability was found.

In Fig. 14, the results for a similar set of calculations are presented. Now, a dispersion of $\Delta\tau/\bar{\tau}=0.3$ is assumed for the equivalence ratio waves. This results in a weaker forcing of the entropy waves in the flame front. The findings are consistent with Fig. 13 with the main difference being that the system remains stable, because the base case without entropy fluctuations does not have highly unstable eigenfrequencies. It appears, that for realistic assumptions for the wave dispersion (e.g., $\Delta\tau/\bar{\tau}=0.3$) the entropy waves do not substantially deteriorate the system stability.

The validity of this statement is not restricted to the triggering of entropy waves by equivalence ratio fluctuations, since the nature of the source of an entropy wave (e.g., pressure pulses) does not effect the strength of its dissipation in the combustor.

Conclusions

The study presented in the paper was made in order to answer the question to what extent equivalence ratio waves and entropy waves must be taken into account in the framework of the stability analysis of gas turbine combustors. The following conclusions can be made.

- The dispersion of the waves can be incorporated in network type stability analysis codes in a simple analytical way if the residence time distribution can be quantified in advance by the computation of the scalar transport or the measurement of the flowfield in simple cases.
- The dispersion of the equivalence ratio waves can only lead to a moderate damping during convection from the injector to the flame (in the frequencies range which is usually most susceptible to instabilities).
- The dispersion of the entropy waves due to aerodynamic dispersion in the combustor is strong even in the low frequency domain.
- The flame of an externally premixed system behaves different from the flame of a gas turbine burner, due to the fluctuating equivalence ratio in the flame. As a consequence, models which use transfer functions for premixed systems (obtained analytically or computationally) cannot draw a realistic picture. The equivalence ratio fluctuation and its dispersion must be taken into account. If the transfer function is obtained experimentally for the burner with fuel injector, the effect of the equivalence ratio waves on the fluctuation of the acoustic velocity downstream of the flame can be incorporated to some degree indirectly in the acoustical model, although the equivalence ratio does not appear as an explicit variable.
- The stability analysis on the basis of models which take the equivalence ratio but not its dispersion into account, tends to predict a much too unstable system behavior.
- Entropy waves deteriorate the system stability only in the low frequency domain and only, if the dispersion is not taken into account.
- For dispersion parameters of both waves, which are realistic for gas turbine combustors with high mixing intensities, no major destabilizing effect of the entropy waves was found.

In summary, the study reveals that it is very important to take the equivalence ratio waves realistically into account, whereas it appears not to be mandatory to incorporate entropy waves into the stability analysis of gas turbine combustors.

Nomenclature

A = cross-sectional area
c_p = specific heat at constant pressure
c = speed of sound
C = parameter of the delay time distribution
f = frequency
g = Green's function
G = transfer function
h = specific enthalpy
k = wave number
L = segment length
M = Mach number
p = pressure
$\dot{Q}$ = heat flux
s = entropy and indep. var. of Laplace transformation
t = time
T = absolute temperature
u = velocity
v = specific volume
Z = impedance

Greek Symbols

δ = impulse function
Δ = difference
ϕ = equivalence ratio
κ = ratio of specific heats
ρ = density
τ = delay time
ω = $2\pi f$
Ψ = scalar quantity

Superscripts and Subscripts

air = air side (fuel injector)
b = backward direction
c = combustor and nozzle
d = downstream of the flame
exit = downstream end of segment
f = forward direction
fl = flame
fuel = fuel side (fuel injector)
inj = fuel injector
inlet = upstream end of segment
s = supply with burner/injector
u = upstream of the flame
$\tilde{}$ = average quantity
$\bar{}$ = fluctuating quantity

Appendix: Default Values for the Model Parameters

$$u_1 = 90 \text{ m/s},$$

$$\phi_1 = 0.5,$$

$$T_1 = 700 \text{ K},$$

$$T_5/T_4 = 2.5$$

$$\Delta C/C = 0$$

$$l_{1\to 2} = 0.3 \text{ m},$$

$$A_3/A_2 = 10,$$

$$l_{3\to 4} = 0.1 \text{ m},$$

$$l_{5\to 6} = 1.0 \text{ m},$$

$$\tau_{\text{fl}} = 0.5 \text{ ms},$$

$$D = 1,$$

$$\omega_0 = 75 \text{ s}^{-1}.$$

References

[1] Keller, J. J., 1995, "Thermoacoustic Oscillations In Combustion Chambers of Gas Turbines," AIAA J., **33**, No. 12, pp. 2280–2287.
[2] Hubbard, S., and Dowling, A. P., 1998, "Acoustic Instabilities in Premixed Burners," AIAA 98-2272, 4th AIAA/CEAS Aeroacoustics Conference, Toulouse, France, June 1998.
[3] Polifke, W., Paschereit, C. O., and Döbbeling. K., 1999, "Suppression of

Combustion Instabilities Through Destructive Interference of Acoustic and Entropy Waves,'' 6th Int. Congress on Sound and Vibration, Copenhagen.
[4] Lieuwen, T., Torres, H., Johnson, C., and Zinn, B. 1999, ''A Mechanism of Combustion Instability in Lean Premixed Gas Turbine Combustors,'' ASME Paper 99-GT-3.
[5] Davies, P. O. A. L., 1988, ''Practical Flow Duct Acoustics,'' J. Sound Vib., **124**, p. 91–115.
[6] Deucker, E., 1995, ''Ein Beitrag zur Vorausberechnung des akustischen Stabilitätsverhaltens von Gasturbinen-Brennkammern mittels theoretischer und experimenteller Analyze von Brennkammerschwingungent,'' VDI Fortschrittsberichte, Reihe 6, No. 317.
[7] Fleifil, M., et al., 1996, ''Response of a Laminar Premixed Flame to Flow Oscillations: A Kinematic Model and Thermoacoustic Instability Results,'' Combust. Flame, **106**, pp. 487–510.
[8] Ohtsuka, M., et al., 1998, ''Combustion Oscillation Analysis of Premixed Flames at Elevated Pressures,'' ASME Paper 98-GT-581.
[9] Peracchio, A. A., and Proscia, W. M., 1998, ''Non-Linear Heat-Release/Acoustic Model for Thermoacoustic Instability in Lean Premixed Combustors,'' ASME paper 98-GT-269.
[10] Lenz, W., ''Die dynamischen Eigenschaften von Flammen und ihr Einfluss auf die Entstehung selbsterregter Brennkammerschwingungen,'' dissertation, Universität Karlsruhe, 1980.
[11] Dowling, A. P., 1997, ''Nonlinear Self-Excited Oscillations of a Ducted Flame,'' J. Fluid Mech., **346**, pp. 271–290.
[12] Marble, F. E., and Candel, S. M., 1977, ''Acoustic Disturbances from Gas Non-Uniformities Convected through a Nozzle,'' J. Sound Vib., **55**, No. 2, pp. 225–243.

Instability of a Premix Burner With Nonmonotonic Pressure Drop Characteristic

W. Polifke
e-mail: polifke@td.mw.tum.de

A. Fischer
e-mail: fischer@td.mw.tum.de

T. Sattelmayer
e-mail: sattelmayer@td.mw.tum.de

Lehrstuhl für Thermodynamik,
Technische Universität München,
85747 Garching, Germany

Instabilities in combustion systems have frequently been reported to occur when slight changes in operating conditions lead to significant and abrupt changes in flame shape or flame position, i.e., changes in the mode of flame stabilization. The present paper offers an explanation and mathematical model of this observation. The analysis rests on the assumption that changes in the mode of flame stabilization are accompanied by a significant variation of the pressure drop across burner and flame, such that the pressure drop-flow rate characteristic locally displays a negative slope. In the limit of low frequencies (Helmholtz mode), it is then straightforward to show that an oscillatory instability can result from such behavior. An analytical stability criterion is derived, relating the nondimensionalized gradient of the pressure drop characteristic to the Helmholtz number of the burner. The physical mechanism of the instability is explained, and it is observed that the Rayleigh criterion need not be satisfied for this kind of instability to occur. In order to extend the stability analysis to higher frequencies, the transfer matrix for a burner with nonmonotonic pressure drop is derived in the limit of low Mach number and negligible fluctuations of the rate of heat release. The transfer matrix is employed in stability analysis based on a linear acoustic model of a combustion system. Experimental results obtained with an externally premixed swirl burner are presented. The pressure drop characteristic, the observed onset of instability and the instability frequency match the model predictions very well. [DOI: 10.1115/1.1519267]

1 Introduction

In the recent literature on thermo-acoustic instabilities in premixed combustion systems, a variety of possible mechanisms have been identified. Deuker [1], Fleifil et al. [2], and Dowling [3] discuss how a flame front with given flame speed responds to a perturbation of the inflow conditions. Krüger et al. [4] have continued Deuker's work, making use of computational fluid dynamics to extract the frequency response of a flame from a time-dependent numerical simulation. The frequency response is then used in a linear stability analysis of the combustion system (''network analysis''). In premixed combustion systems, modulations of the fuel equivalence ratio created by acoustic fluctuations of velocity or pressure at the fuel injector will—after a certain time lag—result in fluctuations of the heat release rate. This mechanism of self-excited instability has been investigated by Keller [5], Lieuwen et al. [6], Polifke et al. [7], Schuermans et al. [8], Straub and Richards [9], and others. The analysis is formulated either in terms of relative phases between acoustic and equivalence ratio fluctuations, [6,9], or the transfer matrix of the flame is determined from the linearized response of the heat release rate to modulations of the fuel concentration and then used in network stability analysis, [5,7,8]. In sequential combustion [10], a similar mechanism of instability has been identified by Ni et al. [11]. In this situation, modulation of the self-ignition time due to acoustic perturbations of the flow in the premixing section cause time-lagged fluctuations of the flame position and the heat release rate. Coherent vortical structures have been found responsible for combustion instabilities in jet diffusion flames, [12,13]. With a combination of experimental, numerical, and analytical methods, Paschereit et al. [14] have shown that this mechanism may also be active in premixed swirling flames.

In the investigations just cited, experimental evidence supplements in general the theoretical or numerical treatment, and one may conclude that each of the instability mechanisms discussed can be held responsible for thermo-acoustic instabilities for certain burner and combustor geometries or certain operating conditions. On the other hand, there is ample experimental evidence, [15], that combustion systems are prone to instabilities whenever the operating conditions are such that slight changes in burner mass flow rate, fuel equivalence ratio or pilot fuel ratio, say, result in significant or abrupt changes in flame shape or flame position, i.e., changes in the mode of flame stabilization. One then sometimes speaks suggestively of a *bi-stable flame*.

To fix ideas, consider a premix swirl burner, with the flame stabilized by a central recirculation zone as well as an outer recirculation zone in the upstream corners of the combustor. The central recirculation zone may be due to a spherical vortex breakdown, [16], or a central lance, see, e.g., [9]. If the fuel flow to the combustor is gradually reduced, the flame front will tend to move away from the burner mouth, similar to the ''lift-off'' phenomenon familiar in diffusion flames. More than this, it may well be that at a certain fuel flow rate one of the two recirculation zones extinguishes, resulting in a sudden change of the flame shape. If this occurs, the pressure drop across burner and flame will typically decrease noticeably.[1]

It is not compulsory that oscillatory behavior results from such a change in the mode of flame stabilization. However, a ''runaway'' mechanism may come into play here, which indeed can give rise to a dynamic instability: As the flame front moves away from the burner mouth and the pressure drop across burner and flame is reduced, an increase in the air flow rate through the burner and a corresponding further reduction in equivalence ratio

Contributed by the International Gas Turbine Institute (IGTI) of THE AMERICAN SOCIETY OF MECHANICAL ENGINEERS for publication in the ASME JOURNAL OF ENGINEERING FOR GAS TURBINES AND POWER. Paper presented at the International Gas Turbine and Aeroengine Congress and Exhibition, New Orleans, LA, June 4–7, 2001; Paper 2001-GT-035. Manuscript received by IGTI, Dec. 2000, final revision, Mar. 2001. Associate Editor: R. Natole.

[1] A similar scenario can be developed, e.g., for a partially piloted premix flame as the pilot fuel ratio is increased or decreased beyond a certain point.

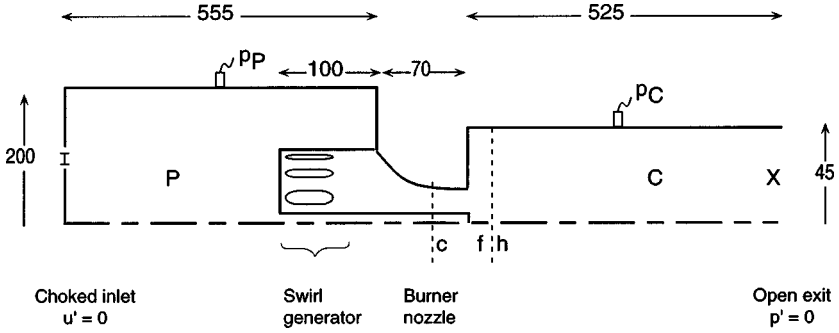

Fig. 1 Sketch of the test rig (not to scale): I—choked inlet to plenum, P—plenum, C—combustion chamber, X—exit. Flow is from left to right. All dimensions are in mm. The nominal cross-sectional area of the burner is evaluated in the throat of the burner at c.

will occur. Consequently, the flame will be pushed even further downstream, the burner pressure drop will decrease even more. Eventually, rising pressure in the combustor or decreasing pressure in the air supply will counteract the elevated air mass flow rate through the burner and attempt to bring it back to its nominal value. However, due to the inertia and the compliance of the gas in burner and plenum or combustor, a certain time delay is associated with this recovery process. Consequently, a self-excited instability may develop if the time lag is such that the fluctuations of flow rate and pressure drop obey a certain phase relation.

Although this mechanism of instability of a bi-stable flame is intuitively appealing, it has not yet been discussed in the literature. Combustion instability mechanisms identified previously—flame front kinematics, equivalence ratio modulations and coherent structures—do not appear to capture the essential features of the dynamics. It is the goal of this paper to analyze bi-stable flame dynamics quantitatively and to establish precisely under which conditions oscillatory behavior may occur.

To this purpose, a lumped parameter model of a combustor with a bi-stable flame is developed. The analysis rests on the assumption that changes in flame stabilization mode are accompanied by a significant variation of the pressure drop across burner and flame. In the limit of low frequencies (Helmholtz approximation for the acoustics of air supply and combustor), it is then possible to show analytically that an oscillatory instability can occur, provided that the slope of the pressure drop—flow rate characteristic of the burner is negative. More precisely, a stability criterion is developed in terms of the normalized gradient of the pressure drop characteristic and the Helmholtz number of the burner at the Helmholtz frequency of the combustion system. The physics of the instability mechanism is explained, it is pointed out that although the interaction of the burner flow and heat release does play a decisive role, fluctuations of the heat release rate need not be present. It follows that the famous Rayleigh criterion, [3], need not be satisfied for this kind of instability to occur. In this respect, one is not dealing with a ''proper'' thermo-acoustic instability here and should instead speak of a *burner flow instability* or a *pressure loss instability* in order to do justice to its hydrodynamic nature.

Because the proposed instability mechanism is of course not restricted to low frequencies, the analytical treatment is then extended to higher frequencies. The transfer matrix of a bi-stable burner is derived and used in network stability analysis of the combustor acoustics. It is found that for an externally premixed swirl burner, the onset of instabilities observed in experiments as well as the instability frequencies match very well the model predictions. The paper concludes with a simple design rule for premix burners, which may be derived from the analysis presented.

Before the discussion of analytical and numerical results, experimental observations are reported in the next section. These findings lend support to the ideas developed above and shall be used to validate predictions of the acoustic model.

2 Experimental Setup and Results

The concept of a pressure loss instability mechanism for bi-stable flames was first formulated during development work on a premix burner for stationary gas turbines, [15], and subsequently refined in the present work. Experiments at the Lehrstuhl für Thermodynamik with a generic, swirl-stabilized premix burner operated at atmospheric pressure without air preheat corroborate these ideas.

The test rig is shown in Fig. 1. Through a choked inlet nozzle I a homogeneous mixture of air and natural gas enters the cylindrical plenum chamber P. At the downstream (right) end of the plenum chamber, the burner is located. The hot section C of the rig is of rectangular cross section, open to the ambiance at the exit X. One side wall of the hot section is made of glass, making possible optical observation of the flame. Pressure taps as well as microphones are installed to measure both mean and fluctuating values of pressure p_P in the plenum and pressure p_C in the combustion chamber, respectively.

The burner used in the tests comprises a cylindrical centerbody, a tangential swirl generator at the upstream end and a nozzle at the downstream end (see Fig. 1). The flame is stabilized with the help of the inner and outer recirculation zones in the wake of the center-body and the backward-facing step, respectively. The burner was designed to allow the study of generic aspects of premixed swirl stabilized flames, and does not mimic any particular burner design presently used in industry. With the possibility of easily changing the diameter of the centerbody and the length of the tangential entry slits, the swirl angle and the strength and size of the recirculation zones can be varied in a wide range. It is emphasized that in the tests reported here, fuel was not injected in or near the burner, but upstream of the choked inlet of the plenum chamber, using static mixer elements to completely homogenize the combustible mixture and thereby eliminate any effects of equivalence ratio fluctuations as well as entropy waves (see, e.g., [17]) on combustion stability.

Time-averaged pressure drop[2] data from four runs with thermal power P in the range from 61 kW to 106 kW are shown in Fig. 2. In these test runs, ignition occurred at high excess air ratios ($\lambda \approx 1.4$ to 1.5), then the air flow was very gradually reduced to (near) stoichiometric conditions. During each run, the fuel flow rate was held constant, so a higher air excess ratio λ corresponds to higher burner mass flow rate $\dot{m}_B$ and vice versa.

For two cases with power $P = 61$ kW and 75 kW, no instability was observed throughout the entire operating range. The pressure

[2]The use of time-averaged pressure data is in line with the quasi-stationary approximation used throughout this paper.

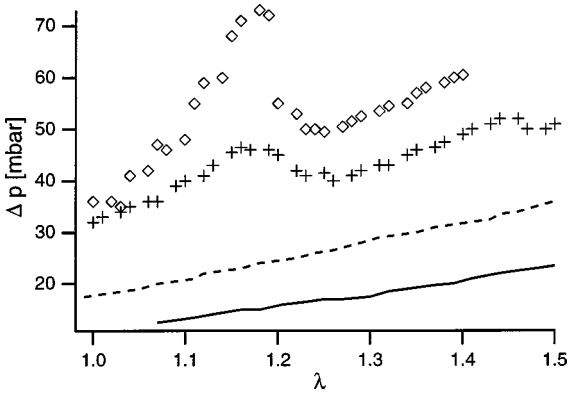

Fig. 2 Pressure drop characteristic, i.e., difference $p_P - p_C$ of the mean pressures in plenum and combustor versus air excess ratio λ for power output $P = 61$ kW (——), 75 kW (– – –), 95 kW (+), and 106 kW (◇). Strong combustion oscillations were observed with $P = 95$ kW for $\lambda < 1.26$ and with $P = 106$ kW for $\lambda < 1.24$.

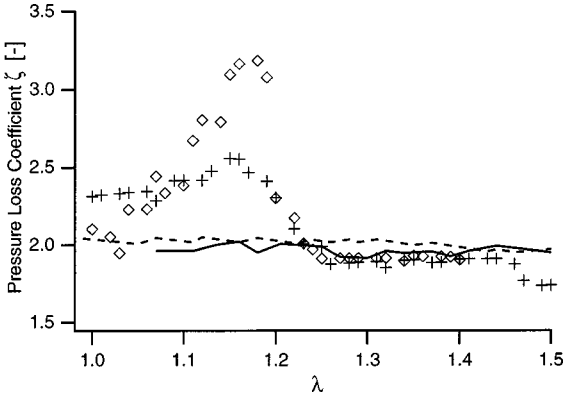

Fig. 4 Pressure drop coefficient ζ versus air excess ratio λ for power output $P = 61$ kW (——), 75 kW (– – –), 95 kW (+), and 106 kW (◇). Strong combustion oscillations were observed with $P = 95$ kW for $\lambda < 1.26$ and with $P = 106$ kW for $\lambda < 1.24$.

loss characteristic curve shows a monotonic increase of the pressure drop $\Delta p \equiv p_P - p_C$ across burner and flame with air excess ratio λ, see Fig. 2. With higher power, strong combustion noise was encountered for $\lambda < 1.26$ (95 kW) and $\lambda < 1.24$ (106 kW) at frequencies in the range 300–320 Hz. Remarkably, the onset of the instabilities corresponds with a region where the pressure drop characteristic displays a negative slope (Fig. 2).

Changes in flame shape and stabilization mode were observed, which also are in line with the ideas put forward in this paper. With decreasing air excess ratio λ, the flame shape changed from an elongated V-shaped flame to a much more compact and intense flame stabilized by both an inner and an outer recirculation zone shortly behind the area expansion, see Fig. 3. With decreasing air excess ratio, the flame eventually flashed back into the premixing nozzle (not shown).

Evaluating a pressure loss coefficient ζ according to

$$\Delta p = \frac{\rho}{2} \zeta u^2, \tag{1}$$

where ρ and u are density and velocity in the burner nozzle, respectively, it could be observed that different pressure loss coefficients are associated with the different flame shapes and flame stabilization mechanisms. For the two low-power stable test runs, the pressure loss coefficient was almost constant with a value of $\zeta \approx 2$ throughout the range of air excess ratios covered in the test runs, see Fig. 4. For the two test runs with power $P = 95$ kW and 106 kW, respectively, an increase of the pressure loss coefficient ζ correlates with the onset of the instability.

Except for the fact that the instability does not die out once the slope of the pressure loss characteristic is again positive at air excess ratios below $\lambda \approx 1.16$ and $\lambda \approx 1.18$, these observations lend support to the proposed instability mechanism. Admittedly, other mechanisms—e.g., flame front dynamics or heat transfer between the flame and the center body of the burner nozzle or the front panel—may also play a role here. Also, it cannot be ruled out that the increase in pressure drop observed is a consequence rather than the cause of the instability.

Clearly, the experimental evidence needs corroboration from theory and modeling. In the next sections, analytical and numerical models of burner and combustor behavior are worked out and the concepts developed so far only in a qualitative manner are formulated more precisely. It will be seen that stability limits and eigenfrequencies observed in the experiment agree well with those predicted by the acoustic model, supporting the ideas put forward in this paper.

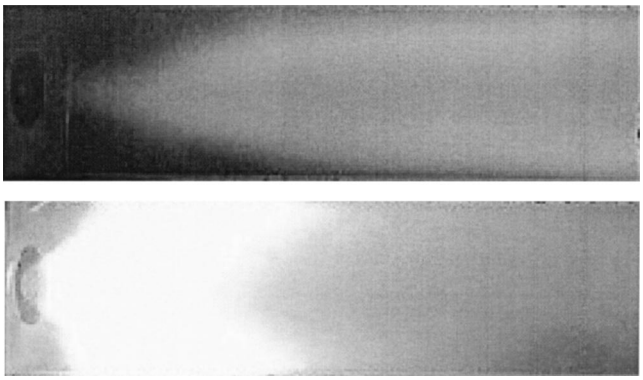

Fig. 3 Flame shape near lean blow out (top) and near stoichiometric (bottom)

3 Lumped Parameter Analysis of a Bi-Stable Burner

In this section, an analytical model and stability criterion for a bi-stable burner in a generic combustor is developed and analyzed. The combustor layout is representative of a gas turbine, and similar—albeit not identical—to the test rig described in the previous section. The analysis is developed in the framework of a lumped parameter model valid only in the limit of low frequencies, where spatial variations of acoustic quantities are assumed to be negligible (*Helmholtz approximation*). The use of such a restricted framework is justified by its simplicity; the essential aspects of the system dynamics can be analyzed clearly and understood easily with the lumped parameter model. A general acoustic formulation, which encompasses the Helmholtz limit as well as high-frequency behavior, is subsequently developed and applied to stability analysis of the test rig in Sections 5 and 6.

Consider a combustion system as shown in Fig. 5, representative of a gas turbine combustor. Air flows from a plenum P through a burner B into a combustion chamber C and leaves through a choked exit X. For the moment, fluctuations of heat release rate or fuel concentration, coherent structures and flame front dynamics are dismissed. Instead, the question how *fluctuations of the pressure drop* across burner and flame may affect system stability is investigated.

In a stationary situation, the difference in static pressure between plenum and combustor equals

$$p_P - p_C = \Delta p(\dot{m}_B), \tag{2}$$

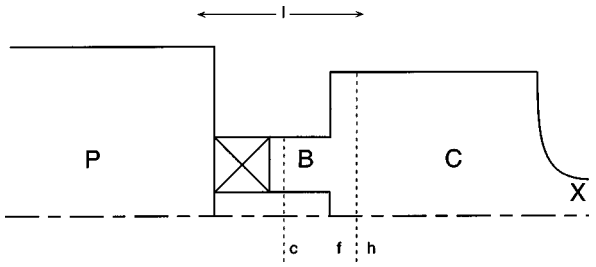

Fig. 5 Exemplary sketch of a premix combustion system. P—plenum chamber, B—inside burner, cross section with nominal area A_B, l—(virtual) length of the burner, f–h—position of flame, C—combustion chamber, X—choked exit. Flow is from left to right.

where $\Delta p(\dot{m}_B)$ is the (stationary) pressure drop across burner and flame, while $\dot{m}_B$ is the mass flux (units kg/m^2-s) inside the burner. For given geometry, operating pressure and fuel flow rate, the pressure drop Δp depends as indicated primarily on the mass flux.

If at time t the difference in static pressure between plenum and combustor is not equal to the pressure drop $\Delta p(\dot{m}_B(t))$ corresponding to the momentary mass flux $\dot{m}_B(t)$, then this pressure mismatch will accelerate or decelerate the flow through the burner. Momentum balance across the burner yields in this case

$$p_P(t)-p_C(t)=\Delta p(\dot{m}_B(t))+l\frac{d\dot{m}_B t}{dt}. \tag{3}$$

Here a virtual length l

$$l\approx A_B\int_1^2\frac{1}{A(x)}dx, \tag{4}$$

has been introduced, pertaining to a nominal cross-sectional area A_B of the burner (see Paschereit and Polifke [18]).

The total mass of gas inside the combustion chamber will change with time if the influx $\dot{m}_B$ through the burner is not equal to the efflux at the exit X.

$$\dot{m}_B A_B-\dot{m}_X A_X=V_C\frac{d\rho_h}{dt}. \tag{5}$$

The subscript h stands for ''hot.'' It is assumed here that the density ρ_h of the gas in the combustor is spatially uniform throughout the combustor. This approximation implies that the flame is short compared with the combustor length and that the combustor is *acoustically compact*, i.e., its length is much smaller than acoustic wave lengths. The first condition is not essential in the present context, a correction could be introduced which accounts for a cold section of the combustor upstream and a hot section downstream of the flame front. The second condition restricts the stability analysis presented in this Section to the low-frequency regime (Helmholtz limit).

As already mentioned, the boundary conditions are

$$p_P=\text{const. (plenum condition)}, \tag{6}$$

$$\dot{m}_X=\text{const. (choked combustor exit)}. \tag{7}$$

To carry out a linear stability analysis for the combustion system, the temporal evolution of small perturbations is investigated. Formally, perturbations are introduced as primed quantities, i.e., $v\rightarrow v+\varepsilon v'$ with $\varepsilon\ll 1$, where v stands for any dynamic variable of the system of Eqs. (3) to (7). The boundary conditions imply

$$p'_P=0, \tag{8}$$

$$\dot{m}'_X=0. \tag{9}$$

Neglecting terms of second or higher order in ε, one obtains—again in the quasi-stationary approximation—from Eq. (3) for the pressure drop

$$-p'_C=\frac{\partial\Delta p}{\partial\dot{m}_B}\dot{m}'_B+l\frac{d\dot{m}'_B}{dt}. \tag{10}$$

The pressure fluctuations in the combustion chamber depend (a) on the fluctuations of the mass flux into the chamber times the slope of the pressure drop characteristic and (b) the rate of change of the mass flux times the virtual length. This second term represents the inertia of the gas in the burner. Introducing a dimensionless parameter

$$\chi\equiv\frac{1}{c_c}\frac{\partial\Delta p}{\partial\dot{m}_B}, \tag{11}$$

where c_c is the speed of sound upstream of the flame, the last result is rewritten conveniently

$$-p'_C=c_c\chi\dot{m}'_B+l\frac{d\dot{m}'_B}{dt}. \tag{12}$$

Using the relations $p'/p=\gamma\rho'/\rho$ and $c^2=\gamma p/\rho$ valid for isentropic flow (γ is the ratio of specific heats), one obtains from mass conservation (5) the following relation

$$\dot{m}'_B=\frac{V_C}{A_B}\frac{d\rho'_h}{dt}=\frac{V_C}{c_h^2A_B}\frac{dp'_C}{dt}, \tag{13}$$

which involves the compliance of the gas in the combustion chamber.

A system of two coupled ordinary differential Eqs. (12) and (13) has been derived for the unknowns $\dot{m}'_B$ and p'_C, i.e., fluctuations of mass flux density and pressure just downstream of the flame. Invoking the usual assumption $\dot{m}'_B(t)\sim p'_C(t)\sim\exp\{st\}$ for the time dependence, two algebraic equations are obtained:

$$\begin{pmatrix}1 & c_c\chi+sl\\ \dfrac{sV_C}{c_h^2A_B} & -1\end{pmatrix}\begin{pmatrix}p'_C\\ \dot{m}'_B\end{pmatrix}=0. \tag{14}$$

Nontrivial solutions require that the determinant of the matrix vanishes, i.e.,

$$s^2+s\frac{c_c\chi}{l}+\omega_0^2=0, \tag{15}$$

where in analogy with a Helmholtz-resonator the parameter

$$\omega_0=c_h\sqrt{\frac{A_B}{lV_C}} \tag{16}$$

is identified as the Helmholtz frequency of the combustion system. The burner with nominal cross-section A_B and length l represents the ''neck'' of the Helmholtz resonator, the combustor itself the resonator volume. The following eigenvalues are found:

$$s_{1,2}=-\frac{c_c}{2l}[\chi\pm\sqrt{\chi^2-\mathcal{H}^2}], \tag{17}$$

where $\mathcal{H}\equiv 2\omega_0 l/c_c$ can be interpreted as (twice) the Helmholtz number[3] of the mixing tube at the Helmholtz frequency of the combustor.

Four types of solutions can be identified, depending on the sign of χ and the relative magnitude of χ and $\mathcal{H}$:

1. $0<\mathcal{H}<\chi$.

In this case, both eigenvalues $s_{1,2}$ are purely real and negative, i.e., perturbations will decay monotonically, the system is stable.

[3]The product of wave number k and geometrical length l is known as the Helmholtz number $\mathcal{H}\equiv kl=2\pi l/\lambda$. For an acoustically compact element, $l\ll\lambda$ and $\mathcal{H}\ll 1$.

2. $0<\chi<\mathcal{H}$.

The square root term in (17) is purely imaginary, therefore the solution will be oscillatory. However, with $\chi>0$, the amplitude of oscillations will decay with time, the system is stable.

3. $-\mathcal{H}<\chi<0$.

Again the solution is oscillatory, but with exponentially increasing amplitudes, i.e., the system is unstable. For very small negative gradients of the pressure drop characteristic, the frequency of the oscillation is close to the combustor's Helmholtz frequency and the growth rates are small. As χ approaches $-\mathcal{H}$, the frequency goes to zero while the growth rate of one of the eigenmodes becomes maximal. It may well be that the violent low-frequency oscillations which are frequently observed at lean blow out, are related to this limit. Recall that entropy waves are not considered in this paper; the low frequencies predicted by the present analysis are not related to convective time scales!

4. $\chi<-\mathcal{H}<0$.

In this case the linear stability analysis predicts a ''runaway'' instability, i.e., monotonously increasing amplitudes of perturbations. The real system can obviously not support ever increasing mass flux—either the flame would blow out, or soon reach a state where the slope of the pressure drop characteristic is less steep and settle into a limit cycle.

4 Physical Mechanism of the Pressure Loss Instability

The analysis presented in the previous section has presented a mechanism of dynamic instability of a combustion system, although no mention has been made of fluctuations of heat release rate. What is the physics of this instability, and is it appropriate to speak of a thermo-acoustic instability?

The pressure drop characteristic of burner and flame appears as the main parameter controlling system stability, besides the inertia and the compliance of the gas in the burner and the combustor, respectively. The instability mechanism analyzed above requires that χ—the nondimensionalized slope of the steady-state pressure drop characteristic—be negative. One might argue that such behavior is quite unusual, because in general the pressure drop through an orifice or a nozzle, say, increases with increasing mass flow rate. Admittedly, a premix flame front could exhibit a negative χ, because for fixed fuel flow, an increase in air flow rate will decrease the temperature ratio across the flame sheet and reduce the drop of static pressure across the flame sheet. Unfortunately, this pressure drop by itself is rather small, and indeed often insignificant compared to other pressure loss effects.

However, for a swirl stabilized premix burner, the pressure loss depends in a sensitive manner on the size and location of the recirculation zones which stabilize the flame, because these factors control the effective exit area of the burner. In turn, the size and strength of recirculation zones respond to changes in the position of the flame front, as the decrease in density across the flame decreases the swirl number and disturbs the radial pressure balance. It is concluded that a decrease in burner pressure drop with increasing mass flux seems possible for a premix swirl burner, whenever flame shape or position, i.e., the mode of flame stabilization, change drastically, and in particular when the flame lifts off or blows off or flashes back into the premixing section.

Note that in formulating (3) and (11), an assumption of quasi-stationary behavior has been invoked, i.e., it has been assumed that the momentary pressure drop depends on the momentary mass flux in the same way as in the stationary case. This assumption is not always well justified and probably overly restrictive. Indeed, Polifke et al. [19] have argued that vortex dynamics can effect negative values of χ and pressure loss instability even in situations where the steady-state pressure loss characteristic does not display anomalous behavior, [19]. Further exploration of these questions shall be the topic of future work.

To continue our argument, it is assumed that the burner behavior is represented by a pressure drop characteristic as depicted schematically in Fig. 6. In steady state, the mass flux $\dot{m}_B$ through the burner is $\dot{m}_0=\dot{m}_X$, the pressure difference between plenum and combustion chamber equals Δp_0. Imagine that a perturbation displaces the system to point a. Now the mass flow rate through the burner is too small to balance the efflux at the combustor exit, and the pressure p_C will decrease. Plenum pressure p_P is by assumption constant; it follows that the pressure difference p_P-p_C will increase, trying to increase the mass flux back to its steady-state value $\dot{m}_0$. However, due to the inertia of the fluid in the burner, the increase in mass flow rate cannot occur immediately. Consequently, once the mass flow rate is back to normal (point b in the figure), the pressure difference p_P-p_C is significantly elevated. This will further increase the mass flux through the burner, until eventually the pressure difference is back to nominal (point c). The reader can complete the cycle back into the vicinity of the starting point a.

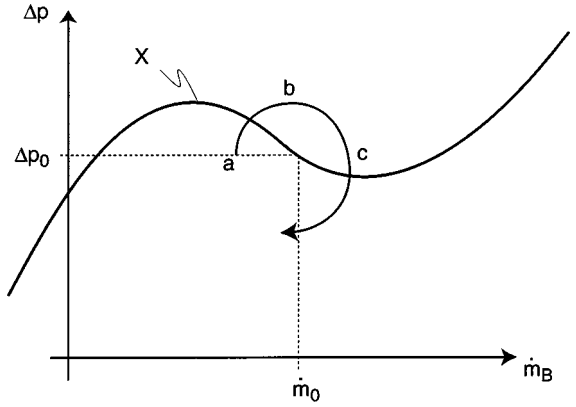

Fig. 6 Sketch of a pressure loss characteristic with negative slope. If the mass flux increases beyond point X, the mode of flame stabilization changes, pressure drop decreases and the system may become unstable.

Will the amplitude of such an oscillation around the steady-state operating point $(\dot{m}_0,\Delta p_0)$ increase or decrease with time? An increase is possible only if the oscillatory state is energetically favorable over the steady state, i.e., if the loss of energy associated with the pressure loss over burner and flame is lower than in steady state. This requires that over one cycle of the oscillation,

$$\int_0^T (p_P-p_C)'\dot{m}_B' dt<0. \tag{18}$$

In other words, an initial perturbation will damp out with time, unless high mass flow rates are correlated with low pressure difference and vice versa. In the quasi-stationary limit, this is possible only if the pressure drop—mass flow rate characteristic displays a negative slope as indicated in Fig. 6. This argument is confirmed by the analytically determined eigenvectors. With the eigenvalues $s_{1,2}$ given by Eq. (17),

$$-\frac{p_c'}{c_c}=\frac{\chi}{2}\left(1\pm\sqrt{1-\left(\frac{\mathcal{H}}{\chi}\right)^2}\right)\dot{m}_B', \tag{19}$$

and Eq. (18) cannot be satisfied for $\chi>0$.

The reader familiar with the work on instabilities in pumping systems, [20], and multiphase flows, [21], will already have noted that the low-frequency analysis presented here shows similarities to lumped parameter models of dynamic instabilities for such systems.

Concerning Rayleigh's criterion for thermo-acoustic instabilities: it should be clear by now that fluctuations of the heat release rate do not play an essential role in the instability mechanism presented and that Rayleigh's criterion need not be satisfied for

the instability to occur. Therefore it does not seem appropriate to refer to the present instability mechanism as a ''proper'' thermoacoustic instability.

In general, one should expect that fluctuations of flame shape or position at an operating point with negative χ will also modulate the heat release rate $\dot{Q}$. The corresponding fluctuations in volume production at the flame front will enhance or decrease the propensity to or intensity of combustion oscillations, depending on the relative phases of the various mechanisms.

5 Transfer Matrix of a Burner Nozzle With Bi-Stable Flame

The physical mechanism of the pressure loss instability is most easily understood with a lumped parameter model for the interplay between plenum, burner, and combustion chamber, as it was presented above. However, while this kind of analysis is limited to low frequencies, there is no reason to assume that the instability mechanism should not also be active at higher frequencies, involving acoustic modes of the system. Indeed, the instability frequencies in the range of 300–320 Hz observed in the experiments (see Section 2) are an order of magnitude higher than the Helmholtz frequency ω_0 of the test rig.

To analyze this regime, it is necessary to cast our understanding of bi-stable burner behavior developed so far into a form which is compatible with acoustic analysis, i.e., to derive the corresponding *transfer matrix*, [8,18]. Once this is achieved, the transfer matrix can be integrated into a network representing the acoustic behavior of a combustion system. It will also become clearer how additional effects due to fluctuations in heat release rate or flame velocity, say, could be integrated into the analytical description.

As usual, a quasi-one-dimensional analysis is developed, assuming that both burner and flame are acoustically compact. The starting point is the unsteady Bernoulli equation,

$$\frac{\partial \phi}{\partial t}+\frac{1}{2}u^2+\frac{\gamma}{\gamma-1}\frac{p}{\rho}=F(t), \tag{20}$$

where the velocity $\mathbf{u}$ is the gradient of its potential, $\mathbf{u}=\nabla\phi$. Integrating from a position c inside the burner (corresponding to B in the low-frequency limit, c.f. Figs. 5 and 1, to a position f just *upstream* of the *flame* yields

$$\frac{\partial}{\partial t}\int_c^f u\,dx+\left[\frac{1}{2}u^2+\frac{\gamma}{\gamma-1}\frac{p}{\rho_c}\right]_c^f+\frac{\Delta p}{\rho_c}=0, \tag{21}$$

where a pressure drop Δp has been introduced to account for losses which the flow incurs as it changes from the orderly swirling flow inside the burner nozzle through a vortex breakdown and the flame front into a highly turbulent flow state with recirculation zone and strong gradients downstream of the combustor area expansion. The brackets $[v]_c^f$ stand for the difference v_f-v_c of any variable v. Introducing perturbations $u\rightarrow u+\varepsilon u'$, with $\varepsilon\ll 1$, and assuming a harmonic time dependence for the perturbation, $u'(t)\sim\exp(-i\omega t)$, one obtains to first order in ε

$$i\omega\int_c^f u'dx+\left[uu'+\frac{p'}{\rho_c}\right]_c^f+\frac{1}{\rho_c}\frac{\partial\Delta p}{\partial\dot{m}}(\rho_c u_c)'=0. \tag{22}$$

The integral on the l.h.s. may again be expressed as a suitably defined virtual length l, see [18]. For the experiment considered in this work, the Mach numbers M are quite small, and terms of first order in M may be neglected with good accuracy. For the pressure downstream of the flame sheet, it is a general result that $p_h=p_f+\mathcal{O}(M)$. Introducing the wave number $k\equiv\omega/c$, one obtains eventually

$$\left[\frac{p'}{\rho_c c_c}\right]_c^h+(\chi+ik_c l)u_c'=\mathcal{O}(M). \tag{23}$$

How does this result for a bi-stable burner compare with the earlier formulation proposed by Paschereit and Polifke [18]? If a pressure loss $\Delta p=\rho_c\zeta u_c^2/2$ with a constant pressure loss coefficient ζ is assumed, then $\chi=\zeta M$. In this case, the differences between Eq. (23) and Eq. (14) in Ref. [18] are due to ''Borda-loss'' terms, which arise due to changes in the cross-sectional of plenum and combustion chamber. These terms have been explicitly considered in [18], while in the present analysis they have been lumped into the overall pressure loss Δp. We conclude that (23) is consistent with the earlier formulation developed in [18].

A second equation coupling fluctuating quantities across the burner stems from mass conservation—as it was the case for the lumped parameter model. Starting with

$$u_h'=u_f'+\left(\frac{T_h}{T_c}-1\right)u_f\frac{\dot{Q}'}{\dot{Q}}+\mathcal{O}(M), \tag{24}$$

which may be derived from the Rankine-Hugoniot relations for a thin flame sheet, [22,17], it is again assumed that fluctuations of heat release rate do not play an essential role in the pressure drop instability mechanism, $\dot{Q}'\approx 0$. This leads to

$$u_c'A_c=u_h'A_h+\mathcal{O}(M), \tag{25}$$

where the change in cross-sectional area A from c to h is considered explicitly. Temperatures or densities do not appear in (25). On first sight, this result seems to violate mass conservation, which for the steady state requires

$$\rho_c u_c A_c=\rho_h u_h A_h\,. \tag{26}$$

However, the result (25) for velocity fluctuations up and downstream of the flame sheet is consistent with the result for the ''fluctuating flame position'' discussed by Schuermans et al. [8]. This implies that the flame is merely convectively transported back and forth by acoustic velocity fluctuations.

Equations (23) and (25) represent the transfer matrix of a bi-stable burner. The derivation presented in this section may be summarized as follows:

$$\begin{pmatrix} \dfrac{p_h'}{\rho_h c_h} \\ u_h' \end{pmatrix}=\begin{pmatrix} \xi & -\chi-ik_c l \\ 0 & \alpha \end{pmatrix}\begin{pmatrix} \dfrac{p_c'}{\rho_c c_c} \\ u_c' \end{pmatrix}, \tag{27}$$

with $\xi=\rho_h c_h/\rho_c c_c$ the ratio of specific impedances and $\alpha\equiv A_c/A_h$ the ratio of areas on both sides of the flame, respectively. In situations where fluctuations of the heat release rate $\dot{Q}'$ are significant, the velocity-velocity coupling coefficient will primarily be affected. The area ratio α would have to be replaced by an appropriate expression, see [8,17].

6 Network Stability Analysis

For quantitative validation of the pressure loss instability mechanism against experimental results, a simple network model of plane-wave acoustics in the test rig (see Fig. 1), making use of the transfer matrix (27) for a bi-stable burner, was constructed and solved.[4] The upstream end of the plenum is modeled as an acoustically closed end ($u'=0$). The plenum and the combustion chamber are represented as simple ducts, where acoustic waves travel back and forth without dissipation. Mach number effects—although probably insubstantial—are considered. At the downstream end, where the combustion chamber is open to the ambiance, the corresponding boundary condition $p'=0$ is set. Temperature, speed of sound, density, and Mach number in the plenum and the combustion chamber are set according to the ex-

[4]The Helmholtz mode of the test rig, where the plenum chamber acts as the resonator volume and the burner as its ''neck,'' has a frequency of approximately 30 Hz. Obviously, the instability observed in the experiment is not the Helmholtz mode, and a low-frequency analysis is not appropriate here.

perimental conditions for $P=95$ kW and $\lambda=1.2$. More details on the network model may be found in [8,17], where similar formulations were developed.

Lacking direct measurements of the burner transfer matrix at the operating conditions used in this study, burner and flame are modeled as a combination of two transfer matrices: first a matrix which represents the change in area from the plenum to the narrowest cross section of the nozzle (corresponding to location c in Figs. 5 and 1), followed by the transfer matrix (27) for a variable pressure loss with virtual length l and combustion chamber area expansion α. The virtual length is set to $l=0.17$ m, equal to the geometrical length of the burner, although considering Eq. (4) it should perhaps be smaller than this value.

With all transfer matrices given in analytical form, it is not necessary to employ graphical methods as they have been derived from control theory for network stability analysis, [23]. Instead, one may directly search for the eigenfrequencies ω_m of the system. The cycle increment ς of an oscillatory mode—the relative decrease or increase of oscillation amplitudes per cycle—can then be determined from the real and imaginary parts of the eigenfrequency

$$\varsigma(\omega_m)\equiv\exp\left\{-\frac{2\pi\Im(\omega_m)}{\Re(\omega_m)}\right\}-1. \tag{28}$$

The cycle increment of an eigenmode equals the percentage by which the amplitude of an infinitesimal perturbation grows during one cycle of the oscillation; negative cycle increments indicate stability.

The lowest eigenmode of the network model reproduces correctly the findings of the lumped parameter model (not shown), which confirms that indeed the transfer matrix (27) and the acoustic model encompass the low-frequency analysis discussed in Sections 3 and 4.

Searching for eigenmodes in the vicinity of 320 Hz, with varying normalized pressure drop gradient χ, the data shown in Fig. 7 are obtained. We indeed find stable and unstable eigenmodes in the correct frequency range. As with the low-frequency analysis, a self-excited instability may occur for $\chi<0$. Differing from the low-frequency Helmholtz mode, the frequency of these acoustic eigenmodes does not change drastically with χ, and the cycle increment displays a maximum of a few percent for a certain value of the pressure drop gradient, after which the instability becomes less strong. While obviously the gradient of the pressure loss characteristics has a strong influence on the growth rate and a noticeable one on frequency, it is found that frequency and cycle increment of the acoustic modes are insensitive to the value chosen for the virtual length l: With l varying between 0.1 m and 0.3 m, both f and ς change by only a small fraction of a percent (not shown).

To summarize, the results of the network analysis compare well with the experimental findings and confirm qualitatively the proposed instability mechanism and the transfer matrix (27) for an externally premixed bi-stable burner.

7 Summary and Conclusions

It has been shown that a pressure loss instability mechanism may be active in combustion systems whenever the pressure loss across burner and flame decreases with increasing mass flow. Such rather unusual behavior may be expected for premixed swirl-stabilized flames, where the pressure loss depends strongly on the location and size of recirculation zones and the location and shape of the flame front, which influence each other strongly. Different operating conditions may therefore exhibit qualitatively different flame shapes and correspondingly very different pressure loss coefficients. In the transition region between two different modes of flame stabilization, a pressure loss characteristic with a negative slope may occur. The suggestive term ''bi-stable flame'' is used to characterize this regime of operation.

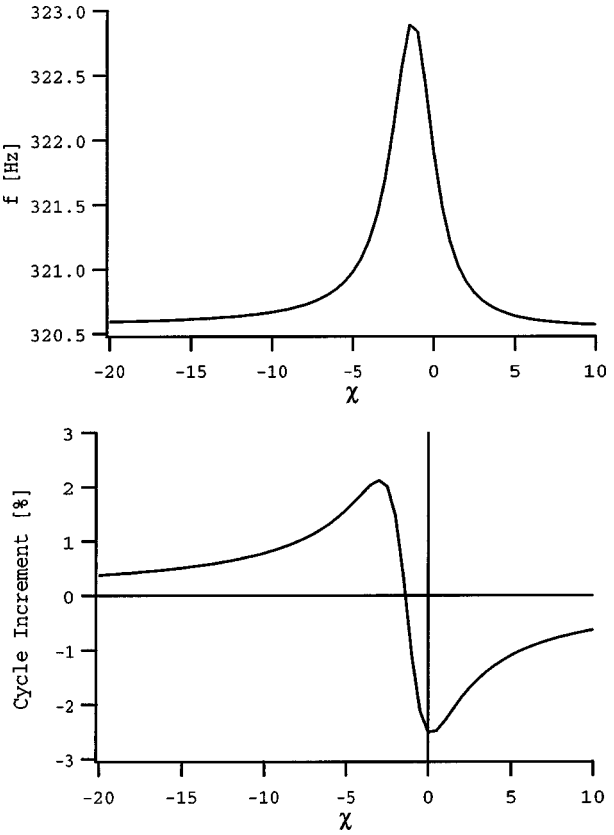

Fig. 7 Frequency f (top) and cycle increment ς (bottom) of first acoustic mode as a function of the nondimensionalized gradient χ of the press drop characteristic

The physics of the instability mechanism has been explained. An instability criterion analogous to the Rayleigh criterion has been formulated, which states that for instability to occur, high mass flow rates must correlate with low pressure difference between plenum and combustion chamber. A low-frequency lumped parameter formulation as well as a transfer matrix, required for network stability analysis, have been formulated for a burner with a bi-stable flame and solved analytically and numerically, respectively.

The onset and frequency of unstable combustion observed in an atmospheric combustion test rig correspond well with theoretical expectations and numerical results.

A simple rule for burner design and development of gas turbine operating concepts may be deduced from this study: burner flow instabilities are likely to occur in a combustion system whenever the pressure loss characteristic of burner and flame displays a negative slope, caused, e.g., by significant changes in the mode of flame stabilization. Therefore, burner designs or operating concepts which exhibit such behavior must be avoided.

Acknowledgment

Discussions with Hanspeter Knöpfel and Thomas Ruck on the possible relation between changes in burner pressure drop and combustion stability are gratefully acknowledged.

Nomenclature

A = cross-sectional area (m^2)
$\mathcal{H}$ = Helmholtz number
M = Mach number
P = power (W)
$\dot{Q}$ = rate of heat release per unit area (W/m^2)

$\Re$ = real part of complex number
$\Im$ = imaginary part of complex number
T = temperature (K)
V = volume (m^3)
c = speed of sound (m/s)
f = frequency (Hz)
i = $\sqrt{-1}$
k = wave number (1/m)
l = virtual length of burner (m)
$\dot{m}$ = mass flux through burner (kg/m^2-s)
p = pressure (Pa)
s = eigenvalue
t = time (s)
u = velocity (m/s)
Δp = (quasi-)stationary pressure drop across burner (Pa)
α = area ratio A_c/A_h
χ = gradient of pressure drop Δp w.r.t mass flux $\dot{m}_B$
ε = small quantity
γ = ratio of specific heats
ϕ = velocity potential (m^2/s)
λ = air excess ratio
ω = angular frequency (1/s)
ρ = density (kg/m^3)
ς = cycle increment
ξ = ratio of specific impedances $\rho_h c_h/\rho_c c_c$
ζ = pressure loss coefficient

Subscripts

B = burner
C = combustion chamber
P = plenum
X = exit
c = cold
f = just upstream of flame front
h = hot

References

[1] Deuker, E., 1995, ''Ein Beitrag zur Vorausberechnung des akustischen Stabilitätsverhaltens von Gasturbinen-Brennkammern mittels theoretischer und experimenteller Analyse von Brennkammerschwingungen,'' PhD thesis, RWTH Aachen.

[2] Fleifil, M., Annaswamy, A. M., Ghoneim, Z. A., and Ghoniem, A. F., 1996, ''Response of a Laminar Premixed Flame to Flow Oscillations: A Kinematic Model and Thermoacoustic Instability Results,'' Combust. Flame, **106**, pp. 487–510.

[3] Dowling, A. P., 1999, ''Thermoacoustic Instability,'' *6th Int. Congress on Sound and Vibration*, Copenhagen, Denmark, pp. 3277–3292.

[4] Krüger, U., Hoffmann, S., Krebs, W., Judith, H., Bohn, D., and Matouschek, G., 1998, ''Influence of Turbulence on the Dynamic Behavior of Premixed Flames,'' ASME Paper No. 98-GT-323.

[5] Keller, J. J., 1995, ''Thermoacoustic Oscillations in Combustion Chambers of Gas Turbines,'' AIAA J., **33**(12), pp. 2280–2287.

[6] Lieuwen, T., Torres, H., Johnson, C., and Zinn, B. T., 1999, ''A Mechanism of Combustion Instability in Lean Premixed Gas Turbine Combustors,'' ASME Paper No. 99-GT-003.

[7] Polifke, W., Paschereit, C. O., and Döbbeling, K., 1998, ''Coupling of Acoustic and Entropy Fluctuations in a Premixed Combustor With Choked Exit,'' *27th Symposium (International) on Combustion*, Boulder, CO, The Combustion Institute, Pittsburgh, PA.

[8] Schuermans, B. B. H., Polifke, W., and Paschereit, C. O., 1999, ''Modeling Transfer Matrices of Premixed Flames and Comparison with Experimental Result,'' ASME Paper No. 99-GT-132.

[9] Straub, D. L., and Richards, G. A., 1998, ''Effect of Fuel Nozzle Configuration on Premix Combustion Dynamics,'' ASME Paper No. 98-GT-492.

[10] Joos, F., Brunner, P., Schulte-Werning, B., Syed, K., and Eroglu, A., 1996, ''Development of the Sequential Combustion System for the ABB GT14/GT26 Gas Turbine Family,'' ASME Paper No. 96-GT-315.

[11] Ni, A., Polifke, W., and Joos, F., 2000, ''Ignition Delay Time Modulation as a Contribution to Thermo-Acoustic Instability in Sequential Combustion,'' ASME Paper No. 2000-GT-0103.

[12] Schadow, K. C., and Gutmark, E. J., 1992, ''Combustion Instability Related to Vortex Shedding in Dump Combustors and their Passive Control,'' Prog. Energy Combust. Sci., **8**, pp. 117–132.

[13] Gutmark, E. J., and Grinstein, F. F., 1999, ''Flow Control with Noncircular Jets,'' Annu. Rev. Fluid Mech., **(31)**, pp. 239–273.

[14] Paschereit, C. O., Flohr, P., Polifke, W., and Bockholts, M., 2000, ''Fluid Dynamic Instabilities in a Swirl Stabilized Burner and Their Effect on Heat Release Fluctuations,'' *Proceedings of Flow Induced Vibrations*, Luzern.

[15] Knöpfel, H. P., and Ruck, T., 1999, private communication.

[16] Sattelmayer, T., Felchlin, M. P., Haumann, J., Hellat, J., and Styner, D., 1992, ''Second-Generation Low-Emission Combustors for ABB Gas Turbines: Burner Development and Test at Atmospheric Pressure,'' ASME J. Eng. Gas Turbines Power, **114**, pp. 118–125.

[17] Polifke, W., Paschereit, C. O., and Döbbeling, K., 2001, ''Constructive and Destructive Interference of Acoustic and Entropy Waves in a Premixed Combustor With a Choked Exit,'' Int. J. Acoust. Vib., **6**(3), pp. 135–146.

[18] Paschereit, C. O., and Polifke, W., 1998, ''Investigation of the Thermo-Acoustic Characteristics of a Lean Premixed Gas Turbine Burner,'' ASME Paper No. 98-GT-582.

[19] Polifke, W., Hirsch, C., Fischer, A., and Sattelmayer, T., 2001, ''Instabilität eines Vormischbrenners mit nicht-monotoner Druckverlust-Kennlinie,'' *20. VDI Flammentag*, Essen, Sept., VDI Bericht **1629**, pp. 277–282.

[20] Greitzer, E. M., 1981, ''The Stability of Pumping Systems—The 1980 Freeman Scholar Lecture,'' ASME J. Fluids Eng., **103**, pp. 193–242.

[21] Yadigaroglu, G., 1981, ''Two-Phase Flow Instabilities and Propagation Phenomena,'' *Thermal and Fluids Engineering*, McGraw-Hill, New York.

[22] Chu, B. T., 1953, ''On the Generation of Pressure Waves at a Plane Flame Front,'' *4th Symposium (International) on Combustion*, pp. 603–612.

[23] Polifke, W., Paschereit, C. O., and Sattelmayer, T., 1997, ''A Universally Applicable Stability Criterion for Complex Thermoacoustic Systems,'' *18. Deutsch-Niederländischer Flammentag*, Delft, VDI Bericht, **1313**, pp. 455–460.

Y. Suzuki

T. Satoh

Japan Defense Agency,
Propulsion Division,
3rd Research Center,
Technical Research & Development Institute
(TRDI),
1-2-10 Sakae, Tachikawa,
Tokyo 190-8533 Japan

M. Kawano

Kawasaki Heavy Industries, Ltd.,
Research & Development Section 2,
Aero Engine Research & Development Center,
1-1 Kawasaki,
Akashi 673-8666 Japan

N. Akikawa

Y. Matsuda

Kawasaki Heavy Industries, Ltd.,
Material Engineering Section,
Aero Engine Engineering Department,
Gas Turbine Division,
1-1 Kawasaki,
Akashi 673-8666 Japan

Combustion Test Results of an Uncooled Combustor With Ceramic Matrix Composite Liner

A reverse-flow annular combustor with its casing diameter of 400 mm was developed using an uncooled liner made of a three-dimensional woven ceramic matrix composite. The combustor was tested using the TRDI high-pressure combustor test facility at the combustor maximum inlet and exit temperature of 723 K and 1623 K, respectively. Although both the material and combustion characteristics were evaluated in the test, this report focused on the combustion performance. As the results of the test, the high combustion efficiency and high heat release ratio of 99.9% and 1032 W/m^3/Pa were obtained at the design point. The latter figure is approximately twice as high as that of existing reverse-flow annular combustors. Pattern factor was sufficiently low and was less than 0.1. Surface temperatures of the liner wall were confirmed to be higher than the limit of the combustor made of existing heat-resistant metallic materials.
[DOI: 10.1115/1.1501916]

Introduction

To improve performance of gas turbine engines for advanced aircraft, high inlet and exit temperatures are imposed on the combustor with decreasing of its size and weight. To protect the liner wall of the combustor against the high temperature combustion gases, the amount of wall-cooling air might increase and more efficient wall-cooling techniques must be applied for the liner wall. However, the increasing of cooling air deteriorates engine performance and the complication of cooling techniques leads to high manufacturing cost.

In effort to develop a 50 kN-thrust class augmented turbofan engine ([1]), the transpiration-cooling liner wall was developed for a 1873 K (1600°C) level straight-through annular combustor with a heat release rate of about 1.1×10^3 W/m^3/Pa ([2]). In the program, an effort was made to minimize the amount of cooling air and manufacturing cost. However, if an uncooled liner made of nonmetallic materials would be applicable for the combustor, a higher engine performance and a lower manufacturing cost could be realized at the same time. Reference [3] mentioned an R&D program for applying ceramic matrix composite (CMC) liners to a straight-through combustor with emphasis on material.

Compared to the straight-through combustor, the reverse-flow type, suitable for turboshaft engines, has several disadvantages as to the liner cooling: a relatively large surface area to be cooled and a relatively low incoming-flow velocity to decrease the convection heat transfer on the cooling side. Because of these reasons, advantage of the uncooling was expected to be more vivid in the reverse case than in the straight-through case. Hence the reverse-flow type, rather than the straight-through type, was selected as a configuration of the present combustor.

In this study, a full-scale reverse-flow annular combustor was designed and fabricated. The uncooled liner made of three-dimensional woven CMC was applied to the combustor. The size of the combustor was designed to be smaller than that of the metallic combustor in the 900-shp class engine (named KSX) previously fabricated ([4]). The KSX combustor has a film-cooling liner wall made of metal and its heat release rate is 0.6×10^3 W/m^3/Pa. The present study aimed to achieve 1000-W/m^3/Pa-class heat release rate with a shorter liner than that employed in the KSX. The fabricated combustor was submitted to a combustion test using TRDI's combustor test facility. This paper describes summary of the design and test results focusing on the combustion performance rather than the material characteristics.

Outline of Combustor Design

Design Point and Targets. Conditions at the design point are listed in Table 1. All figures except the inlet air pressure were determined based on the system study of the 1400-shp-class turbo shaft engine. This class engine was expected to be realized using a combustor with a similar cross-sectional area of the KSX combustor while operating at a higher heat release rate of 1000-W/m^3/Pa-level. Although the inlet pressure presented at the table is lower than that of the system study of the 1400-shp engine, the maximum pressure, which can be provided by the test facility described later, has been selected as the inlet air pressure. However, the corrected air mass flow was adjusted to be the same as that of the 1400-shp combustor.

The design was carried out to make a shorter combustor than the KSX combustor (see Fig. 1) with its casing diameter of 400 mm and liner length of 115 mm. The design targets are listed in

Contributed by the International Gas Turbine Institute (IGTI) of THE AMERICAN SOCIETY OF MECHANICAL ENGINEERS for publication in the ASME JOURNAL OF ENGINEERING FOR GAS TURBINES AND POWER. Paper presented at the International Gas Turbine and Aeroengine Congress and Exhibition, New Orleans, LA, June 4–7, 2001; Paper 2001-GT-088. Manuscript received by IGTI, Dec. 2000, final revision, Mar. 2001. Associate Editor: R. Natole.

Table 1 Conditions at the design point

Inlet air temperature	723 K
Inlet air pressure	686 kPa
Exit gas temperature	1623 K
Air/fuel ratio	36.9

Table 2 Design targets

Heat release rate	$\geqslant 10^3$ W/m^3/Pa
Combustion efficiency	$\geqslant$99%
Pressure loss	$\leqslant$5%
Pattern factor	$\leqslant$0.13

Table 2. As shown in Fig. 2, the heat release rate in the table was placed at the top level among the current reverse-flow combustors. The other design targets were selected to realize high combustor exit temperature and high heat release rate, while satisfying the prerequisites of high combustion—efficiency and stability.

Design Results. The design results at the design point are shown in Table 3. The heat release rate and the pressure loss of the design results satisfied those of the design targets. The heat release rate at the design point was calculated by Eq. (3) described later. In the calculation, the fuel mass flow (G_f) was selected as the value at the design point. The combustion efficiency of η_b was set to be 100%. The combustor inlet air flow was determined for the corrected air mass flow to be the same value of the KSX combustor. The pressure loss was estimated by considering the pressure drops produced in the diffuser, across the liner, and during the combustion. The casing diameter was set to be the same as that of the KSX. All figures concerning dimensions indicates that the present combustor is more compact than the KSX combustor. To make air-fuel ratio in primary zone of 23.5 (the same value at the KSX), the air passed through the 16 air-blast fuel nozzles and 32 primary holes (whose diameter was about 10 mm) was set to be 60.3% of the total airflow. Another 34.4% was supplied through 64 dilution holes whose diameter was about 6 mm.

Experimental Apparatus and Tests

The Hardware Description. A full-annular reverse-flow combustor with the uncooled CMC liners was fabricated for testing to obtain confirmation of satisfactory performance to be expected. The cutaway view of the combustor is shown in Fig. 3. The inner and outer liners photographed before the testing are also shown in Fig. 4. These liners are made of the three-dimensional woven CMC material. SiC fiber (Tyranno ZMI™) was used as reinforcement. The concept of a three-dimensional woven structure is illustrated in Fig. 5. For SiC matrix formation, Polymer Impregnation and Pyrolysis (PIP) process ([5]) was applied. In this process, glass powder for crack sealing was also impregnated into the cavities of the three-dimensional woven preform.

An air-blast-type fuel injector (see Fig. 6) was employed in the present model. This injector had co-rotating double swirlers: core-air stream swirling in the same direction of outer-air stream. Springs were inserted between the liners and the fuel nozzles for easing the stress caused by difference of each thermal expansion.

Facility Installation. The combustor was installed in the combustor test facility located at the Sapporo test center of the TRDI. This facility (see Fig. 7) is supplied with air from a compressor capable of furnishing pressure of about 700 kPa and temperature of 473 K. After the supplied air enters the facility, the air is divided into two lines: a line for cooler and a line for heat exchanger. To mingle the airs through the cooling and heating lines at appropriate ratios, the inlet temperature for the test combustor can be varied from 333 K to 823 K rapidly. The inlet pressure is also changeable rapidly by a pressure regulator in the range between 108 and 686 kPa.

Measurement System and Test Method. The sensors equipped to the combustor are shown in Figs. 8 and 9. Pressure and temperature rakes were mounted at the combustion inlet. An array of water-cooled pressure/temperature rake probes movable in the circumferential direction was equipped at the exit. The pressure probes can serve also as gas sampling probes, with connection to an analyzer for determining concentrations of CO, CO_2, O_2, NO_x and unburned hydrocarbons. The combustion efficiency was obtained by the gas sampling. The surface temperature profile of the liner wall was measured by means of two arrays of 15 thermocouples stuck at two circumferential locations on both combustion- and cooling-side surfaces. The axial and circumferential locations of the thermocouples are indicated in Fig. 9. Ceramic bond was used to stick the thermocouples on the liner without boring holes. The thermo-paint was also employed to obtain temperature profiles on cooling sides of the inner and outer liners.

To obtain combustor performance at the operating conditions covered from the idle to the design point, the test conditions such as inlet temperature, inlet pressure, air mass flow and air-fuel ratio were varied parametrically with gradual increasing of the heat release rate. Pressure loss through the combustion chamber was obtained without burning.

After the performance test, the low cycle fatigue test was carried out. During the LCF test, the test condition was varied periodically from the idle to the design point. A 65-cycle test was finally carried out until the first detection of cracks by bore-scope inspection.

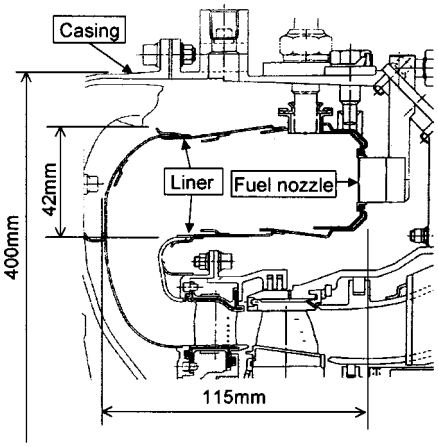

Fig. 1 Cross section of the KSX combustor

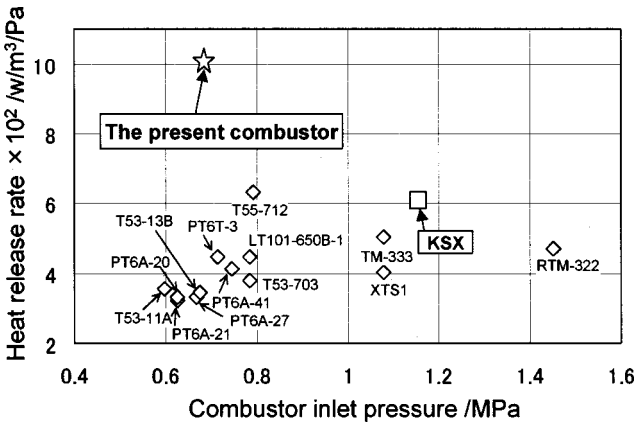

Fig. 2 Comparison of the heat release rate of the present combustor with other reverse flow combustors

Table 3 Design results

Heat release rate	1009 W/m^3/Pa
Combustor inlet air flow	1.55 kg/s
Pressure loss	4.7%
Casing diameter	400 mm
Inner liner diameter	255 mm
Outer liner diameter	336 mm
Liner length	97 mm
Air flow distribution	For primary zone 60.3% For intermediate and dilution zone 34.4% For turbine cooling 5.3%

Test Results and Discussion

Combustion Efficiency. The combustion efficiency η_b was calculated by

$$\eta_b = 100 - \frac{EI_{co}}{10} \times 0.2358 - \frac{EI_{UHC}}{10}. \quad (1)$$

The Emission Index of CO (EI_{CO}) and of unburned hydrocarbon (EI_{UHC}) were calculated by the equation presented in [6] using each gas molecular-weight measured by the gas sampling. To correlate the combustion efficiencies obtained at various operating conditions, the well-known reaction rate parameter θ ([7]) expressed as

$$\theta = \frac{\left(\frac{P3}{9.80665}\right)^{1.75} \times A\text{ref} \times D\text{ref}^{0.75} \times \exp\left(\frac{T3}{300}\right)}{Wa} \quad (2)$$

was employed. As an example, exhaust gas concentrations and η_b at the test condition of $\theta = 2.7 \times 10^7$ are shown in Table 4. The values of η_b at various test conditions are plotted against the θ parameter in Fig. 10. All of the data lie on a single line.

Figure 10 reveals excellent efficiencies of 99.9% at the design point and 99.5% at the idle condition. The efficiency at the design point satisfied the design target shown in Table 2 and the value at the idle point was also confirmed to be high enough. It is valuable to note that both efficiencies exceeded those of the KSX combustor: about 0.2% at the design point and about 1.5% at the idle (see the dotted line in Fig. 10). Concerning the excellent combustion efficiency at the design point, two reasons can be considerable. The one was decreasing of quenching beside the liner wall. The other was increased combustion gas temperature resulting from a higher surface temperature on the uncooled liners. For the good efficiency at the idle condition, two reasons can be considerable.

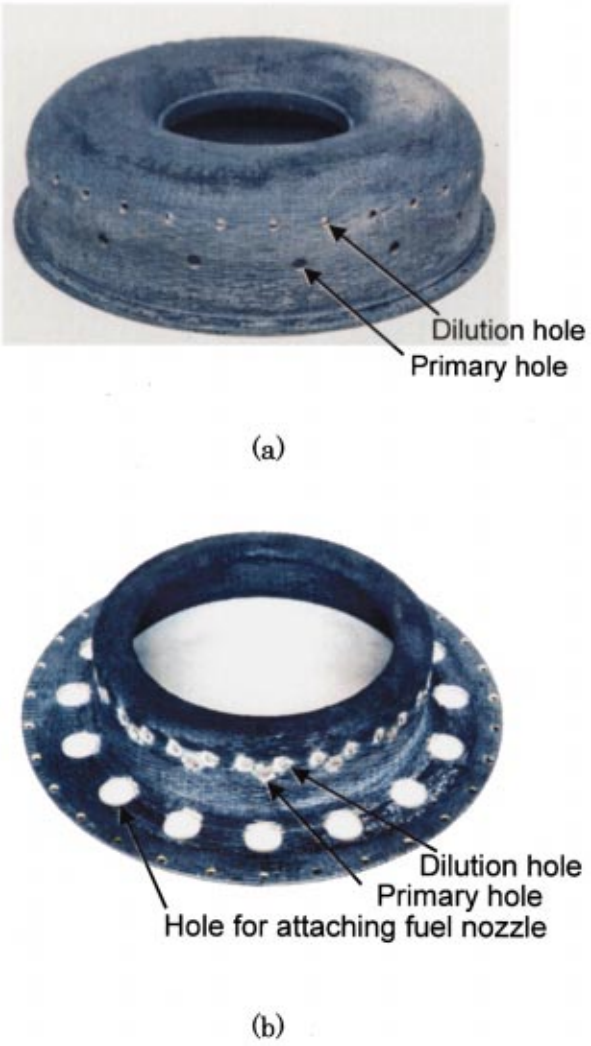

Fig. 4 Ceramic matrix composite liners, (*a*) outer liner, (*b*) inner liner

The one was the decreasing of quenching, same as the above. The other was recirculation in the combustion chamber strengthened by increasing air mass flow through primary holes.

Maximum Exit Temperature and Heat Release Rate. The maximum value of the averaged combustor exit temperature was calculated by the combustion efficiency at the design point and the lower specific energy of fuel supplied per unit time. The calculated value of 1616 K was almost equal to the design condition

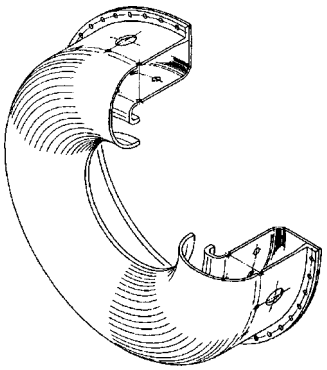

Fig. 3 Cutaway view of the combustor

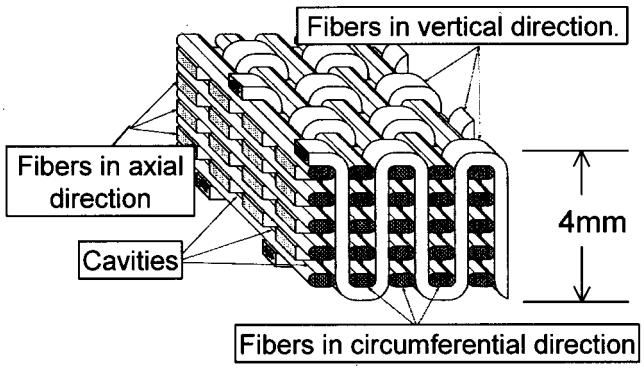

Fig. 5 Three-dimensional woven ceramic matrix composite

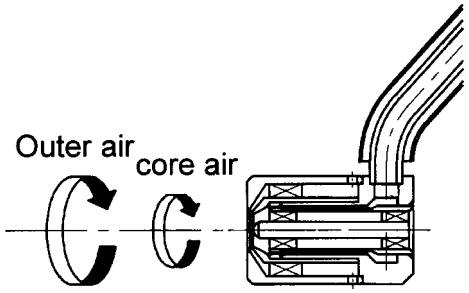

Fig. 6 Air-blast-type fuel injector

shown in Table 1. The heat release rate L_b is the total calorification per unit volume and unit time, and is calculated by

$$L_b = \frac{G_f \times H_u \times \eta_b}{V_l \times P3}. \tag{3}$$

At the design point, Eq. (3) gave us the heat release rate of 1032 W/m^3/Pa (9×10^7 kcal/hr/m^3/atm) that was slightly larger than the design target shown in Table 2.

Pressure Loss. The pressure losses obtained in the test are plotted against the corrected air flow determined by

$$Wa^* = \frac{Wa\sqrt{\frac{T3}{To}}}{\frac{P3}{Po}} \tag{4}$$

(see Fig. 11). Figure 11 indicates that the value at the design point estimated from the experimental data is 0.3% less than the design result shown in Table 3. Under burning condition, the fundamental loss due to combustion of about 0.1% would be added to the cold-flow case. Even though we consider the increment of this 0.1%, the pressure loss is still less than the design result.

Combustor Exit Temperature Distribution and Pattern Factor. Figure 12 shows an example of the temperature distribution obtained at the combustor exit. To evaluate nonuniformity of the distribution, the pattern factor

$$PF = \frac{T4_{\max} - T4_{\text{ave}}}{T4_{\text{ave}} - T3} \tag{5}$$

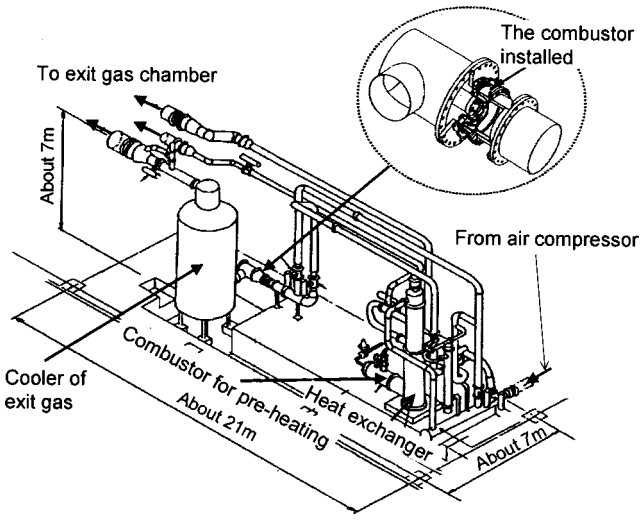

Fig. 7 Test facility

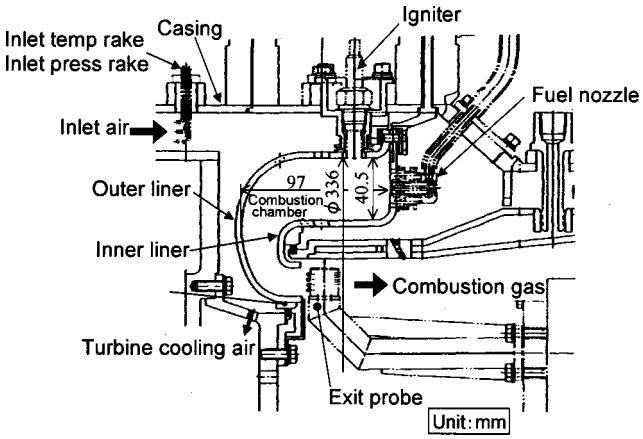

Fig. 8 Cross section of the combustor installed in the test facility, including arrangement of sensors

was calculated, where the maximum temperature $T4_{\max}$ and the average temperature $T4_{\text{ave}}$ at the combustor exit were derived from the distribution as shown in Fig. 12. From Ref. [4], PF has been considered to have a strong correlation with a parameter named ϕ, which is expressed as

$$\phi = Wa^a \times P3^b \times T3^c \times \Delta T^d. \tag{6}$$

When the test data are plotted in ϕ and Wa coordinates using Eqs. (5) and (6) while all variables except Wa are almost constant, the value of power "*a*" can be determined by specifying a correlation curve between PF and Wa with an exponential equation ($PF = C \times Wa^a$). The other powers *b*, *c*, and *d* are also determined by the same way. The values of the powers finally employed are shown in Fig. 13.

From all the temperature distributions obtained, it was found that the local hot area including $T4_{\max}$ always appeared at the same zone in circumferential location (see the Zone A in Fig. 12). The amount of air flow through both primary and dilution holes located upstream of the hot area was diminished, because the thermocouple cables stuck on the combustion-side surface passed through these holes. As a result, the local air-fuel ratio decreased and then the local hot area was created.

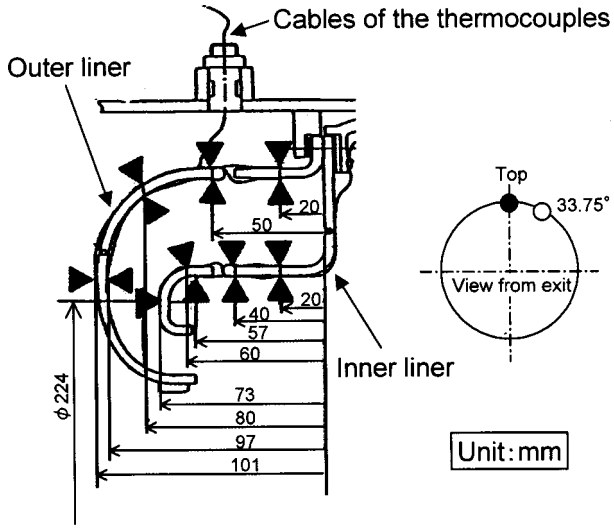

Fig. 9 Surface temperature measuring points. (▲=the measuring points in axial location, ●=fuel nozzle point in circumferential location, ○=point between fuel nozzles in circumferential location.)

Table 4 The result of gas sampling at $\theta = 2.7 \times 10^7$

CO (ppm)	CO_2 (%)	O_2 (%)	NO_x (ppm)	UHC (ppmC)	η_b (%)
73.34	2.81	16.76	90.8	0.12	99.87

To estimate the pattern factor (PF) at the design point, the values of PF were plotted against ϕ after removing the data in the local hot area mentioned above (see Fig. 13). From the figure, the design target value (see Table 2) is well satisfied by the pattern factor of 0.093 at value of ϕ corresponding to the design point.

Surface-Temperature Distributions and Low Cycle Fatigue Test Results. The combustion and cooling-side temperatures on the inner liner at the design point were plotted against distance from the surface for the fuel nozzle to be attached (see Fig. 14). The estimated hot gas temperatures along the combustor axis in the primary and dilution zones were also depicted in Fig. 14 as reference temperatures. As already described, the temperatures were obtained by the thermocouples attached to the liner surface (see Fig. 9). When the heat release rate increased, some of the thermocouples on combustion side were separated from the surface. Hence fewer data points are plotted for the combustion side. At the design point, the temperature of the combustion side reached to about 1600 K, which was far beyond the temperature capability of the metallic material. The measured temperature on the combustion side was considered to be reliable values, because the glass layer, which was formed in excess of about 1500 K, was observed. The maximum temperature on the cooling side was about 1000 K. It was also considered to be appropriate, since the thermo-paint indicated about 1000–1100 K at the same place.

After the 65-cycle low cycle fatigue test was carried out following the performance test, some cracks near dilution holes were

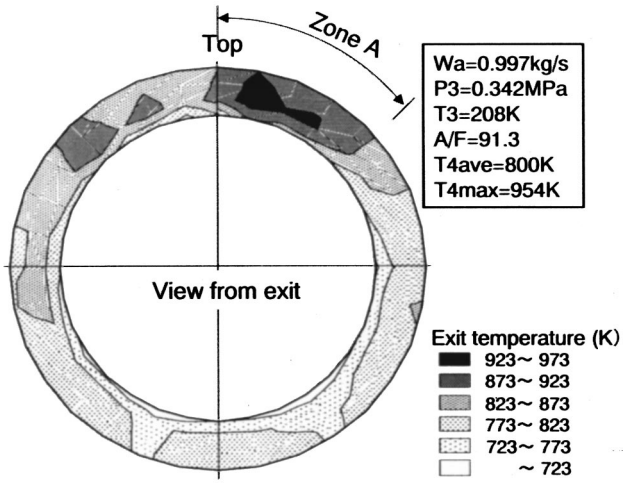

Fig. 12 Temperature distribution at combustor exit

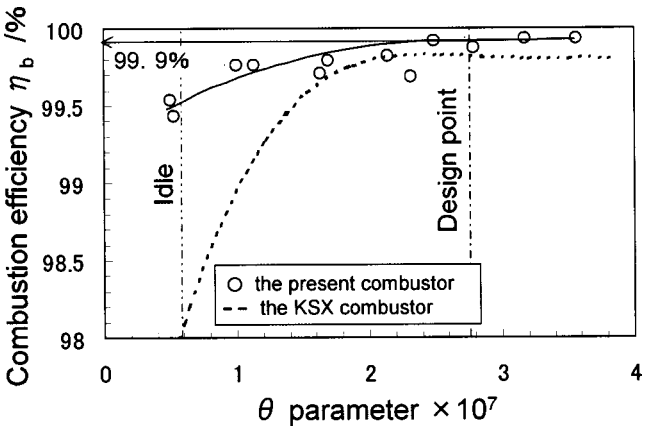

Fig. 10 Combustion efficiency against 0 parameter

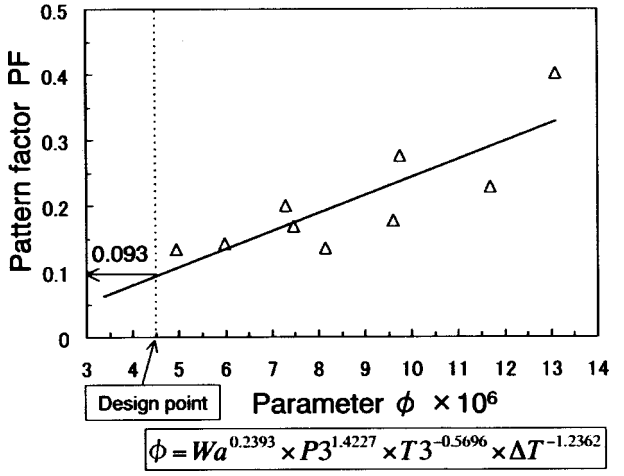

Fig. 13 Pattern factor against parameter ϕ

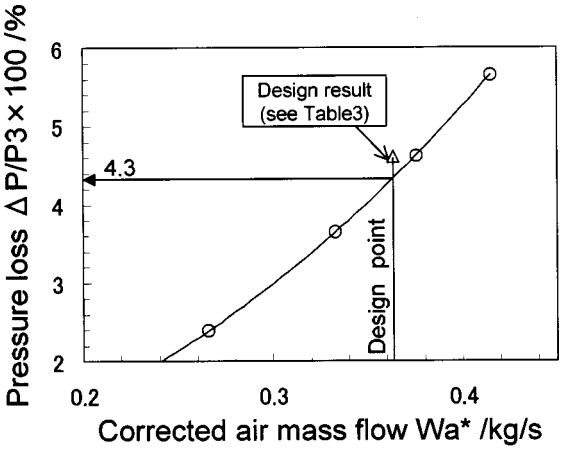

Fig. 11 Pressure loss against corrected air mass flow

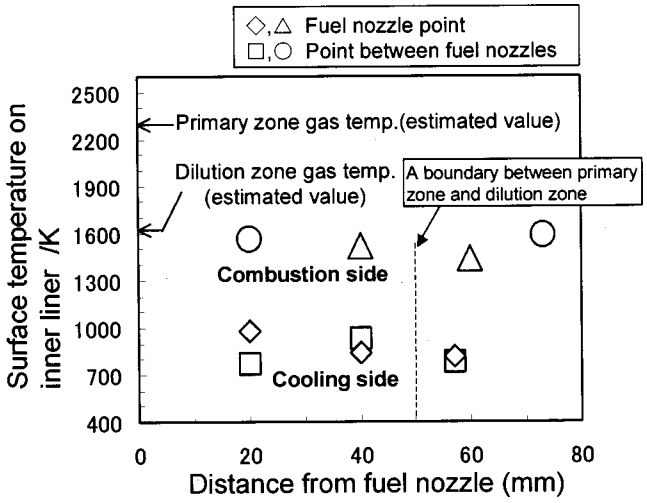

Fig. 14 Surface temperature of the inner liner

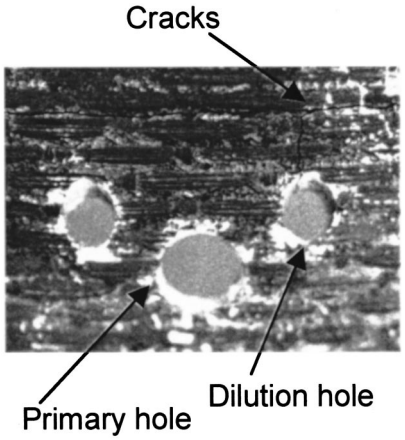

Fig. 15 Cracks near dilution holes on the inner liner

detected on the inner liner by visual inspection (see Fig. 15). On the outer liner, a few cracks were detected near a primary hole and by the nondestructive inspection. But exfoliation of the linear wall that might harm turbine blades didn't exist. This crack formation was caused due to the repeated thermal stress by the temperature gap of about 600 K between each side of the linear wall.

Conclusions

With a view to realizing a high-heat-release rate combustion in the turboshaft engines, a full-annular reverse-flow combustor with uncooled liners made of a three-dimensional woven ceramic matrix composite (CMC) was fabricated. Evaluation of the combustion performance was carried out in terms of heat release rate, combustion efficiency, pressure loss through the combustion chamber, and pattern factor derived from the combustor exit-temperature distribution. A surface temperature survey on the CMC liner was also performed with a set of crack detection. Confirmation was obtained on its combustion performance fully satisfying all design targets with exceeding performance of the larger 900-shp-class metallic combustor previously fabricated. Although some cracks were found on the liners, these excellent performances gave a considerably higher heat release rate (1032 $W/m^3/Pa$) than that of existing metallic combustors.

Additional work will be focused at improving durability of the combustor to apply for a future gas turbine engine. To achieve this, a further development of CMC is necessary with superior strength reliability by evaluating the durability of the three-dimensional woven CMC material, improving the process to increase strength, and reduce thermal stress. The surface temperature profile and crack formations of the CMC liners observed in the present study would provide useful information to consider the future development.

Nomenclature

a, b, c, d = powers in Eq. (6)
A_{ref} = combustor reference area (m^2)
D_{ref} = maximum diameter of combustor casing (m)
C = constant
EI_{CO} = Emission Index of CO
EI_{UHC} = Emission Index of unburned hydrocarbon
G_f = mass flow rate of fuel (kg/s)
H_u = lower specific energy of fuel (JP-4) (J/kg)
L_b = heat release rate ($W/m^3/Pa$)
$P0$ = sea-level static pressure (Pa)
$P3$ = combustor inlet air pressure (Pa)
PF = pattern factor
$T0$ = sea-level static temperature (K)
$T3$ = combustor inlet air temperature (K)
$T4$ = combustor exit gas temperature (K)
V_1 = combustion chamber volume (m^3)
Wa = combustor inlet air mass flow (kg/s)
Wa* = corrected combustor inlet air mass flow (kg/s)
ΔT = temperature rise through combustion chamber ($T4_{ave} - T3$) (K)
ΔP = deference of inlet and exit pressure
η_b = combustion efficiency
θ = reaction rate parameter (θ parameter)
ϕ = parameter to estimate the PF at the design point (see Eq. (6))

Subscripts

ave = average condition
max = maximum condition

References

[1] Miyake, M., 2000, "Engine Development in Japan Defense Agency," J Gas Turb. Soc. Jpn., **28**(5), pp. 352–356 (In Japanese).
[2] Sugiyama, Y., Takamura, R., Koide, Y., Watanabe, T., Hoshi, J., Kuyama, T., Kawano, M., and Nakahata, T., 1995, "Research and Development of 1600°C-Level Combustor With High Release Rate," ISABE 95-7099, *Proceedings of Twelfth International Symposium on Air Breathing Engines*, F. Billig, ed., AIAA, Reston, Va, pp. 1077–1087.
[3] Nishino, K., Igashira, K.-I., Take, K., and Suemitsu, T., 1999, "Development of a Combustor Liner Composed of Ceramic Matrix Composite (CMC)," ASME J. Eng. Gas Turbines Power, **121**, pp. 12–17.
[4] Kawano, M., et al., 1994, "Development of Reverse-Flow Annular Combustor for Small Turboshaft Engines," *Proceedings of the 34th Conference on Aerospace Propulsion*, Japan Society of Aeronautical and Space Science, Tokyo, Japan, pp. 170–175 (In Japanese).
[5] Matsuda, Y., Akikawa, N., and Satoh, T., 2001, "Manufacturing of 3-D Woven SiCf/SiC Composite Combustor Liner," *Ceramic Engineering and Science Proceedings*, American Ceramic Society, Westerville, OH, **22**, No. 3, pp. 463–470.
[6] Society of Automotive Engineers, Inc., 1980, "Procedure for the Continuous Sampling and Measurement of Gaseous Emissions From Aircraft Turbine Engines," Aerospace Recommended Practice, Paper No. ARP 1256A.
[7] Lefebvre, A. H., 1988, *Gas Turbine Combustion*, McGraw-Hill, New York.

Studies of Jet Fuel Freezing by Differential Scanning Calorimetry and Cold-Stage Microscopy

N. Widmor
J. S. Ervin
S. Zabarnick
M. Vangness

Mechanical Engineering Department,
University of Dayton,
300 College Park,
Dayton, OH 45469-0210

Aircraft which fly at high altitude or encounter extremely cold environments have the potential for fuel freezing and, consequently, catastrophic failure of the fuel system. Thus, it is important to study the freezing of hydrocarbon jet fuels. In the current work, a differential scanning calorimeter is used to study thermal characteristics and phase transitions of freezing jet fuel. In addition, a cold-stage microscope is used to record images of the resulting crystalline microstructure. A kinetic representation for the freezing of jet fuel is presented. Kinetic mechanisms that describe the liquid-to-solid phase transformation in fuels are necessary for the development of computational fluid dynamics models that can be used by aircraft designers. [DOI: 10.1115/1.1492836]

Introduction

Operation of aircraft at high altitude for long periods subjects jet fuel to low temperatures. These conditions increase the fuel viscosity and, thus, limit the ability of the fuel to flow. Moreover, prolonged exposure to low temperatures can cause the fuel to solidify. The U.S. Air Force uses a specialty fuel, JPTS, which not only has a low freeze-point temperature, but also has excellent thermal-oxidative stability properties. Unfortunately, JPTS has logistical disadvantages and is more costly than JP-8, the primary jet fuel of the U.S. Air Force ([1]). The thermal-oxidative stability characteristics of JP-8 have been addressed by the JP-8 + 100 additive package. However, the low-temperature properties of JP-8 have gone unstudied until recently ([1]). In addition, commercial aircraft makers and commercial airlines desire to avoid fuel freezing under severe environmental conditions. Thus, there is both military and commercial interest in low-temperature jet fuel research.

With jet fuel at low temperatures, paraffin crystallization can cause line or filter blockage. An economical alternative to the use of specialty fuels is the employment of relatively inexpensive fuel additives. Additives which enhance the low-temperature behavior of jet fuels have not been used previously in aircraft. Thus, there is a need to increase our fundamental understanding of how newly developed additives influence the freezing of jet fuel.

There have been numerous low-temperature studies ([2–4]) of diesel fuels, crude oils, and lubricating oils which have used differential scanning calorimetry (DSC) alone or in combination with microscopy. In contrast, there have been relatively few such studies of the freezing of jet fuel. Moreover, it is believed that the present work is one of the first investigations ([5]) to examine the freezing of jet fuel using a DSC in combination with a cold-stage microscope. The DSC measures the heat flow from (to) a material as it is cooled (heated) and can indicate phase transition temperatures and determine thermodynamic properties such as specific heat and heat of fusion. Such properties are important for numerical simulation of the phase-change dynamics. The cold-stage microscope cools the fuel and simultaneously provides images of the fuel microstructure that assist the interpretation of DSC measurements.

The understanding of the freezing of jet fuels is complicated by the fact that individual jet fuel samples possess a range of freezing characteristics that results from the varying source petroleum and refinery processing. In addition, jet fuels consist not of a single compound, but are a complex hydrocarbon mixture whose behavior can be further complicated by the presence of additives. The effects of changing concentrations of species that continuously precipitate from solution during the freezing process makes the phase-change process more difficult to understand. In addition, the growth of precipitating structures in hydrocarbon fuels depends strongly on the cooling rate. The DSC has been used in previous research ([6]) of the freezing of hydrocarbon blends to indicate the relative degree of freezing with respect to temperature and cooling rate. A semi-empirical kinetic model for nonisothermal crystallization of binary, isomorphous mixtures was developed, and it was believed that this model could be extended to multicomponent mixtures. Similar techniques involving the DSC are used here for jet fuel. In the current work, the use of a semi-empirical kinetic representation for the freezing of jet fuel is considered. Kinetic mechanisms are necessary for the development of computational fluid dynamics models that can be used in aircraft design. Additives alter the behavior of fuels, and the DSC is also used to analyze the effects of additives on jet fuel freezing. The combination of the DSC and microscope not only increase the understanding of hydrocarbon freezing processes but also assist the screening of low-temperature additives.

Experimental

For the differential scanning calorimetry (DSC) studies (TA Instruments, DSC 2920) performed here, open aluminum pans were used for both the sample and reference. The DSC measures the temperature difference between the sample and reference pans and reports the heat flow from the sample. A syringe is used to fill the sample pan (20 μl), and the mass is recorded. A liquid nitrogen cooling accessory (LNCA) cools the sample to a prescribed temperature and allows it to equilibrate above temperatures expected for fuel freezing. The sample is then further cooled at a prescribed rate over a given temperature range. (The same process can be conducted for melting.) At the relatively low temperatures of this study, the maximum cooling rate of the DSC is limited to 5.0 K/min. The reproducibility of the temperature measurement of the DSC is within 0.2 K.

A cold-stage microscope system is used to obtain crystal growth images during the freezing process. Here, the microscope (Olympus BX50) incorporates phase contrast and cross-polarization optics. A 10X objective lens is used together with a digital camera (Sony DKS). The sample (20 μL) is placed on a microscope slide with an elevated cover slip, and the slide resides

Contributed by the International Gas Turbine Institute (IGTI) of THE AMERICAN SOCIETY OF MECHANICAL ENGINEERS for publication in the ASME JOURNAL OF ENGINEERING FOR GAS TURBINES AND POWER. Paper presented at the International Gas Turbine and Aeroengine Congress and Exhibition, New Orleans, LA, June 4–7, 2001; Paper 2001-GT-378. Manuscript received by IGTI, Dec. 2000, final revision, Mar. 2001. Associate Editor: R. Natole.

Table 1 Freeze point, cloud point, and pour point data

Fuel	Freeze Point Temperature (K)	Cloud Point Temperature (K)	Pour Point Temperature (K)
F2827	229.8	225.2	220.2
F3219	226.9	222.3	217.2
F3775	218.7	215.9	212.2

on the cold stage (Linkam) that cools the fuel. Using liquid nitrogen as the coolant, the sample is cooled at the same rate as the DSC while images of the fuel are recorded. Two Jet A fuel samples (F2827 and F3219) and one JPTS fuel sample (F3775) are used in these experiments.

Cloud point, pour point, and freeze point temperatures were measured using a Phase Technology Series 70V Petroleum Analyzer (using ASTM D5773-95, D5949-96, and DD5972-96, respectively). The pour point measurements were obtained at 1 K intervals, and appear in Table 1. It is important to note that the ASTM freeze point temperature is the measured temperature at which the last solid crystals vanish during *heating*. Thus, the freeze point temperature is actually a *melting* temperature.

Kinetics of Fuel Crystallization. Fuel freezing in aircraft fuel systems is generally a nonisothermal process. Moreover, the cooling rate is believed to strongly influence crystal growth and the resulting microstructure of the precipitating phase. Hammami and Mehrotra [6] performed studies of nonisothermal crystallization involving binary mixtures of even and odd-numbered normal-alkanes. In their analysis, they combined Eq. (1) from the theory of Ozawa [7]

$$x_r = \frac{x(T)}{x_\infty} = 1 - \exp\left(\frac{-\chi(T)}{|\lambda|^m}\right) \tag{1}$$

with a semi-empirical expression for the crystallization function, $\chi(T)$, defined as

$$\chi(T) = C_1 (T_m^0 - T)^{m+1} \exp\left(\frac{-C_2}{T(T_m^0 - T)^2}\right). \tag{2}$$

In Eq. (1), x_r is the relative crystallinity, x_∞ is the crystallinity at the termination of the crystallization process, x is the crystallinity at temperature T (K), and λ is the constant cooling rate (K/min). With regard to Eq. (2), Hammami and Mehrotra [6] represented C_1 as a constant that is not strongly temperature dependent and C_2 as a constant associated with the free energy of nucleation. In addition, T_m^0 (K) represents the measured equilibrium melting temperature. From preliminary work, we have found T_m^0 to be well defined and reproducible, and this observation is supported by experiments conducted elsewhere ([8]) using crystalline polymers. The melting point, rather than the temperature associated with the inception of paraffin crystals, is often assumed to be a more accurate measure of the equilibrium solid-liquid coexistence temperature ([6]). Equation (2) was derived ([9]) assuming homogeneous crystallization and one-dimensional crystal growth. Hammami and Mehrotra [6], combined Eqs. (1) and (2) with a set of mixing rules to model the crystallization kinetics of a binary, isomorphous mixture. Moreover, they believed that their model could be extended to a multicomponent isomorphous mixture. The current work presents an extension of their model to represent the kinetics of crystallization of normal alkanes from freezing jet fuel samples.

DSC measurements provide plots of crystallization exotherms for jet fuel samples. The exotherms can be integrated ([6]) with respect to temperature and can provide values of the relative crystallinity, $x_r(T)$:

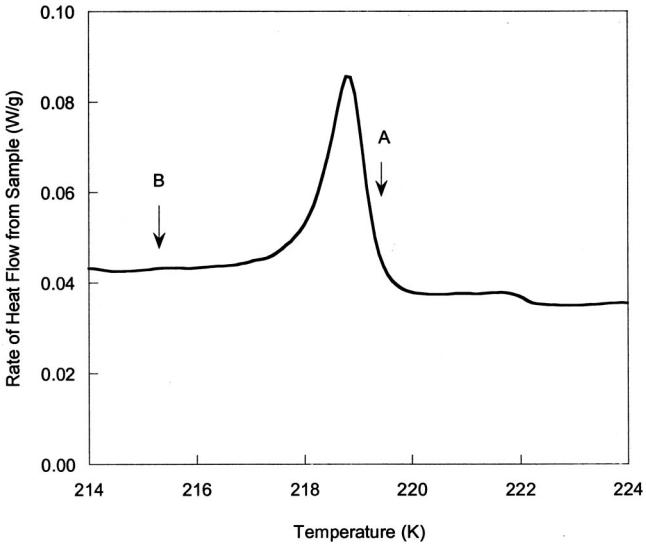

Fig. 1 Jet A (F3219) exotherm measured by differential scanning calorimetry (DSC) at a 1.0 K/min cooling rate. Indicated locations along the curve correspond to images of Fig. 2.

$$x_r = \frac{\int_{T_S}^{T} \left(\frac{dQ}{dt}\right) dT}{\int_{T_S}^{T_\infty} \left(\frac{dQ}{dT}\right) dT}. \tag{3}$$

In Eq. (3), T_s (K) is the temperature associated with the initiation of crystal formation and T_∞ (K) represents the temperature at which crystal formation is complete. Thus, x_r represents the extent of completion of the crystallization process during freezing. In the current work, exotherms and values of x_r (Eq. (3)) were generated using cooling rates of 0.25, 0.5, 1.0, 2.5, and 5.0 K/min.

Results and Discussion

DSC Exotherms for Jet Fuels. Figure 1 shows DSC measurements of the rate of heat evolution together with the fuel temperature from a cooled Jet A fuel sample (F3219). Below 228 K, the jet fuel of Fig. 1 was cooled at a constant rate of 1.0 K/min. Locations along the cooling rate-temperature curve are assigned letters which correspond to the microscope images of Fig. 2. Moving from right-to-left as the fuel cools, the exotherm begins to rise above the baseline as crystals begin to form in the fuel. Consequently, Fig. 2(*a*) shows the appearance of initial fuel crystals. The crystals of Fig. 2(*a*) are largely in the shape of plates, and the formation of similarly shaped wax plates have been observed in studies of the freezing of diesel fuels ([10]). In addition to the plates, Fig. 2(*a*) shows that there are a few ''ribbon-shaped'' crystals. Relatively large normal alkanes have heat of fusion values that are significantly larger than other classes of fuel species (iso-alkanes, cyclo-alkanes, and aromatics). As a consequence, it is believed that most of the exothermic response is due to normal alkane crystallization, and we expect that the large normal alkanes in the jet fuel will crystallize first (n-C_{16} to n-C_{18}) ([5]). Figure 1 shows that the large peak in the exotherm is centered near 219 K. When the cooling curve of Fig. 1 returns to the baseline, the freezing process is considered complete. After the exotherm returns to the baseline, Fig. 2(*b*) (location B Fig. 1) shows that crystals are generally larger than those imaged at the higher temperature of Fig. 2(*a*) (location A Fig. 1). In addition, Fig. 2(*b*) shows that the crystal population increases at the lower temperature (location B Fig. 1).

As jet fuels come from a variety of refinery sources, they may have different low-temperature characteristics. Thus, it is impor-

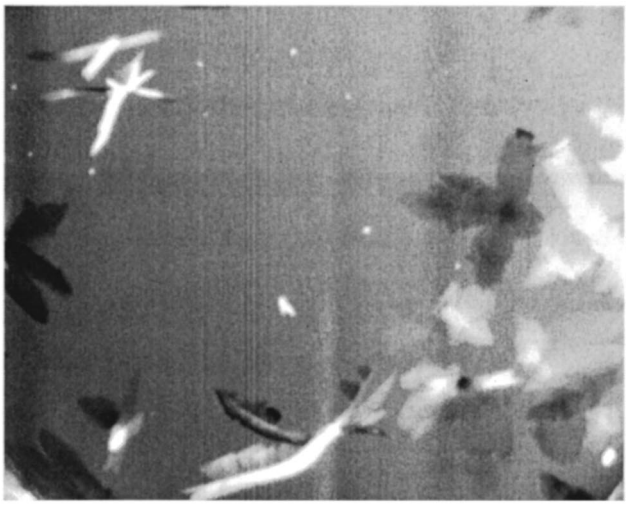

(*a*)

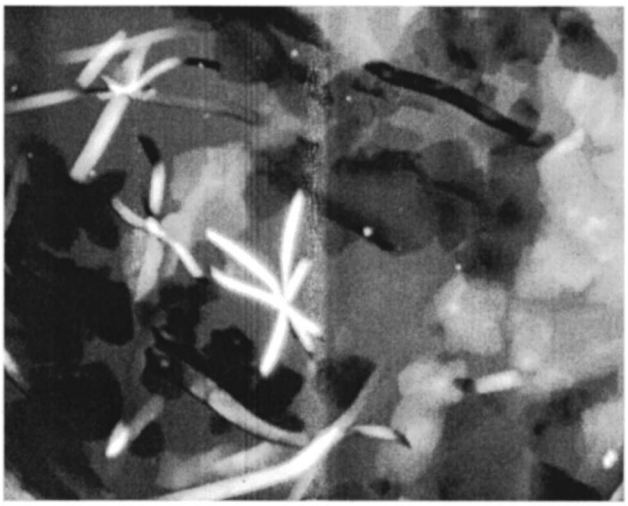

(*b*)

Fig. 2 Images of fuel crystals forming using cold-stage microscopy with a cooling rate of 1.0 K/min. (*a*) and (*b*) correspond to points on the curve of Fig. 1 (magnification 40×).

tant to study different jet fuel samples. Figure 3 shows DSC curves (cooling rate of 1.0 K/min) for two Jet A fuel samples (F3219 and F2827) and one sample of JPTS (F3775). The large JPTS peak (A3) is located at a lower temperature than that of the Jet A peaks (A1 and A2). JPTS fuel is designed for high altitude, low temperature flight, and its freeze point specification is 6 K lower than that of Jet A. Thus, the location of the JPTS exothermic peak relative to the Jet A samples is expected. The ''shoulders'' (labeled B1–B3) at the base of the peaks correspond to the measured cloud point temperatures (temperatures where crystallization begins, Table 1) of the fuel samples. Beyond the cloud point temperature, the heat flow curve reaches a maximum, and the fuel sample continues to solidify. On the low-temperature side of the exothermic peak, the measured pour points (Table 1) are located where the exotherm returns to the baseline. The heat flow curve of fuel F2827 is centered near 223 K with a freeze point near 230 K. For fuel F3219, the large exothermic peak is located near 218 K and has a freeze point temperature near 226 K, which is just at the JP-8 specification limit. Thus, F3219 is a ''worst case'' fuel for JP-8 low-temperature behavior and is being used in the fuel additive studies. Figure 3 shows three symbols on the

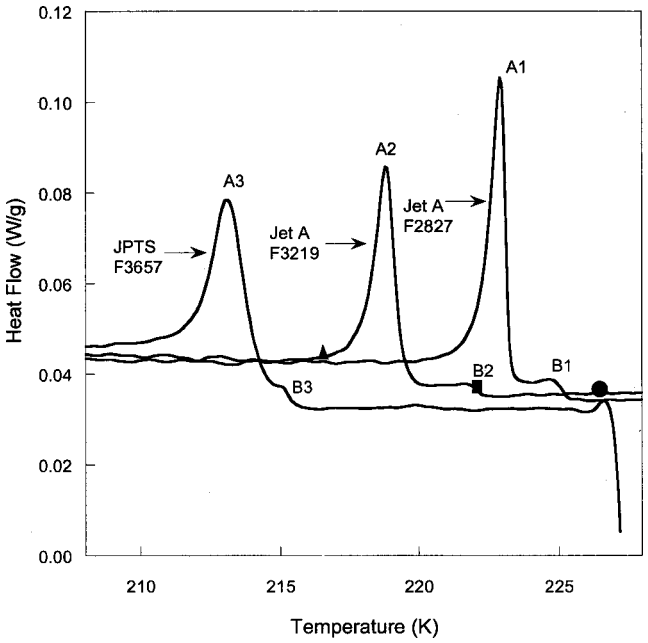

Fig. 3 Differential scanning calorimetry (DSC) measurements for three fuel samples at a cooling rate of 1 K/min

F3219 curve to further clarify the concepts of freeze point (circle), cloud point (rectangle), and pour point (triangle).

Kinetics of Liquid-Solid Phase Transformation. Figure 4 shows calculated and measured values of the relative freezing fraction for the JPTS (F3775) fuel sample for cooling rates between 0.5 K/min and 5.0 K/min. A more satisfactory fit of the kinetic expression of Eqs. (1) and (2) was obtained by introducing another variable, n, to replace the exponent, $m+1$, on term $(T_m^0 - T)$ of Eq. (2). The added complexity of replacing $m+1$ in Eq. (2) with n is reasonable because Eqs. (1) and (2) were originally intended for use in relatively simple binary n-alkane mixtures rather than in more complex mixtures like jet fuel. (The variable m was otherwise retained in Eq. (1).) The new variable n was used in all nonlinear regression analyses that were performed using commercially available software (Table Curve 3D, Jandel Scientific) that employs the Levenburg-Marquardt procedure ([11]).

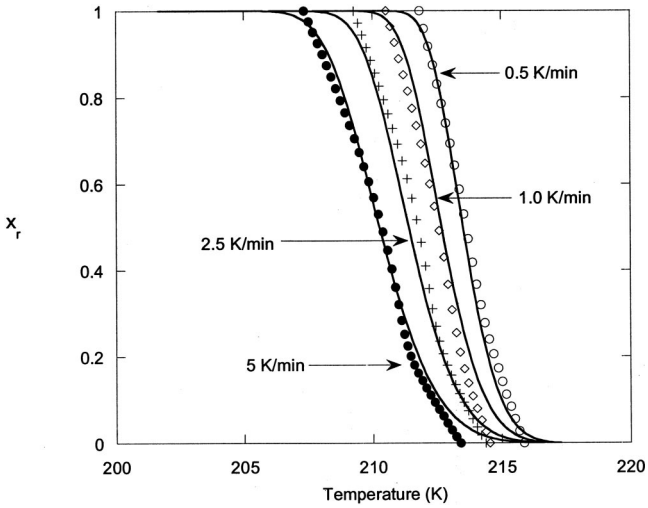

Fig. 4 Predicted and measured relative freezing fraction for JPTS (F3775) with different cooling rates

Table 2 Parameters obtained by nonlinear regression and used in Eqs. (1) and (2)

Fuel	C_1	C_2	m	n
JPTS	1.67904×10-6	22870.4	1.20197	6.35765
Jet A (F3219)	2.24352×10-4	10.8435	0.834486	4.28286

Figure 4 shows that the nonlinear fit (Table 2) of Eqs. (2) and (3) provides a reasonable description of the freezing process of JPTS for cooling rates between 0.5 and 5.0 K/min.

Locations along the temperature axis ($x_r=0$) of Fig. 4 essentially represent the initiation of fuel crystallization. Figure 4 shows that as the cooling rate is increased from 0.5 K/min to 5.0 K/min, the measured temperature at which freezing begins is shifted to lower temperatures. The kinetic model overpredicts the temperature of freezing, and the overprediction is greatest for the cooling rate of 5.0 K/min. However, the model does reflect the downward shift in freezing initiation temperatures as the cooling rate is increased. The shift in freezing initiation to lower temperatures is believed to be a consequence of supercooling of the fuel. Hydrocarbon mixtures which contain larger n-alkane species ($C_{25}-C_{50}$) and are supercooled show a similar shift in temperature as the cooling rate is increased ([6]). In a different experiment ([12]), detailed images of this JPTS jet fuel (F3775) freezing under conditions of a two-dimensional buoyancy-induced flow with imposed surface temperatures were obtained. Freezing began on a cooled aluminum test surface (cooling rate of 1 K/min) at 215.1 K (±0.5 K). Moreover, Fig. 4 shows that at a cooling rate of 1.0 K/min that the JPTS fuel begins to freeze in the DSC experiment at 214.6 K. Thus, with the same cooling rate, the temperature at which the freezing of JPTS begins is essentially the same in two different experiments. The agreement of initial crystallization temperatures between essentially nonflowing (DSC) and flowing experiments illustrates the potential for using DSC measurements to develop correlations that can be used in numerical simulations to predict phase-change behavior over a range of flow conditions. In computational fluid dynamics simulations of the freezing of jet fuel, it is desirable to incorporate the effects of supercooling. The values given in Table 2 correspond to the constants of Eqs. (1) and (2), which can be incorporated within future computational simulations in which x_r is a progress variable and supercooling behavior can be represented. Numerical simulations will assist in the interpretation of experiments and the design of fuel systems that have a wide range of flow and cooling conditions.

Figure 5 shows the calculated and measured relative freezing fraction for the Jet A (F3219) fuel sample. As with Fig. 4 (JPTS fuel) for each cooling rate, the fit of Eq. (1) is better near $x_r=1$ than that near crystal initiation ($x_r=0$). With the values listed in Table 2 for this fuel, Eq. (1) overpredicts the temperature of the onset of freezing, and the difference between measurement and prediction increases with increasing cooling rate. Although the present kinetic model overpredicts the temperature of crystal initiation, the discrepancy is not fatal. This kinetic representation still provides a reasonable representation for x_r beyond crystal initiation and can be used in numerical simulations of fuel freezing. In the experiment ([12]) used for the visualization of the freezing of flowing Jet A fuel (F3219), freezing begins on the aluminum test surface (cooling rate of 1 K/min) at 220.5 K (±0.5 K). At a cooling rate of 1.0 K/min, Fig. 5 shows that the Jet A fuel (F3219) initially freezes in the DSC experiment at 221.6 K. As in the case of the JPTS fuel (Fig. 4), two different experiments indicate that the onset of crystallization for this Jet A fuel (cooling rate of 1 K/min) occurs near 221 K. The measurement of similar temperatures occurring at the initiation of crystal formation corroborates each experimental technique. Moreover, Fig. 4 and 5 together underscore the importance of supercooling in the freezing of jet fuels.

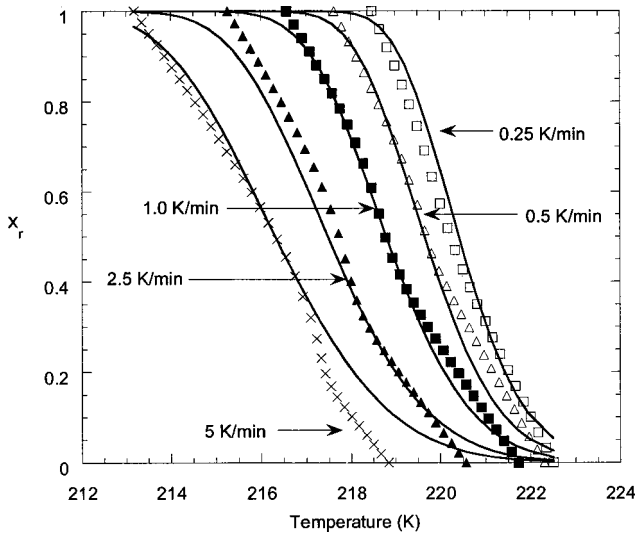

Fig. 5 Predicted and measured relative freezing fraction for Jet A (F3219) with different cooling rates

Additive Studies. The rate at which a hydrocarbon mixture is cooled affects the nucleation rate of normal alkanes from solution. In addition, the rate of change in local concentrations of species precipitating from solution can influence the local transport properties and crystal growth. Additives have been used to modify nucleation and growth processes of freezing diesel fuel. Flow improver additives such as ethylene vinyl acetate copolymers cocrystallize with normal alkanes and have protruding functional groups that interfere with incorporation of free normal alkanes found in diesel fuels. Consequently, smaller crystals result. It is desirable to form numerous small crystals that do not block fuel system filters or flow passages. In addition, flow improver additives are often designed to create multitudes of nuclei to which precipitating wax molecules attach and form crystals. The cooling rate has an important influence on crystal formation in hydrocarbon fuels and, thus, could have an effect on the behavior of low-temperature additives. As a consequence, DSC studies were performed in which the cooling rates of both neat fuel and fuel containing an additive were varied. In large-scale experiments ([1]), the proprietary additive 3607 greatly improved the low-temperature characteristics of fuel F3219 and was selected for this study.

Figure 6 shows values of an effective specific heat for a neat Jet A fuel (F3219) which includes heat of fusion contributions for cooling rates of 1.0 K/min, 2.5 K/min, and 5.0 K/min. Figure 6 shows that as the cooling rate is increased from 1.0 K/min to 5.0 K/min, the large peak in the neat fuel trace shifts from 218.5 K to 217.2 K. In contrast, Fig. 7 shows that the large peak associated with the fuel containing additive 3607 shifts less than 1 K (from 218.3 K to 217.6 K) as the cooling rate is increased from 1.0 K/min to 5.0 K/min. In addition, Fig. 7 shows that there is a more rapid rise and narrower width in the large peaks when contrasted with those of Fig. 6. The more rapid rise in the specific heat values of Fig. 7 implies a faster nucleation rate at a given temperature for the additized fuel. When contrasted with Fig. 6 at the lowest cooling rate, Fig. 7 shows that the additive acts to slightly depress the temperature at which crystallization begins. As the cooling rate increases, Fig. 7 shows that the additive reduces the level of supercooling that can be achieved before crystal nucleation begins. Presumably, the additive becomes a source for heterogeneous crystal nucleation. Figure 7 shows that the behavior of cold flow additives varies with cooling rate in a manner that is not well understood.

The small changes in the DSC exotherms shown here indicate that the additive works primarily by altering crystal morphology

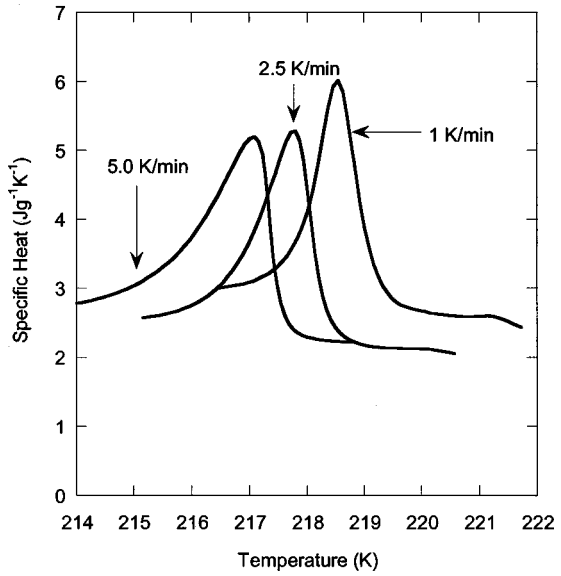

Fig. 6 Measured specific heats for neat Jet A fuel (F3219) and different cooling rates

rather than by significantly changing the temperature at which crystallization begins. To supplement the thermal analysis provided by DSC measurements, we have also used low-temperature microscopy to observe changes in crystal structure during cooling. Figure 8 shows images of the fuel (near 219 K) containing additive 3607 and cooled at a rate of 1.0 K/min. The presence of the additive results in numerous ''long and narrow'' crystals rather than the plate-like crystals of the neat fuel of Fig. 2. The formation of numerous, narrow crystals is the type of behavior expected from ''pour point'' type additives.

Conclusions

In the current work, the DSC was used to detect phase transitions in the cooling of jet fuels. In addition, the DSC demonstrated differences in the low-temperature characteristics of two Jet A fuel samples and a JPTS fuel. By varying the cooling rate over a large range, the effect of supercooling on crystallization within jet fuel was shown to be important. In addition, correlations for liquid-to-solid phase-change kinetics were developed.

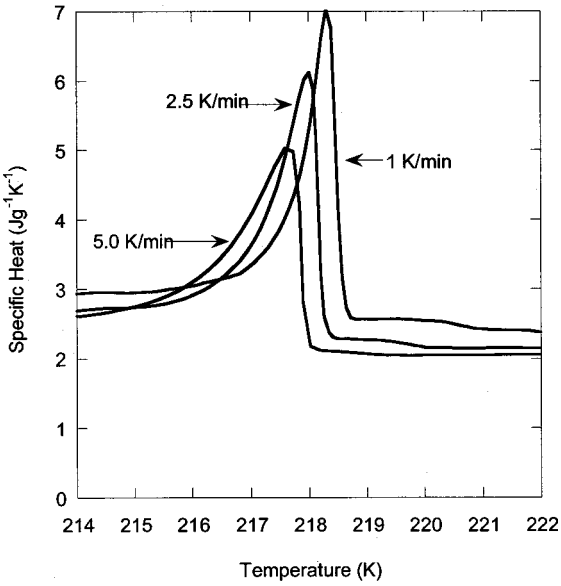

Fig. 7 Measured specific heats for additized Jet A fuel (F3219) and different cooling rates

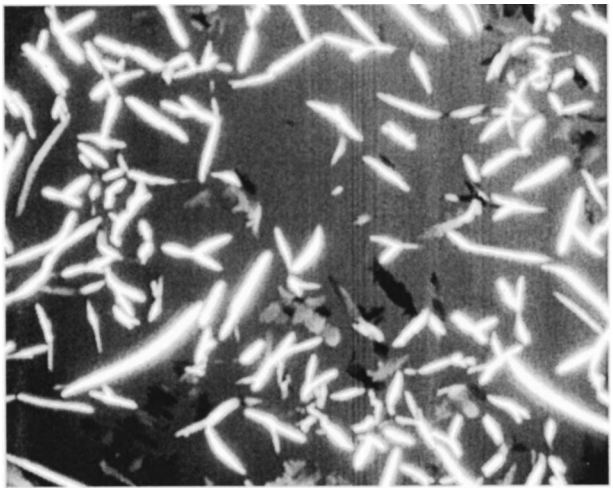

Fig. 8 Images of crystals forming from Jet A containing additive 3607 using cold-stage microscopy with a cooling rate of 1.0 K/min (magnification 40×)

The DSC is a useful instrument in the study of the freezing of jet fuel. The DSC can be used to develop kinetic models of fuel crystal formation and growth and can provide specific heat measurements. Both kinetic growth models and specific heat measurements are important for the development of engineering computational fluid dynamics models. The cold-stage microscope provides information concerning crystal morphology that varies with cooling rate and can also be used in future numerical simulations that involve multiphase flows.

Acknowledgments

This work was supported by the U.S. Air Force, Warner Robins Air Logistic Command, U-2 Special Programs Office, Robins Air Force Base, Warner Robins, Georgia, under Project No. 205 (Project Manager: Capt. Bernard Frank) and the U.S. Air Force Research Laboratory, Propulsion Directorate, Propulsion Sciences and Advanced Concepts Division, Wright-Patterson Air Force Base, Ohio, under Contract No. F33615-97-C-2719.

Nomenclature

C_1 = constant in Eq. (2)
C_2 = constant in Eq. (1)
dQ/dT = differential heat transfer rate (W)
m = exponent used in Eq. (1) and (2)
n = exponent used in nonlinear regression
T = temperature (K)
T_m^0 = measured equilibrium melting temperature (K)
T_S = crystal formation initiation temperature (K)
x_r = relative crystallinity (dimensionless)
$x(T)$ = crystallization as function of temperature (dimensionless)
x_∞ = crystallinity at termination of crystallization process (dimensionless)
λ = cooling rate (K/min.)

References

[1] Ervin, J. S., Zabarnick, S., Binns, E., Dieterle, G., Davis, D., and Obringer, C., 1999, ''Investigation of the Use of JP-8+100 With Cold Flow Enhancer Additives as a Low-Cost Replacement for JPTS,'' Energy Fuels, **13**, pp. 1246–1251.

[2] Noel, F., 1972, ''Thermal Analysis of Lubricating Oils,'' Thermochim. Acta, **4**, pp. 377–392.

[3] Letoffe, J. M., Claudy, P., Garcin, M., and Volle, J. L., 1995, ''Crude Oils: Characterization of Waxes Precipitated on Cooling by D.S.C. and Thermomicroscopy,'' Fuel, **74**, pp. 92–95.
[4] Aboul-Gheit, A. K., Abd-el-Moghny, T., and Al-Eseimi, M. M., 1997, ''Characterization of Oils by Differential Scanning Calorimetry,'' Thermochim. Acta, **306**, pp. 127–130.
[5] Zabarnick, S., and Widmor, N., 2001, ''Studies of Jet Fuel Freezing By Differential Scanning Calorimetry,'' Energy & Fuels, **15**, pp. 1447–1453.
[6] Hammami, A., and Mehrotra, A. K., 1996, ''Non-Isothermal Crystallization Kinetics of Binary Mixtures on N-Alkanes: Ideal Eutectic and Isomorphous Systems,'' Fuel, **75**, pp. 500–508.
[7] Ozawa, T., ''Kinetics of Non-isothermal Crystallization,'' Polymer, **12**, pp. 150–158.
[8] Roberts, D. E., and Mandelkern, L. J., 1955, ''Thermodynamics of Crystallization in High Polymers: Natural Rubber,'' J. Am. Chem. Soc., **77**, pp. 781–786.
[9] Hammami, A., and Mehrotra, A. K., 1992, ''Non-isothermal Crystallization Kinetics of n-Paraffins With Chain Lengths Between Thirty and Fifty,'' Thermochim. Acta, **211**, pp. 137–153.
[10] Lewtas, K., Tack, R. D., Beiny, D., and Mullin, J., 1991, ''Wax Crystallization in Diesel Fuel: Habit Modification and the Growth of n-Alkane Crystals,'' *Advances in Industrial Crystallization*, Butterworth Heinemann, Oxford, UK.
[11] Bevington, P. R., 1969, *Data Reduction and Error Analysis for the Physical Sciences*, McGraw-Hill, New York.
[12] Atkins, D., and Ervin, J. S., 2001, ''Freezing of Jet Fuel Within a Buoyancy-Driven Flow in a Rectangular Optical Cell,'' Energy & Fuels, **15**, pp. 1233–1240.

K. P. Vanoverberghe[1]
e-mail:
koen.vanoverberghe@mech.kuleuven.ac.be

E. V. Van den Bulck

Department of Mechanical Engineering,
Applied Mechanics and Energy Section,
Katholieke Universiteit Leuven,
Celestijnenlaan 300A,
3001 Heverlee, Belgium

M. J. Tummers

W. A. Hübner

Department of Applied Physics,
Thermal and Fluid Sciences Section,
Technische Universiteit Delft,
Lorentzweg 1,
2628CJ Delft, The Netherlands

Multiflame Patterns in Swirl-Driven Partially Premixed Natural Gas Combustion

Five different flame states are identified in a compact combustion chamber that is fired by a 30 kW swirl-stabilized partially premixed natural gas burner working at atmospheric pressure. These flame states include a nozzle-attached tulip shaped flame, a nonattached torroidal-ring shaped flame (SSF) suitable for very low NO_x emission in a gas turbine combustor and a Coanda flame (CSF) that clings to the bottom wall of the combustion chamber. Flame state transition is generated by changing the swirl number and by premixing the combustion air with 70% of the natural gas flow. The flame state transition pathways reveal strong hysteresis and bifurcation phenomena. The paper also presents major species concentrations, temperature and velocity profiles of the lifted flame state and the Coanda flame and discusses the mechanisms of flame transition and stabilization. [DOI: 10.1115/1.1520159]

Introduction

The interest in low NO_x combustion originates from the demand of cleaner burners with increased flame stability, turndown ratio and thermal efficiency. A promising technique is the use of near premixed swirl stabilized combustion. Flames as such are investigated by Qi et al. [1] where the authors present an experimental study based upon photography and mean and fluctuating temperatures. Several researchers, [2–5], have reported on the scaling characteristics of burners that implement this technique. Their studies have indicated the low NO_x potential of such burners. During the course of this experimental work, interesting and not yet reported phenomena were discovered with regard to the flame pattern behavior. Although some flame patterns have been reported by Beér and Chigier [6], only the attached flame received considerable attention. The objective of this paper is to report the existence of multiflame patterns in enclosed swirl driven partially premixed combustion as well as to present the transition pathways between the different flame states. In-flame data allows the explanation of the phenomena.

Experimental Details

General Configuration. The study of different flame states, burning in a quartz glass octagonal combustion chamber, is carried out by means of the visual observation of the flame and by quantitative in-flame data, including the temperature field, the distribution of the major species and velocity measurements. The temperature field and the distribution of the major species such as O_2, NO_x, CO, and unburned hydrocarbons (UHC) in the combustion chamber have been measured with a 3-mm quartz probe with quench section and a fine wire 100-μm type B thermocouple. The flow field has been measured using the two-dimensional LDA technique. Axial, tangential, and radial velocity data are obtained in hot conditions and tight confinements.

Burner. The experimental natural gas burner used in this study has been designed and manufactured by the International Flame Research Foundation (IFRF) in IJmuiden, The Netherlands Dutch Slochteren natural gas and dry combustion air at 25 deg is supplied to the burner while parameters such as (1) swirl intensity, (2) stoichiometric ratio, and (3) degree of premix of the natural gas-air mixture are controlled. The composition of the used fuel is methane 83.2%, ethane 3.8%, propane and higher hydrocarbons 1.2%, N_2 10.3%, CO_2 1.4%. The Wobbe number equals 42.94 MJ/m^3 at 20°C. The 30 kW burner is schematically shown in the left part of Fig. 1. The right part of Fig. 1 shows the dimensions of the burner that are referenced to the outer diameter of the combustion air duct D_0 which equals 27 mm. The burner consists of a swirl generator and a burner quarl joined together via a cylindrical duct. A fuel rod is placed in the center of the burner. The inlet swirl is generated by means of a moveable block swirler which is installed upstream of the cylindrical duct. Detailed information on the calibration and design of the moveable block swirlers as well as on the generic research burner is available in Beér and Chigier [6], Weber and Dugué [7], and Borman and Ragland [8]. The quarl is made of refractory material and has an opening angle of 20 deg. The central fuel rod conducts the natural gas which is injected radially in the swirling combustion air near the burner exit through a set of 24 holes ($d_{\text{hole}}=0.5$ mm). Hence, an annular channel is formed between the duct and the fuel rod, $D_0/D_{\text{fuel rod}}=27/18$ mm, respectively. The swirl number can be continuously varied in a range from 0–1.12.

Although an overall stoichiometric ratio (SR), defined as the ratio of actual applied combustion air to the theoretical combustion air requirement, of 1.10 is kept, the mixing of the natural gas and the combustion air can be altered considerably by the use of two mixing points at different locations. The total gas stream is split up and by means of mass flow controllers, an adjustable amount of gas is mixed upstream with the combustion air in a first mixing point. This mixing point is located sufficiently upstream of the burner entrance such that a homogeneous mixed flow is established at the inlet of the swirl generator. At the end of the fuel rod (= second mixing point), the balance of the gas is radially injected into the swirling air-gas mixture totaling 30 kW in any case. A dimensionless ratio, degree of premix (DPX) can be defined as

$$\text{DPX}=\left(\frac{\dot{m}_{\text{upstream}}}{\dot{m}_{\text{total}}}\right)_{\text{natural gas}} \tag{1}$$

in order to quantify the partial premixed operating conditions of

[1]To whom correspondence should be addressed.

Contributed by the Combustion and Fuels Division of THE AMERICAN SOCIETY OF MECHANICAL ENGINEERS for publication in the ASME JOURNAL OF ENGINEERING FOR GAS TURBINES AND POWER. Manuscript received by the C&F Division Aug. 2001; final revision received by the ASME Headquarters July 2002. Associate Editor: P. Malte.

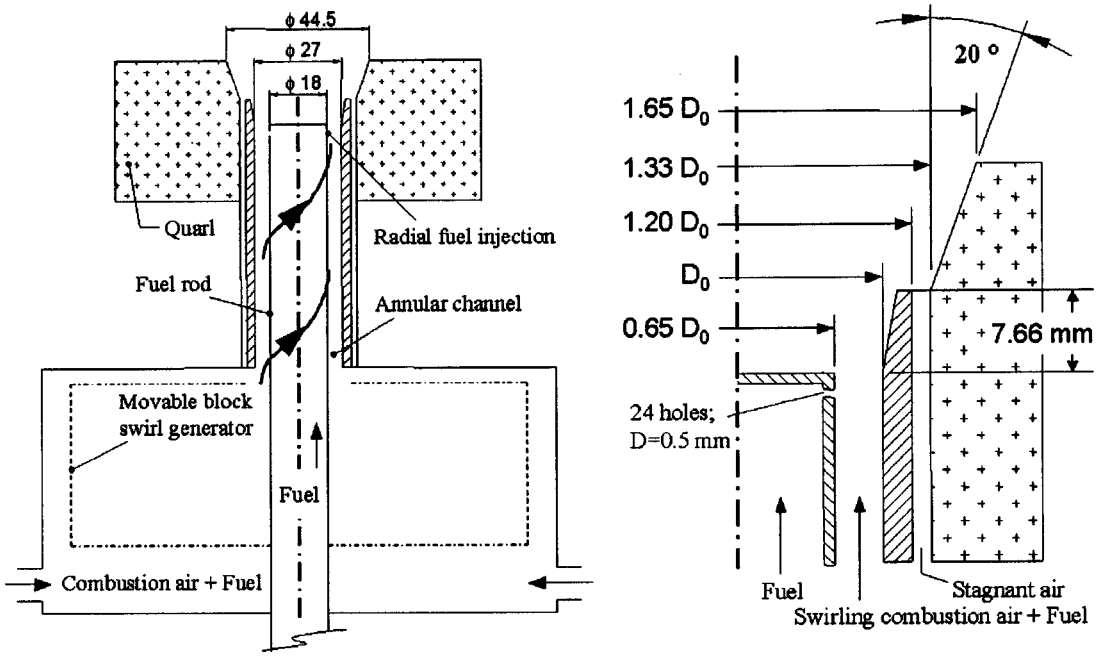

Fig. 1 (left). Experimental 30 kW IFRF burner. Overview, including swirl generator, fuel rod, annular channel and burner quarl with 20 deg opening angle. (right). Characteristic dimensions of the experimental IFRF burner. For 30 kW, D_0=27 mm.

the burner. In this study, the DPX ranges between 0 and 1 and can be set in a continuous way. A value of zero indicates that all the fuel enters at the burner exit. Consequently, a value of one indicates that all the fuel is fully mixed with the combustion air upstream. The Reynolds number in the annular duct equals 19000 for the 30 kW burner operating at a 1.10 stoichiometric ratio as is the case for the results that follow. The momentum ratio of the radial injected fuel to the axial flow of air-fuel mixture equals 3.5% for a DPX=0.7.

Setup Details. A side and top view schematic drawing including dimensions of the combustion chamber is depicted in Fig. 2. The burner is installed in the bottom with the flame burning upward and the combustion products pass through the annular section that is formed by the octagon and the stopper (D_{stopper} =190 mm) into the exhaust. The diameter and length of the confinement are 255 and 310 mm, respectively, and the setup runs under atmospheric pressure conditions.

For convenience, the axis system originates in the center of the burner and *R*, *X*, and *H* represent both the horizontal and vertical directions. The laser beams of the LDA system pass through the windows and the receiving optics are placed in a 180-deg forward scatter arrangement. Some practical constraints limit the velocity measurements to a certain extent. First, the beam separation (50 mm) in conjunction with the focal length (350 mm) of the transmitting lens restrict the position of the measuring volume (MV). Regions lower than 6 mm in the center and 11 mm near the wall cannot be reached. Second, the supporting bars of the octagonal chamber block the beams if the MV traverses further than 38 mm in the *X*-direction. Consequently only radial velocity data can be obtained within this region of the *X-H* plane. Third, the glass windows reflect and disperse the laserlight in the near-wall regions and fouling of the windows by the seeding (ovendried micron-sized Al_2O_3 particles) mandates regular cleaning of the glass. Velocity bias is present in LDA measurements and the ''transit time'' weighting method is applied in the statistical postprocessing of the LDA data, according to Tummers [9].

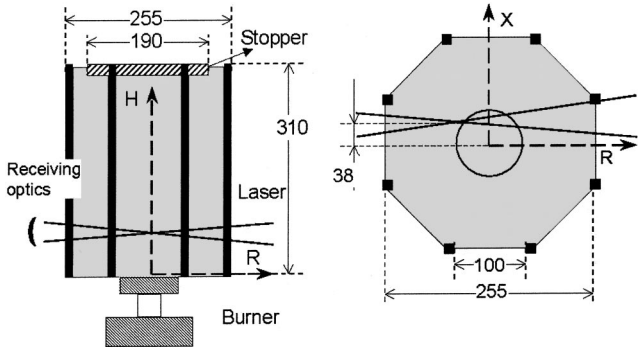

Fig. 2 Schematic drawing of the octagonal quartz glass confinement with the burner installed in the bottom. Dimensions are in millimeter. (left). Side view including *H-R* axes. (right). Top view including *X-R* axes.

Results and Discussion

Flame State Identification. This section presents the identification of different flame states. A vast set of experiments has examined the combined effects of the degree of premix with the swirling intensity of the mixture, the flame confinement and the overall stoichiometry of the combustion. Proper setting of the parameters lead to the set of five basic flame types which are shown in the schematic drawing of Fig. 3.

First, there exists the *nozzle stabilized flame* (NSF). This IFRF ''as-is'' flame type is the regular flame which has already been reported by Sayre et al. [5], Weber et al. [3], and Vanoverberghe et al. [10]. With intermediate or high degree of swirl, it is principally a tulip-shaped blue flame that is stably attached to the divergent burner quarl and it encloses a large torroidal vortex internal reverse flow zone (IRZ), located in the center of the flame. A low swirl version of the NSF also exists and features an opening flame brush at the top of the flame. The NSF is stabilized both by means of the refractory walls of the quarl, controlling the expanding flow, as well as by the recirculation of hot gases igniting the air-fuel mixture close to the burner exit. Visual boundary obser-

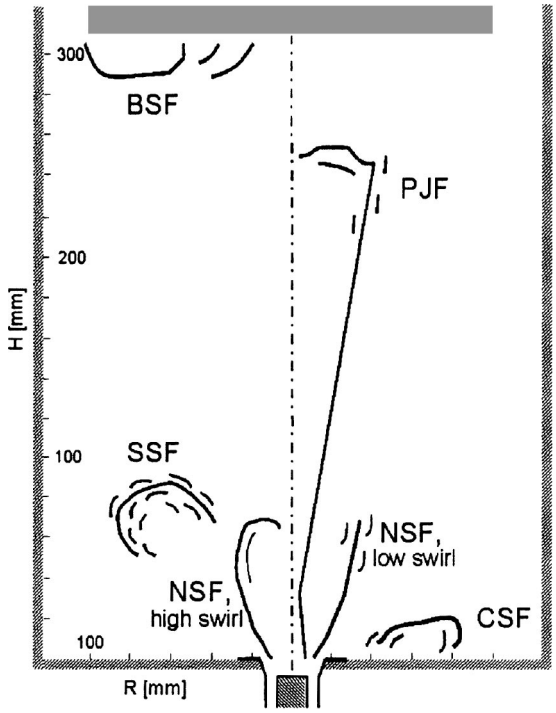

Fig. 3 Schematic drawing of five flame states. Nozzle stabilized flame (NSF); swirl stabilized flame (SSF); Coanda stabilized flame (CSF); pinched jet flame (PJF); backwall stabilized flame (BSF).

vation and in-flame data analysis show that the height and width of the flame are of order of 2.5 and 2 times, respectively, the characteristic diameter D_0 of the burner, revealing a compact flame. This flame pattern is the result of intense mixing of fuel and air due to high shear and high turbulence at the burner exit, resulting in a high combustion intensity.

A second flame type, the *swirl stabilized flame* (SSF), is identified by its lifted nature, forming a torroidal ring burning at an elevated position downstream from the burner head. The maximum elevated position is approximately at $3\,D_0$ and is strongly affected by the swirling intensity. In fact, the flame can be positioned anywhere below $3\,D_0$. The inner diameter of the ring approximates $3\,D_0$ and is wider than the compact NSF. The width and the height of this torroidal flame are, respectively, about $1.9\,D_0$ and $1.5\,D_0$. Inside this ring, a noncombusting recirculation zone is observed. The SSF flame can easily be produced as will be explained in the next section and behaves like a stable flame with no physical anchor points in neither the near-burner region nor the walls of the confinement. In addition the existence of this atmospheric flame with a very low NO_x emission at 1.10 stoichiometric ratio may be of interest to the application of this particular flame in modern gas turbine combustors, operating at 30 bars and 1.5 stoichiometric ratio.

A third flame type looks like a ''sunflower.'' This flame pattern is closely attached to the burner face and the adjacent refractory bottom. It is a flat ring and exhibits a more spread-out character than does the SSF. This flame type is referred to as the *Coanda stabilized flame* (CSF). Its inner diameter equals $2.7\,D_0$ and the flame stretches along the radial position. The height is below $1.2\,D_0$ and the width approximates $1.8\,D_0$. This flame type can be produced with moderate and even low swirl numbers which is in contrast with Leuckel [11] and Beér and Chigier [6], where the researchers report a high swirl requirement in combination with trumpet-shaped wide angle and short nozzles. The diverging angle of the quarl is only 20 deg which is smaller than the 35 deg reported by Beér and Chigier [6]. Despite a dominant axial momentum of the flow, it is remarkable that the CSF flame can exist since the unburned mixture has to change direction over 90 deg without any substantial assistance from the swirl. The wide sunflower pattern and especially the low swirl requirement make these flames suitable for industries where high and uniform radiant heating of large heat sink areas are required.

From the tests with respect to the effect of premix, it revealed that both ring-shaped flames require a minimum of 0.5 DPX setting.

A fourth flame behaves like a trumpet shaped jet flame featuring a pinched section with a high concentration of UHC inside. The flame is referred to as the *pinched jet flame* (PJF). A large recirculation zone is observed at the outside of the jet flame. The jet flame may be fitted into long ceramic tubes for indirect radiative heat exchange purposes.

Last, a fifth flame which stabilizes against the backwall (*backwall stabilized flame*, BSF) is only of interest for full study of the transition pathways and the accompanying setup criteria.

The tests revealed that the different flame states can also be obtained in horizontal firing and except for the BSF, they are independent of the presence of the backwall. The diameter of the cylindrical confinement can easily be adjusted between 200 and 400 mm. Below a diameter of 200 mm, the flame hits the confinement whereas exceeding 400 mm diameter causes a less stable SSF with a flame brush expanding and contracting randomly. The CSF behaves likewise indicating that a low pressure and the external recirculation zone (ERZ) in the corner of the confinement play a role in flame stabilization.

Flame State Transition Pathways. The study of the transition pathways from one flame state to another is illustrated by means of Fig. 4. The experiments have revealed that the flame states can only persist within certain ranges of DPX and swirl number. In the following discussion, the emphasis lies on determining the transition pathways and also highlighting the multiflame capabilities of the burner where identical input conditions lead to very different flame states. NO_x emissions in mg/Nm^3 based upon 3% O_2 dry flue gas conditions are also reported to illustrate the low NO_x potential of some of the flames.

Figure 4 shows in abcis the degree of swirl versus the five flame states in ordinate. The NO_x numbers are printed adjacent to the lines. The left flame transition map is representative for a DPX $=0$. Beginning with a maximum swirl intensity ($S=1.12$), the attached NSF flame exists. Decreasing the swirl changes the flame pattern slightly since the flame becomes less compact and the flame brush at the top of the flame does not curl back into the IRZ anymore. No transition to other flame states occurs.

Mixing gas upstream into the combustion air (increasing DPX) gives rise to the different flame states. In the middle diagram of Fig. 4, the transition pathways between the different flame states are exemplified for a DPX $=0.7$. The solid lines denote a steady flame whereas the dashed lines signify that a sudden transition takes place. First, a NSF exists at maximum swirl. The NSF still holds with decreasing swirl until the transition to the SSF which occurs at $S\approx 0.78$. Decreasing the swirl further more brings the flame in the CSF mode at $S\approx 0.62$. Next, lowering the swirl maintains this CSF upon the $S\approx 0.16$ point where the flame abruptly detaches and the BSF state is established. Reversing the track by increasing the swirl reveals an important hysteresis between $S\approx 0.16$ and $S\approx 0.62$. At the latter point, the BSF reattaches suddenly to a PJF flame. Video recording indicates that the flame front exhibits a fast transit along the centerline towards the burner head. The PJF in turn, returns to the NSF after the swirl has been increased above 0.84. Different from this first pathway, a second pathway exists that starts from the regular NSF to the SSF as described above. Instead of bringing down the flame front into the CSF state, swirl is increased again and raises the SSF into its maximum elevated position. This SSF state is stable provided that the swirl level does not exceed a value of 0.98. Above that swirl

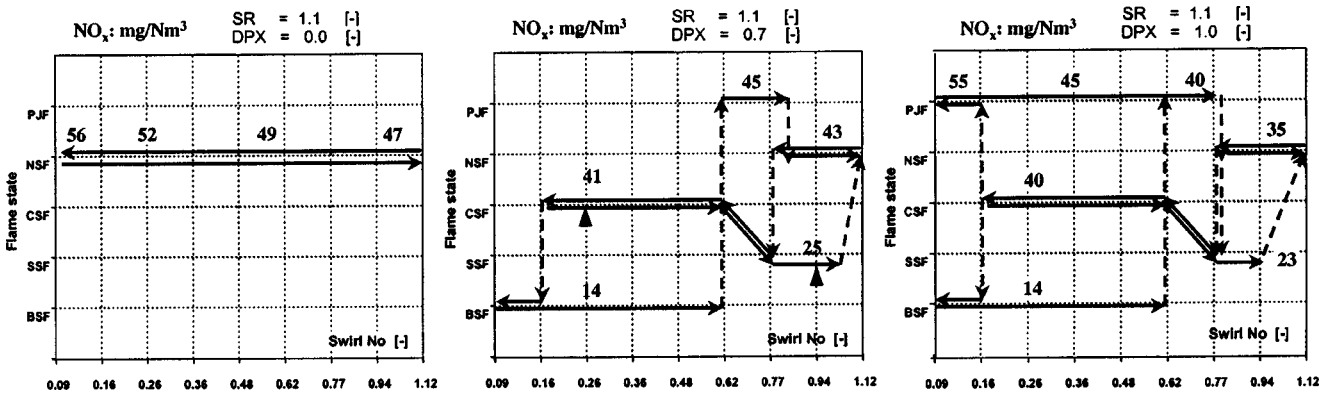

Fig. 4 Flame state transition pathways for various degree of premix ratios. The stoichiometric air to fuel ratio (A/F) equals 1.1. The numbers on the plot denote NO_x emissions in mg/Nm^3 based upon 3% O_2 dry flue gas. (Conversion for NO_x:1 mg/Nm^3 = 0.4872 ppm). (left). DPX=0.0; (middle). DPX=0.7; (right). DPX=1.0.

level the SSF becomes unstable and a little disturbance may cause a transition to the attached NSF. The latter is indicated by means of the sloped dashed line. It is clear from Fig. 4 that hysteresis, bifurcation and even a trifurcation area exist in the diagram. One recognizes the CSF-BSF area at lower swirl numbers. Next, there exists either a NSF or a SSF for the high swirling intensities. Last, a small trifurcation area can be distinguished, allowing either PJF, NSF or SSF flame states for exactly the same input conditions.

The right diagram of Fig. 4 presents the transition pathways for the fully premixed burner (DPX=1.0). In principle, comparable transition pathways show up although an exception must be made at lower swirl numbers. The CSF pathway acts like a pitchfork at $S \approx 0.16$, since the transition bifurcates and both the BSF as well as the PJF can be achieved. Both are stable conditions and no transition from one to the other occurs. Probability values are 70% and 30%, respectively, for the BSF and the PJF cases. The return into the PJF goes with increasing swirl. The BSF is stable until $S \approx 0.62$ is reached where than the BSF flips to the PJF and only the PJF remains. The PJF exists until $S \approx 0.78$ is reached and further increase of the swirl forces the flame to flip back to either the NSF or the SSF state. The second dominant pathway follows NSF-SSF-CSF at higher swirl numbers. The CSF can be lifted to the SSF state. In turn, the SSF transits back to the NSF. Note further that the transition point to NSF at $S \approx 0.94$ comes earlier than for the DPX=0.7 case indicating that a somewhat less stable SSF arises with the fully premixed operation. Bifurcation and trifurcation phenomena show up again.

Finally to complete the picture, a discussion with respect to the NO_x numbers leads to the following conclusions. First, for the nonpremixed attached NSF, the NO_x number ranges from 56 down to 47 mg/Nm^3 with increasing swirl. In general, this indicates that high swirl provides an intense internal recirculation zone which recycles flue gas back into the flame and thus reduces the flame temperature. Even the fully premixed PJF behaves in the same way that decreasing the swirl increases the NO_x proving that ERZ structures alter as well. Second, additional gain in NO_x reduction (e.g., from 47 down to as low as 35 mg/Nm^3 for a high swirl fully premixed NSF) is achieved by premixing the air with the fuel. Peaks in volumetric heat release are diminished and hence local temperature fluctuations flatten. Third, the 23 mg/Nm^3@3% O_2 (= 11.2 ppm@3% O_2 or 3.7 ppm@15% O_2) number indicates the very low NO_x potential for the premixed SSF and in-flame measurements prove that no fuel bypasses the active flame zone (no UHC) nor does incomplete combustion (no CO) occur. The substantial benefit of the SSF compared with the NSF is attributed to the lower flame temperature resulting from a more spread-out combustion process in the SSF case. Moreover, velocity measurements have revealed that more combustion products are recirculated in the large IRZ system which is set up by the SSF. The CSF results in much higher NO_x for a comparable flame pattern but this is due to proximity of the bottom preventing the flame to cool as efficient as in the fully lifted state. Finally, it should be noted that the low NO_x values for the BSF coincide with high CO numbers (400 ppm) as the flame quenches against the backwall stopper.

In-Flame Measurements. Detailed in-flame measurements have been performed on the SSF and the CSF in order to determine the flowfield in the combustion chamber where primarily the SSF has been studied for its low NO_x property, whereas the CSF has been investigated since this remarkable flame state features a flat radial spread-out nature although a low swirl number applies. Data are presented for a DPX=0.7 since this setting has shown up as a good engineering compromise for a low NO_x feature, an excellent flame stability and a good turndown behavior. The swirl numbers are S=0.94 and S=0.26 for the SSF and the CSF, respectively (indicated by the triangles in Fig. 4).

Figure 5 and Fig. 6 present in-flame data for the SSF and the CSF in reference to the diverging quarl, the annular channel and the central fuel rod. The left plot includes a limited number of contour lines of CO, UHC, temperature and mean axial velocity (U). The right plot shows a quiverplot of the velocities in the near-burner region including axial and radial velocity data.

Swirl Stabilized Flame. The CO=5000 ppm contour may be seen as a boundary for the time-averaged flame brush. The UHC =5000 ppm C_3 contour combined with an 800°C isotherm is representative for the flow path of unburned fuel-air mixture. Figure 5 also includes −5, 0, 5, and 10 m/s axial velocity contours. The figure reveals that fresh unburned mixture is injected into the combustion chamber and flows along an oblique plane towards the lifted SSF. The jet penetrates approximately 40 mm before combustion starts. The opening angle of the unburned mixture cone approximates 40 deg with respect to the centerline of the burner. Within the flame, a maximum temperature of 1450°C is observed ($|R|=80$ mm; $H=85$ mm) The swirling flow system experiences a vortex structure such that the central core of the flame encloses a large and strong recirculation zone. The air-fuel jet leaving the burner can be seen as a high velocity region of annular conical form. High velocities (≈31 m/s) at the burner exit exist, only gradually decreasing in magnitude due to mixing and entrainment of recirculated flue gas together with dispersion in radial direction. Both the UHC and mean axial velocity profiles show sharp gradients at the boundary of the fresh mixture with the internal recirculation zone, indicating shear layers. Reverse axial velocities approximate −5 m/s and reveal a uniform recirculation profile along the centerline of the burner.

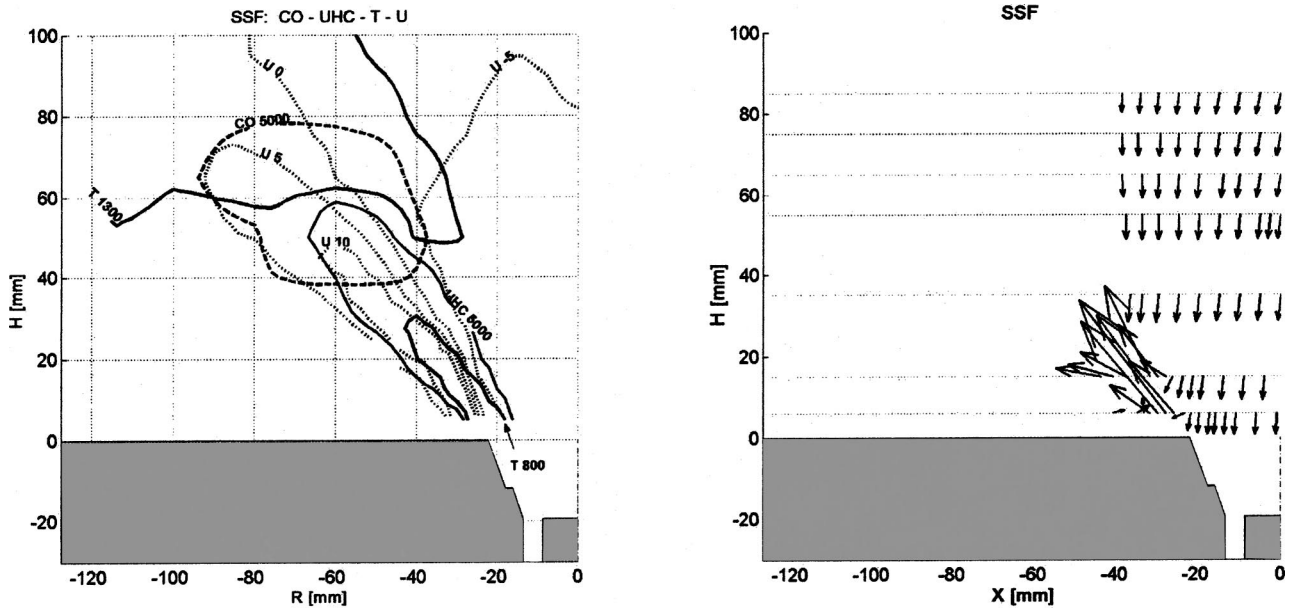

Fig. 5 (left). Flame composition, isotherms and axial velocity contourlines of the SSF. UHC_3 5000 ppm; dashed line=CO 5000 ppm, 800, and 1300°C isotherms. Dotted line=−5, 0, 5, and 10 m/s axial velocity. (right). SSF mean velocities in the near-burner region, maximum velocity of 31 m/s recorded near the burner rim, reverse flow velocity equals −5 m/s along the burner centerline.

Coanda Stabilized Flame. Figure 6 shows a CO =5000 ppm, an UHC=5000 ppm C_3 contour combined with two isotherms (800 and 1600°C) as well as −4, 0 and 3 m/s axial velocity contours. It reveals that fresh unburned mixture exits the annular channel and is deflected into a radial direction. The mixture heats up, is ignited and the combustion process raises the temperature inside the CSF up to 1730°C ($|R|=75$ mm, $H=8$ mm). The flame clings to the bottom and the combustion products detach at $|R|=90$ mm and flow further upwards at the outer side of the combustion chamber. The contour of zero axial velocity confirms that a large eddy system is set up within the confinement. A substantial amount of flue gas is recirculated along the inner core of the combustion chamber, the flow mixes and chemical active species together with the enthalpy of the recirculation gas provide a fast combustion and a stable flame. From the quiverplot in Fig. 6, a narrow region of unburned mixture exits at high velocity (≈24 m/s) following the opening angle of the burner quarl. Along the centerline, a much wider region of reverse flow is present with an almost uniform axial downward velocity profile (≈−7 m/s).

A limited set of LDA data has visualized the cold flow field of the CSF, yet the results are preliminary. Although the Coanda flow pattern is preserved, the profiles change in magnitude. The reverse velocities in the recirculation zone are roughly twice as strong. A detailed cold flow study is ongoing and this will be the subject of subsequent publications on this matter.

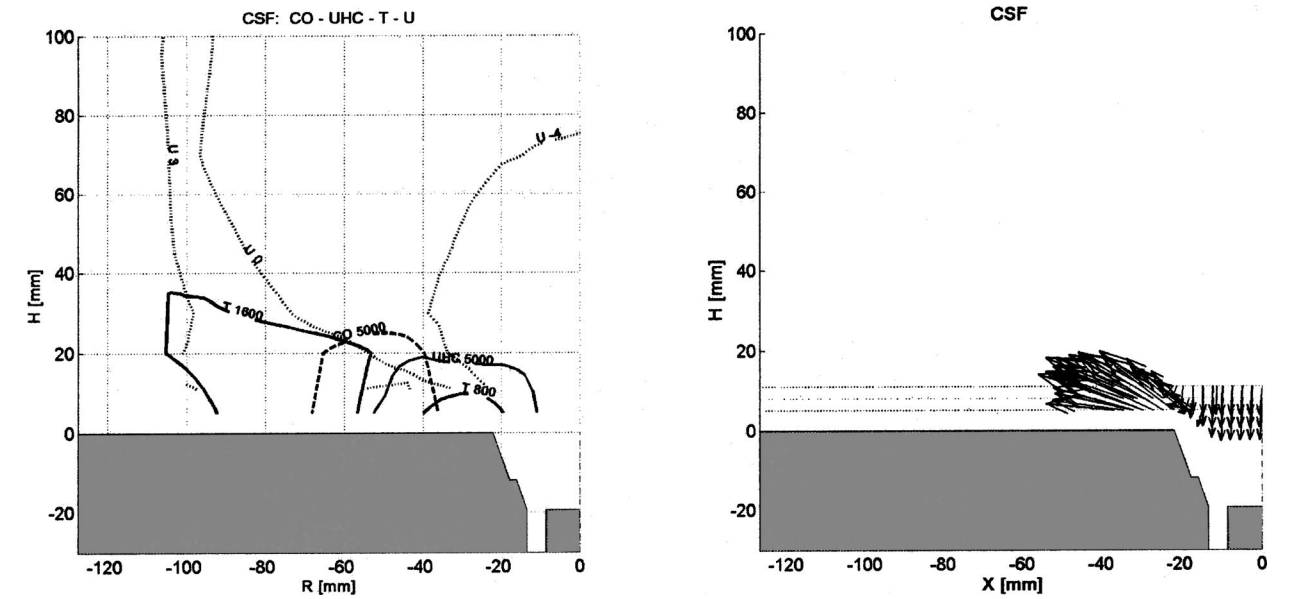

Fig. 6 (left). Flame composition, isotherms and axial velocity contourlines of the CSF. UHC_3 5000 ppm; dashed line=CO 5000 ppm, 800 and 1600°C isotherms. Dotted line=−4, 0, and 3 m/s axial velocity. (right). CSF mean velocities in the near-burner region, maximum velocity of 24 m/s recorded near the burner rim, reverse flow velocity equals −7 m/s along the burner centerline.

Mechanisms of Flame Stabilization and Transition

Time-averaged 5000 ppm CO contours as well as visual observation (Vanoverberghe et al. [10]) could suggest a torroidal ring shaped SSF and CSF flame. The measurements however show that flames with a similar appearance can exist where the flame brush is open at the bottom, allowing reactants to enter. The schematic in Fig. 3 depicts this averaged shape of a crosscut of the SSF as well as the Coanda flame. For the lifted SSF, fresh unburned mixture, which already has been preheated by the IRZ system, enters through a whirling conical sheet into the flame brush. The gradual divergence of the flowfield provides a well-defined match between the longitudinal velocity and the turbulent flame speed and flame stabilization is established. A similar discussion holds for the CSF but differs in that the applied swirl is low ($S \approx 0.26$) and the idea is that the reverse flow system creates momentum to balance the axial outflowing momentum of the exiting air-fuel mixture such that it forces the unburned mixture outward. However, there is a deficit in this balance and a low-pressure region is created in the corners of the confinement since the radial jet entrains stagnant gas and consequently the pressure is reduced. The Coanda [12] effect finally takes over and allows a stable flame clinging to the bottom.

A continuous transition between the CSF, a ''low position'' SSF and ''high position'' SSF exists and the flame can be positioned anywhere between the refractory bottom and its maximum elevation by varying the swirl number. To address this mechanism of the continuous transition two items play a role. First, the jet changes direction due to differences in pressure and momentum forces from the IRZ as well as the ERZ. High swirl induces a low pressure along the centerline and consequently a large IRZ is established. The velocity profiles of the SSF and the CSF, respectively, reveal that the IRZ widens and increases in strength, hence deflecting the conical jet more strongly. The reason for this is that within the tight combustion chamber, the conical jet entrains more stagnant gas from the ERZ as it whirls less with decreased swirl number. Consequently, the pressure in the ERZ field is reduced and this pulls the SSF down to the CSF position when the swirl number is reduced. Second, changing fluid dynamics such as swirl alters the combustion kinetics (turbulent flame speed). For example, high swirl is expected to produce excess turbulence which results in large tangential velocity gradients and a negative flame stretch, causing the flame surface area density and therefore the volumetric burning rate to decrease. Following the idea of faster combustion with less swirl (within a certain range) the flame stabilizes closer to the burner exit and an intermediate SSF (with respect to its position) burns in the combustion chamber.

Summary

This study has identified five different flame states among which four of them are suitable in various domestic and industrial applications. A comprehensive survey of flame pattern behavior is presented. It is stressed that the burner is well documented in literature and hence it provides fully reproducible study objects with the information provided in the paper. The study has proved that proper settings of swirl and premixing degree can be retained as predominant factors in the setup and transition between different flame states. Not yet reported hysteresis, bifurcation, and even trifurcation phenomena have shown up. In the discussion of the transition pathways, quantitative details in terms of exact settings including swirl intensities and degree of premix are given.

In a next step, the combined contour plots of stable chemical species (CO and UHC), temperature and velocity data have been presented for the SSF and the CSF. The data clearly show the time-averaged locations of the unburned mixture, the flame, and the recirculation zones. The mechanisms of flame stabilization and the transition between the SSF and CSF ring-shaped flames are addressed. The flame repositioning of this low NO_x SSF may offer an interesting prospect for abatement of combustion instabilities, i.e. ''humming'' which has been recognized as an important issue in modern gas turbine combustors. Because of the variable distance downstream of the gas nozzle, this burner configuration and operation might be used to control combustion instabilities in gas turbines as the time lag between fuel injection and combustion is considered an important driving force for the onset of pressure oscillations in gas turbine combustors, Lieuwen et al. [13].

Acknowledgments

This research has partially been conducted at the Technische Universiteit Delft. We thank Prof. K. Hanjalić and Prof. D. J. E. Roekaerts of the T. U. Delft for making their facilities available to us.

Nomenclature

BSF = backwall stabilized flame
CSF = Coanda stabilized flame
DPX = degree of premix
D_0 = characteristic diameter
NSF = nozzle stabilized flame
PJF = pinched jet flame
SSF = swirl stabilized flame
S = swirl number
SR = stoichiometric ratio
UHC = unburned hydrocarbons
$\dot{m}$ = mass flow

References

[1] Qi, S., Gupta, A. K., and Lewis, M. J., 1997, ''Effect of Swirl on Combustion Characteristics in Premixed Flames,'' ASME Paper No. 97-GT-276.

[2] Driscoll, J. F., Dahm, W. J. A., and Wu, M. S., 1993, ''Scaling Characteristics of Aerodynamics and Low NO_x Properties of Industrial Natural Gas Burners, The Scaling 400 Study, Part III: The 30 kW Test Results,'' GRI Topical Report 93/0478 or IFRF Doc. No. F40/y/10, GRI, Chicago.

[3] Weber, R., Driscoll, J. F., Dahm, W. J. A., and Waibel, R. T., 1993, ''Scaling Characteristics of Aerodynamics and Low NO_x Properties of Industrial Natural Gas Burners, The Scaling 400 Study, Part I: Test Plan,'' IFRF Doc. No. F40/y/8, IFRF, IJmuiden.

[4] Peters, A. A. F., and Weber, R., 1994, ''Mathematical Modeling and Scaling of Fluid Dynamics and NO_x Characteristics of Natural Gas Burners,'' Int. ASME/EPRI Power Generation Conference, Phoenix, AZ.

[5] Sayre, A., Lallemant, N., Dugué, J., and Weber, R., 1994, ''Scaling Characteristics of Aerodynamics and Low NO_x Properties of Industrial Natural Gas Burners, The Scaling 400 Study, Part IV: The 300 kW BERL Test Results,'' GRI Topical report 94/0186 or IFRF Doc. No. F40/y/11, IFRF, IJmuiden.

[6] Beér, J. M., and Chigier, N. A., 1983, *Combustion Aerodynamics*, Robert E. Krieger, Melbourne, FL.

[7] Weber, R., and Dugué, J., 1992, ''Combustion Accelerated Swirling Flows in High Confinements,'' Prog. Energy Combust. Sci., **18**, pp. 349–367.

[8] Borman, Gary L., and Ragland, Kenneth W., 1998, *Combustion Engineering*, WCB McGraw-Hill, New York, Chap. 6, pp. 216–221.

[9] Tummers, M. J., 1999, ''Investigation of a Turbulent Wake in an Adverse Pressure Gradient Using Laser Doppler Anemometry,'' Ph.D. thesis, T.U. Delft.

[10] Vanoverberghe, K., and Van den Bulck, E., 2000, ''Low Swirl, Coanda Stabilized and Partially Premixed Natural Gas Flames,'' ECSBT2, 2nd European Conference on Small Burner and Heating Technology, Stuttgart, Mar. 16-17, pp. 53–62.

[11] Leuckel, W., 1968, ''Swirl Intensities, Swirl Types and Energy Losses of Different Swirl Generating Devices,'' Doc. No. GO2/a/16, International Flame Research Foundation, IJmuiden, The Netherlands.

[12] http://www.allstar.fiu.edu/aero/coanda.htm

[13] Lieuwen, T., Torres, H., Johnson, C., and Zinn, B. T., 1999, ''A Mechanism of Combustion Instability in Lean Premixed Gas Turbine Combustors,'' ASME Paper No. 99-GT-003.

Low NO_x Emission From an Ambient Pressure Diffusion Flame Fired Gas Turbine Cycle (APGC)

G. Vermes
Consultant,
1460 Elm Street,
Stratford, CT 02139

L. E. Barta
Combustion Consultants International, Inc.,
Bükkös Part 72,
Szentendre, Hungary

J. M. Beér
Massachusetts Institute of Technology,
Building 66, Room 548,
Cambridge, MA 02139
e-mail: jmbeer@mit.edu

The prospects of reduced NO_x emission, improved efficiency, stable, and oscillation-free combustion, and reduced construction costs achieved by an "Inverted Brayton Cycle" applied to midsize (0.5 to 5.0 MWe) power plants are discussed. In this cycle, the combustion products of an atmospheric pressure combustor are expanded in the gas turbine to subatmospheric pressure and following heat extraction are compressed back to slightly above the atmospheric, sufficient to enable a controlled fraction of the exhaust gas to be recirculated to the combustor. Due to the larger volume flow rate of the gas, the polytropic efficiency of both the turbine and compressor of this small machine is increased. Because of the low operating pressure and flue gas recirculation, both of which are instrumental to low NO_x formation, the combustor can be operated in the diffusion flame mode; this, on the other hand, assures good flame stability and oscillation-free combustion over wide ranges of the operating variables. For the task of obtaining very low NO_x formation, the well-tested multi annular swirl burner (MASB) is chosen. Recent computational and experimental development of the MASB by Siemens-Westinghouse as a topping combustor is discussed. It is shown that the MASB operated in rich-quench-lean mode is capable of single-digit NO_x emission. The emissions are further lowered in the APGC by ambient pressure combustion, and by the injection of the recirculated gas in the quench zone of the combustor. Results of a computational optimization study of the ambient pressure gas turbine cycle (APGC) are presented. [DOI: 10.1115/1.1520160]

Introduction and Background

The trend in power generation gas turbine technology for several decades has been to build turbines of increasing size. The application of these large units in combined cycles led to 360 MW plants (60 Hz) of two 130 MW gas turbines plus a condensing steam turbine with the associated heat recovery steam generators. The permitting and erection time of these plants is much shorter than those of the usual 2×1000 MW coal-fired steam plants (let alone the time required building a nuclear plant). Nevertheless, with respect to gas turbine unit size, governmental action and economic conditions have created a new situation during the last few years. A large number of smaller, cleaner, and more efficient power plants have been built following federal legislation (PURPA) which enabled independent power producers (IPPs) to obtain standby electricity from, and sell back surplus electric power to, electric utilities at commercial rates. In this system of "distributed" power generation, plants were moved closer to the customers to reduce cost under the financial drive of electricity industry deregulation; but this also demanded compliance with tight environmental regulations and the use of a clean fuel. Reassessment of the long-term availability of natural gas which led to the permission of natural gas use for base load power generation, and the rapid development of highly efficient GT/steam combined cycles, played important roles to satisfy these requirements.

Parallel with this development of electric utilities, there is an increasing demand for the extension of the generating unit size down to the 1 to 4 MWe range suitable for hospitals, shopping centers, military bases, etc., for producing their own power. These middle-range gas turbine plants are also subject to strict environmental controls, especially for their NO_x emission. The present contribution is intended to show that the application of a novel gas turbine cycle with an atmospheric pressure combustor and flue gas recirculation (APGC) can provide a cost competitive, reliable, and very low NO_x emission solution to this challenging problem.

Contributed by the Combustion and Fuels Division of THE AMERICAN SOCIETY OF MECHANICAL ENGINEERS for publication in the ASME JOURNAL OF ENGINEERING FOR GAS TURBINES AND POWER. Manuscript received by the C&F Division Aug. 2001; final revision received by the ASME Headquarters June 2002. Associate Editor: P. Malte.

The Ambient Pressure Gas-Turbine Cycle (APGC)

A competitive, middle-range gas turbine should show the following characteristics:

- very low emissions, especially of NO_x, necessary in a residential environment;
- high efficiency, to be price competitive within the network, and to reduce CO_2 emission; and
- unattended operation with broad limits of flame stability, free from combustion oscillations.

The following three main features of the APGC, [1], make it capable of responding to the above challenges:

1 atmospheric pressure combustor, capable of reducing the NO_x emissions of a conventional high pressure GT combustor by about a factor of three,
2 compatibility with the use of the multi annular swirl burner (MASB), a well-tested rich-quench-lean low NO_x combustor that is operating in the inherently stable diffusion-flame mode, and
3 flue-gas recirculation (FGR) (not available in the conventional gas turbine cycle) which, when used in the quench zone of the burner, can further reduce NO_x emission.

The Cycle Arrangement

The schemes of a conventional regenerative gas turbine cycle and the proposed ambient pressure gas turbine combustor cycle (APGC) are illustrated by Fig. 1 and Fig. 2, respectively. The

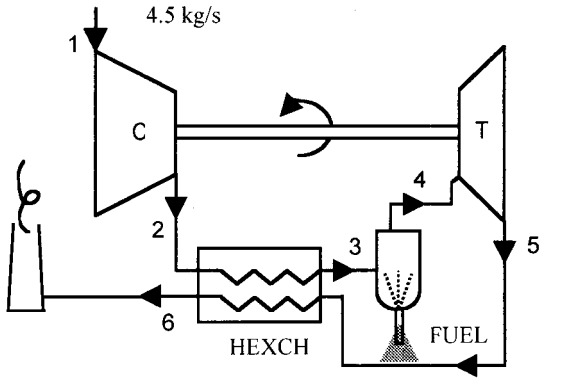

	1	2	3	4	5	6
°C:	15	369	499	1138	565	482
bar:	1.0	13	13	12.9	1.09	1.0

Fig. 1 Conventional regenerative cycle

calculated example is based on a 1.1 MWe turbine,[2]. To accommodate the ambient pressure combustor, the usual sequence of the machinery components of the gas turbine is altered. Referring to Fig. 2, the working fluid (air) enters the expander first (state 3) and the compressor second (state 6). This may be referred to as an ''inverted Brayton cycle,'' [3]. This way, the combustion process takes place at ambient pressure as opposed to the conventional gas turbine, where the combustor operates at elevated pressure (13 bar in the example chosen). Other combustor parameters being equal, the reduced pressure results in an approximately threefold reduction in thermal NO_x emission at atmospheric pressure, [4,5].

The small size of the 1 MW machine results in blade paths of small dimensions for the conventional turbine. The small dimensions have a deleterious effect on component efficiency. The conventional cycle used as a basis for comparison has only 84% polytropic (stage) compression efficiency average (the last stage had to be made centrifugal), resulting in 78% adiabatic efficiency for the entire compressor; the turbine (expander) overall efficiency is 87%. In the APGC, the 10–12 times larger specific volume results in about three times larger dimensions and this makes it possible to count on better efficiency; 94% and 89% were assumed for the turbine (expander) and the compressor, respectively.

The low pressure level of the APGC has an important consequence on the mechanical design of the component machinery. Casing of conventional turbines and compressors have to be designed to withstand a 10–12 bar pressure differential whereas the APGC machinery is designed for a 1 bar pressure differential.

Considering that failure in the conventional machine results in an explosion whereas failure in the APGC machinery causes an implosion, the reduced pressure and the reduced risk in the APGC should result in physically larger but less material-sensitive design.

An important, additional inherent advantage of the APGC relates to blade cooling. In the conventional turbine, the cooling air is available at the compressor exit temperature (in the cited example, this is 369°C). The amount of blade cooling air depends on the temperature difference between the desired metal temperature, about 800°C, and the 369°C air temperature, i.e., 431°C. In the APGC turbine, the cooling air is at 15°C, resulting in a 785°C temperature difference, thereby reducing significantly the necessary cooling air flow.

Because of thermodynamic reasons (cycle efficiency), the compressor inlet temperature has to be kept as low as possible. Because of no limitation on the level of air preheat in the fuel-rich first stage of the combustor, a larger than usual fraction of the exhaust heat can be utilized for preheating the combustion air in the first heat exchanger (HEX-1). Nevertheless, a second heat exchanger is necessary to cool the flue gas further before entry to the compressor. HEX-2 may be a steam generator or water heater depending on local conditions.

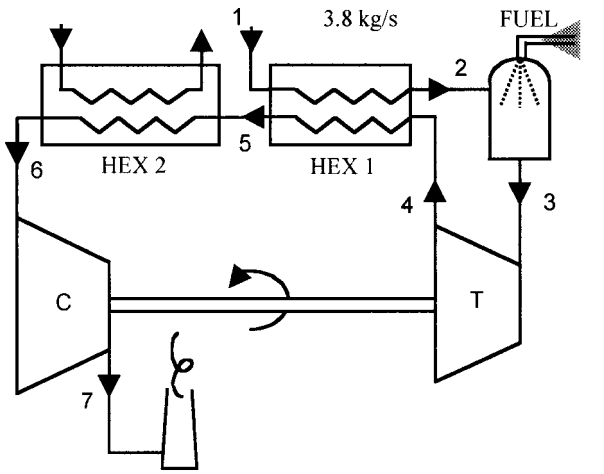

	1	2	3	4	5	6	7
°C:	15	315	1204	557	227	71	460
bar:	1.0	0.97	0.94	0.09	0.08	0.08	1.0

Fig. 2 Ambient pressure combustor gas turbine cycle

The Multi-Annular Swirl Burner (MASB)

The recent (second half of the 1990s) regulatory trend indicates that so-called ''single digit'' NO_x ($\leq$9 ppm(v)) will become a necessity for small ($<$10 MW) gas turbines used for the generation of electricity in residential areas. Gas turbines available on the market offer NO_x levels of 15–25 ppm, using ultra lean premix (ULPM) combustion of natural gas. The combustors are operated at air/fuel ratios close to the lean limit of flammability and have therefore some design and operational limitations. To guard against blow off, most ULPM combustors require a diffusion flame pilot. At turn down, there is an increased risk of flash back especially with silo type combustors and some designs revert back to diffusion flame operation. To restrict the NO_x reliably to the single digit level, post-combustion cleanup systems are applied which require ammonia injection to convert the NO_x to N_2. This entails, however, additional capital and operating costs, guarding against ammonia ''slip'' and the need for the periodic disposal of catalyst material classed as toxic solid waste in environmental regulations.

Theoretical considerations supported by experimental data show that single digit NO_x emissions can be achieved by the appropriate design of a combustor operated at atmospheric pressure and in the fuel-rich, fast-quench, fuel-lean (R-Q-L) combustion sequencing mode. The multi-annular swirl burner (MASB), an all metallic gas turbine combustor (Fig. 3, [6–11]) has shown such very low NO_x emissions. It is a recuperative burner; the combustion air is introduced axially, it cools the concentric annular walls of the combustor, and enters the burner as combustion air at the successive stages of the combustion. In a further development, the head of the MASB was redesigned to provide for fast mixing and rapid ignition of the fuel-rich mixture (Fig. 4, [10]). It consists of two coaxial radial swirlers with an annular mixing space between them. The fuel gas enters the annular mixing space through the inner cylinder and the combustion air through the outer cylinder, both swirling in the same direction. The mixture exits the annulus through a divergent quarl and because the degree of swirl exceeds

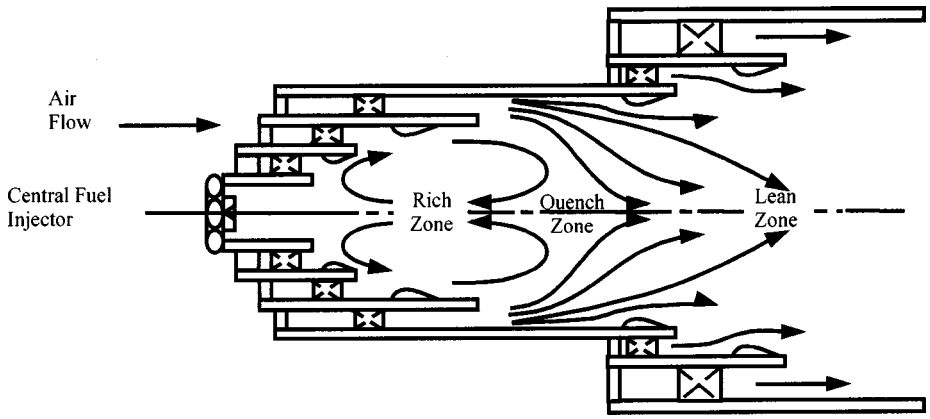

Fig. 3 Conceptual arrangement of the multi-annular swirl burner based on J. M. Beér's patented design

the critical value for vortex breakdown, an internal vortex is produced that is instrumental to the rapid ignition of the fuel-rich mixture.

In a series of USDOE sponsored computational and experimental studies carried out by Westinghouse with the experiments at the University of Tennessee Institute of Space Technology, [8,9], a full-size MASB (18″ diameter) was tested as a topping combustor of a pressurized fluidized bed combined cycle (PFBC). In the topping combustor, the temperature of the PFBC's hot combustion products is raised from 870°C to 1260°C by the combustion of Syngas. These are combustion conditions similar to those in the APGC when flue gas recirculation is applied, and therefore conclusions can be drawn from the topping combustor tests for expected NO_x emissions from the APGC.)

Computed lines of NO_x generation together with experimental data for a 14″ and 18″ MASB are shown in Fig. 5, [11]. In the computations, a Chemkin code [12] was used, and the flow was assumed to be ''plug flow,'' or ''well stirred-plug flow'' with 5 ms residence time for the well stirred zone and the rest of the residence time in plug flow.

The MASB generated NO_x emission varied in the range of 5 to 15 ppm under the conditions of 7.3 bar pressure, fuel-rich zone

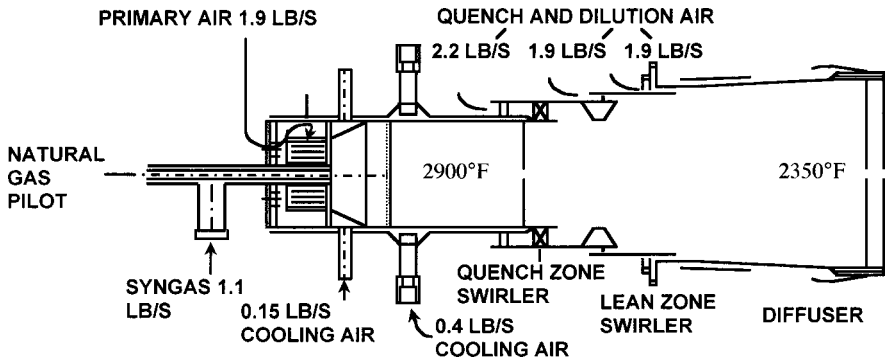

Fig. 4 The multi-annular swirl burner (MASB), [6,10]

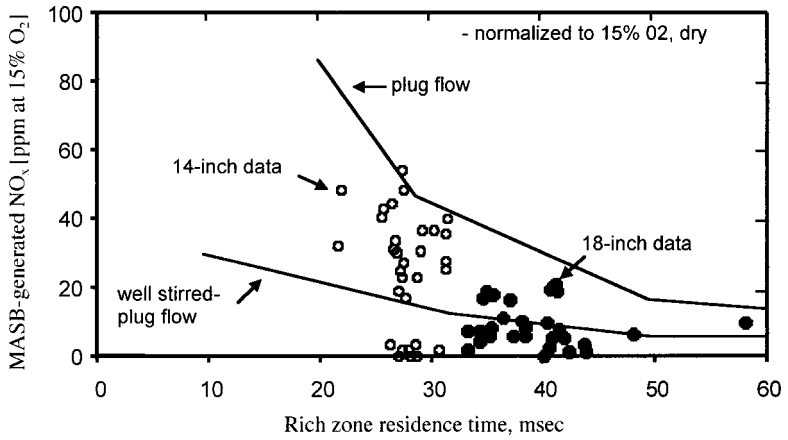

Fig. 5 MASB generated NO_x versus rich zone residence time. Comparison of calculated and experimental data, [11].

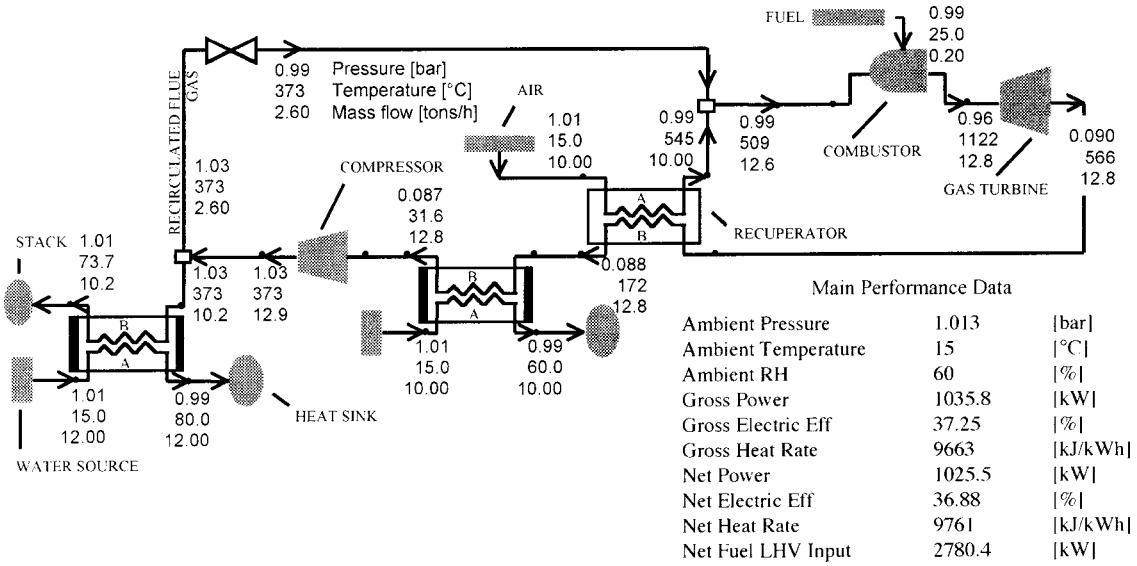

Fig. 6 Ambient pressure gas turbine cycle with flue gas recirculation

equivalence ratio of $\phi = 1.3$, and with 14.7 vol% O_2 in the vitiated air entering the MASB (simulated combustion products of the PFBC).

In the APGC, further reduction of the NO_x emission can be expected partly because of the lower operating pressure of the combustor, and also due to the use of flue gas recirculation, [13]. The O_2 depleted flue gas can be employed effectively as the quenching medium in an R-Q-L combustor; it reduces the NO_x formation in the quench zone while the fuel rich mixture is getting cooled. These results support the targeted single digit NO_x emissions from the MASB in the ambient pressure gas turbine cycle.

It is noteworthy that while realistic combustor tests on conventional gas turbines have to be performed in full-size, pressurized combustion facilities, the APGC turbine will need combustion tests only at atmospheric pressure. Therefore, demonstration tests of the MASB could be performed less expensively with a much more modest engineering effort in a combustion research laboratory, such as a university facility.

APGC Computational Studies

Cycle arrangements were computed by the use of "Thermoflex," a thermal engineering software, [14]. The basic thermodynamic cycle considered is shown in Fig. 6. The pressure (bar), the temperature (°C) and the mass flow (ton/h) are given at every reference point in the graph by three vertically arranged numbers. The main performance data are also shown in Fig. 6. While maintaining the fuel input and the gas mass flow rate through the turbine constant, several variants of this cycle were computed,

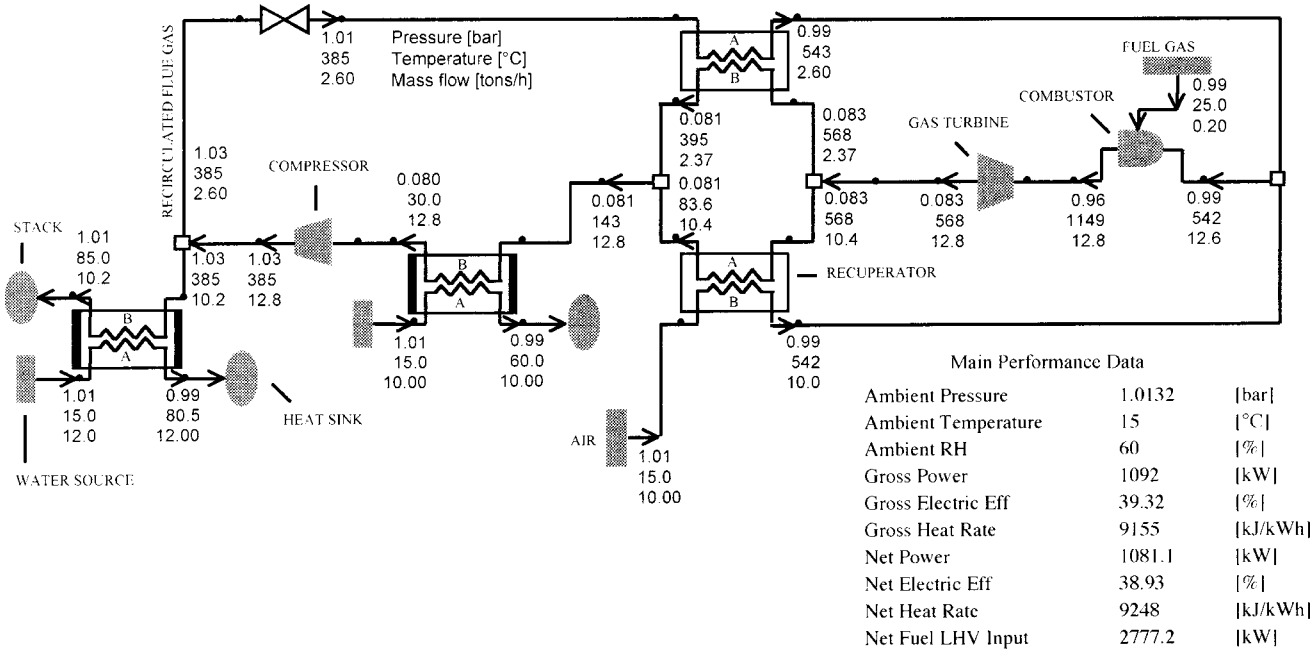

Fig. 7 Ambient pressure gas turbine cycle with both air and recirculated flue gas preheat

e.g., without and with flue gas recirculation, with the recirculated flue gas entering directly the combustor, or flowing through the recuperator before entry to the combustor.

Examination of the results shows that net electric efficiencies of 36.8–39.1% (LHV) and cogeneration efficiencies up to 88% can be obtained with the APGC, and that flue gas recirculation has a twofold effect upon the electric efficiency: It reduces the waste gas heat loss on account of the decreased mass flow rate of the stack gas, but it may also lower the sensible heat input to the combustor resulting in some loss of efficiency. This latter case arises when the recirculated flue gas enters the combustor directly, without getting preheated in the recuperator. The loss can, however, be restored by preheating the recirculated flue gas in the recuperator together with the combustion air, as shown in Fig. 7.

Summary

• Legislative reorganization of the power generation sector of the U.S. (and other) economy(s) expanded the market for 1–4 MWe gas turbines. It is expected that gas turbine plants in this size range would need to comply in the future with strongly tightened NO_x emissions regulations.

• Rearrangement of the traditional combustion turbine cycle into the ambient pressure gas turbine cycle (APGC) provides the opportunity for very low NO_x emissions obtainable with the multi-annular swirl burner (MASB).

• The MASB is operated in the highly stable diffusion flame mode as a rich-quench-lean staged-air combustor.

• Compared to the conventional high-pressure combustor, the rate of thermal NO_x formation is strongly reduced in the atmospheric pressure MASB.

• Recirculated flue gas of depleted O_2 concentration can be used effectively to reduce the temperature with a minimum of NO_x formation in the quench zone of the combustor. This is a further potential source of ''single digit'' NO_x burners.

• Computations using the ''Thermoflow'' code show that electric cycle efficiencies in the range of $\eta = 36.9–39.1\%$ (LHV) are obtainable, with the lower value for the case when the recirculated flue gas bypasses the recuperator, and the higher efficiency when both the combustion air and the recirculated fluegas flow through the recuperator before entering the burner.

• The APGC has special promise for the 0.5–5.0 MWe performance range. Improved polytropic efficiency of the turbine and compressor and the lighter construction of the containment vessels are additional advantages of this system.

Acknowledgment

The authors thank Mr. Donald McGaffigan for his assistance in the preparation of the manuscript and the computer graphic design of the figures.

References

[1] Vermes, G., and Beér, J. M., 2001, ''Ambient Pressure Gas Turbine System,'' U.S. Patent No. 6,298,654 B1, Oct. 9.

[2] Vermes, G., 1990, ''TG 15 Alternative Fuels Combustor Development,'' Textron-Lycoming Report MO. 071390GV1.

[3] Wilson, D. G., 1984, *The Design of High Efficiency Turbomachinery and Gas Turbines*, The MIT Press, Cambridge, MA.

[4] Hung, W. S. Y., 1995, ''An Experimentally Verified NO_x Emission Model for Gas Turbine Combustors,'' ASME Paper No. 75-GT-71.

[5] Toof, J. L., 1986, ''A Model for the Prediction of Thermal, Prompt, and Fuel NO_x Emission From Combustion Turbines,'' ASME J. Eng. Gas Turbines Power, **108**, pp. 340–347.

[6] Beér, J. M., 1989, British Patent No. 45652/65 (1965); U.S. Patent No. 4,845.940.

[7] Lew, H. G., DeCorso, S. M., Vermes, G., Carl, D., Havener, W. J., Schwab, J., and Notardonato, J., 1982, ''Low NO_x and Fuel Flexible Gas Turbine Combustors,'' ASME J. Eng. Gas Turbines Power, **104**.

[8] Garland, R. V., Pillsbury, P. W., and Dowdy, T. E., 1991, ''Design and Test of Candidate Topping Combustor for Second Generation PFB Applications,'' ASME Paper No. 91-GT-113.

[9] Domeracki, W. F., Dowdy, T. E., and Bachovchin, D. M., 1995, ''Topping Combustor Status for Second Generation Pressurized Fluid Bed Cycle Application,'' ASME Paper No. 95-GT-106.

[10] Beér, J. M., Dowdy, T. E., and Bachovchin, D. M., 1997, U.S. Patent No. 5636510.

[11] Domeracki, W. F., Dowdy, T. E., and Bachovchin, D. M., 1994, ''Status of Topping Combustor Development for Second Generation Pressurized Fluid Bed Cycles,'' ASME Paper No. 94-GT-176.

[12] Kee, R. J., Rupley, F. M., and Miller J. A., 1989, ''CHEMKIN II,'' Sandia Report SAND 89-8009, U.S. D.O.E. Sandia National Laboratories, Livermore, CA.

[13] Moorman, R. J., and Long, C. H., 1973, ''Design, Development and testing of a Swirl Type Gas Burner With Fuel Gas Recirculation for NO_x Control,'' ASME 73-PWR-21, pp. 1–9.

[14] *Thermoflow*, 1999, a thermal engineering software, Thermoflow, Inc., Sudbury, MA.

A High-Efficiency Solid Oxide Fuel Cell Hybrid Power System Using the Mercury 50 Advanced Turbine Systems Gas Turbine

W. L. Lundberg

S. E. Veyo

Siemens Westinghouse Power Corporation,
Stationary Fuel Cells,
1310 Beulah Road,
Pittsburgh, PA 15235-5098

M. D. Moeckel

Caterpillar Incorporated,
14009 Old Galena Road,
Mossville, IL 61552

The conceptual design of a 20 MWe-class hybrid power generating system that integrates a Siemens Westinghouse pressurized solid oxide fuel cell generator with a Mercury 50 gas turbine is discussed. The Mercury 50 was designed and developed by Caterpillar/Solar Turbines during the U.S. Department of Energy (DOE) Advanced Turbine Systems (ATS) program, and the hybrid system design concept was evaluated during a recently completed project that was part of the DOE high efficiency fossil power plant (HEFPP) program. While achieving a high power system efficiency by the hybrid cycle approach was important, the focus of the design study was to select the solid oxide fuel cell (SOFC) generator capacity such that the low specific cost of the ATS gas turbine and the high efficiency of the more expensive pressurized solid oxide fuel cell (PSOFC) generator would combine optimally to produce an attractively low cost of electricity (COE) for the overall power system. The system cycle and physical characteristics are described; power, efficiency, and emissions estimates are presented; and estimates of system cost and COE are provided. In addition, two bottoming cycle options (steam turbine and ammonia turbine) are described, and performance and cost projections for each are reviewed.
[DOI: 10.1115/1.1499727]

Introduction

The purpose of the U.S. Department of Energy high efficiency fossil power plant (DOE HEFPP) program was to evaluate fossil-fueled power plant concepts that would achieve, in addition to high efficiency, a cost of electricity (COE) that was less than the COE produced by conventional-technology power systems. In a recently completed HEFPP project, Siemens Westinghouse, with subcontractor Caterpillar, developed and evaluated a 20 MWe-class power system concept for a pressurized solid oxide fuel cell (PSOFC)/gas turbine (GT) hybrid power system, utilizing the Mercury 50 gas turbine, that would meet that objective. The Mercury 50, developed by Caterpillar/Solar Turbines during the DOE Advanced Turbine Systems (ATS) program, is a 4.5 MWe engine that achieves high Brayton cycle efficiency with recuperation. The premise of the Siemens Westinghouse/Caterpillar HEFPP conceptual design study was that a high-efficiency Siemens Westinghouse PSOFC generator could be integrated optimally in a hybrid-cycle system with the Mercury 50 ATS-GT to achieve, in addition to a high system efficiency, an attractively low COE. The study, results of which are summarized in this paper, found that the optimum integration of the PSOFC and Mercury 50 technologies resulted in a 10 MWe-class power block which could be operated independently, or doubled to provide the 20 MWe-class capacity of interest to the HEFPP program.

Power System Description

A simplified cycle diagram for the PSOFC/ATS-GT power system is presented in Fig. 1. The hybrid cycle, in which the fuel cell generator operates at compressor discharge pressure, achieves high-efficiency operation due to the inherently high efficiency of the fuel cell generator itself, the extended processing to power by the gas turbine of the fuel energy that was not converted to power by the fuel cell, the attendant reduction in the supply of fuel to the gas turbine combustor, and the operation of the fuel cell generator at elevated pressure. To preclude a sulfur reaction with SOFC nickel-bearing components, the fuel processing system indicated in the figure is designed to reduce the fuel sulfur content from the specified 4 ppmv source level to 0.1 ppmv prior to SOFC entry.

It is noted that the world's first PSOFC/GT hybrid cycle power system, a 220 kWe system sponsored by Southern California Edison, has been designed and built by Siemens Westinghouse Power Corporation. It is for proof-of-concept purposes, and with the exception of incorporating a simpler fuel processing system and a two-shaft gas turbine, the system is based on the cycle depicted in Fig. 1. It has undergone factory and site acceptance testing, and its capability for safe, controlled startup, operation (with high efficiency), and shutdown has been demonstrated. Continued operation and testing of the power system are planned. A view of the system is presented in Fig. 2, and additional detail on the 220 kWe PSOFC/GT power system and program is provided in papers by Veyo et al. [1] and Veyo and Vora [2].

The 20 MWe-class PSOFC/ATS-GT power system concept is depicted in Fig. 3. Two PSOFC/ATS-GT power blocks, each of 10 MWe-class capacity, are evident in the figure, separated on the site by balance-of-plant (BOP) support equipment. Each power block consists of one recuperated Mercury 50 gas turbine, which supplies pressurized, preheated air to four PSOFC generator modules, and expands hot exhaust received from the modules. Note that in this system concept, and provided the BOP equipment is available, one power block could be operated, delivering power to the AC grid, while the other block is down for maintenance. The area occupied by the 20 MWe-class system is 0.55 acre.

Each SOFC generator module employs Siemens Westinghouse solid oxide fuel cells. Each cell is tubular, having an active length of 1500 mm and a diameter of 22 mm. In each generator module, the cells are installed in 20 576-cell substacks. An individual substack is depicted in Fig. 4. A single PSOFC generator module, with DC power rating of approximately 2 MWe, is 11 m in overall

Contributed by the International Gas Turbine Institute (IGTI) of THE AMERICAN SOCIETY OF MECHANICAL ENGINEERS for publication in the ASME JOURNAL OF ENGINEERING FOR GAS TURBINES AND POWER. Paper presented at the International Gas Turbine and Aeroengine Congress and Exhibition, New Orleans, LA, June 4–7, 2001; Paper 2001-GT-521. Manuscript received by IGTI, Dec. 2000, final revision, Mar. 2001. Associate Editor: R. Natole.

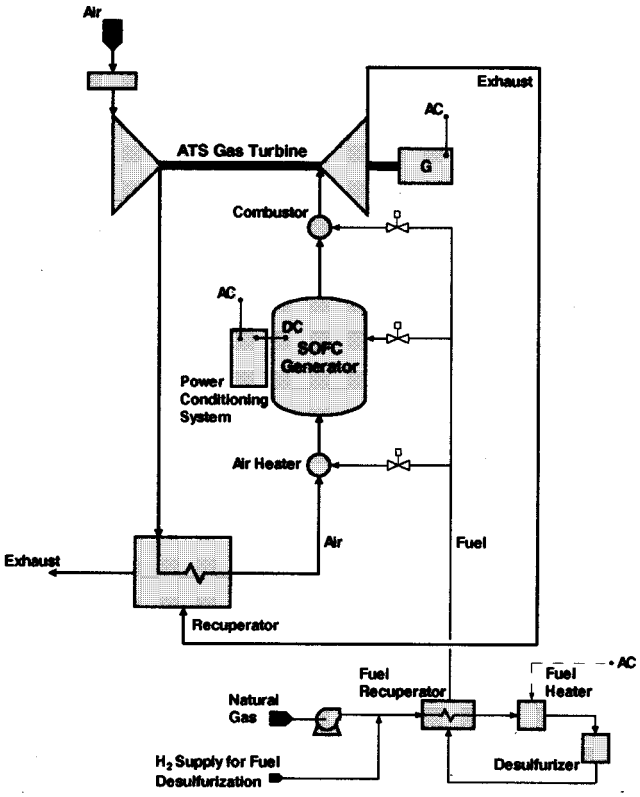

Fig. 1 Simplified PSOFC/ATS-GT hybrid power system cycle

length, and has an outer diameter of approximately 3.5 m. The DC power outputs of the four modules in each power block are combined and bused to the block power conditioning system where DC is converted to AC form and stepped to AC grid voltage. The Mercury 50 gas turbine operates with a pressure ratio of 9.5:1, a combustor exit temperature of approximately 1150°C, and generates approximately 4.5 MWe. Some modification of the Mercury 50 is required, as described later, for it to send recuperator outlet air to the PSOFC module inlets and to receive SOFC exhaust (vitiated air) as its oxidant at the combustor air inlet. The SOFC exhaust is hotter than the normal Mercury 50 combustor inlet air (870°C versus 620°C), which results in a reduction of the rate at which fuel is supplied to the combustor. Note that the study assumed the gas turbine would operate at Mercury 50 design conditions rather than at potentially different conditions which could be dictated by a hybrid-cycle optimization.

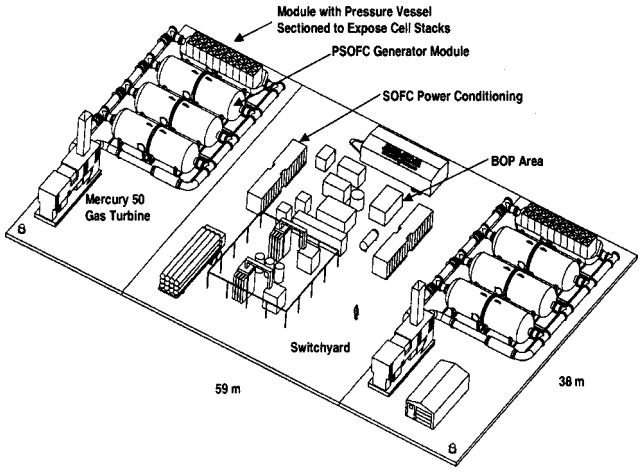

Fig. 3 20-MWe PSOFC/ATS-GT power system site

Results of the study to determine the optimum PSOFC generator sizing for combination with a single Mercury 50 gas turbine are presented in Fig. 5. They show the effect of varying the number of 576-cell substacks to be included in the generator configuration. As the number of cell stacks increases, the estimated system efficiency increases because the SOFC current density is able to move progressively to lower values, and the cell voltage to higher values. The optimizing parameter is the COE. Initially, the COE decreases with the addition of cell stacks, a direct response to the improving system efficiency. However, the SOFC cost effect eventually becomes controlling, and the crossover between efficiency dominance and cost dominance occurs at the minimum-COE point, and defines the optimum number of cell substacks that should be included in the SOFC generator. The analysis indicates that number is 72, but 80 was chosen because it results in small COE increase, but an increase in the system efficiency of nearly 6/10 of one percentage point. The 80 substacks are packaged in four horizontal pressure vessels, as indicated in Fig. 3. The

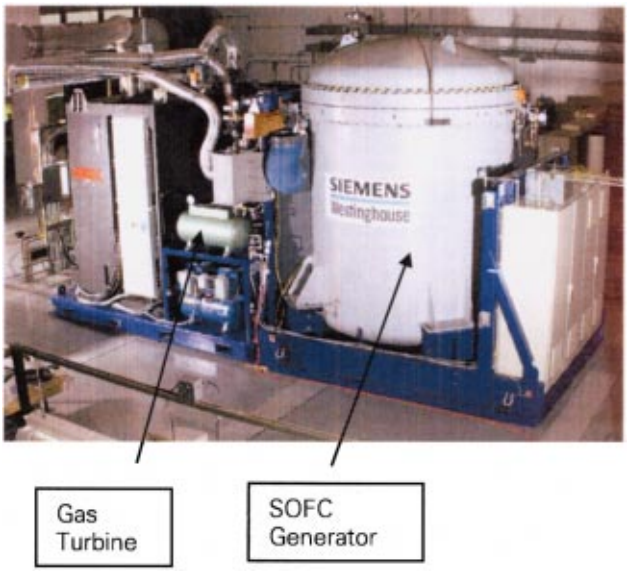

Fig. 2 220-kWe PSOFC/GT power system

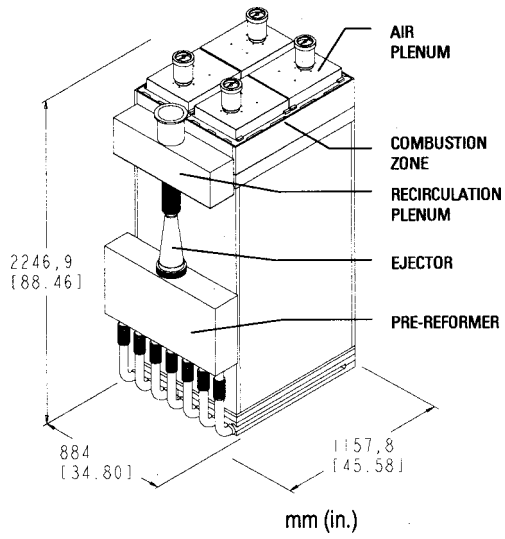

Fig. 4 Basic building block (576-cell substack)

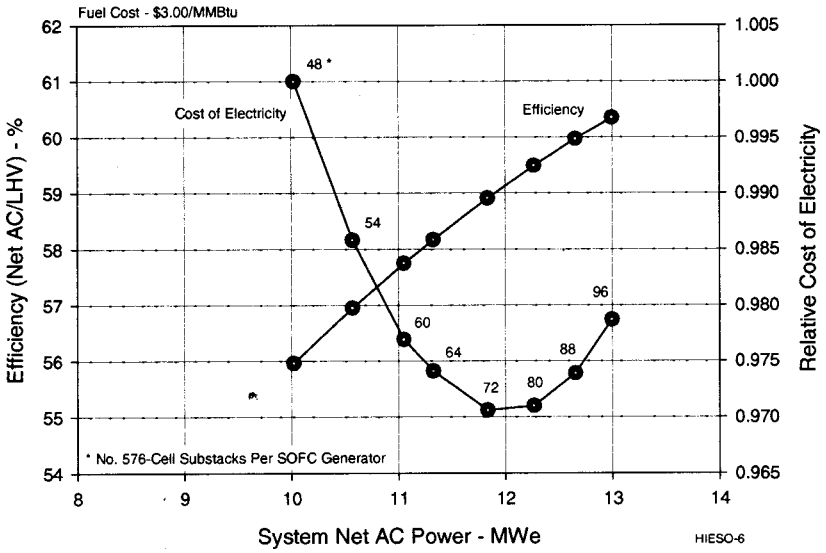

Fig. 5 PSOFC generator sizing

minimum-COE power system, a power block consisting of four PSOFC generator modules and one Mercury 50 gas turbine generates approximately 12.5 MWe at an efficiency of nearly 60 percent (Net AC/LHV). For HEFPP study purposes, two such power blocks were needed to compose the required 20 MWe-class power system.

The Solar Turbines Mercury 50 Advanced Turbine Systems (ATS) Gas Turbine

Integration of Mercury 50 Gas Turbine To Pressurized Solid Oxide Fuel Cell (PSOFC) System. Selection and integration of a well matched gas turbine engine to the pressurized solid oxide fuel cell subsystem is a key factor in determining the lowest cost of electricity (COE) integrated system. The Mercury 50 recuperated gas turbine engine, shown in Figs. 6 and 7, was chosen as the gas turbine to integrate in this low-COE PSOFC/ATS-GT concept system.

The Mercury 50 was chosen due to its high thermal efficiency, power rating, modular design, reliability, and low cost of maintenance. The design point specifications and pertinent fuel cell integration points of the Mercury 50 as a stand alone gas turbine engine at 27°C, sea level intermittent rating, and 15°C ambient, sea level conditions for both intermittent and continuous ratings are as follows:

Parameter	27°C Inter	15°C Inter	15°C Cont
Hours of Operation per Year	2500–5000	2500–5000	8760
Turbine electric power (MWe)	4.21	4.57	4.43
Overall efficiency-gen (percent)	40.0	41.5	41.1
Natural gas fuel flow (kg/h)	790	827	814
Overall airflow (kg/s)	16.0	16.6	16.6
Recuperator airflow (kg/s)	15.4	16.0	16.0
Recuperator air outlet temp. (°C)	631	621	611
Recuperator air outlet pres. (kPa)	879	909	909

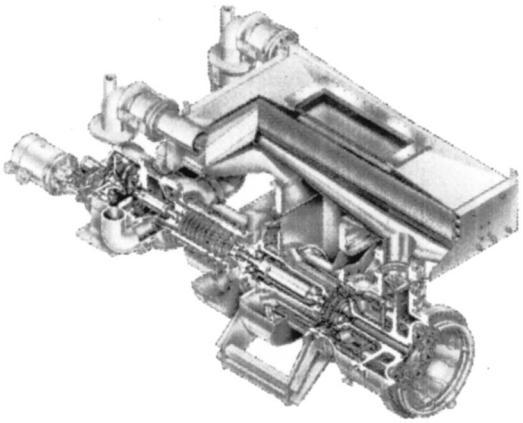

Fig. 6 Mercury 50 recuperated gas turbine

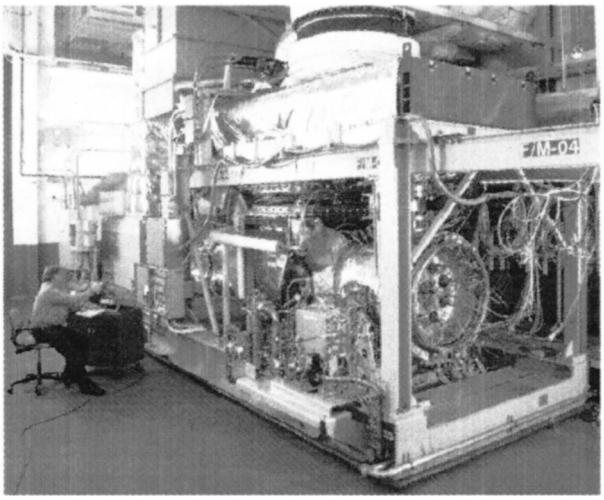

Fig. 7 Mercury 50 undergoing test at solar turbines; San Diego, CA

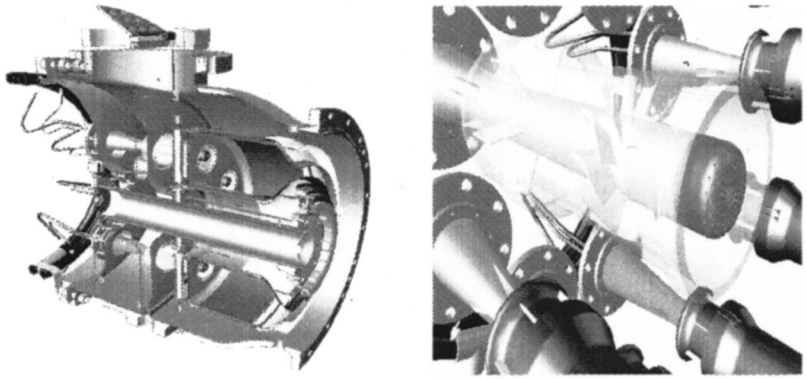

Fig. 8 Mercury 50 combustor and injectors

The performance quoted is based on the following parameters:

Generator efficiency (percent)	97.0
Gearbox efficiency (percent)	98.7
Inlet air relative humidity (percent)	60
Compressor inlet delta *P* (kPa)	0
Exhaust delta *P* (percent)	3.8
Compressor pressure ratio	9.33
Combustor outlet temp. (°C)	1207-Int/1193-Cont
Combustor TRIT (°C)	1163-Int/1150-Cont
Compressor flow (kg/s)	16.6
Recuperator gas flow (kg/s)	16.7
Fuel added (kg/s)	0.23
Air lost (kg/s)	0.09
Combustor delta *P* (PSOFC) (percent)	3.0
Compressor adiabatic eff. (percent)	87.5
Expander adiabatic eff. (percent)	87.6
Recuperator effectiveness (percent)	92
Recuperator air out temp. (°C)	621-Int/611-Cont

Modifications to the Mercury 50. The PSOFC/ATS-GT power system was optimized by Siemens Westinghouse with input from Caterpillar Research regarding the Mercury 50 performance. The PSOFC/ATS-GT system optimized for the lowest cost of electricity resulted in the Mercury 50 turbine operating very near its 15°C/sea level design point. The lowest COE point resulted in the Mercury 50 running at a pressure ratio of 9.5:1 versus a design point of 9.3:1 which resulted in a power output of 4.8 MWe versus a design point of 4.6 MWe. A minor adjustment to the compressor variable geometry was made by opening stators 5.7 deg to rematch the Mercury 50 to the integrated PSOFC/ATS-GT optimum point. Combustor outlet TRIT was maintained at 1163°C with overall thermal efficiency of the engine dropping only 0.5 point.

The combustor will be receiving airflow from the PSOFC module, containing 16 percent oxygen at 870°C versus an engine design point airflow temperature from the recuperator of 620°C. The eight injectors of the combustion system shown in Fig. 8 will need to be resized to maintain the proper optimum combustion characteristics; however, the combustor is required to raise the engine flow 336°C versus a normal temperature rise of 587°C for the base Mercury 50 engine design point on a 15°C day. Modifications to the combustor main case would need to take place to be able to withstand the 870°C PSOFC exhaust. Incorporating internal insulation, similar to that used in the PSOFC exhaust piping would be the prime path; however, redesign of the combustor case using high-temperature materials should be investigated in any future design.

Physically, the modular and innovative design of the Mercury 50 with the combustion section at one end of the engine, make the Mercury 50 easy to accommodate connection to a PSOFC system. As shown in Fig. 6, the Mercury 50 normally has a single connection between the recuperator air outlet and the combustor at the 12 o'clock position. The recuperator air outlet will be extended axially outward for connection with the PSOFC inlet and the turbine combustor section will be rotated 90 deg for easy connection with the PSOFC exhaust as depicted in Fig. 9.

Solar's Role in Advanced Turbine Systems (ATS) and Mercury 50 Status

On Sept. 14, 1995, Solar Turbines, a wholly owned subsidiary of Caterpillar Inc., was awarded a six-year contract to develop two sizes of ATS products. In developing the Mercury 50 gas turbine concept, Solar considered current marketplace requirements in conjunction with the DOE/industry ATS program objectives. The most significant demand peak was noted at approximately 5 MWe in output, driven primarily by the industrial power generation and emerging distributed generation market segments for whom efficiency and first cost are key requirements.

In response, Solar developed the Mercury 50 gas turbine, which was announced to the public in 1998 at the ASME Turbomachinery Exhibition in Orlando, FL. It is an optimized recuperated gas turbine, nominally sized at 4.2 MWe on a 27°C (80°F) day (4.9 MWe at ISO conditions). This environmentally superior system incorporates a highly flexible combustion system that can be configured for either ultra lean-premixed or catalytic combustion, with an ultimate goal of 5 ppmv NO_x on natural gas without the use of add-on post-combustion pollution control devices. The Mercury 50 gas turbine is a single-shaft machine designed around an optimized recuperated cycle that is targeted to meet the rapidly expanding demand for highly efficient, environmentally superior turbine-based power systems in the industrial power generation markets.

The Mercury 50, as of mid Oct. 2000, continues in a field demonstration phase with multiple units in developmental test at selected field sites where 6000 hours have been accrued. A single engine has accumulated over 2500 hours. At the DOE host site at Rochelle Municipal Utilities in Rochelle, IL, a Mercury 50 ATS engine is operating in economic dispatch mode and has accumulated 1000 hours of operation. Shipment of commercial units is planned for mid 2002.

Mercury 50 Gas Turbine Design

Increases in firing temperatures and compression ratios, combined with the use of advanced cooling, sealing and materials technologies have been the traditional approaches to improving turbine performance. While such technology improvements can offer significant benefits, industrial gas turbine users have traditionally avoided new technologies out of concern for the potential impacts on overall reliability. Instead, they prefer a sensible balance between the demonstrated benefits of key technologies and the high reliability requirements demanded by their processes.

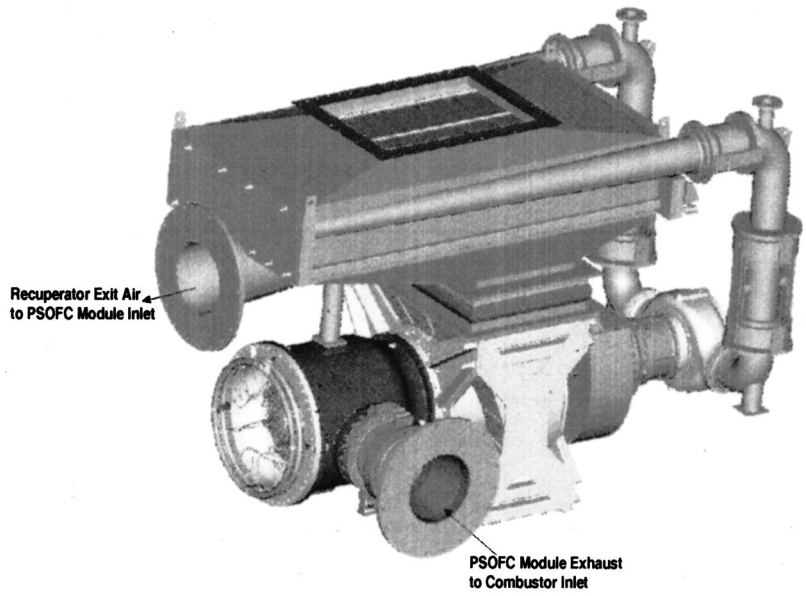

Fig. 9 Modifications required for PSOFC integration

This led Solar to evaluate the use of compound cycles based upon demonstrated technologies as the approach most likely to yield a step improvement in efficiency without unduly risking reliability in the process. Initially, a wide variety of candidate cycles was assembled for consideration. The benefits and drawbacks of each concept were qualitatively assessed against key customer buying criteria, including performance, cost, risk, growth capability, reliability and customer acceptance. From this process, two cycles were carried forward as potential solutions: intercooled and recuperated (ICR) and recuperated.

Recuperation of the classic Brayton cycle gas turbine is a well-known method of improving cycle efficiency that involves the addition of a heat exchanger to recover some portion of the exhaust heat that would otherwise be lost to the cycle. The differential between the exhaust gas temperature and the compressor discharge temperature determines the extent of the efficiency improvement that can be realized. Intercooling the Brayton cycle involves the addition of an interstage heat exchanger, to reject a portion of the heat generated during the compression process, which significantly reduces the work input required by the compressor. The combination of intercooling and recuperation into an ICR cycle produces an increase in both specific power and thermal efficiency. This enables the recovery of a greater portion of the thermal energy in the exhaust gas at the expense of an increase in the complexity of the machine. Figure 10 graphically contrasts the flow paths associated with simple and recuperated cycles.

Primary Surface Recuperator. Recuperated cycles have been applied to gas turbines in the past with varied degrees of success. In general, bulky tube-shell or plate-fin heat exchangers were added onto existing turbines via somewhat elaborate and often cumbersome piping and support arrangements, with little or no attempt made to optimize the cycle. The result was a lukewarm performance improvement accompanied by poor thermal transient response, thermal cracking and other mechanical performance problems within the recuperator that often failed to meet customer expectations. Yet, when a prime mover, such as Solar's Mercury 50 gas turbine, is designed to incorporate the recuperator from the start, significant gains can be realized without causing the mechanical performance issues that have occurred in the past.

At the heart of the Mercury 50 gas turbine lies Solar's proven primary surface recuperator (PSR). As outlined in Fig. 11, the construction is rugged and the modular nature of the design gives it superior flexibility to handle thermal stresses. Air cells are constructed from 0.1-mm (0.004-in.) thick sheets of Type 347SS folded into a corrugated pattern. This folded shape maximizes the primary surface area that is in direct contact with exhaust gas on

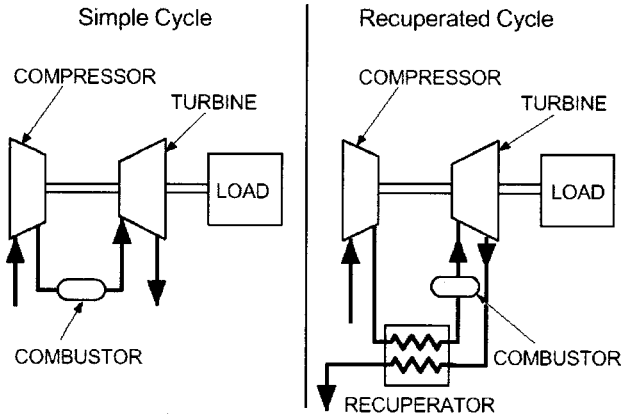

Fig. 10 Comparison of simple and recuperated cycles

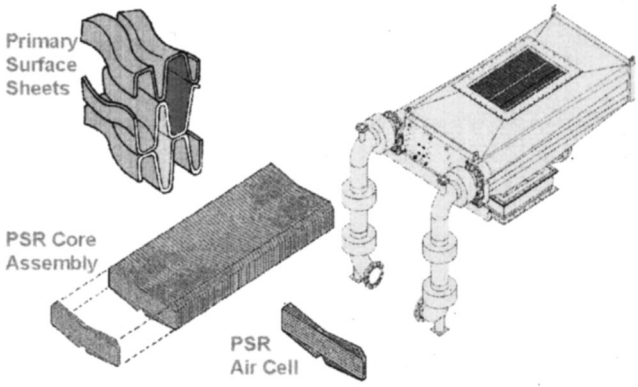

Fig. 11 Construction of the primary surface recuperator

Table 1 Estimated power system performance/power block

Parameter	
Compressor air intake rate	16.6 kg/s
Compressor pressure ratio	9.5:1
Gas turbine combustor exhaust temperature	1160°C
SOFC gross AC power	7.9 MWe
Gas turbine gross AC power	4.8 MWe
Power block net AC power	12.3 MWe
Fuel flow to the SOFC generator	0.31 kg/s
Fuel flow to the gas turbine	0.14 kg/s
Power system efficiency (Net AC/LHV)	59.9 percent
Carbon dioxide emission	340 kg/MWh
NO_x emission	0.04 kg/MWh
SO_x emission	0
Exhaust temperature	360°C
Exhaust flow rate	16.9 kg/s

one side and compressor discharge air on the other. Pairs of these sheets are welded together around the perimeter to form air cells.

There are no internal welds or joints within the air cells, which are the basic building block of the PSR. Groups of these cells are sandwiched together via an arrangement of clamping bars and are welded to intake and discharge headers to form the recuperator assembly. Developed by engineers at Caterpillar Inc. in the early 1970s for vehicular applications, the PSR has undergone numerous refinements and has been successfully applied to a variety of gas turbines over the years. To date, Solar's PSRs have accumulated in excess of 2.3 million operating hours with few of the incipient problems typical of alternative recuperator technologies.

Simplified Flow Path. The complex flow path of the recuperated cycle also provided design challenges that were effectively addressed in the layout. The recuperator is supplied with air from the compressor discharge plenum on one end, while heated air is collected at the other end and supplied to the combustor. Turbine exhaust is collected at the bottom center of the recuperator and discharged from the top. On a conventional turbine, this flow path requires a somewhat complex series of piping, elbows, flanges.

Electric Power Generator. Net shaft power is delivered at the turbine cold-end through a helical-gear gearbox to an air-cooled AC generator. For 60 Hz output, which was the basis for this project, the 14,200 rpm turbine shaft speed is reduced by the gearing to 1800 rpm, the generator design speed. Mercury 50 AC generators are available that can deliver design output voltages in the 3,300 V–13,800 V range, the high value being assumed in this study. The study also assumed that Mercury 50 power output would be delivered directly to the utility AC grid; no consideration was given to an overall power management system that would integrate and deliver to the grid the combined power outputs of the PSOFC generator modules and the Mercury 50 gas turbine.

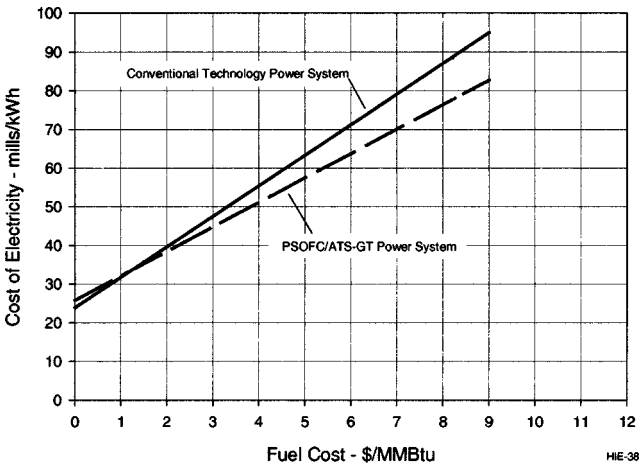

Fig. 12 Cost of electricity estimates

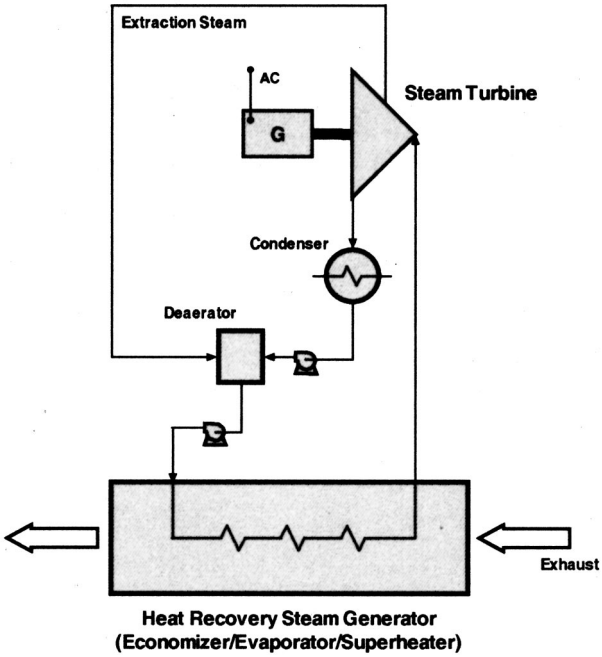

Fig. 13 Steam turbine cycle

Power System Performance and Cost Estimates

System performance estimates are summarized in Table 1. They are based on SOFC operation with a peak cell temperature of 1020°C and an SOFC fuel utilization of 85 percent. The estimated cell voltage and current density are 0.742 volts and 296 mA/cm^2.

The NO_x emission estimate was based upon an NO_x concentration of 5 ppmv, the Mercury 50 program goal without the need for post-combustion pollution control devices. Near-zero SO_x is projected due to the assumed desulfurization of all power system fuel.

The power system installed-cost estimate is $1170/kWe. It includes costs related to site preparation, equipment procurement, shipping, and installation, as well as allowances for G&A, sales

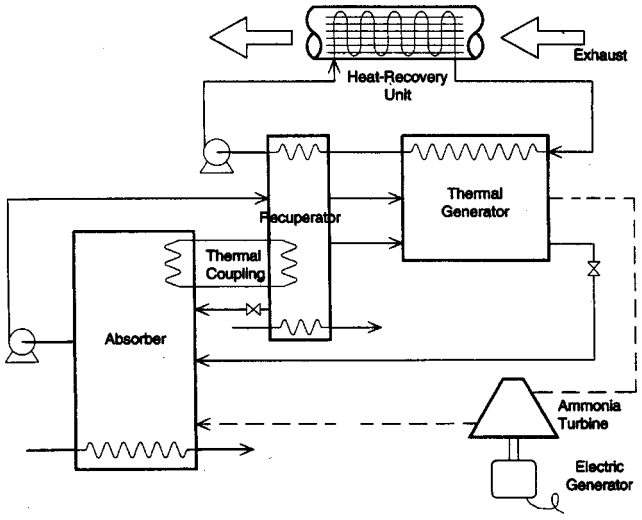

Fig. 14 Ammonia-water power system cycle

Table 2 Energy flows in the ammonia-water power cycle

Components	Heat Rate kW	Power Generation kW
Heat recovery unit	10,305	
Generator—heat from transfer fluid	9,224	
Recuperator		
Heat from transfer fluid	1,081	
Heat rejected to water	3,095	
Absorber—heat rejected to water	5,129	
Turbine power		2,081
Electric generator power		1,977
Pumping power		70
Net power		1,907

Table 3 Estimated power system performance, with bottoming cycles

Parameter	Baseline PSOFC/ATS-GT Power System	With Steam Turbine Cycle	With Ammonia-Water Cycle
SOFC AC power, MWe	15.8	15.9	15.9
Gas turbine AC power, MWe	9.6	9.6	9.6
Bottoming cycle AC power, MWe	···	1.6	1.9
Power system net AC power, MWe	24.7	26.2	26.5
Power system efficiency (NetAC/LHV), %	59.9	63.6	64.4
Carbon dioxide emission, kg/MWh	340	317	313
NO_x emission, kg/MWh	0.040	0.038	0.038
SO_x emission	0	0	0
Exhaust temperature, °C	360	215	94
Exhaust flow rate, kg/s	33.9	33.9	33.8
Installed cost, $/kWe	1,170	1,220	1,260

and marketing, and profit. Mature technologies were assumed. COE estimates were developed for the system, operating at its design point, and also for a competing technology, which was assumed to be a 20 MWe-class gas turbine/steam turbine combined cycle. The cost and efficiency estimates for the conventional-technology system were $830/kWe and 47.9 percent, taken from the 1997 Gas Turbine World Handbook. COE estimates for the two power systems are graphed in Fig. 12 as functions of fuel cost. At the reference HEFPP study fuel cost, $3/MMBtu, the COE estimate for the PSOFC/ATS-GT power system is approximately 6 percent less than the conventional-technology value. As the figure indicates, the COE advantage of the advanced power system will increase with increasing fuel cost.

Bottoming Cycle Options. As indicated in the performance summary, the power system exhaust exits the recuperator at 360°C with a flow rate of 16.6 kg/s per power block. Assuming the flows from two blocks were collected and combined, two analyses were done to assess the performance of bottoming-cycle-equipped PSOFC/ATS-GT power systems. In one, the added cycle was composed of a heat recovery steam generator (HRSG) and steam turbine, while in the other it was an ammonia-water absorption system power cycle in which the additional power was produced by the expansion of pressurized ammonia gas across an ammonia turbine.

The cycle for the steam turbine system is depicted in Fig. 13. The HRSG is a once-through unit, consisting of economizer, evaporator, and superheater sections. The evaporator generates steam a 31.0 bara (450 psia) for supply to the turbine, superheated 28°C (50°F). The deaerator operates on steam extracted from the steam turbine at 1.5 bara (22 psia), 0.14 bar (2 psi) above the deaerator pressure. The steam turbine was assumed to be a condensing unit, and the condenser operating pressure was set at 0.04 bara (0.6 psia).

The ammonia-water system cycle, depicted in Fig. 14, consists of a heat-recovery unit, thermal generator, internal recuperator, ammonia absorber, and turbine plus electric generator. The system requires three solution pumps, one transfer-fluid pump, and a cooling-water pump. Only one solution pump is shown in Fig. 14, the other two are integrated in the recuperator. For better control and integration of the power cycle, a closed flow loop with water as transfer fluid is used for heat recovery. This approach maintains low pressure drop on the exhaust gas side and thereby minimizes the backpressure on the gas turbine exhaust. About 90 percent of the heat from the transfer fluid is used for generating vapor in the thermal generator. The countercurrent heat and mass transfer processes in the thermal generator facilitate an efficient heat extraction from the transfer fluid. The remaining heat is used in the recuperator, which is an integrated heat and mass transfer unit for recuperating internal and external heats. Ammonia vapor in the generator is internally superheated. The vapor then drives the tur-

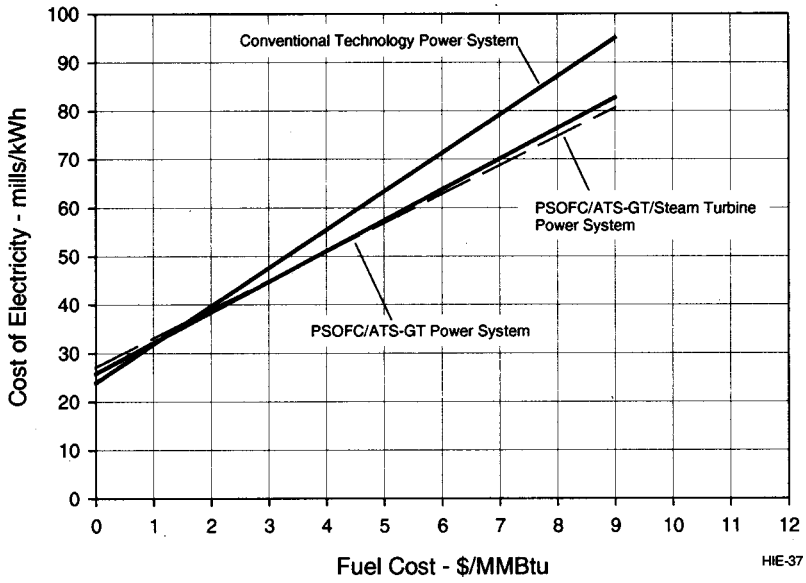

Fig. 15 Cost of electricity for steam bottoming cycle option

bine and the resulting low-pressure ammonia vapor flows to the absorber, where it is absorbed in the strong (high absorbing capacity) solution from the generator. The resulting weak (low absorbing capacity) solution is pumped to the recuperator, where it is divided into three streams for balancing the heat and mass transfer from different sections of the recuperator. As shown in Fig. 14, one stream from the recuperator returns to the absorber, and also the recuperator and absorber are thermally coupled. Heat integration in the recuperator is a key design feature of the power cycle, because the overall conversion efficiency of the cycle depends on the thermal performance of the recuperator.

Energy flows in the major components are summarized in Table 2. The total thermal energy recovered from the exhaust gas stream is 10,305 kWth, which is 77.3 percent of the residual LHV of the exhaust gas. Of this, about 20 percent is converted to electric power. After accounting for pumping losses, the net electric power produced by the ammonia-water cycle is 1907 kWe.

Performance estimates for the baseline PSOFC/ATS-GT power system are compared in Table 3 with estimates for the system when equipped with the bottoming cycle options described above. The Table 3 entries all apply to 20 MWe-class power systems, each composed of two 10 MWe-class PSOFC/ATS-GT power blocks.

As Table 3 shows, equipping the power system with either bottoming cycle will attractively increase the overall system power output and efficiency, but it will also increase the system cost. As Fig. 15 indicates, the steam-cycle-equipped power system, due to its higher cost, and also to its higher O&M cost, will not show significant COE advantage until high fuel costs are reached. Similar COE predictions were obtained by the analysis of the ammonia-water bottoming cycle system. It is noted that the analysis did not take economic advantage of the reduced hybrid system emissions. Factoring in the effects of carbon and NO_x emission taxes would, of course, increase the COE attractiveness of the hybrid power system with bottoming cycle.

Conclusions

(1) A low-cost 60 percent efficient 20 MWe-class PSOFC/ATS-GT hybrid power system concept has been developed that employs the Mercury 50 ATS gas turbine. (2) The system installed-cost estimate is $1170/kWe, and when operated on $3/MMBtu natural gas fuel, its estimated COE is approximately 6 percent less than the COE of a less expensive, less efficient, conventional-technology GT/ST combined cycle power system. Increased COE advantage is achieved at higher fuel costs. (3) Adding a bottoming cycle (steam turbine or ammonia-water power cycle) to the baseline PSOFC/ATS-GT power will increase the system power output and efficiency to approximately 64 percent. (4) However, adding the bottoming cycle will not necessarily result in increased economic advantage (relative to the baseline PSOFC/ATS-GT power system) until high fuel costs are reached due to increases in the system installed and O&M costs.

Acknowledgments

The development of the Siemens Westinghouse tubular solid oxide fuel cell is supported by the United States Department of Energy, National Energy Technology Laboratory, Morgantown, WV, under a cooperative agreement, contract DE-FC26-97FT34139. The conceptual design of the PSOFC/ATS-GT power system was supported by the United States Department of Energy National Energy Technology Laboratory, Pittsburgh, PA, under contract DE-AC26-98FT40455, and by the Siemens Westinghouse Power Corporation and Caterpillar Incorporated.

The ammonia-water power system concept, its analysis, and the concept discussion presented above were developed by the Energy Concepts Company, Annapolis, MD.

References

[1] Veyo, S. E., Shockling, L. A., Dederer, J. T., Gillett, J. E., and Lundberg, W. L., 2000, ''Tubular Solid Oxide Fuel Cell/Gas Turbine Hybrid Cycle Power Systems—Status,'' ASME Paper No. 2000-GT-550.

[2] Veyo, S. E., and Vora, S. D., 2000, ''Tubular SOFC Field Units—What, Where, When,'' *Fuel Cell Seminar Proceedings*, Nov., Portland, OR, Courtesy Associates, Washington, DC.

A Thermodynamic Analysis of Tubular Solid Oxide Fuel Cell Based Hybrid Systems

A. D. Rao[1]

G. S. Samuelsen

Advanced Power and Energy Program,
University of California,
Irvine, CA 92697-3550

The goals of a research program recently completed at the University of California, Irvine were to develop analysis strategy for solid oxide fuel cell (SOFC) based systems, to apply the analysis strategy to tubular SOFC hybrid systems and to identify promising hybrid configurations. A pressurized tubular SOFC combined with an intercooled-reheat gas turbine (SureCell™ cycle) is chosen as the base cycle over which improvements are sought. The humid air turbine (HAT) cycle features are incorporated to the base cycle resulting in the SOFC-HAT hybrid cycle which shows an efficiency of 69.05 percent while the base cycle has an efficiency of 66.23 percent. Exergy analysis identified the superior efficiency performance of the SOFC component. Therefore, an additional cycle variation added a second SOFC component followed by a low pressure combustor in place of the reheat combustor of the gas turbine of the SOFC-HAT hybrid. The resulting dual SOFC-HAT hybrid has a thermal efficiency of 75.98 percent. The single SOFC-HAT hybrid gives the lowest cost of electricity (3.54¢/kW-hr) while the dual SOFC-HAT hybrid has the highest cost of electricity (4.02¢/kW-hr) among the three cycles with natural gas priced at $3/GJ. The dual SOFC-HAT hybrid plant cost is calculated to be significantly higher because the fraction of power produced by the SOFC(s) is significantly higher than that in the other cases on the basis of $1100/kw initial cost for the SOFC. The dual SOFC-HAT hybrid can only be justified in favor of the single SOFC-HAT hybrid when the price of natural gas is greater than $14/GJ or if a severe carbon tax on the order of $180/ton of CO_2 is imposed while natural gas price remains at $3/GJ. [DOI: 10.1115/1.1499728]

Introduction

The majority of electricity in the U.S. is generated by the combustion of fossil fuels to heat either steam or ''air'' for use in Rankine or Brayton cycles. Until recently, the industry has operated these power plants under regulations that have guaranteed a reasonable return on investment. In the past decade, however, a number of factors have coalesced influencing the manner in which power will be generated in the years to come.

Potential for Regulation on Greenhouse Gas Emissions. Due to the projected increases in fossil fuel usage world wide, emissions of carbon dioxide (CO_2) to the atmosphere are expected to increase by about 60 percent over the 1990 level by 2015. CO_2 is the primary constituent in the earth's atmosphere that contributes to the greenhouse effect. The greenhouse effect is the entrapment of heat by the earth's atmosphere by gases such as CO_2; the sun's radiation falling on the earth's surface is reradiated as infrared heat which is absorbed by the greenhouse gases. It should be noted that the CO_2 generated from a given fuel per unit of power produced is inversely proportional to the thermal efficiency of a power plant, assuming complete utilization of the fuel. Thus, the CO_2 emissions may be reduced by increasing cycle efficiency.

Concern Over Emissions From Coal-Fired Plants. In addition to CO_2, pollutants such as oxides of sulfur, oxides of nitrogen, carbon monoxide, and unburned hydrocarbons are introduced into the atmosphere when traditional power generation technologies relying on combustion are used. The amount of pollutants emitted to the atmosphere depend on the degree of pollution abatement measures incorporated; these pollution abatement measures, however, tend to increase the plant operating and capital costs significantly in case of coal fired plants.

Deregulation. The breakup of the historic vertically integrated electric utility by deregulation is resulting in the appearance of merchant power producers selling in a market driven atmosphere. This is creating the marketplace for distributed power generation which is gaining much attention from industry and could be a major market for fuels cells if configurations can be identified that are efficient and simple so that the plant capital cost and process controllability are not compromised.

Thus, these factors have now made it a propitious time for a new approach to power generation; an approach that will change the way the fossil fuels are used by introducing advanced technologies that efficiently produce electricity while minimizing the environmental impact; fuel cells hold this promise.

Analysis Tools

Existing solid oxide fuel cell (SOFC) models do not fully integrate the heat and mass transfer with the electrochemistry while existing system models do not include simulation capabilities for the required power cycle equipment (e.g., SOFC). Thus, the capabilities required to perform tubular SOFC-based hybrid cycle analysis have been developed (Rao and Samuelsen [1]) which include analytical models for the tubular SOFC as well as the secondary equipment such as a gas turbine, reformer or partial oxidation reactor, shift reactor, humidifier, steam turbines, compressor, gas expander, heat exchangers, and pump. In addition to these equipment models, modules for functions such as separating a component from a stream, splitting a stream or combining streams and ''controller'' to automatically iterate in order to meet the desired design criteria are incorporated. Another important capability that is included is to be able to arrange the various components or modules as defined by the user in order to configure different hybrid systems.

[1]Senior Fellow, Fluor, Aliso Viejo, CA 92698.

Contributed by the International Gas Turbine Institute (IGTI) of THE AMERICAN SOCIETY OF MECHANICAL ENGINEERS for publication in the ASME JOURNAL OF ENGINEERING FOR GAS TURBINES AND POWER. Paper presented at the International Gas Turbine and Aeroengine Congress and Exhibition, New Orleans, LA, June 4–7, 2001; Paper 2001-GT-522. Manuscript received by IGTI, Dec. 2000, final revision, Mar. 2001. Associate Editor: R. Natole.

The system model may be used by cycle analysts from industry (e.g., equipment manufacturers, engineering and consulting firms, electric utility companies) for verifying performance of proposed cycles, as well as for developing new cycles.

Exergy Analysis

Exergy analysis may be applied to point the direction towards making changes to the system configuration in order to improve the thermal efficiency. It also allows a quantitative understanding of the dependence of the thermal efficiency on cycle operating parameters such as the pressure ratio, and provides means for quantitatively verifying the superiority of one cycle over another with respect to the thermal efficiency. The analysis consists of calculating the maximum work potential of each of the streams in the system as the stream is brought in thermodynamic equilibrium with the environment. The amount of this work potential destroyed across each major equipment within the system is also determined. Unlike the conventional definition of exergy, the maximum work potential is being defined to also include the work that may be produced from a stream when its temperature is lower than the ambient temperature. In such cases, a heat engine is hypothesized using the environment as its heat source and the stream as its heat sink. In this manner, the refrigeration potential of streams such as liquefied natural gas (when supplied to a power plant as fuel) may be taken into account. A potential use of the refrigeration potential of liquefied natural gas may be to cool the inlet air of a gas turbine in order to reduce the compressor work and thus increase the thermal efficiency (and the net power output) of the engine.

When the kinetic and potential energy effects may be neglected, exergy (χ) is defined as (Vogler and Weissman [2]):

$$\chi = W_{\text{sensible}} + W_{\text{expansion}} + W_{\text{concentration}} + W_{\text{chemical}}$$

where W_{sensible} is the reversible work that may be obtained by a heat engine taking heat from the stream (at temperature T) and rejecting heat to the environment (at temperature T_o), $W_{\text{expansion}}$ is the reversible work that may be obtained from the stream at pressure P by expansion (after conversion of the sensible heat) to the pressure of the environment (P_o), $W_{\text{concentration}}$ is the additional work that may be obtained by reversibly diffusing a noncombustible component i within the stream at partial pressure P_i through a membrane to the environment where it may be at a partial pressure of P_{oi}, and W_{chemical} is the work (after cooling and expansion) that may be produced by oxidation of the combustibles that may be present in the stream with enough excess air such that the partial pressure of the CO_2 corresponds to that in the ambient. Thus,

$$\chi = -\int (1 - T_o/T) C_p dT + RT\left[\ln(P/P_o) + \sum \ln(P_{io}/P_i)\right] - \Delta G_{\text{reax}}$$

where the integral in the first term on the right-hand side of the above equation is evaluated from the initial to the final temperature of the stream, C_p is the specific heat of the stream, ΔG_{reax} is the Gibbs free energy change for the oxidation reaction of the combustibles at the temperature of the environment. The first term on the right-hand side of the equation above (within the integral) defines the maximum work that may be obtained based on the Carnot cycle efficiency. For systems containing an electrochemical device such as a fuel cell and for systems where streams leaving the system have compositions very different from that of the ambient air, the Carnot cycle efficiency does not suffice.

This first term in the above equation as defined in Vogler and Weissman [2] is modified to include the work potential of streams that contain water in the form of vapor which could undergo a phase change when equilibrated with the environment, and is also applied to streams that are colder than the environment. This term (W_{heat}) is thus redefined as

$$W_{\text{heat}} = -\int (1 - T_o/T) dH$$

where H is the enthalpy which may include both sensible as well as latent heats. When $T < T_o$, it may be shown that the expression $W_{\text{heat}} = -\int (1 - T/T_o) dH$ still applies where dH is now the heat rejected by the reversible heat engine to the stream.

The second term is also modified in order to be able to handle streams that contain water as a vapor or as a liquid and may undergo phase change:

$$W_{\text{expansion}} = -\Delta G_{\text{expansion}}$$

where $\Delta G_{\text{expansion}}$ is the Gibbs free-energy change of the stream as its pressure is reduced to that of the environment. Note that for a reversible process occurring at constant temperature T_o,

$$\Delta H = T_o \Delta S - W_s$$

or

$$W_s = -\Delta H + T_o \Delta S = -\Delta G$$

where ΔH, ΔS, and ΔG are the enthalpy, entropy, and Gibbs free-energy changes while W_s is the shaft work.

The proposed next step in the path for the stream to equilibrate with the environment is the reversible isothermal oxidation reaction at T_o of the combustibles present in the stream utilizing the ambient air:

$$W_{\text{chemical}} = -\Delta G_{\text{chemical}}.$$

The proposed final step in the path for the stream to equilibrate with the environment is the reversible isothermal expansion at T_o of component i through a hypothetical reversible membrane to its partial pressure in the ambient air (by allowing the component to reversibly exchange through a selective membrane between the stream and a chamber, and similarly between the ambient air and a second chamber, the two chambers being connected by a turboexpander operating reversibly between the two pressures):

$$W_{\text{concentration}} = -\Delta G_{\text{concentration}}.$$

The components considered for this type of expansion are water vapor and carbon dioxide. The oxygen and nitrogen could also be expanded but in the reverse direction while producing work, since a concentration gradient may exist for these components between the system and the environment (the concentration in the environment being typically higher). Such considerations would, however, lead to misleading results or provide impractical guidance for cycle improvements.

Hybrid Systems Analysis

Systems identified for analysis and the results obtained by the application of the model are presented in the following.

Base Cycle—Westinghouse SureCell™ Configuration. A fuel cell based hybrid cycle consists of combining a fuel cell with a heat engine to maximize the overall system efficiency. One example of such a Hybrid cycle is the SureCell™ system as proposed by Westinghouse and depicted in Fig. 1 (Bevc and Parker [3]).

The system consists of an intercooled/reheat gas turbine integrated with a pressurized tubular solid oxide fuel cell (SOFC). Atmospheric air is compressed in an intercooled compressor, comprised of a low-pressure (LP) compressor and a high-pressure (HP) compressor. The discharge air from the HP compressor is preheated against the turbine exhaust in a recuperator and then provided to the SOFC as its oxidant. Fuel is also preheated in the turbine exhaust, supplied to the SOFC (after desulfurization) and to the gas turbine reheat or LP combustor. The exhaust from the SOFC, consisting of the depleted air and the depleted fuel, is supplied to the HP combustor of the gas turbine. The exhaust from the HP combustor enters the HP expander where it is expanded to

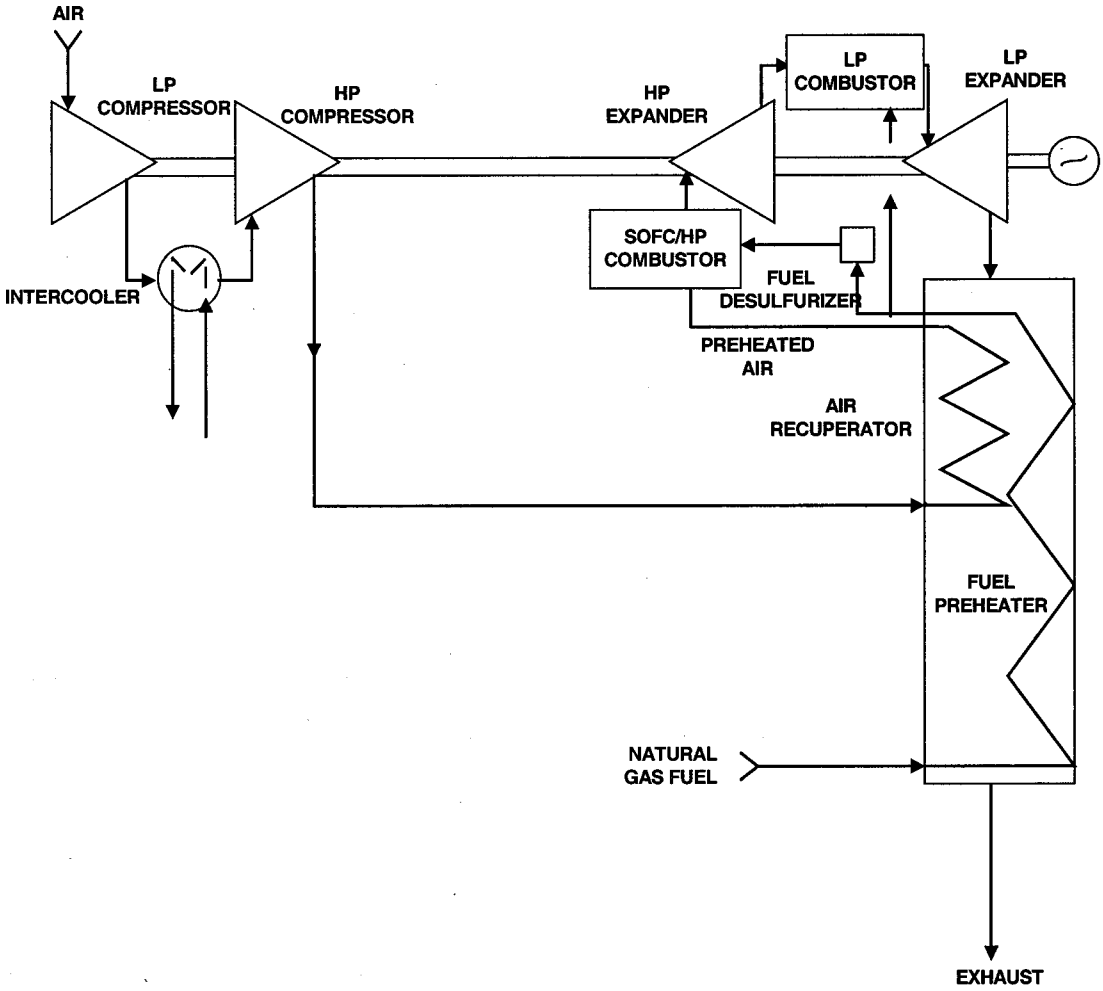

Fig. 1 Base cycle-SureCell™ system as proposed by Westinghouse (Bevc and Parker [3])

a pressure which is higher than atmospheric and then supplied to the LP combustor where the additional fuel is fired. Additional air and/or fuel may also be fed to the HP combustor. The hot exhaust from the LP combustor is then expanded in the LP expander to near atmospheric pressure and then supplied to the heat recovery unit. The power developed by the expanders drives the compressors and the electric generator.

The cycle thermal efficiency for this base cycle is developed for various pressure ratios. The cycle thermal efficiency is not a strong function of pressure ratio. The thermal efficiency of the cycle increases from 65.5 percent to 66.59 percent on a lower-calorific value of the fuel as the pressure ratio is decreased from 15 to 6.5. In order to explain this trend the cycle configuration is further analyzed by developing the exergy changes across each of the components of the system at three different pressure ratios. The results are summarized in Table 1 as relative exergies, that is, these exergies are presented as percentage of the exergy contained in the total fuel stream (entering the SOFC and the low pressure (LP) combustor). The exergy contained in the stack gas is also included in this table. The remaining two streams crossing the system boundary are the ambient air (LP compressor inlet) whose exergy is zero (the dead state) and the fuel which has the relative exergy of 100 percent. As seen by the data, the total exergy loss for the case with a pressure ratio of 6.5 is the lowest verifying the thermal efficiency trend.

As the cycle pressure ratio is reduced, the exhaust temperature from the LP turbine increases which in turn increases the temperature of the preheated air supplied to the SOFC. This increase in temperature more than offsets the decrease in efficiency of the SOFC operating at a lower pressure in the range of pressure ratios investigated. Furthermore, the irreversibilities in the LP combustor are reduced at the lower pressure ratio because the temperature of the oxidant stream entering this combustor increases as the expansion ratio of the high pressure (HP) turbine decreases. Also, the contribution to exergy loss by the intercooler is reduced as the cycle pressure ratio is decreased since less heat is rejected in the intercooler as the compression ratio of the LP compressor is reduced.

A pressure ratio of 8.8 is chosen for this base cycle (and not a lower pressure ratio) based on the constraint of limiting the tur-

Table 1 Base cycle—exergy destruction data (without generator/inverter losses)

Pressure Ratio	6.5	8.8	15
Component	**Exergy, % of Total Fuel Input**		
LP compressor	0.83	0.86	0.87
Intercooler	1.58	2.09	2.63
HP compressor	0.82	0.80	0.80
Recuperator+fuel preheater	2.53	2.05	1.43
SOFC	11.57	11.44	11.63
HP combustor	3.18	3.19	3.14
HP expander	0.81	0.86	0.84
LP combustor	9.77	10.14	10.54
LP expander	1.10	1.08	1.10
Stack gas	5.64	5.54	6.00
Total	31.33	29.25	23.98

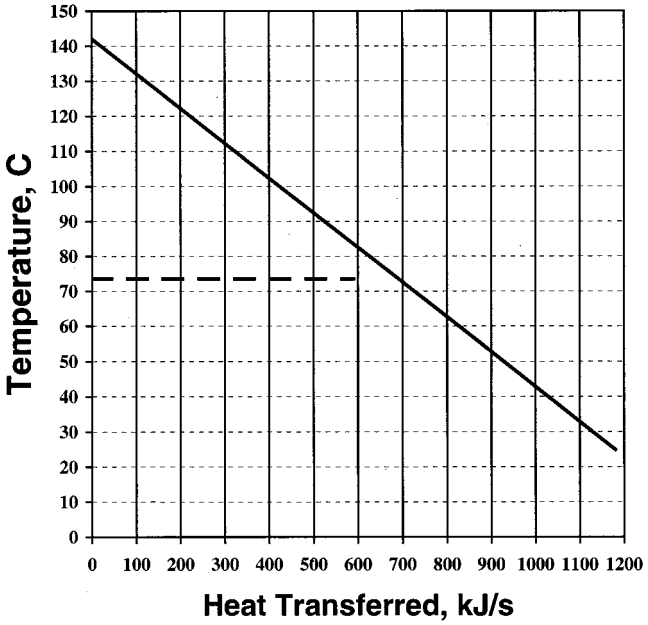

Fig. 2 Heat transfer from a gas to generate steam

bine exhaust temperature to a maximum of 635°C as set by the chosen design basis for this evaluation. The pressure ratio of 8.8 is also consistent with the pressure ratio touted for the SureCell™ hybrid by Westinghouse (Bevc and Parker [3]).

Enhancement of the thermal performance of the cycle may be accomplished by minimizing the exergy losses due to the intercooler and the stack gas. Modifications aimed at these components of the cycle are next attempted in order to maximize the cycle efficiency. The modifications however, should be such that the resulting cycle is not complex, thus not compromising its controllability and cost.

Conventional approach to recovery of heat has been via a Rankine cycle by generating steam. Inspection of the temperature of the heat available in the intercooler and in the stack gas indicates that only low pressure steam may be generated, the quantity and the pressure being limited by the saturation temperature of the steam corresponding to its pressure. Figure 2 depicts the heat transfer if steam were generated by half of the heat rejected by the air in the intercooler (for the case with a pressure ratio of 8.8).

As can be seen from the figure, the temperature of the gas (represented by the solid line) decreases as heat is transferred while the water/steam (represented by the dashed line) remains at a constant temperature being a single component. Thus, when as much as half of this heat is utilized for steam generation, the pressure of steam that may be generated corresponding to the saturation temperature of 73.5°C (allowing a 10°C temperature difference in the heat exchanger) will be only 0.34 bar, a pressure that is too low to generate power in a steam turbine economically. Another disadvantage with steam generation in addition to the above is that due to the diverging temperature difference between the gas and the steam/water mixture, the exergy loss in heat transfer is increased. If, however, a fluid that has a variable boiling point is utilized to recover the low temperature heat rejected in the intercooler, the quantity of heat recovered as well as the exergy destruction may be reduced.

The humid air turbine (HAT) cycle (Rao [4]) which utilizes generation of ''steam'' by directly contacting pressurized air with hot water in a countercurrent humidifier and circulating the water leaving the humidifier to recover heat rejected in the intercooler and from the stack gas could potentially be applied in this hybrid system to enhance the overall cycle efficiency.

The humidifier, by introducing water vapor into the combustion air would increase the amount of motive fluid available for expansion in the turbines, while recovering the low temperature heat from the intercooler and the stack gas. Within the humidifier, the water evaporates at successively higher temperatures as the air moves up the humidifier column (as its water vapor content increases) with hot water flowing countercurrently downwards exchanging mass and heat with the pressurized air stream. Furthermore, the water evaporates at temperatures much lower than the boiling point or saturation temperature of pure water since the phase change occurs within the humidifier in the presence of air (at the prevailing partial pressure of water vapor in the air stream). This combined humidifier and water circulating subsystem makes it possible to recover low temperature heat without being constrained by the boiling temperature of pure water while reducing the exergy destruction during heat transfer.

Single Solid Oxide Fuel Cell–Humid Air Turbine (SOFC-HAT) Hybrid. The resulting hybrid cycle as depicted in Fig. 3 incorporates humidification of the air before it is preheated in the recuperator and fed to the SOFC. The air leaving the compressor is first cooled in an aftercooler and then introduced into the humidifier column where it comes into countercurrent contact with hot water. A portion of the water is evaporated into the air stream, the heat required for the humidification operation being recovered from the intercooler and the stack gas by circulating water leaving the humidifier.

A potential disadvantage with this cycle is that the partial pressure of the oxygen in the air stream entering the SOFC is reduced which decreases the mass transfer rate of the oxygen to the cathode surface and through the cathode while increasing the cathode concentration and activation polarizations. On the other hand, the cycle may optimize at a high pressure ratio such that it off-sets the reduction in the concentration of the oxygen in the air stream with the net effect that the partial pressure of the oxygen is not significantly effected.

The efficiency of this hybrid cycle is determined to be also a weak function of the pressure ratio but increases with pressure in direct contrast to the SureCell™ configuration. The optimum efficiency of the cycle may lie beyond the maximum pressure ratio of 15 for the SOFC as constrained by the chosen design criteria for this investigation. The efficiency of the cycle at a pressure ratio of 15 is 69.05 percent based on the lower calorific value of the fuel to the system. The exergy destruction in each of the components of the cycle for the maximum efficiency case is compared to exergy destruction of the base cycle at the pressure of 8.8 in Table 2.

The SOFC-HAT hybrid has significantly less exergy destruction which verifies its significantly higher thermal efficiency as compared to the base cycle. The fuel consumption of the SOFC-HAT case is higher than the base cycle per unit of inlet air flow because of the high concentration of water vapor in the combustion air. Thus, the exergy destruction in the various components of the system of the SOFC-HAT hybrid are reduced per unit flow of fuel to the system. Additionally, in the case of the SOFC-HAT hybrid, the exergy destruction is reduced by the incorporation of recovery of heat from within the cycle and utilizing this heat for the humidification operation as can be seen by the data presented in Table 3 which also explains the relationship of the overall thermal efficiency of this case and the pressure ratio.

As the pressure ratio increases, more heat is removed from the air in the intercooler but since this heat is recovered for the humidification operation, the cycle is not penalized as is the base case cycle. Furthermore, the power developed by the expanders is increased by a much more significant amount than the power consumption of the air compressors as compared to the base case since additional motive fluid (water vapor) is added to the expanding fluid.

The performance of the SOFC in the base case and in the SOFC-HAT is compared in Table 4. The thermal efficiency of the fuel cell is slightly lower for the SOFC-HAT than that in the base

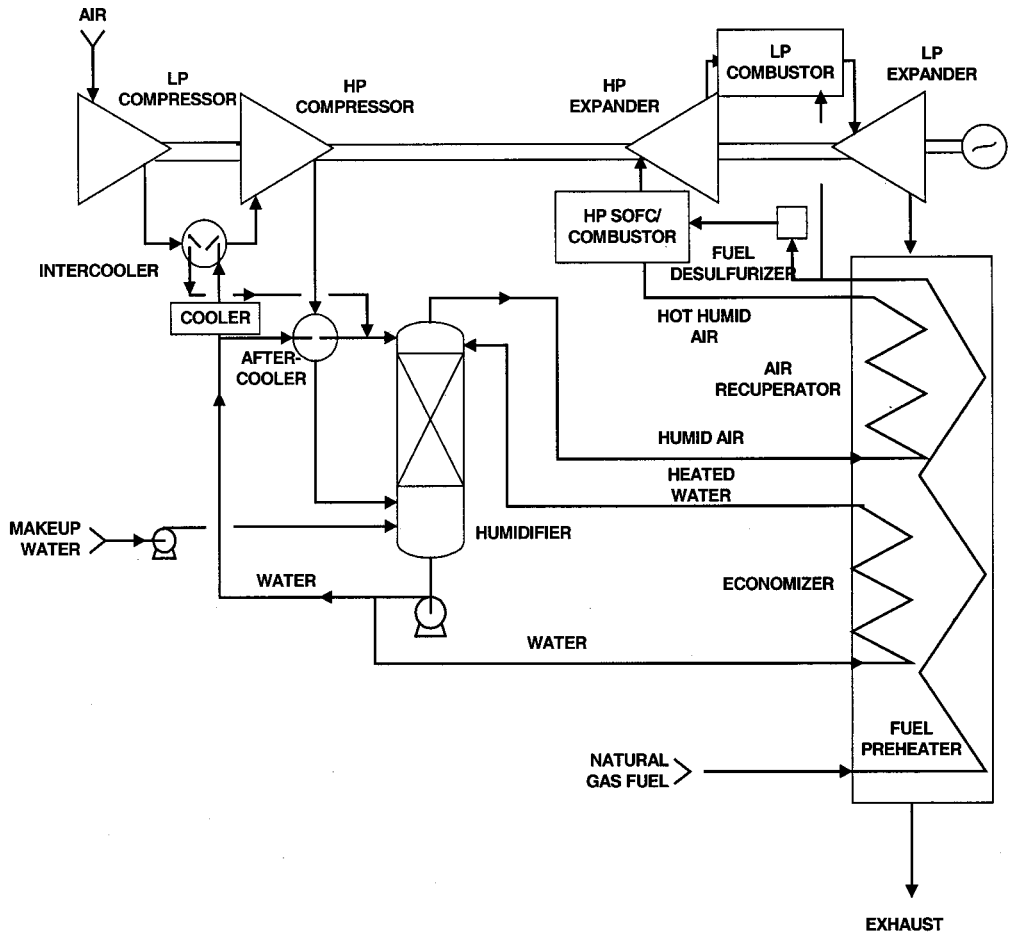

Fig. 3 Single SOFC-HAT hybrid

case. For a given operating pressure of the SOFC in the HAT-based system, as pointed out previously the lower concentration of the oxygen in the air stream entering the SOFC tends to decrease the mass transfer rate of the oxygen to the cathode surface and through the cathode itself which has the effect of decreasing the capacity of the cell as well as in increasing the cathode concentration and activation polarizations. However, the higher operating pressure of the SOFC in the HAT-based system more than compensates these effects such that the capacity of the SOFC is actually increased while the thermal efficiency is only slightly compromised over the SOFC in the base case.

Based on the exergy destruction data as presented in Table 2, it appears that the SOFC and the LP combustor destroy about the same amount of exergy when expressed as a fraction of the total fuel input to the cycle. However, when the exergy destruction by

Table 2 Exergy destruction in SOFC hybrid cycles as percent of total fuel input

	Base Cycle	Single SOFC-HAT Hybrid
LP compressor	0.86	0.7
Intercooler	2.09	0.58
HP compressor	0.80	0.72
Aftercooler	···	0.30
Humidifier	···	0.16
Economizer	···	0.24
Cooler	···	0.29
Recuperator and fuel preheater	2.05	1.71
HP SOFC	11.44	11.51
HP combustor	3.19	2.87
HP expander	0.86	0.81
LP combustor	10.14	10.19
LP expander	1.08	1.09
Stack gas	5.54	4.54
Total	38.05	35.71

Table 3 Reduction in exergy destruction by humidification as percent of total fuel input

	Base Cycle	Single SOFC-HAT Hybrid
Intercooler	2.09	0.58
Aftercooler	···	0.30
Humidifier	···	0.16
Economizer	···	0.24
Cooler	···	0.29
Stack gas	5.54	4.54
Total	7.63	6.11

Table 4 SOFC performance comparison

	Base Cycle	Single SOFC-HAT Hybrid
Current density mA/cm^2	295.7	304.9
Power per tube, Watts	193.7	198.9
Thermal efficiency, % fuel energy to SOFC (lower calorific value)	47.35	47.28

Table 5 Exergy destruction in SOFC versus LP combustor for SOFC-HAT hybrid

	% of Exergy Entering SOFC or LPCombustor
SOFC	10.62
HP combustor	2.65
Subtotal (SOFC and HP combustor)	13.27
LP combustor	16.03

these components is expressed as a percentage of the total exergy entering that component (Table 5), the result reveals that the SOFC is a much more efficient component. Thus, further gain in efficiency may be expected by minimizing combustion by adding an LP SOFC.

Dual Solid Oxide Fuel Cell–Humid Air Turbine (SOFC-HAT) Hybrid. The resulting hybrid is depicted in Fig. 4 and is similar to the previous case incorporating humidification of the compressed air before it is preheated in the recuperator. However, the system consists of the additional SOFC followed by an LP combustor in place of the reheat combustor of the gas turbine. The cycle thermal efficiency as developed for various pressure ratios indicates that for this cycle also the efficiency is essentially independent of the pressure ratio. It shows an efficiency of 75.98 percent at a pressure ratio of 15 which is slightly higher than that obtained at a pressure ratio of 8.8. Once again, the pressure ratio of the cycle is limited to 15 based on the design basis established for this investigation. The exergy destruction in each of the components of the cycle for this maximum efficiency case is compared to the corresponding exergy destruction of the previous two cases in Table 6 which verifies the higher efficiency of this dual SOFC-HAT case.

Table 6 Exergy destruction in SOFC hybrid cycles as percent of total fuel input

	Base Cycle	Single SOFC-HAT Hybrid	Dual SOFC-HAT Hybrid
LP compressor	0.86	0.7	0.52
Intercooler	2.09	0.58	0.43
HP compressor	0.80	0.72	0.54
Aftercooler	···	0.30	0.22
Humidifier	···	0.16	0.11
Economizer	···	0.24	0.17
Cooler	···	0.29	0.22
Recuperator and fuel preheater	2.05	1.71	1.22
HP SOFC	11.44	11.51	8.55
HP combustor	3.19	2.87	2.09
HP expander	0.86	0.81	0.61
LP SOFC	···	···	7.91
LP combustor	10.14	10.19	1.54
LP expander	1.08	1.09	0.78
Stack gas	5.54	4.54	4.20
Total	38.05	35.71	29.11

Results and Discussions

The overall performance of the three hybrid cycles is compared in Table 7. The current density of the SOFC in each of the cases is compared. The current density of the dual SOFC-HAT hybrid's LP

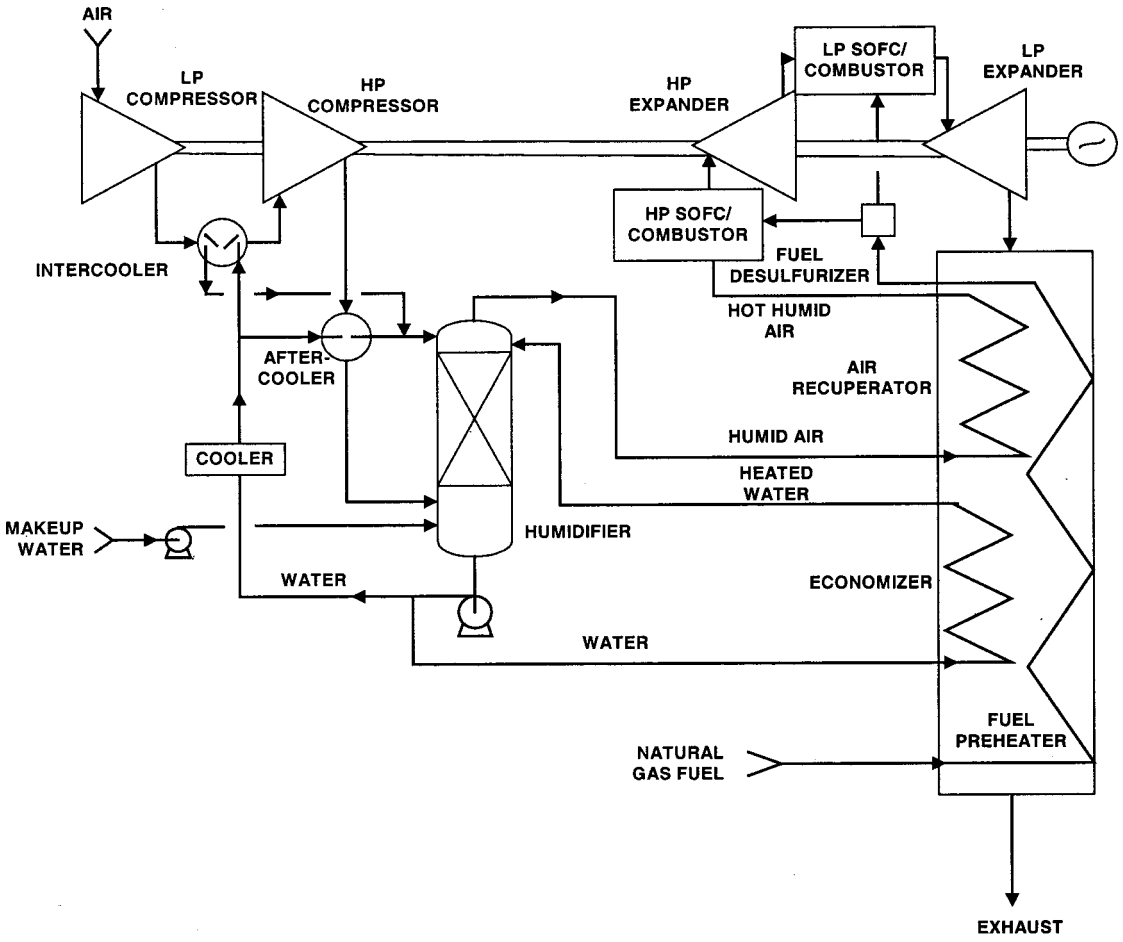

Fig. 4 Dual SOFC-HAT hybrid

Table 7 Performance comparison of SOFC hybrid cycles

	Base Cycle	Single SOFC-HAT Hybrid	Dual SOFC-HATHybrid
Cycle pressure ratio	8.8	15.0	15.0
SOFC power, % of total	56.5	53.7	68.4
Gas turbine power, % of total	43.5	46.3	31.6
SOFC current density, mA/cm^2	193.7	198.9	198.6/161.1
Specific power output. kW/kg/s	665.3	969.5	1431.8
Exergy destroyed, % of total fuel input	38.05	35.71	29.11
CO2 emissions, kg/MW-hr	0.08994	0.08627	0.07840
Thermal efficiency, % fuel (lower calorific value)	66.23	69.05	75.98

SOFC is significantly lower than that in the other SOFCs because this SOFC operates at a much lower pressure while the concentration of diluents (water vapor and carbon dioxide) in the oxidant stream to the SOFC is high. The fraction of the total power developed by the SOFC(s), however, remains to be the highest with the dual SOFC-HAT hybrid while it is the lowest with the single SOFC-HAT hybrid. The specific power output defined as the net power developed by the cycle per unit of air entering the system (which has an inverse relationship to the size of the turbomachinery required to generate a unit of power) is significantly increased by combining the SOFC with the HAT cycle; as much as a 46 percent increase is realized. This increase is due to the introduction of water vapor into the pressurized air stream which increases the working fluid for the expanders as well as the higher operating pressure of the cycle. Thus, power developed by the gas turbine as a fraction of the total power generated is increased when the HAT cycle is incorporated into a single SOFC-based hybrid. Further increase in the specific power is realized by including the second SOFC, the specific power output being more than doubled over the base case. However, the fraction of total power generated by the SOFCs is increased.

The greenhouse gas emissions of CO_2 are significantly reduced as the system thermal efficiency is increased, these emissions being inversely proportional to the efficiency.

The exergy losses through the stack gas for the three cases are presented in Table 8. The loss of exergy due to the large amount of moisture carried by the stack gas in the HAT based hybrids is, however, not significantly higher than that in the base case. Thus, only small gain in efficiency may be expected if a cycle is devised to recover the remaining exergy in the water vapor. Recovery of this water for recycle and recovery of the latent heat for cogeneration (production of hot water for district heating) purposes may, however, be considered.

The relative plant costs expressed as $/kW and economics of the three cases are summarized in Table 9. The base cycle cost of $1000/kW is based on the projected cost by Siemens Westinghouse when full manufacturing and production occurs. The cost of the HAT-based hybrids were estimated based on the relative difference in cost of the turbomachinery, the heat exchange, the humidifier, and water treatment equipment derived from the Gas Research Institute Report [5]. Natural gas is assumed to cost $3/GJ on a lower calorific basis and the plant on-stream factor of 0.9 is utilized to calculate the cost of electricity. The total capital requirement, and the operating and maintenance (O&M) costs are estimated as fractions of the plant cost based on projected values taken from the Electric Research Institute's Technical Assessment Guide [6].

The single SOFC-HAT hybrid results in the minimum cost of electricity while the dual SOFC-HAT hybrid has the maximum cost of electricity among the three cases. The plant cost of the dual SOFC-HAT hybrid is significantly higher because the fraction of power produced by the SOFC(s) is significantly higher than that in the other cases. The cost of the SOFC per unit of power produced by the SOFC is significantly higher than that of the gas turbine. Also as pointed out previously, the power density of the LP SOFC is significantly lower which also contributes towards increasing the plant cost. The dual SOFC-HAT hybrid can only be justified in favor of the single SOFC-HAT hybrid when the cost of natural gas is greater than $14/GJ or if a severe carbon tax is imposed on power plants.

The plant cost of the single SOFC-HAT hybrid is lowest because the fraction of power produced by the SOFC is significantly lower than that in the other cases. This case represents a healthy tradeoff between efficiency and plant cost.

The cost of the SOFC module(s) in the HAT-based hybrids is derived from the projected cost of Siemens Westinghouse which is

Table 8 Exergy loss in stack gas as percent of fuel input

	Base Cycle	Single SOFC-HAT Hybrid	Dual SOFC-HAT Hybrid
Due to temperature	4.07	2.98	2.52
Due to partial pressure of H_2O and CO_2	1.47	1.56	1.68
Total exergy lost	5.54	4.54	4.20

Table 9 Relative plant costs and cost of electricity with natural gas at $3/GJ

	Base Cycle	Single SOFC-HAT Hybrid	Dual SOFC-HAT Hybrid
Plant cost, $/kW	1000	960	1240
Total capital requirement[1], $/kW	1074	1031	1332
Thermal efficiency, % Fuel (lower calorific value)	66.23	69.05	75.98
Capital charge, ¢/kW-hr	1.53	1.47	1.90
Fuel cost, ¢/kW-hr	1.47	1.41	1.28
Fixed O&M costs[2], ¢/kW-hr	0.08	0.08	0.1
Variable O&M costs[3], ¢/kW-hr	0.60	0.58	0.74
Cost of electricity, ¢/kW-hr	3.68	3.54	4.02

[1]1.074 percent of plant cost

[2]0.08×10^{-3} of plant cost

[3]0.6×10^{-3} of (plant cost)×(on-stream factor)

$1100/kW. With the single SOFC-HAT hybrid, the cost of electricity remains less than the competitive 5¢/kW-hr even when the cost of the SOFC is 50 percent higher than this projected value.

Summary and Conclusions

The Westinghouse SureCell™ hybrid configuration is chosen as the base cycle over which improvements are sought. The SureCell™ hybrid combines a pressurized tubular SOFC with an intercooled-reheat gas turbine. One variation considered applies HAT cycle features to an SOFC hybrid design. Generation of ''steam'' by directly contacting pressurized air with hot water in a countercurrent humidifier and circulating the water leaving the humidifier to recover heat rejected in the gas turbine intercooler and the stack gas is applied. The resulting SOFC-HAT hybrid cycle shows an efficiency as high as 69.05 percent based on the fuel lower calorific value at a pressure ratio of 15 while the base case has an efficiency of 66.23 percent at the pressure ratio of 8.8. The efficiency of the base case corresponding to a pressure ratio of 8.8 is chosen for the comparison because the efficiency of the cycle at this pressure is higher than that at a pressure ratio of 15 (the efficiency of this hybrid configuration decreases as the pressure ratio is increased; at pressure ratios below 8.8, the efficiency increases slightly but at the lower pressure ratios, the turbine exhaust temperature increases beyond the temperature limit of 635°C which is set by strength of the last stage turbine blades). The pressure ratio of 8.8 is also consistent with the pressure ratio touted for the SureCell™ hybrid by Westinghouse that forms the basis for the configuration of the base case).

Exergy destruction data, which quantifies the amount of lost work due to thermodynamic irreversibilities, were developed for all the components within the system and identified the superior efficiency performance of the SOFC component. Therefore, an additional cycle variation added a second SOFC component followed by a LP combustor in place of the reheat combustor of the gas turbine of the SOFC-HAT hybrid. The resulting dual SOFC-HAT hybrid cycle has a thermal efficiency as high as 75.98 percent.

Assuming a natural gas cost of $3/GJ, the single SOFC-HAT hybrid gives the lowest cost of electricity (3.54¢/kW-hr) while the dual SOFC-HAT hybrid has the highest cost of electricity (4.02¢/kW-hr) among the three cycles analyzed. The plant cost of the dual SOFC-HAT hybrid is calculated to be significantly higher because the fraction of power produced by the SOFC(s) is significantly higher than that in the other cases on the basis of $1100/kw initial cost for the SOFC. The dual SOFC-HAT hybrid can only be justified in favor of the single SOFC-HAT hybrid when the cost of natural gas is greater than $14/GJ or if a severe carbon tax is imposed on power plants (on the order of $180/ton of CO2 emitted with natural gas priced at $3/GJ).

The plant cost of the single SOFC-HAT hybrid is lowest of the three cycles because the component of power produced by the SOFC is significantly lower than that in the other cases. This case represents a healthy tradeoff between efficiency and plant cost.

References

[1] Rao, A. D., and Samuelsen, G. S., 2000, ''Analysis Strategies for Tubular SOFC based Hybrid Systems,'' presented at the ASME Turbo Expo Conference, Munich, May.

[2] Vogler, T. C., and Weissman, W., 1988, ''Thermodynamic Availability Analysis for Maximizing a System's Efficiency,'' Chem. Eng. Prog., **84**(3), pp. 35–42.

[3] Bevc, F. P., and Parker, W. G., 1995, ''SureCell™ Integrated Solid Oxide Fuel Cell Power Plants for Distributed Power Applications,'' *PowerGen 1995 Americas*, Dec. 5–7.

[4] Rao, A. D., 1989, ''Process for Producing Power,'' U.S. Patent No. 4,289,763, May 16.

[5] Gas Research Institute Report, ''Evaluation of Advanced Gas Turbine Cycles,'' GRI-93/0250, Aug.

[6] Electric Research Institute's Technical Assessment Guide, 1982.

Internal Reforming Solid Oxide Fuel Cell Gas Turbine Combined Cycles (IRSOFC-GT)—Part II: Exergy and Thermoeconomic Analyses

A. F. Massardo
Mem. ASME
e-mail: massardo@unige.it

L. Magistri
e-mail: Loredana.Magistri@unige.it

Thermochemical Power Group (TPG),
Dip. di Macchine, Sistemi Energetici e Trasporti,
Universita di Genova,
Via Montallegro 1,
16145 Genova, Italy

The aim of this work is to investigate the performance of internal reforming solid oxide fuel cell (IRSOFC) and gas turbine (GT) combined cycles. A mathematical model of the IRSOFC steady-state operation was presented in Part I of this work coupled to the thermodynamic analysis of a number of proposed IRSOFC-GT combined cycles, taking into account the influence of several technological constraints. In the second part of this work, both an exergy and a thermoeconomic analysis of the proposed cycles have been carried out using the TEMP code developed by the author. A suitable equation for IRSOFC cost evaluation based on cell geometry and performance has been proposed and employed to evaluate the electricity generation cost of the proposed combined systems. The results are presented and the influence of several parameters is discussed: external reformer operating conditions, fuel-to-air ratio, cell current density, compressor pressure ratio, etc. Diagrams proposed by the author for cost versus efficiency, cost versus specific work, and cost versus system pressure are also presented and discussed.
[DOI: 10.1115/1.1492837]

Introduction

Part I of this work (Massardo and Lubelli [1]) presented an analysis of atmospheric and pressurised solid oxide fuel cells (SOFCs) associated with gas turbine (GT) systems, from an electrochemical and thermodynamic point of view.

The proposed cycles, significantly simpler than those of other systems presented in the literature, can be analyzed to show that fuel cell technology can be well integrated with mature gas and steam cycle technology to yield functional high efficiency power generation schemes (65 to 70% with atmospheric cells; 70 to 75% with pressurised cells). The specific work of the proposed systems is also considerably higher than for classical gas-steam combined plants.

Nevertheless, in order to utilize SOFC-GT systems it is necessary to achieve low initial and running costs. Therefore, the importance of a joint thermodynamic and economic analysis is quite evident.

A thermoeconomic approach which combines thermodynamic analysis with economic considerations to optimize the system (Agazzani et al., [2], Agazzani and Massardo [3], Agazzani et al. [4], and Massardo and Scialò [5]) may be used to solve this problem.

In this work the thermoeconomic analysis of IRSOFC-GT combined cycles has been carried out using the tool TEMP (thermo economic modular program) developed by the authors. The modular organization of the code enables the user to perform quickly and reliably a direct thermoeconomic analysis (DTA) of the IRSOFC-GT cycles.

Thanks to the adoption of apt cost functions for the different components of the cycles (including SOFC and steam reformer) the analysis is particularly well suited for cost versus efficiency, cost versus specific work, and cost versus system operative pressure evaluation.

Exergy Analysis

The IRSOFC mathematical model described in Part I of this work (Massardo and Lubelli [1]) has been integrated into the TEMP code, a simulator tool for the thermoeconomic analysis of advanced thermal energy systems developed by the author (Agazzani and Massardo [3]). In this way the complete energy analysis of the proposed IRSOFC-GT combined cycles can be obtained, taking into account several technological constraints already discussed in Part I.

The results of the exergy analysis carried out on the FCGTI system (atmospheric fuel cell) are shown in Fig. 1: These results have been obtained for a current density equal to 3000 A/m^2, the external reformer being at equilibrium condition, a fuel to air ratio 3.5%, and a compressor pressure ratio equal to 16. The second law efficiency is 68.7% and the SOFC irreversibility rate is about 23% of the total, while the combustion chamber value is about 25.8%. This result can be explained taking into account that the second-law efficiency of the SOFC is very high, 94.5%, due to the ordered electrochemical conversion that takes place inside the cell. The low-efficiency value of the combustion chamber justifies the high irreversibility rate of this component (moreover it must be taken into account that the fuel burned in the combustion chamber is a very small part of the whole system input fuel).

Other components that show high irreversibility rates are the reformer (6%), the expander (6.4%), the compressor (4.5%), the evaporator (4.2%), and the stack (12.8%).

The influences of compressor pressure ratio and external reformer operative conditions have been investigated and the results are shown in Fig. 2: When the external reformer operates at equilibrium condition the pressure ratio influence is quite evident in the cell and the combustion chamber, while the other irreversibility distributions remain practically constant. When the external

Contributed by the International Gas Turbine Institute (IGTI) of THE AMERICAN SOCIETY OF MECHANICAL ENGINEERS for publication in THE ASME JOURNAL OF ENGINEERING FOR GAS TURBINES AND POWER. Paper presented at the International Gas Turbine and Aeroengine Congress and Exhibition, New Orleans, LA, June 4–7, 2001; Paper 2001-GT-380. Manuscript received by IGTI, Dec. 2000, final revision, Mar. 2001. Associate Editor: R. Natole.

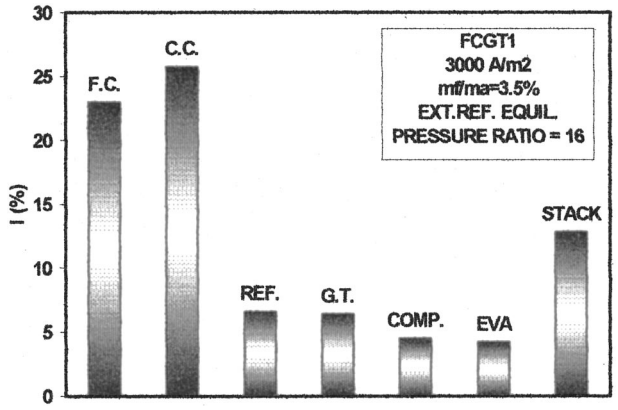

Fig. 1 Irreversibility rate distribution (%) for the FCGT1 layout

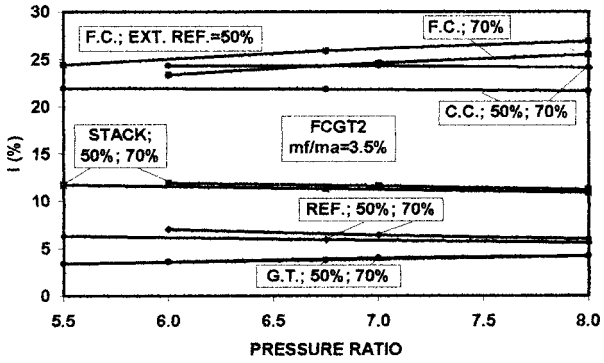

Fig. 4 FCGT2 layout irreversibility rates versus plant pressure and ER operative conditions

reformer operates at 50% of this equilibrium condition there is an increase in the cell irreversibility rate and a corresponding decrease in the combustion chamber value versus the pressure ratio.

The results of the exergy investigation carried out on the FCGT2 system are shown in Fig. 3; the results have been obtained for the same conditions as Fig. 1, but for a pressure ratio equal to 6.0 and external reformer at 70% of the equilibrium condition (the complete reformer equilibrium condition does not respect the cell temperature constraint −1300K−see Fig. 16 Part I). The second-law efficiency is 68%, while the fuel cell irreversibility rate is 23.3%, the combustion chamber irreversibility rate is 24.3% (in this case only the exhaust fuel from the cell is burned), and the external reformer irreversibility rate is 7%. In this configuration the rate of the recuperator is high (8.7%) too, and the expander and compressor show reduced values: 3.6 and 3.3%, respectively.

The stack value is similar to the data of the FCGT1 system (12%). The influence of pressure ratio (in its feasible region) and the external reformer conditions are shown in Fig. 4. With an increasing pressure ratio the irreversibility rate increases for the recuperator, the external reformer, while for the cell decreases, and remains practically constant for the burner.

Figure 5 shows the behavior of the second law efficiency of the two atmospheric cell layouts (FCGT1 and FCGT2) versus the compressor pressure ratio. The figure shows also the influence of the external reformer conditions and of the fuel-to-air ratio.

Figure 6 represents the exergy analysis results of the FCGT3 layout (current density 3000 A/m^2; pressure ratio 8; fuel-to-air ratio 3.5%; external reformer at equilibrium). The second-law ef-

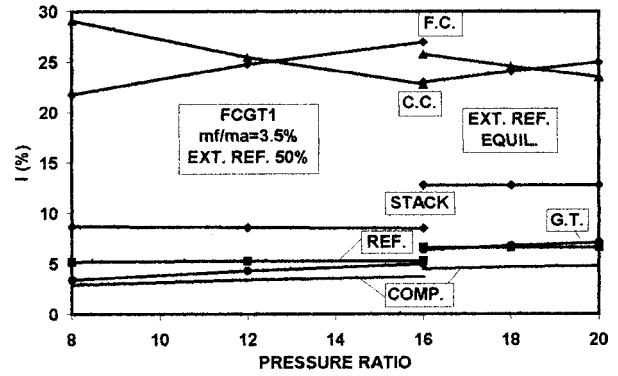

Fig. 2 Irreversibility rate distribution (%) for the FCGT2 layout

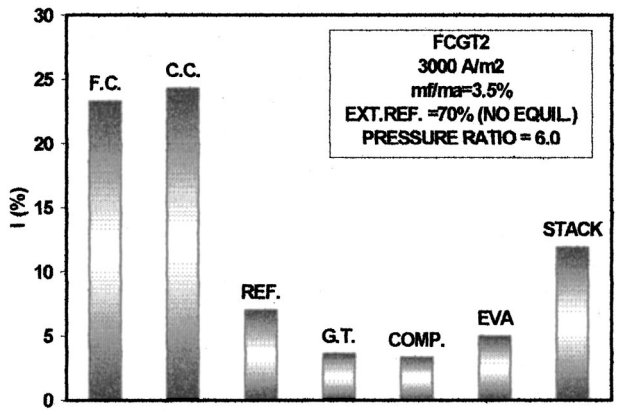

Fig. 3 FCGT1 layout irreversibility rates versus plant pressure and ER operative conditions

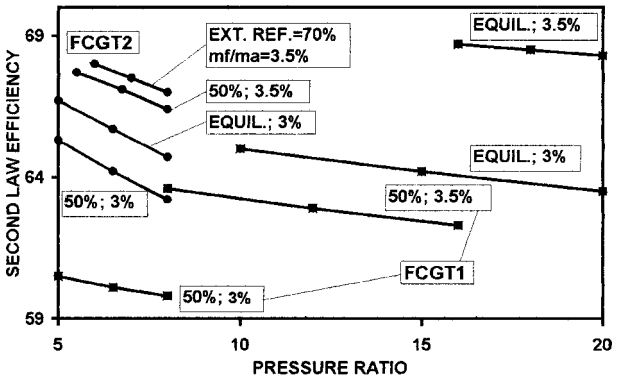

Fig. 5 Second-law efficiency versus pressure ratio (FCGT1 and FCGT2 plant)

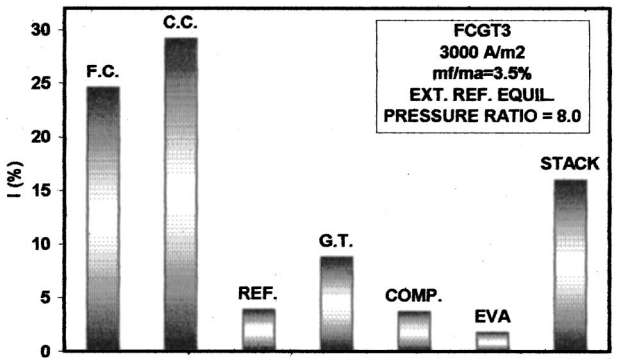

Fig. 6 FCGT3 layout irreversibility rate versus plant pressure and ER operative conditions

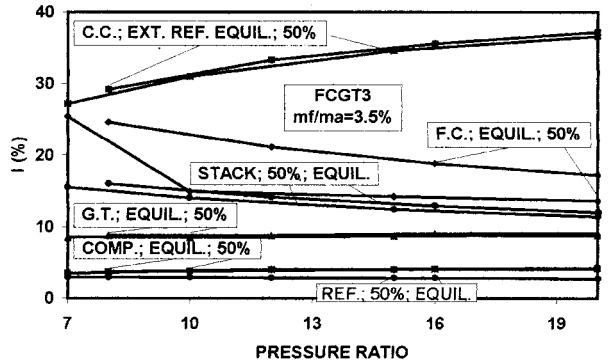

Fig. 7 Irreversibility rate (%) distribution for the FCGT3 layout

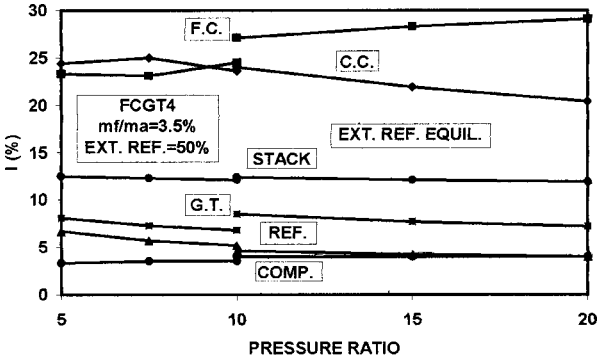

Fig. 9 FCGT4 layout irreversibility rate versus plant pressure and ER operative conditions

ficiency is 72.5%. The fuel cell irreversibility rate is 24.6%, while the irreversibility rate of the two combustion chambers is 29.2% (15.7% and 13.5%, respectively). The stack value is 16%; the gas turbine value 8.8%; the compressor 3.7%, and the reformer 3.9%. In this case too the cell second-law efficiency is very high (94.5%). The pressure ratio and external reformer influence is shown in Fig. 7. The effect of a pressure ratio increase is evident. In fact, the cell irreversibility rate is drastically reduced, while the value for the first combustion chamber, behind the fuel cell, falls more slowly, and the corresponding value for the second combustor downstream from the turbine increases. Such behavior can be explained taking into account that the cell is pressurised, and thus when β increases, with a TIT practically constant, the turbine outlet temperature falls, and more and more fuel must be burned in the second combustion chamber, then increasing the exergy destruction. The influence of the external reformer operating conditions is less evident in this case.

For the FCGT4 layout the results are shown in Fig. 8 and Fig. 9. In this case (Fig. 8) the pressure ratio is 10, and the cell irreversibility rate is high (27.1%), while the combustion chamber irreversibility rates are, respectively, 15.4% and 8.6% (total 24%). Stack value is 12.4%, ER 4.6%, GT 8.5%, and evaporator 5.7%. Low values are shown by compressor and recuperator.

In Fig. 9 we may observe that the cell irreversibility rate increases slowly with the pressure ratio (from 27 to 30%), while both combustion chamber rates decrease. The influence of the external reformer operating conditions is more evident than in the previous FCGT3 system.

Finally, Fig. 10 displays the second-law efficiency versus the system pressure ratio, assuming external reformer conditions and fuel-to-air ratio as parameters. The data for the FCGT4 plant are more sensitive to the pressure ratio, while the results for the FCGT3 plant are more constant in the feasible pressure ratio range. The influence of the fuel to air ratio is also evident for both the configurations, while better results can be obtained with the external reformer at equilibrium. However, all efficiency values, especially for lower pressure ratios, are very high.

Direct Thermoeconomic Analysis (DTA)

The thermoeconomic analysis employed here is similar to classical thermoeconomic functional analysis (TFA) but employs an original direct approach developed by the author (Agazzani and Massardo [3]) to carry out the direct thermoeconomic analysis (DTA), and optimization (DTO). In DTA, the analyzed plant is subdivided into a set of units, each one including one or more physical components, connected by material flows. The schematization of the plant in single units, interconnected by material and mechanical workstreams, is the ''physical structure of the system,'' and a new study of the system has been introduced, called ''functional productive analysis.'' The graphical representation is called the ''functional productive diagram.'' The complete mathematical formulation of this functional productive analysis has been presented by Agazzani and Massardo [3]. By means of the ''functional productive analysis'' the functional exergy flows between the components can be evaluated, together with marginal and average unit costs for each functional exergy flow. Therefore, the global thermoeconomic performances of the components (internal economy) are defined. The ''functional productive diagram'' of the four combined IRSOFC-GT systems presented in Part I are shown in Figs. 11–14. The thermoeconomic analysis has been carried out using a modular simulator called TEMP: Once the thermodynamic and exergy analyses are completed, TEMP sequentially calls all the modules that have thermoeconomic purposes. Each thermoeconomic module utilized calculates its one functional purpose. In this way all the functional exergy flows of the functional diagram are analyzed and the functional productive analysis is performed.

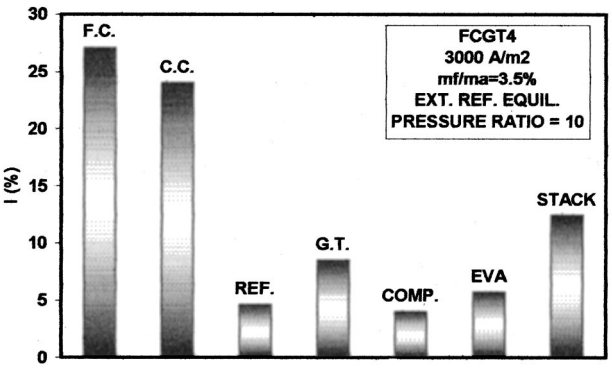

Fig. 8 Irreversibility rate (%) distribution for the FCGT4 layout

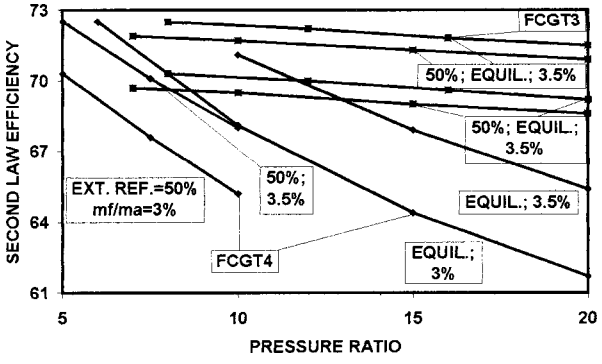

Fig. 10 Second-law efficiency versus pressure ratio (FCGT3 and FCGT2)

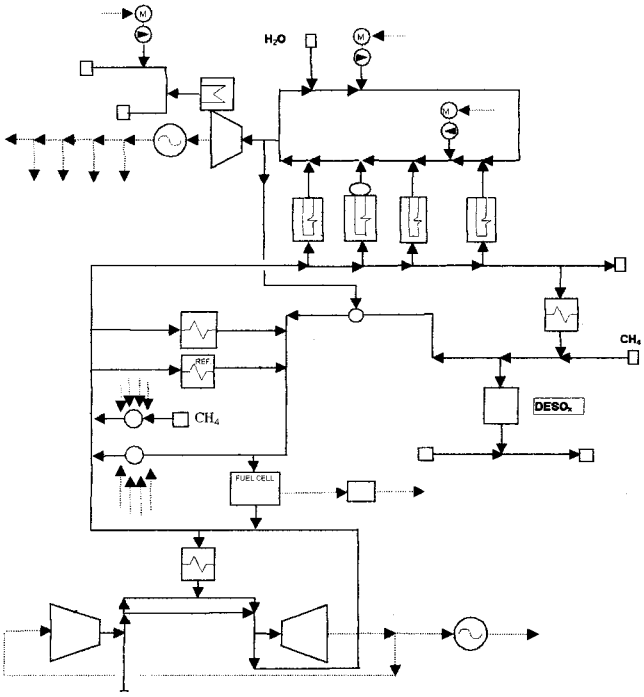

Fig. 11 Functional production diagram of the FCGT1 configuration

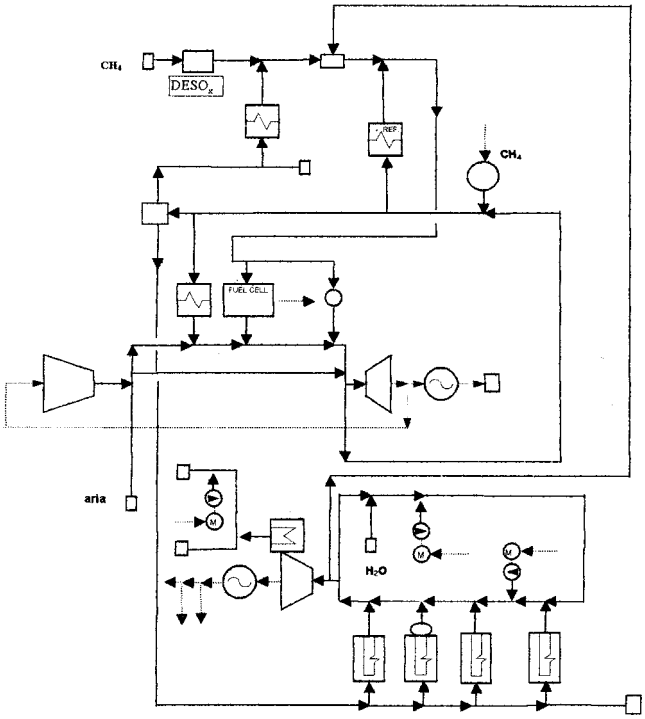

Fig. 13 Functional productive diagram of the FCGT3 configuration

Besides, each module estimates the capital cost Z by means of a ''cost equation'' function written in terms of geometric and manufacturing variables, or a ''costing equation'' function, written in terms of performance and stream variables. Further information about the component cost functions are reported in Agazzani et al. [2], Agazzani and Massardo [3], Agazzani et al. [4], Massardo and Scialò [5], and Traverso and Massardo [6]. Instead, a description of the approach used for cost-costing equations of the new modules (IRSOFC and external reformer) will be presented in the next paragraph.

Cost Evaluation

The thermoeconomic technique used here must have reliable and updated cost functions for the plant components.

Determining these functions is rather complicated since it is difficult to consider every factor that contributes to estimates the final purchase cost of a component. They must be related to the thermodynamic parameters of the plant and factors covering every type of item. Furthermore, it must be possible to update them by taking into account the progress of both performance improvement and market prices. In particular, for DTA there is a need to evaluate the capital cost for each unit as a function of its product and the sizing variable. The following equation has been used to evaluate the capital cost rate of a unit ''r:''

$$Z_r = \frac{\Xi_r \cdot \mathrm{FCR} \cdot \Phi_r}{3.6 \cdot 10^5 \cdot N} \tag{1}$$

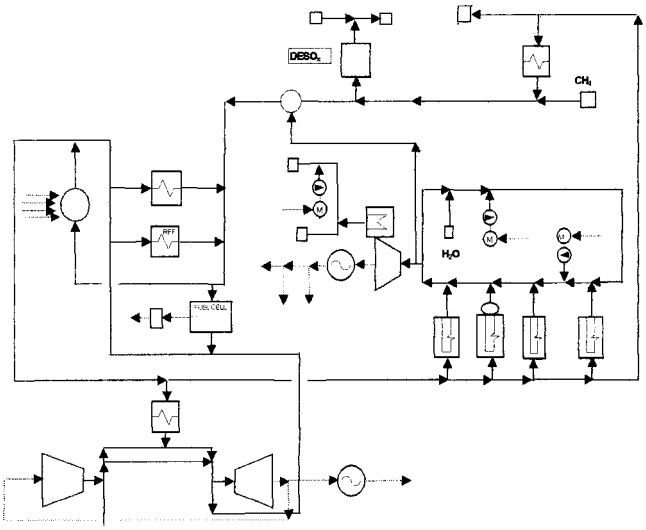

Fig. 12 Functional productive diagram for the FCGT2 configuration

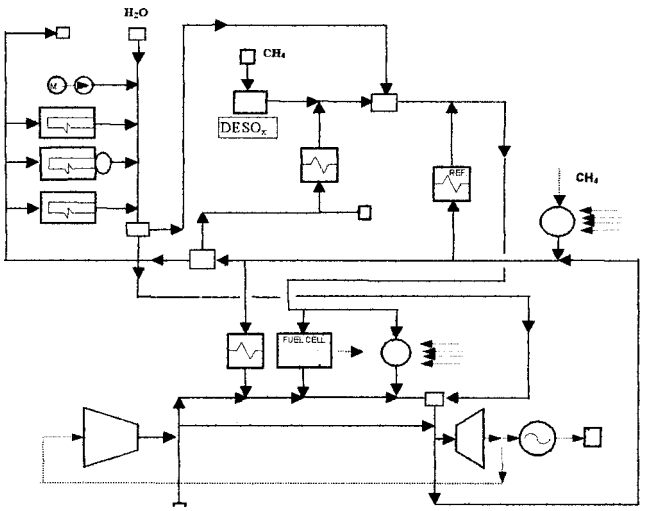

Fig. 14 Functional productive diagram for the FCGT4 configuration

where Φ_r is the maintenance factor; FCR the annual fixed charge rate %; N the number of operating hours per year, and Ξ_r the purchased equipment cost (PEC). The following standard values have been considered: FCR=18.2%; $\phi_r=1.06$; $N=8000$ (h/y). These values can be easily modified to take into account different financial scenarios. Every purchased equipment cost has been escalated by means of an escalation index (Massardo and Scialò [5]).

IRSOFC Cost Evaluation

Fuel cell costs are inevitably less well established than gas, steam, combined cycles, etc. The production costs of SOFCs have not been firmly established yet; moreover, the production cost of the cell stack segments depends on the type of SOFC: planar type or tubular. Studies of SOFCs are generally at the development stage of several kW or decines of kW class modules or stacks. On the other hand, a variety of designs, production methods, and raw materials, being interrelated factors, have been studied actively in many institutions. Price of materials per weight and the rate of material utilization have a direct effect upon the production cost. Therefore, to calculate costs, it is necessary to make some assumptions about: (i) technical specifications of the estimated SOFC; (ii) materials; (iii) production equipment; (iv) employment of workers; (v) power sources.

The total production costs of SOFCs can be calculated, as suggested by Itoh et al. [7], in the following order: (a) decision on the production process and the yield rate in each step; (b) definitive calculations of the material weight by taking the yield rate and the material cost; (c) the estimation of the equipment cost and maintenance expenses; (d) the calculation of light, heat, labor, and miscellaneous expenses. The cited authors suggest a cost for the planar-type SOFC of about 1000 $/kWe (the cheapest of all the types); taking into account that the material cost o the planar-type covers nearly (60%) of the total because of the large consumption of expensive materials (especially for the separator), the cell cost can be reduced by decreasing the thickness of the separator and/or the electrolyte. Labor expenses, which represent the second largest cost in this SOFC type—20%—are cheaper than those for other types. On the other hand, costs for the electrochemical vapor deposition (EVD) tubular type, and the pressure plasma (PS) type have been, respectively, about 5000 $/kWe and 2500 $/kWe. The cited authors also noted that the manufacturing cost of the tubular type by EVD technique is very expensive.

Another important aspect of the problem is related to the relationship between cost and power density (kW/m^2). Production costs decrease sharply with power density (see Fig. 15(*a*)) up to 5 kW/m^2.

In the case of the planar-type SOFC, a sufficiently profitable power density for commercial application is evident, while for the tubular type the convenience is not so clear. The reduction of the cost with the power density is evident and depends on the reduction of materials and related costs (labor, etc.) for a fixed SOFC power.

On the other hand, Krist et al. [8] suggested that SOFCs manufactured by a wide variety of traditional ceramic methods and atmospheric pressure spraying cost $500 to $600/m^2 ($250 to 300/kW at 2 kW/m^2); vacuum processes are considerably more expensive, increasing the cost of production by $200 to 300 m^2, while the use of a ceramic interconnector increases the cost by roughly $500/m^2 (all the data are reported in Fig. 15(*a*), together with the Itoh's curves).

The IRSOFCs used in the combined cycles investigated here have a potential equal to about 0.7V at the operative conditions (current density 3000 A/m^2; utilisation fuel factor 0.8), the same value as in Itoh's paper, and the power density, calculated on the basis of cell surface and power (obtained in the cell module of the TEMP code), is always within the range 1.9 to 2.6 kW/m^2, as shown in Fig. 15. Moreover, the maximum cell cost, that is considered interesting for this study is 2000 $/kWe, and by including

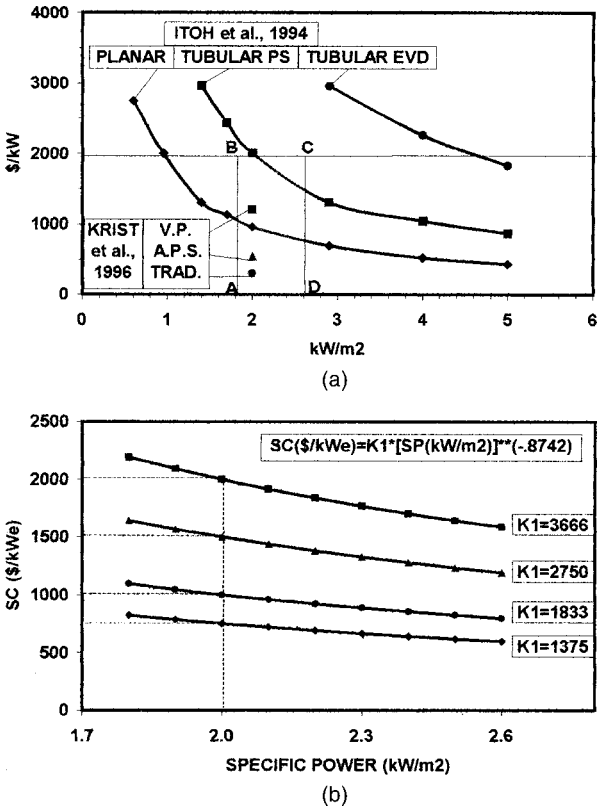

Fig. 15 (*a*) Specific production cost versus specific power (TRAD.=traditional), (*b*) proposed equation for solid oxide fuel cell (SOFC) specific cost evaluation

this constraint in the analysis it is possible to define the ''ABCD'' area in Fig. 15(*a*). All the data of Krist et al. [8] are inside the area considered; the curve of the planar type evaluated by Itoh et al. [7] is also well inside the area ''ABCD,'' while the PS tubular cell is just inside the area considered (right top corner). The EVD tubular solution is completely outside the region considered (its cost is too high) and it will not be considered in the following thermoeconomic analysis.

Taking into account the results shown in Fig. 15, the IRSOFC cost can be obtained through the use of the following expression:

$$Z_c(\$) = \mathrm{SC}_c \cdot P_c \tag{2}$$

where SC_c is the specific cost of the cell per kWe evaluated with the following equations:

$$\mathrm{SC}_c = K_1 \cdot \mathrm{SP}_c^{-0.8742} \tag{3}$$

and the meaning of the constant K_1 is shown in Fig. 15(*b*).

Obviously, the applicability of Eq. (3) is for SP in the range 1.8 to 2.6 (kW/m^2); however, it can easily be extended to high specific power values.

In this way the COE (cost of electricity) of the plant including SOFCs, can be evaluated. In fact, to evaluate the cell cost it is necessary to know the cell power and the cell electrochemical surface, both evaluated inside the IRSOFC module of the TEMP code (Massardo and Lubelli [1]). The constant K_1 can easily be modified in the analysis and the proposed range (see Fig. 15(*b*)) agrees well with the data reported in literature, as already confirmed by Stephenson and Ritchey [9], where the cell cost per kW was assumed to be equal to 1000 $/kWe, without considering the power density influence.

Obviously, all the cell and plant operative parameters are included in the cost function equation through the cell power and surface calculation.

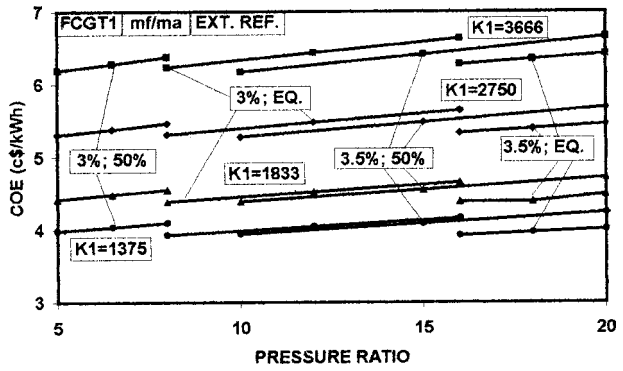

Fig. 16 Cost of electricity (COE) for the FCGT1 configuration

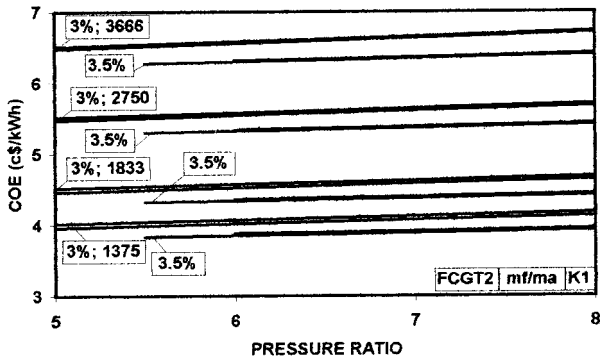

Fig. 17 Cost of electricity (COE) for the FCGT2 configuration

Another important cost to be evaluated is the cost of the external reformer. The external reformer is similar to the steam reformer widely used in chemical plants. However, in the cycles considered here the reformer always operates at very high temperature, and therefore the cost of the catalizers can be reduced when compared to a classical steam reformer (Costamagna [10]). An extensive research into the reformer cost has been carried out, mainly in the field of chemical engineering, but also based on several communications (Hoffman [11], Costamagna [10], and Pietsch, [12]) and the following cost equation has been used:

$$Z_{ER} = K_{ER}\phi_{ER} \tag{4}$$

where the exergy flows ϕ_{ER} is evaluated with the reformer module of the TEMP code. Obviously, Eq. (4) can be considered a first attempt to evaluate the reformer cost and more work needs to be carried out in a similar way to that already done for the selective catalytic reactor (SCR) for NO_x abatement (Agazzani et al. [4]).

Thermoeconomic Analysis Results

The thermoeconomic analysis has been carried out in the operating conditions already established in Part I of this work (Massardo and Lubelli [1]) where all technological constraints are verified. The size of the plants has been defined by fixing the inlet air mass flow rate to 10 kg/s, so that the average power plant value is around 10 MW. The investigation has been carried out assuming the following values for the constant K_1 of Eq. (3): 3666, 2750, 1833, 1375 \$/kWe, to simulate different technological levels in the SOFC production cost (with these values the SC at SP $=2\ kW_e/m^2$ is, respectively, 2000, 1500, 1000, 750 $\$/kW_e$ as shown in Fig. 15(*b*)).

The complete thermoeconomic results are reported in Massardo and Magistri [13], where the internal economy of the systems (unitary exergetic costs, marginal costs, etc.) is also included. Here, only the overall result, COE, will be presented and discussed.

Figure 16 shows the results obtained for the FCGT1 layout, the COE is reported versus the compressor pressure ratio (in this case the cell is atmospheric), the external reformer is considered at equilibrium condition and at 50% of the equilibrium, and the fuel-to-air ratio is 3.0% and 3.5%, respectively. Obviously, the most important effect is due to the K_1 value: the COE reduction is high when K_1 passes from its maximum to minimum value, and the results are particularly interesting when K_1 is in the low value region. All the results have been obtained with a specific power around 2.0 kWe/m^2, while the influence of the fuel-to-air ratio is not very high (when m_f/m_a increases the COE is slightly reduced). The effect of compressor pressure ratio is more evident, but over the whole range the COE reduction is about 10%. The best thermoeconomic performances are always obtained at the minimum allowable compressor pressure ratio. All the cell temperatures are under the limit imposed in Part I (1300 K), but the maximum values are present where the COE is minimum, and some attention must be given to the cell temperature influence on the cell life. However, it is important to remember that the FCGT1 layout suffers from the intermediate heat exchanger maximum temperature limit, usually not verified in the results shown. To avoid this problem the FCGT2 layout has been proposed, and the thermoeconomic results of such a configuration are shown in Fig. 17. In this case the compressor pressure ratio is low $(5 \div 8)$, and the COE is not very sensitive to it, while the influence of m_f/m_a and external reformer condition is similar to the previous case. Also in this case the specific power is around 2 kW/m^2, while the cell temperature constraint is always verified. The effect of K_1 constant is quite evident, and the COE level is similar but higher than the previous case FCGT1.

The thermoeconomic performance of the FCGT3 layout is presented in Fig. 18. In this case, despite the pressurized cell configuration, the influence of the pressure ratio is very weak, and the effects of fuel-to-air ratio and external reformer condition are also reduced. The reduction of the COE with the compressor pressure ratio is mainly correlated to the increase in the specific power of the cell (from 2.28 to 2.39). Nevertheless, the most important data in the cited figure show that the COE is greatly reduced if compared to the previous data (Figs. 16 and 17), where atmospheric cells are used.

A different behavior has been obtained for the configuration FCGT4 (Fig. 19). In this case the pressure ratio influence is evident (COE reduces with β), and the influence of m_f to m_a ratio is now again evident, while the external reformer condition mainly affects the specific power (2.37 equilibrium; 2.28 at 50% of the equilibrium). The optimum COE result can be obtained for $m_f/m_a = 3.5\%$, external reformer at equilibrium and low β value; and this COE is similar to the FCGT3 best result.

A very useful way to analyze the thermoeconomic performance of the proposed layouts is the use of the cost/efficiency and cost/specific work diagrams as suggested for gas turbine based cycles

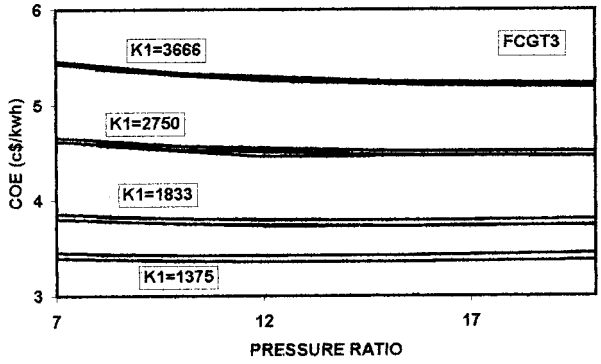

Fig. 18 Cost of electricity (COE) for the FCGT3 configuration

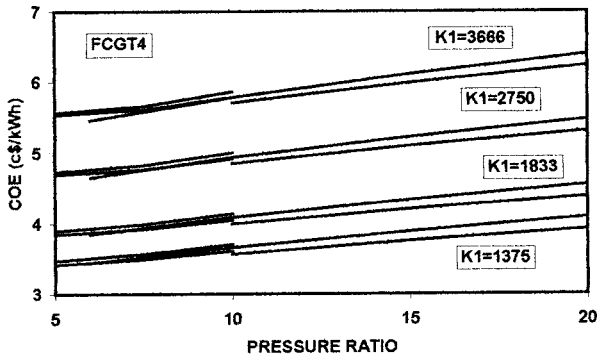

Fig. 19 Cost of electricity (COE) for the FCGT4 configuration

by the author (Massardo and Scialò [5] and Traverso and Massardo [6]). Fig. 20 shows the COE versus plant efficiency and Fig. 21 shows COE versus plant specific work. The complete data are reported in Massardo and Magistri [13]); here only the results obtained for $K_1 = 1833$\$/kWe are shown.

The efficiency influence on the COE of the systems is quite evident. In fact, the efficiency increase allows the COE reduction to be obtained for FCGT1, FCGT2, and FCGT4 layouts; analysing the data of the FCGT3 plant, a different behavior is evident:

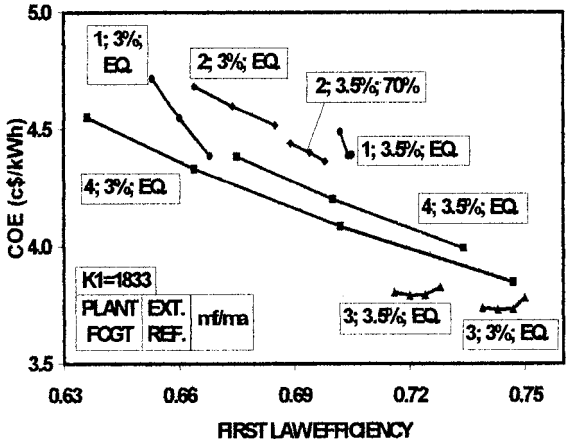

Fig. 20 Cost of electricity (COE) versus system efficiency ($K_1 = 1833$)

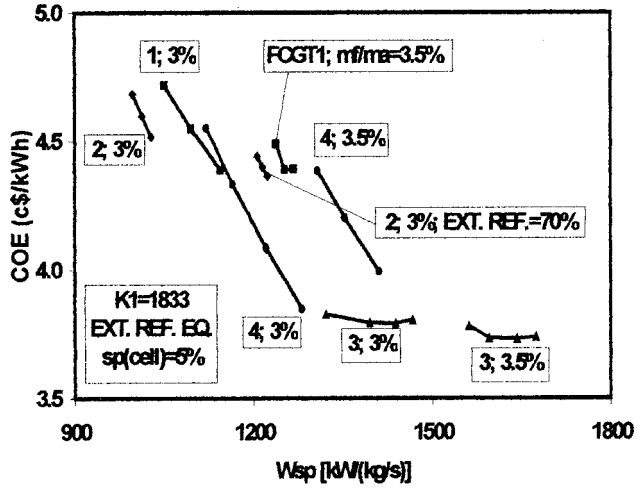

Fig. 21 Cost of electricity (COE) versus system specific work ($K_1 = 1833$)

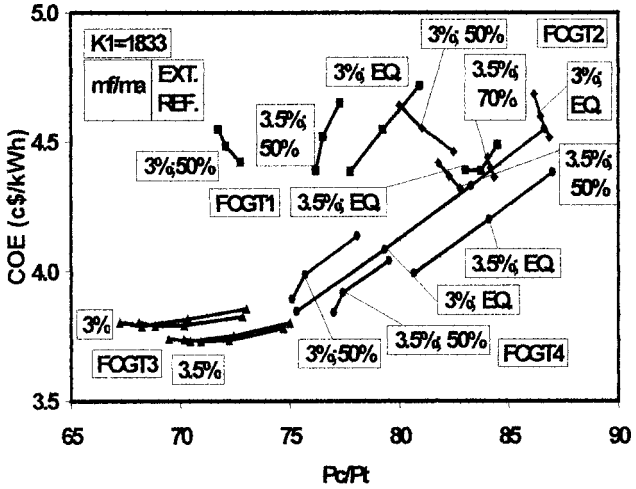

Fig. 22 Cost of electricity (COE) versus power ratio (cell/total, $K_1 = 1833$)

The minimum COE for such plants does not correspond to the maximum efficiency of the whole system. However, the efficiency variation range for the FCGT2 (ER 70%) and FCGT3 plants is small, while the range for FCGT1, and, mainly for FCGT4 is very large (0.64 to 0.75).

Figure 21 shows the thermoeconomic results versus plant specific work (the ratio between the plant power and the compressor inlet mass flow rate: 10 kg/s). In this case the effect of the specific work is evident on the COE value for the FCGT1, 2 and 4 plants; when the specific work increases the correspondent COE is greatly reduced. The FCGT3 layout shows a different behavior: The minimum COE value is just in the middle of the specific work range, i.e., the continuous increase of the specific work does not allow a reduction in cell system cost.

The results shown in Figs. 20 and 21 are very interesting, also taking into account the high level of efficiency and specific work that can be obtained, and the COE values (mainly when K_1 is under 1833).

Another noteworthy aspect of the systems under investigation is the very high ratio between the cell power and the whole plant power, and the consequent high value of the cell capital cost compared to the capital cost of the whole plant ($\geqslant$80%). Figure 22 shows the COE data versus cell-to-plant power ratio (Pc/Pt) for $K_1 = 1833$.

From a general point of view it is possible to observe that the minimum COEs are obtained in the area of the minimum Pc/Pt ratio, mainly for FCGT3 layout (Pc/Pt is always under 74%, and values under 70% are shown, too). The FCGT4 plant data also show the high influence of the power ratio, while the atmospheric plant FCGT2 shows a different behavior.

Conclusions

This paper has presented an assessment of the performance of a number of IRSOFC gas turbine (GT) combined cycles for a range of cycle and economic parameters. The main conclusions of this work are as follows:

- Solid oxide fuel cell technology can be well integrated with gas and steam turbines to yield high efficiency power generation schemes. The proposed system efficiencies are high (65–70% for atmospheric cells; 74–76% for pressurized cells), and also the specific work is considerably higher than for classical gas-steam combined cycles.
- An exergy analysis shows the reduced irreversibility rate of the cell system and the corresponding high value for the combus-

tion chamber, where used. The influence of the main parameter on the second-law efficiency values has also been investigated.

• The COE of the proposed systems has been obtained through the use of a thermoeconomic analysis, with a suitable fuel cell cost equation. The cell cost equation is based on cell power and electrochemical surface evaluation, both of which dependent on the operating conditions of the cell and of the plant. The technological level is taken into account through the use of a proper constant K_1.

• The thermoeconomic results obtained with the TEMP code have been presented and discussed; the influence of compressor pressure ratio, fuel-air ratio, external reformer condition, specific work, efficiency and cell-to-plant power ratio have been investigated.

• The COE of the pressurized configurations is lower than that of the atmospheric ones, mainly due to the efficiency increase and the power ratio (Pc/Pt) reduction.

• Economic results presented here must be considered not only as an absolute solution but mainly for the thermoeconomic comparison of different SOFC-GT combined cycles.

• A future stage of the work will consider the comparison between the thermoeconomic results presented here, the results previously presented by the author (Massardo and Scialò [5] Agazzani and Massardo [3], and Agazzani et al. [2]) for gas, steam, and combined plants and the results for mixed flow systems (STIG, RWI, HAT, etc., Traverso and Massardo [6]). In this way a complete view of the gas turbine based plants will be possible not only from a thermodynamic point of view, but also from a thermoeconomic one.

• Taking into account that IRSOFC-GT systems have CO_2 and NO_x emissions particularly reduced the environmental impact is greatly reduced, also taking into account the possible influence of CO_2 taxation (Massardo et al. [14]) and Borchiellini et al. [15]).

Acknowledgments

This work has been sponsored by the MURST of Italy through the grant ''Cofinanziamento 1999.''

Nomenclature

APS = atmospheric pressure spray
CC = combustion chamber
COE = cost of electricity ($/kWh)
COMP = compressor
EVA = evaporator
EVD = electrochemical vapor deposition
FC = fuel cell
FCR = annual fixed charge rate, %
GT = gas turbine
K = constant
I = irreversibility rate
IR/ER = internal/external reformer, respectively
m = mass flow rate, kg/s
N = number of operating hours per year
PEC = purchased equipment cost, $
PS = pressure plasma
SC = specific cost, $/kW$_e$
SOFC = solid oxide fuel cell
SP = specific power, kW$_e$/m^2
TIT = turbine inlet temperature, K
VP = vacuum process
Z = capital cost, $
$\Delta p\%$ = pressure loss percentage, %
Ξ_r = capital cost rate of a unit ''r''
β = pressure ratio
η_{is} = isentropic efficiency
ϕ = exergy flows, J/kg

Subscripts

a, f = air, fuel
c, t = cell, total
r = unit ''r''

References

[1] Massardo, A. F., and Lubelli, F., 2000, ''Internal Reforming Solid Oxide Fuel Cell—Gas Turbine Combined Cycles (IRSOFC-GT).—Part I: Cell Model and Cycle Thermodynamic Analysis,'' ASME J. Eng. Gas Turbines Power, **122**, pp. 27–35.
[2] Agazzani, A., Massardo, A. F., and Satta, A., 1995, ''Thermoeconomic Analysis of Complex Steam Plants,'' ASME Paper No. 95-CPT-038.
[3] Agazzani, A., and Massardo, A. F., 1997, ''A Tool for Thermoeconomic Analysis and Optimization of Gas, Steam and Combined Plants,'' ASME J. Eng. Gas Turbines Power, **119**, pp. 885–892.
[4] Agazzani, A., Frangopoulos, C., and Massardo, A. F., 1998, ''Environmental Influence on the Thermoeconomic Optimization of a Combined Plant With No$_x$ Abatement,'' ASME J. Eng. Gas Turbines Power, **120**, pp. 557–565.
[5] Massardo, A. F., and Scialo, M., 2000, ''Thermoeconomic Analysis of Gas Turbine Based Cycles,'' ASME J. Eng. Gas Turbines Power, **122**, pp. 664–671.
[6] Traverso, A., and Massardo, A. F., 2002, ''Thermoeconomic Analysis of Mixed Gas-Steam Cycles,'' Appl. Therm. Eng., **22**, pp. 1–21.
[7] Itoh, I., Mori, M., Mori, N., and Abe, T., 1994, ''Production Cost Estimation of Solid Oxide Fuel Cells,'' J. Power Sources, **49**.
[8] Krist, K., Wright, D., Romeo, C., and Chen, T. P., 1996, ''Cost Projections for Solid Oxide Fuel Cell Systems,'' 1996 *Fuel Cell Seminary*, Orlando FL, Nov., pp. 497–500.
[9] Stephenson, D., and Ritchey, I., 1997, ''Parametric Study of Fuel Cell Gas Turbine Combined Cycle Performance'' ASME Paper No. 97-GT-340.
[10] Costamagna, P., 1998, ''private communication,'' Stanford University, Stanford, CA.
[11] Hoffman M., 1999, ''private communication,'' University of California, Davis, CA.
[12] Pietsch T., 1998, ''private communication,'' Rolls Royce Eng., Advanced Centre, Derby, UK.
[13] Massardo, A. F., and Magistri L., 1999, ''Thermoeconomic and Environomic Analysis of SOFC Combined Cycles,'' DIMSET TN 1/99, University of Genoa (in Italian).
[14] Massardo, A., Santarelli, M., and Borchiellini, R., ''Carbon Exergy Tax (CET): Impact on Conventional Energy Systems Design and Its Contribution to Advanced Systems Utilisation,'' *ECOS 2000*, Twentee, NL, pp. 139–156.
[15] Borchiellini, R., Massardo, A. F., and Santarclli, M., 1999, ''Carbon Tax vs. CO_2 Effects on Environomic Analysis of Existing Power Plants,'' Proceedings ECOS '99, June 8–10, Tokyo, pp. 287–293.

Control System Design for Active Lubrication With Theoretical and Experimental Examples

I. F. Santos
e-mail: ilmar@fem.unicamp.br

A. Scalabrin
e-mail: scala@fem.unicamp.br

DPM–Department of Mechanical Design,
UNICAMP–State University of Campinas,
Campinas, Sao Paulo 13083-970, Brazil

This work focuses on the theoretical and experimental behavior of rigid rotors controlled by tilting-pad journal bearings with active oil injection. Initially the mathematical model of the active bearing is presented: The equations that describe the dynamics of hydraulic actuators are introduced into the equations of the lubricant, resulting in a new form of Reynolds' equation for active lubrication. The global model of the system is obtained by coupling the equation of motion of the rigid rotor with the stiffness and damping of the active oil film. This global model is then used to design the control system of the active bearing based on root locus curves. The active system stability is analyzed by calculating its eigenvalues and frequency response curves. The theoretical and experimental results show that this kind of bearing can significantly reduce the vibration level of rotating machinery. [DOI: 10.1115/1.1451757]

Introduction

The need of rotating machines of high efficiency, working at severe pressure and flow condition, demands continuous monitoring and control of vibration levels. The development of new mechanisms for dissipating vibration energy is of fundamental importance in order to keep low machine vibration levels. One of the ways of reducing vibration amplitudes in rotating machines is use of hydrodynamic bearings. Among the hydrodynamic bearings, the tilting-pad journal bearings (TPJB) are those which show the best stability properties. Nevertheless, in many cases, due to aerodynamic excitations and oil film damping reduction during full load condition (high maximum continuous speed), the amount of damping is not enough to ensure a reasonable stability margin. Thus, further mechanisms to dissipate vibration energy must be connected to such bearings, for instance squeeze-film dampers ([1]) and ([2]).

Another way of creating such kind of mechanisms is by using control techniques. Feedback control systems have also been applied to tilting-pad bearing with this goal, but are still in research and development stages. The first theoretical publications related to active tilting-pad journal bearings were presented by Ulbrich and Althaus [3] using piezo-actuators, and Santos and Ulbrich [4] using hydraulic actuators. The first experimental publications related to this topic can be found in Santos [5] and Santos [6]. In this context, a new type of dissipation mechanism is being developed, named active lubrication ([7–10]). To manufacture tilting-pad bearings actively lubricated, orifices are machined in the pad surface. Such orifices are connected to servovalves by means of pipelines. The lubricant is injected through the orifices into the bearing gap with a controllable pressure, allowing changes in hydrodynamic pressure distribution and consequently in the oil film properties (damping and stiffness).

Some authors have been investigated the combination of control techniques with hydrostatic lubrication ([11]) which results in active-control fluid bearings (ACFBs). Some others have been applied control techniques to squeeze-film dampers ([12]) which result in hybrid squeeze-film dampers (HSFDs). There is no doubt that these kind of active hydraulic devices, including active lubrication, are for a new generation of rotating machines ([11,13]). They will easily be applied to compressors and turbines (turbogenerators) in the next future, after crossing through the stages of research and development in laboratories of universities and industries. The benefits of actively lubricated bearings, active-control fluid bearings, and hybrid squeeze-film dampers are strongly related to the feasibility of compensating dynamical excitations, which are the source of the vibration problems. Moreover they allow adjustment of different levels of damping and stiffness, according to the acceptance limits of vibration in machines. An advantage of active lubricated bearings is the possibility of generating large control forces using small space. That is one of the principal advantages when compared to magnetic bearings. In case of control failure, the possibility of operating in the conventional way without large damages and without cross-coupling effects make active lubricated tilting-pad bearings a very attractive machine element.

An overview about different types of active actuators to control rotor vibrations is presented by Ulbrich [14], namely, magnetic, piezo, and hydraulic actuators. The recent theoretical developments related to active lubrication show the feasibility of changing the bearing properties by using a constant injection pressure ([7–10]). In this paper the mathematical model including the feedback control law for changing dynamically the injection pressure is presented. It leads to a modified Reynolds equation for the active lubrication cases. With the damping and stiffness of the active oil film, it is possible to construct the global linear mathematical model for the rotor-bearing system and design the feedback control system. The goal is to reduce the vibration level and increase the damping level of a rigid rotor.

Experimental Facilities

The rigid rotor coupled to the tilting-pad bearing actively lubricated is shown in Fig. 1. Figure 2 illustrates the interior of the bearing, built by four pads which are orthogonally arranged in the *y* and *z*-directions. It is possible to see the orifices machined on the pad surface. Figure 3 shows the pipeline connection of the electronic injection and two different pad geometries: with 5 and 15 orifices. The pads are built by two parts, which attached to each other by screws create a small sealed reservoir fulfilled by pressurized oil. These reservoirs are shown in the scheme of operational principle (see Fig. 4, active lubrication). In Fig. 1 the test rig is presented, focusing on the servovalves, and pipelines attached to the bearing. The oil (lubricant) coming from the servovalves is controlled using a feedback control law. The feedback

Contributed by the International Gas Turbine Institute (IGTI) of THE AMERICAN SOCIETY OF MECHANICAL ENGINEERS for publication in the ASME JOURNAL OF ENGINEERING FOR GAS TURBINES AND POWER. Paper presented at the International Gas Turbine and Aeroengine Congress and Exhibition, Munich, Germany, May 8–11, 2000; Paper 2000-GT-643. Manuscript received by IGTI, Nov. 1999; final revision received by ASME Headquarters, Feb. 2000. Associate Editor: D. Wisler.

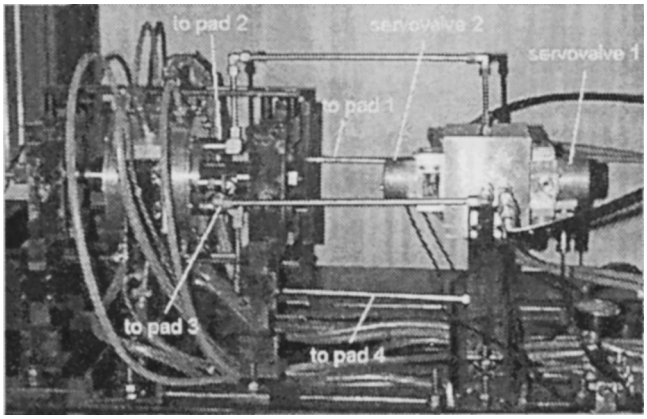

Fig. 1 Coupling between servovalves and bearing by means of pipelines

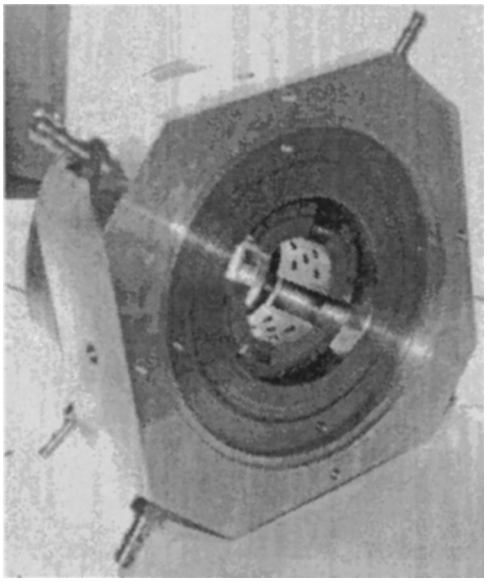

Fig. 2 Tilting-pad journal bearing with orifices machined on the pad surfaces

law is designed using displacement and velocity signals as shown in the scheme presented in Fig. 4. It is important to point out that the influence of the piping injection system on the rotational motion of the tilting-pad is very small. The piping line contributes with a very low torsional stiffness which can easily be calculated using the piping line dimensions. Comparing the torsional stiffness of the pad resulted from the oil film to the piping stiffness the first one can be neglected. High response servovalves of MOOG are used in this application. The valves show 90-deg phase lag at the frequency of 350 Hz. More details about the operational principle can be found in Santos and Russo [9].

Mathematical Model

The mathematical model of the rotor-bearing-actuator system is obtained in four steps: (1) initially the equations that describe the behavior of the hydraulic actuators are obtained; (2) the model of the bearing fluid film behavior based on the Reynolds equation is developed; (3) the model of the global system is constructed, including the equations of the rigid rotor and the active bearing; (4) and finally the control system is designed.

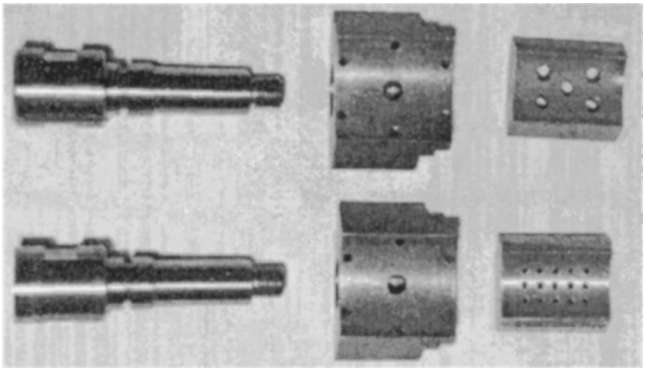

Fig. 3 Details of the pad parts and pipeline connections for injecting oil into the bearing gap. From left to right one can see feedline, the inferior part of the pad and the superior one (with 5 and 15 orifices), which attached to each other by screws create a small sealed reservoir.

Hydraulic Actuators. The behavior of the hydraulic actuators is determined by equations that relate the pressure and flow in the servovalve with the pressure in the bearing fluid film and the flow of oil through the orifices of the pads.

Considering that no load is applied to the servovalve, the flow through it is determined by the electrical input signal. This input signal is a function of the rotor displacement and velocity. Assuming that the rotor motion is harmonic, it is possible to obtain an analytical expression for the flow in the servovalve. Considering the *y*-direction, one gets ([15])

$$Q_y(t)=\omega_V^2 K_V Y\sqrt{\frac{G_1^2+G_2^2\omega^2}{(-\omega^2+\omega_V^2)^2+(2\xi_V\omega_V\omega)^2}}\,e^{j(\omega t+\phi_y)} \tag{1}$$

where

$$\phi_y=\arctan\left[\frac{-G_1 2\xi_V\omega_V\omega+\omega G_2(-\omega^2+\omega_V^2)}{G_1(-\omega^2+\omega_V^2)+\omega^2 G_2 2\xi_V\omega_V}\right]. \tag{2}$$

When the servovalve is coupled with the actuators (active bearing) the flow and pressure in the servovalve depend also on the load conditions. In this case, the expression that relates the flow and the pressure are nonlinear and can be linearized adopting the servovalve coefficient K_{PQ} ([9]). Applying this linearized relation to servovalve 1 and the pads 1 and 3, the following equations are obtained:

$$Q_1(t)=Q_y(t)+K_{PQ}(P_{inj1}(t)-P_{inj3}(t)) \tag{3}$$

$$Q_3(t)=-Q_y(t)-K_{PQ}(P_{inj1}(t)-P_{inj3}(t)). \tag{4}$$

The flow between the servovalve and the bearing can also be described considering the flow through the orifices of the pads. Assuming an incompressible oil, no pipe deformation and considering a laminar flow, one gets the velocity of oil injection into the bearing gap. Integrating the oil velocity over the orifices areas, the flow through the bearing pads becomes

$$Q_1(t)=\sum_{i=1}^{s}\left[\frac{\pi d_{O_i}^2}{128\mu l_{O_i}}(P_{inj1}(t)-p_1(\overline{x,z},t))\right] \tag{5}$$

$$Q_3(t)=\sum_{i=1}^{s}\left[\frac{\pi d_{O_i}^2}{128\mu l_{O_i}}(P_{inj3}(t)-p_3(\overline{x,z},t))\right]. \tag{6}$$

By coupling the flow equations of the servovalve, Eqs. (3) and (4), with the flow equation of the bearing, Eqs. (5) and (6), one gets the injection pressure equation:

$$P_{\mathrm{inj1}}(t)=C_1\cdot p_1(\overline{x,z},t)+C_2\cdot p_3(\overline{x,z},t)+C_3\cdot Q_y(t) \tag{7}$$

$$P_{inj3}(t)=C_1\cdot p_3(\overline{x,z},t)+C_2\cdot p_1(\overline{x,z},t)-C_3\cdot Q_y(t). \tag{8}$$

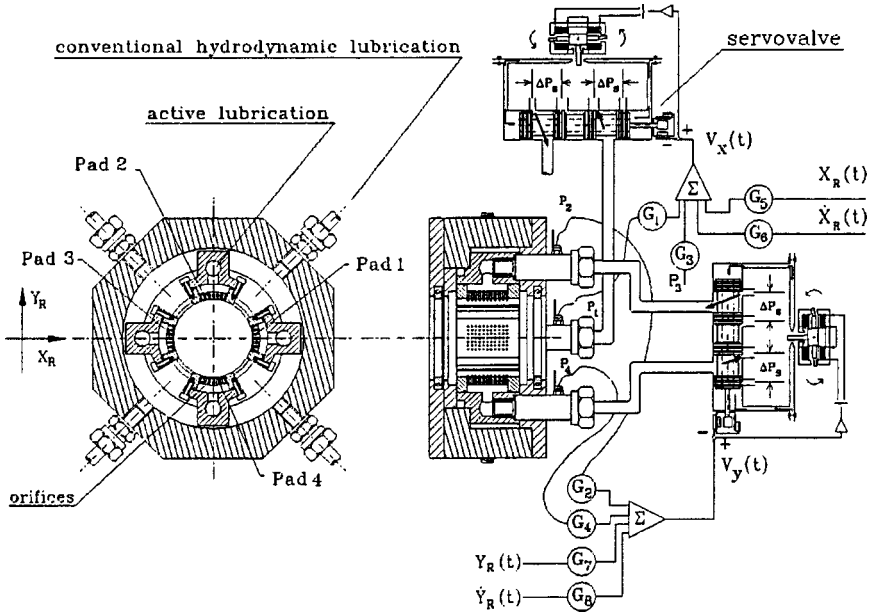

Fig. 4 Scheme of the operational principle of the active lubrication

Active Lubrication Equations. Once the hydraulic actuators behavior is determined, and the injection pressure equations are obtained, the next step is to obtain the equations that describe the bearing fluid film behavior.

The characteristics of the hydrodynamic bearing are obtained from the fluid film pressure distribution over the bearing pads, as described by Reynolds equation. Considering the injection in the radial direction, this equation is modified with the introduction of terms that represent the pressure injection of the oil coming from the chambers of the pads. This modified equation is presented in Santos and Russo [9], where the injection pressure is constant. Considering the dynamic pressure injection described by Eqs. (7) and (8), the modified Reynolds equations, applied again to pads 1 and 3, become

$$\frac{\partial}{\partial \bar{x}}\left(\frac{h_1^3}{\mu}\frac{\partial p_1}{\partial \bar{x}}\right)+\frac{\partial}{\partial \bar{z}}\left(\frac{h_1^3}{\mu}\frac{\partial p_1}{\partial \bar{z}}\right)-\frac{3}{\mu l_o}\sum_{i=1}^{s}\mathcal{F}_i(\bar{x},\bar{z})\cdot[p_1\cdot(1-C_1)-C_2\cdot p_3]=6U\frac{\partial h_1}{\partial \bar{z}}+12\frac{\partial h_1}{\partial t}-\frac{3}{\mu l_o}\sum_{i=1}^{s}\mathcal{F}_i(\bar{x},\bar{z})\cdot C_3\cdot\omega_V^2\cdot K_V\cdot Y\cdot\sqrt{\frac{G_1^2+(\omega\cdot G_2)^2}{(-\omega^2+\omega_V^2)^2+(2\cdot\xi_V\cdot\omega_V\cdot\omega)^2}}\cdot e^{j\cdot(\omega\cdot t+\phi_y)} \tag{9}$$

$$\frac{\partial}{\partial \bar{x}}\left(\frac{h_3^3}{\mu}\frac{\partial p_3}{\partial \bar{x}}\right)+\frac{\partial}{\partial \bar{z}}\left(\frac{h_3^3}{\mu}\frac{\partial p_3}{\partial \bar{z}}\right)-\frac{3}{\mu l_o}\sum_{i=1}^{s}\mathcal{F}_i(\bar{x},\bar{z})\cdot[p_3\cdot(1-C_1)-C_2\cdot p_1]=6U\frac{\partial h_3}{\partial \bar{z}}+12\frac{\partial h_3}{\partial t}+\frac{3}{\mu l_o}\sum_{i=1}^{s}\mathcal{F}_i(\bar{x},\bar{z})\cdot C_3\cdot\omega_V^2\cdot K_V\cdot Y\cdot\sqrt{\frac{G_1^2+(\omega\cdot G_2)^2}{(-\omega^2+\omega_V^2)^2+(2\cdot\xi_V\cdot\omega_V\cdot\omega)^2}}\cdot e^{j\cdot(\omega\cdot t+\phi_y)} \tag{10}$$

where the left side terms represent the hydrodynamic pressure distribution along pads 1 and 3, which are coupled by the function that describes the position of the orifices ($\Sigma_{i=1}^{s}\mathcal{F}_i(\bar{x},\bar{z})$). The first term on the right side of the equations gives the influence of the bearing clearance shape h and the rotor velocity U (both dependent on the geometry and operational conditions of the system) on the hydrodynamic pressure; the second term on the right side gives the influence on the hydrodynamic pressure determined by the bearing clearance variation with respect to time, which represents the vibration movement between the rotor and the bearing pads. Finally, the third term on the right side of the equations gives the influence of the hydraulic control system terms, including the rotor displacement amplitude Y, the feedback gains G_1 and G_2 and the servovalve parameters ξ_V and ω_V. This term is also dependent on the system vibration frequency (ω) and phase (ϕ_y), which gives the lag between the injection pressure and the rotor movement, and is presented in Eq. (2).

Therefore, to solve the modified Reynolds equation and calculate the bearing stiffness and damping coefficients, one must consider that the entire system vibrates with the same frequency ω. The main characteristic of the modified Reynolds' equation, Eqs. (9) and (10), is that the pressures of the pads located in the same direction are coupled, i.e., the two equations cannot be solved independently.

Global Model. The mathematical model of the global system (rotor+bearing+active lubrication) is obtained calculating the stiffness and damping of the active bearing (which are function of the control gains) and introducing these active hydrodynamic forces into the rigid rotor dynamic equation. Figure 5 shows the global system including the rigid rotor, the rotor supports A and B and the active bearing coupled with the servovalves (point C of the rotor). The global model does not ignore the rotational motions of the pads. The stiffness and damping coefficients regarding rotor and tilting-pad motions are calculated using the modified Reynolds equation and perturbation method, assuming synchronous movements. It results in damping and stiffness matrices of order 3×3 for each rotor-pad system, where the coefficients depend on the synchronous frequency and feedback control gains. The global model is created using four degrees-of-freedom for describing the rotor movements (vertical and horizontal linear displacements and rotations around the vertical and horizontal axis)

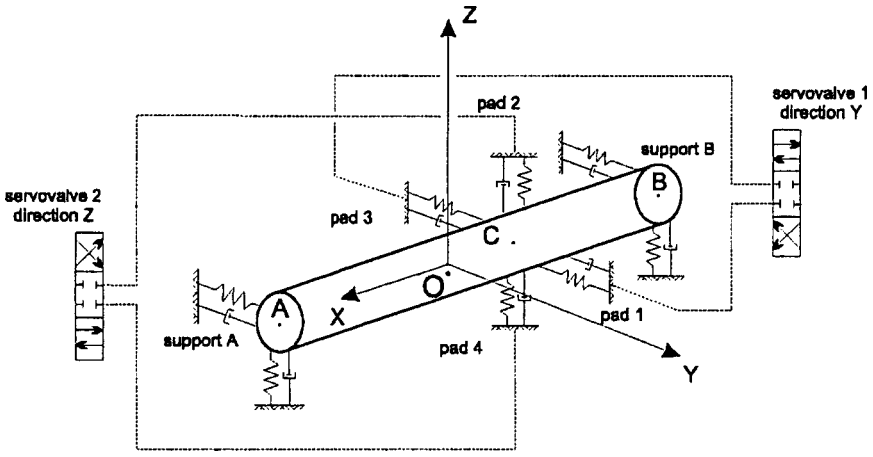

Fig. 5 Global system—rigid rotor, active bearing, and servovalves

and the four additional degrees-of-freedom for describing the tilting motion of the four pads. Summarizing, the global model of the test rig has eight degrees-of-freedom.

The global model in the state-space form is described by the following equation ([15]):

$$\begin{Bmatrix} \dot{\mathbf{q}}_G \\ \ddot{\mathbf{q}}_G \end{Bmatrix} = \begin{bmatrix} 0 & I \\ -\mathbf{M}_G^{-1}\cdot\mathbf{K}_G & -\mathbf{M}_G^{-1}\cdot(\mathbf{D}_G - \Omega\cdot\mathbf{G}_G) \end{bmatrix} \cdot \begin{Bmatrix} \mathbf{q}_G \\ \dot{\mathbf{q}}_G \end{Bmatrix} + \begin{Bmatrix} 0 \\ -\mathbf{M}_G^{-1}\cdot\mathbf{f}_G \end{Bmatrix}$$

$$\dot{\mathbf{q}}_\mathbf{E} = \mathbf{A}\cdot\mathbf{q}_E + \mathbf{f}_E \tag{11}$$

where Ω is the rotor rotational speed, $\mathbf{q}_G$ is the displacement vector, $\mathbf{M}_G$, $\mathbf{D}_G$, $\mathbf{G}_G$, and $\mathbf{K}_G$ are the mass, damping, gyroscopic and stiffness matrices of the global system, respectively, and $\mathbf{f}_G$ is the vector of perturbations.

System Control. The design of the control system is defined by five steps:

(i) Definition of the structure of the feedback law. In this case a very simple output signal was choosen,

$$\begin{cases} \dot{\mathbf{q}}_E(t) = \mathbf{A}(t,\mathbf{u})\cdot q_E(t) \\ \mathbf{y}(t) = \mathbf{C}\cdot\mathbf{q}_E(t) \end{cases}, \tag{12}$$

leading to the control vector $\mathbf{u}$ with $\mathbf{G}$ as gain matrix

$$\mathbf{u} = \mathbf{G}\cdot\mathbf{y} = \mathbf{G}\cdot\mathbf{C}\cdot\mathbf{q}_E = \{G_1 y \;\; G_3 z \;\; G_2\dot{y} \;\; G_4\dot{z}\}^T$$

which means that one uses a PD-control with the displacement and velocity signal of the rotor.

(ii) This information is used in Eqs. (1), (9), and (10). The modified Reynolds equation for actively lubricated bearings is solved, and rotor-bearing equilibrium position is found.

(iii) After solving the modified Reynolds equation one calculates the damping $\mathbf{D}_G$ and stiffness $\mathbf{K}_G$ matrices as a function of the different gain values G_1, G_2, G_3 and G_4.

(iv) These matrices ($\mathbf{D}_G$ and $\mathbf{K}_G$) are introduced into Eq. (11), and the eigenvalues of the state matrix $\mathbf{A}$ are calculated as function of $\mathbf{D}_G$ and $\mathbf{K}_G$, or as function of G_1, G_2, G_3 and G_4.

(v) The root locus curve method is then applied, aiming at achieving a more damped rotor-bearing system.

In other words, modifying the feedback gains over a certain range, one also modifies the stiffness and damping matrices and, consequently, the behavior of the system. The stability of the global system is analyzed by calculating its eigenvalues for each gain adopted and by calculating the frequency response curves for different gain values.

Theoretical and Experimental Results

Figure 6 presents the variation of the real part of the system eigenvalues as a function of the displacement feedback gains, and Fig. 7 presents the variation of the real part of the eigenvalues as a function of the velocity feedback gains. The rotor angular velocity adopted in the presented simulations is $\Omega = 18$ Hz or ($\approx$1080 rpm or 113 rad/s).

Figure 6 presents the eigenvalues of the system related to the translation and rotational modes of the rotor in directions *y* and *z* and also some eigenvalues related to the pads tilting modes. The main goal is to analyze the translation modes of the rotor. When the displacement gain has a value of $G_1 = 5$ V/mm (right side of the graphic) the eigenvalue associated with the *y* displacement has a value of -100 rad/s (point A) and the eigenvalue associated with the *z* displacement has a value of -130 rad/s (point B).

It can be seen that, as the values of the gains decrease, the real part of these eigenvalues also decreases, indicating that the system stability (associated with the translation modes of the rotor) increase. When the gains achieve a certain value ($G_1 \approx -17$ V/mm for the *y*-direction and $G_3 \approx -13$ V/mm for the *z*-direction), respectively, the eigenvalues "bifurcate" (points A′ and B′), indicating that the imaginary part of the eigenvalues becomes null and the movement of these coordinates is overdamped.

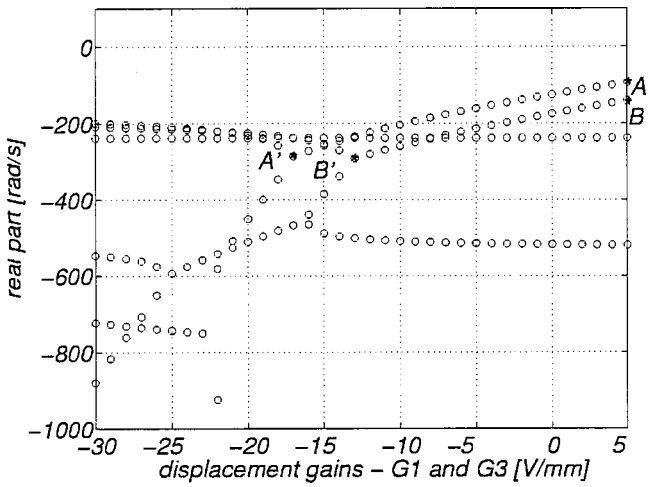

Fig. 6 Real part of the eigenvalues as a function of displacement feedback gains G_1 and G_3. Point A is related to the *y*-direction and point B to the *z*-direction.

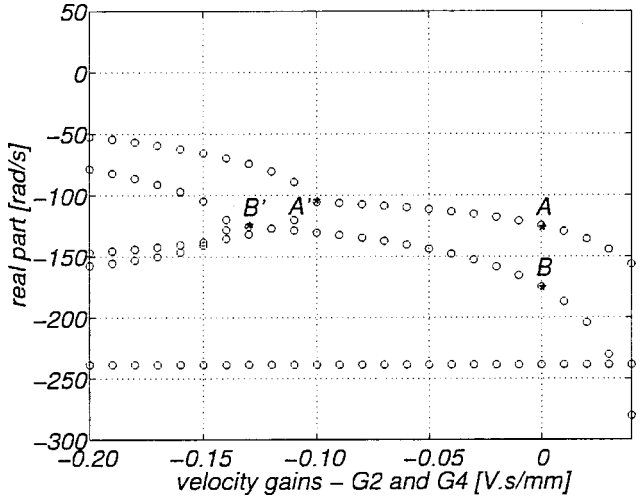

Fig. 7 Real part of the eigenvalues as a function of velocity feedback gains G_2 and G_4. Point A is related to the *y*-direction and point B to the *z*-direction.

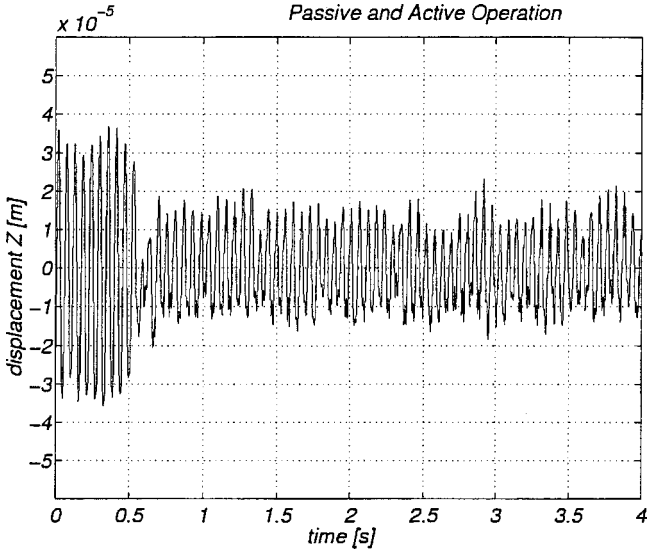

Fig. 9 Experimental results showing the vibration amplitude of the rotor, when the control system is turned on after 0.5 s

Analyzing the variation of the velocity gains (Fig. 7) one can see that, as the gains G_2 and G_4 decreases from positive values to negative values, the real part of the eigenvalues increases. But when the velocity gains become smaller the real part of the eigenvalues also opens, as was observed in Fig. 6, points A′ and B′.

This behavior of the real part of the eigenvalues shows that the passive system (without feedback control) is already well damped and when the control system is applied the system becomes overdamped. This makes the theoretical and experimental analyses of the influence of the control system on the test rig (Fig. 1 and Fig. 5) more difficult. Another approach to observe the control system behavior is to choose different feedback loops and calculate the frequency response curves for these control systems.

Figure 8 shows the frequency response curves of the rigid rotor in the speed range of zero until 400 rad/s (≈64 Hz or 3820 rpm) for five cases: (a) passive case or conventionally lubricated rotor-bearing system (with no radial oil injection); (b) with radial injection at constant pressure or hybridly lubricated (with no feedback control); (c) actively lubricated using a displacement feedback control law with $G_1 = -10$ V/mm; (d) actively lubricated using a velocity feedback control law with $G_2 = -0.1$ V.s/mm; and (e) actively lubricated using a feedback control with both displacement and velocity signals ($G_1 = -10$ V/mm and $G_2 = -0.1$ V.s/mm). It is important to point out that pad and rotor movements are synchronous, and damping and stiffness bearing coefficients are calculated at each rotational speed in the mentioned range.

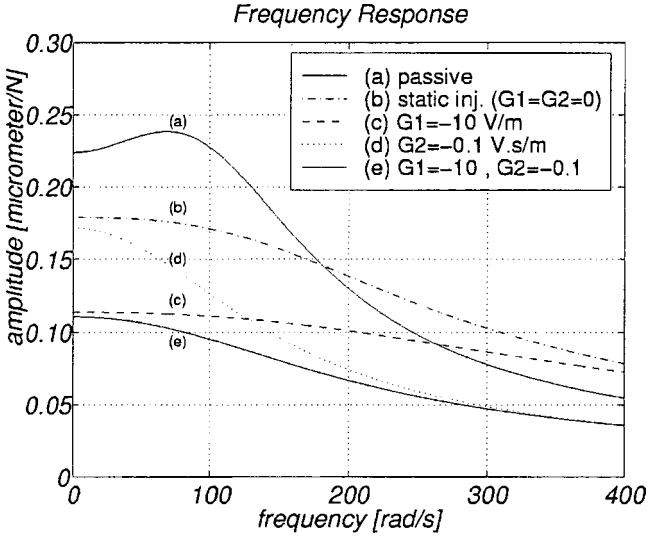

Fig. 8 Frequency response curves of the rotor for five different cases: (*a*) ——conventionally lubricated; (*b*) —·—·—·— hybridly lubricated; (*c*) — — —actively lubricated with displacement feedback control; (*d*) · · · · actively lubricated with velocity feedback control; (*e*) ——actively lubricated with displacement and velocity feedback control

(a) The frequency response curve of the rotor (test rig shown in Fig. 1) shows again that the passive system is well damped for the passive case. It can be easily seen through the low resonance peak and low amplification factor. (b) Adding to the conventional hydrodynamic lubrication the radial oil injection with constant pressure, the vibration amplitude of the rotor can be reduced for low frequencies, but not for high frequencies. (c) Working with actively lubricated bearing, when only the displacement feedback is used, the vibration amplitude of the rotor at low frequencies is reduced even more, but at high frequencies the amplitude is still higher than the passive case. (d) When the velocity displacement is used while designing the feedback control law, the vibration amplitude of the rotor at high frequencies is significantly reduced. (e) Combining velocity and displacement signals with proper control gains the frequency response curve of the rotor has the lowest amplitude in the whole frequency range, resulting in a very well damped rotor-bearing system.

Based on the theoretical investigations presented, the output control system was designed and experimentally implemented on the test rig (Fig. 1). Figure 9 shows the rotor displacement in the *z*-direction when an angular velocity of the rotor Ω is set at 18.1 Hz or 113.7 rad/s. The system operates without control until 0.5 s, when the control system is turned on.

It can be clearly seen from Fig. 9 that when the control system is operating the rotor amplitude (caused by the imbalance) reduce significantly. The amplitude ratio between the passive system (amplitude ≈30 μm) and the active system (amplitude ≈15 μm) is 2/1. This is almost the same amplitude ratio observed in Fig. 8 when a frequency excitation of 18.1 Hz or 113.7 rad/s is set. The vibration amplitude of the rotor drops from ≈0.23 μm/N (passive case) to ≈0.11 μm/N (active case with displacement and velocity feedback control law).

Conclusions and Future Aspects

In this work a theoretical and experimental investigation of rigid rotors controlled by tilting-pad bearings with active lubrication was presented.

The complete set of equations for describing the behavior of active oil film was presented. It was taken into account the dynamics of the hydraulic system and the feedback control law, leading to the modified Reynolds equation for active lubrication cases. The main characteristic of these equations is the frequency dependency and the need of simultaneously solving the pressure distribution for the pair of pads in each direction. Theoretical results agree very well with the experimental ones, and the mathematical model becomes a very helpful tool aiming at developing and designing active lubricated bearings. The reduction of rotor vibrations could be seen theoretically as well as experimentally.

The test rig has a relative light rotor, which operates at the low rotational speed of 18.1 Hz supported by a bearing with minimum radial clearance. This combination of parameters leads to system eigenvalues with large magnitudes of damping, nearly overdamped. Although the rotor-bearing system is already well damped, a further increase of damping can clearly be seen when the control system is turned on, which shows the feasibility of active lubrication. Additional tests are being carried out at higher rotor speeds where the magnitudes of damping are not so large. The test rig is also being modified aiming at having a heavier rotor operating with maximum bearing clearance or worn bearings. Such a combination of parameters will lead to a lower damped rotor-bearing system. These tests will also show the influence of the active lubrication and the reduction of vibration amplitudes in the case of low damped rotating systems.

From the technological point of view it was experimentally demonstrated the operational principle of active lubrication. One concludes that actively lubricated bearings can become a very important tool to reduce vibration in rotating machines and improve their stability. Further theoretical and experimental investigations are being carried on, focusing new control strategies, advantages and disadvantages of such a kind of damping mechanism, with the main goal of industrial applications in centrifugal compressors.

Penalties on power loss for bearings operating with active lubrication are being investigated as well. Comparison of power loss for bearings with passive and active lubrication will more clearly show the chances of industrial applications from the economical and performance point of view.

Acknowledgment

The Brazilian research foundation Fundação de Amparo *à* Pesquisa do Estado de São Paulo (FAPESP) is gratefully acknowledged for the support given to this project. The Machinery Dynamics Group of the Danish company Odegaard & Danneskiold-Samsoe A/S is acknowledged for its interest and motivation related to the industrial application of the results of this research project.

Nomenclature

$\mathbf{A}$ = state-space matrix
$\mathbf{C}$ = measurement matrix
C_1, C_2, C_3 = coefficients of the pressure of injection expression
$\mathbf{D}_G$ = global damping matrix
$\mathbf{G}$ = control gain matrix
$\mathbf{G}_G$ = global gyroscopic matrix
G_1, G_3 = displacement feedback gains in directions y and z
G_2, G_4 = velocity feedback gains in directions y and z
$\mathbf{K}_G$ = global stiffness matrix
K_{PQ} = coefficient of linearization of the servovalve
K_V = flow gain of the servovalve
$\mathbf{M}_G$ = global mass matrix
P_{inji} = pressure of injection in pad $i=1,2,3,4$
Q_1, Q_3 = flow through pads 1 and 3
Q_y = flow through servovalve 1 in no-load condition
U = rotor tangential velocity
Y = rotor displacement amplitude in horizontal direction
d_O = orifice diameter
$\mathbf{f}_E$ = vector of state-space forces
$\mathbf{f}_G$ = vector of external forces
h_i = bearing gap in pad $i=1,2,3,4$
l_o = orifice length
p_i = pressure distribution over pad $i=1,2,3,4$
$\mathbf{q}_E$ = vector of state-space coordinates
$\mathbf{q}_G$ = vector of global coordinates
$\mathbf{u}$ = control vector
$\mathbf{y}$ = output vector
Ω = rotor angular velocity
ω = harmonic vibration frequency of the rotor and the pads
ω_V = natural frequency of the servovalve
ξ_V = damping factor of the servovalve
ϕ_y = phase between rotor movement and servovalve response
μ = oil viscosity
$\mathcal{F}$ = function that describes the orifices position

References

[1] Mohan, S., and Hahn, E. J., 1974, "Design of Squeeze Film Damper Supports for Rigid Rotors," ASME J. Eng. Ind., **96**, No. 3, p. 976.
[2] Shiau, T. N., Rao, J. S., Chang, J. R., and Choi, S. T., 1999, "Dynamic Behavior of Geared Rotors," ASME J. Eng. Gas Turbines Power, **121**, pp. 494–503.
[3] Ulbrich, H., and Althaus, J., 1989, "Actuator Design for Rotor Control," *12th Biennial ASME Conference on Vibration and Noise*, Vol. 1, ASME, New York, pp. 17–22.
[4] Santos, I. F., and Ulbrich, H., 1992, "Actively Controlled Tilting Pad Journal Bearings," *ISROMAC - The International Symposium on Transport Phenomena and Dynamics of Rotating Machinery*, Honolulu, Vol. 2, pp. 423–431.
[5] Santos, I. F., 1993, *Aktive Kippsegmentlagerung—Theorie und Experiment* (Schwingungstechnik, 189), VDI-Verlag, Dusseldorf.
[6] Santos, I. F., 1995, "On the Adjusting of the Dynamic Coefficients of Tilting-Pad Journal Bearings," STLE Tribol. Trans., **38**, No. 3, pp. 700–706.
[7] Santos, I. F., 1994, "Design and Evaluation of Two Types of Active Tilting-Pad Journal Bearings," *IUTAM Symposium on Active Control of Vibration*, Bath, England, pp. 79–87.
[8] Santos, I. F., 1995, "Strategien für die Erhöhung der Dämpfungsreserve von kippsegmentgelagerten Rotorsystemen," *Schwingungen in rotierenden Maschinen*, Vol. 3, pp. 3–12.
[9] Santos, I. F., and Russo, F. H., 1998, 'Tilting-Pad Journal Bearings with Electronic Radial Oil Injection,' ASME J. Tribol., **120**, pp. 583–594.
[10] Santos, I. F., and Nicoletti, R., 1999, 'THD Analysis in Tilting-Pad Journal Bearings Using Multiple Orifice Hybrid Lubrication,' ASME J. Tribol., **121**, pp. 892–900.
[11] Bently, D. E., Grant, J. W., and Hanifan, P., 1999, "Active Control Fluid Bearings for a New Generation of Machines," *Orbits, Second/Third Quarters*, Vol. 20, No. 2, pp. 15–20.
[12] El-Shafei, A., and Hathout, J. P., 1995, "Development and Control of HSFDs for Active Control of Rotor-Bearing Systems," ASME J. Eng. Gas Turbines Power, **117**, pp. 757–766.
[13] Ulbrich, H., 1993, "Haben aktive Lagerungen Zukunft?," *Schwingungen in rotierenden Maschinen*, Vol. 2, Vieweg Verlag, pp. 18–27.
[14] Ulbrich, H., 1998, "Active Vibration Control of Rotors," *Fifth International IFToMM Conference on Rotor Dynamics*, Vieweg Verlag, Braunschweig, pp. 16–31.
[15] Scalabrin, A., 1999, "Utilização de Mancais Segmentados com Injeção Electrônica para Controle de Rotores - Teoria e Experimento," Master thesis, Department of Mechanical Design, State University of Campinas, Brazil.

A Harmonic Wavelets Approach for Extracting Transient Patterns From Measured Rotor Vibration Data

V. C. Chancey
Department of Biomedical Engineering,
Duke University,
Durham, NC 27708-0281

G. T. Flowers

C. L. Howard

Department of Mechanical Engineering,
Auburn University,
Auburn, AL 36849-5341

Vibration analysis is a powerful diagnostic tool for rotating machinery problems. Traditional approaches to vibration signature analysis have focused on the Fourier transform, which tends to average out transient effects. Recent work in the area of wavelets has allowed for the characterization of signals in frequency and in time, which, if properly interpreted, can provide substantial insight, particularly with regard to transient behaviors. There are many different types of wavelets, but the harmonic wavelet was developed specifically for vibration analysis. It uses an algorithm based upon the fast Fourier transform (FFT), which makes it particularly attractive to many in the vibration analysis community. This paper considers the harmonic wavelet as a tool for extracting transient patterns from measured vibration data. A method for characterizing transient behaviors using the harmonic wavelet is described and illustrated with simulation and experimental results. [DOI: 10.1115/1.1520156]

Introduction

Rotating machinery provides the backbone of numerous industries, from the turbine-compressor trains used in the petrochemical industry to the steam turbines utilized in the production of electrical power. The aerospace industry is also heavily dependent on turbomachinery. From the compressors and turbines used in modern jet aircraft to the impressive example found in the space shuttle main engine (SSME) turbopumps, rotating machinery is an essential element of industrial society. When this machinery fails, production delays, determination of the cause of the failure, and replacing the defective part(s) cost those industries millions of dollars each year. In response to this situation, the field of machinery diagnostics has developed. Prior to the advent of the fast Fourier transform (FFT) spectrum analyzer, a maintenance plan involved periodically taking apart the equipment and inspecting it. Today, a predictive approach is used in many industries. Several parameters may be used for condition monitoring, including temperature, pressure, oil analysis, noise, and vibration. Of these, Wowk [1] notes that vibration analysis is the single most important component of a successful maintenance program.

In the diagnosis of an existing problem, current analysis methods often cannot be used to distinguish between specific causes. For example, vibrations due to unbalance, eccentricity, and a bent shaft or bowed rotor may be of similar amplitude and frequency, leading to similar time traces and Fourier diagrams. Another instance of difficult vibration diagnosis is with wear on the surface of a bearing race. In the initial stages of wear, the resulting vibration causes distinct peaks to be seen in the frequency domain. However, after wear develops along the entire surface of the race, the vibration signal becomes more like random noise (Vance [2]). This is representative of one of the limitations of current vibration analysis methods utilizing the FFT: the inability to monitor transient and nonrepeating vibration signals. Fourier methods, based on infinitely long periodic signals, tend to average out these transitory signals, while it is often too complicated to note a growth or decay in a specific part of the signal with a time trace.

If an efficient method could be developed which would allow the extraction of these transient (but oscillatory) signals from the overall vibration pattern, additional insight and diagnostic ability could result. This method should be grounded in current methods, to function as a supplement to and extension of FFT technology. Drawing on such familiar concepts as the FFT, filter banks, and time-frequency methods, researchers in varied fields such as signal processing, geophysics, vision research, electrical engineering, and image processing concurrently developed wavelets in order to improve their signal analysis, in time (or space) as well as frequency (Hubbard [3]). Although the basic ideas of modern wavelets were developed beginning in the mid-1970s, the main deterrent to their widespread application was that no one realized that pyramid algorithms, quadrature mirror filters, and subband coding were, in essence, all the same.

Wavelets, as an analysis tool, have the unique ability to simultaneously gather information about both the time and frequency domains. The current work is intended to demonstrate the use of harmonic wavelets (HW) in analyzing transient signals, including those with changing frequency and those with multiple frequencies of interest. Newland [4,5] developed harmonic wavelets specifically in response to his own vibration analysis investigations. The HW has been shown to be a favorable choice for vibration analysis because of the use of the FFT and the inverse fast Fourier transform (IFFT) in the HW algorithm. The algorithms for the FFT and IFFT are readily available for use, and many vibration analysts have a good understanding of their results. In addition, the Fourier coefficients are generated as an intermediate step in determining the HW coefficients.

Analysis Approach

A recent study by Chancey et al. [6] showed that using the absolute harmonic wavelet coefficients (AHWC) for sinusoidal signals allows the identification of a particular frequency content's amplitude within a given signal as a function of time, or scaled time. This methodology is only appropriate for use with oscillatory signals, but these type signals are usually the expression of vibrations in rotating machines.

Contributed by the International Gas Turbine Institute (IGTI) of THE AMERICAN SOCIETY OF MECHANICAL ENGINEERS for publication in the ASME JOURNAL OF ENGINEERING FOR GAS TURBINES AND POWER. Paper presented at the International Gas Turbine and Aeroengine Congress and Exhibition, New Orleans, LA, June 4–7, 2001; Paper 2001-GT-241. Manuscript received by IGTI, Dec. 2000, final revision, Mar. 2001. Associate Editor: R. Natole.

Table 1 Implementation of the HW transform

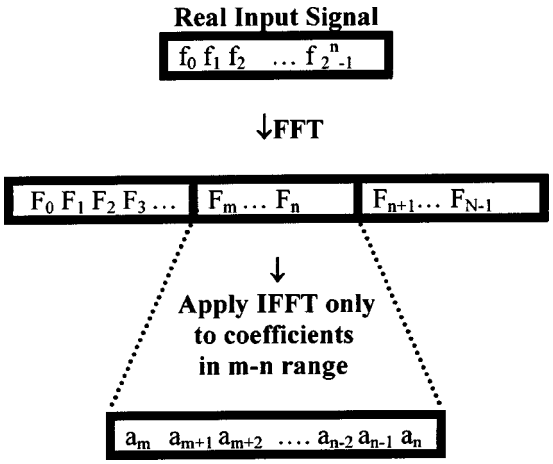

In order to provide a proper foundation for the discussion, we should first consider some basic points of the harmonic wavelet algorithm. There have been a number of improvements over the last few years, but in its original form, the family of harmonic wavelets was defined as

$$w(2^j t-k)=\frac{e^{i4\pi(2^j t-k)}-e^{i2\pi(2^j t-k)}}{i2\pi(2^j t-k)} \tag{1}$$

where j denotes a level or octave and k represents an integer shift within the level. The representation of a function by these wavelets becomes similar to general wavelet theory representation as shown in Eq. (2) where a signal may be expressed as the summation of the product of wavelet coefficients and their respective shifted and scaled wavelet. Each level corresponds to a scaled version of the entire signal length and j contains information about the length of each wavelet and span of its coefficient.

$$f(t)=\sum_{j=-\infty}^{\infty}\sum_{k=-\infty}^{\infty} a_{j,k}w(2^j t-k) \tag{2}$$

Newland [7] proved that this family could be generalized to some m,n level ($m\leqslant n$, m, and n not necessarily integers) with the Fourier transform of the redefined wavelet given by

$$W_{m,n}(\omega)=\left\langle \begin{array}{ccc} \dfrac{1}{(n-m)2\pi} & & m2\pi\leqslant\omega\leqslant n2\pi \\ & \text{for} & \\ 0 & & \text{all other } \omega \end{array} \right\rangle \tag{3}$$

thus removing the restrictions ($2^j 2\pi\leqslant\omega\leqslant 2^j 4\pi$) on bandwidth present in the original formulation. Newland [8,9] published a revised algorithm based on simply calculating the coefficients of a selected band of frequencies. Any number of FFT semi-coefficients now can be selected as input to an IFFT and thus obtain HW coefficients for a select band of frequencies if desired. Table 1 illustrates this procedure. Note that to calculate the HW coefficients for a frequency range from m to n, only the Fourier semi-coefficients in that range are used in the application of the inverse FFT.

Now assume that the vibration signal to be analyzed is of the form

$$f(t)=\sum_{i=1}^{M} g_i(t)\cos(\omega_i t-\phi_i). \tag{4}$$

The function $f(t)$ is assumed to have M components. The amplitude of each component is attenuated by a growth (or decay) function $g_i(t)$. The frequency, ω_i, and phase angle, ϕ_i, are associated with the ith component of $f(t)$.

To learn what information the resulting harmonic wavelet coefficients contain, one begins by rewriting Eq. (4) as

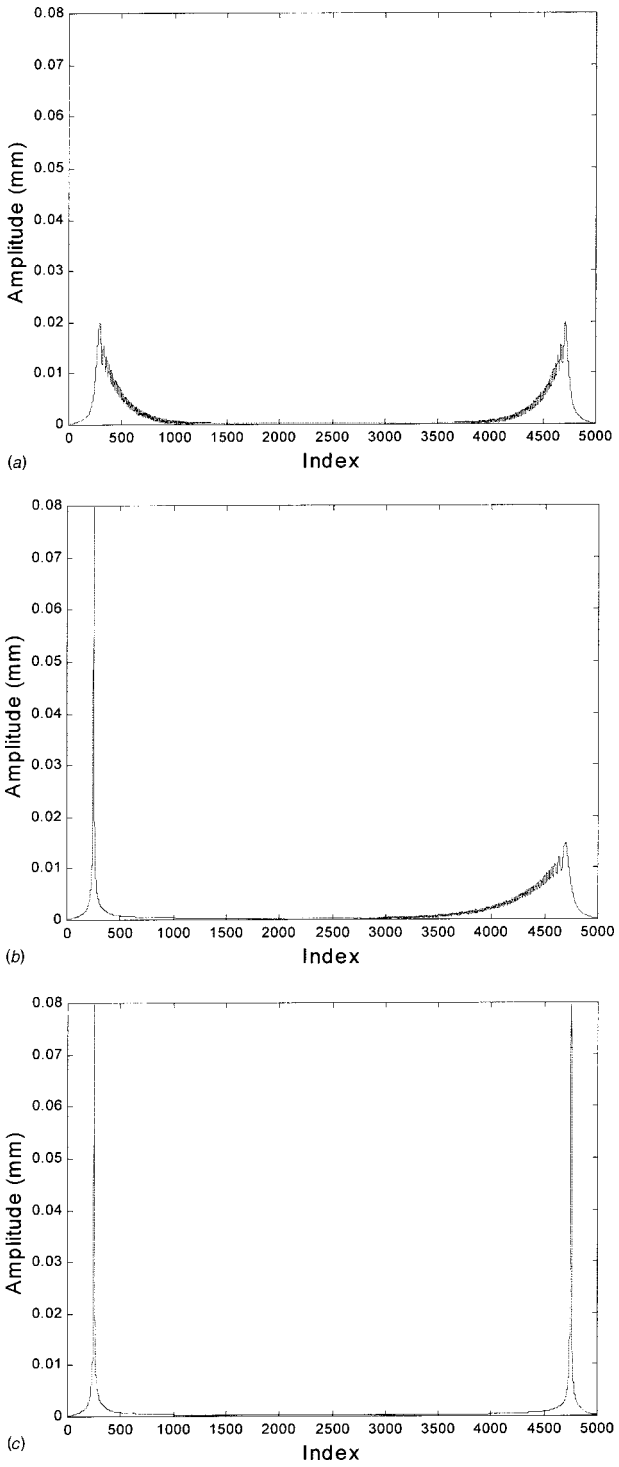

Fig. 1 (*a*) Absolute Fourier coefficients for $x(t)=e^{-0.5t}\cos([10+2t]\pi t)$ over a 25-sec time interval; (*b*) absolute Fourier coefficients for $x(t)=e^{-0.5t}\cos([10+2t]\pi t)$ over a 25-sec time interval shifted as described above; (*c*) absolute Fourier coefficients for $x(t)=e^{-0.5t}\cos(10\star 2\pi t)$ over a 25-sec time interval

$$f(t)=\sum_{i=1}^{M}\left[g_i(t)\cos(\phi_i)\cos(\omega_i t)+g_i(t)\sin(\phi_i)\sin(\omega_i t)\right]. \tag{5}$$

Now consider the Fourier transforms (Morrison [10]) for each component of the terms in Eq. (5). Application of the Fourier transform gives

$$g_i(t)\cos(\phi_i)\cos(\omega_i t)\Leftrightarrow\frac{1}{2}\cos(\phi_i)G_i(\omega-\omega_i)+\frac{1}{2}\cos(\phi_i)G_i(\omega+\omega_i) \tag{6a}$$

and

$$g_i(t)\sin(\phi_i)\sin(\omega_i t)\Leftrightarrow\frac{1}{2j}\sin(\phi_i)G_i(\omega-\omega_i)-\frac{1}{2j}\sin(\phi_i)G_i(\omega+\omega_i). \tag{6b}$$

Remember that the IFFT is applied only to the m to n frequencies of interest, designated here by terms with argument $(\omega-\omega_i)$ in Eq. (6). By adding the terms containing $\omega-\omega_i$ in Eqs. (6*a*) and (6*b*) and taking the IFFT of the sum, the following relationship between the frequency terms and the corresponding time function is produced.

$$\frac{1}{2}G_i(\omega-\omega_i)\left[\cos(\phi_i)+\frac{1}{j}\sin(\phi_i)\right]\Leftrightarrow\frac{1}{2}g_i(t)[\cos(\omega_i t-\phi_i)+j\,\sin(\omega_i t-\phi_i)] \tag{7}$$

The harmonic wavelet coefficients, a_k, associated with the level containing ω_i are the time domain terms of Eq. (7) (when temporally discretized for the $(n-m)$ time increments in the associated level). If only the frequency spectrum of the component $g_i(t)\cos(\omega_i t-\phi_i)$ (of the original signal $f(t)$) is completely contained in the bandwidth region ω_m to ω_n, then the absolute value of the associated HW coefficients gives

$$|a_k|=\frac{1}{2}|g_i(t_k)| \tag{8}$$

where t_k denotes the temporal position of each coefficient within its level. If there is overlap between the spectra of two or more signal components, the $|a_k|$ (AHWC) represent the absolute value of the time signal corresponding to that part of the frequency spectrum which belongs to the bandwidth in question.

Note here that $g_i(t_k)$ should always be positive or always negative. With this restriction, the AHWC provide a straightforward representation of the amplitude variation of a particular frequency component of a signal, implying the growth signature is now available as a means of vibration analysis and characterizing system behavior. In order to properly interpret AHWC results, it is preferred to have a constant single frequency, or a simple set of frequencies, per level in the analysis to identify the growth associated with a particular frequency or level. Practically, such amplitude growth of a constant single frequency may sometimes be difficult to achieve as rotordynamic vibration phenomena often involve frequencies that are functions of the rotor speed. Figure 1(*a*) shows the Fourier coefficients for an example signal where there the frequency is linearly increased (at a rate of 2 Hz/s) from a base value (10 Hz) for a time interval of 25 seconds. The frequency content of the resulting signal is relatively broadband. Note that in Figure 1(*a*), the Fourier coefficients above an index value of 2500 are the mirror images of those below 2500. The indices below 2500 are associated with the positive frequency components, while those above 2500 are associated with negative frequency components.

One possible approach to the problem of variable frequency (and resulting broadband representation in the Fourier domain) lies in consideration of the basic form of the signal

$$f(t)=\sum_{i=1}^{M}g_i(t)\cos([\omega_i+\alpha(t)]t+\phi_i) \tag{9}$$

where $\alpha(t)$ is function of time. This relationship can be expressed as

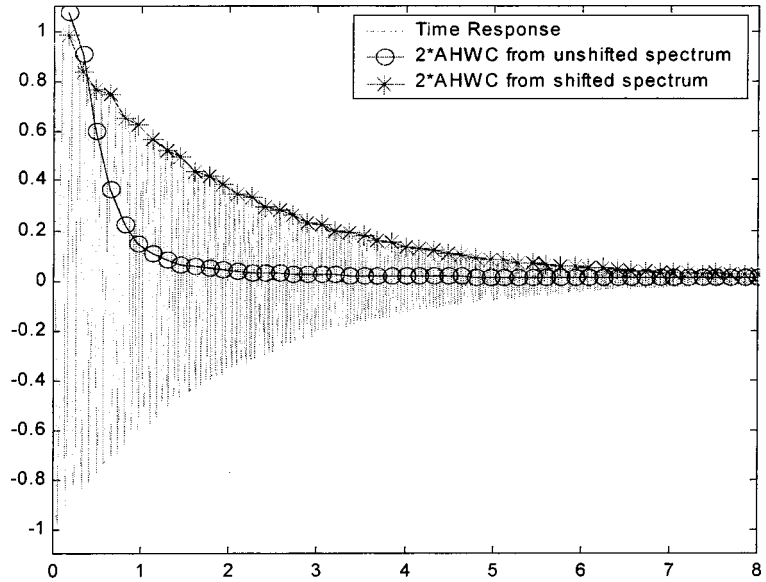

Fig. 2 AHWC for $x(t)=e^{-0.5t}\cos([10+2t]2\pi t)$ calculated as described from the shifted spectrum (Fig. 1(*b*)) compared to AHWX from the unshifted spectrum (Fig. 1(*a*)) for an initial eight-second interval

$$f(t)=\frac{1}{2}\sum_{i=1}^{M} g_i(t)e^{jt\alpha(t)}e^{j(\omega_i t+\phi_i)} + \frac{1}{2}\sum_{i=1}^{M} g_i(t)e^{-jt\alpha(t)}e^{-j(\omega_i t+\phi_i)}. \quad (10)$$

If one premultiplies the signal by $e^{-jt\alpha(t)}$, one obtains

$$f'(t)=e^{-jt\alpha(t)}f(t)=\frac{1}{2}\sum_{i=1}^{M} g_i(t)e^{j(\omega_i t+\phi_i)} + \frac{1}{2}\sum_{i=1}^{M} g_i(t)e^{-j(t[\omega_i+2\alpha(t)]+\phi_i)}. \quad (11)$$

The FFT of the resulting function, $f'(t)$, consists of two nonzero parts. As shown in Fig. 1(*b*), the components above 2500 are no longer a mirror image of those below 2500. The region associated with the positive frequency components (those below 2500) is now centered around an index of 250, which represents a frequency of 10 Hz. The coefficients in this part of the spectrum are indistinguishable from the Fourier coefficients associated with a similar signal with a constant frequency, as shown in Fig. 1(*c*). The other nonzero portion of the spectrum in Fig. 1(*b*), associated with the negative frequency components (those above 2500), is even more broadband than the unshifted signal in Fig. 1(*a*). However, the harmonic wavelet algorithm only uses the positive frequency components, so these broadband components can be ignored.

This proposed shifting procedure works very well when the

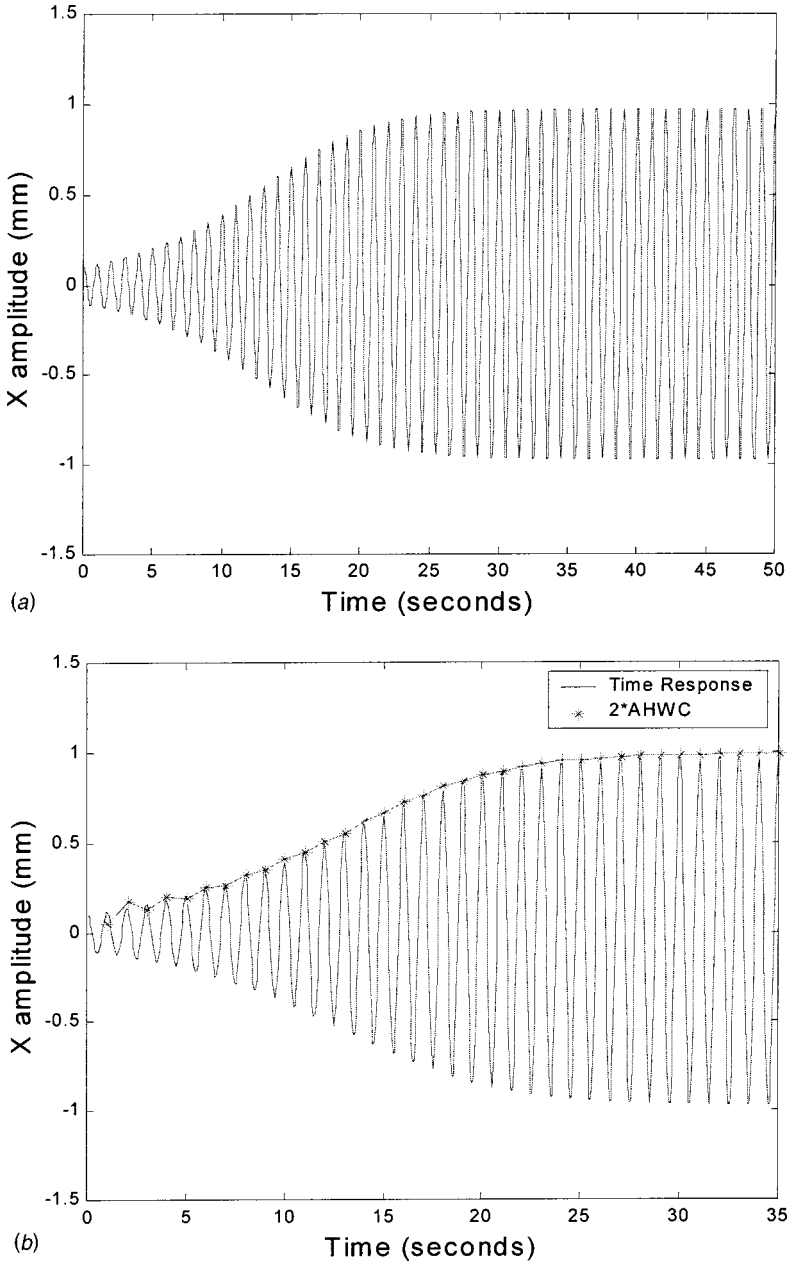

Fig. 3 (*a*) Case 1 time response with $d_1=0.01$, $b_s=1$, $c_{1s}=30$, $m_s=1$, $k_s=4\pi^2$, $c_s=0.01$, $m_s\omega^2 u=0$; (*b*) Case 1 time response superimposed with absolute harmonic wavelet coefficients in the transient response region

frequency variation is identical for all frequencies. It can center the components associated with a single frequency variation function about the base frequencies. This frequency centering allows the AHWC to correctly identify any growth function associated with the frequency variation (Fig. 2). However, for rotor vibrations, sub and superharmonics of the running speed are common, which means that at least some frequencies will have different frequency variation functions. The frequency components associated with variation functions different from the one used in implementing the shifting will also be shifted but will not be centered about a nominal frequency. This may result in increased overlap or broadening of the bandwidths of these components. As a result, this procedure should be used with great care.

Simulation Studies

In order to illustrate some of the basic ideas associated with using the harmonic wavelet for transient vibration analysis, a simple rotor model, consisting of a Jeffcott rotor with imbalance and a general forcing function added to the system, is considered. The governing equations are

$$m_s\ddot{x}+c_s\dot{x}+k_sx=f_x(x,y,t)+m_s\omega^2u\cos(\omega t) \tag{12a}$$

$$m_s\ddot{y}+c_s\dot{y}+k_sy=f_y(x,y,t)+m_s\omega^2u\sin(\omega t) \tag{12b}$$

Let us examine the response characteristics that we might observe for two different forcing functions. First, we will consider the response for forcing functions of the following form, which will be referred to as Case 1.

$$f_x(x,y,t)=-d_1(b_s\dot{x}^2-c_{1s})\dot{x} \tag{13a}$$

$$f_y(x,y,t)=-d_1(b_s\dot{y}^2-c_{1s})\dot{y}. \tag{13b}$$

The system is unstable about the origin, so any perturbation will result in exponentially growing oscillations that will eventu-

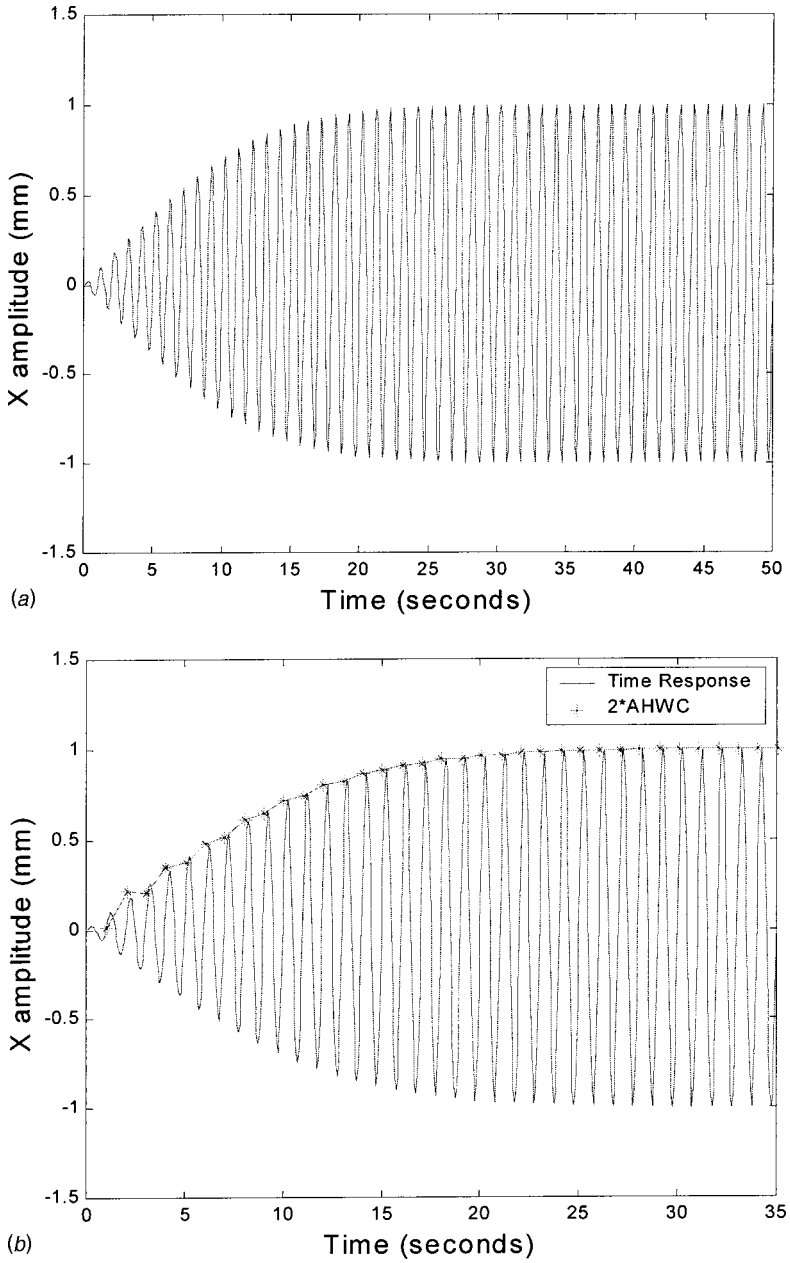

Fig. 4 (*a*) Case 2 time response with $d_2=0.005$, $\omega=2\pi$, $m_s=1$, $k_s=4\pi^2$, $c_s=0.01$, $m_s\omega^2u=1$; (*b*) Case 2 time response superimposed with absolute harmonic wavelet coefficients in the transient response region

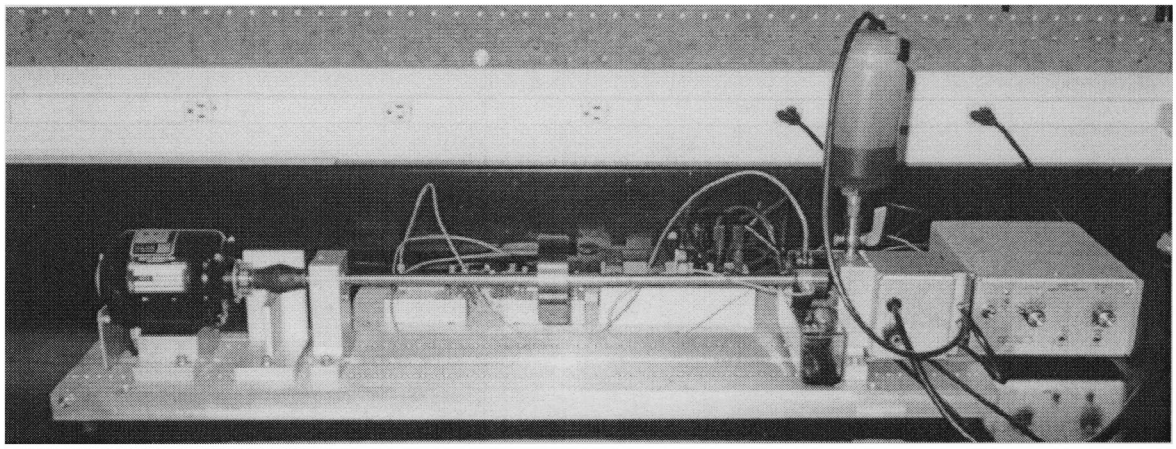

(*a*)

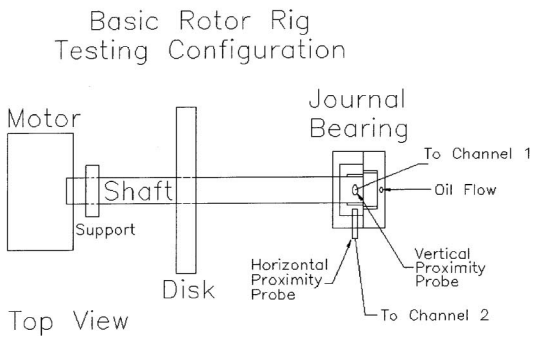

(*b*)

Fig. 5 (*a*) Photograph of experiment test rig; (*b*) experiment setup for oil whirl testing

ally be limited by the nonlinear damping terms. For one set of parameters, the response shown in Fig. 3(*a*) was observed.

Next, let us consider the response for forcing functions of the following form, which will be referred to as Case 2.

$$f_x(x,y,t) = -d_2\dot{x}^3 \tag{14a}$$

$$f_y(x,y,t) = -d_2\dot{y}^3 \tag{14b}$$

This system is driven to high amplitude oscillations through the imbalance resonating with the natural frequency. Again, vibration levels are limited by nonlinear damping.

Comparison of the Fig. 3(*a*) and 4(*a*) shows that the steady-state behaviors of both systems are nearly identical in terms of frequency and amplitude. Fourier analysis of the steady-state signal will provide no information that allows an analyst to distinguish between the two signals. As can be seen in the time responses, the difference between the two signals lies in the growth characteristics of each signal. Analysis of the transient regions using the AHWC is shown in Fig. 3(*b*) for Case 1 and in Fig. 4(*b*) for Case 2. The Case 1 signal grows in an exponential manner consistent with linearly unstable behavior until the growth is limited by the nonlinear effects. Likewise, the Case 2 signal grows in a linear manner consistent with resonance until it, too, is limited by the nonlinear effects.

It is interesting to note that, for the simulation signals shown here, simple inspection of the time traces will allow one to discern the growth patterns without using wavelets. However, in many cases, the change in overall vibration level due to a particular source may be only a relatively small percentage and its effect may be largely lost in any time trace. Using the AWHC, one is able to selectively examine the growth (or decay) pattern associated with a specific frequency band, which gives additional capability to discern between the various possible causes of a vibration problem.

Experimental Study

Experimental data from a bench-top rotor system was collected and analyzed in order to illustrate the absolute harmonic wavelet analysis approach discussed earlier. The test apparatus consisted of a standard Bentley-Nevada rotor test kit equipped with an oil whirl/whip demonstrator. A photograph of the rig is shown in Fig. 5(*a*) and a schematic diagram is shown in Fig. 5(*b*). The rotor shaft is supported at one end by a journal bearing supplied with dyed SAE 5 oil. The oil supply was fed by gravity from a container above the bearing, collected below the bearing, and returned by a siphon pump to the supply reservoir. Two proximity probes, one vertical and one horizontal, were located near the journal to measure the vibration of the shaft/journal associated with the oil whirl phenomenon. The fluid film bearing consisted of a journal inserted into a Pyrex casing with bearing clearance measured to be approximately 0.635 mm (25 mils). The rotor rig shaft assembly included a steel disk placed approximately in the center of the shaft. An electric motor and a support were at the opposite end of the rotor from the journal bearing and probes. Vibration data collected from the probes was collected and stored using a signal analyzer. For each test, the running speed was constant. Typical data results and observations are discussed below from a single test series with a running speed of approximately 1538 RPM (25.625 Hz), unless otherwise noted.

The time response can be viewed in terms of three distinct regions of responses, as shown in Fig. 6(*a*), where vibration data

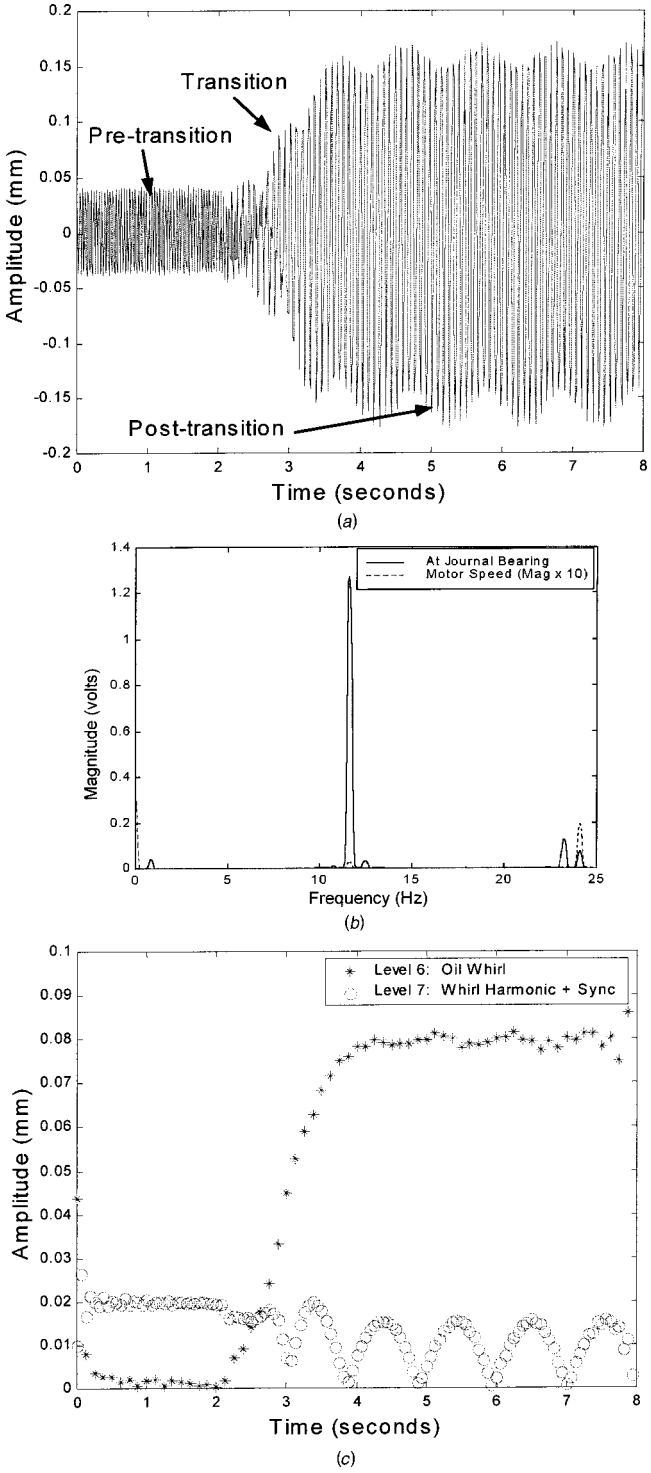

Fig. 6 (*a*) Oil whirl vibration data, (*b*) the frequency spectrum during oil whirl of vibration at the journal bearing end and of the motor speed at 1448 rpm (magnified ×10) allows the correlation of supersynchronous vibrations present during oil whirl; (*c*) overlaid AHWC from levels associated with oil whirl and synchronous when compared to the time response reflect amplitude variation associated with changing conditions of the onset of oil whirl

just prior to and including transition was recorded. The first (pre-transition) is the steady-state response that occurs when the rotor is side-loaded. This is accomplished with a spring loaded (for quick release) slide mechanism that contacts the shaft with a cloth pad. The second response is the transient vibration (referred to as transition) that results when the rotor side-loading is abruptly released. The third region (post-transition) contains the steady-state responses (resulting from oil whirling) that occur after the transient motion has settled out.

Figure 6(*b*) shows the steady-state post-transition frequency distribution for a test series with operating speed at 1448 RPM. The three major peaks in the frequency spectrum for the vibration at the journal bearing end appear at 11.625 Hz, 23.25 Hz (2× oil whirl frequency), and 24.125 Hz. From the spectrum given by the motor/rotor speed, it is determined that the shaft speed (1448 rpm) is associated with the peak at 24.125 Hz, or the second of the two higher frequency peaks appearing in the vibration spectrum. The interaction of the second harmonic of oil whirl (which is slightly less than the rotor speed) and the rotor speed creates the beating effect seen in the post-transition time trace.

Figure 6(*c*) shows the AHWC for the total time interval shown in Fig. 6(*a*). Because the oil whirl frequency is approximately 50% of synchronous as shown Fig. 6(*b*), the contributions from oil whirl and synchronous vibration fall into different levels (level 6 and level 7, respectively). This allows HW analysis using Newland's original algorithm (based on octaves) to be used. The shape of the growth curve associated with oil whirl appears as a relatively nice exponential function, similar to the results from case 1 of the simulation studies. This is in keeping with cross-coupled driven linear instability that is the source of this vibration.

However, the contributions from synchronous whirling and the second harmonic of oil whirl fall in the same level (level 7), producing the bouncing of the AHWC that can be seen in Fig. 6(*c*). In an effort to separate these two frequencies from unrelated vibration sources, nonoctave frequency bandwidths were applied in the harmonic wavelet analysis. (The transition to oil whirl could be clearly seen using the octave bandwidths and was not re-examined using the nonoctave bandwidths. Chancey et al. [6]) In this example case, the two frequencies of interest were a single Hertz apart. The frequency range examined by the algorithm had to be small in order to isolate the components associated with each effect in separate levels. This resulted in the use of an extremely short frequency range: a 1.0 Hz range encompassing the second harmonic of the oil whirl, and another 1.0 Hz range including the effects of synchronous whirling. Valuable information can be gained from these representations. In Fig. 7(*a*), the frequency band was centered about 24.625 Hz, or the second harmonic of oil whirl. As can be seen (ignoring the spurious first data point), the AHWC track zero amplitude until the transition into oil whirl begins at about two seconds. The amplitude slowly increases until it reaches a steady-state value of approximately 0.02 mm. The rotor speed of 25.625 Hz was examined in Fig. 7(*b*). As anticipated, the AHWC track the vibration amplitude due to imbalance in the first part of the signal, again ignoring the false first data point. After a slight decline during transition, the amplitude remains stable, as expected. Part of the unexpected decline can be attributed to an initial overestimation of amplitude in the first part of the signal. The ability to separate close frequencies in real data is a very powerful tool for analysis of vibration signals.

Conclusion

A strategy for assessing transient characteristics in measured vibration data has been presented. The technique uses the filtering and frequency banding capabilities of the harmonic wavelet, with the absolute harmonic wavelet coefficients (AHWC) for each level serving as a measure of the vibration characteristics. The technique was described, including a (limited) method for dealing with signals that have a variable frequency. Results from simulation and experiments for oil whirl are presented to illustrate the method. It was shown that the AHWC can provide valuable insights into the causes of vibration problems and can serve as powerful diagnostic tools.

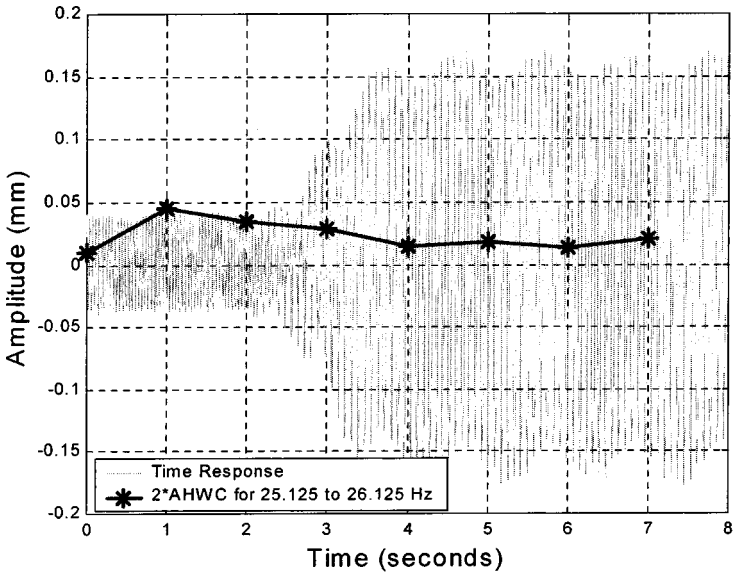

(*a*)

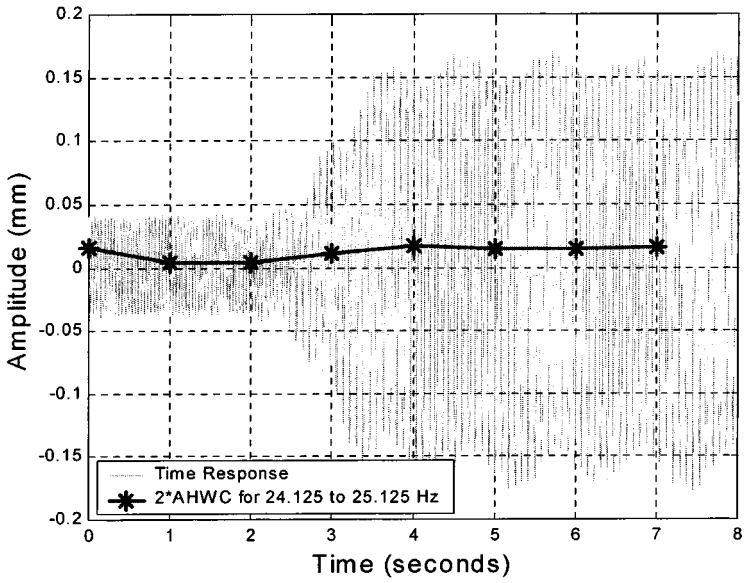

(*b*)

Fig. 7 (*a*) Nonoctave AHWC for the second harmonic of oil whirl; (*b*) nonoctave AHWC for synchronous vibration

Acknowledgments

This work was supported by NASA under Grant No. NGT8-52851. The Government has certain rights in this material. Appreciation is expressed to S. G. Ryan for his advice and assistance in this research effort.

Nomenclature

ω = speed or frequency, rad/s
t = time, s
j = sqrt{(−1)}, unless used as an integer subscript
f_i = discrete values of the input signal
F_i = semi-coefficient output from the FFT
$f(t)$ = function representing data or signal
$g(t)$ = growth function
$w(t)$ = harmonic wavelet functional form
$W(\divideontimes)$ = Fourier transform of the harmonic wavelet
$a_{j,k}$ = wavelet coefficient at level j translated by k, particularly used as a_k for the harmonic wavelet coefficient within a given level
i,j,k = indices for wavelet decomposition
m,n = the combination represents the beginning and end of a particular level in the use of a form of the harmonic wavelet transform, a new level where the original harmonic wavelet family is redefined

References

[1] Wowk, V., 1991, *Machinery Vibration: Measurement and Analysis*, McGraw-Hill, New York.
[2] Vance, J. M., 1988, *Rotordynamics of Turbomachinery*, John Wiley and Sons, New York.
[3] Hubbard, B. B., 1996, *The World According to Wavelets: The Story of a Mathematical Technique in the Making*, A. K. Peters, Wellesley, MA.
[4] Newland, D. E., 1993, "Harmonic Wavelet Analysis," Proc. R. Soc. London, Ser. A, **443**, pp. 203–225.

[5] Newland, D. E., 1993, *An Introduction to Random Vibrations, Spectral & Wavelet Analysis*, Longman, Singapore.
[6] Chancey, V. C., Flowers, G. T., and Howard, C. L., 2000, ''Characterization of Transient Behaviors in Rotordynamic Vibrations From Experimental Data Using Harmonic Wavelets,'' Int. J. Vib. Acoust., **6**(1), pp. 15–22.
[7] Newland, D. E., 1994, ''Harmonic and Musical Wavelets,'' Proc. R. Soc. London, Ser. A, **444**, pp. 605–620.
[8] Newland, D. E., 1997, ''Practical Signal Analysis: Do Wavelets Make Any Difference,?'' 1997 ASME Design Engineering Technical Conferences, Sacramento, CA, 12 pp.
[9] Newland, D. E., 1997, ''Application of Harmonic Wavelets to Time-Frequency Mapping,'' *Fifth International Congress on Sound and Vibration*, University of Adelaide, South Australia, pp. 2043–2053.
[10] Morrison, N., 1994, *Introduction to Fourier Analysis*, John Wiley and Sons, New York, pp. 238–256.

A Multipoint Measurement Technique for the Enhancement of Force Measurement With Active Magnetic Bearings

J. T. Marshall
Pratt & Whitney
East Hartford, CT 06108

M. E. F. Kasarda
Department of Mechanical Engineering,
Virginia Tech,
Blacksburg, VA 24061-0238

J. Imlach
Imlach Consulting Engineering,
Anchorage, AK 99504

Active magnetic bearings (AMBs) have the unique capability to act concurrently as support bearings and load cells for measuring shaft forces. Current state-of-the-art methods for force measurement rely on models with limited accuracy due to effects which are difficult to characterize such as fringing, leakage, and variations in material properties. In addition, these effects may be a function of actual air gaps which are difficult to determine in a dynamic operating environment. This paper discusses a new force measurement methodology that inherently accounts for these types of effects and other system uncertainties by utilizing multiple sets of current pairs in opposing actuators, in conjunction with a calculation algorithm, to accurately determine the force applied by the AMB. This new multipoint methodology allows for the determination of bearing forces from information on basic actuator geometry and control currents only, with no knowledge of actual operating air gaps required. The inherent nature of the methodology accounts for model uncertainties such as fringing, leakage, and other system unknowns. Initial static experimental test results are presented demonstrating 3% error in measuring the nominal determined bearing load, and a variation in calculated forces of less than 5% in most cases (8% in one case) when the location of the rotor within the bearing stator is modified. For the analogous conventional single-point measurements, the results show 15% error and 23% variation. [DOI: 10.1115/1.1519268]

Introduction

The active magnetic bearing (AMB) is a feedback mechanism that supports a load by levitating it in a magnetic field. AMBs can provide unprecedented dynamic control of systems, which can be used to minimize vibration and noise. Magnetic bearings can also be used to eliminate such impediments as mechanical wear and the need for continuous lubrication. Advantages also include considerably higher rotational operating speeds than conventional rolling element bearings. One of the most promising capabilities for many applications is the ability of the AMB to act concurrently as both a support bearing and non-invasive force sensor. The feedback nature of the AMB allows for its use as a load cell to continuously measure forces necessary for levitation based on information about the magnetic flux density in the air gaps. This measurement capability may be exploited for monitoring the health of rotating machinery or to improve the process control of such products as textile fibers and photographic films where changes in shaft loads may indicate changes in product quality, [1]. AMBs are also an enabling technology allowing for the development of highly accurate and flexible thrust measurement systems (TMSs) for rocket and gas turbine performance testing, [2].

In the context of their applications, many researchers have addressed fundamental issues associated with using AMBs as load cells. Limitations stem from deducing magnetic flux information within the bearing gaps from monitored control currents because of hysteresis and saturation effects. Allaire [3] discusses limitations in measuring pump impeller forces due to this problem. Recently Knopf [4] reported a force measurement system utilizing Hall effect devices in each of the gaps of the AMB actuator, which eliminate saturation and hysteresis concerns. While this provided much improved results, the Hall effect sensors are both fragile and difficult to use.

Inaccuracies in force models due to such effects as magnetic fringing and leakage have also been problematic and have warranted the development of elaborate calibration techniques. Fittro et al. [5] detail the calibration of a radial magnetic bearing system by making static force measurements in a laboratory calibration test apparatus outside of the pump where the bearings will be used. Baun et al. (1996) similarly describe the static testing of a thrust bearing in a laboratory set up outside of the actual pump impeller force measurement test rig. Knopf and Nordman [4] discuss two calibration procedures appropriate for field applications. However, the first procedure requires accurate external loading of the test fixture, while the second procedure requires a priori knowledge of bearing forces under certain conditions, limiting their usefulness. Guinzburg and Buse [7,8] discuss the issues surrounding a complicated calibration procedure associated with their test apparatus. Additionally, none of the fringing correction factors used in these procedures takes into account the effect of gap length variations on fringing, which Imlach [2] has shown to have a significant impact on the accuracy of force measurements.

Presented here is a new methodology effectively resulting in a system identification approach for force measurement in the field. The methodology utilizes multiple sets of current pairs in opposing actuators, in conjunction with a calculation algorithm, to accurately determine the force applied by the AMB in the axis of the opposing actuators. The procedure was initially developed for system 1D work to determine operating gap lengths, [9], and is loosely based on well-established rotor balancing techniques using ''influence coefficients'' to determine a benchmark, or calibration, of system conditions. In the AMB scenario, perturbation currents replace ''trial weights'' and information on the state of the system is determined by examining the ''response'' of the system to the perturbation. This new multipoint methodology allows for

Contributed by the International Gas Turbine Institute (IGTI) of THE AMERICAN SOCIETY OF MECHANICAL ENGINEERS for publication in the ASME JOURNAL OF ENGINEERING FOR GAS TURBINES AND POWER. Paper presented at the International Gas Turbine and Aeroengine Congress and Exhibition, New Orleans, LA, June 4–7, 2001; Paper 2001-GT-246. Manuscript received by IGTI, Dec. 2000, final revision, Mar. 2001. Associate Editor: R. Natole.

the determination of bearing forces from information on the actuator geometry and control currents only, with no knowledge of actual operating actuator air gaps required. The inherent nature of the methodology accounts for model uncertainties such as fringing and leakage, and minimum calibration is required.

The multipoint methodology utilizes multiple sets of current pairs to determine the bearing force, as opposed to single-point state-of-the-art measurement techniques. The single-point measurement techniques are usually performed with bearing current information and assumed gaps, or are performed with the use of delicate Hall probes for the direct measurement of magnetic flux density. The ability to accurately account for fringing and leakage effects in either of these single-point methods is problematic, and is usually handled only by the application of a constant derating factor with no additional accounting for changes in gap length. In the multi-point methodology, as a force measurement is determined, an ''effective gap'' is also inherently determined by the procedure which accounts for uncertainties such as fringing and leakage effects.

The viability of the multi-point methodology is demonstrated here through the use of magnetic finite element analysis (MFEA) and actual experimental test data. MFEA data was generated for an E-core actuator and target for application to the rocket TMS scenario, [2]. Experimental testing was performed using a static test setup on a small rotor, and measurements were made with the multipoint method for several different loading conditions and for five different rotor positions (resulting in five different air gap pair lengths) within the bearing stator for each of the load cases. Future work will extend the application of this technique to dynamic measurements.

Approach

The multipoint force measurement technique that has been developed during this project takes advantage of the fact that an AMB feedback system will keep the supported target (shaft) at a predetermined fixed location between two opposing actuators with great accuracy. The multiple points required by the technique are obtained by increasing the current into one side of the double-acting actuator in small increments and recording the currents for both sides of the actuator for each of these increments after initial transients are dissipated and the rotor is re-centered within the actuator. This is simply performed by adding a perturbation current to the control effort already levitating the load as shown in Fig. 1.

In order to maintain the target location once a perturbation current is injected, the new current level in the opposing actuator is determined by the controller in order to balance out the additional electromagnetic force generated by the injected perturbation current. By monitoring the current in both sides of the actuator after a perturbation current is injected, a data point is determined for use in the algorithm. This procedure is repeated several times with different levels of perturbation current injected in order to generate a series of measured ''current pairs'' (or ''multiple points'') which are then utilized to determine the supported load and position of the rotor.

The fundamental force equation for a double-acting magnetic

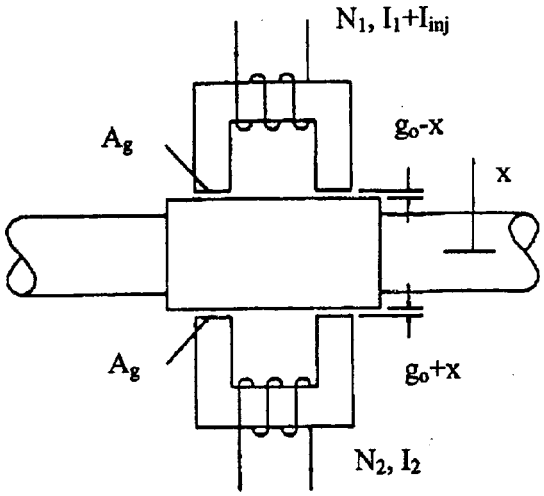

Fig. 1 Double-acting magnetic actuator with injection current

bearing is presented in many locations, including Imlach [2] and Baun et al. [6]. For a double-acting actuator, the net force on the target is given by

$$F_{th}=\varepsilon k_{th}\left(\frac{i_1^2}{(2g_1+b_{th})^2}-\frac{i_2^2}{(2g_2+b_{th})^2}\right) \tag{1}$$

where $k_{th}=\mu_0 A_g N^2$ is a proportionality constant relating force to the coil current and gap width, ε is a derating factor, and $b_{th}=L_i/\mu_r$ is the iron path length converted into an equivalent air gap.

In order to utilize the multipoint algorithm, a common substitution has to be made into the force equation. This substitution treats the gaps g_1 and g_2 as

$$g_1=g_0-x \tag{2}$$

$$g_2=g_0+x \tag{3}$$

resulting in

$$F_{th}=\varepsilon k_{th}\left(\frac{i_1^2}{(2(g_0-x)+b_{th})^2}-\frac{i_2^2}{(2(g_0+x)+b_{th})^2}\right) \tag{4}$$

where g_0 is the radial clearance of the bearing and x is the displacement of the target from the bearing centerline. In this manner, there are only two unknowns that need to be determined for a set of current pairs, which are the force, F, and the displacement, x.

The multipoint computer algorithm basically searches for overlaps among the solution spaces made up of x and F combinations for each of the current pair sets. The algorithm does this by first creating a vector of potential displacements (x) between the physical bounds of $\pm g_0$. The algorithm then generates a matrix of unique force values for each value of x and each of the current pair data sets. Equation (5) demonstrates the basic form of this matrix.

$$F_{x,I1,I2}=\begin{bmatrix} F(-g_0;I_{10},I_{20}) & F(-g_0;I_{11},I_{21}) & \cdots & F(-g_0;I_{1n},I_{2n}) \\ F(-g_0+x;I_{10},I_{20}) & F(-g_0+x;I_{11},I_{21}) & \cdots & F(-g_0+x;I_{1n},I_{2n}) \\ \cdots & \cdots & \cdots & \\ F(-g_0+nx,I_{10},I_{20}) & F(-g_0+nx,I_{11},I_{21}) & \cdots & (-g_0+nx,I_{1n},I_{2n}) \end{bmatrix} \tag{5}$$

Table 1 Comparison of MFEA generated data and algorithm-predicted values

	MFEA Data		Predicted Data		% Error	
Set #	Force (N)	x (mm)	Force (N)	x (mm)	Force	x
1	0	2.00	1.549	1.99	0.031	0.100
2	215	−5.05	215.5	−5.05	0.010	0.000
3	−50	0.05	−53.5	0.0512	0.070	0.012
4	−300	2.08	−301.05	2.084	0.021	0.040

where x is the spatial step size and n is chosen such that $nx = 2g_0$ and $-g_0+nx=+g_0$. By scanning across each row (a distinct spatial location), the forces are compared and when they are approximately equal (within a specified accuracy limit), the ''true'' force and displacement, x, is found. In theory, the F value that overlaps *all* current pairs on a distinct row, coupled with its associated x, represent the only physically realizable state. This approach is based on the idea that the AMB controller will maintain a given target location irrespective of the level of bias current in the actuator. Initial results show that the method works well with only three to five sets of current pairs necessary for accurate results. This procedure was initially verified with numerically generated data utilizing magnetic finite element analysis (MFEA) software. Sets of current pairs were generated by MFEA models for an ''E-core'' planar actuator as presented by Imlach [2]. Using only the current pairs and information on the actuator configuration, the multi-point calibration algorithm was able to predict the bearing forces, as well as the location of the target relative to the actuator (operating gap length) to within a 0.10% error. Table 1 shows the results of several MFEA generated data sets and the associated error of the algorithm predictions (note that the percentage error numbers are based on full-scale actuator force and displacement, 5000 N and 10.0 mm, respectively).

The ability of the algorithm to predict the operating gap and force of the MFEA data within 0.10% error demonstrates the potential of the multipoint approach for obtaining high-accuracy force measurements.

Test Apparatus. After the success of the MFEA study, a static experimental test was developed for additional verification and investigation of the multipoint measurement approach. The static force measurement apparatus used for the testing is shown in Fig. 2. Although there are two AMBs in the setup, only one was used for measuring static forces during these initial tests. The bearing on the right in Fig. 2 was used only as a pivot point and was not activated. By shimming the rotor within the disabled right bearing with a thin ring of material, an approximate pin joint was created. By hanging different masses on the overhung end of the shaft, different bearing loads were created, giving a testing envelope large enough for the study. Since the testing was performed statically, bearing forces, F_{det}, were determined by weighing the masses and using these values in a calculation of the moment balance about the disabled bearing. The worst-case uncertainty of this mechanical measurement is for the heaviest load trial, since it involves four masses and each contains a certain level of uncertainty on its weight and location. This maximum uncertainty is $\pm 4.3\%$. However, for comparison with the AMB measurements, some of the effect of this uncertainty is accounted for, or eliminated, by the constant derating factor, ε, which was determined empirically from initial measured data.

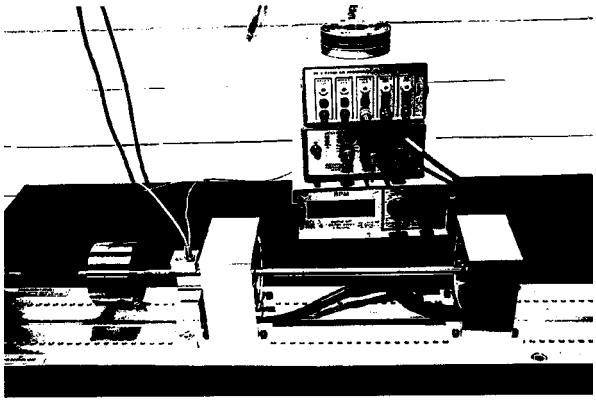

Fig. 2 Experimental setup for force measurement

The AMBs used in the study are an eight-pole, heteropolar design with a digital PID controller manufactured by Revolve Magnetic Bearings, Inc. The bearings have a maximum rated load capacity of 53.4 N, and the saturation current is 3.0 A. The inner diameter of the stator is 35 mm, with a nominal diametric gap of 0.762 mm. External Bently Nevada proximity probes were used in order to obtain direct vertical and horizontal position measurements. These additional position sensors were used only to quantify the displacement of the rotor within the stator for the test cases, and they were not used in the multipoint force predictions.

In order to utilize the multipoint measurement algorithm, several sets of current pairs are required. Because the controller for the bearings used did not allow for the injection of additional current, the necessary current pairs were obtained by modifying the top bias current to achieve the same effect. The controller uses a model of Eq. (4), which uses $(i_{\text{bias}}+i_{\text{pert}})$ instead of i_1. By increasing the bias current in the top half of the actuator, the controller comes to a different, and higher, steady-state overall coil current. In an effort to eliminate inconsistencies due to hysteresis, whose effects are beyond the scope of this paper, all sweeps were conducted from low to high values. Although it was not possible to use the same bias values for the different load cases, the increments were equal for each case.

Experimental Test Results. Once the data was collected, it was processed by the multipoint routine using Eq. (4) and the predicted force and displacement were recorded for each current pair case. For the actuators used in this experiment $k_{th} = 4.313\ \text{N mm}^2/\text{A}^2$, $b_{th}=0.02709$ mm ($\mu_r=3000$ was used as given in the bearing specifications). A constant derating factor, ε, is used as a scale factor for all cases which was determined, based on initial measurements of known loads as compared to mechanically measured loads, to be 0.88. Once determined, it provided accurate results across a large range of loads without modification ($\sim 16-47$ N, where the maximum rated load capacity of the bearing is 53.4 N). Although the constant derating factor of $\varepsilon=0.88$ was determined empirically for these tests, future studies will address the determination of this factor a priori.

For comparison, a state-of-the-art single-point prediction of force using monitored currents was also made. That is, Eq. (4) was used for the single-point method with the same values for all fixed parameters, including the derating factor, as were used in the multipoint method. To calculate the force in this manner for each case, a single current pair was chosen and used along with gaps inferred from the position measured by the proximity probe. The force predictions determined from both approaches for multiple rotor locations are presented in Tables 2–5. Each table represents

Table 2 Data table for case 1 (F_{det}=16.73 N)

Vertical Position (mm)	Multipoint Algorithm Predicted Values X (mm)	F (N)	Single-Point Predictions F (N)
0.127	0.118	16.73	17.57
0.0635	0.075	16.99	16.24
0	0.030	16.95	15.17
−0.0635	−0.015	16.99	14.32
−0.127	−0.060	16.95	13.61
Percent Spread		1.55	23.67
Percent Error		1.15	−8.06

Table 4 Data table for case 3 (F_{det}=37.94 N)

Vertical Position (mm)	Multipoint Algorithm Predicted Values X (mm)	F (N)	Single-Point Predictions F (N)
0.127	0.136	37.63	36.39
0.0635	0.092	38.21	34.30
0	0.045	38.12	32.52
−0.0635	−0.004	37.72	31.05
−0.127	−0.057	37.01	29.85
Percent Spread		3.16	17.24
Percent Error		−0.53	−13.49

a different load case, and the force determined from a moment balance (F_{det}) is given within the title of each table. The first column of each table is the vertical position of the rotor. The controller allows for position offsets from the central location, the centerline of the bearing. The centerline is defined as 0 mm, so that "−0.127" is 0.127 mm below the centerline. The next two columns are the results of the multipoint computer algorithm for displacement and force, respectively. The final column is the single-point force prediction for the different spatial cases. Listed below the double line are the measures of how well each method predicts the force values. The first measure is percent spread, which is defined as

$$\% \text{ Spread} = \left(\frac{\Delta F^{\text{calc}}_{\text{max}-\text{min}}}{F_{\text{det}}} \right) \cdot 100\% \tag{4}$$

where $\Delta F^{\text{calc}}_{\text{max}-\text{min}}$ is the minimum calculated force value subtracted from the maximum calculated value and F_{det} is the assumed true value. This percentage tells how much the calculated force values differ over the range of spatial locations (or how precise the data is). The next measure is percent error. This is simply defined as

$$\% \text{ Error} = \left(\frac{F_{\text{avg}} - F_{\text{det}}}{F_{\text{det}}} \right) \cdot 100\% \tag{5}$$

where F_{avg} is the average value of the predicted force for all positions and F_{det} is again the assumed true value. Equation (5) gives a measure of how closely the measurement methods predict the nominal predetermined force. For both of these percentages, a low value is desired, with 0% being the ideal case.

For each unique loading, the multipoint algorithm was able to calculate the bearing force within ±3% error despite the different rotor locations within the bearing. The analogous single-point values show 8–15% error from the determined bearing loads. When the multipoint method is used, the percentage spread values are well below 5% (with the exception of the last data point for Case 2, causing an 8% spread), while the single-point values exhibit 16–23% of the determined bearing load value in spread.

The multipoint code also gives a prediction for the displacement of the rotor. These values are also shown in Tables 2–5. The relatively large discrepancy between the algorithm and the mechanically measured displacement values may indicate that the algorithm values are reflective of an effective displacement (or effective gap) which accounts for system uncertainties such as fringing and leakage effects. This effective gap that is determined allows for the effective use of Eq. (4) for accurate force determination. It is the speculation of the authors that any uncertainty in geometry, rotor-stator alignment, material properties, or magnetic field effects is being accounted for in this effective displacement determined by the multipoint approach. While tracing the origin of the uncertainty is difficult, the fact that the uncertainties are inherently accounted for in the algorithm makes identifying their origin extraneous in determining an accurate force measurement as is demonstrated by the accuracy of the test results presented in Tables 2–5.

In regards to the determination of an effective gap by the procedure, recall that the theoretical validation tests shown in Table 1 produced exceptional position predictions. When using MFEA, many of the uncertainties of the experimental setup do not exist. The magnetic properties of the actuator and target are known precisely, gaps and flux fields are uniform, and any fringing and leakage follow the theoretical models contained within the MFEA code. When actual hardware is used, each of these quantities becomes a potential source of error for force measurement techniques. These physical uncertainties are inherently addressed in the multipoint measurement technique making this a powerful and robust approach for exploiting the force measurement capabilities of AMBs.

Summary

Active magnetic bearings (AMBs) have the unique capability to act concurrently as support bearings and load cells for measuring shaft forces. This unique capability has been exploited in laboratory environments in the past, but not without difficulty, and the requirement to tightly control experimental conditions. The goal of the work presented here is to establish robust techniques for achieving accurate force measurements with AMBs in harsh field conditions, such as in a rocket thrust measurement system (TMS) or in a factory environment. It has been shown that a new methodology utilizing multiple sets of current pairs in opposing actuators, in conjunction with a calculation algorithm, has been developed which accurately determines the force applied by the AMB in the axis of the opposing actuators. *This new multipoint meth-*

Table 3 Data table for case 2 (F_{det}=26.82 N)

Vertical Position (mm)	Multipoint Algorithm Predicted Values X (mm)	F (N)	Single-Point Predictions F (N)
0.127	0.135	28.20	27.05
0.0635	0.086	27.53	25.22
0	0.039	27.31	23.84
−0.0635	−0.038	27.40	22.51
−0.127	−0.063	26.02	21.35
Percent Spread		8.13	21.25
Percent Error		1.76	−10.54

Table 5 Data table for Case 4 (F_{det}=48.49 N)

Vertical Position (mm)	Algorithm Predicted Values X (mm)	F (N)	Single-Point Predictions F (N)
0.127	0.132	46.71	45.77
0.0635	0.088	47.28	42.97
0	0.044	48.04	40.92
−0.0635	−0.006	47.55	39.01
−0.127	−0.053	47.42	37.68
Percent Spread		2.74	16.68
Percent Error		−2.25	−14.89

odology allows for the determination of bearing forces from information on basic actuator geometry and control currents only, with no knowledge of actual operating air gaps required. The inherent nature of the methodology accounts for model uncertainties such as fringing, leakage, and other system unknowns.

The methodology utilizes multiple sets of current pairs to determine the bearing force, as opposed to single-point state-of-the-art measurement techniques. The single-point measurement techniques are usually performed with bearing current information and assumed gaps, or are performed with the use of delicate Hall probes for the direct measurement of magnetic flux density. Accurately accounting for fringing and leakage effects in either of these single-point approaches is problematic, and no universally accepted method for this exists. In the multipoint methodology presented here, an effective gap is inherently determined which appears to account for uncertainties in geometry, rotor-stator alignment, material properties, and/or magnetic field effects such as fringing and leakage.

The viability of the multi-point methodology has been demonstrated through the use of magnetic finite element analysis (MFEA) and actual experimental test data. The MFEA validation was conducted in order to prove the merit of the fundamental idea that multiple current pairs could be used in order to provide accurate position and force information for a magnetic bearing. A MFEA model using an ''E-core'' actuator was created and several current pairs were generated for different force and displacement conditions. Using only the current pairs and bearing geometry, the calibration code was able to provide predictions of force and displacement within 0.10% error of the MFEA-generated data.

A test rig for the experimental verification of the multipoint force measurement methodology was constructed in order to experimentally validate this approach. Experimental testing was performed using a static test setup on a small test rotor, and measurements were made with the multipoint method for several different loading conditions and for five different rotor positions (resulting in five different air gap pair lengths) within the bearing for each load case. The multipoint method provided accurate, precise predictions of force with little dependence on rotor position within the bearing stators. The error of the multipoint force measurement technique for all load and rotor positions was within 3% relative to the nominal determined bearing load, as compared to an error of 15% for the analogous single-point force measurement method. The percent spread on the multipoint measured load for all rotor positions was within 5% for three of the four cases and within 8% for the fourth. Single-point force calculations were also performed which varied as much as 23% for different rotor positions for a given load.

Future tests of this multipoint force measurement technique are planned in order to improve the procedure and to better characterize the full benefits of this methodology. Additional tests will include evaluations of the methodology in a rotating shaft scenario to test the dynamic measurement capabilities of the approach, an investigation into hysteretic and eddy current effects on the procedure, the a priori identification of the constant derating factor, and efforts to improve the overall accuracy of the technique. The initial test results presented here demonstrate the potential of the multipoint approach for obtaining high accuracy force measurements in the presence of system uncertainties in both laboratory and field applications of active magnetic bearings.

Acknowledgments

The authors would like to acknowledge the National Science Foundation (NSF) for supporting the work presented in this paper under Grant No. DMI-9733124. The authors would also like to acknowledge NASA Stennis Space Center and Revolve Magnetic Bearings for their support on this project.

Nomenclature

A_g = pole face area
b_{th} = equivalent iron length
F_{det} = determined bearing load
F_{th} = theoretical force prediction
g_0 = nominal radial air gap
g_1 = top air gap
g_2 = bottom air gap
I_1 = top current
I_2 = bottom current
I_{inj} = injected current
I_{bias} = bias current
I_{t1} = top current, Trial 1
I_{b1} = bottom current, Trial 1
I_{b2} = bottom current, Trial 2
k_{th} = proportionality constant
L_i = iron path length
N = number of coils
x = rotor position
ε = constant derating factor
μ_0 = magnetic permeability of air
μ_r = relative magnetic permeability

References

[1] Kasarda, M. E., 1999, ''Magnetic Bearings for Improved Process Control,'' 1999 NSF Grantees Conference Proceedings, Long Beach, CA, Jan.

[2] Imlach, J., Kasarda, M. E. F., and Balaji, P. A., 2000, ''Enhancements to AMB Force Measurement Procedures for Application to a Rocket Thrust Measurement System,'' ASME Paper No. 2000-GT-414.

[3] Allaire, P. E., Fittro, R. L., Maslen, E. H., and Wakefield, W. C., 1995, ''Measured Force/Current Relations in Solid Magnetic Thrust Bearings,'' ASME Paper No. 95-GT-400.

[4] Knopf, E., and Nordmann, R., 1998, ''Active Magnetic Bearing for the Identification of Dynamic Characteristics of Fluid Bearings—Calibration Results,'' *Proceedings of the Sixth International Symposium on Magnetic Bearings*, Cambridge, MA, Aug., Technomic, Lancaster, PA, pp. 52–61.

[5] Fittro, R. L., Baun, D. O., Maslen, E. H., and Allaire, P. E., 1997, ''Calibration of an 8-Pole Planar Radial Magnetic Actuator,'' ASME Paper No. 97-GT-018.

[6] Baun, D. O., Fittro, R. L., and Maslen, E. H., 1996, ''Force Versus Current and Air Gap Calibration of a Double Acting Magnetic Thrust Bearing,'' ASME Paper No. 96-GT-121.

[7] Guinzburg, A., and Buse, F. W., 1994, ''Axial and Radial Forces on a Pump Impeller Obtained With a Magnetic-Bearing Force Measurement Rig,'' *Proceedings, Fourth International Symposium on Magnetic Bearings*, Aug. ETH, Zurich, pp. 537–545.

[8] Guinzburg, A., and Buse, F. W., ''Magnetic Bearings as an Impeller Force Measurement Technique,'' *Proceedings of the Twelfth International Pump Users Symposium*, Mar., pp. 69–76.

[9] Kasarda, M. E., Imlach, J., Balaji, P. A., and Marshall, J. T., 2000, ''The Concurrent Use of Magnetic Bearins for Rotor Support and Force Sensing for the Nondestructive Evaluation of Manufacturing Processes,'' *Smart Structures and Materials 2000: Smart Structures and Integrated Systems*, Norman M. Wereley, ed., Proc. SPIE, SPIE, Bellingham, WA, **3985**, pp. 352–363.

Rotordynamic and Bearing Upgrade of a High-Speed Turbocharger

B. C. Pettinato
e-mail: bpettina@Elliott-turbo.com

P. DeChoudhury

Elliott Company,
901 North Fourth Street,
Jeannette, PA 15644-1473

The paper discusses the redesign of a high-speed turbocharger for improved bearing life and mechanical operation. The bearings were changed from a pair of combination journal/thrust bearings to a pair of redesigned journal bearings with double acting thrust bearing at the center of the unit. Internal oil passages, drain cavities, and seals were also revised. These modifications resulted in reduced oil leakage across end seals, reduced coke buildup at the turbine, increased thrust load capacity, and improved rotordynamics. Both the analytical and experimental results, which consisted of bearing performance and vibration data of original and modified systems are presented. [DOI: 10.1115/1.1519273]

Introduction

Turbochargers are a special class of turbomachinery used to increase engine power by providing compressed air for combustion. They can typically be found on diesel engines, which are used as prime movers in land and marine applications. Bearing and rotordynamic challenges for these units are complicated by a lack of industrial standards to guide design practices as related to the dynamics of turbochargers, and also by a lack of condition monitoring to provide information on the vibration and thermal state of the turbocharger. Failures, when they occur, are without warning and difficult to diagnose. Consequently, turbocharger reliability is often handled through scheduled maintenance.

The turbocharger discussed herein was used on a series of diesel locomotives operated by a major world railway. The units were overhauled on a six-month cycle to prevent failures, thereby leading to high maintenance costs. The end user attempted to increase the turbocharger bearing life by enlarging the active thrust bearing. While an improvement, the modification was insufficient to increase scheduled maintenance from a six-month cycle to an 18-month cycle, which was the overall objective. A more extensive redesign was required.

The redesign and analysis of the turbocharger are presented in detail. The existing turbocharger was modified to provide improved mechanical performance of the thrust bearing with extended life expectancy, and improved rotordynamic characteristics. The modified turbocharger kept the same footprint, and used most existing parts. In addition to providing extended life expectancy, it was expected that the modifications would accommodate any possible future aerodynamic upgrades. Both the original and the modified designs were tested on a dedicated test stand.

Original Turbocharger

A cross-sectional schematic of the original turbocharger center housing and rotating assembly is shown in Fig. 1. This assembly defines the rotor-bearing system and consists of the bearings, seals and turbocharger rotor.

The rotor was supported by bearings in both the radial and axial directions. The active thrust collar was located at the turbine end of the machine integral to the shaft, while the inactive thrust collar was located at the compressor end. As shown in Fig. 1, the active thrust collar and bearing were in close proximity to the hot turbine end. Since the active thrust bearings had a history of failing by wiping, it was suspected that there was insufficient oil film thickness, which could be caused, in part, by the elevated temperatures at the turbine end. Hot temperatures, at the turbine end of the shaft, could have further aggravated problems by causing thermal deformation at the thrust collar, journal, and bearing surfaces. Hot temperatures would also contribute to oil coking on the bearings.

The bearings were combination journal/thrust bearings. The journal bearings were three-axial-groove style. The thrust bearings were fixed geometry, with a compound tapered-land bearing on the active turbine end, and a flat-plate bearing on the inactive impeller end.

The flow throughout the turbocharger can be identified in Fig. 1. Oil entered the turbocharger through an orifice inlet, and was split at a tee, directed to both the turbine and compressor end bearings. The oil lubricated the journal bearing first, and then was forced toward the thrust bearing sequentially, which resulted in sequential heating of the oil and hotter temperatures. The close proximity of the thrust bearings to the end seals exposed the seals to significant quantities of oil, thereby increasing leakage into the turbine and compressor sections. The remaining oil exited through the drain cavity.

Observations. Diagnosis of the failure mechanism relied primarily on inspection during turbocharger overhauls, and after bearing failures. The bearings appeared to fail gradually by wiping. Successive inspections of numerous turbochargers revealed bearings in various stages of wear, with the land portions increasing, and the tapers decreasing in arc length as shown in Fig. 2. As wear propagated, the tapers would become less capable of supporting load, and the bearings would fail completely, damaging the thrust collar in the process. The gradual nature of the failures suggested that the bearings were often in boundary lubrication and that the film thickness was insufficient.

In addition to wiping of the active thrust face, the failures were accompanied by significant coke buildup on the turbine disk. It was further noted that there was coke buildup on the turbine end bearing as well. The source of the coke buildup originated primarily from oil leakage across the turbocharger end seals in combination with the hot diesel exhaust gas.

A buffer gas system using the impeller discharge air was used to balance part of the thrust load, and also to prevent oil leakage into the turbine section, and exhaust gas leakage into the bearing cavity, [1]. However, frequent operation at idle speed reduced the buffer supply pressure and the effectiveness of the system. Furthermore, the buffer system was susceptible to fouling, and sometimes did not work at all.

The operating environment was also very demanding on the

Contributed by the International Gas Turbine Institute (IGTI) of THE AMERICAN SOCIETY OF MECHANICAL ENGINEERS for publication in the ASME JOURNAL OF ENGINEERING FOR GAS TURBINES AND POWER. Paper presented at the International Gas Turbine and Aeroengine Congress and Exhibition, New Orleans, LA, June 4–7, 2001; Paper 2001-GT-249. Manuscript received by IGTI, Dec. 2000, final revision, Mar. 2001. Associate Editor: R. Natole.

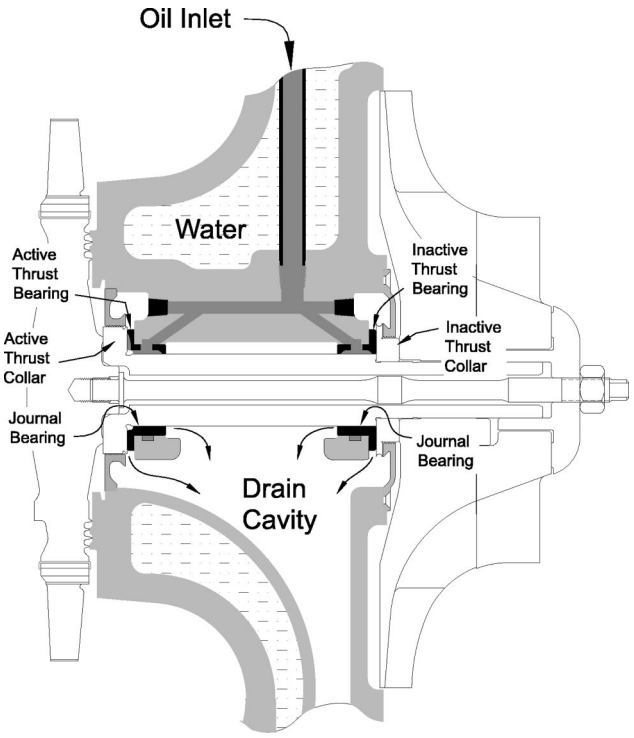

Fig. 1 Cross-sectional layout of the original turbocharger

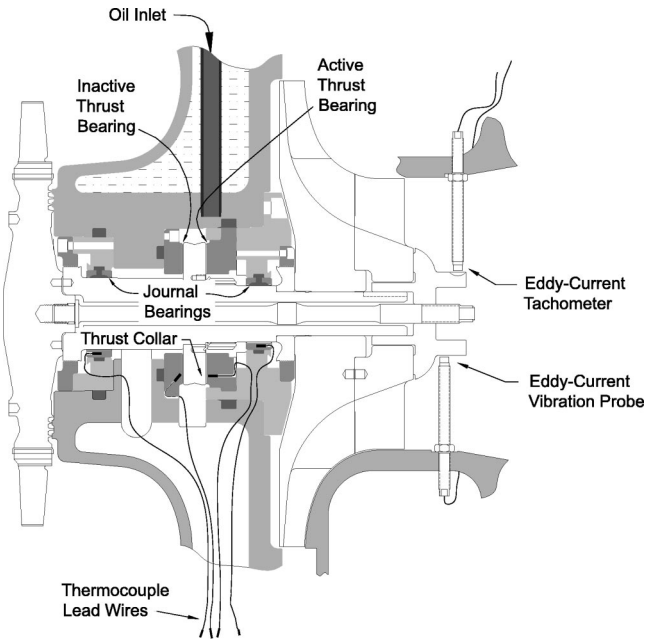

Fig. 3 Cross-sectional layout of the modified turbocharger with instrumentation

lubricant. Both the diesel engine and the turbocharger were connected to a common oil supply. Oil contamination and degradation are considered typical consequences of lubricating a diesel locomotive engine. Lubricant oxidation caused by high temperature; and contamination, from fuel oil, soot, and water, can significantly modify lubricant properties. Lubricant viscosity can vary, by as much as a full grade due to degradation over the operating life of the lubricant, [2,3].

Turbocharger Redesign

A major upgrade was required to improve the mechanical life of the turbocharger. The upgrade presented several challenges. The redesign would need to provide satisfactory operation over a wide speed range and be insensitive to variations in oil properties. In addition to improving unit reliability, the redesign also needed to handle both the existing loads and potentially higher loads from future aerodynamic upgrades.

The Modified Turbocharger. The modified turbocharger is shown in Fig. 3. Load capacity, rotordynamics, flow rate, and balance of flow, as well as oil coking and leakage problems were addressed. The combination journal/thrust bearings, used on the original design, were changed to a pair of journal bearings and a double acting thrust bearing. Here, the active thrust bearing has been moved to the center of the unit, away from the hot turbine end. While minimal modification to the existing unit was desirable to keep costs low, it was determined that a new intermediate casing was required to fit the larger thrust bearings, and to increase the oil inlet and drainage capacity.

The oil inlet area to the turbocharger was increased 180%. Internal oil passages were also increased, thus reducing pressure drops within the unit and allowing for increased flow. Instead of metering the oil supply at the case inlet, the supply oil was orifice metered at each bearing, which improved flow distribution. Since the journal bearings no longer supplied oil to the thrust bearings, the journal bearings could be designed to force oil to the center of the unit away from the end seals. The end seals were changed to a windback design to keep oil from migrating down the shaft. These modifications resulted in reduced leakage across the end seals; and would decrease coking at the turbine disk and bearings. The oil drain area was increased by 54%, reducing the chance of foaming and heat buildup.

The changes required to implement the redesign were minimal. The modified unit kept the same footprint. Most existing parts were reusable. Some external piping changes, however, were required.

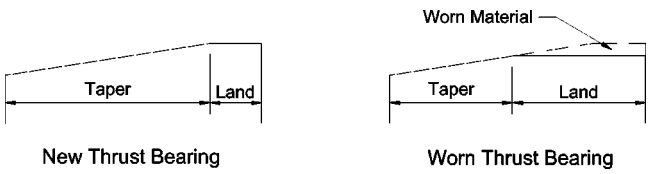

Fig. 2 Reduction of thrust bearing tapers due to wearing of the lands

Analysis

The theoretical analysis of the original and modified units is presented. The study consisted of aerodynamic modeling to determine the thrust load at nominal and worst case conditions, as well as bearing and rotordynamic modeling of original and modified units. Flow calculations were performed to ensure proper oil supply at the bearings. The analyses were instrumental in defining the scope of the problems and the extent of the required modifications.

Thrust Loading. The thrust load was determined using worst-case assumptions at the compressor nominal operating speed of 17,085 rpm, and at the maximum permissible speed of the aluminum impeller, 20,799 rpm, which was beyond the anticipated maximum speed of 20,000 rpm. Results are summarized in Table 1. As shown, the original thrust bearing was severely undersized.

The thrust bearing was enlarged on the outer diameter; resulting in a 131% increase in bearing area (Fig. 4). The bearing geometry was improved, by changing from eight rectangular shaped sectors

Table 1 Analytical evaluation of active thrust bearings

	Analytical Results				Extrapolated From Measurement	
	Nominal Speed (17,085 RPM)		Maximum Speed (20,799 RPM)		(20,000 RPM)	
	Original Bearing	Modified Bearing	Original Bearing	Modified Bearing	Original Bearing	Modified Bearing
Thrust Load	6770 N	6770 N	12184 N	12184 N		
Unit Load	2682 kPa	1165 kPa	4833 kPa	2096 kPa		
Min.Film Thickness	15 μm	43 μm	10 μm	33 μm		
Max. Metal Temp.	112°C	96°C	131°C	103°C	118°C	91°C
Max. Oil Film Temp.	124°C	103°C	144°C	111°C		
Flow Rate	9.5 lpm	18.5 lpm	19.3 lpm	31.0 lpm	7.6 lpm	11.0 lpm

to ten square shaped sectors. Oil distribution was also improved, by feeding fresh oil from the common supply between each pad, instead of receiving throw-off oil from the journal bearing.

Thrust bearing designs were analyzed using CFD analysis as developed by Brockett et al. [4]. The method consisted of solving the generalized Reynold's and three-dimensional energy equations as formulated from the boundary conditions. These boundary conditions consisted of zero oil pressure at the periphery of each pad and constant sump temperature at each pad inlet. The analysis considered mechanical deformation of both the bearing and thrust collar, and also the centrifugal inertia of the fluid, as well as thermal conductivity from the oil film into the thrust bearing. Results of the analysis are shown in Table 1. The modified bearing was predicted to have roughly three times the film thickness of the original design. Since the original design had a film thickness less than the tolerance on flatness and parallelism, rubs were likely to occur. In addition, the high theoretical film temperatures, for the original bearings, could contribute to oil coking problems, as had been observed in the field, and thermal distortion of the bearing surface. In contrast, the lower film and metal temperatures along with the increased film thickness of the modified design would result in improved bearing performance. The high theoretical flow rate required of the new thrust bearing was a major concern. Testing, however, showed that the active thrust bearing required only 11.0 lpm to achieve acceptable performance.

The larger thrust bearing required an increased thrust collar diameter. The thrust collar slid over the shaft and butted against a shoulder at the shaft center. The collar thickness was sized at 19 mm thereby limiting axial mechanical deformation to less than 9 μm at the 12,184 N loading. The added thickness also provided a larger heat sink to reduce thermal deformation.

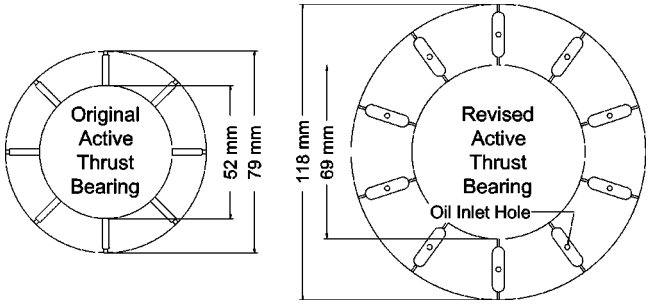

Fig. 4 Thrust bearing redesign and comparison

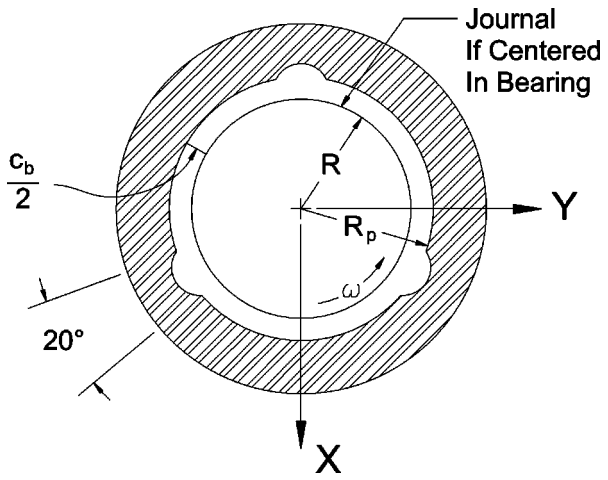

Fig. 5 Three-axial-groove journal bearing

Schematics of the three-axial-groove journal bearing (Fig. 5) and three-lobe journal bearing (Fig. 6) are shown. The three-axial-groove journal bearing was a circular geometry with three oil inlet grooves located 120 deg apart. The three-lobe journal bearing was similar in design. The lobes, however, were preloaded thereby forming a converging-diverging wedge. The additional clearance at leading and trailing edges of each lobe reduced shear forces in the oil, thereby reducing the bearing power loss and metal temperature.

The theoretical worst-case bearing metal temperatures were analyzed. Results are presented in Tables 1 and 2. As shown in the tables, the modified turbocharger, with enlarged active thrust bearing and three-lobe journal bearings had theoretically superior thermal characteristics as compared to the original turbocharger with three-axial-groove journal bearings. Active thrust bearing metal temperatures were reduced from a theoretical maximum of 131°C to 103°C. Journal bearing metal temperatures were reduced from a theoretical maximum of 127°C to 105°C.

Vibration And Rotordynamics. A rotordynamic evaluation consisting of critical speed, unbalance response, [5–7], and stability analyses, [8], was conducted to examine the existing unit, and to determine the effect of the modifications. A summary of the analyses of both units is provided.

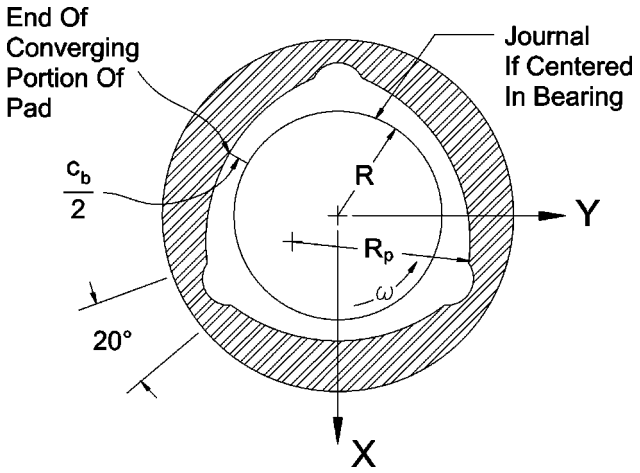

Fig. 6 Three-lobe journal bearing

Table 2 Predicted maximum journal bearing metal temperatures with 82°C inlet oil

	Analytical Results	Extrapolated from Measurement
Original Turbocharger T.E. Three-Ax-Grv Brg	127°C	109°C
Original Turbocharger C.E. Three-Ax-Grv Brg	127°C	108°C
Modified Turbocharger T.E. Three-Lobe Brg	104°C	91°C
Modified Turbocharger C.E. Three-Lobe Brg	105°C	93°C

T.E. = Turbine End C.E. = Compressor End

As shown in Table 3, the original unit operated well below the first rigid support critical speed. The modified unit was designed with similar shaft properties, thus keeping the flexible critical speeds well removed from the operating speed range. The overall length of the rotor was kept the same, but with a slight reduction in bearing span. The total weight of the modified turbocharger rotor increased slightly. Examination of Table 3 shows that the rigid support critical speeds of the two units were nearly identical.

Unbalance peak responses were predicted for both the original and modified turbochargers. As shown in Table 3, the low speed peak response, of the original turbocharger, had considerably higher amplification factor than the modified turbocharger. The low speed peak responses of both the original and modified turbochargers were, however, well below the minimum continuous speed of 5000 rpm. Peak responses, in the operating speed range of 5000 to 20,000 rpm, were essentially well damped.

The accuracy of the shaft model was checked by modal analysis. The first free-free bending mode was found to be highly sensitive to thru-bolt tension. However, at 136 N-m bolt torque, the rotor behaved similar to the rotordynamic model. The predicted free-free bending mode was located at 433 Hz while the bending mode from modal analysis was determined to be 449 Hz. The measured mode shapes were similar. The rotordynamic characteristics of the modified rotor can be seen in more detail in the critical speed map, Fig. 7, with the three-lobe bearing principal stiffness values superposed.

Table 3 Comparison of rotordynamic analysis results: original versus modified turbocharger

Item	Original Turbocharger On Three-Axial-Groove Bearings		Modified Turbocharger On Three-Lobe Bearings	
Rigid Support Critical Speeds:				
1st	45,021 CPM		44,665 CPM	
2nd	129,662 CPM		139,361 CPM	
Bearing Span	136 mm		134 mm	
Overall Length	396 mm		396 mm	
Total Rotor Weight	30.6 kg		33.0 kg	
Unbalance Response				
	Peak Response (AF)*		Peak Response (AF)	
	Turbine End Bearing	Compressor End Bearing	Turbine End Bearing	Compressor End Bearing
Out-Of-Phase Unbalances At Ends	2350 rpm (16.7)	2350 rpm (16.9)	1200 rpm (2.35)	1400 rpm (5.24)
In-Phase Unbalances At Ends	8800 rpm (<1.0)	-	-	7800 rpm (<1.0)
	-	-	19200 rpm (1.20)	19000 rpm (<1.0)
Stability Log Dec At 20,799 rpm	−1.946		0.394	
Whirl Frequency	5833 cpm		4364 cpm	

* Peak response in rpm, amplification factor (AF) in parenthesis

The flexible rotor stability of the two units is presented in Fig. 8. As shown, the original design had negative logarithmic decrement when using the zero preload three-axial-groove journal bearings. Use of the three-axial-groove design on the modified unit also resulted in negative logarithmic decrement. The improved stability characteristics of the three-lobe bearings were obtained through bearing preload, as compared to the zero preload three-axial-groove design, [9,10]. The cross-coupled stiffness coefficients for three-lobe bearings were considerably less than the three-axial-groove bearings contributing to improved stability. Thus, the three-lobe journal bearings provided a stable design with positive logarithmic decrement.

Turbocharger Testing

The turbochargers were tested on a dedicated test stand. Exhaust from a 1050 kW gas turbine was used to power the turbocharger while the impeller end was operated under varying load conditions. The test stand is described in further detail by Schwartz et al. [11].

The turbochargers were instrumented (Fig. 2), such that shaft vibration, casing vibration, and bearing metal temperatures could be monitored. A modified nosepiece was used to provide a sensing surface for the eddy-current probes. The bearings were instrumented with thermocouples, in accordance with API standards, [12]. Monitoring of oil flow rate, inlet, and drain temperatures was provided by the test facility.

Test Procedure. A series of tests was conducted to ensure unit reliability, quantify the improvements of the redesign, and determine any required changes prior to production. The planned test procedure consisted of operating both the original and modified turbochargers at all field conditions. The turbochargers were run from 5000 rpm idle speed up to 20,000 rpm. While the oil used in the field was SAE 40 grade, the oil used at the test facility was SAE 30 grade. The SAE 30 oil was delivered at temperatures ranging from 54.4 to 79.4°C to simulate the inlet viscosity range of the SAE 40 oil.

The oil inlet flow of the original turbocharger was limited to 17 lpm due to a high pressure-drop, 393 kPa, at the pipe inlet. Attempts to increase the flow rate to 23 lpm were not possible because of this high pressure loss. The original unit was run and held at a series of speeds ranging from 5000 rpm to 15,000 rpm. When the original turbocharger reached a speed of 19,500 rpm, a thrust collar to thrust bearing rub occurred. Due to the rub, no additional tests, at different inlet temperatures, were conducted for the original design.

The modified turbocharger was tested over a full range of operating conditions at 30 lpm oil inlet flow. Inlet oil viscosity was varied over a wide range by changing inlet oil temperature. Speeds were varied from below idle speed to 20,000 rpm without any problems.

Thermal Results. Bearing metal temperatures were measured for each bearing, as tested. The hottest bearings were the turbine end journal bearing and active thrust bearing. These bearing temperatures are presented in Figs. 9 and 10 for the nominal inlet viscosity as a function of speed. The flow rate, as shown in the legend, represents the total flow to the turbocharger. The left vertical axis represents metal temperature as recorded during the test, using SAE 30 oil, at 66.7°C oil inlet temperature, which would provide the nominal inlet viscosity. The right vertical axis represents the expected metal temperature; using SAE 40 oil at the nominal inlet temperature of 73.9°C. Results for the original and modified designs are presented. The temperatures for the original design were extrapolated beyond the shutdown speed of 19,500

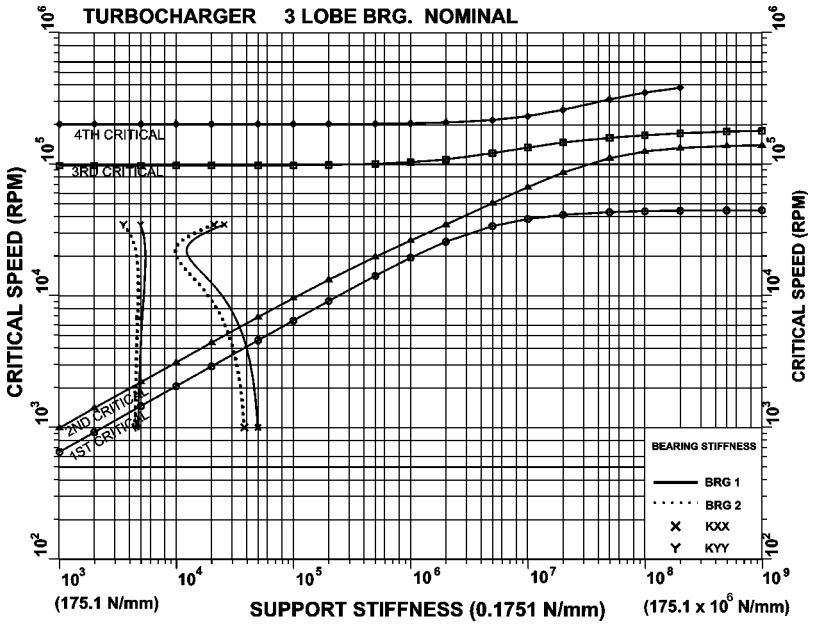

Fig. 7 Critical speed map, modified turbocharger

rpm to 20,000 rpm as shown by the open circle. Some uncertainty was present in the 19,500 rpm temperature data due to the emergency shutdown.

Examining data for the original unit, in Figs. 8 and 9 shows that the bearing metal temperatures increased rapidly with speed. Based on these results bearing metal temperatures would have reached approximately 95.6°C for the turbine end journal bearing, 93.9°C for the compressor end journal bearing, 103.9°C for the active thrust bearing, and 88.3°C for the inactive thrust bearing when using SAE 30 oil. The results using SAE 40 oil, at the nominal inlet temperature, would be roughly 7.2 to 8.3°C higher. The active thrust bearing is estimated to have a maximum temperature of 111.1°C when using SAE 40 oil at the nominal inlet temperature of 73.9°C.

Examining data for the modified unit in Figs. 9 and 10 shows that bearing metal temperatures increased slowly with speed. Bearing metal temperatures, for the modified turbocharger, were cooler than expected. Examining the results with SAE 30 oil at 66 to 68°C inlet temperature, the turbine end journal bearing metal temperature reached 78.3°C. Compressor end journal bearing temperatures were similar, reaching 79.4°C. The active thrust bearing metal temperature shown in Fig. 9 reached 77.8°C. The inactive thrust bearing metal temperature reached 63.3°C. Results using SAE 40 oil at 73.9°C inlet temperature would be roughly 7.2 to 8.3°C higher. Overall, the temperatures of the four modified bearings are estimated to be below 87.8°C, when using SAE 40 oil, at the nominal 73.9°C inlet temperature.

Expected bearing metal temperatures, at the maximum recommended 82°C inlet temperature, using SAE 40 oil, are summarized in Tables 1 and 2 for both sets of bearings. Under these conditions, bearing metal temperatures for the modified design are roughly 28°C cooler than the original design. The improvement of bearing thermal characteristics is proven for the modified design.

Vibration Results. Vibration data is presented for each unit, as tested, under varying conditions. The data are presented in the form of cascade plots. The horizontal axis shows the vibration frequency while the vertical axis is used to indicate speed and amplitude.

The cascade diagram, of the original turbocharger, is presented

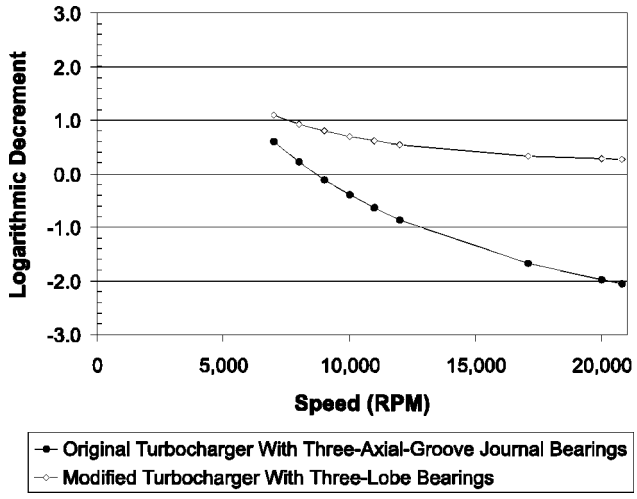

Fig. 8 Stability comparisons

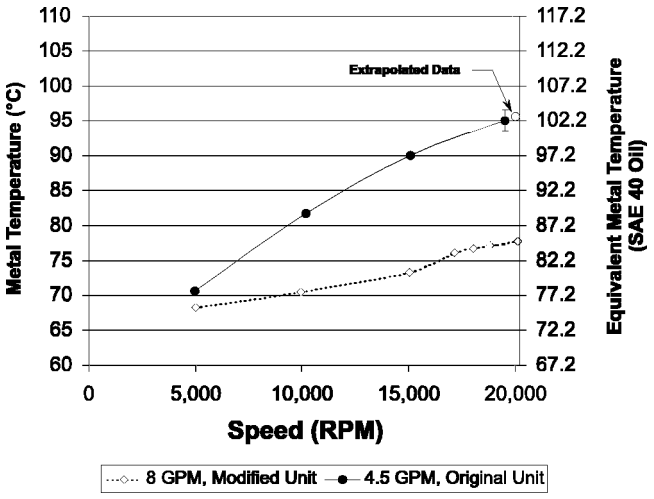

Fig. 9 Turbine end journal bearing metal temperatures

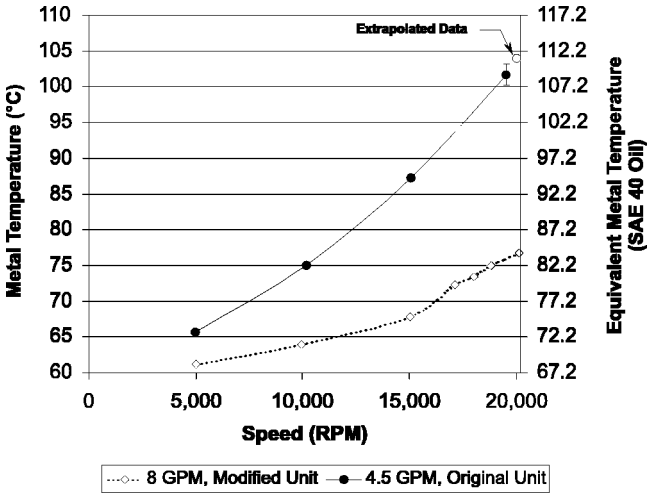

Fig. 10 Active thrust bearing metal temperatures

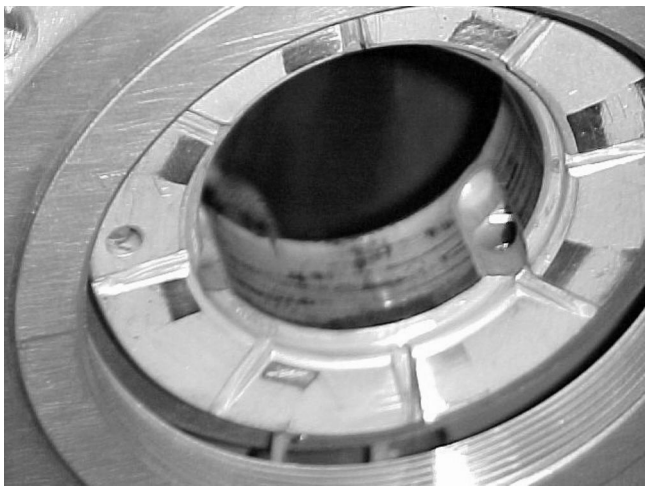

Fig. 12 Original active thrust bearing after rubbing

for the runup in Fig. 11. Subsynchronous vibration was observed on the unit at low speeds during startup, but was not present over 3000 rpm. Running the unit up through the 5000 rpm idle speed, subsynchronous vibration was again observed, this time coming in at 47% of 7700 rpm running speed. Subsynchronous vibration remained fairly steady while the synchronous vibration climbed with speed. At 16,500 rpm, the vibration became purely synchronous with respect to shaft speed. Synchronous amplitude continued to increase rapidly until it began spiking at 19,500 rpm reaching amplitudes of 315 μm total vibration. At this speed, the spectral data indicated that multiple frequencies of vibration were present. Disassembly of the unit showed that a rub had occurred on the thrust bearing (Fig. 12).

The modified unit was then tested at 30 lpm using the three-lobe journal bearings. These bearings were anticipated to provide stable operation throughout the speed range. The cascade diagram, of the modified turbocharger with three-lobe journal bearings, is presented for 30 lpm flow and nominal inlet viscosity in Fig. 13. The unit was run from below 5000 rpm at idle speed to 20,000 rpm. Subsynchronous vibration was of very low amplitude, 11.4 μm at the nose occurring beyond 6200 rpm operating speed. The synchronous vibration generally increased with speed, reaching maximum amplitude of 48 μm at 20,000 rpm. Since 30 lpm was the desired flow rate, additional tests were conducted at maximum and minimum inlet viscosities by running at 55.6°C and 79.4°C oil inlet temperature, respectively. Changing the inlet temperature of the oil had little effect on the operation of the unit. The modified design had been proven to be stable over the operating region, as predicted.

Conclusions

Failure mechanisms for a diesel engine turbocharger were investigated. Deficiencies in the original design were identified and corrected through design modification. The overall findings are summarized as follows:

- The original turbocharger had high unit thrust loading and low minimum fluid film thickness, possibly causing frequent thrust bearing failure. Also, the ability to increase oil flow to the bearing was restricted by the existing hardware design.

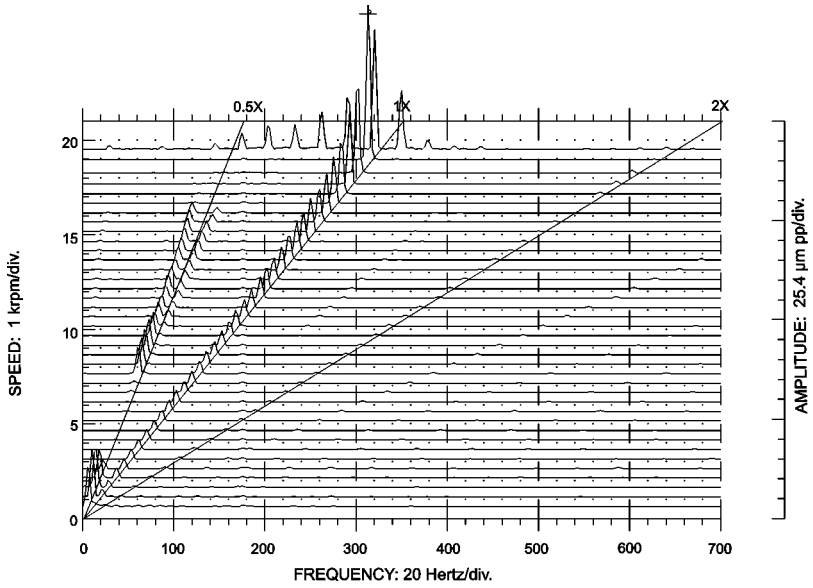

Fig. 11 Cascade diagram, original turbocharger with three-axial-groove journal bearings, 17 lpm, nominal inlet viscosity

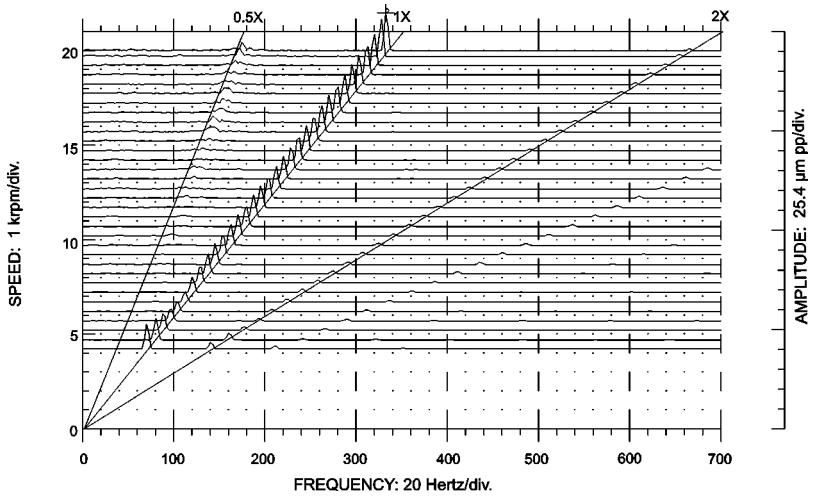

Fig. 13 Cascade diagram, modified turbocharger with three-lobe journal bearings, 30 lpm, nominal inlet viscosity

• The modified thrust bearing resulted in reduced unit load and increased minimum film thickness. The delivery of the oil to the journal bearings, and the thrust bearings, were both optimized to result in optimum temperature rise and metal temperature.

• The predicted maximum metal temperature in the thrust bearing of the original unit was considerably higher than the modified thrust bearing. This was verified during tests of the original and modified unit.

• In the original unit, the turbine end journal bearing and active thrust bearing showed signs of wiping. The modified unit showed no signs of bearing wiping.

• Analysis showed that the original rotor-bearing system with three axial groove journal bearings was unstable. Tests showed that the original unit had high synchronous vibration, combined with subsynchronous vibration.

• The modified unit with three-lobe journal bearings was predicted to be stable. Test data showed that the modified unit had low synchronous vibration. Also, no instability of concern was observed at 30 lpm oil flow over a wide range of inlet oil temperature and viscosity.

• The original unit was unable to reach speed of 20,000 rpm during the test due to high vibration caused by rub at 19,500 rpm, and also showed high metal temperatures. The modified unit was able to reach 20,000 rpm speed with low synchronous vibration and negligible subsynchronous vibration. The bearing metal temperatures were relatively low, and were insensitive to a wide flow range and inlet oil temperature.

• A successful mechanical redesign of a diesel engine turbocharger was completed. Most existing parts were reusable. Some piping changes, however, were required.

Acknowledgments

The authors are indebted to the Elliott Company for permission to publish this paper.

References

[1] Petrock, W., and Stewart, W. A., 1970, ''Critical Factors in the Application of Diesel Engines to Rail Traction,'' Proc. Inst. Mech. Eng., **184**, Part 3, pp. 25–31.
[2] Hoffman, J. G., 1979, ''Crankcase Lubricants for Four-Cycle Railroad and Marine Diesel Engines,'' Lubr. Eng., **35**, pp. 189–197.
[3] Pratt, T. N., et al., 1981, ''HVI and MVI Locomotive Diesel Engine Oil—Open Forum,'' Lubr. Eng., **37**, pp. 577–591.
[4] Brockett, T. S., Barrett, L. E., and Allaire, P. E., 1996, ''Thermoelastohydrodynamic Analysis of Fixed Geometry Thrust Bearings Including Runner Deformation,'' Tribol. Trans., **39**, pp. 555–562.
[5] Lund, J. W., Arwas, E. B., Cheng, H. S., Ng, C. W., and Pan, C. H., 1965, ''Rotor-Bearing Dynamics Design Technology, Part III: Design Handbook for Fluid Film Type Bearings,'' Technical Report AFAPL-TR-65-45, Aero Propulsion Lab, WPAFB, OH.
[6] DeChoudhury, P., Zsolcsak, S. J., and Barth, E. W., 1976, ''Effect of Damping on the Lateral Critical Speeds of Rotor-Bearing Systems,'' J. Eng. Ind., **98**, pp. 505–513.
[7] Lund, J. W., and Orcutt, F. K., 1967, ''Calculations and Experiments on the Unbalance Response of a Flexible Rotor,'' J. Eng. Ind., **89**, pp. 785–796.
[8] Lund, J. W., 1974, ''Stability and Damped Critical Speeds of a Flexible Rotor in Fluid-Film Bearings,'' J. Eng. Ind., **96**, pp. 509–517.
[9] Garner, D. R., Lee, C. S., and Martin, F. A., 1980, ''Stability of Profile Bore Bearings: Influence of Bearing Type Selection,'' Tribol. Int., **13**, pp. 204–210.
[10] Flack, R. D., and Lanes, R. F., 1982, ''Effects of Three-Lobe Bearing Geometries on Rigid-Rotor Stability,'' ASLE Trans., **25**, pp. 221–228.
[11] Schwartz, R., Reichert, B. A., and Chapman, K. S., 1997, ''Development of a Turbocharger Test Stand,'' *Proceedings of the PCRC Gas Machinery Conference*, Austin, TX.
[12] American Petroleum Institute Standard 670, 1993, *Vibration, Axial-Position, and Bearing Temperature Monitoring Systems*, 3rd Ed., American Petroleum Institute, Washington, DC.

Experimental Study of Aerodynamic and Structural Damping in a Full-Scale Rotating Turbine

J. J. Kielb
Rolls-Royce,
P.O. Box 420,
Speed Code T-10B,
Indianapolis, IN 46241

R. S. Abhari
Turbomachinery Lab,
Swiss Federal Institute of Technology,
Zurich 8126, Switzerland

Damping in turbomachinery blades has been an important parameter in the study of forced response and high-cycle fatigue, but because of its complexity the sources and physical nature of damping are still not fully understood. This is partly due to the lack of published experimental data and supporting analysis of real rotating components. This paper presents the results of a unique experimental method and data analysis study of multiple damping sources seen in actual turbine components operating at engine conditions. The contributions of both aerodynamic and structural damping for several different blade vibration modes, including bending and torsion, were determined. Results of the experiments indicated that aerodynamic damping was a large component of the total damping for all modes. A study of structural damping as a function of rotational speed was also included to show the effect of friction damping at the blade and disk attachment interface. To the best of the authors' knowledge, the present paper is the first report of independent and simultaneous structural and aerodynamic damping measurement under engine-level rotational speeds. [DOI: 10.1115/1.1496776]

Introduction

One of the most important factors in controlling turbomachinery blade forced response and flutter is the damping that exists in the system. Early work in the experimental investigation of vibrations in a blade-disk assembly is best summarized in a survey by Srinivasan [1]. Because of the complexity of the components that are involved in studying damping, it is has been difficult to measure and predict the actual levels that are seen during engine operation. Often times the damping is assumed to be a certain value, based on practical experience and lore, when forced response predictions are completed in the design phase. There has been a minimal amount of published experimental data on aerodynamic and structural damping in blades operating at engine conditions to confirm these assumptions.

Turbine blade damping is composed of three major sources: material (due to inherent material properties), structural (due to the frictional contacts), and aerodynamic (due to the motion induced unsteady pressure around the blade). Srinivasan and Cutts [2] showed that material damping is negligibly small, for typical metal alloys used in the construction of blades, and can often be ignored. Structural damping has been difficult to analyze because of the complexity associated with frictional contacts. The majority of research has been focused on contact kinematics models for predicting the damping from wedge-type dampers and shroud contacts, including Yang and Menq [3] and Sanliturk et al. [4]. A recent experimental technique and damping reduction method for isolating the structural damping was reported in Jeffers et al. [5]. Aerodynamic damping has been studied more carefully in recent years with advancements in computational fluid dynamics, including Chiang and Kielb [6] and Abhari and Giles [7]. This usually involves performing CFD calculations that consider the forcing function and aerodynamic damping in two separate categories. The latter category includes blade motion in the CFD prediction to determine the aerodynamic damping.

The current study used an experimental method of measuring the blade damping in an actual high-pressure turbine disk with and without air loading at engine representative conditions. The objective was to measure both structural and aerodynamic damping for several different modes and investigate how these parameters change with differences in the operating conditions. These differences include variations in rotor speed, inlet pressure, and axial rotor/stator spacing. A companion paper by Kielb et al. [8] shows the forcing function measurement from on-blade pressure transducers for the same experiments and operating conditions.

Experimental Method

The experimental method consisted of two separate sets of studies, both performed in The Ohio State University Turbine Research Facility. Figure 1 shows a diagram of the approach for measuring both structural and aerodynamic damping sources. Part(a) involved using a shock tunnel to obtain the representative temperatures, pressures, and rotational speeds for a steady-state time frame of 50 to 100 ms. During this set of experiments blade loading, vibratory response, and total damping (including aerodynamic and structural) were acquired. More extensive explanations of the experimental method and shock tunnel facility can be found in Kielb et al. [8] and Dunn et al. [9], respectively. Part(b) of the experiments involved using the same facility to investigate the vibratory response in vacuum while providing dynamic actuation from on-blade piezoelectric ceramics. This study provided the first reported rotating application of the piezo-actuation and damping reduction method reported by Jeffers et al. [5]. Many of the details of the current method are omitted in this paper for brevity. Without the aerodynamic forces around the blade, it was possible to quantify the amount of structural damping by itself at engine representative speeds. By combining data from both sets of experiments the relative contributions of both aerodynamic and structural damping to the total blade damping were determined.

Contributed by the International Gas Turbine Institute (IGTI) of THE AMERICAN SOCIETY OF MECHANICAL ENGINEERS for publication in the ASME JOURNAL OF ENGINEERING FOR GAS TURBINES AND POWER. Paper presented at the International Gas Turbine and Aeroengine Congress and Exhibition, New Orleans, LA, June 4–7, 2001; Paper 2001-GT-262. Manuscript received by IGTI, Dec. 2000, final revision, Mar. 2001. Associate Editor: R. Natole.

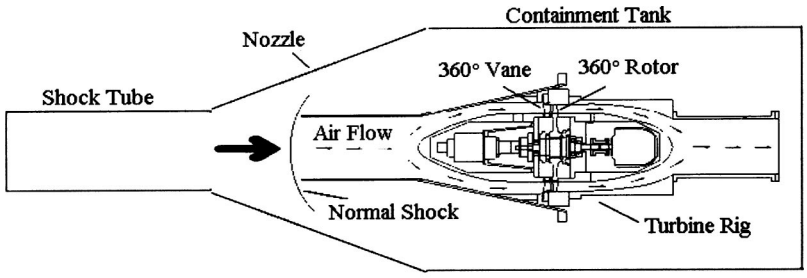

a) Aerodynamic Excitation - Engine Representative Pressure and Temperature

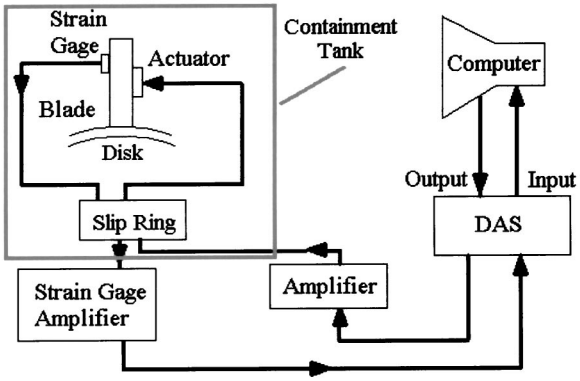

b) Piezoelectric Excitation - Vacuum and Ambient Temperature

Fig. 1 Diagram of approach to experimental method

Turbine Rig. To make the experiments as realistic as possible actual engine hardware from a full-scale turbine rig was chosen for the study. The actual vane nozzles and rotor blades of the Honeywell TFE 731-2 high pressure turbine were used. Several studies have already been completed using this turbine rig, such as the work of Dunn and Hause [10] and Dunn et al. [11]. The rig hardware was recalled for use in the current study and new instrumentation was added.

For the purpose of studying forced response the valve on the shock tunnel was opened just before the rotor reached a resonant speed, allowing it to accelerate through resonance as the sudden air loading entered the test section.

The Campbell diagram, experimentally measured during the spin tests in vacuum, for the TFE 731-2 turbine can be seen in Fig. 2, showing the four modes of interest. The resonant frequencies plotted in Fig. 2 represent an average of the response for the instrumented blades during the piezo excitation experiments. Figure 3 shows the mode shapes in the range of 0–20 kHz obtained from a finite element modal analysis.

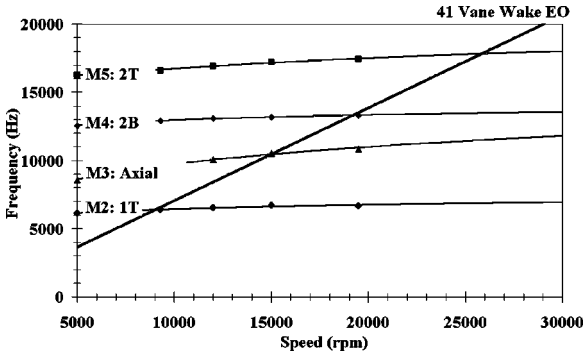

Fig. 2 Experimental Campbell diagram for instrumented airfoils (obtained from vacuum spin tests)

Instrumentation. The structural response of the blades was measured using precision metal foil resistive strain gages. The gages were placed in areas of high strain, as predicted by finite element analysis, at three spanwise locations (base, midspan, and tip) as seen in Fig. 4. Nine strain gages were used over the sum of six blades. Four of these blades had additional instrumentation, while the other two had only strain gages. This gage placement was done to quantify the change in response due to the addition of

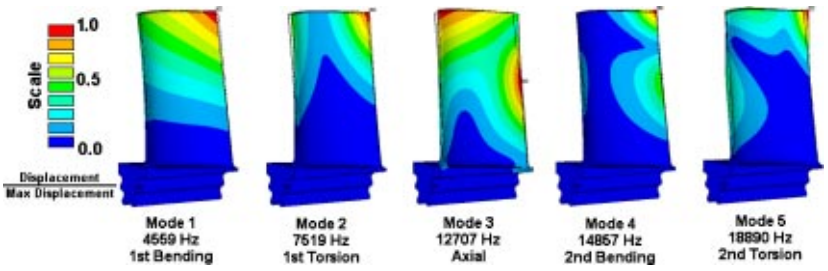

Fig. 3 Finite element analysis mode shapes

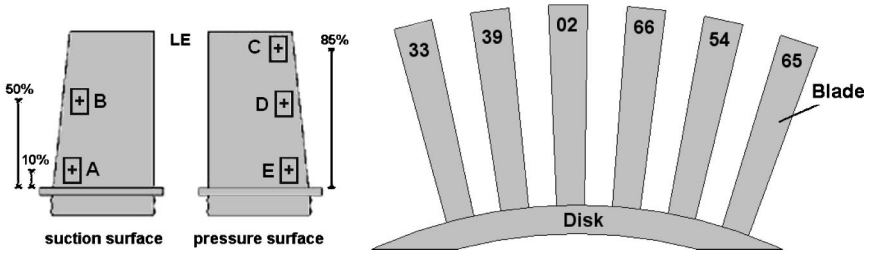

Fig. 4 Strain gage locations and blade distribution

the other instrumentation. The distribution also allowed for a sampling of the mistuned response of the blade and disk assembly.

For blade actuation flush-mounted piezoelectric ceramic actuators were chosen, because of their functionality in a rotating environment and the well-controlled frequency output over a wide range. Many of the problems seen in other recent experimental efforts that used piezoelectric actuators stemmed from the existence of cross-talk between the high-voltage excitation signals and the low-voltage strain gage signals. In the past, managing this effect required that the power to the actuator be shut off so that only the decay in the response would be available. In the current study a combination of data acquisition and post-processing techniques were used to minimize the cross-talk contamination to the strain gage measurements, allowing for the actuators to be simultaneously powered while monitoring the blade response. This arrangement provided a well-controlled vibratory response measurement with a high signal-to-noise ratio, see Jeffers et al. [5].

The piezo was installed near the base of the blade on the trailing edge because it provided the best actuation for exciting the modes of interest and it created the least amount of intrusiveness for the damping measurement. Pockets were electro-discharge machined (EDM) into the blade so that the piezo and lead wires were flush to the surface, minimizing interference with the aerodynamics. The actuators were constructed by shaping piezo wafers made by Rainbow™ Ceramics to fit the pocket and then attaching electrodes. The piezo assembly was coated with insulating film and glued flush to the surface of the blade as shown in the photo in Fig. 5. Only two actuators were used, but the piezos also excited neighboring blades by vibration coupling through the disk.

Data Acquisition. Data were acquired using two different sets of hardware for the aerodynamic and piezoelectric excitation techniques, respectively. During the aerodynamic excitation experiments, the strain gages were wired through a fully programmable, computer-controlled amplifier. This acquisition system has been used for many previous experiments.

During the piezoelectric actuation, data were acquired by using an 18-bit data acquisition system. The piezoelectric actuators were powered with both swept sign and chirp forms of excitation. The swept sine routine provided an AC signal that varied from 1–20 kHz with user-defined resolutions. The signal-processing unit simultaneously recorded and computed the transfer function of the blade response. This technique was useful for obtaining very accurate data in high noise environments, but it was slow. It was preferable to avoid long acquisition times to prevent excessive bearing temperatures. A faster alternate method was to use a chirp excitation that provided a burst of all frequencies within a specified range. This method was slightly less accurate in the presence of high noise, but it provided a tenfold decrease in the amount of time needed to acquire the same amount of data. The signal-to-noise ratio using chirp and sweep approaches were typically about 22 and 25, respectively. Consequently, chirp excitations were used for almost all of the runs, although some runs were repeated with the sweep method to prove that both forms of excitation provided similar results.

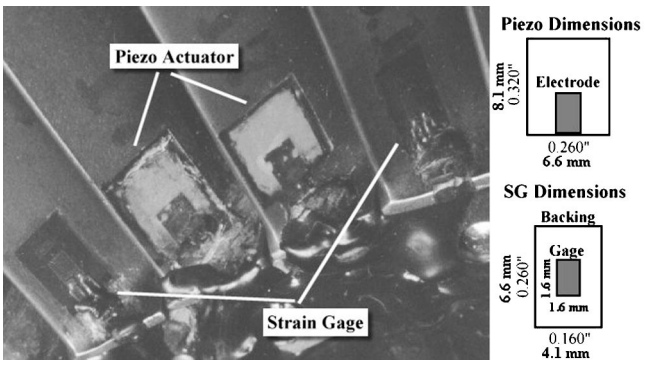

Fig. 5 Piezos and strain gages on subsection of rotor

Bench Tests. To prove the feasibility of the excitation technique and guide the full-scale experiments, several bench studies were performed. These studies allowed for carefully monitored control of the excitation and provided the opportunity to quantify the signal-to-noise ratios for the piezoelectric actuation method. The same data acquisition system was used for the bench tests, except the slip ring was not needed, making the signals much cleaner. The bench studies involved mounting a single blade in a broach block, allowing for a simulation of the firtree constraint on the blade. This constraint was varied for different speeds by adjusting the load applied to the bottom of the blade. A calibration of the associated torque applied to two set screws, that forced a small shim against the bottom of the blade, was performed using a load cell so that the force needed to simulate a particular speed was determined.

Signal Noise Reduction. The capacitive cross-talk was minimized by shielding the wires as much as possible. In this application it was difficult to completely shield the wires, since very fine gage leads were needed on the blade surface. By using a combination of shielding and keeping the power lines on separate connectors, the noise was minimized to the point that the remaining interference could be removed during post-processing.

Data Reduction. The strain gage data were Fourier decomposed using the fast Fourier transform routine. The capacitive cross-talk was removed from the signals obtained during the piezo excitation experiments by subtracting the baseline noise signal from the data. It became necessary to find a more accurate damping reduction method than the simple half-power technique because of the low-system damping levels identified in the absence of air. The data points were curve fitted using the single-degree-of-freedom equation of motion in Eq. (1), with a unique weighting function that allowed the curve fit to focus on the peak response being employed. More detail on this technique can be found in Jeffers et al. [5].

Table 1 Overall uncertainty due to both experimental and data reduction errors for various ranges of ζ and resolution

Resolution (Hz)	$\zeta * e^{-4}$	ω_r (kHz)	Overall Error in $\zeta * e^{-4}$
1	5	7.5	±0.66
1	20	18	±0.50
10	5	7.5	±1.09
10	20	18	±2.56
100	20–100	0–20	±10.00

$$\frac{A}{F} = \frac{1}{\sqrt{\left(1-\left(\frac{\omega_r}{\omega}\right)^2\right)^2 + \left(2\zeta\frac{\omega_r}{\omega}\right)^2}} \tag{1}$$

Intrusiveness of Measurement Components. Due to the relatively small size of the blade, compared to the size of the transducer, and the amount of instrumentation that was used, it was necessary to recognize the extent to which the transducers altered the actual measurements. There were two main sources of intrusiveness: parasitic damping contributed by both the actuator and the strain gage, and the reduction in stiffness due to the removal of blade material for the flush-mounted actuator. The added damping due to instrumentation was found to be minimal, measuring less than 5×10^{-4} in the critical damping ratio, ζ, which is defined by Eq. (2).

$$\zeta = c/c_c \tag{2}$$

The reduction in stiffness due to transducer installation showed an average reduction in the resonant frequency of less than 5%. The latter effect helped the data reduction slightly, since the responses of the instrumented blades were shifted away from the nominal blade responses, making each peak response more isolated. In most cases the altering of the blade response due to the transducers was minimal and deemed not to significantly change the conclusions about the damping in the system.

Error Analysis. All sources of error in the experimental method were investigated to determine the largest sources of uncertainty. For the piezo excitation experiments, little error originated from the experimental components themselves. The majority of the uncertainty in the damping calculation was attributed to the data reduction and curve-fitting methods. The removal of the cross-talk provided a minimal 1% error in ζ. The single-degree-of-freedom curve fit showed small uncertainty levels for low damping ratios (below $5e^{-1}$) as seen in Table 1. The repeatability of the damping calculations was investigated by taking data during a series of repeated experiments in which the blade was removed and re-installed in the broach block between runs. The standard deviations were found to be no larger than $0.6e^{-4}$, indicating that the damping ratio could be reduced in a repeatable manner.

For the aerodynamic excitation runs the majority of the error was attributed to the small sampling of data during the short duration experiment. These experiments showed a high signal-to-noise ratio in the strain gage signals (over 10) as seen in Kielb et al. [8]. The frequency resolution of the fast Fourier transform results from the aerodynamic excitation experiments was much lower than the resolution from the vacuum tests (100 Hz compared with 1.25 Hz) because of the limited run time. This created difficulty when computing the damping ratio with the single-degree-of-freedom method, since there were few points in the response with which to fit a curve around resonance. It was also necessary to make sure that there was a small change in speed during the run to allow the blade to reach the steady-state resonant response, since there was an excitation source of rapidly increasing frequency. By analyzing small time windows of 10 ms, the speed change was assured to be less than ±2.5% over the time frame and the frequency resolution was 100 Hz. Even with this careful data reduction procedure the resulting damping calculation had the potential to make ζ seem about 20% higher than it truly was for the aerodynamic excitation experiments. While this appears to be a high value, it is small when put into the context of the comparisons between the isolated structural damping and aerodynamic damping. The effect of rotor acceleration was the major issue affecting the uncertainty in the aerodynamic excitation results presented.

Results

Mistuning. The measured vibratory responses captured the mistuned dynamics of the blade and disk assembly. Since each blade inherits small geometric differences from the manufacturing process, the resonant frequencies are slightly mistuned from each other. In addition, the transducers, pockets, and wire channels in the six instrumented blades created an even larger source of mistuning, which incidentally had a beneficial affect of allowing for a clearer identification of a particular resonance. As a result of the mistuning, the measured vibratory response showed multiple peak responses, rather than a single isolated peak. For the purpose of this investigation each peak response was attributed to a particular blade strictly to make decisive conclusions about the damping levels. This paper is not focused on identifying the mistuned response; rather the behavior is mentioned to clarify how the vibratory response was handled for reducing data.

Vibratory Response in Vacuum. Examples of vibratory response measurements on two different blades at the same speed are shown in Figs. 6 and 7. These figures show the strain signals obtained at both the midspan and base of two neighboring blades. The graphs labeled as (a) and (b) show the experimental runs where the blade is excited over a wide frequency range (0–20 kHz) with a coarse frequency resolution of 6.25 Hz. Mode 2 (1st torsion) and mode 4 (2nd bending) exhibited the largest responses throughout most of the study. The wide frequency range experiments were used mostly for viewing the characteristics of the response. In order to obtain an accurate damping and resonant frequency measurement, a narrower frequency range was selected during data acquisition, allowing for a finer frequency resolution. The graphs labeled as (c) and (d) show results from the smaller frequency range of interest (12–14 kHz) for the 2nd bending mode. These experiments used a smaller resolution of 1.25 Hz. It should be emphasized that the high resolution experiments were taken separately (and at slightly different operating conditions) from the lower resolution experiments, causing a slight difference in the peak responses.

The mistuned response is quite obvious from these plots, making it difficult to associate a specific peak resonance with a particular blade. The highest peak response was associated with the blade that the gage was attached to in this case, and generally in all the other cases. This conclusion was made by comparing the results from different sensors during the same runs and by using the large database of bench tests on isolated blades. Figure 6 clearly shows a large resonance of blade 66 at approximately 12.6 kHz on both gages and some smaller peaks. The peak at approximately 12.8 kHz was determined to be the response of blade 54 by comparing this plot with that in Fig. 7. In addition, the bench data from blade 54 isolated in the broach block had a similar resonant frequency, which allowed for a confidant identification of the peak resonance.

Change in Blade Response With Rotational Speed. As the centrifugal load on the blade increases due to the change in rotational speed, the normal force between the blade and disk contact interfaces also increases, causing the energy dissipation through friction to decrease. In the turbine used for the current study the only form of structural damping came from this frictional force, so it was necessary to quantify the decrease in structural damping

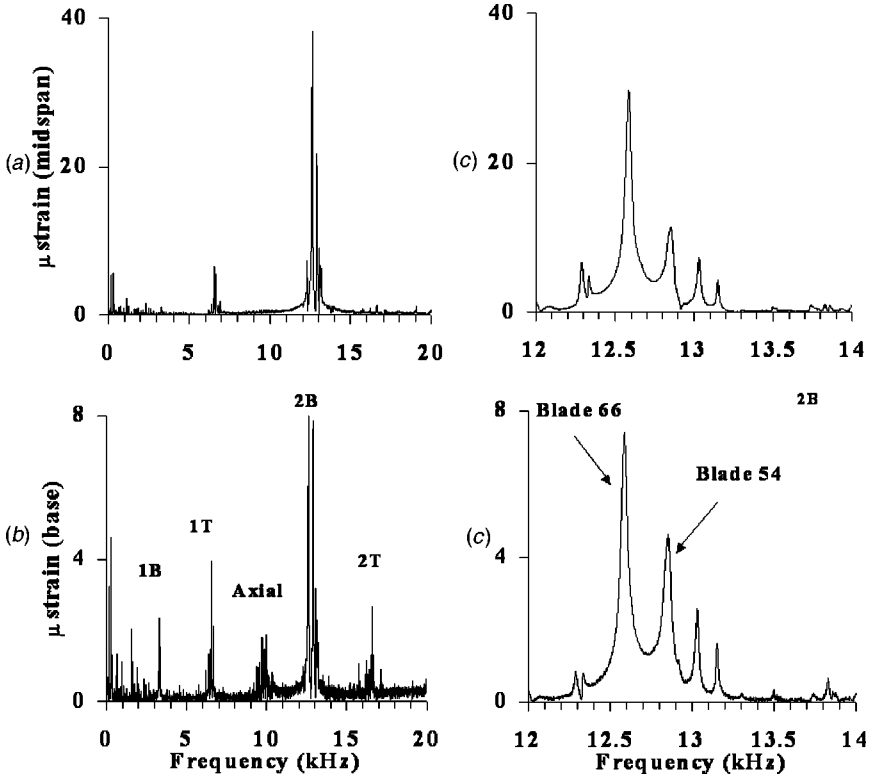

Fig. 6 Response of blade 66 in vacuum at 9300 rpm for two frequency resolutions and two gage locations

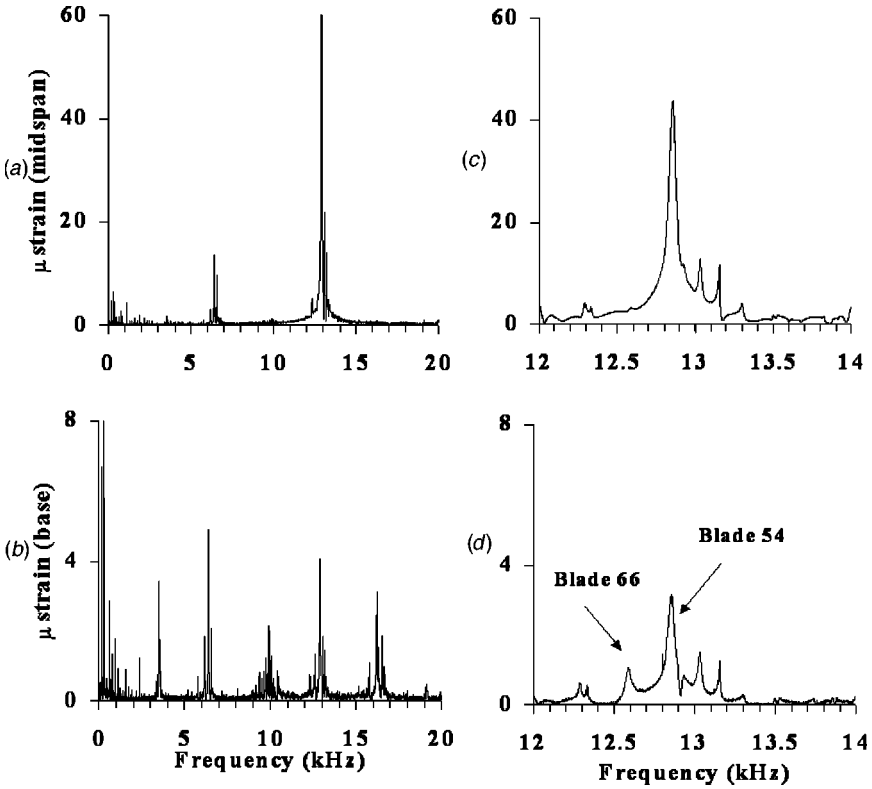

Fig. 7 Response of blade 54 in vacuum at 9300 rpm for two frequency resolutions and two gage locations

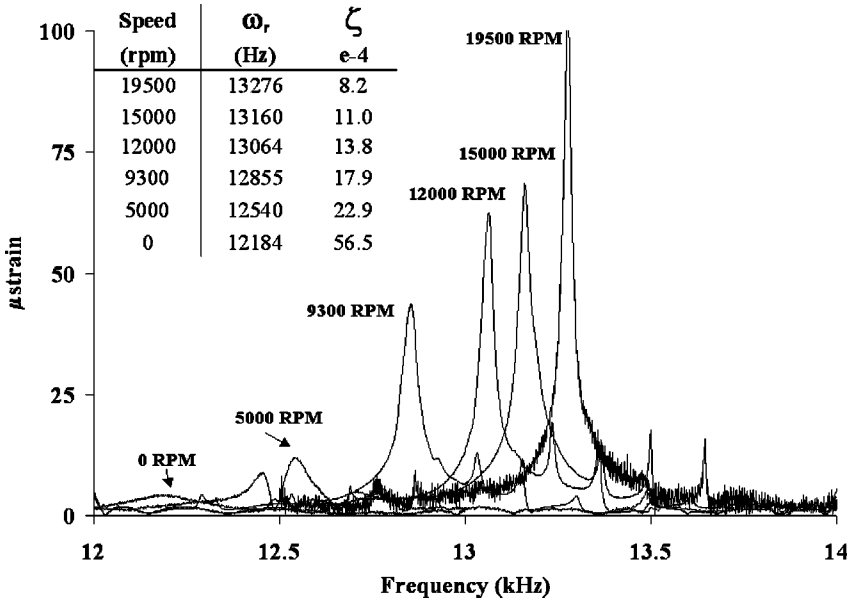

Fig. 8 Second bending vibratory response in vacuum of blade 54 at six different rotational speeds

with increasing rotational speed. This set of experiments in vacuum also helped to precisely define the run conditions (exact frequency and associated rotational speed) for the aerodynamic excitation experiments.

The mode 4 (2nd bending) vibratory responses of blade 54 (SG31) at different speeds are plotted in Fig. 8. The increases in both the amplitude of the peak response and the resonant frequency are seen from the curves. The smaller damping at higher speeds is also evident, since the width of the resonant peak at the half power points is narrower. The computed resonant frequency and damping for each response is listed in the same figure.

Figure 8 provides a visual display of the change in response

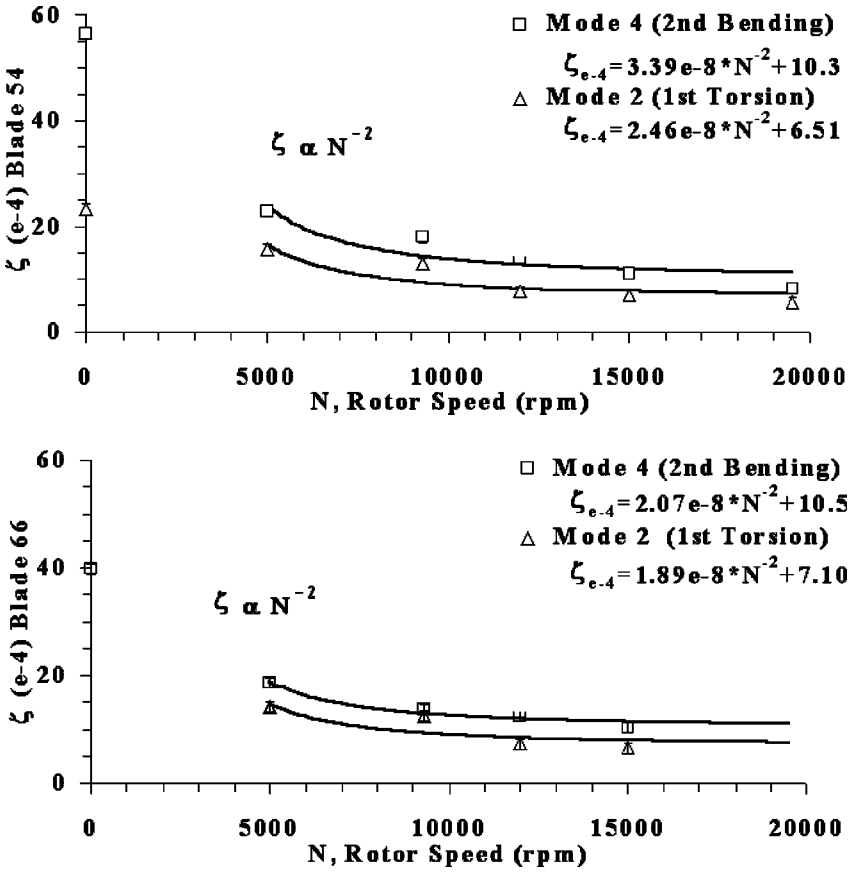

Fig. 9 Change in structural damping with rotational speed for 2B and 1T modes

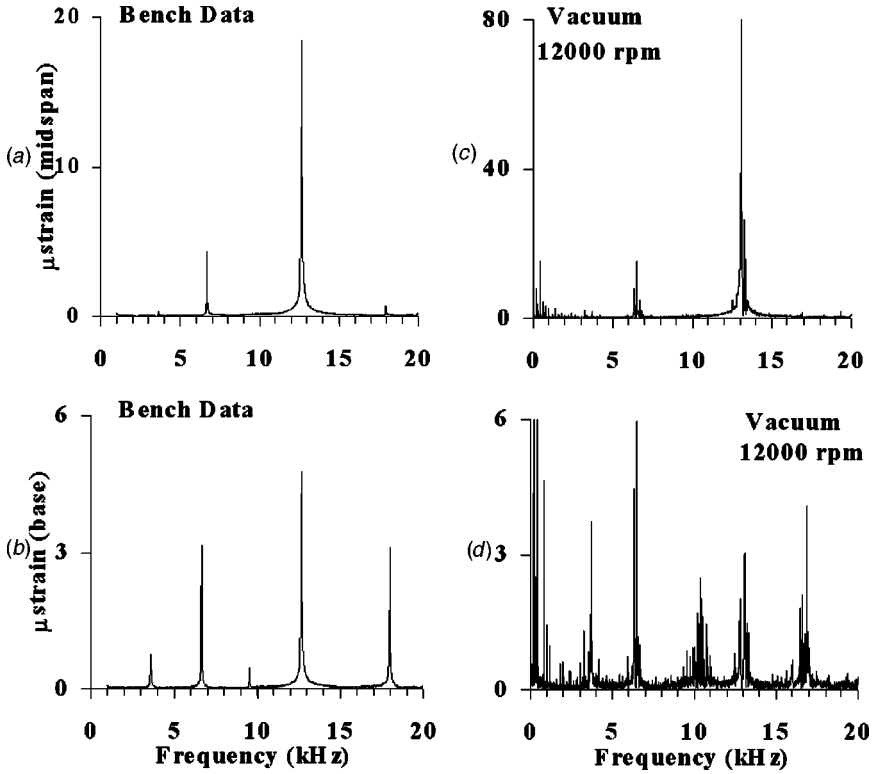

Fig. 10 Comparison of blade 54 vibratory response in the Broach block and the spinning rotor in vacuum

with speed, but to analyze the details of the change in structural damping, the critical damping ratio was plotted for two different modes on two blades in Fig. 9. These plots suggest that the damping is proportional to 1 over the square of the speed, especially for speeds above 5000 rpm (20% of design speed), as seen in the least squares curve-fit solutions in Fig. 9. Since the centrifugal load is proportional to the square of the rotational speed and inversely proportional to damping, the data suggests that the measured damping was solely from this increased speed. The only exception occurred for lower speeds (less than 20% of design speed) where nonlinear effects, from the more complex friction interfaces, and less repeatable blade loading conditions exist. As expected there were slightly higher damping levels for the bending mode due to the larger energy dissipation in the firtree interface.

Comparison of Rotating Results With Broach Block Experiments. The static experiments in the broach block and the rotating experiments in the disk were compared to see how well the bench simulations represented the realistic rotating response. Figure 10 shows the vibratory responses for the simulated speed of 12,000 rpm in the broach block and the corresponding responses at a speed of 12,000 rpm the vacuum spin tests. The relative peak of each mode was similar in both the broach block and the rotor. The actual levels of strain response were slightly higher for the rotating test since a higher excitation voltage was used to drive the piezo. It is once again evident from the plots in (b) that the mistuned response is being measured. The data from the broach block (a, b) provide a ''clean'' response for attributing each resonance to a particular blade.

The resonant frequency and damping differences between the static and rotational experiments for the 2nd bending and 1st torsion modes are summarized in the plots in Fig. 11 and the results of Table 2. It was difficult to accurately determine which speed the bench experiments actually simulated, since the contact force-to-speed calibration, mentioned in the bench test discussion had many uncertainties. Also, the bench tests were not performed in vacuum so the comparisons are not straightforward. It should be noted that the containment tank for the rotating runs was not completely at vacuum, which resulted in a small amount of air (approximately 7 mbar or 5 torr) that could introduce a slight amount of damping. With the exception of mode 3 for blade 66, the damping levels appear to be almost the same in both the rotor and the bench experiments, indicating that the ambient air during the bench tests did not add significant aerodynamic damping. The small decrease in resonant frequency for the rotating experiments in vacuum (with the blades mounted in the disk) is expected, since the blade and disk system modes are usually slightly less stiff than the isolated blade modes.

Comparison of Damping in Air and in Vacuum at Rotational Speed. The goal of using two different excitation methods was to quantify the effect of the aerodynamic excitation on the vibratory response of the blade. It was necessary to first compare the vibratory responses from the two forms of blade actuation. Of course the aerodynamic excitation methods were the most realistic for classifying the structural response of a turbine blade in operation. The vibratory responses over a wide frequency range for both methods during the 2nd bending mode experiments can be seen in the plots of Fig. 12. The strain gage signals from the two different gages on blade 54 show expected response levels for the five modes of interest. It is clear that the piezoelectric excitation method does indeed provide a feasible excitation for classifying the vibratory response in vacuum, when compared to the responses from the aerodynamic excitation experiments. At first glance there were two indications of the aerodynamic damping from the two strain gage signals (Fig. 12(*c*) and (*d*)). The first is the larger peak amplitude for the response in vacuum. There is also an indication that the resonant frequency decreases and the width of the peak decreases during the vacuum experiments.

To determine the damping levels of the 2nd bending and 1st torsion responses a small frequency range around resonance was analyzed. Fig. 13 shows the 2nd bending vibratory responses for

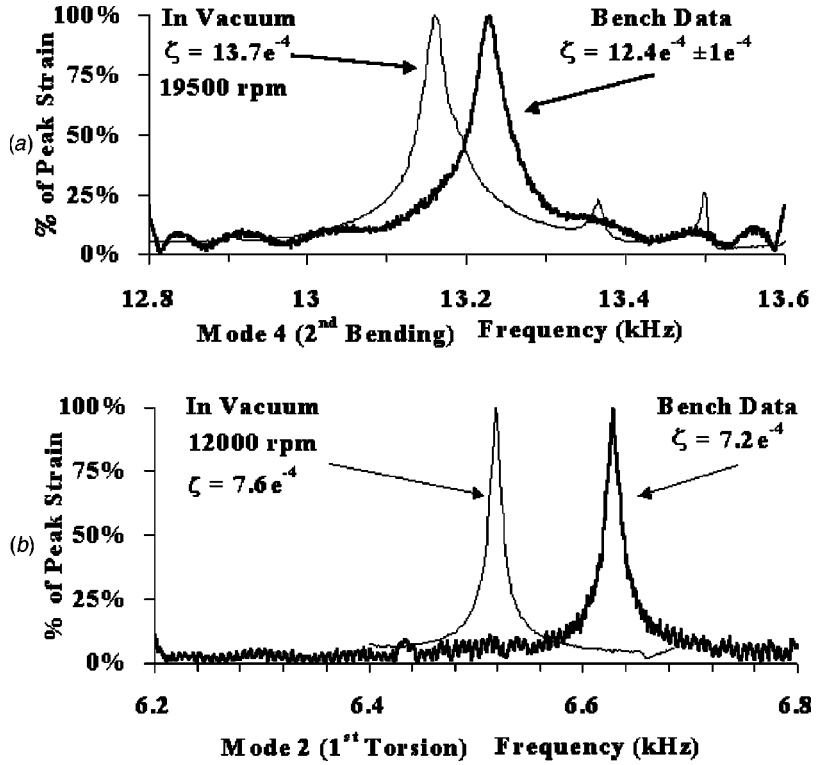

Fig. 11 Comparison of blade 54 damping in the Broach block and the spinning rotor in vacuum

both excitation experiments. These plots provide a more detailed view of the damping increase with aerodynamic excitation. The resonant responses from both gages showed a reduction in resonant frequency and wider peak resonance. This conclusion is confirmed with the results of the single-degree-of-freedom damping reduction technique shown in Table 3. A similar assessment was made for the 1st torsion mode as seen in Fig. 14. It should be noted that the 1st torsion mode was excited at much lower strain levels (up to ten times less), which increased the uncertainty in the damping. The responses were nondimensionalized in both peak strain and frequency for making the comparison more obvious. The aerodynamic damping for 1st torsion appears to be over twice as large as for 2nd bending, which was not expected. The authors were also surprised that the aerodynamic damping level was as high as 1%. In both cases the aerodynamic damping was found to be a major component of the total damping, since the increase in critical damping ratio, ζ, was over five times the isolated structural damping.

Since the damping levels in both modes indicated that a large component of the total damping was due to the aerodynamic loading on the blade, the effects of inlet pressure and axial vane to blade spacing on damping and peak response were investigated. The shock tunnel experiments were performed with two different turbine rig inlet pressures and two different axial spacings. A change in the inlet pressure resulted in a change in the flow Reynolds number, and hence the sensitivity of the aerodynamic damping to flow viscosity. Variation in the axial spacing resulted in a substantial reduction of the unsteady forcing function. The results from this change in the inlet pressure and axial spacing are used to elucidate any nonlinearity in the blade response. The variation in

Table 2 Comparison of bench test and rotor measured resonant frequency and damping

	Mode 2 1st Torsion		Mode 3 Axial		Mode 4 2nd Bending	
	ω_r (Hz)	$\zeta \pm 1$ (e-4)	ω_r (Hz)	$\zeta \pm 1$ (e-4)	ω_r (Hz)	$\zeta \pm 1$ (e-4)
Bl54 Rotor 12000 rpm	6519	7.6	10376	4.8	13064	13.7
Bl54 Bench 12000 rpm*	6628	7.2	11432	4.0	13532	12.4
Bl54 Rotor 15000 rpm	6690	6.9	10650	3.3	13160	11.1
Bl66 Rotor 12000 rpm	6658	7.2	10271	5.9	12788	12.4
Bl66 Bench 12000 rpm*	6966	6.8	11025	8.0	13230	12.6 6
Bl66 Rotor 15000 rpm	6816	6.5	10555	4.5	12906	10.3

*simulated rotational speed in the broach block

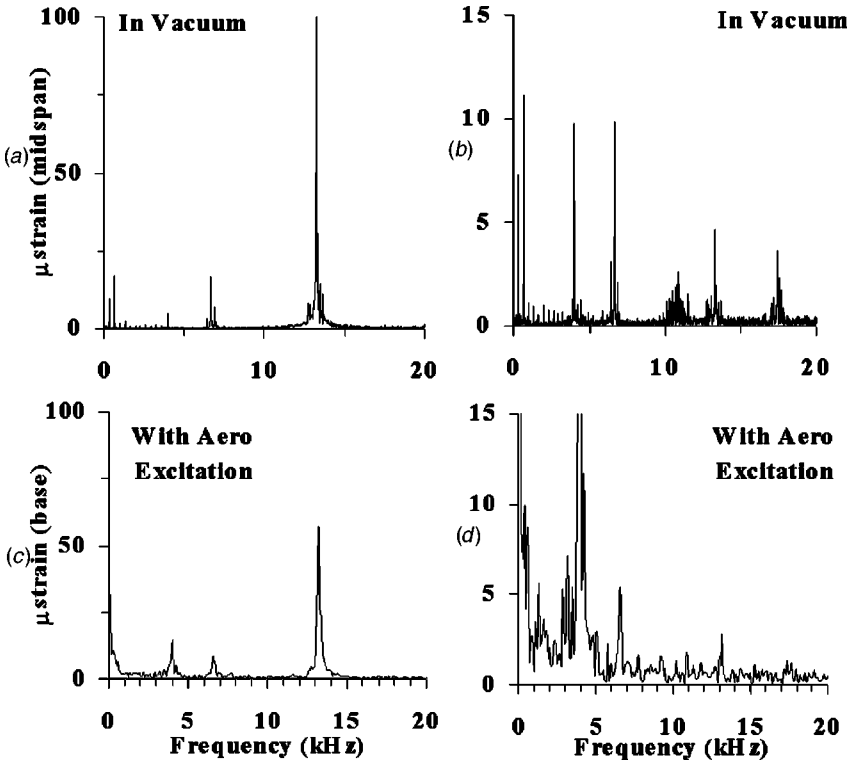

Fig. 12 Large frequency range vibratory response at 19,500 rpm in vacuum and with 2B aerodynamic excitation

damping and vibratory response with the change in inlet pressure for the 2nd bending mode can be seen in Fig. 15(*a*). The response was very similar for both inlet pressures, with the response at the lower pressure having a slightly higher peak strain and lower damping. For all practical purposes the two responses can be considered to be the same, due on the uncertainty in the measurement, indicating that the change in response with an increased inlet pressure is negligible. The change in response with two different spacings between the vane and blade can be seen in Fig. 15(*b*). The damping at both spacings was very similar, but the peak strain was

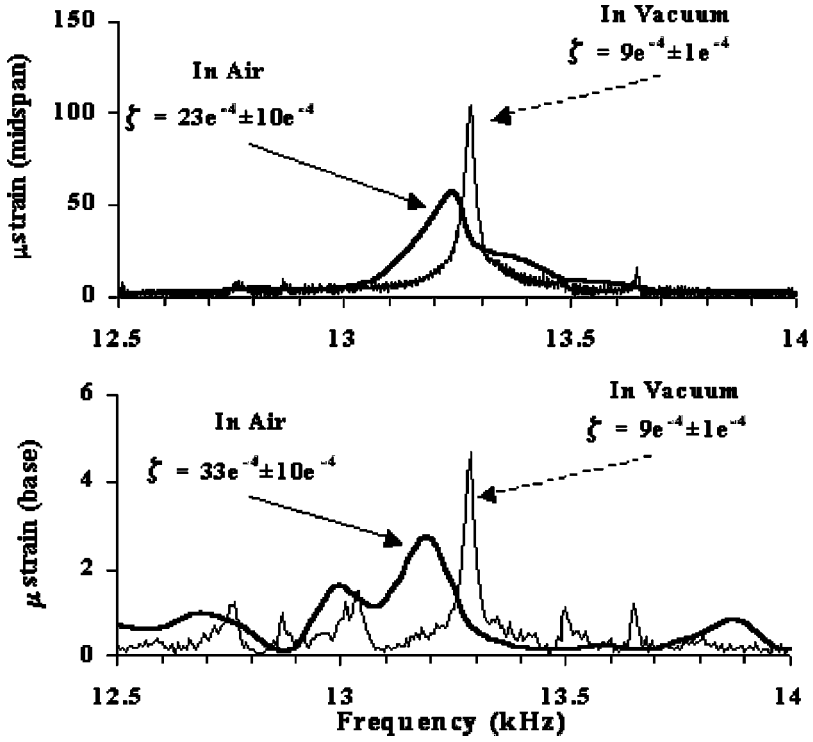

Fig. 13 Vibratory response of 2B at 19,500 rpm in vacuum and with air loading

Table 3 Comparison of frequency and damping of two blades during the 2B excitation in both vacuum and air

			ω_r (Hz)		ζ (e-4)	
Gage	Bl	Loctn	Vac	Air	Vac	Air
SG31	54	Mid	13288	13250	9.0±1	23.0±10
SG32	54	Base	13288	13250	9.0±1	33.0±10
SG33	66	Mid	13038	13090	9.0±1	33.0±10
SG34	66	Base	13038	13090	9.0±1	35.0±10

higher with the spacing that was 14% higher than the nominal value. This was an unexpected result, since the pressure loading at the nominal spacing was measured to be as much as four times higher by Kielb et al. [8]. It is possible that with a 14% increase in spacing the wake and potential interaction could constructively interfere, causing a higher loading for this mode. This is only speculation and the investigation of the coupled pressure loading and vibratory response for this mode is left as a future task.

Conclusions

Turbine blade vibratory response was analyzed with and without the aerodynamic loading on the blade during engine operation. The unique piezoelectric actuation method provided continuous blade excitation at high frequency while monitoring the structural response in a spinning rotor. The historical problem with this method of cross-talk interfering with the measurement signals was resolved through experimental methods and post-processing. The resulting experimental technique provided a method with low uncertainty and intrusiveness for determining the components of structural and aerodynamic damping in the total blade damping.

The first series of experiments in the evacuated spin facility showed the existence of mistuned vibratory response in the blade and disk system, but the resonant peaks were far enough apart to classify the nature of the response and damping characteristics.

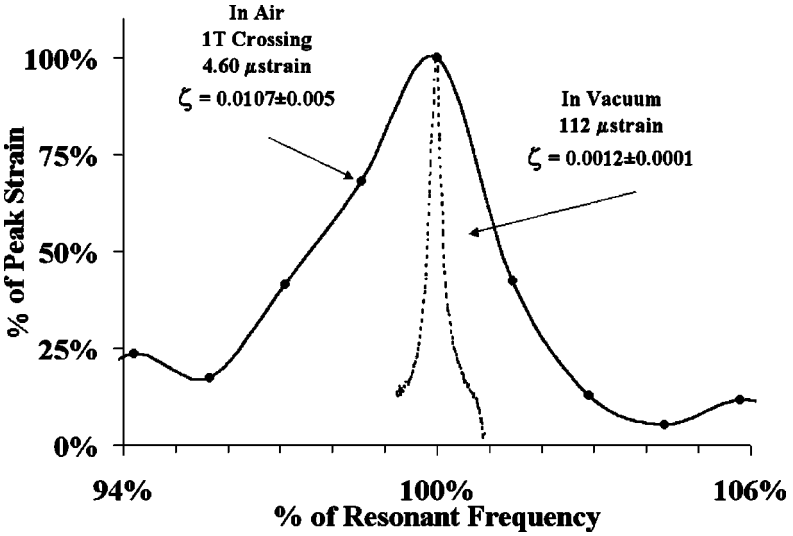

Fig. 14 Vibratory response of 1T in vacuum and with air loading

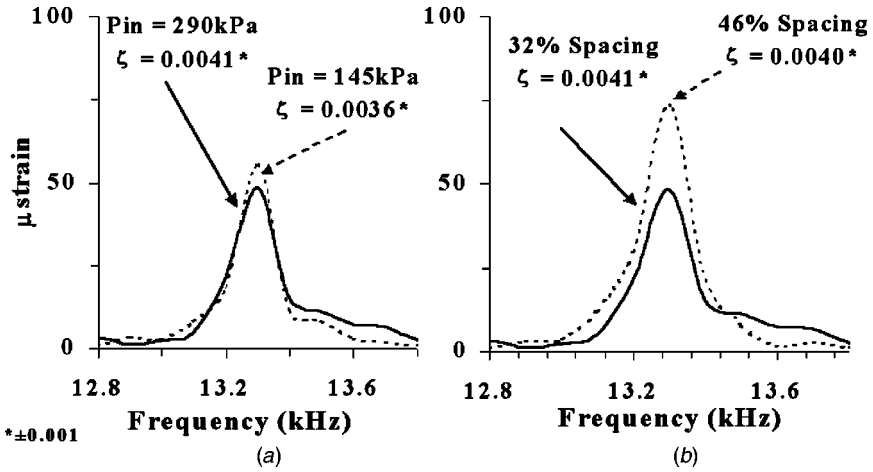

Fig. 15 Variation in damping and peak response for 2B with (*a*) change in inlet pressure and (*b*) change in axial vane to blade spacing

The damping was shown to be inversely proportional to the square of the speed, proving that the only significant damping present in the experiments in vacuum was attributed to friction between the blade and the disk attachment.

A comparison of the rotating results with bench test results showed similar vibratory responses and the ambient air during the bench test did not have a significant effect on the damping level. Comparisons of rotating vibratory responses in vacuum and with engine representative pressures during operation showed that the aerodynamic damping was a large part of the total blade damping for both 1T and 2B modes adding as much as a factor of 10 in the critical damping ratio. The authors were rather surprised at the significant level of aerodynamic damping (compared to structural) for this turbine blade. The aerodynamic damping was slightly higher for the 1T mode than the 2B mode. Similar damping levels were seen from experiments at different axial rotor/stator spacings and different inlet pressures, indicating that for this case blade resonant response appears to be responding in a linear manner. As far as the authors are aware, this paper presents the first experimental measurement of forced response of an actual rotating turbine bladed-disk at engine representative conditions where aerodynamic and structural damping were individually quantified for different modes.

Acknowledgments

This study was supported through NASA and the GUIde Consortium. The authors would like to express their thanks to Mike Dunn, Charlie Haldeman, Ryan Jeffers, Tony Giang, Jeff Barton, and Joe Panovsky for their help with this program.

Nomenclature

A = amplitude of response
F = amplitude of forcing function
N = rotational speed in rpm
c = damping coefficient
c_c = critical damping coefficient
ω = frequency
ω_r = resonant frequency
ζ = critical damping ratio

References

[1] Srinivasan, A. V., 1984, ''Vibrations of Bladed-Disk Assemblies—A Selected Survey,'' ASME J. Vib., Acoust., Stress, Reliab. Des., **106**, pp. 165–168.
[2] Srinivasan, A. V., and Cutts, D. G., 1984, ''Measurement of Relative Vibratory Motion at the Shroud Interfaces of a Fan,'' ASME J. Vib., Acoust., Stress, Reliab. Des., **106**, pp. 189–197.
[3] Yang, B. D., and Menq, C. H., 1997, ''Characterization of Contact Kinematics and Application to the Design of Wedge Dampers in Turbomachinery Blading,'' ASME Paper No. 97-GT-97.
[4] Sanliturk, K. Y., Ewins, D. J., and Stanbridge, A. B., 1999, ''Underplatform Dampers for Turbine Blades: Theoretical Modeling, Analysis, and Comparison With Experimental Data,'' ASME Paper No. 99-GT-335.
[5] Jeffers, T., Kielb, J., and Abhari, R., 2000, ''A Novel Technique For Measurement of Rotating Blade Damping,'' ASME Paper No. 2000-GT-0359.
[6] Chiang, H., and Kielb, R., 1993, ''An Analysis System for Blade Forced Response,'' ASME J. Eng. Gas Turbines Power, **115**, pp. 762–770.
[7] Abhari, R. S., and Giles, M., 1997, ''A Navier-Stokes Analysis of Airfoils in Oscillating Transonic Cascades for the Prediction of Aerodynamic Damping,'' ASME Paper No. 95-GT-182.
[8] Kielb, J. J., Abhari, R. S., and Dunn, M. G., 2001, ''Experimental and Numerical Study of Forced Response in a Full-Scale Rotating Turbine,'' ASME Paper No. 2001-GT-0263.
[9] Dunn, M. G., Moller, J. C., and Steele, R. C., 1989, ''Operating Point Verification Data for a Large Shock Tunnel Test Facility,'' WDRC-TR-89-2027, May.
[10] Dunn, M. G., and Hause, A., 1982, ''Measurement of Heat Flux and Pressure in a Turbine Stage,'' ASME J. Eng. Gas Turbines Power, **104**, pp. 215–223.
[11] Dunn, M. G., Rae, W. J., and Holt, J. L., 1984, ''Measurement and Analysis of Heat Flux Data in a Turbine Stage,'' ASME J. Eng. Gas Turbines Power, **106**, pp. 229–233.

Forced Response of Turbine Engine Bladed Disks and Sensitivity to Harmonic Mistuning

J. A. Kenyon
Air Force Research Laboratory,
Propulsion Directorate,
Wright-Patterson AFB, OH 45433

J. H. Griffin
Department of Mechanical Engineering,
Carnegie Mellon University,
5000 Forbes Avenue,
Pittsburgh, PA 15213

The mistuned forced response of turbine engine bladed disks is treated using harmonic perturbations in the properties of a continuous ring. A continuous shear spring is attached to the ring in which the stiffness is allowed to vary along the ring annulus. The modes of such a structure with a single harmonic mistuning pattern are shown to obey the Mathieu equation, which is solved to obtain the natural frequencies and modes of the mistuned system. The forced response of the system is then examined to determine the sensitivity of the system to small mistuning. The model is extended to include multiple harmonics, allowing for the possibility of general mistuning. An expression for the maximum amplitude magnification due to small mistuning is developed by showing that high response is caused by distortion of the structural modes. A method to intentionally mistune systems for maximum forced response is demonstrated, and numerical results demonstrate the accuracy of the analytical prediction. The intentionally mistuned system response is shown to be robust with respect to small random mistuning. Such a result might be useful for designing a test rotor for screening new bladed disk designs or for establishing the root cause of fatigue problems. [DOI: 10.1115/1.1498269]

Introduction

Turbine engine bladed disks belong to a class of structures generally referred to as periodic. Such structures exhibit families of extended modes with closely spaced natural frequencies. The close proximity of the natural frequencies to one another makes such structures sensitive to small imperfections which break down the periodicity of the system. These imperfections are referred to as mistuning since one of its manifestations is a variation in the natural frequencies of the individual blades on the disk. In modern bladed disks, discrete blades may be replaced by an integrally machined blade and hub system, but the term mistuning has endured and has come to include any variation between nominally identical sectors of the system.

A rich literature exists on mistuning, its effects on turbine engine forced response, and the efforts of researchers to understand and model the phenomena associated with mistuning. Srinivasan [1] provides a good review of much of the earlier literature, particularly the development of modeling and statistical methods in the 1980s and early 1990s. The statistics of mistuned forced response were deemed important because the small variations in blade and disk properties associated with mistuning are random parameters that are impossible to control and often difficult to accurately measure. Thus, predicting the statistics of mistuned response was believed to be more practical than trying to predict response in a given system.

Statistical methods generally attempt to predict fleet durability using limited data. In other words, the likelihood that response amplitudes will be above a critical value is determined, often through the use of Monte Carlo simulations. With Monte Carlo simulations, mistuning is introduced in a system as a random variable, and the statistics of the forced response are determined. Thousands of simulations may be necessary to obtain accurate results, which can become computationally expensive and time consuming, especially for full finite element models of realistic bladed disks. As a result, reduced-order modeling techniques based on cyclic symmetric finite element models have been developed to reduce the computational effort in modeling mistuned response. Two primary methods have evolved. The first uses the concept of component mode synthesis, in which the bladed disk is divided into blade and disk portions which are modeled separately ([2,3]). This provides a convenient way to introduce mistuning of individual blades. The second reduced-order method computes the mistuned modes of the system as a linear combination of the nominal tuned system modes ([4]). This method is convenient since it uses the results from a cyclic symmetric finite element model with no additional modeling requirements. Bladh et al. [5,6] recently introduced a similar technique, using a Craig-Bampton component mode synthesis to obtain the tuned system modes.

Other recent ideas that have received attention are intentional mistuning and harmonic mistuning. Intentional mistuning refers to a systematic introduction of variations in particular system properties to obtain a desired response. Harmonic mistuning is significant because the periodicity of the system requires that any pattern of perturbations in system properties be decomposable into Fourier components. Mignolet et al. [7] examined harmonically mistuned oscillator models, and determined that the harmonically mistuned systems exhibited many of the same qualities as their randomly mistuned counterparts. Castanier and Pierre [8] considered the effect of intentional mistuning with harmonic patterns on forced response, and in a related paper ([9]) discussed the implications of such mistuning on the sensitivity of forced response to additional random mistuning.

In this paper, the concept of harmonic mistuning is used as an approach to help understand the sensitivity problem. A continuous model of a ring is developed to model a mistuned bladed disk. The ring model is similar to that used by Huang [10]. Mistuning is introduced in the model by harmonically varying the stiffness of a continuous ring-to-ground shear spring. The sensitivity of the ring's response to single-harmonic mistuning patterns is studied to gain insight into the physical mechanisms behind the sensitivity, and then the approach is generalized to include any number of harmonics in the mistuning pattern. This model is used to investigate maximum forced response on a bladed disk.

A goal of this research is to explore how to mistune a given

Contributed by the International Gas Turbine Institute (IGTI) of THE AMERICAN SOCIETY OF MECHANICAL ENGINEERS for publication in the ASME JOURNAL OF ENGINEERING FOR GAS TURBINES AND POWER. Paper presented at the International Gas Turbine and Aeroengine Congress and Exhibition, New Orleans, LA, June 4–7, 2001; Paper 2001-GT-274. Manuscript received by IGTI, Dec. 2000, final revision, Mar. 2001. Associate Editor: R. Natole.

system so that its forced response is both maximized and robust to small additional mistuning. Robustness means that small random mistuning due to manufacturing tolerances or inaccuracies in measuring blade characteristics will have little impact on the forced response of the system, making the response predictable. Maximizing the response of a bladed disk provides a test case for screening new designs or for establishing root cause for fatigue problems with existing designs. Moreover, the robustness of the maximum response means that such test results truly represent the worst-case scenario for that design.

Single Harmonic Mistuning

Formulation. For this study, a bladed disk is modeled as a continuous ring with motion only in the circumferential direction, Fig. 1, similar to that of Huang [10]. The stiffness of the blades is modeled by a continuous shear spring, with stiffness κ^* and units of force/length squared. The stiffness will later be varied to introduce mistuning. The equation of motion for the ring is

$$\frac{1}{c^2}\frac{\partial^2 u}{\partial t^2}=\frac{1}{R^2}\frac{\partial^2 u}{\partial \theta^2}-\kappa u+f, \tag{1}$$

where c is the wave speed of the ring material, R is the radius of the ring, f is an applied distributed force, u is the displacement of the ring, and θ is the angular coordinate. The stiffness $\kappa=\kappa^*/EA$ is a normalized form of κ^*, where E represents the elastic modulus of the ring material and A is the cross-sectional area of the ring. It can be shown that (1) is equivalent to the equations of motion for the harmonic oscillator model often used in the literature, Fig. 2 (see for example [7,11]).

To represent N discrete blades, the continuous series of shear springs is discretized into N segments at angular positions $\theta_j=j\Delta\theta$, where $\Delta\theta=2\pi/N$. A finite central difference approximation is used for the second derivative of u with respect to θ. To obtain a possible equation of motion, mass is needed as the coefficient of $\partial^2 u_j/\partial t^2$. The mass of a single segment is $m=\rho AR\Delta\theta$, where ρ is the density of the ring material. Therefore, mass is obtained by replacing c^2 with E/ρ, the elastic modulus divided by density, and multiplying through by $EAR\Delta\theta$. Defining the blade stiffness, $k_j=EAR\Delta\theta\kappa_j$, the coupling stiffness, $k_c=EA/R\Delta\theta$, and the force term, $F_j=EAR\Delta\theta f_j$, leads to

$$m\frac{d^2u_j}{dt^2}+k_ju_j+2k_cu_j-k_c(u_{j+1}+u_{j-1})=F_j. \tag{2}$$

This equation is identical to the equation of motion jth mass in the harmonic oscillator, Fig. 2, with damping $c_j=0$, which is consistent with the derivation for the ring (see Eq. (1) of [7]). Therefore, the ring model should demonstrate physical behavior analogous to that of the discrete mass-spring system, which is often used to model a single family of modes in a mistuned bladed disk.

The natural modes of the system can be obtained by solving the homogeneous problem, $f=0$. The shear spring stiffness is allowed to vary harmonically in θ, $\kappa(\theta)=\kappa_0(1+\varepsilon\cos n\theta)$, where n represents the harmonic wave number of the mistuning pattern and ε is the amplitude of the perturbation in the tuned stiffness κ_0. Using separation of variables and defining

$$\alpha=(R^2\omega^2/c^2)-R^2\kappa_0 \tag{3}$$

yields the equation for the mistuned natural modes of the ring,

$$\frac{d^2U(\theta)}{d\theta^2}+(\alpha-R^2\kappa_0\varepsilon\cos n\theta)U(\theta)=0. \tag{4}$$

Equation (4) is a form of the well-known Mathieu equation ([12]).

Modes of a Harmonically Mistuned System. The modal Eq. (4) is solved using two techniques. First, a perturbation solution is obtained that is valid for small mistuning. Its value is that it gives relatively simple, analytical expressions for how mistuning affects the modes. Thus, the perturbation solution can be used to identify how different physical mechanisms such as frequency splitting and mode distortion contribute to the response. Secondly, the modes are calculated using a truncated matrix approach that converges to the exact solution for all values of mistuning perturbation ε.

In the perturbation solution the eigenvalues α and the eigenfunctions U are assumed to be of the form

$$\alpha_j=\alpha_j^{(0)}+\varepsilon\alpha_j^{(1)}+\varepsilon^2\alpha_j^{(2)}+\varepsilon^3\alpha_j^{(3)}+\ldots \tag{5}$$

$$U_j=U_j^{(0)}+\varepsilon U_j^{(1)}+\varepsilon^2U_j^{(2)}+\varepsilon^3U_j^{(3)}+\ldots. \tag{6}$$

The expressions (5) and (6) are substituted in (4). The resulting problem is then solved using standard perturbation methods and the requirement that the individual functions $U_j(\theta)$ are periodic ([13]). The solution is shown here to first order in ε, resulting in three possible cases for α and U based on the relationship between j and n:

Case 1: $j=0$.

$$\alpha_0=0 \tag{7a}$$

$$U_0=A_0-\varepsilon\frac{R^2\kappa_0A_0}{n^2}\cos n\theta \tag{7b}$$

Case 2: $j=n/2$.

(a). Cosine mode.

$$\alpha_{n/2}^C=\frac{n^2}{4}+\frac{R^2\kappa_0}{2}\varepsilon \tag{8a}$$

$$U_{n/2}^C=A_{n/2}\cos\frac{n}{2}\theta-\varepsilon\frac{R^2\kappa_0A_{n/2}}{4n^2}\cos\frac{3n}{2}\theta \tag{8b}$$

(b). Sine mode.

$$\alpha_{n/2}^S=\frac{n^2}{4}-\frac{R^2\kappa_0}{2}\varepsilon \tag{9a}$$

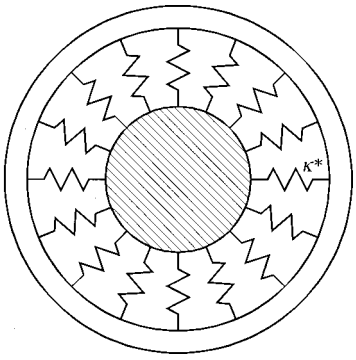

Fig. 1 Circular ring with a continuous ring-to-ground shear spring

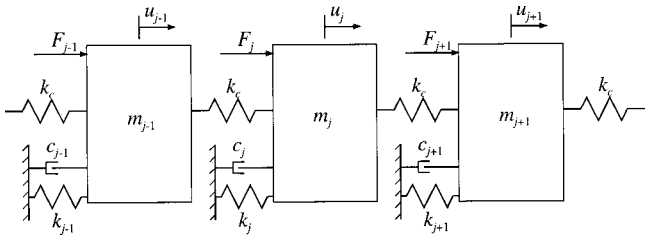

Fig. 2 Discrete mass-spring model of bladed disks

$$U^S_{n/2} = B_{n/2} \sin\frac{n}{2}\theta - \varepsilon \frac{R^2\kappa_0 B_{n/2}}{4n^2} \sin\frac{3n}{2}\theta \tag{9b}$$

Case 3: $j \notin \{0, n/2\}$.

$$\alpha_j = j^2 \tag{10a}$$

$$U_j = A_j \cos j\theta + B_j \sin j\theta + \varepsilon R^2\kappa_0 \left\{ \frac{1}{2n(2j-n)} [A_j \cos(j-n)\theta + B_j \sin(j-n)\theta] - \frac{1}{2n(2j+n)} [A_j \cos(j+n)\theta + B_j \sin(j+n)\theta] \right\} \tag{10b}$$

Examination of this solution yields significant insight into the frequency splitting and mode distortion phenomena that characterize mistuning. Frequency splitting refers to when the natural frequencies of a complimentary pair of modes, which are repeated in a tuned system, separate and are no longer equal, as indicated by (8*a*) and (9*a*). First, frequency splitting is seen to occur when $j = n/2$, or when the mistuning has a harmonic component n which is twice the number of nodal diameters j in the mode. For instance a 4th nodal diameter mode will split for mistuning harmonic component $n = 8$. In general, splitting will occur when j is any integer multiple of $n/2$ ([14]). If general mistuning is represented by a Fourier series, it is these components of the Fourier series which will result in frequency splitting.

Mode distortion occurs as the result of additional harmonic terms in the solution. The harmonic content of the modes is consistent with Huang [10] and Kim et al. [14]. Such mode distortion is important in two respects. First, mode distortion is associated with localization, in which the energy of the modal response is restricted to a small region of the bladed disk. Second, mode distortion means that the mode may be excited by forcing functions of more than one engine order. Conversely, a single-engine order excitation may excite several modes in a family.

The second solution technique assumes that the eigenfunctions will be of the form of a Fourier series,

$$U = \sum_{j=0}^{\infty} A_j \cos j\theta + B_j \sin j\theta. \tag{11}$$

Substituting this into (4) and using orthogonality results in a number of expressions involving the Fourier coefficients A_j and B_j. For cosine modes, the following expressions are obtained:

$$(\alpha - j^2)A_j - R^2\kappa_0\varepsilon(A_{n-j} + A_{n+j})/2 = 0, \quad j < n \tag{12a}$$

$$(\alpha - j^2)A_j - R^2\kappa_0\varepsilon(A_0 + A_{2j})/2 = 0, \quad j = n \tag{12b}$$

$$(\alpha - j^2)A_j - R^2\kappa_0\varepsilon(A_{j-n} + A_{n+j})/2 = 0, \quad j > n. \tag{12c}$$

Similar expressions are found for the sine modes in terms of B_j. If the number of terms in the series is limited, $j \leqslant M$ for integer M, these expressions can be written in matrix form,

$$\mathbf{Ax} = \mathbf{0}, \tag{13}$$

where $\mathbf{x} = \{A_0 A_1 B_1 \ldots A_M B_M\}^T$. The eigenvalues of the matrix are α, which have the same definition as before. The eigenvectors are vectors of the Fourier coefficients for each mode. This technique, called the truncated matrix approach, is mathematically equivalent to the subset of nominal modes reduced-order modeling technique developed by Yang and Griffin [4] and results in a representation of the modes of the ring that rapidly converges to the exact solution as M increases.

Sensitivity of Forced Response to Mistuning of a Single Harmonic. This section uses the results from the previous section to investigate the sensitivity of forced response to single harmonic mistuning patterns. With the engine order of the excitation E and the mistuning harmonic n held constant, the mistuning perturbation amplitude ε was incremented, and a forced response analysis was performed by summing the modal response. Proportional damping was assumed, with the modal damping ratio approximately equal to 0.003 for each mode. In the simulations, the frequency was incremented in sufficiently small intervals so that the error in the peak amplitude was less than 1%. The maximum response at any point on the ring was determined over the range of frequencies, and the ratio of this response amplitude to the tuned response amplitude, $u_{\max}/u_{\text{tuned}}$, was calculated.

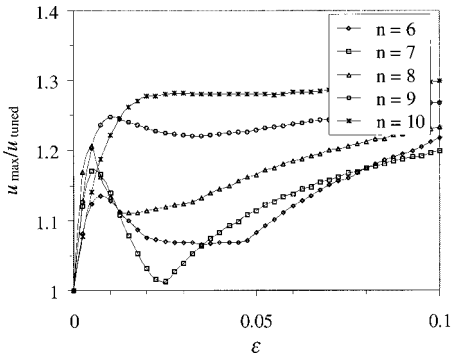

Fig. 3 Mistuned response sensitivity curves

The maximum response of the system is plotted in Fig. 3 as a function of perturbation amplitude ε for several n with $E = 4$. The slopes of these curves indicate the sensitivity of the system to mistuning in a particular harmonic. Some important observations can be made from the figure. First, nearly all of the sensitivity curves exhibit a steep slope near $\varepsilon = 0$, indicating the inherent sensitivity of nearly tuned systems. However, the curves all show other regions where the slope is small or zero. These regions are relatively insensitive to additional mistuning perturbations, at least in the harmonic component indicated. Finally, the harmonic component $n = 2E$ produced the steepest initial slope in the response curves. This corresponds to a response in the $j = n/2$ splitting modes, indicating that these modes are the most sensitive to small mistuning for the assumed damping. The harmonics just above and below this, $n = 2E + 1$ and $n = 2E - 1$, gave the next highest sensitivity to small mistuning, as indicated by the slopes of these curves for small ε. Initial sensitivity tended to decrease as n moved away from $2E$. Although the results shown in the figure are for $E = 4$, these were found to be true in general.

The mechanics behind the response of the $j = n/2$ splitting modes were further investigated by repeating the sensitivity analysis for $E = 4$, $n = 8$ while truncating various terms in the modal equations. The results are shown in Fig. 4. Using the "exact" solution from the truncated matrix as a basis for comparison, the

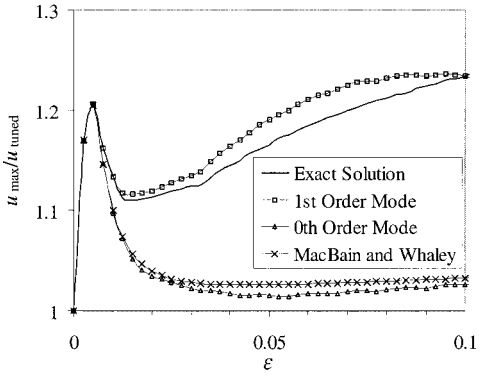

Fig. 4 The effects of various terms on the solution for splitting modes

effects of limiting the terms included in the response can be seen in the other curves. First, the response was truncated to include only the $j=n/2$ split modes. The first-order perturbation solution with only these modes agrees relatively well with the truncated matrix solution over the range of ε considered. This indicates that the sensitivity of the response of the split modes is dominated by a single-mode pair and by the first-order terms in these modes. The modes were then truncated to zeroth order, eliminating the dependence of the mode shape on ε. This curve is also plotted in Fig. 4. It predicts the quick peak and drop in amplitude for small ε, but does not predict the subsequent increase in response as ε grows.

These results give an explanation of the mechanisms at work in the sensitivity of splitting modes. The response consists primarily of two modes, the split sine and cosine modes corresponding to $j=n/2$. The initial high slope and peak occur solely because of frequency splitting, which means the sine and cosine modes can no longer combine into a pure traveling wave response. However, as ε continues to increase, the higher-order terms, which represent distortion in the mode, become more important. This leads to the increasing response for $\varepsilon>0.01$.

The results for the splitting modes were compared with the results of MacBain and Whaley [15], who used a receptance approach to develop a simple expression for the maximum response of the splitting modes in terms of a non-dimensional parameter S/ζ. This parameter represents the ratio of the amount that the natural frequencies are split to the damping in the system (see Eq. 21 of [15]). The comparison is also shown in Fig. 4. For this comparison, the frequency split was calculated in terms of ε using the truncated matrix solution for the natural frequencies, and the damping ratios were assumed to be the same as before. The initial peak in the response agrees exactly with their result, though the two solutions diverge immediately after that initial peak. This is to be expected, however, because MacBain and Whaley did not include any distortion terms in the expression for the modes. The result from the zeroth-order truncated solution, which likewise has no distortion terms, can be seen to agree quite well with MacBain and Whaley. It should also be noted that the maximum amplitude magnification agrees with the numerical results of Ewins [16]. From this analysis, it can be shown that the sensitivity of the splitting modes is inversely proportional to the damping as the mistuning goes to zero.

The sensitivity of modes that do not split must also be considered. Because the harmonic mistuning patterns around $n=2E$ produced the most sensitive response, Fig. 3, these will be used to examine the sensitivity of nonsplitting modes to mistuning. It is assumed that for a lightly damped system, only a single-mode pair will respond significantly at a particular frequency, which is consistent with the results for splitting modes. Therefore, only a single mode pair j will be considered. Introducing the harmonic pattern $n=2E+z$, where z is a positive integer, and truncating the modes in (10*b*) to include only the dominant terms in the modes with $2n(2j-n)$ in the denominators leads to expressions for the cosine and sine modes,

$$U_E^C = A_E[\cos E\theta - \beta\cos(E+z)\theta], \tag{14a}$$

$$U_E^S = B_E[\sin E\theta + \beta\sin(E+z)\theta], \tag{14b}$$

where

$$\beta = -\frac{\varepsilon R^2\kappa_0}{2n(2E-n)} \tag{15}$$

represents the amount of harmonic distortion in the mode. The coefficients A_E and B_E are found by normalizing the modes so that their lengths are unity.

$$A_E = B_E = 1/\sqrt{\pi(1+\beta^2)} \tag{16}$$

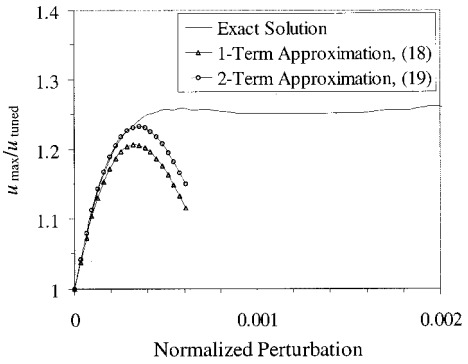

Fig. 5 Forced response approximation for nonsplitting modes

Calculating the forced response for an engine order E excitation, determining the point θ on the disk where the maximum response occurs, and using (16), an expression for the maximum mistuned response of an undamped disk is

$$u_{max} = \frac{f_0}{\omega_E^2-\omega^2}\left(\frac{1+\beta}{1+\beta^2}\right), \tag{17}$$

where f_0 is the amplitude of the exciting force, ω_E is the natural frequency of the $j=E$ mode, and ω is the excitation frequency. Noting that the tuned response is $u_{tuned}=f_0/(\omega_E^2-\omega^2)$, a simple expression for the amplitude magnification is obtained.

$$\frac{u_{max}}{u_{tuned}} = \frac{1+\beta}{1+\beta^2} \tag{18}$$

The expression for the amplitude magnification can be further refined by including both of the first-order terms in the analysis. Following the same procedure, the expression

$$\frac{u_{max}}{u_{tuned}} = \frac{1+(1+\eta)\beta}{1+(1+\eta^2)\beta^2} \tag{19}$$

is obtained, where

$$\eta = z/(4E+z). \tag{20}$$

These approximations are compared to computed sensitivity data in Fig. 5 for $n=2E+2$, $E=6$. To facilitate the comparison, the perturbation ε is normalized to correspond to a given j and n by dividing by the denominator of (15). Furthermore, β in (18) and (19) is normalized on the abscissa by dividing by $R^2\kappa_0$. In this way, these results can be applied generally to any system with given $R^2\kappa_0$ for mode j and harmonic n mistuning. It is clear in the figure that the approximate expressions do a good job of predicting both the initial slope of the sensitivity curve and the initial peak value. In addition, the improvement in the agreement achieved by adding the additional term suggests that the disagreement seen is due to truncation error. Comparable agreement was seen in the approximations for nonsplitting modes for all $n>2E$. A similar approach was taken to obtain expressions for $n<2E$. It should be noted that damping does not appear in the expressions for the response due to mode distortion.

These results are significant in several ways. First, a single mistuned mode pair can generally be used to study mistuning sensitivity for small perturbations ε. Second and perhaps more importantly, the initial sensitivity and peak in response as a function of ε are governed by first-order terms in the solutions for the modes. This suggests that a linear superposition can be used to include additional harmonics in the mistuning pattern and in the modes. The simplified modes can then be used to investigate maximum mistuned response for small mistuning. Finally, the

sensitivity of the forced response in splitting modes depends on damping, but damping has no direct effect on the sensitivity of the response in distorted modes that do not split.

Multiple Harmonic Mistuning

Formulation of Modes. Clearly, mistuning in general is not limited to variation patterns with only one harmonic component. As a result, multiple harmonics must be included in the mistuning pattern to understand general mistuned response. With a single harmonic perturbation pattern, the modes of the system satisfy the Mathieu Eq. (4). To include additional harmonics, the perturbation term is expanded into a Fourier cosine series including phase,

$$\frac{d^2U(\theta)}{d\theta^2}+\left[\alpha+\varepsilon R^2\kappa_0\left(\sum_{m=1}^{M}\delta_m\cos(m\theta-\phi_m)\right)\right]U(\theta)=0, \tag{21}$$

where $M=N/2$ if the number of blades N is even or $(N-1)/2$ if N is odd. Here, a single perturbation parameter ε is retained to allow for a proper perturbation solution. The Fourier coefficient δ_m scales the perturbation for each individual harmonic, and ϕ_m is the phase. The inclusion of the phase angle precludes the use of sine terms in the series expansion. The eigenvalue α is the same as in (3).

Substituting the power series expansion for α and U, (5) and (6), into (21) and isolating the various powers of ε results in a recursive system of ordinary differential equations for the perturbation terms, $U_j(\theta)$. As before, the solution was carried out to first order in ε, and different cases were determined based on the relationship between the mode j and the harmonic number m. The results are summarized below.

Case 1: $j=0$.

$$\alpha_0=0 \tag{22a}$$

$$U_0=A_0\left[1-\varepsilon R^2\kappa_0\sum_{m=1}^{M}\frac{\delta_m}{m^2}\cos(m\theta-\phi_m)\right] \tag{22b}$$

Case 2: $j=m/2$ *for Any Even* $\boldsymbol{m}$ *Where* $\delta_m\neq 0$.

(a) Cosine mode.

$$\alpha^C_{m/2}=j^2+\varepsilon\delta_{2j}R^2\kappa_0/2 \tag{23a}$$

$$U^C_{m/2}=A_{m/2}\left\{\cos j\theta-\varepsilon\frac{\delta_{2j}R^2\kappa_0}{16j^2}\cos 3j\theta-\varepsilon R^2\kappa_0\times\sum_{m\neq 2j}\delta_m\left[-\frac{1}{2m(j-m)}\cos((j-m)\theta+\phi_m)+\frac{1}{2m(j+m)}\cos((j+m)\theta-\phi_m)\right]\right\} \tag{23b}$$

(b) Sine mode.

$$\alpha^S_{m/2}=j^2-\varepsilon\delta_{2j}R^2\kappa_0/2 \tag{24a}$$

$$U^S_{m/2}=B_{m/2}\left\{\sin j\theta-\varepsilon\frac{\delta_{2j}R^2\kappa_0}{16j^2}\sin 3j\theta-\varepsilon R^2\kappa_0\times\sum_{m\neq 2j}\delta_m\left[-\frac{1}{2m(j-m)}\sin((j-m)\theta+\phi_m)+\frac{1}{2m(j+m)}\sin((j+m)\theta-\phi_m)\right]\right\} \tag{24b}$$

Case 3: $j\notin\{0,m/2\}$.

$$\alpha_j=j^2 \tag{25a}$$

$$U_j=A_j\cos j\theta+B_j\sin j\theta+\sum_{m\neq 2j}\frac{\varepsilon\delta_m R^2\kappa_0}{2m(2j-m)}\times[A_j\cos((j-m)\theta+\phi_m)+B_j\sin((j-m)\theta+\phi_m)]-\sum_{m\neq 2j}\frac{\varepsilon\delta_m R^2\kappa_0}{2m(2j+m)}[A_j\cos((j+m)\theta-\phi_m)+B_j\sin((j+m)\theta-\phi_m)] \tag{25b}$$

Note that in the event of single harmonic mistuning, the solutions obtained here revert to the previous solution, (7)–(10). In fact, this solution is identical to the single harmonic case with additional harmonic terms linearly superimposed on the modes. Furthermore, the solution is consistent with the findings of Huang [10], who determined that for random mistuning the forced response depends on the $(m+j)$th and $(m-j)$th Fourier coefficients of the random mistuning parameter.

Forced Response and Maximum Response Magnification. In a manner analogous to the single harmonic mistuning case, the forced response is derived for a pair of nonsplitting modes with multiple harmonics in the mistuning pattern. These modes can arise in the case of an engine order E excitation if there is no $n=2E$ harmonic component in the Fourier decomposition of the mistuning pattern. Again, the modes are truncated to include the dominant first-order term for each harmonic, namely the $\cos((j-m)+\phi_m)$ term. Defining $\beta_m=\varepsilon\delta_m R^2\kappa_0/[2m(2j-m)]$, the $j=E$ modes can be expressed:

$$U^C_E=A_E\left[\cos E\theta+\sum_{m\neq 2E}\beta_m(\cos(E-m)\theta+\phi_m)\right], \tag{26a}$$

$$U^S_E=B_E\left[\sin E\theta+\sum_{m\neq 2E}\beta_m(\sin(E-m)\theta+\phi_m)\right]. \tag{26b}$$

The modes are normalized for unit length to find A_E and B_E, yielding

$$A_E=B_E=C=\left[\pi\left(1+\sum_{m\neq 2E}\beta_m^2\right)\right]^{-1/2}. \tag{27}$$

Using the same technique and nomenclature used to derive (17), an expression for the forced response of the system can be found.

$$u=\frac{\pi C^2 f_0}{\omega_E^2-\omega^2}\left[\cos(E\theta-\omega t)+\sum_{m\neq 2E}\beta_m\cos((E-m)\theta+\phi_m-\omega t)\right] \tag{28}$$

This result is similar to Chang and Wickert [17]. By inspection, the forced response is maximized at $\theta=0$, with ϕ_m chosen to be either zero or π so that the sign of $\beta_m\cos(\phi_m)$ is positive, giving terms with the same sign at $\theta=0$. This phase requirement is important. It physically means that the forced response is maximized when the harmonic components of the mistuning pattern are in phase or out of phase by 180 deg. The resulting mistuning pattern is symmetric about the blade that exhibits the strongest response, which is consistent with Whitehead [18]. As a consequence of this requirement, the harmonic components of the mode will also be in phase and reinforce the response. Using this result gives an expression for the amplitude of the maximum forced response on a disk with M harmonics in the mistuning pattern,

$$u_{\max}=\frac{\pi C^2 f_0}{\omega_E^2-\omega^2}\left[1+\sum_{m\neq 2E}\beta_m\right]. \tag{29}$$

With (27) and again using $u_{\text{tuned}}=f_0/(\omega_E^2-\omega^2)$, an expression for the amplitude magnification is obtained.

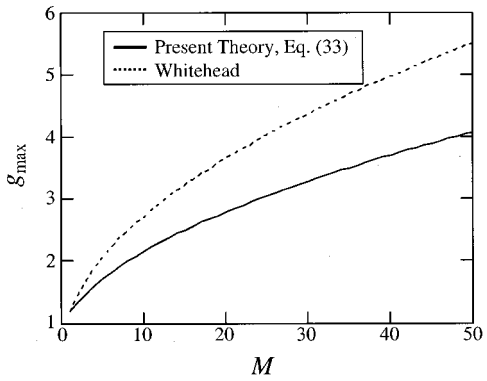

Fig. 6 Maximum amplitude magnification as a function of number of harmonics

$$\frac{u_{\max}}{u_{\text{tuned}}} = \frac{1+\sum_{m\neq 2E}\beta_m}{1+\sum_{m\neq 2E}\beta_m^2} \tag{30}$$

In the case of single harmonic mistuning, (30) reverts to (18).

The result in (30) provides an opportunity for calculating the worst possible response in a bladed disk due to mode distortion. It can be shown that in the range of β_m of interest for small mistuning, $0<\beta_m<1$, a local maximum is obtained if all β_m are equal, or for all $(p,q)\in\{0,1,\ldots,M\}$, $\beta_p=\beta_q=\beta$. Therefore, (30) becomes

$$g(\beta)=\frac{u_{\max}}{u_{\text{tuned}}}=\frac{1+M\beta}{1+M\beta^2}. \tag{31}$$

For a given M, the value of β giving the largest amplitude magnification is determined by maximizing g, resulting in an expression for the worst possible mistuning β^*,

$$\beta^*=(-1+\sqrt{1+M})/M. \tag{32}$$

Substituting this expression in (31) yields the value of the maximum possible amplitude magnification.

$$g_{\max}=(1+\sqrt{1+M})/2 \tag{33}$$

The behavior of the maximum response $g_{\max}$ is shown as a function of M in Fig. 6. The result of Whitehead [18,19] is also shown for comparison. Whitehead [18,19] predicted that the highest amplitude magnification possible was related to the number of blades N on the disk by

$$g_{\max}=(1+\sqrt{N})/2. \tag{34}$$

Since the maximum number of harmonics on the disk is $N/2$ for N even or $(N-1)/2$ for N odd, (34) can be approximated in terms of M by replacing N with $2M$, which is shown in the figure. As a result, the predicted worst-case amplitude magnification from Whitehead is greater than that predicted here in (33) by a factor of approximately $\sqrt{2}$. The difference in the results arises because the expression derived by Whitehead is based on aerodynamic modes and assumes that the contribution from all tuned modes can sum in phase. The results derived here in (25*b*) indicate that this is not feasible for distorted structural modes. The sine (odd) and cosine (even) modes do not localize in the same location on the disk and cannot superpose their maxima in a single location. Sinha [20] used optimization methods to numerically determine the highest ''actual'' amplitude magnification for a ten bladed disk of 1.64 ($R2$ of Fig. 2 in [20]). This compares well with a value of 1.62 predicted by (33) when $M=4$ (the harmonic that causes splitting was eliminated). Similarly, Dye and Henry [21] found a highest magnitude amplification for a 43-bladed disk of 2.82, compared to a value of 2.74 using (33) with $M=19$. Note that both the $m=2j$ and the $m=j$ harmonics were eliminated for this result.

It should be observed that the expression (33) derived here for the maximum amplitude magnification does not necessarily indicate the maximum response that will occur in a real bladed disk. This expression is limited in three ways. First, the derivation of the modes and forced response expressions used to arrive at (33) assumed small mistuning, which allowed for the truncation of higher order terms in the modes. Thus the maximum obtained is a local maximum and a more severe response may be possible for larger mistuning. In addition, large mistuning may distort the modes sufficiently so that a different mode pair than that considered here dominates the response. Secondly, the system was assumed to be very lightly damped, so that only the contribution of a single pair of modes was considered. Finally, the model considered here is limited to only a single family of modes. For closely spaced families of modes, the contribution of another mode family may lead to a response greater than that predicted by this analysis.

Numerical Example and Robustness

The results of the previous section are demonstrated with a numerical example consisting of a discrete mass-spring model, Fig. 2. The example serves several practical purposes. First, it validates the results with a well-known model and shows that they apply for discrete representations of bladed disks as well as for the continuous system representation. In addition, it allows for a discussion of robustness. Since the maximum amplitude magnification represents a local maximum in forced response, this point should be relatively robust so that the sensitivity of the system to random mistuning about this point should be small.

The example problem represents a single mode family of a bladed disk with 24 blades. Each mass is set to unity. The other properties of the system are chosen so that the system is sensitive to mistuning. The response to an $E=4$ traveling wave excitation was determined for the system. Intentional mistuning was introduced in the system for maximum forced response according to the results of the previous sections. The number of harmonics in the system was determined based on the number of blades. In this case, with $N=24$ blades and disallowing harmonics which split the modes, the number of harmonics in the mistuning pattern is $M=10$. From this, the maximum amplitude magnification $g_{\max}=2.16$ was predicted from (33), and the optimum value of β^* to obtain this response was calculated from (32). The mistuning of each harmonic δ_m was determined from the definition of β_m and used as the input parameter for intentionally mistuning the system.

It was found that the forced response obtained by mistuning the system in this manner was approximately 21% lower than predicted. This was attributed to the truncation of terms in the modes to obtain the expressions in the previous section. As a result of the differences with the theory, an optimization routine was used to obtain the maximum forced response of the system. The routine, which is commercially available, uses a Nelder and Mead [22] simplex algorithm to maximize the forced response with respect to multiple inputs, the various harmonic components of mistuning. It was assumed that the phases of the input mistuning harmonics were zero in accordance with the results of the previous section. The harmonic mistuning components determined by the theory derived here were used as an initial guess for the optimization. After the optimization, the mistuning pattern resembled the initial guess from the theory except that the individual blade mistuning was greater. The maximum forced response found by the optimization algorithm was 1.98, which is bounded by the predicted maximum of 2.16 from the theory, (33). Furthermore, this numerical result is within 10% of the analytically predicted result. It should be noted that the optimization routine allowed frequency splitting, though it was found that mistuning in the harmonics which cause frequency splitting was generally small at the local maximum for the system.

Table 1 Maximum response amplitude magnification

Number of Blades	Numerical Result	Present Theory	Whitehead
12	1.42	1.72	2.23
18	1.70	1.91	2.62
24	1.98	2.16	2.95
30	2.22	2.37	3.24

The harmonic mistuning patterns corresponding to maximum forced response were obtained for a number of systems with various numbers of blades, and the amplitude magnification of the response of each system was calculated. The results are shown in Table 1. In addition, the amplitude magnification predicted by the expression developed here in (33) and that predicted by Whitehead [18,19] are shown. The amplitude magnification predicted by the theory presented here can be seen to provide an upper bound on the actual maximum response, but the value of the response is closer to the numerical result than that of Whitehead. In addition, the agreement between the numerically obtained maximum and the predicted maximum improve as the number of blades increases. This probably occurs because a higher number of blades in the discrete system more closely represents the continuous system for which the theoretically predicted maximum was derived.

The maximum forced response provides a local extremum with respect to all harmonic mistuning components. This means that the gradient of the response with respect to the harmonic mistuning components is zero. Thus, the maximum forced response is robust with respect to small random mistuning in addition to the intentional mistuning, which can occur in a real system as a result of manufacturing tolerances, wear, or error in measuring system parameters.

The robustness of the system intentionally mistuned for maximum forced response was investigated by examining how the variation in the response changes with the variation in the stiffness. Monte Carlo simulations were performed in which small random stiffness variations were projected onto the intentionally mistuned baseline system. The standard deviation of the response for 1000 simulations was determined for a given standard deviation in stiffness and normalized by the expected response value to obtain a percent standard deviation in the response. Finally, this result was normalized by the standard deviation of mistuning to obtain the relative variation of the response. If the response variation is thought of as a function of the stiffness variation, this quantity represents the slope of the function, and serves as a direct measure of the sensitivity of the system. The results of this analysis are shown for a range of stiffness variations in Fig. 7.

It can be seen in Fig. 7 that the relative variation in the response decreases significantly when the random variation in the stiffness is reduced for the intentionally mistuned system. This does not occur for the tuned system. The relative variation in the response remains approximately constant for the tuned system as the variation in the random mistuning is reduced. Therefore, the sensitivity of the intentionally mistuned system to small random mistuning is much less than the sensitivity of the tuned system, indicating that the intentionally mistuned system is robust with respect to small random mistuning.

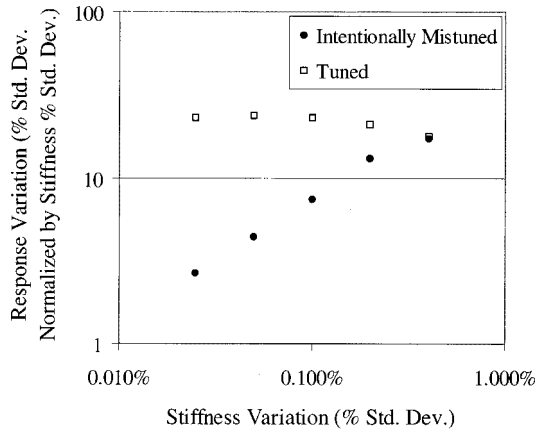

Fig. 7 Reduction in sensitivity near worst-case mistuning

Conclusions

A continuous model of turbine engine bladed disks has been developed and shown to be equivalent to mass-spring models that have been used extensively in the literature. Two solution methods, the perturbation solution and the truncated matrix approach, were developed to determine the natural modes of the system. The advantage of the perturbation solution is that it provides simple algebraic expressions for the natural frequencies and modes of the system as a function of mistuning amplitude, mistuning harmonic number, and mode wave number. The truncated matrix approach gives very accurate representations of the modes.

The primary mechanisms behind amplitude magnification in mistuned bladed disks have been explored. In cases when the mistuning causes the natural frequencies of a mode pair to split, this splitting determines the sensitivity of the system to small mistuning, since the sine and cosine modes cannot combine into a pure traveling wave response. For those modes in which the frequencies do not split, distortion in the mode shape leads to amplitude magnification. In either case, mistuned response for small mistuning is dominated by first-order terms. This indicates that linear superposition of first-order harmonic components may be used to obtain the modes for multiple harmonic mistuning. Furthermore, in lightly damped systems such as bladed disks, only a single-mode pair in a family must be considered to obtain a reasonable estimate of the effect of mistuning on response. These results significantly simplify the analysis when multiple harmonics are considered.

The modes of the mistuned system with multiple harmonics in the mistuning pattern are similar to those of the system with single harmonic mistuning. Additional harmonics enter the mode through the linear superposition of additional harmonic terms in its Fourier expansion. The forced response of nonsplitting modes has been examined, and an expression was derived for the maximum amplitude magnification due to distortion of the structural modes from small mistuning. This maximum occurs with the harmonics in the mode superimposed in phase. Since extremely large forced response results from the superposition of numerous harmonics in the mistuned mode, this is a product of mode distortion rather than frequency splitting.

A simple numerical example using a discrete mass-spring system has been used to verify the results of this investigation. The continuous system result was used to estimate the mistuning pattern that would give rise to the maximum response. Using this estimate as an initial guess, an optimization algorithm was used to determine the blade stiffnesses that would give the maximum response. After optimization, the response was within 10% of the analytically predicted maximum. Similar agreement between numerical results and analytically predicted response maxima was demonstrated for bladed disk systems with various numbers of blades.

The response of an intentionally mistuned worst-case system was shown to be robust. In general, robustness is a desirable feature since it insures that the response is predictable. For the intentionally mistuned bladed disk considered here, the response is much greater than that of the tuned system, which often may not be practical. However, robust maximum response can be useful in some circumstances. Since the known response represents the worst possible response for a nominal system, this provides an ideal way to develop a trial case for screening new bladed disk designs or for establishing root cause for existing fatigue prob-

lems. Because of the robustness of the response, a bladed disk produced in this manner truly represents the worst case that will be seen in a fleet of engines.

Acknowledgments

The authors wish to acknowledge the contribution of Mr. C. Li, whose initial exploratory research in this area during his M.S. program at Carnegie Mellon University provided a convenient and useful starting point for the work described in this paper.

References

[1] Srinivasan, A. V., 1997, ''Flutter and Resonant Vibration Characteristics of Engine Blades,'' ASME J. Eng. Gas Turbines Power, **119**(4), pp. 742–775.
[2] Kruse, M. J., and Pierre, C., 1996, ''Forced Response of Mistuned Bladed Disks Using Reduced-Order Modeling,'' *Proceedings of the 37th AIAA/ASME/ASCE/AHS/ASC Structures, Structural Dynamics, and Materials Conference*, Salt Lake City, UT, AIAA, Washington, DC, **4**, pp. 1938–1950.
[3] Yang, M.-T., and Griffin, J. H., 1997, ''A Reduced Order Approach for the Vibration of Mistuned Bladed Disk Assemblies,'' ASME J. Eng. Gas Turbines Power, **119**, pp. 161–167.
[4] Yang, M.-T., and Griffin, J. H., 2001, ''A Reduced Order Model of Mistuning Using a Subset of Nominal System Modes,'' ASME J. Eng. Gas Turbines Power, **123**, pp. 893–900.
[5] Bladh, R., Castanier, M. P., and Pierre, C., 2000, ''Component-Mode-Based Reduced Order Modeling Techniques for Mistuned Bladed Disks, Part I: Theoretical Models,'' ASME Paper No. 2000-GT-0360.
[6] Bladh, R., Castanier, M. P., and Pierre, C., 2000, ''Component-Mode-Based Reduced Order Modeling Techniques for Mistuned Bladed Disks, Part II: Application,'' ASME Paper No. 2000-GT-0360.
[7] Mignolet, M. P., Hu, W., and Jadic, I., 2000, ''On the Forced Response of Harmonically and Partially Mistuned Bladed Disks. Part I: Harmonic Mistuning,'' Int. J. Rotating Mach., **6**(1), pp. 29–41.
[8] Castanier, M. P., and Pierre, C., 1997, ''Consideration on the Benefits of Intentional Blade Mistuning for the Forced Response of Turbomachinery Rotors,'' *Proceedings of the 1997 ASME International Mechanical Engineering Congress and Exposition*, **AD-55**, ASME, New York, pp. 419–425.
[9] Castanier, M. P., and Pierre, C., 1998, ''Investigation of the Combined Effects of Intentional and Random Mistuning on the Forced Response of Bladed Disks,'' AIAA Paper No. 98-3720.
[10] Huang, W.-H., 1982, ''Vibration of Some Structures With Periodic Random Parameters,'' AIAA J., **20**(7), pp. 1001–1008.
[11] Wei, S.-T., and Pierre, C., 1988, ''Localization Phenomena in Mistuned Assemblies With Cyclic Symmetry, Part I: Free Vibrations,'' ASME J. Vib., Acoust., Stress, Reliab. Des., **110**, pp. 429–438.
[12] Abramowitz, M., and Stegun, I. A., ed., 1964, *Handbook of Mathematical Functions With Formulas, Graphs, and Mathematical Tables*, National Bureau of Standards Applied Mathematics Series, 55, U.S. Department of Commerce, Washington, D. C., reprint (1968), pp. 721–746.
[13] Nayfeh, A. H., 1981, *Introduction to Perturbation Techniques*, John Wiley and Sons, New York, pp. 234–247.
[14] Kim, M., Moon, J., and Wickert, J. A., 2000, ''Spatial Modulation of Repeated Vibration Modes in Rotationally Periodic Structures,'' ASME J. Vibr. Acoust., **122**(1), pp. 62–68.
[15] MacBain, J. C., and Whaley, P. W., 1984, ''Maximum Resonant Response of Mistuned Bladed Disks,'' ASME J. Vib., Acoust., Stress, Reliab. Des., **106**, pp. 218–223.
[16] Ewins, D. J., 1969, ''The Effects of Detuning upon the Forced Vibrations of Bladed Disks,'' J. Sound Vib., **9**(1), pp. 65–79.
[17] Chang, J. Y., and Wickert, J. A., 2001, ''On the Response of Modulated Doublet Modes to Traveling Wave Excitation,'' J. Sound Vib., **242**, pp. 69–83.
[18] Whitehead, D. S., 1998, ''The Maximum Factor by Which Forced Vibration of Blades Can Increase Due to Mistuning,'' ASME J. Eng. Gas Turbines Power, **120**, pp. 115–119.
[19] Whitehead, D. S., 1966, ''Effect of Mistuning on the Vibration of Turbomachine Blades Induced by Wakes,'' J. Mech. Eng. Sci., **8**(1), pp. 15–21.
[20] Sinha, A., 1997, ''Computation of the Maximum Amplitude of a Mistuned Bladed Disk Assembly via Infinity Norm,'' *Proceedings of the 1997 ASME International Mechanical Engineering Congress and Exposition*, **AD-55**, ASME, New York, pp. 427–432.
[21] Dye, R. C. F., and Henry, T. A., 1969, ''Vibration Amplitudes of Compressor Blades Resulting from Scatter in Blade Natural Frequencies,'' ASME J. Eng. Power, **91**, pp. 182–187.
[22] Nelder, J. A., and Mead, R., 1965, ''A Simplex Method for Function Minimization,'' Comput. J. (UK), **7**, pp. 308–313.

Effects of Multistage Coupling and Disk Flexibility on Mistuned Bladed Disk Dynamics

R. Bladh
Graduate Student

M. P. Castanier[1]
Assistant Research Scientist
e-mail: mpc@umich.edu

C. Pierre
Professor,
Fellow ASME

Department of Mechanical Engineering,
The University of Michigan,
2250 G. G. Brown Building,
Ann Arbor, MI 48109-2125

The effects of disk flexibility and multistage coupling on the dynamics of bladed disks with and without blade mistuning are investigated. Both free and forced responses are examined using finite element representations of example single and two-stage rotor models. The reported work demonstrates the importance of proper treatment of interstage (stage-to-stage) boundaries in order to yield adequate capture of disk-blade modal interaction in eigenfrequency veering regions. The modified disk-blade modal interactions resulting from interstage-coupling-induced changes in disk flexibility are found to have a significant impact on (a) tuned responses due to excitations passing through eigenfrequency veering regions, and (b) a design's sensitivity to blade mistuning. Hence, the findings in this paper suggest that multistage analyses may be required when excitations are expected to fall in or near eigenfrequency veering regions or when the sensitivity to blade mistuning is to be accounted for. Conversely, the observed sensitivity to disk flexibility also indicates that the severity of unfavorable structural interblade coupling may be reduced significantly by redesigning the disk(s) and stage-to-stage connectivity. The relatively drastic effects of such modifications illustrated in this work indicate that the design modifications required to alleviate veering-related response problems may be less comprehensive than what might have been expected. [DOI: 10.1115/1.1498267]

1 Introduction

Dynamic analyses of bladed disks or blisks found in turbomachinery rotors typically involve several idealizations of true conditions. Two such idealizations are of particular interest to the investigation reported in this paper: (a) spatial repetitiveness (cyclic symmetry) of a single rotor stage; and (b) isolated, dynamically independent rotor stages.

The cyclic characteristic (a) enables analysts to reduce both modeling and computational efforts considerably by modeling and analyzing a fundamental disk-blade sector, rather than the entire assembly. However, cyclic symmetry implies that all sectors are identical, i.e., that the system is tuned. Over the past decades, many researchers have conclusively shown that this assumption can be a potentially disastrous idealization of a bladed disk's true behavior—see for instance Wagner [1], Dye and Henry [2], Ewins [3,4], El-Bayoumy and Srinivasan [5], Irretier [6], and Wei and Pierre [7,8]. In reality, individual blades exhibit small structural differences—blade mistuning—which may stem from manufacturing and material tolerances or in-service wear. These variations destroy cyclic symmetry and thus require modeling the full bladed disk assembly. More importantly, mistuning may lead to qualitatively different dynamic behavior than that experienced by a perfectly tuned rotor. In particular, mistuning may inhibit the even distribution of vibration energy among blades, and therefore confine most of the energy to only a few blades. This way, mode shapes may become spatially localized, and some blades may experience forced response deflections that are much larger than those predicted by a tuned analysis.

Analyzing each stage independently in accordance with assumption (b) implies that the analyst must choose some boundary conditions that best describe the constraints imposed by adjacent stages. In current practice, this is typically dealt with by imposing either fully clamped conditions or axial restraints alone, or by modeling adjacent stages as uniformly distributed masses and stiffnesses (to preserve cyclicity). Such approximate constraints may well yield reasonable descriptions of the ''global'' vibration characteristics of a rotor stage in a multistage assembly. However, it may be suspected that the approximate boundary conditions will in general not accurately describe the disk flexibility locally at the interstage (stage-to-stage) boundaries. This will lead to inconsistent representations of the interaction between families of disk- and blade-dominated modes. The mixture of blade and disk dominance (i.e., the disk-blade modal interaction) in veering regions is a critically important factor in determining a design's sensitivity to mistuning. Studies by Wei and Pierre [8] and by Óttarsson and Pierre [9] show that the severity of vibration energy localization is to a large extent governed by the level of structural interblade coupling, which results from the disk-blade modal interaction. Thus, when considering a rotor design from a mistuning sensitivity point of view, misrepresentations of the disk flexibility and structural interstage coupling can potentially result in severely misguided conclusions.

The purpose of this paper is to make evident the importance of accurate interstage boundary modeling through inclusion of multistage effects. The multistage effects are demonstrated using finite element models of simplified example single and two-stage rotors. The paper describes important general implications of multistage coupling on the free and forced vibration characteristics of tuned and mistuned configurations. Its effect on the response in eigenfrequency veering regions is given particular attention, since the level of structural interblade coupling, and thus the mistuning sensitivity, are manifested by the local veering characteristics.

This paper is organized as follows. Section 2 introduces the simple finite element single and two-stage models used in this study. Section 3 illustrates and discusses general implications of multistage dynamics in the free and forced response, with and without blade mistuning. Section 4 demonstrates more specifically the impact of disk flexibility and structural interstage coupling on the forced response in eigenfrequency veering regions, by using

[1]To whom correspondence should be addressed.

Contributed by the International Gas Turbine Institute (IGTI) of the THE AMERICAN SOCIETY OF MECHANICAL ENGINEERS for publication in the ASME JOURNAL OF ENGINEERING FOR GAS TURBINES AND POWER. Paper presented at the International Gas Turbine and Aeroengine Congress and Exhibition, New Orleans, LA, June 4–7, 2001; Paper 2001-GT-277. Manuscript received by IGTI, Dec. 2000, final revision Mar. 2001. Associate Editor: R. Natole.

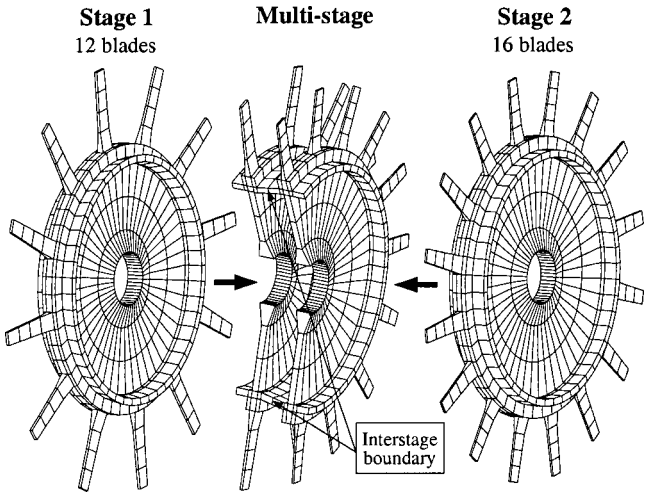

Fig. 1 Finite element meshes for the single and two-stage example rotor models

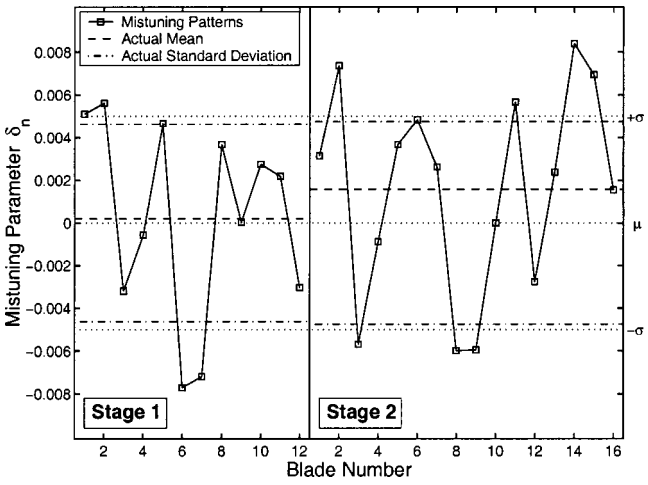

Fig. 2 Employed random blade mistuning patterns

single and multistage models with varying interstage boundary conditions and disk flexibility. Important findings and conclusions from this study are summarized in Section 5.

2 Description Of Example Models

Figure 1 depicts the simple example single and two-stage rotor models employed in this study. A portion of the multistage model has been cut out in Fig. 1 in order to better illustrate the assembled geometry. The models are constructed entirely from eight-noded brick (linear solid) elements. It should be noted that the stage geometries are very simple, and that the finite element meshes are very coarse, compared to those of typical industrial finite element models. Furthermore, the aspect ratio of the blades is unrealistically high for both stages. However, the modeled stages still exhibit the essential characteristics of realistic rotors, such as disk and blade-dominated mode families and their interactions (i.e., eigenfrequency veerings).

The stage 1 model features 12 blades, each with length 60 mm and base width 7.5 deg ($\sim$13 mm). The blades are slightly tapered along the radial direction, from 5-mm thickness at the base to 2-mm thickness at the tip. The stage 2 model features 16 blades, each with length 48 mm. The stage 2 blades are otherwise identical to those of stage 1. The stage 1 disk has an outer radius of 100 mm, while the outer radius of the stage 2 disk is 104 mm. Both disks have an inner radius of 20 mm, and both disks are clamped at their respective outward rims. The two stages are considered to be welded together at the interstage boundary. Moreover, a uniform structural damping coefficient of 0.5% is used for both stages in the forced response, while any viscous damping is assumed negligible.

For the mistuned results, a single random mistuning pattern is used for each stage with the mistuning parameter distribution depicted in Fig. 2. The two mistuning patterns were sampled from a uniform distribution of mean zero ($\mu=0$) and standard deviation 0.5% ($\sigma=0.005$), where one mistuning value, δ_n, is assigned to each blade. Note that a 0.5% standard deviation among the blade modal stiffnesses approximately corresponds to 0.25% standard deviation among blade natural frequencies. Blade mistuning is introduced to the finite element models by varying Young's modulus in the blade elements:

$$E_n=(1+\delta_n)E_o, \quad n=1, \ldots, N, \tag{1}$$

where n is the blade number and N is the total number of blades in the stage.

3 Features Of Multistage Response

Before proceeding to explore the free and forced response of multistage assemblies, one important feature of any multistage model first needs to be clarified. When studying coupled multistage models, the concept of ''tuned'' bladed disks becomes questionable. Typically, adjacent stages will not have the same number of blades (sectors), and the cyclicity and harmonic content of adjacent stages will therefore be incompatible. As a result, coupling of individual stages to form multistage rotors will inherently introduce some level of disorder to each stage, which will here be referred to as a stage-periodicity mismatch effect. This stage-periodicity mismatch effect can also be described as a form of ''disk mistuning,'' as opposed to the more commonly considered blade mistuning.

For the particular model used in this work, the effect of stage-periodicity mismatch is very small. In fact, although frequency pair splitting is readily observed, the relative frequency split induced by the stage mismatch is only on the order of 0.001% for the investigated model. As a result, ''tuned'' nodal diameter mode shapes are readily identified for both stages, while no circumferential mode localization is observed due to the stage-periodicity mismatch effect alone. Consequently, the notation ''tuned'' will therefore still be used in this work to denote cases where blade mistuning has not been added explicitly. Furthermore, note that the blade number combination of the employed two-stage model (12 and 16 blades) may be somewhat unusual in that the two stages share several nodal-diameter symmetries. In fact, the investigated two-stage model does exhibit cyclic symmetry. The model can be subdivided into four identical 90-deg sectors containing three stage 1 and four stage 2 blades each, and it will therefore behave as a complicated ''four-bladed'' rotor. As a result, the interstage coupling may be stronger and the stage-periodicity mismatch effect less pronounced for this model compared to models with more ''incompatible'' blade number combinations (e.g., prime numbers). Furthermore, note that the interstage coupling and thus the dynamic characteristics of the two-stage assembly should be different if the two stages are arbitrarily rotated with respect to each other.

3.1 Free Vibrations. An interesting, but not unexpected, result in the free vibrations of multistage assemblies is that most mode shapes are confined to either stage. While this is common for most modes, it is particularly apparent for blade-dominated modes. As illustrative examples, the deformed meshes pertaining to (a) a typical blade-dominated mode shape and (b) a typical disk-dominated mode shape that feature distinct stage 2 confinement are shown in Fig. 3. The relative stage participations for the lower modes of the investigated multistage model are plotted in

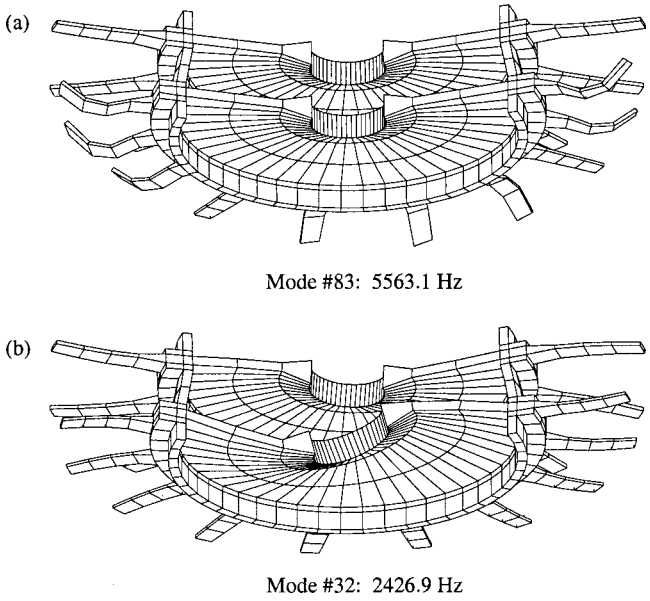

Fig. 3 Deformed finite element shapes for (*a*) a blade-dominated mode and (*b*) a disk-dominated mode, which are both confined to stage 2 (lower stage)

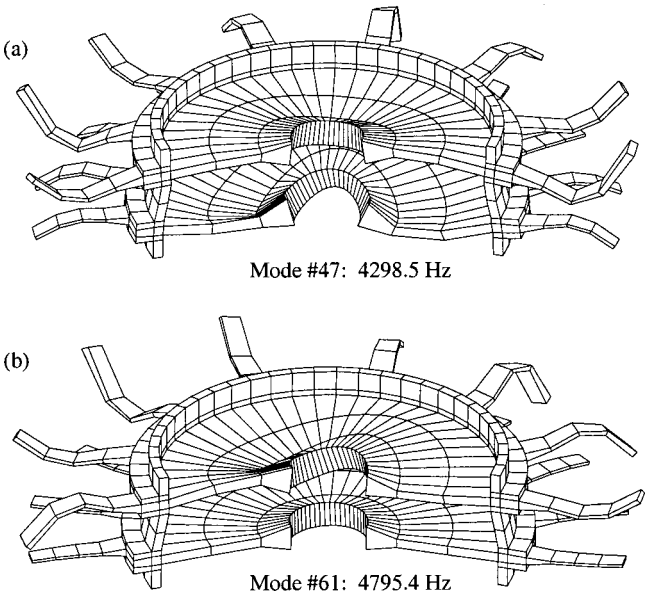

Fig. 5 Deformed finite element shapes for (*a*) a multistage system mode and (*b*) a mixed disk-blade mode confined to stage 1 (upper stage)

Fig. 4. The relative participation of stage i for the kth mode, R_k^i, is obtained from a stage-wise comparison of strain energies:

$$R_k^i = \frac{\mathbf{u_k^{i^T}} \mathbf{K_i} \mathbf{u_k^i}}{\sum_{p=1}^{M} \mathbf{u_k^{p^T}} \mathbf{K_p} \mathbf{u_k^p}}, \tag{2}$$

where $\mathbf{u_k^p}$ is the stage p portion of the kth mode shape; $\mathbf{K_p}$ is the stage p stiffness matrix; and M is the total number of stages. In this representation, it is clear that relatively few modes exhibit significant participation of both stages, which are here denoted system modes. In fact, for this model, system modes only occur when disk-dominated modes of both stages are relatively close in frequency. To physically illustrate these two fundamental mode types, one system mode and one stage-confined mode are depicted in Fig. 5. The system mode in Fig. 5(*a*) exhibits significant participation from both stages, where, interestingly, stage 1 (upper) features more blade-dominated motion and stage 2 (lower) displays more disk-dominated motion. Moreover, Fig. 5(*b*) illustrates a mixed disk-blade multistage mode shape that exhibits significant stage 1 confinement.

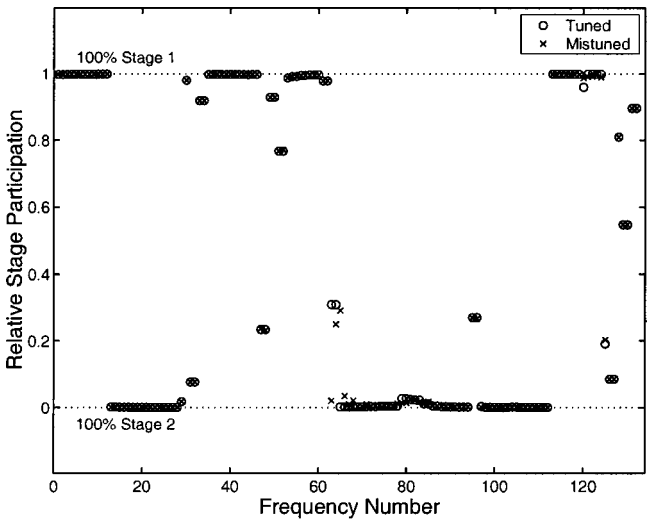

Fig. 4 Stage 1 strain energies relative to total multistage strain energies for "tuned" and blade mistuned multistage modes below 8000 Hz

It is further notable from Fig. 4 that the blade mistuning patterns employed in this particular case do not alter the stage participation factors to any significant degree. This stage participation ''invariance'' with respect to mistuning is likely a result of the strong confinement to either stage that is observed for the blade-dominated mode families of the investigated model. For other models, however, it is quite possible that significant stage-to-stage interaction could be observed for families of blade-dominated modes, if they are sufficiently close in frequency for two or more stages. In such cases, the effect of mistuning on stage participation may also become more pronounced.

The dynamic characteristics of single-stage tuned bladed disks are conveniently summarized in plots of natural frequencies versus the number of nodal diameters (harmonics), as shown in Figs. 6 and 7. The nearly horizontal connecting lines correspond to assembly modes that are dominated by blade motion. The characteristic blade motion of each family of blade-dominated modes is indicated on the right of Figs. 6 and 7, where F=Flexural; A=Axial (edgewise bending); and T=Torsion. Moreover, modes located on the slanted connecting lines are dominated by disk motion. The rapid increase of the eigenfrequencies of the disk-dominated modes is due to stiffening of the disk as the circumferential wavelength decreases with increasing number of nodal diameters.

For sufficiently low levels of stage-periodicity mismatch effects, the nodal-diameter representation of single-stage free-vibration characteristics may also be useful for multistage assemblies. Figure 8 illustrates the two ''tuned,'' blade-dominated, and stage-confined multistage mode shapes indicated in Figs. 6 and 7 (modes 54 and 83). The mode shapes are here represented by the normalized axial deflection for one node at each blade tip. Mode 54 is seen to exhibit significant stage 1 confinement, whereas mode 83 is confined to stage 2. Together with Figs. 3 and 5, Fig. 8 clearly illustrates the tuned-like spatially extended characteristic observed for the multistage mode shapes, despite the stage-periodicity mismatch. Hence, by examining the multistage mode

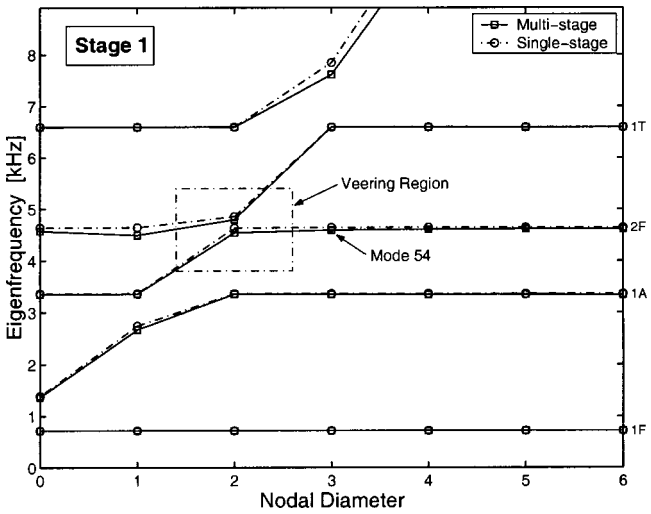

Fig. 6 Natural frequencies versus number of nodal diameters for the tuned stage 1 model with fixed interstage boundaries, and for the "tuned" multistage model for modes confined to stage 1

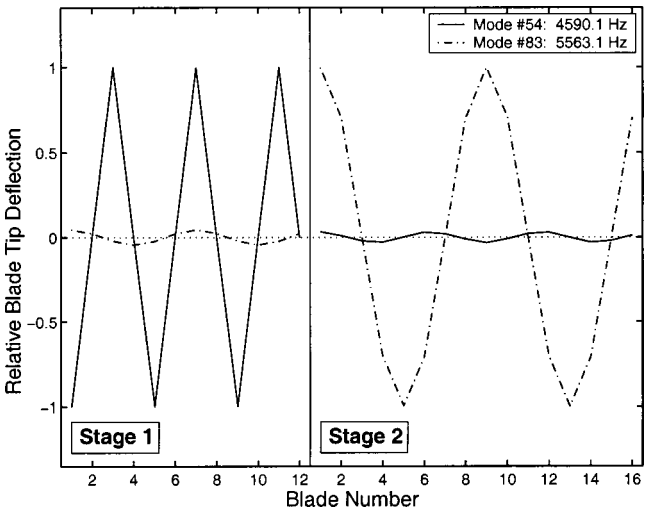

Fig. 8 "Tuned" multistage mode shapes 54 and 83

shapes with respect to stage participation, zero crossings (for nodal diameter designation), and, for certain particularly non-obvious system modes, single-stage versus multistage natural frequency proximity, the multistage modes could be divided into stage 1 and stage 2 frequencies as shown in Figs. 6 and 7. It should be noted that this identification process may be infeasible for more realistic models that may feature both more system modes and much more complex eigenfrequency veering regions. However, the stage identification is carried out here in order to better demonstrate the effect of interstage coupling relative to traditional single-stage analyses.

For the identified stage 1 multistage natural frequencies in Fig. 6, it is observed that the interstage coupling does not significantly alter the global characteristics from a clamped interstage single-stage representation. Clearly, however, the disk is more flexible in the multistage model, which is manifested by the slight shift downwards of the disk-dominated modes. In contrast, the blade-dominated modes are practically unchanged. The shift of disk-dominated modes is also observed for stage 2 in Fig. 7. For stage 2, however, the inclusion of multistage effects clearly has a more dramatic effect on the global characteristics as well. From having a group of three relatively close families of distinctly blade-dominated modes in the single-stage representation, the multistage model shows evidence of a second family of disk-dominated modes being present in the lower harmonics of this frequency range, due to the added disk flexibility. This second family of disk-dominated modes features one-nodal-diameter "softening" (i.e., a drop in natural frequency), which is observed for many rotor models (e.g., see Bladh et al. [10]). The result is a significant interaction at one nodal diameter between this second family of disk-dominated modes and all three blade-dominated mode families, which is not seen for the single-stage model. This is clearly a drastic change in the free-vibration characteristics that is certain to affect the stage 2 forced response for excitations in this region.

An important implication of the modified disk flexibility is that the characteristics of the eigenfrequency veerings are also modified. An example of an affected eigenfrequency veering region is highlighted in Fig. 6. This veering modification means that the mixture of blade and disk dominance (i.e., the disk-blade modal interaction) among the two mode pairs representing the veering is altered. As mentioned in the Introduction, this modification of the disk-blade modal interaction may have a critical impact on mistuning sensitivity. For instance, consider the mistuned single and multistage mode shapes in Fig. 9. The depicted modes correspond in natural frequency order to the tuned multistage mode shapes depicted in Fig. 8, but can otherwise only be compared qualitatively with tuned modes or with each other, due to the "irregular" effect of mistuning. As illustrated in Fig. 9, the single and multistage representations of the stage 1 mistuned mode shapes (mode 54) exhibit similar levels of "localization," or lack thereof. On the other hand, the levels of localization exhibited by the mistuned stage 2 mode shape (mode 83) in single and multistage representations are vastly different. Here, the single-stage model predicts a strongly localized mode, while the "actual" multistage mode shape exhibits a much milder deviation from a tuned, spatially extended behavior. Thus, from a mistuning sensitivity perspective, multistage dynamic analyses may be needed in order to yield sufficiently accurate representations of disk flexibility and structural interstage coupling. This will be explored further in the sections to follow.

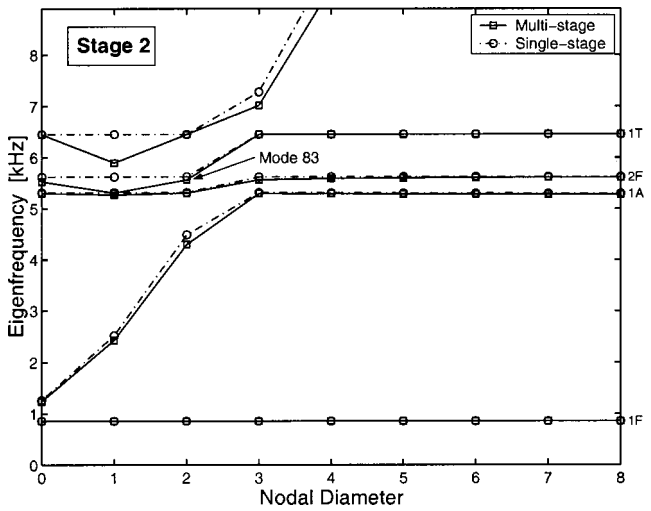

Fig. 7 Natural frequencies versus number of nodal diameters for the tuned stage 2 model with fixed interstage boundaries, and for the "tuned" multistage model for modes confined to stage 2

3.2 Forced Response. The forced response examples included in this section are based on stage-wise independent engine order (EO) excitations, which are harmonic in time and differ only in phase from blade to blade. The engine order excitations are

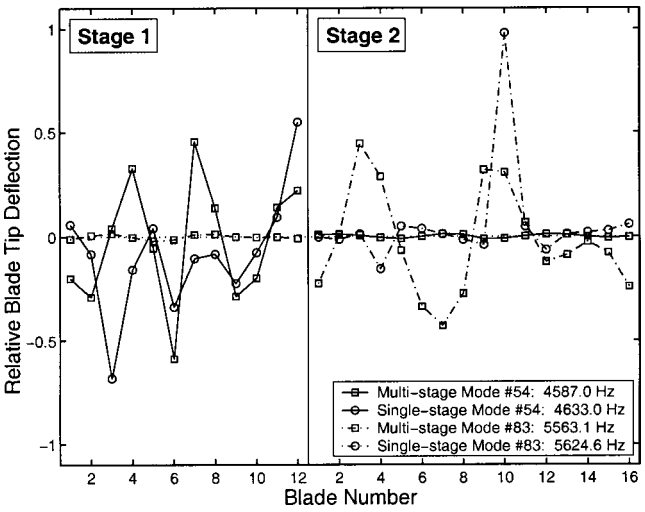

Fig. 9 Mistuned single and multistage mode shapes 54 and 83

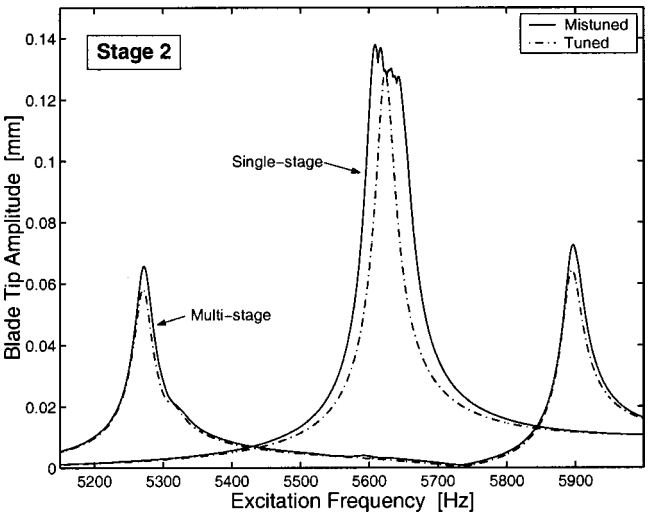

Fig. 11 Stage 2 forced response from engine order 15 excitation (15EO=−1EO), using tuned and mistuned finite element single and multistage models

applied to one stage at a time. This will isolate and better demonstrate the effects of interstage coupling, as it eliminates any subresonances that may be induced by adjacent stage excitations. Specifically, stage 1 is subjected to an engine order 10 (10EO) excitation in the frequency range 4–5 kHz, and stage 2 is subjected to an engine order 15 (15EO) excitation in the frequency range 5–6 kHz. As indicated by the employed engine orders, it is here assumed that the wakes behind the stationary vanes immediately upstream are the dominating sources of excitation. Whereas this excitation may be realistic from an engine order perspective, the blade surface force applied here is highly unrealistic: a single point load on one blade tip node in the axial direction (axis of rotation). However, while unrealistic, it is quite adequate for demonstrative purposes. Furthermore, note that the applied engine order excitations are equivalent to counterrotating engine order 2 (−2EO) and 1 (−1EO) excitations for stages 1 and 2, respectively. Hence, the applied excitations will pass through the harmonic 2 veering region of stage 1 (see Fig. 6), and through the harmonic 1 region of stage 2 that exhibited a drastic change in the free vibration characteristics due to interstage coupling (see Fig. 7).

Figures 10 and 11 depict each stage's response amplitudes resulting from the above excitations. The amplitudes are here represented by the axial displacement magnitude of one blade tip node for the maximum responding blade in each stage. As shown in Fig. 10, the shift in disk flexibility due to interstage coupling observed in Fig. 6 results in a significantly changed veering response behavior for stage 1. Specifically, the added disk flexibility has moved the mode pairs comprising the veering to lower resonant frequencies: the upper mode pair from 4860 Hz to 4795 Hz, and the lower mode pair from 4635 Hz to 4540 Hz. As an important consequence, the upper mode pair, which is clearly disk-dominated and therefore low-responding in the single-stage representation, exhibits much more blade participation in the multistage response. Conversely, the lower mode pair goes from being distinctly blade-dominated to having significant disk participation. Hence, the disk-blade modal interaction has changed to make the sensitivity to mistuning much less pronounced. This is clearly demonstrated by the mistuned results depicted in Fig. 10, where the maximum amplitude magnification due to blade mistuning goes from 48% in the clamped interstage case to only 25% in the multistage case.

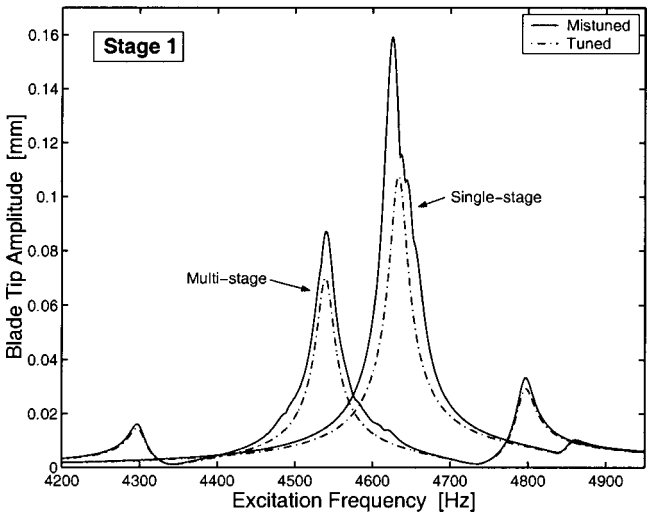

Fig. 10 Stage 1 forced response from engine order 10 excitation (10EO=−2EO), using tuned and mistuned finite element single and multistage models

Moreover, note that even when disregarding blade mistuning, the interstage coupling has a very significant effect on tuned response amplitude levels. The maximum tuned response amplitude for the single-stage model is as much as 54% larger than for the multistage model. Hence, a design based on the tuned single-stage response with applicable safety factors, would in reality (i.e., in a multistage assembly) enjoy an additional safety factor in this particular case. However, it must be emphasized that the design-endangering opposite scenario might be just as likely to occur for other models.

The stage 2 forced response depicted in Fig. 11 demonstrates a similarly dramatic change in response behavior due to interstage coupling. Here, the blade-dominated harmonic 1 mode pair at 5620 Hz has ''disappeared'' in favor of two more disk-dominated mode pairs at approximately 5270 Hz and 5890 Hz, respectively. The increased disk dominance leads to a maximum tuned response amplitude for the multistage model that is 50% lower than that of the single-stage stage 2 model, which features a more blade-dominated response. Note that the stage 2 excitation case exhibits negligible mistuning sensitivity for both single and multistage representations. Also, note that the blade-dominated family of modes at 5320 Hz does not respond to the applied excitation, since the edgewise blade motion (1A; see Fig. 7) of this mode family cannot be excited by the applied force.

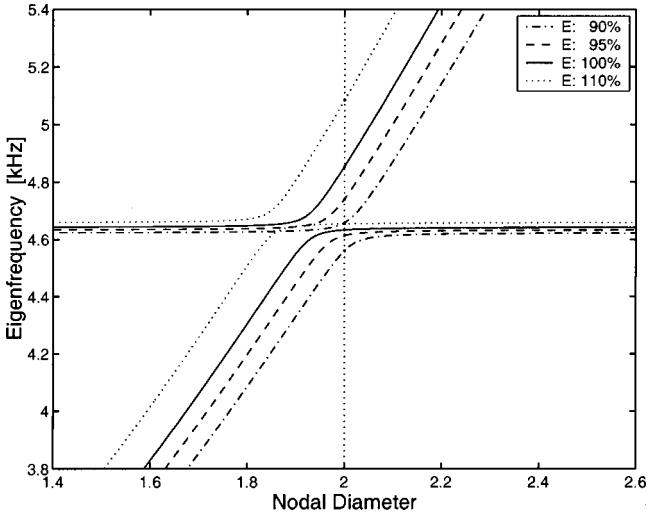

Fig. 12 Detailed view over the stage 1 eigenfrequency veering region indicated in Fig. 6 (single-stage) using a pseudo-continuous interblade phase angle description for varying levels of disk Young's modulus (E)

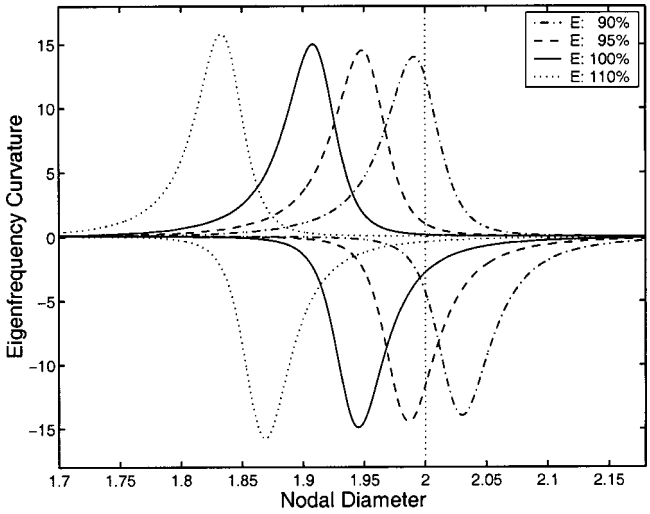

Fig. 13 Upper and lower eigenfrequency curvatures in the stage 1 veering region depicted in Fig. 12 for varying levels of disk Young's modulus (E)

An interesting observation is the existence of subresonances for the multistage model in both tuned and mistuned configurations. For instance, consider the subresonance appearing for stage 1 in Fig. 10 at 4295 Hz. At this resonant frequency, the response is dominated by the motion of a mixed disk-blade two-nodal-diameter mode pair (modes 47 and 48 in Fig. 4) with a stage 1 to stage 2 participation ratio of approximately 1:4, and is thus confined to stage 2. Hence, even though the driving excitation is applied to the least responsive part of this pair of system modes, stage 1's mode participation is sufficient to generate resonance. This observation is important, since it demonstrates that the capture of interstage flexibility alone may not be enough—adjacent stage dynamics may also impact significantly the ''true'' dynamic behavior of a stage in a multistage rotor assembly.

4 Veering Response Sensitivity

4.1 Effects of Disk Flexibility. In this section, the influence of disk flexibility is investigated in more detail. This study is motivated by the significant differences in eigenfrequency veering characteristics and response that resulted from interstage-coupling-induced changes in disk flexibility shown in the previous section. The effective disk flexibility is determined by design (geometry), material, boundary conditions (interstage coupling), and operating conditions (excitation engine orders, centrifugal stiffening). Hence, while interstage coupling has significant impact as shown in the previous section, it is only one contributing factor out of several. However, a full-scale parametric study involving all factors is far beyond the scope of this paper. Thus, to limit the simulation space, only the stage 1 model (single-stage; see Fig. 1) with fixed interstage boundaries is considered, where Young's modulus (E) in the disk part is modified to artificially simulate one or more of these factors.

Figure 12 shows the detailed behavior of the stage 1 model in the eigenfrequency veering highlighted in Fig. 6 for different values of disk Young's modulus. Note that 100% E corresponds to the stage 1 model used in Section 3. The results in Fig. 12 were obtained using the pseudo-continuous interblade phase-angle representation outlined in Bladh et al. [10], which enables computation of fictitious noninteger harmonic (nodal-diameter) modes. This approach can be used effectively to obtain approximations of local veering characteristics, such as local veering curvatures and a veering's true distance to an integer engine order excitation. The local lower (negative values) and upper (positive values) veering curvatures pertaining to the disk flexibility levels in Fig. 12 were computed using a standard fourth-order finite difference scheme and are plotted in Fig. 13. As demonstrated by Fig. 12, the main effect of decreasing the disk flexibility (i.e., increasing E) is to shift the location of the veering to lower interblade phase angles or nodal diameters (i.e., from right to left), while the upward shift in blade-dominated mode frequencies is marginal. This is consistent with the modifying effect of the interstage coupling on disk flexibility observed in the previous section. Furthermore, it is clear from the resulting curvatures in Fig. 13 that the disk flexibility variations have a rather mild effect on the local curvatures, as the obtained maximum curvatures do not change significantly.

An important effect of the veering shift observed in Figs. 12 and 13 is that, as the disk flexibility is decreased (i.e., increasing E), the lower integer harmonic (actual) mode pair will go from disk-dominated (on slanted line) to blade-dominated (on horizontal line) via a mixed disk-blade mode type, and vice versa for the upper mode pair. Hence, at some disk flexibility level, when the center of the veering is located at integer harmonic two, both upper and lower mode pairs will be of the mixed disk-blade type. This has a strong impact on the tuned forced response through the veering, as shown in Fig. 14. As the lower mode pair goes from being largely disk-dominated to blade-dominated, its resulting maximum blade-tip response amplitudes increase monotonically, while, logically, the opposite trend is observed for the upper mode pair response.

Interestingly, the mistuned responses depicted in Fig. 15 indicate that the maximum mistuned response amplitude does not exhibit this monotonic behavior. Instead, there exists some intermediate disk flexibility level, or, equivalently, veering-excitation proximity level, for which the amplification due to mistuning (i.e., the ratio of mistuned to tuned response) has a local maximum. To further elucidate the significance of the veering shift, the maximum tuned and mistuned responses were obtained as a function of closely spaced values of disk Young's modulus. These results are shown in Fig. 16, where both tuned and mistuned responses from veering (-2EO) excitation are shown to exhibit a distinct minimum for a specific flexibility level. Figure 17 shows the resulting mistuned-to-tuned response amplitude magnifications, maximum veering curvature, and distance between veering center and applied excitation as functions of disk flexibility. It is observed from Fig. 17 that the flexibility level of minimum amplification corresponds to the case of a perfectly centered veering. Furthermore, Fig. 17 clearly demonstrates the existence of intermediate disk

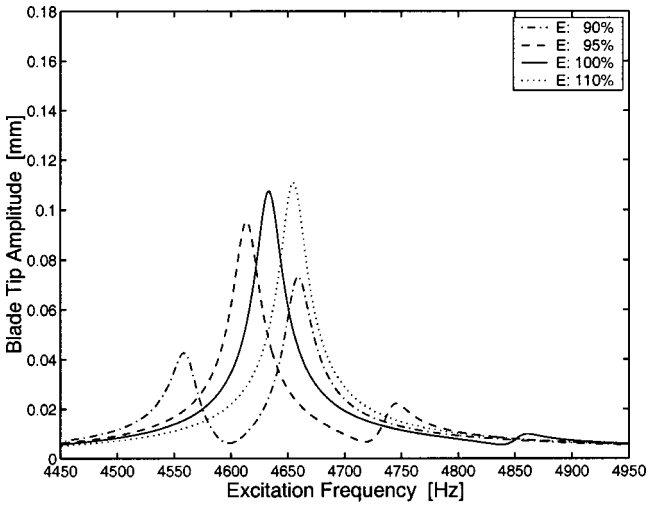

Fig. 14 Tuned stage 1 forced response from engine order 10 excitation (10EO=−2EO) using the single-stage finite element model for varying levels of disk Young's modulus (E)

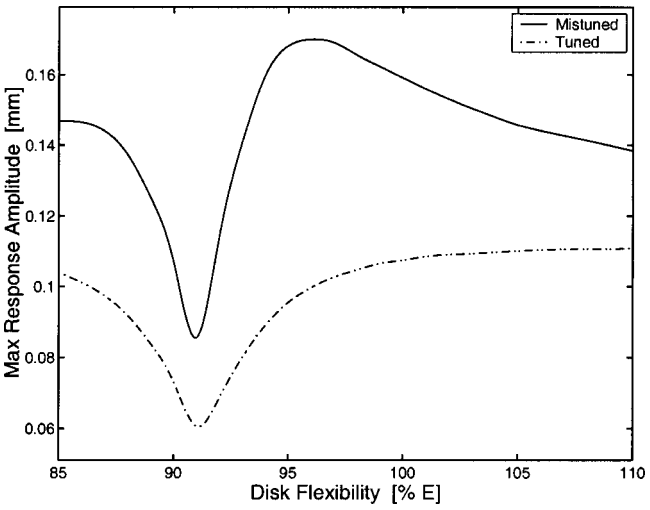

Fig. 16 Maximum tuned and mistuned stage 1 forced responses from engine order 10 excitation (10EO=−2EO) as a function of disk Young's modulus (E) using the single-stage finite element model

flexibility/veering-excitation proximity levels that yield local amplification maxima on either side of a perfectly centered veering.

While the findings in this section are thoroughly consistent, much work remains to get a clear picture of mistuning sensitivity, and, in particular, to get a firm basis for its quantification. However, the findings in this section support the hypothesis that mistuning sensitivity maxima are obtained for a delicate balance of disk and blade participation in the highest-responding eigenfrequency veering mode pair. It is hypothesized that significant flexible blade motion is needed to ''absorb'' the external excitation and to allow the elastic differences among the blades (mistuning) to come into play. The disk motion is needed to communicate the vibration energy between sectors, leading to a transfer of energy from low-responding blades to high-responding blades. For a scenario in which the mode pair is too disk-dominated, the elastic discrepancies among the blades will not be sufficiently amplified due to mostly disk-induced rigid-body participation of the blades, hence the relative insensitivity to mistuning. In the other extreme, where the mode pair is too blade-dominated, the relative insensitivity to mistuning is instead due to the fact that sector-to-sector communication is largely disabled by the minimal disk participation, even though the elastic blade differences are amplified. The proposed hypothesis does not necessarily contradict existing ideas concerned with veering characteristics (local curvature, veering-excitation proximity, etc.). However, if true, this consideration may potentially make the issue of defining a quantitative measure of mistuning sensitivity even more delicate. On the other hand, it may allow the analyst to more quickly identify potentially ''dangerous'' veerings.

4.2 Effects of Interstage Coupling. In this section, it will be investigated whether there are some types of ''standard'' interstage boundary conditions that will result in single-stage dynamic characteristics that could be adequate for practical purposes. Clearly, it would be desirable to avoid multistage analyses as far as possible, since they add significant complexity in terms of modeling, and, in addition, make the task of interpreting the results more cumbersome.

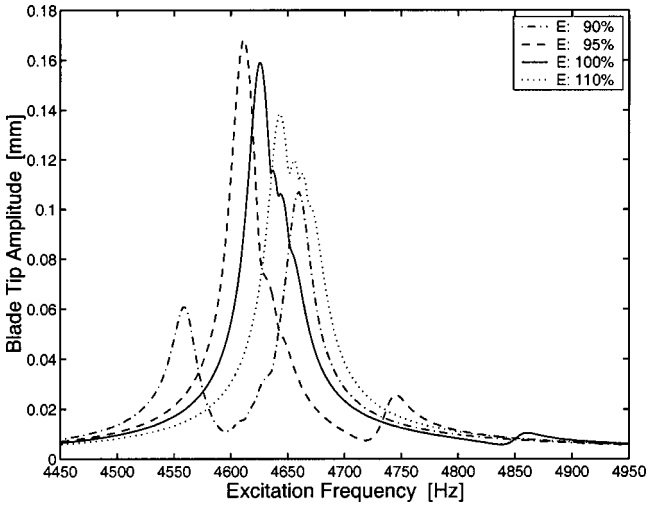

Fig. 15 Mistuned stage 1 forced response from engine order 10 excitation (10EO=−2EO) using the single-stage finite element model for varying levels of disk Young's modulus (E)

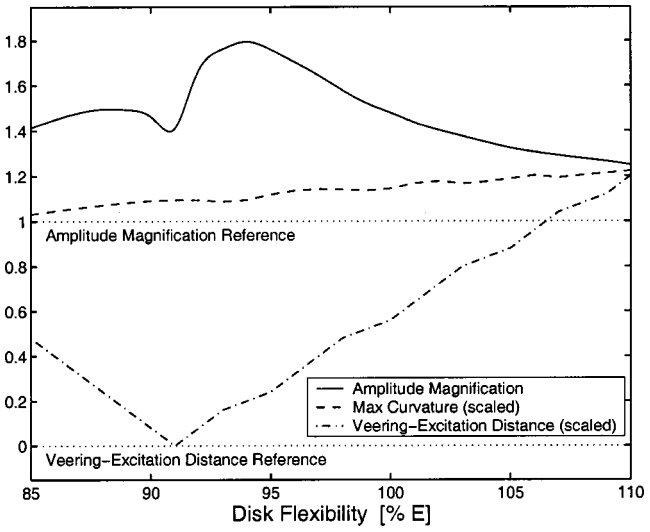

Fig. 17 Mistuned stage 1 response amplification from engine order 10 excitation (10EO=−2EO) and local eigenfrequency veering characteristics as functions of disk Young's modulus (E)

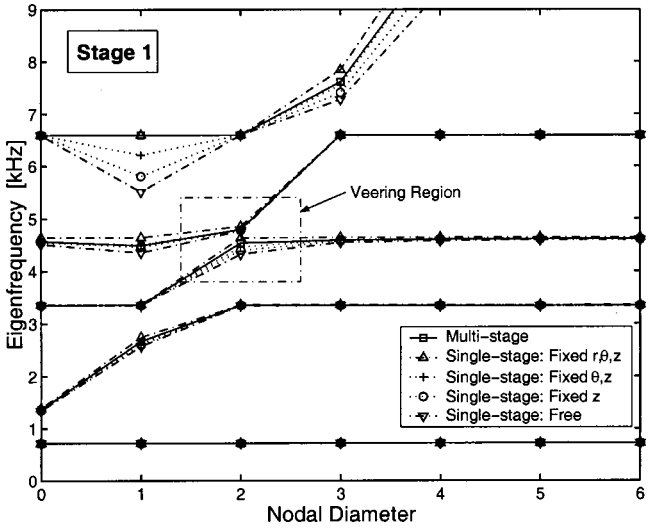

Fig. 18 Natural frequencies versus number of nodal diameters for the tuned stage 1 rotor model using different interstage boundary conditions, plus identified harmonics of the "tuned" two-stage model

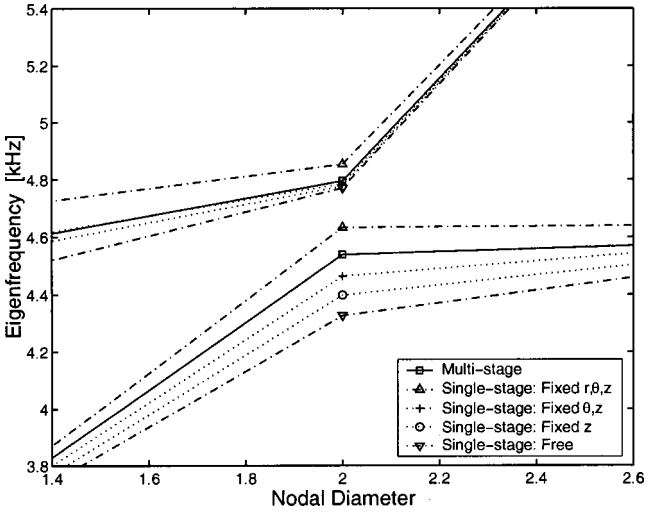

Fig. 19 Detailed view of the eigenfrequency veering region indicated in Fig. 18

As mentioned in the Introduction, current practice is to analyze each rotor stage independently, using a set of interstage boundary conditions that the analyst feels will best describe the constraints imposed by adjacent stages. Typically, this implies imposing either fully clamped conditions or axial restraints alone, or, in more elaborate cases, modeling of adjacent stages as uniformly distributed masses and stiffnesses (to preserve cyclicity). Clearly, the latter modeling approach will benefit from moving local boundary effects well away from the part of interest by virtue of Saint-Venant's principle ([11]). However, it will not take into account the incompatible harmonics of adjacent stages, and thus any stage-periodicity mismatch effects.

Figure 18 depicts the tuned natural frequencies versus the number of nodal diameters for various plausible, ''standard'' interstage boundary conditions—i.e., combinations of fixed radial (r), tangential (θ), and axial (z) directions—using the stage 1 model, plus the corresponding results for the two-stage model. Note that the models used for this case are the same as those in Section 3. As shown in Fig. 18, the imposed boundary constraints yield a reasonable description of the ''global'' vibration characteristics of stage 1 compared to the results obtained with the multistage model. However, these approximate boundary conditions do not provide consistent representations in the eigenfrequency veerings, and thus fail to accurately describe the interaction between families of disk-dominated modes (slanted lines) and blade-dominated modes (horizontal lines). This unfortunate circumstance is clearly demonstrated in Fig. 19, which depicts a detailed view over the frequency veering region indicated in Fig. 18. As shown, the upper disk-dominated mode pair is fairly well represented by all boundary approximations, except for fully clamped conditions. In contrast, the approximate representations of the lower mode pair exhibit significant discrepancies from the ''true'' multistage behavior. While the fully clamped approximation predicts an overly blade-dominated mode pair, the others predict too much disk dominance. This is clearly a vital deficiency, since the disk-blade modal interaction in veering regions is a critically important factor in determining a design's sensitivity to mistuning, as shown in Section 4.1.

Figures 20 and 21 depict the forced response resulting from an excitation through the veering in Fig. 19 (-2EO). As expected, the upper resonance is approximated reasonably well by all the relaxed boundary conditions, since they also gave reasonable predictions of the free modes of vibration. For the lower resonance, the approximations are well off in terms of the resonant frequencies, which follows from the relatively wide scattering of the predicted eigenfrequencies in Fig. 19. Note, however, that the relaxed boundary conditions nevertheless yield reasonably accurate predictions of the maximum tuned response, since these are disk-dominated responses. In the mistuned case, the relaxed approximations tend to exaggerate the amplification due to mistuning, but they still provide reasonable approximations of the maximum mistuned response amplitude. Note that in both the tuned and mistuned cases, the clamped condition does not yield responses that are even reasonably close to the multistage responses. It is also worth mentioning that, for obvious reasons, the single-stage approximations are unable to display any subresonances induced by adjacent stage dynamics exhibited by the multistage model.

It is realized that the model used in this study is highly simplified, and thus, it may not be representative of multistage effects for more realistic models. Therefore, in an effort to prove the findings of this study more general, two additional multistage cases are presented in this section, in which the stiffness of the disks and interstage rims is significantly different from the origi-

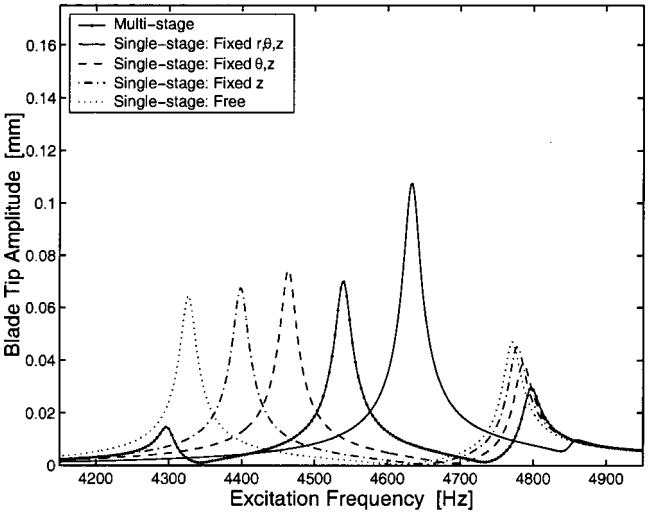

Fig. 20 Stage 1 tuned finite element forced responses from engine order 10 excitation (10EO=−2EO) using different interstage boundary conditions, plus the "tuned" multistage finite element response

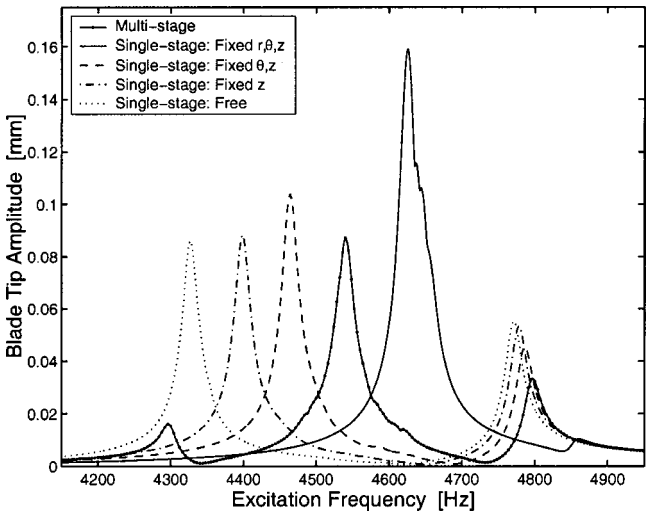

Fig. 21 Stage 1 mistuned finite element forced responses from engine order 10 excitation (10EO=−2EO) using different interstage boundary conditions, plus the blade mistuned multistage finite element response

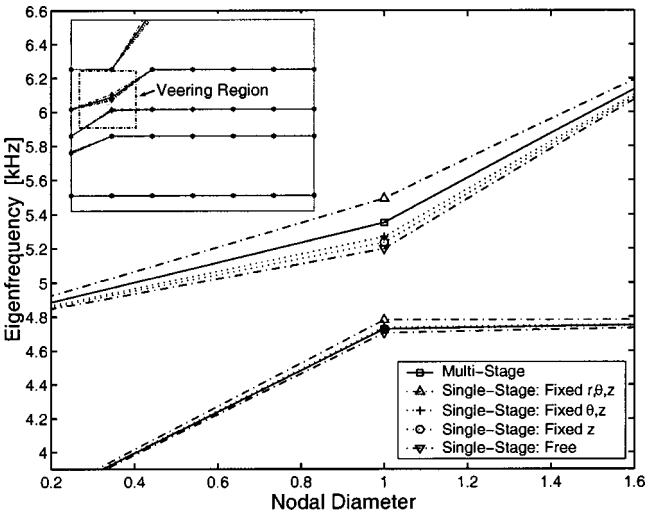

Fig. 22 Detailed view of the indicated eigenfrequency veering region (upper left) for the tuned stage 1 rotor model using different interstage boundary conditions, plus identified harmonics of the "tuned" two-stage model, with a fourfold increase of Young's modulus in disks and interstage rims

nal model. For the first case, the stiffness of the disks and interstage rims is increased uniformly by using a Young's modulus (E) that is four times higher than that of the original model. From plate vibration theory (e.g., Meirovitch [12]), it is found that plate modal stiffness follow $\omega^2 \propto Eh^2$, where h is the plate thickness. Hence, in an approximate sense, the fourfold increase in Young's modulus corresponds to a model with a twofold increase in thickness for the disks and interstage rims. In the second case, only Young's modulus of the disks are increased by a factor four, while the interstage rims are unchanged. While this is clearly a very artificial way to alter a model, these two additional cases are nevertheless believed to establish that similar interstage coupling effects are likely to occur even though model characteristics may differ significantly.

An important observation made for both these additional cases is that the stage-periodicity mismatch here results in slight deterioration of the spatially extended characteristic for a few blade-dominated modes of higher harmonics. Hence, the stiffer disks increase the mistuning sensitivity of the two-stage model significantly, considering the extremely low level of ''disk mistuning'' that is being induced by the stage-periodicity mismatch. However, since the eigenfrequency veering region under investigation in this section is located at lower harmonics, the harmonics of the modes surrounding the veering are readily identified in spite of this deterioration.

The uniform stiffening of the entire disks leads to drastically different free vibration characteristics, as shown in Fig. 22. The significantly stiffer stage 1 disk has shifted the disk-dominated modes to higher frequencies to form a harmonic 1 veering instead of the original harmonic 2 veering. Moreover, it is observed from Fig. 22 that the features of the veering and the boundary approximations are reversed in this case. Here, the boundary approximations exhibit significant discrepancies for the upper (disk-dominated) mode pair, while the lower mode pair has too much blade dominance to be affected by the differing disk flexibilities to any significant extent. Consequently, the approximations of the lower blade-dominated resonance are tightly clustered in frequency, as depicted in Fig. 23. Note, however, that all approximate boundary conditions predict similarly exaggerated tuned maximum resonant amplitudes, overshooting the true multistage amplitude by 12–21%.

When stiffening only the disks without the interstage rims, the free-vibration characteristics are similar to the previous case in that the veering occurs at harmonic 1. However, upon closer examination, the local veering characteristics are found to be drastically different, as depicted in Fig. 24. The more flexible interstage rims have shifted the disk-dominated modes to slightly lower frequencies relative to the previous case. Therefore, the veering is now comprised of an upper disk-dominated mode pair and a lower mode pair that is very close to having significant disk participation. In this case, it is particularly notable how well the natural frequency of the more blade-dominated lower mode pair is approximated by the fully clamped condition, while the relaxed boundary conditions are well off target. Recall that the fully clamped condition resulted in the worst approximations in the original disk flexibility case. However, for the upper mode pair, it is again the clamped approximation that is the most off target. Hence, as shown in Fig. 25, the clamped condition predicts the true multistage resonant frequency very well. However, it is still off considerably in terms of expected maximum amplitude. The

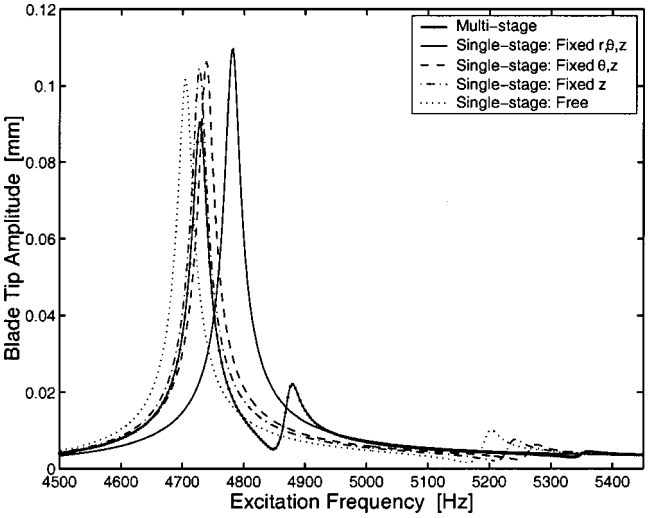

Fig. 23 Stage 1 tuned finite element forced responses from engine order 11 excitation (11EO=−1EO) using different interstage boundary conditions, plus the "tuned" multistage finite element response, with a fourfold increase of Young's modulus in disks and interstage rims

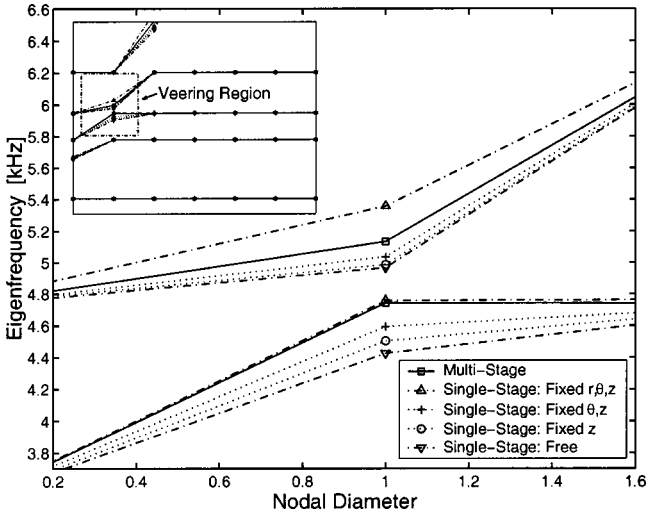

Fig. 24 Detailed view of the indicated eigenfrequency veering region (upper left) for the tuned stage 1 rotor model using different interstage boundary conditions, plus identified harmonics of the "tuned" two-stage model, with a fourfold increase of Young's modulus in disks alone

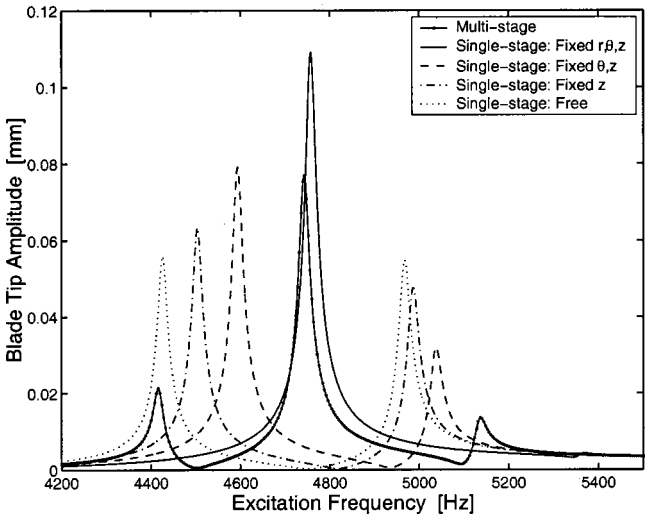

Fig. 25 Stage 1 tuned finite element forced responses from engine order 11 excitation (11EO=−1EO) using different interstage boundary conditions, plus the "tuned" multistage finite element response, with a fourfold increase of Young's modulus in disks alone

relaxed boundary conditions, on the other hand, are well off target in terms of resonant frequency, and, except for the "fixed θ,z" case, well off in terms of maximum resonant amplitude as well.

The examples presented in this section demonstrate that interstage coupling and adjacent stage dynamics have a significant impact on free and forced response behavior for multistage rotor models with widely different characteristics. Furthermore, these examples show that there is no "standard" interstage boundary condition to be used in single-stage analysis that will consistently yield sufficiently good approximations of true multistage behavior. Rather, the performance of such boundary conditions is governed by local veering characteristics, including disk-blade mode dominance, and can therefore only be employed with confidence (if at all) on a case-to-case basis.

5 Conclusions

This paper explored the effects of multistage coupling on the dynamics of bladed disks with and without blade mistuning. Both free and forced responses of an example two-stage finite element rotor were examined.

Several important implications of multistage coupling were identified in this work. One important observation was that a form of "disk mistuning" is inherent in the coupled multistage system, due to different numbers of sectors for adjacent stages. Furthermore, the reported work demonstrated the importance of proper treatment of interstage (stage-to-stage) boundaries in order to yield adequate capture of a design's disk-blade modal interaction in eigenfrequency regions, also denoted structural interblade coupling. The modifications to the disk-blade modal interactions resulting from structural interstage coupling effects were found to have a significant impact on (a) tuned responses due to excitations passing through eigenfrequency veering regions, and (b) a design's sensitivity to blade mistuning. Hence, the findings in this paper suggest that multistage analyses may in fact be required when excitations are expected to fall in or near eigenfrequency veering regions or when the sensitivity to blade mistuning is to be adequately accounted for.

Furthermore, the observations in this paper support the hypothesis that mistuning sensitivity maxima are obtained for a delicate balance of disk and blade participation in the highest-responding eigenfrequency veering mode pair. Significant flexible blade motion is needed to "absorb" the external excitation and to allow the structural differences among the blades to come into play. The disk motion is needed to communicate the vibration energy between sectors, leading to vibration energy localization by partial reflections. This consideration may allow the analyst to more quickly identify potentially "dangerous" eigenfrequency veerings.

The found sensitivity of eigenfrequency veering response complicates significantly the dynamic analysis of multistage rotor systems. These findings suggest that multistage analyses should be performed when excitations are expected to fall in or near eigenfrequency veering regions. However, the found sensitivity also opens up the possibility of reducing the severity of unfavorable excitation cases by redesigning the disk(s) and interstage connectivity. The relatively drastic effects of such modifications illustrated in this work indicate that the design modifications required to alleviate veering-related response problems may be less comprehensive than what might have been expected.

References

[1] Wagner, J. T., 1967, "Coupling of Turbomachine Blade Vibrations Through the Rotor," ASME J. Eng. Power **89**, pp. 502–512.

[2] Dye, R. C. F., and Henry, T. A., 1969, "Vibration Amplitudes of Compressor Blades Resulting From Scatter in Blade Natural Frequencies," ASME J. Eng. Power **91**, pp. 182–188.

[3] Ewins, D. J., 1969, "The Effects of Detuning Upon the Forced vibrations of Bladed Disks," J. Sound Vib., **9**, pp. 65–79.

[4] Ewins, D. J., 1973, "Vibration Characteristics of Bladed Disc Assemblies," J. Mech. Eng. Sci., **15**, pp. 165–186.

[5] El-Bayoumy, L. E., and Srinivasan, A. V., 1975, "Influence of Mistuning on Rotor-Blade Vibrations," AIAA J., **13**, pp. 460–464.

[6] Irretier, H., 1983, "Spectral Analysis of Mistuned Bladed Disk Assemblies by Component Mode Synthesis," *Vibrations of Bladed Disk Assemblies*, ASME, New York, pp. 115–125.

[7] Wei, S. T., and Pierre, C., 1988, "Localization Phenomena in Mistuned Assemblies With Cyclic Symmetry, Part I: Free Vibrations," ASME J. Vib., Acoust., Stress, Reliab. Des., **110**, pp. 429–438.

[8] Wei, S. T., and Pierre, C., 1988, "Localization Phenomena in Mistuned Assemblies With Cyclic Symmetry, Part II: Forced Vibrations," ASME J. Vib., Acoust., Stress, Reliab. Des., **110**, pp. 439–449.

[9] Ottarsson, G. S., and Pierre, C., 1995, "On the Effects of Interblade Coupling on the Statistics of Maximum Forced Response Amplitudes in Mistuned Bladed Disks," *Proc. 36th AIAA/ASME/ASCE/AHS Structures, Structural Dynamics, and Materials Conference*, New Orleans, LA, AIAA, Washington, DC, **5**, pp. 3070–3078.

[10] Bladh, R., Castanier, M. P., and Pierre, C., 1999, "Models of Rotor Mistuning and the Prediction of Mistuned Blade Forced Response," *Proc. 4th National Turbine Engine High Cycle Fatigue Conference*, Monterey, CA, Universal Technology Corp., Dayton, OH.

[11] Timoshenko, S. P., and Goodier, J. N., 1970, *Theory of Elasticity*, McGraw-Hill, New York.

[12] Meirovitch, L., 1967, *Analytical Methods in Vibrations*, Macmillan, New York.

Optimization of Intentional Mistuning Patterns for the Reduction of the Forced Response Effects of Unintentional Mistuning: Formulation and Assessment

B.-K. Choi
School of Mechanical and Aerospace Engineering,
The Institute of Marine Industry,
Gyeongsang National University,
Tongyoung, Kyongnam 650-160, Korea

J. Lentz
Honeywell Engines and Systems,
Department 93-31/301-125,
P.O. BOX 52181,
Phoenix, AZ 85072-2181

A. J. Rivas-Guerra

M. P. Mignolet

Department of Mechanical and Aerospace Engineering,
Arizona State University,
Tempe, AZ 85287-6106

The focus of the present investigation is on the use of intentional mistuning of bladed disks to reduce their sensitivity to unintentional random mistuning. The class of intentionally mistuned disks considered here is limited, for cost reasons, to arrangements of two types of blades (A and B, say). A two-step procedure is then described to optimize the arrangement of these blades around the disk to reduce the effects of unintentional mistuning. First, a pure optimization effort is undertaken to obtain the pattern(s) of the A and B blades that yields small/the smallest value of the largest amplitude of response to a given excitation in the absence of unintentional mistuning. Then, in the second step, a pattern screening technique based on a recently introduced measure of localization is used to determine which of the patterns does have a large/small sensitivity to random unintentional mistuning. In this manner, expensive Monte Carlo simulations can be eliminated. Examples of application involving both simple bladed disk models and a 17-blade industrial rotor clearly demonstrate the significant benefits of using this class of intentionally mistuned disks. [DOI: 10.1115/1.1498270]

Introduction

In the context of turbomachinery, mistuning refers to blade-to-blade variations in their structural and/or geometrical properties. Much of the vast literature on this topic (see, for example, Refs. [1–14]) has assumed these differences to be small and to arise either during the manufacturing process or as a result of in service wear. The motivation for considering such small variations is that their effects on the forced response of bladed disks can be extremely large, i.e., fluctuations of the blade properties by 1–2% can lead to increases of the amplitude of vibration of some blades by 100% or more, as often reported in the above studies. Interestingly, the large sensitivity of the tuned system to these small variations has been linked (see, for example, Ref. [6]) to its high level of symmetry.

In this light, it would appear beneficial to design bladed disks *not to be tuned*, i.e., to exhibit intentional mistuning, to reduce the sensitivity of their forced response to unintentional mistuning, i.e., the unavoidable manufacturing and/or in service wear variations. Certainly, the consideration of intentional mistuning is not new: Kaza and Kielb [3,4] demonstrated the value of alternate mistuning to raise the flutter speed, a concept used in a Westinghouse turbomachine. In the context of forced response, however, it is only recently that Castanier and Pierre [15–16] and Kenyon and Griffin [17] have investigated the use of harmonic patterns of mistuning and have shown that the magnification of the forced response due to unintentional mistuning can be significantly reduced ([15–16]). In particular, it was observed in these studies that the magnitude of the intentional mistuning must typically be of the order of or larger than that of the unintentional one for this design strategy to yield a benefit. Other studies of amplitude magnification ([18,19]) have also demonstrated that while some mistuning causes an increase in peak response, further mistuning often reverses the effect and decreases the sensitivity. This has been shown experimentally by Mehmed and Murthy [20] who intentionally mistuned a propfan and observed a decrease in the maximum response.

Note then that the use of different sets of blades on the same rotor is a complex and/or expensive proposition: for disks with inserted blades it implies the manufacturing of different types of blades, the tracking of these different variants, and the implementation of a systems that assures that the right blades have been inserted in the right slots. For blisks, the manufacturing issues may be less severe, although there are definite costs associated with the programming of different blade geometries on the manufacturing machines, and possibly more importantly with the necessary inspections for certification. In light of the above comments, it is highly desirable to optimize the benefit-over-cost ratio of intentional mistuning.

The formulation and assessment of such an optimization strategy is the focus of the present investigation. In particular, this effort aims at answering the questions of how well this approach would perform, how the optimization search could be conducted, and providing some insight into why such an intentional mistuning reduces the sensitivity to additional variations in blade properties. To this end, both simple (one and two degrees-of-freedom per blade) and complex (REDUCE reduced-order model of an industrial impeller) models of bladed disks have been considered.

Optimization Approach

In view of the complexity and cost of intentional mistuning, one should *optimize* the pattern (i.e., arrangement of blades) to reduce as much as possible the amplification of the forced re-

Contributed by the International Gas Turbine Institute (IGTI) of THE AMERICAN SOCIETY OF MECHANICAL ENGINEERS for publication in the ASME JOURNAL OF ENGINEERING FOR GAS TURBINES AND POWER. Paper presented at the International Gas Turbine and Aeroengine Congress and Exhibition, New Orleans, LA, June 4–7, 2001; Paper 2001-GT-293. Manuscript received by IGTI, Dec. 2000, final revision, Mar. 2001. Associate Editor: R. Natole.

sponse to a given excitation or set thereof. Accordingly, it is suggested here that an acceptable intentional mistuning pattern, i.e., maximizing the benefit-over-cost ratio, must be such that

1. it yields a *large* decrease in sensitivity to unintentional mistuning, and
2. it involves a minimum number of types of blades, ideally 2.

It is proposed here to address this optimization problem sequentially. That is, the disk will first be assumed to support only two different types of blades (blades A and B, say) and their arrangement that yields the smallest amplification of the forced response due to unintentional mistuning will be sought. Having established the increased cost of this mistuned design over a tuned one (blades C, say), the process can then be repeated with three types of blades, then four and so on until the cost increase is no longer justified by the reduction of sensitivity to mistuning.

The process described above has some rather dramatic computational implications. Indeed, for each mistuning pattern considered, it requires the determination of the largest amplitude of blade response that can be observed on a disk exhibiting both intentional and unintentional mistuning. At this point in time, however, reliable estimates of this largest amplitude can only be obtained by time consuming Monte Carlo simulations (with the possible use of a Weibull distribution fit ([12,15])). Accordingly, a straightforward application of the proposed optimization strategy could only be done for very simple bladed disk models. It is thus proposed to proceed slightly differently by

1. performing the optimization *in the absence of unintentional mistuning*, and
2. obtaining a qualitative/quantitative estimate of the sensitivity of a given intentionally mistuned disk to additional unintentional (random) mistuning.

In this manner, the optimization effort (i.e., step (1)) requires only one forced response evaluation per intentionally mistuned disk considered, as opposed to an entire population.

Even with this simplification, care must be taken in selecting the optimization algorithm, as mistuning has a very nonlinear effect on the forced response. By switching the order of the blades around the disk, dramatic differences can be obtained in the variability of the blade-to-blade amplitudes of vibration as exemplified in particular by the harmonic mistuning analysis of Mignolet et al. [11]. It might thus be suspected that there exists a series of local optima in the complex, high dimensional space over which the optimization must take place. In this light, two different optimization algorithms were used and assessed: a simple genetic algorithm and a combination of subproblem approximation and steepest descent algorithms. Since the last two techniques are rather standard optimization approaches (e.g., available within ANSYS), they will not be described in any further details here at the contrary of the simple genetic algorithm which is presented next.

Simple Genetic Algorithm. Genetic optimization algorithms are based on the transformation of a population of individual objects/design (here bladed disks) through a series of generations using the Darwinian principle of reproduction and naturally occurring genetic operations of selection, crossover, and mutation. As the evolution process they mimic, these algorithms are intrinsically stochastic in nature—both the initial population and the transition from one generation to the next are random. Genetic algorithms are particularly well suited for the present effort because the design variables only admit discrete values (i.e., a specific blade is only of type A or B) and there are multiple optima (differing for example by a rotation of the disk), see Refs. [21], [22] for further details.

The simple genetic algorithm used here relies on a population of n_{pop} bladed disks (referred to as ''chromosomes'') each of which is a random arrangement of N ''genes'' (the type A or B of the different blades). Accordingly, each bladed disk can be characterized by a sequence of N A and B letters, i.e., AABBBBAABABBA . . . which evolves from one generation to the next according to the rules of selection, crossover, and mutation until all the chromosomes yield essentially similar values of the fitness or objective function (selected here as the maximum amplitude of blade response in a frequency sweep at the selected engine order).

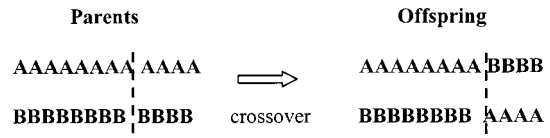

Fig. 1 Graphical description of the single-point crossover technique

The selection operator determines those members of the population that survive to participate in the production of members at the next generation. Selection is based on the value of the fitness of the individual members and is such that members with greater fitness levels (smaller maximum amplitude of blade response) tend to survive. In the fitness proportionate selection used here, each individual bladed disk i in the population is first assigned a probability of selection $p_s(i)$ given as

$$p_s(i) = 1 - \frac{A_{\max}^{(i)}}{\sum_{j=1}^{n_{pop}} A_{\max}^{(j)}} \tag{1}$$

where $A_{\max}^{(i)}$ denotes the maximum amplitude of blade response on disk i. Then, n_{pop} individuals (not necessarily all different) of the population at generation g are selected, according to the probabilities $p_s(i)$, for further potential genetic processing, i.e., crossover and mutation, to generate the population $g+1$. Note that population members with a higher fitness are likely to be selected more often than those with a lower fitness.

Crossover (or recombination) is the general process by which two chromosomes (the ''parents'') are split into segments and recombined to form two new chromosomes (the ''offspring''). The single point crossover technique used in the present investigation is schematically exemplified in Fig. 1 and can be described as follows. Given a pair of parents, the crossing site is first chosen at random among the $N-1$ possible locations. Then, the two parent chromosomes are each sliced at the selected crossing site, into two segments apiece. Appropriate segments from different parents are then concatenated to yield the two offspring.

Note that this process does not necessarily take place for all pairs of chromosomes forming the population, rather the crossover only occurs for each such pair with a fixed probability p_c. When crossover does not take place (event of probability $1-p_c$), the two offspring are simply identical to the parents. In both cases, the offspring proceed next to the final stage of mutation.

Mutation is the process by which the genes of the offspring are varied from their parent counterparts. In the present binary situation (i.e., blades are either of type A or B), the mutation was accomplished by independently allowing, with probability p_m, each of the genes to switch type. This probability plays a very important in the convergence of the genetic algorithm to an optimum, or near optimum, solution. Indeed, if p_m is large, the mutation process is very frequent and the diversity of the population is high. This situation is desirable in the first few generations to span properly the space of possible solutions but, toward the end of the process, a high mutation rate may force the disappearance of the optimum solution. Accordingly, the probability of mutation was selected here as a exponentially decreasing function of the generation number g as

$$p_m(g) = p_m(0)\exp[-\tau g/g_{\max}] \tag{2}$$

where $g_{\max}$ is the maximum number of generation.

Table 1 Values of the parameters of the simple genetic algorithm

Population size (n_{pop})	35
Chromosome length (N) =number of blades on disk	12
Crossover probability (p_c)	0.70
Mutation probability (see Eq. (2))	$p_m(0)=0.99$, $\tau=5$
Max. number of generations (g_{max})	500

Experimentation with the above algorithm has shown that the chromosome with the highest fitness (disk with the lowest maximum amplitude of blade response) may disappear from one generation to the next due to the operations of crossover and mutation. To remedy this situation, the ''one elite reservation'' strategy was used according to which the best disk is retained unchanged from one generation to the next, i.e., it is automatically selected and no mutation nor crossover is performed on it.

At the completion of the above procedure, composed of the selection, crossover, and mutation, the old population (at generation g) is replaced by the new one (generation $g+1$) and the process is repeated until the maximum number of generations is attained. At each generation, the minimum, maximum, and average objective function values (largest amplitude of blade response) is determined. The evolution of these three quantities through the generations provides, as will be seen later, a good indication of the convergence of the process.

Shown in Table 1 are the values of the algorithm parameters, population size, probabilities of crossover, mutation, etc., that led to the optimum results presented in this paper. These values were obtained after several trials and were retained because they led to the smallest value of the largest amplitude of blade response.

Application to a Simple Bladed Disk Model

To gain some perspective on the feasibility and benefits of the proposed optimization effort, the single-degree-of-freedom per blade model shown in Fig. 2 was first considered with several different values of the coupling stiffness and damping coefficient. The computations proceeded as follows. The bladed disk model

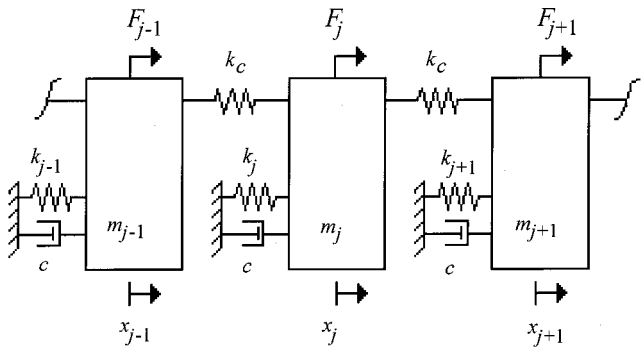

$$F_j = F_o \cos\left(\omega t + \frac{2\pi r(j-1)}{N}\right)$$

$m_t = 0.0114$ kg $\quad k_t = 430{,}300$ N/m $\quad c = 0.143$ Ns/m

$N = 12$ blades $\quad F_o = 1$ N $\quad r = 4$

k_j: normal distribution of mean k_t and standard deviation σ

Fig. 2 Single-degree-of-freedom per blade disk model

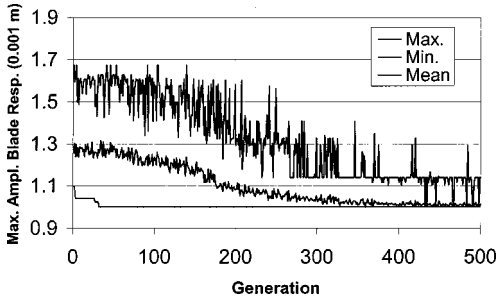

Fig. 3 Convergence plot of the simple genetic algorithm, single-degree-of-freedom model, k_C=8,606 N/m

and engine order of the excitation were first selected. The simple genetic algorithm described above was then used to obtain the intentionally mistuned disk formed of blades A and B such that the maximum of its response over the entire frequency range was the smallest possible. This optimization was accomplished with the parameter values given in Table 1.

To assess the convergence of the simple genetic algorithm, the minimum, maximum, and mean value over the population of disks of the largest amplitude of blade response was monitored as a function of the generation number. A typical plot of the evolution of these three values is shown in Fig. 3. Note that the minimum value over the population of the largest amplitude of blade response is associated with the optimum A/B pattern. Thus, it is clearly seen from Fig. 3 that the optimum A/B pattern is obtained within a small number of generations, i.e., of the order of 40. In the ensuing generations, the exponentially decreasing mutations (see Eq. (2)) and constant crossover homogenize the population as demonstrated by the convergence of the mean (and eventually the maximum) largest amplitude of blade response in the population to its minimum value. Accordingly, the simple genetic algorithm converged.

Once the ''best'' intentionally mistuned disk was obtained, its sensitivity to unintentional mistuning was assessed by adding various levels of random mistuning and evaluating the largest response over the resulting population of disks (10,000 disks). This effort was conducted at the frequency that yielded the largest response of the purely intentionally mistuned disk.

The value of the coupling stiffness k_C was first set to 45,430 N/m to represent an average to large blade-to-blade coupling level and the two sets of blades A and B were selected to have natural frequencies 5% lower and 5% higher, respectively, than the tuned ones (type C). Under these conditions, the genetic optimization algorithm yielded the configuration 7A5B the highest responding blade of which experiences an amplitude of vibration of 0.79 times the tuned value. To assess the sensitivity of this and other noted A/B patterns, the simulation effort described above was undertaken in the range of 0–5% of frequency mistuning. These results, shown in Fig. 4, clearly demonstrate the benefit of using the 7A5B pattern of intentional mistuning, especially at reasonably low levels of random unintentional mistuning. For example, with 1.5% of mistuning, the largest magnification observed on the tuned disk is 1.45 versus 0.95 for the 7A5B one! At higher mistuning level, the different curves become closer but the one corresponding to the 7A5B disk remains the lowest one.

Other A/B patterns of interest here are the 2B1A and 3A3B whose amplitude magnification curves are also shown in Fig. 4. Interestingly, it is seen that the pattern 2B1A which does lead to a large reduction (18%) of the response in the absence of unintentional mistuning (i.e., for $\sigma=0$) also exhibits a very large sensitivity to this random mistuning and performs for $\sigma\neq 0$ approximately as the tuned disk. On the contrary, the pattern 3A3B displays a larger response than the tuned disk for $\sigma=0$ but

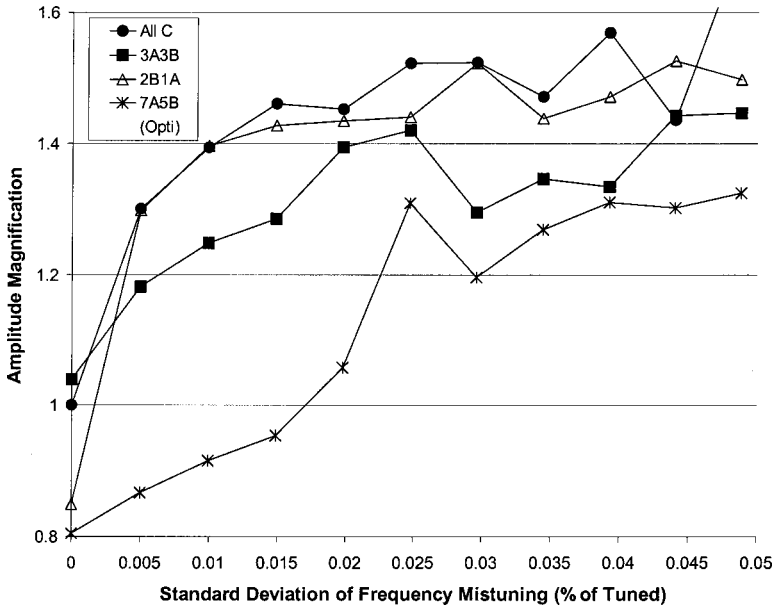

Fig. 4 Amplification factor of the forced response with respect to the tuned disk as a function of the level of unintentional mistuning, single-degree-of-freedom model, k_C=45,430 N/m. Blades C are tuned, A and B have natural frequencies 5% lower and higher, respectively, than tuned. The notation 3A3B refers to disks formed of two groupings AAABBB or $(AAABBB)_2$ and similarly 2B1A represents $(BBA)_4$.

is much less sensitive to the effects of unintentional mistuning and thus yields smaller amplitude magnifications for $\sigma \in [0.005,0.025]$.

This effort was repeated for weakly coupled blades, i.e., $k_C = 8{,}606$ N/m and led to the optimum pattern 2A2B. As in the previous case, this computation was followed by a sensitivity analysis to unintentional mistuning. Specifically, the amplitude magnification factor obtained in a 10,000-disk Monte Carlo simulation was plotted as a function of the standard deviation of frequency mistuning for the tuned configuration and various A/B

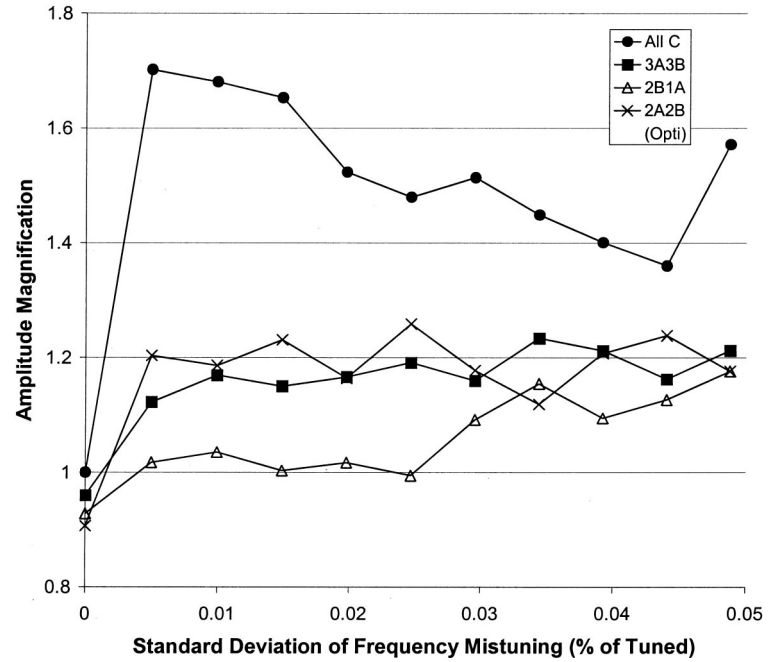

Fig. 5 Amplification factor of the forced response with respect to the tuned disk as a function of the level of unintentional mistuning, single-degree-of-freedom model, k_C=8,606 N/m. Blades C are tuned, A and B have natural frequencies 5% lower and higher, respectively, than tuned. The notation 2A2B refers to disks formed of three groupings AABB or $(AABB)_3$ and similarly 2B1A represents $(BBA)_4$.

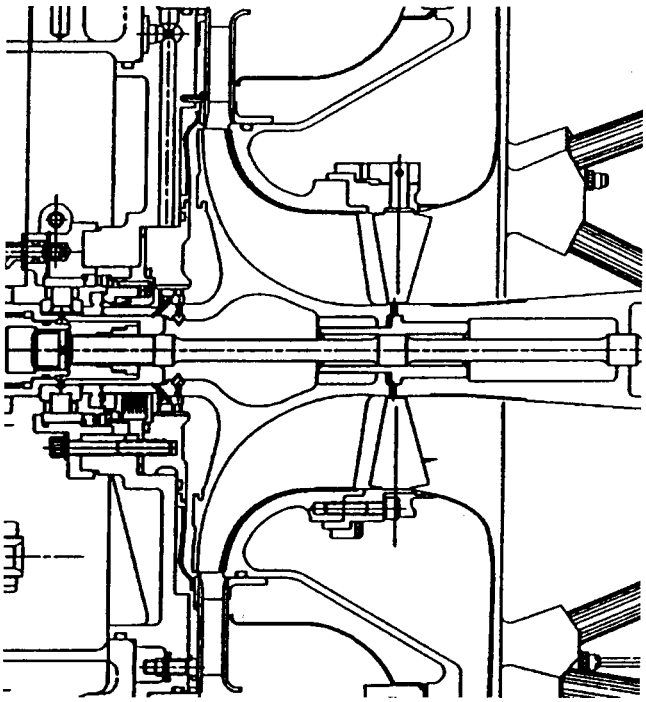

Fig. 6 Typical APU load compressor with inlet guide vanes

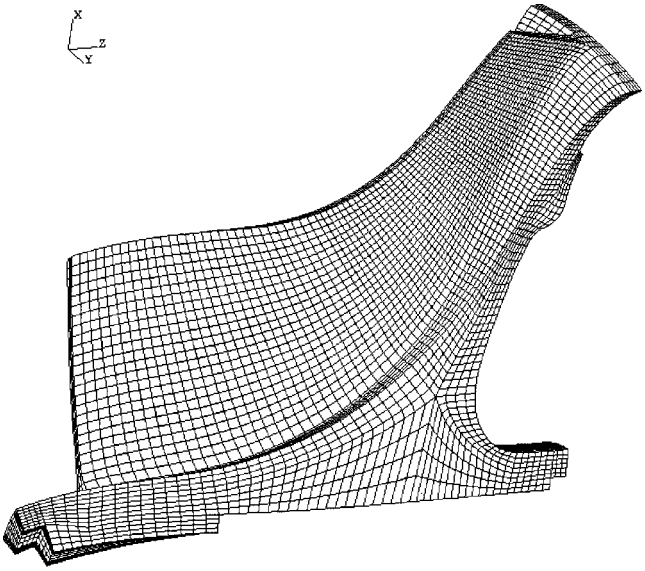

Fig. 7 Single sector structural model of the 17-blade centrifugal compressor rotor

patterns, see Fig. 5. As in Fig. 4, note first the large reduction in the amplitude magnification obtained by selecting the 2A2B pattern over the tuned one (all C), i.e., from 1.72 to 1.22 at low standard deviation of mistuning. Interestingly, it is also seen from Fig. 5 that the optimal solution, i.e., 2A2B, does not yield the lowest amplitude magnification when unintentional mistuning is present. Indeed, the curves corresponding to the systems 3A3B and 2B1A are generally slightly below their 2A2B counterpart for $\sigma \neq 0$. Nevertheless, the amplitude magnification is always less for the optimal A/B pattern than it is for the tuned disk.

Additional study cases with the model of Fig. 2 and a related two-degree-of-freedom per blade system ([23]) confirm the general observations stated above.

Application to an Industrial Rotor

A 17-bladed centrifugal compressor was selected to exemplify the optimization strategy described above to an industrial rotor. The compressor considered is an Auxiliary Power Unit (APU) load compressor with upstream inlet guide vanes (IGV's), see Fig. 6. The blisk rotor is known to be subjected to a strong upstream disturbance from the IGV's that excites the 5th characteristic blade mode. Accordingly, it is with this excitation that the optimization was conducted.

Computational Models and Free Response. Both finite element (ANSYS) and reduced-order (REDUCE, [24]) models of the rotor were generated. The finite element model shown in Fig. 7 was built using cyclic symmetry and consisted of 17,474 eight-noded solid elements per sector. Specifically, the airfoil and disk portion of the model required 24,900 and 41,844 degrees-of-freedom, respectively. In contrast, the reduced-order model (ROM) consists of 30 cantilever blade modes, and 30 disk-induced modes, for a total of 60 degrees-of-freedom per sector. The tuned natural frequencies corresponding to the finite element and reduced-order models matched reasonably well as can be seen in Fig. 8. Further improvements of the REDUCE code [25] are expected to improve the slight frequency discrepancies in the frequency veering zone near 17 kHz for nodal diameters 3 through 5. These modes are fairly complex and involve a significant amount of blade and disk coupling. In this context, note that the response of the disk can exhibit multiple nodal diameters due to the periodicity. For example, the major 3 nodal diameter mode of the system has significant contributions of the minor nodal diameters of 14, 20, 31, and so on. An example of such a complex mode shape for the nodal diameter 3 family is shown in Fig. 9.

Forced Response. The objective of the present application was to evaluate the benefits of intentional mistuning in reducing the sensitivity to random mistuning of the response of the rotor to the IGV engine order excitation (=14). The external loading was represented as a single unit load located along the leading edge of the airfoil and normal to the surface of the blade. This excitation is clearly a simplification of actual engine conditions in which the blades are subjected to unsteady pressure loads. Structural damping was estimated from test data and used in the ROM forced response calculations. Finally, the viscous damping associated with the blade/air interaction was not considered.

To assess the benefits of intentional mistuning, it was first desired to establish the sensitivity of the otherwise tuned rotor to small unintentional mistuning. This baseline was obtained by proceeding with a simulation of 50 random rotors (to maintain a reasonable simulation time) the results of which were fitted with the Weibull distribution to estimate the largest amplitude of response. The results of these computations, shown in Fig. 10, are consistent with known findings, i.e., a fairly large rise in amplification for small levels of mistuning and then a sharp decay in response with further mistuning. To confirm the adequacy of the number of simulations (50), 200 random rotor simulations were also conducted for standard deviations of mistuning of 1% and 5%, see Fig. 10. Clearly, there is only a slight change in the predicted percentiles of the response thereby validating the use of only 50 simulations.

The effects of intentional mistuning on the maximum forced response of the rotor were considered next. Following the previous discussion, this analysis was initially done without any unintentional mistuning and only patterns of two blades were considered. While blade "C" always corresponded to a tuned one, blade "A" was softer than tuned, i.e., with a Young's modulus reduced from its tuned counterpart by 2.5%, 5%, 7.5%, and 10%. These changes in blade stiffness can be construed as originating from a uniform distribution with standard deviations of 0.72%, 1.44%, 2.16%, and 2.88%. The combination of subproblem approximation and steepest descent algorithms, as available in ANSYS, was

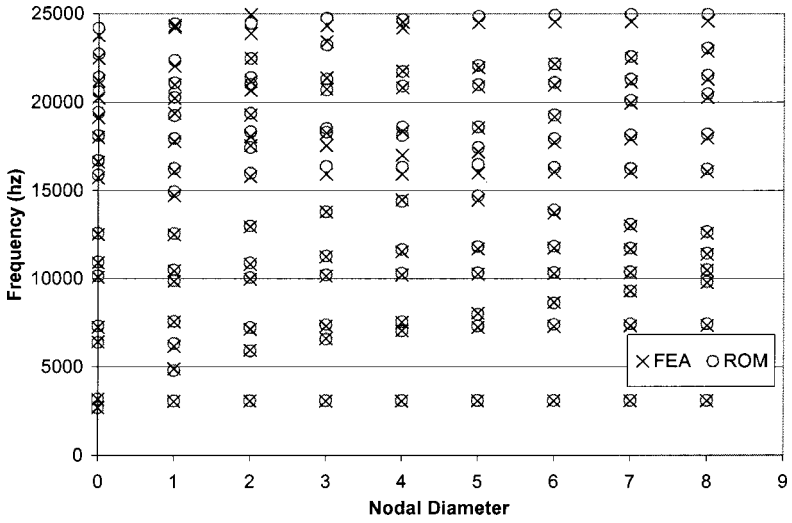

Fig. 8 Natural frequencies versus number of nodal diameters for the tuned rotor in Fig. 7 by finite element and ROM

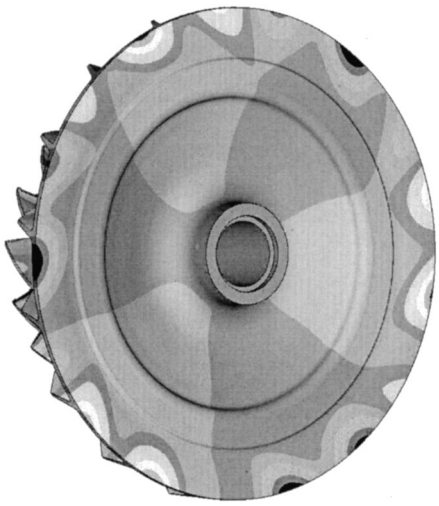

Fig. 9 Complex mode shape of the compressor disk for a nodal diameter 3 mode

used to obtain the optimum patterns of the A and C blades. A typical convergence plot, see Fig. 11, demonstrates that convergence occurred uneventfully and fairly rapidly. In addition to these optimum patterns, the fixed arrangements $(CA)_8C$ (high-low-high) and 9C8A (approximate 1 per rev) were also tested. The largest amplitude found on these disks (in the absence of random unintentional mistuning) is also shown in Fig. 10. Note in particular that the optimized pattern shows a considerable reduction in the amplitude of response, even with respect to the tuned value. As a random disk, its response is very much in the left tail of the distribution as its highest response is lower than the 0.5% percentile!

The optimized pattern corresponding to the 7.5% decrease in stiffness, i.e., 2CAC3A2C8A, was used to estimate the sensitivity of the response of such intentionally mistuned disks to random (unintentional) mistuning. The results, see Fig. 12, clearly show that this pattern has a much reduced sensitivity to unintentional mistuning as compared to the tuned (all C) disk for low values of the standard deviation of mistuning. When the level of unintentional mistuning becomes comparable to its intentional counterpart, the benefits of using different blades becomes substantially reduced but no worsening has been noted.

As a final assessment of the benefits of the optimized pattern, a

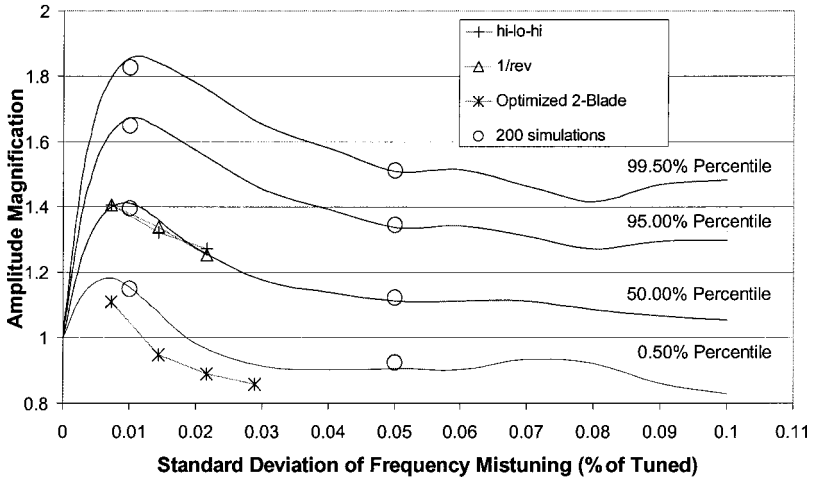

Fig. 10 Amplitude magnification for the nominal and intentionally mistuned rotors

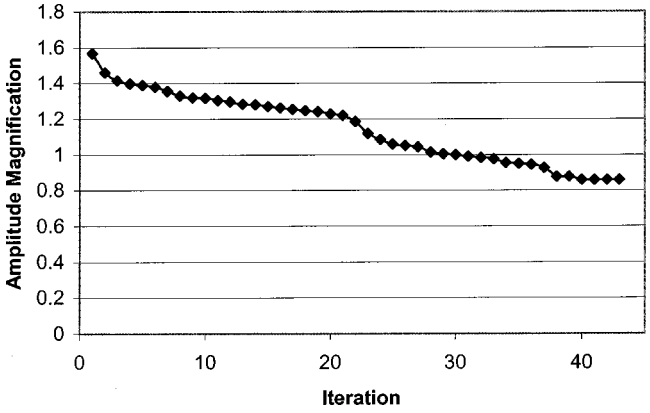

Fig. 11 Typical convergence plot of the combination of subproblem approximation and steepest descent algorithms

comparison of the above results with those produced with approximate 1 and 3 per rev arrangements of A and C blades (i.e., 9C8A and 3C3A3C3A3C2A, respectively) is shown in Fig. 13.

Pattern Screening by Localization Assessment

The previous sections have clearly demonstrated the potential benefits of intentional A/B mistuning to reduce the sensitivity of the response of bladed disks to unintentional mistuning. Unfortunately, neither the optimization algorithms nor the results presented provide any physical insight into the features of the optimum A/B patterns that lead to this reduced sensitivity. Obtaining such an understanding would not only shed some new light on the general applicability of intentional mistuning but it may also provide a mean of assessing the sensitivity of A/B patterns to random mistuning *without performing extensive simulation studies*. That is, it could provide a direct approach for screening the insensitive A/B patterns from the sensitive ones. The reduction of the computational effort associated with the elimination of the Monte

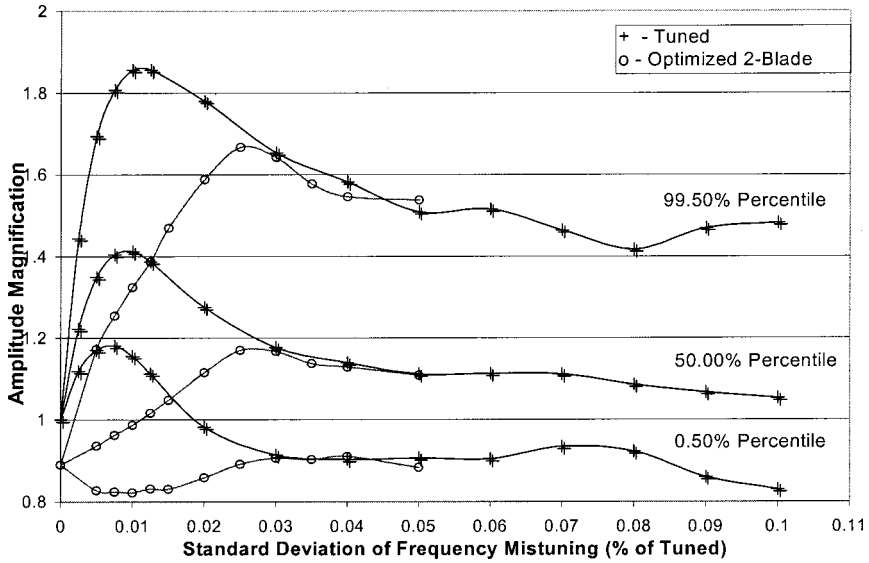

Fig. 12 Sensitivity of the tuned and optimized intentionally mistuned disks to unintentional random mistuning

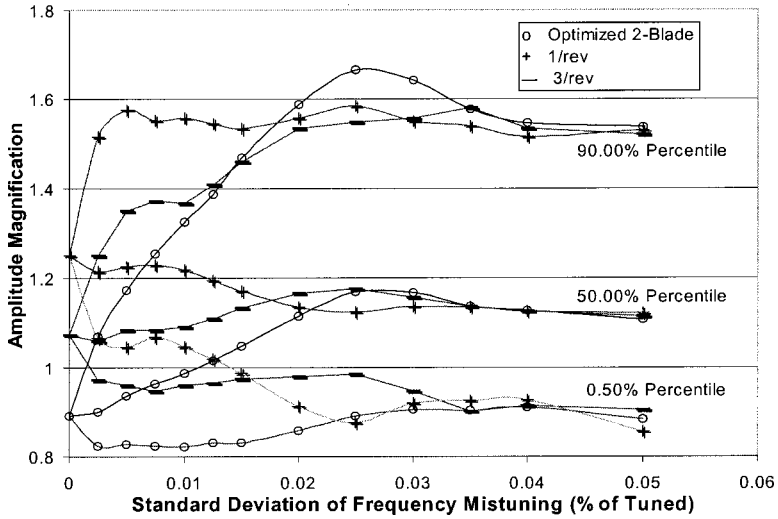

Fig. 13 Sensitivity of the optimized and some harmonically intentionally mistuned disks to unintentional random mistuning

Carlo simulations would be particularly significant in the present optimization context. This section focuses on addressing these issues from a localization point of view.

It is generally well accepted that the amplitude magnification that is associated with mistuning originates in the localization of the forced response of the disk ([6,7]). The *quantitative* evaluation of localization is, however, a difficult task ([26–29]). Indeed, these authors have shown that the mean localization factor, as specified by Wei and Pierre [6], is not an appropriate measure of localization because (i) it is dominated by damping effects not by mistuning and (ii) it does not account for the disk-to-disk variability of the localization of the forced response. In addition to these criticisms, a recent study ([30]) has emphasized the need to consider blade-to-blade variations of the localization.

Fortunately, a simple alternative for the quantification of localization was provided in [30]. Indeed, noting that the localization of the forced response is indicative of a spatial decay of the influence (or statistical correlation) of the properties of a specific blade on the response of others, they have argued that the number of blades over which a non-negligible correlation exists is in fact a measure of localization. Further, to estimate this number of blades, they suggested a simple iterative algorithm that relies on the computation of the exact forced response of partially mistuned disks in which only a sector of s blades is mistuned (the ''mistuned'' sector), the remaining ones being tuned (the ''baseline'' sector). Specifically, the amplitude of response of the central blade of the mistuned sector is computed with increasing values of $s = 1,3,5, \ldots$ until the error in predicting the response of the central blade drops and stays below a specified error margin (10% say). The corresponding value of the mistuning width s then serves as the measure of localization around that blade.

Using this novel measure of localization, Rivas-Guerra and Mignolet [30] have demonstrated that the largest possible amplitudes (A) of response occur for blades that are very strongly localized, e.g., $s=3$. Further, the wedge shape of the domain (A, s) indicated that an increase of localization of these high responding blades would produce an increase in their forced response. In the present context of large differences in blade properties, e.g., A blades versus B blades, the above concepts must be slightly altered. Specifically, for the disks exhibiting both intentional and small unintentional mistuning, it is only the latter variability that is removed in the ''baseline'' sector. For disks with only intentional mistuning, it would appear appropriate at first to replace the A or B blades in the ''baseline'' sector by tuned blades. However, proceeding with such a replacement changes dramatically the disk as the stiffnesses of the A, B, and tuned blades are quite different (of the order of 10% difference in all of the above examples). The outcome of such computations does not represent any longer the linear sensitivity measure of the response of one blade with respect to the stiffness of another but rather quantifies nonlinear effects associated with large structural modifications. Thus, following the spirit of the discussion of Rivas-Guerra and Mignolet [30], it was decided to induce only small changes in the blades present in the baseline sector bringing them closer to the tuned configuration. Specifically, the stiffness of the blades softer (respectively, stiffer) than the tuned ones have their stiffnesses increased (respectively, decrease) by the factor $(1+\sigma)$ (respectively, $(1-\sigma)$) where σ denotes the standard deviation (as a fraction of tuned) of unintentional mistuning.

The application of these concepts to intentionally mistuned disks will be exemplified on the single-degree-of-freedom example of Fig. 2. The scatter plot of the amplitude of response of the blade versus the mistuning widths s required to achieve a 10% accuracy is shown in Fig. 14 for $k_C = 8{,}606$ N/m, for both the 2B1A and 2B2A patterns without unintentional mistuning. In analyzing this figure, note first that it exhibits a total of 24 symbols, 12 triangles, and 12 squares, consistently with the two 12-blade disks. However, the periodic nature of the 2A2B and 2B1A disks and of the engine order excitation implies a similar periodicity of the blade responses so that only three different amplitudes exist for the 2B1A disk and four for its 2A2B counterpart. Further, the ensuing discussion will only focus on the localization (i.e., width of mistuning, s) of the maximum responding blade since it is only this quantity which is being considered in the proposed optimization process.

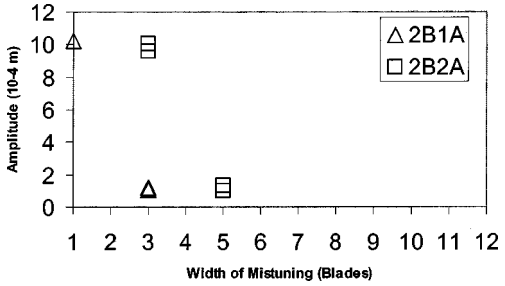

Fig. 14 Scatter plot of the width of partial mistuning required to achieve an accuracy of 10% on the amplitude of response of the blades of 2B1A and 2B2A disks, $k_C = 8606$ N/m, no random mistuning

Then, surprisingly, it is seen that the maximum amplitude of the 2B1A system can accurately be obtained with a one-blade mistuned sector while a three-blade width is required for the 2B2A system. Accordingly, the 2B1A system is more localized without random mistuning than its 2B2A counterpart and thus its capability for further localization, and consequently further increases in the maximum amplitude of response, can be expected to be lower than for the 2B2A system. This expectation is not only confirmed by the smallest slope around $\sigma = 0$ on Fig. 5 but also by the scatter plots of these two patterns obtained with unintentional mistuning (1% in frequency), see Figs. 15 and 16.

Indeed, it can be observed that approximately 10% of the blades of the 2B2A randomly mistuned disks are now localized to a one-blade sector while none did so in the absence of uninten-

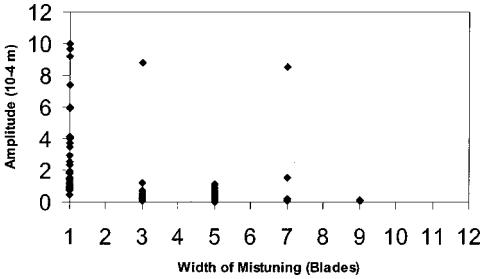

Fig. 15 Scatter plot of the width of partial mistuning required to achieve an accuracy of 10% on the amplitude of response of the blades of ten randomly mistuned 2B1A disks, $k_C = 8606$ N/m

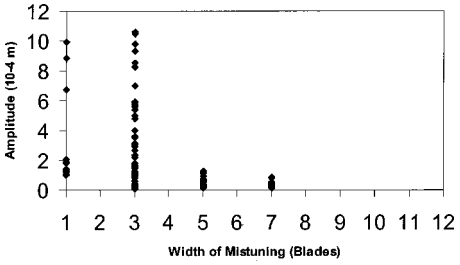

Fig. 16 Scatter plot of the width of partial mistuning required to achieve an accuracy of 10% on the amplitude of response of the blades of ten randomly mistuned 2B2A disks, $k_C = 8606$ N/m

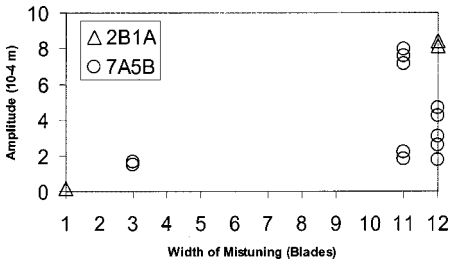

Fig. 17 Scatter plot of the width of partial mistuning required to achieve an accuracy of 10% on the amplitude of response of the blades of 2B1A and 7A5B disks, k_C=45,430 N/m, no random mistuning

tional mistuning. This situation of course does not happen for the 2B1A disks since the width of mistuning for the largest responding blade was already $s=1$! In fact, it is seen from Fig. 15 that mistuning has a beneficial effect on the localization of the 2B1A disks as a substantial fraction of them are now less localized (higher values of s) than they were before. In regards to the amplitudes of response, it should first be noted that the largest overall amplitude on the ten random disks is actually slightly smaller than it was on the tuned system. In fact, the 40 blades that would exhibit a high response in the tuned case all experience a decrease in their amplitude of response because of unintentional mistuning.

Following the discussion of Rivas-Guerra and Mignolet [30], it is suggested here that the decreases in localization and amplitude of response are in fact related. As specific examples of this situation, consider the amplitudes of (in 10^{-4} m) 8.808 (seen at $s=3$ on Fig. 15) and 8.516 and 1.513 (seen at $s=7$ on Fig. 15) which were all observed on high responding blades of the tuned case (tuned amplitude of 10.24810^{-4} m requiring a width of mistuning $s=1$, see Fig. 14). Other similar simultaneous decreases in localization and amplitude of response can also be noted in connection with the low responding blades of the tuned disk.

According to these observations, it can be stated that the response of any of the randomly mistuned disks considered in Fig. 15 is more global than for the pure 2B1A pattern and that this decrease of the localization has generally been accompanied by a decrease in amplitude as suggested in Ref. [30]. In some sense it would appear that the 2B1A achieves a maximum of localization in the absence of unintentional mistuning so that the inclusion of these variations induces a decrease in localization and thus a very low sensitivity to random unintentional mistuning.

The analysis of the results obtained for $k_C=45{,}430$ N/m generally confirms the above observations: The pattern with the lowest sensitivity to unintentional mistuning is the one that exhibits localization of the response at the smallest value of s (highest localization) when this random mistuning is not present. This situation is visible in the scatter plot of Fig. 17: The highest response of the 7A5B disk (with the lowest sensitivity to unintentional mistuning) is localized for $s=11$ while the disk 2B1A does not localize within the 10% accuracy, i.e., $s=N=12$. Its response is thus global as the tuned disk.

Summary

This investigation focused on the use of intentional mistuning of bladed disks to reduce their sensitivity to an unintentional random mistuning originating for example in the manufacturing process or in service wear. More specifically, it was proposed, for complexity/cost reasons, to limit the number of different blades to two (A and B, say) and to optimize the arrangement of these blades around the disk to reduce the effects of unintentional mistuning.

The strategy proposed to address this optimization problem relies on the following two steps:

(i) optimization of the arrangement of A and B blades to yield patterns that exhibit small/the smallest maximum amplitudes of forced response of the disk in the absence of unintentional mistuning.
(ii) the qualitative assessment of the sensitivity of the A/B blade patterns to unintentional mistuning by using a novel localization measure.

In regards to its overall goals, the findings of this investigation can be summarized as follows:

(1) The A/B pattern yielding the smallest maximum amplitude of response in the absence of unintentional mistuning is not always optimal when unintentional mistuning is factored in but the amplitude magnification of this A/B pattern is always less, most often much less, than that of the tuned system.
(2) The inclusion of the localization measure in the optimization effort permits efficiently the selection of the least sensitive of the A/B patterns retained in the first step of the approach, i.e., in the optimization per say. In this manner, a further decrease of the amplitude magnification may be achieved.

The following specific observations were also made.
(3) The largest amplitude on the disk in the absence of mistuning can be reduced by up to 20–30% by using a disk with an A/B blade pattern as opposed to a tuned one, see Figs. 4, 5, and 12.
(4) The amplitude magnification due to unintentional mistuning is often *dramatically* reduced. In Fig. 5, the largest amplification due to unintentional mistuning is 1.7 (largest amplitude$=1.7\times$tuned) without intentional mistuning but it is only 1.1 at that same standard deviation of random mistuning with an A/B pattern. Similar decreases can also be seen in Figs. 4 and 12.
(5) The standard deviation of unintentional mistuning at which the maximum magnification occurs tends to be pushed toward higher levels. For example, in Fig. 12 it occurs at 0.5%–1% without intentional mistuning and at 2.5%–3.5% with intentional mistuning which creates an additional benefit when the variability of the frequencies of the manufactured blades is low. That is, the response penalty for achieving very tight manufacturing control of the geometric parameters of the airfoils has been substantially reduced.
(6) The optimized pattern may or may not appear as variations of simple harmonic patterns, the patterns 7A5B, 3A3B, 2A2B, 2A1B, on the 12-blade disk may appear as distorted 1, 2, 3, and 4 harmonics of mistuning but the distortion plays an important role in reducing the amplitude magnification. Further, the 2CAC3A2C8A arrangement obtained in connection with the 17-blade industrial rotor is not close to any specific harmonic pattern. It would appear that patterns of two blades close to simple harmonics are in general less robust to unintentional mistuning than those that are not.
(7) The sensitivity of an intentionally mistuned disk to random unintentional mistuning appears to be directly related to the width of mistuning s needed to accurately obtain the maximum response of the disk. Specifically, the lower the value of s, the higher the disk is already localized, and thus the lower its sensitivity to unintentional mistuning will be. This observation provides a simple mean to screen A/B patterns that are very sensitive to unintentional mistuning from those that are only slightly so without performing any Monte Carlo simulation study.
(8) The above findings have consistently been obtained in connection with both simple (one and two-degree-of-freedom) disk models and an industrial rotor modeled by REDUCE, compare Figs. 4, 5, and 12.
(9) Two different optimization algorithms, one based on steepest descent and one genetic algorithm, have been tested and shown to perform well in finding the A/B pattern yielding the smallest maximum response in the absence of unintentional mistuning.

Acknowledgments

The financial support of this investigation by the NASA grant NAG-1-2233 and the PRDA Contract F33615-98-C-2922 ''Bladed Disk Contaminated Modes and Unsteady Aerodynamic Response Study'' is gratefully acknowledged.

References

[1] Ewins, D. J., 1969, ''The Effects of Detuning Upon the Forced Vibrations of Bladed Disks,'' J. Sound Vib., **9**, pp. 65–79.
[2] Whitehead, D. S., 1966, ''Effect of Mistuning on the Vibration of Turbomachines Blades Induced by Wakes,'' J. Mech. Eng. Sci., **8**, pp. 15–21.
[3] Kaza, K. R. V., and Kielb, R. E., 1984, ''Flutter of Turbofan Rotors With Mistuned Blades,'' AIAA J., **22**(11), pp. 1618–1625.
[4] Kaza, K. R. V., and Kielb, R. E., 1985, ''Vibration and Flutter of Mistuned Bladed-Disk Assemblies,'' J. Propul., **1**(5), pp. 336–344.
[5] Basu, P., and Griffin, J. H., 1986, ''The effect of Limiting Aerodynamic and Structural Coupling in Models of Mistuned Bladed Disk Vibration,'' ASME J. Vib., Acoust., Stress, Reliab. Des., **108**, pp. 132–139.
[6] Wei, S. T., and Pierre, C., 1988, ''Localization Phenomena in Mistuned Assemblies With Cyclic Symmetry—Part I: Free Vibrations,'' ASME J. Vib., Acoust., Stress, Reliab. Des., **110**(4), pp. 429–438.
[7] Wei, S. T., and Pierre, C., 1988, ''Localization Phenomena in Mistuned Assemblies With Cyclic Symmetry—Part II: Forced Vibrations,'' ASME J. Vib., Acoust., Stress, Reliab. Des., **110**, pp. 439–449.
[8] Sinha, A., and Chen, S., 1989, ''A Higher Order Technique to Compute the Statistics of Forced Response of a Mistuned Bladed Disk,'' J. Sound Vib., **130**, pp. 207–221.
[9] Wei, S.-T., and Pierre, C., 1990, ''Statistical Analysis of the Forced Response of Mistuned Cyclic Assemblies,'' AIAA J., **28**(5), pp. 861–868.
[10] Lin, C. C., and Mignolet, M. P., 1997, ''An Adaptive Perturbation Scheme for the Analysis of Mistuned Bladed Disks,'' ASME J. Eng. Gas Turbines Power, **119**, pp. 153–160.
[11] Mignolet, M. P., Hu, W., and Jadic, I., 2000, ''On the Forced Response of Harmonically and Partially Mistuned Bladed Disks. Part I: Harmonic Mistuning,'' Int. J. Rotating Mach., **6**(1), pp. 29–41.
[12] Mignolet, M. P., Hu, W., and Jadic, I., 2000, ''On the Forced Response of Harmonically and Partially Mistuned Bladed Disks. Part II: Partial Mistuning and Applications,'' Int. J. Rotating Mach., **6**(1), pp. 43–56.
[13] Yang, M.-T., and Griffin, J. H., 2001, ''A Reduced Order Model of Mistuning Using a Subset of Nominal System Modes,'' ASME J. Eng. Gas Turbines Power, **123**(4), pp. 893–900.
[14] Petrov, E., Sanliturk, K., Ewins, D. J., and Elliott, R., 2000, ''Quantitative Prediction of the Effects of Mistuning Arrangement on Resonant Response of a Practical Turbine Bladed Disc,'' *5th National Turbine Engine High Cycle Fatigue (HCF) Conference*, Chandler, AZ, Mar. 7–9.
[15] Castanier, M. P., and Pierre, C., 1997, ''Consideration on the Benefits of Intentional Blade Mistuning for the Forced Response of Turbomachinery Rotors,'' *Proceedings of the ASME Aerospace Division*, **AD-Vol. 55**, pp. 419–425.
[16] Castanier, M. P., and Pierre, C., 1998, ''Investigation of the Combined Effects of Intentional and Random Mistuning on the Forced Response of Bladed Disks,'' AIAA Paper No. AIAA-98-3720.
[17] Kenyon, J. A., and Griffin, J. H., 2000, ''Intentional Harmonic Mistuning for Robust Forced Response of Bladed Disks,'' *5th National Turbine Engine High Cycle Fatigue (HCF) Conference*, Chandler, AZ, Mar. 7–9.
[18] Ottarsson, G., and Pierre, C., 1995, ''On the Effects of Interblade Coupling on the Statistics of Maximum Forced Response Amplitudes in Mistuned Bladed Disks,'' *Proceedings of the 36th Structures, Structural Dynamics, and Materials Conference and Adaptive Structures Forum*, New Orleans, LA, Apr. 10–13, **5**, pp. 3070–3078.
[19] Kruse, M. J., and Pierre, C., 1996, ''Forced Response of Mistuned Bladed Disks Using Reduce-Order Modeling,'' *Proceedings of the 37th Structures, Structural Dynamics, and Materials Conference*, Salt Lake City, UT, Apr. 15–17, pp. 1938–1950.
[20] Mehmed, O., and Murthy, D. V., 1988, ''Experimental Investigation of Propfan Aeroelastic Response in Off-Axis Flow With Mistuning,'' *Proceedings of the 24th AIAA/SAE/ASEE Joint Propulsion Conference*, Boston, MA.
[21] Goldberg, D. E., 1989, *Genetic Algorithms in Search, Optimization & Machine Leaning*, Addision-Wesley, Reading, MA.
[22] Gen, M., and Cheng, R., 1997, *Genetic Algorithms & Engineering Design*, John Wiley and Sons, New York.
[23] Mignolet, M. P., Rivas-Guerra, A. J., and Delor, J. P., 2001, ''Identification of Mistuning Characteristics of Bladed Disks From Free Response Data—Part I,'' ASME J. Eng. Gas Turbines Power, **123**, pp. 395–403.
[24] Castanier, M. P., Ottarsson, G., and Pierre, C., 1997, ''A Reduced-Order Modeling Technique for Mistuned Bladed Disks,'' ASME J. Vibr. Acoust., **119**, pp. 439–447.
[25] Bladh, R., Castanier, M. P., and Pierre, C., 2002, ''Component-Mode-Based Reduced Order Modeling Techniques for Mistuned Bladed Disks, Part I: Theoretical Models,'' ASME J. Eng. Gas Turbines Power, to appear.
[26] Castanier, M. P., and Pierre, C., 1993, ''Individual and Interactive Mechanisms for Localization and Dissipation in a Mono-Coupled Nearly Periodic Structure,'' J. Sound Vib., **168**(3), pp. 479–505.
[27] Cha, P. D., and Morganti, C. R., 1994, ''Numerical Statistical Investigation on the Dynamics of Finitely Long, Nearly Periodic Chains,'' AIAA J., **32**(11), pp. 2269–2275.
[28] Castanier, M. P., and Pierre, C., 1997, ''Predicting Localization via Lyapunov Exponent Statistics,'' J. Sound Vib., **203**(1), pp. 151–157.
[29] LaBorde, B. H., 1999, ''Assessment of Predictive Capabilities of Mistuning Effects on the Resonant Response of Bladed Disks,'' M. S. thesis, Arizona State University, Tempe, AZ, Dec.
[30] Rivas-Guerra, A. J., and Mignolet, M. P., 2003, ''Local/Global Effects of Mistuning on the Forced Response of Bladed Disks,'' ASME J. Eng. Gas Turbines Power, to appear.

Development of High-Speed Gas Bearings for High-Power Density Microdevices

F. F. Ehrich

S. A. Jacobson

Gas Turbine Laboratory,
Massachusetts Institute of Technology,
77 Massachusetts Avenue,
Cambridge, MA 02139

A 4.2-mm diameter silicon rotor has been operated in a controlled and sustained manner at rotational speeds greater than 1.3 million rpm and power levels approaching 5 W. The rotor, supported by hydrostatic journal and thrust gas bearings, is driven by an air turbine. This turbomachinery/bearing test device was fabricated from single-crystal silicon wafers using micro-fabrication etching and bonding techniques. We believe this device is the first micro-machine to operate at a circumferential tip speed of over 300 meters per second, comparable to conventional macroscale turbomachinery, and necessary for achieving high levels of power density in micro-turbomachinery and micro-electrostatic/electromagnetic devices. To achieve this level of peripheral speed, micro-fabricated rotors require stable, low-friction bearings for support. Due to the small scale of these devices as well as fabrication constraints that limit the bearing aspect ratio, the design regime is well outside that of more conventional devices. This paper focuses on bearing design and test, and rotordynamic issues for high-speed high-power micro-fabricated devices.
[DOI: 10.1115/1.1498273]

Introduction

Based on an original concept by A. H. Epstein et al. [1,2], an effort was undertaken in 1994 to design and develop a family of high-power-density microdevices involving millimeter/micron scale turbomachinery, combustion systems, and electrostatic/electromagnetic energy-conversion components, manufactured within the complex of micro-electro-mechanical systems (MEMS) fabrication technology. The work was conducted by a team of faculty, staff, and students under the direction of A. H. Epstein at the M.I.T. Gas Turbine Laboratory. The activity was sponsored and encouraged by ARO and DARPA.

A fundamental enabling technology needed was the ability to spin silicon rotating elements, supporting the turbomachinery and electrical components, at peripheral speeds of several hundred meters per second, over two orders of magnitude faster than silicon rotors have previously achieved. A full set of demanding requirements was evolved for the bearing/rotordynamic system that, though commonplace for full-scale rotating machinery, was unprecedented for microdevices.

Objectives—Operational Requirements

- High tip speed—Achieve a challenging goal of 500 m/s.
- Extended life—Sustain hundreds of hours of operation with minimal wear and no deterioration in performance.
- Low energy dissipation; low leakage—Limit viscous drag losses to no more than 5 W; and leakage loss to no more than 10% of main turbomachinery flow.
- Acrobatic attitude capability—Operate at any attitude with respect to the gravitational or acceleration field.
- Shock resistance—Withstand 100 Gs of acceleration without detriment to operation.
- Stability—Operate stably, with high as-manufactured imbalance, without any vibratory or divergent behavior that would jeopardize performance or life. (A systematic balancing operation was not considered feasible.)
- Temperature capability—Operate at elevated temperatures typical in gas turbine engines.

Objectives—Configuration Requirements

- Fabrication—Limit to multidie wafer-level batch fabrication operations to exploit the low cost potential of MEMS systems.
- Wafer levels—Include a minimum number of separately fabricated (and subsequently bonded) wafers to minimize the complexity and cost of the devices as well as the as-manufactured imbalance of the rotors.
- Bearing pressurization—Include the facility for pressurizing bearings internally from tapped pressures (and, where appropriate, air-impingement starter air).

Objectives—Applications Requirement

- Rotordynamic system—Develop the total rotordynamic system integrated with the individual bearings.
- Universality of application—Anticipate and accommodate all the various devices that had been conceived and contemplated (including single wafer rotors, and two-wafer rotors), without requiring redevelopment of the rotor/bearing system for each individual device.

Design

The micro-bearing/rotor system was designed in the context of a micro-bearing experimental test vehicle (the ''microrig'') by F. F. Ehrich with contributions by S. A. Jacobson [3] for the drive-turbine detailed design, R. Walker for the thrust bearing detailed design, K. S. Breuer et al. [4] for the journal bearing detailed design, K. S. Chen [5] for the stress analysis, and M. Spearing and K. S. Chen [6] for the material characterization. Further contributions were made by C. C. Lin et al. [7] in his work on the fabrication and initial test of the first microrigs. Subsequent refinement and development of the rotor/bearing system design was accomplished by L. Fréchette et al. [8] in the context of the design of a single-wafer micromotor compressor, and by J. M. Protz [9] in the context of a two-wafer rotor microjet engine.

Figure 1 shows a cross section of the microrig. A 4.2-mm diameter rotor is enclosed in a fusion-bonded stack of five aligned, through-etched wafers. The rotor is a planar disk with a radial-

Contributed by the International Gas Turbine Institute (IGTI) of THE AMERICAN SOCIETY OF MECHANICAL ENGINEERS for publication in the ASME JOURNAL OF ENGINEERING FOR GAS TURBINES AND POWER. Paper presented at the International Gas Turbine and Aeroengine Congress and Exhibition, New Orleans, LA, June 4–7, 2001; Paper 20001-GT-478. Manuscript received by IGTI, Dec. 2000; final revision, Mar. 2001. Associate Editor: R. Natole.

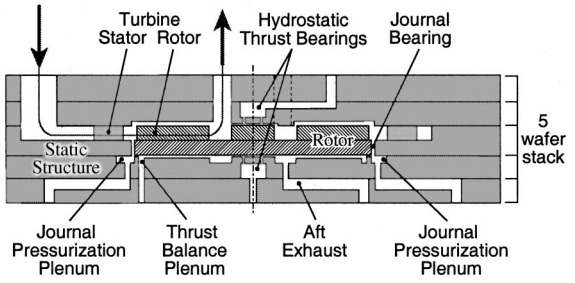

Fig. 1 Schematic cross section of micro-bearing rig. The rotor is 4.2 mm in diameter and 450 μm thick (0.15 μm thick blades and 300 μm long journal bearing). The rotor is centered in a rectangular die structure with dimensions 15 mm×15 mm ×2.3 mm. There are two semi-circular journal pressurization plenums that can be pressurized differentially to provide side-load.

inflow turbine on its front side. Pressurized nitrogen enters the device near the outer edge and flows radially inward through a set of stator vanes and then through the rotor blades, exhausting axially near the center of the device. A gas journal bearing on the periphery of the rotor provides radial support. A pair of gas thrust bearings on the device centerline provides axial support. The turbine is designed to provide sufficient power to overcome viscous drag in the bearings, blade tips, and backside of the rotor.

Bearing Type Selection. One of the attractions of micro-fabricated MEMS devices is the ability to produce parts in large batches. Batch production requires fabrication repeatability and high yield, and these issues call for minimizing device complexity ([4]). Standard bulk micro-fabrication technology limits the structures in MEMS devices to two-dimensional extruded-like forms. Fabrication and assembly precision are limited to dimensional and assembly (wafer-bonding alignment) accuracy tolerances of about 1–2 microns for devices up to 1 cm.

With these constraints in mind, a study of different bearing options was performed. High-speed rolling-element bearings could not be micro-fabricated based on current technology. The dissipation of this type of bearing at the desired scale would also be too large and the life too short. The standard toolbox of materials that can be micro-fabricated does not include one with significant magnetic properties so that a magnetic bearing was not considered feasible. While miniature conventionally machined ball bearings are available and could potentially be coupled to a micro-fabricated device, available units with adequate life were rated up to only 500,000 rpm, less than one-fourth the required rotation rate for our rotors. In addition, dissipation levels of such ball bearings were estimated to be an order of magnitude larger than our design specifications would allow. Moreover, the use of such bearings is incompatible with the requirements of batch fabrication.

The design focused on gas-lubricated bearings as they are most compatible with batch micro-fabrication while promising relatively low dissipation levels and stable operation at high rotational speeds. The small scale of the device along with fabrication limitations (etch depth and etch aspect ratio constraints) put these bearings well outside the standard design space, making the development of these bearings a major design and development challenge.

Thrust Bearings. As shown in Fig. 2, there are two main types of gas-lubricated thrust bearings: hydrodynamic and hydrostatic. Hydrodynamic bearings rely on the rotor rotation to provide viscous pumping action in the bearing and to elevate the pressure on the bearing face as a function of the axial bearing gap size, generating stiffness to inhibit axial motion. Hydrostatic bearings act independently of rotor motion and rely on a source of high-pressure fluid supplied through a series of restrictors, including the bearing gap, to generate a pressure that is a function of the axial gap size, generating stiffness to inhibit axial motion.

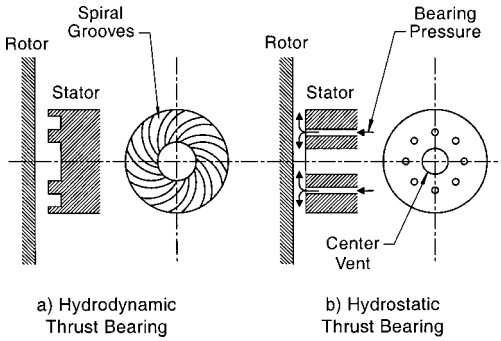

Fig. 2 Schematic comparing generic types of gas thrust bearings

Since the thrust bearing was considered a less daunting challenge than the journal bearing, research and development efforts focused initially on designing and demonstrating the hydrostatic thrust bearing (Fig. 2(b)). With proper pressurization controlled by the operator, the hydrostatic design can provide axially centered operation even with no rotation, allowing the rotor to be floated prior to spinning it up.

The long-term goal of this project is to micro-fabricate a self-contained gas turbine engine. Hydrostatic thrust bearings may not provide sufficient stiffness for this device given the expected pressure ratio of the compressor. A next generation microrig has been designed by C. W. Wong [10] with hydrodynamic thrust bearings to investigate their advantages, namely elimination of bearing-pressurization airflow, high stiffness capability, and considerable simplification in system construction.

Journal Bearings. As shown in Fig. 3, there are also two generic types of gas-lubricated journal bearings: hydrodynamic and hydrostatic. Hydrodynamic journal bearings rely on the rotor to drag fluid around the bearing at high speed, generating stiffness as the dragged fluid interacts with a rotor that has moved off-center

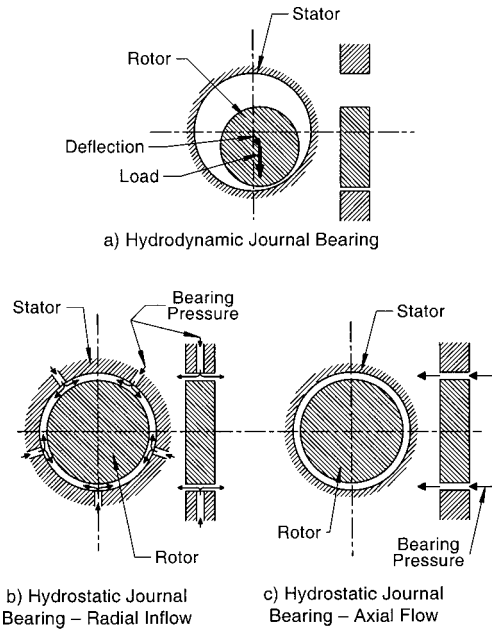

Fig. 3 Schematic comparing generic types of gas journal bearings

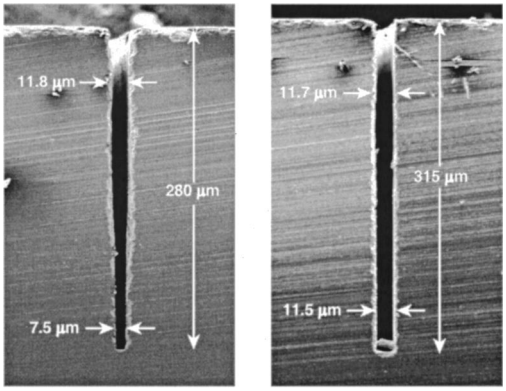

(a) A 1998 journal (b) A CY2000 journal

Fig. 4 Journal bearing etch test cross section

imposing an asymmetric flow field. Hydrostatic bearings rely on a source of high-pressure fluid supplied either radially (Fig. 3(b)) or axially (Fig. 3(c)) through a series of restrictors, including the bearing gap, to generate stiffness.

The hydrodynamic bearing was chosen for initial development since it was considerably simpler in configuration and required considerably less pressurized airflow (needed to side-load the rotor) than a radial-inflow hydrostatic journal bearing. That initial selection did not anticipate the difficulty in operation of the hydrodynamic bearing. The hydrodynamic bearing is very difficult to stabilize at low speed in the context of the microdevice. Moreover, for stable operation and sufficient stiffness at high speed, a hydrodynamic bearing must operate with large eccentricity, very close to the wall ([11–14]). Such close clearance operation involves very high-energy dissipation and makes the bearing extremely vulnerable to catastrophic rubs precipitated by rotor imbalance. Additionally, the application of side-load may require accurate real-time measurement of the minimum clearance—not readily available experimentally, and probably unfeasible in operating devices.

As will be noted in the discussion of the bearing development, the journal bearing design has evolved using a very simple axial-flow configuration hydrostatic system (Fig. 3(c)) that was discovered to be already inherent in the original design. The hydrostatic operation of the bearing exploits the configuration's inherent stability at low speed, and its centered rotor (with no imposed eccentricity) to accommodate operation with high imbalance and low-energy dissipation. Moreover, the axial-flow variant has a flow usage substantially less than originally anticipated. Hydrodynamic operation remains an available option should current effort on hydrostatic operation fall short of our ultimate requirements.

Overall Configuration. A cross-sectional schematic of the microrig is shown in Fig. 1. Micro-fabrication is typically a two-dimensional process in which a mask is photolithographically transferred to the surface of a silicon wafer. Material is removed from the wafer through an etching process that eats away the parts of the wafer unprotected by the mask. All of the deep etching (>10 microns) utilized for this project used a process known as deep reactive ion etching (DRIE), an anisotropic process that etches straight down into the wafer leaving relatively straight-walled extruded-like structures ([15]). The journal bearing clearance etch is the most critical of the required etches, requiring a depth on the order of 300 microns and a width on the order of 11 microns for an aspect ratio of between 25 and 30. Figure 4 shows an example of a cross section through an early journal bearing etch test for devices built in 1998 with the bearing gap varying from about 7 to 13 microns along its length. That early effort is compared to a more recent achievement with a virtually constant width etch.

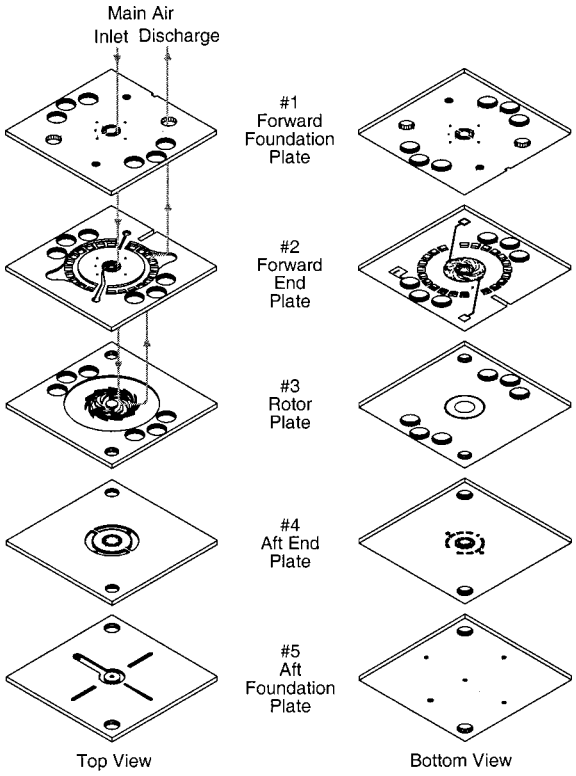

Fig. 5 Micro-bearing rig, exploded view

Effective three dimensionality is achieved by a serial sequence of two-dimensional etches, each with a different etch depth and photo-lithographic mask, on both the front and back sides of the several wafers, followed by bonding the wafers together in an aligned fashion. Figure 5 shows an exploded view of the five individual wafers of which the microrig is composed. The inlet flow to the turbine is distributed in a circumferential plenum and flows radially inward through a radial-inflow turbine. The rotor is supported axially by two centrally located hydrostatic thrust bearings. The journal bearing is located on the rim of the rotor. This design resulted from several design considerations and constraints:

- The microrig was designed as a flexible platform. In its basic configuration (Fig. 1), it serves as a microbearing and microturbomachinery test vehicle. The design also allows the introduction of an electrostatic induction motor (or generator) on the back of the rotor. Electrostatic operation results in a substantial attraction force on the rotor towards the back side of the device. In anticipation of this, the aft thrust bearing (1.8-mm diameter) was sized larger than the forward thrust bearing (1.4-mm diameter). The hydrostatic thrust bearing consists of a plenum linked to the bearing gap by fixed orifice restrictors. There are 18 fixed orifice restrictors at a radius of 0.75 mm on the aft side and 14 restrictors at a radius of 0.55 mm on the forward side. These restrictors are nominally 100 microns long and 10 microns in diameter. With the rotor axially centered, the gap in each of the thrust bearings is 1.5 ± 0.1 microns. Early designs of the thrust bearings included a center vent. However, the center vent was removed in the course of development for configuration simplification.
- Several features of the bearings required tight tolerances, including the fixed orifice restrictors. Substantial resources were invested in micro-fabrication process development to ensure dimensional repeatability from device to device. Repeatability is a strong function of the photolithography and the etch parameters.

In addition, the device geometry, particularly the mix of small and large features, can play an important role, and the device layout and process steps have taken this into account.

• Care has been taken in setting the device specifications to obtain reasonable device yield, to exploit the fact that it was often easier to consistently match feature dimensions in a given location on a wafer, than across a wafer or between different wafers. As an example, repeatability of the thrust bearing restrictors is made difficult by their small size. In setting the acceptable tolerance range for the restrictors, a much tighter tolerance is set on consistency between restrictors on a given device than on the specific dimensions associated with them. Our current process control is such that the restrictor length can vary by up to 10 microns and the restrictor diameter by about 1 micron between different wafer builds. However, uniformity is better between devices on the same wafer, and within a single device, the lengths tend to be uniform within a micron and the diameters within a few tenths of a micron, which is acceptable for device performance.

• The journal bearing is on the disk outer diameter for fabrication ease, as well as to maximize the bearing footprint. Microfabrication constraints limit the bearing-clearance etch aspect ratio.

• Two separate plenums are included on the aft side of the rotor over the end of the journal bearing, each covering somewhat less than half of the circumference. An applied pressure difference to these plenums results in a side load on the rotor, necessary for hydrodynamic operation since, in its small scale and silicon construction, the mass of the rotor is insufficient to provide a side load of the order of magnitude required to stabilize the hydrodynamic bearing. For hydrostatic operation, these plenums are equally pressurized.

• An additional plenum on the aft side of the rotor, inboard of the rotor radius, is used to balance the axial load on the rotor as the turbine pressurization is changed, relieving the load on the thrust bearings.

Development

Macrorig. In order to accelerate the pace of development while the initial fabrication process development was in progress, the construction and experimental test of an overscale model of the rotor/bearing system (termed the ''macrorig'') was undertaken. The model was designed by F. F. Ehrich and rendered in precise 26X scale, the minimum necessary to enable complete instrumentation—particularly of rotor dynamic deflection/orbit—with journal bearing clearance adjusted for full simulation of all pertinent dimensionless parameters. The rig was operated with vertical centerline to simulate virtual absence of meaningful radial gravitational load in full microscale. Capability was included for precisely adjusted tilting of the centerline to develop a controlled component of the gravitational force on the rotor in the radial direction. The research program was designed and conducted by D. J. Orr [11]. A number of important findings and a considerable amount of data were acquired:

• It was found that the rotor had a high imbalance in its as-manufactured state. The system could not be operated with side load (that is, hydrodynamically stabilized) until a precision balancing of the rotor was accomplished. There was good correspondence between the analytic formulation of the hydrodynamic bearing behavior to the experimental results from the macrorig with a balanced rotor ([4,11–14]).

• Inherent hydrostatic stiffness of the journal bearing associated with axial flow through the bearing clearance (Fig. 3(c)) was discovered and characterized (Fig. 6). With an axial pressure differential applied across the journal bearing, there is a pressure drop associated with the flow entering the bearing, with the flow passing through the bearing from viscous effects including the development of the boundary layer in the gap (significant due to the short length of the bearing and low Reynolds number of the flow), and finally with the flow exiting the bearing. Each of these losses can be viewed as a resistance, and several of these resistances are functions of the local journal bearing clearance. The variation in internal bearing pressures as a function of local dynamic clearance changes results in a variation in the pressure forces on the rotor journal that results in a restoring force and an inherent stiffness. This effect was not purposely designed for in the original layout of the microrig, and its appearance was unexpected and fortuitous. Subsequent to its being uncovered, L. San Andres of Texas A&M helped us identify the phenomenon as the ''Lomakin effect,'' as described by Childs [16]. As a consequence of this initially unexpected stiffness at both low and high speed, it was possible to run to high speed even in the as-manufactured highly imbalanced state with no applied side-load. Operation was generally characterized by prominent asynchronous precession frequency, which was generally suggestive of the system's natural frequency. The indications of precession were most pronounced even under very modest side-load when stimulated by the nonlinear asynchronous response to synchronous excitation at rotation speeds which were whole number multiples of the natural frequency (i.e., subharmonic response), and fractional multiples of the natural frequency (i.e., superharmonic response) ([17]). The measured natural frequencies were then a key parameter in the characterization of the stiffness (Fig. 6).

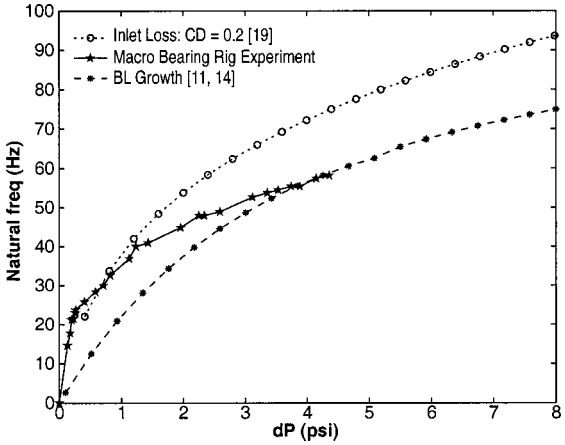

Fig. 6 Hydrostatic journal bearing natural frequency—macrorig ([11])

• It was possible to run the rotor to high multiples of natural frequency (i.e., many times higher than the reference number of 2 suggested by conventional analysis ([4,14]) of the system without hydrodynamic stiffness when unloaded or lightly loaded. Some mapping of the instability boundary was accomplished.

Microrig

Device Fabrication. First generation microrig devices were designed by C. C. Lin and fabricated by Lin with the help of R. Ghodssi and R. Khanna. Lin conducted initial testing of these devices, verifying the thrust bearing design. Fabrication and operational details of this first generation device are described in Lin et al. [7]. Second generation devices were designed by L.G. Fréchette and fabricated by Fréchette and X. Zhang. These devices were tested by Fréchette, C.W. Wong, and S.A. Jacobson, and achieved sustained operation at high speeds. Fabrication and basic operational details for the second generation devices are included in Fréchette et al. [8]. Each device build, produced in the MIT Microsystems Technology Laboratory (MTL), consisted of a bonded stack of five 100-mm wafers and produced 12 devices. Results presented in this paper come from devices produced in several builds of the second-generation device.

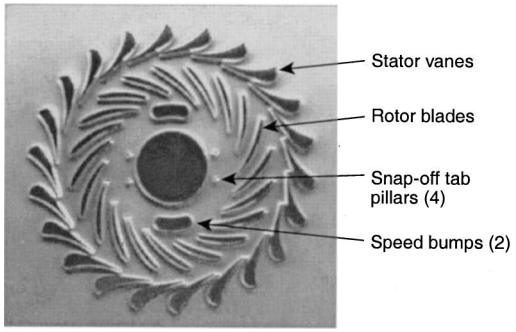

Fig. 7 View of the rotor plate showing the 4.2-mm diameter microturbine with 150 μm tall stator and rotor blades, two symmetric speed bumps, and four pillars for the snap-off tabs. In this picture, the journal bearing gap has not been etched or the snap-off tabs severed.

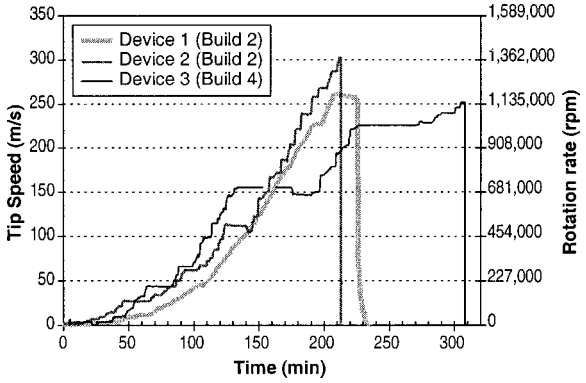

Fig. 8 Operation of three microrig devices to high speed for sustained periods of time

Testing. The microrig mounts in an acrylic package using o-rings to create sealed fluidic connections. Plastic tubing connects the package to a gas handling system, which includes a high-pressure nitrogen source, valves to distribute pressures to the various ports, pressure sensors, mass flow meters, a PC-based data acquisition system, and a fiber optic speed sensor.

At the conclusion of device fabrication, the rotor is held fixed internally by four silicon tabs in an axially centered position. The flow rate versus pressure characteristic is measured for each of the thrust bearings in this position. This test is repeated once the tabs are snapped off, freeing the rotor, with the rotor pushed to an axial eccentricity of ± 1. Data from this series of tests is compared to flow models to confirm fabrication precision and to test for leaks. This data also allows the use of the thrust bearings as an axial position sensor. The thrust bearings exhaust to ambient and thus are independent of the turbine and journal bearing pressurization, and are only weakly dependent on rotation. A fixed pressure is supplied to one of the thrust bearings; the static test data then indicates the flow rate through that bearing associated with centered operation. The pressure supplied to the opposite thrust bearing is then controlled throughout a run to maintain the appropriate mass flow in the original thrust bearing, resulting in axially centered operation. For initial tests, the thrust bearings were pressurized in the range of 40–80 psi. This provided sufficient stiffness to the degree that the axial position of the rotor was not strongly affected by the level of pressurization on the rotor faces for typical runs.

A fiber optic speed sensor detects the passage of two diametrically opposite features on the silicon rotor. These two features, referred to as speed bumps in Fig. 7, are at the same level as the blades and the thrust-bearing hub, and are located on the rotor in the exhaust flow from the turbine. The output from this sensor is a low-duty cycle square wave with frequency twice that of the rotor rotation rate. The speed sensor signal is monitored on a spectrum analyzer during a run. The speed signal is also occasionally sampled at a high-data rate for a short-time period for post-processing a more finely resolved power spectrum. Figure 8 shows the rotation rate of three devices as they are slowly accelerated in a stable manner. As the turbine supply pressure increases, the pressures applied to the hydrostatic journal bearing are also increased according to a predetermined schedule. Device 1 was brought up to a tip speed of 260 m/s (1.2 million rpm) and was held there for 20 minutes (a pressure leak resulted in a slight deceleration). The rotor was then rapidly decelerated to stop. Device 2 reached a tip speed of 303 m/s (1.37 million rpm) and Device 3 reached a tip speed of 250 m/s (1.1 million rpm) prior to crashing. These devices were each run for approximately 10^8 revolutions.

The operating schedule is one suspect in the cause of the crash of Devices 2 and 3. More dies are currently being tested to help map out safe areas of operation. However, a significant problem in consistently achieving high-speed operation is believed to be rotor imbalance. Balance is limited by our ability to align the placement of the feature masks relative to one another on each side and on opposite sides of the rotor wafer, and by the uniformity of the blade etches across a rotor.

The mass flow rates supplied to Device 2 are shown in Fig. 9. The flow rates supplied to each of the two semi-circular journal pressurization plenums (Q_{jp1} and Q_{jp2}) are essentially equal (as required by hydrostatic operation), lying on top of each other in Fig. 9. The thrust balance plenum was sealed with negligible leakage. Also shown in Fig. 9 is an aggregate of the back plenum flows normalized by the main turbine flow. This ratio peaks at a value of 0.3 at low speed, but decreases to 0.13 at the highest speed and is continuing to trend down. Analysis of the bearing dynamics discussed in the next section indicates that the device may operate at high speeds with an axial differential pressure across the journal bearing much lower than anticipated in our early look at hydrostatic journal bearings and with flow sufficiently small compared to the main engine flow to meet device loss requirements.

Experimental Estimation of the Rotor Natural Frequency and Stiffness. As previously noted, the speed sensor involved the positioning of two bumps on the rotor surface (as shown in Fig. 7) and the introduction of a stationary fiber optic probe which both illuminated the surface of the disc and the rotation bumps, and also measured the energy which they reflected. This produced a sensed signal that included two pulses per revolution, one for each passing of a bump in the field of vision of the fiber optic probe. Although the major signal was expected to have a principal fre-

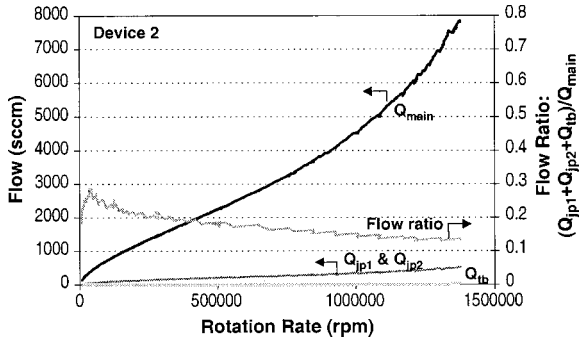

Fig. 9 Measurement of journal and thrust-balance plenum flow rates in a microrig compared to the main flow through the turbine

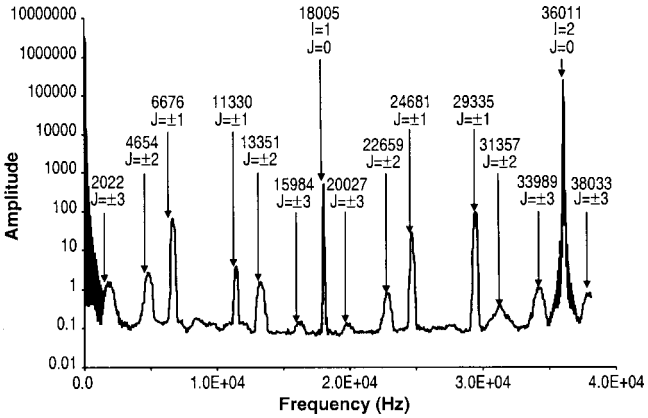

Fig. 10 Frequency spectrum of the speed sensor signal as measured on the microrig. There is no way to distinguish whether this is indicative of a 6676 Hz or an 11,330 Hz precession frequency.

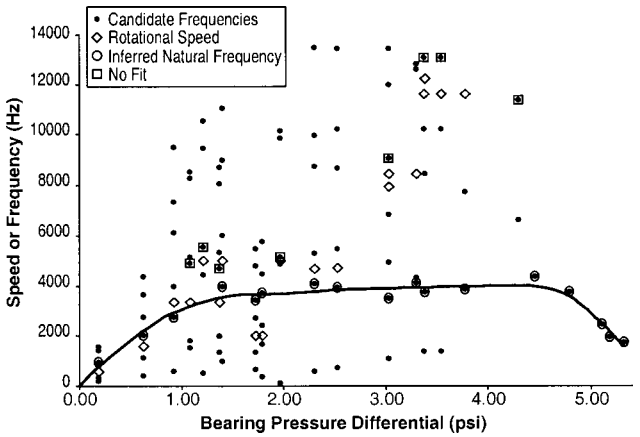

Fig. 12 Precession frequencies selected as possibly representative of the system natural frequency

quency of two times the rotational speed ($2\,\Omega_{\text{rotation}}$), early observations of the typical signal's waveform suggested the presence of asynchronous precession velocities of the rotor also manifest in the signal's spectrum, as shown in Fig. 10. Precession velocity of the rotor in the direction of the speed bump's rotation speed at the time of its passing the fiber optic probe's field of vision would result in a shorter pulse width in the sensed signal. Similarly, precession velocity of the rotor opposite to the direction of the speed bump's rotational speed at the time of its passing the fiber optic probe's field of vision would result in a longer pulse width in the sensed signal. Analysis of such a pulse width modulated signal suggested that we might expect to see a spectrum (Fig. 11) with a large number of response frequencies for any single precession frequency:

$$\Omega_{\text{spectral}} = I\ \ \Omega_{\text{rotation}} + J\ \ \Omega_{\text{precession}} \tag{1}$$

where I and J are integers. The most prominent of these spectral components were found to be for values of $J = \pm 1$ giving the primary candidate frequencies:

$$\Omega_{\text{spectral}} = I\ \ \Omega_{\text{rotation}} \pm\ \ \Omega_{\text{precession}}\,. \tag{2}$$

The spectral component $(I,J) = (0,1)$ would then represent the precession frequency. But as suggested in a typical measured spectrum shown in Fig. 10, there is no systematic way to identify which of the spectral components that are inferred to have an index $J = \pm 1$ is the one which has the indices $(I,J) = (0,1)$ and can be associated with the actual precession frequency. Figure 11 illustrates this point by showing the calculated spectrum from an analytic model of the sensor signals for $\Omega_{\text{precession}}/\Omega_{\text{rotation}} = 0.37$ and 0.63. Only a single figure is shown for the two results because they are actually *identical*.

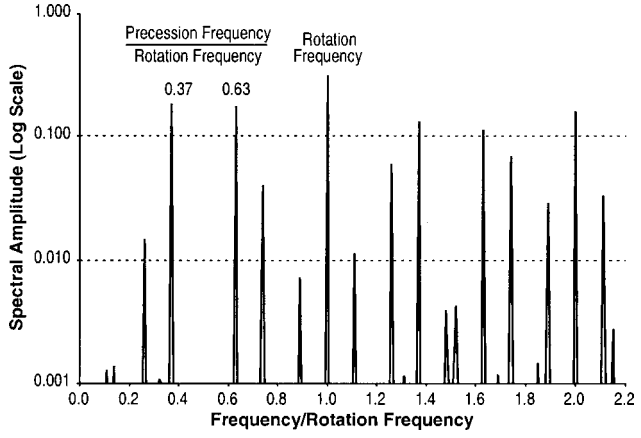

Fig. 11 Frequency spectrum of the speed sensor signal from an analytic model for $\Omega_{\text{precession}}/\Omega_{\text{rotation}} = 0.37$ and 0.63 (identical result for both cases)

Although a precession frequency is not always evident on test of the microdevices, we believe that the principal precession activity that we do see is at or near the natural frequency (Ω_{natural}) of the system, as excited by broad-band noise at operating points with low damping or from sub or super or ultra-subharmonic response to synchronous (imbalance) excitation acting on system nonlinearities ([17]). It therefore becomes a principal objective of experimental data reduction to resolve this ambiguity in identifying the actual principal precession frequency from among the many candidate frequencies observed.

It is inferred from analytic models of hydrostatic stiffness that the stiffness and hence the natural frequency of the rotor in a fixed design geometry is principally a function of the bearing differential pressure ΔP. We therefore array all of the candidate frequencies (that is, where $J = \pm 1$) from the experimentally derived spectra for all the measurement points from all the experimentally tested devices on a single graph as a function of ΔP as in Fig. 12. We then seek to identify a set of representative points, one from each spectrum, which form a continuous curve with the generic characteristics we might expect from the functional relationship between Ω_{natural} and ΔP as also shown in Fig. 12. The identified curve constitutes a very preliminary and tentative evaluation of the relationship between Ω_{natural} and ΔP, pending more conclusive resolution of two outstanding issues:

(1) From the set of 25 experimental spectra, the identified curve involves only 17 data points with 8 spectra failing to yield candidate frequencies that fall on the identified curve. It is hypothesized that the eight maverick points may represent the effect of hydrodynamic stiffening as seen by the rotor orbiting with a dynamic eccentricity ratio $\varepsilon_{\text{dynamic}}$ greater than 0.65. At lower dynamic eccentricity ratios, hydrodynamic stiffness is negligible and we expect to operate with simple constant linear hydrostatic stiffness. We would then expect the dynamic eccentricity amplitude response curve to vary with normalized rotation speed as shown in Fig. 13 with no penetration of hydrodynamic stiffening. The precise analytic model of operation at higher dynamic eccentricities, typical of transcritical operation with large imbalance, is quite complex (involving nonlinear anisotropic stiffness and damping as well as significant cross-coupled coefficients all of which are functions of dynamic eccentricity and rotation speed) and is still under study. But one may anticipate the findings of such an analysis by examining the behavior of a simple model approximating the hydrodynamic effects with isotropic stiffness that is negligible at low dynamic eccentricity ratios and rises sharply as the dy-

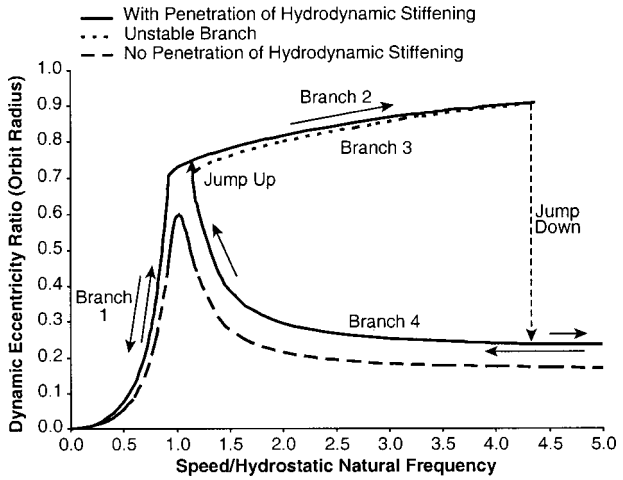

Fig. 13 Amplitude response curves—peak amplitude without and with penetration into the regime of hydrodynamic stiffening from a simplified perspective

namic eccentricity ratio approaches 1. This simple model suggests that the dynamic eccentricity amplitude response curve might resemble that shown in Fig. 13 with a characteristic ''rightward-leaning'' critical peak. That type of response curve would result in a natural frequency characteristic as shown in Fig. 14, with natural frequencies in the large amplitude transcritical regime substantially greater than the hydrodynamic natural frequencies typical of small amplitude dynamic eccentricities. Figure 14 also shows that the eight experimental data points which did not fall on the hypothesized hydrostatic natural frequency curve could well be indicative of large amplitude transcritical operation of the rotor whose frequency has been elevated by hydrodynamic stiffening.

(2) The hypothesized relationship between rotor natural frequency and differential bearing pressure ΔP deviates markedly from available analytic predictions. The measured frequencies are more than two times the value predicted by available analyses (Orr [11] and Piekos [14] modeling the inherent boundary layer growth effect, and Breuer [18], based on Tang and Gross [19], modeling the inherent entrance effect). The analytic predictions for Ω_{natural} rise monotonically in the range of ΔP of interest while the experimental data show a linear rise, followed by a relative constant level of Ω_{natural} with rising ΔP followed by a distinct

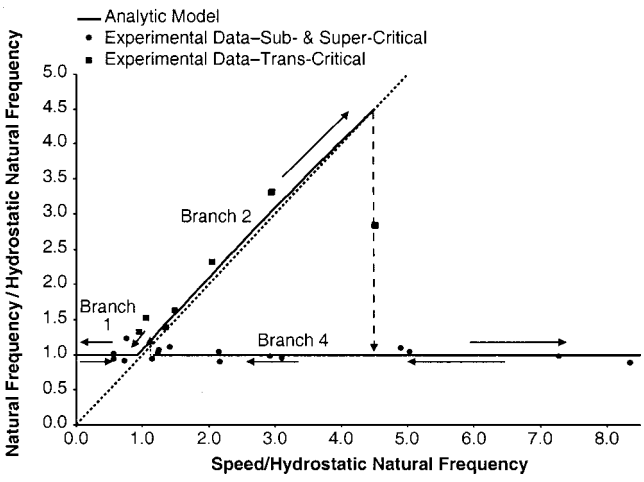

Fig. 14 Frequency response curve—peak amplitude with penetration into the regime of hydrodynamic stiffening in transcritical operation

fall-off of Ω_{natural}. These discrepancies are under study but have yet to be resolved or replicated in an analytic model.

Discussion

Stability Issues. If the hypothesized deduction of natural frequency proves to be correct, it implies that the microrig is capable of operating stably at multiples as high as ten times the natural frequency instead of two times the natural frequency as predicted by simple analysis of the hydrostatic bearing when operating at low (i.e., essentially zero) eccentricity ratio. The macrorig ([11]) was also able to operate stably at speeds that were as high as seven times the natural frequency when operating at low eccentricity ratio. There is precedent for this finding of high values of ''whirl ratio'' in hydrostatic (radial injection) bearing operation in the work of Larson and Richardson [20]. They measured whirl ratios of approximately 2 at very low values of ΔP but identified whirl ratios approaching 6 at elevated values of differential bearing pressure. They suggest that the whirl ratio R has a form that can be expressed as

$$R = \Omega_{\text{instability}} / \Omega_{\text{natural}} = 2 + C \quad \Omega^2_{\text{natural}} \tag{3}$$

where the constant C is related to the bearing geometry and operating parameters. Orr [11] was able to correlate the measured instability boundary of the macro-rig rotor with this type of functional relationship.

The data from the microrig are not yet sufficient to confirm the applicability of this functional format of the instability boundary. But, if it does pertain, we can use it to project the probable maximum speed potential of the microrig rotor. Based on a typical stable operating point at which a speed of 1,102,500 rpm or 18,375 Hz was achieved where the natural frequency of 1755 Hz was indicated (at a bearing pressure differential of 5.32 psi), we would infer that the constant C had a value no less than $2.750e^{-6}$ Hz^{-2}. This then implies that, at a bearing pressure differential of 3.30 psi with a natural frequency of 4120 Hz, stable operation at a speed of no less than 201,000 Hz or 12,000,000 rpm might be feasible—well above the required maximum speed.

Imbalance. We define imbalance as the ratio of the rotor center of mass offset from geometric center to the mean bearing gap. High levels of imbalance make transcritical operation difficult. Our operating protocols have been designed to allow us to transition to supercritical operation at low speeds ($\sim$30,000 rpm) where the imbalance loading for this size device is not large. When the device operates supercritically, the rotor will typically spin about its center of mass, and thus an imbalance level less than 1 is necessary for operation. We do not currently have the capability to measure the degree of imbalance in a rotor. However, we do understand the precision level to which we can align masks and wafers, and the uniformity of our etching process. Assuming that these contributions to imbalance are independent and can be combined in an rms sense, the average imbalance for an optimized microrig rotor is estimated to be about 0.05 for a device taken from the center of a wafer, where etch uniformity is best. These devices have been run up to 1.4 million rpm. For devices fabricated near the edge of a wafer, the imbalance for an otherwise optimized rotor is about 0.11. These devices typically only reach about a half million rpm before crashing, although one edge device nearly reached one million rpm—still considerably lower than the maximum speeds achieved with devices from the center of the wafer.

These results lead us to believe that imbalance is a leading factor resulting in high speed crashes, probably precipitated by small asymmetries in side-load which cause off-center operation and result in large amplitude subharmonic pseudo-resonant peak amplitudes ([17]). We have worked on fabrication process improvements to decrease the imbalance. However, with current technology, it will be difficult to reduce imbalance below about 0.03 for the microrig with process improvements alone. The de-

sign for the gas turbine engine device includes a rotor formed from two wafers and has two sets of blades, compounding the imbalance issue. An optimized gas turbine two-wafer rotor is expected to have imbalance levels of about 0.20, which is unlikely to allow high-speed operation. We plan to initiate an effort to investigate dynamic balancing of the rotors, if improvements in as-manufactured imbalance and improvements in operating protocols are insufficient to eliminate the problem.

Accomplishments and Future Program

A high-speed rotordynamic system and the associated gas journal and thrust bearings have been designed and partially developed for high-power-density micro-turbomachinery and micro-electrostatic/electromagnetic devices. The 4.2-mm diameter silicon rotor, driven by an air turbine, has been operated in a stable, controlled and sustained manner at rotational speeds greater then 1.3 million rpm. This turbomachinery/bearing test device was fabricated from single-crystal silicon wafers using micro-fabrication etching and bonding techniques. This device is believed to be the first micromachine to operate at a circumferential tip speed of over 300 meters per second, comparable to conventional macroscale turbomachinery and fundamental to achieving high power-density.

Continuing development work is aimed at:

- achieving the full design speed of 500 meters/second (rotational speed of 2,400,000 rpm).
- completing analytic characterization of the journal bearing so that its design may be optimized for achieving the required range of stable operation at the minimum leakage flow and scaled for application to a variety of high-power-density microdevices
- developing viable hydrodynamic thrust bearings in order to achieve a major simplification in the system design and bearing capability.
- demonstrating a feasible operating protocol that will afford a simple automatic starting sequence without resort to an external energy source other than that introduced in an air-impingement starter.
- achieving consistency of rotor as-manufactured imbalance at a level that allows acceleration of single-wafer rotor devices through low speeds to stable high-speed operation.
- developing a dynamic or geometric balancing procedure for microrotors, recognizing that required as-manufactured balance may not be achievable in two-wafer rotor devices.

Acknowledgments

This work was sponsored by the US Army Research Office, Drs. R. Paur and T. Doligowski, program managers, and DARPA, Dr. R. Rosenfeld, program manager. The authors would also like to acknowledge the contributions to the micro-bearing device development from the MIT micro-engine team, in particular Kenny Breuer, Alan Epstein, Luc Frechette, C.C. Lin, D.J. Orr, Ed Piekos, Nick Savoulides, Marty Schmidt, Chee Wei Wong and Xin Zhang. The authors also wish to thank Luis San Andres for his assistance.

References

[1] Epstein, A. H., et al., 1997, ''Micro-Heat Engines, Gas Turbines, and Rocket Engines—The MIT Microengine Project,'' 28th AIAA Fluid Dynamics Conference, 4th AIAA Shear Flow Control Conference, Snowmass Village, CO, AIAA Paper No. 97-1773.

[2] Epstein, A. H., Sentura, S. D., Waitz, I. A., Lang, J., Jacobson, S. A., Ehrich, F. F., Schmidt, M. A., Ananthasuresh, G. K., Spearing, M. S., Breuer, K. S., and Nagle, S., 1998, ''Microturbomachinery,'' World Intellectual Property Organization, International Publication Number WO 98/02643 and U.S. Patent #5,932,940.

[3] Jacobson, S. A., 1998, ''Aerothermal Challenges in the Design of a Microfabricated Gas Turbine Engine,'' AIAA Paper No. 98-2545.

[4] Breuer, K. S., Ehrich, F. F., Fréchette, L., Jacobson, S., Orr, D. J., Piekos, E., Savoulides, N., and Wong, C. W., 2000, ''Challenges for Lubrication in High Speed MEMS,'' *NanoTribology*, Stephen Hsu, ed., Kluwer, Dordrecht, The Netherlands.

[5] Chen, K. S., 1999, ''Materials Characterization and Structural Design of Ceramic Micro Turbomachinery,'' Ph.D. thesis, Department of Aeronautics and Astronautics, M.I.T., Cambridge, MA.

[6] Spearing, S. M., and Chen, K. S., 1997, ''Micro-Gas Turbine Materials and Structures,'' presented at 21st Annual Cocoa Beach Conference and Exposition on Composites, Advanced Ceramics, Materials and Structures.

[7] Lin, C. C., Ghodssi, R., Ayon, A. A., Chen, D. Z., Jacobson, S., Breuer, K. S., Epstein, A. H., and Schmidt, M. A., 1999, ''Fabrication and Characterization of a Micro Turbine/Bearing Rig,'' MEMS '99, Orlando, FL, Jan.

[8] Fréchette, L. G., Jacobson, S. A., Breuer, K. S., Ehrich, F. F., Ghodssi, R., Khanna, R, Wong, C. W., Zhang, X., Schmidt, M. A., and Epstein, A. H., 2000, ''Demonstration of a Microfabricated High-Speed Turbine Supported on Gas Bearings,'' Solid-State Sensor and Actuator Workshop, Hilton Head Island, SC.

[9] Protz, J. M., 2000, ''An Assessment of the Aerodynamic, Thermodynamic, and Manufacturing Issues for the Design, Development, and Microfabrication of a Demonstration Microengine,'' Ph.D. Thesis, Department of Aeronautics and Astronautics, M.I.T., Cambridge, MA.

[10] Wong, C. W., 2001, ''Design, Fabrication, Experimentation and Analysis of High-Speed Microscale Gas Bearings,'' M. S. thesis, Department of Mechanical Engineering, M.I.T., Cambridge, MA.

[11] Orr, D. J., 2000, ''Macro-Scale Investigation of High Speed Bearings for MEMS Devices,'' Ph.D. thesis, Department of Aeronautics and Astronautics, M.I.T., Cambridge, MA.

[12] Piekos, E. S., Orr, D. J., Jacobson, S. A., Ehrich, F. F., and Breuer, K. S., 1997, ''Design and Analysis of Microfabricated High Speed Gas Journal Bearings,'' 28th AIAA Fluid Dynamics Conference, 4th AIAA Shear Flow Control Conference, Snowmass Village, CO, AIAA Paper 97-1966.

[13] Piekos, E. S., and Breuer, K. S., 1998, ''Pseudospectral Orbit Simulation of Non-Ideal Gas Lubricated Journal Bearings for Microfabricated Turbomachines,'' ASME Paper No. 98-Trib-48.

[14] Piekos, E. S., 2000, ''Numerical Simulation of Gas-Lubricated Journal Bearings for Microfabricated Machines,'' Ph.D. thesis, Department of Aeronautics and Astronautics, M.I.T., Cambridge, MA.

[15] Ayon, A. A., Braff, R., Lin, C. C., Sawin, H. H., and Schmidt, M. A., 1999, ''Characterization of a Time Multiplexed Inductively Coupled Plasma Etcher,'' J. Electrochem. Soc., **146**(1), pp. 339–349.

[16] Childs, D. W., 1993, *Turbomachinery Rotor Dynamics*, John Wiley and Sons, New York, Chap. 4 and 5.

[17] Ehrich, F. F., 1995, ''Nonlinear Phenomena in Dynamic Response of Rotors in Anisotropic Mounting Systems,'' ASME J. Vibr. Acoust., **118**, pp. 154–161.

[18] Breuer, K. S., 1999, personal communication.

[19] Tang, I. D., and Gross, W. A., 1962, ''Analysis and Design of Externally Pressurized Gas Bearings,'' ASLE Trans., **5**, pp. 261–284.

[20] Larson, R. H., and Richardson, H. H., 1962, ''A Preliminary Study of Whirl Instability for Pressurized Gas Bearings,'' ASME J. Basic Eng., **84**.

J. A. Vázquez[1]

E. H. Maslen
e-mail: ehm7s@Virginia.edu

Department of Mechanical and
Aerospace Engineering,
University of Virginia,
122 Engineer's Way,
Charlottesville, VA 22904-4746

H.-J. Ahn
e-mail: ahj@amed.snu.ac.kr

D.-C. Han
e-mail: amed.snu.ac.kr

School of Mechanical and
Aerospace Engineering,
Seoul National University,
Kwanak-ku, Shilim-dong San 56-1,
Seoul, Korea

Model Identification of a Rotor With Magnetic Bearings

The experimental identification of a long flexible rotor with three magnetic bearing journals is presented. Frequency response functions are measured between the magnetic bearing journals and the sensor locations while the rotor is suspended horizontally with piano wire. These frequency response functions are compared with the responses of a rotor model and a reconciliation process is used to reduce the discrepancies between the model and the measured data. In this identification, the wire and the fit of the magnetic bearing journals are identified as the sources of model error. As a result of the reconciliation process, equivalent dynamic stiffness are calculated for the piano wire and the fit of the magnetic bearing journals. Several significant numeral issues that were encountered during the process are discussed and solutions to some of these problems are presented.
[DOI: 10.1115/1.1499730]

Introduction

Construction of rotordynamic models for turbomachinery is a reasonably mature engineering discipline. However, it is well known that many effects arise in the assembly of real machines that cause the actual behavior to differ from that inferred by the model. It is possible to calculate transfer functions between engineering input and engineering output from in situ measurements. However, it is not possible to calculate internal states (these states can be used in predictions of unbalance response, etc.) from this measurements. As a result, it is common to make ad hoc adjustments to engineering models once experimental data is available in order to bring the model into agreement with this data. Typically, these apparent errors in the original model are confined to relatively small portions of the model: large, abrupt changes in rotor diameter; fits between rotor and disks; seals, and so forth.

These discrepancies can be conveniently modeled as feedback mechanisms in which the dynamics of the feedback are unknown: The identification problem is then to determine these unknown dynamics. Determination of these unknown dynamics can be cast as a control synthesis problem by designing a ''controller'' wrapped around the nominal engineering model which attempts to force the output of the composite system (model and controller) to match the experimental data (Fig. 1).

To complete the paradigm, the data must be converted into a description of a dynamic system whose response to the known test inputs is the known test outputs. This dynamic system is combined with the nominal engineering model and the controller is designed to drive the difference between responses of the two systems to zero (Fig. 2). The mathematical basis for this approach was described in detail in [1].

The state-space model for the system in Fig. 2 is

$$\begin{Bmatrix} \dot{\hat{z}} \\ \dot{z} \end{Bmatrix} = \begin{bmatrix} \hat{\mathbf{A}} & 0 \\ 0 & \mathbf{A} \end{bmatrix} \begin{Bmatrix} \hat{z} \\ z \end{Bmatrix} + \begin{bmatrix} \hat{\mathbf{B}}_c \\ \mathbf{B}_c \end{bmatrix} u_c + \begin{bmatrix} 0 \\ \mathbf{B}_k \end{bmatrix} f_k \tag{1}$$

$$e_{y_m} = \begin{bmatrix} \hat{\mathbf{C}}_m & -\mathbf{C}_m \\ 0 & 0 \end{bmatrix} \begin{Bmatrix} \hat{z} \\ z \end{Bmatrix} + \begin{bmatrix} 0 \\ \varepsilon \mathbf{D}_{12} \end{bmatrix} f_k \tag{2}$$

$$y_k = [0 \quad \mathbf{C}_k] \begin{Bmatrix} \hat{z} \\ z \end{Bmatrix} + \varepsilon \mathbf{D}_{21} u_c \tag{3}$$

$$f_k = \mathbf{K}(s) y_k . \tag{4}$$

The constant matrices $\mathbf{A}$, $\mathbf{B}_c$, and $\mathbf{C}_m$ are the state-space equations of the nominal rotor model. The constant matrices $\hat{\mathbf{A}}$, $\hat{\mathbf{B}}_c$, and $\hat{\mathbf{C}}_m$ represent the state-space realization of the identified rotor. This state-space realization is calculated from the experimental frequency response functions ([2]). $\mathbf{D}_{12}$ and $\mathbf{D}_{21}$ are full rank matrices and ε is a very small number. These values do not affect the results but are needed to avoid numerical problems.

Any suitable method for designing the feedback controller may be used: $\mathcal{H}_\infty$, $\mathcal{H}_2$, etc. ([3]). The identification process is a matter of following the steps:

1. Measure frequency response functions of the actual rotor-bearing system.

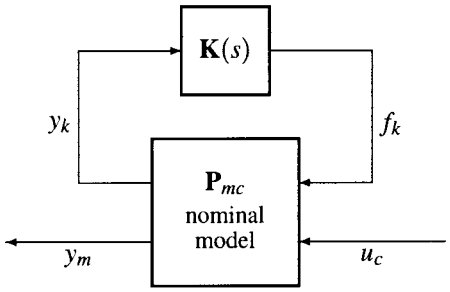

Fig. 1 Reconciled model representation

[1]Currently at DuPont Engineering, Beech Street Engineering Center, 101 Beach Street, Wilmington, DE 19880-0840. e-mail: jose.a.vazquez@usa.dupont.com.

Contributed by the International Gas Turbine Institute (IGTI) of THE AMERICAN SOCIETY OF MECHANICAL ENGINEERS for publication in the ASME JOURNAL OF ENGINEERING FOR GAS TURBINES AND POWER. Paper presented at the International Gas Turbine and Aeroengine Congress and Exhibition, New Orleans, LA, June 4–7, 2001; Paper 2001-GT-566. Manuscript received by IGTI, Dec. 2000, final revision, Mar. 2001. Associate Editor: R. Natole.

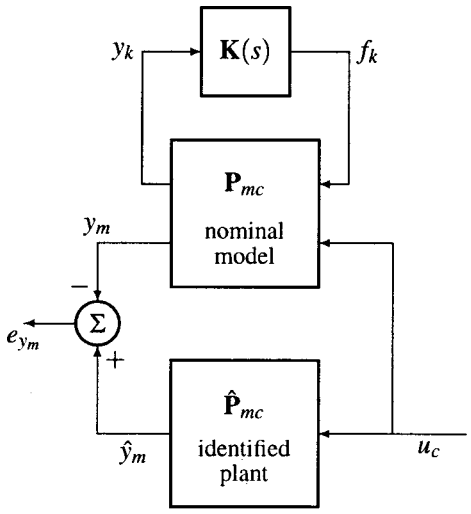

Fig. 2 Model identification block diagram

2. Identify a dynamic system from frequency response functions (state-space model for the transfer functions): $\hat{\mathbf{A}}$, $\hat{\mathbf{B}}_c$, and $\hat{\mathbf{C}}_m$.

3. Construct a nominal engineering model (rotor, bearing, seals, etc.): $\mathbf{A}$, $\mathbf{B}_c$, and $\mathbf{C}_m$.

4. Identify the points of likely modeling uncertainty (interference fits, seal locations, aerodynamic cross-coupling, etc.): $\mathbf{C}_k$, $\mathbf{D}_k$.

5. Assemble the error supermodel (consists of engineering model coupled to the experimentally identified model, Fig. 2).

6. Turn the controller synthesis crank⇒produces $\mathbf{K}(s)$.

If the controller is designed properly, the reconciled model will be matched to the measured data in the sense that, when the original test signals are applied to this modified model, its output will match the original data.

In the present work, we present an experimental exploration of the method, as applied to a two-meter-long flexible rotor with three magnetic actuators. In addition, several significant numerical issues that were encountered during the reconciliation process are discussed and solutions to some of these problems are presented.

Experimental Rig

The experimental rig consists of a long, flexible rotor supported by three magnetic bearings. The geometry of this rotor is illustrated in Fig. 3. The bearing layout of this rotor is intended to be representative of a large boiler feed pump. The rotor is approximately 2.5 m long and weighs 783 N. The continuous running speed of the pump is 5200 rpm. This rotor is part of an experimental rig that has been used for the experimental verification of fault tolerance methods in magnetic bearings ([4,5]).

In the present work, the rotor is suspended horizontally with piano wire. Frequency response functions are measured between all the bearing locations and sensor location using impact excitation. That is, the rotor is excited at the bearings using an instrumented hammer while the response is measured at the sensor locations, using accelerometers. A total of nine frequency response functions are measured for the rotor.

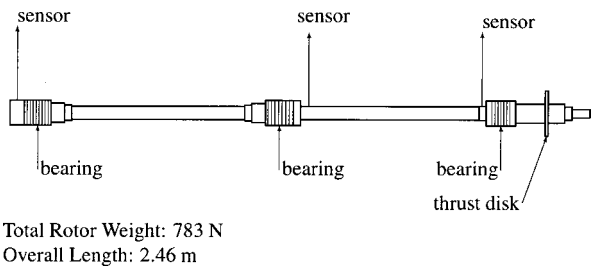

Fig. 3 Three-bearing rotor

Transfer Function Identification

Polynomial transfer functions are extracted from the frequency response data by the iterative method presented by Sanathanan and Koerner [6] and later modified by Gähler and Herzog [2]. This method is usually referred as the SK iteration method. Polynomials of order 18 were used to represent the rotor. This is the lowest-order polynomial that produced an acceptable match to the experimental data frequency response functions.

Transfer Functions of Multiple Inputs and Multiple Outputs (MIMO) Systems. Identification of systems with multiple inputs and multiple outputs (MIMO) can be accomplished by a series of frequency response functions measured at multiple outputs due to a single inputs (SIMO). All the transfer functions of the MIMO system should have the same denominator since the poles of the system are the same. The original SK iteration method was developed for SISO systems but can be easily expanded to MIMO systems by coupling the equations for all the transfer functions and solving for the complete set of coefficients simultaneously.

Assume $G_1(j\omega_k)$ and $G_2(j\omega_k)$ are two frequency response functions for which it is desired to fit polynomial transfer functions $g_1(s)$ and $g_2(s)$ with the same denominator.

$$g_1(j\omega)=\frac{{}^1p_{m_1}(j\omega)^{m_1}+{}^1p_{m_1-1}(j\omega)^{m_1-1}+\ \ldots\ +{}^1p_1(j\omega)+{}^1p_0}{q_n(j\omega)^n+q_{n-1}(j\omega)^{n-1}+\ \ldots\ +q_1(j\omega)+q_0} \tag{5}$$

$$g_2(j\omega)=\frac{{}^2p_{m_2}(j\omega)^{m_2}+{}^2p_{m_2-1}(j\omega)^{m_2-1}+\ \ldots\ +{}^2p_1(j\omega)+{}^2p_0}{q_n(j\omega)^n+q_{n-1}(j\omega)^{n-1}+\ \ldots\ +q_1(j\omega)+q_0}$$

or

$$g_1(j\omega)=\frac{P_1(j\omega)}{Q(j\omega)},\quad g_2(j\omega)=\frac{P_2(j\omega)}{Q(j\omega)}. \tag{6}$$

The error functions for each of the polynomial transfer functions can be written as

$$\varepsilon 1_k=\left|G_1(j\omega_k)-\frac{P_1(j\omega_k)}{Q(j\omega_k)}\right|,\quad \varepsilon 2_k=\left|G_2(j\omega_k)-\frac{P_2(j\omega_k)}{Q(j\omega_k)}\right| \tag{7}$$

following the development of ([2,6]), the error functions are written as

$$\begin{aligned}\varepsilon 1'_k&=\varepsilon 1_k Q(j\omega_k)=|G_1(j\omega_k)Q(j\omega_k)-P_1(j\omega_k)|\\ \varepsilon 2'_k&=\varepsilon 2_k Q(j\omega_k)=|G_2(j\omega_k)Q(j\omega_k)-P_2(j\omega_k)|.\end{aligned} \tag{8}$$

The coefficients of the transfer functions can be obtained by minimizing the summation of the error for all the experimental points, or

$$E=\sum_{k=1}^{N}\left[|\varepsilon 1'_k|_1^2 W_{k,L}+|\varepsilon 2'_k|_2^2 W_{k,L}\right] \tag{9}$$

where

$${}_1W_{k,L}=\frac{1}{|Q(j\omega_k)_{L-1}G_1(j\omega_k)|^2} \tag{10}$$

$${}_2W_{k,L}=\frac{1}{|Q(j\omega_k)_{L-1}G_2(j\omega_k)|^2} \tag{11}$$

and L is the iteration step in the process. Taking the partial derivatives of Eq. (9) with respect to each of the coefficients and setting equal to zero yields a set of algebraic equations. This set of equa-

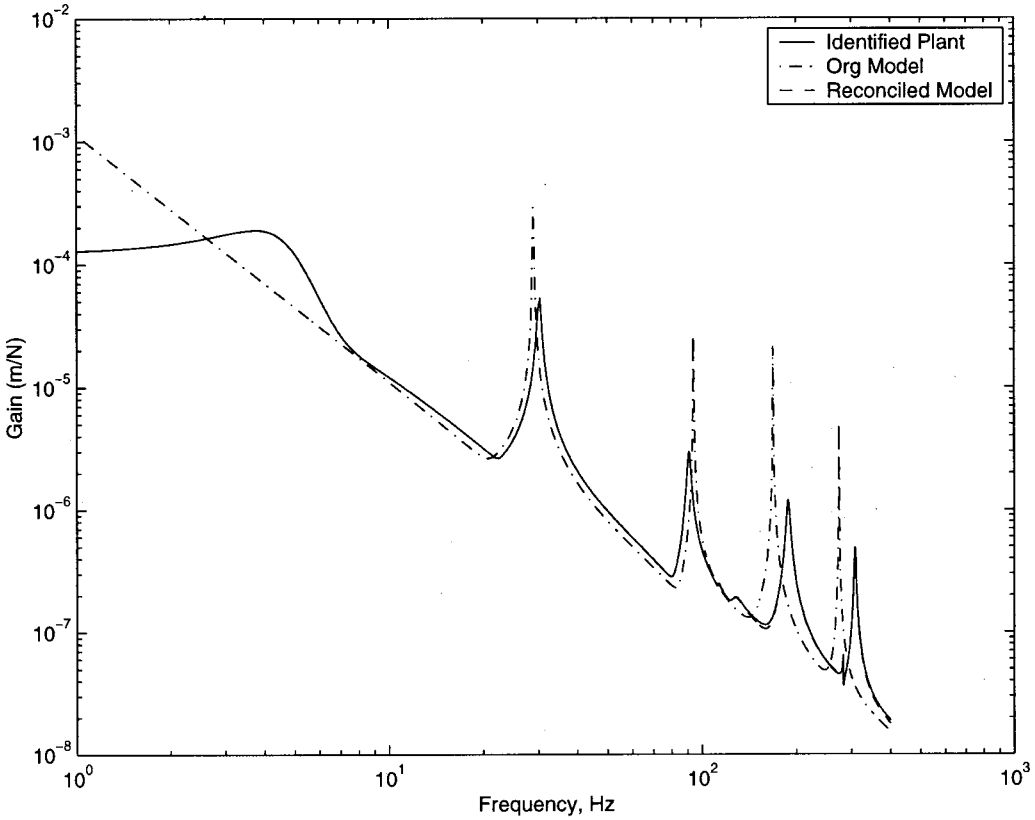

Fig. 4 Maximum singular value of the identified frequency response function, the original model, and the reconciled model

tions is linearly dependent because we have a free parameter coming from the ratio of the numerator and denominator. It is customary to normalize the denominator coefficients either to the lowest-order coefficient (q_0) or the highest-order coefficient (q_n). We normalize with respect to the highest order coefficient by setting $q_n=1$. In the original presentation of the SK iteration, the authors chose $q_0=1$ but that choice produces problems when the plant contains poles at the origin (as in the case of a free-free rotor).

The algorithm was presented for two frequency response functions with the same denominator but it can be expanded to any number of frequency response functions without modification. For the work presented here, nine transfer functions of order 14 are fitted simultaneously (with the same denominator).

Poles Outside the Measurement Range and Unstable Transfer Functions. When identifying systems with poles at very low frequency, it is possible to have poles that are outside the range of measurement. In the case of a suspended rotor, it is not possible to avoid this problem. In principle, a rotor suspended by wire and excited in the plane perpendicular to the plane of the wires will have two poles at the origin (if the effect of the wire is neglected). If the effect of the wire is included, the first two poles are not exactly at the origin but very close to it. The difficulty with these very low frequency modes is that accelerometers, normally used for frequency response function measurements, have a minimum frequency response of about 5 Hz.

This means that there is a region at low frequency for which there is no experimental data. However, the fitting algorithm will try to find the low-frequency poles below the measurement range, even though data at these frequencies is not available. For the work presented here, the effects of poles below the range of measurement were manifested in two ways. First, two pairs of poles were placed at 4.44 Hz and 4.47 Hz, just below the minimum frequency for the experimental data. Second, one of these sets of poles is placed in the right half-plane, very close to the imaginary axis. These poles are largely an artifact of the fitting process and cannot be avoided.

The first effect is easily accounted for in the reconciliation process by allowing the method to modify the model to account for these modes. The second effect is not acceptable because it makes the identified plant unstable. The controller synthesis algorithms considered here can produce only stable closed loop systems. In our setup (Fig. 2), the controller synthesis algorithm is not able to move the poles of the identified plant (measured transfer func-

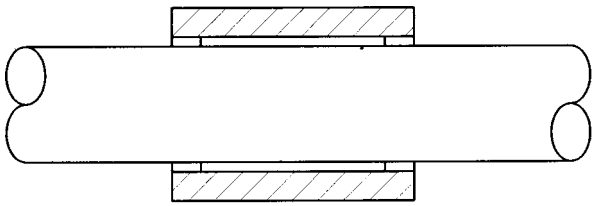

Fig. 5 Magnetic bearing journal

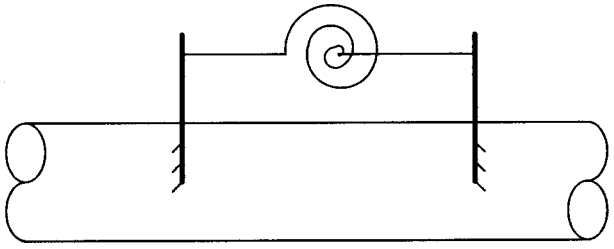

Fig. 6 Magnetic bearing journal model

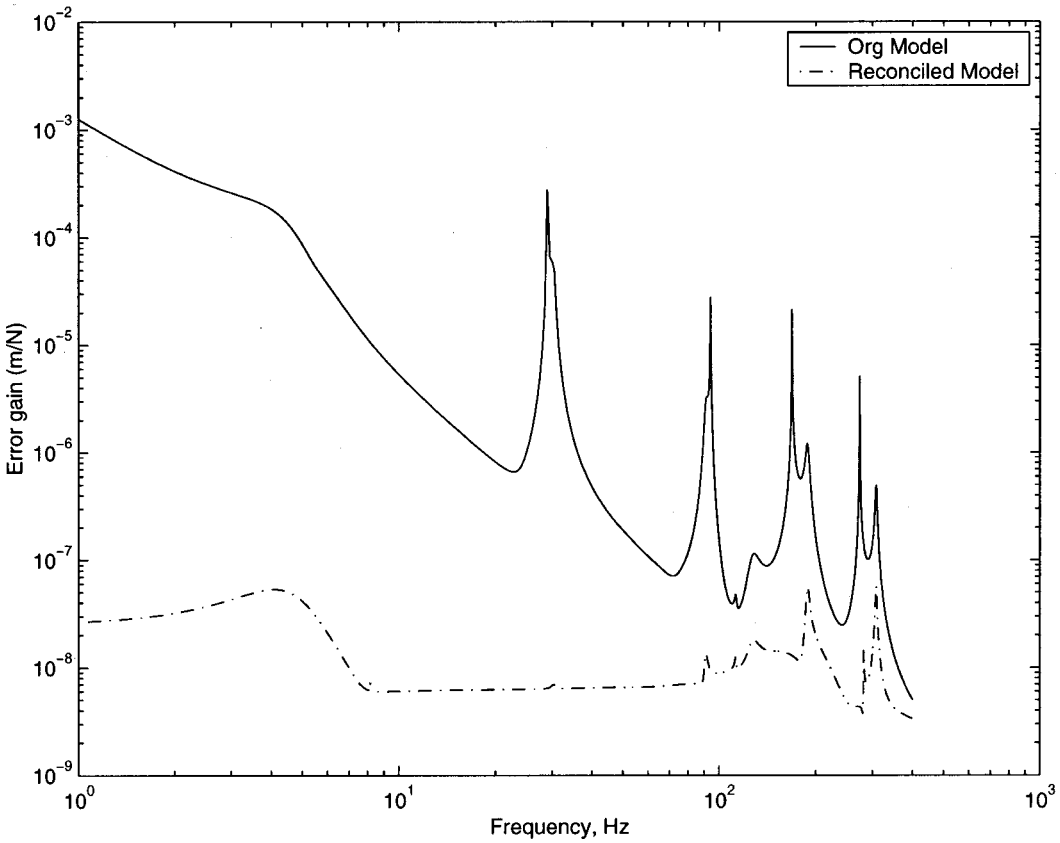

Fig. 7 Maximum singular value of the error gain for the original model and the reconciled model

tions). Therefore, if the identified plant is unstable, the controller synthesis problem has no solution. This problem was fixed by manually mirroring the unstable poles into the left half-plane. The process is accomplished by modifying the weighting function at each iteration. For the SK iteration method, the calculated denominator polynomial is used as part of the weighting function in the next iteration. Therefore, after each iteration, the roots of the denominator are calculated. If any root is in the right half-plane, the real part of the root is changed in sign and the new polynomial is used as the weighting function for the next iteration until convergence is reached.

Table 1 Comparison between the eigenvalues of the nominal model, identified rotor-bearing system, and the reconciled model

Nominal Model		Identified System		Reconciled Model	
Log Dec	Frequency (Hz)	Log Dec	Frequency (Hz)	Log Dec	Frequency (Hz)
0.0	0.00	2.93	4.44	2.93	4.44
0.0	0.00	2.18	4.47	2.18	4.47
0.0	29.07	0.07	30.33	0.07	30.33
				1.36	47.28
				1.53	51.57
				21.39	63.75
0.0	94.11	0.08	90.89	0.08	90.89
		0.04	112.85	0.04	112.85
		0.27	126.96	0.27	126.96
				2.51	148.53
				1.69	159.65
0.0	168.64	0.08	188.39	0.08	188.39
				1.19	215.67
				6.01	251.75
		0.01	282.08	0.01	282.08
0.0	273.83	0.04	308.11	0.04	308.11
				6.02	675.66
				6.29	901.20
				6.17	1218.97
				6.27	5142.99
				6.28	7040.11

Overparametrization. The reconciliation method requires a representation of the plant in state-space form. Once the transfer functions of the system are calculated, they must be converted to state-space form. Even though this process is trivial for SISO and SIMO system, it is not the case for MIMO systems ([7]). The resulting state-space realization of the plant contains redundant states. This overparametrization makes the plant difficult to observe, making the reconciliation process more difficult (numerical problems). In ([7]), a method is presented to calculate the state space form without redundant states. The method is a maximum singular value approximation of the state space model to the plant transfer functions. This method was applied to the transfer function of the rotor. Unfortunately, the results of the approximation are not adequate for this system. At this point the authors do not have an explanation for the poor approximation and more work is required in this area. The larger model with redundant states was used for the remainder of the work.

Rotor Model

A model of the rotor is assembled from calculated undamped mode shapes. Two rigid-body modes and four flexible mode shapes are used. The magnetic bearing journals were included in the model as lumped masses. The stiffening effect of the attachment of these journals to the rotor was purposely neglected. The idea is to identify this effect through the reconciliation process. Figure 4 shows a comparison between the measured and calculated frequency response functions of the rotor. The maximum singular value ([8]) is used to condense the comparison of the nine

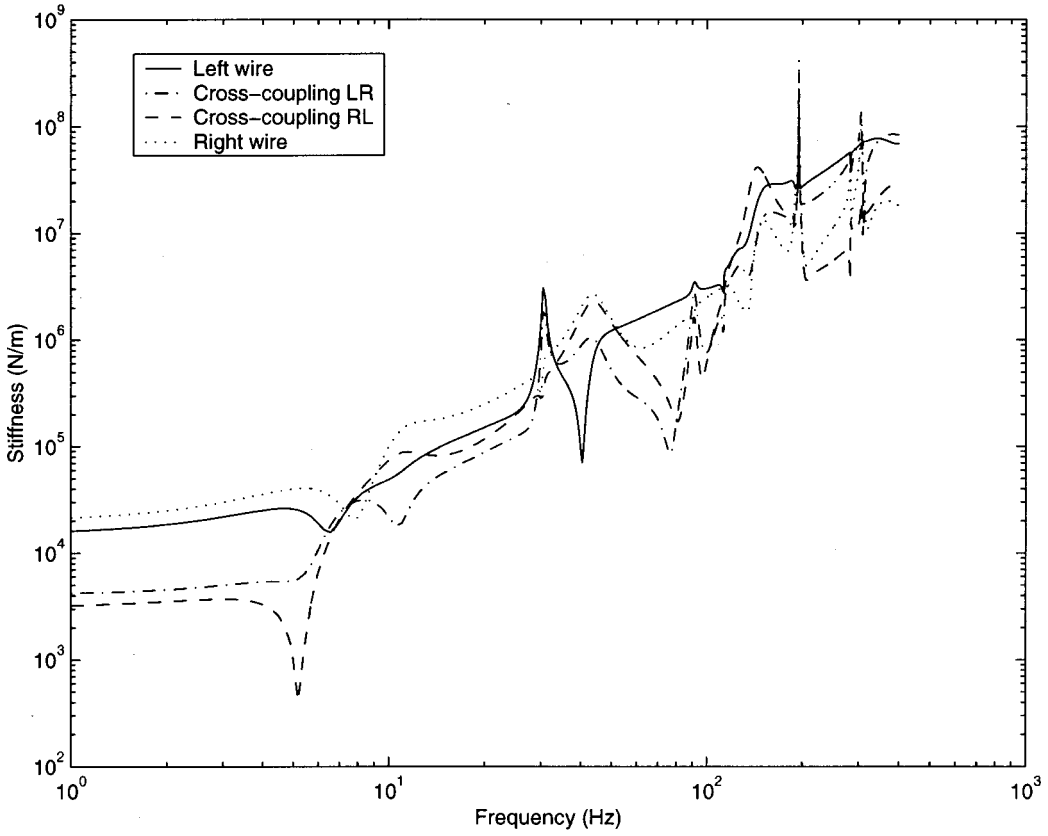

Fig. 8 Calculated wire dynamic stiffness

frequency response functions into a single plot[2]. The identified plant shows a peak response at 4.45 HZ. This peak is the response of the poles at 4.44 Hz and 4.47 Hz introduced by the fitting algorithm as a consequence of the poles below the minimum measurement frequency. The model is underpredicting the first, third, and fourth bending natural frequencies of the rotor while overpredicting the second natural frequency.

Figure 7 shows the maximum singular value of the error gain between the rotor model and the measured plant. The maximum singular value allows summarizing the maximum error from the nine frequency response functions in a single plot.

Keep in mind that the response below 5 Hz is an artifact of the identification process and that there is no measured data available in this region. It is included in the error gain because the reconciliation process will try to match that part of the system.

Unknown Dynamic Mechanisms

The next step in the reconciliation process is the identification of the locations where error is entering the model through unknown dynamic mechanisms. We propose that error is entering the model through the wire and through stiffening effects at the magnetic bearing journals.

Wire Model. The effect of the wire is inserted as a dynamic system acting between the rotor and ground. This model allows the reconciliation process enough room to match the low-frequency modes introduced by the fitting algorithm. It is very important to provide this mechanism, otherwise the reconciliation process will expend a lot of energy trying to correct the error at low frequency while neglecting the error at high frequency.

Shrink Fit/Collect Model. Figure 5 shows a simplified view of a magnetic bearing journal. These components are attached to the rotor through double acting collets. These components grab the rotor and restrict the bending in this area, producing a stiffening effect similar to shrink fits. The model used for these mechanisms is a dynamic rotational stiffness (dynamic system) acting between the rotation states in that section of the shaft (Fig. 6). The dynamic moments generated by these models are applied between the relative rotations of sections of the shaft.

Discussion of Results

The model of the rotor was reconciled using the method explained in ([1]), the controller synthesis method for this problem was LQG ([3]). Figure 7 shows the error gain for the reconciled system. The error is reduced by three orders of magnitude.

The error is reduced considerably at low frequencies but not as much for high frequency. Table 1 shows a comparison of the eigenvalues of the original model, the identified rotor and the reconciled model. The damping of the eigenvalues is shown in the form of the logarithmic decrement. If the eigenvalue s is defined of the form $s=p\pm j\omega_d$, the logarithmic decrement is defined as $\delta=-2\pi p/\omega_d$. The reconciled model matches exactly all the eigenvalues of the identified plant. The reconciliation process introduces several additional modes but they are all very well damped and have very little effect on forced response.

Figure 8 shows the calculated dynamic stiffness of the wire. Both direct and cross-coupling stiffnesses are shown. Figure 9 shows the calculated dynamic stiffness at the collets. The cross-coupling effects between collets and between the collets and wire models are not shown to simplify the plots. These dynamic

[2] $\overline{\sigma}(A)=\max_{x\neq 0} x^T A^T A x/x^T x$

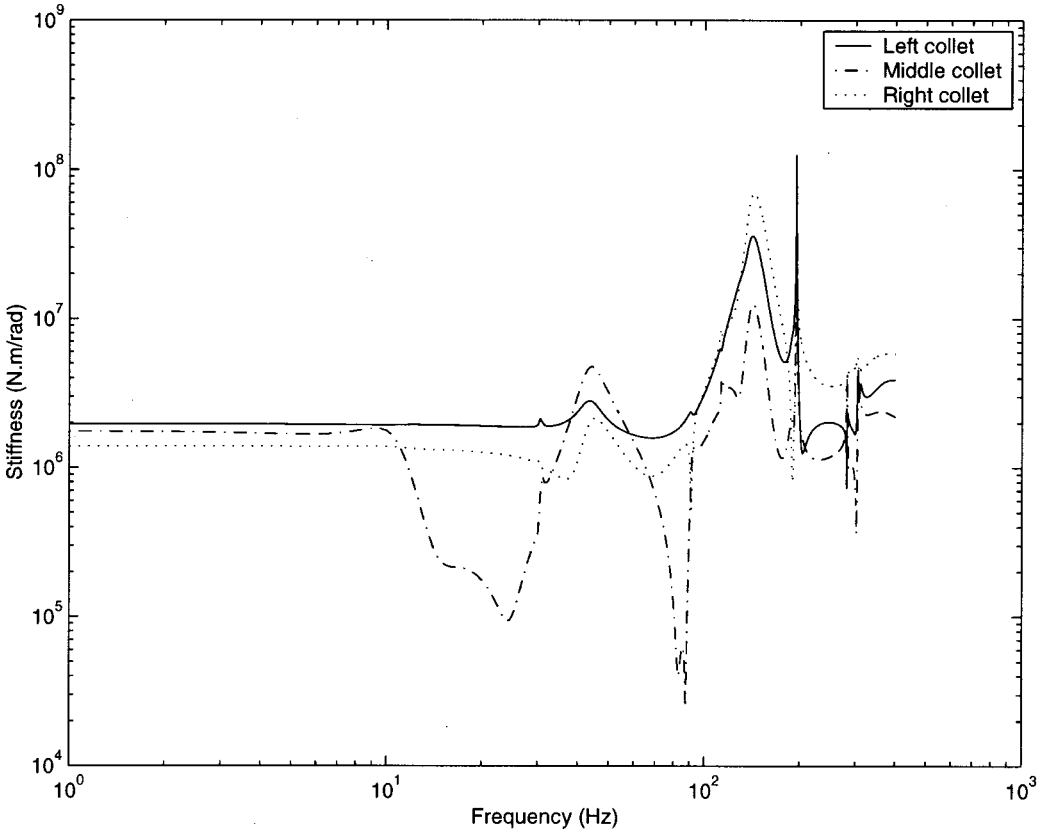

Fig. 9 Calculated dynamic stiffness at the collets

mechanisms are calculated as transfer functions of order equal to the sum of the orders of the identified plant and the original rotor model.

Up to 20 Hz, the stiffness of the wires can be identified with the combined effect of a spring and damper. The stiffness at low frequency is 15,000 N/m at the left wire and 21,000 N/m at the right wire. This is the expected value to produce the natural frequencies at 4.44 Hz and 4.47 Hz. Up to 20 Hz, the effect of the collets can be easily identified with constant springs of $1.96*10^6$ Nm/rad, $1.75*10^6$ Nm/rad and $1.39*10^6$ Nm/rad. This agree with the estimated rotational stiffness of the magnetic journal sleeves of $2.6*10^6$ Nm/rad. This stiffness was estimated assuming rigid attachment between the sleeves and the rotor. Including a flexible attachment decreases the effective stiffness of the sleeve on the rotor.

After 20 Hz there is a lot of activity in all the calculated dynamic stifnesses. This may be because the dynamic stiffnesses start fighting the effects of each other. At present, this problem cannot be eliminated. The next step is to design a weighting function that will penalize the dynamics of the wire at high frequency. In this manner, the controller synthesis algorithm will put more emphasis on the collet transfer functions and reduce the effort on the wire transfer functions. At the time of writing this paper, we are in the process of testing this approach.

Conclusions

The reconciliation method was applied to a two meter long flexible rotor with three magnetic bearing journals. The rotor is hung horizontally with piano wire and frequency response functions are measured between the magnetic bearing journals and the sensor locations. Transfer functions are calculated from these frequency response functions with the same denominator (MIMO system) using a modified version of the SK iteration method.

The identified transfer functions are used in the reconciliation method to modify a nominal model of the rotor. The wire used to suspend the rotor and the fit of the magnetic bearing journals are identified as the main source of error in the model. The reconciled rotor has all the eigenvalues of the reconciled plant plus some additional eigenvalues introduced by the reconciliation method. These additional eigenvalues are all very well damped and cause no adverse consequences.

The reconciliation process reduced the error between the model response and the measured response by several orders of magnitude, demonstrating the effectiveness of the method. The identified dynamics of the wire and the fit of the magnetic bearing journals show the expected behavior at low frequency. At high frequencies, the dynamic system shows a lot of activity. The authors postulate that this activity is the result of the synthesis algorithm, where the calculated effects are fighting each other. The next step is to explore the use of cost functions for the wire transfer functions that will penalize the activity of the wire at high frequency.

Nomenclature

$\mathbf{A}, \mathbf{B}_c, \mathbf{C}_m$ = nominal rotor model in state-space format

$\hat{\mathbf{A}}, \hat{\mathbf{B}}_c, \hat{\mathbf{C}}_m$ = state-space realization of the identified rotor (extracted from measured frequency response functions)

$\mathbf{B}_k, \mathbf{C}_k$ = input and output matrices of the locations of the unknown dynamic mechanisms

$\mathbf{D}_{12}, \mathbf{D}_{21}$ = full rank matrices

e_{y_m} = error between the rotor model and the identified plant

f_k = unknown dynamic forces

$\mathbf{K}(s)$ = unknown dynamic mechanism calculated by the reconciliation process

u_c = excitation applied to the system
y_k = response at the locations of the unknown dynamic mechanisms acting on the system
y_m = calculated response of the model at the measurement locations
$\hat{y}_m$ = measured response of the plant
z = states of the rotor model
$\hat{z}$ = states of the identified rotor
ε = very small number

References

[1] Maslen, E. H., Vázquez, J. A., and Sortore, C. K., 2002, ''Reconciliation of Rotordynamic Models With Experimental Data,'' ASME J. Eng. Gas Turbines Power, **124**, pp. 351–356.

[2] Gähler, C., and Herzog, R., 1994, ''Identification of Magnetic Bearing Systems,'' *Proceedings of the Fourth International Symposium on Magnetic Bearings*, ETH Zurich, Aug., pp. 293–298.

[3] Zhou, K., Doyle, J. C., and Glover, K., 1996, *Robust and Optimal Control*, Prentice-Hall, Englewood Cliffs, NJ.

[4] Maslen, E. H., and Meeker, D. C., 1995, ''Fault Tolerance of Magnetic Bearings by Generalized Bias Current Linearization,'' IEEE Trans. Magn., **31**(3), May pp. 2304–2314.

[5] Maslen, E. H., Sortore, C. K., Williams, R. D., Fedigan, S. J., and Aimone, R. J., 1999, ''Fault Tolerant Magnetic Bearings,'' ASME J. Eng. Gas Turbines Power, **121,** pp. 504–508.

[6] Sanathanan, C. K., and Koerner, J., 1963, ''Transfer Function Synthesis as a Ratio of Two Complex Polynomials,'' IEEE Trans. Autom. Control, Jan., pp. 56–58.

[7] Gähler, C., Mohler, M., and Herzog, R., 1997, ''Multivariable Identification of Active Magnetic Bearing Systems,'' JSME Int. J., Ser. C, **40**(4), pp. 584–592.

[8] Maia, N. M. M., 1991, ''Fundamentals of Singular Value Decomposition,'' *Proceedings of the 9th IMAC Conference*, Society for Engineering Mechanics, Bethel, CT, **II**, pp. 1515–1521.

Dynamic Modeling and Validation of a Lorentz, Self-Bearing Motor Test Rig

L. S. Stephens
e-mail: stephens@engr.uky.edu

D.-G. Kim

Department of Mechanical Engineering,
University of Kentucky,
521 CRMS,
Lexington, KY 40506

A new type of self-bearing motor that uses Lorentz-type forces to generate both bearing force and motoring torque has been developed. The motor stator is of slotless construction with four three-phase windings. The motor rotor is constructed of 16 surface mounted permanent magnets (PM's). The main advantage of the design is that it eliminates the tradeoff between motoring torque and bearing force with PM thickness as found in previous designs. This paper presents the dynamic model for the self-bearing motor and illustrates how the model is integrated into the overall system model of the motor test rig. The dynamic model is validated against experimentally measured transfer functions with good agreement between the two. [DOI: 10.1115/1.1499731]

Introduction

Self-bearing motors (also termed bearingless motors) combine magnetic bearing and motoring functionality into a single actuator to perform both radial force and torque production. The advantages of such designs are a higher power density and a shorter shaft length, making them advantageous for high-speed applications such as flywheels and high-speed compressors where rotordynamic limitations often prevail. Some self-bearing motor designs can be operated in servo-mode, and find applications in space-based pointing systems that require low weight and low power consumption. The motor in this paper is such a design. Salazar et al. [1] reviewed the existing English language literature on self-bearing motors and identified six different types discussed in over 90 contributions since the mid 1970's. One type is the permanent magnet (PM) self-bearing motor which has been studied by Chiba et al. [2], Schoeb and Bischel [3], and Okada et al. [4], among others. One commonality of the recent PM designs is that attractive forces between the rotor and stator (reluctance-type forces) provide the bearing function, and magnetic forces on current carrying conductors (Lorentz-type forces) produce the motoring torque. As a consequence, an inherent tradeoff between motoring torque and bearing force exists as thicker permanent magnets lead to larger torque but increase the path reluctance for the bearing flux leading to smaller bearing forces.

In previous work, Carroll et al. [5], Kim and Stephens [6], Steele and Stephens [7], and Stephens and Kim [8], the authors proposed a new PM self-bearing motor design that uses Lorentz-type forces to produce both the bearing forces and the motoring torque. It was shown that this design eliminates the tradeoff between torque and bearing force such that both increase with PM thickness. A similar approach was also proposed by Okada et al. [9]. This paper describes the dynamic modeling and experimental validation of a test rig that has been constructed for the Lorentz self-bearing motor. While many of the system components have well known models, the main contributions of the paper are (1) that it illustrates how the force-current-displacement relationship for the new type of self-bearing motor is integrated into the overall system model; and (2) it presents an experimentally validated model for the new type of self-bearing motor that can be used by researchers to develop controllers and simulations for new applications.

Contributed by the International Gas Turbine Institute (IGTI) of THE AMERICAN SOCIETY OF MECHANICAL ENGINEERS for publication in the ASME JOURNAL OF ENGINEERING FOR GAS TURBINES AND POWER. Paper presented at the International Gas Turbine and Aeroengine Congress and Exhibition, New Orleans, LA, June 4–7, 2001; Paper 2001-GT-567. Manuscript received by IGTI, Dec. 2000, final revision, Mar. 2001. Associate Editor: R. Natole.

Test Rig Description

Figure 1 shows the Lorentz self-bearing motor test rig and the feedback loop components. The rig consists of a conventional eight-pole active magnetic bearing (AMB) on the outboard end of a shaft (outboard is the end furthest from the encoder) with inductive probes measuring radial displacements, $x_{b,s}$ and $y_{b,s}$. The slotless self-bearing motor is assembled near the midspan of the shaft and uses inductive probes to measure the radial displacements $x_{m,s}$ and $y_{m,s}$. The opposite end of the shaft is connected to a rotary optical encoder providing the angular position and velocity measurements, θ and ω. The coupling connection uses a Jarno interface and an aluminum coupling such that the encoder ball bearings support one end of the shaft through the coupling, while the other end of the shaft is free to move radially, pivoting about the coupling as illustrated in the figure. In order to stabilize the shaft, either the conventional AMB or the self-bearing motor, or both can be used.

The feedback loop of the system consists of the five sensor measurements, $x_{b,s}$, $y_{b,s}$, $x_{m,s}$, $y_{m,s}$, θ that are conditioned and fed into a dSPACE DS1103 motion control system. This system is used to implement the controllers for the conventional AMB and the self-bearing motor. An additional analog stage is also used to construct the control current requests for the self-bearing motor. A group of 16 PWM transconductance power amplifiers then generate the self-bearing motor and the conventional AMB control currents.

Dynamic modeling of the system for controller design requires detailed models for the shaft rotordynamics, the self-bearing motor and conventional AMB actuators, sensors, power amplifiers, and the controller. Figure 2 shows the block diagram structure used to model the system for controller design. Each of these components is discussed below in the context of this figure.

Shaft Rotordynamic Model

The shaft assembly is shown in detail in Fig. 3, along with the first free-free flexible lateral modeshape. The shaft assembly consists of a sensor target for the conventional AMB, a stack of thin laminated journals for the conventional AMB, a sensor target for the motor bearing, the self-bearing motor rotor with permanent magnets attached, and the jarno coupling interface. The x and y displacements of each of these locations are identified in Fig. 3.

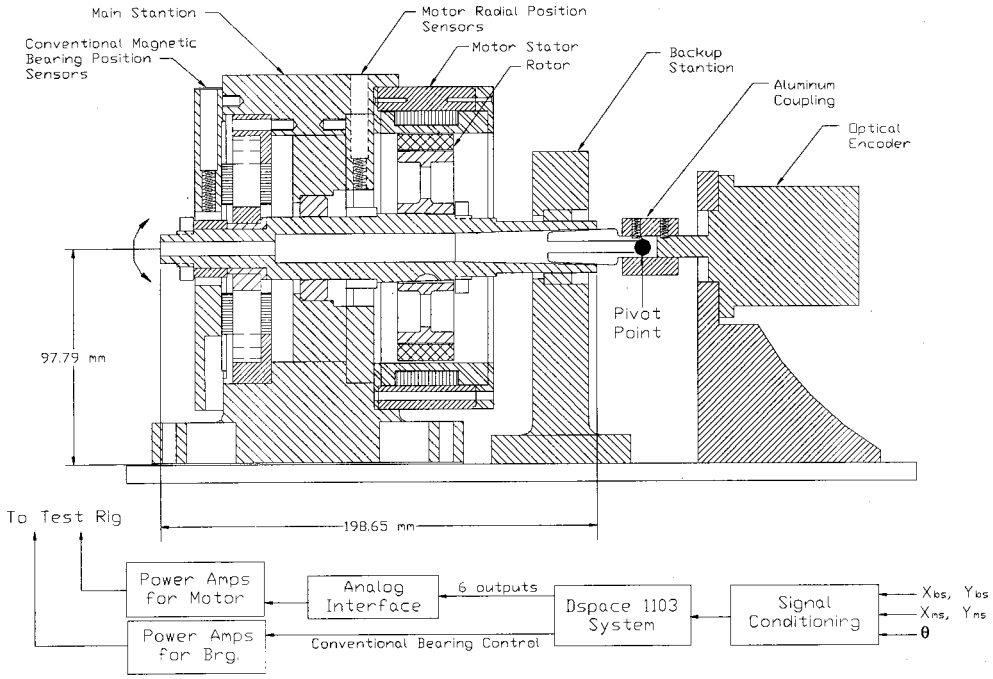

Fig. 1 Experimental test rig

The lateral rotordynamic model of the shaft is generated using 35 lumped mass stations connected by massless springs and neglecting gyroscopics. The first shaft flexible body mode is also shown in Fig. 3 with natural frequency of 2792 Hz, which is within the control bandwidth of 3 kHz (limited by power amplifiers). The natural frequency of flexible modes 2 and 3 are 5625 Hz, and 9271 Hz, respectively. For angular motion of the shaft, a single rigid-body decoupled mode is also included. Under these assumptions, the governing dynamic equations have the second-order form

$$\begin{bmatrix} [M_x] & 0 & 0 \\ 0 & [M_y] & 0 \\ 0 & 0 & J \end{bmatrix} \begin{bmatrix} \ddot{\mathbf{x}} \\ \ddot{\mathbf{y}} \\ \ddot{\theta} \end{bmatrix} + \begin{bmatrix} [K_x] & 0 & 0 \\ 0 & [K_y] & 0 \\ 0 & 0 & 0 \end{bmatrix} \begin{bmatrix} \mathbf{x} \\ \mathbf{y} \\ \theta \end{bmatrix} = \begin{bmatrix} \mathbf{F}_x \\ \mathbf{F}_y \\ T_\theta \end{bmatrix} \tag{1}$$

where $[M_x]$, $[M_y]$, $[K_x]$, and $[K_y]$ are 35×35 mass and stiffness matrices in the x and y directions, $\mathbf{x}$ and $\mathbf{y}$ are the 35×1 displacement vectors, J is the polar moment of inertia for the rigid-body model of the shaft angular motion, and θ is the angular displacement of the shaft. The second-order form is readily converted to $2^*(2N+1)(N=35)$ first-order ordinary differential equations and then reduced by truncating all lateral vibration modes except the rigid-body modes (bouncing and tilting) and the first six flexible modes. The reduced-order model is then of the form

$$\ddot{\mathbf{z}}=[A]\mathbf{z}+[B]\mathbf{u} \tag{2a}$$

$$\mathbf{y}_o=[C]\mathbf{z} \tag{2b}$$

where $\mathbf{z}$ is the state vector, $\mathbf{u}$ is the vector of force inputs and $\mathbf{y}_o$ is the vector of displacement outputs. The rotordynamic transfer function matrix, $[G_p]$ of Fig. 2, relating the displacement outputs, $\mathbf{y}_o$, to the force inputs, $\mathbf{u}$, is then computed using the resolvent as

$$[G_p]=[C][sI-A]^{-1}[B] \tag{3}$$

where the outputs of interest are the displacements at the conventional-bearing sensor locations, x_{bs} and y_{bs}, the self-bearing motor sensor locations, $x_{m,s}$ and $y_{m,s}$, the jarno coupling connection point, x_j and y_j and the angular orientation of the shaft, θ. The inputs of interest are the corresponding force inputs due to the conventional AMB, $F_{x,b}$ and $F_{y,b}$, the self bearing motor, $F_{x,m}$ and $F_{y,m}$, the jarno coupling connection, $F_{x,j}$ and $F_{y,j}$ and the self-bearing motor torque, T_θ. The input and output vectors for the rotor model in Fig. 2 are then

$$\mathbf{y}_o=[x_{b,s}\ \ y_{b,s}\ \ x_{m,s}\ \ y_{m,s}\ \ x_j\ \ y_j\ \ \theta]^T \tag{4}$$

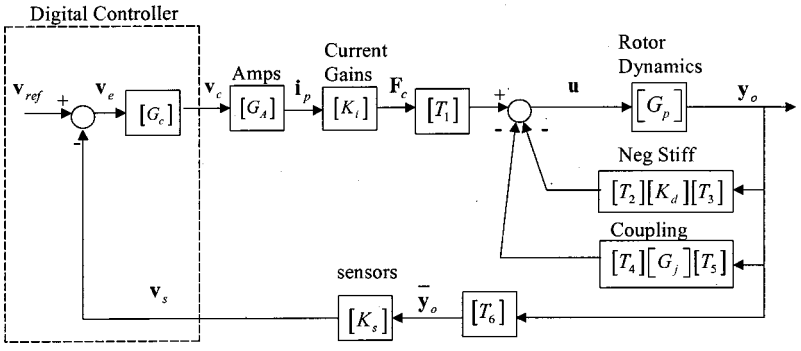

Fig. 2 Block diagram for modeling and controller design

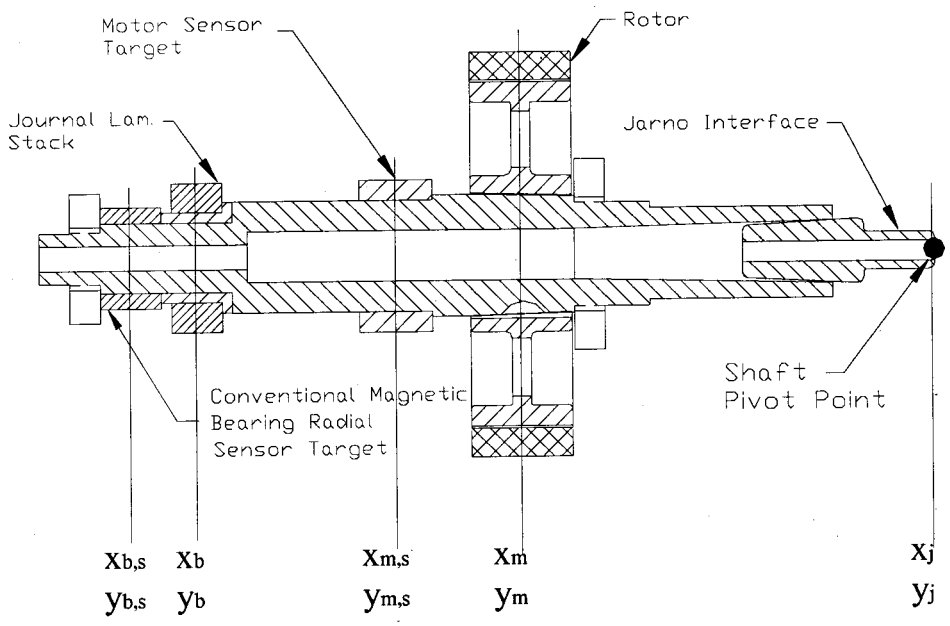

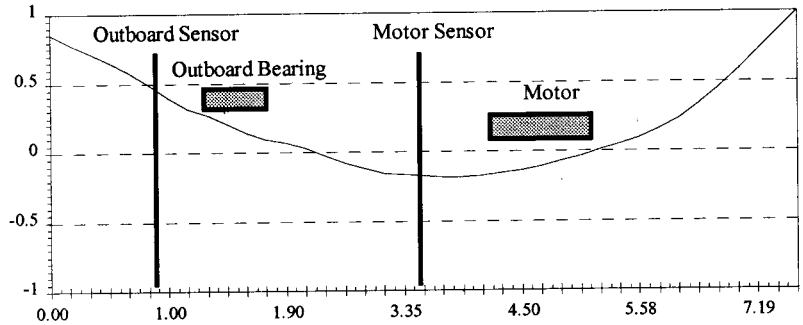

Fig. 3 Rotor with first flexible body mode (2792 HZ)

$$\mathbf{u}=[F_{x,b}\ \ F_{y,b}\ \ F_{x,m}\ \ F_{y,m}\ \ F_{x,j}\ \ F_{y,j}\ \ T_\theta]^T. \tag{5}$$

The test rig shaft is connected to the encoder shaft through the jarno coupling. Referring to Fig. 1, the coupling provides a lateral stiffness and some structural damping for the shaft, but allows the shaft to pivot angularly about a point. The coupling is modeled in Fig. 2 using the transfer function matrix, $[G_j]$ of the form

$$\begin{bmatrix} F_{x,j} \\ F_{y,j} \end{bmatrix} = \underbrace{\begin{bmatrix} cs+k & 0 \\ 0 & cs+k \end{bmatrix}}_{[G_j]} \begin{bmatrix} x_j \\ y_j \end{bmatrix} \tag{6}$$

where c is the damping coefficient and k is the lateral spring stiffness that are estimated later using experimental data. The matrices $[T_4]$ and $[T_5]$ are transformation matrices that select the outputs from the vector, $\mathbf{y}_o$ and distribute the force inputs into vector, **u**.

Actuator Models

A. Conventional Active Magnetic Bearing (AMB) Model. The conventional AMB is a standard eight-pole heteropolar magnetic bearing with the properties described in Table 1. The force current displacement relationship is therefore

$$\begin{bmatrix} F_{x,b} \\ F_{y,b} \end{bmatrix} = \underbrace{\begin{bmatrix} K_{i,b} & 0 \\ 0 & K_{i,b} \end{bmatrix}}_{[K_{i,b}]} \begin{bmatrix} i_{x,b} \\ i_{y,b} \end{bmatrix} + \underbrace{\begin{bmatrix} K_p & 0 \\ 0 & K_p \end{bmatrix}}_{[K_{d,b}]} \begin{bmatrix} x_b \\ y_b \end{bmatrix} \tag{7}$$

where the conventional AMB current gain and negative stiffness are computed using the well-known relationships:

$$K_{i,b}=\frac{4\alpha\mu_o AN^2 I_b}{g_{o,b}^2} \tag{8}$$

$$K_p=\frac{4\alpha\mu_o AN^2 I_b^2}{g_{o,b}^3} \tag{9}$$

and where α is the flux leakage factor, A is the pole cross-sectional area, N is the number of turns per pole, I_b is the bias current, and $g_{o,b}$ is the nominal radial air gap. Table 2 gives the values of $K_{i,b}$ and K_p for two different operating points of the self-bearing motor. As Table 2 indicates, the open-loop AMB properties are independent of the self-bearing motor. The primary uncertainty in the conventional AMB force and current gains is due to the flux leakage and fringing effects at the edge of the poles

Table 1 Summary of self-bearing motor and active magnetic bearing properties

	Property	Sym.	Uns.	Val.
Self-Bearing Motor	No. of pole pairs	M	⋯	8
	No. of segments	N_{seg}	⋯	4
	No. of winding stations/seg.	N_s	⋯	12
	No. of wires/winding station	N_w	⋯	85
	Radial thickness of PM	t_m	mm	7.75
	Rad. thickness of coil windings	t_c	mm	3.87
	Nominal radial air gap	$g_{o,m}$	mm	0.762
	Rotor outer radius	R	mm	50.8
	Motor length	L	mm	25.4
	PM flux density	$\overline{B_m}$	Tesla	0.77
	Recoil permeability	μ_R	⋯	1.10
	Remnance flux density	B_r	Tesla	1.08
	Magnet leakage factor	K_{ml}	⋯	1.82
	Flux concentration factor	C_ϕ	⋯	0.80
	Peak inst. current/phase	I_{pk}	Amps	12.0
	Max. cont. current/phase	I_{rms}	Amps	3.0
Conv.	Pole area	A	mm^2	137.1
AMB	No. of turns/pole	N	⋯	60
	Bias current	I_b	Amps	3.0A
	Nominal radial air gap	g_{ob}	mm	0.40
	Flux leakage factor	α	⋯	0.60

(teeth). The flux correction factor was estimated experimentally using a Gaussmeter and a 0.010 inch thick Hall probe and found to be 0.6 with a ± 10 percent uncertainty.

B. Lorentz Self-Bearing Motor Model. Figure 4 shows the layout of the Lorentz self-bearing motor consisting of $M=8$ permanent magnet pole pairs attached to the rotor and $N_{\text{seg}}=4$ individually controlled winding segments attached to the stator. Each winding segment in the motor is an arc of $\pi/2$ radians and is attached to a slotless back iron. The slotless construction reduces cogging torque and increases load generation capacity (Casemore and Stephens [10]). The windings occupy $N_s=12$ stations along each winding segment ID with $N_w=85$ individual wires per station. Figure 5 shows the control loop for the self-bearing motor. As this figure indicates, each segment has a unique control current, i_1-i_4, that is divided into three phases, producing Lorentz-type forces F_{1x}, F_{2y}, F_{3x}, and F_{4y}, using a total of 12 phases. Stephens and Kim [8] showed that if the four segment currents are related to the three directional control currents, $i_{x,m}$, $i_{y,m}$, and i_θ by

$$\begin{aligned} i_1&=(i_\theta-i_{x,m})\\ i_2&=(i_\theta-i_{y,m})\\ i_3&=(i_\theta+i_{x,m})\\ i_4&=(i_\theta+i_{y,m}) \end{aligned} \tag{10}$$

then, independent bearing forces and motoring torque are generated for small rotor eccentricities. (Note that in Fig. 5, these equations are constructed using voltage commands, V_{cx}, V_{cy}, and $V_{c\theta}$, to construct segment voltage commands, V_1-V_4, that are then sent to transconductance power amplifiers.) The bearing force and motoring torque relationships are of the form

$$\begin{bmatrix} F_{x,m}\\ F_{y,m}\\ T_0 \end{bmatrix} = \underbrace{\begin{bmatrix} K_{ixx} & (\overline{K_{xy,w}}+K_{ixy}) & 0\\ -(\overline{K_{xy,w}}+K_{ixy}) & K_{ixx} & 0\\ 0 & 0 & K_{i\theta} \end{bmatrix}}_{[K_{i,m}]} \begin{bmatrix} i_{x,m}\\ i_{y,m}\\ i_\theta \end{bmatrix} + \underbrace{\begin{bmatrix} K_{xx,m} & \overline{K_{xy,L}} & 0\\ -\overline{K_{xy,L}} & K_{xx,m} & 0\\ 0 & 0 & 0 \end{bmatrix}}_{[K_{d,m}]} \begin{bmatrix} x_m\\ y_m\\ \theta \end{bmatrix} \tag{11}$$

where $[K_{i,m}]$ is the self-bearing motor current gain matrix, and $[K_{d,m}]$ is the self-bearing motor negative stiffness (destabilizing) matrix, and where the entries in these matrices are computed using the following equations:

Table 2 Open-loop force coefficients for self-bearing motor and active magnetic bearing

	Property	Sym.	Units	$i_\theta \approx 0$ $\theta=0$	$i_\theta=12$ A $\theta=\pm 11.25$ deg
Self-Bearing Motor	Torque gain	$K_{i\theta}$	N-m/A	2.0	2.0
	Bearing force direct current gain	K_{ixx}	N/A	17.8	17.8
	Bearing force cross Cpled. current gain	K_{ixy}	N/A	0	± 1.1
	Negative stiffness due to PM's	$K_{xx,m}$	N/mm	-101	-101
	Position stiff. due to Lorentz forces	$\overline{K_{xy,L}}$	N/mm	0	± 24.9
	Side pull due to winding flux	$\overline{K_{xy,w}}$	N/A	0	± 0.29
AMB	Bearing force current gain	$K_{i,b}$	N/A	28.7	28.7
	Neg. stiff. due to bias current	K_p	N/mm	-218.9	-218.9

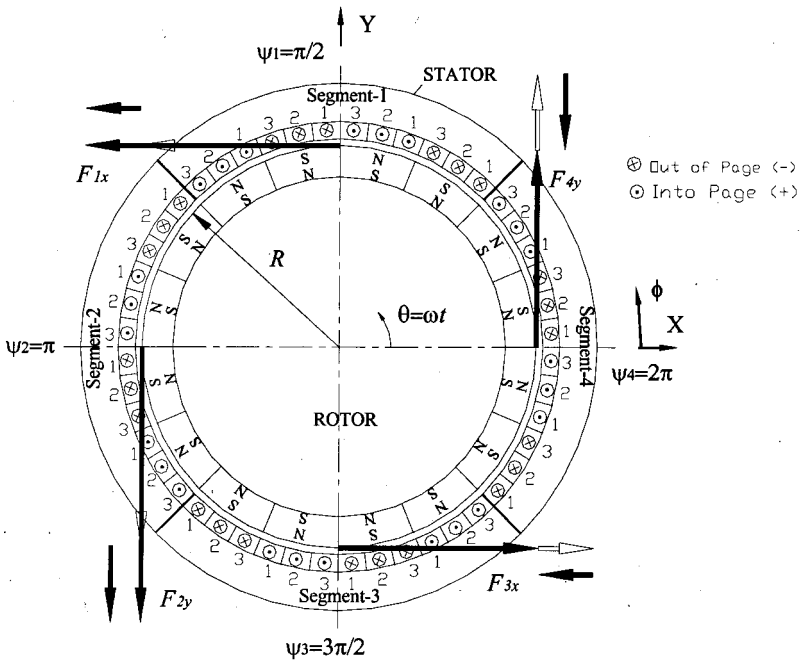

Fig. 4 Self-bearing motor layout

(torque gain) $$K_{i\theta}=\epsilon\frac{2\sqrt{2}\pi MRLN_w\overline{B_m}}{3} \quad (12)$$

(direct current gain) $$K_{ixx}=\epsilon\frac{4MN_w\overline{B_m}L}{3}\pm 0.5 \text{ percent} \quad (13)$$

(cross-coupled current gain)

$$K_{ixy}=0\pm 6 \text{ percent } K_{ixx} \quad (M=8) \quad (14)$$

(PM neg. stiffness) $$K_{xx,M}=-\frac{\pi RLB_r^2t_m^2\mu_RK_{ml}C_\phi}{\mu_o[t_m+\mu_RK_{ml}C_\phi(g_{o,m}+t_c)]^3} \quad (15)$$

(Lorentz side pull) $$\overline{K_{xy,L}}=0\pm\frac{2M\epsilon\pi B_r\mu_RK_{ml}C_\phi Lt_mN_wi_\theta}{3[t_m+\mu_RK_{ml}C_\phi(g_o+t_c)]^2} \quad (16)$$

(winding flux side pull) $$\overline{K_{xy,w}}=0\pm\frac{2\sqrt{2}\mu_oRLN_w^2i_\theta}{9[t_m+t_c+g_{o,m}]^2} \quad (17)$$

where $\epsilon=\cos(M\gamma)$ is a factor that depends on the phase angle, γ, between the winding currents and the rotor position. The torque current gain and the direct force current gain provide the independent bearing forces and motoring torque for the self-bearing motor. All other force coefficients are destabilizing. Two of these parameters vary a small amount with angular position, θ. These

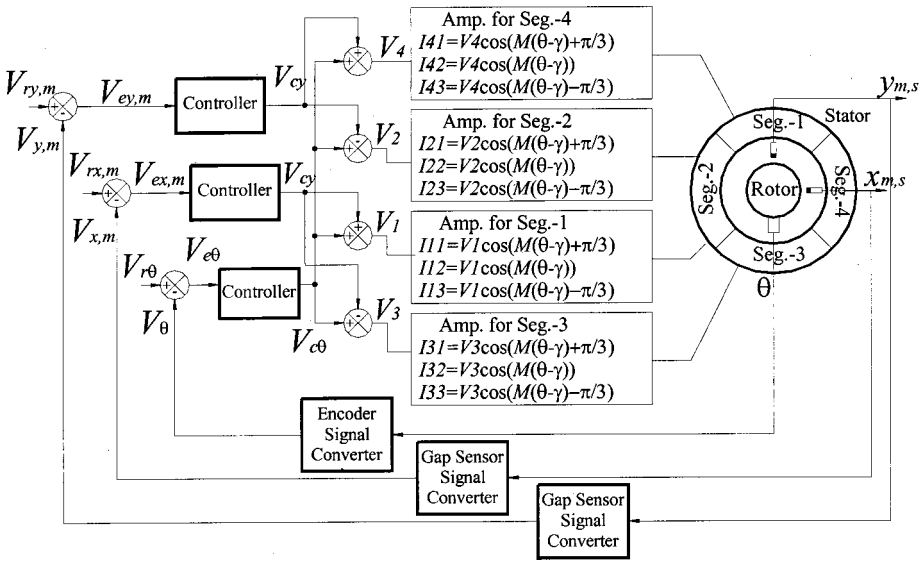

Fig. 5 Control of self-bearing motor

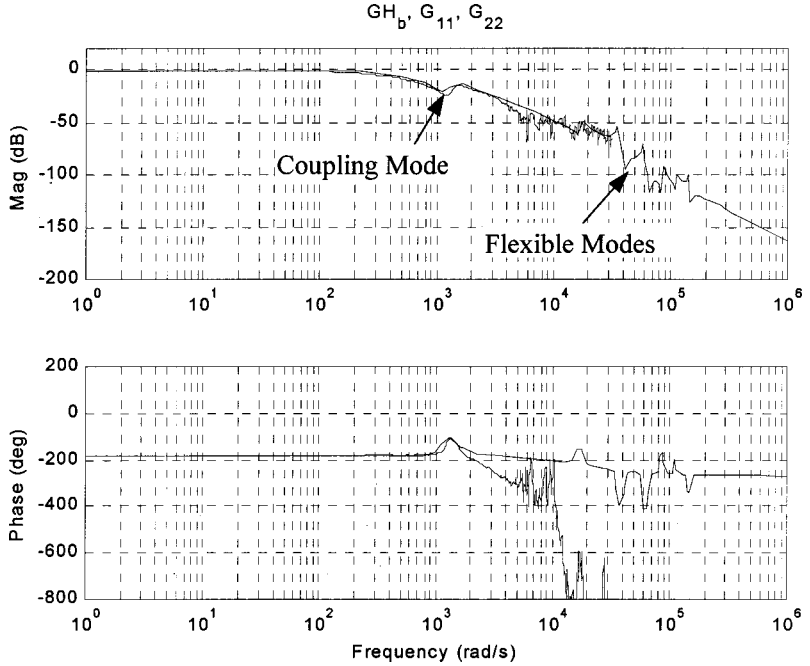

Fig. 6 Conventional active magnetic bearing open-loop transfer functions

parameters are the direct current gain, K_{ixx}, which varies ± 0.5 percent, and the cross-coupled current gain, K_{ixy}, which has a nominal value of zero but varies up to ± 6 percent of K_{ixx}. These gains vary sinusoidally with rotor angular position. K_{ixx} has its extreme values at $\theta=0$ deg, 11.25 deg . . . and its nominal values at the midpoint of these angles. K_{ixy} has its nominal values at $\theta=0$ deg, 11.25 deg . . . and its extreme values at the midpoint of these angles. Another two of these parameters vary with the torque control current, i_θ. These are the Lorentz side pull force $\overline{K_{xy,L}}$, which arises due to an imbalance in the Lorentz-type forces on the rotor, and the winding flux side pull force, $\overline{K_{xy,w}}$, which arises due to an imbalance in the winding flux when both a nonzero bearing force and motoring torque are requested from the motor. (For further derivations and discussion of the self-bearing motor force and torque gains, see Stephens et al. [8].)

Table 1 summarizes the construction of the self-bearing motor, including the variables used in Eqs. (12)–(17), and Table 2 gives the corresponding values of the negative stiffness and current gains for the self bearing motor when operating at two different conditions. The first is the condition at which the experimental results were taken. This is the unloaded condition where the angular control current is $i_\theta=0.05$ A (measured during experiment) and the angular position is $\theta=0$ deg. Note that for this condition all of the cross-coupled terms are zero. The second condition is $i_\theta=12$ A and $\theta=11.25$ deg which corresponds to the maximum loaded condition and the location of the rotor where the variation

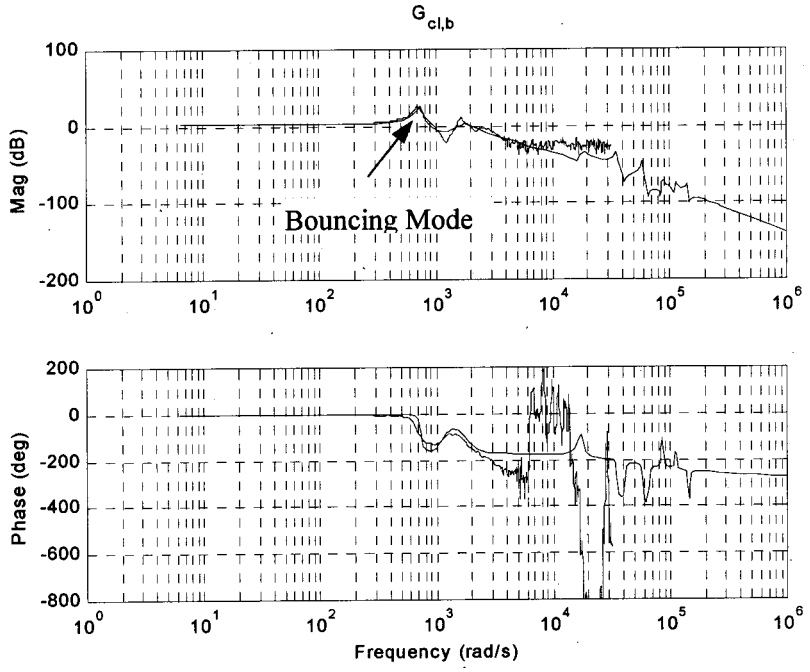

Fig. 7 Conventional active magnetic bearing closed-loop transfer functions

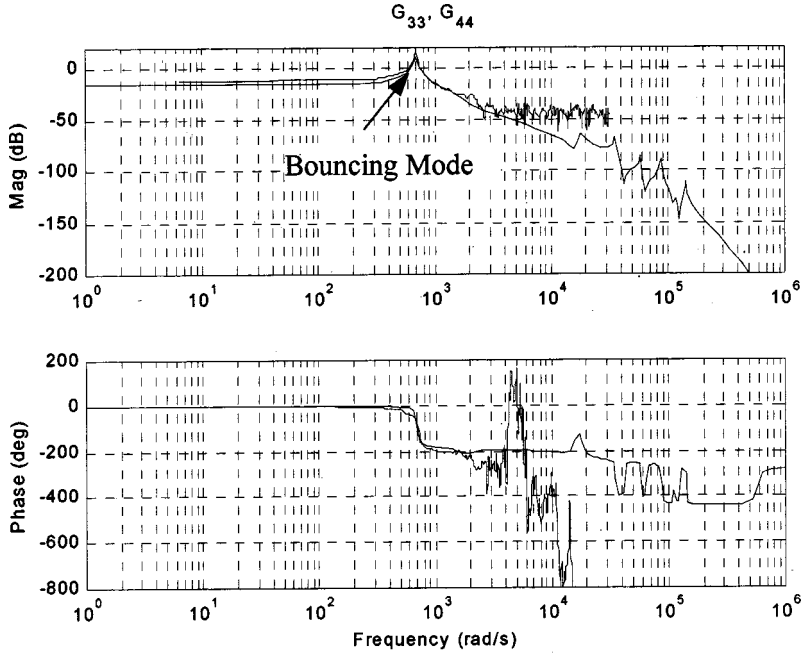

Fig. 8 Self-bearing motor radial position direct open-loop transfer functions

in gains is a maximum. At this condition, the cross-coupled gains are nonzero and must be considered to evaluate closed-loop stability and performance. Finally, $[K_{i,m}]$ and $[K_{i,b}]$ are augmented diagonally to form $[K_i]$ in Fig. 2, and $[K_{d,m}]$ and $[K_{d,b}]$ are augmented diagonally to form $[K_d]$ in Fig. 2. Again, $[T_1]$, $[T_2]$, and $[T_3]$ are transformation matrices that select the appropriate input and output variables.

Power Amplifiers and Sensors

The power amplifiers are PWM transconductance amplifiers. The transfer functions of these devices were measured and fitted with a first-order transfer function with a bandwidth of 3 Khz and unity DC gain. The power amplifier transfer function matrix is constructed as

$$[G_A] = \frac{G_{dc}BW}{s+BW}[I_{5\times5}] \tag{18}$$

where G_{dc} is the DC gain, BW is the bandwidth in rad/s and $[I_{5\times5}]$ is a 5×5 identity matrix.

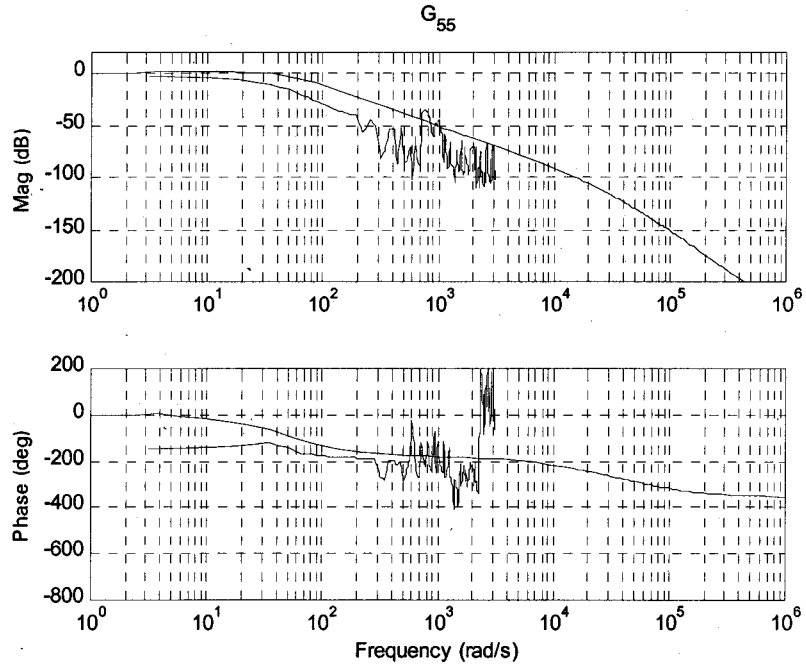

Fig. 9 Self-bearing motor angular position open-loop transfer function

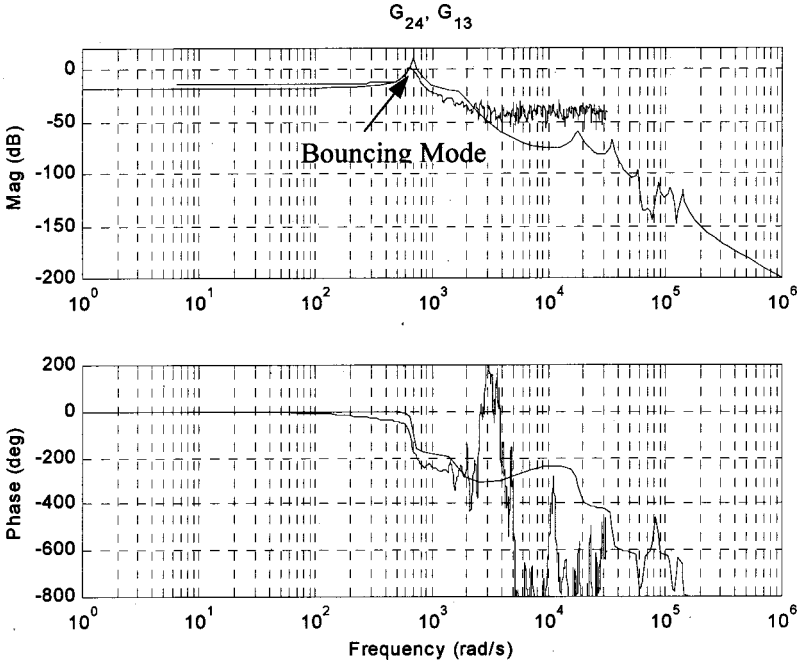

Fig. 10 Active magnetic bearing radial sensor to motor radial force transfer function

The radial position sensors are inductive type probes and the encoder is an optical type. The bandwidths of these sensors are significantly larger (>10 Khz) than the bandwidth of any other subsystem, therefore they are modeled as pure gains. The sensitivity of the conventional bearing inductive probes, the self-bearing motor inductive probes, and the encoder is 9016 V/m, 8436 V/m and 1.6 V/rad, respectively. The sensor transfer function matrix is then

$$\underbrace{\begin{bmatrix} V_{xb} \\ V_{yb} \\ V_{xm} \\ V_{ym} \\ V_{\theta} \end{bmatrix}}_{\mathbf{v}_s} = \underbrace{\begin{bmatrix} 9016 & 0 & 0 & 0 & 0 \\ 0 & 9016 & 0 & 0 & 0 \\ 0 & 0 & 8436 & 0 & 0 \\ 0 & 0 & 0 & 8436 & 0 \\ 0 & 0 & 0 & 0 & 1.6 \end{bmatrix}}_{[K_s]} \underbrace{\begin{bmatrix} x_{b,s} \\ y_{b,s} \\ x_{m,s} \\ y_{m,s} \\ \theta \end{bmatrix}}_{\overline{\mathbf{y}_o}} \tag{19}$$

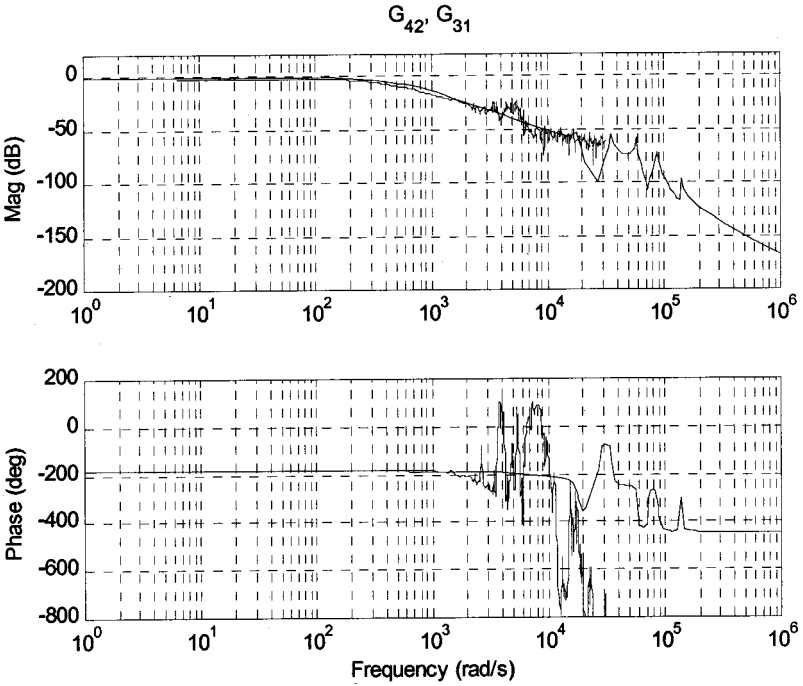

Fig. 11 Self-bearing motor radial sensor to active magnetic bearing force transfer function

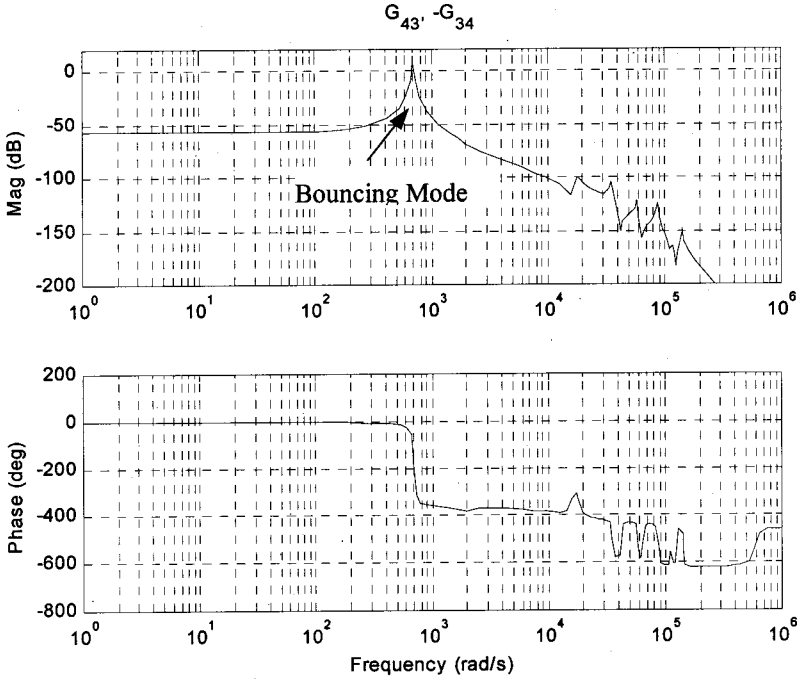

Fig. 12 Self-bearing motor cross-coupled transfer functions for $i_\theta = 12$ A and $\theta = 11.25$ deg

where $\mathbf{v}_s$ is the sensor output vector and $[T_6]$ is the transformation matrix that selects the appropriate outputs from $\mathbf{y}_o$.

Controller

The controllers are implemented on the digital motion control card. The rate of throughput for the controller is greater than 10 KHz which is much greater than the largest frequency of control (3 KHz as limited by the power amplifiers), therefore a continuous system model is used for the controller. Decoupled PD controllers are used to stabilize the shaft lateral motion using either the conventional AMB or the self bearing motor, or both. The general form of the controller transfer function matrix is then

$$\underbrace{\begin{bmatrix} V_{cx,b} \\ V_{cy,b} \\ V_{cx,m} \\ V_{cy,m} \\ V_{c\theta} \end{bmatrix}}_{\mathbf{v}_c} = \begin{bmatrix} G_{pd,b} & 0 & 0 & 0 & 0 \\ 0 & G_{pd,b} & 0 & 0 & 0 \\ 0 & 0 & G_{pd,m} & 0 & 0 \\ 0 & 0 & 0 & G_{pd,m} & 0 \\ 0 & 0 & 0 & 0 & G_{pd,\theta} \end{bmatrix} \underbrace{\begin{bmatrix} V_{ex,b} \\ V_{ey,b} \\ V_{ex,m} \\ V_{ey,m} \\ V_{e\theta} \end{bmatrix}}_{\mathbf{v}_e} \tag{20}$$

where $G_{pd,b}$, $G_{pd,m}$ and $G_{pd,\theta}$ are the PD controllers of the form $k_d s + k_p$ for the conventional AMB, self-bearing motor bearing function, and the self-bearing motor angular torque function, respectively. Note that in this control configuration, the self-bearing motor is a servo-motor, where the angular velocity can be generated using the appropriate reference input signal. The motor is used in servo-mode for these experiments in order to investigate the effect of the variability in open loop gains (Eqs. (12)–(17)) with rotor angular position. Alternatively, the motor can operate at a constant angular velocity by using the encoder to estimate the angular velocity, ω, and feeding back this quantity. For this test rig, the stabilizing gains used for the conventional AMB ($G_{p,b}$) are $k_p = 4.5$ and $k_d = 0.001$. The stabilizing gains used for the motor angular motion ($G_{p\theta}$)$k_p = 2.0$, and $k_d = 0.5$. These controllers are used in the next section to validate the model using experimental data.

Experimental Results

Transfer functions were measured for the test rig in two different configurations. The first configuration was with the rotor stabilized using only the jarno coupling and the conventional AMB. The second configuration again used the jarno coupling and conventional AMB to stabilize the shaft but added the self-bearing motor to stabilize the angular position and to inject open-loop forces onto the rotor.

A Conventional Active Magnetic Bearing (AMB) Configuration. In the first configuration the only effect present from the self-bearing motor is the negative stiffness due to the permanent magnets. By injecting a sine sweep input at each of the conventional AMB control inputs, $\mathbf{v}_c$, and measuring the conventional AMB sensor responses, $\mathbf{v}_s$, the following open-loop transfer function matrix was constructed for the system:

$$\begin{bmatrix} V_{x,b} \\ V_{y,b} \end{bmatrix} = \begin{bmatrix} GH_b & 0 \\ 0 & GH_b \end{bmatrix} \begin{bmatrix} V_{cx,b} \\ V_{cy,b} \end{bmatrix} \tag{21}$$

where the cross terms are zero because no cross-coupling effects are present in the conventional AMB and the diagonal terms, GH_b, are identical due to symmetry between the x and y-axes. Figure 6 shows the experimental bode plot of GH_b along with that resulting from the model. Good agreement is seen between the model and the experimental results. Figure 6 indicates that the flexible body rotor modes present in the model response are essentially below the experimental response noise floor of about -45 dB. The first vibration mode of the open loop system results from the jarno coupling support which was modeled in Eq. (6). The experimental results indicate that the natural frequency of this mode is at $\omega_n = 1550$ rad/s. Using a modal mass, m, of 15 percent of the total mass of the shaft (3.9 lbs.) and a damping ratio of $\xi = 0.15$ for the coupling interface, the stiffness and damping of Eq. (6) were estimated as $k = m\omega_n^2$ and $c = 2\xi m \omega_n$.

Results were also generated for the closed-loop transfer func-

tion matrix. For this measurement the sine sweep was injected at the conventional AMB reference input, $\mathbf{v}_{\text{ref}}$, and the sensor responses, $\mathbf{v}_s$, were measured as

$$\begin{bmatrix} V_{x,b} \\ V_{y,b} \end{bmatrix} = \begin{bmatrix} G_{cl,b} & 0 \\ 0 & G_{cl,b} \end{bmatrix} \begin{bmatrix} V_{rx,b} \\ V_{ry,b} \end{bmatrix} \tag{22}$$

where, again, the cross terms are zero because there is no cross coupling for the conventional bearing and the diagonal terms are identical due to symmetry. Figure 7 shows the modeled and experimental results of the closed-loop transfer function. Figure 7 indicates that closing the loop on the conventional bearing introduces the stabilizing ''bouncing mode'' of the rotor in its bearings. The closed-loop measurements show that the conventional AMB has a phase margin of 8 deg, a gain margin of 67 and a closed-loop stiffness of 369.7 N/mm. This set of test results indicates that the rotor model, conventional AMB model, PM negative stiffness model and feedback component models accurately characterize the system.

B Self-Bearing Motor Configuration. The second experimental configuration is with the conventional AMB control loops closed, the self-bearing motor angular control loop closed, and the self-bearing motor radial (bearing) control loops open. In this configuration, the shaft is stabilized in the x and y-directions using the jarno coupling and the conventional AMB, and stabilized in the θ direction using the self-bearing motor. The motor was tested in the servo-loop mode at the home position ($\theta=0$) in order to evaluate the effect of the actuator gains (which vary with angular position) and compare them to the model. The following transfer function matrix was measured:

$$\underbrace{\begin{bmatrix} V_{x,b} \\ V_{y,b} \\ V_{x,m} \\ V_{y,m} \\ V_{\theta} \end{bmatrix}}_{\mathbf{v}_s} = \underbrace{\begin{bmatrix} G_{11} & 0 & G_{13} & G_{14} & 0 \\ 0 & G_{22} & G_{23} & G_{24} & 0 \\ G_{31} & G_{32} & G_{33} & G_{34} & 0 \\ G_{41} & G_{42} & G_{43} & G_{44} & 0 \\ 0 & 0 & 0 & 0 & G_{55} \end{bmatrix}}_{[G_{sb}]} \underbrace{\begin{bmatrix} V_{cx,b} \\ V_{cy,b} \\ V_{cx,m} \\ V_{cy,m} \\ V_{r\theta} \end{bmatrix}}_{\mathbf{v}_{\text{exp}}} \tag{23}$$

where $[G_{sb}]$ is the experimental transfer function matrix and $\mathbf{v}_{\text{exp}}$ is the vector of experimental inputs. (The input and output locations are shown in Figs. 2 and 5.) The diagonal terms, G_{11} and G_{22}, are the open-loop transfer functions for the conventional AMB, GH_b, as measured in Eq. (21) and shown previously in Fig. 6. These were measured again using the second test configuration and found to be the same as in the first configuration, as expected. The diagonal terms G_{33} and G_{44} are the direct open-loop transfer functions between the self-bearing motor x and y-direction control inputs and sensors, respectively. Figure 8 shows that $G_{33}=G_{44}$ due to symmetry as in the case of the conventional AMB. Note that the open-loop bearing force produced by the self-bearing motor acts against the rotor with the closed loop conventional AMB. Therefore, the bouncing mode of the rotor appears, as it should, in this transfer function. The last diagonal term in $[G_{sb}]$, G_{55}, is the closed-loop transfer function for angular position control using the motor. Figure 9 shows the model and experimental transfer functions. There is a slight inaccuracy in the model as the break frequency of the experimental transfer function is seen to be lower. The most likely reason for this is that the inductance of the motor was not included in the model, which would account for the lower bandwidth.

The off-diagonal terms of $[G_{sb}]$ arise due to two effects: (i) multiple sensors and (ii) the cross-coupled terms in the self-bearing motor. Since there are two radial sensors in the x-direction (one for the conventional AMB and one for the motor) and two in the y-direction, clearly an input at either the motor or the AMB results in a response at both sensor locations. This gives rise to the off-diagonal terms, G_{13}, G_{24}, G_{31}, and G_{42}. Figures 10 and 11

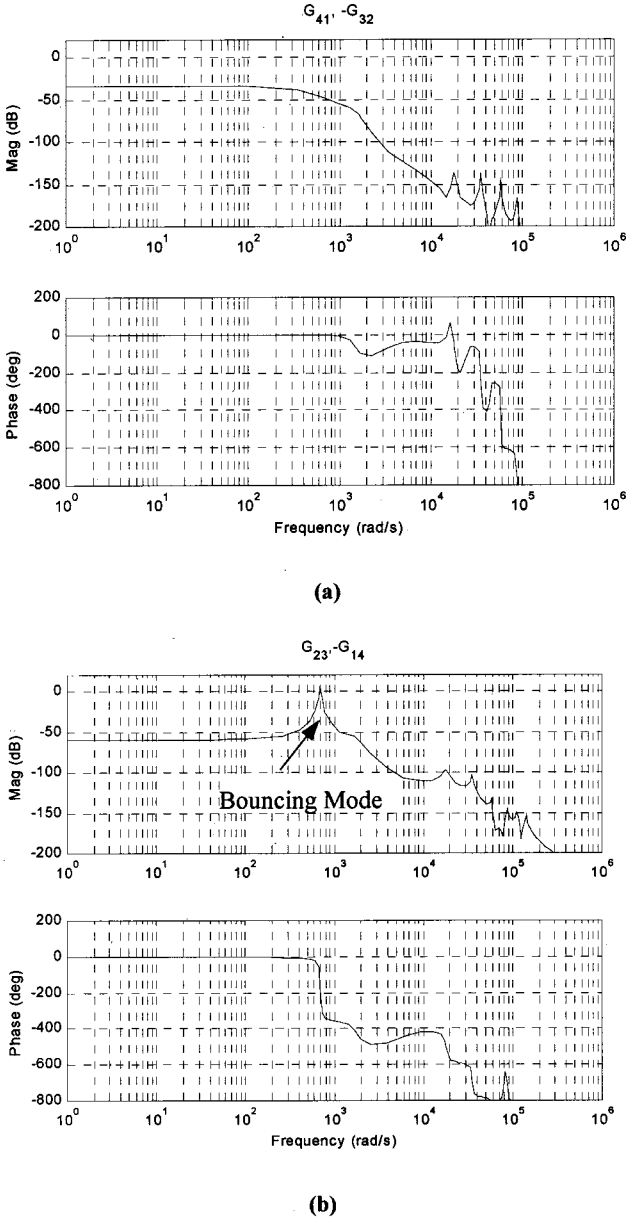

Fig. 13 Self-bearing motor and conventional active magnetic bearing cross-coupled force transfer functions for $i_\theta=12$ A and $\theta=11.25$ deg

show the modeled and experimental results for these transfer functions indicating that $G_{24}=G_{13}$ and $G_{42}=G_{31}$. Note that since open-loop forces by the self-bearing motor act on the system with the conventional AMB closed, the ''bouncing'' mode occurs in G_{24} and G_{13}. However, open-loop inputs from the AMB act on the system with the SB motor-bearing feedback loops open, therefore, the bouncing mode does not appear in G_{42} and G_{31}.

Finally, the self-bearing motor cross-coupling effects described in Eqs. (11)–(17) give rise to the off-diagonal terms G_{34}, G_{43}, G_{14}, G_{23}, G_{41}, and G_{32}. The model results indicate that $G_{34}=-G_{43}$ and $G_{14}=-G_{23}$, and arise due to cross coupling in both the current gain matrix, $[K_{i,m}]$, and the negative stiffness matrix, $[K_{d,m}]$. The model results further indicate that $G_{41}=-G_{32}$ and arise only due to the cross-coupling in the negative stiffness matrix, $[K_{d,m}]$.

For the experimental results, no external torque was applied to the motor and the motor was stabilized at an angular position of $\theta=0$. Under this no load condition the motoring current was mea-

sured as $i_\theta = 0.05$ amperes. As Table 2 indicates for this condition, all of the self-bearing motor cross-coupled gains are essentially zero. This was confirmed experimentally by measuring the cross-coupled transfer functions which were found to be less than -45 dB (the noise floor) in magnitude.

The maximum current for the self-bearing motor is 12 A which corresponds to a peak torque of 24 N-m. It is impractical to apply such a large torque to the test rig in its present form, therefore experimental results were not obtained for this condition. However, Figs. 12, 13(*a*), and 13(*b*) show the modeled results for the cross-coupled force gains when the motor is under full load ($i_\theta = 12$ A), and the rotor position is 11.25 deg (this corresponds to the position where the cross-coupled gains are a maximum). These plots indicate that the cross-coupled terms are quite small but may become significant at certain frequencies (1 dB at 710 rad/s in Fig. 12). These terms introduce an added instability to the system that must be addressed either by design (design the motor to minimize the cross coupled gains in Eqs. (12)–(17)), application (apply the motor in lightly loaded situations where i_θ, and hence the cross-coupled gains are essentially negligible) or accept the variations in gain as uncertainties in the system and design robust controllers to handle them. For the motor design in this paper, the cross-coupled gains were minimized during design (see Stephens and Kim [8]).

Conclusions and Summary

This paper presented an experimentally validated model for a new type of self-bearing motor that uses Lorentz forces to produce both bearing forces and motor torque. The results indicated that the self-bearing motor has several cross-coupled terms in the force-current-displacement relationship, but that these cross-coupled terms are quite small over all operating conditions. Experimental transfer functions compared well with the model. The model derived and validated in this paper can be used in future studies to design higher-order controllers and evaluate the new self-bearing motor design for use in new applications.

Acknowledgments

The author expresses his appreciation to Airex Corporation of Dover, NH, and to the U.S. Air Force for sponsorship of this research under contract F04701-98-C-0019. The author also wishes to thank Barrett Steele and Zhaohui Ren of the UK Bearings and Sealing Laboratory for helping with data collection and assembling the figures.

References

[1] Salazar, A. O., Chiba, A., and Fukao, T., 2000, ''A Review of Developments in Bearingless Motors,'' *Proc. 7th Int. Symp. Magn. Bearings*, ETH, Zurich, Aug. pp. 335–339.
[2] Chiba, A., Rahman, M. A., and Fukao, T., 1991, ''Radial Forces in Bearingless Reluctance Motor,'' IEEE Trans. Magn., **27**, Mar., p. 786.
[3] Schoeb, R., and Bischel, J., 1994, ''Vector Control of Bearingless Motor,'' *Proc. 4th Int. Symp. Magn. Bearings*, ETH Zurich, pp. 327–332.
[4] Okada, Y., Miyamoto, S., and Ohishi, T., 1996, ''Levitation and Torque Control of Internal Permanent Magnet Type Bearingless Motor,'' IEEE Trans. Control Sys. Tech., **4**(5), pp. 565–571.
[5] Carroll, D., Sedgewick, J., and Stephens, L. S., 1999, ''Long Life, Fault Tolerant, Spacecraft Sensor Gimbal/Bearing System Final Report,'' United States Air Force Research Laboratory/VSDV, Contract No. F29601-98-C-0188, Mar.
[6] Kim, D. G., and Stephens, L. S., 2000, ''Fault Tolerance of a Lorentz-Type Slotless, Self Bearing Motor According to the Coiling Schemes,'' *Proc. 7th Int. Symp. Magn. Bearings*, ETH, Zurich, Aug., pp. 219–224.
[7] Steele, B. A., and Stephens, L. S., 2000, ''A Test Rig for Measuring Force and Torque Production in a Lorentz, Slotless Self Bearing Motor,'' *Proc. 7th Int. Symp. Magn. Bearings*, ETH, Zurich, Aug., pp. 407–412.
[8] Stephens, L. S., and Kim, D. G., 2000, ''Analysis and Simulation of a Lorentz-type, Slotless Self-Bearing Motor,'' *Proceedings of the 1st IFAC Conference on Mechatronics*, Darmstadt, Germany, Sept., Elsevier Sci. Ltd., Amsterdam.
[9] Okada, Y., Konishi, H., Kanebako, H., and Lee, C., 2000, ''Lorentz Force Type Self Bearing Motor,'' *Proc. 7th Int. Symp. Magn. Bearings*, ETH Zurich, Aug., pp. 353–358.
[10] Casemore, M. A., and Stephens, L. S., 1999, ''Actuator Gains for a Toothless Permanent-Magnet Self-Bearing Motor,'' IEEE Trans. Magn., **35**(6).

Predicted Effects of Shunt Injection on the Rotordynamics of Gas Labyrinth Seals

N. Kim
Graduate Assistant,
Weatherford International, Inc.,
Houston, TX

S.-Y. Park
Graduate Assistant

D. L. Rhode[1]
Professor

Mechanical Engineering Department,
Texas A&M University,
College Station, TX

A recent CFD perturbation model for turbomachinery seal rotordynamics was extended for labyrinth shunt injection with an arbitrarily high pressure gas. A large number of measured cases with labyrinth injection pressure at approximately 13.8 bars (200 psi) were computed and compared with measurements. The drastically reduced (negative) cross-coupled stiffness, which is the primary advantage from the use of shunt injection in gas labyrinth seal applications, was well predicted. The agreement with measurements for k, C, and C_{eff} was within about 40%, 60% and 10%, respectively. In addition, it was found that moving the injection toward the high pressure end of the seal gives k, C, and C_{eff} values that are rotordynamically only slightly more stabilizing. Further, the radial distributions of the flow perturbation quantities give support to the two-control volume approach for developing bulk-flow models for labyrinth seal rotordynamics.
[DOI: 10.1115/1.1520539]

Introduction

Labyrinth-type gas seals are fluid dynamic devices with numerous applications that often require either a minimum or a fixed leakage. Labyrinth seals can be rotordynamically self-exciting, because the rotor generally whirls within the seal housing. This rotor vibration is a very important problem for recent turbomachines designed for higher shaft speed, higher pressure, and higher efficiency (small clearance) operating conditions. Specifically, the whirling motion of a rotor causes an asymmetric flow in the seal, which generates an uneven pressure distribution along the circumference resulting in rotordynamic forces on the rotor. Two important effects on the rotordynamic forces of labyrinth seals are the entering swirl velocity and the gas density. The book by Childs [1] offers a good survey of the rotordynamic behavior of labyrinths.

In an effort to increase rotordynamic stability, shunt injection of high pressure gas through the stator housing has been used in certain applications for a long time. The injection flow is usually supplied by a very large number of closely spaced (circumferentially) high pressure ports. Various injection angles (measured from the tangent) have been used depending on the application. Shunt injection has proven to be rotordynamically beneficial in many cases, although there have been cases in which they were not satisfactory, [2]. In addition, a major disadvantage of shunt injection is the large increase of labyrinth leakage. Specifically, Soto and Childs [3] measured cases with a 100% increase of leakage due to the presence of shunt injection. It was further found that shunt injection at an angle against rotation gives a large stabilizing effect, i.e., a drastically reduced (even negative) cross-coupled stiffness was measured, [3]. In spite of its importance in stabilizing rotor motion, there has been no rigorous theoretical analysis of shunt injection. The flowfield is very complex, i.e., unsteady, three-dimensional, turbulent, and highly compressible with two flow exits as shown in Fig. 1. One expects that the only reliable theoretical approach would employ an appropriate numerical model.

An appropriate model is the computational fluid dynamics (CFD) perturbation model based on the disturbed boundary condition (PDBC) for liquid seals with a plain whirling rotor [4] and with a tilted whirling rotor [5]. It showed very successful comparisons with measurements for rotordynamic forces and moments. The model assumes that the rotor undergoes a circular orbit of small radius compared to the normal seal clearance, resulting in corresponding disturbances in the flowfield inside the seal. Mathematically, the perturbation of the flow variables such as velocities and pressure was assumed to respond to the disturbed flow boundary conditions on the whirling rotor surface. One advantage of the PDBC model is that it can be applied to any axisymmetric seal geometry for a variety of flow conditions (including the compressibility effect), which will be presented in a following section.

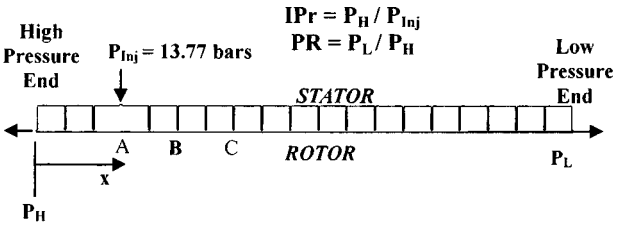

(a) Overall seal configuration

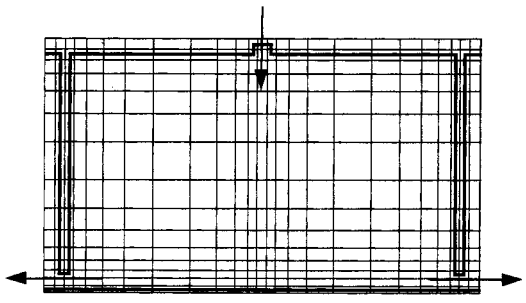

(b) Extremely coarse grid example for the injection cavity

Fig. 1 Injection labyrinth seal configuration (not to scale). [Tooth clearance=0.22 mm (0.00866 in.); tooth height=3.175 mm (0.125 in.); tooth pitch=3.175 mm (0.125 in.); seal length =63.5 mm (2.5 in.); shaft radius=64.69 mm (2.54684 in.)], [Injection Location A: $x/L=0.16$; B: $x/L=0.26$; C: $x/L=0.37$].

[1]To whom correspondence should be addressed.

Contributed by the International Gas Turbine Institute (IGTI) of THE AMERICAN SOCIETY OF MECHANICAL ENGINEERS for publication in the ASME JOURNAL OF ENGINEERING FOR GAS TURBINES AND POWER. Paper presented at the International Gas Turbine and Aeroengine Congress and Exhibition, New Orleans, LA, June 4–7, 2001; Paper 2001-GT-239. Manuscript received by IGTI, Dec. 2000, final revision, Mar. 2001. Associate Editor: R. Natole.

Objectives

The first of three main objectives of the present investigation is to extend the recent quasi three-dimensional CFD perturbation model to allow shunt injection of arbitrarily high pressure gas at any axial location. The second objective is to validate the extended model by comparing the predicted rotordynamic force coefficients with measurements. The third objective is to examine the distributions of the flow perturbations as well as the effect of injection axial location.

Mathematical Model

For small amplitude motions about a centered rotor position, the reaction forces F_y and F_z can be modeled by a linearized set of equations, [1].

$$-\begin{Bmatrix} F_y \\ F_z \end{Bmatrix} = \begin{bmatrix} K & k \\ -k & K \end{bmatrix} \begin{Bmatrix} y \\ z \end{Bmatrix} + \begin{bmatrix} C & c \\ -c & C \end{bmatrix} \begin{Bmatrix} y' \\ z' \end{Bmatrix} + \begin{bmatrix} M & m \\ -m & M \end{bmatrix} \begin{Bmatrix} y'' \\ z'' \end{Bmatrix} \tag{1}$$

where y, y', y'' and z, z', z'' are displacements, velocities, and accelerations in the y and z lateral directions. K and k are the direct and the cross-coupled stiffness coefficients, C and c are the direct and cross-coupled damping coefficients, and M and m are the direct and cross-coupled inertia coefficients, respectively. Among the above force coefficients, the tangential components k and C are more important in the determination of rotor stability.

The flow field formed in the eccentric seal clearance, as shown in Fig. 2, is basically unsteady, three-dimensional, and turbulent. Thus the governing equations are the time-averaged turbulent Navier-Stokes equations for the cylindrical coordinate system in a fixed reference frame on the stator:

$$\rho \frac{\partial u}{\partial t} + \rho \left[u \frac{\partial u}{\partial x} + v \frac{\partial u}{\partial r} + \frac{w}{r} \frac{\partial u}{\partial \theta} \right] = -\frac{\partial p}{\partial x} + \frac{\partial \tau_{xx}}{\partial x} + \frac{1}{r} \frac{\partial}{\partial r}(r \tau_{xr}) + \frac{1}{r} \frac{\partial \tau_{x\theta}}{\partial \theta} \tag{2a}$$

$$\rho \frac{\partial v}{\partial t} + \rho \left[u \frac{\partial v}{\partial x} + v \frac{\partial v}{\partial r} + \frac{w}{r} \frac{\partial v}{\partial \theta} - \frac{w^2}{r} \right] = -\frac{\partial p}{\partial r} + \frac{\partial \tau_{rx}}{\partial x} + \frac{1}{r} \frac{\partial}{\partial r}(r \tau_{rr}) + \frac{1}{r} \frac{\partial \tau_{r\theta}}{\partial \theta} - \frac{1}{r} \tau_{\theta\theta} \tag{2b}$$

$$\rho \frac{\partial w}{\partial t} + \rho \left[u \frac{\partial w}{\partial x} + v \frac{\partial w}{\partial r} + \frac{w}{r} \frac{\partial w}{\partial \theta} + \frac{vw}{r} \right] = -\frac{1}{r} \frac{\partial p}{\partial \theta} + \frac{\partial \tau_{\theta x}}{\partial x} + \frac{1}{r} \frac{\partial \tau_{\theta\theta}}{\partial \theta} + \frac{\partial \tau_{\theta r}}{\partial r} + \frac{2}{r} \tau_{\theta r} \tag{2c}$$

and the continuity equation is given by

$$\frac{\partial \rho}{\partial t} + \frac{\partial}{\partial x}(\rho u) + \frac{1}{r} \frac{\partial}{\partial r}(r \rho v) + \frac{1}{r} \frac{\partial}{\partial \theta}(\rho w) = 0. \tag{3}$$

The symmetric Reynolds stress tensor is given as

$$[\tau_{ij}] = \begin{bmatrix} 2\mu_e \frac{\partial u}{\partial x} - \Pi & \mu_e \left\{ \frac{\partial u}{\partial r} + \frac{\partial v}{\partial x} \right\} & \mu_e \left\{ \frac{1}{r} \frac{\partial u}{\partial \theta} + \frac{\partial w}{\partial x} \right\} \\ \mu_e \left\{ \frac{\partial u}{\partial r} + \frac{\partial v}{\partial x} \right\} & 2\mu_e \frac{\partial v}{\partial r} - \Pi & \mu_e \left\{ r \frac{\partial}{\partial r}\left(\frac{w}{r} \right) + \frac{1}{r} \frac{\partial v}{\partial \theta} \right\} \\ \mu_e \left\{ \frac{1}{r} \frac{\partial u}{\partial \theta} + \frac{\partial w}{\partial x} \right\} & \mu_e \left\{ r \frac{\partial}{\partial r}\left(\frac{w}{r} \right) + \frac{1}{r} \frac{\partial v}{\partial \theta} \right\} & 2\mu_e \left\{ \frac{1}{r} \frac{\partial w}{\partial \theta} + \frac{v}{r} \right\} - \Pi \end{bmatrix} \tag{4}$$

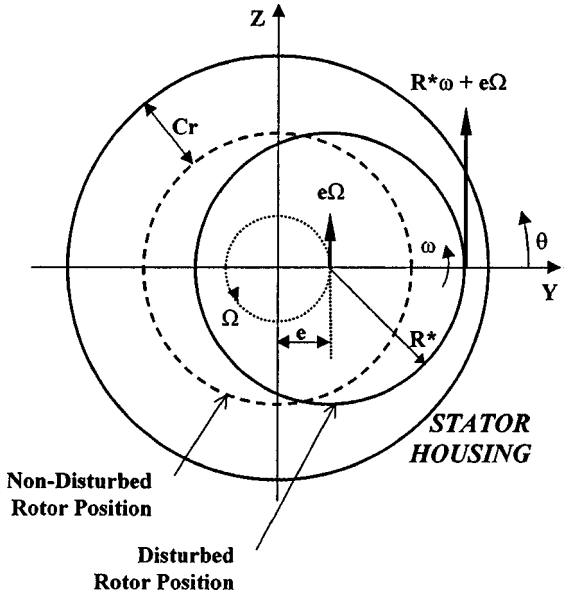

Fig. 2 Geometrical and kinematical relationship in a whirling rotor, [Ω: whirling speed; ω: rotating speed]

with

$$\Pi = \frac{2}{3} \rho k + \mu_e \left\{ \frac{\partial u}{\partial x} + \frac{1}{r} \frac{\partial}{\partial r}(rv) + \frac{1}{r} \frac{\partial w}{\partial \theta} \right\}$$

where μ_e is the effective turbulent viscosity. It is modeled as the sum of the laminar viscosity and the turbulent viscosity, i.e., $\mu_e = \mu + C_\mu \rho k^2/\varepsilon$ where $C_\mu = 0.09$. Following the k-ε turbulence model, the governing equations for the turbulent kinetic energy k and the turbulent energy dissipation ε are

$$\rho \frac{\partial k}{\partial t} + \frac{\partial}{\partial x_i}(\rho u_i k) = \frac{\partial}{\partial x_i}\left(\frac{\mu_e}{\sigma_k} \frac{\partial k}{\partial x_i} \right) + \tau_{ij} \frac{\partial u_i}{\partial x_j} - \rho \varepsilon \tag{5}$$

$$\rho \frac{\partial \varepsilon}{\partial t} + \frac{\partial}{\partial x_i}(\rho u_i \varepsilon) = \frac{\partial}{\partial x_i}\left(\frac{\mu_e}{\sigma_\varepsilon} \frac{\partial \varepsilon}{\partial x_i} \right) + \frac{\varepsilon}{k}\left[c_1 \tau_{ij} \frac{\partial u_i}{\partial x_j} - c_2 \rho \varepsilon \right] \tag{6}$$

where a tensor notation is employed, and the empirical constants are $c_1 = 1.44$, $c_2 = 1.92$, $\sigma_k = 1$, and $\sigma_\varepsilon = 1.3$, [6]. The working fluid is assumed to be quasi-ideal-gas and the equation of state is

$$p = Z \rho R T \tag{7}$$

where Z is the compressibility factor and R is the universal gas constant. To compute the temperature field, the energy equation in terms of the total enthalpy is solved.

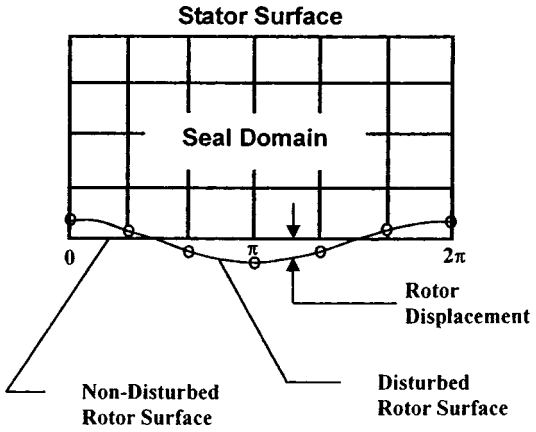

Fig. 3 Geometrical representation of the Taylor series expansion of variable on the displaced rotor surface [Ω: whirling speed; ω: rotating speed]

$$\rho\frac{\partial h}{\partial t}+\frac{\partial}{\partial x_i}(\rho u_i h)=\frac{\partial}{\partial x_i}\left[u_j\tau_{ij}+\frac{c_p\mu_e}{\mathrm{Pr}}\frac{\partial T}{\partial x_i}\right] \tag{8}$$

where the total enthalpy is defined as $h=c_pT+1/2u_iu_i$ and Pr is the turbulent Prandtl number.

Complete solutions of the above fully three-dimensional, unsteady governing equations, [7], for the present seal situations would require massive computer resources in practice. Less resources are required to solve the fully three-dimensional perturbation equations solved for simple seals with incompressible flow by Athavale and Hendricks [8]. However, observe that the fluid boundary deformation (i.e., circumferential variation of radial clearance) is periodic circumferentially and temporally when the rotor is whirling on a circular orbit about the housing center position. Assuming that the eccentricity of the rotor is small compared to the seal radial clearance (Fig. 2), one can approximately decompose the position of the whirling rotor surface into a steady, axisymmeric part and an unsteady, asymmetric part. In terms of a Fourier series expansion up to first order, the position of the displaced rotor surface, (i.e., R), is approximately given as (see Figs. 2 and 3)

$$R(\theta,t)=R^*+\varepsilon Re\{Ce^{j(\Omega t-\theta)}\} \tag{9}$$

where R^* represents the concentric-rotor (i.e., undisturbed) surface location, j indicates an imaginary number, and C is the seal clearance. For the case of tilted whirling motion the clearance C should be multiplied by the local eccentricity function $\varphi(x)$ to reflect the axial variation of the rotor eccentricity, [4]. It is assumed that the flow variables such as velocities, pressure and density can be expressed in an analogous manner to have a steady and axisymmetric part, and an unsteady and asymmetric part as

$$\Phi(x,r,\theta,t)=\Phi_0(x,r)+\varepsilon Re\{\hat{\Phi}_1(x,r)e^{j(\Omega t-\theta)}\} \tag{10}$$

where Φ is a generic flow variable, the zeroth-order variable Φ_0 represents the undisturbed part, while the complex first-order variable $\hat{\Phi}_1$ is the disturbed part varying only in the x-r space. The perturbation parameter ε is defined as the ratio of rotor disturbance to seal radial clearance, i.e., e/C, where $e\ll C$. It is implied in the choice of the modeled disturbance Eq. (10) that the small disturbance rotor whirl motion gives correspondingly periodic (first-order) flow disturbances. When the complex function is defined as $\hat{\Phi}_1=\Phi_{1c}+j\Phi_{1s}$, one obtains a simpler form of Eq. (10) as

$$\Phi(x,r,\theta,t)=\Phi_0(x,r)+\varepsilon\{\Phi_{1c}(x,r)\cos(\Omega t-\theta)-\Phi_{1s}(x,r)\sin(\Omega t-\theta)\}$$

from which one finds that Φ_{1c} and Φ_{1s} are to be determined to represent the flow disturbance in the x-r plane.

By substituting Eqs. (4), (7), and (10) into Eqs. (2) and (3) for pressure, velocities and the density, one obtains the zeroth-order and the first-order axisymmetric equation sets.

Zeroth-Order Equations. Continuity equation:

$$\frac{\partial}{\partial x}(\rho_0u_0)+\frac{1}{r}\frac{\partial}{\partial r}(r\rho_0v_0)=0.$$

General momentum equation:

$$\frac{\partial}{\partial x}(\rho_0u_0\Phi_0)+\frac{1}{r}\frac{\partial}{\partial r}(r\rho_0v_0\Phi_0)=\frac{\partial}{\partial x}\left(\mu_e\frac{\partial\Phi_0}{\partial x}\right)+\frac{1}{r}\frac{\partial}{\partial r}\left(r\mu_e\frac{\partial\Phi_0}{\partial r}\right)+S(\Phi_0)$$

where the source terms for each variable are given as

$$S(u_0)=-\frac{\partial p_0}{\partial x}+\frac{1}{3}\frac{\partial}{\partial x}\left(\mu_e\frac{\partial u_0}{\partial x}\right)+\frac{1}{r}\frac{\partial}{\partial r}\left(r\mu_e\frac{\partial v_0}{\partial x}\right)-\frac{2}{3}\frac{\partial}{\partial x}\left\{\mu_e\left(\frac{\partial v_0}{\partial r}+\frac{v_0}{r}\right)\right\}-\frac{2}{3}\frac{\partial}{\partial x}(\rho_0k)$$

$$S(v_0)=-\frac{\partial p_0}{\partial r}+\frac{1}{3}\frac{1}{r}\frac{\partial}{\partial r}\left(r\mu_e\frac{\partial v_0}{\partial r}\right)-\frac{2}{3}\frac{v_0}{r}\frac{\partial\mu_e}{\partial r}-\frac{2}{3}\frac{\partial}{\partial r}\left(\mu_e\frac{\partial u_0}{\partial x}\right)-\frac{4}{3}\frac{\mu_e}{r^2}v_0+\frac{\partial}{\partial x}\left(\mu_e\frac{\partial u_0}{\partial r}\right)+\rho_0\frac{w_0^2}{r}-\frac{2}{3}\frac{\partial}{\partial r}(\rho_0k)$$

$$S(w_0)=-\frac{\rho_0v_0w_0}{r}-\frac{w_0}{r^2}\frac{\partial}{\partial r}(r\mu_e).$$

First-Order Equations. Continuity equation in complex function form:

$$\frac{\partial}{\partial x}(\rho_0\hat{u}_1)+\frac{1}{r}\frac{\partial}{\partial r}(r\rho_0\hat{v}_1)=-\frac{\partial}{\partial x}(\hat{\rho}_1u_0)-\frac{1}{r}\frac{\partial}{\partial r}(r\hat{\rho}_1v_0)+j\left\{\frac{1}{r}(\rho_0\hat{w}_1+\hat{\rho}_1w_0)-\hat{\rho}_1\Omega\right\}.$$

General momentum equation in complex function form:

$$\frac{\partial}{\partial x}(\rho_0u_0\hat{\Phi}_1)+\frac{1}{r}\frac{\partial}{\partial r}(r\rho_0v_0\hat{\Phi}_1)=\frac{\partial}{\partial x}\left(\mu_e\frac{\partial\hat{\Phi}_1}{\partial x}\right)+\frac{1}{r}\frac{\partial}{\partial r}\left(r\mu_e\frac{\partial\hat{\Phi}_1}{\partial r}\right)+S(\hat{\Phi}_1)$$

where the source terms for each variable are given as

$$S(\hat{u}_1)=-\frac{\partial\hat{p}_1}{\partial x}+\frac{1}{3}\frac{\partial}{\partial x}\left(\mu_e\frac{\partial\hat{u}_1}{\partial x}\right)+\frac{1}{r}\frac{\partial}{\partial r}\left(r\mu_e\frac{\partial\hat{v}_1}{\partial x}\right)-\mu_e\frac{\hat{u}_1}{r^2}-\frac{2}{3}\frac{\partial}{\partial x}\left\{\mu_e\left(\frac{\partial\hat{v}_1}{\partial r}+\frac{\hat{v}_1}{r}\right)+\hat{\rho}_1k\right\}-\rho_0\left\{\hat{v}_1\frac{\partial u_0}{\partial r}+\hat{u}_1\frac{\partial u_0}{\partial x}\right\}-\hat{\rho}_1\left\{v_0\frac{\partial u_0}{\partial r}+u_0\frac{\partial u_0}{\partial x}\right\}-\mathbf{j}\left\{\frac{\mu_e}{r}\frac{\partial\hat{w}_1}{\partial x}-\frac{2}{3}\frac{1}{r}\frac{\partial}{\partial x}(\mu_e\hat{w}_1)-\rho_0\frac{w_0\hat{u}_1}{r}+\rho_0\Omega\hat{u}_1\right\}$$

$$S(\hat{v}_1) = -\frac{\partial \hat{p}_1}{\partial r} + \frac{1}{3}\frac{\partial}{\partial r}\left(\mu_e \frac{\partial \hat{v}_1}{\partial r}\right) - \frac{2}{3}\frac{\partial}{\partial r}\left(\mu_e \frac{\partial \hat{u}_1}{\partial x}\right) + \frac{\partial}{\partial x}\left(\mu_e \frac{\partial \hat{u}_1}{\partial r}\right)$$
$$-\frac{2}{3}\frac{1}{r}\frac{\partial}{\partial r}(\mu_e \hat{v}_1) - \frac{7}{3}\frac{\mu_e \hat{v}_1}{r^2} + \frac{\mu_e}{r}\frac{\partial \hat{v}_1}{\partial r} - \frac{2}{3}\frac{\partial}{\partial r}(\hat{\rho}_1 k)$$
$$-\rho_0\left\{\hat{v}_1\frac{\partial v_0}{\partial r} - 2\frac{w_0 \hat{w}_1}{r} + \hat{u}_1\frac{\partial v_0}{\partial x}\right\} - \hat{\rho}_1\left\{v_0\frac{\partial v_0}{\partial r} - \frac{w_0^2}{r} + u_0\frac{\partial v_0}{\partial x}\right\} - \mathbf{j}\left\{\frac{\mu_e}{r}\frac{\partial \hat{w}_1}{\partial r} - \frac{2}{3}\frac{1}{r}\frac{\partial}{\partial r}(\mu_e \hat{w}_1) - \frac{7}{3}\frac{\mu_e \hat{w}_1}{r^2} - \rho_0\frac{w_0 \hat{v}_1}{r} + \rho_0 \Omega \hat{v}_1\right\}$$

$$S(\hat{w}_1) = -\frac{7}{3}\frac{\mu_e \hat{w}_1}{r^2} - \frac{\hat{w}_1}{r}\frac{\partial \mu_e}{\partial r} - \rho_0\left\{\hat{v}_1\frac{\partial w_0}{\partial r} + \frac{v_0 \hat{w}_1}{r} + \frac{w_0 \hat{v}_1}{r} + \hat{u}_1\frac{\partial w_0}{\partial x}\right\} - \hat{\rho}_1\left\{v_0\frac{\partial w_0}{\partial r} + \frac{v_0 w_0}{r} + u_0\frac{\partial w_0}{\partial x}\right\} - \mathbf{j}\left\{-\frac{\hat{p}_1}{r} + \frac{7}{3}\frac{\mu_e \hat{v}_1}{r^2} + \frac{\hat{v}_1}{r}\frac{\partial \mu_e}{\partial r} + \frac{1}{3}\frac{\mu_e}{r}\frac{\partial \hat{v}_1}{\partial r} - \frac{2}{3}\frac{\mu_e}{r}\frac{\partial \hat{u}_1}{\partial x} + \frac{1}{r}\frac{\partial}{\partial x}(\mu_e \hat{u}_1) - \frac{2}{3}\frac{\hat{\rho}_1 k}{r} - \frac{\rho_0 w_0 \hat{w}_1}{r} + \rho_0 \Omega \hat{w}_1\right\}.$$

The equation sets for the zeroth and first-order variables were solved using a finite volume computer code utilizing the SIMPLEC algorithm, [9], with the QUICK differencing scheme, [10], for convection terms.

Boundary Conditions. Previous quasi three-dimensional (i.e., two-dimensional computations) rotordynamic seal models solve incompressible flows, [11,12]. They utilize the perturbation coordinate transformation in deriving the first-order governing equations and boundary conditions to align the first-order displaced rotor surface (Figs. 2 and 3) with a grid line in the transformed plane. For CFD perturbation problems, this approach introduces complications, including a large increase in the number of first-order source terms in the equations. The present approach, as discussed by Kim and Rhode [4,5], uses the same computational grid for the first-order equations as that for the zeroth-order equations for the undisplaced rotor surface. The boundary condition for the first-order equations can be obtained by the Taylor series expansion of each variable, including the zeroth and first-order terms, at the grid points on the undisturbed rotor surface in Fig. 3, toward the corresponding disturbed rotor surface, i.e., open circles in Fig. 3, [13]. On the other hand, the boundary values for all the first-order variables on the stator surface should be specified as zero. The first-order boundary values on the rotor were taken from standard dynamics relations that account for rotor displacement, whirl and shaft speed. Details can be found in a work by Kim and Rhode [5].

The flow disturbance values at both exits, i.e., at the high pressure reservoir and low pressure reservoir, should be properly modeled. Based on recent numerical experiments with similar labyrinths, the axial variation of the first-order velocities were approximated as zero gradient. In addition, the Dirichlet boundary conditions for the mean values of the first-order pressures were specified using the bulk energy equation between the seal exit and downstream chamber.

Injection slot inlet (Fig. 1 (*a*)):

$$\hat{\Phi}_1(x_{\text{in}}, r) = 0; \quad \{\hat{\Phi}_1 = \hat{u}_1, \hat{v}_1, \hat{w}_1\}$$

$$\left|\frac{\partial \hat{p}_1'(x,r)}{\partial r}\right|_{x_{\text{in}}} = 0$$

where $\hat{p}_1'$ represents the first-order pressure-correction quantity, [9].

Seal Exits (Fig. 1 (*a*)):

$$\left|\frac{\partial \hat{\Phi}_1(x_{\text{ex}}, r)}{\partial x}\right|_{x_{\text{ex}}} = 0; \quad \{\hat{\Phi}_1 = \hat{u}_1, \hat{v}_1, \hat{w}_1\}$$

$$\hat{P}_1(x_{\text{ex}}) = -p_d(1-\xi_{\text{ex}})\left\{\frac{U_0(x_{\text{ex}})\hat{U}_1(x_{\text{ex}}) + W_0(x_{\text{ex}})\hat{W}_1(x_{\text{ex}})}{ZRT_{\text{ex}}}\right\}$$

where the subscript ex signifies the condition at seal exit while *d* signifies the downstream chamber condition. Note that one would obtain the same result for the above Dirichlet pressure boundary conditions at the seal exit if one assumes the process from the seal exit to the downstream chamber to be isentropic or isothermal. Based on the findings from a previous series of concentric-rotor CFD computations, the minor loss coefficient ξ_{ex} can be assumed in a range between 0.9 to 1.1 for most applications. A value of 1.0 was used here for ξ_{ex}. The approximate and empirical nature of this exit boundary condition may reduce the accuracy of the numerical results. However, it is apparent that any small change in the exit conditions of a seal has little effect on the resultant rotordynamic forces, [14].

Rotordynamic Force Coefficients. The relations between the radial and tangential forces and the rotordynamic force coefficients can be obtained from Eq. (1) as

$$\frac{F_r}{e} = -K - c\Omega + M\Omega^2$$

$$\frac{F_\theta}{e} = k - C\Omega - m\Omega^2.$$

By integrating the pressure on the rotor surface up to the first-order terms, one obtains the force components at a particular whirling speed as

$$-\frac{F_r}{e} = \pi \int_L \left|\frac{\partial p_0(x,r)}{\partial r}\right|_{R*} R^* dx + \frac{\pi}{C}\int_L p_{1c}(x, R^*) R^* dx$$

$$-\frac{F_\theta}{e} = \frac{\pi}{C}\int_L p_{1s}(x, R^*) R^* dx.$$

By using the above relations and subsequent least-square approximation in terms of the whirling speed, one can obtain the force coefficients for the different flow conditions.

Results and Comparison With Experiment

Cases Considered. The geometry of the shunt-injected labyrinth seal used for validation of the present rotordynamic model has 19 teeth as shown in Fig. 1(*a*). An exaggerated grid arrangement in the cavity section with the injection slot is shown in Fig. 1(*b*). The pressure at the shunt injection is higher than that at the high pressure end of the seal. Thus the injected flow splits so that some of it exits from the high pressure end and the remainder from the low pressure end. This is apparently the most challenging test case employed thus far for labyrinth rotordynamic models because of the presence of (a) the fairly large number (19) of tooth throttlings, (b) complicated turbulent mixing from the injection against rotation (30 deg from tangent) giving a complicated swirl velocity field, (c) a more complicated overall seal mass balance (two exits), (d) the high level (compared to previous model test cases) of the injection pressure P_{Inj} and the high pressure P_H, and (e) the significant compressibility effects due to tooth-clearance Mach numbers of 0.8, for example.

The primary parameters that determine the flow conditions are the pressure ratio ($PR = P_L/P_H$), shunt injection pressure ratio ($IPr = P_H/P_{\text{Inj}}$), and the rotor shaft speed. In this investigation P_{Inj} was fixed at 13.8 bars (200 psi). In addition the axial location

Table 1 Grid independence results [rpm=4680, $IPr=0.85$, $PR=0.65$]

NI×NJ	Mass [Kg/s]	Deviation [%]	k [kN/m]	Deviation [%]
795×45	0.16501	0.56	1631.0	2.05
668×45*	0.16593	2.52	1664.5	8.86
507×41	0.17012		1517.1	
NI×NJ	C [kN-s/m]	Deviation [%]	K [kN/m]	Deviation [%]
795×45	0.3999	3.23	823.83	1.45
668×45*	0.4129	4.61	835.80	3.38
507×41	0.3938		864.08	

* Production Grid

of the injection (A, B, or C in Fig. 1(a)) is of particular interest. Because the test specimen has a large number of closely spaced (circumferentially) injection holes, the approximation that the injection enters through a circumferential "slot" of the same injection flow area as that of the actual holes is quite reasonable. Specifically, the test specimen injection jets pass through the circumferentially closely spaced holes at an angle of 30 degrees from the tangent in the direction opposite that of rotation. This swirl angle and the close circumferential spacing mixes the jets together immediately upon entering the injection cavity as if they entered as a sheet through a circumferentially uniform "slot."

Table 1 shows the results of grid independence tests where the pressure ratio $PR=0.45$, the injection pressure ratio $IPr=0.85$ and the shaft speed is 4680 rpm. The percentage discrepancy of the solution values between consecutive grids shown in the table justify the present choice of 668×45 grid. The mass flow and force coefficients from the production grid deviate from the finest grid tested by less than 3.23%.

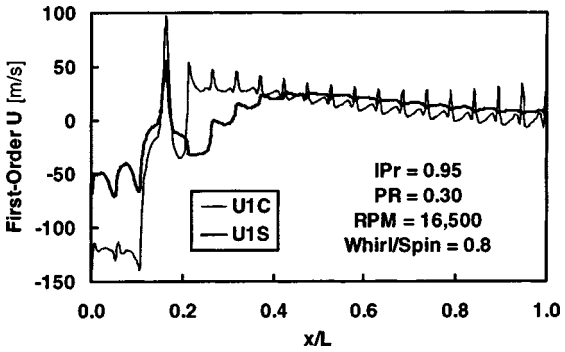

Fig. 6 Axial distribution of the first-order axial velocity components

Flow Perturbation Distributions. Figures 4 through 6 show the axial distribution of the first-order variables at the radial location midway between the rotor and the tooth tips for the conditions shown. The thin and thick data curves represent the values of the cosine and sine components, respectively, as shown. It is interesting that the cosine components for all variables experience a local sharp peak at the abrupt flow contraction at each tooth, whereas the sine components generally change in a somewhat less peaked manner. The appearance of these peaks in the first-order cosine variables is in good agreement with previous results at the abrupt flow contraction at the seal inlet of an incompressible bushing (i.e., smooth-plain) seal, [4]. Furthermore, the peaks in the pressure distribution in Fig. 4 are also in agreement with the results of Ishii et al. [7] who used a fully three-dimensional CFD model. By comparing the order of magnitude of the first-order velocities, one finds that the swirl velocity disturbances are the largest and the radial velocity disturbances (not shown for brevity)

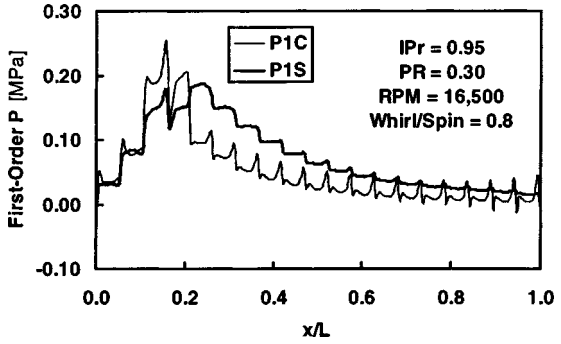

Fig. 4 Axial distribution of the first-order pressure components

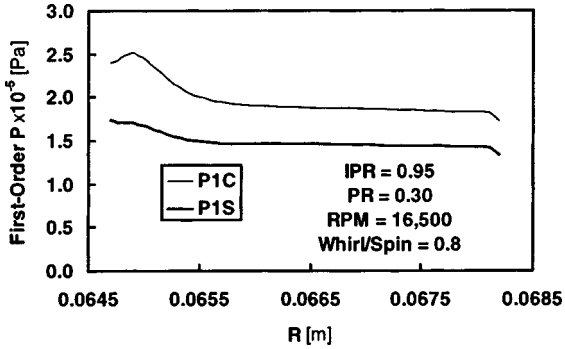

Fig. 7 Radial distribution of the first-order pressure components at injection location A ($x/L=0.16$)

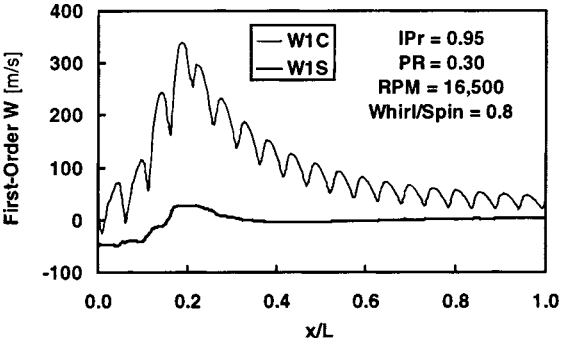

Fig. 5 Axial distribution of the first-order circumferential velocity components

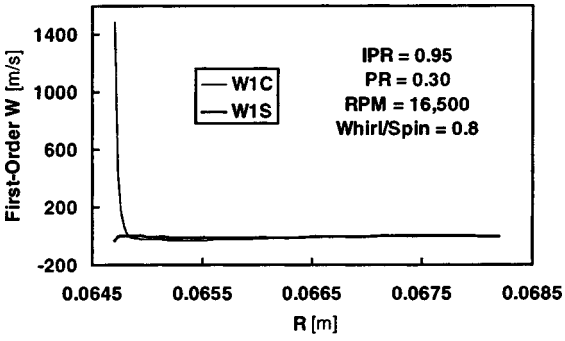

Fig. 8 Radial distribution of the first-order circumferential velocity components at injection location A ($x/L=0.16$)

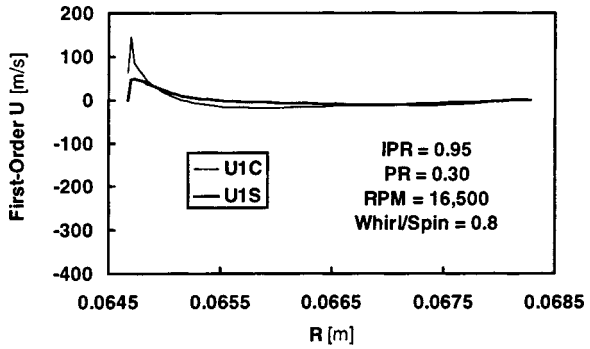

Fig. 9 Radial distribution of the first-order axial velocity components at injection location A ($x/L=0.16$)

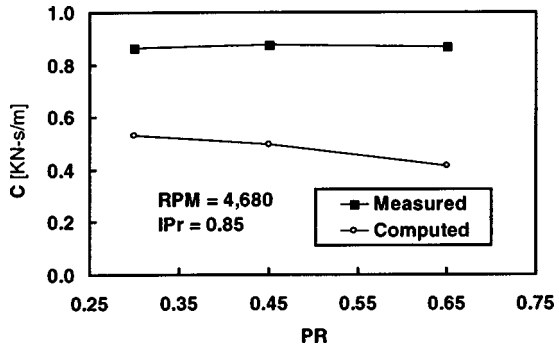

Fig. 12 Variation of direct damping with pressure ratio for injection location A ($x/L=0.16$)

the smallest. It is shown that for all velocity variables the cosine component has a more prominent peak at each tooth passage. This results from the fact that the cosine component represents the flow disturbance at the circumferential location where the maximum rotor displacement occurs as explained in the model formulation. Therefore the cosine component is more sensitive to the presence of each tooth clearance, for example, and consequently shows sharper peaks than does the sine component as shown in the figures.

The radial variations of the first-order variables at the axial position of the injection slot are shown in Figs. 7 through 9 for the same operating conditions as that of Figs. 4 through 6. The radial distribution of all flow disturbance variables has approximately two distinctive regions, i.e., inside the cavity and near the rotor. It is clearly seen that the variation inside the cavity is negligible whereas that of the velocities near the rotor is abrupt. Notice that this observation provides specific justification for the use of multivolumes in bulk-flow labyrinth models. In such models the flow variables for the control volume inside the cavity and that near the rotor are assumed to have different bulk values. The abrupt changes of the variables near the rotor decrease as the flow progresses toward the low pressure exit (P_L) of the seal.

Comparison With Experiments. The computed force coefficients are compared with measurements, [3], for the cross-coupled stiffness (k), the direct damping (C), and the effective damping (C_{eff}) in Figs. 10 through 14. The operating conditions for the test cases are that the shaft speeds are 4680 rpm and 16,500 rpm, the injection pressure ratio ($IPr=P_H/P_{\text{Inj}}$) is 0.85 and the seal pressure ratio (P_L/P_H) ranges from 0.3 to 0.65. It was found that the mass flow rates were about 8.6% under predicted on average, considering the entire set of test cases involved. The zeroth-order solutions contribute an unavoidable source of uncertainty to the first-order solution because a large part of the first-order equations consists of zeroth-order variables and their derivatives.

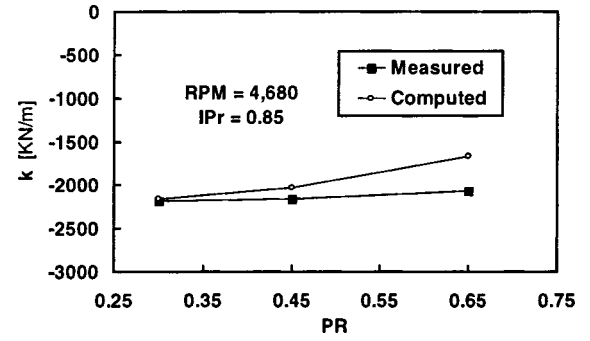

Fig. 10 Variation of cross-coupled stiffness with pressure ratio for injection location A ($x/L=0.16$)

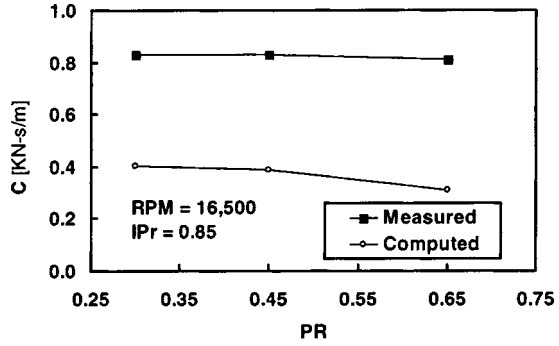

Fig. 13 Variation of direct damping with pressure ratio for injection location A ($x/L=0.16$)

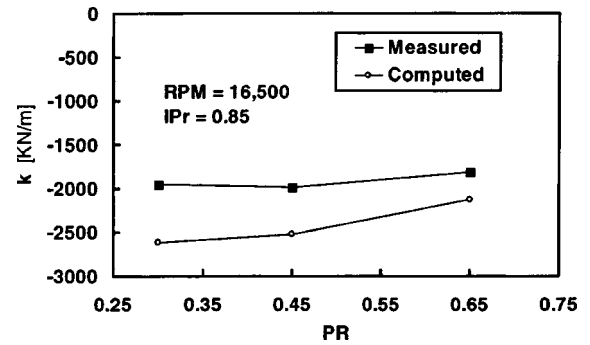

Fig. 11 Variation of cross-coupled stiffness with pressure ratio for injection location A ($x/L=0.16$)

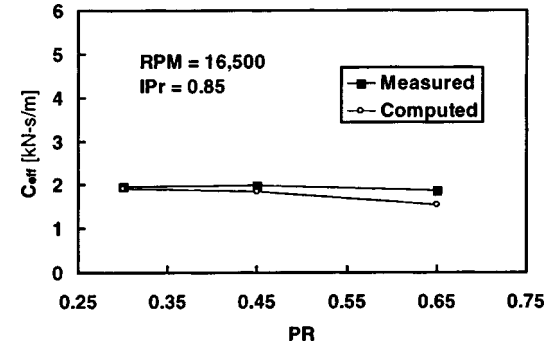

Fig. 14 Variation of effective damping with pressure ratio for injection location A ($x/L=0.16$)

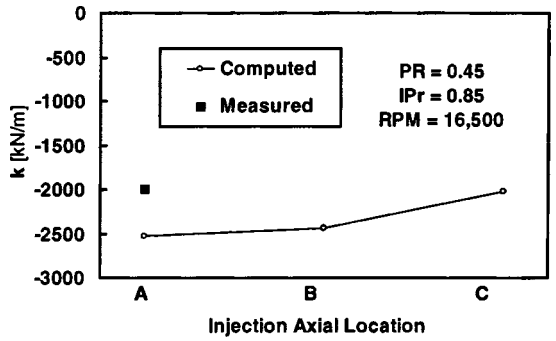

Fig. 15 Variation of cross-coupled stiffness with shunt injection location

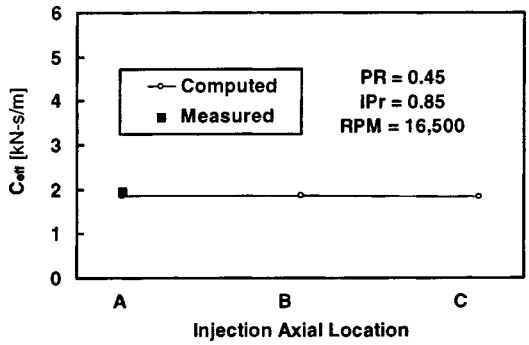

Fig. 17 Variation of effective damping with shunt injection location

Comparison with measurements for the cross-coupled stiffness are given in Figs. 10 and 11. From the figures one finds that the cross-coupled stiffness is slightly overpredicted at a low shaft speed and is underpredicted at a high shaft speed. However, the present model simulates the stabilizing effect of the shunt injection reasonably well, i.e., it gives a negative cross-coupled stiffness value for most operating conditions as was experimentally found. In addition the model generally gives the correct trends, unlike the larger discrepancies for labyrinths often found with previous models. The computed results are usually within 30% of the measurements and thus are quite satisfactory, especially considering the challenging flow complexities. Specifically this includes the approximations that the nineteen circumferentially spaced injectors have been simulated with a circumferential slot of the same flow area, the complicated injection turbulent mixing and swirl velocity, substantial compressibility effect, and high shaft speeds with a large number of teeth. Further, it has been found that the present model underpredicts the direct damping generally less than 60% as shown in Figs. 12 and 13. Also note that the slope of the predicted curves is quite reasonable. The computed effective damping coefficient $C_{\text{eff}}=C(1-k/C\Omega)$ has been used to compare seals in practical applications, and Fig. 14 shows it to be in excellent agreement with measurements (within 4.0%). As done with the measured values, the computed effective damping was evaluated with the whirl speed equal to the spin speed.

Effect of Injection Axial Location. Note in Figs. 4 through 6 that the maximum for both components of a flow disturbance quantity occurs at the injection axial location. This observation indicates the potential significance of locating the injection at an appropriate axial position in order to maximize the stabilizing effect of the injection which is related to reducing the zeroth-order overall swirl velocity. The predicted effect of the axial location of injection on the force coefficients is shown in Figs. 15 through 17.

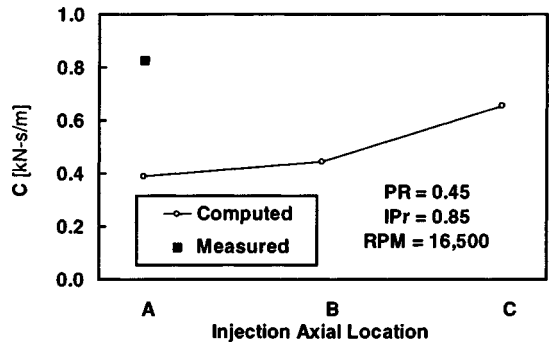

Fig. 16 Variation of direct damping with shunt injection location

The alphabetic notation A, B, and C used for the axial location is found in Fig. 1(*a*). For these three locations as shown in the figures the cross-coupled stiffness and direct damping become more stabilizing and less stabilizing, respectively, as the injection location is moved toward the high pressure end (Fig. 1(*a*)) of the seal. Further, it is shown that the change in magnitude of the cross-coupled stiffness is smaller (28%) than that of the direct damping (40%). These counterbalancing effects on stability have only a slight effect on C_{eff} as shown in Fig. 17.

Summary

A recent quasi three-dimensional CFD perturbation model (i.e., two-dimensional computations) was extended to allow shunt injection of a high pressure gas at any axial location. The model avoids the complicated perturbation coordinate transformation used by previous quasi three-dimensional models. Thus it allows rotordynamic force computations of any radial-clearance seal of axisymmetric geometry. The model was validated against measurements at challenging conditions where bulk models often give about 200% error due to the presence of (a) injection flow exiting from both ends of the seal, (b) injection against rotation giving complicated turbulent mixing of swirl momentum, (c) high shaft speed, (d) significant compressibility effects due to fairly high injection supply pressure, and (e) the fairly large number (19) of labyrinth teeth. Specific findings for the cases considered include

1 comparisons with the present measurements over a fairly large number of operating conditions show that k, C, and C_{eff} agree with measurements for the present complicated cases generally within about 40%, 60%, and 10%, respectively.

2 Very large values were found in the injection labyrinth cavity for all pressure and velocity flow perturbations except for the sine component of the circumferential velocity. However, for the cases considered, the axial location of the injection appears to have only a slight effect on rotordynamic stability (i.e., in terms of C_{eff}). Specifically, moving the injection toward the high pressure end of the seal gives k and C values that are more stabilizing and less stabilizing, respectively.

3 The radial distributions of the flow perturbation quantities show negligible variation within the cavity and abrupt variations within the tooth clearance. This finding supports the use of a two-control volume approach for those developing bulk-flow models for labyrinth seal rotordynamics.

Acknowledgments

The authors appreciate the financial assistance for a portion of this project by the Texas Advanced Technology Program and also the Texas A&M University Supercomputer Center.

Nomenclature

C = seal clearance
C, c = direct and cross-coupled damping coefficients
C_{eff} = effective damping coefficient ($C(1-k/C\Omega)$)
c_μ, c_1, c_2 = empirical constants (k-ε model)
D, d = rotor diameter
e = radius of rotor whirling motion
F = fluid reaction force
j = imaginary number
K, k = direct and cross-coupled stiffness coefficients
k = turbulent kinetic energy
L = seal length
M, m = direct and cross-coupled inertia coefficients
p = pressure
P_{Inj} = pressure at shunt injection
P_L = pressure at low pressure end of seal
P_H = pressure at high pressure end of seal
PR = ratio of P_L/P_H
IPr = ratio of P_H/P_{Inj}
p = near-wall first grid point
R^* = radial location of undisplaced rotor surface
Re = real part of a complex function
t = time
$\hat{U}_0, \hat{W}_0$ = area mean zeroth-order velocities
$\hat{U}_1, \hat{W}_1$ = area mean first-order velocities
x, y, z = cartesian coordinates
x, r, θ = cylindrical coordinates

Greek Symbols

ε = turbulent kinetic energy dissipation rate
ε = relative eccentricity of rotor (e/C); perturbation parameter
Φ = generic dependent variables
$\hat{\Phi}_1$ = complex function of dependent variable
θ = coordinate in circumferential direction
ρ = density of fluid
τ = shear stress
ξ = pressure minor loss coefficient at the seal exit
ω = rotor spin speed (Fig. 2)
Ω = rotor whirling speed (Fig. 2)

Superscripts

$'$ = time derivative (d/dt); (Eq. (1))
$'$ = pressure correction term
$\hat{}$ = complex function (over hat)

Subscripts

ex, in = seal exit and inlet
i, j = tensor index
p = first grid point near the wall
r, θ, x = cylindrical coordinates
0, 1 = zeroth and first-order quantities, respectively
1c = cosine component of first-order variable
1s = sine component of first-order variable

Abbreviations

CFD = computational fluid dynamics
PDBC = perturbation with disturbed boundary condition

References

[1] Childs, D. W., 1993, *Turbomachinery Rotordynamics: Phenomena, Modeling and Analysis*, John Wiley and Sons, New York.
[2] Gelin, A., Pugnet, J. M., Bolusset, D., and Friez, P., 1996, "Experience in Full-Load Testing Natural Gas Centrifugal Compressors for Rotordynamic Improvements," ASME Paper No. 96-GT-378.
[3] Soto, E. A., and Childs, D. W., 1998, "Experimental Rotordynamic Coefficient Results for (a) a Labyrinth Seal With and Without Shunt Injection and (b) a Honeycomb Seal," ASME Paper No. 98-GT-008.
[4] Kim, N., and Rhode, D. L., 2000, "CFD-Perturbation Seal Rotordynamic Model for Tilted Whirl About Any Pivot Axial Location," *Proceedings of the 8th International Symposium on Transport Phenomena and Dynamics of Rotating Machinery*, Honolulu, (ISROMAC-8), **II**, pp. 1116–1123.
[5] Kim, N., and Rhode, D. L., 2000, "A New CFD-Perturbation Model for the Rotordynamics of Incompressible Flow Seals," ASME Paper No. 2000-GT-402.
[6] Launder, B. E., and Spalding, D. B., 1974, "The Numerical Computation of Turbulent Flows," Comput. Methods Appl. Mech. Eng., **3**, pp. 269–289.
[7] Ishii, E., Kato, C., Kikuchi, K., and Miura, H., 2000, "Fully Three-Dimensional Computation of Rotordynamic Coefficients in a Labyrinth Seals," ASME J. Turbomach., in press.
[8] Athavale, M. M., and Hendricks, R. C., 1996, "A Small Perturbation CFD Method for Calculation of Seal Rotordynamic Coefficients," Int. J. Rotating Mach., **2**, pp. 167–177.
[9] Van Doormaal, J. P., and Raithby, D. G., 1984, "Enhancements of the SIMPLE Method for Predicting Incompressible Fluid Flows," Numer. Heat Transfer, **2**, pp. 147–163.
[10] Leonard, B. P., 1979, "A Stable and Accurate Convective Modeling Procedure Based on Quadratic Upstream Interpolation," Comput. Methods Appl. Mech. Eng., **19**, pp. 59–98.
[11] Dietzen, F. J., and Nordmann, R., 1987, "Calculating Rotordynamic Coefficients of Seals by Finite-Difference Techniques," ASME J. Tribol., **109**, pp. 388–394.
[12] Arghir, M., and Frene, J., 1997, "Rotordynamic Coefficients of Circumferentially-Grooved Liquid Seals Using the Averaged Navier-Stokes Equations," ASME J. Tribol., **119**, pp. 556–567.
[13] Yao, L. S., 1980, "Analysis of Heat Transfer in Slightly Eccentric Annuli," ASME J. Heat Transfer, **102**, pp. 279–284.
[14] Millsaps, K. T., and Martinez-Sanchez, M., 1993, "Dynamic Forces From Single Gland Labyrinth Seals: Part II-Upstream Coupling," ASME Paper No. 93-GT-322.

Chebyshev Polynomials Fits for Efficient Analysis of Finite Length Squeeze Film Damped Rotors

F. A. Rodrigues
e-mail: fabiano@mecasola.ec-lyon.fr

F. Thouverez

C. Gibert

L. Jezequel

Ecole Centrale de Lyon—Laboratoire de Tribologie
et Dynamique des Systemes,
36, Avenue Guy de Collongue
B. P. 163,
69131 Ecully Cedex, France

The nonlinear behavior of the hydrodynamic forces generated by squeeze film dampers makes dynamical analyses of rotor-bearing systems incorporating such devices a complex and often long task. When steady-state orbits are to be sought, approximate methods (e.g., harmonic balance method, trigonometric collocation method) can be used in order to save computation cost. However, numerical integration in the time domain cannot be avoided if one wishes to calculate transient responses, or to carry out more meticulous analyses concerning the effects of the damper nonlinear nature on the motion of the system. For finite length squeeze film dampers, neither the short nor the long bearing approximations can be suitably applied, and the fluid pressure field has to be estimated numerically, thus rendering rotordynamics predictions even longer and, for engineering purposes computationally prohibitive. To surmount this problem, the present paper proposes a straightforward procedure to derive polynomial expressions for the squeeze film damper (SFD) forces, for given damper geometry and boundary conditions. This is achieved by applying Chebyshev orthogonal polynomial fits over force data generated by numerically solving the two-dimensional pressure field governing equation. For both transient and steady-state calculations, the use of the SFD forces polynomial expressions is seen to be very efficient and precise. [DOI: 10.1115/1.1423319]

1 Introduction

One of the major concerns in the design of modern rotating machinery is the improvement of its power-to-weight ratios. As an outcome of this tendency, operating speeds have been increased and shafts have become slender. These features have aggravated the problems of vibration and dynamic loads transmission to the support structure. The squeeze film damper (SFD) turned out to be one of the most attractive technical solutions to remedy these problems, thanks to its relative constructional simplicity and important damping capability. Despite its beneficial influence in rotordynamics performance, the highly nonlinear squeeze film damper behavior often brings about some difficulties in the prediction of rotor response at the design stage.

When transient responses are to be calculated, numerical integration methods in the time domain have to be used, even though computation can be very expensive. This shortcoming becomes even more acute when the order of the mechanical system model becomes larger. Ditto for time-step reductions, which are sometimes necessary to achieve the desired accuracy. In order to avoid the computational cost of numerical integration, recent works (e.g. [1–6]) have focused on the application of approximate methods to find squeeze film damped rotors steady-state orbits. Some of them ([4–6]) also carried out a complementary stability analysis based on the Floquet theory.

With the aim of allowing a fast evaluation of the fluid forces, simplified one-dimensional damper models, namely, short and long bearing approximations for constant fluid properties, were used in all the works cited above. These approximations are obtained by assuming one of the pressure gradients, circumferential or axial, to be negligible in comparison to the other, a condition that depends on the length-to-diameter ratio, λ, and on the damper extremity boundary conditions. The short bearing approximation is suitable for small λ and weak flow restrictions at the damper ends, whereas the long bearing approximation applies, in practical situations, for tight sealed dampers ([7]). However, usual SFD configurations have partially sealed extremities in order to improve the damping capability ([8]), without causing overheating problems. In this case, the damper cannot be considered either short or long, making unavoidable the two-dimensional modeling of the fluid pressure field.

Some researchers have attempted to derive simple formulations for finite SFDs to shun the need for numerically solving the two-dimensional problem. Rezvani and Hahn [9] advocate the use of the approximations suggested by O'Donohue et al. [10] and by Rohde and Li [11], which are based on the assumption that the axial pressure profile is parabolic. As they pointed out, the accuracy of these approximations is limited to finite dampers having L/D ratios lower than 1 ([9]). Barret et al. [12] proposed the introduction of a correction factor to the short bearing theory, obtained assuming isoviscous flow and open ends boundary conditions. Fuerst et al. [13] managed to obtain a closed-form solution for the two-dimensional Reynolds equation by employing a superposition technique and Bessel-Fourier series, also considering the fluid to have constant viscosity and the damper to have open ends. The assumption of constant fluid properties in these two latter works restrains their applicability when the variation of oil viscosity along the damper length is important, since it may lead to significant errors in the SFD force estimation ([14]).

In addition to the simplifications based on damper geometry and fluid properties, cavitation is also very often treated in a fairly simplified way in SFD models by employing the Gumbel boundary conditions. This approach may yield satisfactory results for highly loaded SFD executing circular centered orbits. Under different circumstances, the use of the more realistic Reynolds boundary conditions, which satisfy flow continuity at the cavitation inception, is necessary. The determination of the pressure field becomes then a free boundary problem, so that iterative techniques are required to handle it ([15]), thus making the calculation of the hydrodynamic forces even longer.

Since the determination of the damper pressure field from two-dimensional or iterative equations commonly requires a great deal of time, its coupling with the resolution of the system equations of motion is unattractive, even computationally prohibitive. In the

Contributed by the Structures and Dynamics Division of THE AMERICAN SOCIETY OF MECHANICAL ENGINEERS for publication in the ASME JOURNAL OF ENGINEERING FOR GAS TURBINES AND POWER. Manuscript received by the S&D Division, Mar. 2000; final revision, May 2001. Editor: H. D. Nelson.

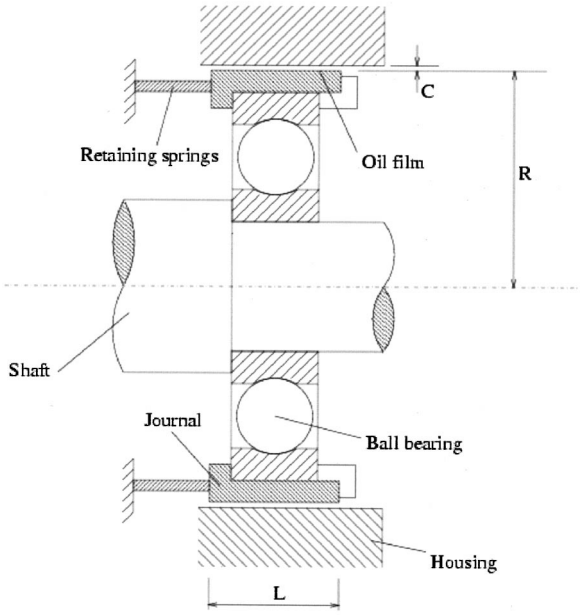

Fig. 1 Schematic view of a squeeze film damper (SFD)

present paper, this problem is overcome by the use of Chebyshev orthogonal polynomials. For given damper geometry and boundary conditions, the differential equation governing the pressure distribution in the film is solved numerically for specified journal motion states. The force data generated are then fitted with the aid of the Chebyshev polynomials, a procedure that results in the derivation of SFD forces polynomial expressions. These expressions can then be used in dynamics analyses of different systems, on condition that the SDF geometry and boundary conditions remain the same.

The fluid pressure field is assumed to be governed by the Reynolds equation, which implies that inertia effects are completely neglected. In this case, the Chebyshev polynomial fits furnish expressions for the radial and tangential damping forces as functions of the journal eccentricity and velocities. Nonetheless, the idea of applying Chebyshev fits is not restricted to inertialess models. Assuming that damping and inertia effects can be decoupled ([16,17]), Chebyshev fits may be also used to obtain radial and tangential inertia force expressions as functions of the journal eccentricity and accelerations. Since the Reynolds equation is still widely used for squeeze film damped rotors analyses, e.g. [18–20], despite the alternative formulations developed to take fluid inertia effects into account, e.g., [16,17,21,22], it will be used to illustrate the application of the proposed approach.

To demonstrate the usefulness of the Chebyshev fits, simulations including transient as well as steady-state and stability calculations for a Jeffcott rotor incorporating SFD are carried out. In a first numerical example, the results obtained by using the classical short and long bearing approximations, the finite differences scheme and the Chebyshev polynomial fit are compared in regards to time and accuracy. Afterwards, the method is applied to a more complex example, where the Reynolds cavitation conditions are employed, an end seal leakage coefficient is introduced and an axially varying viscosity is accounted for, a problem whose analytical solution is not known to the authors.

2 Pressure Field Governing Equation

Figure 1 shows the schematic view of a SFD. The cylindrical journal is prevented from rotating by the use of retaining springs such as spring bars or a squirrel cage. The support stiffness is usually designed so that static loads are compensated and the damper journal is initially held centrally within the clearance space, though some designs may supply preloading. In any case, the retaining springs shall be flexible enough to allow the journal free translation within the clearance, which provides the squeezing action that produces hydrodynamic forces in the fluid.

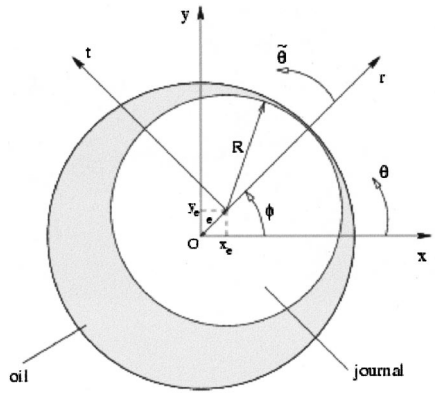

Fig. 2 Cross section and coordinate frames of the squeeze film damper (SFD)

According to the SFD cross section depicted in Fig. 2, the Reynolds equation for incompressible flow of a Newtonian fluid can be written in the local coordinate frame (**r**, **t**) as ([23]):

$$\frac{1}{R^2}\frac{\partial}{\partial\tilde{\theta}}\left(\frac{h^3}{12\mu}\frac{\partial P}{\partial\tilde{\theta}}\right)+\frac{\partial}{\partial z}\left(\frac{h^3}{12\mu}\frac{\partial P}{\partial z}\right)=-\dot{\phi}\frac{dh}{dt}-\dot{e}\cos\tilde{\theta} \quad (1)$$

where the fluid thickness h for an aligned journal is given by

$$h=C(1-\varepsilon\cos\tilde{\theta}).$$

Without further assumptions, the Reynolds Eq. (1) provides no analytical expressions for the pressure distribution in the fluid. Consequently, a numerical method, for instance a finite difference scheme, is required to solve Eq. (1). The SFD hydrodynamic forces are then obtained by integrating the pressure field over the journal surface:

$$f_{sr}=\int P(\tilde{\theta},z)\cos\tilde{\theta}Rd\tilde{\theta}dz\approx\sum_{i}^{Ni}\sum_{j}^{Nj}P_{i,j}\cos\tilde{\theta}_jR\Delta\tilde{\theta}\Delta z$$
$$f_{st}=\int P(\tilde{\theta},z)\sin\tilde{\theta}Rd\tilde{\theta}dz\approx\sum_{i}^{Ni}\sum_{j}^{Nj}P_{i,j}\sin\tilde{\theta}_jR\Delta\tilde{\theta}\Delta z. \quad (2)$$

Though accurate, the numerical solution of the Reynolds equation is excessively long. This feature is all the more undesirable since industrial rotating machine finite element models are often of considerable size, so that rotordynamic predictions require extensive computation time.

When the Reynolds equation is used as the pressure distribution governing equation, the SFD forces for a given damper configuration are functions of only three variables, e, $\dot{e}$, and $\dot{\phi}$, provided that the boundary conditions are axisymmetric. It is noteworthy that several modified or extended forms of the Reynolds equation verifying this observation have been developed to introduce eventually important effects such as journal misalignment ([24]), use of a porous damper ([25]), lubrication with bubbly oil ([26]), or with a non-Newtonian fluid ([27]), among others, that are not accounted for in the classical Reynolds Eq. (1). Although the Chebyshev fits are applied in the present paper only to the latter equation, the extension of the method to the works cited above is immediate.

3 Chebyshev Orthogonal Polynomials Fit

The main idea of this work is based on the remark made above. As functions of three variables, the radial and tangential SFD viscous forces can be approximated as triple series involving variables e or ε, $\dot{e}$, and $\dot{\phi}$:

$$f^v_{sr}(\varepsilon,\dot{\phi},\dot{e}) \cong \sum_{k=0}^{p^r_u} \sum_{l=0}^{P^r_v} \sum_{z=0}^{P^r_z} C^r_{k,l,z} T_k(\varepsilon) T_l(\dot{\phi}) T_z(\dot{e}) = \tilde{f}^v_{sr}(\varepsilon,\dot{\phi},\dot{e})$$
$$f^v_{st}(\varepsilon,\dot{\phi},\dot{e}) \cong \sum_{k=0}^{P^t_u} \sum_{l=0}^{P^t_v} \sum_{z=0}^{P^t_z} C^t_{k,l,z} T_k(\varepsilon) T_l(\dot{\phi}) T_z(\dot{e}) = \tilde{f}^v_{st}(\varepsilon,\dot{\phi},\dot{e}) \quad (3)$$

where $C^r_{k,l,z}$ and $C^t_{k,l,z}$ are constants, T_k, T_l, T_z constitute the polynomial basis over which the forces are projected, and P^r_u, P^r_v, P^r_z and P^t_u, P^t_v, P^t_z are the polynomials' truncation orders.

The coefficients $C_{k,l,z}$ can be determined by invoking the orthogonality properties of the chosen polynomials. The use of the Chebyshev polynomials makes the integrals required to evaluate these coefficients quite straightforward ([28]). These polynomials are given by

$$T_n(\zeta) = \cos(n \arccos(\zeta)) \quad -1 < \zeta \quad 1 \quad n = 0,1,2,\ldots \quad (4)$$

and satisfy the following weighted orthogonality property:

$$\int_{-1}^{1} w(\zeta) T_n(\zeta) T_m(\zeta) d\zeta = \begin{cases} 0 & n \neq m \\ \pi/2 & n = m \neq 0 \\ \pi & n = m = 0 \end{cases} \quad (5)$$

where $w(\zeta) = (1-\zeta^2)^{-1/2}$ is the weighting function.

Note that this orthogonality property applies only when ς is within the interval $[-1, 1]$. Therefore, the variables ε, $\dot{e}$, and $\dot{\phi}$ have to be normalized, using the change of coordinates,

$$\eta = \frac{2\varepsilon - \varepsilon_{\max} - \varepsilon_{\min}}{\varepsilon_{\max} - \varepsilon_{\min}}; \quad \kappa = \frac{2\dot{\phi} - \dot{\phi}_{\max} - \dot{\phi}_{\min}}{\dot{\phi}_{\max} - \dot{\phi}_{\min}};$$
$$\xi = \frac{2\dot{e} - \dot{e}_{\max} - \dot{e}_{\min}}{\dot{e}_{\max} - \dot{e}_{\min}}. \quad (6)$$

The SFD forces fit is performed over data generated from the numerical solution of the pressure field governing equation, for given damper geometry and boundary conditions. Thus, the normalization limits $\varepsilon_{\min}$, $\varepsilon_{\max}$, $\dot{\phi}_{\min}$, $\dot{\phi}_{\max}$, $\dot{e}_{\min}$, and $\dot{e}_{\max}$ are defined beforehand. Obviously, these limits depend on the mechanical system in which the SFD is incorporated. Hence, in order to avoid incorrect evaluations of the hydrodynamic forces, the normalization limits should be set so that a wide range of instantaneous motions is covered. Besides, in lieu of using the Chebyshev polynomials as defined by Eq. (4) when estimating the SFD forces, one would better use the form

$$T_n(\zeta) = \zeta^n - \binom{n}{2} \zeta^{n-2}(1-\zeta^2) + \binom{n}{4} \zeta^{n-4}(1-\zeta^2)^2 - \ldots. \quad (7)$$

Some particular Chebyshev polynomials derived from this formula are presented in the Appendix. It was observed during numerical tests that the use of Eq. (7) permits a certain level of extrapolation without distorting the values of the SFD radial and tangential forces. The presence of the arc-cosine in Eq. (4) prevents the normalized variables from exceeding the limit values of 1 and -1, thus preventing the possibility of extrapolation if this equation is employed.

The coefficients $C_{k,l,z}$ are obtained as follows. Consider the integral

$$A_{i,j,s} = \int_{-1}^{1}\int_{-1}^{1}\int_{-1}^{1} \tilde{f}(\eta,\kappa,\xi) T_i(\eta) T_j(\kappa) T_s(\xi) \times w(\eta) w(\kappa) w(\xi) d\eta d\kappa d\xi. \quad (8)$$

The substitution of the term $\tilde{f}(\eta,\kappa,\xi)$ by Eq. (3) yields

$$\begin{aligned} A_{i,j,s} = & \int_{-1}^{1}\int_{-1}^{1}\int_{-1}^{1} C_{0,0,0} T_0(\eta) T_i(\eta) T_0(\kappa) \\ & \times T_j(\kappa) T_0(\xi) T_s(\xi) w(\eta) w(\kappa) w(\xi) d\eta d\kappa d\xi \\ & + \int_{-1}^{1}\int_{-1}^{1}\int_{-1}^{1} \sum_{k=1}^{P_u} \sum_{l=1}^{P_v} \sum_{z=1}^{P_z} C_{k,l,z} T_k(\eta) \\ & \times T_i(\eta) T_l(\kappa) T_j(\kappa) T_z(\xi) T_s(\xi) \\ & \times w(\eta) w(\kappa) w(\xi) d\eta d\kappa d\xi. \end{aligned} \quad (9)$$

Utilizing the orthogonality property, Eq. (5), it follows

$$A_{0,0,0} = \pi^3 C_{0,0,0} \quad \text{for} \quad i,j,s = 0 \quad (10a)$$

$$\begin{aligned} A_{i,j,s} &= \sum_{k=1}^{P_u} \sum_{l=1}^{P_v} \sum_{z=1}^{P_z} C_{k,l,z} \left(\frac{\pi}{2}\right)^3 \delta_{ik}\delta_{jl}\delta_{sz} \\ &= \left(\frac{\pi}{2}\right)^3 C_{i,j,s} \quad \text{for} \quad i,j,s \neq 0 \end{aligned} \quad (10b)$$

where δ_{ij} is the Kronecker delta.

From Eqs. (8), (9), (10*a*), and (10*b*), the following general expression can be derived for the coefficients $C_{k,l,z}$:

$$C_{k,l,z} = \frac{8}{(1+\delta_{k0})(1+\delta_{l0})(1+\delta_{z0})\pi^3} \int_{-1}^{1}\int_{-1}^{1}\int_{-1}^{1} \tilde{f}(\eta,\kappa,\xi) \times T_k(\eta) T_l(\kappa) T_z(\xi) w(\eta) w(\kappa) w(\xi) d\eta d\kappa d\xi. \quad (11)$$

These integrals can be performed by the Gauss-Chebyshev quadrature method. The coordinates of the points used in the integration are defined by

$$\eta_i = \cos\left(\frac{2i-1}{2Q_\eta}\pi\right) \quad i = 1,\ldots,Q_\eta;$$
$$\kappa_j = \cos\left(\frac{2j-1}{2Q_\kappa}\pi\right) \quad j = 1,\ldots,Q_\kappa; \quad (12)$$
$$\xi_s = \cos\left(\frac{2s-1}{2Q_\xi}\pi\right) \quad s = 1,\ldots,Q_\xi.$$

The evaluation of the Chebyshev polynomials and the weighting function at the quadrature points in the integral (11) yields

$$\begin{aligned} C_{k,l,z} = & \frac{8}{(1+\delta_{k0})(1+\delta_{l0})(1+\delta_{z0}) Q_\eta Q_\kappa Q_\xi} \\ & \times \sum_{i=1}^{Q_\eta} \sum_{j=1}^{Q_\kappa} \sum_{s=1}^{Q_\xi} \tilde{f}(\eta,\kappa,\xi) \cos\left(\frac{2i-1}{2Q_\eta} k\pi\right) \\ & \times \cos\left(\frac{2j-1}{2Q_\kappa} l\pi\right) \cos\left(\frac{2s-1}{2Q_\xi} z\pi\right). \end{aligned} \quad (13)$$

To determine the coefficients $C_{k,l,z}$ from the above expression, the generation of the SFD forces, $\tilde{f}(\eta,\kappa,\xi)$, to be fitted is carried out by directly defining the variables η, κ, and ξ on the quadrature points.

The fit procedure just described can be extended to derive SFD forces polynomial expressions functions of four or more variables. While algebraically straightforward, performing curve fits with more than three variables is computationally cumbersome. The inertia effects are thus more easily taken into account by making

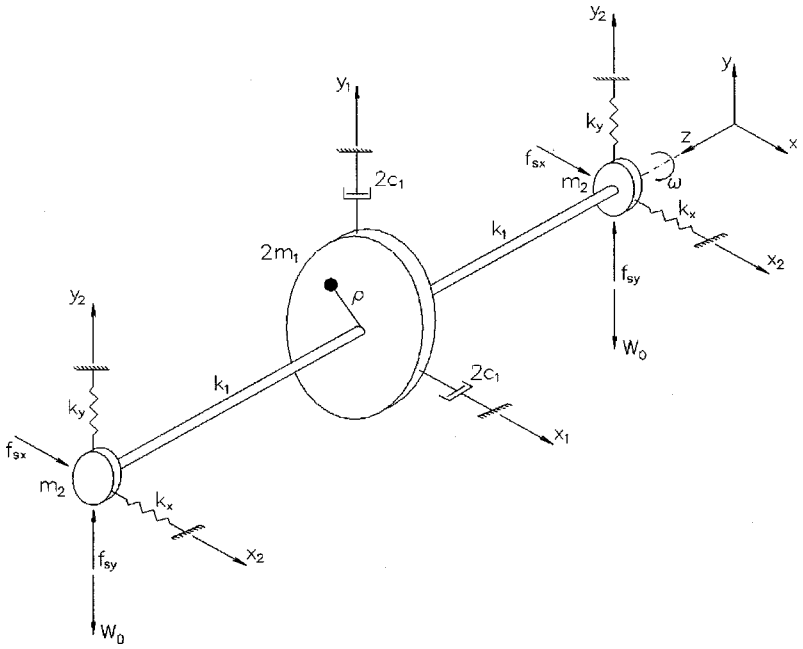

Fig. 3 Squeeze film damped flexible rotor—Jeffcott model

the hypothesis that viscous and inertia forces can be decoupled ([16,19]). Under such assumption, in addition to Eq. (3), one might similarly write

$$f^i_{sr}(\varepsilon,\ddot{\phi},\ddot{e}) \cong \sum_{k=0}^{P^r_u}\sum_{l=0}^{P^r_v}\sum_{z=0}^{P^r_z} C^r_{k,l,z}T_k(\varepsilon)T_l(\ddot{\phi})T_z(\ddot{e}) = \tilde{f}^i_{sr}(\varepsilon,\ddot{\phi},\ddot{e}) \tag{14}$$

$$f^i_{st}(\varepsilon,\ddot{\phi},\ddot{e}) \cong \sum_{k=0}^{P^t_u}\sum_{l=0}^{P^t_v}\sum_{z=0}^{P^t_z} C^t_{k,l,z}T_k(\varepsilon)T_l(\ddot{\phi})T_z(\ddot{e}) = \tilde{f}^i_{st}(\varepsilon,\ddot{\phi},\ddot{e}).$$

Once the inertia and viscous forces polynomial expressions have been derived, the total SFD forces are calculated from

$$f_{sr}(\varepsilon,\dot{\phi},\ddot{\phi},\dot{e},\ddot{e}) = \tilde{f}^v_{sr}(\varepsilon,\dot{\phi},\dot{e}) + \tilde{f}^i_{sr}(\varepsilon,\ddot{\phi},\ddot{e})$$

$$f_{st}(\varepsilon,\dot{\phi},\ddot{\phi},\dot{e},\ddot{e}) = \tilde{f}^v_{st}(\varepsilon,\dot{\phi},\dot{e}) + \tilde{f}^i_{st}(\varepsilon,\ddot{\phi},\ddot{e}).$$

4 Numerical Examples

In order to test the accuracy and numerical efficiency of the proposed method, the unbalance response of a Jeffcott rotor mounted on identical SFDs (Fig. 3) is studied. Thanks to the system symmetry about the rotor midpoint, the governing equations of motion in the stationary coordinate frame can be written as ([29])

$$[M]\{\ddot{s}\} + [C]\{\dot{s}\} + [K]\{s\} = \{f_e\} + \{f_{nl}\} \tag{15}$$

where

$$[M] = \begin{bmatrix} m_1 & 0 & 0 & 0 \\ 0 & m_1 & 0 & 0 \\ 0 & 0 & m_2 & 0 \\ 0 & 0 & 0 & m_2 \end{bmatrix}; \quad [C] = \begin{bmatrix} c_1 & 0 & 0 & 0 \\ 0 & c_1 & 0 & 0 \\ 0 & 0 & 0 & 0 \\ 0 & 0 & 0 & 0 \end{bmatrix};$$

$$[K] = \begin{bmatrix} k_1 & 0 & -k_1 & 0 \\ 0 & k_1 & 0 & -k_1 \\ -k_1 & 0 & k_1+k_x & 0 \\ 0 & -k_1 & 0 & k_1+k_y \end{bmatrix};$$

$$\{s\} = \begin{Bmatrix} x_1 \\ y_1 \\ x_2 \\ y_2 \end{Bmatrix}; \quad \{f_e\} = \begin{Bmatrix} \rho m_1 \omega^2 \cos(\omega t) \\ \rho m_1 \omega^2 \sin(\omega t) \\ 0 \\ W_0 \end{Bmatrix}; \quad \{f_{nl}\} = \begin{Bmatrix} 0 \\ 0 \\ f_{sx} \\ f_{sy} \end{Bmatrix}.$$

The following is defined for the rotor:

$$m_1 = 45\ \text{kg}; \quad m_2 = 15\ \text{kg}; \quad c_1 = 30\ \text{N.s/m};$$

$$\rho m_1 = 0.014\ \text{m.kg}; \quad k_1 = 6.0\times 10^7\ \text{N/m};$$

$$k_x = 2.5\times 10^7\ \text{N/m}; \quad k_y = 2.0\times 10^7\ \text{N/m}.$$

The frequency response curves are obtained using the harmonic balance method, following the work by Hahn and Chen [5]. An explicit expression of the force Fourier coefficients functions of the response Fourier coefficients can be derived from the SFD forces polynomial expressions, but a daunting deal of symbolic algebraic manipulation would have to be performed for it. Hence an alternating frequency/time domain (AFT) method ([30]) was used instead. To ensure continuity through the response curves, the pseudo-arc length continuation method ([31]) is used. Stability analyses of the periodic motions were carried out using the Floquet matrix transition method ([4,31]). For the transient calculations, the equations of motion were integrated using the fourth-order Runge-Kutta method with constant time-step.

4.1 Application to a Classical Squeeze Film Damper (SFD) Model. In this first numerical example, classical assumptions of the lubrication theory are made, i.e., the fluid is considered to be isoviscous and the damper ends to be open. The following parameters are defined for the SFD: $R = 0.03$ m, $L = 0.06$ m, $C = 0.5$ mm, and $\mu = 0.0275$ Pa.s. Cavitation is accounted for by the Gumbel boundary conditions. The SFD is considered to have a single land without geometrical discontinuities, a coherent hypothesis for end fed and hole with check valves fed dampers ([32]). It is noteworthy that for circumferential groove feeding systems, Arauz and San Andres [33] have shown experimentally that the classical hypothesis that grooves are regions of constant pressure, and consequently boundary conditions of the problem, is incorrect. The groove contribution to the total SFD force can be taken into account by superposing it to the SFD film lands contri-

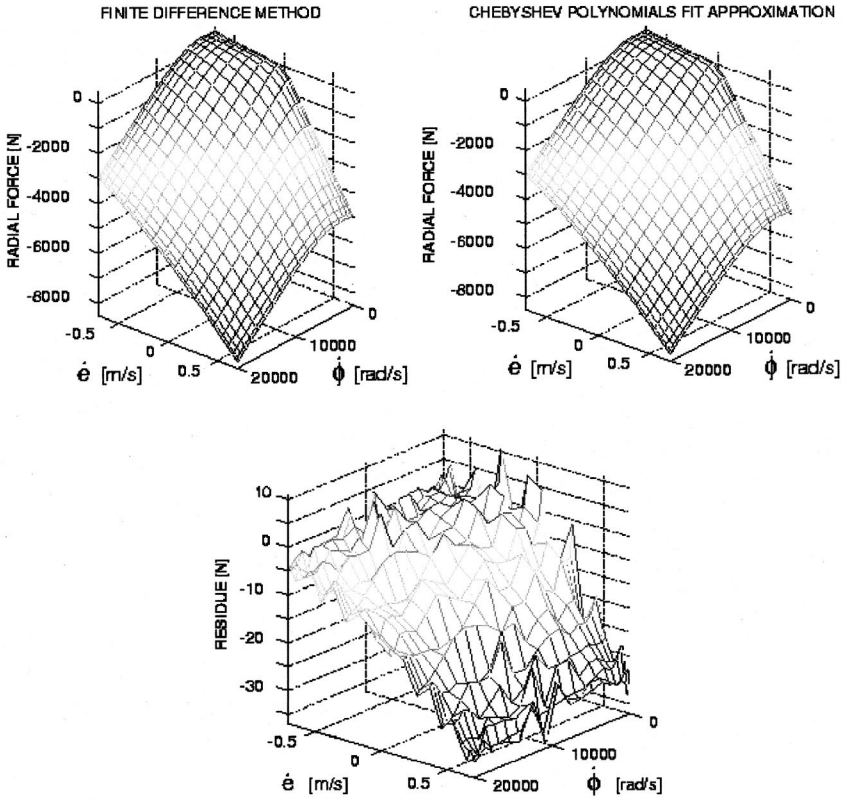

Fig. 4 Inspection of the fit quality: radial force function of $\dot{e}$ and $\dot{\phi}$ for $\varepsilon=0.5$

bution ([33]). Hence, Chebyshev fits can likewise be utilized to obtain polynomial expressions for the groove contribution on the SFD hydrodynamic forces.

4.1.1 Fitting Procedure. The parameters used for the Chebyshev polynomials fit are

$$\varepsilon_{\min}=0; \quad \varepsilon_{\max}=0.94; \quad \dot{e}_{\min}=-0.7\ \text{m/s}; \quad \dot{e}_{\max}=0.7\ \text{m/s};$$

$$\dot{\phi}_{\min}=0; \quad \dot{\phi}_{\max}=20{,}000\ \text{rad/s}; \quad Q_\eta=Q_\kappa=Q_\xi=20;$$

$$P_u^r=P_u^t=16; \quad P_v^r=P_v^t=14; \quad P_z^r=P_z^t=10.$$

An easy and direct visualization of the fit quality is not possible due to the three variables dependence feature of the radial and tangential forces. Nevertheless, two quite conclusive forms of inspection can be performed: the first one by plotting the SFD forces as functions of the radial $\dot{e}$ and precession $\dot{\phi}$ velocities for fixed values of eccentricity, as shown in Fig. 4, and the second one by examining the relative errors of the SFD forces polynomial approximations at the quadrature points in a one-dimensional graph, as shown in Fig. 5.

Figure 4 compares the Chebyshev polynomials fit to the forces calculated by the finite difference scheme for $\varepsilon=0.5$, taking the radial component as an example. It can be seen that the polynomial approximation agrees very well with the finite difference reference force values, and the residue is almost negligible. An even better trend is observed for the tangential force thanks to its

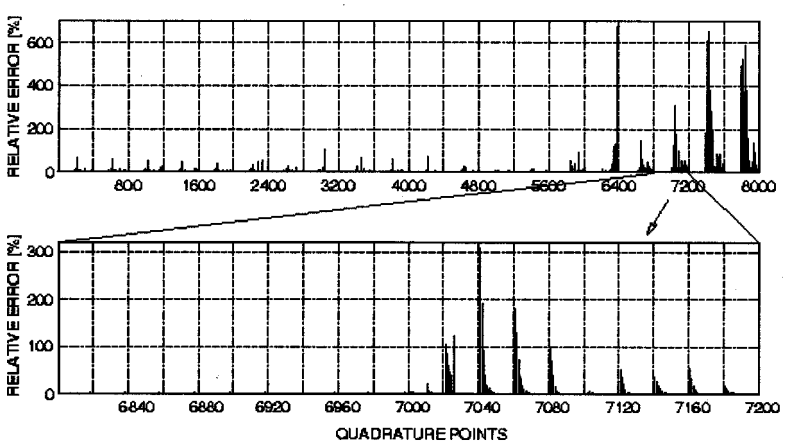

Fig. 5 Inspection of the fit quality: radial force relative error at quadrature points

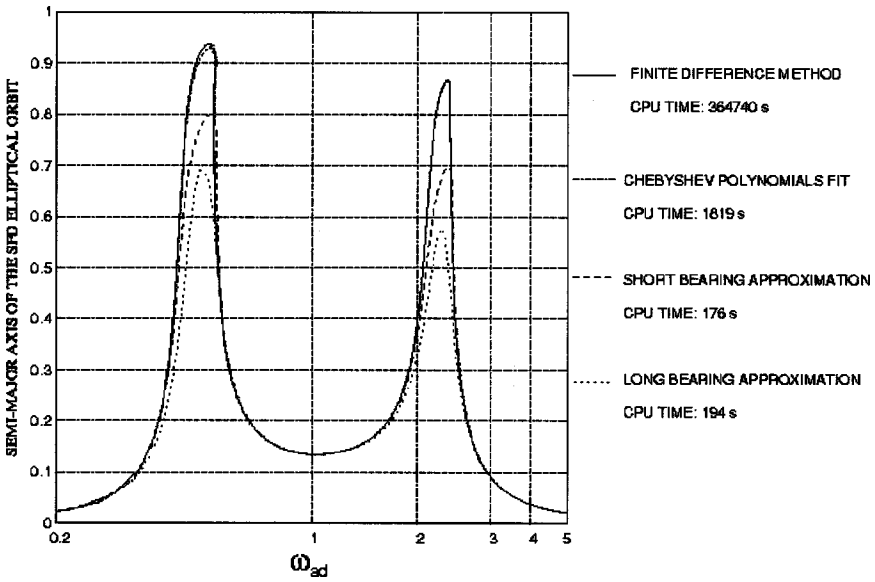

Fig. 6 Comparison of unbalance responses calculated using different squeeze film damper (SFD) forces models

smoother behavior especially for $\dot{e} \leqslant 0$. The more complex behavior of the radial force in this range is due to its change in sign, which occurs at specific set of values of ε and $\dot{\phi}$, for fixed negative radial velocities. Consequently, a better fitting of the radial force is obtained in general for $P_z^r > P_v^r$. And to reach the same fit quality for the tangential forces, lower values of P_z^t and P_v^t can be defined.

Figure 5 shows the relative errors, E_{rel}, of the polynomial approximation in comparison to the finite difference calculations, at the quadrature points, once again making use of the radial force as example. By defining the quadrature points so that $\varepsilon_{\max}=\varepsilon_1>\varepsilon_2>\ldots>\varepsilon_{20}=\varepsilon_{\min}$, $\dot{e}_{\max}=\dot{e}_1>\dot{e}_2>\ldots>\dot{e}_{20}=\dot{e}_{\min}$, $\dot{\phi}_{\max}=\dot{\phi}_1>\dot{\phi}_2>\ldots>\dot{\phi}_{20}=\dot{\phi}_{\min}$, the relative errors one-dimensional array is arranged in the following order:

$$E_{\text{rel}}(1)=E\text{rel}(\varepsilon_1,\dot{e}_1,\dot{\phi}_1)$$
$$\vdots$$
$$E_{\text{rel}}(20)=E\text{rel}(\varepsilon_{20},\dot{e}_1,\dot{\phi}_1)$$
$$E_{\text{rel}}(21)=E\text{rel}(\varepsilon_1,\dot{e}_2,\dot{\phi}_1)$$
$$\vdots\vdots$$
$$E_{\text{rel}}(400)=E\text{rel}(\varepsilon_{20},\dot{e}_{20},\dot{\phi}_1)$$
$$E_{\text{rel}}(401)=E\text{rel}(\varepsilon_1,\dot{e}_1,\dot{\phi}_2)$$
$$\vdots\vdots\vdots$$
$$E_{\text{rel}}(8000)=E\text{rel}(\varepsilon_{20},\dot{e}_{20},\dot{\phi}_{20}).$$

The first graph in Fig. 5 provides therefore an approximate idea of the relative error variation as a function of $\dot{\phi}$. It can be seen that relative errors are larger for small precession velocities. The second graph zooms a region of the first one, thus allowing a qualitative analysis of the relative error evolution as a function of $\dot{e}$ for a fixed value of $\dot{\phi}$.

The most prominent peaks observed in the graphs of Fig. 5 are related to quadrature points at which the force magnitudes are very small. This is the case of regions in the neighborhood of sign changes in the radial force. Hence, taking the relative error as the fit quality parameter, the SFD forces polynomial description provided by the Chebyshev fits is more accurate for higher force magnitudes. Nevertheless, the absolute errors obtained for small force magnitudes are also small, as can be noticed in Fig. 4. Consequently, the existence of large fit relative errors is not really problematic for the calculation of rotor unbalance responses, since the external dynamic load may dominate over the SFD forces when these are small. However, it was observed that stability analyses can indeed be affected, especially at very small eccentricities. An easy way to surmount this problem is to carry out one Chebyshev fit for moderate to large eccentricity values and another one for small eccentricity values, thus deriving different force expressions for the two eccentricity ranges.

The truncation orders necessary to obtain a satisfying fit quality are very sensitive to the predefined value $\varepsilon_{\max}$, especially P_u^r and P_u^t. The use of Chebyshev fits can yield good results, even for very high eccentricity ratios, on condition that the truncation orders are large enough to furnish an accurate polynomial description of the singular behavior of the hydrodynamic forces when $\varepsilon \rightarrow 1$. Unfortunately, a universal criterion based on which the truncation orders could be systematically specified does not exist. So, the derivation of the SFD forces polynomial expressions shall consist in an iterative process. Thanks to the Chebyshev polynomials orthogonality, this iterative process can be performed quite efficiently, since the truncation orders can be progressively increased, without changing the already calculated coefficients, until a good fit is achieved.

4.1.2 Comparison to Classical Lubrication Models. The main objective of this first numerical example is to compare, in terms of computation cost and numerical accuracy, the results obtained when the SFD forces are estimated by the short and long bearing approximations ([3,23]), by a finite difference scheme and by the forces expressions obtained from the Chebyshev polynomials fit.

Some rotor response simulations are shown in Figs. 6, 7, and 8. Figure 6 presents the dimensionless semi-major axis of the steady-state elliptical orbits of the rotor's unbalance response for zero static load, from $\omega_{ad}=0$ to 5, where $\omega_{ad}=\omega/\sqrt{k_1/m_1}$. Taking the response calculated by the use of the finite difference scheme as a reference, it can be seen that the application of neither the short bearing approximation nor the long bearing approximation are suitable to determine finite length SFD forces, although they do it much faster than the finite difference scheme. On the other hand, the use of the SFD forces polynomial approximation results in an

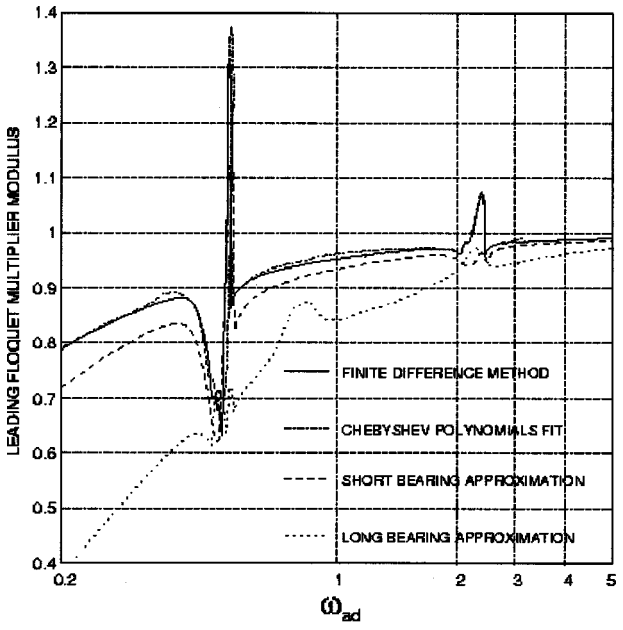

Fig. 7 Stability analysis results for different squeeze film damper (SFD) forces models

unbalance response almost identical to that obtained by the finite difference scheme, with the advantage of performing the calculation much more efficiently.

The precision of the calculations using the Chebyshev polynomials fits is confirmed by the stability results. Floquet theory states that the orbit becomes unstable when the leading Floquet multiplier modulus exceeds the value of one ([4,31]). From Fig. 7 it can be noted that the short and long bearing approximations fail to provide accurate results, since neither predicts the bifurcation point at $\omega_{ad} \approx 2.22$, whereas the SFD forces polynomial expressions are quite precise. In this stability analysis, in addition to the radial and tangential forces expressions obtained using the fit parameters defined above, two other expressions derived for $0 < \varepsilon < 0.1$, $P_u^r = P_u^t = 6$, $P_v^r = P_v^t = 5$, $P_z^r = P_z^t = 4$ were used whenever the eccentricity decreased below 0.1.

Finally, the accuracy of the polynomial approximations was tested for transient analyses, taking as example the prediction of a quasi-periodic motion observed at $\omega_{ad} = 2.3$. From Fig. 8 it can be seen that even for such a complex rotor motion, the Chebyshev fits are able to provide good results. As pointed out before, a certain level of extrapolation is allowed, what can be inferred from the fact that the orbit eccentricity reaches values as high as 0.95, while the fit was performed for $\varepsilon_{\max} = 0.94$. It is interesting to note that, only for this specific simulation, the numerical integration was carried out over 11,600 integration points, thus necessitating 46,400 SFD forces evaluations, approximately six times more than the $Q_\eta . Q_\kappa . Q_\xi = 8000$ necessary to do the preprocessing before the application of the Chebyshev fits. In the light of the CPU times indicated in Fig. 8, this simple comparison evidences the potential time gain that may be provided by the use of the Chebyshev polynomials fits.

4.2 Application to a More Complex Squeeze Film Damper (SFD) Model. The same damper geometry is treated in this second numerical example, but conditions supposed to be more realistic are accounted for in the film pressure distribution model. Firstly, the Reynolds boundary conditions are mimicked by using the Murty's algorithm ([34]). Secondly, a constant end leakage coefficient, $Cl = 0.005\,\mathrm{mm^2/Pa.s}$, is introduced to simulate the presence of seals. The boundary conditions at the damper extremities are thus expressed by ([7]):

$$q_z(\tilde{\theta}, z_{\text{extremities}}) = Cl[P(\tilde{\theta}, z_{\text{extremities}}) - P_0] \tag{16}$$

where q_z is the locally exiting flow rate and P_0 is the ambient pressure. And thirdly, the temperature is assumed to vary linearly in the axial direction, from $T_i = 30°\mathrm{C}$ at the damper midspan ($z = 0$) to $T_0 = 50°\mathrm{C}$ at the damper extremities. The expression of the oil viscosity as a function of the temperature is written as

$$\mu = \alpha \exp(\beta / T) \tag{17}$$

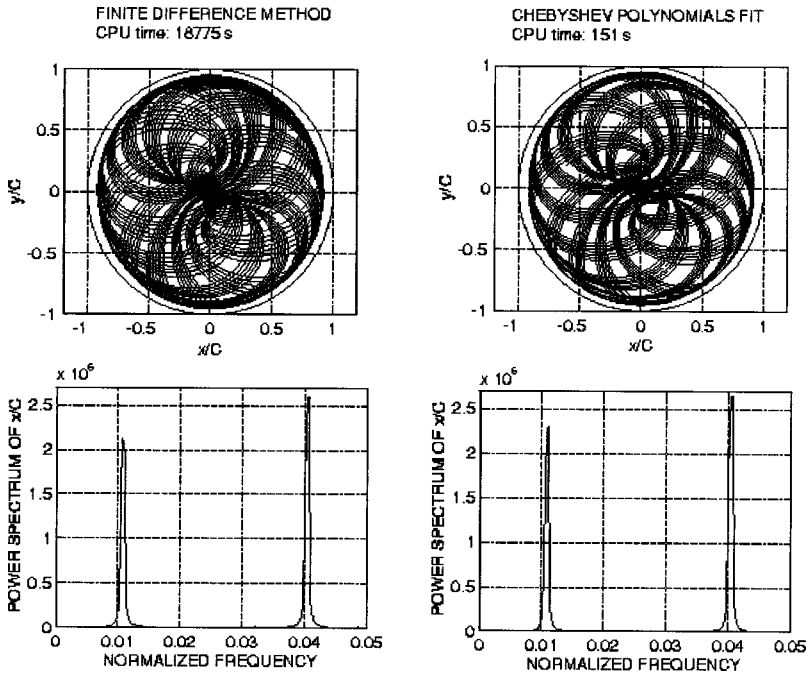

Fig. 8 Comparison of quasi-periodic orbits obtained by numerical integration for $\omega_{ad} = 2.3$

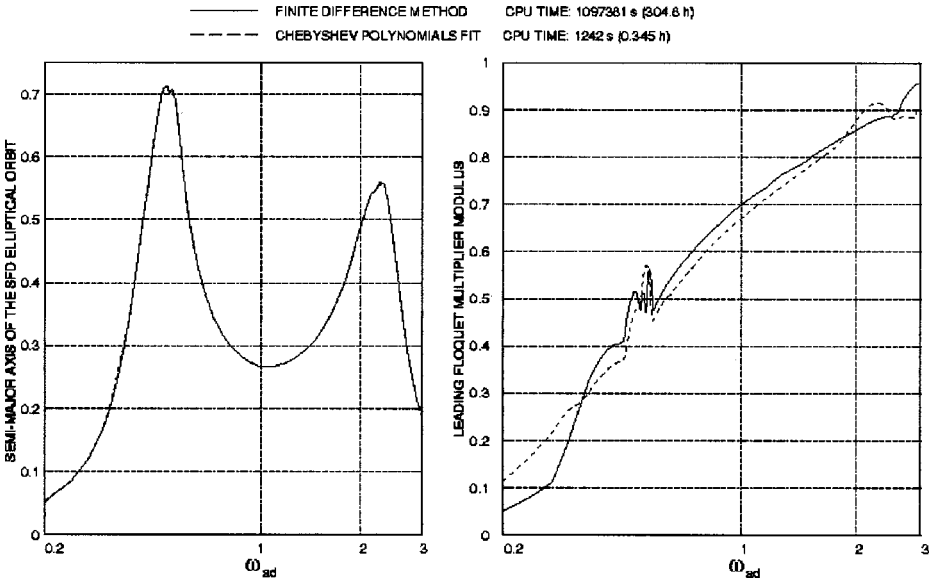

Fig. 9 Comparison of results obtained by the finite difference method and the Chebyshev polynomials fit

where the temperature as a function of the axial coordinate is

$$T = 2(T_0 - T_i)|z|/L + T_i \,. \tag{18}$$

From the data presented in [14] for SAE 30 engine oil, the values $\alpha = 2.9045e-8$ Pa.s and $\beta = 4673.077°$C are obtained by employing a least square approach.

The Chebyshev polynomials fits are performed for the following set of parameters:

$$\varepsilon_{\min} = 0; \quad \varepsilon_{\max} = 0.8; \quad \dot{e}_{\min} = -0.5 \text{ m/s}; \quad \dot{e}_{\max} = 0.5;$$

$$\dot{\phi}_{\min} = 0; \quad \dot{\phi}_{\max} = 10{,}000 \text{ rad/s} \quad Q_\eta = Q_\kappa = Q_\xi = 20;$$

$$P_u^r = P_u^t = 12; \quad P_v^r = P_v^t = 10; \quad P_z^r = P_z^t = 8.$$

The rotor parameters defined previously are kept for the simulations, but the unbalance is doubled. Figure 9 presents a comparison between the rotor unbalance responses obtained by evaluating the SFD forces via a finite difference scheme and via their polynomial approximations. It can be seen that the agreement is excellent in the orbit amplitudes and satisfactory in the stability analyses. The time saving provided by the SFD forces polynomial expressions is striking. The explanation for the huge CPU time taken by the finite difference scheme lies on the use of the Reynolds boundary conditions, which make the determination of the pressure field an iterative process. It seems obvious that the numerical resolution of the pressure field governing equation during rotordynamics simulations is of little interest to industrial applications, despite its accuracy. Nevertheless, the same precision level can be ensured in a much more efficient way by the utilization of Chebyshev fits. Hence, the derivation of hydrodynamic forces polynomial approximations proves to be a quite attractive way to speed up squeeze film damped rotors calculations, without the need of making simplifying hypotheses in the fluid behavior modeling stage.

5 Conclusions

In this paper a new approach for studying the performance of finite length SFDs is presented. It consists in the application of Chebyshev polynomials fits over force data generated from the numerical solution of any pressure field governing equation, so as to derive SFD forces polynomial expressions.

To illustrate the use of the above approach, the classical two-dimensional Reynolds equation is assumed to govern the film pressure distribution. In this case, the radial and tangential viscous forces can be approximated as triple series involving variables ε, $\dot{e}$, and $\dot{\phi}$, provided that the damper boundary conditions are axisymmetric. If inertia effects are to be accounted for, radial and tangential inertia forces expressions can be obtained as functions of ε, $\ddot{e}$, and $\ddot{\phi}$, by assuming that viscous and inertia effects can be decoupled ([16,19]). In theory, Chebyshev fits can be used to derive hydrodynamic forces as functions of more than three variables, but computationally the cost might become unattractive.

The simulation results presented in this work showed, as expected, that the short and long bearing approximations may not be suitable for estimating finite length dampers forces. Coupling the evaluation of the damper forces by a two-dimensional finite difference scheme with the calculation of the system nonlinear responses is inconceivable, because this procedure is seen to be too computationally expensive. The use of polynomial approximations to evaluate the SFD forces is shown to be an interesting alternative, since it allows for expeditious and accurate computation on the dynamics of rotors supported by finite length SFDs.

A significant deal of time is all the same required to do the preprocessing by numerically solving the film pressure governing equation, before performing Chebyshev fits. However, the force data generation is carried out only once, and the number of SFD forces evaluations necessary is usually significantly lower than that required for one single rotor response calculation. Hence, the time spent to obtain SFD forces polynomial expressions may be largely compensated when dynamic analyses are carried out. The time savings are even more important when the determination of the pressure field involves an iterative process, as for thermo-elasto-hydrodynamic analyses ([35]), or for the use of the Reynolds boundary conditions.

The main disadvantage of the proposed approach is inherent to its numerical nature, namely, how to know if a sufficiently accurate fit has been carried out, inasmuch as the judgement of the fit quality is somehow subjective. To assure that the truncation orders are high enough for accurate rotordynamics calculations, a standard way of verification of numerical procedures can be employed: successive refinement until convergence. In the context of this work, refinement means increase in truncation orders. Nonetheless, convergence can be efficiently achieved thanks to the orthogonality of the Chebyshev polynomials and to calculation speed provided by the SFD forces polynomial expressions.

Nomenclature

C = SFD radial clearance
$C_{k,l,z}$ = Chebyshev fit coefficients
c_1 = damping at the rotor mid-point
e = eccentricity
$\dot{e}_{\min}$, $\dot{e}_{\max}$ = $\dot{e}$ normalization limits
f_{sr}, f_{st} = SFD forces in the local coordinate frame
h = film thickness
L = SFD length
k_1 = stiffness of rotor segments
k_x, k_y = stiffness of retaining springs
m_1 = lumped mass at the rotor midpoint
m_2 = lumped mass at the damper station
P = pressure in the fluid film
P_u, P_v, P_z = polynomials truncation orders
Q_η, Q_κ, Q_ξ = number of quadrature points
R = SFD radius
T_n = Chebyshev polynomials
w = weighting function
x_e, y_e = journal center displacements
ε = e/C dimensionless orbit radius
$\varepsilon_{\min}$, $\varepsilon_{\max}$ = ε normalization limits
λ = L/D SFD length-to-diameter ratio
η, κ, ξ = ε, $\dot{e}$, $\dot{\phi}$ normalized counterparts
ϕ = attitude angle of the journal
$\dot{\phi}_{\min}$, $\dot{\phi}_{\max}$ = $\dot{\phi}$ normalization limits
ρ = mass eccentricity of the rotor
μ = fluid viscosity
ω = angular speed of the rotor
$(\dot{})$ = derivation with respect to time

Appendix

Particular Chebyshev polynomials of the first kind:

$$T_0(\zeta)=1$$

$$T_1(\zeta)=\zeta$$

$$T_2(\zeta)=2\zeta^2-1$$

$$T_3(\zeta)=4\zeta^3-3\zeta$$

$$T_4(\zeta)=8\zeta^4-8\zeta^2+1$$

$$T_5(\zeta)=16\zeta^5-20\zeta^3+5\zeta$$

References

[1] Chu, F., and Holmes, R., 1998, "Efficient Computation on Nonlinear Responses of a Rotating Assembly Incorporating the Squeeze-Film Damper," Comput. Methods Appl. Mech. Eng., **164**, pp. 363–373.
[2] Nataraj, C., and Nelson, H. D., 1989, "Periodic Solutions in Rotor Dynamic Systems With Nonlinear Supports: A General Approach," ASME J. Vibr. Acoust., **111**, pp. 187–193.
[3] El-Shafei, A., and Eranki, R. V., 1994, "Dynamic Analysis of Squeeze Film Damper Supported Rotors Using Equivalent Linearization," ASME J. Eng. Gas Turbines Power, **116**, pp. 682–691.
[4] Zhao, J. Y., Linnet, I. W., and McLean, L. J., 1994, "Stability and Bifurcation of Unbalanced Response of a Squeeze Film Damped Flexible Rotor," ASME J. Tribol., **116**, pp. 361–368.
[5] Hahn, E. J., and Chen, P. Y. P., 1994, "Harmonic Balance Analysis of General Squeeze Film Damped Multidegree-of-Freedom Rotor Bearing Systems," ASME J. Tribol., **116**, pp. 499–507.
[6] Shiau, T. N., Hwang, J. L., and Chang, Y. B., 1993, "A Study on Stability and Response Analysis of a Nonlinear Rotor System With Mass Unbalance and Side Load," ASME J. Eng. Gas Turbines Power, **115**, pp. 218–226.
[7] Tichy, J. A., 1987, "A Study of the Effect of Fluid Inertia and End Leakage in the Finite Squeeze Film Damper," ASME J. Tribol., **109**, pp. 54–59.
[8] Jung, S. Y., San Andrés, L. A., and Vance, J. M., 1991, "Measurements of Pressure Distributions and Force Coefficients in a Squeeze Film Damper Part II: Partially Sealed Configuration," Tribol. Trans., **34**, pp. 383–388.
[9] Rezvani, M. A., and Hahn, E. J., 1993, "Limitations of the Short Bearing Approximation in Dynamically Loaded Narrow Hydrodynamic Bearing," ASME J. Tribol., **115**, pp. 544–549.
[10] O'Donoghue, J. P., Koch, P. R., and Hooke, C. O., 1969–1970, "Approximate Short Bearing Analysis and Experimental Results Obtained Using Plastic Bearing Liners," Proc. Inst. Mech. Eng., **184**, Pt. 3L, pp. 190–196.
[11] Rohde, S. M., and Li, D. F., 1980, "A Generalized Short Bearing Theory," J. Lubr. Technol., **102**, pp. 278–282.
[12] Barret, L. E., Allaire, P. E., and Gunter, E. J., 1980, "A Finite Length Bearing Correction Factor for Short Bearing Theory," J. Lubr. Technol., **102**, pp. 283–290.
[13] Fuerst, A., Weber, H. I., and Brito, G. C., 1998, "Application and Remarks on the Finite Bearing Solution (FBS)," IFToMM Fifth International Conference on Rotor Dynamics, Darmstadt, pp. 560–570.
[14] Arauz, G. L., and San Andrés, L. A., 1993, "Experimental Pressures and Film Forces in a Squeeze Film Damper," ASME J. Tribol., **115**, pp. 134–140.
[15] Amendola, M., 1996, "Cavitation in Hydrodynamic Lubrication: A Parallel Algorithm for a Free-Boundary Problem," PhD thesis, IMECC-Unicamp.
[16] Reinhardt, E., and Lund, J. W., 1975, "The Influence of Fluid Inertia on the Dynamic Properties of Journal Bearings," J. Lubr. Technol., **97**, pp. 159–167.
[17] El-Shafei, A., 1991, "Unbalance Response of a Jeffcott Rotor Incorporating Long Squeeze Film Dampers," ASME J. Vibr. Acoust., **113**, pp. 85–94.
[18] Ramesh, K., and Kirk, G., 1999, "Nonlinear Response of Rotors Supported on Squeeze Film Dampers," *Proceedings of DETC99 17th Biennial ASME Vibrations Conference*, Las Vegas, NV.
[19] Inayat-Hussain, J. I., Kanki, H., and Mureithi, N. W., 1999, "On The Effectiveness of Squeeze-Film Dampers for Vibration Attenuation in Rotating Machinery," *Proceedings of Inter-Noise 99*, Fort Lauderdale, FL.
[20] Chu, F., and Holmes, R., 2000, "The Damping Capacity of the Squeeze Film Damper in Suppressing Vibration of a Rotating Assembly," Tribol. Int., **33**, pp. 81–97.
[21] Szeri, A. Z., Raimondi, A. A., and Giron-Duarte, A., 1983, "Linear Force Coefficients for Squeeze-Film Dampers," J. Lubr. Technol., **105**, pp. 326–334.
[22] San Andres, L., and Vance, J. M., 1987, "Effects of Fluid Inertia on Finite Length Squeeze-Film Dampers," ASLE Trans., **30**, pp. 384–393.
[23] Gohar, R., 1988, *Elastohydrodynamics*, (Ellis Horwood Series in Mechanical Engineering), Ellis Horwood, Chicester, UK.
[24] Cookson, R. A., Feng, X. H., and Kossa, S. S., 1983, "The Effect of Journal Misalignment on the Oil-Film Forces Generated in a Squeeze Film Damper," ASME J. Eng. Gas Turbines Power, **105**, pp. 560–564.
[25] Zhang, S., and Yan, L., 1991, "Development of an Efficient Oil Film Damper for Improving the Control of Rotor Vibration," ASME J. Eng. Gas Turbines Power, **113**, pp. 557–562.
[26] Chamniprasart, K., Al-Sharif, A., Rajagopal, K. R., and Szeri, A. Z., 1993, "Lubrication With Binary Mixtures: Bubbly Oil," ASME J. Tribol., **115**, pp. 253–260.
[27] Jaw-Ren, Lin, 1998, "Squeeze Film Characteristics on Finite Journal Bearings: Couple Stress Fluid Model," Tribol. Int., **31**, pp. 201–207.
[28] Worden, K., and Tomlinson, G. R., 1988, "Developments in Force State Mapping for Nonlinear Systems," *Proceedings, VI International Modal Analysis Conference*, pp. 1471–1479.
[29] McLean, L. J., and Hahn, E. J., 1983, "Unbalance Behavior of Squeeze Film Damped Multi-Mass Flexible Rotor Bearing Systems," ASME J. Lubr. Technol., **105**, pp. 22–28.
[30] Ren, Y., and Beards, C. F., 1994, "A New Receptance-Based Perturbative Multi-Harmonic Balance Method for the Calculation of the Steady State Response of Non-Linear Systems," J. Sound Vib., **172**, pp. 593–605.
[31] Nayfeh, A. H., and Balachandran, B., 1995, *Applied Nonlinear Dynamics*, John Wiley and Sons, New York.
[32] Wang, J., and Hahn, E. J., 1995, "Transient Analysis of Squeeze-Film Dampers With Oil Hole Feed," Tribol. Trans., **38**, pp. 837–844.
[33] Arauz, G. L., and San Andrés, L., 1994, "Effect of a Circumferential Feeding Groove on the Dynamic Force Response of a Short Squeeze Film Damper," ASME J. Tribol., **116**, pp. 369–377.
[34] Murty, K. G., 1974, "Note on a Bard-Type Scheme for Solving the Complementarity Problems," Opsearch, **11**, pp. 123–130.
[35] Freund, N. O., and Tieu, A. K., 1993, "A Thermo-Elasto-Hydrodynamic Study of Journal Bearing With Controlled Deflection," ASME J. Tribol., **115**, pp. 550–556.

Identification of the Modal Parameters of a Flexibly Supported Rigid Casing

N. Feng
Lecturer

E. J. Hahn
Professor

School of Mechanical and Manufacturing Engineering,
The University of New South Wales,
Sydney NSW 2052 Australia
e-mail: e.hahn@unsw.edu.au

Satisfactory means for evaluating the vibration behavior of gas turbine installations where it is impractical to obtain a satisfactory model of the support structure and where it has natural frequencies in the operating range are not yet available. This paper investigates the feasibility of identifying the modal parameters of a flexibly supported rigid casing to predict the unbalance response of the contained rotor. Assumed known are the location of the principal axes of inertia of the casing. Numerical experiments demonstrate that the identification procedure works well even with a measurement accuracy of only two significant digits. Thus, the procedure is expected to be practically feasible, though no sensitivity studies have yet been carried out to determine the limitations imposed by the assumed location of the principal axes. [DOI: 10.1115/1.1519265]

Introduction

The evaluation of the vibration behavior of gas turbine installations where the rotor support structure or casing has natural frequencies in the operating range has still not been satisfactorily developed for situations where it is impractical to obtain a satisfactory model of the casing either theoretically, (e.g., using finite elements), or experimentally, (e.g., modal testing), even though the interaction between a rotor and/or casing can significantly modify the dynamic behavior of the rotor. To enable these effects to be predicted, various techniques have been proposed to devise an equivalent casing which results in the same system dynamic response over the speed range of interest, [1–5]. Of these techniques, that of Feng and Hahn [5] proved promising in theory, but experimental evaluation showed that its identification capability was too susceptible to measurement error, [6], for practical implementation in its present form.

Feng and Hahn [5] sought to identify stiffness, damping, and mass matrices for an equivalent casing. A more promising approach, i.e., one which is more tolerant to measurement errors, would seem to be to identify instead modal parameters for an equivalent casing as proposed by Cheli et al. [4]; and in a preliminary investigation, excellent unbalance response identification was achieved for a symmetrically supported casing with symmetrically positioned connections to a rotor over a speed range in which only the rigid body modes of the casing contributed to the response, [7]. These assumptions of symmetry are far too restrictive. To study the more general case where such symmetries need not exist, it is assumed, in the first instance, that the casing can be modeled as a flexibly supported rigid body. Gas turbine casings which are sufficiently flexible as to exhibit flexural modes over the speed range of interest would also need to have these flexural modes identified. Such casing identification falls outside the scope of this paper.

Identification in Terms of Translational Degrees-of-Freedom

Theory. The technique for identifying the casing modal parameters in terms of selected translational degrees-of-freedom is discussed in [7] and is briefly summarized here. The equations of motion for the casing depicted in Fig. 1 are

$$\mathbf{M}\ddot{x}+\mathbf{C}\dot{x}+\mathbf{K}x=f \tag{1}$$

or in terms of modal parameters,

$$\mathbf{m}\ddot{q}+\mathbf{c}\dot{q}+\mathbf{k}q=\mathbf{A}^T f \tag{2}$$

where

$$q=\mathbf{A}^{-1}x \tag{3}$$

In case of harmonic excitation, Eq. (2) becomes

$$(-\Omega^2\mathbf{m}+i\Omega\mathbf{c}+\mathbf{k})\mathbf{A}^{-1}X=\mathbf{A}^T F \tag{4}$$

where the nonzero elements F_c in F, being the forces transmitted from the rotor to the casing, can be expressed in terms of the relative motion X_{rc} between the rotor and casing as

$$F_c=-(i\Omega\mathbf{C}_b+\mathbf{K}_b)X_{rc}\,. \tag{5}$$

No restrictions of symmetry apply to the bearing damping and stiffness matrices in Eq. (5). They could, for example, represent hydrodynamic bearings via linearised stiffness and damping coefficients which are here assumed known. By imposing orthonormal conditions to the mode shapes in the modal matrix $\mathbf{A}$, it is possible to force $\mathbf{A}^{-1}=\mathbf{A}^T$, so that Eq. (4) becomes

$$(-\Omega^2\mathbf{m}+i\Omega\mathbf{c}+\mathbf{k})\mathbf{A}^T X=\mathbf{A}^T F \tag{6}$$

or in decoupled form one has the $j(j=1,2,\ldots,m)$ equations:

$$(-\Omega^2 m_j+i\Omega c_j+k_j)\sum_{i=1}^{n} a_{ji}X_i-\sum_{i=1}^{n} a_{ji}F_i=0. \tag{7}$$

The parameters to be identified in the jth equations are m_j, c_j, k_j and $a_{ji}(i=1,2,\ldots n)$. Because every term in Eq. (7) contains one mode shape element only, normalization to ensure that $\Sigma_{i=1}^{n}a_{ji}^2=1$ can be performed after the parameter identification.

For each mode shape, i.e., for each j, Eq. (7) constitutes a set of nonlinear simultaneous equations (as many equations as speed values Ω for which X and F values are available) in the parameters to be identified. They may be solved using nonlinear regression.

Illustrative Example Using Translational Degrees-of-Freedom. In Ref. [7], a symmetrically supported foundation block with symmetrical connections to a rotor (Fig. 2) was identified numerically via this identification procedure using seven degrees-of-freedom distributed symmetrically on the top surface as shown in Fig. 3. Full details of the solution procedure, including the use of modification factors to cater for contributions of the

Contributed by the Structures and Dynamics Division of THE AMERICAN SOCIETY OF MECHANICAL ENGINEERS for publication in the ASME JOURNAL OF ENGINEERING FOR GAS TURBINES AND POWER. Manuscript received by the S&D Division Nov. 2000; final revision received by the ASME Headquarters May 2002. Associate Editor: M. Mignolet.

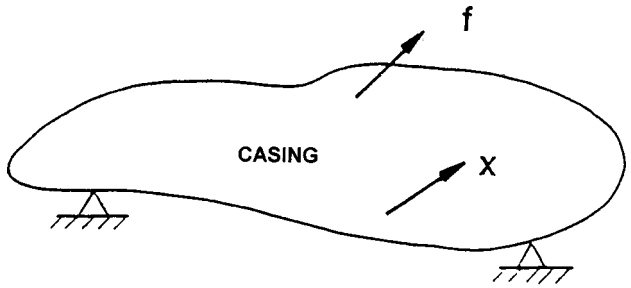

Fig. 1 Casing schematic

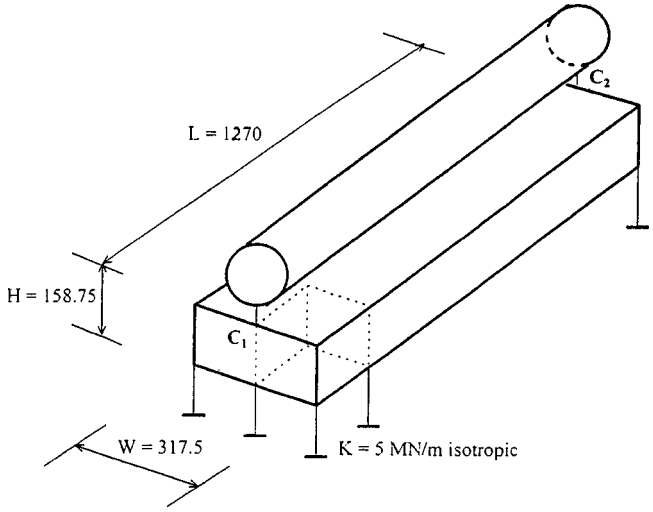

Fig. 2 Symmetric foundation

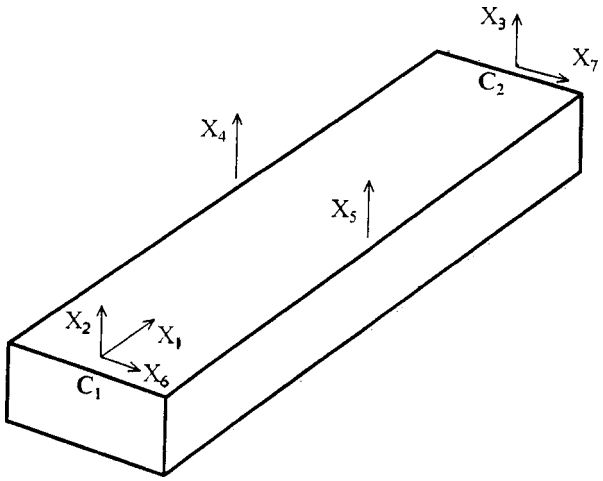

Fig. 3 Location of the seven degrees-of-freedom

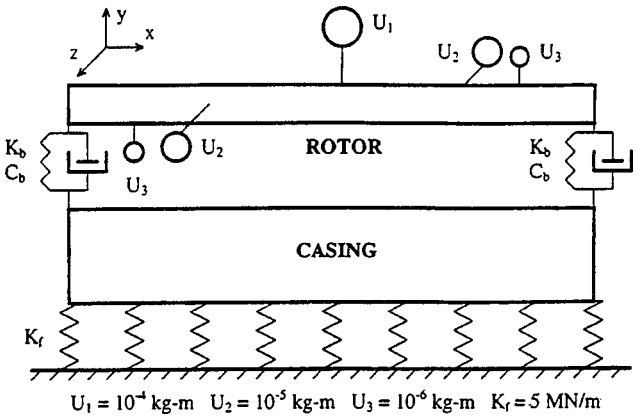

Fig. 4 Unbalance distribution No. 1

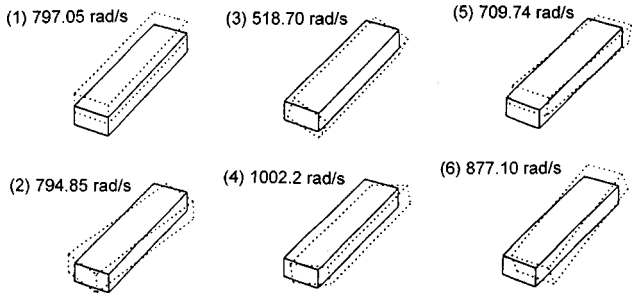

Fig. 5 Rigid-body modes of block

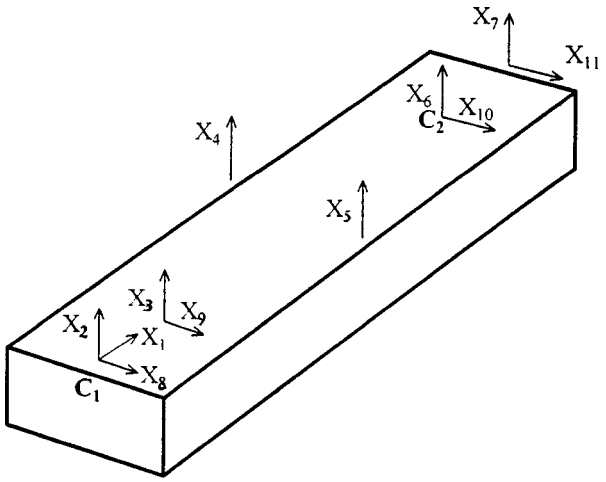

Fig. 6 Location of the 11 degrees-of-freedom

retained degrees-of-freedom, are given in this reference. The identification was over the speed range of 300 to 1200 rad/s using a 10 rad/s interval and using the unbalance distribution shown in Fig. 4 to generate the measured responses. Finite element codes were used to find relevant natural frequencies and mode shapes, and nonlinear regression was used to solve the equations obtained from Eq. (7), [8]. Over this speed range, only the rigid-body modes of the block were found to be relevant and these are shown in Fig. 5. Hence, without loss of generality, this rectangular block could be used to model any flexibly supported rigid body, including a rigid casing.

The identifications in Ref. [7] were for symmetric connections and symmetric supports. To ensure that the technique was suited for more general situations, the symmetry of the rotor connections to the block was disturbed by moving the second rotor connection C_2 towards the center by 1/8 of the casing length, and the degrees-of-freedom associated with connection C_2 were moved with it. The total number of degrees-of-freedom still completely define the six modes of interest and an attempt was made to identify the same casing using measurements at those points. However, the results obtained were unsatisfactory in that the modal properties of the casing, which are independent of the measurement locations, had changed somewhat. To overcome this problem, four more degrees-of-freedom were added to form a symmetric distribution of the degrees-of-freedom as shown in Fig. 6. Thus, neglecting damping terms for simplicity, Eq. (7) has the form

Table 1 Modal parameters of the casing with unsymmetric connections (11 degrees-of-freedom)

	ω(rad/s)		$\mathbf{a_{ji}}$			$\mathbf{m_j}$
Mode	actual	identified	ji	actual	identified	identified
1	797.05	796.95	13	1	.9132	85.847
2	794.85	794.13	2, 10	−.75	−.7525	59.817
3	518.70	517.52	34		.7256	82.091
4	1002.2	1001.1	44		−2.739	302.81
5	709.74	708.82	51		6.195	53.651
6	877.10	879.40	61		−4.333	64.400

$$(\mathbf{k}-\Omega^2\mathbf{m})\begin{bmatrix} 0 & a_{12} & a_{13} & a_{14} & a_{15} & a_{16} & a_{17} & 0 & 0 & 0 & 0 \\ 0 & 0 & 0 & 0 & 0 & 0 & 0 & a_{28} & a_{29} & a_{2,10} & a_{2,11} \\ 0 & 0 & 0 & a_{34} & a_{35} & 0 & 0 & a_{38} & a_{39} & a_{3,10} & a_{3,11} \\ 0 & 0 & 0 & a_{44} & a_{45} & 0 & 0 & a_{48} & a_{49} & a_{4,10} & a_{4,11} \\ a_{51} & a_{52} & a_{53} & 0 & 0 & a_{56} & a_{57} & 0 & 0 & 0 & 0 \\ a_{61} & a_{62} & a_{63} & 0 & 0 & a_{66} & a_{67} & 0 & 0 & 0 & 0 \end{bmatrix}\begin{Bmatrix} X_1 \\ X_2 \\ \vdots \\ X_{11} \end{Bmatrix} - \begin{bmatrix} a_{12} & a_{16} & 0 & 0 \\ 0 & 0 & a_{28} & a_{2,10} \\ 0 & 0 & a_{38} & a_{3,10} \\ 0 & 0 & a_{48} & a_{4,10} \\ a_{52} & a_{56} & 0 & 0 \\ a_{62} & a_{66} & 0 & 0 \end{bmatrix}\begin{Bmatrix} F_2 \\ F_6 \\ F_8 \\ F_{10} \end{Bmatrix} = 0. \tag{8}$$

The form of this modal matrix was obtained by considering the possible rigid-body mode shapes for this block as shown in Fig. 5. The six rigid-body modes involve predominantly three translational modes of the mass center of the block and three rotational modes about the principal axes of inertia of the block, with some coupling present because of the spring supports. Thus, if one considers the first mode, a small vertical translational displacement of the block will induce oscillations in the vertical direction only, for the resultant force in the other two translational directions and the resultant moment about any of the principal axes of inertia (here corresponding to the *x*, *y*, *z* axes located at the mass center) are zero. Hence, this mode is a pure translational mode with no coupling. The mode shape elements in the first row corresponding to the measurement degrees-of-freedom affected by this motion, viz degrees-of-freedom X_2, X_3, X_4, X_5, X_6 and X_7 in Fig. 6, are a_{12}, a_{13}, a_{14}, a_{15}, a_{16}, and a_{17}.

The second mode is similarly a pure rotational mode about the *y*-axis through the mass center. The remaining modes are more complicated as some coupling is present. For example, the third mode appears to be predominantly a rotation about the *x*-axis. If a small rotation $\Delta\theta_x$ is imparted to the rigid body, not only is there a resultant moment about the *x*-axis, but also a resultant force in the *z*-direction whereas the resultant moments about the other two axes and the resultant forces in the other two directions are zero. Hence, the affected measurement degrees-of-freedom for this mode shape will be X_4, X_5, X_8, X_9, X_{10}, and X_{11}, necessitating corresponding mode shape elements a_{34}, a_{35}, a_{38}, a_{39}, $a_{3,10}$, and $a_{3,11}$. Similar analyses show that mode shape 4, while predominantly a rigid-body translation in the *z*-direction also involves rotation about the *x*-axis; that mode shape 5, while predominantly rigid-body translation in the *x*-direction also involves rotation about the *z*-axis; and that mode shape 6, while predominantly rotation about the *z*-axis, also involves translation in the *x*-direction.

In each mode, one mode shape element is arbitrarily chosen as unity, another mode shape element is selected to be identified and the remaining are defined either geometrically from these two utilizing the geometric constraints pertaining to what are assumed to be rigid modes (actually, because finite element analysis was used to determine the actual mode shapes some bending contributions could appear) or according to orthogonality requirements. Twelve-digit ''measurement'' accuracy was used to ensure that numerical roundoff error did not significantly affect the values of the identified parameters. Tables 1 and 2 summarize the identification results. These are comparable in accuracy to those for the casing with symmetric rotor connections discussed in Ref. [7], but are not perfect.

Since it was unclear whether the imperfections in the identifications were due to the possible influence of flexural modes, or due to a poor choice for the location of the translational degrees-of-freedom used for measurement, or due to numerical error buildup (which would indicate potential problems with the approach when applied to more general cases such as a nonsymmetrically supported block), it was decided to eliminate all possibilities of flexural modes by ensuring the foundation was always rigid and so only had six (rigid-body) modes. Such an approach would also clearly indicate whether the six measurement degrees-of-freedom were satisfactorily located. Use of finite element software to generate the response was avoided by solving the equations of motion for a flexibly supported rigid block, using the motions of the mass center and the rotations about the principal

Table 2 Orthonormal mode shapes of the casing with unsymmetric connections (11 degrees-of-freedom)

Mode	$\mathbf{a_{j1}}$	$\mathbf{a_{j2}}$	$\mathbf{a_{j3}}$	$\mathbf{a_{j4}}$	$\mathbf{a_{j5}}$	$\mathbf{a_{j6}}$	$\mathbf{a_{j7}}$	$\mathbf{a_{j8}}$	$\mathbf{a_{j9}}$	$\mathbf{a_{j,10}}$	$\mathbf{a_{j,11}}$
1	0	.40825	.40825	.40825	.40825	.40825	.40825	0	0	0	0
2	0	0	0	0	0	0	0	.56569	.42426	−.42426	−.56569
3	0	0	0	.32360	−.32360	0	0	.44457	.44457	.44457	.44457
4	0	0	0	−.62872	.62872	0	0	.22882	.22882	.22882	.22882
5	.76709	.36291	.27218	0	0	−.27218	−.36391	0	0	0	0
6	−.64156	.43392	.32544	0	0	−.32544	−.43392	0	0	0	0

axes of inertia through the mass center, i.e., the so-called mass center coordinates, as the six degrees-of-freedom.

Identification in Terms of Mass Center Coordinates

Theory. The equations of motion for a rigid casing using the casing mass center coordinates with the *x*, *y*, and *z*-axes corresponding to the principal axes of inertia of the casing, are given by (see Appendix A):

$$\mathbf{M}\ddot{u}+\mathbf{C}\dot{u}+\mathbf{K}u=f_d=\mathbf{D}f \tag{9}$$

or in terms of modal parameters with harmonic excitation by

$$(-\Omega^2\mathbf{m}+i\Omega\mathbf{c}+\mathbf{k})\mathbf{A}^{-1}U=\mathbf{A}^TF_d\,. \tag{10}$$

In such a case, the mass matrix is diagonal and contains the four independent parameters m_f, I_x, I_y, and I_z. Note that the modal matrix **A** is now necessarily of order 6 and differs from that in the previous section. Also, one can now no longer assume that $\mathbf{A}^{-1}=\mathbf{A}^T$. Instead, since

$$\mathbf{I}=\mathbf{m}^{-1}\mathbf{m}=\mathbf{m}^{-1}\mathbf{A}^T\mathbf{M}\mathbf{A}=\mathbf{A}^{-1}\mathbf{A} \tag{11}$$

$$\mathbf{A}^{-1}=\mathbf{m}^{-1}\mathbf{A}^T\mathbf{M} \tag{12}$$

and Eq. (10) becomes

$$(-\Omega^2+i\Omega\mathbf{c}\mathbf{m}^{-1}+\mathbf{k}\mathbf{m}^{-1})\mathbf{A}^T\mathbf{M}U=\mathbf{A}^TF_d\,. \tag{13}$$

In decoupled form one has the j equations ($j=1,2\ldots m$):

$$(-\Omega^2+i\Omega c_j/m_j+k_j/m_j)\sum_{i=1}^{6}a_{ji}M_iU_i-\sum_{i=1}^{6}a_{ji}F_{d_i}=0. \tag{14}$$

The parameters to be identified in the jth equation are now $c_j/m_j=2\zeta_j\omega_j$, $k_j/m_j=\omega_j^2$, $M_i(i=1,4,5,6)$ and $a_{ji}(i=1,2,\ldots,6)$. Note that the M_is are the same for all the modes and will generally be identified independently m times. Compared to that in the previous section, this approach limits the degrees-of-freedom to six (i.e., $m\leqslant 6$), satisfies the orthogonality requirement as expressed by Eq. (11) automatically, and does not require the normalization procedure. It is applicable to any flexibly supported rigid casing.

Illustrative Examples Using Mass Center Coordinates. For comparison purposes the example casing used was a rigid block with the same dimensions and mass as the one in Fig. 2. To simplify data input the 64 springs at the corners of each brick element, were replaced with springs at $x=\pm\sqrt{(11L/128)}$ and $z=\pm\sqrt{(W/8)}$ from the mass center with isotropic stiffnesses of $K_f=80$ MN/m, i.e., 16 times the individual spring stiffnesses. Such a support arrangement will result in the same natural frequency for the purely translational first mode. Unsymmetric casing supports were formed by varying the above stiffness values and their locations. Also, since rotor connection locations do not alter the casing parameters, only the earlier unsymmetric connection locations are presented. The responses were measured at 10 rad/s intervals over the speed range of 300 to 1300 rad/s at the points shown in Fig. 7. For such an arrangement, **D** and **G** become

$$\mathbf{D}=\begin{bmatrix} 1 & 0 & 0 & 0 & 0 & 0\\ 0 & 1 & 1 & 1 & 0 & 0\\ 0 & 0 & 0 & 0 & 1 & 1\\ 0 & 0 & 0 & -\frac{W}{2} & \frac{H}{2} & \frac{H}{2}\\ 0 & 0 & 0 & 0 & \frac{L}{2} & -\frac{3L}{8}\\ -\frac{H}{2} & -\frac{L}{2} & \frac{3L}{8} & 0 & 0 & 0 \end{bmatrix} \tag{15}$$

and

$$\mathbf{G}=\begin{bmatrix} 1- & -\frac{4H}{7L} & \frac{4H}{7L} & 0 & 0 & 0\\ 0 & \frac{3}{7} & \frac{4}{7} & 0 & 0 & 0\\ 0 & -\frac{3H}{7W} & -\frac{4H}{7W} & \frac{H}{W} & \frac{3}{7} & \frac{4}{7}\\ 0 & \frac{6}{7W} & \frac{8}{7W} & -\frac{2}{W} & 0 & 0\\ 0 & 0 & 0 & 0 & \frac{8}{7L} & -\frac{8}{7L}\\ 0 & -\frac{8}{7L} & \frac{8}{7L} & 0 & 0 & 0 \end{bmatrix}. \tag{16}$$

As a convenient check on theory and computer implementation, the symmetrically supported casing was again identified. Thus, Eq. (13), on neglecting the damping terms for simplicity, has the form

$$(\mathbf{k}\mathbf{m}^{-1}-\Omega^2)\begin{bmatrix} 0 & a_{12} & 0 & 0 & 0 & a_{16}\\ 0 & 0 & a_{23} & 0 & a_{25} & 0\\ 0 & 0 & a_{33} & a_{34} & 0 & 0\\ 0 & 0 & a_{43} & a_{44} & 0 & 0\\ a_{51} & 0 & 0 & 0 & 0 & a_{56}\\ a_{61} & 0 & 0 & 0 & 0 & a_{66} \end{bmatrix}\mathbf{M}U$$

$$=\begin{bmatrix} 0 & a_{12} & 0 & 0 & 0 & a_{16}\\ 0 & 0 & a_{23} & 0 & a_{25} & 0\\ 0 & 0 & a_{33} & a_{34} & 0 & 0\\ 0 & 0 & a_{43} & a_{44} & 0 & 0\\ a_{51} & 0 & 0 & 0 & 0 & a_{56}\\ a_{61} & 0 & 0 & 0 & 0 & a_{66} \end{bmatrix}\begin{bmatrix} 0\\ F_2+F_3\\ F_5+F_6\\ \frac{H}{2}(F_5+F_6)\\ L\left(\frac{F_5}{2}-\frac{3F_6}{8}\right)\\ L\left(\frac{3F_3}{8}-\frac{F_2}{2}\right) \end{bmatrix}. \tag{17}$$

The form of the modal matrix is again obtained by considering the possible rigid-body mode shapes (Fig. 5). Thus, for the first mode, if a small vertical translational displacement Δy is imparted to the block, the resultant force in the *y*-direction is nonzero,

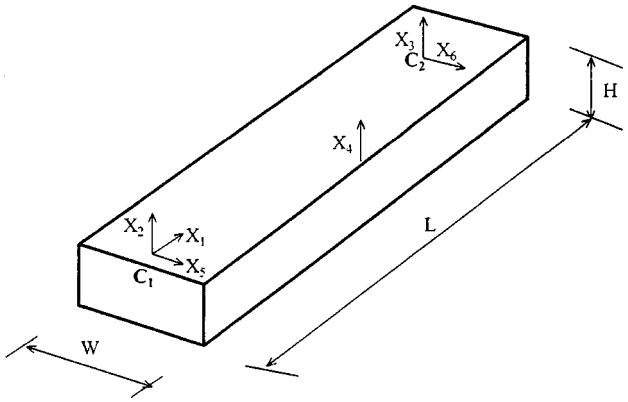

Fig. 7 Location of the measurement points

Table 3 Modal parameters of the symmetric rigid casing (mass center coordinates)

	ω_j (rad/s)		a_{ji}				$\mathbf{M}_i$	
Mode	actual	iden'd	ji	actual	iden'd		actual	iden'd
1	798.01	798.01	16	0	-2×10^{-5}	m_f	502.49	502.49
2	821.14	821.14	23	0	7×10^{-9}	I_y	71.761	71.760
3	579.98	579.97	33	.1682	.1682	I_x	5.2765	5.2767
4	1202.8	1202.8	43	−.06241	−.06241	I_x	5.2765	5.2765
5	719.87	719.87	51	−.4261	−.4262	I_z	68.595	68.595
6	891.42	891.42	61	.3203	.3203	I_z	68.595	68.594

whereas the resultant forces in the other two directions and the resultant moments about the three axes are zero. Hence, the affected degree-of-freedom for this mode shape will be U_2, necessitating the corresponding nonzero mode shape element a_{12}. The additional mode shape element a_{16} was added to see if it will be correctly identified to be zero. Similarly for the second mode shape, a pure rotational mode about the *y*-axis, the affected degree-of-freedom was found to be U_5, necessitating the corresponding nonzero mode shape element a_{25}. Again, the additional mode shape element a_{23} was added to see if it will be correctly identified to be zero. The remaining modes again involve some coupling. Thus, the third mode, predominantly a rotation about the *x*-axis, upon imparting a small rotation about the *x*-axis, will involve motions about the *x*-axis as well as in the *z*-direction. Hence, the affected degrees-of-freedom for this mode shape will be U_3 and U_4, necessitating corresponding mode shape elements a_{33} and a_{34}. Similarly, one can determine the to be identified mode shape elements for modes 4, 5, and 6.

For each mode, two of the parameters in **M** were combined with the unknowns in **A**. Because the first elements in modes 5 and 6 do not involve excitation forces (i.e., there are assumed to be no excitation forces in the *x*-direction), the decoupled equation for the fifth mode ($j=5$ in Eq. (14)) reads after some simplification:

$$\left(-I_z\Omega^2+\frac{k_5 I_z}{m_5}\right)\left(\frac{a_{51}m_f}{I_z}U_1+a_{56}U_6\right)=a_{56}L\left(\frac{3F_3}{8}-\frac{F_2}{2}\right) \tag{18}$$

with a similar equation for the sixth mode. Hence, on specifying $a_{56(66)}$ as unity, one can define the parameters to be identified as $k_{5(6)}I_z/m_{5(6)}$, I_z and $m_f a_{51(61)}/I_z$ ($a_{51(61)}$ now being relative magnitudes). The orthogonality requirement (from Eq. (12)) states that

$$a_{51}a_{61}+a_{56}a_{66}I_z/m_f=0 \tag{19}$$

so that

$$a_{61(51)}=-m_f a_{51(61)}/I_z. \tag{20}$$

This enables a_{61} and a_{51} in turn (and also m_f) to be determined. Similarly, the decoupled equation for mode 1 using the already identified I_z enables in the identification of k_1/m_1 (i.e., ω_1^2), m_f and a_{16}. This identified m_f was then used in modes 2, 3, and 4 in identifying ω_2, ω_3, ω_4, a_{23}, a_{33}, a_{43}, I_y and I_x.

Table 3 summarizes the identification results. The better agreement here compared with Table 1 is mainly due to the elimination of the effect of the flexibility of the casing. The results presented so far are all based on 12-digit measurement data accuracy. Equally good agreement pertained even when the input measurement data were rounded off to two digits.

Next, an unsymmetrically supported casing was analyzed with the spring locations and stiffnesses as shown in Fig. 8. In such a case the modal matrix **A** (in Eq. (17)) is full and the number of parameters to be identified in each mode is 10, viz:, ω_j, four inertia terms, and five mode shape elements (here the a_{j6} were all specified to be unity). With 12-digit measurement input data accuracy, excellent identification of inertial properties and mode shapes was again obtained. Actual and identified natural frequencies were identical to five significant figures as were most of the identified parameters for all six mode shapes, with just a handfull of parameters differing minimally with errors never exceeding 0.04%. Identification was then carried out using the input measurement data rounded off to two digits. Some of the first trial identified parameters, i.e., m_f, I_x, I_y, I_z, and ω_j, are shown in Table 4 under T1. Note that the inertial properties of the casing are still as listed in Table 3. There was no satisfactory convergence for mode 4; i.e., for all initial values tried, the search either failed to converge or converged to the other modes. Because all the parameters in **M** were identified five times independently (would have been six times had satisfactory convergence been achieved for mode 4), it was clear that they were in error. Convergence was achieved by accepting the average of reasonably common parameter values as known parameters, and reidentifying the remaining parameters. Thus, m_f was first removed as an unknown by assuming its average value of 502.36 from modes 5 and 6, resulting in nine unknowns in each mode. The corresponding second trial identification results for the remaining inertial parameters are summarized in Table 4 under T2. Mode 4 was identified based on the responses of $\Omega=700$ to 1300 rad/s. Since the I_x and I_y values are still scattered, the next step was to assume as known the average value of $I_z=68.667$ from modes 5 and 6, resulting in eight unknowns for each mode. The corresponding third trial identification results are shown in Table 4 under T3. Average values of Ix

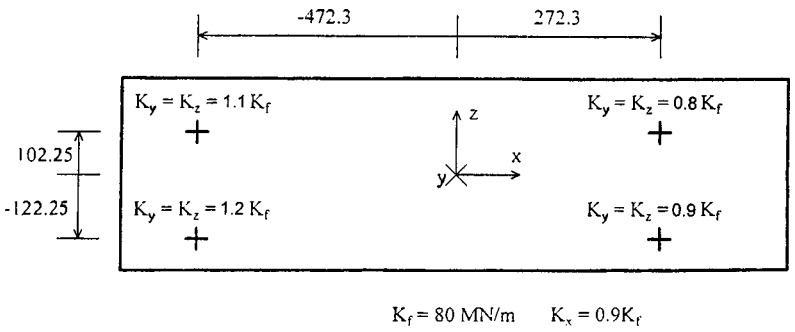

Fig. 8 Unsymmetrically supported casing

Table 4 Modal parameters of the unsymmetrically supported rigid casing (two-digit data)

	m_f	I_x			I_y			I_z		ω(rad/s)				
Mode	T1	T1	T2	T3	T1	T2	T3	T1	T2	Actual	T1	T2	T3	T4
1	491.48	−35.652	10.815	5.4780	47.464	76.287	70.908	44.909	52.195	765.00	765.94	765.59	765.33	765.30
2	330.17	5.5950	5.0211	5.3586	76.380	69.648	70.501	31.995	42.849	823.61	817.39	822.66	824.75	825.36
3	375.25	295.72	5.8370	5.3755	125.49	80.866	85.586	14.724	26.223	543.45	542.09	543.58	544.08	544.64
4	-	-	2.6898	5.2018	-	13.311	69.005	-	17.232	1259.0	-	1262.9	1259.9	1258.7
5	502.00	4.7616	4.7716	5.4966	81.514	82.214	81.325	67.677	67.768	626.74	626.78	626.75	626.55	626.71
6	502.72	13.868	13.735	7.4114	68.432	68.826	69.467	69.502	69.566	1002.2	1001.5	1001.5	1002.0	1002.0

	a_{j1}			a_{j2}			a_{j3}			a_{j4}			a_{j5}		
	Actual	T3	T4	Actual	T3	T4	Actual	T3	T4	Actual	T3	T4	Actual	T3	T4
1	4.23	4.01	4.02	2.22	2.10	2.11	.379	.372	.373	−1.55	−.889	−.934	−.989	−.680	−.707
2	.147	.146	.143	.0345	.0316	.0300	.176	.184	.184	10.1	9.95	9.96	5.23	5.27	5.33
3	−.0906	−.106	−.124	.867	.783	.774	−3.96	−3.53	−3.35	−19.8	−17.4	−16.4	3.54	2.73	3.13
4	.0151	.0402	.0479	−.553	−.482	−.483	2.83	2.27	2.28	−42.8	−34.6	−34.0	5.27	4.62	4.47
5	−.258	−.260	−.260	.402	.403	.402	.0988	.0970	.0976	.106	.100	.106	−.189	−.166	−.190
6	.108	.107	.107	−.270	−.269	−.270	−.0510	−.0507	−.0508	.0142	.0300	.0334	−.182	−.171	−.173

$=5.3821$ from modes 1 to 5, and $I_y=69.970$ from modes 1, 2, 4, and 6 were then used to identify the remaining six unknowns. The final results are shown in Table 4 under T4 and indicate significant improvement.

Note that all the identified natural frequencies are relatively insensitive to measurement data accuracy and are never far removed from the actual values. As a result the responses based on the identified foundation are expected to have error in amplitudes rather than in locations of the resonant peaks.

Finally, for the unbalance distribution shown in Fig. 4, Fig. 9 shows the unbalance responses at the left end, one quarter distance, and halfway from the left end of the rotor for the actual rotor casing system and for the identified (two-digit data) rotor casing system, calculated using impedance matching and influence coefficients as outlined in Appendix B. As expected, the unbalance responses are virtually unaffected by the remaining discrepancies between the actual and identified parameters. Similar unbalance responses are shown in Fig. 10 corresponding to the unbalance distribution in Fig. 11. Again, the unbalance responses are virtually unaffected by the remaining discrepancies between the actual and the identified parameters, so that the identified casing is excitation independent, in that it predicts the correct unbalance response for an unbalance distribution totally different from that which was used to excite the casing for identification purposes.

Discussion and Conclusions

Based on the modal parameter approach, a casing identification technique is developed for a flexibly supported casing exhibiting rigid mode vibration in the speed range of interest. Numerical examples show that this approach is far more tolerant to measurement errors than direct identification of mass and stiffness matrix elements. Identification is achieved from response data with only two-digit measurement data accuracy, an accuracy attainable with practical measurement technology. The identified natural frequencies are always close to the actual ones, and the inaccuracy in mode shape has little effect on the system responses.

The identification of rigid-body casing modal parameters in terms of selected translational degrees-of-freedom does not exclude the possible influence of flexible modes, rendering identification error determinations difficult, whereas the use of mass center coordinates overcomes this problem.

The repeatedly but independently identified mass matrix elements provided a useful means of reducing the number of unknowns in the iteration equations as well as a useful indication of the presence and likelihood of error. To be consistent, the same element values of **M** should be used for all the modes in the final identification.

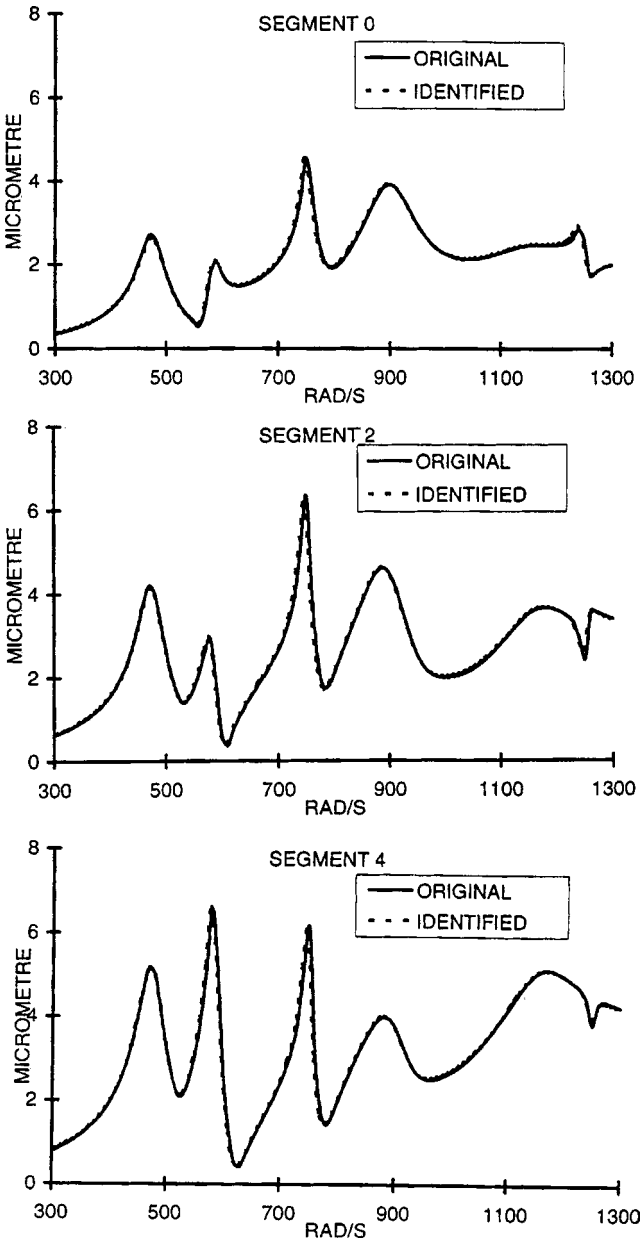

Fig. 9 Unbalance responses for unbalance distribution No. 1

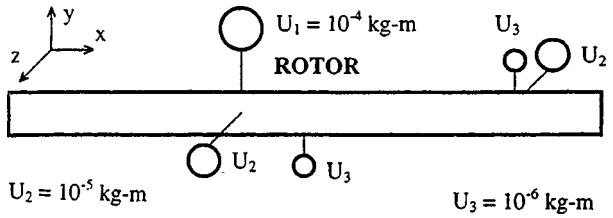

Fig. 10 Unbalance responses for unbalance distribution No. 2

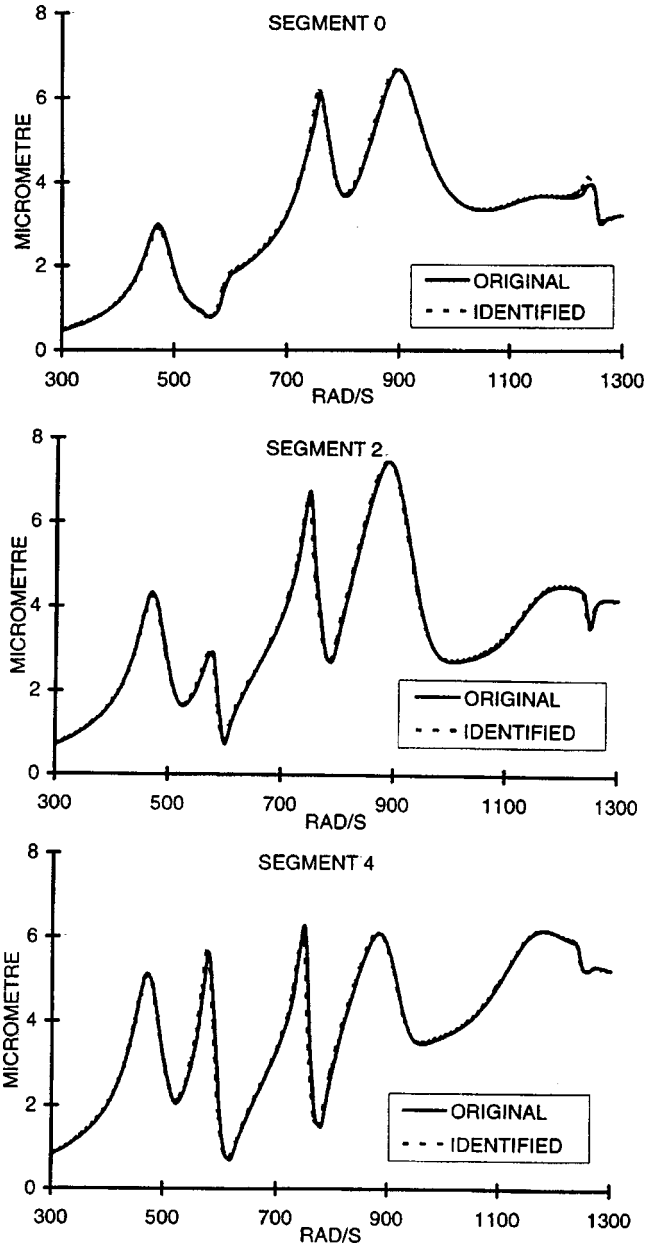

Fig. 11 Unbalance distribution No. 2

The above techniques were restricted to a symmetric casing and neglected flexible casing modes. Extension to more general casings with possibility of casing flexure are left for future work.

Acknowledgments

This work was jointly supported by the Australian Research Council and by Pacific Power International.

Nomenclature

$\mathbf{A}, \mathbf{A}_1, \mathbf{A}_2$ = casing modal matrices
b_x, b_y, b_z = distances of casing support locations from casing mass center
$\mathbf{C}, \mathbf{C}_b$ = casing and bearing damping matrices, respectively
C_x, C_y, C_z = casing support damping in x, y, z directions, respectively
$\mathbf{c}$ = modal damping matrix $= \mathbf{A}^T\mathbf{C}\mathbf{A}$
$\mathbf{D}$ = matrix defined in Appendix A
d_x, d_y, d_z = distances of connections from casing mass center
F_c = subset vector of F containing all nonzero elements
$f; F$ = forces acting on casing; amplitudes thereof
$f_d; F_d$ = $\mathbf{D}f$; amplitudes thereof
$\mathbf{G}$ = matrix defined in Appendix A
$\mathbf{K}, \mathbf{K}_b$ = casing and bearing stiffness matrices, respectively
K_f = lumped casing support stiffness
K_x, K_y, K_z = casing support stiffness in x, y, z directions, respectively
$\mathbf{k}$ = modal stiffness matrix $= \mathbf{A}^T\mathbf{K}\mathbf{A}$
$\mathbf{M}$ = casing mass matrix
$\mathbf{m}$ = modal mass matrix $= \mathbf{A}^T\mathbf{M}\mathbf{A}$
m = assumed number of retained (relevant) modes
m_f = casing mass
n = number of degrees-of-freedom of casing
$q; Q$ = modal displacements of the casing; amplitudes thereof
$u; U$ = casing displacements in terms of casing mass center coordinates, $= \mathbf{G}x$; amplitudes thereof
$x; X$ = casing displacements in terms of translational coordinates; amplitudes thereof
x, y, z = translational displacements of casing mass center
r, s, t = number of force applications in the x, y, and z directions, respectively
$x_{rc}; X_{rc}$ = relative displacements of the rotor in bearings; amplitudes thereof
$\theta_x, \theta_y, \theta_z$ = angular displacements of casing mass center
ζ = modal damping ratio
Ω = excitation frequency
ω = natural frequency

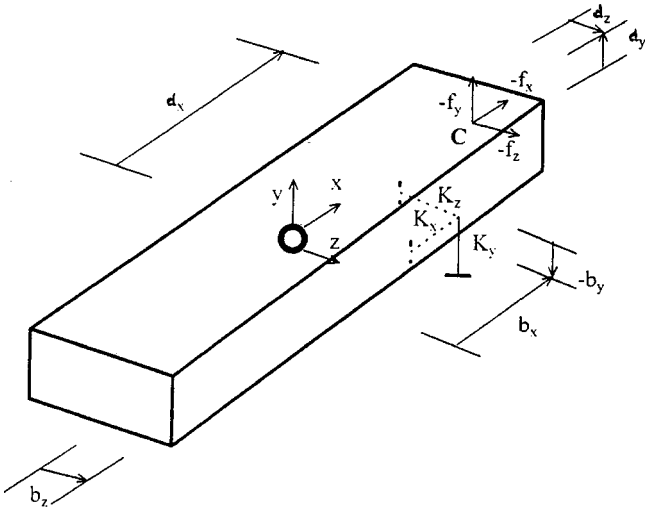

Fig. 12 Rigid casing schematic

Appendix A

Assuming the coordinate axes at the mass center coincide with the principal axes of inertia, the linearized equations of motion for the x and θ_x degrees-of-freedom of the rigid block shown in Fig. 12 are [9]:

$$m_f\ddot{x}+\sum C_x\dot{x}-\sum b_yC_x\dot{\theta}_z+\sum b_zC_x\dot{\theta}_y+\sum K_xx-\sum b_yK_x\theta+\sum b_zK_x\theta_y=\sum f_x \tag{A1}$$

$$I_x\ddot{\theta}_x-\sum b_zC_y\dot{y}+\sum b_yC_z\dot{z}+\sum b_z^2C_y\dot{\theta}_x+\sum b_y^2C_z\dot{\theta}_x-\sum b_xb_zC_y\dot{\theta}_z-\sum b_xb_yC_z\dot{\theta}_y-\sum b_zK_yy+\sum b_yK_zz+\sum b_z^2K_y\theta_x+\sum b_y^2K_z\theta_x-\sum b_xb_zK_y\theta_z-\sum b_xb_yK_z\theta_y=\sum d_yf_z-\sum d_zf_y \tag{A2}$$

where the summations cover all the external forces and moments acting on the rigid casing. Corresponding equations of motion for the y, z, θ_y, and θ_z degrees-of-freedom are obtained by cyclic permutation of x, y, and z. These equations in matrix form are

$$\mathbf{M}\ddot{u}+\mathbf{C}\dot{u}+\mathbf{K}u=\mathbf{D}f, \tag{A3}$$

where

$$u=\{x,y,z,\theta_x,\theta_y,\theta_z\}^T \tag{A4}$$

$$f=\{f_{x1},f_{x2},\ldots,f_{xr},f_{y1},f_{y2},\ldots,f_{ys},f_{z1},f_{z2},\ldots,f_{zt}\}^T \tag{A5}$$

$$\mathbf{D}=\begin{bmatrix} 1 & 1 & \cdots & 1 & 0 & \cdots & \cdots & \cdots & \cdots & \cdots & \cdots & 0 \\ 0 & \cdots & \cdots & 0 & 1 & 1 & \cdots & 1 & 0 & \cdots & \cdots & 0 \\ 0 & \cdots & \cdots & \cdots & \cdots & \cdots & \cdots & 0 & 1 & 1 & \cdots & 1 \\ 0 & \cdots & \cdots & 0 & -d_{z1} & -d_{z2} & \cdots & -d_{zs} & d_{y1} & d_{y2} & \cdots & d_{yt} \\ d_{z1} & d_{z2} & \cdots & d_{zr} & 0 & \cdots & \cdots & 0 & -d_{x1} & -d_{x2} & \cdots & -d_{xt} \\ -d_{y1} & -d_{y2} & \cdots & -d_{yr} & d_{x1} & d_{x2} & \cdots & d_{xs} & 0 & \cdots & \cdots & 0 \end{bmatrix} \tag{A6}$$

$$\mathbf{M}=\begin{bmatrix} m_f & & & & & \\ & m_f & & & 0 & \\ & & m_f & & & \\ & & & I_x & & \\ & 0 & & & I_y & \\ & & & & & I_z \end{bmatrix} \tag{A7}$$

$$\mathbf{K}=\begin{bmatrix} \sum \mathbf{K}_x & 0 & 0 & 0 & \sum b_z\mathbf{K}_x & -\sum b_y\mathbf{K}_x \\ 0 & \sum \mathbf{K}_y & 0 & -\sum b_z\mathbf{K}_y & 0 & \sum b_x\mathbf{K}_y \\ 0 & 0 & \sum \mathbf{K}_z & \sum b_y\mathbf{K}_z & -\sum b_x\mathbf{K}_z & 0 \\ 0 & -\sum b_z\mathbf{K}_y & \sum b_y\mathbf{K}_z & \sum (b_z^2\mathbf{K}_y+b_y^2\mathbf{K}_z) & -\sum b_xb_y\mathbf{K}_z & -\sum b_xb_z\mathbf{K}_y \\ \sum b_z\mathbf{K}_x & 0 & -\sum b_x\mathbf{K}_z & -\sum b_xb_y\mathbf{K}_z & \sum (b_x^2\mathbf{K}_z+b_z^2\mathbf{K}_x) & -\sum b_yb_z\mathbf{K}_x \\ -\sum b_y\mathbf{K}_x & \sum b_x\mathbf{K}_y & 0 & -\sum b_xb_z\mathbf{K}_y & -\sum b_yb_z\mathbf{K}_x & \sum (b_x^2\mathbf{K}_y+b_y^2\mathbf{K}_x) \end{bmatrix} \tag{A8}$$

with a similar expression for **C**.

When measuring the responses, it is the translational motions at selected points that are measured rather than the mass center motions. These motions are related via the transformation:

$$u=\mathbf{G}x. \tag{A9}$$

These translational coordinates (the measured points) in x correspond to those in the force vector f and are selected so as to reflect the vibration modes of interest. When the measured points are defined, the transformation matrix **G** can be established from geometric relations. It can also be derived from the **D** matrix. Thus, let $\mathbf{A}_1$ be the modal matrix corresponding to x and $\mathbf{A}_2$ the modal matrix corresponding to u. On substituting Eq. (A9) into Eq. (A3), since $x=\mathbf{A}_1q$, Eq. (A3) becomes

$$\mathbf{A}_1^T\mathbf{D}^{-1}\mathbf{M}\mathbf{G}\mathbf{A}_1\ddot{q}+\mathbf{A}_1^T\mathbf{D}^{-1}\mathbf{C}\mathbf{G}\mathbf{A}_1\dot{q}+\mathbf{A}_1^T\mathbf{D}^{-1}\mathbf{K}\mathbf{G}\mathbf{A}_1q=\mathbf{A}_1^Tf. \tag{A10}$$

Also, since $u=\mathbf{A}_2 q$, Eq. (*A*3) becomes

$$\mathbf{A}_2^T\mathbf{M}\mathbf{A}_2\ddot{q}+\mathbf{A}_2^T\mathbf{C}\mathbf{A}_2\dot{q}+\mathbf{A}_2^T\mathbf{K}\mathbf{A}_2 q=\mathbf{A}_2^T\mathbf{D}f. \quad (A11)$$

Thus,

$$\mathbf{A}_2^T=\mathbf{A}_1^T\mathbf{D}^{-1} \quad (A12)$$

and

$$\mathbf{A}_2=\mathbf{G}\mathbf{A}_1. \quad (A13)$$

Hence,

$$\mathbf{G}^T=\mathbf{D}^{-1}. \quad (A14)$$

Appendix B

To calculate the unbalance responses of the rotor casing system using the casing modal parameters, the influence coefficients of the casing at the connection points may be found, following a similar approach to that in Ref. [7]. Thus, since $u=\mathbf{A}_2 q$, Eq. (*A*3) is decoupled as

$$\ddot{q}_j+2\zeta_j\omega_j\dot{q}_j+\omega_j^2 q_j=A_{2_j}^T D_j f/m_j \quad (j=1,2,\ldots,m) \quad (B1)$$

with solution, upon harmonic excitation of

$$Q_j=\frac{A_{2_j}^T D_j F}{m_j(s^2+2\zeta_j\omega_j s+\omega_j^2)} \quad (B2)$$

where $s=j\Omega$. From Eqs. (*A*9) and (*A*14), since $u=\mathbf{A}_2 q$

$$X=\mathbf{G}^{-1}U=\mathbf{D}^T\mathbf{A}_2 Q=\mathbf{A}_1 Q \quad (B3)$$

so that

$$X=\sum_{j=1}^{m}\frac{A_{1_j}^T F}{m_j(s^2+2\zeta_j\omega_j s+\omega_j^2)}A_{1_j}. \quad (B4)$$

The influence coefficients are then given by

$$G_{ik}(s)=\sum_{j=1}^{m}\frac{A_{1_{ij}}A_{1_{kj}}}{m_j(s^2+s\zeta_j\omega_j s+\omega_j^2)}(i,k=1,2,\ldots,m). \quad (B5)$$

References

[1] Cottin, N., Felgenhauer, H. P., and Natke, H. G., 1984, "On the Parameter Identification of Elastomechanical Systems Using Input and Output Residuals," Arch. Appl. Mech., **54**(5), pp. 378–387.

[2] Leuridan, J. M., Brown, D. L., and Allenmang, R. J., 1983, "Direct System Parameter Identification of Mechanical Structures With Application to Modal Analysis," *8th International Seminar on Modal Analysis*, Katholieke Universiteit Leuven, Leuven, pp. 201–208.

[3] Lees, A. W., 1988, "The Least Square Method Applied to Identify Rotor/Foundation Parameters," *Proc. Intl Conference on Vibrations in Rotating Machinery*, IMechE, Edinburgh, IMechE, London, pp. 209–215.

[4] Cheli, F., Dedini, F. G., and Vania, A., 1992, "Supporting Structure Effect on Rotating Machinery Vibration," *Proc. Intl Conference on Vibrations in Rotating Machinery*, IMechE, Bath, IMechE, London, pp. 543–548.

[5] Feng, N. S., and Hahn, E. J., 1995, "Including Foundation Effects on the Vibration Behavior of Rotating Machinery," Mech. Syst. Signal Process., **9**(3), pp. 243–256.

[6] Feng, N. S., and Hahn, E. J., 1996, "Experimental Identification of the Foundation Dynamic Stiffness Parameters of Rotor-Bearing-Foundation Systems," *Proceedings of the 6th International Symposium on Transport Phenomenon and Dynamics of Rotating Machinery*, Honolulu, Pacific Center of Thermal-Fluids Engineering, Honolulu, HI, **1**, pp. 48–57.

[7] Feng, N. S., and Hahn, E. J., 1996, "Turbomachinery Foundation Identification Using Foundation Modal Parameters," *Proceedings ISMA-21 Noise and Vibration Engineering Conference*, **III**, Katholieke Universiteit Leuven, Leuven, pp. 1503–1513.

[8] IMSL, 1995, STAT/LIBRARY, IMSL Inc., Version 3.0.

[9] Meriam, J. L., 1975, *Dynamics*, SI Version, 2nd Ed., John Wiley and Sons, New York.

Predicted Geometry Effects on Oil Vapor Flow Through Buffer-Gas Labyrinth Seals

S.-Y. Park
Graduate Assistant

D. L. Rhode
Professor

Mechanical Engineering Department,
Texas A&M University,
College Station, TX 77843

Mass transport characteristics of buffer-gas labyrinth seals operating in the flooded, nonmist regime were studied using numerical simulations. Discussion is given of the extension, to account for oil vapor mass transport, of a finite volume computer code that was previously validated using nonoil labyrinth hot-film anemometer as well as leakage measurements. A parametric study was conducted to obtain a first understanding of oil vapor transport from the liquid film on the stator wall and to assist oil seal designers. Various geometry effects with various oil film lengths were investigated. It was found in the present investigation that increasing the buffer gas pressure can increase the oil vapor mass flow to the process gas due to increased evaporation from the liquid oil film. In addition, it was found that buffer-gas mass flow is mainly affected by the clearance and the total flow area of the buffer-gas injection. [DOI: 10.1115/1.1520540]

Introduction

A labyrinth seal is a noncontacting device used to reduce leakage flow or to maintain a certain leakage to provide desired cooling, buffering, or purging between two regions of different pressure. The present work focuses on its application to isolate process gas from oil-vapor-contaminated bearing gas by injecting a noncontaminated buffering gas into the seal (see Fig. 1). If the injection gas pressure is high enough, a portion of it flows axially through the seal in both directions in order to exit from both axial ends of the seal.

In such a buffered oil labyrinth there can be a small amount of oil vapor ''back diffusion,'' which is the phenomenon wherein oil vapor from the oil sump is diffused in the direction opposite to that of the seal fluid throughflow, i.e., toward the process gas end of the seal. This diffusion is due to the difference between the oil vapor concentration of the bearing chamber (saturated) and that of the process gas (essentially zero concentration). The injection pressure of the buffer gas is often increased above the threshold pressure (required to prevent bearing gas flow to the process gas) in an attempt to isolate bearing oil vapor from the process gas. However, even for very high injection pressures, a significant amount of oil vapor has been found on the process gas side of the seal. Turbomachinery designers attribute this to the presence of a liquid film inside the labyrinth (called ''flooding'') that in some cases is believed to form during startup of the turbomachine.

Based on conversations with manufacturers, it appears that there are several operating regimes for oil labyrinths. One of these is the ''nonflooded'' regime that apparently results from favorable bearing system design and favorable machine startup conditions. It is believed that the axial length of the oil film within the seal depends on details of the oil pump-bearing system behavior during machine startup, as well as the design of the bearing-seal system. However, the regime that is considered here is the ''flooded, nonmist'' regime (i.e., without the presence of significant oil mist particles). This latter regime is applicable for (a) the nonmist type of bearing lubrication, (b) low and moderate peripheral speeds, (c) the presence of an effective centrifugal slinger to prevent oil particles from entering the seal, and (d) a teeth-on-stator labyrinth configuration with fairly low velocities. The configuration of (d) above allows the centrifugal force on a fluid (gas) particle within the seal to inhibit any oil particles within the seal from substantially leaving the liquid oil film that rotates at fairly low circumferential velocity around the radially outer portion of the stator housing (see Fig. 1).

Previous Work

No investigation has been reported that gives design information, design insight or a parametric understanding regarding the oil film mass transfer in the flooded buffer-gas labyrinth seal. However for the nonflooded operating regime (i.e., no oil evaporation), Park and Rhode [1] presented design curves for buffered and nonbuffered labyrinths. Specifically, the minimum (i.e., critical) pressure and flow rate at which noncontaminated buffer gas must be injected to prevent oil vapor from leaking to the process gas was given for a range of seal geometries and operating conditions. In addition, the vapor flow and bearing gas flow for a wide range of bearing and injection (where present) pressures were given for buffered as well as nonbuffered labyrinths.

Boyman and Suter [2] provided an interesting paper on the identification of contaminant transport mechanisms in a buffered labyrinth. However, important information regarding operating conditions and geometric dimensions was not provided. They measured back diffusion using propane gas in a teeth-on-rotor labyrinth seal. Using a true-scale (i.e., full-size) test model, the minimum buffer-gas flow rates that prevent back diffusion were found, and a large-scale model was employed to visualize the flow behavior using a colored dye.

Concerning related work on nonseal geometries, for the case of tritium back diffusion in a laboratory against ventilation air flow passing through a small clearance around a closed door, the amount of back diffused tritium was calculated and an emergency evacuation strategy was discussed by Nguyen [3]. Similarly, the contaminant back diffusion and contaminant surface transport in a simple pipe ventilation system were investigated by Verma et al. [4]. The latter also computed the minimum purge gas flow rate necessary to prevent the contaminant from entering a clean chamber for various gases.

For impinging two-dimensional slot jet flow, Alkire and Ju [5] obtained experimental correlations for the Sherwood number for three different flow regions as functions of Reynolds number, Schmidt number, radial distance from the slot to the opposing wall, and the axial distance from the slot jet. Also, similar correlations were made for a submerged oblique impinging slot jet by Chin and Agarwal [6]. Significant decreases of the mass transfer

Contributed by the Structures and Dynamics Division of THE AMERICAN SOCIETY OF MECHANICAL ENGINEERS for publication in the ASME JOURNAL OF ENGINEERING FOR GAS TURBINES AND POWER. Manuscript received by the S&D Division July 2000; final revision received by the ASME Headquarters Sept. 2002. Associate Editor: M. Mignolet.

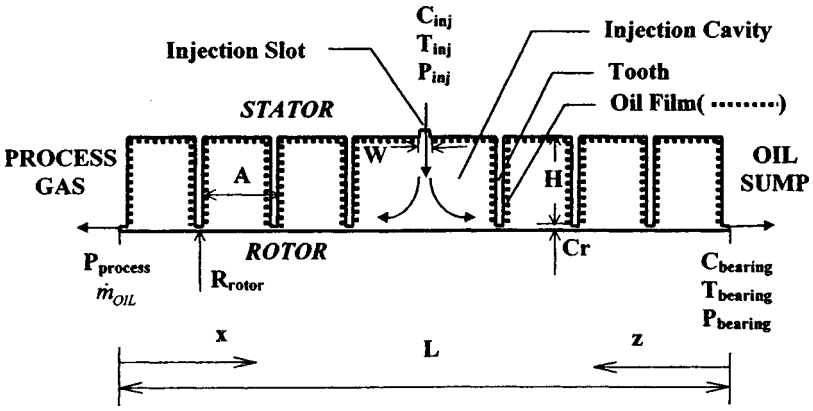

Fig. 1 Schematic diagram of the buffer-gas labyrinth seal

rate were observed for a slot jet angle smaller than 60 deg, but the variation of nozzle height had only a small effect on the mass transfer.

Recently, the mass transfer characteristics of an impinging slot jet on a rotating cylinder were investigated by Pekdemir and Davies [7]. They found the length of the potential core region is at most the ratio of the slot height H (see Fig. 1) to the slot width W equal to approximately 4. For H/W>4, the Sherwood number shows some dependency upon H/W. In addition, Chen and Modi [8] investigated the turbulent jet impingement mass transfer and heat transfer on a plain wall, using numerical simulation with the k-ω turbulence model. Ignoring the very slight density change caused by the concentration distribution, the concentration field was uncoupled from the velocity field so that the concentration field could be solved after obtaining the velocity solution. Then a finer grid was used to solve the concentration distribution by interpolating the fluid flow from the coarser grid solution. It was reported that the ratio H/W in the range from 2 to 8 had a very small effect on the Sherwood number.

All the back diffusion studies previously investigated are for laminar flow, i.e., Re=1~3. However, preliminary computations for turbulent flow in the present study of the buffer-gas seal confirmed that no back diffusion occurs in the seal due to the high buffer-gas exit velocity opposing the oil back diffusion. Stated differently, convection toward the bearing dominates over oil vapor back-diffusion attempting to enter the seal.

As mentioned above, no investigation has reported oil transport information from a thin oil film on an interior wall of a labyrinth seal. Further, the proprietary "in-house" design methods of turbomachinery manufacturers could not be based on oil vapor mass transfer information from the liquid film within a flooded labyrinth. Due to the present vacuum of information for flooded oil labyrinths, nearly any useful information from numerical or experimental techniques will be very helpful.

Objective

The objective of the present investigation is to obtain a parametric understanding and design insight of the factors influencing the characteristics of the buffered oil labyrinth in the flooded, nonmist operating regime. There is an extremely wide range of oil labyrinth designs, bearing designs, operating conditions, machine transients, etc., that exhibit important effects on oil labyrinth behavior. Further, for each specific turbomachine, a large number of bearing-seal system geometric and operational details are required in order to predict the transients of the liquid oil film axial length. Thus to obtain a generic basic understanding, the oil film axial length had to be considered as a parameter to be varied in this parametric study.

Numerical Model

The numerical model employed herein uses the well known finite volume approach, [9], employing the SIMPLEC algorithm, [10], with the high-Re k-ε turbulence model and the QUICK, [11], convective difference scheme. The present numerical work involves the extension (for the transport of chemical species) of a computer code that has been extensively validated against a wide variety of measurements over a wide range of nonoil labyrinth swirl flow conditions. Quite reasonable agreement with hot-film anemometer measured distributions within a labyrinth chamber was found by Demko, Morrison, and Rhode [12]. Also, good agreement (usually within 8 percent) with orifice meter measurements of labyrinth leakage was obtained by Rhode and Hibbs [13] and by Rhode and Adams [14]. Further, using a very similar numerical method, good agreement with labyrinth leakage measurements has been found by Zimmermann and Wolf [15] and by Wittig et al. [16].

The continuity, momentum, energy, and concentration transport equations can be expressed in the following common form using cylindrical two-dimensional axisymmetric coordinates

$$\frac{1}{r}\left[\frac{\partial}{\partial x}(\rho u r\phi)+\frac{\partial}{\partial r}(\rho v r\phi)-\frac{\partial}{\partial x}\left(r\Gamma_\phi\frac{\partial\phi}{\partial x}\right)-\frac{\partial}{\partial r}\left(r\Gamma_\phi\frac{\partial\phi}{\partial r}\right)\right]=S_\phi \tag{1}$$

where ϕ and S_ϕ represent the generalized dependent variable and the source term according to each governing equation, respectively. For example, $\phi=C$, $\Gamma_\phi=\mu_t/Sc_t=\rho D_{AB}$, and $S_\phi=0$ in the concentration equation.

The mass transfer model involving the thin liquid oil film is developed under the following main assumptions: (a) the density variation of the buffering gas (air) due to the oil vapor concentration distribution is small enough that the concentration computation can be uncoupled from the velocity field computation; (b) the oil film has the saturated concentration value at each computed local temperature; (c) the oil film exists only on the stator wall because the centrifugal force along the rotor prevents a film; and (e) the existence of the oil film is considered as a steady-state boundary condition. Assumption (c) above is easily justified by considering that the centrifugal force cause-effect relationship in the buffer labyrinth is very similar to that in the bearing chamber. Specifically, there is a large amount of experimental evidence by, for example, Wittig et al. [17] and by Chew [18] giving various details of the thin liquid oil film circumferentially flowing around the radially outer housing of the bearing chamber in aircraft gas turbines.

One can calculate the saturated wall concentration for each computed local temperature using

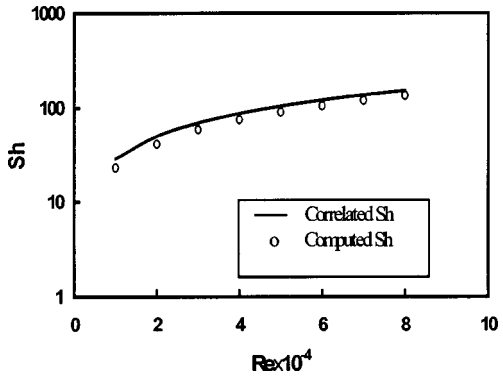

Fig. 2 Comparison of computed and empirical-correlation Sherwood number with Reynolds number for pipe flow

$$C_{\mathrm{SAT}}=\frac{P_{\mathrm{SAT}}}{\Re T_{\mathrm{SAT}}} \tag{2}$$

where $\Re$ [Nm/(Kgmol K)] is the universal gas constant, and the saturation pressure (P_{SAT}) for the computations was obtained for a common bearing oil by fitting a least squares curve to the tabular pressure and temperature data that was obtained from a lubricating oil manufacturer. Also, the molecular mass diffusivity ($D_{AB}=2.3744\times10^{-6}\,\mathrm{m^2/sec}$) of the oil was calculated by following the procedure of Rohsenow and Hartnett [19] and Özisik [20].

To avoid computing within the near wall region, the concentration wall function was utilized. Specifically, the empirical *P*-function proposed by Jayatilleke [21] was used to relate the oil vapor concentration flux from the wall to the oil vapor concentration at the near wall grid point. The concentration flux at the cavity base wall can be expressed as

$$D_{AB}\left.\frac{\partial C}{\partial r}\right|_{\mathrm{WALL}}=\frac{\mu}{\rho \mathrm{Sc}}\left(\frac{C_{\mathrm{WALL}}-C_P}{y_P}\right) \quad y^+\leqslant 11.63 \tag{3}$$

$$D_{AB}\left.\frac{\partial C}{\partial r}\right|_{\mathrm{WALL}}=\frac{C_\mu^{1/4}k^{1/2}(C_{\mathrm{WALL}}-C_P)}{\mathrm{Sc}_t(U^++P)}y^+>11.63 \tag{4}$$

where

$$U^+=\frac{1}{\kappa}\ln(Ey^+)$$

$$P=9.24\left[\left(\frac{\mathrm{Sc}}{\mathrm{Sc}_t}\right)^{3/4}-1\right]\left[1+0.28\exp\left(\frac{-0.007\mathrm{Sc}}{\mathrm{Sc}_t}\right)\right]$$

where y_P in Eq. (3) is the distance from the wall to the nearest grid point, and C_P is the concentration value at the nearest grid point.

Following the recommendation of Jayatilleke [21], the turbulent Schmidt number in the model has been calibrated to give concentration solutions that match an appropriate experimental correlation. Specifically, the correlation of Dittus and Boelter [22], which is $\mathrm{Sh}=0.023\,\mathrm{Re}^{0.8}\,\mathrm{Sc}^{0.4}$, was selected and used in Sherwood number form. Specifically, fully developed turbulent pipe flow was computed in which the wall had a liquid ammonia film. For each different Reynolds number computation, a different grid system was used so that a near-wall grid point of approximately $y^+=20$ was maintained. The local mass transfer coefficient and Sherwood number are defined as

$$h_m=\frac{D_{AB}\left.\frac{\partial C}{\partial r}\right|_{\mathrm{WALL}}}{C_{\mathrm{WALL}}-C_{\mathrm{REF}}}, \quad \mathrm{Sh}=\frac{h_m D_h}{D_{AB}}. \tag{5}$$

The Sherwood number is the dimensionless mass transfer coefficient. The radially averaged bulk concentration value at each axial location has been used as the reference concentration value, C_{REF}, to evaluate the Sherwood number. As shown in Fig. 2, the turbulent Schmidt number of 0.5 gives reasonable agreement with the correlated Sherwood number.

The concentration axial gradient at the process gas exit of the seal was set to zero. This boundary condition was verified with a series of numerical experiments. Specifically, a fictitious length of annular channel without a liquid film was added to the process gas end of the seal. The resulting mass flow of oil vapor in the channel was essentially identical to that for the presently used $\partial C/\partial x=0$ at the junction where the channel begins ($x=0$ in Fig. 1). In addition, the concentration boundary condition along the rotor surface was specified as zero normal gradient.

The oil vapor mass flow rate has been evaluated from each solution at the process gas end of the seal and at each tooth tip location by numerically evaluating the following relation:

$$\dot{m}_{\mathrm{OIL}}=M_{\mathrm{OIL}}2\pi\int_{Ri}^{Ro}\left[uC-D_{AB}\frac{\partial C}{\partial x}\right]_x r\,dr. \tag{6}$$

The first term inside the bracket of Eq. (6) represents the oil vapor transport due to convection, and the second is that due to diffusion. The convection term is the dominant term.

Results

Figure 1 shows the buffer-gas labyrinth seal that attempts to prevent oil vapor from reaching the process gas by injecting buffer-gas through the injection slot. The injection slot is located at the center of the injection cavity so that the pitch of the injection cavity is twice that of other cavities. The thickness of each tooth is 0.38 mm (0.015 in.), and the length of the seal (L) and the radius of the rotor (R_i) are 30.86 mm (1.22 in.) and 100.13 mm (3.94 in.), respectively.

Actual buffer-gas labyrinth seals typically have a series of 16 or more equally spaced injection holes around the circumference instead of a slot. Because these consecutive holes are circumferentially very closely spaced, the strong turbulent diffusion mixes the jets together very quickly. Therefore the effect of the total hole area can be approximated as that of an axisymmetric slot of the same total area. Considering the uncertainties from the standard k-ε turbulence model, this is a very reasonable approximation.

To investigate the geometry effects, the injection slot width (W), the cavity depth (H), the tooth pitch (A), and the radial clearance (Cr) are varied. The injection slot width is varied from 0.25 mm to 0.76 mm; the cavity depth from 2.54 mm to 7.62 mm; the pitch from 3.81 mm to 7.62 mm; and the clearance from 0.18 mm to 0.36 mm. The variation of the clearance and the injection slot width substantially change the buffer mass flow rate. Also, the pitch and the cavity depth are related to the area of the oil film covering the stator wall.

The seal operating conditions in the present study are given in Table 1. The buffer gas enters the injection cavity with zero oil concentration. The oil vapor concentration at the bearing end of the seal, C_{bearing}, is considered to be the saturated concentration value for the given bearing temperature, T_{bearing}. The saturated oil concentration on the stator wall and the bearing oil concentration are obtained using Eq. (2).

Grid Independence. For grid independence testing, the total air mass flow rate through the injection slot and the vapor mass flow rate to the process side were obtained and compared for three different grids. Two different seal geometries were considered, each with a different value of clearance and cavity depth. All grid systems have many highly nonuniform regions in the x and r-directions. As shown in Tables 2(a) and 2(b), grid sizes of 140×37 and 140×27 were selected, as they are considered to be sensibly grid independent.

Table 1 Operating condition

	Operating Condition
RPM	12,000
P_{inj}	169 kPa
$P_{bearing}$	100 kPa
$P_{process}$	100 kPa
T_{inj}	298 °K
$T_{bearing}$	344 °K
C_{inj}	0.0 kgmol/m^3
$C_{bearing}$	3.2×10^{-6} kgmol/m^3

Flow Field and Concentration Distributions. The flow structure of an impinging jet, such as the buffer throughflow jet, can be categorized into the following flow regions: jet flow, stagnation, wall jet (cross flow), and jet entrainment. The jet flow region extends from the slot to the beginning of the stagnation region near the rotor under the injection slot. The wall jet region starts just after the stagnation zone along the rotor. The jet entrainment region is the region adjacent to the jet flow region where a portion of the surrounding fluid is entrained by the jet.

A generalized impinging jet flow can be divided into three zones: potential core, developing, and developed. The characteristics of these flow zones depend on the turbulence intensity in the slot. For the case of an impinging jet on a stationary flat plate, the jet potential core extends approximately five slot widths, [23]. For the present geometry in Fig. 1, the distance from the jet origin to the rotor is about 10 slot widths, so even though the rotor is not a flat plate, the developing and the developed zones may exist after the potential core region. The developing zone is an important region for oil vapor transport because a large shear stress is generated along the boundary of the jet. This large shear stress facilitates the entrainment of high concentration recirculated fluid and generates turbulence which promotes intense mixing between the jet and the recirculated flow.

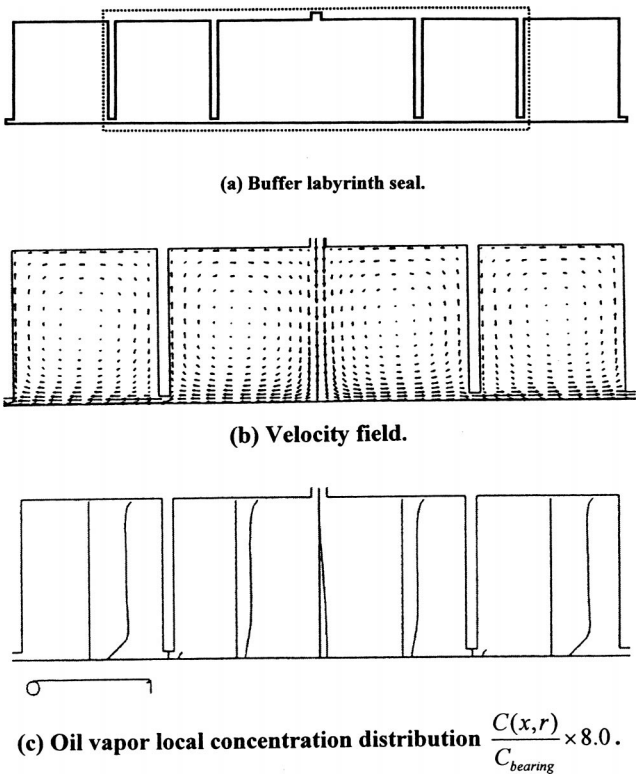

Fig. 3 Flow fields and radial concentration distribution of the seal

Table 2 Grid independence

(a) Cr = 0.25 mm (0.01 in), W = 0.51 mm (0.02 in), H = 5.08 mm (0.2 in), A= 3.81 mm (0.15 in).

Grid Size NI×NJ	$\dot{m}_{AIR}$ [Kg/s]	$\dot{m}_{OIL}$ [Kg/s]	$\frac{\dot{m}_{finer}-\dot{m}_{coarser}}{\dot{m}_{finer}}$ [%]	
			$\dot{m}_{AIR}$	$\dot{m}_{OIL}$
117×27	6.82×10^{-2}	2.13×10^{-6}	1.4	2.5
140×37	6.72×10^{-2}	2.18×10^{-6}	0.43	1.6
197×41	6.75×10^{-2}	2.15×10^{-6}	-	-

(b) Cr = 0.36 mm (0.014 in), W = 0.51 mm (0.02 in), H = 2.54 mm (0.1 in), A= 3.81 mm (0.15 in).

Grid-Size NI×NJ	$\dot{m}_{AIR}$ [Kg/s]	$\dot{m}_{OIL}$ [Kg/s]	$\frac{\dot{m}_{finer}-\dot{m}_{coarser}}{\dot{m}_{finer}}$ [%]	
			$\dot{m}_{AIR}$	$\dot{m}_{OIL}$
117×17	9.72×10^{-2}	2.18×10^{-6}	0.13	9.4
140×27	9.74×10^{-2}	2.40×10^{-6}	0.03	0.4
179×31	9.74×10^{-2}	2.41×10^{-6}	-	-

Figure 3(*b*) shows only three cavities in the middle of the buffer-gas labyrinth seal. The flow enters through the injection slot located on the cavity stator wall of the wide, injection cavity and bifurcates to both the process side and the bearing side of the seal. There are two recirculation zones in the injection cavity and one zone in the others. The recirculated flow has a high oil vapor concentration due to the presence of the oil film on the stator wall. Specifically, the liquid oil film on the stator wall constitutes a source of oil vapor via evaporation at the liquid-air interface. Because of the entrainment and intense turbulent mixing of the jet with the recirculation flow, the high oil vapor concentration that occurs near the stator wall contaminates the throughflow jet and is thus convected (i.e., carried) by the jet to the adjacent labyrinth cavities.

There are two main differences between the basic flowfield of the present study and that of the general impinging jet. One of these is that the impingement wall is herein a high rotating surface, and the other is that no oil film is herein considered on the impinged wall (rotor surface). Stagnation and wall jet regions along the impinged surface would be the most active and important zones for the heat and mass transfer of the general impinging jet, [24], but these two regions have a very small effect on the oil vapor mass transfer since the oil film exists only on the stator wall. The entrainment region is expected to be the most important region in the present situation.

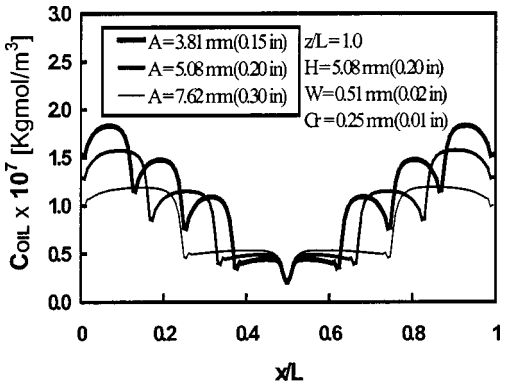

Fig. 4 Axial oil vapor bulk concentration distribution for various tooth pitch (*A*) values

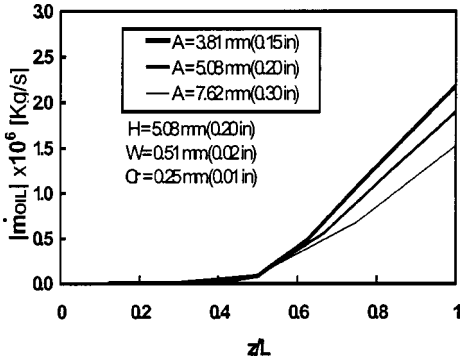

Fig. 5 Variation of seal-exit oil vapor mass flow with tooth pitch (*A*) and oil film length (*z*/*L*)

Starting at the injection slot ($x/L=0.5$) in Fig. 3(*c*), a fluid particle of buffer gas enters the injection cavity with zero oil vapor concentration, and its concentration increases as it flows radially inward and then toward either the bearing end of the seal or the process gas end of the seal. This increase is primarily the result of turbulent oil vapor diffusion from the recirculation zone within each cavity (higher concentration) with which the throughflow jet particle (lower concentration) comes in contact. The recirculation zones have higher vapor concentration because of the evaporation of liquid oil along the stator surfaces of the seal, as well as any vapor that may enter the seal from the bearing sump via (molecular) back-diffusion (see Introduction). Because of the presence of the evaporating oil film on the stator wall, a maximum concentration value (for a particular cavity) is seen there, along with a minimum value on the rotor wall where the centrifugal force prevents a film from forming. Inside a labyrinth cavity, except near the walls, the radial concentration distribution is fairly constant due to the turbulent diffusion mixing in the recirculation zone. The concentration within a cavity shows a larger magnitude compared to that of the throughflow-jet along the rotor because low vapor concentration buffer gas is predominantly found along the rotor. The cavity with the lowest cavity-average concentration is the injection cavity due to its turbulent diffusion mixing with the zero-concentration entering throughflow jet. The average concentration within a cavity increases toward either end of the seal because the concentration of the throughflow jet that is mixing with the cavity recirculation zone increases toward either end of the seal.

Effects of Tooth Pitch (*A*). The tooth pitch, defined in Fig. 1, has a large effect on the oil concentration field because the surface area of the film-coated teeth directly affects the amount of the evaporation source of the vapor. The bulk concentration shown here is defined as

$$C_{\mathrm{BULK}}(x)=\frac{\int_{Ri}^{Ro} C\rho urdr}{\int_{Ri}^{Ro} \rho urdr}. \tag{7}$$

In the bulk concentration distribution of Fig. 4, the effect of the pitch is shown. A local minimum of the bulk concentration is found at the impingement point ($x/L=0.5$) on the rotor, as well as at each tooth clearance, where the throughflow jet exclusively occurs. As expected, this results from the low vapor concentration of the buffer jet. Observe that C_{OIL} increases significantly as the tooth pitch decreases, i.e., as the number of teeth (oil evaporating surface area) increases. For all cases, the bulk concentration at the locations occupied by the throughflow-jet has a smaller value than that in the recirculation zone locations because the throughflow-jet consists predominantly of low vapor-concentration buffer gas. The diffusion of oil vapor into the throughflow-jet begins at the injection slot and continues as the jet continues along the rotor. Thus the local concentration values along the rotor increase gradually toward either end of the seal as seen in Fig. 3(*c*). The concentration distribution of the three different pitch cases shown (Fig. 4) are essentially symmetric, which means negligible vapor back diffusion from the bearing toward the process end (defined in the Introduction), is occurring at the present operating condition. The reason for negligible vapor back-diffusion is that vapor convection toward the bearing dominates over vapor back-diffusion toward the process gas. Also, observe that the concentration distribution under the injection slot ($x/L=0.5$) for each pitch case is the same. This is not surprising because the number of teeth (i.e., amount of oil evaporation surface) in the seal cannot affect the vapor diffusion from the injection cavity to the entering buffer jet.

Even though the larger pitch has slightly more buffer-gas mass flow, the smaller tooth pitch gives more vapor mass flow toward the process side. This is because the smaller tooth pitch gives more teeth and thus more oil evaporation surface area. Figure 5 shows the vapor mass flow due to the different pitch values of Fig. 4 and to various oil film lengths (z/L). As expected, the vapor mass flow increases as the oil film length (z/L) increases, and as the pitch decreases for a given film length. The slope of the vapor mass flow rate in Fig. 5 changes dramatically near $z/L=0.5$ because of the buffer-gas injection there. This is because any liquid film occurring between the injection slot and the process gas is carried efficiently to the process end of the seal by the buffer gas. Observe that the maximum vapor mass flow occurs for $z/L=1.0$ and for the smallest pitch. As shown in Fig. 5, the vapor mass flow decreases by approximately 30 percent as the pitch increases from 3.81 mm (0.15 in.) to 7.62 mm (0.3 in.).

Effects of Cavity Depth (*H*). Figures 6 and 7 show the concentration and oil vapor mass flow for various cavity depths. Basically, increasing the cavity depth means lengthening the oil film,

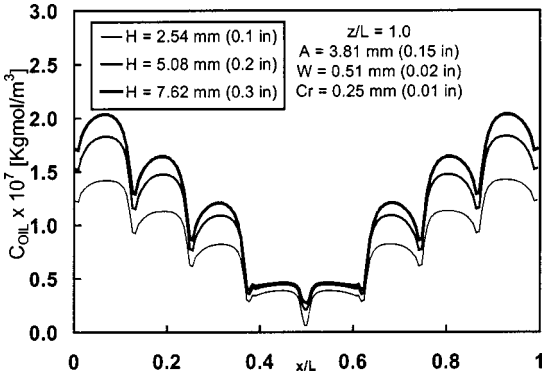

Fig. 6 Axial oil vapor bulk concentration distribution for various cavity depth (*H*) values

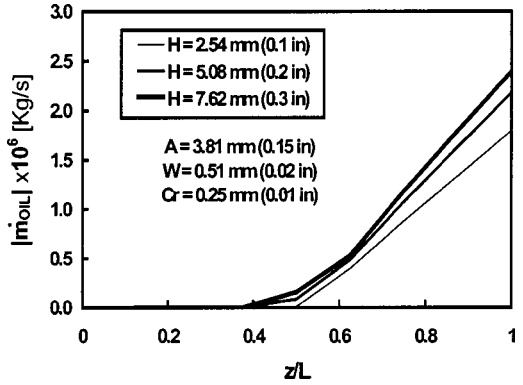

Fig. 7 Variation of seal-exit oil vapor mass flow with cavity depth (*H*) and oil film length (*z*/*L*)

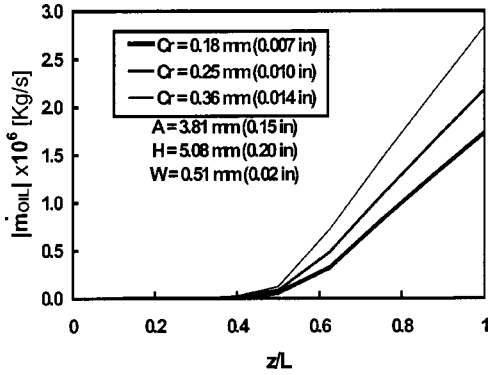

Fig. 9 Variation of seal-exit oil vapor mass flow with tooth clearance (*Cr*) and oil film length (*z*/*L*)

increasing the recirculation zone size, and increasing the area for vapor diffusion from the injection cavity to the entering buffer jet. The concentration distribution in Fig. 6 is again symmetric and similar in shape to that of Fig. 4. However, the concentration variation with cavity depth under the injection slot ($x/L=0.5$) is quite different here. Increasing the cavity depth gives the entering buffer jet more length in which the entrainment region plays a role in increasing the concentration under the slot. Due to the lengthened oil film and the resulting increased mixing time in the injection cavity, the vapor mass flow and the concentration increase as the cavity depth increases. As shown in Fig. 7, the vapor mass flow increases by approximately 33 percent as cavity depth increases from 2.54 mm (0.1 in.) to 7.62 mm (0.3 in.).

Effects of Tooth Clearance (*Cr*). The tooth clearance is generally considered to be one of the most important dimensions in seal design. Increasing the seal clearance massively increases the buffer-gas mass flow for a given injection pressure. In the injection cavity, as shown in Fig. 8, the clearance variation has a small effect on the bulk concentration distribution, but as the throughflow passes across the cavities, the larger clearance has a somewhat smaller vapor concentration because the increased buffer gas flow dilutes the oil vapor bulk concentration in the throughflow jet. However, the larger clearance increases the vapor mass flow as shown in Fig. 9. Also, note that for $z/L<0.5$, the vapor mass flow change is small, but for $z/L>0.5$ the slope increases gradually with increasing clearance. As shown in Fig. 9, the vapor mass flow decreases by approximately 39 percent as the clearance decreases from 0.36 mm (0.014 in.) to 0.18 mm (0.007 in.).

Effects of Injection Slot Width (*W*). The injection slot width also has a significant effect on the velocity field, the concentration distribution, and the oil vapor mass flow as shown in Figs. 10, 11, and 12. Unlike increasing the clearance, widening the slot for the present cases increases the pressure inside the injection cavity slightly, and this slightly increases the buffer-gas mass flow toward the process side as shown in Fig. 10. Thus, the increased buffer-gas mass flow in this situation is not responsible for the large concentration changes shown in Fig. 11. Specifically, observe the decrease of concentration between $W=0.25$ mm and $W=0.51$ mm. Because the narrow slot of $W=0.25$ mm has almost the same buffer-gas flow with only half the flow area, the injection velocity and hence the turbulence energy production are much higher. Thus the oil evaporation and vapor diffusion in the injection cavity are substantially higher for $W=0.25$ mm. When the slot width is widened from $W=0.25$ mm to 0.51 mm, the bulk concentration at the process side exit decreases about 30 percent,

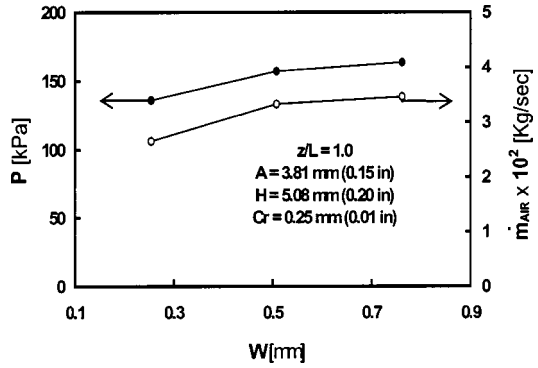

Fig. 10 Variation of injection cavity pressure and the buffer-gas mass flow to the process side with injection slot width (*W*)

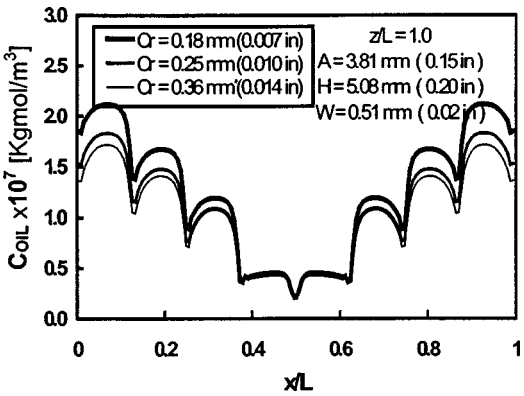

Fig. 8 Axial oil vapor bulk concentration distribution for various tooth clearance (*Cr*) values

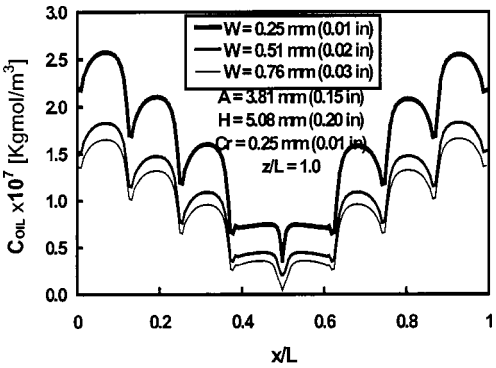

Fig. 11 Axial oil vapor bulk concentration distribution for various injection slot width (*W*) values

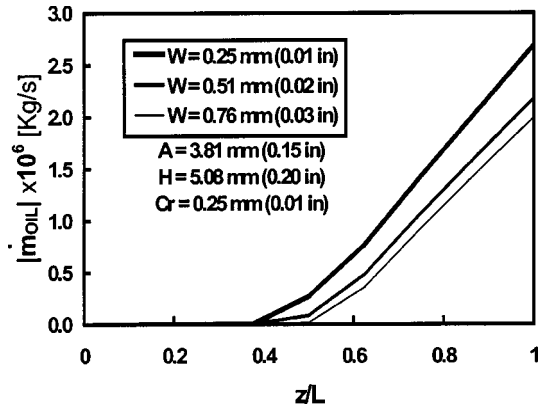

Fig. 12 Variation of seal-exit oil vapor mass flow with injection slot width (W) and oil film length (z/L)

and the process side bulk exit velocity increases about 20 percent. As a result, the vapor mass flow shows about 17 percent reduction (see Eq. (6)).

Summary

The vapor mass transfer characteristics for the flooded, nonmist regime of a buffer-gas labyrinth were investigated for the first time. Discussion is given of the extension, to account for vapor transport, of a finite volume computer model that was previously validated using nonoil labyrinth measurements. Specifically, a parametric study was conducted to (a) understand vapor mass transfer within the seal and (b) assist designers in minimizing vapor flow to the process gas. To understand the convective and diffusive vapor characteristics within the seal, radial and axial vapor concentration distributions were obtained and examined for various buffer-gas seal geometries. The specific geometry dimensions considered include tooth pitch, tooth clearance, cavity depth, and injection slot width. For the cases considered it was found that increasing the buffer-gas flow rate (i.e., the pressure) to prevent back diffusion of vapor from the bearing can increase the vapor flow to the process gas.

For the cases considered, it was determined that

1 an increase of the pitch and a decrease of the cavity depth reduce the surface area of the oil film so that the vapor concentration and the vapor mass flow rate decrease.

2 an increase of the seal clearance greatly increases the buffer-gas mass flow rate. Consequently, the vapor concentration is slightly reduced due to the dilution of the throughflow vapor concentration at increased injection rates. However, the vapor mass flow rate is increased because the large increase of buffer gas flow carries out more vapor.

3 an enlarged injection slot width reduces the injection cavity turbulence energy, and thus the liquid evaporation and diffusivity there, so that the throughflow vapor concentration is substantially reduced. Thus the vapor mass flow rate decreases because of the diluted vapor concentration and other local effects.

4 the oil film length, i.e., the film surface area, has a very strong effect on the vapor mass transport to the process side of the seal.

Finally, it has been shown for the flooded, nonmist regime that the vapor mass flow can be drastically reduced with slight changes of seal geometry, but it is impossible to completely stop oil vapor transport.

Acknowledgment

The authors are indebted to the Texas Advanced Technology Program for partial support and to the Supercomputer Center at Texas A & M University for a grant of SGI Power Challenge CPU time.

Nomenclature

A = tooth pitch (mm)
C = oil vapor concentration (kgmol/m^3)
Cr = clearance of the seal (mm)
C_μ = constant for turbulent model
D_{AB} = diffusion coefficient (m^2/s)
D_h = hydraulic diameter ($=2Cr$) (m)
E = constant for the law of the wall
H = cavity depth (mm)
h_m = mass transfer coefficient (m/s)
k = turbulent kinetic energy (m^2/s^2)
L = seal length (mm)
NI, NJ = number of grid lines in (x,r) coordinate system
M = molecular weight (kg/kgmol)
$\dot{m}$ = mass flow rate (kg/s)
P = pressure (Pa)
$\Re$ = universal gas constant (Nm/(kgmol K))
Re = Reynolds number ($=\rho U2Cr/\mu$)
R_i = Rotor radius (mm)
Sc = laminar Schmidt number ($=\nu_l/D_{AB}$)
Sc$_t$ = turbulent Schmidt number ($=\nu_t/D_{AB}$)
Sh = Sherwood number ($=h_m2Cr/D_{AB}$)
T = temperature (K)
u, v = velocities in (x,r) coordinate system (m/s)
W = injection slot width (mm)
x = axial position from process end of seal (mm)
y^+ = dimensionless distance from wall ($=y\sqrt{\tau_w/\rho}/\nu$)
z = oil film length from bearing end of seal (mm)

Greek Symbols

κ = von Kàrmàn constant
μ = dynamic viscosity (kg/(ms))
ρ = density (kg/m^3)
ν = kinetic viscosity (m^2/s)

Subscript

AIR = air
bearing = bearing side
BULK = radially averaged quantity
inj = injection slot
l = laminar
OIL = oil vapor
process = process side
REF = reference
SAT = saturation/saturated
t = turbulent

References

[1] Park, S.-Y., and Rhode, D. L., 2003, "Predicted Effects of Bearing Sump and Injection Pressure on Oil Labyrinth Leakage," ASME J. Eng. Gas Turbines Power, **125**, pp. 316–325.
[2] Boyman, T., and Suter, P., 1978, "Transport Phenomena in Labyrinth-Seals of Turbomachines," *AGARD CP-237*, pp. 8-1–8-10.
[3] Nguyen, D. H., 1994, "Transport Phenomena and Occupational Consequences of a Tritium Release," Nucl. Technol., **106**, pp. 630–372.
[4] Verma, N. K., Haider, A. M., and Shadman, F., 1993, "Contamination of Ultrapure Systems by Back-Diffusion of Gaseous Impurities," J. Electrochem. Soc., **140**, pp. 1459–1463.
[5] Alkire, R., and Ju, J. B., 1987, "High Speed Selective Electroplating With Impinging Two-Dimensional Slot Jet Flow," J. Electrochem. Soc., **134**, pp. 294–299.
[6] Chin, D. T., and Agarwal, M., 1991, "Mass Transfer from an Oblique Impinging Slot Jet," J. Electrochem. Soc., **138**, pp. 2613–2650.
[7] Pekdemir, T., and Davies, T. W., 1998, "Mass Transfer from Rotating Circular Cylinders in a Submerged Slot Jet of Air," Int. J. Heat Mass Transf., **41**, pp. 3441–3450.

[8] Chen, Q., and Modi, V., 1999, ''Mass Transfer in Turbulent Impinging Slot Jets,'' Int. J. Heat Mass Transf., **42**, pp. 873–887.
[9] Patankar, S. V., 1980, *Numerical Heat Transfer and Fluid Flow*, McGraw-Hill, New York.
[10] Van Doormaal, J. P., and Raithby, G. D., 1984, ''Enhancements of the Simple Method for Predicting Incompressible Fluid Flows,'' Numer. Heat Transfer, **7**, pp. 147–163.
[11] Leonard, B. P., 1979, ''A Stable and Accurate Convective Modeling Procedure Based on Quadratic Upstream Interpolation,'' Comput. Methods Appl. Mech. Eng., **19**, pp. 59–98.
[12] Demko, J. A., Morrison, G. L., and Rhode, D. L., 1989, ''The Prediction and Measurement of Incompressible Flow in a Labyrinth Seal,'' ASME J. Eng. Gas Turbines Power, **111**, pp. 697–702.
[13] Rhode, D. L., and Hibbs, R. I., 1993, ''Clearance Effects on Corresponding Annular and Labyrinth Seal Flow Leakage Characteristics,'' ASME J. Tribol., **115**, pp. 699–704.
[14] Rhode, D. L., and Adams, R. G., 2001, ''Computed Effect of Rub-Groove Size on Stepped Labyrinth Seal Performance,'' STLE Tribol. Trans., **44**(4), pp. 523–532.
[15] Zimmermann, H., and Wolf, K. H., 1987, ''Comparison Between Empirical and Numerical Labyrinth Flow Correlations,'' ASME Paper No. 87-GT-86.
[16] Wittig, S., Schelling U., Kim, S., and Jacobsen, M., 1987, ''Numerical Predictions and Measurements of Discharge Coefficients in Labyrinth Seals,'' ASME Paper No. 87-GT-188.
[17] Wittig, S., Glahn, A., and Himmelsbach, J., 1994, ''Influence of High Rotational Speeds on Heat Transfer and Oil Film Thickness in Aero-Engine Bearing Chambers,'' ASME J. Eng. Gas Turbines Power, **116**, pp. 395–401.
[18] Chew, J. W., ''Analysis of the Oil film on the Inside Surface of an Aero-Engine Bearing Chamber Housing,'' ASME Paper No. 96-GT-300.
[19] Rohsenow, W. M., and Hartnett, J. P., 1973, *Handbook of Heat Transfer*, McGraw-Hill, New York.
[20] Özisik, M. N., 1985, *Heat Transfer—A Basic Approach*, McGraw-Hill, New York.
[21] Jayatilleke, C. L. V., 1969, ''The Influence of Prandtl Number and Surface Roughness on the Resistance of the Laminar Sublayer to Momentum and Heat Transfer,'' Prog. Heat Mass Transfer, **1**, pp. 193–329.
[22] Winterton, R. H. S., 1998, Int. J. Heat Mass Transf., **41**.
[23] Gardon, R., and Akfirat, C., 1965, ''The Role of Turbulence in Determining the Heat-Transfer Characteristics of Impinging Jets,'' Int. J. Heat Mass Transf., **8**, pp. 1261–1272.
[24] Viskanta, R., 1993, ''Heat Transfer to Impinging Isothermal Gas and Flame Jets,'' Exp. Therm. Fluid Sci., **6**, pp. 111–134.

Design Study of Part-Flow Evaporative Gas Turbine Cycles: Performance and Equipment Sizing—Part I: Aeroderivative Core

N. D. Ågren[1]
e-mail: niklas@comsol.se

M. O. J. Westermark

Department of Chemical Engineering/Energy Processes, Royal Institute of Technology, SE-100 44 Stockholm, Sweden

The evaporative gas turbine cycle is a new high-efficiency power cycle that has reached the pilot testing stage. This paper presents calculation results of a new humidification strategy based on part flow humidification. This strategy involves using only a fraction of the compressed air for humidification. Thermodynamically, it can be shown that not all the air needs to be passed through the humidification system to attain the intrinsic good flue gas heat recovery of an EvGT cycle. The system presented also includes live steam production and superheating by heat from the hottest flue gas region. The humidifier only uses the lower temperature levels flue gas heat, where it is best suited. The analyzed system is based on data for the aeroderivative Rolls Royce Trent as a gas turbine core. Part II of this two-part paper presents the results based on data for the industrial gas turbine ABB GTX100. Simulation results include electric efficiency and other process datas as functions of degree of part flow. A detailed model of the humidifier is also used and described, which produces sizing results both for column height and diameter. Full flow humidification generates an electric efficiency of 51.5% (simple cycle 41%). The efficiency increases when the humidification air flow is reduced, to reach a maximum of 52.9% when air flow to the humidification amounts to around 12% of the intake air to the compressor. At the same time, total heat exchanger area is reduced by 50% and humidifier volume by 36% compared to full flow humidification. This calls for a recommendation not to use all the compressed air for humidification. [DOI: 10.1115/1.1476924]

Introduction

Since the proposal of the EvGT cycle (evaporative gas turbine cycle), also known as the HAT cycle, in the late 1980s (Rao [1]), a considerable amount of theoretical assessments and thermodynamic evaluations have been presented in the literature. The main advantages identified with the evaporative gas turbine cycle are electric efficiencies in level with combined cycles, and ultra-low NO_x emissions. At the same time, the EvGT system is projected to require less capital investment/kW than the combined cycle, because of the absence of the steam turbine system in the bottom cycle (Nilsson [2]). The EvGT is also a realistic alternative in small-scale sizes (1−10+MW), where the combined cycle is ruled out. Another advantage is quick startup and shutdown behavior and other flexibilities normally associated with a simple cycle gas turbines. These advantages can qualify the cycle for, e.g., peak load plants and distributed power production (campuses, hospitals). The high efficiency and projected high-power density also qualifies it for offshore use, especially in, e.g., Norway that has high CO_2 taxes.

The first demonstration of the EvGT technology has been realized in Sweden. The first experimental results have been reported by Ågren et al. [3] and Lindquist et al. [4,5].

Part flow humidification is a refined humidification strategy for EvGT cycles. This method involves a bypass of the compressed air around the humidification system, which means that a part of the compressed air is led directly to the combustion chamber, or the recuperator where applicable. Agren et al. [6,7] presented one variant of the part flow layout and predicted it competitive to a full flow EvGT because of major savings in heat exchanger equipment with none or minor efficiency decreases. The optimal portion of compressed air led through the humidification system of various humid air cycles has been stated in some patents: See Nakamura et al. [8], Nakamura et al. [9], and Westermark [10].

This paper presents simulation results of a new part flow layout of the EvGT process. It involves water addition to the compressed air with both steam boilers and a humidification system. The boilers produce steam by heat recovery from the high temperature level flue gas (above the boiling point). The humidification system evaporates water by heat recovery in the low temperature region of the flue gas (below the boiling point), thereby acting where is best suited.

In-depth design and sizing calculations for the humidifier are sparse in literature. Specifically, the height and diameter evaluation for this unit is lacking. In depth sizing calculations of the humidification column is presented in this work. This is a two-part paper where Part I presents a system with high pressure (35 bar) aeroderovative as the gas turbine core engine (Rolls Royce Trent). Part II of the paper presents the results from a system with an intercooled industrial gas turbine (ABB GTX100, modified to intercooled version) as core engine.

System Description

Figure 1 shows the system that was simulated in this study. The gas turbine data are taken from the Rolls Royce Trent. This is a high-pressure nonintercooled aeroderivative with a pressure ratio

[1]Currently at Comsol AB, Tegnérgatan 23, SE-111 40 Stockholm, Sweden.

Contributed by the International Gas Turbine Institute (IGTI) of THE AMERICAN SOCIETY OF MECHANICAL ENGINEERS for publication in the ASME JOURNAL OF ENGINEERING FOR GAS TURBINES AND POWER. Paper presented at the International Gas Turbine and Aeroengine Congress and Exhibition, New Orleans, LA, June 4–7, 2001; Paper 2001-GT-112. Manuscript received by IGTI, Dec. 2000, final revision, Mar. 2001. Associate Editor: R. Natole.

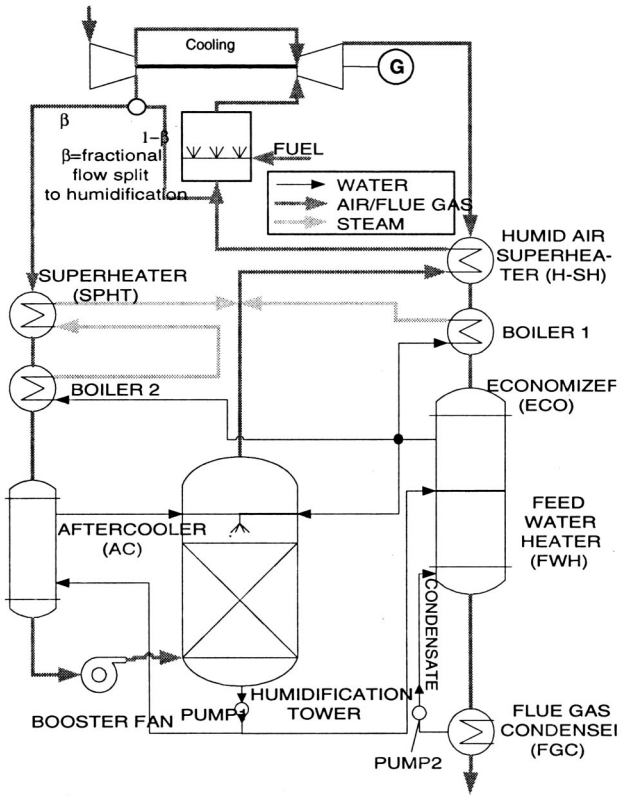

Fig. 1 Flowsheet of the part-flow process

of 35. The cycle is only evaluated with regard to power production, not heat production. The flue gas condenser (FGC) is included in the system for water recovery, but the condensation heat is disposed of. The condensate is used as feed water for the humidification circuit. The condensation temperature is calculated for a water balance, i.e., the plant is self-sufficient with water. The theory and practice of water balancing in an EvGT plant has been described by Ågren et al. [3].

The water addition to the compressed air is done by both boilers at high temperature levels, and the humidification system at low temperature levels. The humidifier is with other words utilized to recover heat below the boiling point, where conventional boilers are useless. The two boilers are treated separately, but in real practice the boiler tubes can be installed in the same boiler house.

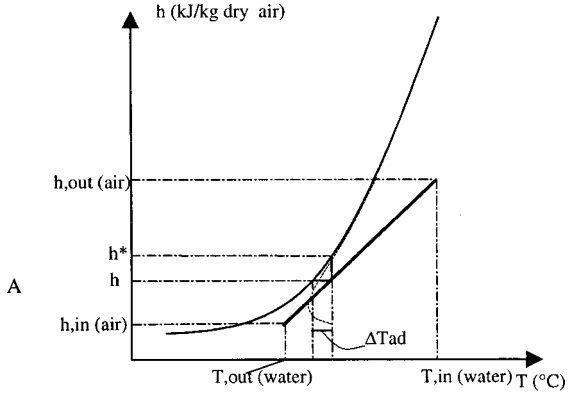

Fig. 2 Operating line and saturation curve for an air humidifier

The dry Trent is not possible to recuperate, since the compressor outlet temperature is always higher than the expander outlet temperature (see Appendix A).

This means that the dry air portion of the humid air can never surpass the temperature it had at the compressor outlet. Therefore, the end heater before the combustion chamber in Fig. 1 is called a humid air superheater (H-SH).

The compressed air stream splitter after the cooling bleed is where the air is variably bypassed the humidification system. The mass flow fraction led to the humidifier is called β.

The condensate is preheated in the FWH to the same temperature as the tower outlet water, to avoid unnecessary thermodynamic irreversibilities. However, the live superheated steam leaving the SPHT is mixed with the lower temperature humid air from the humidfier and the saturated steam leaving BOILER1. This is done to avoid dewout in the mixing point.

In practice, a small waste bleedoff from the water stream leaving the tower should be used to make up for impurity buildup in the circuit (Ågren et al. [3]). This is, however, not included in the calculations since it probably doesn't affect the results to a large extent.

A booster fan for the air used in the humidifier is used to make up for the pressure drop in the humidification circuit.

Part Flow Concept

To appreciate the process synthesis for evaporative gas turbine cycles it is necessary to understand the humidification column modeling. This paragraph starts with a brief recapitulation. For details, please refer to Mickley [11], Perry [12], or Ågren [13].

The operating conditions and sizing of a humidifier are dealt with by the air-water saturation curve and the operating line in a diagram with air enthalpy h on the ordinate and the water temperature on the abscissa.

An example is depicted in Fig. 2. The upper solid curve is the saturation curve for saturated humid air. The lower solid curve is the operating line, and is the result of a differential heat and mass balance between the gas and water phases. Detailed calculations reveal that the operating line in fact is slightly curved. This is, however, scarcely visible in a graphical plot. The operating line

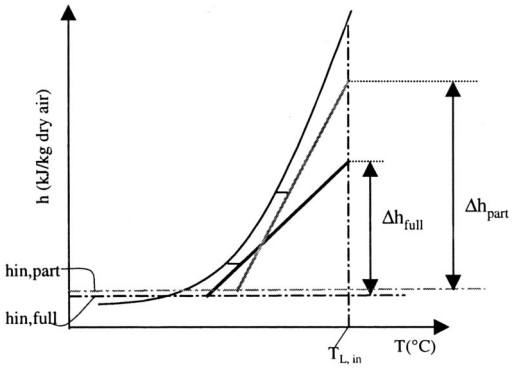

Fig. 3 Humidifier operating lines at full and part flow

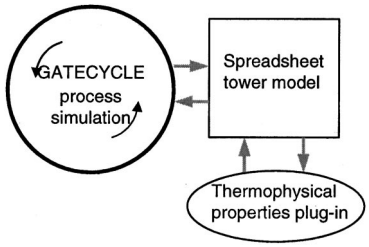

Fig. 4 Data flows between the used software

Table 1 Library data for RR Trent (open sources)

Inlet air flow:	155.7 kg/s
Compressor inlet pressure (after duct):	1.007 bar
Compressor outlet temperature	579°C
Compressor outlet pressure	35.28 bar
Expander outlet temperature	434°C
Expander outlet pressure (before HRSG)	1.038 bar
Combustor outlet temperature	1336°C
Combustor efficiency	99.9%
Combustor pressure drop (% of inlet pressure)	1%
Generator efficiency	98.3%
Shaft power	50.8 MW
Total cooling flow (% of comp. intake)	22%

Table 2 Heat exchanger assumptions

	ΔT_{min} (°C)	U (W/m^2,°C)
SPHT	30	100
H-SH	30	100
Boiler	10 (at drum)	300
AC	15	300
FWH	15	300
ECO	15	300

Table 3 Auxiliaries' efficiencies

	Isentropic	Shaft+Bearing	El. Drive
booster	0.7	0.9	0.95
pumps	0.85	0.9	0.95

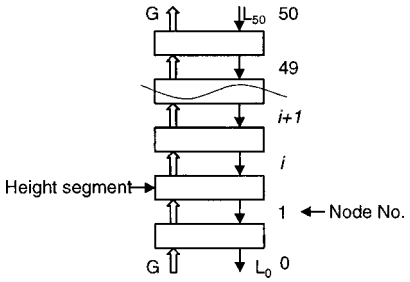

Fig. 5 Tower calculation segments

connects the water temperature and the air enthalpy at any point in the column. An arbitrary point A on the operating line of the column is marked in Fig. 2. The thin vertical solid line from A is the tieline that connects the bulk humid air enthalpy (h) and the humid air enthalpy for the state at the water-air interface (h^*). According to the enthalpy potential model (Mickley, [11]), the distance h^*-h constitutes the driving force for enthalpy transfer in terms of an enthalpy difference. The tieline is here taken as vertical, which means that the resistance against mass and heat transfer is assumed to be entirely on the gas side. The horizontal solid line $T-T_{ad}=\Delta T_{ad}$ is usually stated to some minimum value as a boundary condition for design calculations (T_{ad} is by some authors named as the wet bulb temperature). In this work ΔT_{ad} is selected to 4°C, as recommended by Strigle [14]. The fine dotted curved line in Fig. 2 is an approximate h-T plot of the state of the bulk air throughout the column.

For a given gas turbine package, an integrated humidification system can be laid out in different ways. Some boundary conditions must be set to be able to manageably analyze the whole system. These are minimum approach temperature in heat exchangers and the minimum difference between the air adiabatic temperature of saturation and the water temperature, ΔT_{ad}, in the

Table 4 Various system results based on 155.7 kg/s compressor intake

β	Humidification Rate (kg H2O/kg intake air)	Cooling Flow (kg/kg intake air)	η_{el} (LHV)	Fuel Energy Consumption (MW) LHV	Net Electric Power (MW)
Dry	-	0.220	0.410	122.4	51.0
1	0.237	0.332	0.515	211.3	108.9
0.8	0.228	0.327	0.519	205.3	106.5
0.6	0.218	0.324	0.523	199.3	104.1
0.4	0.208	0.318	0.527	192.7	101.5
0.2	0.193	0.310	0.529	185.0	97.9
0.1	0.181	0.304	0.528	179.4	94.8
0.05	0.169	0.300	0.525	174.9	91.8
0.025	0.160	0.293	0.522	171.9	89.7

Table 5 Humidification distribution and booster effect

β	Dry Air Flow to Humidifier (kg/s)	Evaporated Water in Humidifier (kg/s)	Steam Flow From Boilers (kg/s)	Power Consumption of Booster Fan (kW)
1	104.03	12.9	24.0	504
0.8	83.79	11.8	23.7	407
0.6	63.20	10.6	23.4	307
0.4	42.46	9.3	23.0	208
0.2	21.49	7.6	22.5	109
0.1	10.83	6.1	22.0	58
0.05	5.45	4.8	21.6	31
0.025	2.75	3.5	21.4	16

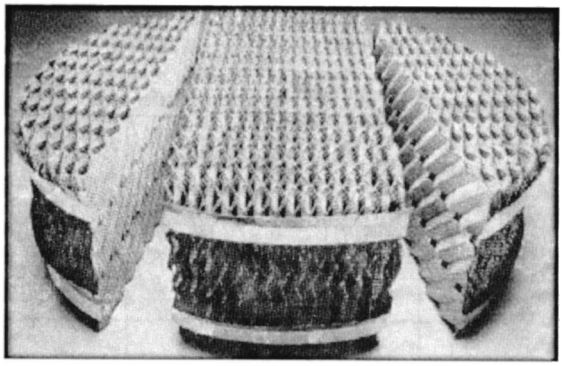

Fig. 6 Intalox© structured metal packing 2T (Norton Chemical Proc. Prod. Corp.)

column (the ''pinch''). This ''pinch'' should not be confused with the Pinch concept in Linnhoff March pinch technology.

For the column, the inlet water temperature (vertical dash-dotted line in Fig. 3) is determined by the security margin against boiling, taken as 10°C below boiling point in this work. The outlet massflow of water is matched to comply with the amount of water that can be heated in the economizer and the aftercooler (see Fig. 1). Inputs to the column calculation will then be: system pressure, ω and T of inlet air, inlet water temperature, and outlet water flow. The enthalpy of the inlet air is marked by the horizontal dash-dotted line in Fig. 3. The operating line is then confined within the area limited by the dash-dotted lines and the saturation curve. The slope of the operating line is roughly given by $L \cdot c_{p,L}/G$ (cf. Ågren [13]). The horizontal position of the operating line is given by the minimum ΔT_{ad} (denoted by the tiny waist in the Fig. 3). Thereby the operating line is determined. A full-flow case is shown with the black operating line. If the dry air flow through the column is cut to 50% of the full flow $G(\beta=0.5)$, the slope of the new part flow operating line will have a slope $1/\beta=2$ times that of the full flow, with conserved water flows. Also, the inlet air temperature, and thereby enthalpy, may be slightly altered. With a retained minimum ΔT_{ad}, the part flow operating line will be represented by the gray line in Fig. 3. The enthalpy rise (kJ/kg dry air) is also denoted in the figure, and it can be seen that $\Delta h_{\text{part}} > \Delta h_{\text{full}}$. The transferred heat (kW) in the column for full and part flows are

$$Q_{\text{full}} = G\Delta h_{\text{full}} \tag{1}$$

$$Q_{\text{part}} = \beta G \Delta h_{\text{part}}. \tag{2}$$

If we assume for a moment that the same amount of heat (kW) is recovered by the humidification systems in both cases, then $Q_{\text{full}} = Q_{\text{part}}$ or

$$\Delta h_{\text{part}}/\Delta h_{\text{full}} = 1/\beta, \tag{3}$$

which is equal to 2 in the example above. The Q of different part flow cases will however not be exactly the same. The actual cases must be calculated because it is not possible to analytically foresee the relation between the enthalpy rise in part or full flow cases. The difference in Δh cannot be seen by altering the water flow in a constant air flow system either.

The above theoretical reasoning leads to the important conclusion that if a percentage of the compressed air is bypassed the humidification system, the heat recovery potential is not impaired to the same extent as the airflow is decreased. The part flow concept is based on this notion.

However, according to Fig. 3, the water outlet temperature from the humidifier will increase if $L \cdot c_{p,L}/G$ is increased, and the recovery of heat from the flue gas will be penalized. A good strategy is therefore to avoid unnecessary thermal loading of the lower section humidifier in order to keep L low. This can be dealt with by, e.g., steam production from the highest temperature levels of the flue gas, leaving the lower temperature region heat to the humidification system.

Computational

The mass and energy balancing were performed with GATECYCLE 5.31 (©GE Enter Software). Since GATECYCLE is not yet suitable for humidifier calculations, the humidification process was simulated separately in a spreadsheet program. A datalink to GATECYCLE from the spreadsheet program was created with CYCLE-link (©GE Enter Software). All the calculations could then be controlled and run from the spreadsheet console. For the humidification calculations, thermophysical properties plugins were installed in the spreadsheet program. (SteamTab and MoistAirTab, ©ChemicaLogic Corp.).

Modeling

Turbo Package Adaption. To employ a gas turbine model with reasonable component efficiencies, firing temperatures, first

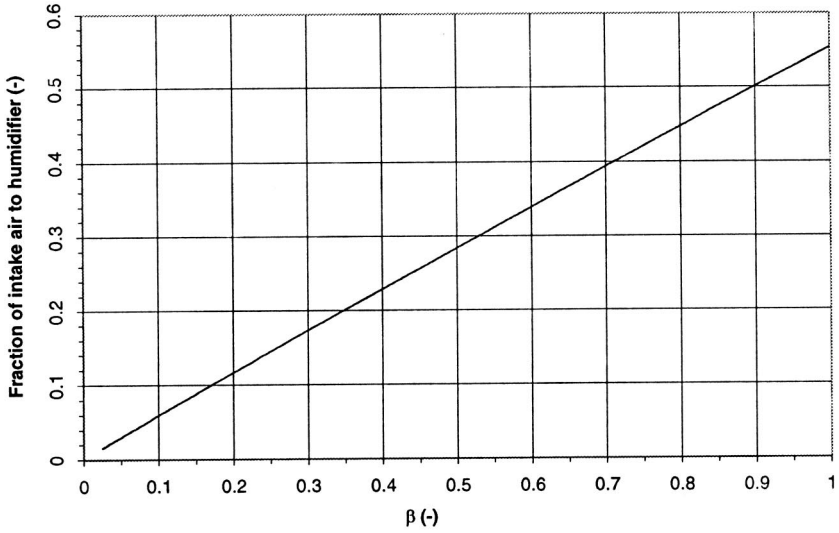

Fig. 7 Conversion from β to fraction of compressor intake air used in the humidifier circuit

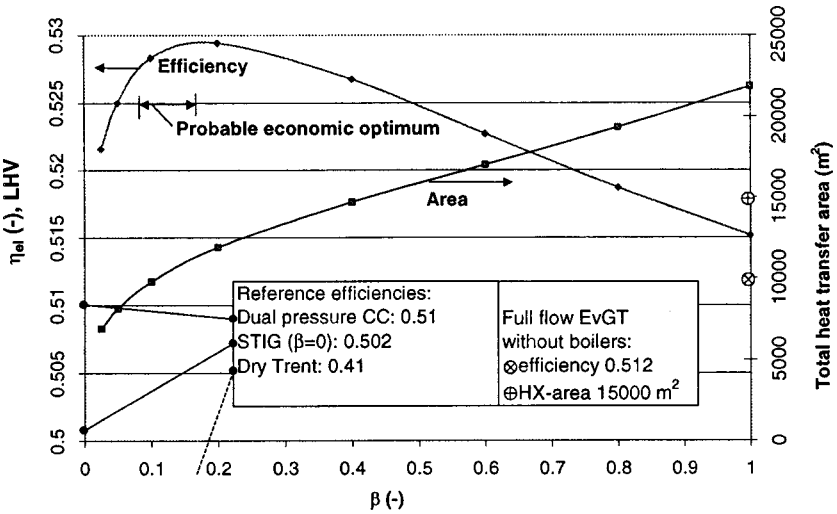

Fig. 8 Electric efficiency and total heat transfer area versus β

rotor temperatures etc., data for an existing gas turbine were used. This reflects present technology concerning materials and aerodynamics. However, the EvGT introduces significant changes in operating conditions for the gas turbine. In the EvGT models in this work, the compressor airflow and other engine characteristics are kept constant, which means that the expander is exposed to higher volumetric flow than at dry design conditions. The expander probably needs redesign because of this (compressor redesign is also an option if a retained expander volumetric flow is chosen). In this work, the existing dry data are, however, accepted, to show the process potential of 155.7 kg/s inlet air to the compressor with the same turbo prerequisites as a dry cycle. (See Fig. 4.)

Data for the Rolls Royce Trent were retrieved from the GATECYCLE GT library. The machine was then built in GATECYCLE component by component in a dry model and the data from the library model were used to mimic the Trent. The library data used to fit the dry model are presented in Table 1.

The dry model was adapted to the library data and the following additional data could be retrieved: compressor polytropic efficiency: 0.895, expander polytropic efficiency: 0.876. These data together with applicable data from Table 1 were then used in the evaporative cases. A flow sheet of the dry model is shown in Appendix A.

In the evaporative cases, the compressor flow was kept constant, whereas the expander volumetric flow changed according to the added water vapor. (See Tables 2–5.)

Gas Expander Cooling. The cooling of the gas expander was mimicked by running a dry case of the RR Trent based on databank data, selecting right cooling air fraction of compressor intake air. In the dry Trent case it is 22%, extracted from the compressor outlet. In the dry model, this amount was equally distributed to the first nozzle cooling port and first rotor cooling port in the GATECYCLE expander model. This resulted in a reported first-stage rotor temperature of 1253°C. In the evaporative cases, the combustor outlet temperature from Table 1 was used. But the flow of hot combustion gas from the combustor is higher because of the added water vapor, which is why a larger amount of cooling air is needed. In the evaporative runs, the cooling air flow was thus controlled to meet the first-stage rotor tem-

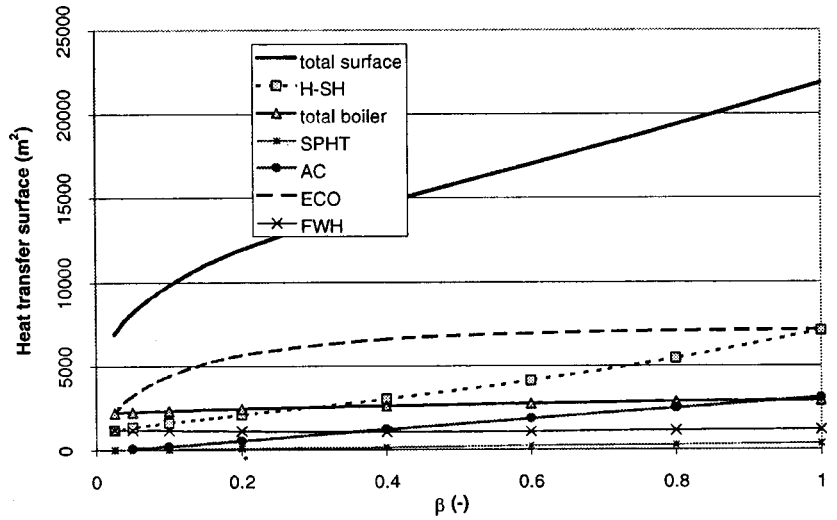

Fig. 9 Distribution of heat transfer surface versus β

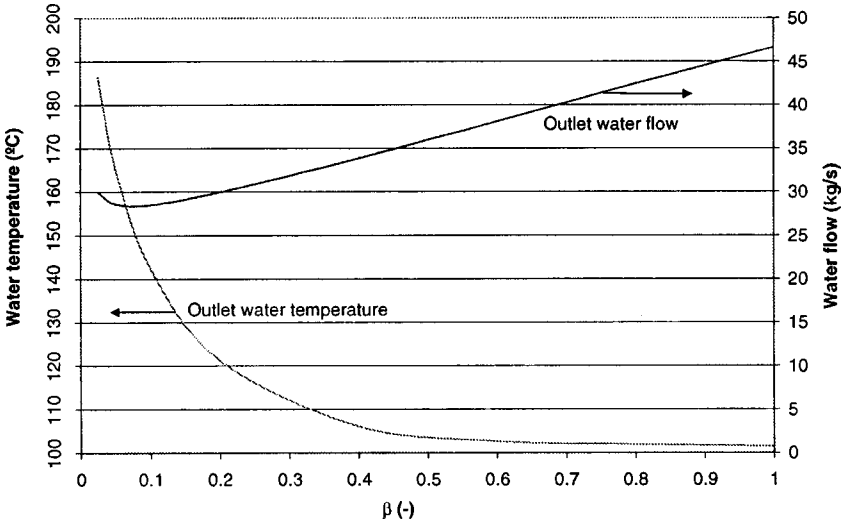

Fig. 10 Column water outlet temperature and water flow versus β

perature of 1253°C. This is reasonable, because it is the same assumption as is done in the GATECYCLE library model of the dry engine.

Humidifier Model. The enthalpies of humid air in the humidification spreadsheet model were calculated as

$$h = h_{da} + \omega h_{\mathrm{H_2O}} \ \text{(kJ/kg dry air)} \tag{4}$$

where h_{da} and $h_{\mathrm{H_2O}}$ are the enthalpies of dry air and pure steam, respectively, expressed in kJ/kg. These values are functions of temperature and the partial pressure of dry air and steam, respectively. The steam data are from *IAPWS Formulation 1995 for the Thermodynamic Properties of Ordinary Water Substance for General and Scientific Use* and the dry air data are taken from the Hyland-Wexler correlations (Hyland and Wexler [15]). The humidity is calculated as

$$\omega = \frac{M_{\mathrm{H_2O}}}{M_{da}} \cdot \frac{p_{\mathrm{H_2O}}}{p_{\mathrm{total}} - p_{\mathrm{H_2O}}}. \tag{5}$$

The above equations are based on the assumption that steam and air exist in an ideal mixture, i.e., no enthalpy of mixing is accounted for. A discussion about this is found further on in the sources of error section.

To calculate the operating line and states of the leaving and exiting streams, the humidification column is divided into 50 height segments, where the state points are calculated at nodes number 0–50, see Fig. 5. The states at node 50 represent the top of the column and number 0 the bottom. L denotes liquid water rate (kg water/s) and G dry air rate (kg dry air/s). G is constant throughout the column. The water temperature is first distributed into 50 equidistant steps. The water temperature at node i is then

$$T_{L,i} = T_{L,0} + \frac{i(T_{L,50} - T_{L,0})}{50}. \tag{6}$$

The states at the bottom (node 0) are given to explain why a net energy stream downwards can be calculated as

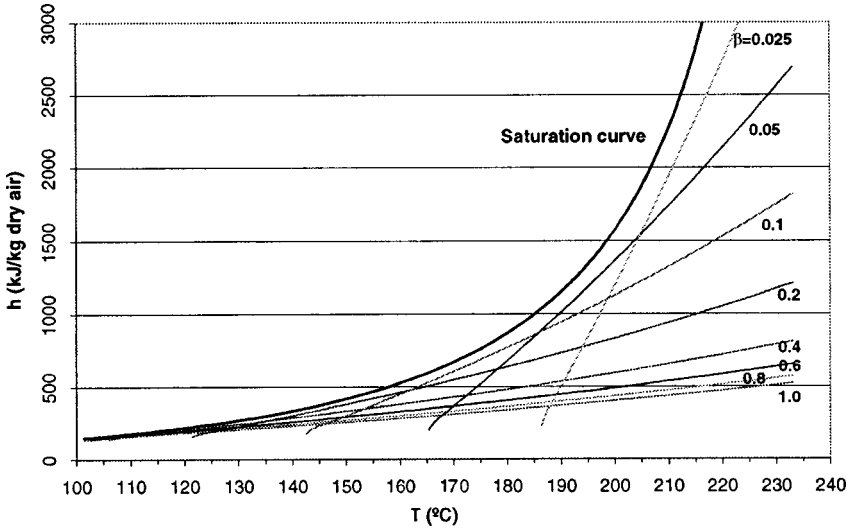

Fig. 11 Operating lines for all part flow cases

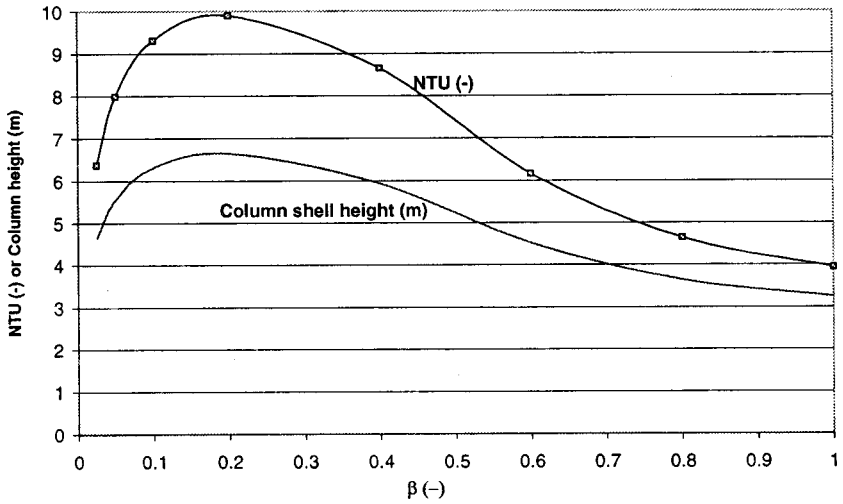

Fig. 12 NTU and column shell height versus β

$$\dot{E}_{\text{net},0} = L_0 \cdot h_{L,0} - G \cdot (h_{da,0} + \omega_0 h_{\text{H}_2\text{O},0}) \tag{7}$$

and a net mass flow H_2O downwards (both liquid and gaseous)

$$\dot{m}_{\text{net},0} = L_0 - \omega_0 G. \tag{8}$$

But for a flow process at steady-state operation (with no leakage), the net streams of mass and energy downwards must be the same at any height coordinate, or

$$\dot{E}_{\text{net},0} = \dot{E}_{\text{net},i} = \dot{E}_{\text{net}} \tag{9}$$

$$\dot{m}_{\text{net},0} = \dot{m}_{\text{net},i} = \dot{m}_{\text{net}}. \tag{10}$$

With constant net flows we can substitute Eq. (8) in Eq. (7) for any node $1 < i < 50$ and arrive at

$$(\dot{m}_{\text{net}} + \omega_i G) \cdot h_{L,i} - G \cdot (h_{da,i} + \omega_i h_{\text{H}_2\text{O},i}) - \dot{E}_{\text{net}} = 0. \tag{11}$$

The humid air exit is assumed to be saturated with water. For calculational convenience, this assumption is used from node 1 and upwards. It can be shown that this does not affect the final results much, even though the air approach to the saturation curve happens gradually (see Fig. 2). Assuming saturated conditions, the unknowns ω_i, $h_{da,i}$ and $h_{\text{H}_2\text{O},i}$ in Eq. (11) are functions of only bulk air temperature, $t_{G,i}$. This temperature can then be found for each node 1–50 by iterations until Eq. (11) is satisfied.

This way the input values for the column is inlet water temperature (fixed to 10°C below boiling point), inlet air flow, temperature and humidity, outlet water temperature, and flow. The output values will be inlet water flow and outlet humid air temperature and humidity (and thus flow rate). Also a full representation of the operating line $h = f(T_L)$ will be produced. This model resembles the one presented by Enick et al. [16], but is more accurate since it takes into account the slight curvature of the operating line (see section Part Flow Concept above).

Column Sizing. The calculation of the effective packing height is based on the number of transfer units (NTU) method. The detailed deduction can be found in Perry [12] and is also used for humidification processes by Mickley [11]. The required packing height Z is then stated by $Z = \text{HTU} \cdot \text{NTU}$, where HTU is the height of a transfer unit. The NTU in a humidification column is

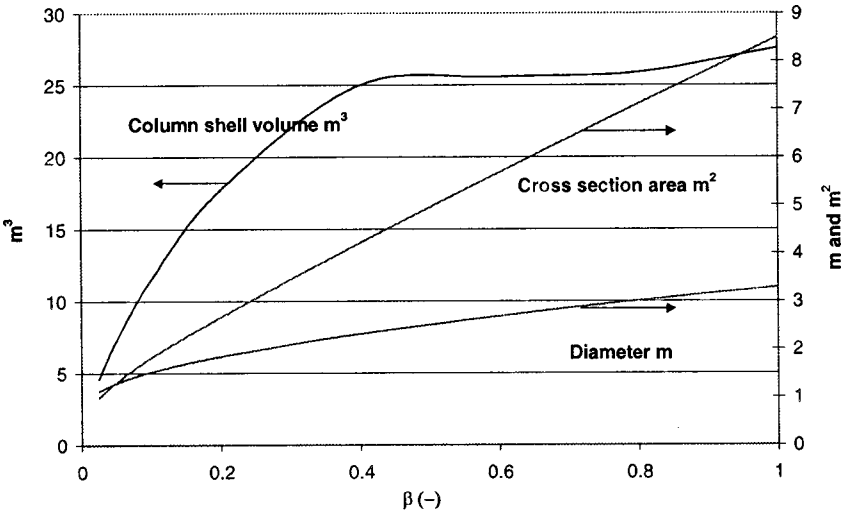

Fig. 13 Humidification column dimensions

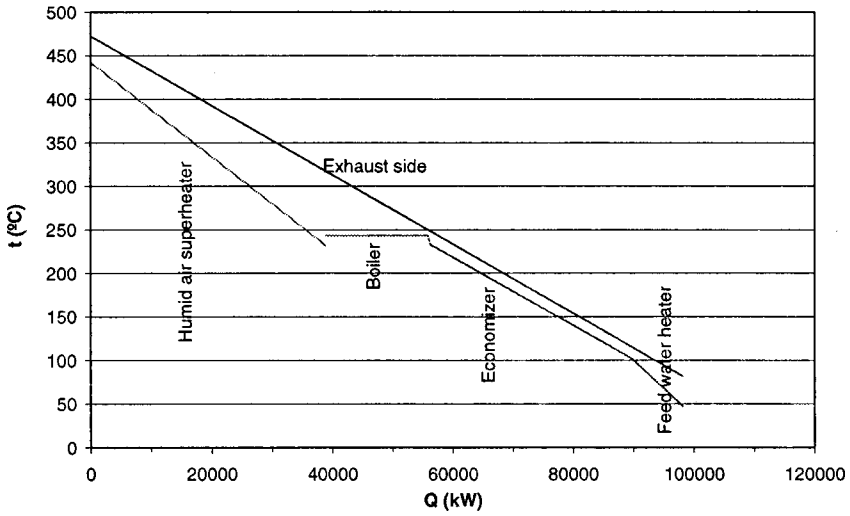

Fig. 14 Flue gas heat recovery diagram for $\beta=1$

taken as the reciprocal of the enthalpy driving force $1/(h^*-h)$, integrated over h. The NTU can thus be seen as the total enthalpy rise divided by an average driving force.

$$\mathrm{NTU}=\int_{h,\mathrm{in}}^{h,\mathrm{out}}\frac{dh}{(h^*-h)} \tag{12}$$

With reference to Fig. 2 and Fig. 5 the NTU-integral was evaluated numerically with a finite difference $\Delta\mathrm{NTU}_i$ for each node. A sum of all the difference steps gives the total NTU:

$$\Delta\mathrm{NTU}_i=\frac{h_i-h_{i-1}}{\frac{1}{2}[(h_i^*-h_i)+(h_{i-1}^*-h_{i-1})]} \tag{13}$$

$$\mathrm{NTU}=\sum_{i=1}^{50}\Delta\mathrm{NTU}_i\,. \tag{14}$$

The HTU of a packing is a function of the geometry and specific surface of the packing and mass and heat transfer coefficients (flow patterns and physical properties of the fluids). A packing with large void fraction and small specific surface has a higher HTU value, whereas a more effective packing with smaller channels and rugged surfaces is more effective and has a smaller HTU value. In practice, the HTU is determined empirically for a special packing and application. For this work, the structured packing Norton Intalox © 2T metal packing was selected, see Fig. 6. Predicted HTU data for the described EvGT process were acquired from the reseller Thurne Teknik AB, Sweden, and is about 0.57 m. The total shell height is taken as $Z+1$ m to allow for distributors, connections and fixtures.

The diameter of the column was calculated with aid of generalized pressure drop correlations and empirical packing factors as provided by the packing manufacturer Norton Corp. The packing diameter was designed for a maximum pressure drop of 400 Pa/m of packing at the top of the packing.

Additional Assumptions and Boundary Conditions. The ambient conditions for all calculations were: $T=15°\mathrm{C}$, $p=1.013$ bar, RH=60%. The electric efficiency based on LHV is calculated accounting for auxiliaries (booster fan and water pumps). The fuel is natural gas (LHV=47.45 MJ/kg).

The pressure drops over the humidification system were taken as 3% of compressor outlet pressure, and 2% of system pressure in the water system.

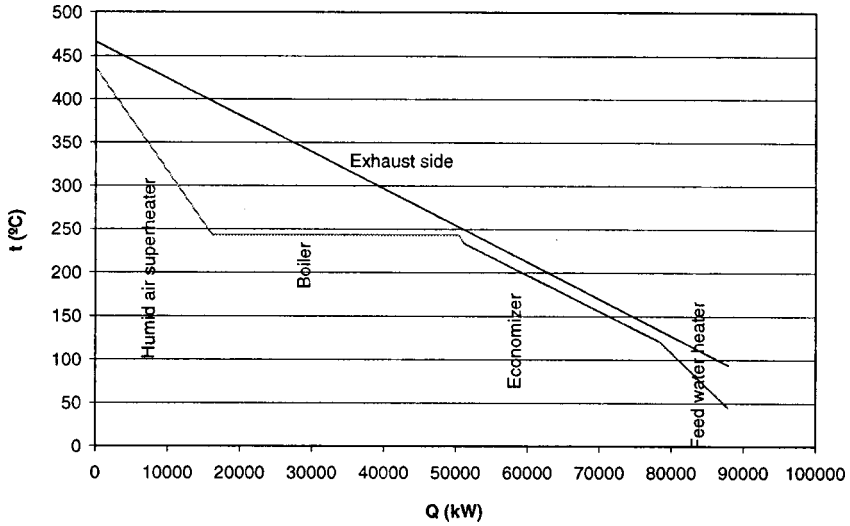

Fig. 15 Flue gas heat recovery diagram for $\beta=0.2$

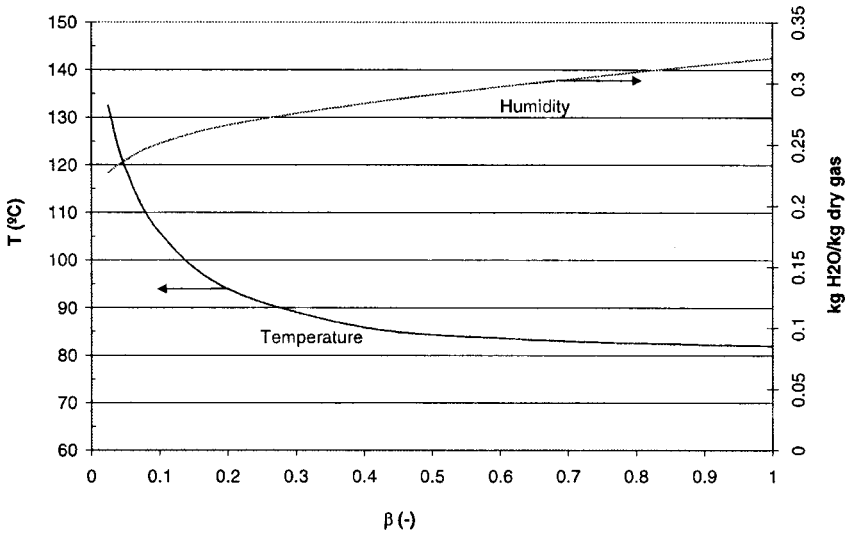

Fig. 16 Temperature and humidity of flue gas at FWH exit versus β

Results and Discussion

All calculations were made with the part flow fraction β as main parameter. β expresses the fraction of compressed air (after cooling extraction) that is led to the humidification system. If F denotes the airflow in kg/s after cooling extraction, then $F\beta$ kg/s goes to the humidification system and $F(1\text{-}\beta)$ kg/s goes directly to the combustion chamber (see Fig. 1). This value is intuitive since $\beta=1$ represents full flow humidification and $\beta=0$ represents no humidification (STIG). It might also be desired to express the air fraction used for humidification on basis of compressor intake air. Since the cooling flow varies slightly over the cases (see Appendix D), the relation between β and fraction of compressor intake is not fully linear. For the reader's convenience the relation is plotted Fig. 7.

Figure 8 shows one of the more important curves from the parametric calculations. The electric efficiency for full flow ($\beta=1$) is 51.5%. When the air is gradually bypassed around the humidification system, the efficiency increases. An efficiency optimum of 52.9% arises slightly below $\beta=0.2$.

As stated earlier, a decrease in air fraction led to the humidification system (introduction of part flow humidification) is not identical to a proportional decrease in heat recovery potential in the humidification system. One penalty, though, for part flow humidification (in specific at very low values of β) is that the tower outlet water temperature will be higher. This impairs the heat recovery potential in the economizer. On the other hand, full-flow mode degrades the system by exposing the entire compressed air stream to the pressure drops in the humidification section. This pressure drop is regained with the booster fan (see Fig. 1), of which the compression work steals efficiency points. Yet another penalty for full flow mode, that is specific for high pressure nonintercooled aeroderivatives, is that the cycle cannot be recuperated. The temperature after the compressor (579°C for the Trent) can never be regained since the expander outlet temperature always is lower. This means that the dry gas portion of the working medium will always be temperature degraded when entering the combustor after the humidification pass. This causes extra fuel consumption.

These pros and cons must be weighed against each other and an intermediate fraction of air should be employed for humidification. Only the fraction needed for sufficient humidification heat recovery should be used. The rest should be bypassed directly to the combustor. The optimum concerning efficiency in this case proves to be at $\beta=0.2$, a considerably higher efficiency than is predicted for a combined or STIG cycle.

Figure 8 also depicts the total heat transfer area needed for the different cases. The total area decreases monotonously with decreased β. Consider that the total plant investment is assumed to follow some function that increases with increased total heat exchanger area. For a minimum production cost, fuel expenses (including CO_2 taxes) and capital costs must be weighed against each other. A production cost minimum will then in most cases probably appear somewhat to the left of the efficiency optimum (see Fig. 8). The exact optimum depends on local fuel prices, taxes, and interest rates.

Figure 9 shows the heat transfer area for each heat transfer component. The economizer area trend is rather flat from $\beta=1$ down to 0.4. This is because the tower outlet water temperature is rather constant in this region (see Fig. 10). As the tower outlet water temperature increases, below $\beta=0.4$, less heat transfer can take place and the economizer area is decreased. The humid air superheater (H-SH) area monotonically decreases with decreasing β. The reason is that less dry air ballast is used in the humidification when employing part flow.

The outlet temperature from the humidifier is presented in Fig. 10. In the full-flow case, the temperature is 101.5°C. This temperature is governed by the operating line and its ''pinch'' location against the saturation curve, as shown in Fig. 11.

The minimum ΔT_{ad} value is set to 4°C for all cases. The value on the abscissa for the bottom end of the operating line is the tower outlet temperature. The outlet water temperature is virtually

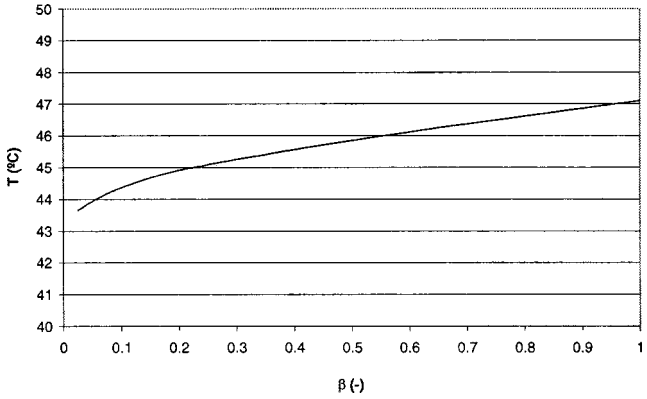

Fig. 17 End condensation temperature versus β

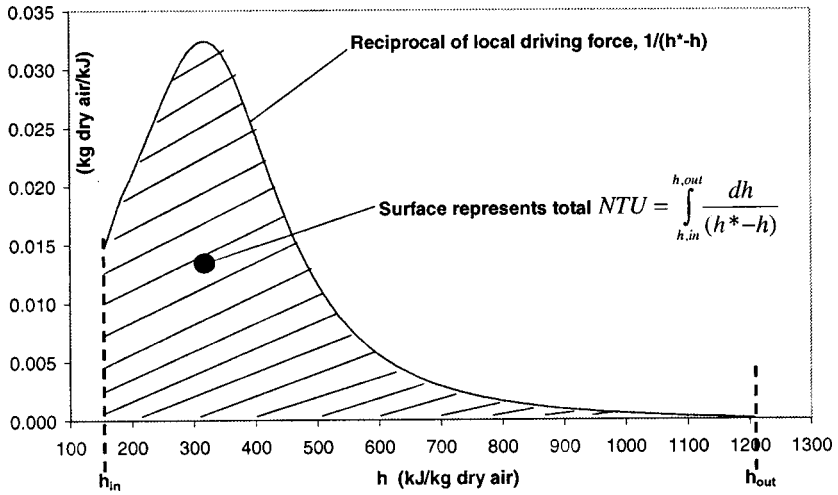

Fig. 18 Graphical representation of number of transfer units for $\beta=0.2$

unaffected in the region $\beta=1$ to 0.6, because the "pinch" is located very near the bottom end. As less air is led through the humidification ($\beta<0.60$), the operating lines will gradually get steeper and hence the tower outlet water temperature will increase. The outlet water temperature limit for $\beta\rightarrow 0$ is 233°C and can be deducted both from Fig. 10 and Fig. 11, and equals the tower inlet water temperature. This limit value is of no practical importance, since it reflects a case where the air flow is so minute that it does not affect the water at all, and practically no humidification takes place.

In the calculations, the outlet water flow from the tower (for a given β) is selected to match the maximum flow the economizer can handle to produce water of 233°C. This flow is thus governed by the stipulated minimum temperature difference in the economizer. Since different flows give different tower outlet water temperatures, which in turn affects the capacity of the economizer, the water flow match will be an iterative procedure. The results for each β can be seen in Fig. 10. At full flow ($\beta=1$) the water flow is 47 kg/s. As less air is used for humidification, the tower outlet water flow decreases. This decrease can be explained as follows: A lower humidifier air flow reduces the steam production in boiler 2 (Fig. 1), which causes a decrease in water content in the gas turbine and the flue gases. This lowers the thermal capacity (mc_p) of the flue gas, allowing less water flow on the cold side. Also the thermal load on the humidifier is reduced, because of less aftercooling and economizer effect. Because of the lower humidification rate, the firing is decreased, which also lowers the thermal capacity of the flue gas (less combustion CO_2 and H_2O).

Approaching very low β-values (very small air flow through the humidifier), the tower outlet water temperatures will increase very rapidly (see Fig. 10). This has the new effect that very low temperature rise is needed in the ECO to "top off" the water up to 233°C. Therefore, more water can be fed to the economizer again. This explains the existence of a minimum flow at $\beta=0.1$ in Fig. 10.

Figure 12 above discloses the number of transfer units (NTU) required for each part flow case. The number of transfer units is proportional to the effective packing height Z required in the humidfication column, $Z=\text{HTU}*\text{NTU}$. HTU=0.57 m for the Intalox 2T structured packing used for this work (data courtesy of Norton Co.). The NTU is 4 for full flow and reaches a maximum of around 10 at $\beta=0.2$, to fall again below $\beta=0.2$. The limit for $\beta\rightarrow 0$ is NTU=0. Again, this is of no practical importance, since it represents a packing height approaching 0, a tower with no heat recovery effect at all (no air traveling through the column). The

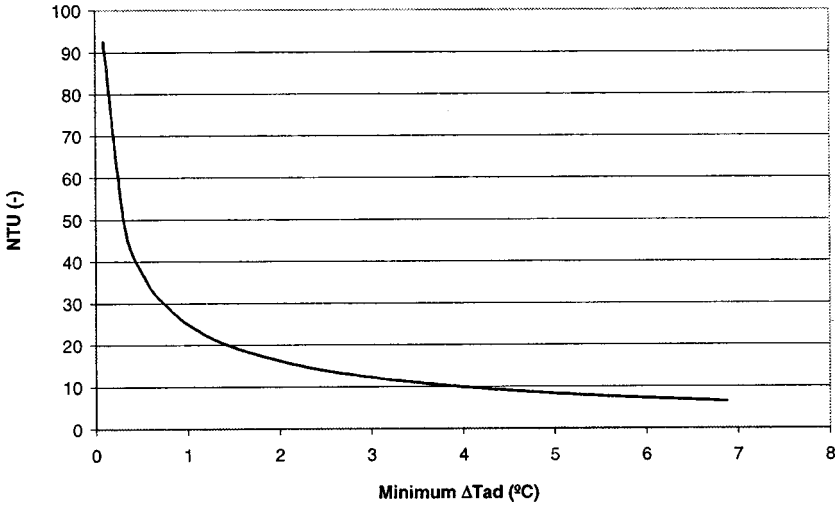

Fig. 19 Example of calculated number of transfer units as a function of minimum adiabatic temperature difference in a column for $\beta=0.2$

shape of the curve in Fig. 12 can be deducted from Fig. 11; The NTU is simply the ratio between total enthalpy transfer and the mean driving force.

Figure 13 compiles the dimensions of the column. The diameter depends on the packing geometry, hydrodynamics, thermophysical properties, and flow relations of the gas and water phase (generalized correlations courtesy of Norton Corp.). The diameter is naturally reduced with reduced air flow. The total volume has an inflexion region in midrange part flow, because of higher column height in this region than for full flow (see Fig. 12).

Figure 14 and Fig. 15 show the heat release diagrams for the flue gas train in two flow cases. One noticeable phenomenon is that the temperature of the flue gas exit of the feed water heater is lower for the full-flow case (82°C) than that of the part flow case (94°C). The energy content of the FWH exit can be regarded as lost to the surroundings. It may at first sight appear puzzling that the part flow case has higher electric efficiency (see Fig. 8), whereas the exit flue gas has higher temperature. The explanation is that a very large amount of the flue gas enthalpy is represented by the latent heat of water vapor. So, the true enthalpy flow lost to the surroundings is depending on both temperature and, to a larger extent, water content. Figure 16 indicates that the flue gas of the $\beta=0.2$ case indeed has a lower water content than the $\beta=1$ case, even though it has a higher temperature.

Figure 17 shows the temperature that the end condenser must cool the flue gas to, to make the plant self-sufficient with water. The condenser temperature decreases as less air flow is employed for humidification. This is because the condensing temperature for self-support of water is only a function of fuel consumption per kg compressor intake air (cf. Agren et al. [3]), and the fuel energy consumption decreases with decreasing air flow through the humidifier (see Appendix D).

Finally, some plots for the humidification tower for $\beta=0.2$ are presented in Fig. 18 and Fig. 19. With the help of the definition of NTU, Fig. 18 can be constructed. The curve is the reciprocal of the local enthalpy driving force, $1/(h^*\text{-}h)$, at any height coordinate in the tower. $h^*\text{-}h$ can be read off from Fig. 11 as the vertical distance between the operating line and the saturation curve. If the values of $1/(h^*\text{-}h)$ are summed and integrated over h, the NTU can be graphically represented as the surface between the curve and the abscissa in Fig. 18. h_{in} is the enthalpy of the dry air entering the tower, and h_{out} is the enthalpy of the humid air leaving the column.

The path along the abscissa from h_{in} to h_{out} in Fig. 18 can be regarded as some travelled enthalpy distance for the air between the entry (bottom) and the exit (top) of the column. If an integration is done along this path, every small enthalpy rise dh requires a differential NTU, $d\text{NTU}=dh/(h^*\text{-}h)$, or, a differential height segment $dZ=\text{HTU}\cdot d\text{NTU}$ of column packing. This dNTU can be graphically seen as the additional slice of surface beneath the curve. The conclusion from the hump in the curve is that the lower part of the column is more packing demanding, because of lower driving force (see Fig. 11). This result implies that it may be reasonable to use denser packing with lower HTU (more effective) at the bottom section of the column. The top part of the column does not consume much NTU at all, why maybe a packing with wider channels and higher HTU can be used there. This can also be reasonable because the volumetric flow in the top part of the columns is higher, and with a less dense packing, the capacity is higher for a given pressure drop. However, for simplicity the packing Intalox 2T has been used for the entire column in this study (Fig. 6).

As stated before, the ''pinch,'' or the minimum difference between water temperature and the air adiabatic temperature of saturation is chosen to 4°C for all calculation cases, as recommended by Strigle [14]. However, a test series of different values of ΔT_{ad} for $\beta=0.2$ was run and the results are shown in Fig. 19. The lower ΔT_{ad}, the higher the NTU, and the higher the tower. If ΔT_{ad} is chosen too small, the height will be too large, or, as $\Delta T_{ad}\rightarrow 0$, NTU$\rightarrow\infty$. This is because the driving force becomes smaller when the minimum ΔT_{ad} gets smaller. The difference 4°C is a reasonable compromise, since the tower height is reasonable and the tower outlet temperature is reasonably low.

Sources of Error. The gas mixture in the humidification tower has been regarded as an ideal mixture. Thus, the properties were calculated with steam tables and databases for pure air at their respective partial pressures, according to Dalton's law of partial pressures. Although this ideal mixture model is frequently used in psychrometrics, a more accurate method would be to, instead of partial pressures, use an approximate fugacity correlation and use the fugacity $\Phi_i=\gamma_{ij}p_i$ at the property calculation of each component. The fugacity coefficient γ_{ij} takes into account the molecular interaction between the different components i and j (e.g., air and water). A good overview of the importance of fugacity models is given by Wark [17]. At the elevated temperatures and pressures present in the EvGT process, the coefficient will be somewhat below unity, implying higher volatility than predicted from Dalton's law. This will increase saturation humidity for a given temperature. A single check with a refined interaction model for air-water systems (Hyland and Wexler [15]), shows a deviation of about 2 deg in dew point. The Hyland-Wexler moist air model is however not reliable above 100°C and was consequently not employed in this work. Our ideal mixing assumption slightly affects the NTU results, but does probably not affect the performance trends for different part flows. Our estimation is, however, that the column height values in this study are slightly overestimated because of this.

There is a newly started project at the department of the authors that aims at finding new property models for high pressure and high-temperature air-water mixtures. Experiments are planned within this project.

The Lewis relation is assumed to hold as described by Mickley [11]. This assumption is stated by Enick et al. [16] not to generate any significant errors even for high humidities as is the case in evaporative cycles.

Conclusions

A study of a part flow evaporative gas turbine system with additional live steam injection has been simulated. The gas turbine core was the high pressure aeroderivative Rolls Royce Trent. The fraction of compressed air after cooling bleed used for the humidification system (β) was varied between 1 and 0. Main results are as follows:

- Part-flow humidification proves favorable regarding electric efficiency, an efficiency optimum of 52.9% was found at $\beta=0.2$. This corresponds to 12% of the compressor intake air used for humidification.
- The total area of heat exchanger equipment decreases monotonously when the fraction of compressed air used for humidification is lowered. A 50% heat exchanger area saving is made if 20% instead of 100% of the compressed air after cooling bleed is used for humidification. At the same time an efficiency increase of 1.4 points is achieved.
- Detailed sizing results (height, diameter) for the humidification column are presented for an array of different part flow cases.

The presence of a pronounced optimum in efficiency can be explained by the fact that the high pressure nonintercooled aeroderivative gas turbine cannot be recuperated because of low gas turbine exit temperatures. The favors of part flow humidification are therefore exceptional. For total plant profit optimum, the tradeoffs between performance and plant investment has to be considered. Judging from Fig. 8 it is advised to employ a part-flow fraction slightly lower than $\beta=0.2$ if maximum efficiency is favored.

Acknowledgments

Alstom Power, Elforsk, Sydkraft, Vattenfall, Elkraft (DK), and Statens Energimyndighet (Swedish National Energy Administration) are gratefully acknowledged for financial support. Anna C. Berglund of Thurne Teknik AB is acknowledged for providing data for Norton's tower internals products.

Nomenclature

β = fraction of compressed air led to humidifier circuit. This value is defined on a basis of the accessible air flow after turbine cooling bleed (see Fig. 1.)
ω = humidity ratio (kg H_2O/kg dry air)
L = liquid water flow (kg/s)
G = dry air flow (kg dry/s)
h = bulk humid air enthalpy (kJ/kg dry air)
h^* = humid air enthalpy at liquid-air interface (kJ/kg dry air)
T = temperature (°C)
T_{ad} = adiabatic temperature of saturation (°C)
RH = percent relative humidity (%)
p = pressure (bar)
M = molecular weight (kg/kmole)
$\dot{E}$ = net energy flow downwards in humidifier (kW)
c_p = heat capacity at constant pressure (kJ/kg, °C)
LHV = lower heating value (MJ/kg)
NTU = number of transfer units
HTU = height of a transfer unit (m)
Z = packing height (m)

Subscripts

da = pertaining to dry air portion
H_2O = pertaining to H_2O part in humid air
L = pertaining to liquid phase
G = pertaining to air phase

Appendix A

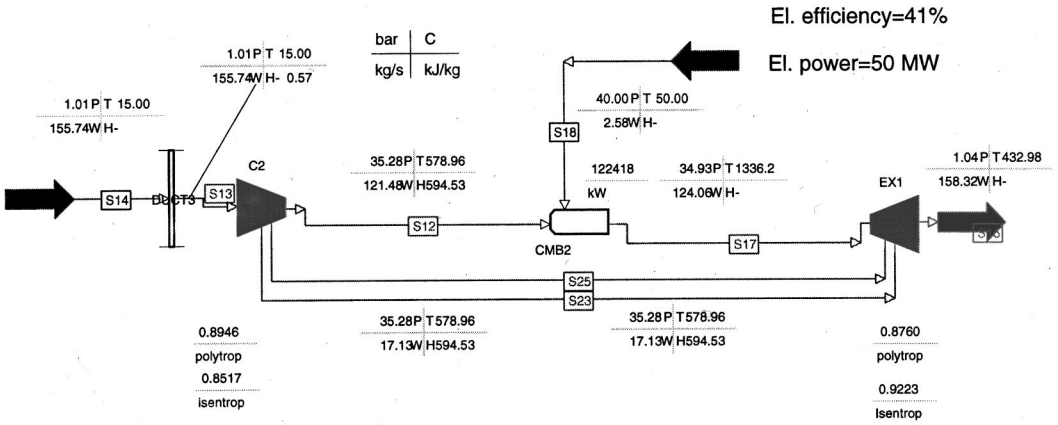

DRY ROLLS ROYCE TRENT MODEL

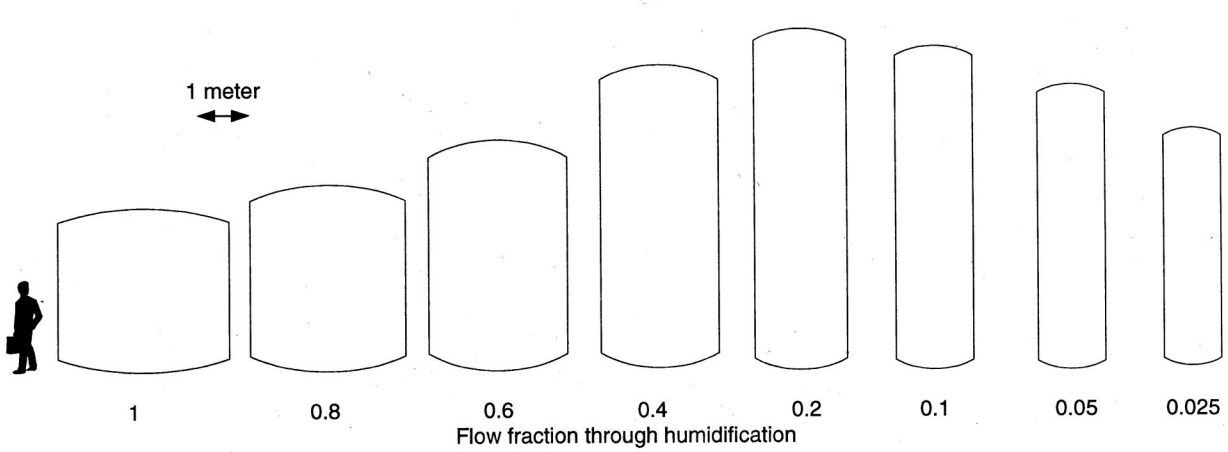

RELATIVE SIZE SCALE OF HUMIDIFIER

Appendix B

Full-Flow EvGT Case (β=1)

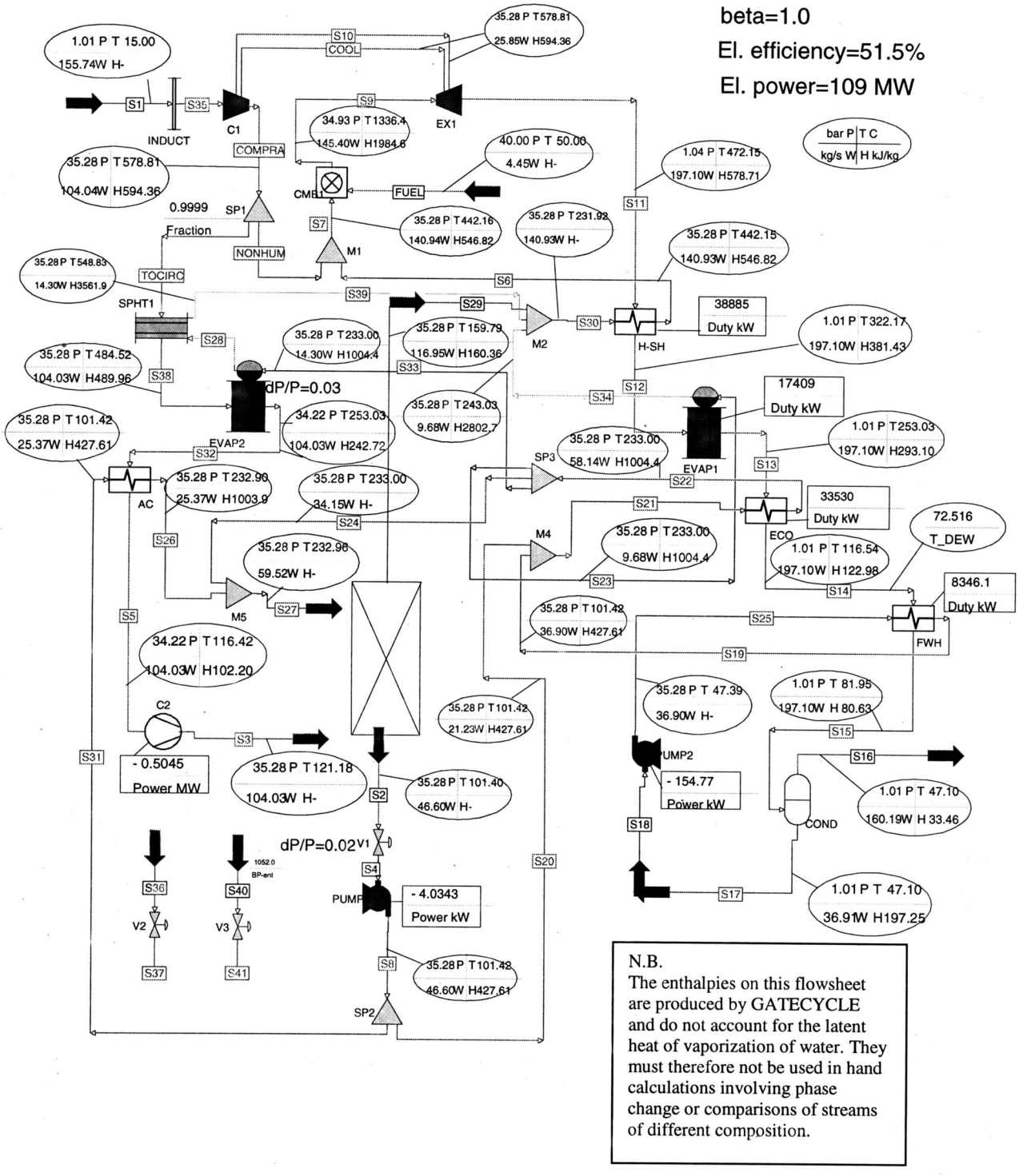

Appendix C

Part-Flow Case (β=0.2)

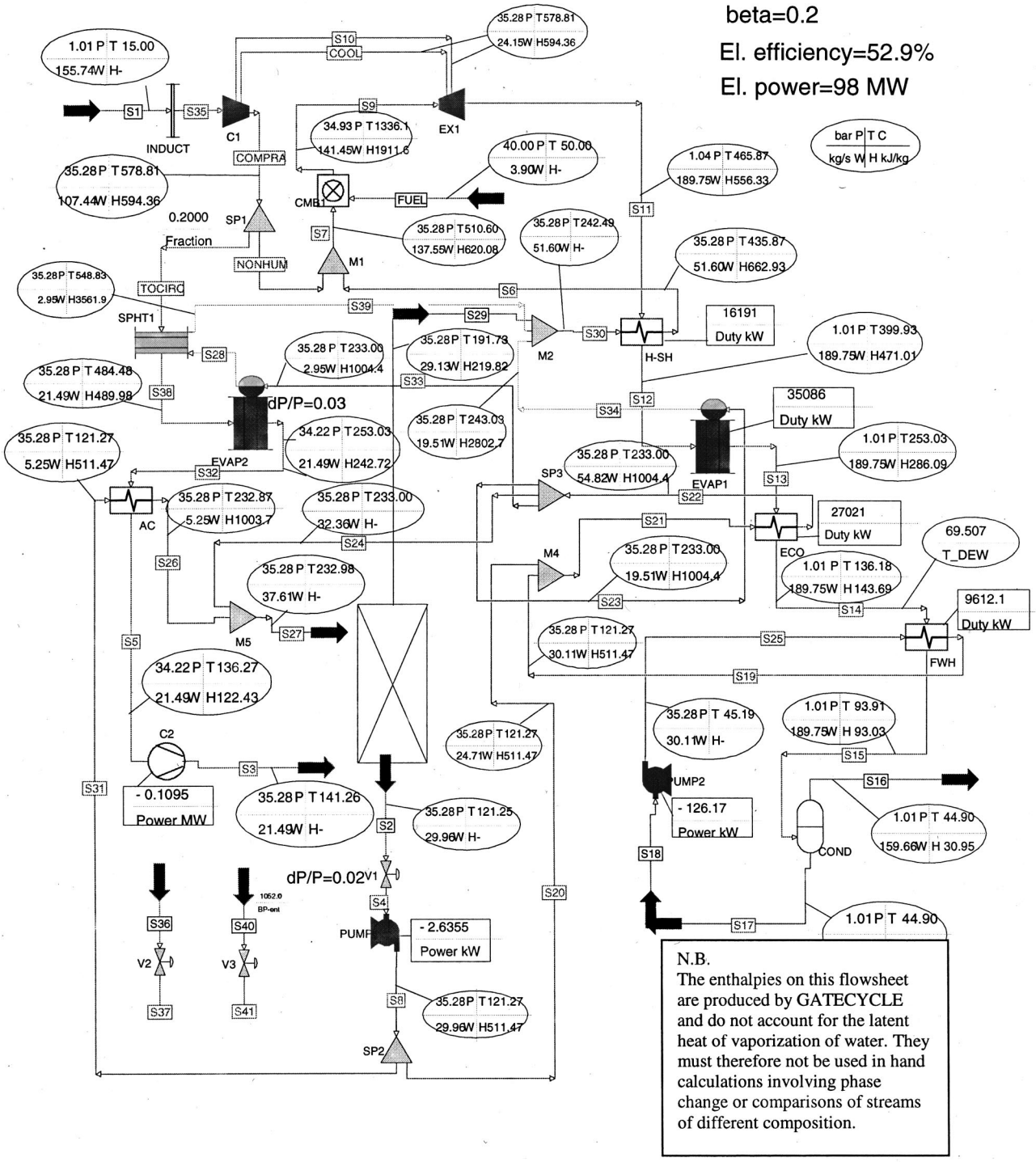

References

[1] Rao, A. D., 1989, ''Process for Producing Power,'' U.S. Patent No. 4,829,763, May 16.

[2] Nilsson, P. A., ed., 1996, ''EvGT—Evaporative Gas Turbine—Block 3,'' Technical Report, Lund Institute of Technology, Department of Heat and Power Technology, Lund, Sweden.

[3] Ågren, N., Westermark, M., Bartlett, M., and Lindquist, T., 2000, ''First Experiments On An Evaporative Gas Turbine Pilot Power Plant: Water Circuit Chemistry and Humidification Evaluation,'' ASME Paper No. 2000-GT-168.

[4] Lindquist, T., Rosén, P., and Torisson, T., 2000, ''Evaporative Gas Turbine Cycle—A Description of a Pilot Plant and Operating Experience,'' accepted for 2000 ASME International Mechanical Engineering Congress and Exposition, Nov. 5–10, Orlando, FL.

[5] Lindquist, T., Rosén, P., and Torisson, T., 2000, ''Theoretical and Experimental Evaluation of the EvGT-Process,'' accepted for 2000 ASME International Mechanical Engineering Congress and Exposition, Nov. 5–10, Orlando, FL.

[6] Ågren, N., Cavani, A., and Westermark, M., 1997, ''New Humidification Concept for Evaporative Gas Turbine Cycles Applied to a Modern Aeroderivative Gas Turbine,'' *Proceedings, ASME Advanced Energy Systems Division*, M. L. Ramalingam et al., eds., ASME, New York, **37**, pp. 223–230.

[7] Ågren, N., Cavani, A., and Westermark, M., 1997, ''New Humidification Concept in Evaporative Gas Turbine Cycles,'' *Proceedings of the TAIES'97, Thermodynamic Analysis and Improvement of Energy Systems*, Chinese Society of Engineering Thermophysics, Beijing, China, June 10–13, Beijing World Publishing Corp., Beijing, China.

[8] Nakamura, H., Takahashi, T., Narazaki, N., Yamamoto, F., Sayama, N., 1985, ''Regenerative Gas Turbine Cycle,'' U.S. Patent 4,537,023, Aug. 27.

[9] Nakamura, H., Takahashi, T., Narazaki, N., Yamamoto, F., and Sayama, N., 1987, ''Regenerative Gas Turbine Cycle,'' U.S. Patent 4,653,268, Mar. 31.

[10] Westermark, M., 1996, ''Method and Device for Generation of Mechanical Work and, if Desired, Heat in an Evaporative Gas Turbine Process,'' International Patent Application No. PCT/SE96/00936.

[11] Mickley, H. S., 1949, ''Design of Forced Draught Air Conditioning Equipment,'' Chem. Eng. Prog., **45**, pp. 739ff.

[12] *Perry's Chemical Engineers' Handbook*, 7th Ed., 1997, McGraw-Hill, New York.

[13] Ågren, N., 2000, ''Advanced Gas Turbine Cycles With Water-Air Mixtures as Working Fluid,'' doctoral thesis, Royal Institute of Technology, Stockholm, Sweden.

[14] Strigle, R., 1994, *Packed Tower Design and Applications, Random and Structured Packings*, 2nd Ed., Gulf Publishing Corp., Houston, pp. 150–159.

[15] Hyland, W., and Wexler, A., 1983, ''Formulations for the Thermodynamic Properties of Dry Air and Saturated Air-Water Mixtures,'' ASHRAE Trans., **89**(2A), pp. 520–535.

[16] Enick, R. M., Klara, S. M., and Marano, J. J., 1995, ''A Robust Algorithm for High-pressure Gas Humidification,'' Comput. Chem. Eng., **19**, pp. 1051–1061.

[17] Wark, K., 1995, *Advanced Thermodynamics for Engineers*, McGraw-Hill, Singapore.

Design Study of Part-Flow Evaporative Gas Turbine Cycles: Performance and Equipment Sizing—Part II: Industrial Core

N. D. Ågren[1]
e-mail: niklas@comsol.se

M. O. J. Westermark

Department of Chemical Engineering/Energy Processes, Royal Institute of Technology, SE-100 44 Stockholm, Sweden

This is Part II of a two-part paper and presents calculation results of a part-flow EvGT cycle based on gas turbine data for the ABB GTX100 (modified for intercooling). The evaporative gas turbine cycle is a new high-efficiency cycle that has reached the pilot testing stage. This paper presents calculation results of a new humidification strategy based on part-flow humidification. This strategy involves using only a fraction of the compressed air for humidification. Thermodynamically, it can be shown that not all the air needs to be passed through the humidification system to attain the intrinsic good flue gas heat recovery of an EvGT cycle. The presented system also includes live steam production and superheating, by heat from the hottest flue gas region, for injection. The humidifier then only uses the lower temperature levels, where it is best suited. The analyzed system is based on data for the ABB GTX100.gas turbine in intercooled mode. Part I of this two-part paper presents the results based on data for the aeroderovative Rolls Royce Trent. Simulation results include electric efficiency and other process data as function of degree of part flow. A detailed model of the humidifier is used, which produces sizing results both for column height and diameter. Paper I includes detailed description of the modeling. For the GTX100 system, full-flow humidification generates an electric efficiency of 52.6% (simple cycle 36.2%). The efficiency is virtually unaffected if the air portion to humidification is cut to 60% of accessible compressor air (represents 48% of compressor intake). If 30% of air from the compressor after cooling bleed (24% of intake) is led to the humidifier, the efficiency is reduced to 52.2%. On the other hand is the total heat exchanger area reduced by 20% and column volume by 50%. This calls for a recommendation not to use all the compressed air for humidification. It is recommended to use 15–30% of compressor intake air. The exact economic optimum depends on local fuel prices, CO_2 *taxes, interest rates, etc.* [DOI: 10.1115/1.1476925]

Introduction

This is Part II of a two-part paper ([1]). This Part II presents simulation results of a new part-flow layout of the EvGT process, based on gas turbine data of the industrial gas turbine ABB GTX100 modified to include intercooling. In Part I, the introduction to the subject of part flow humidification in evaporative gas turbine cycles is presented, as well as extensive modeling description of the humidifier. Part I also presents simulation results of a system based on gas turbine data of a Rolls Royce Trent aeroderivative. It is strongly advised to read Part I of the paper before continuing with this part, since Part I includes a more general discussion of the EvGT and part flow humidification. This part concentrates on the results and discussion of evaporative intercooled industrial gas turbines.

The system involves water addition to the compressed air with both a heat recovery steam boiler and a humidification system. The boiler produces steam by heat recovery from the highest temperature of the flue gas (above the boiling point). After the boiler, the humidification system recovers heat in the lower temperature region (below the boiling point). The virtue of the humidification system is its capability of producing water vapor below the boiling point of water, why it is situated where is best suited. Evaporation heat for the humidifier is also taken from the aftercooler and the intercooler. System performance and sizing of equipment is evaluated with the fraction of air to the humidifier as a parameter.

System Description

Figure 1 shows the system that was simulated in this study. The gas turbine data are taken from the ABB GTX100. This is a gas turbine with intermediate pressure ratio, 20 and an electric efficiency of 36% for simple cycle without evaporation. The EvGT system is only evaluated with regard to power production, not heat production.

The water addition to the compressed air is done by both a steam boiler at the highest temperature level of the flue gas (above boiling point), and the humidification system, that uses the heat at low temperature levels (below boiling point). The humidifier is with other word used where it is of best suited. The advantage with an EvGT humidification system is that it can produce water vapor below the boiling point at the governing total pressure. The humidification system also picks up heat from the aftercooler and the intercooler. All water streams destined for the humidification column are heated to 10°C below boiling point. This is done to avoid cavitation at any geometric irregularities in the flow path. The gas turbine is modeled as intercooled and the intercooler's lowest temperature region is used to preheat the recycled condensate feed. This feed is mixed with the tower outlet water when it reaches the temperature of the tower outlet water. This is done to avoid unnecessary mixing irreversibilities. The flue gas condenser (FGC) is included in the system for water recycling but the condensation heat is disposed of. The FGC flue gas exit temperature is calculated for a water balance, i.e., the plant made is self sufficient with water. The theory and practice of water balancing in an EvGT plant has been described by Agren et al. [2].

[1]Currently at Comsol AB, Tegnérgatan 23, SE-111 40 Stockholm, Sweden.

Contributed by the International Gas Turbine Institute (IGTI) of THE AMERICAN SOCIETY OF MECHANICAL ENGINEERS for publication in the ASME JOURNAL OF ENGINEERING FOR GAS TURBINES AND POWER. Paper presented at the International Gas Turbine and Aeroengine Congress and Exhibition, New Orleans, LA, June 4–7, 2001; Paper 2001-GT-113. Manuscript received by IGTI, Dec. 2000, final revision, Mar. 2001. Associate Editor: R. Natole.

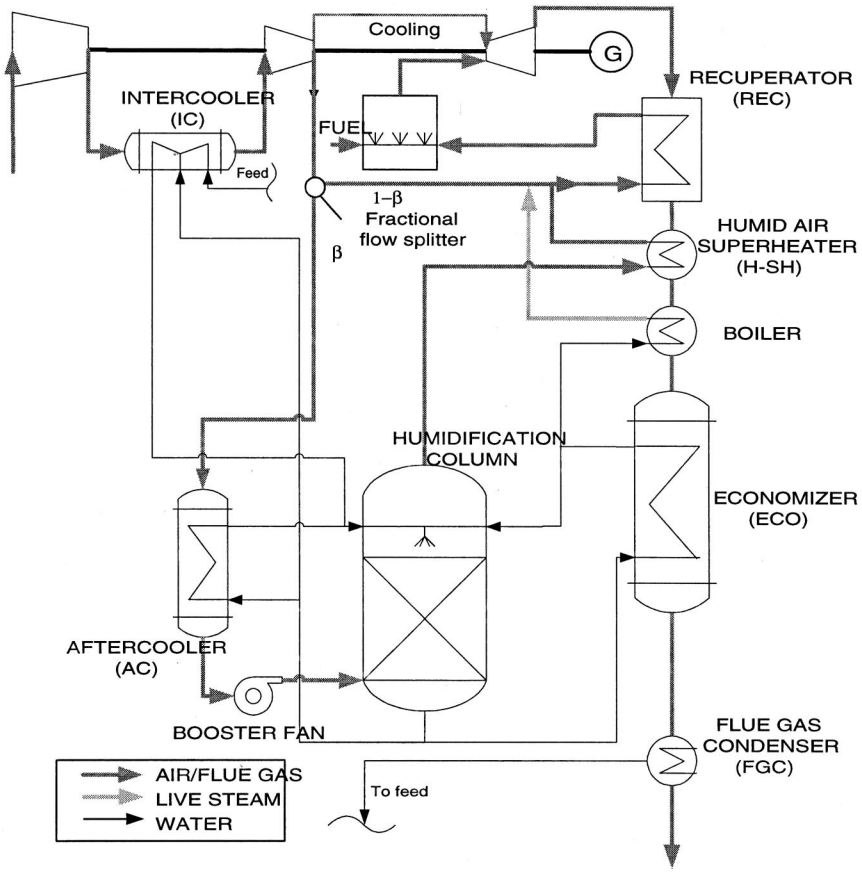

Fig. 1 Flowsheet of the part-flow process

The heat exchangers were modeled with assumptions of approach minimum temperature difference and overall heat transfer coefficients (see Table 1). The humid air superheater is not included in Table 1. It was instead designed to heat the humid air to 225°C, which is enough to avoid dewout in the mixing point before the recuperator (Fig. 1). No steam boiler is used before the aftercooler, because of the relatively low temperature of the compressed air.

The compressed air stream splitter after the cooling bleed is where the air is variably bypassed the humidification system. The mass flow fraction led to the humidifier is called β.

In practice, a small waste bleedoff from the water stream leaving the tower should be used to make up for impurity buildup in the circuit ([2]). This is, however, not included in the calculations since it probably doesn't affect the results to a large extent.

A booster fan for the humidification air is used to make up for the pressure drop in the humidification circuit.

Assumptions

Turbo Package Adaption. To employ a gas turbine model with reasonable component efficiencies, firing temperatures, first rotor temperatures, etc., data for an existing gas turbine were used. This reflects present technology concerning materials and aerodynamics. However, the EvGT introduces significant changes in working conditions for the gas turbine. In the EvGT models in this work, the compressor airflow, and characteristics are kept constant, which means that the expander is exposed to higher volumetric flow than at dry design conditions. The expander probably needs redesign because of this (compressor redesign is also an option if a retained expander volumetric flow is chosen). In this work, the existing dry data are, however, accepted, to show the process potential of the EvGT with the same turbo-prerequisites as a dry cycle.

Data for the ABB GTX100 were retrieved from the GATECYCLE GT library. The machine was then built in GATECYCLE component by component in a dry model and the data from the library model were used to mimic the unit. The library data used to fit the dry model to are presented in Table 2.

The dry model was adapted to the library data and the following additional data could be retrieved: compressor polytropic efficiency: 0.901, expander polytropic efficiency: 0.853. These data

Table 1 Heat exchanger assumptions

	ΔT_{min} (°C)	U (W/m^2, °C)
IC	30	100
REC	30	100
Boiler	10 (at drum)	300
AC	15	300
ECO	15	300

Table 2 Library data for ABB GTX100 (open sources)

Inlet air flow	118.9 kg/s
Compressor inlet pressure (after duct)	1.007 bar
Compressor outlet temperature	450°C
Compressor outlet pressure	20.3 bar
Expander outlet temperature	554°C
Expander outlet pressure (before heat recovery units)	1.038 bar
Combustor outlet temperature	1358°C
Combustor efficiency	99.9%
Combustor pressure drop (% of inlet pressure)	3%
Generator efficiency	95.8%
Shaft power	43.3 MW
Total cooling flow (% of comp. intake)	19%

Table 3 Various system results based on 118.9 kg/s compressor intake

β	Humidification rate (kg H2O/kg intake air)	Cooling flow (kg/kg intake air)	η_{el} (LHV)	Fuel energy cons. (MW) LHV	Net Electric power (MW)
dry	-	0.19	0.362	115.9	41.5
1	0.187	0.222	0.526	149.1	78.3
0.8	0.185	0.221	0.526	148.8	78.3
0.6	0.182	0.220	0.526	148.2	77.9
0.4	0.177	0.220	0.524	147.1	77.1
0.2	0.167	0.219	0.519	144.7	75.1
0.1	0.156	0.219	0.512	142.2	72.9
0.05	0.147	0.217	0.506	139.9	70.8
0.025	0.139	0.215	0.500	138.0	69.0

Table 4 Auxiliaries' efficiencies

	Isentropic	Shaft+Bearing	El. Drive
Booster fan	0.7	0.9	0.95
pumps	0.85	0.9	0.95

Table 5 Humidification distribution and booster effect

β	Dry Air Flow to Humidifier (kg/s)	Evaporated Water in Humidifier (kg/s)	Steam Flow From Boiler (kg/s)	Power Consumption of Booster Fan (kW)
1	92.5	17.4	4.8	737.7
0.8	74.1	16.0	6.0	594.5
0.6	55.6	14.5	7.2	451.8
0.4	37.1	12.6	8.4	307.8
0.2	18.6	9.9	10.0	161.1
0.1	9.3	7.4	11.1	84.3
0.05	4.7	5.3	12.1	43.9
0.025	2.3	3.6	12.9	22.8

together with applicable data from Table 2 were then used in the evaporative cases. A flow sheet of the dry model is shown in Appendix A.

In the evaporative cases, the compressor flow was kept constant, whereas the expander volumetric flow changed according to the added water vapor.

Gas Expander Cooling. The cooling of the gas expander was mimicked by running a dry case of the RR Trent based on data-bank data, selecting right cooling air fraction of compressor intake air. In the dry GTX case it is 19%, extracted from the compressor outlet. In the dry model, this amount was equally distributed to the first nozzle cooling port and first rotor cooling port in the GATECYCLE expander model. This resulted in a reported first-stage rotor temperature of 1275°C. In the evaporative cases the combustor outlet temperature from Table 2 (1358°C) was used. But the flow of hot combustion products from the combustor is higher because of the added water vapor, which is why a larger amount of cooling air is needed. In the wet runs, the cooling air flow was thus controlled to meet the first stage rotor temperature of 1275°C. This is reasonable, because it is the same assumption as is done in the GATECYCLE library model of the dry engine. It proved not to be much difference in cooling flow between the dry reference and the evaporative cases, because the intercooling makes the cooling air colder, why it counterbalances the extra mass flow from the combustor (see Table 3 and Appendix D).

Additional Assumptions and Boundary Conditions. The ambient conditions for all calculations were $T=15°C$, $p=1.013$ bar, RH=60%. The electric efficiency (LHV) is calculated accounting for auxiliaries (booster fan and water pumps). The fuel is natural gas (LHV=47.45 MJ/kg).

Tables 1 and 4 show additional component assumptions. The humid air superheater is used to heat the air to 225°C which is necessary to avoid dewout in the mixing point with the steam. The pressure drop over the humidification system were taken as 3% of compressor outlet pressure, which is compensated by the booster fan.

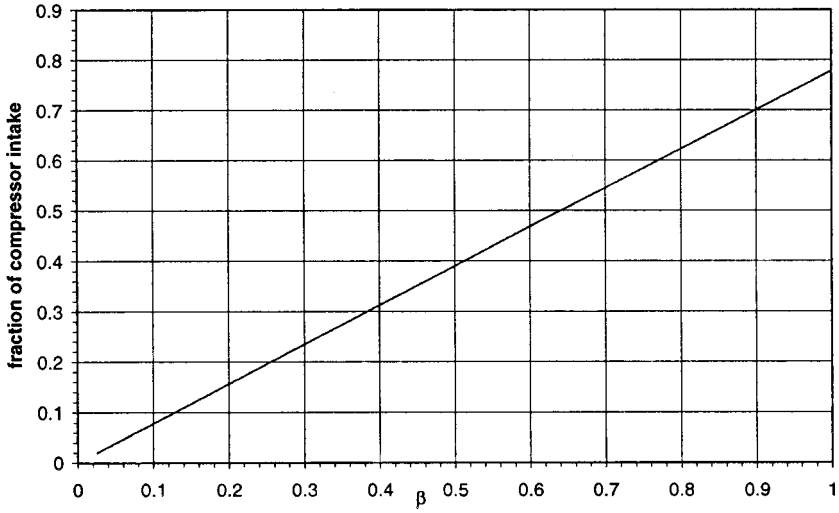

Fig. 2 Conversion from β to fraction of compressor intake air used in the humidifier circuit

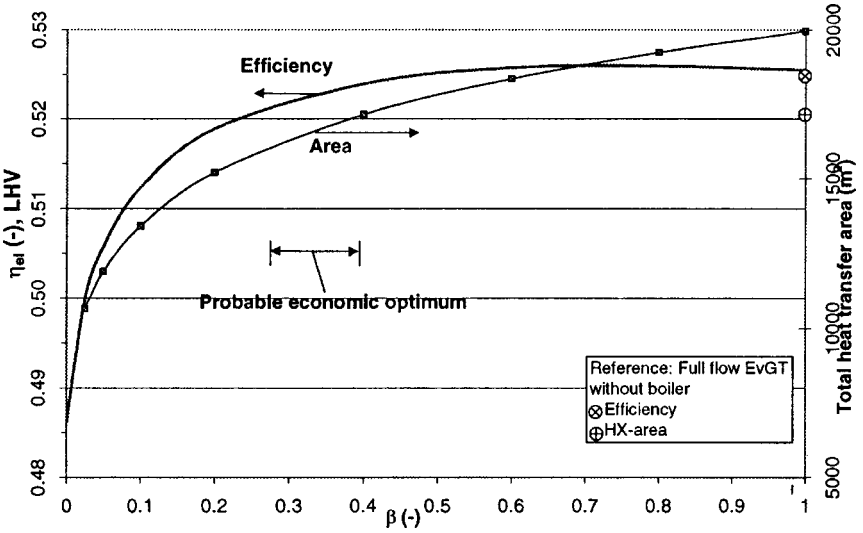

Fig. 3 Electric efficiency and total heat transfer area versus β

Results and Discussion

All calculations were made with the part flow fraction β as main parameter. β expresses the fraction of available compressed air after cooling extraction that is led to the humidification system. If F denotes the airflow in kg/s after cooling extraction, then $F\beta$ kg/s goes to the humidification system and $F(1-\beta)$ kg/s goes directly to the recuperator (see Fig. 1). This value is intuitive since $\beta=1$ represents full flow humidification and $\beta=0$ represents no humidification (STIG). It might also be desired to express the air fraction used for humidification on basis of compressor intake air. Since the cooling flow varies slightly over the cases (see Table 3 and Appendix D), the relation between β and fraction of compressor intake is not fully linear. For the reader's convenience the relation is plotted Fig. 2.

Figure 3 shows one of the more important curves from the parametric calculations. The electric efficiency for full flow ($\beta=1$) is 52.6%. When the air is gradually bypassed around the humidification system, the efficiency trend is essentially flat. When the humidification air fraction approaches 0.5, the efficiency starts to fall.

As stated in Part I of this paper, a decrease in air fraction led to the humidification system (introduction of part flow humidification) is not identical to a proportional decrease in heat recovery potential in the humidification system. One penalty, though, for part flow humidification (in specific at very low values of β) is that the tower outlet water temperature will be higher. This impairs the heat recovery potential in the economizer and intercooler. On the other hand, full flow mode degrades the system by exposing the entire compressed air stream to the pressure drops in the humidification section. This pressure drop is regained with the booster fan (see Fig. 1), of which the compression work steals efficiency points.

These pros and cons apparently counterbalance each other in the β region 1–0.5.

Figure 3 also depicts the total heat transfer area needed for the different cases. The total area decreases monotonously with decreased β. Consider that the total plant investment is assumed to follow some function that increases with increased total heat exchanger area and cost of pipes, channels, and booster fan, etc. For an minimum production cost, fuel expenses (including CO_2 taxes) and capital costs must be weighed against each other. A production cost minimum will then probably appear somewhere in the region noted in Fig. 3. In this region, the efficiency drop is only 0.3 efficiency points whereas the area saving is around 20% compared with full flow. So, only the fraction needed for sufficient humidification heat recovery (and total efficiency) should be used.

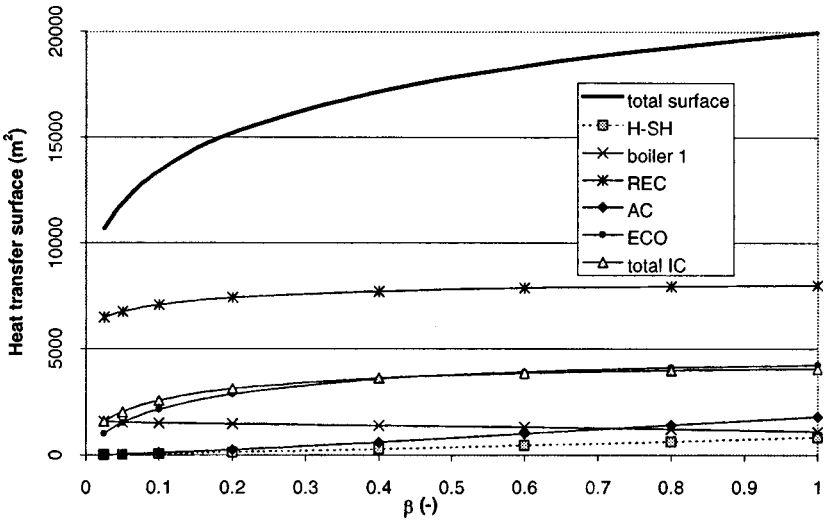

Fig. 4 Distribution of heat transfer surface versus β

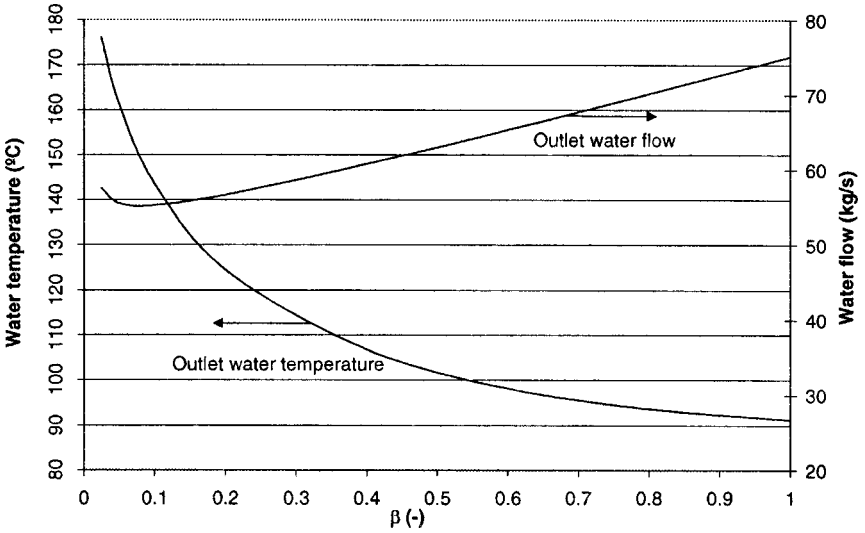

Fig. 5 Column water outlet temperature and water flow versus β

The rest should be bypassed directly to the combustor to save capital costs. The exact total economic optimum depends on local fuel prices, taxes, and interest rates.

Figure 4 shows the heat transfer area for each heat transfer unit. The recuperator area is rather constant in a large part of the region. This is because the mass flow (air+humidity) is rather constant, as well as the cold stream entry temperature. The moderate drop below $\beta=0.2$ is because of lower humidity and slightly higher cold inlet temperature. The ECO and IC areas tend to fall steeper below $\beta=0.4$ than above 0.4. This is because the tower outlet water temperature does not increase very fast in the region $\beta=0.4-1$ (see Fig. 5). As the tower outlet water temperature increases more rapidly below $\beta=0.4$, less heat transfer can take place and the ECO and IC area is decreased. The boiler area is increasing when leading less air to the humidification system, because more heat is available due to smaller H-SH and REC.

The outlet temperature from the humidifier is presented in Fig. 5. In the full flow case, the temperature is 101.5°C. This temperature is governed by the working line and its ''pinch'' location against the saturation curve, as shown in Fig. 6.

The minimum ΔT_{ad} value is set to 4°C for all cases. The value on the abscissa for the bottom end of the working line is the tower outlet water temperature. The outlet water temperature increases only about 4°C in the region $\beta=1$ to 0.6 (Fig. 5), because the ''pinch'' is located very near the bottom end (Fig. 6). As less air is led through the humidification ($\beta<0.60$), the working lines will gradually get steeper and hence the tower outlet water temperature will increase faster and faster. The outlet water temperature limit for $\beta\rightarrow 0$ is 203°C and can be deducted both from Fig. 5 and Fig. 6. This equals the tower inlet water temperature. This limit value of the outlet temperature is of no practical importance, since it reflects a case where the air flow is so minute that it does not affect the water at all, and practically no humidification takes place.

In the calculations, the outlet water flow from the tower, for a given β, is selected to match the maximum flow the economizer can handle to produce water of 203°C. This flow is thus governed by the minimum temperature difference in the economizer. Since different flows give different tower outlet water temperatures, which in turn affects the capacity of the economizer, the water flow match is an iterative procedure. The results for each β can be seen in Fig. 5. At full flow ($\beta=1$) the water flow is 75 kg/s. As less air is used for humidification, the tower outlet water flow decreases. This is because the AC can produce less water, and the

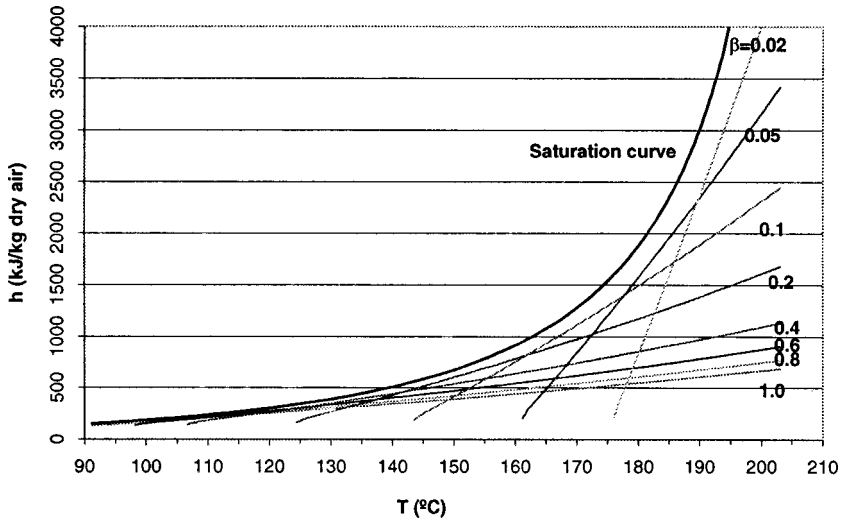

Fig. 6 Working lines for all part flow cases

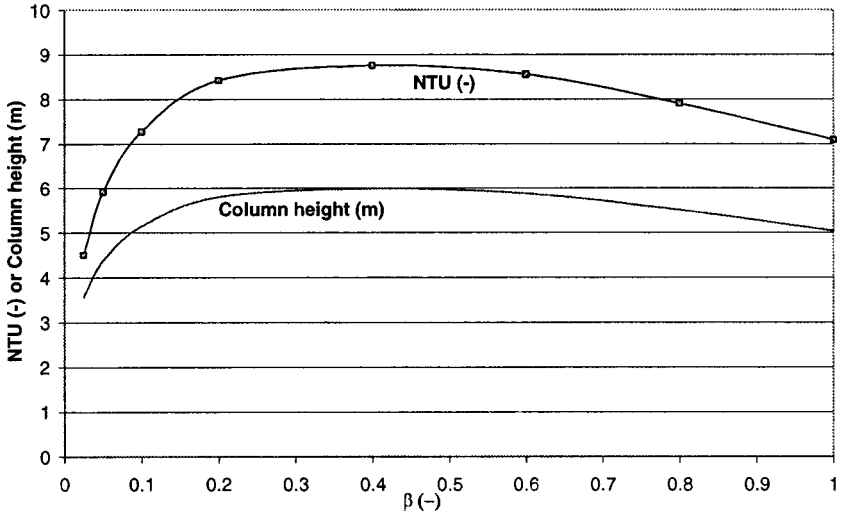

Fig. 7 Number of transfer units and column shell height versus β

total water addition to the air is somewhat less. At very low β values (very small air flow through the humidifier), the tower outlet water temperatures will increase very rapidly (see Fig. 5). This has the new effect that very low a temperature rise is needed in the ECO to "top off" the water up to 203°C. Therefore, more water can be fed from the humidifier again. This explains the existence of a flow minimum at $\beta=0.1$ in Fig. 5.

Figure 7 above discloses the number of transfer units (NTU) required for each part flow case. The number of transfer units is proportional to the effective packing height Z required in the humidification column, $Z=\text{HTU}^*\text{NTU}$. HTU=0.57 m for the Intalox 2T structured packing used for this work (data courtesy of Norton Co.). The NTU is 7 for full flow and reaches a maximum of slightly less than 9 at $\beta=0.45$, to fall again below $\beta=0.45$. The limit for $\beta\rightarrow 0$ is NTU=0. Again, this is of no practical importance, since it represents a packing height approaching 0, a tower with no heat recovery effect at all (no air traveling through the column). The shape of the curve in Fig. 7 can be deducted from Fig. 6. The NTU is simply the ratio between total enthalpy transfer and the mean driving force (see Fig. 6). The total column shell height in Fig. 7 is taken as $Z+1$ to allow for distributors and fixtures.

Figure 8 complies the dimensions of the column. The diameter depends on the packing geometry, hydrodynamics, physical properties, and flow relations between the liquid and gas phase (generalized Ergun correlations courtesy of Norton Corp.). The diameter is naturally reduced with reduced air flow.

Figure 9 and Fig. 10 show the heat release diagrams for the flue gas train in two flow cases. The energy content of the ECO hot exit can be regarded as lost to the surroundings. One noticeable phenomenon is that the temperature of the flue gas exit of the feed ECO is slightly lower for the full flow case (106°C) than that of the part flow case (113°C). This trend is monotonical for the whole range of part flow cases from $\beta=1$ to $\beta=0.025$. All the exhaust temperatures are shown in Fig. 11. On comparing Figs. 3 and 11, it may at first sight appear puzzling that, e.g., the part flow case $\beta=0.6$ has essentially the same efficiency as the full flow case $\beta=1$, whereas the $\beta=0.6$ case has indeed a higher stack temperature. The explanation is that a very large amount of the flue gas enthalpy is represented by the latent heat of water vapor. So, the true enthalpy flow lost to the surroundings is dependent on both temperature and, to a larger extent, on the humidity of the flue gas.

Figure 12 shows the temperature that the end condenser must cool the flue gas to fully support the humidification with feed water. Thereby the system doesn't need any fresh feed water. The

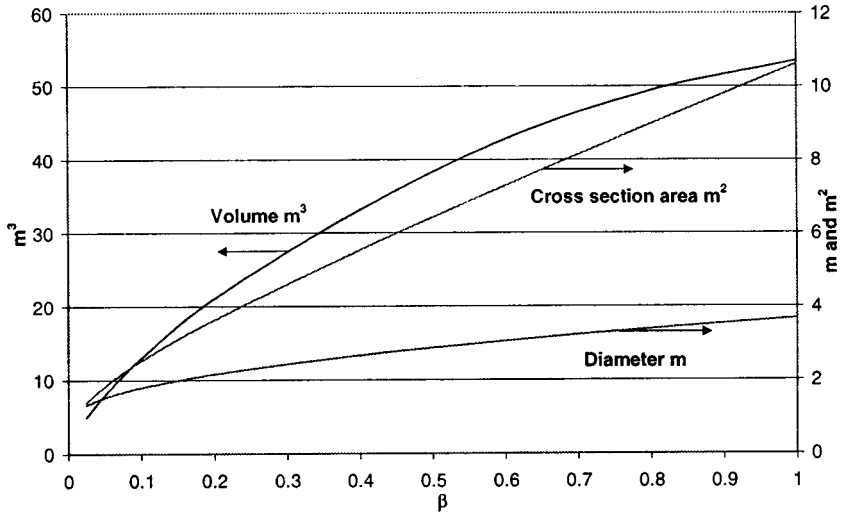

Fig. 8 Humidification column shell dimensions

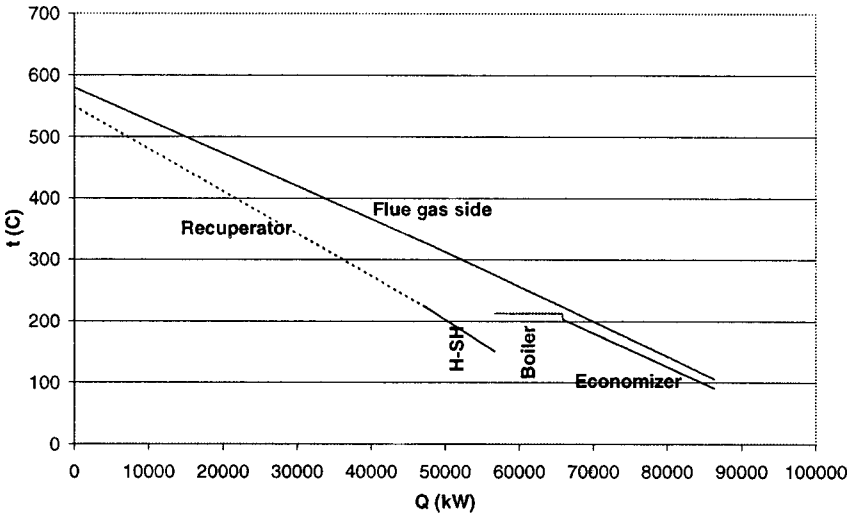

Fig. 9 Flue gas heat recovery diagram for $\beta=1$

condenser temperature is fairly constant throughout the cases. This is because the condensing temperature for self-support of water is only a function of fuel consumption per kg compressor intake air (see Ågren et al. [2]), and the fuel energy consumption does not vary very much (see Table 3 and Appendix E).

As stated in Part I, the ''pinch,'' or the minimum difference between water temperature and the air adiabatic temperature of saturation is chosen to 4°C for all calculation cases, as recommended by Strigle [3]. However, a test series of different values of ΔT_{ad} for $\beta=0.2$ was run and the results are shown in Fig. 13. The lower ΔT_{ad}, the higher the NTU, and the higher the tower. If ΔT_{ad} is chosen too small, the height will be too large, or, as $\Delta T_{ad}\rightarrow 0$, NTU$\rightarrow\infty$. This is because the driving force becomes smaller when the minimum ΔT_{ad} gets smaller. The difference 4°C is a reasonable compromise, since the tower height is reasonable and the tower outlet temperature is reasonably low.

Sources of Error. The gas mixture in the humidification tower has been regarded as an ideal mixture. Thus, the properties were calculated with steam tables and databases for pure air at their respective partial pressures, according to Dalton's law of partial pressures. As further discussed in Part I of this paper, this is a somewhat conservative assumption, which slightly underestimates the volatility in a humidifier. However, the presented trends for efficiency versus humidifier flow are not likely to change.

Conclusions

A study of a part flow evaporative gas turbine system with additional live steam injection has been simulated. The gas turbine core was an intercooled version of ABB GTX100. The fraction of compressed air after cooling bleed used for the humidification system (β) was varied between 1 and 0. Main results are

- part-flow humidification down a to a β of around 60% (48% of compressor intake) leaves the electric efficiency virtually unaffected. In this region, the thermodynamic penalties and advantages of part flow discussed above apparently counterbalance each other. If the air fraction to the humidifier is cut even more, the electric efficiency will start to drop.
- the total area of heat exchanger equipment decreases monotonously when the fraction of compressed air used for humidification is lowered.
- a 20% heat exchanger area saving and 50% column volume saving is made if 30% instead of 100% of the compressed air after cooling bleed is used for humidification. At the same

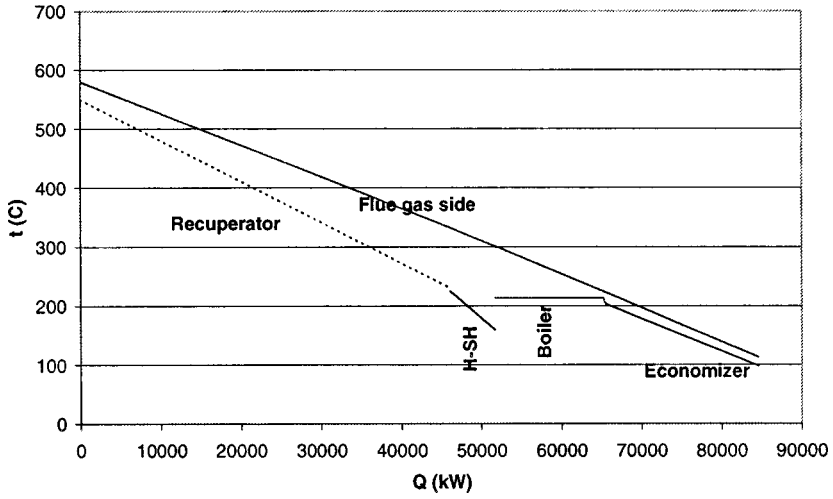

Fig. 10 Flue gas heat recovery diagram for $\beta=0.2$

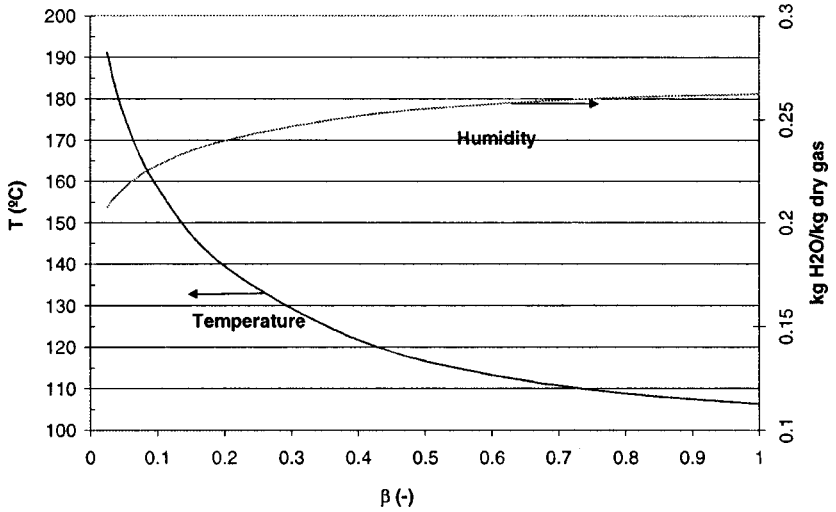

Fig. 11 Temperature and humidity of flue gas downstream ECO, versus β

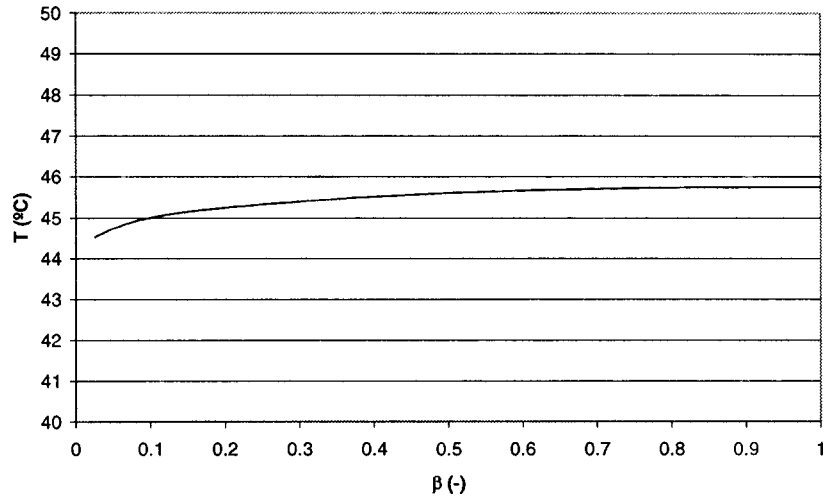

Fig. 12 End condensation temperature versus β

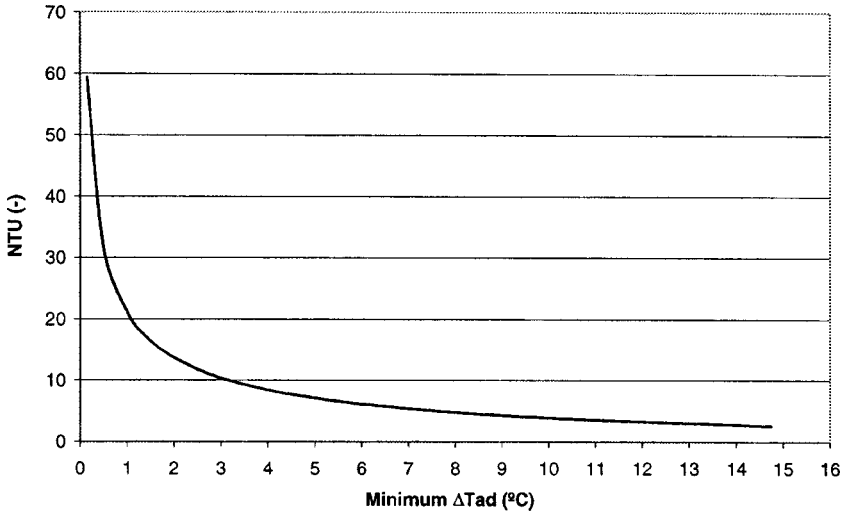

Fig. 13 Example of calculated number of transfer units as a function of minimum adiabatic temperature difference in a column for β=0.2

time the efficiency decrease is only 0.4 efficiency points (from 52.6 to 52.2%). This example corresponds to 24% of compressor intake air.

The relevance of part flow humidification is demonstrated for an intercooled industrial gas turbine. For total plant profit optimum, the tradeoffs between thermal and environmental performance, and plant investment have to be considered. Judging from Fig. 3 it is advised to employ a part flow fraction between β=0.2–0.4 (corresponding to 15–30% of compressor intake air). For a minimum production cost, fuel expenses (including CO_2 taxes) and capital costs have to be evaluated locally. Hence, the exact total economic optimum depends on local fuel prices, taxes, and interest rates.

Acknowledgments

Alstom Power, Elforsk, Sydkraft, Vattenfall, Elkraft (DK), and Statens Energimyndighet (Swedish National Energy Administration) are gratefully acknowledged for financial support. Anna C. Berglund of Thurne Teknik AB is acknowledged for providing data for Norton's tower internals products.

Nomenclature

β = fraction of compressed air led to humidifier. This value is defined on a basis of the accessible air flow after turbine cooling bleed (see Fig. 1.)
ΔT_{ad} = difference between dry bulb temperature and adiabatic temperature of saturation (°C)
RH = percent relative humidity (%)
p = pressure (bar)
LHV (MJ/kg) = lower heating value (mJ/kg)
NTU = number of transfer units
HTU = height of a transfer unit (m)
Z = packing height (m)

Appendix A

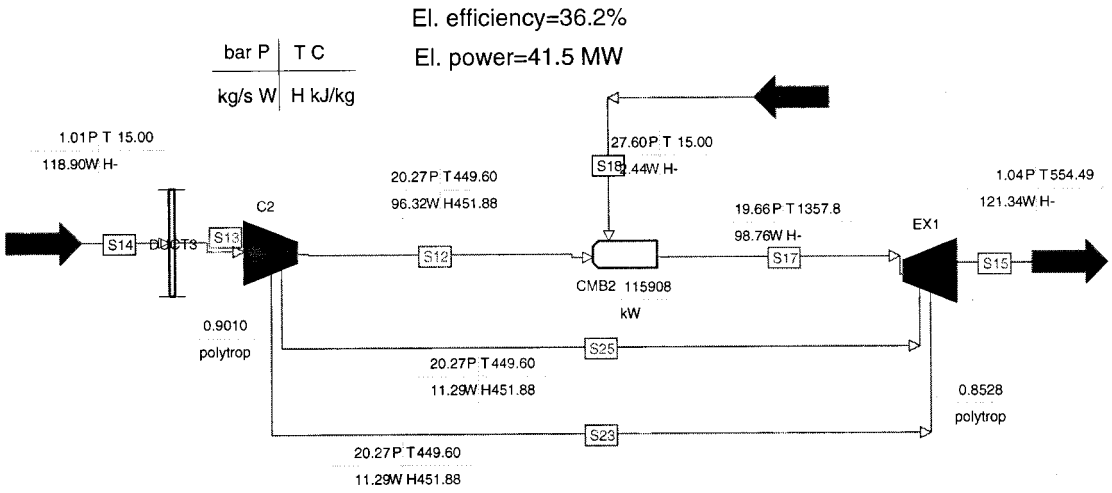

DRY ABB GTX100 MODEL

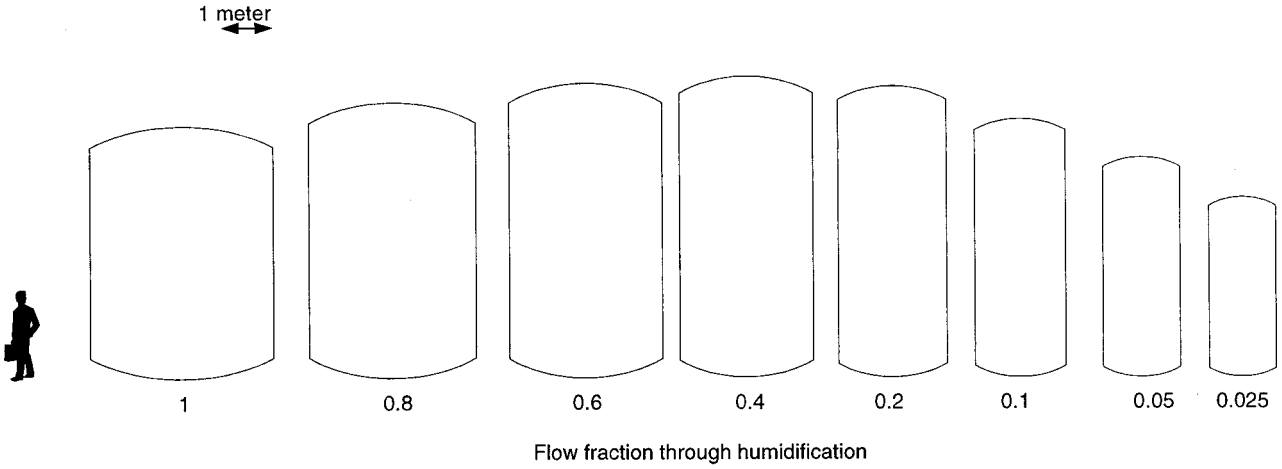

RELATIVE SIZE SCALE OF HUMIDIFIER COLUMN

Appendix B

Full-flow EvGT case (β=1)

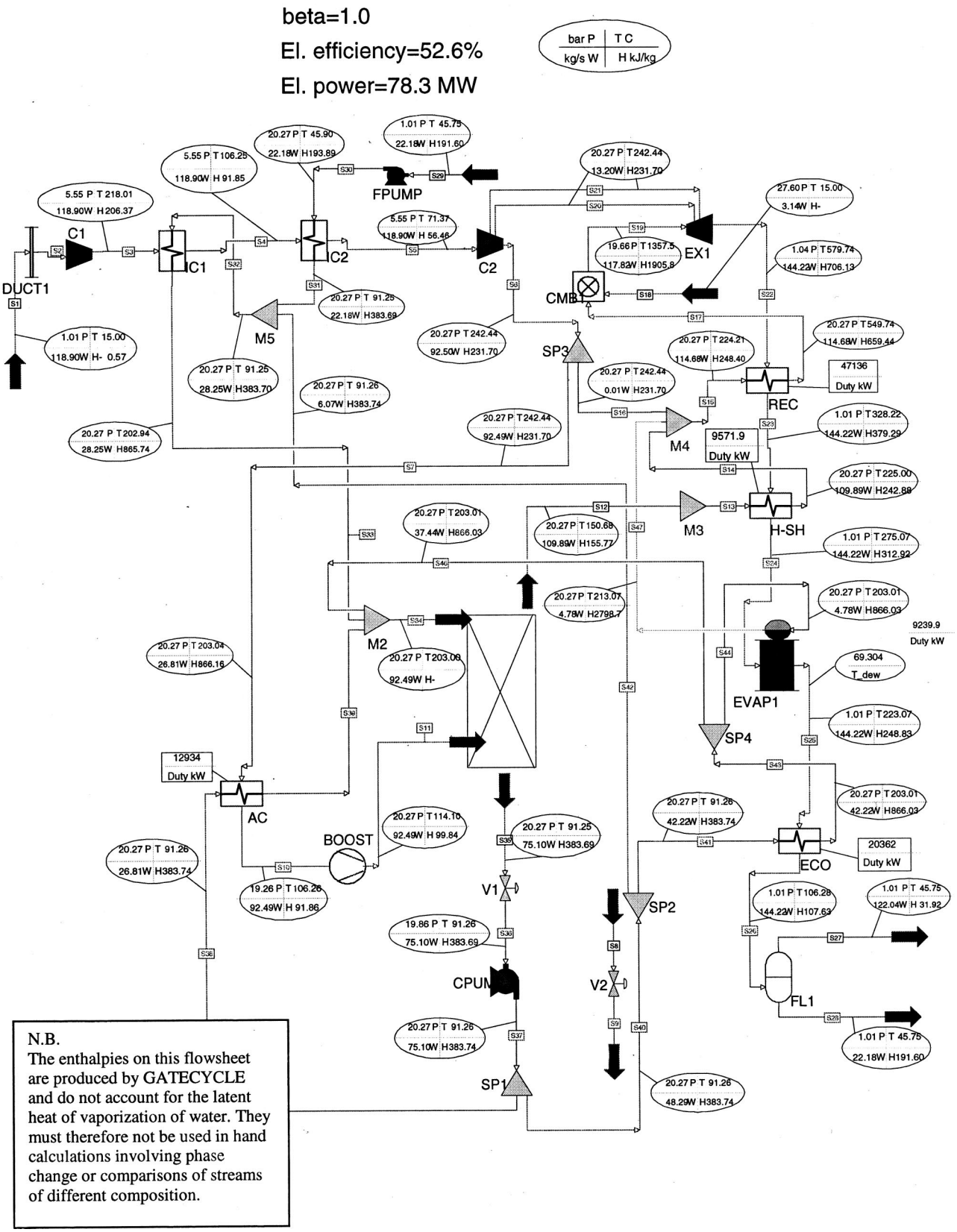

Appendix C

Part-flow case (β=0.4)

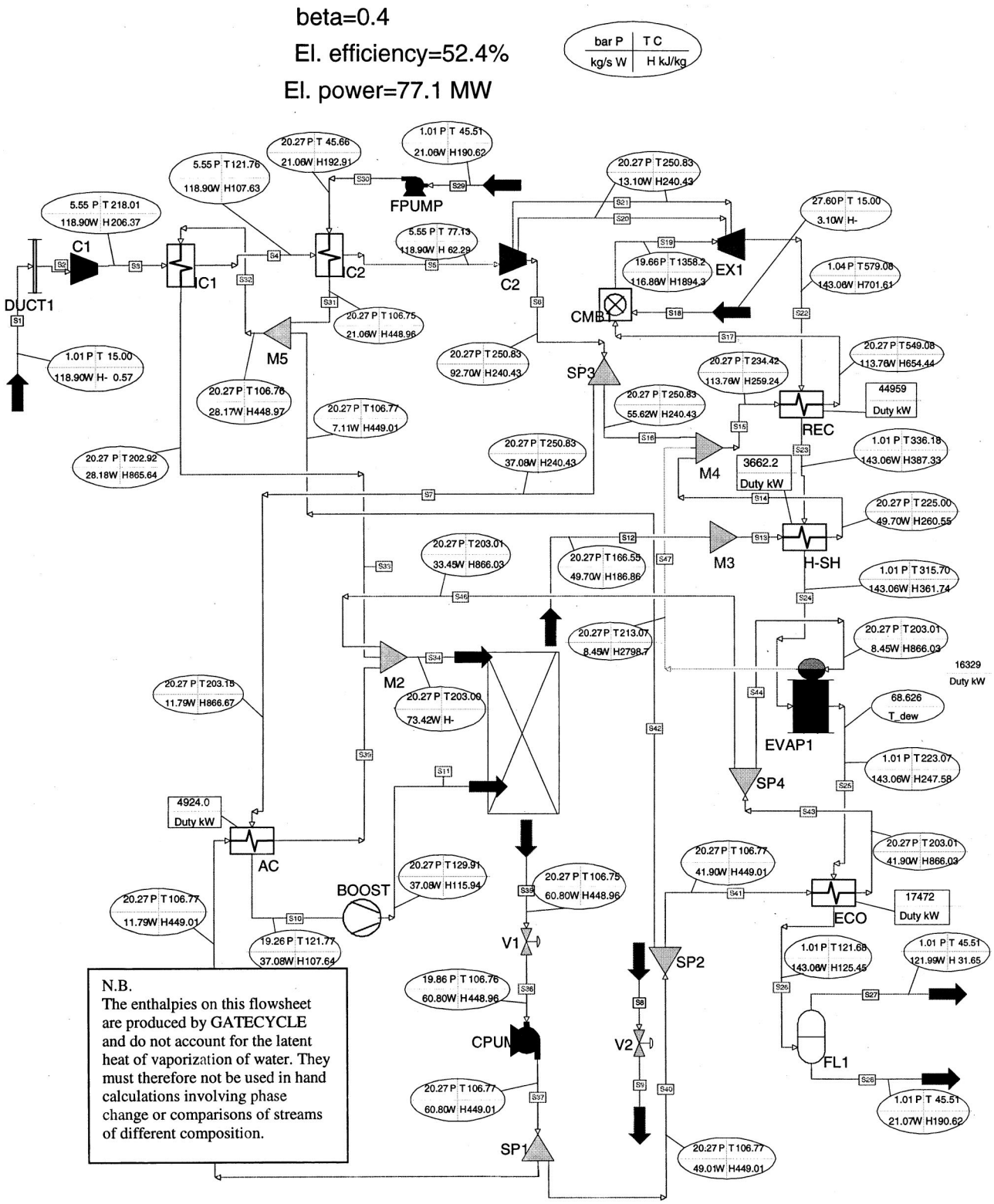

Appendix D

Part-flow case (β=0.2)

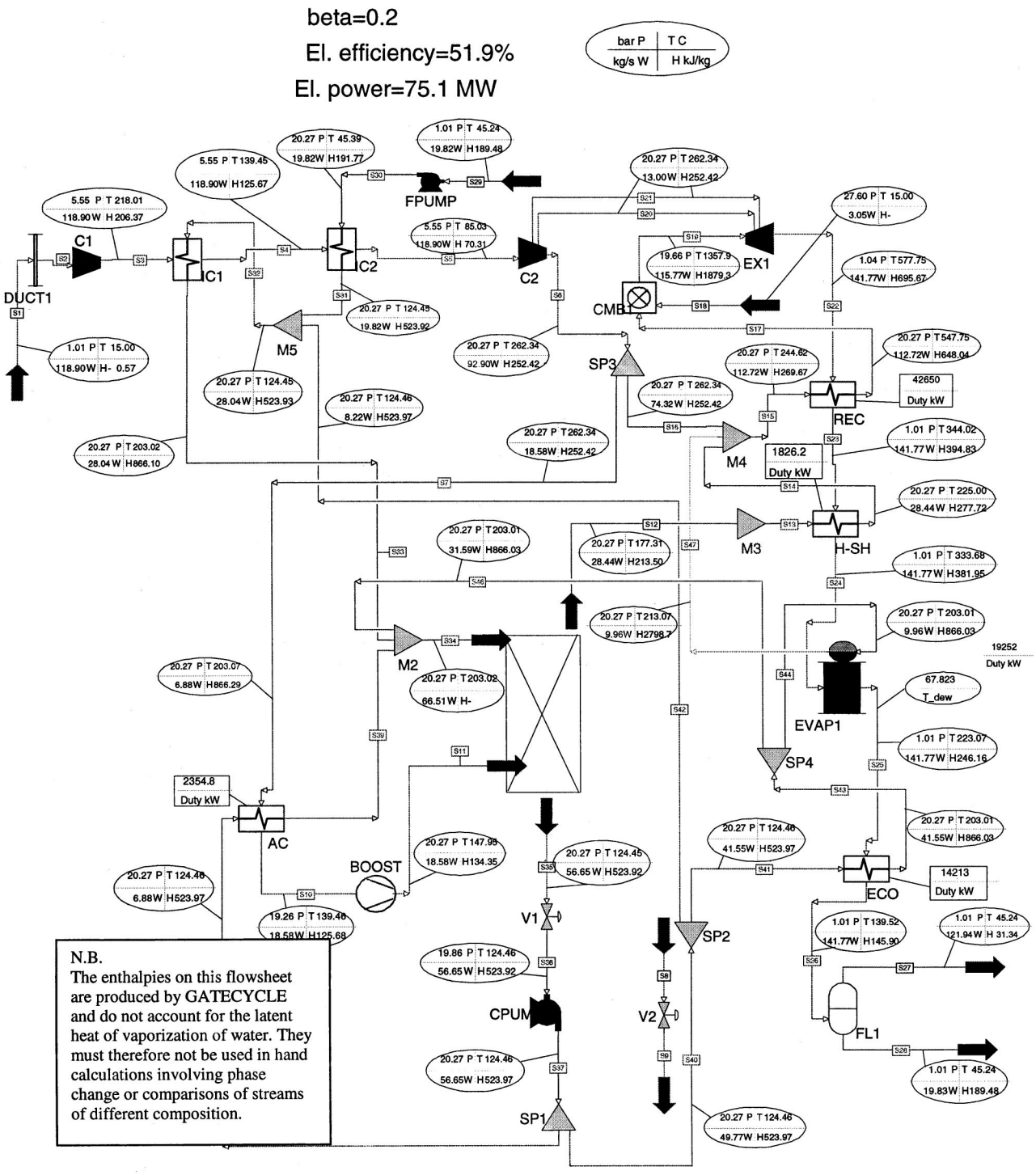

References

[1] Ågren, N. D., and Westermark, M. O. J., 2003, ''Design Study of Part-Flow Evaporative Gas Turbine Cycles: Performance and Equipment Sizing—Part I: Aerodynamic Core,'' ASME J. Eng. Gas Turbines Power, **125**, pp. 201–216.

[2] Ågren, N., Westermark, M., Bartlett, M., and Lindquist, T., 2000, ''First Experiments On An Evaporative Gas Turbine Pilot Power Plant: Water Circuit Chemistry and Humidification Evaluation,'' ASME Paper No. 2000-GT-168.

[3] Strigle, R., 1994, *Packed Tower Design and Applications, Random and Structured Packings*, 2nd Ed., Gulf Publishing Corp., Houston, TX.

Technical Risks and Mitigation Measures in Combustion Turbine Project Development

D. Grace
Senior Engineer

J. Scheibel
CT Technical Manager

EPRI,
3412 Hillview Avenue,
Palo Alto, CA 94304

Project developers, insurers, financiers, and maintenance organizations have an interest in quantifying technical risks and evaluating risk mitigation alternatives for combustion turbine (CT) power plants. By identifying exposure to risk early in the project development process, optimal procurement decisions, and mitigation measures can be adopted for improved financial returns. This paper describes a methodology used to quantify all nonfuel O&M costs, including scheduled and unplanned maintenance, and business interruption costs due to unplanned outages. The paper offers examples that demonstrate the impact of technical risk on project profitability. An overview of activities required for addressing technical risk as part of the equipment selection and procurement process is provided, and areas of technical improvements for reducing life cycle costs are described. [DOI: 10.1115/1.1496771]

Introduction

The potential impact on project profitability of risks associated with the electricity market, fuel prices, regulatory activities, and various mitigation alternatives are typically quantified during project development. By contrast, technology risk evaluations are often subjective and anecdotal. Even though technology-related risks can be difficult to quantify, these risks should also be assessed to determine their effect on project profitability and rate of return. As project developers continue to select advanced technologies to obtain competitive advantages in heat rate, emissions performance and specific costs, a quantitative risk assessment becomes more critical ([1]).

To reduce financial exposure to technical risk, long-term maintenance agreements and other forms of O&M contracts are becoming more prevalent in the financial structure of new CT plant project development. Maintenance contracts, extended warranties, parts costs guarantees, machinery breakdown insurance, and business interruption insurance are all approaches to control negative financial consequences to unforeseen technical problems. These risk mitigation methods are becoming more common as developers incorporate the next generation of gas turbines into their development plans as a means to be competitive in the marketplace. Unfortunately, technical risk and mitigation issues are often addressed late in the project development process, resulting in less optimal technology procurement decisions and higher costs for risk mitigation. At this late stage, some alternatives may no longer be available or feasible.

To achieve early recognition of technical risk factors and quantify identified risks, a comprehensive methodology is required. The analysis includes a statistically based assessment of unplanned maintenance events and costs, scheduled maintenance variability and parts life evaluation, detailed estimation of total nonfuel O&M costs, and pro forma assessment of cash flow impacts. Combined with an overall project financial analysis, the methodology provides a means of quantifying the impact of technical risk on project financial performance, as well as a means of assessing the benefits of fixed price approaches to mitigating the risk.

Contributed by the International Gas Turbine Institute (IGTI) of THE AMERICAN SOCIETY OF MECHANICAL ENGINEERS for publication in the ASME JOURNAL OF ENGINEERING FOR GAS TURBINES AND POWER. Paper presented at the International Gas Turbine and Aeroengine Congress and Exhibition, New Orleans, LA, June 4–7, 2001; Paper 2001-GT-472. Manuscript received by IGTI, Dec. 2000, final revision, Mar. 2001. Associate Editor: R. Natole.

Areas of Technical Risk

Quantitative risk involves both event cost and probability of occurrence. To obtain a proper perspective, an estimate of the overall maintenance costs associated with operating the plant and a valuation of the other costs associated with electricity production needs to be considered with technical risk costs. Some cost items, such as those associated with operating personnel, consumables, and periodic maintenance, can be estimated at a single value (i.e., these are deterministic variables). Some cost categories involving uncertainty, such as unplanned maintenance and scheduled maintenance, vary over a range (i.e., these are stochastic variables). In the approach described in this paper, the latter costs are estimated with probability distributions based on statistical data and a Monte Carlo simulation to determine the range of costs expected.

In this methodology, the following major areas of uncertainty related to technical risk are addressed: scheduled maintenance frequency, unplanned maintenance frequency, costs, and outage duration. Other cost components of operations and maintenance are handled deterministically. The uncertainty in frequency and cost directly impacts the maintenance costs for the unit. Unplanned maintenance and forced outages also decrease revenue due to fewer operating hours, and therefore also impact the profitability of the plant in the form of business interruption and reduction from planned revenues.

Approach to Quantifying Risk

Using this approach, the major stochastic variables are defined statistically, based on actual fleet data, theoretical modeling, and field experience. Probability distributions are assigned to the failure rate data, with distribution type, mean, and standard deviation values determined from fleet statistics. Three categories of failure events are defined in this analysis: minor, major, and catastrophic. Events are classified according to their magnitude of cost and time-to-repair duration. Examples of minor events include trips due to loss of flame, software errors, and minor repairs such as fuel gas control valve repair. Examples of major events include shutdown and repair to correct high bearing vibrations, as well as repair of fuel gas line leaks, combustion liners, and fuel gas nozzles. Catastrophic events include significant CT repair, such as repair of turbine wheel microcracking, stage 2/3 wheel spacer modifications, and generator ground problems.

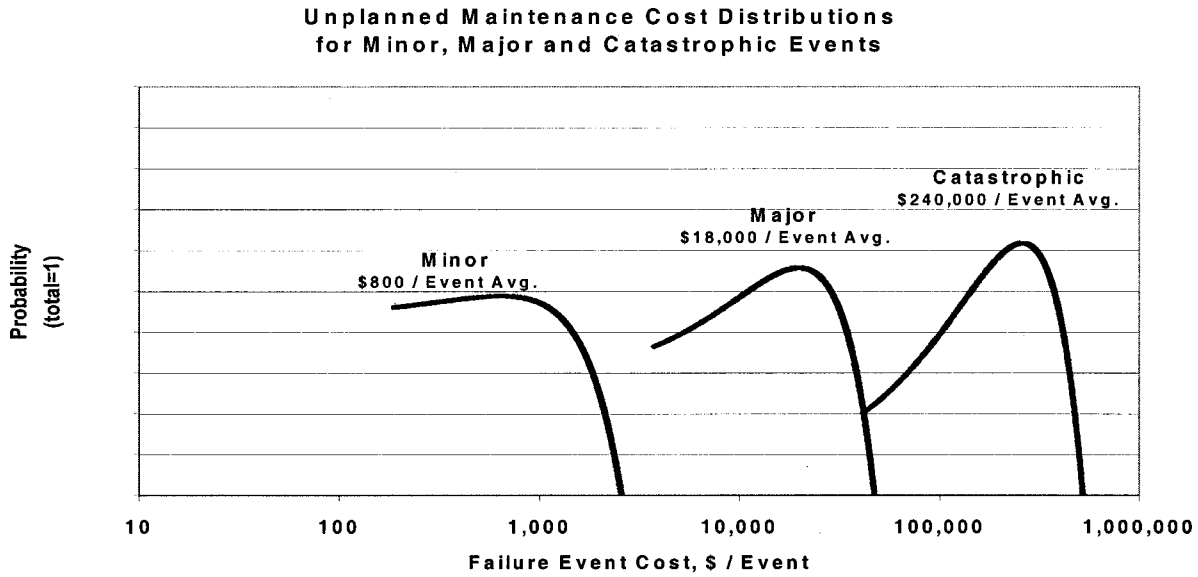

Fig. 1 Unplanned maintenance event costs

Within each event category, a probability distribution for repair cost and repair duration is determined from the statistical data. Figures 1 and 2 show the generalized probability distributions of cost per event and time to repair. Statistical data from a subset of the fleet of F-class gas turbines is used, although the analysis methodology is also applicable to other classes of turbines with operating experience.

An analysis of the statistical data indicates several correlation factors. Failure event frequency for minor and major events decreases with time after initial model introduction. Therefore, a ''learning curve'' effect is included in the modeling to account for CT model maturity. In addition, minor and major events are sensitive to the duty cycle (or ''mission'') of the gas turbine (i.e., peaking, cyclic, or base load duty). Therefore, these effects are included as well. Engineering judgement is exercised in extrapolating roughly five years of F-class data forward another ten years, based on previous experience with older classes of machines. For example, Figure 3 shows the mean value for major event frequency (i.e., failure rate) as a function of calendar year for peaking, cyclic, and base load duty.

The key unplanned maintenance dependent variables—outage hours and maintenance costs—are statistical distributions determined from the failure rate (i.e., events per time period), outage hours, and cost distributions. Unplanned outage hours and unplanned maintenance costs are determined from the three types of event statistics (i.e., minor, major, and catastrophic) for the selected duty cycle by summing as follows (for 8760 hours per year):

- unplanned outage hours $= \Sigma((\text{failure rate})_{\text{Type}} \times \text{service factor} \times 8760 \times (\text{outage hours per event})_{\text{Type}})$
- unplanned maintenance cost $= \Sigma((\text{failure rate})_{\text{Type}} \times \text{service factor} \times 8760 \times (\text{cost per event})_{\text{Type}})$

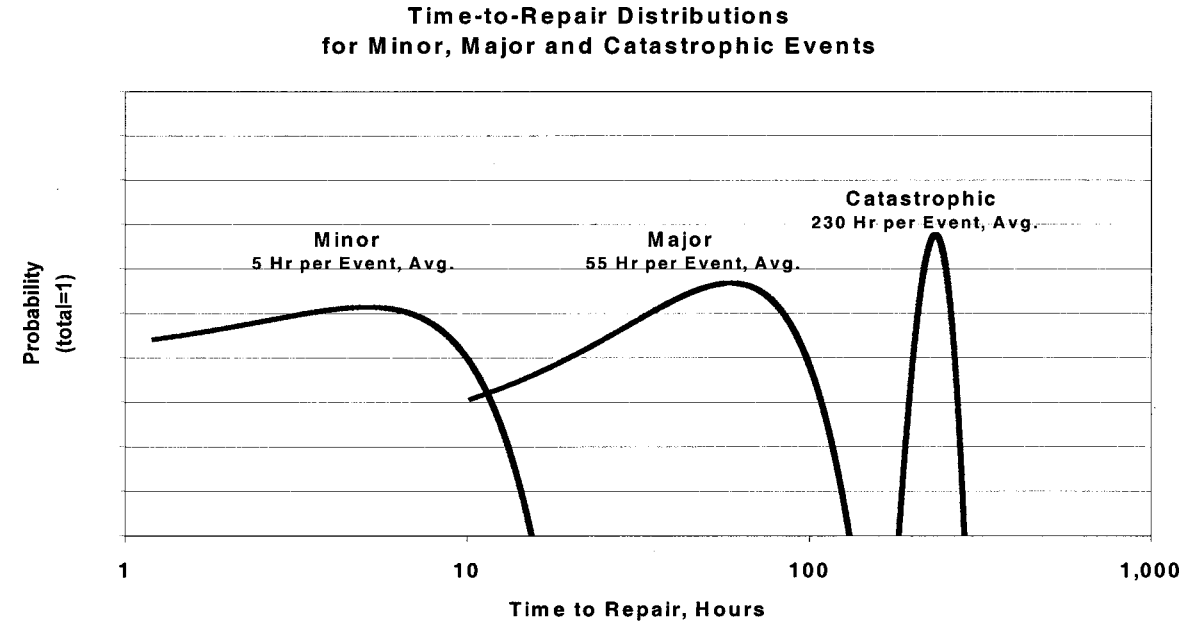

Fig. 2 Time-to-repair to unplanned maintenance events

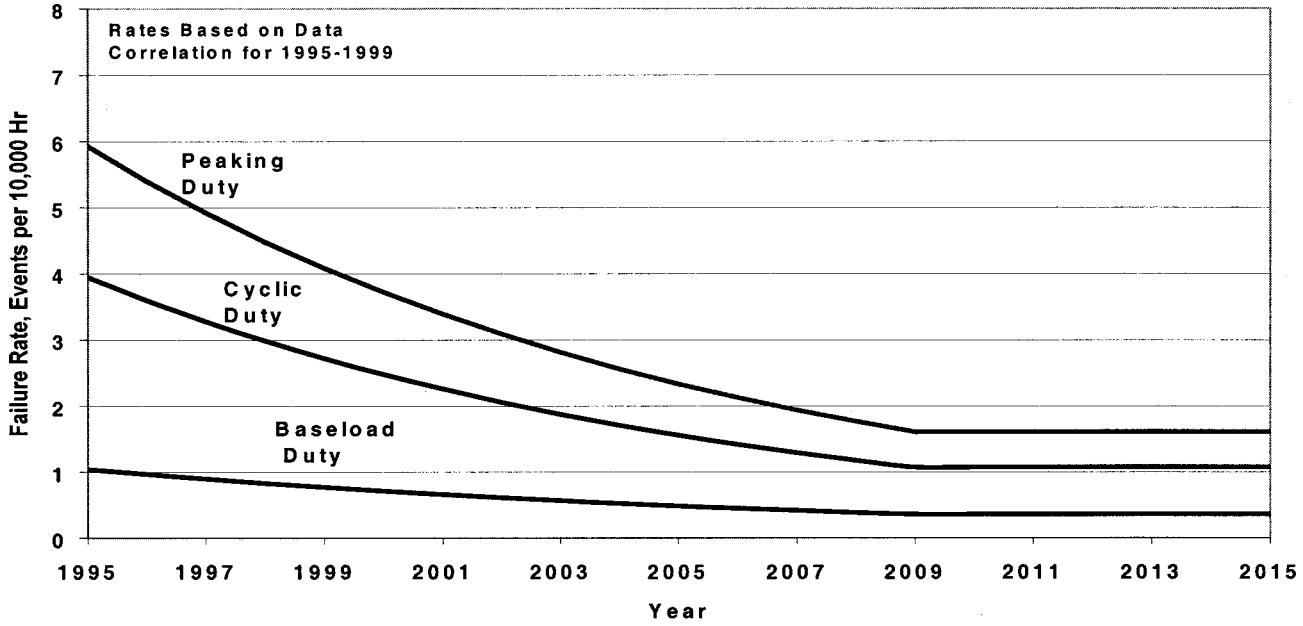

Fig. 3 Failure rate as a function of duty cycle and year after model introduction

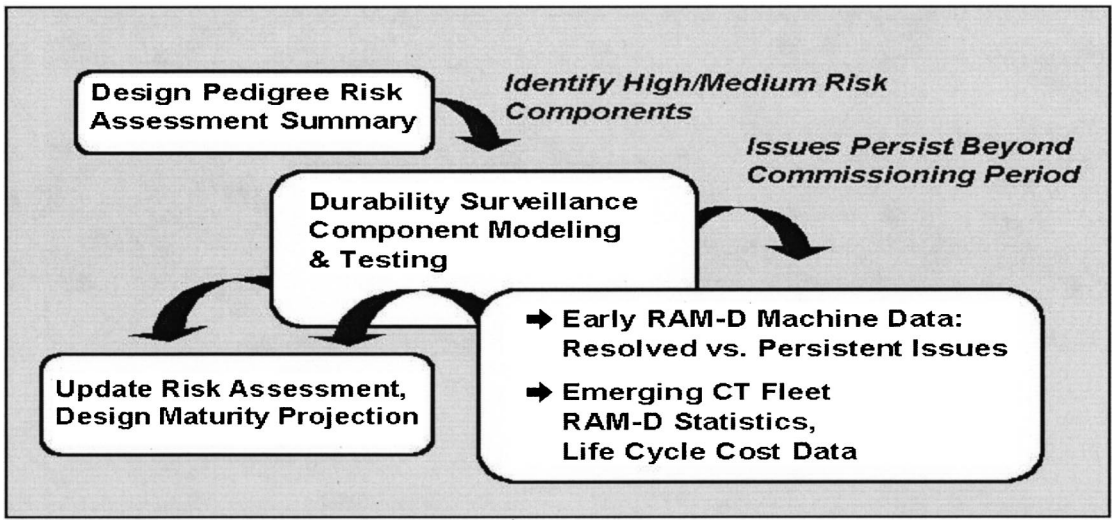

Fig. 4 EPRI risk assessment program

The key stochastic variables for scheduled maintenance are expected life for repair and replacement of major parts. Overall life and its variability are determined from a statistical analysis (mean value and standard deviation) of the intervals between scheduled hot gas path inspections). The recommended frequency of scheduled maintenance is based on vendor-specific algorithms for relating operating hours and number of starts (i.e., factored hours and starts, or equivalent operating hours, as applicable).

Component repair and replacement costs and relative life estimates are based on a combination of vendor guidelines, analytical estimates, and industry experience ([2]). Figure 4 indicates the general approach used to derive risk judgements and RAM-D data inputs.

Early experience with the advanced F-class machines indicates significant reductions in serviceable life of some hot gas path parts on the order of 50% or more for some components. This includes higher scrap rates during refurbishment cycles. Many owners have identified these replacement parts costs to be the dominant maintenance issue. Durability and repair yield data are relatively scarce, and gathering such data is further complicated by a continuing evolution of design modifications. Fleet leaders experience, tempered by engineering judgement, has been used to estimate hot section component service lives.

Fleet statistics are determined from the Operational Reliability Analysis Program (ORAP). ORAP is an automated system for monitoring and reporting the reliability, availability, maintainability, and durability (RAM-D) of over 1500 gas and steam turbine driven units, covering various applications, duty cycles, and plant arrangements for both simple and combined cycles.

O&M Cost Framework

The plant operation and maintenance costs are consolidated in a software tool, the CT Project Risk Analyzer ([3]). The software, built as a Microsoft Excel-based workbook with multiple spreadsheets, is the analysis framework for determining O&M costs and quantifying technical risk mitigation alternatives and benefits. The

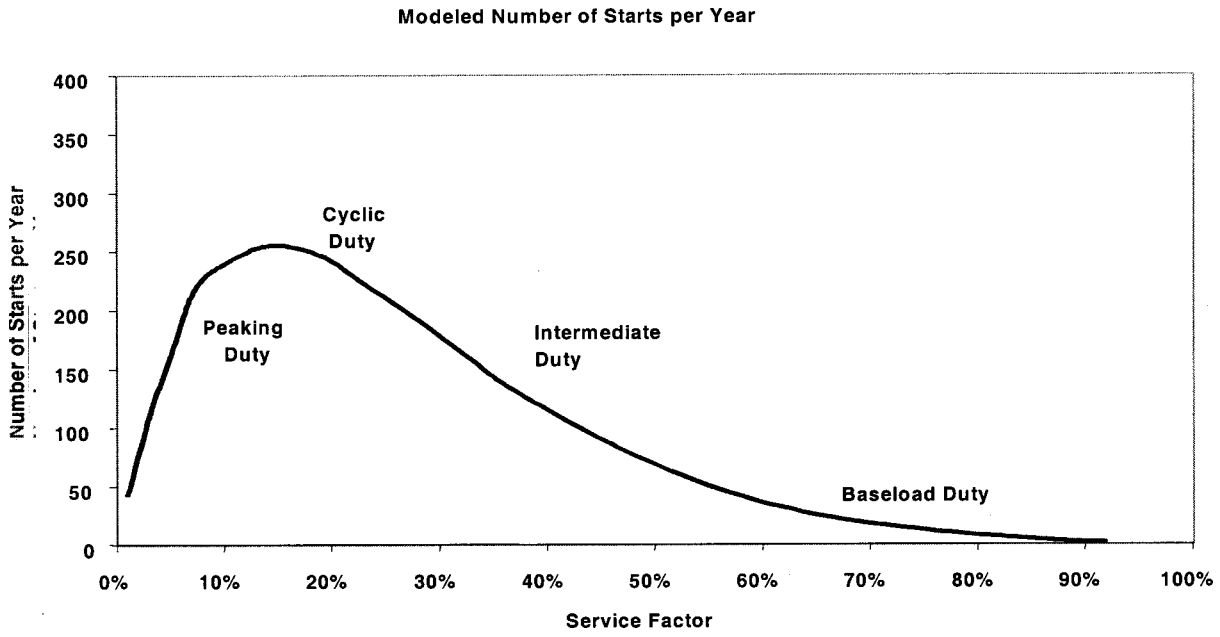

Fig. 5 Modeled number of starts per year

workbook uses an add-in software product for performing the statistically based Monte Carlo simulations on the stochastic variables and determining the cost and probability distributions.

The CT Project Risk Analyzer provides a means to estimate all nonfuel operating costs (i.e., labor, materials, and consumables), scheduled maintenance (including parts replacement and repair costs), and unplanned maintenance. In addition, risk mitigation costs for maintenance contracts, extended warranties, machinery breakdown, and business interruption insurance can be included. The spreadsheet provides cash flow projections for O&M components, a present worth and annualized cost analysis, as well as a cost-benefit comparison of mitigation options. Thus, the framework software consolidates both statistical and conventional costs into a unified cost structure.

The CT Project Risk Analyzer also provides a framework for studies of O&M cost sensitivity to various parameters. For instance, the typical sensitivity of maintenance costs to service factor can be determined. To do this, a model of the number of starts as a function of service factor was developed using the results of a production cost modeling study in the western U.S. (see Fig. 5). Although specific site locations and local supply and demand characteristics can affect the number of starts per year, the curve represents an average finding for the area.

Figure 6 shows typical maintenance cost estimates, as a function of service factor and number of starts. The relatively high annualized maintenance cost at low service factors is due to the significant number of starts per year assumed for peaking duty and cycling duty plants. For plants with many starts but low service factor, the maintenance costs can be similar, whether operating at 15% or 50% service factor. This is due to the high number of starts characteristic of peaking duty plants.

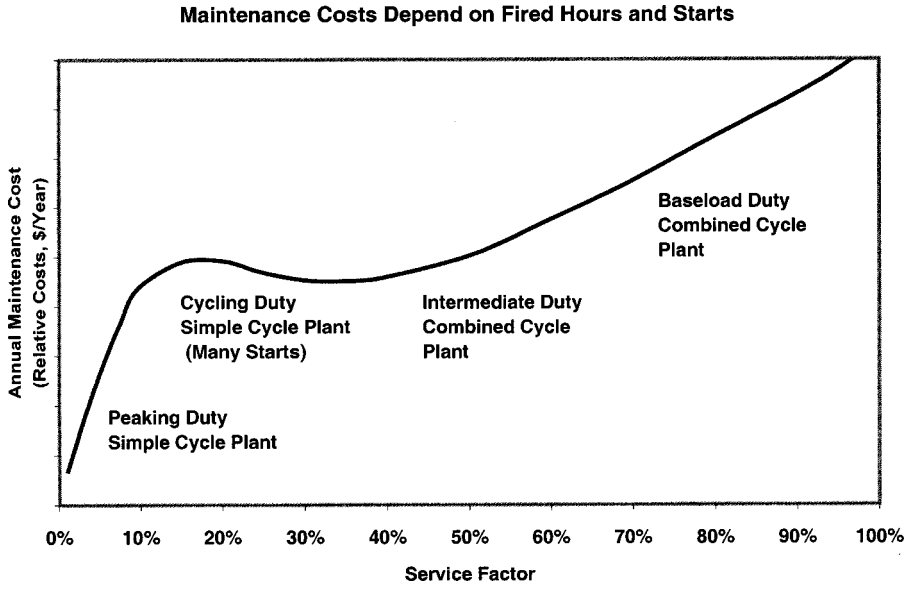

Fig. 6 Annual maintenance cost

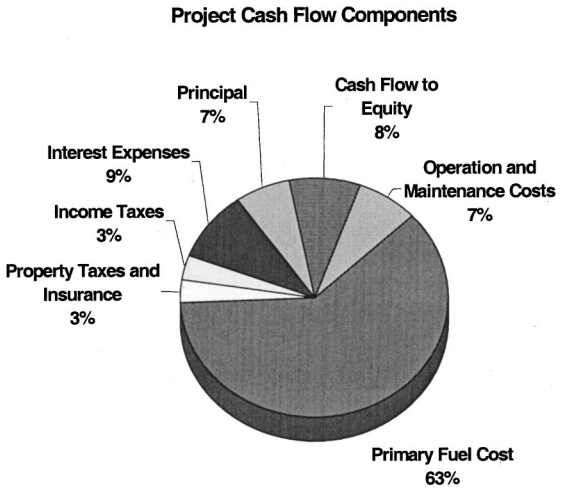

Fig. 7 Relative distribution of project cash flow

Project Costs Including O&M

Project cash flow and financial performance is readily determined with the use of an overall performance and costing model such as state-of-the-art power plant (SOAPP-CT) software. When combined with inputs from the CT Project Risk Analyzer, impacts on financial performance due to changes in O&M costs can be estimated.

The following examples assume assessment of a combined-cycle power plant operating at 70% service factor (moderate base-load duty), configured with two F-class gas turbines, two heat recovery steam generators (HRSG's), and a single steam turbine. Financial assumptions include a natural gas price of $3.50/MMBtu, electricity sales at $40/MWh (average price), a base case internal rate of return (IRR) of 18% and a 20-year economic life. A similar approach can be used for specific gas turbine models operating at any other duty conditions.

Figure 7 shows the relative distribution of costs from an overall project cash flow perspective. Fuel costs have the largest impact on project profitability; maintaining operating efficiency and minimizing fuel cost is clearly an important factor. O&M costs are also a significant portion of cash outflow; the annualized O&M costs for the CT-based plant represent about 6–8% of the revenue cash flow for a combined-cycle plant operating at moderate base load duty. Allocating the O&M costs into major components shows that about one-half of the O&M budget for advanced F-class CT-based plants is dedicated to scheduled maintenance parts repair and replacement—a typical result (see Fig. 8).

Plant Profitability Sensitivity and Risk

Technology risk primarily affects scheduled maintenance and unplanned maintenance. Variability in these areas can significantly affect plant net revenue and plant profitability. The CT Project Risk Analyzer results, combined with an overall plant financial analysis, enable sensitivity studies on variables of interest. For example, the variability in plant profitability can be determined as a function of the variability in maintenance frequency.

Figure 9 shows the variability in plant profitability, as measured by either net present value at a 12% discount rate (NPV_{12}) or IRR after taxes. The arithmetic mean at 18% IRR occurs at about 56% probability. For this example, the difference in NPV_{12} from the 80th percentile to the 20th percentile is about $14 million, due only to variability in maintenance frequency. The IRR varies from 16.7% to 19.4% for the same percentile range in probability (due to the use of annualized maintenance estimates and consistent escalation with inflation for all parameters, the shape of the IRR and NPV curves overlap, which does not necessarily occur in general). For a project with an initial capital cost of roughly $250 million, a $14 million variation in NPV due only to variability in maintenance frequency is significant, representing 5.6 percent of the initial cost.

The sensitivity of profitability to hot gas path (HGP) parts costs was also examined. For a project initially at 18% IRR, a 35% reduction in replacement costs for HGP components increased IRR to 19%, equivalent to a $5 million dollar improvement in NPV_{12} for the nominally $250 million plant (see Fig. 10). Note that over the 20-year life of the project, the total HGP components cost about $30 million; a 35% HGP parts cost reduction of $10.5 million is equivalent to about $5 million in NPV_{12} (after taxes).

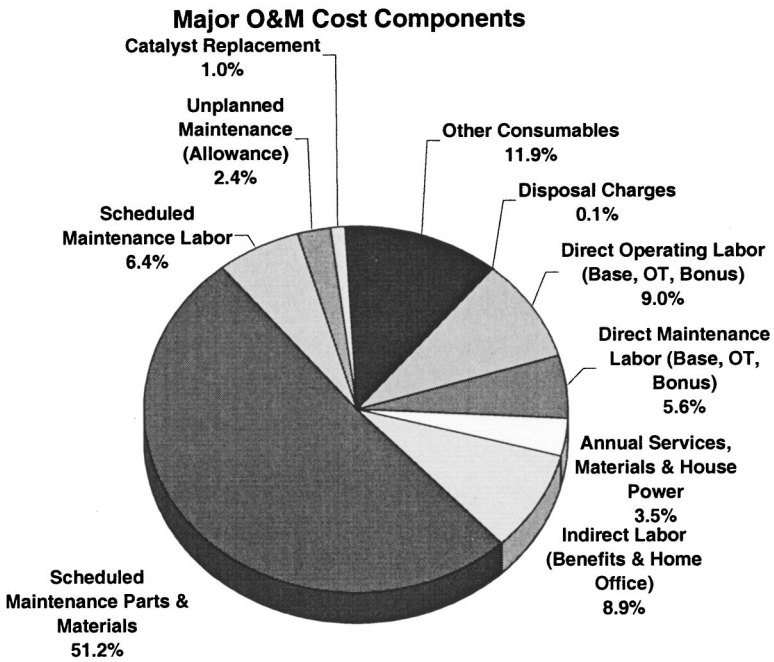

Fig. 8 Major cost components of CT operations and maintenance

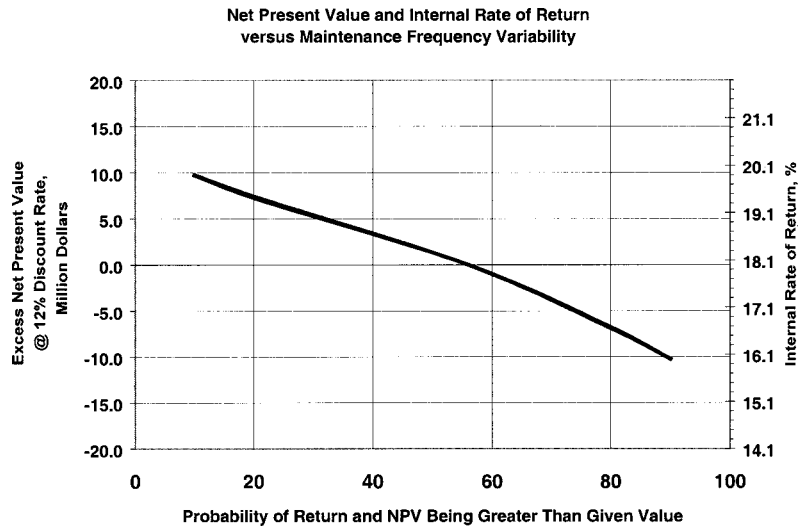

Fig. 9 Plant profitability sensitive to variability in maintenance frequency

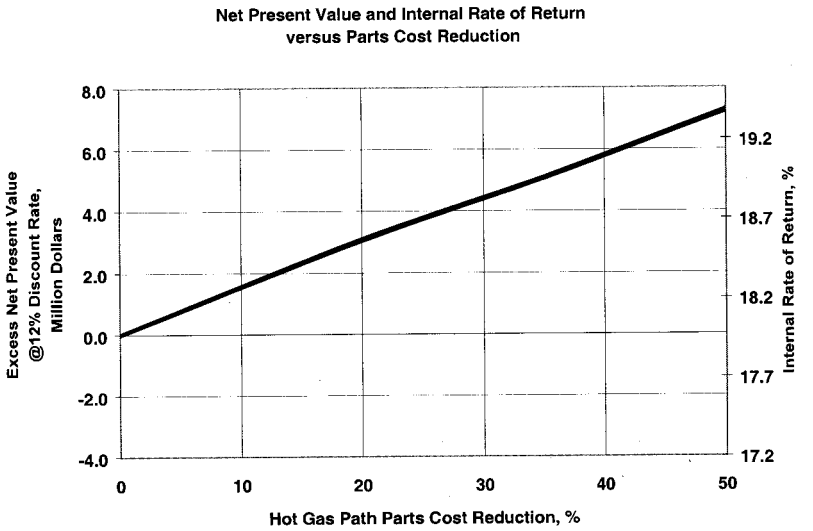

Fig. 10 Plant profitability sensitive to reduction in hot gas path parts cost

Technical Risk Mitigation Alternatives

Maintenance contracts, often called ''long term service agreements'' or ''long term programs,'' are a rapidly growing business for the original equipment manufacturers (OEM) and third-party service suppliers. Although the contracts are individually tailored to each situation, contracts typically cover the supply of parts, material, labor, and expertise required to perform the major inspections and maintenance on the unit or component. A wide variety of contracts are available, ranging from simply a prenegotiated parts agreement to a broad scope O&M agreement in which all O&M costs, including unplanned maintenance, are covered on a fixed price basis. In these contracts, a bonus is generally negotiated for performance exceeding requirements, while liquidated damages apply when requirements are not met.

Insurance provides another means of controlling technology risk costs. Machinery breakdown insurance covers the cost to repair accidental damage or failure, subject to significant deductible amounts. Business interruption insurance can be used to cover loss of income and extra expenses when operations are curtailed or suspended due to equipment failure.

Extended warranties may also be available from the OEM to provide more financial recourse for the buyer, if the equipment fails to meet contract performance requirements or minimum parts life requirements. Of course, extended warranties, maintenance contracts, and insurance policies cost money. These risk mitigation measures also provide benefits—the financial value of which is difficult to quantify because technical risk is involved. However, the risks should be quantified to the extent necessary to identify the impact on profitability of risk mitigation, or at least identify the extent to which higher-than-expected costs are reduced. The CT Project Risk Analyzer provides the framework for such economic comparisons.

Life-Cycle Cost Reduction

In addition to financial approaches, a number of technical approaches are improving CT availability/reliability, mitigating risk, and reducing overall maintenance life-cycle cost. These developments, when viewed collectively, ensure that advanced machines will progress along an improving, although perhaps not entirely steady, design maturity path over the next decade. A unified ap-

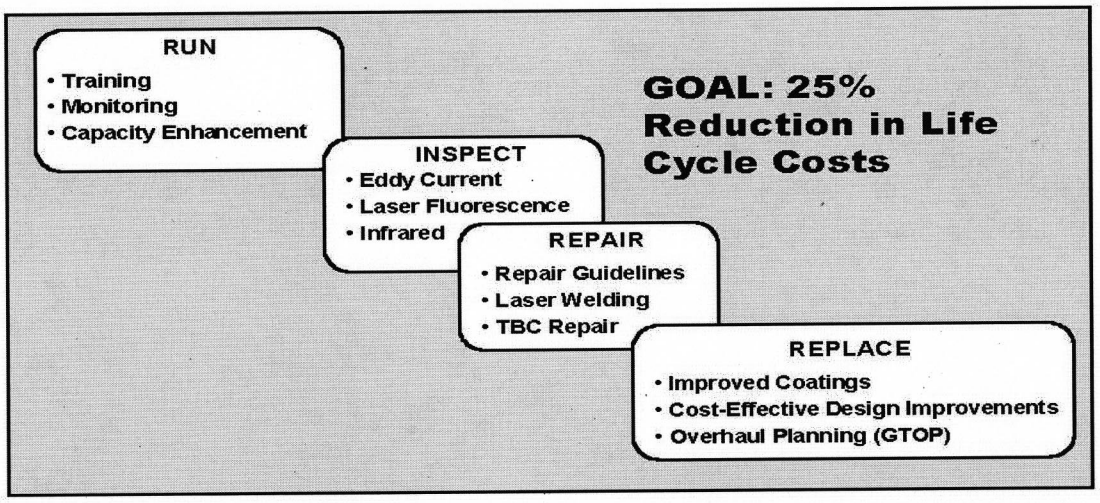

Fig. 11 Technical areas of improvement of life cycle costs

proach to risk assessment also enables refinement of the information and tools for O&M assessment and identification of areas in which the most improvement can be made (see Fig. 11).

Enhanced on-line monitoring techniques can improve life-cycle costs. On-line monitoring provides levels of machine status information suitable for supporting the trading floor, the plant operators, and the asset manager. Sensor information can be processed and remotely accessed via the company Intranet or over secured Internet sites. Monitored machine performance, including wear and tear incurred over a start/run/shutdown mission, determine the profitability of a trading position. Plant operators and asset managers/engineers use diagnostic software capable of discerning early trends in deterioration as machine fleet histories are accumulated in mega-process history databases. Neural networks and artificial intelligence techniques, such as fuzzy logic, will efficiently screen data for abnormal conditions, determine likely causes, and recommend counter measures. New sensors for detecting compressor instabilities, burner dynamics, blade hot spots, and material degradation are required to supplement normal control instrumentation.

New inspection techniques provide an early indication of problems that decrease parts life and can enable more timely remedial action. Inspection of the combustion section and hot gas path are prescribed maintenance activities typically performed visually or assisted by borescope. Techniques are nearing readiness for evaluating the degree of metallic coating degradation based on changes in electromagnetic properties, such as impedance. Other techniques suitable for field use will be required to assess thermal barrier coating thickness and bond integrity. Such inspections probes may be introduced through borescope ports or the engine exhaust using flexible lances. Other concepts under investigation include addition of certain easily detectable trace elements that track thickness or diffusion mechanisms and signal loss of oxidation protection.

Improved repair techniques can extend the life of high value parts. Repair is integral to achieving hot section durability goals of 48,000 to 72,000 hours. Sacrificial oxidation protection coatings are assumed to be stripped/recoated once or twice during the component life. If the coating is breached, oxidation damage to the underlying thin-walled casting may render the component unrepairable. Early indications show that as much as one-half of first-stage blades may be scrapped in these cases. Inspection and improved coatings under development will address this issue. Repair of wall loss and cracking in new directionally solidified (DS) alloys and single crystal (SC) alloy materials using precision laser welding techniques seek to restore full structural integrity. Such techniques could extend weld repair beyond blade tip buildups to more highly stressed areas, including trailing edge cracks near the platform or airfoil midspan ([4]).

Improved components using advanced materials, coating systems, and novel air/steam cooling circuits have been accompanied by upgrades in firing temperature. The material innovations in the form of wear extender packages and use of DS alloys and thermal barrier (TB) coatings are now being introduced to improve the durability of conventional machines. As component field experience is accumulated and aero-thermal stress analysis focuses on life limiting critical areas, subtle changes in airfoil shapes, and cooling passages are being introduced in refined designs. Techniques to improve the yield rate of SC castings and reparability are of high priority with manufacturers and their suppliers in reducing the highest cost components.

All the above approaches to reducing technical risk need to be carefully considered before committing to a risk mitigation strategy, especially those strategies that extend beyond the first major maintenance inspection.

Conclusions

Technical risk should be quantified and assessed early in the project development and procurement process. A framework for quantifying technical risks in CT-based power plants provides economic results based on quantitative assessment of the costs associated with the risks. The methodology presented is supported by data on the fleet of gas turbines in service and analysis results from the ongoing EPRI program to reduce CT life cycle costs. Technical risks can significantly impact the project financial performance and economic return to the equity owner, but can be mitigated through both financial and technical approaches. Reducing maintenance costs over time can make a valuable improvement to project financial performance.

Acknowledgments

EPRI gratefully acknowledges Strategic Power Systems, Inc. in its management of the Operational Reliability Analysis Program (ORAP) and the refinement of statistical outage and cost data for use in the CT Project Risk Analyzer framework.

References

[1] EPRIGEN, 1999, ''Technology Risk Assessment in Combustion Turbine Based Power Plants,'' EPRIGEN, Palo Alto, CA, Report No. TR-113988.

[2] EPRIGEN, 1999, ''Combustion Turbine Design Evolution and Risk: Pedigree Matrices for ABB, General Electric, Siemens Westinghouse and Siemens Power Advanced Machines,'' EPRIGEN, Palo Alto, CA, Report No. TR-114081.

[3] EPRI, 2000, ''CT Project Risk Analyzer Workbook Software Version 1.0: User's Manual and Tutorial,'' EPRI, Palo Alto, CA, Report No. 1000338.

[4] Gandy, D. W., Frederick, G., Viswanathan, R., and Stover, J. T., 2000, ''Overview of Hot Section Component Repair Methods,'' ASM Utilities and Energy Sector Conference on Gas Turbine Materials Technologies, Oct. 9–12, St. Louis, Mo.

R. L. McAlpin
P. L. Talley
H. L. Bernstein

Gas Turbine Materials Associates,
San Antonio, TX 78279
e-mail: gtma@texas.net

R. E. Holm
Occidental Chemical Corporation,
Houston, TX 77227-7702
e-mail: Robert_e._holm@oxy.com

Failure Analysis of Inlet Guide Vanes

The common failure modes of variable inlet guide vanes (VIGVs or IGVs) on industrial gas turbines are reviewed. These mechanisms include corrosion, cracking, and wear of the IGVs, their bushings and thrust washers. A new mechanism for IGV failure is described through a case history and metallurgical examination. High-cycle fatigue cracking in multiple IGV's was found at a location different from the expected cracking location. The failure is caused by a combination of wear loss and galling of the IGV metal shafts against the polymer bushings, combined with deterioration of the polymer matrix. Finite element analysis is used to verify the loading mode, maximum stress location, and crack propagation direction. [DOI: 10.1115/1.1494095]

1 Introduction

Inlet Guide Vanes (IGVs) are used to control the air entering a gas turbine. They may be fixed or variable. Variable inlet guide vanes (VIGVs) are used to throttle the airflow—reducing it at startup, and modulating airflow to obtain higher exhaust temperatures for part-load operation in combined cycle applications. This paper addresses materials issues in VIGVs, more commonly referred to as IGVs. (Fixed IGVs have few material issues apart from corrosion.)

There are few technical papers in the open literature that address materials issues in IGVs, apart from those that deal with the corrosion of the materials of construction ([1–3]). (A literature survey did not find any technical papers that deal specifically with IGV materials or IGV failures.) The turbine manufacturers (OEMs) distribute to their customers product information bulletins that do address material issues and failure modes of IGVs, but these are not in the open literature.

This paper reports on a new failure mode and mechanism for the IGV. The failure occurred at the inner diameter, and was caused by deterioration of the inner bushing. This paper also provides a summary of previously reported failure modes for IGVs, as well as a description of some of the materials used.

1.1 Inlet Guide Vane (IGV) Construction and Materials. A typical variable inlet guide vane is shown in Fig. 1. The outer diameter of the IGV is the driven end. The end of the drive shaft includes a thrust washer. The inner diameter of the IGV rests in a bushing and follows the outer diameter rotation.

Materials utilized for IGVs have included the following:

- Type 316 austenitic stainless steel (limited use),
- Type 403 martensitic stainless steel; and
- Custom 450 (also called GTD-450) precipitation hardening stainless steel.

Type 403 stainless IGVs have been plated with NiCd coatings, but this process has been discontinued because of the toxicity of cadmium. Various metallic-ceramic coatings are currently used. Coatings have not been effective on Custom 450.

Materials previously used for inner bushings were various mineral-filled thermosetting polymers (DU and Phenolic bushings). These materials had good hardness, but with limited environmental resistance. More recently, the thermoplastic resin TFE (polytetrafluoroethylene) has been used (Chemlon bushing), and exhibits excellent chemical resistance and high lubricity.

1.2 Known IGV Failure Modes and Inspection. Because IGVs throttle the compressor air, operational failure will affect the engine performance. If the IGV actually breaks off and goes into the compressor, then a massive compressor failure will result. Most reported IGV failures occurred at the outer diameter (driven end) of the IGV, and have been related to cracking or seizing caused by corrosion, wear, high-cycle fatigue, or combined mechanisms.

Inspection practices and recommendations are driven by failure experience. The goal of inspection is to identify critical levels of damage and replace components before a costly failure can result. Common practice is to inspect IGVs for damage at scheduled outages, which may be annual, biannual, or less frequent depending upon the application and potential damage mode. The OEMs provide guidelines addressing inspection procedures, recommended intervals, and some inspection limits.

Pitting corrosion in IGVs is promoted by the presence of liquid water and dissolved salts—chlorides are most often involved. Condensing moisture, airborne fouling, wash water, and ingress of rain water, can all contribute to the occurrence of pitting. Inspection limits for pitting address pit size and distribution. Pitting damage ultimately causes failure by initiating a cracking mechanism.

The limited use of Type 316 stainless steel resulted in failures from stress corrosion cracking. Stress corrosion cracking requires material susceptibility in a specific environment or corrosive agent, and an applied or residual stress. Usually, aqueous chlorides are the causative agent for stress corrosion cracking in Type 316 stainless steel and the corrosive conditions that promote stress corrosion cracking can be less aggressive than the conditions for pitting.

Wear loss in bushings, thrust washers, and the mating spindle surfaces on the IGVs causes looseness. Looseness can promote cyclic bending loads, and high local contact stresses on the load-bearing surfaces. Inspection concentrates on clearances between the IGV inner button and bushing. Growth of corrosion products on the thrust washer can also push the IGV inward and cause binding, which increases loads and may also lead to cracking.

High-cycle fatigue cracking can result after wear or corrosion damage has accumulated or advanced to a sufficient degree to cause crack initiation. High-cycle fatigue loading is driven by flow-induced vibration. Crack propagation rates in IGVs are expected to be slow, with loads controlled by operating (throttle) cycles and vibration. The normal location for crack inspection is at the outer diameter (driven) end of the IGVs, at the fillet between the thrust collar and airfoil. One design places an additional

Contributed by the International Gas Turbine Institute (IGTI) of THE AMERICAN SOCIETY OF MECHANICAL ENGINEERS for publication in the ASME JOURNAL OF ENGINEERING FOR GAS TURBINES AND POWER. Paper presented at the International Gas Turbine and Aeroengine Congress and Exhibition, New Orleans, LA, June 4–7, 2001; Paper 2001-GT-428. Manuscript received by IGTI, Dec. 2000, final revision, Mar. 2001. Associate Editor: R. Natole.

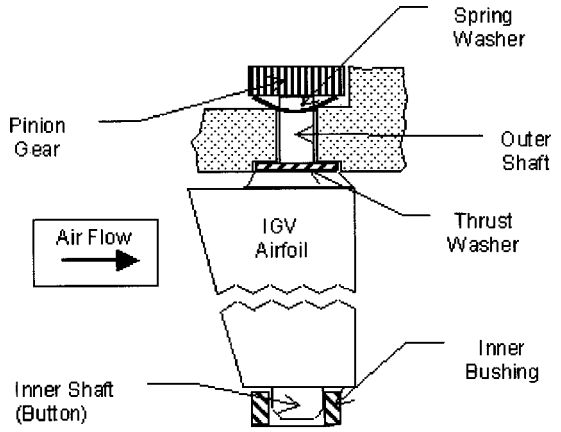

Fig. 1 Diagram of variable inlet guide vane (IGV), viewed from suction side

Fig. 3 Plan view of opened crack segment. Arrows locate two origins at the bottom corners on opposite sides of the airfoil. (Scale divisions=0.01 in.)

radius cut in the airfoil base at this location. Crack initiation at the leading edge near the outer end has also been observed. Inspection by penetrant testing can verify the presence of cracks.

2 Case History

A single cracked IGV was found in a General Electric MS7001E (Frame 7E) gas turbine, after 84,000 operating hours. Failure of a second IGV resulted during subsequent service, after an additional 8000 hours. Inspection then found cracking in several more IGVs. The IGVs were made from GTD-450, and exhibited normal metallurgical properties. The IGVs contained widespread pitting corrosion; however, the sizes of the pits were within G.E. allowable inspection limits for Type 403 material.[1]

2.1 Fracture Examination. Cracking on the IGVs initiated at the inner end of the airfoil, at the leading edge corner of the inner support button. On the fractured IGV, the cracking propagated to failure at the trailing edge, shown in Fig. 2. The fracture location was opposite from the expected location for fatigue cracking failures, which is at the outer diameter end.

The cracking resulted by high-cycle fatigue, as observed macroscopically, and verified by scanning electron microscopy (SEM) fractography techniques. The opened segment from the first crack is shown in Fig. 3. Two cracks initiated from the two leading edge corners, at the suction and pressure sides, and joined into a single propagating crack front. Cracking in all the IGVs was verified to be high-cycle fatigue, with the same initiation points, and following this same crack path.

[1]Corrosion limits for IGVs made from GTD-450 are not publicly available.

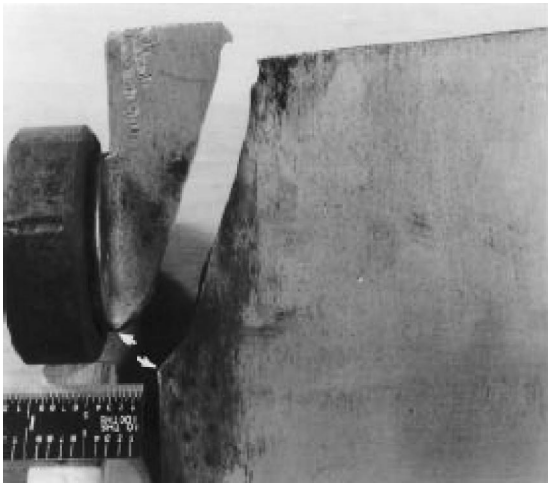

Fig. 2 Failed IGV. The inner end segment includes the bushing in place on the button. Arrows located at the crack initiation point.

Fig. 4 Large corrosion pit (arrow) at IGV crack origin

On the initially cracked IGV, the suction side crack originated at a large pit, of 70 mils (1.8-mm) diameter (Fig. 4). The pit is slightly smaller than the maximum size allowed by the G.E. inspection requirement for this location in Type 403 material. The large pit may have been an accelerating factor in the cracking, but not a primary factor in the cracking occurrence. Cracking in other IGVs initiated by high-cycle fatigue in the absence of pitting corrosion.

2.2 Metal Button Wear. The opposite sides of the support buttons on the IGVs showed different wear conditions (Fig. 5). The pressure side surfaces were generally smooth, while wear on the suction sides formed a very rough texture. Aerodynamic forces on the IGVs are expected to produce contact loads along the suction side and toward the trailing edge. Patches of adhered material from the polymer bushings were also present. Minimum diameters were aligned with the visual wear, and indicated up to 9 mils (0.20 mm) wear loss. The button diameters were within acceptable inspection limits.

Metallographic examination revealed the button pressure side surfaces were smooth, microscopically flat, and essentially featureless. Mixed wear modes forming broad and shallow wear pits were documented on the button suction sides. Galling produced a deformed surface layer at edges of the wear pits (Fig. 6). Abrasive wear formed groove-type metal loss by cutting and rubbing, while

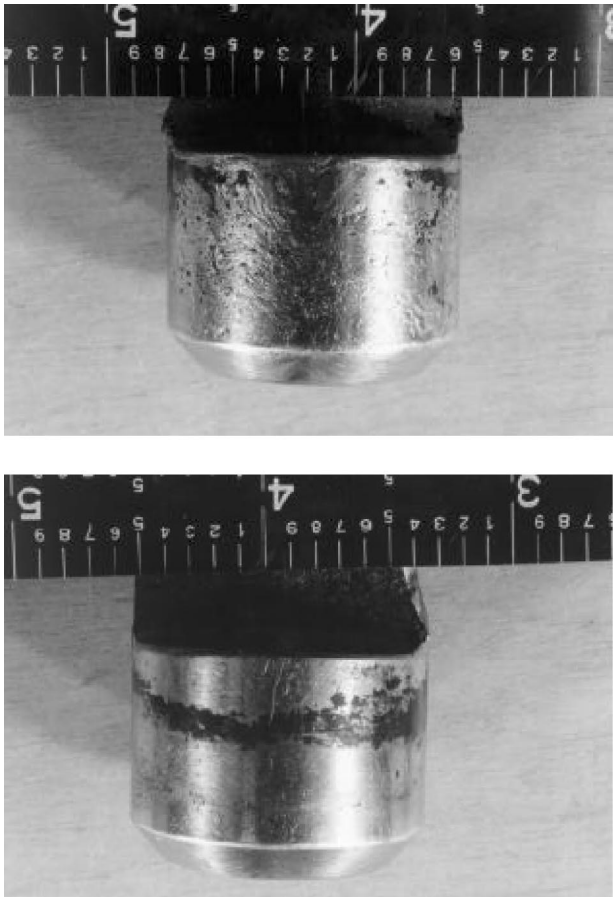

Fig. 5 Button surface conditions on suctions side (*a*) and pressure side (*b*) surfaces. (Scale divisions=0.1 in.)

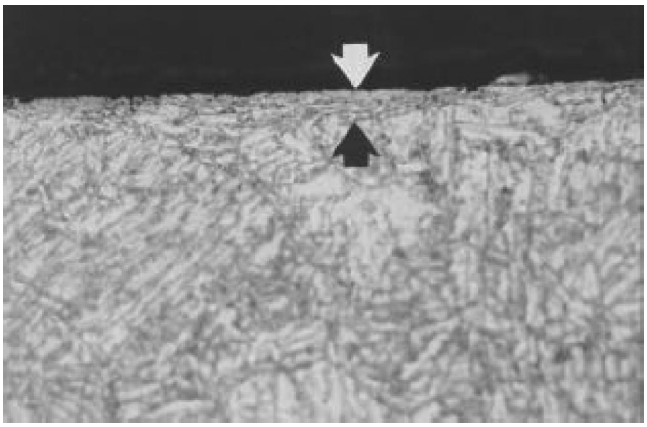

Fig. 6 Microstructure of galling layer (between arrows) on button contact surface (original 1000X—Vilella's reagent)

adhesive wear caused surface roughening from compressive buildup of wear particles and tensile stretching of a surface deformed layer (Fig. 7).

2.3 Polymer Bushing Deterioration. Compared to a new bushing, the bushing from a failed IGV demonstrated a 5% mass loss. Both wear loss and deformation from contact loads were indicated by dimensional measurements, which showed decreases of both inside and outside diameters, and an increase in the axial

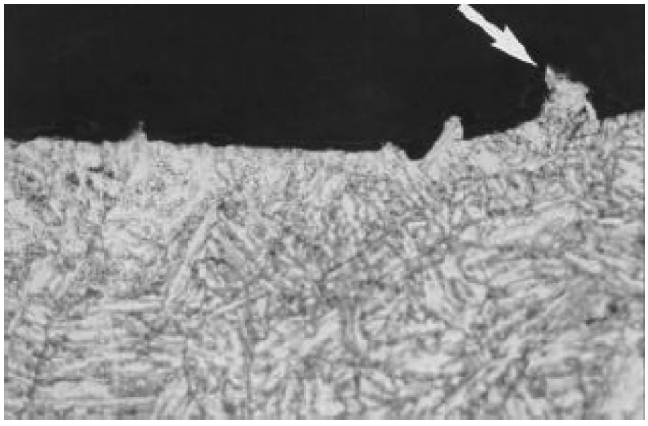

Fig. 7 Adhesive wear features (arrow) on button contact surface (original 1000X—Vilella's reagent)

Fig. 8 Metallic wear particles (bright) on bushing contact surface (original 20X)

height of the bushing. Wear loss of up to 6 mils (0.15 mm) was indicated. Density of the failed bushing had also decreased by 4%, which denotes swelling of the polymer.

The bushing inner diameter surface contained shallow wear grooves and pit-type features, and a buildup of fine metallic particles (Fig. 8), which resulted from wear of the metal button against the polymer. X-ray microanalysis confirmed the metal particles were the same composition as the IGV button. The wear surfaces also exhibited a buildup of mineral filler particles originating from the polymer formulation. Other than hydrocarbon residues, which could result from lubricants, no extraneous materials were found on the bushing wear surfaces.

The TFE resin matrix of the polymer bushing had deteriorated, confirmed by both infrared spectroscopy (IR) and durometer hardness testing. Hardness of a new bushing measured 61 Shore D with 0 creep. Hardness of the failed bushing was 56 Shore D, with 5 points creep.[2] Weakening of the polymer matrix is indicated by the loss in hardness, and the creep response indicates a ''tacky'' or adhesive behavior, denoting a loss in lubricity.

3 Stress Analysis

A simplified three-dimensional model of the IGV was developed. The airfoil of the IGV was approximated as a flat plate, with

[2]Durometer hardness is reported after an initial 5-seconds dwell, and creep is reported from the hardness decrease after an additional 15-seconds dwell.

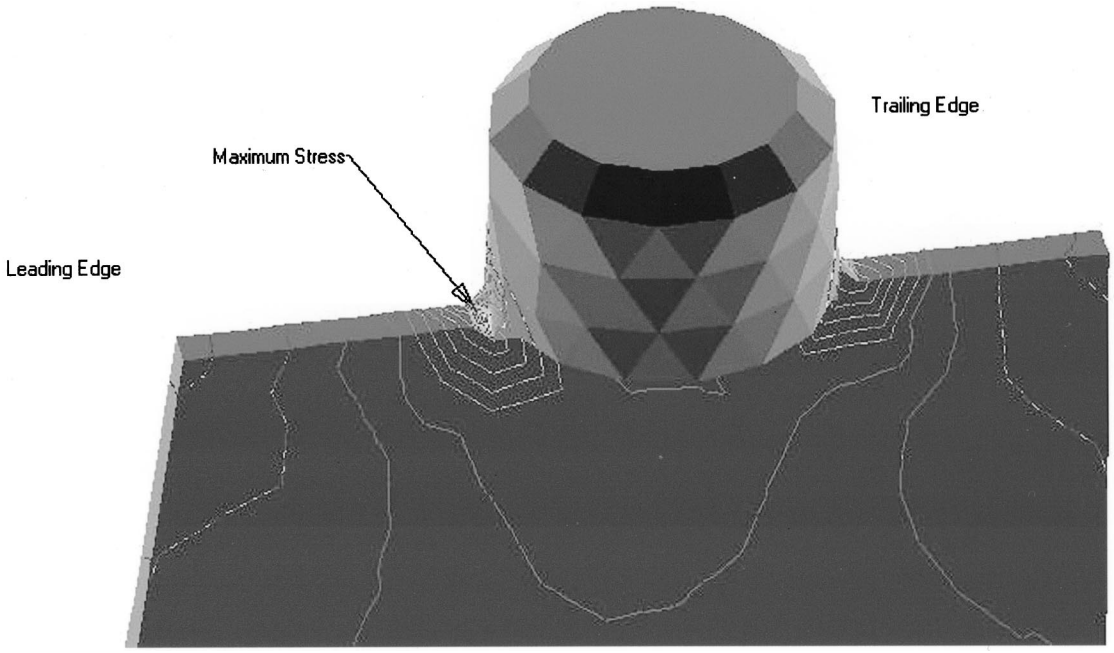

Fig. 9 Results of the simplified stress analysis showing the equivalent, or Von Mises, stress contours. Maximum stress occurs at the crack origin.

a cylindrical button offset to the trailing edge, as on the IGV. Fillets were added between the button and the airfoil. Measurements were taken of the IGV to ensure accuracy of the model.

This solid model was analyzed using the Aegis finite element analysis program, with tetrahedral elements and a linear elastic, static analysis. For the model, the airfoil was fixed at the outer diameter end and torque was applied to the button, to represent binding. The results are shown in Fig. 9, for the equivalent, or von Mises, stress.

The maximum stress occurred at the leading edge corner of the bottom of the button. The orientation of the maximum stress is along a curve pointing towards the trailing edge. Cracking in all the IGV samples started at this same corner, and grew in the same direction, concurring with this simplified stress analysis.

4 New Failure Mode

The cause of cracking and failure in the IGVs is galling and mechanical wear between the bushing and IGV buttons. Cracking resulted by high-cycle fatigue, and was driven by increased operational stresses caused by the button galling. Long-term deterioration of the bushings is a primary factor in the failure mechanism. Both mechanical damage and environmental aging of the polymer resin are indicated.

While the polymer bushing is staked in place to prevent rotation, deformation of the bushing and the combined wear of the bushing and the IGV button allow the bushing to move in its socket and to cant in position relative to the button. Contact stresses are increased both by the angular displacement and the buildup of wear debris, which ultimately causes galling of the button on the bushing. Galling increases the operational stress to promote the fatigue cracking.

5 Discussion

In the case history presented, recommendations for bushing replacement were based upon clearance measurements. No recommendation had been made based upon total operating hours. These polymer bushings had operated for over 84,000 hours. Wear on the IGV button was also within the inspection limits. However, deterioration of the bushing was a combination of both wear and dimensional swelling, so that, neither clearance or button measurements would identify the need for replacement.

The failure denotes the need to identify both a lifetime limit for the polymer bushings, and a minimum clearance limit. Even if inspection results show proper clearances, a required bushing replacement should be set at the major inspection interval of 48,000 hours. Bushing replacement before polymer deterioration can also increase the IGV service life by minimizing wear on the support button.

The clearance inspection requirement includes only a maximum limit. With zero clearance between the button and bushing, binding may be occurring. For this reason, a minimum clearance of 1 to 2 mils (0.04 to 0.08 mm) should be required.

6 Summary

Most failures of IGVs result from cracking or seizing at the outer diameter (driven end). The failures are caused by corrosion, wear, high-cycle fatigue, and combined mechanisms. Inspection procedures have been defined by failure experience to address the known mechanisms.

A new failure mode for IGVs resulting from binding and cracking at the inner diameter end was documented. The primary failure cause is long-term aging of the polymer bushings, and wear of the IGV buttons is a factor. Deterioration of the bushing was a combination of both wear and resin damage, which produces dimensional swelling and loss of lubricity.

The normal inspection procedure based on clearance measurements would not identify the need for bushing replacement. Replacement at a service limit of 48,000 hours should prevent the failure and minimize wear on the IGV buttons. Also, there is a need to maintain a minimum clearance between the bushing and IGV button.

Acknowledgments

The authors wish to thank Occidental Chemical Corporation and Gas Turbine Materials Associates for their support of this work and their willingness to share these results with the technical community. The authors also wish to thank Ms. Julie Nicholls for the preparation of this manuscript.

References

[1] Haskell, R. W., ''Gas Turbine Compressor Operating Environment and Material Evaluation,'' GE Reference No. GER-3601, GE Company, Schenectady, New York.

[2] Henthorne, M., T. Debold, and R. Yinger, 1972, ''Custom 450, A New High-Strength Steel,'' *Corrosion/72*, NACE.

[3] Kolkman, H. J., and Mom, A. J. A., 1984, ''Corrosion and Corrosion Control in Gas Turbines Part I: The Compressor Section,'' ASME Paper No. 84-GT-255.

Dwell Sensitive Fatigue Response of Titanium Alloys for Power Plant Applications

M. R. Bache

W. J. Evans

I.R.C. in Computer Aided Materials Engineering,
Department of Materials Engineering,
University of Wales,
Swansea SA2 8PP, UK
e-mail: irc@Swansea.ac.uk

The phenomenon of "dwell sensitivity" in the $\alpha+\beta$ and near α titanium alloys and the intrinsic relationship with quasi-cleavage facet formation is discussed. In the present paper, particular emphasis is placed upon the role of "cold creep" and ambient temperature strain accumulation under cyclic loading. A process of stress redistribution between microstructurally distinct regions that demonstrate different strengths is proposed as the fundamental cause of facet development and subsequent dwell failures. A model to describe the redistribution process is validated through a matrix of fatigue testing designed to assess the effects of microstructural form, stress axiality, and periods of dwell loading at peak stress on cyclic strain accumulation. [DOI: 10.1115/1.1494094]

Introduction

The introduction of titanium alloys for ambient to mid temperature components in the fan and high-pressure compressor stages of modern gas turbines has contributed significantly to the efficiency improvements gained since the early designs of the Whittle era. Their relative high strength, low density, and corrosion resistance offer clear advantages over alternative materials particularly steels. Initially, alloy development and production were both driven by the needs of the aerospace industry and in particular, the necessity to improve on power to weight ratios of aeroengines. Environmental legislation during the 1990s has forced the aero manufacturers to further improve future engine designs through a combination of increased thrust and reduced emissions. At the same time, land and marine gas turbines are rapidly gaining favor for energy production and propulsion, respectively, and with increased processing capacity and the development of low-cost alloy variants ([1]), titanium alloys are now being introduced into a wider range of automotive, offshore, and biomedical applications.

Pure titanium consists of a close packed hexagonal alpha phase up to 882°C where a structural transformation occurs to form a body-centered cubic beta phase. Early attempts at alloying utilized this dual phase characteristic to produce materials with specific mechanical properties. For instance, the $\alpha+\beta$ titanium alloy Ti-6Al-4V (Ti 6/4), introduced in the 1950s, contains aluminum to stabilize and strengthen the alpha phase while the addition of vanadium, as a beta stabilizer, offers a greater proportion of the more ductile beta phase during hot forming operations such as forging and rolling. Mechanical performance is controlled via heat treatment to control microstructural development. Aero gas turbine fan blade and disk applications utilize Ti 6/4 alloys to the present day, normally in a fine grained mill annealed α or bimodal $\alpha+\beta$ form (Figs. 1(*a*) and 1(*b*)). This is in recognition of the ambient temperature dwell sensitivity noted in alternative coarser grained variants. It is vital that knowledge of the dwell phenomenon is taken on board by the new generation of designers in all the relevant industrial sectors but especially amongst the gas turbine community.

"Dwell sensitivity" in titanium alloys was discovered during the early 1970s. Increasing HP compressor temperatures exceeded the capabilities of Ti 6/4, hence the need for more advanced high-temperature alloys which led to the introduction of creep resistant near alpha alloys such as IMI685 and IMI829 (the term "near α" indicates a relatively large proportion of α stabilising elements compared to β stabilizers). Their improved temperature capability was achieved by a combination of specific chemical additions (e.g., the use of silicon) and a coarser grain size which, for instance, reduced grain boundary cavitation. In terms of defect tolerance, a lifing technique gaining popularity around this time, these alloys offered good resistance to crack growth due to an optimized α/β basketweave microstructure (Fig. 1(*c*)). Their performance at elevated temperatures was unsurpassed. However, it was as a consequence of utilizing IMI685, in particular, as a fan disk material that operators experienced some well-documented, premature in-service and test rig failures ([2]). A typical aircraft takeoff and landing sequence applies one major cyclic load reversal to critical rotating disk components with the cruise period acting as a hold or dwell period at relatively high stress. Subsequent research has identified the crucial role played by microstructure, texture, and the anisotropic mechanical response in dwell sensitive failures. The improved understanding of crack initiation and the very early stages of crack growth that developed from such work, has assisted designers who are currently adopting a "total life" philosophy for component lifing. This approach amalgamates "life to first crack" and "defect tolerance" principles and through its intimate understanding of deformation and fracture in titanium alloys will in part overcome the inefficient and extremely conservative use of these alloys. This paper explores some of these specific findings with the emphasis placed upon ambient temperature response.

Quasi-Cleavage Facets

The fracture surfaces of the fan disk failures mentioned above were invariably characterized by quasi-cleavage facets. These are a natural feature of both cyclic or time dependent fracture in $\alpha+\beta$ alloys. The term "quasi-cleavage" is commonly used within the titanium community in recognition of the fact that the facets are found to have a near basal plane crystallographic orientation. They are considered to develop due to the progressive separation of intense slip bands under the action of a tensile stress normal to the slip plane ([3]). It is important to emphasize that they are not a brittle phenomenon as normally inferred by the use of the term "cleavage." Plasticity and a process of stress redistribution within the alloy has been implicated in their formation ([4]). This results from the presence of "strong" and "weak" regions due to an in-homogenous distribution of slip systems and microstructure. Grains with their basal plane lying near perpendicular to the principal stress axis will not allow slip and will therefore act as a

Contributed by the International Gas Turbine Institute (IGTI) of THE AMERICAN SOCIETY OF MECHANICAL ENGINEERS for publication in the ASME JOURNAL OF ENGINEERING FOR GAS TURBINES AND POWER. Paper presented at the International Gas Turbine and Aeroengine Congress and Exhibition, New Orleans, LA, June 4–7, 2001; Paper 2001-GT-424. Manuscript received by IGTI, Dec. 2000, final revision, Mar. 2001. Associate Editor: R. Natole.

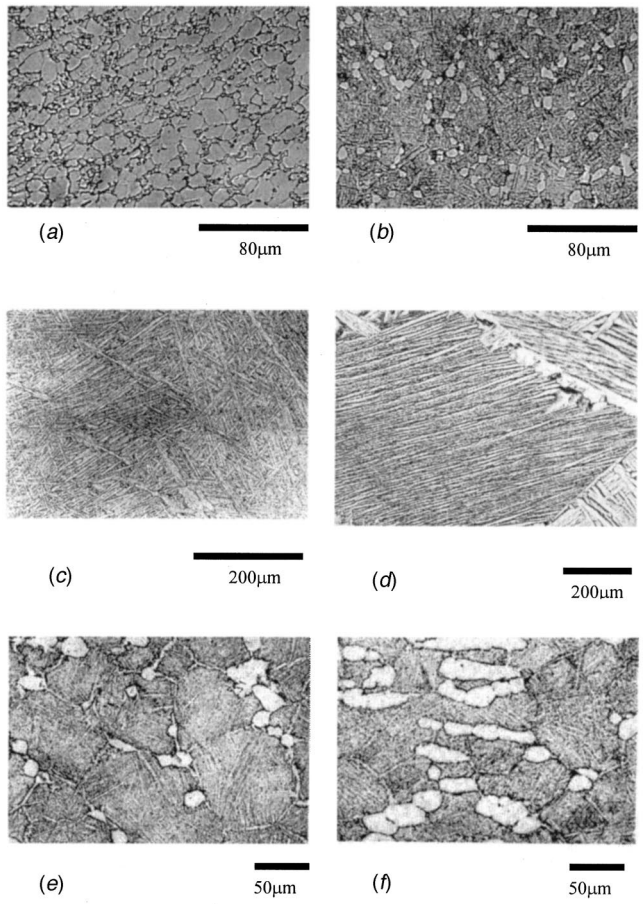

Fig. 1 Titanium alloy microstructures, (*a*) mill annealed Ti 6/4, (*b*) bimodal Ti 6/4, (*c*) basket weave, Timetal 685, (*d*) aligned, Timetal 685, (*e*) rolled bar, Timetal 834, (*f*) forged disk, Timetal 834

strong region. Such grains often promote facets in spite of their unfavorable orientation. A model to account for this observation based upon the Stroh pile up theory has been promoted by the present authors (Fig. 2 and [5]).

"Cold Creep" and Cyclic Strain Accumulation

A fundamental requirement of the redistribution model is the ability of this class of alloy to deform by a process commonly termed ''cold creep.'' This is the accumulation of permanent or plastic strain under conditions of static loading at stresses near to or above the monotonic yield stress. This process will readily occur in the $\alpha+\beta$ and near α titanium alloys at room temperature. However, a similar effect is also noted under cyclic loading with the classical form of creep curve reproduced (see examples presented in Fig. 3 onwards). Due to the associated cyclic softening demonstrated by these alloys, the accumulation of plastic strain will actually persist under stress levels as low as the cyclic yield stress.

The measurement of strain accumulation during fatigue tests offers an insight into the relative contributions from microstructure, waveform, and stress axiality towards the stress redistribution process. The following data were generated during a previous study concentrating on the dwell sensitivity of the near α alloy Timetal 685 (formerly IMI685). More detailed experimental information has been reported [5,6], but essentially the alloy was assessed in the aerospace recommended basketweave form and the unwanted aligned morphology (Figs. 1(*c*) and 1(*d*), respectively), under pure tension or torsion loading modes. A ''cyclic'' trapezoidal waveform was employed and compared to ''dwell'' loading containing a two minute hold at peak stress. All of the tests illustrated in Figs. 3 to 5 were performed under identical peak stress and stress range conditions (σ_{max}=850 MPa and R=0.1). The following points were noted:

- A comparison between cyclic tests performed on basketweave and aligned specimens under identical stress conditions demonstrates greater strain accumulation for the aligned microstructure (Fig. 3).
- For a given microstructure under identical stress conditions, dwell loading induces a higher rate of strain accumulation and ultimate strain to failure compared to a cyclic waveform. For the case of the basketweave microstructure, illustrated in Fig. 4, this was also accompanied by a reduction in the number of ''cycles to failure'' under dwell, i.e., basketweave material was ''dwell sensitive.''
- Greater strain is accumulated and at a faster rate under a pure torsion fatigue mode compared to pure tension (Fig. 5).

Model Validation

The data illustrated in Figs. 3 to 5 are all consistent with the empirical experience of dwell failures in service and the model proposed to describe stress redistribution. The influence of microstructure in controlling strain accumulation is of particular interest. Despite the fact that the fully transformed aligned form demonstrates the faster and greater ultimate strain accumulation, in terms of the number of stress reversals to instigate failure it has been reported previously that this microstructure is not dwell sensitive ([5]). The band delineating the LCF response for the aligned material in Fig. 6 encompasses all cyclic and two-minute dwell tests on both tubular and solid specimen designs. Although no significant dwell effect was noted, a weaker response was found for tubular specimens when compared to solid testpieces. This was attributed to the relatively large grain size of the aligned microstructure in relation to the thin wall of the tube. The relatively stronger fatigue response demonstrated by basketweave specimens under a cyclic waveform is compromised by the imposition of a dwell period at peak stress, to the extent that the dwell basketweave lives are comparable to those of aligned material tested under either waveform. It is pertinent that, due to the thermal gradients invariably encountered during rapid quenching in order to induce a basketweave morphology, thick section components often contain regions of coarse, α lath alignment within their interior. From the strain-life information illustrated in Fig. 3, these aligned regions should deform relatively easily. However, since they are essentially constrained by a stronger phase (i.e., juxtaposed aligned grains which are not so favorably orientated for easy slip or even basketweave material), they will act to throw stress on to these strong regions and subsequently encourage facet development.

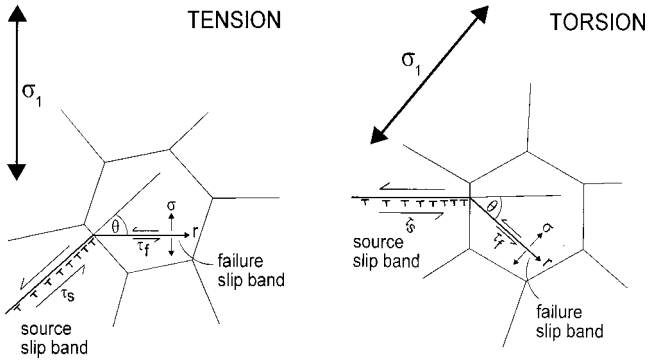

Fig. 2 Slip band model to describe facet formation in alpha-beta and near-alpha titanium alloys under tension and torsion loading configurations

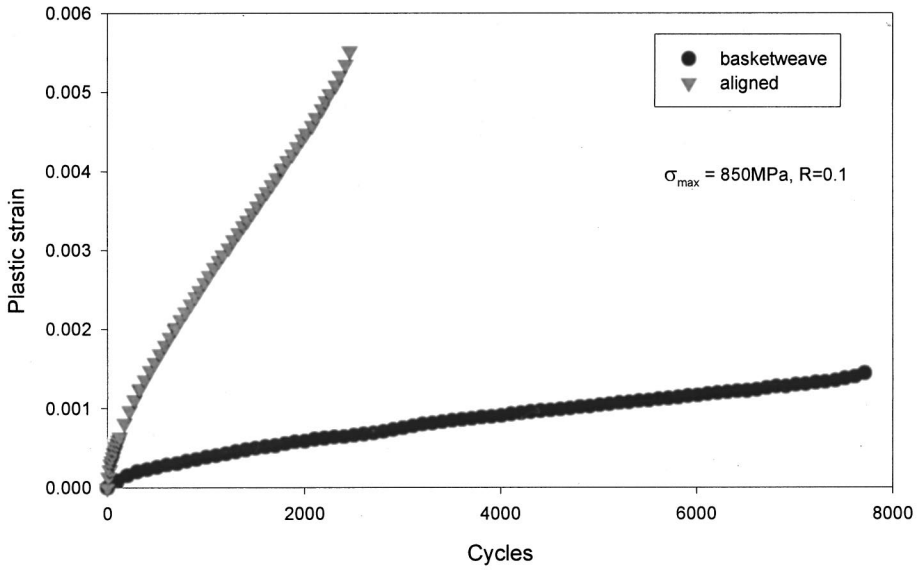

Fig. 3 Comparison of strain accumulation for Timetal 685 in basket weave and aligned microstructural form

This contrast between the strain response in aligned and basketweave materials can be attributed to the fundamental strength differences of the two forms. By normalizing the applied cyclic stress with respect to the appropriate UTS, as measured under monotonic tension, data from comparable stress conditions can be plotted (Fig. 7). Allowing for the fact that tests were not performed at identical conditions, under the normalized criterion, the strain-life properties of the two microstructures are not too dissimilar.

The ability to accumulate plastic strain is clearly enhanced by a hold time at peak stress emphasizing the time-dependent nature of the dwell phenomenon (Fig. 4). However, the lack of dwell sensitivity in the fully transformed, aligned 685 material suggests that enhanced strain accumulation alone does not instigate dwell failures. Rather, a microstructural condition offering an anisotropic mechanical response appears to be more susceptible (i.e., the basketweave microstructure containing regions of alpha lath alignment) which allows for stress to be redistributed between the ''strong'' and weak regions.

One prediction of the Stroh model is that the magnitude of the tensile and shear stresses in the ''strong'' grain or region where the basal facet will eventually develop is directly proportional to the slip band length in the neighboring source or ''weak'' grain. It is pertinent, therefore, to note that dwell sensitivity is most prevalent for coarse grained alloys. The case of the advanced alloy Timetal 834 is, therefore, of interest in this respect since it has been shown to be insensitive to dwell when assessed in rolled bar stock form, but sensitive in the isothermally forged condition (Figs. 1(*e*) and 1(*f*), respectively) ([7]). Despite a similar prior beta grain size in each condition, through the employment of suitable X-ray techniques, forged material was shown to contain relatively large regions with a common basal plane orientation. These

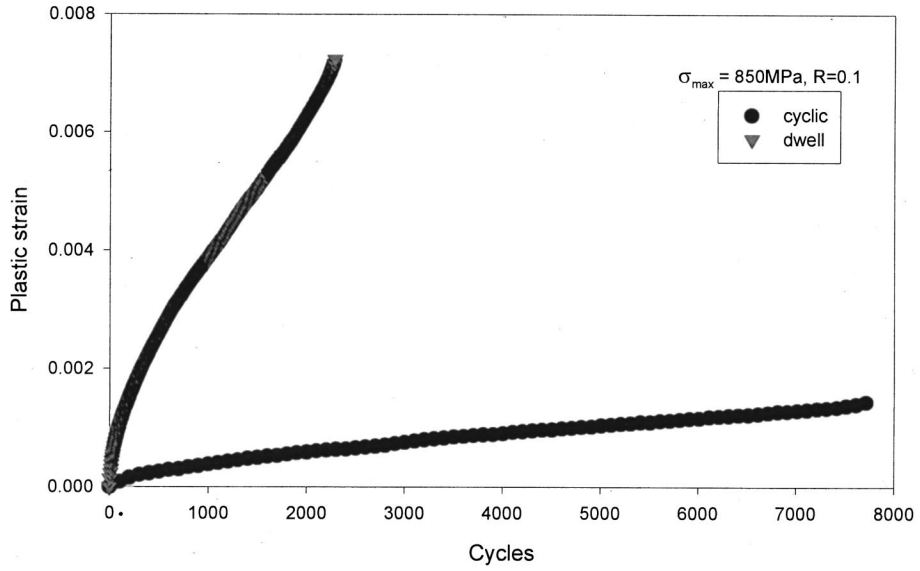

Fig. 4 Strain accumulation under cyclic and dwell waveforms in basket weave Timetal 685

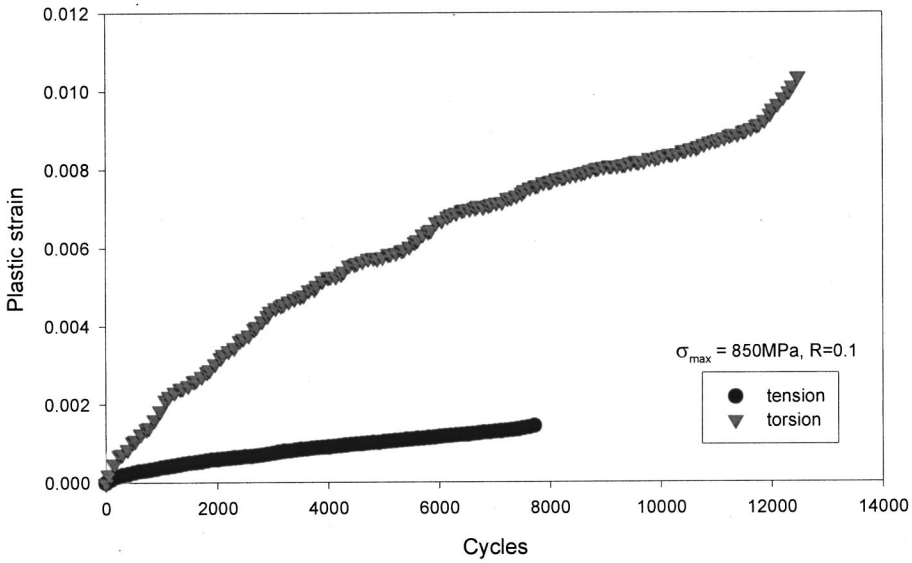

Fig. 5 Strain accumulation under cyclic tension and torsion loading in basket weave Timetal 685

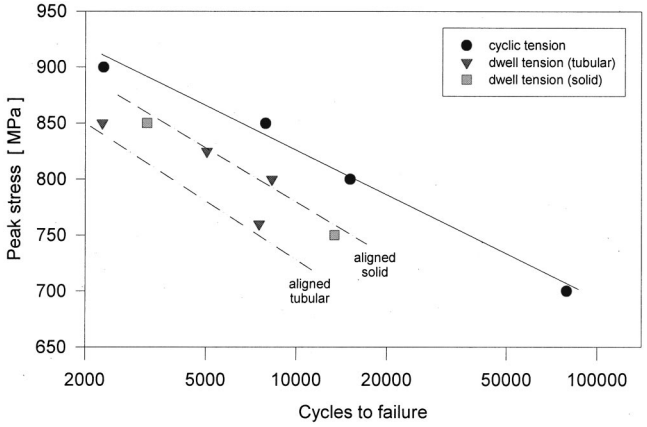

Fig. 6 Cyclic and dwell fatigue response in Timetal 685

extended through juxtaposed phases of transformed beta and primary alpha material. In essence, the forging operation had failed to break up the original prior beta grains to the same extent as rolling in the case of bar stock. More recently, the successful use of an alternative alloy for compressor disk applications, namely Ti 6246, further demonstrates that dwell sensitive behavior can be avoided by selecting processing conditions which minimize anisotropy on the microscopic scale ([8]).

Finally, the evidence presented in Fig. 5 demonstrates the importance of stress axiality. Strain accumulation is clearly enhanced under the shear dominated torsion loading condition. In terms of the redistribution model, Fig. 2, the orientation of the critical basal planes for primary slip and facet formation will be rotated through 45 deg depending on pure tension or torsion conditions. In addition, however, employing a von Mises form of stress criterion, for any given effective stress level a lower resolved tensile stress will be induced perpendicular to the developing basal plane facet under torsion relative to pure tension. This is highlighted by the

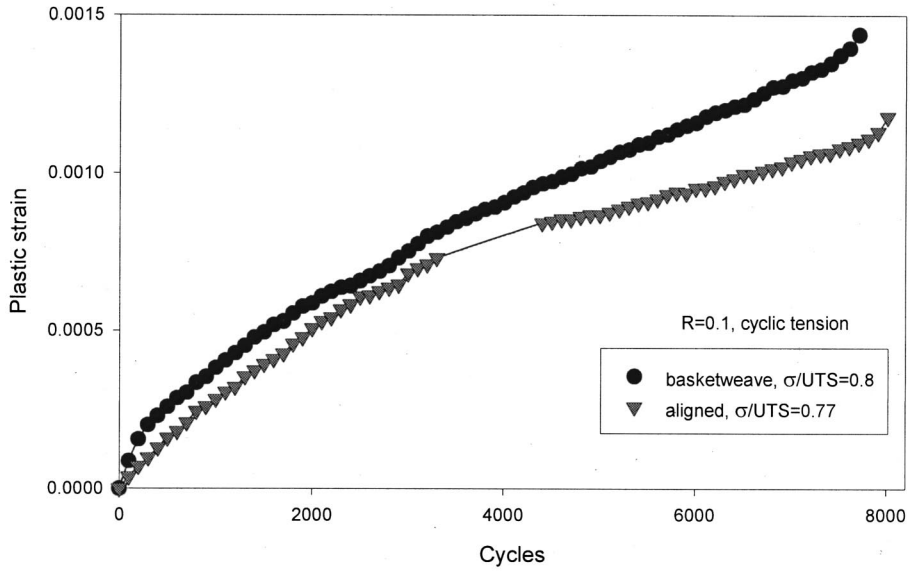

Fig. 7 Strain accumulation in basket weave and aligned forms of Timetal 685 at near equivalent normalized strength conditions (basket weave UTS=1067 MPA, aligned UTS =976 MPa)

subsequent effect on stage II fatigue crack growth. Total fatigue lives (i.e., initiation+crack growth to failure) measured under tension or torsion loading of laboratory specimens of the coarse grained alloy Timetal 685 were indistinguishable ([5,6]). However, for fine grain variants, e.g., Timetal 834, it has been demonstrated that where stage II growth contributes a greater proportion of the total life, the reduction in resolved tensile stress under mixed mode tension plus torsion or pure torsion induces progressively longer fatigue lives ([9]). It is important to recognize that real components will experience complex triaxial stress states while in service so information generated under uniaxial test conditions in the laboratory may not necessarily provide the most useful design data.

Concluding Remarks

The recognition of a ''dwell sensitive'' failure mode in $\alpha+\beta$ titanium alloys has led to a detailed understanding of the associated processes of planar slip, stress redistribution, quasi-cleavage facet formation, crack initiation, and early growth. A fundamental understanding of the anisotropic mechanical behavior, found in these alloys on the microstructural scale, and its subsequent control through alloy chemistry and improved processing techniques, are all required in order to eliminate the over conservative lifing of titanium components subjected to dwell loading. This requirement is especially relevant to gas turbine designs for power generation and propulsion applications in the short to medium term. Due to prevailing economic factors, the conventional titanium alloys will continue to be used for LP and HP compressor applications in preference to potential, high cost, replacement composite, and intermetallic systems.

References

[1] Allen, P. G., Bania, P. J., Hutt, A. J., and Combres, Y., 1996, ''LCB: A Low Cost Beta Alloy for Automotive and Other Industrial Applications,'' *Titanium '95*, P. A. Blenkinsop, W. J. Evans and H. M. Flower, eds., Eighth World Conference on Titanium, Birmingham, Oct. IOM, London, pp. 1680–1687.

[2] Ruffles, P., 1995, ''The Foresight Challenge,'' *Materials World*, **3**, IOM, London, pp. 469–470.

[3] Wojcik, C. C., Khan, K. S., and Koss, D. A., 1988, ''Stage I Fatigue Crack Propagation in a Titanium Alloy,'' Acta Metall., **36**, p. 1261.

[4] Evans, W. J., 1987, ''The Influence of Microstructure on Dwell Sensitive Fatigue in a Near Alpha Titanium Alloy,'' Scr. Metall., **21**, p. 469.

[5] Evans, W. J., and Bache, M. R., 1994, ''Dwell Sensitive Fatigue Under Biaxial Loads in the Near-Alpha Titanium Alloy IMI685, '' Int. J. Fatigue, **16**, pp. 443–452.

[6] Bache, M. R., and Evans, W. J., 1992, ''Tension and Torsion Fatigue Testing of a Near-Alpha Titanium Alloy,'' Int. J. Fatigue, **14**, p. 331.

[7] Bache, M. R., Cope, M., Davies, H. M., Evans, W. J., and Harrison, G., 1997, ''Dwell Sensitive Fatigue in a Near Alpha Titanium Alloy at Ambient Temperature,'' Int. J. Fatigue, **19**(1), pp. S83–S88.

[8] Spence, S. H., Evans, W. J., and Cope, M., ''Dwell Fatigue of Ti6246 at Near Ambient Temperatures,'' *Advances in Fracture Research*, Proceedings of ICF9, Sydney, Australia, p. 1571.

[9] Bache, M. R., Davies, H. M., and Evans, W. J., 1995, ''A Model for Fatigue Crack Initiation in Titanium Alloys,'' *Titanium '95*, Proceedings of the 8th World Conference on Titanium, Birmingham, UK, P. A. Blenkinsop, W. J. Evans, and H. M. Flower eds., Institute of Materials, London, p. 1347.

W. J. Evans

J. P. Jones

M. R. Bache

IRC in Computer Aided Materials Engineering,
Department of Materials Engineering,
University of Wales,
Swansea SA2 8PP, UK
e-mail: irc@Swansea.ac.uk

High-Temperature Fatigue/Creep/Environment Interactions in Compressor Alloys

The high-temperature fatigue response of titanium and nickel alloys destined for high-performance gas turbine applications is considered with particular emphasis given to the role of creep and environmental damage during crack growth. In an attempt to partition the respective contributions from these two rate controlling factors, data are presented for a range of temperature, stress ratio, and pressure conditions. The implications for the extended use of such alloys in future gas turbine designs are discussed.
[DOI: 10.1115/1.1498272]

Introduction

Fatigue crack initiation and growth response in high-performance steels, titanium alloys, and nickel alloys at subzero, ambient, and intermediate temperatures has been characterized in depth over the past 40 years. It is clearly established that the early stages of crack development are strongly influenced by the local microstructure of the alloy. As the cracks grow in size, they are less affected by microstructure but controlled by crack-tip plasticity that, in the more ductile materials, is associated with the formation of characteristic striations. Such information has dominated the principles of alloy development ([1]). Thus fine microstructures are introduced to enhance fatigue crack initiation resistance and to minimize the limitations of small crack growth behavior. Coarser microstructures are often used to impart long crack growth resistance particularly if they increase closure through crack diversion mechanisms as in the case of lamellar morphologies in titanium alloys or crystallographic growth near threshold in nickel alloys.

There are, however, limitations in these well-established routes to improved alloys. Environmental factors can significantly accelerate crack development particularly in the initiation and early growth stages ([2–4]). The actions of the aggressive species do not necessarily fit in with the accepted microstructure criteria. Creep deformation and fracture mechanisms can also modify the fatigue crack development process. Creep behavior is optimized by a different set of microstructural parameters to those required for optimum fatigue performance. For instance, a larger grain size is often preferred. Clearly there are major conflicts for the materials engineer seeking to develop alloys for high-temperature fatigue conditions where creep and environment play a part.

Engineering Design Requirements

In gas turbine design, performance enhancement in the form of higher thrust, reduced fuel consumption, or more efficient power generation is a perpetual necessity. Traditionally these requirements have been met by a succession of alloys with improved mechanical characteristics. It has become increasingly evident, however, that as we move into the 21st century the rate of change in the growth of conventional alloy systems is rapidly diminishing. In the longer term, designer materials such as metal and ceramic matrix composites will evolve to meet the challenges. In the short-to-medium term, cost constraints are demanding that even with current limitations, conventional alloys will continue to be used. This implies more effective mechanical design methods than those currently employed. While this is a general requirement, it is a critical issue for situations in which components experience the combined effects of fatigue/creep/environmental damage.

It is important to appreciate at the outset, two pertinent factors in the development of design methods against fatigue at high temperatures. The first is that actual crack development involves a succession of stages with each one affected differently by creep and/or environment. These stages are

- development of the stress-strain state at the critical, hot spot, location;
- initiation of cracks at the critical feature;
- small crack growth in which the crack area is comparable in size to the grain dimensions of the alloy ([5]); and
- long crack growth when the crack size is significantly larger than the microstructure.

Long cracks are the most widely studied regime and one where the growth rates, da/dN, are usually related to stress intensity factors,

$$\Delta K = Y \Delta \sigma \sqrt{\pi a},$$

with Y a geometry term, $\Delta\sigma$ the range of externally applied stress and "a" the crack dimensions.

The second significant factor is that engineering design methods generally merge the different stages of the fatigue process into two broad but distinct categories ([6]). First, there are the "initiation" or "first detectable crack" criteria which are based on S-N data generated on plain laboratory testpieces or component features. These "safe life" criteria assume the alloys to be defect free and generally apply statistically based scatter factors to arrive at a safe design life. The "initiation" approach ignores crack growth beyond the first engineering crack size that is typically a 0.75-mm long surface flaw. The second and alternative damage tolerant approach adopts the counter argument that defects are always present and that the crack initiation stage is nonexistent. The component life is then determined by how long it takes the crack to grow from the initial flaw size to ultimate failure. The rate of crack propagation is usually addressed through the application of fracture mechanics principles based on long crack growth data. An important variant is the use of the "effective initial flaw size—EIFS" ([7]). This approach addresses two major limitations in the fracture mechanics approach which are the definition of the starting flaw size for calculating residual propagation lives and the growth kinetics of cracks while small and within the vicinity of the flaw. The "worst case" EIFS is derived from a database of pseudo flaw sizes determined from "back tracking" calculations on failed specimens, representative structural features and full

Contributed by the International Gas Turbine Institute (IGTI) of THE AMERICAN SOCIETY OF MECHANICAL ENGINEERS for publication in the ASME JOURNAL OF ENGINEERING FOR GAS TURBINES AND POWER. Paper presented at the International Gas Turbine and Aeroengine Congress and Exhibition, New Orleans, LA, June 4–7, 2001; Paper 2001-GT-477. Manuscript received by IGTI, Dec. 2000, final revision, Mar. 2001. Associate Editor: R. Natole.

component tests. Application of reserve factors to the calculated lives covers uncertainties in the calculation method and provides a declared safe life for the component.

Both approaches to fatigue life prediction have limitations but at lower temperatures where creep and environment have minimal impact, these are generally conservative, and so lead to the straightforward effect that components are heavier or operate at lower stresses than optimum. However, the assumption of similar conservatism at high temperatures is potentially dangerous because of the additional deformation and damage processes due to creep and environment. Clearly, a more efficient design and life prediction capability requires the nature of these interactions to be understood and quantified in full. The objective of the present research was to quantify the impact of creep and environmental factors on the propagation of small and long fatigue cracks. This was considered to be particularly important as the initiation stage of many cracks at temperature is extremely short or even absent.

Experimental Background

Crack propagation behavior at elevated temperature is characterized through a variety of test piece types and by means of a wide range of experimental techniques. The most common specimens are the compact tension (CT) and corner crack (CC) geometries. The CT specimen provides information on long, through section crack shapes. At high temperature, there is a tendency for the crack to tunnel and side grooves are often introduced to offset this problem. The CC specimen focuses on part-through cracks that grow from a slit at one corner of the cross section. It is capable of covering both small and long crack behavior but most importantly, it facilitates high-precision crack growth monitoring using a DC potential difference system. The CC geometry used in this program and the associated stress intensity calibration have been described elsewhere ([3]).

A DCPD system in which a 30-amp current is pulsed for about three seconds during selected loading cycles is a highly sensitive means of monitoring crack growth without inducing detrimental local heating at the crack tip. The platinum PD monitoring wires should be spot welded immediately adjacent to the starter slit for maximum resolution and a linear calibration in terms of crack length. The PD system has the additional advantage that it can also be used to measure crack closure during the fatigue crack growth process. This is achieved by applying the current continuously throughout selected loading cycles as the crack develops ([8]). The most sensitive measurements of closure are obtained under vacuum conditions when oxide on the crack surfaces does not interfere with the current flow. These measurements then allow for the calculation of ''closure-corrected'' fatigue crack growth rates in terms of an ''effective driving force'' or ΔK_{eff}.

Clearly, studies of environmental effects require a capability for carrying out experiments in controlled atmospheres. A typical environmental chamber designed to encapsulate the test specimen and the loading rods of a servohydraulic testing machine has been described previously ([3]).

Crack Growth Response

The data presented in Figs. 1 to 5 demonstrate how applied conditions influence the interaction between fatigue, creep, and environment. The information is for the titanium alloy Ti 6246 but are typical of other alloys and systems.

Under cyclic loading (15 cpm) there is a progressive increase in growth rate as the temperature increases from 20 to 550°C (Fig. 1). The greatest increase occurs at low ΔK and diminishes as the higher rates of crack growth except for the highest temperature (550°C). Between 20°C and 450°C, the enhancement in growth rates is small but there is a significant increase between 450°C and 500°C. It is evident from the graph that the 500°C data set is a transition stage between low-temperature fatigue-dominated growth and high-temperature creep/environment-influenced behavior.

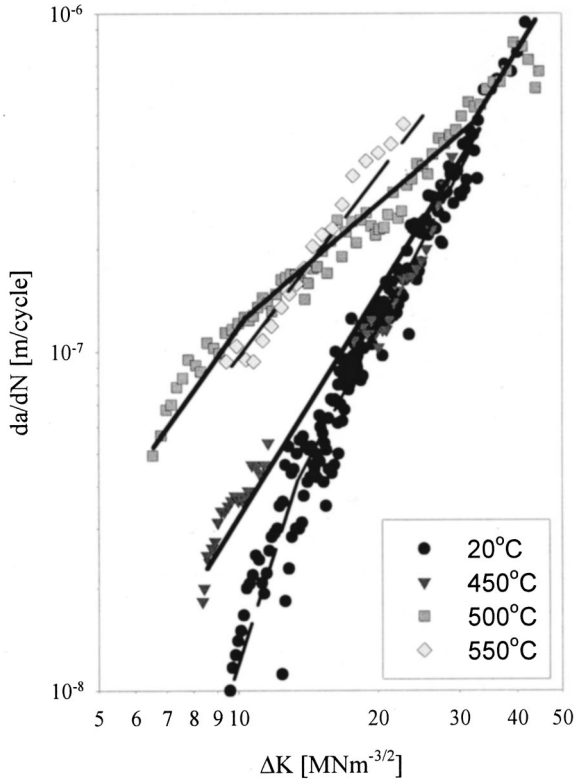

Fig. 1 FCG in Ti 6246 under cyclic loading (15 cpm)

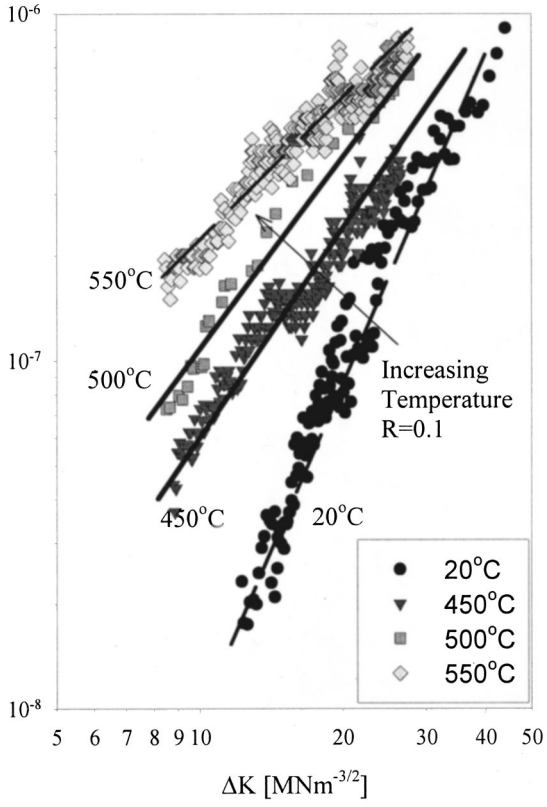

Fig. 2 FCG in Ti 6246 under a two-minute dwell waveform

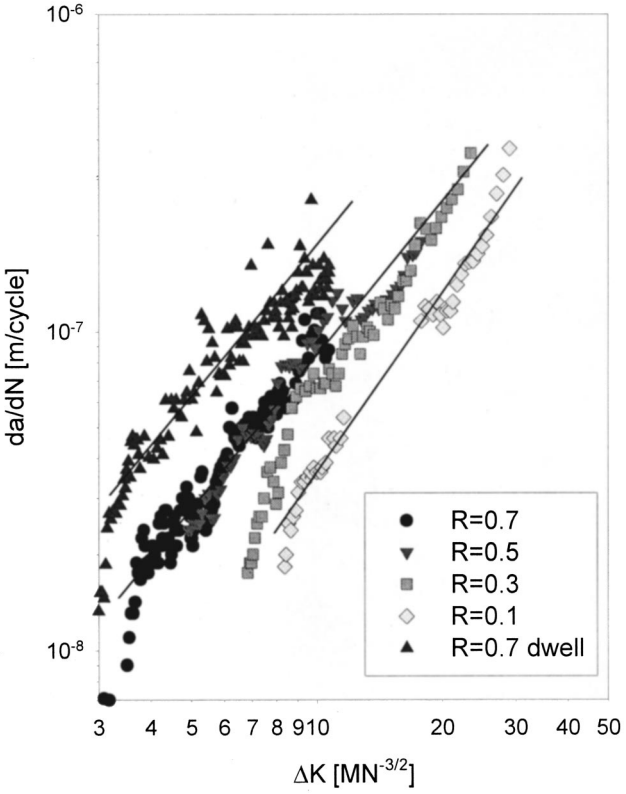

Fig. 3 Effect of mean stress in Ti 6246 at 450°C

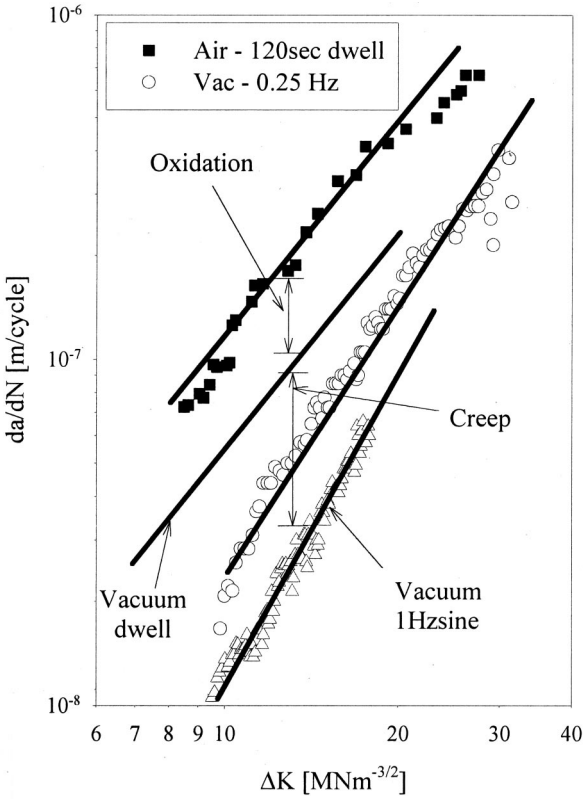

Fig. 5 Environmental influence of FCG in Ti 6246 at 500°C

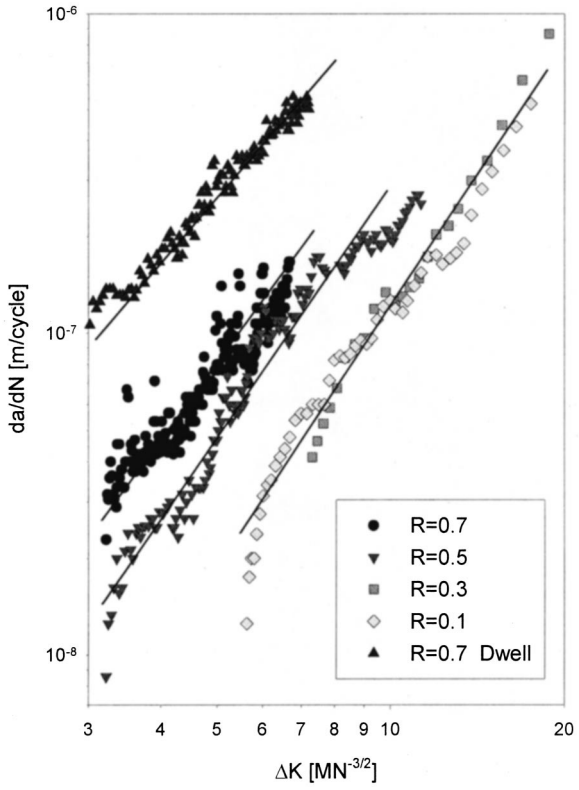

Fig. 4 Effect of mean stress in Ti 6246 at 550°C

When a dwell period (120 secs) at maximum stress is introduced, the transition effect disappears to the extent that there is a progressive increase in growth rates from 20°C to 550°C (Fig. 2). Once again, it appears that the largest enhancement is at low ΔK. However, a comparison with the growth rates of Fig. 1 confirms that creep/environmental damage mechanisms become more significant as times on load increase.

Increases in mean stress (R-value) also cause faster fatigue growth rates for a given ΔK value at any temperature. Near ambient, the R value effects can be rationalized through a correction for crack closure. In Figs. 3 and 4, data covering a range of R values are presented for Ti 6246 at 450°C and 550°C, respectively. At 450°C, there is a change in growth behavior from $R=0.1$ to 0.3 but then the remaining R value data superimpose. Such behavior is rationalized by closure arguments. However, at 550°C the growth rates continue to increase as R increases. The strong R-value dependence in this case does not conform fully with closure correction.

The relative contributions of environment and creep are not clear from the information presented so far. Figure 5 contains crack growth data in air and a hard vacuum (10^{-5} torr). It is evident that the vacuum conditions are associated with significantly lower growth rates. It is apparent, however, that frequency and dwell time still effect growth rates in vacuum. Clearly, a higher frequency reduces rates but a longer dwell period (120 secs) causes a faster rate of propagation. Figure 5 also compares air and vacuum dwell behavior from which the relative contributions of creep and environment can be defined for this particular test condition.

Crack Closure

Crack closure has often been invoked to account for some of the effects observed where there is an environmental-fatigue interaction ([9]). The role of crack-tip plasticity in the promotion of R-value effects under pure fatigue is generally accepted. Changes

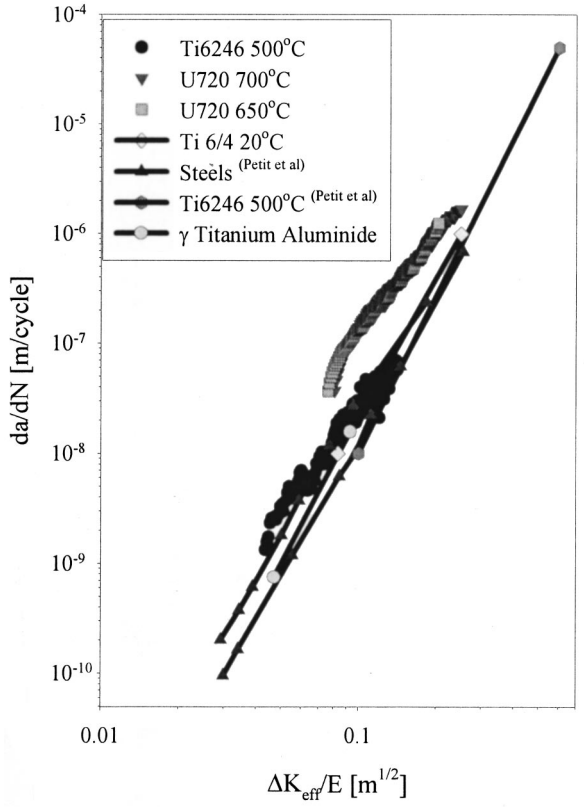

Fig. 6 Intrinsic FCG for a variety of titanium and nickel alloys

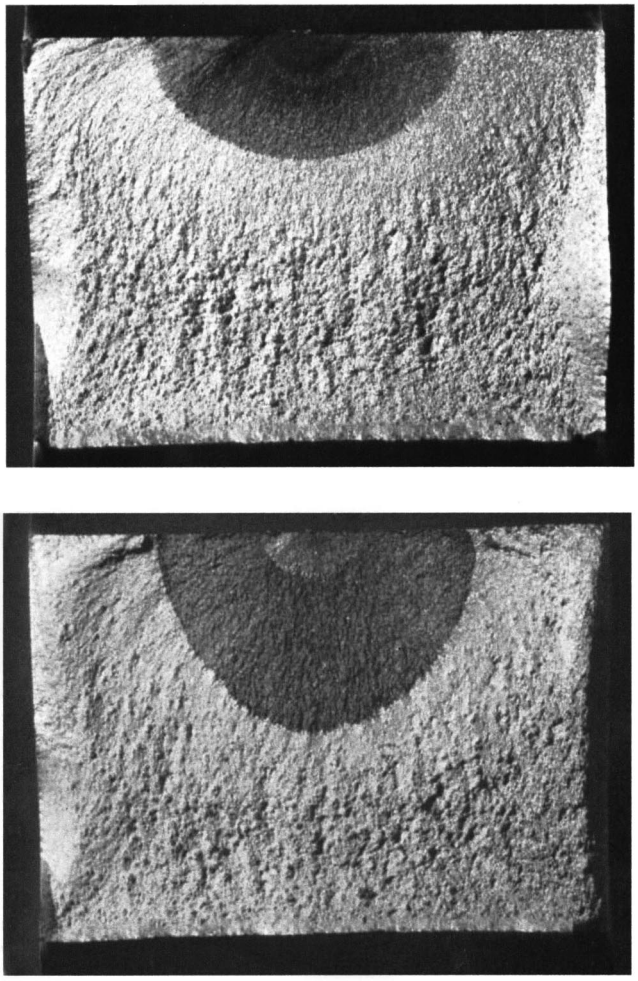

Fig. 7 Fatigue cracks developed in IN718 under hard vacuum (top) and atmospheric pressure (bottom) at 600°C

to the closure state caused by environmental damage have been invoked. These changes include increased crack surface roughness and debris deposited on the crack faces. Petit [10] has used closure corrected data obtained in vacuum to define an intrinsic fatigue crack growth response. He has developed a unified model for a wide range of materials, including steels, aluminum alloys, and titanium alloys, by relating their long crack growth rates to the parameter $\Delta K_{\text{eff}}/E$ with E the elastic modulus at the appropriate test conditions. The ΔK_{eff} is an effective stress intensity factor ($\Delta K_{\text{eff}}=K_{\max}-K_{\text{clos}}$) where $K_{\max}$ is the maximum and K_{clos} the closure stress intensity factors. The intrinsic growth rate relationship is illustrated in Fig. 6 for vacuum data on Ti-6A1-4V at room temperature, Ti 6246 at 500°C, several steels and a high-strength nickel alloy at 650°C and 700°C. The Ti 6246 growth rates are for two basic frequencies: 15 cpm trapezoidal and 30 Hz with the former taken from Fig. 5. The nickel data were also obtained with the trapezoidal waveform at 15 cpm. The Ti-6/4 rates are fundamental to the intrinsic growth response. They were obtained at room temperature under conditions where any time dependency is insignificant. Clearly the Ti 6246 at high frequency and the steels correlate well with the Ti 6246 at high frequency and the steels correlate well with the Ti-6/4 closure corrected data. The lower frequency Ti 6246 and nickel data, while lying close to the intrinsic curve, are displaced slightly to higher growth rates at a given $\Delta K/E$. The low frequency, high temperatures, and vacuum conditions strongly support an interaction with high-temperature creep damage events.

Interaction With the Environment

The effect of environment is epitomized in the crack growth behavior of the nickel alloy IN718 shown in Fig. 7 ([11]). Fatigue crack growth tests were performed on double edge notch (DEN) test-pieces containing a mid-notch starter defect at 600°C. Two important observations have been noted by previous workers. First, air pressure effects the rate of crack propagation. Andrieu et al. [12] have shown that for oxygen partial pressures greater than 10^{-2} torr, growth rates are similar to atmospheric pressure but for partial pressures less than 10^{-3} torr the growth response is similar to the high vacuum condition at 10^{-6} torr. The second observation relates to the shape of the cracks that developed at the notch root. The elliptical shape found under hard vacuum is consistent with the stress field associated with this type of notch. The deeper penetration in the partial vacuum for nominally similar loading conditions is typical of the cracks that develop under conditions where environment is assisting the crack growth process. The shape change is attributed to the ingress of the damaging species to the crack tip and preferential failure of embrittled grain boundaries in the tri-axial stress field at the deepest position of the crack front ([11]). Crack tunnelling is a common observation at temperature and particularly in the presence of dwell cycles at peak stress.

There is continuing debate on the species responsible for environmental degradation. One view is that it is associated with water vapor ([2,10,13]), the other that it involves the ingress and diffusion of oxygen ([14,15]). The water vapor argument has been strongly promoted by Petit to account for differences between crack growth rates in air and the intrinsic, vacuum growth curve. He has developed his ideas for a range of aluminum alloys, titanium alloys, and steels and covered a range of temperature conditions from near ambient to the fatigue-creep-environment regime. The theory is supported by a series of definitive experiments involving controlled traces of water vapor. In essence, it is sug-

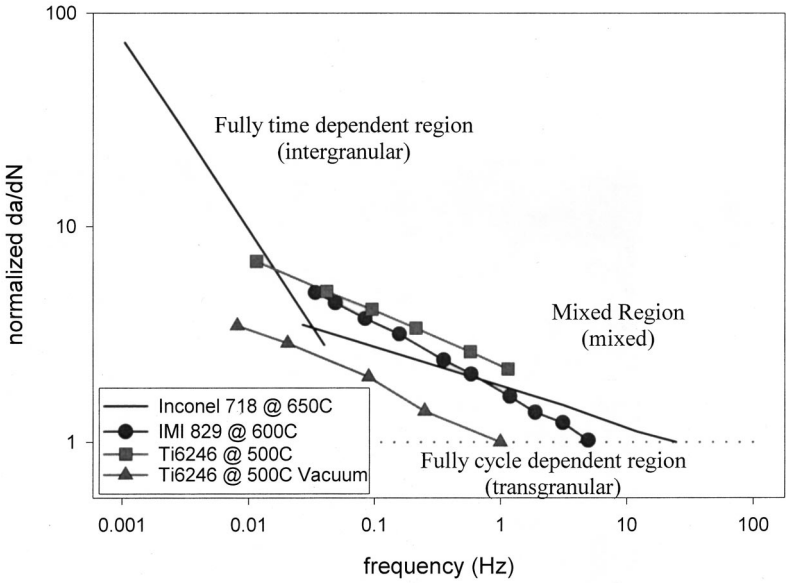

Fig. 8 The role of frequency on fracture mode and normalized growth rates

gested that there is a material/test condition dependent critical growth rate, $(da/dN)_{cr}$, which can be related to the point at which the crack-tip plastic zone becomes equal to the alloy grain size. For rates greater than the critical value, normal crack advance occurs involving, for instance striation formation, but at an accelerated rate due to the adsorption of water vapor. At rates less than $(da/dN)_{cr}$, the water has sufficient time to dissociate and the released hydrogen causes dramatic accelerations in crack growth.

The alternative oxygen model has received support from many authors working on titanium and nickel alloy systems ([4,12,14–17]). In the near alpha titanium alloy, TIMETAL 834, Hardy and colleagues calculate, on the basis of the work of Wallace [18], that oxygen diffusion can produce a saturated oxygen region of a similar size to the intrinsic growth increment during a four-second cycle at 630°C. Other work on titanium alloys at lower temperatures has highlighted dramatic accelerations in crack growth rate as the concentration of internal oxygen increases ([3]). Interestingly, this lower temperature acceleration is associated with increased formation of crystallographic facets and is more marked at high *R* value. The high temperature, accelerated crack growth in TIMETAL 834 is also accompanied by enhanced facet development and a strong *R*-value dependency. It is argued that oxygen promotes facet formation on basal planes (0001) in titanium alloys ([18]). Other authors, including Ghonem and co-workers ([14,15]), have also come out strongly in favor of oxygen enhanced crack growth at high temperatures in titanium alloys.

Oxygen is often considered to be the active species in nickel alloys. This view is encouraged by the fact that there is a highly distinctive change in fracture mode from transgranular (cycle dominated) to intergranular (time-dependent) as the cyclic frequency falls. The change in fracture mode has promoted the construction of a mechanism map detailing the rate of crack propagation and fracture mode in terms of test frequency ([19]) as illustrated in Fig. 8. This employs a normalization method for the crack growth rates in which the measured rate at a given frequency and stress intensity range (ΔK) is divided by the growth rate for fatigue dominated behavior at high frequency. A normalized value of unity, therefore, represents pure fatigue. The approach allows data for titanium alloys to be superimposed on the graph. Clearly the Timetal 829 and Ti 6246 rates show a similar pattern of behavior to the IN 718. This is true also of the Ti 6246 rates for high vacuum conditions. The observation strongly suggests that the observed trend is not caused by oxygen and environmental species but is strongly influenced by creep deformation, possibly through its effect on crack closure.

It has been argued that, in the case of nickel alloys, oxygen can diffuse and cause embrittlement of boundary carbides or form a brittle niobium oxide film thereby leading to intergranular fracture. An alternative view is that oxygen could pin grain boundaries and prevent grain boundary sliding and local slip thereby enhancing the tendency for triple-point wedge cracking in order to accommodate creep deformation. However, the situation is by no means clear and the work of Browning and co-workers ([20]) bring the discussion back full circle to the water vapor theory of Petit. In essence, they found that intergranular cracking could still occur at low oxygen partial pressures provided there was still water vapor present.

An interesting additional factor in the growth rate equation has been highlighted recently by Miller and co-workers ([21,22]). A large number of cracks generally form under high temperature fatigue. While these are small compared with the microstructure, i.e., stage I cracks, their widely different orientations tends to keep their growth independent. However, once a small number cross the microstructural barrier, such as the grain size, they become stage II cracks and rapid coalescence occurs because they are now similarly orientated. This leads to a significant acceleration in growth rate similar to that reported for environmental enhancement. Further insights into this damage process are now essential to allow detailed models to be developed.

Clearly, there is no consensus on the detailed mechanisms responsible for intergranular crack growth. It is accepted, however, that as R-value increases, this time-dependent growth regime becomes more predominant because the cracks are less, or even not, affected by closure thus providing a greater opportunity for the environmental species to act. It is also recognized that as cycle frequency increases, the opportunity for ingress by the environment diminishes so that the fracture mode progressively changes to a transgranular, cycle-dependent mode typical of ambient temperature fatigue. Recognition of these facts, however, is not sufficient. Engineering design demands that the damage mechanisms should be quantified into a ready means for predicting the service lives for these demanding operating conditions.

Conclusions

Conventional metallic alloy systems employed in future gas turbine designs will undoubtedly operate under regimes of stress and temperature where the interaction of fatigue, creep, and environmental degradation will ultimately limit life. The present paper has highlighted the need for a fundamental understanding of these interactions in terms of fatigue crack growth and damage tolerance for a variety of titanium and nickel alloys.

References

[1] Evans, W. J., 1998, ''Optimizing Mechanical Properties in Alpha+Beta Titanium Alloys,'' Mater. Sci. Eng., A, **243**, pp. 89–96.

[2] Petit, J., Mendez, J., Berata, W., Legendre, L., and Muller, C., 1992, ''Influence of Environment on the Propagation of Short Fatigue Cracks in a Titanium Alloy,'' *Short Fatigue Cracks*, edited by K. J. Miller and E. R. de los Rios, eds., Mechanical Engineering Publications, London, **ESIS13**, pp. 235–250.

[3] Bache, M. R., Evans, W. J., and McElhone, M., 1997, ''The Effects of Environment and Internal Oxygen on Fatigue Crack Propagation in Ti-6A1-4V,'' Mater. Sci. Eng., A, **234–236**, pp. 918–922.

[4] Skelton, D., and Knowles, D. M., 1999, *Fatigue '99*, Wu and Wang, eds., Beijing, EMAS, Cradley Heath, West Midlands, UK, pp. 2111–2116.

[5] Ritchie, R. O., and Lankford, J., eds., *Small Fatigue Cracks*, TMS-AIME, Warrendale, PA.

[6] Harrison, G. F., and Boyd-Lee, A. D., 1999, ''Life Extension Methods for Fatigue Critical Aeroengine Components,'' *DERA Conference on Gas Turbines—Materials Make the Difference*, Mechanical Services Sector, DERA, Farnborough, UK, pp. 15-1–15-10.

[7] Asquith, G., and Pickard, A. C., 1988, ''Fatigue Testing of Gas Turbine Components,'' *Full Scale Fatigue Testing of Components and Structures*, K. J. Marsh, ed., Butterworths, London, **V2**, pp. 201–234.

[8] Bache, M. R., 1999, ''Microstructural Influences on Fatigue Crack Growth in the Near Alpha Titanium Alloy Timetal 834,'' *Small Fatigue Cracks: Mechanics, Mechanisms and Applications*, K. S. Ravichandran, R. O. Ritchie, and Y. Murakami, eds., Elsevier, New York, pp. 199–206.

[9] Gangloff, R. P., and Ritchie, R. O., 1985, *Fundamentals of Deformation and Fracture*, B. A. Bilby, K. J. Miller, and J. R. Willis, eds., Cambridge Univ. Press, London, pp. 529–558.

[10] Petit, J., 1992, ''Modelling of Intrinsic Fatigue Crack Propagation,'' *Theoretical Concepts and Numerical Analysis of Fatigue*, A. F. Blom and C. J. Beevers, eds., EMAS, pp. 131–151.

[11] Bache, M. R., Evans, W. J., and Hardy, M. C., 1999, ''The Effects of Environment and Loading Waveform on Fatigue Crack Growth in Inconel 718,'' Int. J. Fatigue, **21**, pp. 69–77.

[12] Andrieu, E., Hochstetter, G., Molins, R., and Pineau, A., 1994, *Superalloys 718, 625 and 706 and Various Derivatives*, E. A. Loria, ed., The Minerals, Metals and Materials Society, pp. 619–631.

[13] Lesterlin, S., Sarrazin-Baudoux, C., and Petit, J., 1995, ''Temperature-Environment Interactions on Fatigue Behaviour in Ti6246 Alloy,'' *Titanium '95: Science and Technology*, edited by P. A. Blenhinsop, W. J. Evans, and H. Flower, eds., The Institute of Materials, The University Press, UK, pp. 1211–1218.

[14] Ghonem, H., and Foerch, R., 1991, ''Frequency Effects on Fatigue Crack Growth Behavior in a Near Alpha Titanium Alloy,'' Mater. Sci. Eng., **138**, pp. 69–81.

[15] Foerch, R., Madsen, A., and Ghonem, H., 1993, ''Environmental Interactions in High Temperature Fatigue Crack Growth of Ti-1100,'' Metall. Trans., **24**, p. 1321.

[16] Hardy, M. C., Bache, M. R., Konig, G., and Henderson, M. B., 1999, ''Influence of Creep and Oxidation on the Elevated Temperature Crack Growth Behaviour of a Near Alpha Titanium Alloy,'' *Life Assessment of Hot Section Gas Turbine Components*, IOM, London.

[17] Bricknell, R. H., and Woodford, D. A., 1981, ''Embrittlement of Nickel Following High Temperature Air Exposure,'' Metall. Trans., **12A**, pp. 425–433.

[18] Wallace, T. A., 1996, ''The Effect of Oxidation Exposure on the Mechanical Properties of Timetal-1100,'' *Titanium '95: Science and Technology*, P. A. Blenkinsop, W. J. Evans, and H. M. Flower, eds., The Institute of Materials, The University Press, UK, pp. 1943–1950.

[19] Weerasooriya, T., 1988, ''Effect of Frequency on Fatigue Crack Growth Rate of Inconel 718 at High Temperature,'' *Fracture Mechanics: 19th Symposium*, ASTM-STP 969, ASTM, Philadelphia, PA, pp. 907–923.

[20] Browning, P. F., Henry, M. F., and Rajan, K., 1997, ''Oxidation Mechanisms in Relation to High Temperature Crack Propagation Properties of Alloy 718 in H_2 /H_2O/Inert Gas Environment,'' *Superalloy 718, 625, 706 and Various Derivatives*, The Minerals, Metal and Materials Society, Warrendale, PA, pp. 665–678.

[21] Miller, K. J., 2000, ''Blind Alleys on the Route to Real Fatigue Solutions: A Historical Perspective,'' *Fatigue 2000, Proceedings of Fourth International Conference of the EIS, Cambridge, UK*, M. R. Bache, P. A. Blackmore, J. Draper, J. H. Edwards, P. Roberts, and J. R. Yates, eds., EMAS, Cradley Heath, West Midlands, UK, Mar. 14.

[22] Miller, K. J., 2000, ''Blind Alleys on the Route to Real Fatigue Solutions: A Historical Perspective,'' *Fatigue 2000—Fracture & Durability Assessment of Materials, Components nad Structures*, M. R. Bache, P. A. Blackmore, J. Draper, J. H. Edwards, P. Roberts, and J. R. Yates, eds., Proceedings of the 4th International Conference on the Engineering Integrity Society, Apr. 10–12, Cambridge, EMAS, Cradley Heath, West Midlands, UK.

Design Development of Unitized Titanium Structure

D. Groneck
The Boeing Company
M/C S064-2400
St. Louis, MO 63166-0516
e-mail: daniel.e.groneck@boeing.com

D. Harmon
PCC Structurals, Inc.,
Portland, OR

Traditional airframe primary structure is fabricated from wrought product forms that are transformed by machining, forming, and joining into structural components. These individual parts are assembled together by fasteners to create the airframe. Significant cost and cycle-time savings can be achieved by switching from multipiece builtup assembly to a single-piece net shape casting. The reduction in number of discrete parts provides a significant reduction in both direct and indirect costs. In particular, the inherent low material costs and excellent producibility characteristics of cast metallic parts may provide a significant contribution to the goal to reduce acquisition costs. Under the program reported herein, and in conjunction with a casting vendor, prototype titanium (Ti-6Al-4V) cast airframe components were designed and fabricated. The typical overall dimensions of each casting are 50 inches×40 inches×30 inches, and weigh approximately 190 pounds per casting. The castings were modeled on generic aircraft fuselage structure, that incorporated smooth inner moldline surface and integral webs and keels, capped by a T-element, web stiffeners, access holes, and other detail features. Multiple castings are joined to create the airframe structure. A rapid prototyping method was utilized to create the pattern, which eliminated the requirement for expensive metal tooling. The prototype castings successfully demonstrated the producibility of this generic airframe structure. [DOI: 10.1115/1.1494099]

1 Technology Background

The increased use of more expensive materials, structural concepts, and complex assemblage of many discrete components can increase the costs for next generation aircraft. Complex structural concepts created with composite material preforms and titanium components are increasingly required to maximize structural efficiency to optimize air vehicle performance. Although the necessity to reduce aircraft weight has driven the increased use of organic matrix composites for fuselage skins and wing structure, metallic structures and assemblies still account for at least two-thirds of airframe weight. With the continued widespread use of metallic materials for airframe assemblies, application of state-of-the-art metals processing technology and advanced structural design concepts can provide breakthrough cost savings for military aircraft systems.

Lean Manufacturing is focused on reducing part count, manufacturing operations, and simplifying the assembly process, resulting in lower cost and higher quality. The product of this effort will be a more unitized airframe with a higher level of integration of subsystems and mounting hardware. This may appear to be a simple strategy, but it requires inputs from experts in a wide variety of fields (design, analysis, manufacturing, procurement, suppliers, etc.) to enable incorporation of the appropriate lessons learned from within the company and supplier base. Emerging metallic materials, processing and manufacturing technologies are enabling to the design development of a highly unitized airframe.

In airframe construction, the center and aft fuselage represent the highest cost on a dollar per pound basis. This is primarily attributed to factors such as high part count and the use of titanium components needed to construct highly loaded assemblies (e.g., tightly spaced frame assemblies and titanium bulkhead components). Airframe construction has traditionally relied upon builtup mechanical assembly of machined hogouts, sheet metal, and forged/machined components to build aircraft assemblies. This philosophy currently represents the lowest risk approach since there is a historical knowledge base; design and analysis activities can be segmented to small subassembly levels with individual load cases and airframe component manufacturing can be rapid, flexible, and straightforward since part details are relatively simple in geometry. The disadvantage of the current design and manufacturing philosophy is that part count is high resulting in higher engineering logistics costs. Also, material efficiency can be poor, component assembly is often problematic due to part distortion and tolerance build-up and modularity is difficult at the system level.

The disadvantage in relying heavily on traditional titanium components is that the costs of manufactured components are increasing due to reduced availability, escalating material costs, and the relative difficulty in machining and forming of component geometries.

1.1 Program Background. One enabler of Lean Manufacturing is the use of castings to replace builtup assemblies of parts. The principal context of this paper is the reporting of a design development program ongoing at The Boeing Company, Phantom Works, St. Louis, MO, to design, fabricate, and test a prototype structural test article of significant size and complexity. Early in the trade study phase, it became apparent that the temperature, stress, and stiffness requirements of the test article required the use of structural high temperature materials. In the line with the desire to meet the weight goal of the test article, the use of titanium materials became the only real choice. Fortunately the upper temperature limit did not require the use of near alpha or titanium aluminide materials, and the selection fell to the Alpha-Beta titanium alloys—either Ti-6Al-4V or Ti-6Al-2Sn-4Zr-2Mo.

A ''one-off'' test article would traditionally be fabricated from a builtup assembly, that would require large number of major structural components, such as keels and frames. These structural components would be fabricated from large hand forging or plate stock, and then undergo extensive (and expensive) machining operations, typically yielding only 15% of the purchased material weight. Other structural elements, such as skins, would be fabricated from sheetmetal, which is formed to the final lofted geometry, using a variety of forming techniques. Each of these fabrication techniques has extensive (and expensive) tooling

Contributed by the International Gas Turbine Institute (IGTI) of THE AMERICAN SOCIETY OF MECHANICAL ENGINEERS for publication in the ASME JOURNAL OF ENGINEERING FOR GAS TURBINES AND POWER. Paper presented at the International Gas Turbine and Aeroengine Congress and Exhibition, New Orleans, LA, June 4–7, 2001; Paper 2001-GT-450. Manuscript received by IGTI, Dec. 2000, final revision, Mar. 2001. Associate Editor: R. Natole.

requirements, driving up the total cost for a one-piece prototype. Builtup assemblies also require a substantial number of clips, angles, doublers, and fasteners to join the major structural elements together. This program's complex geometry requirements meant that unitized structure could provide optimized load paths, resulting in lower overall structural weight. Based on these factors and experience in other prototype programs, it was concluded that typical design and production techniques were too time-consuming and expensive for this design.

An improved procurement process was required to meet the Lean Manufacturing objectives for this prototype program. A shift to modular construction not only had significant cost and weight reduction potential, but reduction in part count would simplify and streamline the supply chain—reducing the bill of material. A design optimized for castings also would offer the efficiency of managing a single source instead of numerous subcomponents from multiple vendors. Indirect and shop floor costs are reduced because these modular assemblies would not require as much touch labor for assembly as traditional structure, resulting in a total lead time reduction in the fabrication and assembly phase. Finally, over 95% of the casting surface is left as-cast, so the total machining activity for this program is substantially reduced.

An initial evaluation revealed that the casting industry was interested in pursuing the large nonsymmetric titanium castings required. After a vendor evaluation, competition, and proposal review, a contract was awarded to PCC Structural Castings of Portland, OR.

1.2 Design Development. Several issues have traditionally prevented large structural titanium castings from being implemented on prototype programs. First of all, castings have a reputation for lengthy prototype development time. The high cost of hard (wax) tooling prevented prototype applications. Also, the confidence in limited material property databases meant the use of casting factors, which usually resulted in an increase in component weight, compared to traditional aircraft structure. Finally, monolithic structures create concerns, as part redundancy is one method used to achieve damage tolerant and supportable structures.

Fortunately, the casting vendors have been working on the issue of ''speed to market,'' essential to prototype production. For this program, the use of stereolithic (SLA) patterns was proposed to serve the place of wax patterns. The manufacturing strategy for these prototype castings utilized the same theory of constraints and capacity analysis tools used for general production castings in their Portland, Oregon facility. A goal of 28 weeks cycle time of delivery from final part submittal to casting delivery to the machining vendor was established.

This program was initiated with preliminary engineering definitions and trimetric views and weight estimates. As engineering models were refined, both sites used Unigraphics solid modeling packages to review the proposed parts. Utilizing data transfer through 4-mm DAT tapes, electronically transferred working files, and paper working models, casting engineers worked concurrently with the Integrated Product Team, early and frequently throughout the design process. This ensured that the vast experience that the casting engineers have with large structural cast titanium alloys was captured.

This exchange took several forms:

- initial face-to-face meetings between the appropriate personnel to establish general design criteria that would be used for all castings.
- conference calls and electronic data exchanges to discuss particular design features of individual castings.
- on-site reviews of the castings at critical process points.

The Integrated Product Team worked together to define the optimal size of the castings, which pushed the physical limits of the casting process. The structural design goal of maximizing the size of the castings, to minimize the number of splice joints that were required, had to be balanced against the practical and physical size limitations at the casting supplier's Large Titanium parts facility. Table 1 lists the casting sizing guidelines. To meet the rapid pace of this program, all processing, with the exception of Hot Isostatic Pressure (HIP) process, was planned to utilize existing in-house facilities. Although each casting is unique, all shared some of the following design features:

- keel and frame segments,
- moldline geometry for skin attachment,
- T- and L-element caps,
- lofted geometry solid surface, with integral buttons, and
- integral lugs for attachment to test fixture.

As a result of this concurrent engineering, a total of 15 castings were defined, with five castings having symmetric configurations, for a total of ten unique casting configurations. Table 2 lists the sizes and weights for representative castings. Part count, relative to traditional structure, was reduced over 65%.

Table 1 Casting facility dimensional guidelines (contact PCC, structurals for complete details)

PROCESS	LIMITING SIZE
SLA	N/A – Individual segments joined
Dip Tanks	Flow coat can be applied to parts of almost unlimited size. For back-up dips, the dip pots are 96 inches in diameter, but molds of larger size can be dipped by manipulating the model at an angle
Casting Furnace	Current pour capacity of 1500 pounds, largest part poured to date is 96 inches long x 18 inches tall
Heat Treat Furnace	95 inches max length
HIP Chambers	Subcontractors' largest chamber is 65 inch diameter x 100 inches tall
Weld Chamber	100 inches
CMM	80 inches wide x 100+ inches long (largest on-site)
X-ray	100" (largest on-site)

1.3 Structural Analysis. With the overall size envelopes of the castings established, detailed structural analysis of the assembly could begin. Three-dimensional finite element models of the prototype assembly were created and surveyed to determine the critical loads. These models included applied air, inertia, and thermal loads corresponding to specific flight, ground handling, transportation, and test conditions. Analysis checks were made on each casting to verify its structural integrity. Yield, ultimate, and stability checks were made to guarantee a positive margin of safety. A variety of proprietary analysis codes, such as ALADAN (for panel buckling) and HOLEBUCK (for panels with holes and penetrations) were used to conduct these checks as well as classical analysis techniques. Factors of safety used in the analysis were

Table 2 Typical casting dimension and weight

Casting	Dimensions [L x W x H] (inches)	Estimated Weight (lbs., each)
Figure 2	53.0 x 38.9 x 27.6	159
Figure 3	50.0 x 38.9 x 31.8	177
Figure 4	50.0 x 39.0 x 21.7	212
Figure 5	50.0 x 38.9 x 27.6	205

1.15 for yield strength and 1.50 for ultimate strength, using material property data from company and subcontractor databases.

Each casting was segregated into zones, each of which would be analyzed and sized separately. Then, P3/PATRAN, a commercially available finite element pre- and post-processor, was used to conduct min/max searches on principal stresses and Von Mises stresses in each zone. The results of the min/max searches were summarized at the faying surfaces of the panel in each zone. Analysis checks were conducted for every critical load condition identified in a zone as a result of the max/min searches. Once a critical load condition was identified, analysts used P3/PATRAN to extract running loads from the finite element model to size that zone.

In addition to gross strength checks, each duct zone or bay was also checked for overall panel stability. A proprietary code called ALADAN was used for this task. Inputs to the code include the panel geometry, material, curvature, running loads from the finite element model, and panel stiffener geometry and location.

1.4 Detail Design. Frame and keel webs were sized for no buckling at 150% design limit load. Typical frame and keel thickness is 0.12 inch. Although the use of tapered thickness webs was investigated, constant thickness webs were used to reduce analysis effort and improve producibility of the prototype castings. The webs receive additional support from 0.60 inch high integral stiffeners. The keel and frame interfaces form a series of bays, 12 to 15 inches per side. Splice straps mechanically join splice interfaces between castings. The use of welding for joining was investigated, but technical risk and tooling costs were too high for this prototype.

After an analysis of the thermal and strength requirements, cost impact, and casting design features, Ti-6Al-4V was selected for these castings. HIP would provide complete healing of porosity and shrinkage as the pores are collapsed during the heat and pressure cycle, creating a homogeneous product. After reviewing the test data, a standard mill anneal was selected for final heat treatment.

Through concurrent engineering, potential problems were identified early. For example, to aid the casting process, access holes were required in the casting. Access holes were used to observe proper investing coverage, and to provide support of thin, unsupported cast walls. Many of these holes could be located in panels where the final part required or could accept access holes, eliminating the need to weld patches prior to final part acceptance. Also, by identifying those areas which were to be subsequently machined and those regions with tight ''as-cast'' tolerances, a gate reference cleanup requirement acceptable to both parties was negotiated.

The selection of corner radii was a tradeoff between structural requirements, producibility, and weight impact concerns. Some titanium alloys require larger corner radii to prevent fillet erosion. Although the selection of Ti-6Al-4V meant that a smaller radius could be selected, a typical 0.25 inch corner and fillet radii was selected with some areas receiving smaller radii to meet specific design requirements. While this results in an increase in fillet radius compared to the 0.12 inch that can be achieved by machining, it is an improvement from the 0.5 inch or greater radius required for machined corner radii. The deep pockets on these designs would require very large diameter cutters for stability, so the overall, a weight reduction is calculated from using the cast radii.

1.5 Positional Tolerances. The SLA process was used to create the prototype pattern. The casting engineers used the provided Unigraphics solid model to create the SLA models. This required the application of a casting factor, addition of chemical milling stock, cast radii, and dividing each casting into SLA subassemblies, that would be joined together prior to gating and investing. The use of solid models also provided the opportunity to add padups and improve the model surface coarseness. One drawback of this process is that the dimensional tolerance of the finished casting is not as accurate as a casting fabricated from a standard tool produced wax pattern. The following positional tolerances were defined for this program:

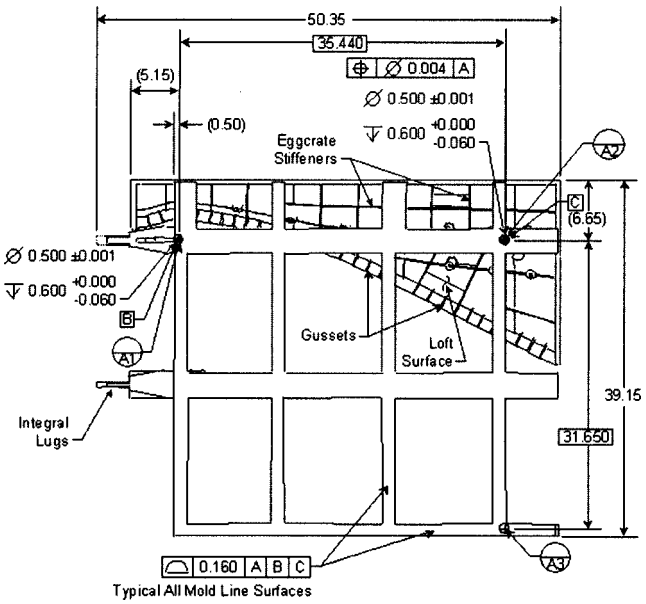

Fig. 1 Casting datum system

- profile tolerance: $+/-0.080$ inch (noncritical),
- web and Frame positional tolerance: $+/-0.040$ inch,
- casting thickness tolerance: $+/-0.020$ inch,
- hole diameter tolerance: $+/-0.015$ inch, and
- hole positional tolerance: $+/-0.040$ inch.

Although 95% of the casting surface was used as-cast, key interfaces did require machining. To accommodate these tolerances, extra machining stock was added to the casting at critical surfaces. The periphery of the casting had 0.250 inch excess stock added, with 0.060 inch added to the interior face of the periphery. Early in the development phase, it became apparent that the region on the frame and keel ends where the splice plates were fastened required additional 0.080 inch machine stock to allow for finish machining. After completion of the first castings, it was determined that the casting shrinkage factor selected was too large. However, this increase in casting size was accommodated by the extra machining pad-up around the periphery of the casting, and a decision was reached to maintain the same casting factor for all castings. This would ensure that the keel and frame interfaces would be consistent. Tight dimensional control of the machined castings is required to meet the modular assembly techniques. Total hole positional tolerances of 0.010 inch and total perimeter and profile tolerances of 0.010 inch on the machined surfaces were specified and are being achieved.

The pattern was conservatively gated to improve mold survivability and to achieve best casting quality. An initial concern was the handling of these non-symmetric castings during investing. The investing robot can handle molds of 4000 pounds. Mold weight after investing, at no time exceeded 2800 pounds, and careful manipulation of the mold is required to prevent excessive collection of slurry during investment.

Typically castings utilize discrete attachment points for assembly. Since these castings are used as the primary structural elements for the system, essentially the entire perimeter of the casting would be a mating surface. A consistent datum management system, as seen in Fig. 1, was established that would be traceable throughout the fabrication and assembly process. First, a pretarget fit of the casting was performed on the Coordinate Measure-

Fig. 2 View of as-cast moldline

ment Machine (CMM). An IGES file of this information was electronically transferred for review and input on any adjustments required to achieve the proper coverage. The casting's datum surfaces were then machined, and a post-targeting inspection was performed and reviewed for final inspection. Next, the machining vendor locates the casting using these same datum features, and probes the casting at critical locations to ensure that it was correctly located on the machine tool. This data is compared to the information collected on the CMM. Finally, the assembly process uses these same datum surfaces to ensure that the machined casting is accurately located in the assembly tool. Views of typical castings are shown in Figs. 2, 3, 4, and 5.

Fig. 3 View of 1515 casting

Fig. 4 View of as-cast moldline

1.6 NDT Requirements. One potential source of difficulty is the radiographic inspection of these nonsymmetric, deep wall castings. A particular concern is that the radiographic technique development time cannot be amortized over a production run of at least several castings. Although inspection is still a significant cycle time driver, several things were done to try to minimize the

Fig. 5 View of integral lugs

impact of radiographic inspection. A supplier quality representative was stationed at the casting source during the development of the first inspection techniques, to provide real-time X-ray technique approval. This eliminated the data submittal and response delays typical of many development programs. During this review, it became apparent that modifications to standard machined part radiographic techniques would result in significant cycle time reductions, without impacting part quality. The castings were zoned for critical sections, with the majority of the casting requiring standard aircraft quality standards. Again, it must be noted that the majority of the casting consists of nominal 0.120 inch thick walls, which minimized NDT detectability issues.

1.7 Summary. Several lessons learned have been incorporated in this program. First of all, the cast surface condition has been improved. This was accomplished through the development of an improved proprietary SLA surface treatment, and by optimizing rework procedures for these large castings. Secondly, dimensional control needs to be monitored. Six dimensional tollgates were instituted in the process: SLA pre-assembly, pre-third chem-mill, post-chem-mill, heat treat setup, final dimensional inspection, and CMM. Finally, as previously noted, radiographic inspection had the following improvements: minimum indication size agreement, use of generic technique/single wall shots, and elimination of surface blemishes prior to radiographic inspection.

This prototype activity has demonstrated that large complex aft fuselage structures, evolving high temperature materials, can be efficiently produced using large titanium castings and a modular assembly approach. Weight and cost objectives were achieved, and existing analysis codes or processes were sufficient to support this prototype activity.

Integrated Vehicle Comparison of Turbo-Ramjet Engine and Pulsed Detonation Engine

T. Kaemming
The Boeing Company,
Mail Code S064-1042,
St. Louis, MO 63166

The pulsed detonation engine (PDE) is a unique propulsion system that uses the pressure rise associated with detonations to efficiently provide thrust. A study was conducted under the direction of the NASA Langley Research Center to identify the flight applications that provide the greatest potential benefits when incorporating a PDE propulsion system. The study was conducted in three phases. The first two phases progressively screened a large matrix of possible applications down to three applications for a more in-depth, advanced design analysis. The three applications best suited to the PDE were (1) a supersonic tactical aircraft, (2) a supersonic strike missile, and (3) a hypersonic single-stage-to-orbit (SSTO) vehicle. The supersonic tactical aircraft is the focus of this paper. The supersonic, tactical aircraft is envisioned as a Mach 3.5 high-altitude reconnaissance aircraft with possible strike capability. The high speed was selected based on the perceived high-speed fuel efficiency benefits of the PDE. Relative to a turbo-ramjet powered vehicle, the study identified an 11% to 21% takeoff gross weight (TOGW) benefit to the PDE on the baseline 700 n.mi. radius mission depending on the assumptions used for PDE performance and mission requirements. The TOGW benefits predicted were a result of the PDE lower cruise specific fuel consumption (SFC) and lower vehicle supersonic drag. The lower vehicle drag resulted from better aft vehicle shaping, which was a result of better distribution of the PDE cross-sectional area. The reduction in TOGW and fuel usage produced an estimated 4% reduction in life cycle cost for the PDE vehicle. The study also showed that the simplicity of the PDE enables concurrent engineering development of the vehicle and engine. [DOI: 10.1115/1.1p-496116]

Introduction

The pulsed detonation engine (PDE) is a cyclic propulsive device that uses the pressure rise associated with detonations to develop thrust. There are several ways to integrate detonative combustion into propulsive devices (Fig. 1). The basic PDE is an air-breathing engine that relies on inlet ram to provide inlet flow. The pulsed detonation rocket engine (PDRE) uses pressure-fed propellants similar to a conventional rocket. However, the PDRE is cyclic and takes advantage of the detonation pressure rise. There are also two possible combinations of the PDE and PDRE. The combined cycle engine integrates the PDRE hardware within the physical limits of a PDE, ramjet or scramjet. A possible implementation of the combined cycle engine is a PDRE-powered ejector ramjet. In the combined cycle engine, the PDE and PDRE can operate at the same time. In the dual mode engine, the PDE and PDRE share the same hardware. Therefore, they cannot operate at the same time. In addition, the dual mode engine must incorporate sufficient configuration flexibility to satisfy the requirements of both engine cycles. The last engine considered was a hybrid combination of the PDE and the turbine-based engine. In the concept shown in Fig. 1, a pulsed detonation combustor replaces a portion of the high-pressure segment of a conventional turbofan. Another possible implementation of the hybrid, though not studied here, is using a pulsed detonation augmentor in the bypass flow of the turbofan.

The first phase of the PDE application study considered using these five engine concepts in a wide variety of air vehicles, including commercial aircraft, micro-aircraft, and rotorcraft. A screening, based principally on engine form, fit and function, reduced this large matrix down to nine engine/aircraft combinations for a first-level evaluation. These configurations were further reduced to a supersonic tactical aircraft, a strike missile and a hypersonic single-stage-to-orbit vehicle. Utilizing a supersonic tactical aircraft application, this paper focuses on the comparison of a conventional turbo-ramjet engine against the PDE.

The PDE performance data used in the study was generated using the Boeing detonation engine cycle analysis and design evaluation (DECADE) cycle code. To date, only limited PDE performance data are available for code validation. Therefore, the PDE performance prediction technology status is markedly less mature than the turbo-ramjet performance prediction technology status.

The engineering study presented in this paper was funded under NASA Task Order #5 NAS1-98103 contract. The author would like to acknowledge the technical assistance of Dr. J. R. Elliott, NASA Langley Research Center, and the support of Mr. Joseph Doychak, NASA Glenn Research Center, in the performance of this study.

Tactical Aircraft Description

The notional tactical aircraft used in this study was designed to provide rapid response, on-demand reconnaissance. Similar to the SR-71, the aircraft would fly at high speed at high altitude. For this study, a cruise of Mach 3.5 at 80,000 feet was selected. The basic sizing mission (Fig. 2) required a mission radius of 700 n. mi. The sizing mission also included a reduced speed dash to simulate weapon delivery for the alternate strike capability of the vehicle.

A vehicle was configured for both a conventional turbo-ramjet engine and a normal pulsed detonation engine (PDE) propulsion system. These vehicles are at a conceptual design status with first level weights, structural layout, aerodynamics, stability, and control and installed propulsion system performance estimates. An

Contributed by the International Gas Turbine Institute (IGTI) of THE AMERICAN SOCIETY OF MECHANICAL ENGINEERS for publication in the ASME JOURNAL OF ENGINEERING FOR GAS TURBINES AND POWER. Paper presented at the International Gas Turbine and Aeroengine Congress and Exhibition, New Orleans, LA, June 4–7, 2001; Paper 2001-GT-451. Manuscript received by IGTI, Dec. 2000, final revision, Mar. 2001. Associate Editor: R. Natole.

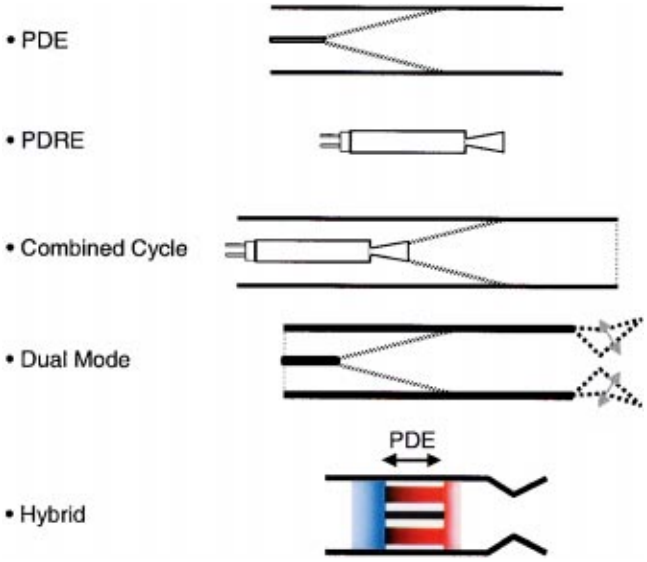

Fig. 1 Pulse detonation technology engine architectures

''as-drawn'' vehicle was synthesized with data packages developed for each major discipline. Using the ''as-drawn'' vehicle as the benchmark, the vehicle was then resized analytically to meet the desired sizing mission performance.

The ''as-drawn'' turbo-ramjet aircraft is 90 feet long with a span of 43.3 feet. Two large turbo-ramjet engines were used. The engine technology status is roughly equivalent to the technology status of the today's advanced production engines. The vehicle assumes a two-person crew seated in tandem to minimize cockpit frontal area. Bay volume is allocated for either reconnaissance equipment or weapons.

The ''as-drawn'' PDE aircraft is 95 feet long with a span of 45.9 feet. Fourteen PDEs were used. Multiple PDEs are required to provide a quasi-steady thrust and inlet airflow. The PDE aircraft was developed using the same design groundrules as the turbo-ramjet aircraft. The most obvious difference between the two aircraft is the engine integration. Boeing's analysis indicates that the thrust density, or thrust-per-unit cross-sectional area, is slightly greater for the turbo-ramjet than the PDE. Thrust density determines the cross-sectional area that must be allocated for the engines. The lower thrust density of the PDE is caused by two factors. First, the cyclic nature of the PDE means that the PDE only develops thrust during a portion of its cycle while a turbine engine develops thrust continuously. Second, the engine pressure ratio of

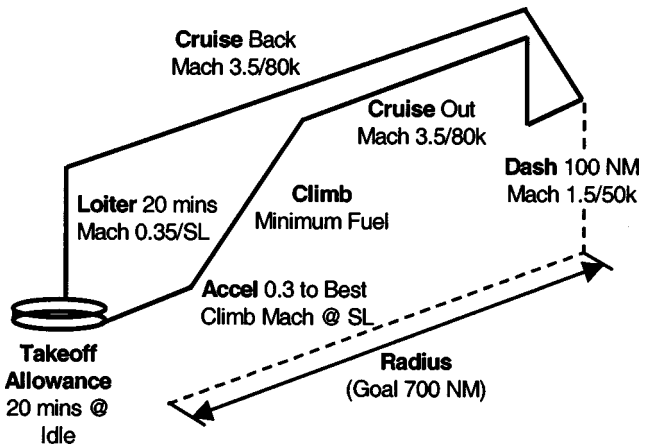

Fig. 2 Tactical aircraft baseline mission

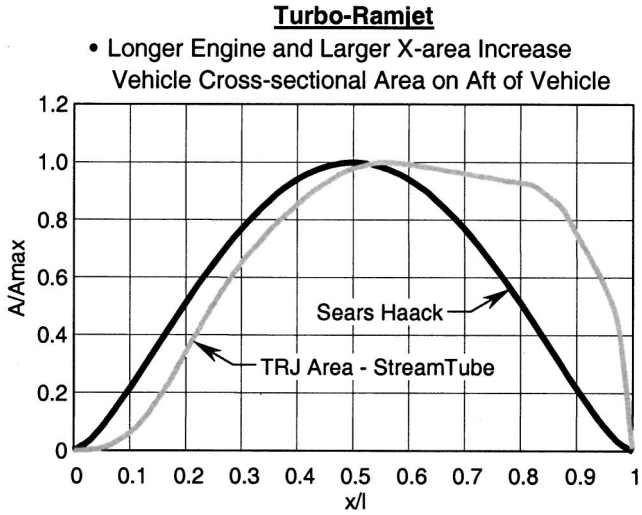

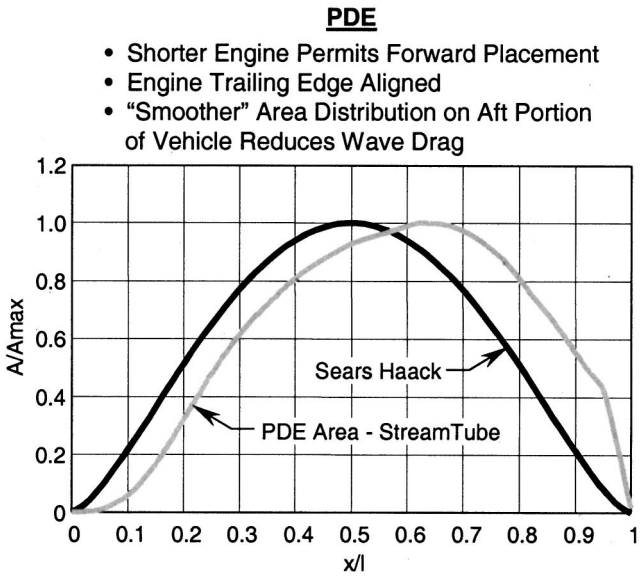

Fig. 3 Comparison of aircraft area distribution

the PDE is the product of the inlet system recovery and the detonation pressure. Therefore, the PDE engine pressure ratio is set primarily by flight conditions. On the other hand, the turbine engine can be designed to have a wide range of engine pressure ratios by changing compressor and turbine designs. The higher engine pressures enable the turbine engine to have significantly higher thrust density than the PDE. The result is that the PDE vehicle must accommodate a larger engine cross-sectional area.

While the maximum cross-sectional area of the PDE-powered vehicle is larger, the integration flexibility of the PDE allows the designer to tailor the overall vehicle area distribution to minimize supersonic drag. During the first design cycle of tactical aircraft for this study, the PDEs were integrated in a cluster near the vehicle centerline, similar to the turbine engine integration. Using similar integrations for both engine types resulted in a poor area distribution for the PDE vehicle. Later in the study, a configuration was developed where the PDEs were laterally integrated along the vehicle trailing edge. Since the trailing edge is swept, the result was a more uniform axial distribution of the PDE. This, in turn, resulted in a more even distribution of the PDE cross-sectional area. The net result was a better area distribution for the PDE vehicle, and therefore, lower supersonic drag (Fig. 3).

It is important to note that this area distribution benefit is only

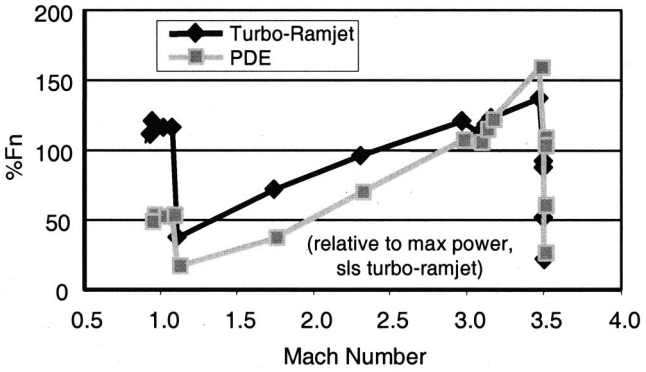

Fig. 4 Engine thrust comparison along baseline mission

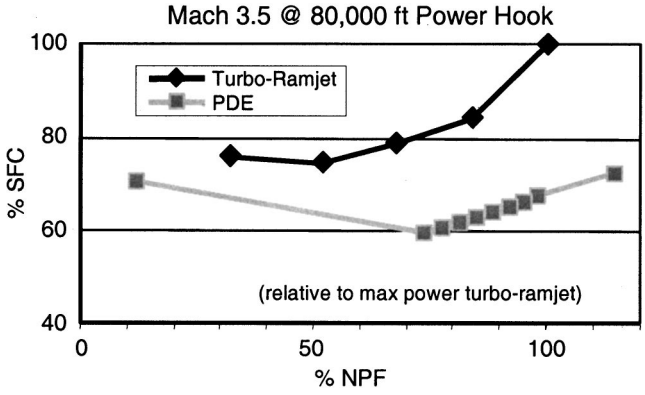

Fig. 5 Engine specific fuel consumption comparison along baseline mission

realized if the vehicle can accommodate an axial distribution of engines. Without this feature, the PDE vehicle would exhibit a markedly higher supersonic drag.

Engine Performance Comparison

Engine performance was estimated for both the turbine engine and the PDE with consistent methods and groundrules. Standard inlet recovery, MIL-E-5007D, was assumed. The PDE must meter the airflow into the engine with an air induction valve. Therefore, the PDE performance includes additional pressure loss for the air valve. Inlet drags were computed using Boeing advanced design methods. The maximum, practical engine nozzle exhaust area was used for both engines. This provided the best overall vehicle performance since most of the mission fuel is spent at high speeds. At high speeds, the engines require very large expansion ratios for efficient nozzle performance. A stream thrust coefficient of 98% was assumed for both engines. The nozzle performance for the PDE was integrated over the entire engine cycle. Thus, the PDE nozzle swept through a wide range of nozzle pressure ratios during each pulse.

The turbo-ramjet engine used here was an available advanced design engine typical of IHPTET (integrated high performance turbine engine technology) Generation 6 performance. The engine operated as a low bypass turbofan from static conditions up to Mach 3. At Mach 3.25 and above, engine operation converted over to the ramjet mode.

The PDE performance was predicted using Boeing's PDE performance code. The PDE performance code is named DECADE, for detonated engine cycle analysis and design evaluation. This code has been validated with a wide range of existing test data, including a wide range of fuels and operating conditions. The code is a classic thermodynamic cycle code, which assures conservation of properties at all conditions.

A comparison of the engine performance is provided in Figs. 4 and 5. Engine thrust, Fig. 4 is total installed vehicle thrust over the sizing mission. For this paper, the thrust has been normalized by the turbo-ramjet sea level static installed thrust. The most important feature in total vehicle thrust is the dramatic difference in thrust lapse characteristics between the two types of engines. The turbo-ramjet engine possesses a much higher thrust at low speeds. This results from the turbofan engine's ability to develop high engine pressure ratios at low speeds. The PDE, on the other hand, has very low thrust at low speeds. This is due to the PDE's dependence on inlet ram to establish engine pressure ratio. At higher speeds, the PDE thrust increases due to increased ram pressure. The PDE thrust increases with speed at a faster rate than the turbo-ramjet. This is clearly illustrated in Fig. 4 where the PDE thrust increased more then 200% between Mach 1 and Mach 3.5. In contrast, the turbo-ramjet engine thrust increased less than 20% over the same Mach range.

The net result of the marked difference in engine thrust lapse is that the turbo-ramjet engine sizes at high speed while the PDE sizes at low speeds. The turbo-ramjet vehicle has trouble getting to the higher Mach numbers, while the PDE vehicle requires a long runway for takeoff. Viable vehicle performance is available from both engines, although their flight performance is dramatically different due to the thrust lapse difference.

The supersonic cruise performance comparison of specific fuel consumption (SFC) versus the net propulsion force (NPF) is provided in Fig. 5. For this comparison, the thrust and specific fuel consumption (SFC) have been normalized to the turbo-ramjet maximum thrust point. Here, the high-speed benefits of the PDE are shown. The PDE has a lower SFC than the turbo-ramjet. At this condition, due to increasing internal air temperatures and decreased thermodynamic benefits for mechanical compression, the turbo-ramjet engine has converted to ramjet operation. Several earlier studies, Refs. [1,2], have shown that the detonative cycle is more efficient at a given cycle pressure than the Brayton cycle, represented here by the ramjet. The detonative cycle efficiency improvement results from lower entropy generated by the combustion process and higher combustion pressure due to the detonation.

The vehicle sizing results that follow dramatically illustrate the high-speed fuel efficiency and the low-speed thrust deficit of the PDE.

Vehicle Performance

Representative data packages for both vehicles were assembled for each major discipline. These included advanced design component weight estimates, trimmed aerodynamic characteristics and the propulsion system performance described above. Vehicle stability and control characteristics were also evaluated. Sufficient control effectiveness and appropriate stability margins were designed into each vehicle.

Using the assembled data packages, Boeing analytical codes were used to size the vehicle for the baseline design mission (Fig. 2). The resultant vehicle take off gross weights (TOGWs) are compared in Fig. 6. The weights have been normalized to the TOGW for the turbo-ramjet vehicle. On this baseline mission, the PDE exhibited an 11% lower TOGW. The weight benefits were approximately equal between the empty weight of the vehicle and the fuel weight required to meet the design mission requirements. These weight benefits were primarily due to the better cruise SFC for the PDE.

As illustrated in Fig. 6, the empty vehicle weight saving is a first-order effector or of vehicle acquisition cost. Similarly, the fuel consumed per flight hour (Fuel/FH) is the first-order effector of vehicle operational and support cost.

The PDE vehicle possessed a much smaller takeoff thrust-to-weight than the turbo-ramjet. At takeoff, the turbo-ramjet had a

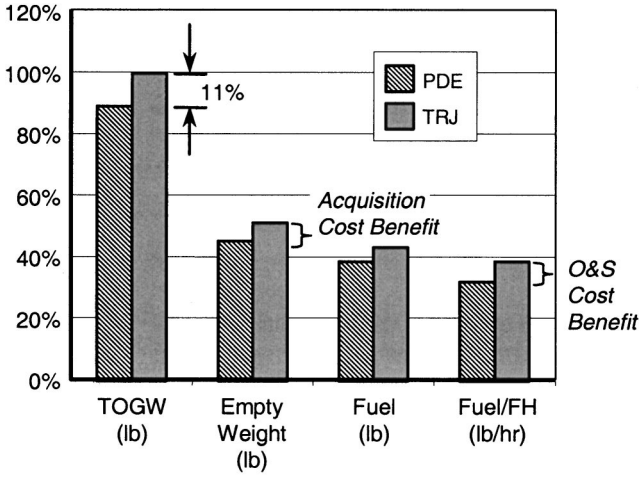

Fig. 6 Tactical aircraft baseline mission sized weights

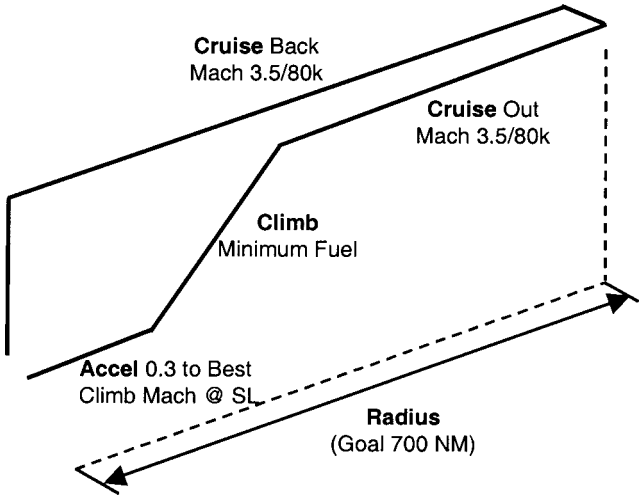

Fig. 7 Alternate mission

thrust-to-weight ratio of 1.12. In sharp contrast, the PDE vehicle had a takeoff thrust-to-weight ratio of only 0.16. For this class of vehicle, a 0.16 thrust-to-weight is unacceptable because the aircraft requires more than 10,000 feet for takeoff. Two options were explored. First, takeoff analyses were conducted which showed that a takeoff thrust-to-weight of 0.24 is required for adequate takeoff performance. When the PDE vehicle was sized with a 0.24 thrust-to-weight, the PDE vehicle lost all of its TOGW advantage as compared to the baseline configuration. The second approach was to off load fuel at takeoff and refuel in flight, similar to the SR-71 concept of operation. With 12,800 lb. of fuel (28% of fuel capacity) to takeoff, climb, and refuel, the PDE retained its TOGW advantage.

Next, a mission study was conducted to explore alternate missions that could achieve the same mission objectives while considering the strengths and weaknesses of the PDE. The intent was to break out of the paradigm of designing the PDE vehicle to mission guidelines and allowances developed for turbine powered vehicles. Compared to the turbo-ramjet, the PDE vehicle consumed more than twice as much fuel in the 20-minute takeoff and landing allowances in the baseline mission. This is largely due to a lack of knowledge in defining PDE idle performance. When coupled with the other low-speed portions of the mission, the PDE was paying a large penalty.

The alternate mission study focused on minimizing any penalties associated with the lack of technical maturity of the PDE and emphasizing the strengths of the PDE. The resulting alternate emission (Fig. 7) was achieved by removing the landing allowances and the dash segment of the baseline mission. This mission is more representative of a dedicated reconnaissance mission.

The ''as-drawn'' vehicles were then sized for the alternate mission. The resulting vehicle weights are presented in Fig. 8. The TOGW benefit for the PDE vehicle has now increased to 21% when the vehicle off loads fuel for takeoff. When the PDE vehicle is sized for takeoff with full fuel load, the TOGW benefit is marginally reduced to 18%.

The alternate mission clearly illustrates the high-speed system level benefits of the PDE.

Vehicle Cost

Estimates of vehicle life cycle costs were made using Boeing advanced design estimating tools. These estimating tools are based heavily on historical vehicle cost trends. The cost study assumed an aircraft production quantity of 100, 300 flight hours per aircraft per year flight rate and 25 years of operation. Only acquisition cost and operating and support, O & S, costs were estimated. Historical vehicle cost data indicate that the research development and test and evaluation, RDT&E, costs are less than 3% of vehicle life cycle costs.

The costs presented here were derived for the baseline mission. Additional cost savings would be realized if the alternate mission was evaluated likewise.

The total estimated aircraft acquisition costs are presented in Fig. 9, along with a breakdown of the cost into major cost contributors. The PDE vehicle is estimated to provide nearly 5% acquisition cost savings. This cost savings comes almost entirely from the savings of the air vehicle costs.

A breakdown of the air vehicle costs into major subsystems is provided in Fig. 10. The air vehicle cost savings exhibited by the PDE vehicle are a direct result of the smaller vehicle weight and the low cost of the PDE. The cost savings are approximately equal between the airframe cost and the propulsion system cost. The cost estimates for this study predict a higher subsystem cost for the PDE than for the turbo-ramjet. This consideration is due to the larger number of engines, the increased auxiliary power unit, APU, size and the need for on-board oxygen generation for the PDE. The larger number of engines adds fuel system complexity. The larger APU is incorporated because no secondary power generation concept has been developed for the PDE thus far. The APU then must provide all vehicle secondary power.

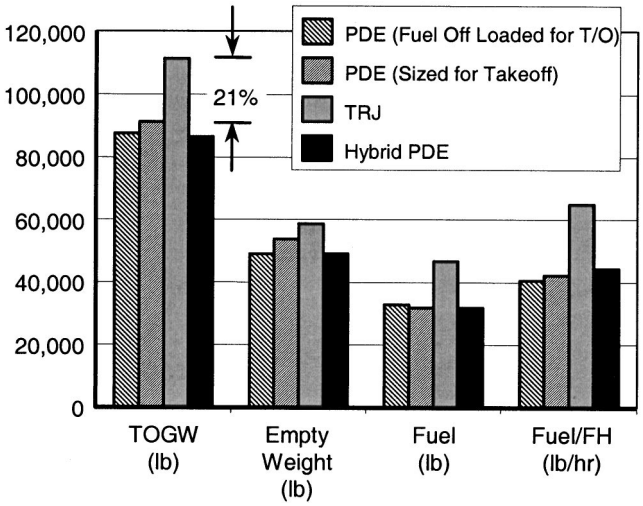

Fig. 8 Sized aircraft weights for alternate mission

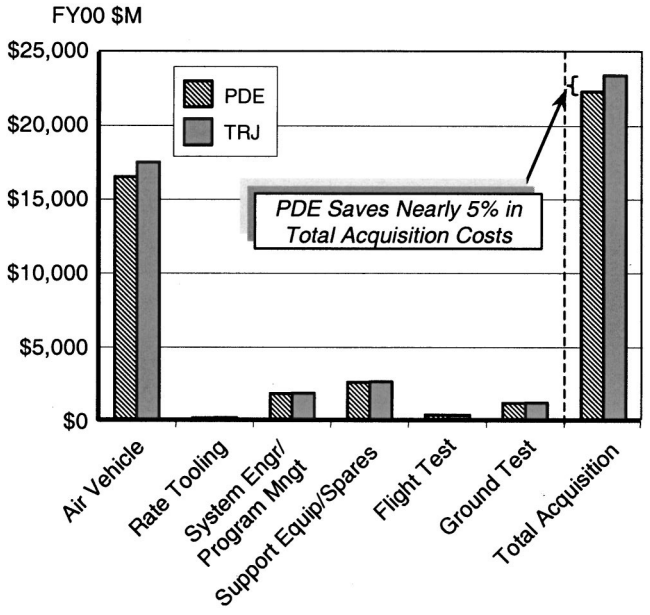

Fig. 9 Total aircraft acquisition cost (baseline mission)

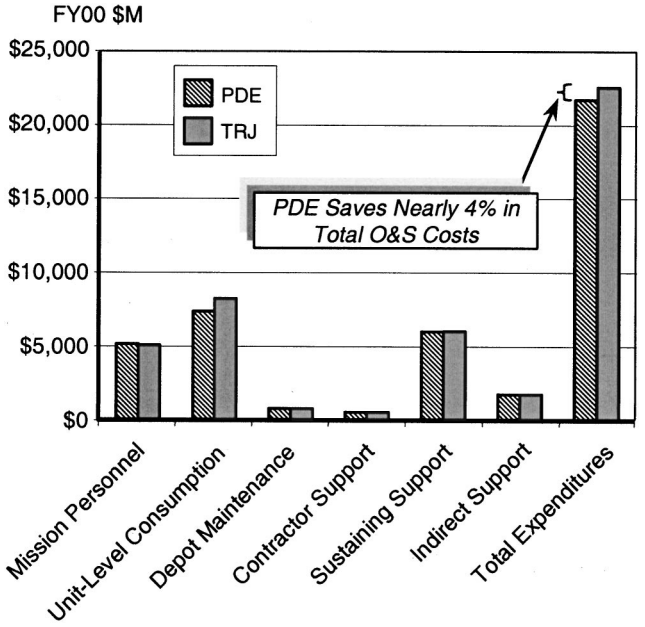

Fig. 11 Relative total operating and support costs (baseline mission)

The on-board oxygen generation systems is required to provide the small amounts of oxygen required by the PDE to initiate the detonations.

The operating and support, O&S, cost estimates (Fig. 11) further illustrate cost savings available with the PDE. The major contributor to the O&S cost savings is in unit-level consumption, which is directly attributable to reduced fuel usage. While a maintenance cost savings has been postulated for the PDE due to its smaller size and its simplicity, no maintenance cost savings were included in this cost study.

An estimate of vehicle life cycle costs was obtained by adding the acquisition and the O&S cost estimates (Fig. 12). The PDE is estimated to provide more than a 4% life cycle cost savings. These life cycle cost benefits were computed for the baseline design mission, where the PDE showed an 11% reduction in TOGW. A larger cost savings would be possible if the alternate mission was utilized for the cost evaluation, where the PDE showed a 21% TOGW reduction.

Development Roadmaps

Development roadmaps for the PDE and the tactical aircraft were developed to aid in research and development planning and investment strategies. For the tactical aircraft, a four-year demonstration and validation phase and a seven-year engineering and manufacturing development phase are envisioned. While the technology base for the tactical aircraft development is judged to be near-term, the technology readiness level of the PDE requires sev-

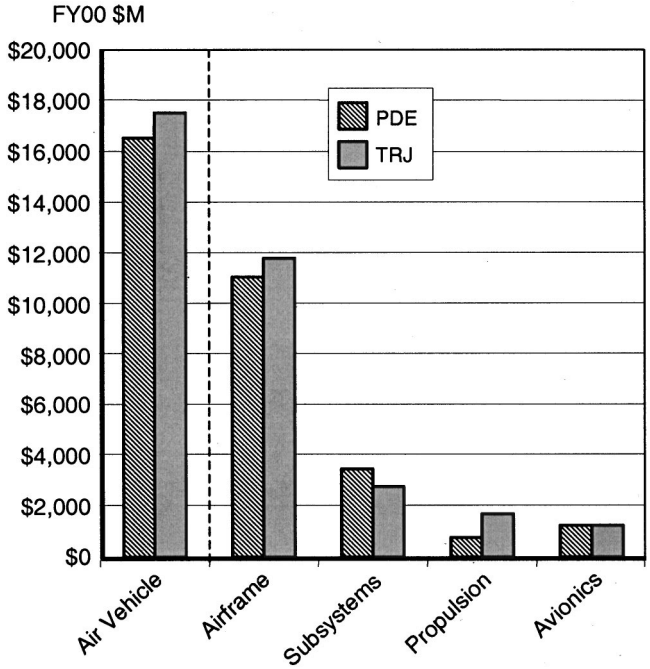

Fig. 10 Relative air vehicle acquisition costs (baseline mission)

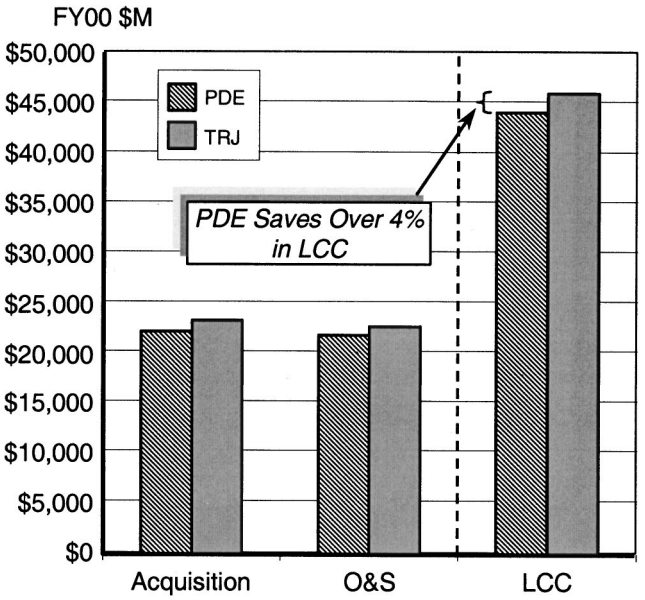

Fig. 12 Relative aircraft life cycle costs

eral years of investment to prepare for integration into an aircraft. Our study estimates that four years of concept exploration and development are necessary to prepare the PDE.

Assuming that the four years of development are accomplished, the simplicity and scalability of the PDE permits an aggressive demonstration and validation of only three years and an engineering and manufacturing development of only three years. When compared with the four and seven-year periods of the aircraft, the PDE appears to enable concurrent engineering of the engine with the air vehicle.

Concurrent engine and aircraft development offers a new paradigm in aircraft acquisition. Cycle time from concept to reality will be dramatically reduced, as would development costs. Small production runs of specialty aircraft would be more affordable. All of this is a direct result of the simplicity of the PDE design and manufacturing. Of course, the benefits are contingent on the PDE technology readiness level being sufficiently advanced to support the aggressive development schedule.

Conclusions

The PDE can show vehicle level performance advantages over conventional turbine based engines. However, performance advantages are only realized when the vehicle is designed to capitalize on the strengths of the PDE with accommodation for its weaknesses. The PDE strengths are in high supersonic fuel efficiency and immense integration flexibility afforded by its low volume and wide range of possible shapes. The PDE can efficiently cruise at high supersonic speeds and can be designed to fit within spaces and shapes impractical for a turbine-based engine. The PDE major weakness is low-speed performance including thrust, fuel consumption, and thrust density. The vehicle must be designed to accommodate modest low speed acceleration and climb capability. These conclusions are based on current PDE performance prediction capabilities and PDE low-speed performance assumptions, both of which require validation.

The cost of purchase and ownership of a PDE can be significantly less than for a turbine engine. This study showed projected life cycle cost savings of approximately 4% for the PDE vehicle compared to the cost of the turbo-ramjet engine vehicle. Additional cost savings are possible if the aircraft were tailored more to the PDE strengths as was demonstrated in the alternate mission study.

The simplicity of the PDE enables a more rapid engine development cycle. Once the PDE technology level matures, it is conceivable that the PDE and the vehicle could be concurrently developed.

It should be noted that the hydrid engine evaluations conducted in this study showed similar overall vehicle benefits as the PDE. Further analyses are necessary to accurately evaluate the system level benefits of the hybrid engine.

References

[1] Wortman, A., Othmer, P., and Rostafinski, W., 1992, ''Detonation Duct Gas Generator Demonstration Program,'' Paper No. AIAA-92-3174.

[2] Bratkovich, T., Aarnio, M., and Bussing, T., 1997, ''An Introduction to Pulse Detonation Rocket Engines (PDRE's),'' Paper No. AIAA-97-2742.

Integrating Subsystems and Engine System Assessments

V. J. Van Griethuysen
AFRL Propulsion Directorate,
AFRL/PRTA Building 18,
1950 Fifth Street
Wright-Patterson AFB, OH 45433

M. R. Glickstein
MRG Technical Services, Inc.,
504 Greenway Drive,
North Palm Beach, FL 33408

E. S. Hodge
Modelogics, Inc.,
4228 Carillon Terrace
Kennesaw, GA 30144

In the past, system and subsystem level assessments for propulsion systems have been a long and drawn out serial process, typically taking several months to a year or more. Data exchange from one subsystem group to the next was a manual process. This was particularly the case when different computer platforms were being utilized to run the models. Each group would optimize their particular subsystem as a separate entity. There were no approaches available to facilitate the evaluation of how a particular subsystem, when combined with the engine, would impact the overall integrated system. The availability of tools to facilitate direct interface of the various subsystem models with engine performance decks was not available. As a result, the lead times for various iterations were such that not all of the groups were even working on the same configuration. Fortunately, software technology has been evolving, and the ability to integrate models is now becoming available. This paper describes work in progress of an innovative methodology for high-level integration of complex flight systems. This new approach will facilitate rapid integration and optimization of propulsion and secondary subsystems in a truly concurrent manner, providing capability for top-level evaluation of complex and highly integrated flight system architectures [DOI: 10.1115/1.1496117]

Background

Engineering, as practiced today in many organizations, is a serial process with a typical product development cycle like the one depicted in Fig. 1. Typically there are long feedback loops, often due to manual data interchange with compartmentalization of the information. With this approach it is easy to see how subsystem groups tend to optimize designs for their ''box'' based on a set of parameters relating strictly to their discipline. They pass this design along and hope the restrictions they've implicitly put on all those subsystems downstream don't cause too much of a problem, i.e., necessity for redesign.

There are several flaws with this process. First, due to the complexity of all the many aspects of the system design, it is impossible for anyone to completely understand everything related to the design. In addition, it takes so long to complete the design process, the product is never fully optimized on a system wide basis. Second, rarely are designers from different disciplines examining and running trade studies on identical versions of the system design, which of course has major implications for quality control. And third, once the design is completed it is impossible to repeat the process to determine the flow of requirements and the reasoning behind all of the original design decisions and constraints.

This classic process results in a product that is not optimized for the overall requirements, but rather for the ''boxes'' within the design process. A suboptimized product design means either the product costs more than it should to produce or the performance or value of the product is low for the cost to produce. Either of these outcomes can mean millions of dollars of lost profit and excess costs to the corporation or government.

The engineering process as described above has been the same for decades. Originally it was done with pencil, paper, and slide rule. Then (as depicted by Fig. 2) in the 1970s people began to apply computational technology to the process, first in the form of calculators to speed up the mathematical calculations, followed by large, centralized computers. These in turn were followed by departmental large-frame computers running proprietary operating systems, and later in the UNIX-based work station environment.

All of these steps were simply automating certain aspects of the process, speeding up the component subprocesses and making incremental decreases in the design cycle time, but left the overall process unchanged. Today the automation approach has taken the form of attempting to automatically transfer data from one computer program to the next. Such efforts have generally failed because the methods and systems that are trying to be linked are difficult to use individually, much less as a group. Also, legacy computer programs were typically designed for manual input and output (I/O), to be stand-alone codes and not necessarily optimized for the most efficient or timely operation. In many instances linking of existing methods offers even less time savings than previous measures.

The reason for such an unexpected result is that, in using this approach of linking legacy programs, engineers spend most of their time trying to understand why the various programs failed to converge to a solution, and spend very little time actually looking at results. Basically, automation of the current engineering process, particularly with legacy codes, has ''hit a wall.'' The problem, simply stated, is that the commercial sector and customers are demanding quicker ''time to market'' for new and more cost effective products. The question is how to get there?

If there is to be revolutionary improvement in engineering approaches, the developmental engineering process must itself be reengineered and in doing so requires bringing together state-of-the-art computing technology and engineering. This is more than simply rewriting mainframe legacy codes or moving analysis codes from UNIX systems to the desktop computer. It means the elimination of the old serial process where functional groups worked their portion of the effort and then passed along the results to the next group. In other words a paradigm shift from the old tried-and-not-so-true approach to a more truly integrated real time and efficient approach or process makes sense.

The new process must be one of concurrent engineering where all the functional groups are working on the same system version in parallel, immediately seeing the results that their design decisions have on the entire system. Traditionally only a few project participants (project leaders, program managers) have been involved in the review of system level results such as cost, reliability, operability, and manufacturability. Now engineers will be involved with this review process. Further, engineers who have

Contributed by the International Gas Turbine Institute (IGTI) of THE AMERICAN SOCIETY OF MECHANICAL ENGINEERS for publication in the ASME JOURNAL OF ENGINEERING FOR GAS TURBINES AND POWER. Paper presented at the International Gas Turbine and Aeroengine Congress and Exhibition, New Orleans, LA, June 4–7, 2001; Paper 2001-GT-452. Manuscript received by IGTI, December 2000, final revision, March 2001. Associate Editor: R. Natole.

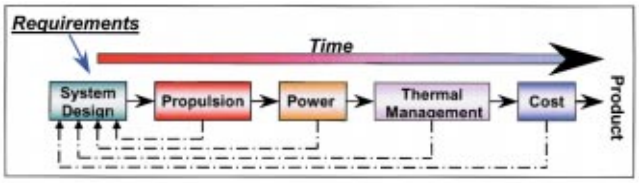

Fig. 1 The serial engineering process

traditionally tried to optimize their discreet part of the problem will now be able to perform global optimizations on the entire system.

The new paradigm for engineering design and development unifies the computing platform by bringing all functions to the desktop in an integrated, easy-to-use environment, one that promotes concurrent engineering and focuses on system optimization instead of subprocess optimization (Fig. 3). A virtual engineering environment that dramatically reduces the time to perform engineering trade studies, while making the engineer's job easier is envisioned for this next generation engineering process. But more importantly, it will allow everyone from the various disciplines working on a project, to be able to focus on their own expertise while simultaneously gaining an immediate ''big picture'' insight of the problem at hand.

The benefits of this new collaborative approach to the design and integration of complex engineering systems have been recognized for several years within industry and the Government, with a variety of methods evolving to take advantage of such benefits. These various approaches have been given several generic names, including collaborative engineering, distributed simulation, and concurrent engineering. All of these attributes, and more, are embodied in initiatives such as the Integrated Product and Process Development (IPPD) approach for doing business ([1]). Rooted from acquisition reforms and the never ending drive to reduce production and life cycle costs due to the diminishing budgets

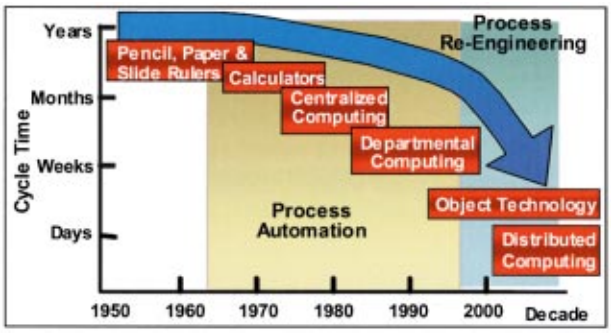

Fig. 2 Technology applied to the engineering process

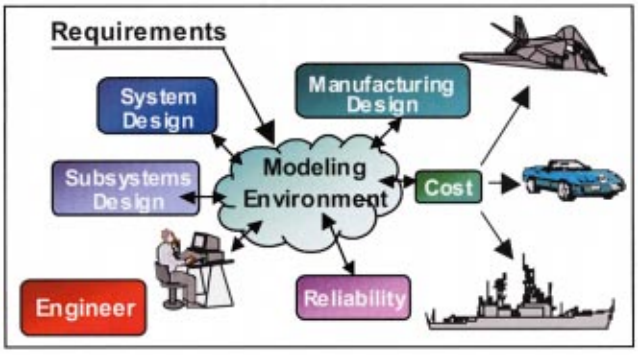

Fig. 3 Concurrent engineering process

within the Research and Development sector, IPPD is gaining momentum. Some of the related tenets, as identified in the DoD Guide to IPPD, include concurrent development of products and processes, maximization of optimization flexibility, multidisciplinary teamwork, and empowerment of decisions to the lowest level possible. Integration tools, such as described in this paper, offer an approach for achieving the goals of the IPPD initiative.

A New Approach

The difficulty of large-scale integration of highly interactive systems, as witnessed during several advanced programs in recent years, has led to a desire to develop a methodology for this purpose. The major stumbling block to simulation of large-scale integrated systems is the difficulty of sharing and passing data between proprietary software models, without a common standard for data structure. Therefore, any approach to software integration must begin with the selection of a data architecture standard for passing information between the software models simulating the components of the physical system.

The direction of this paper now turns to describing the concepts underlying a new approach, aimed at solving the data handling problem, while providing a foundation and methodology for implementating concurrent engineering designs of complex integrated systems. Although initially directed toward developing ''object-based'' simulation tools applicable to the design and evaluation of integrated thermal management systems, the approach is much more broadly applied to the component integration of any system incorporating physical or abstract processes (such as fluid flow, thermal flow, chemical reactions, electrical devices, and data streams). This endeavor is being performed under the support of a Department of Defense Research and Engineering/Air Force sponsored Dual Use Science and Technology (DUS&T) ([2]) program originally titled Thermal Systems Analysis Tools (TSAT).

Rather than inventing new data standards for this work, the well-defined existing protocols of the Microsoft Windows operating system were selected as the basis for data handling. Implicit in this choice is the decision that the simulation methodology would be developed for application on computers operating with MS Windows. However, that choice does not preclude the implementation of the same approach on a UNIX or any other platform. The MS Windows family of operating systems provides the capability to share and pass data among different software applications, either operating on the same computer or remotely across a network. This protocol, called the ''Component Object Model'' (COM) ([3]), defines standards for interoperability within the Windows system. Similarly a broader multiplatform standard protocol, often seen on UNIX systems, is the Common Object Request Broker Architecture (CORBA) ([4]). These two protocols serve as a bridge, allowing communication between the Windows and UNIX environs for example. Therefore, development of simulation methods with one of these protocols does not preclude communication with simulations based on the other protocol. The primary requirement for communication is that some standard be chosen for development.

In the Windows environment, methods are provided for data exchange among applications, as long as certain programming protocols are observed. For example, a PowerPoint slide presentation may use data graphs prepared in an Excel spreadsheet, and subsequent modification of the data in the spreadsheet will be reflected by a change in the PowerPoint slide. Development of these powerful capabilities has been driven by the wide acceptance of the Windows platform as an office productivity tool. To capitalize on this capability, software operating in the Windows environment must adhere to certain programming rules. First, programs and their subelements are written as ''objects,'' adhering to the rules for object oriented programming. In addition, these objects are structured in a way to comply with a Microsoft protocol called ActiveX ([5]). A program so structured is called ActiveX

compliant, and is compatible with and capable of interoperating with other ActiveX programs. Such programs now comprise a large number of applications that run in the Windows environment, including desktop productivity tools and Internet browsers. Taking note of the broad capability for interoperability among business applications, it is logical to conclude that these capabilities could be expanded and applied to engineering applications.

Object Modeling of Integrated Systems. In compliance with the programming rules previously mentioned, modeling of an integrated system proceeds one component at a time, with each software component representing a physical device, such as a heat exchanger, pump, turbine, or other device in the system. Each type of physical component to be included in a system integration must be available as a software component. Furthermore, each of these software components must be built as an ActiveX compliant object, with appropriate definition of required data handling. If these requirements are satisfied, a complex system can be rapidly modeled by selecting the necessary component objects from a prebuilt library, and connecting them together in accordance with the desired system architecture. This of course implies that a means is available to connect components, or more exactly, to pass data in the correct sequence, and format, from each component to the next. Therefore, connectivity or data passing is the next required capability. In addition, several other features must be provided to allow operation of a simulation, once a system is configured. Controllers must be provided to satisfy desired balances between components, and to achieve convergence in the system analysis. Also, a top-level control mechanism must be available to define the calculation sequence of the system component models, and to specify the operating conditions or constraints of the integrated system.

Each type of physical component is modeled as an object, where a particular object may be used one or more times in a system. For instance, a cooling system may utilize several heat exchangers of a similar type, each having a different detailed geometry. A heat exchanger ''object'' is described with its operational details (effectiveness, size, single or multiple pass, flat plate or shell and tube) considered as properties. The object may then be used several times, with the specific properties defined for each usage. A library, consisting of objects, may be built defining many physical components, with the specific details of each object defined whenever the object is used. This is analogous to a mechanic reaching into his toolbox for a crescent wrench, and setting the spacing of the jaws before placing it on a specific nut.

As described, a component object is a computer simulation of a physical object, representing the physical behavior or performance of the modeled object. In addition to physical performance, there are other characteristics that may be included and determined in the component object. Design and optimization of integrated systems may be based on system performance alone, or included within a broader range of optimization metrics, such as system weight, procurement or operational cost, maintenance, or other factors. If models are defined for these different metrics, they are incorporated in the relevant component objects, and the integrated system optimized at a higher level. In addition to components (objects simulating physical devices), connectors (data-passing objects), and controllers (balancing/convergence objects), there is another class of objects that are very important for convenience in building simulations. These are ''utilities'' which provide necessary functions, but do not represent a specific physical device. Examples of useful utilities are fluid or solid material property objects, which provide mechanical or thermodynamic properties at defined environmental state conditions. Since this information may be needed by a wide range of component objects, it is more convenient to build separate utilities that are accessible to all components, than to incorporate such information within each component object. Another class of utilities are processes, such as gas dynamic behavior, that may be required in the definition of specific components. Still another class of utilities provide data management functions, such as logging errors, exhibiting data results in a graphic user interface, and providing links to desktop applications (such as Excel data plotting tools for plotting calculation results).

After a software object is programmed, it can be compiled into executable form, and used in several ways. For example, objects written to be ActiveX compliant are compiled into ''ActiveX Controls,'' which are repesented as icons in a graphical user interface. These component objects are then used in a ''drag and drop'' mode to rapidly configure complex system simulations. Once objects are compiled into ActiveX Controls, they may be executed in any ActiveX compliant environment. Such environments, called ''containers'' for convenience, act as graphical workspaces for building object-based simulations. Among the applications that are used as containers are the Microsoft Office desktop applications, the Internet Explorer browser, and any of the Microsoft Visual Studio programming environments.

An Application—A System Simulation. A library of thermal system components, including the necessary supporting utilities and control objects, has been assembled, in accordance with the described methodolgy. This set of simulation tools and methods, which are being developed under the previously mentioned TSAT program, have been tested and demonstrated in several preliminary simulations of integrated aircraft systems. Figure 4 illustrates the arrangement of one of these simulations. This simulation represents a single-engine fighter aircraft, with integrated thermal management for both the engine and aircraft systems.

Included in this selected simulation are the aircraft, the propulsion system, the engine thermal management system (TMS), and the aircraft environmental control system (ECS). In the selected integration architecture, the engine fuel provides the primary heat sink for the engine TMS, and the engine bypass flow in the fan duct provides the primary heat sink for the ECS system. The engine TMS requirements consist of cooling the engine lubrication oil, which in turn cools the bearings, gearbox, and the starter generator. Heat is additionally generated in the main fuel pump, the hydraulic (fuel-draulic) actuator pump, and the actuators. In addition, cooled air is required for purging the engine bearing compartments. The aircraft thermal management includes the environmental control system (cockpit cooling and avionics), the aircraft gearbox, and the aircraft hydaulic systems.

The system architecture shown in Fig. 4 does not include all of the subsystem components described above, but does include the engine TMS, the primary components of the ECS cooling system, and incorporates a linkage between the fuel system and the ECS system, allowing the fuel to be used as part of the heat sink for the ECS. It should be noted that part of the illustrated sysytem (specifically the fan duct heat exchangers and bypass ducts) are physically within the engine, but are shown externally for clarity. The engine is a parametric model of a current technology turbofan, with characteristics appropriate for an advanced concept strike fighter aircraft.

The system of Fig. 4 has been modeled with the methods and libraries being developed in the TSAT program, and a preliminary performance trade has been conducted to evaluate initial capabilities of the simulations. As applied to this evaluation, the system simulation is assembled on a Visual Basic (VB) ''form,'' as seen in Fig. 5, which provides the required container, or workspace. The simulation is constructed in this graphic environment by selection of the required component objects from a ''toolbox,'' and assembling them in the appropriate order on the form with drag-and-drop methods. The component toolbox appears down the left side of the figure, and the completed model appears in the center window.

Each small block in Fig. 5 represents a physical component in the aircraft system, and is analytically supported by a programmed simulation of the component. In this model, all objects have been programmed in VB, or a combination of VB and FORTRAN. However, they could equally well have been programmed in

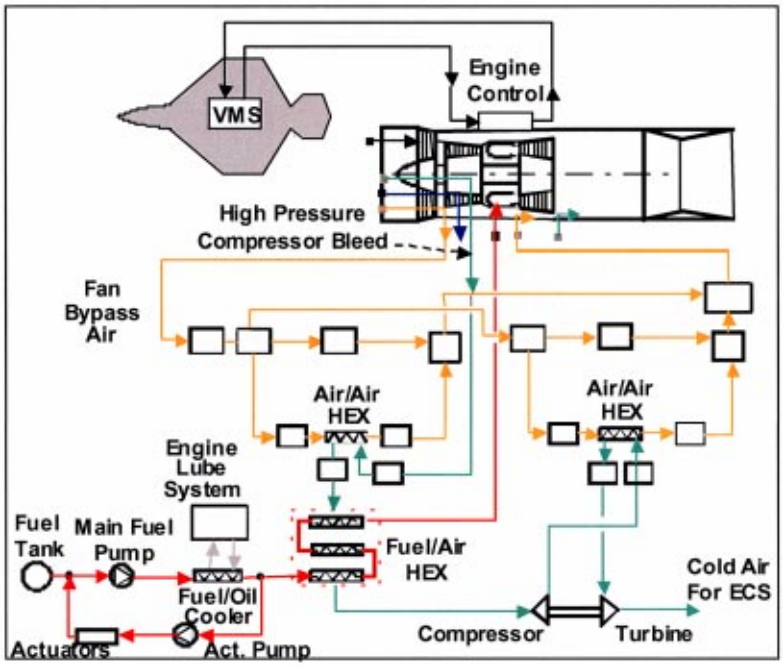

Fig. 4 Schematic of integrated simple flight system

C/C++, or Java. The lines connecting the objects on the form represent ''connectors,'' that pass data from object to object. The model shown on the form is more than a schematic drawing of a system. As the objects are dropped on the form, the necessary computer commands are generated automatically by the Visual Studio (Basic) system to control the operational sequence of the component objects, to allow the objects to communicate, and to control the convergence methods selected to yield global balances of the system components. As each component object is dropped on the form, its corresponding code is loaded into memory and executes for a defined set of initial default conditions. The object then remains in memory in an idle state until an event occurs changing one of the defined object properties. The object then executes to provide a solution corresponding to the new property set. The simulation as shown in Fig. 5 is in ''design mode,'' in which components can be independently run, but the system does not pass data between objects.

When the assembly of the simulation is complete, and the ap-

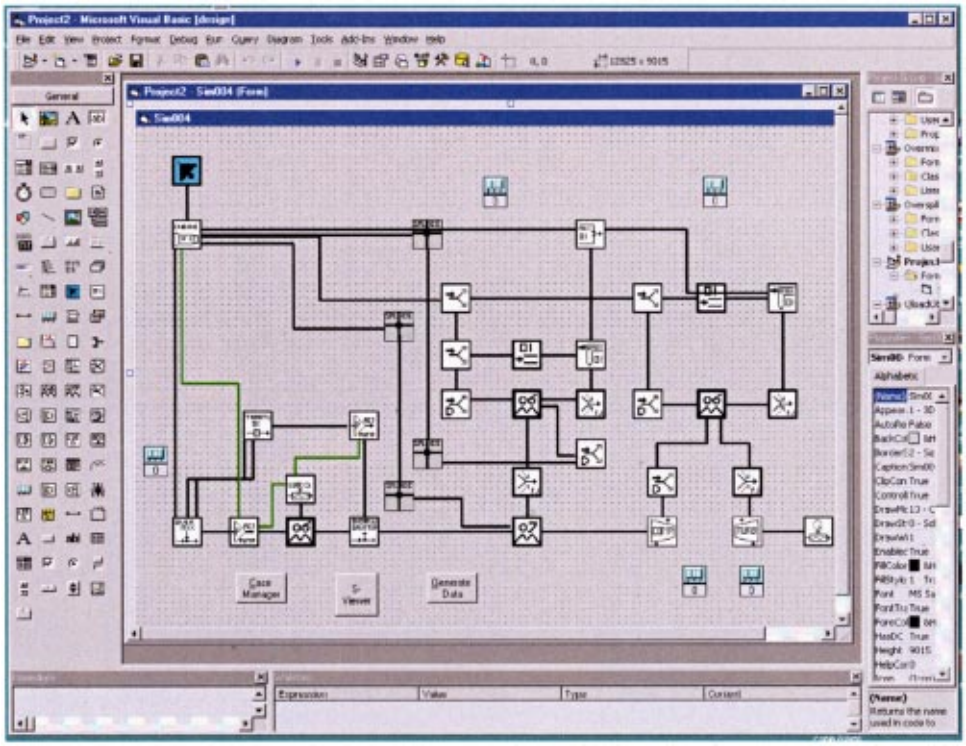

Fig. 5 Simulation modeled on visual basic form

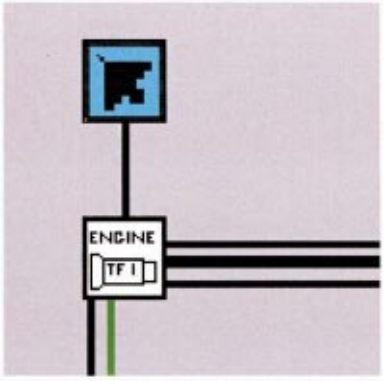

Fig. 6 Engine and aircraft objects

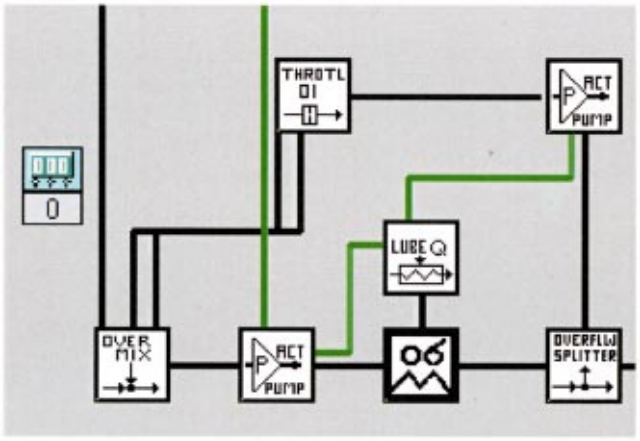

Fig. 7 Engine fuel and thermal management system

propriate system boundary conditions have been defined, the model is executed in ''run mode.'' In this operational mode, the system is operated in a defined sequence, with initial fluid states defined, and data flows sequentially through the connected components. To clarify the methods applied in building the components, and assembling them into an operational simulation, the model will be dissected for further discussion.

The Engine and Aircraft Objects. Figure 6 shows the engine and aircraft objects. The engine in this simulation is a Fortran based parametric (legacy) model of a modern turbofan engine, with capability for varying the various design parameters, and operating over a defined flight envelope. This model began as a conventional stand-alone program, with input and output through external data files. To make this program capable of communicating in an object based environment, it was converted into an object by ''wrapping'' it in an interface routine that is compatible with ActiveX objects. This ''wrapper'' is an interface, written in Fortran, that passes data to the outside world in accordance with the rules of object oriented programming. The wrapper converts data into a form compatible with the internal requirements of the legacy code. The legacy engine model, and its interface wrapper, are compiled into a dynamic link library (DLL), which can be called by a VB object. A VB object is written specifically to interface with this engine DLL, and from this point on the VB object represents the engine. To make the approach actually useable, all information that is required by the engine and all external connected components must be identified, and data passing defined as part of the wrapper and the associated object. For the engine model, these data include information defining all fluid streams that might be connected to other components (such as core fan, bypass bleed air, fuel), various engine internal conditions that might impact thermal management requirements, and power extraction conditions (such as shaft speeds) for deriving mechanical power from the engine.

For control of the engine operation, data that must be supplied includes definition of flight and ambient conditions, in addition to the required thrust, bleed extraction, and power extraction. This information is supplied on a data bus from the aircraft model, with the engine response supplied as feedback to the aircraft. Another data bus supplies the internal engine conditions required for definition of pump operation, and heat generation in the lubrication system.

From this discussion, it is apparent that there are several different types of information that must be passed between component objects in a simulation. These include fluid stream properties, environmental data, thermal loads, shaft power and speeds of connected devices, information for electrical components, and other data types or definitions that may be required.

Engine Thermal Management. Figure 7 shows the engine thermal management subsystem, which manages engine fuel flow, hydraulic power, and lubrication cooling. In this subsystem, fuel flow burned by the engine is defined by the engine model, and fuel conditions as supplied to the subsystem are defined as a boundary condition, or could be defined by a model of the aircraft fuel tank. Fuel is used as the hydraulic fluid in addition to cooling the engine lubrication system.

With recirculation of fuel in the hydraulic actuation system, determination of fuel heating in the loop requires convergence logic, provided by the controller object shown to the left of the subsystem. The multiple connectors shown consist of both fluid stream connectors and engine data bus connectors. The two pumps and the lube oil heating definition are all defined by engine operating conditions, and require such data.

Environmental Control System. The environmental control system, as shown in Fig. 4, is integrated with the engine, and rejects heat into the engine fan duct. Engine high compressor bleed (1) is cooled with fan air, (2) further cooled with fuel, (3) compressed in an external compressor, (4) cooled again with fan air, and (5) expanded in a turbine. This air, cooled in the reverse Brayton cycle, is then used directly or indirectly to provide cockpit and avionics cooling, and other aircraft thermal management. For this model, cold air is used to cool a specified heat load to define the cooling capability of the system. The fan duct cooling system, shown in Fig. 8, includes a heat exchanger (labeled 06), a bypass duct (labeled 01) and a splitter that controls the balance between airflow through the heat exchanger and leakage around it. This balance is defined by matching the static pressures at the exit of the heat exchanger and the leakage duct. In this architecture, the heat exchanger represents an array of heat exchanger modules placed in an annular arrangement in the fan duct. Part of the array is used to precool the air before compression, and the remainder cools the air after compression. Because the single object represents multiple devices, the air stream is divided proportionally prior to cooling, then rejoined afterward. This figure also shows the location of the fuel-air cooler (07), used to subsequently cool bleed air after leaving the fan duct heat exchanger array. Figure 9 illustrates the remainder of the ECS system, including the turbomachinery in the reverse Brayton cycle, and the second fan duct heat exchanger array. For this simple model, the compressor and turbine are defined with constant efficiency, and balances are limited to power and flow balance. In both arrays of fan duct heat exchangers, the fans and leakage streams are mixed and returned to the engine fan stream.

Modeling the cooling system as though it were external to the engine allows the engine cycle to be independently balanced prior to running the thermal system model, then repeating an iteration on the engine cycle to account for the effects of the thermal system integration with the engine.

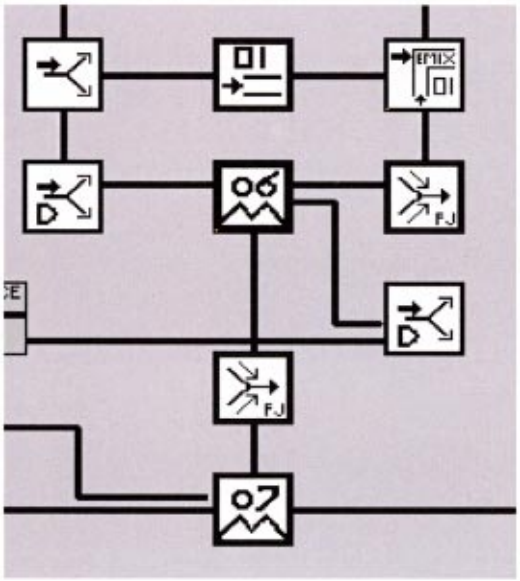

Fig. 8 Precooler heat exchangers in fan duct

A Simple Trade Study. Assembly of the system simulation, as shown in Fig. 5, required about two hours, including definition of the controls and balances. This was based on a system after the architecture had been selected. On completion of the simulation, a design effort is required to define the sizes and other properties of the system components. This is the major technical challenge of system integration, assuring that the system is operational and that its performance satisfies all the desired design requirements over the entire operating envelope, including preflight. This is typically an iterative process, requiring changes in some component properties, and possibly changes in the thermal system architecture. In system modeling with more conventional methods (that is hard wired procedural codes), making architectural changes typically requires a major effort. However, using drag-and-drop object-based modeling, changing architecture only requires rewiring components in the graphic environment, a relatively simple process.

As an example evaluation of the selected architecture, and a demonstration of the capability of the modeling method, a brief trade study is illustrated. The following are assumed as a basis for the evaluation.

The selected architecture has been modeled, component sizes have been adjusted to achieve acceptable operation, and aircraft thermal loads have been defined. At a selected aircraft cruise condition (12.2km/0.9M) (40K/0.9M) the ECS loads have grown, and require maximizing the system cooling capability. With the selected system configuration, and the engine thrust requirement at 60% of intermediate power, two options will be considered to increase the ECS cooling capacity. First, high-compressor bleed flow extraction (which is the refrigerant in the reverse Brayton cycle) will be increased to possibly yield more cooling. Next, the question of coolant return to the engine will be considered. Cooled bleed air can be used as an indirect coolant and subsequently returned to the engine cycle, or used as a direct coolant and exhausted overboard after use. In the first case the cooling turbine exhaust pressure must be above the engine pressure at the selected return location. In the second case, the exhaust pressure can be lower, as long as it satisfies cockpit environment requirements.

To address the question of which options to select, a parametric evaluation is performed to identify the effect of bleed flow rate and coolant return location on cooling capacity. A simple thermal load is applied to the cooled bleed air at the turbine exit. Bleed air flow up to 2.0 kg/sec (260 lb/min) is considered with exit pressures of 55 and 110 kPa (8 and 16 psia). The maximum useful coolant temperature is assumed to be 38°C (100°F). The system simulation is exercised over the range of conditions, and the results are shown in Fig. 10.

From the figure, it is evident that when the exhaust pressure is lowered, the effective cooling capacity is approximately doubled. This is a result of the increased expansion across the turbine, yielding lower discharge temperatures. It is noted that the available cooling capacity reaches a maximum with increased bleed air flow rate. This behavior is due to the characteristic performance of the heat exchangers with increased flow rate.

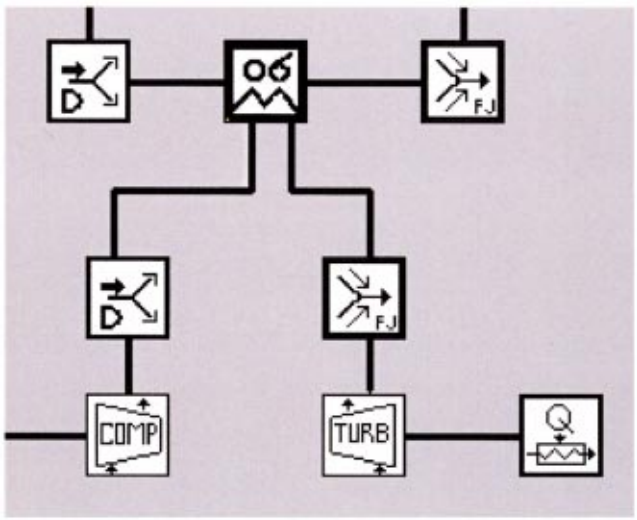

Fig. 9 Environmental contol system

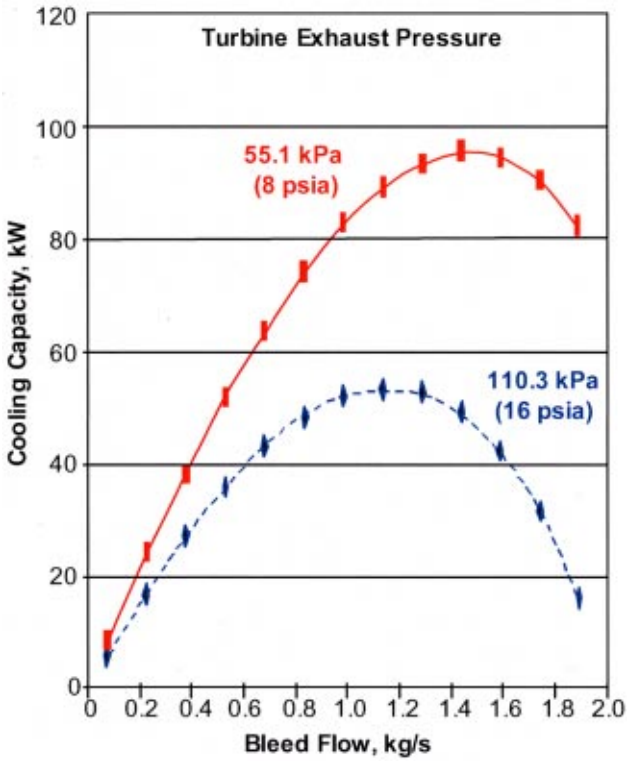

Fig. 10 Cooling capacity as function of bleed flow

Summary

The potential benefits of collaborative and concurrent engineering approaches to the design and development of complex engineering systems, such as for advanced fighter aircraft, have been discussed. Within this framework, a new methodology was also described to aid the engineer in developing system models and performing trade studies to address ''big picture'' issues relative to the system. This methodology is to aid in the development of system level solutions, as opposed to grouping individually optimized components into systems with no concern for system level performance. An example of a first step toward system level optimization is illustrated in the simple trade study of an integrated flight vehicle and its thermal management system.

The effort described within this paper has tremendous potential for changing, and hopefully, improving the way system engineering is and will be accomplished. The referenced program, although nearing completion at the time of publication, has been directed initially toward thermal management related systems, or in other words, the emphasis has been on flow processes concerning heat transfer and thermodynamics relative to fluids, gases and solids. However, through the flexibility of object modeling, the tool discussed is quite capable of being used to model other processess, whether those processes be physical or abstract, simple or complex, small or large. To date, the authors have only scratched the surface to applying the program toward other applications, including electrical systems and automotive refrigeration systems.

Efforts to include validation of the modeling approach presented are incorporated in the program schedule, but as of the writing of this paper have not been initiated. The plan is to utilize test results in the near future of a related fuel system program. The approach entails first validating the components contained in the thermal library, and then validate to the subsystem level. As confidence is gained and system data obtained, the modeling tool will be gradually exercised up to the system level with results compared to existing systems.

Acknowledgment

The authors would like to thank Nick Kuprowicz, of the Engine Integration and Assessment Branch of AFRL, for his review and feedback of this paper.

References

[1] Office of Under Secretary of Defense, 1996, ''DoD Guide to Integrated Product and Process Development (Version 1.0) Feb. 5,'' *http://www.acq.osd.mil/io/se/ippd/guide/table_of_contents.html*.
[2] AFRL Dual Use Office, 2001, ''Air Force Dual Use Science and Technology Program,'' Nov., *http://www.afrl.af.mil/dualuse/*.
[3] Microsoft Corporation, 2000, ''COM: Delivering on the Promises of Component Technology,'' June, *http://www.microsoft.com/com*.
[4] Object Management Group, 2001, ''CORBA Basics,'' Aug., *http://www.omg.org/gettingstarted/corbafaq.htm*.
[5] Microsoft Corporation, 1999, ''How to Write and Use ActiveX Controls for Microsoft Windows CE2.1,'' June, *http://msdn.microsoft.com/library/default.asp?url=/library/en-us/dnce21/html/activexce.asp*.

Application of Pulse Detonation Combustion to Turbofan Engines

M. A. Mawid

T. W. Park

Engineering Research and Analysis Company, Wright-Patterson AFB, OH 45433

B. Sekar

C. Arana

Turbine Engine Division, Propulsion Directorate, Air Force Research Laboratory, Wright-Patterson AFB, OH 45433

The potential performance gain of utilizing pulse detonation combustion in the bypass duct of a turbofan engine for possible elimination of the traditional afterburner was investigated in this study. A pulse detonation turbofan engine concept without an afterburner was studied and its performance was assessed. The thrust, specific fuel consumption (SFC), and specific thrust of a conventional turbofan with an afterburner and the new pulse detonation turbofan engine concept were calculated and compared. The pulse detonation device performance in the bypass duct was obtained by using multidimensional CFD analysis. The results showed that significant performance gains can be obtained by using the pulse detonation turbofan engine concept as compared to the conventional afterburning turbofan engine. In particular, it was demonstrated that for a pulse detonation bypass duct operating at a frequency of 100 Hz and higher, the thrust and specific thrust of a pulse-detonation turbofan engine can nearly be twice as much as those of the conventional afterburning turbofan engine. SFC was also shown to be reduced. The effects of fuel-air mixture equivalence ratio and partial filling on performance were also predicted. However, the interaction between pulse detonation combustion in the bypass duct and the engine fan, for potential fan stall, and engine nozzle have not been investigated in this study. [DOI: 10.1115/1.1494098]

Introduction

Current Air Force planning activities indicate that affordability of future aircraft fighters must be increased and will be the primary metric for the Air Force VAATE initiative. This initiative defines affordability in terms of the ratio of propulsion capability to total cost. In order to meet long-term affordability goals, advanced affordable propulsion concepts need to be identified and their payoffs must be quantified. Advanced propulsion concepts may include engine components such as pulse detonation combustors (PDC) and afterburner (PDA) operating at quasi-constant volume combustion. These components will operate in a mode identical to pulse detonation engines (PDE) and as a result obtaining performance estimates of PDE is of interest.

The pulse detonation engine (PDE) concept utilizes a repetitive unsteady cycle of detonation waves initiation, propagation, and expulsion to produce thrust. The higher performance potential of the PDE concept relative to conventional steady flow propulsion systems, such as turbine and ramjet engines, can only be realized by achieving rapid fuel-air mixing, detonation transition and combustion product scavenging over the PDE cycle. The high pressure behind a detonation must be exploited to the largest possible extent over a repetitive cycle in order to generate high thrust. In general, the combustion process in PDE takes place at supersonic speed and at a quasi-constant volume, for this reason, PDE can achieve better specific fuel consumption relative to conventional steady-flow engines. In addition, the absence of rotating machinery in the flow path and the consolidation of the compression (pressurization), combustion, and thrust generation processes within a single component without the need for precompression to peak operating pressures forms the basis for a propulsion system with a high thrust-to-weight ratio. This propulsion system provides potential for lower cost, simplicity, and a high degree of reliability. The PDE performance potential has in recent years increased interest in exploiting the PDE for aircraft, rocket, and missile applications, [1–6].

Contributed by the International Gas Turbine Institute (IGTI) of THE AMERICAN SOCIETY OF MECHANICAL ENGINEERS for publication in the ASME JOURNAL OF ENGINEERING FOR GAS TURBINES AND POWER. Paper presented at the International Gas Turbine and Aeroengine Congress and Exhibition, New Orleans, LA, June 4–7, 2001; Paper 2001-GT-448. Manuscript received by IGTI, Dec. 2000, final revision, Mar. 2001. Associate Editor: R. Natole.

The PDE cycle, [7–9], begins as a mixture of fuel and air fills the combustor volume. Rapid transition to detonation is induced by rapid energy deposited through a spark or laser-based system. The detonation wave then propagates through the fuel-air mixture and is expelled from the combustion chamber. The expansion waves behind the detonation waves and reaction zone, which are created to match the closed end boundary condition, reduce the combustor pressure to the stagnation condition that exists between the front end of the chamber and the trail of the expansion waves. This process partially scavenges combustion products when the wave is expelled at the exhaust end of the combustor. Once the detonation wave leaves the combustor, expansion waves propagate upstream into the confinement to further scavenging combustion product. After the scavenging process is completed, the filling process begins to recharge the combustion chamber with a detonable mixture of fuel and air.

The level of energy required to initiate and sustain a detonation wave depends on the detonative limits of the fuel mixture, on the ignition delay at the operating conditions within the engine, and on the interaction between the exhaust waves open end and the flow within the detonation tube. A strong coupling between the mixing process, kinetics of combustion, and the geometry of engine, therefore, exists. At an operating frequency of several hundred cycles per second, the time available to complete fuel injection and mixing is no more than a few milliseconds. One way to achieve proper mixing is to exploit the unsteady turbulent flow within the engine. Ignition delay of the fuel air mixture determines the extent of the transition region of the detonation tube. Expansion from the aft end of the detonation tube also interacts with the detonation wave as it traverses the transition region.

To explore the potential benefit of augmenting the conventional turbofan constant pressure combustion with pulse detonative combustion, a new pulse detonation-turbofan (PDTF) system concept is presented in this study. The objective here is to demonstrate the potential performance gain of this new concept as compared to the conventional turbofan engine (Fig. 1). In this pulse detonation-turbofan engine concept, the afterburner is completely eliminated and pulse detonation combustion to augment engine core thrust is induced in the engine bypass duct (Fig. 2). A number of methods can be used to achieve pulse detonation combustion in the bypass duct, such as placing detonation tubes along with a rotary valve in the bypass duct. However, the addition of tubes in the bypass duct

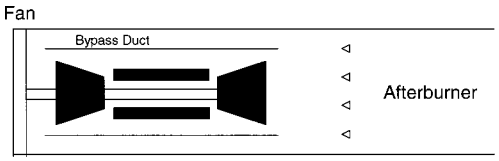

Fig. 1 Standard afterburning turbofan configuration

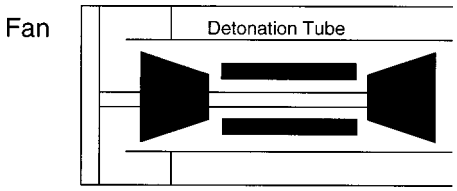

Fig. 2 Pulse detonation turbofan configuration

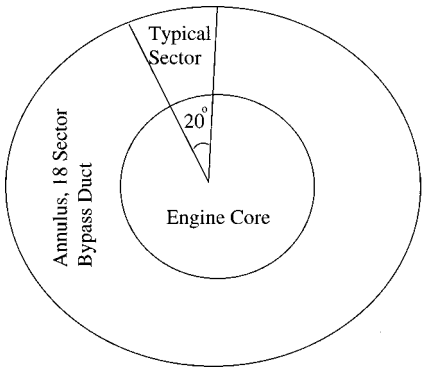

Fig. 3 Side view of bypass duct sector arrangement

will increase overall engine weight and will increase total pressure losses of the bypass duct airflow. In this study, the annulus bypass duct was assumed to have 18 sectors, each with a 20-deg angle (Fig. 3). Detonative combustion is assumed to take place in these sectors in an alternate manner. The number of sectors that would be closed at any one time would be determined based on the pulse detonation frequency and cycle time. A rotary valve design type would be required to regulate the filling and blowdown processes, [8]. The analysis approach, we used to demonstrate concept feasibility, is given in the next section, which is followed by sections on AFRL pulse detonation experiment and modeling efforts, analysis of the new pulse detonation engine concept, results, and conclusion.

Pulse Detonation Turbofan Engine Analysis Approach

The turbofan engine core remains unaffected by the implementation of detonative combustion in the bypass duct. In contrast to the conventional turbofan engine with an afterburner, the pulse detonation bypass duct flow is not mixed with the engine core flow. The bypass duct detonation cycle consists of several fundamental processes that occur during the cycle. Alternate duct sectors are first charged with JP-8/air mixture. These sectors are then closed (sealed) by a rotary valve and ignition energy is deposited at the closed valve end to initiate detonation. Detonation waves then exit and burned gases are expelled. The rotary valve is then opened and the bypass duct sectors are refilled again with JP-8/air mixture while adjacent sectors are fired. The thrust produced in the bypass duct is due to the pressure differential acting upon the interior faces of the sectors and to the momentum imparted to the burned JP-8/air mixture as it is accelerated by the detonation. The burned mixture moves away from the detonation wave at the speed of sound relative to the wave (Chapman-Jouguet conditions). A number of modeling approaches can be used to predict the performance of the pulse detonation turbofan bypass duct concept. These modeling approaches vary in complexity from simple control volume-based to three-dimensional CFD with finite rate chemical kinetics. While simple control volume-based analyses are useful to carry out parametric studies and predict basic performance, more accurate and realistic performance estimates can be made by using multidimensional CFD analyses.

CFD will, therefore, be used to predict the performance of the pulse detonation turbofan concept. CFD modeling of the combustion processes in pulse detonation engines, however, requires an accurate representation of the interaction between fluid mechanics and chemistry, [10–13]. In the present analysis, a single-step chemical reaction model was used to represent the detonation chemistry, [14]. Although we showed in a previous study, [10],

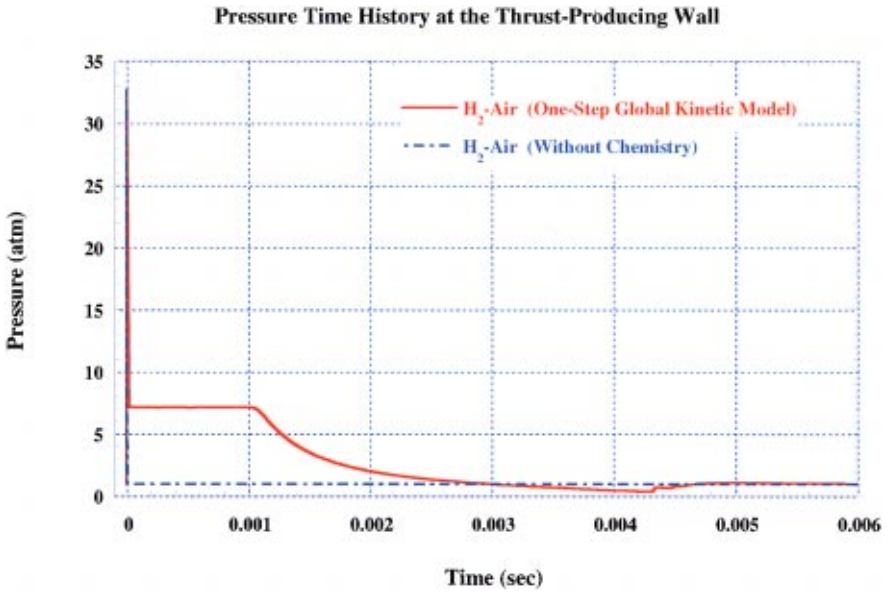

Fig. 4 Computed pressure-time history at the thrust wall for H_2-air single tube experiment

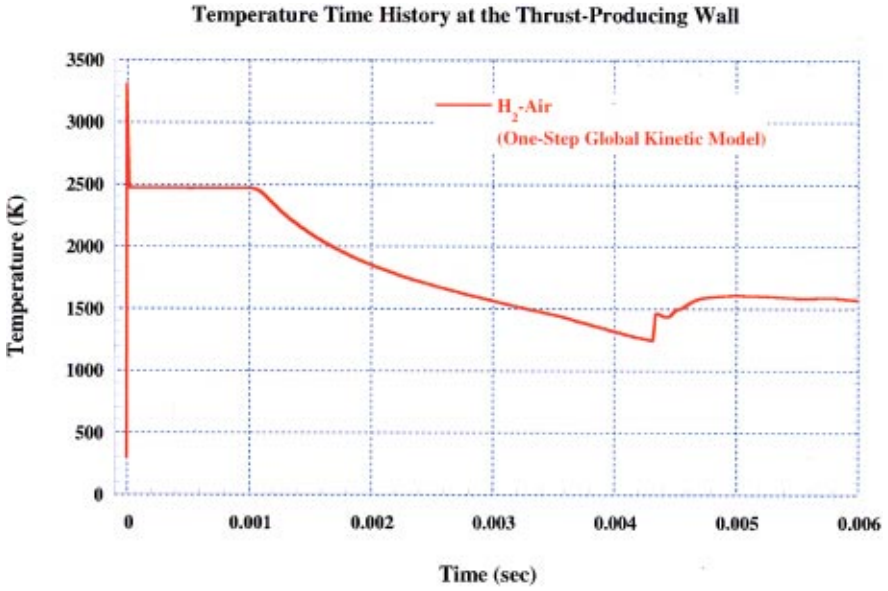

Fig. 5 Computed temperature-time history at the thrust wall for H_2-air single tube experiment

that the use of one-step chemical reaction models overpredicted the initial detonation properties. The use of one-step reaction model can, however, be justified for obtaining very reasonable performance estimates to demonstrate the pulse detonation turbofan concept feasibility. The CFD modeling approach will first be used to model the AFRL pulse detonation experiment, [15,16], and then comparisons between the CFD predictions and the AFRL experimental data for hydrogen-air detonation will be made as will be described in the next section.

Table 1 CFD predictions of Fred Schauer's PDE experiment (H_2-air) excluding initial effects

	Thrust (lbf)	SFC (lbm-fuel/ lbf·hr)	Specific Thrust (lbf/lbm/s)	Total Impulse (lbf·s)	Detonation Speed (ft/s)
Exp.	6.6	0.94	112.5		6394.0
CFD	9.4	0.62	168.2	0.588	6807.7

CFD Analysis for AFRL Pulse Detonation H_2-Air Experiment. The AFRL pulse detonation experiment, [15,16], consisted of a 2 inch in diameter and 36 inches in length single tube, rotary valve, spark ignition plug and a mixer. In this experiment the detonation tube is filled with an H_2-air mixture at atmospheric pressure, temperature, and various mixture strengths. Full and partial tube filling and purging processes can be studied in this experiment. Thrust, ISP and specific fuel consumption can all be measured as a function of the mixture equivalence ratio, tube cycle time (frequency) and filling fraction. The H_2-air chemistry was modeled using a single-step reaction model of the form

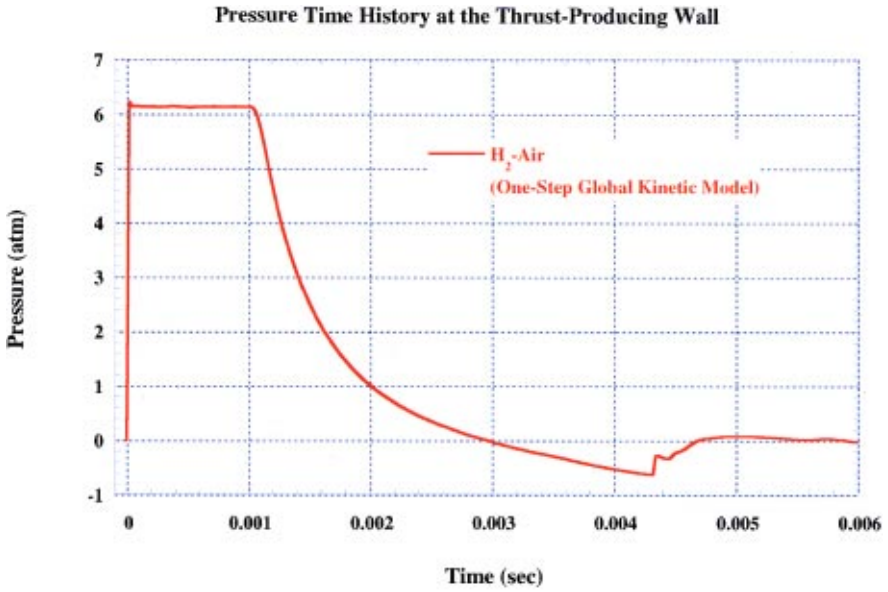

Fig. 6 Computed pressure-time history at the thrust wall for H_2-air single tube experiment

Table 2 CFD predictions of Fred Schauer's PDE experiment (H_2-air) including initial effects

	Thrust (lbf)	SFC (lbm-fuel/ lbf·hr)	Specific Thrust (lbf/lbm/s)	Total Impulse (lbf·s)	Detonation Speed (ft/s)
Exp.	6.6	0.94	112.5		6394.0
CFD	6.6097	0.9364	111.9675	0.4131	6807.7

Table 3 Conventional turbofan cycle

Conventional Turbofan Cycle	Performance
OPR	135
FPR	9.38
TRIT	4113 °R
Bypass ratio	0.8
Total air flow with A/B	1,036,800 PPH
Engine core air flow	576,000 PPH
Duct air flow	460,800 PPH
Total fuel flow with A/B	69,929 PPH
Core fuel flow	20,237 PPH
Total thrust with A/B	45,966 lbf
Total SFC with A/B	1.52 lbm/lbf/hr
Total specific thrust	159.2 lbf/lbm/s
Core (dry) thrust	19,406 lbf
Core SFC	1.04 lbm/lbf/hr
Core specific thrust without A/B air flow	121.3 lbf/lbm/s

$$2H_2+O_2\rightarrow 2H_2O$$

where the pre-exponential factor is 5.5×10^9 (m·kg·sec) and the activation energy is 5×10^7 J/kmole·K. The pulse detonation tube was connected to a large size dump tank (i.e., three times as large the diameter and length of tube) to minimize the effect of the downstream pressure boundary condition. The CFD computations were two-dimensional. The computational grid spacing in the axial and radial directions were 0.02 and 0.5 mm, respectively. Grid-independent analyses were carried out to insure that the results are computational grid independent.

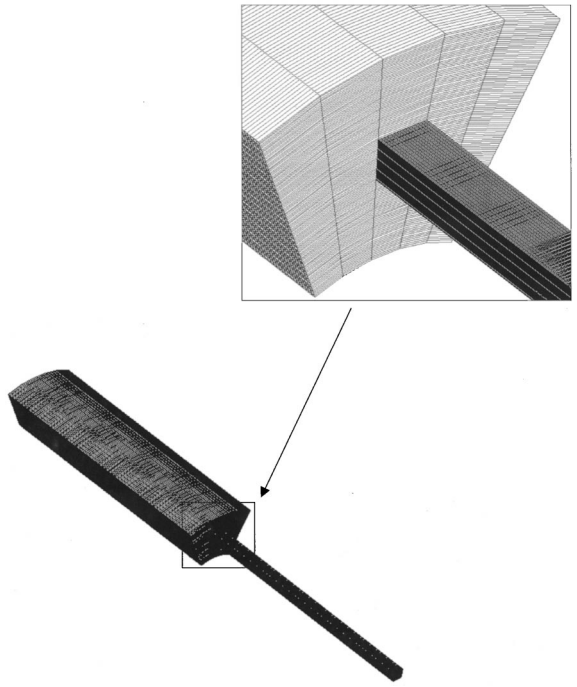

Fig. 7 Computational grid system of the pulse detonative sector with dump tank

Initially, the pulse detonation tube was assumed to be filled with a stoichiometric mixture of H_2-air. The dump tank was assumed to contain only air. To initiate the combustion process, one row of computational cells was considered to represent the ignition source such as a spark igniter or a laser system. The ignition cells were set at a higher temperature and pressure at the start of the computations. The initial temperature, pressure, and Mach number used in the present computations were 298 K, 1 atm, and 0.0, respectively. The mixture equivalence ratio was unity. The flow in the PDE and dump tank was modeled as unsteady and viscous flow. Viscous effects are accounted for here to allow for limited wave-wall interaction. Though the objective here is not to investigate viscous effects on wave shape, but rather to account for as much physics in the simulation as possible.

The numerical model employed in this investigation was based upon a commercial code ''STAR-CD,'' [17]. The code was previously modified to allow for multistep chemical reactions. The chemical reactions were solved using a stiff solver and the effect of chemistry was coupled to STAR-CD through the use of an operator-split-like method. This procedure allows the chemical reactions to be integrated by appropriate and efficient techniques including subcycling the chemistry source terms. The conservation equations for mass, momentum and energy were solved. Second-order temporal and spatial (MARS) schemes were used for the unsteady, convective, and diffusion terms, respectively.

Proper numerical treatment of the chemistry source terms for the global kinetics was not used for resolving the wave speed accurately. For the global one step kinetic model, it is important to use an averaged temperature in the detonation wavefront to control both the temperature and pressure rise. This procedure is equivalent to the use of a limiter function to slow down chemistry such that excessive unphysical heat release may be prevented, [3]. In the present study, the temperature predicted by the analysis was used and no temperature averaging across the wave was performed.

The thrust acting on the pulse detonation tube end wall was computed by integrating the predicted pressure at the closed end wall. However, since the detonation process is intermittent, an average thrust was calculated by using the following relation:

$$F_{\text{avg}}=\frac{\int_0^{T}\text{cycle}[P(t)-P_{\text{drag}}]A dt}{T_{\text{cycle}}} \tag{1}$$

where $P(t)$ is the predicted instantaneous unsteady pressure at the tube closed end wall and P_{drag} is the pressure acting on the left side of the thrust wall during detonation and purging. The cycle time, T_{cycle}, is defined as the time required to fill the detonation tube with a premixed fuel/air mixture, detonation initiation time, time for the detonation to exit the tube, and purge time to reduce the tube pressure to the refill pressure level and is given by

$$T_{\text{cycle}}=T_{\text{fill}}+T_{\text{initiation}}+T_{\text{detonation}}+T_{\text{purge}}. \tag{2}$$

The filling time can be calculated by

$$T_{\text{fill}}=\frac{\text{tube length}}{\text{fuel/air inlet velocity}}. \tag{3}$$

Table 4 PDC Input Conditions

Bypass ratio	0.8
Core air flow	576,000 PPH
Duct air flow	460,800 PPH
Total temperature	1045.9 °R
Total pressure	138 psi
Mach no.	0.34
Number of duct sectors	18

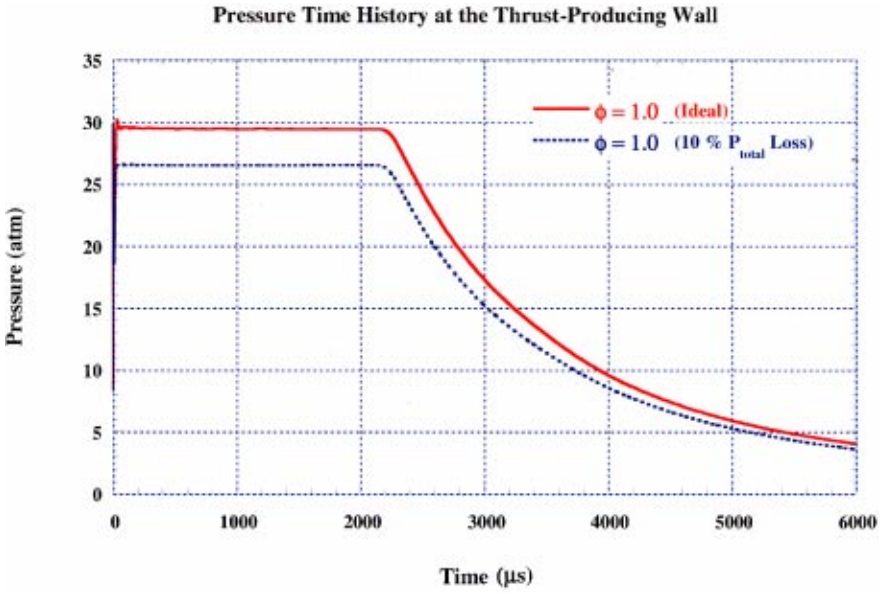

Fig. 8 Pressure-time history at the thrust wall

The products purging time can be achieved using the relation

$$T_{\text{purge}} = \frac{\text{tube length}}{\text{speed of sound at local conditions}}. \quad (4)$$

The detonation time may be evaluated using the relation

$$T_{\text{detonation}} = \frac{\text{tube length}}{\text{absolute detonative velocity}}. \quad (5)$$

The detonation initiation time can be estimated using deflagration to detonation transition time. However, this time interval is usually small compared to the filling time and as such, it may be set to zero. For the AFRL H_2/air analysis, the 16 Hz experimental cycle frequency, which is the inverse of the cycle time, was used to calculate the averaged thrust. It should, however, be mentioned here that the cycle time can also be computed by using the CFD calculations. This was done for the pulse detonation turbofan engine concept as will be shown later.

CFD Results for AFRL Experiment. Figures 4 and 5 show the predicted pressure and temperature time history at the thrust-producing wall. It is seen that the pressure and temperature at the wall rapidly decay immediately after the detonation combustion occurs and the detonation wave starts leaving through the open end of the tube. The wall pressure and temperature then level off and further decay as the detonation wave exits the tube and the blowdown process is initiated. The predicted results here are qualitatively very consistent with previously predicted results, [7,8], for H_2-air mixture. Figure 4 also shows the cold pressure-time history without chemistry. It is seen that the initial pressure wave decays fast to the initial pressure.

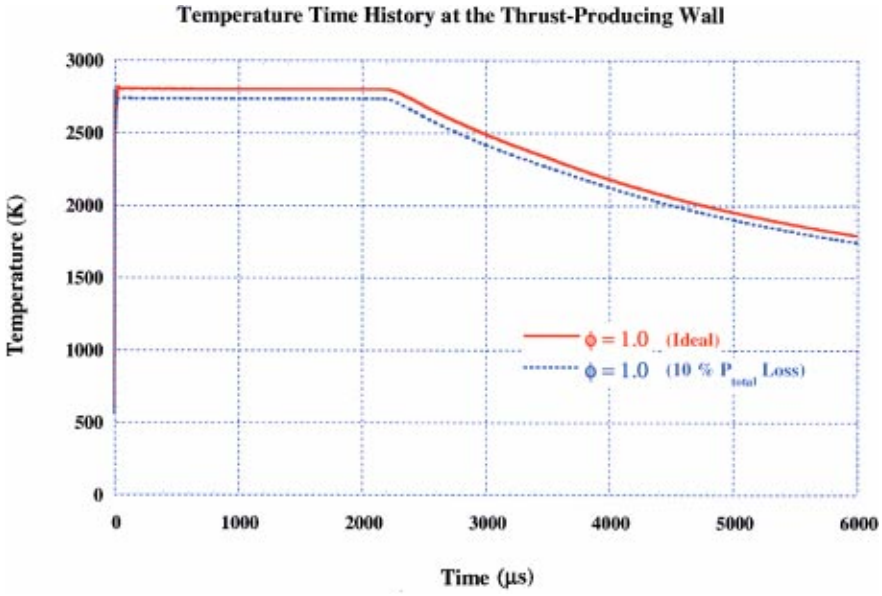

Fig. 9 Temperature-time history at the thrust wall

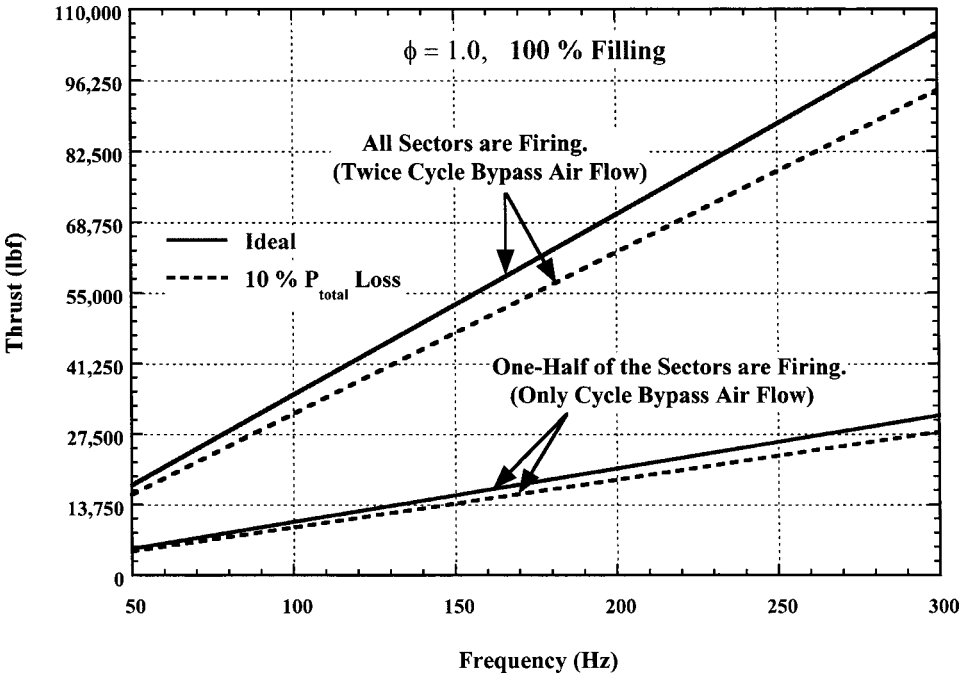

Fig. 10 Thrust versus cycle frequency for the bypass pulse-detonation duct

The predicted wall pressure-time history profile was numerically integrated to obtain an estimate of the thrust produced at the wall. In addition, the time required for the H_2-air mixture to be completely burned was used to calculate the averaged fuel and air mass flow rates. The calculated fuel and air mass flow rates along with the integrated thrust, were used to compute the specific thrust and SFC. Table 1 contains the predicted and measured thrust, SFC, specific thrust, total impulse and detonation speed. It can be seen that the thrust was overpredicted and consequently specific thrust and SFC were over and under predicted. The overpredicted thrust is believed to be due to the detonation initiation method and due to the use of one-step chemical reaction for H_2-air, which overpredicts the combustion heat release as was shown in a previous study, [10]. The contribution of the initial energy deposition to total thrust can be estimated by performing CFD analysis with the same initial conditions, but without chemical reactions. The contribution value can then be used to correct the thrust. Figure 6 shows the predicted pressure-time history when the initial pressure pulse was subtracted out. Table 2 shows the new integrated thrust, SFC and specific thrust based on Fig. 6 and the experimental measurements. It can be clearly seen that the comparison is quite satisfactory and provides confidence in our CFD results for reasonable estimates of pulse detonation performance.

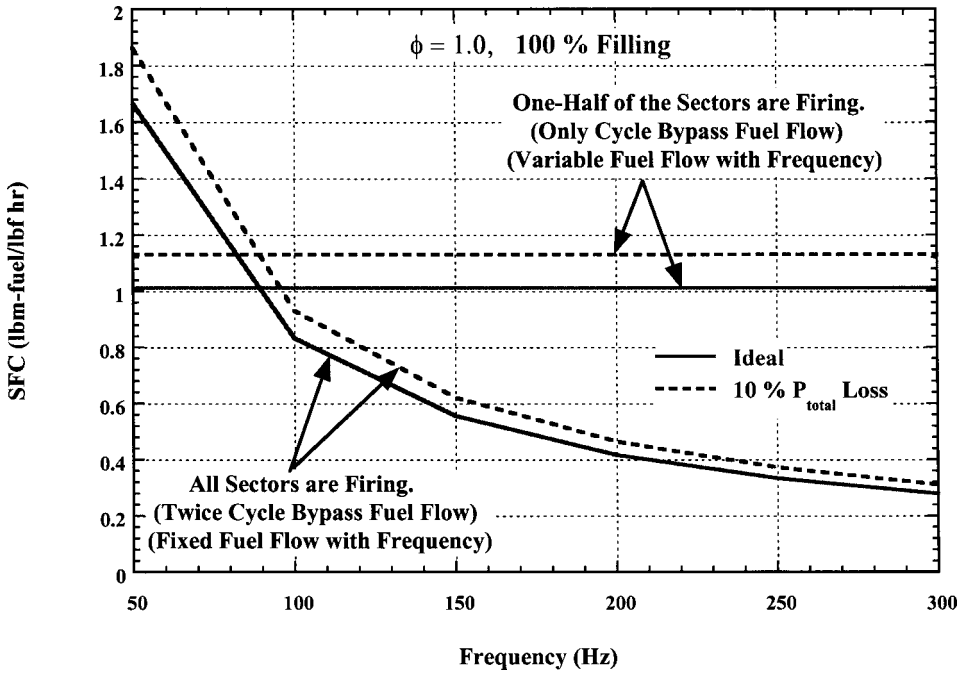

Fig. 11 SFC versus cycle frequency for the bypass pulse-detonation duct

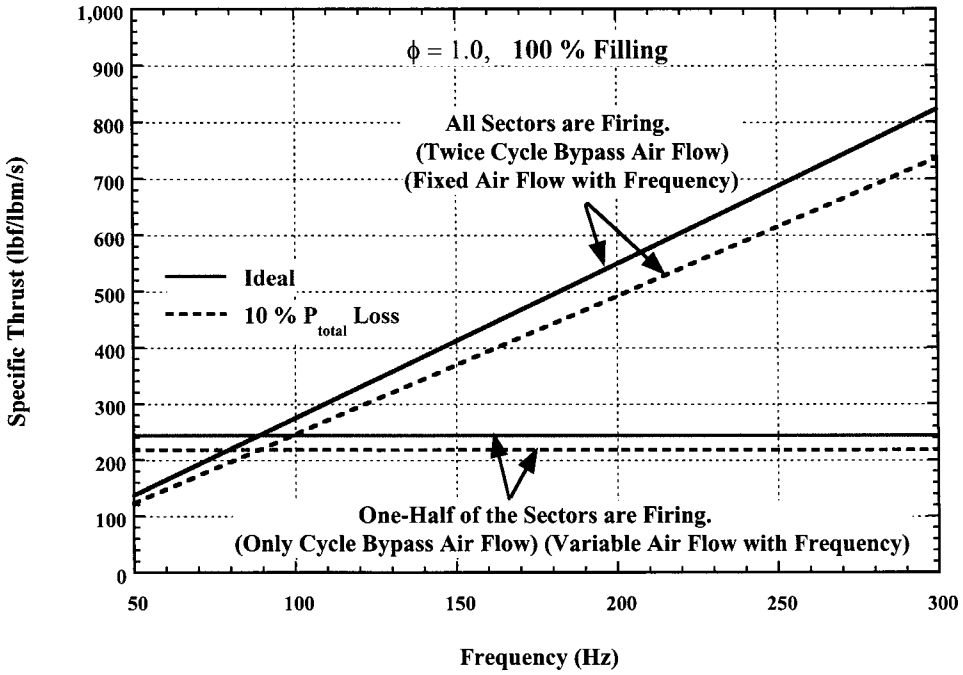

Fig. 12 Specific thrust versus cycle frequency for the bypass pulse-detonation duct

Pulse Detonation Turbofan Analysis

A combined CFD and cycle analysis approach will be used to predict the performance of the pulse-detonation turbofan engine concepts. This will be given in the next two sections.

Conventional Turbofan Cycle Analysis With and Without an Afterburner. An advanced turbofan engine cycle was first selected. This advanced cycle is given in Table 3. The performance numbers were computed using an in-house cycle code. Pressure losses for the engine components were considered. This turbofan engine cycle was not optimized for a particular mission. It rather represents a future goal with a conventional afterburner. Assumed fan and compressor pressure rises are only conceptual.

CFD Analysis for Pulse Detonation Turbofan. Figure 7 shows the computational grid used to model a 20-deg donut-like sector. As mentioned previously, the two-dimensional grid is attached to a three-dimensional large dump tank. The presence of this large dump tank is very important as to reduce the effect of downstream pressure such that the detonation wave can exit the

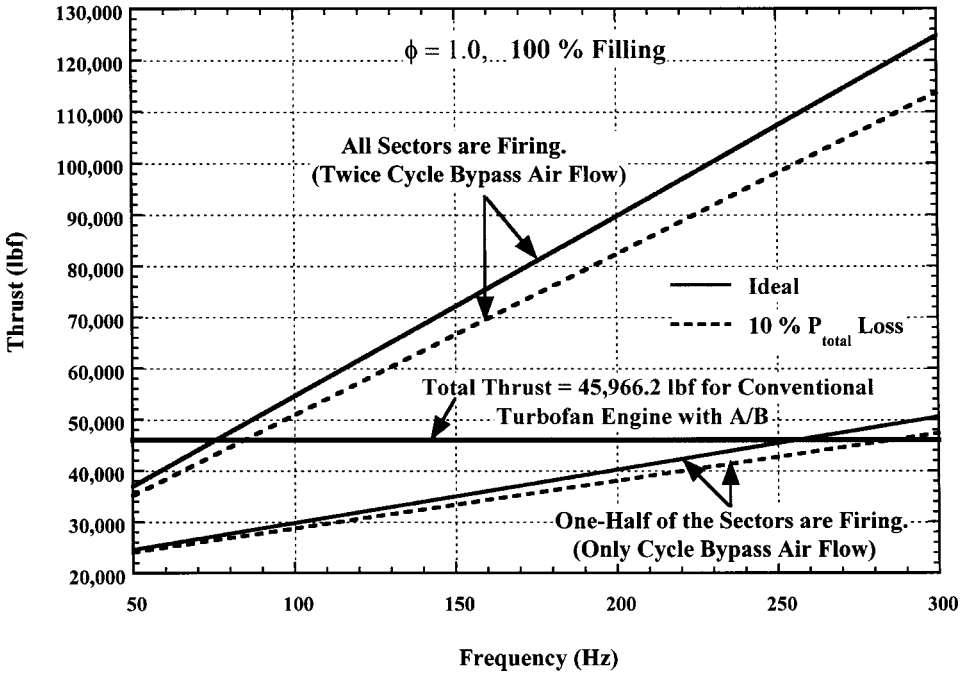

Fig. 13 Total thrust versus frequency for the pulse-detonation turbofan and the conventional turbofan with an afterburner

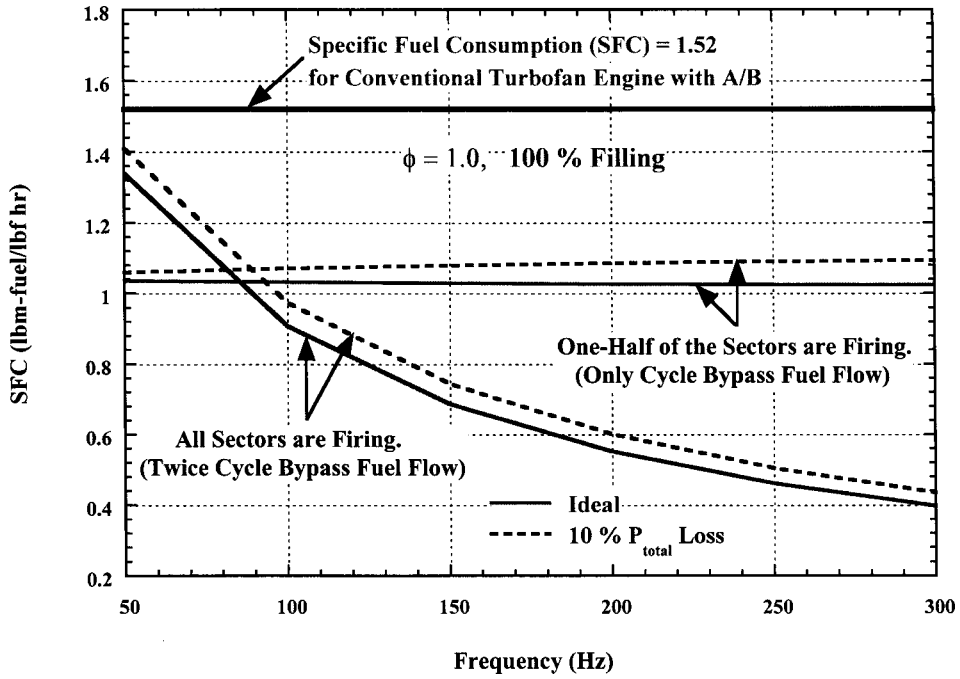

Fig. 14 Total SFC versus frequency for the pulse-detonation turbofan and the conventional turbofan with an afterburner

pulse detonative sector, [18]. The length of this sector is 63 inches. The total number of computation cells used was 252,379 and the spacing in the axial and radial directions were 1.0 mm and 1.2 mm, respectively. This computational grid resolution was sufficiently adequate to provide grid-independent results.

The sector was initially filled with a mixture of C_3H_8-air. Propane was used to simulate the gaseous JP-8 fuel. However, JP-8 thermodynamic data were used in the computations. A one-step global reaction model was used to represent the propane chemistry and is given as, [14],

$$C_3H_8+5O_2\rightarrow 3CO_2+4H_2O$$

where the reaction rate constants are given as $A=4.836\times 10^9$ and $E=1.256\times 10^8$ N·m/kmol·K and the fuel and oxygen exponents

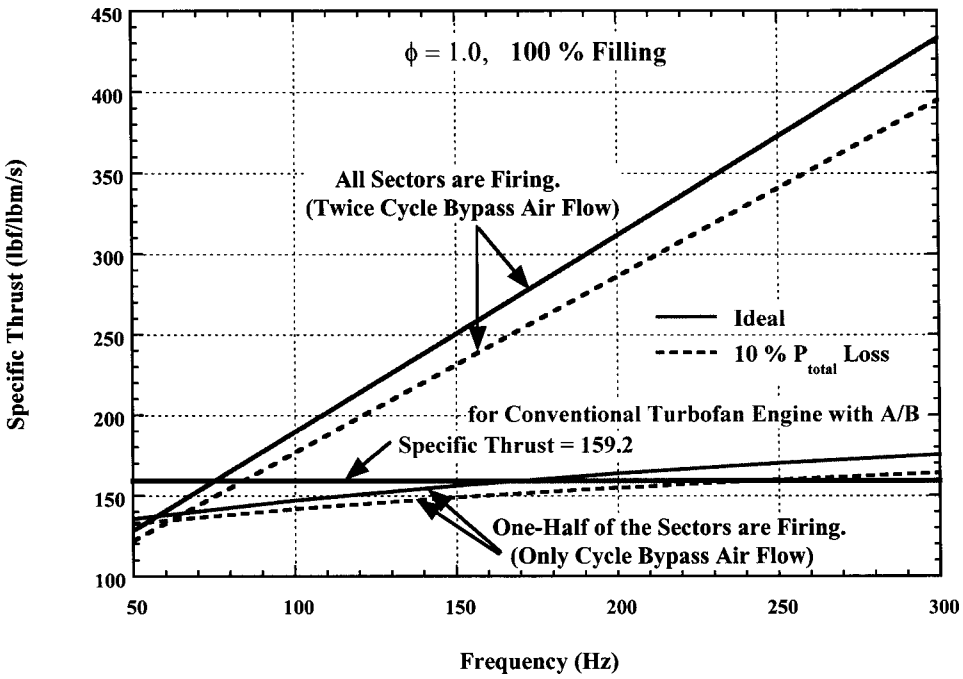

Fig. 15 Total specific thrust versus frequency for the pulse-detonation turbofan and the conventional turbofan with an afterburner

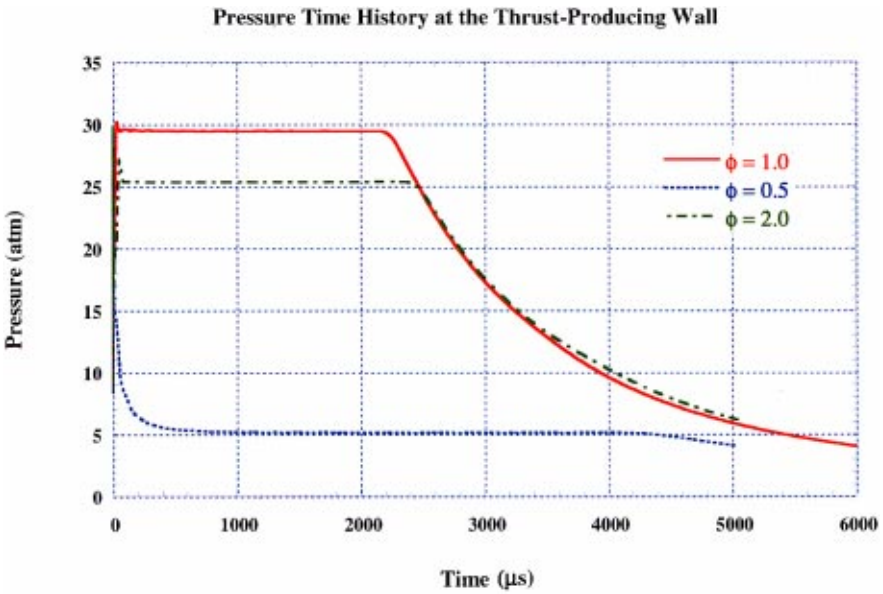

Fig. 16 Pressure-time history at the thrust wall for the fuel-lean, stoichiometric, and fuel-rich cases

are $[C_3H_8]^{0.1}$ and $[O_2]^{1.65}$, respectively. It should be mentioned that currently no reduced or global JP-8 fuel reaction mechanisms are available to model JP-8 fuel under pulse detonation pressure and temperature conditions. Three rows of cells located at the sector end wall were designated as the detonation ignition source initially. These cells were filled with C_3H_8-air combustion products at equilibrium and at a pressure and temperature of 33 atm and 2800 K, respectively. The initial conditions of the C_3H_8-air mixture were given by the cycle parameters as shown in Table 4.

CFD Results for Pulse-Detonation Turbofan. Figures 8 and 9 illustrate the predicted pressure and temperature time history at the sector closed end wall. The solid and dashed lines are for an ideal and 10% total pressure drop cases, respectively. Total pressure drop due to viscous and frictional effects and fuel-air mixing may affect the pulse-detonation turbofan engine concept potential performance gain. It was therefore important to include the total pressure loss effect in the analysis such that a more realistic performance can be predicted. The pressure in detonation cells was initially 33 atm and as detonative combustion occurred, the pressure for the ideal case slightly decayed to a pressure of about 29 atm. Whereas for the case of 10% pressure loss, the pressure rapidly decayed to about 26 atm. The wall pressure for both cases is predicted to level off, after the initial decay, until the detonation wave starts to exit the pulse detonation sector. At this time, the expansion waves produced at the sector exit travel to the closed end of the tube and reduce the wall pressure. When the pressure at

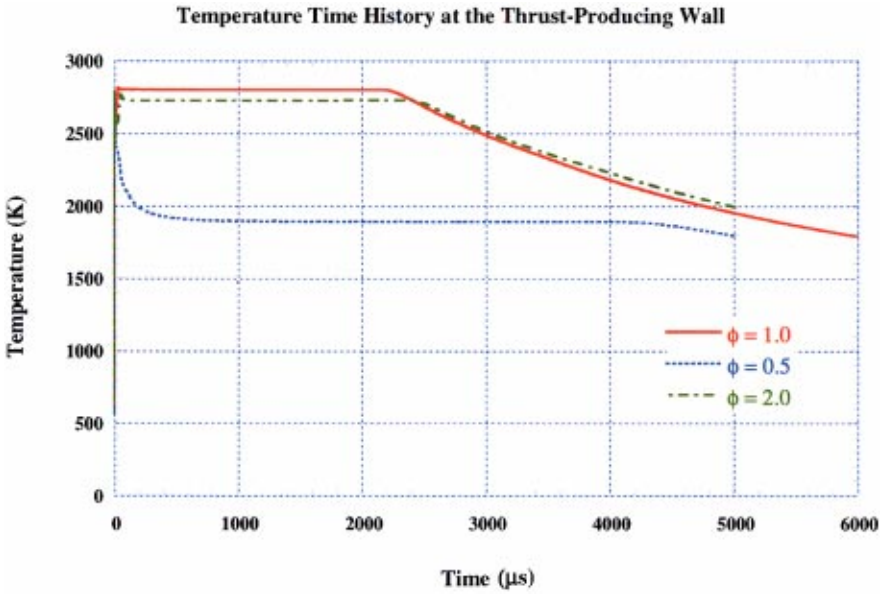

Fig. 17 Temperature-time history at the thrust wall for fuel-lean, stoichiometric, and fuel-rich cases

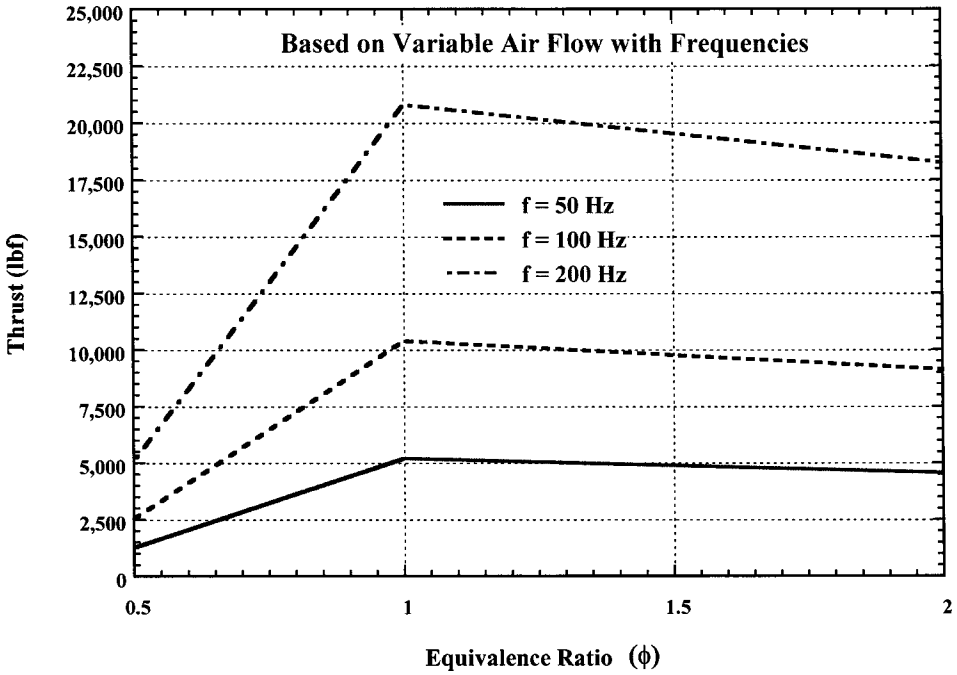

Fig. 18 Thrust versus initial mixture equivalence ratio

closed end wall drops below the initial pressure, purging of the combustion products in bypass sector occurs and the closed end wall opens for a fresh charge of fuel and air for the next cycle. The temperature time history at the closed end wall (Fig. 9) exhibits a similar behavior as that of the pressure.

The pressure-time history profiles shown in Fig. 8 were numerically integrated to obtain the time-averaged thrust force acting on the sector closed end wall, Eq. (1). The cycle time was computed using the input parameters (Table 4) for the filling time and the CFD results for the detonation and purging times. The detonation initiation time was assumed to be negligible. The cycle time for the conditions of Table 4 was about 0.0207 sec and this cycle time gives a cycle frequency of about 50 Hz. However, in order to demonstrate the potential performance gain of using the pulse-detonation turbofan engine concept, the thrust, SFC and specific thrust produced by the bypass pulse detonation duct for a range of cycle frequencies were predicted for the ideal and 10% total pressure loss cases. It should be indicated here that the cycle frequency was varied by decreasing the filling time. The bypass duct length and area were fixed and the inlet velocity and density were varied to maintain constant duct air flow. Figures 10 through 12 show the predicted thrust, SFC, and specific thrust plotted against

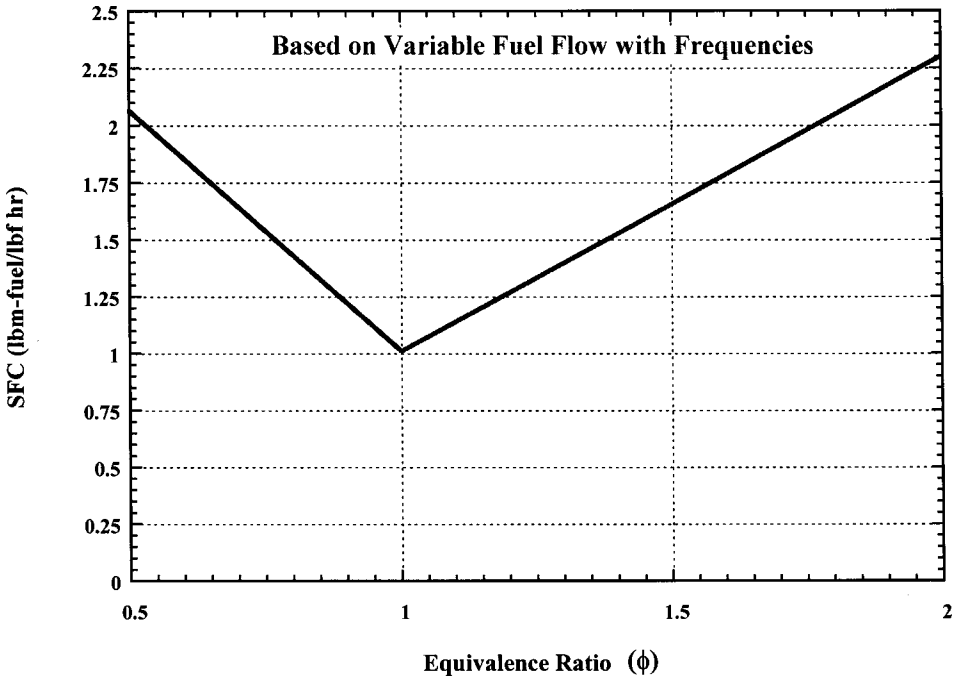

Fig. 19 SFC versus initial mixing equivalence ratio

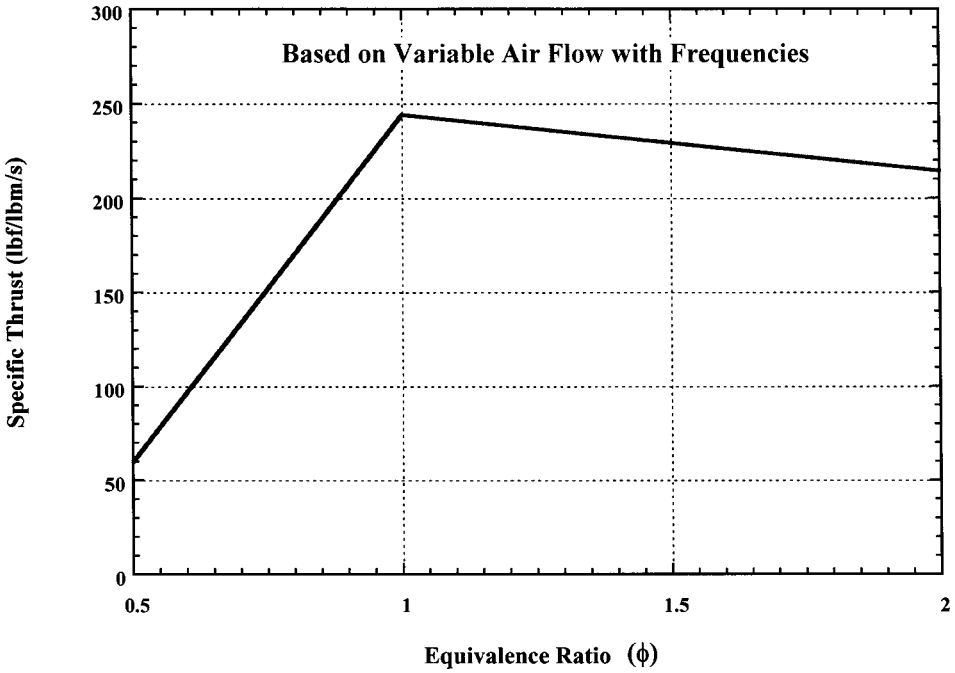

Fig. 20 Specific thrust versus initial mixture equivalence ratio

the cycle frequency, respectively, for the bypass pulse-detonation duct. The mixture equivalence ratio was unity and the bypass duct was assumed to be 100% filled with JP-8-air mixture. It can be seen that as the cycle frequency is increased for 50 Hz to 300 Hz, significant performance gain can be achieved, even for 10% total pressure loss case. Reliable operation with higher cycle frequencies (i.e., above 300) might not be possible due to engine cycle and sizing constraints and the fundamental detonation initiation process limitations.

Figures 13 through 15 show comparisons between the pulse-detonation turbofan and the conventional turbofan with an afterburner for total thrust, total SFC and total specific thrust, for a 50-300 frequency range and for the ideal and the 10% pressure loss cases. In these figures, the turbofan engine core (dry) thrust was added to the pulse detonation bypass duct thrust for various cycle frequencies. The total engine air and fuel flows (i.e., engine core fuel and air flows and bypass duct air and fuel flows) were used to calculate the total SFC and specific thrust. It is clearly seen that for a cycle frequency of 100 Hz and higher, substantial performance gain can be obtained as compared to the conventional turbofan engine with an afterburner (straight lines). In fact for a cycle frequency of 200 Hz, the turbofan cycle performance can be doubled, when pulse detonation combustion is used in the bypass duct. This clearly demonstrates the potential performance benefits of using such pulse detonation turbofan engine concept.

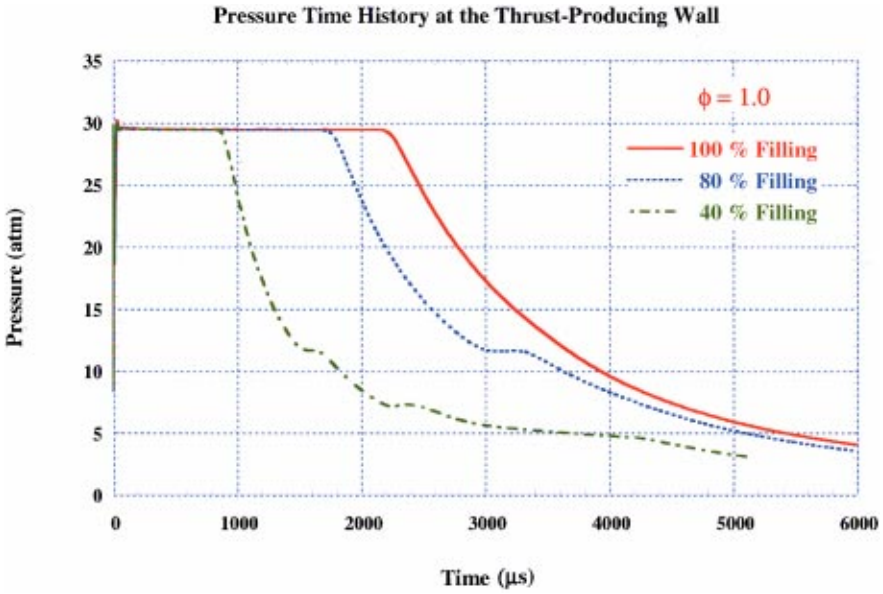

Fig. 21 Pressure-time history at the thrust wall for complete and partial filling of the bypass sector

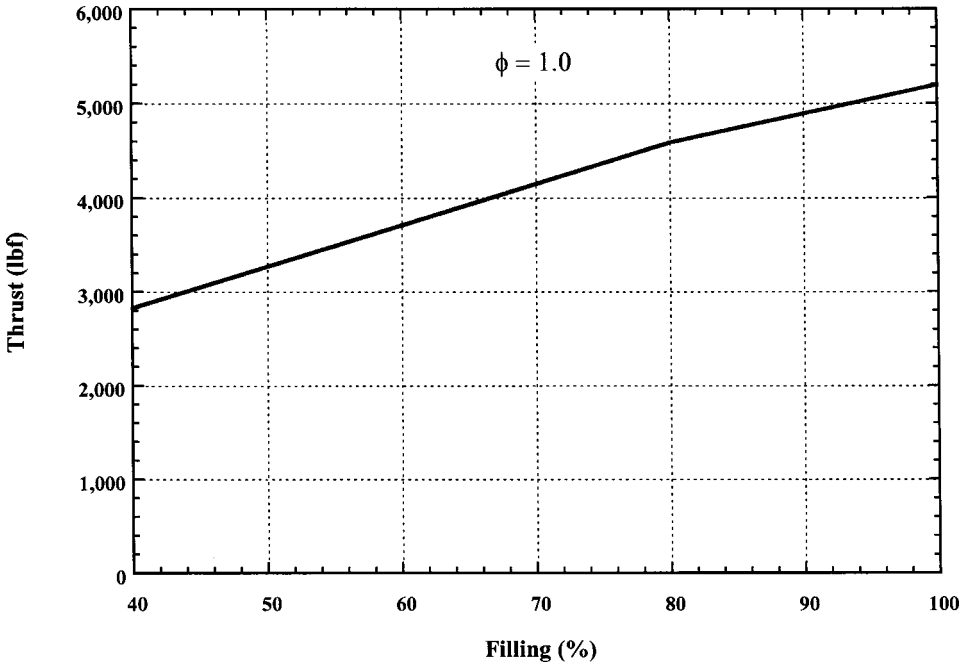

Fig. 22 Thrust versus bypass sector filling percentage

The cycle frequency must, however, be greater than 80 Hz to realize sizable performance gain as shown in Figs. 13 and 15.

Effect of Mixture Equivalence Ratio. The effect of the initial fuel-air mixture stoichiometry on the performance of the pulse-detonation turbofan engine concept was predicted by varying the initial overall mixture equivalence ratio. The initial pressure, temperature, and Mach number were the same as those of Table 4. The ignition (detonation) cells conditions were also maintained at 2800 K and 55 atm for temperature and pressure along with equilibrium products, as was done above.

Figures 16 and 17 show the predicted pressure and temperature time histories for lean, $\phi=0.5$, stoichiometric, $\phi=1.0$, and rich, $\phi=2.0$, mixtures. As is expected, the stoichiometric case maintains a higher wall pressure while the detonation wave is still traversing the bypass sector. As the detonation wave is expelled out of the sector, the stoichiometric and rich cases pressure profiles coincide onto each other. The wall pressure for the lean mixture case is, however, predicted to sharply decay to a pressure that is less than the initial pressure. This behavior can also be seen in the temperature profile (Fig. 17). In fact, the reduction in the

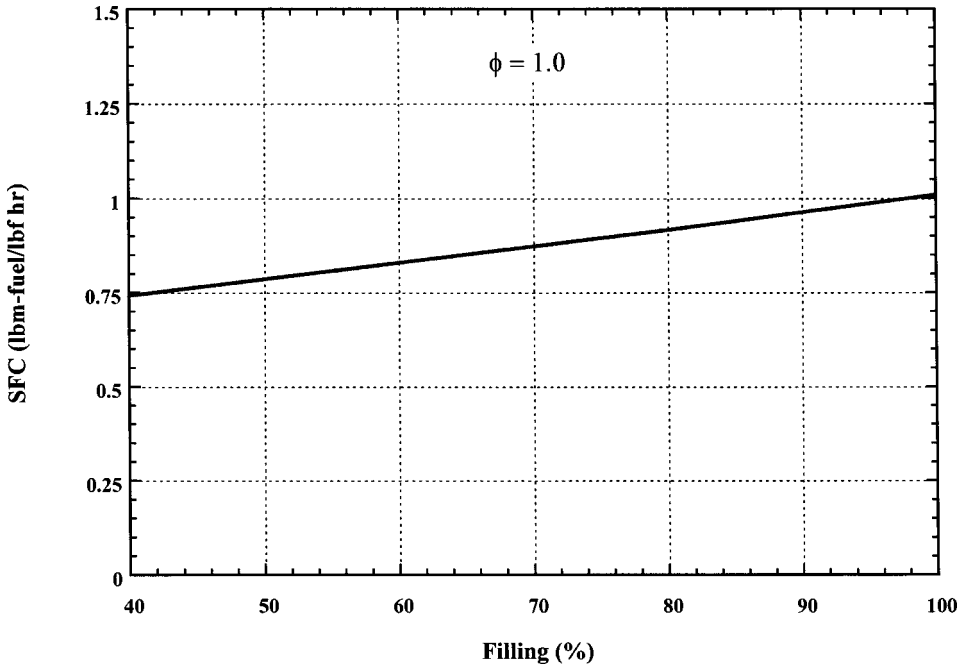

Fig. 23 SFC versus bypass sector filling percentage for different cycle frequencies

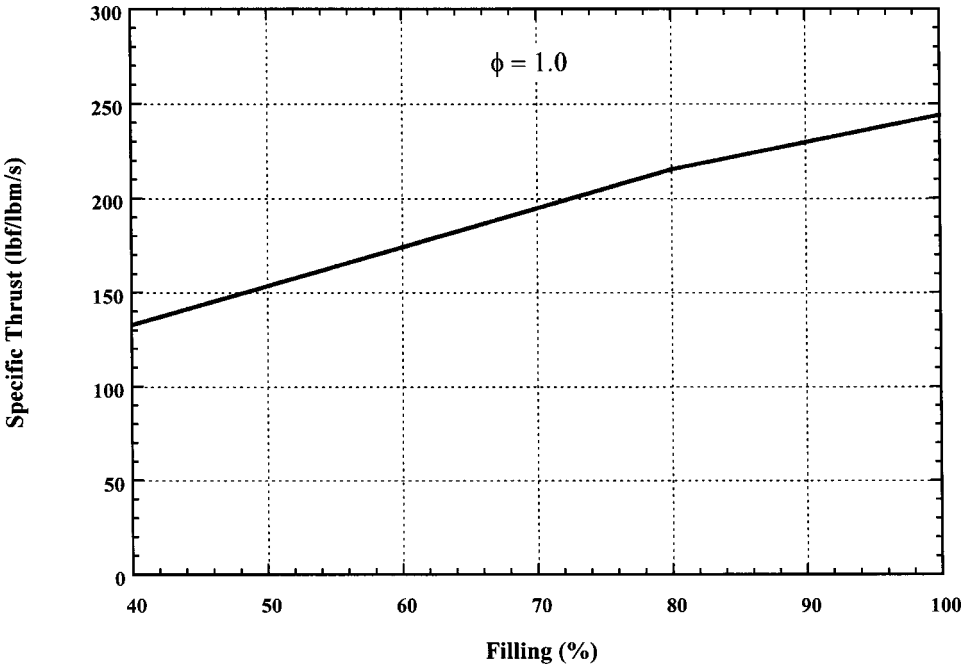

Fig. 24 Specific thrust versus bypass sector filling percentage

heat release and temperature of the reaction zone behind the detonation wave is responsible for the immediate sharp decline in wall pressure.

Figures 18 through 20 display the predicted thrust, SFC, and specific thrust plotted against the initial mixture equivalence ratio and for three different cycle frequencies. Note here that the thrust, SFC, and specific thrust are only for bypass duct alone and no core (dry) engine thrust, fuel flow and air flow were added. It can be seen that the maximum thrust, minimum SFC occur for a stoichiometric mixture, ϕ=1.0. Furthermore, as the cycle frequency is increased, higher thrust, specific thrust, and lower SFC are predicted. In addition, the results show that tradeoffs can be made to optimize performance.

Effect of Sector Partial Fillings. In the above results we assumed that the bypass duct sectors would completely be filled with a premixed fuel-air mixture during every cycle. In reality, however, some sectors may not be filled completely. This could be caused by factors such as distortion of the inlet air profile and fan and bypass sectors rotary valve interaction. As the engine inlet velocity profile is distorted, the average bypass duct inlet velocity of the air flow, upon which the rotary valve motion is designed, is changed. This leads to situations under which the rotary valve is closed before the PD sector is fully filled. It is therefore important to assess the partial filling effect on the performance of the pulse detonation turbofan engine concept as predicted here.

Figure 21 illustrates the predicted wall pressure time history for complete and partial filling of the bypass sector. The initial conditions of temperature and pressure were maintained the same as those of Table 4. The temperature and pressure conditions in the ignition cells were also maintained at 2800 K and 55 atm, respectively. It can be seen that as filling is decreased, the detonation wave is expelled from the sector earlier and the expansion waves traverse towards the sector tube to reduce the wall pressure at an earlier time. Since the average thrust is the area under the pressure-time curve over the cycle time, a reduction in the thrust would, therefore, result, as shown below. It should be indicated here that partial filling of the bypass sectors is equivalent to shortening the sector length with a change in cycle time such as filling time, detonation, and purging times. However, from an engine operational point of view, a variable cycle pulse detonation bypass duct design may not be feasible. This is primarily due to the potential fan bypass duct rotary valve interaction, which could potentially lead to engine fan stall. In the results presented below, the cycle time for 100% filling was therefore used to predict performance.

Figures 22 through 24 show the predicted thrust, SFC and specific thrust as a function of the bypass sector filling percentage. It is seen that the best thrust performance is predicted for 100% filling. The effect of partial filling on SFC is also predicted to diminish.

Conclusions

In this study, the potential performance gain of using pulse detonation combustion in the bypass duct of a turbofan engine was identified. CFD and cycle analyses were used to obtain the bypass duct and engine core performance. The results clearly showed that the pulse detonation turbofan engine concept would have superior performance for an operating frequency of 100 Hz and higher, as compared to the conventional afterburning turbofan engine. A nonideal pulse detonation turbofan engine concept was also analyzed and found to be promising as well. The effect of fuel-air mixture equivalence ratio was also predicted. The results showed that good pulse detonation bypass duct performance can be obtained for lean mixture, provided that cycle frequency is higher than 100 Hz. The effect of bypass sector partial filling was also predicted.

Issues related to interaction between the engine fan and pulse detonation combustion in the bypass duct, fuel-air mixing, liquid fuel injection, and predetonator requirements were not investigated. It should also be indicated that the effect of merging the pulse detonation bypass duct flow with the engine core flow through a nozzle has not been investigated in this study. Moreover, multicycle performance of the new pulse detonation turbofan engine concept still needs to be estimated. The above issues should therefore warrant further investigations of this new pulse detonation turbofan engine concept.

Acknowledgment

The authors would like to thank Dr. Fred Schauer for providing us with the experimental data and operating conditions.

Nomenclature

A = constant cross-sectional area
A/B = afterburner
F_{avg} = average thrust
FPR = fan pressure ratio
f = cycle frequency
OPR = overall pressure ratio
$P(t)$ = unsteady pressure at the tube wall
P_{drag} = pressure acting on left side of thrust wall
PPH = lbm/hr
SFC = specific fuel consumption
T_{cycle} = cycle time
$T_{detonation}$ = detonation time
T_{fill} = filling time
$T_{initiation}$ = initiation time
T_{purge} = purging time
TRIT = turbine rotor inlet temperature
t = time
ϕ = mixture equivalence ratio

References

[1] Lynch, E. D., Edelman, R. B., and Palaniswamy, S., 1992, ''Computational Fluid Dynamic Analysis of the Pulse Detonation Engine Concept,'' AIAA Paper No. 92-0264.
[2] Eidelman, S., Grossmann, W., and Lottati, I., 1990, ''Computational Analysis of Pulsed Detonation Engines and Applications,'' AIAA Paper No. 90-0460.
[3] Eidelman, S., Grossmann, W., and Lottati, I., 1990, ''Air-Breathing Pulsed Detonation Engine Concept: A Numerical Study,'' AIAA Paper No. 90-2420.
[4] Eidelman, S., and Grossmann, W., 1992, ''Pulsed Detonation Engine Experimental and Theoretical Review,'' AIAA Paper No. 92-3168.
[5] Eidelman, S., Grossmann, W., and Lottati, I., 1989, ''A Review of Propulsion Applications of the Pulsed Detonation Engine Concept,'' AIAA Paper No. 89-2446.
[6] Cambier, J. L, and Adelman, H. G., 1988, ''Preliminary Numerical Simulations of a Pulsed Detonation Wave Engine,'' AIAA Paper No. 88-2960.
[7] Bussing, T. R. A., and Pappas, G., 1994, ''An Introduction to Pulse Detonation Engines,'' AIAA Paper No. 94-0263.
[8] Bussing, T. R. A., Hinkey, J. B., and Kaye, L., 1994, ''Pulse Detonation Engine Preliminary Design Considerations,'' AIAA Paper No. 94-3220.
[9] Bratkovich, T. E., and Bussing, T. R. A., 1995, ''A Pulse Detonation Engine Performance Model,'' AIAA Paper No. 95-3155.
[10] Mawid, M. A., Park, T. W., and Sekar, B., 1999, ''Numerical Analysis of Pulse Detonation Engines Using Global and Reduced Hydrocarbon Kinetics,'' AIAA Paper No. 99-4901.
[11] Cambier, J.-L., 1999, ''Preliminary Modeling of Pulse Detonation Rocket Engines,'' AIAA Paper No. 99-2659.
[12] Sekar, B., Palaniswamy, S., Peroomian, O., and Chakravarthy, S., 1998, ''A Numerical Study of the Pulse Detonation Wave Engine with Hydrocarbon Fuels,'' AIAA Paper No. 98-3880.
[13] Lynch, E. D., Edelman, and Palaniswamy, C., 1994, ''Computational Fluid Dynamic Analysis of the Pulse Detonation Engine Concept,'' AIAA Paper No. 94-0264.
[14] Westbrook, C. K., and Pitz, W., 1984, ''A Comprehensive Chemical Kinetic Reaction Mechanism for the Oxidation and Pyrolysis of Propane and Propene,'' Combust. Sci. Technol., **37**, pp. 117–152.
[15] Talley, D., and Schauer, F., 1999, ''Overview of Pulse Detonated Engines (Air Force),'' invited paper at *49th JANNAF Propulsion Meeting*, Tucson, AZ.
[16] Schauer, F., Stutrud, J., and Bradley, R., 1999, ''AFRL's In-House Research Pulse Detonation Engine,'' invited paper at *11th PERC Symposium*, The Pennsylvania State University, University Park, PA, 1999.
[17] Computational Dynamics Limited, 1999, *STAR-CD Manuals*, Version 3.1.
[18] Kailasanath, K., Patnaik, G., and Li, C., 1999, ''Computational Studies of Pulse Detonation Engines: A Status Report,'' AIAA Paper No. 99-2634.

Development of a Temporally Modulated Fuel Injector With Controlled Spray Dynamics

H. Chang
D. Nelson
C. Sipperley
C. Edwards[1]

Thermosciences Division,
Department of Mechanical Engineering,
Stanford University,
Stanford, CA 94305-3032

It is now well established that combustion instability in liquid-fueled gas turbines can be controlled through the use of active fuel modulation. What is less clear is the mechanism by which this is achieved. This results from the fact that in most fuel modulation strategies not only is the instantaneous mass flow rate of fuel affected but so too are the parameters which define the post-atomization spray that takes part in the combustion. Specifically, experience with piezoelectric modulated sprays has shown that drop size, velocity, cone angle, and patternation are all affected by the modulation process. This inability to decouple changes in the fueling rate from changes in the spray distribution makes understanding of the mechanism of instability control problematic. This paper presents the results of an effort to develop an injector which can provide temporal modulation of the fuel flow rate but without concomitant changes in spray dynamics. This is achieved using an atomization strategy which is insensitive to both fuel flow rate and combustor acoustics (an over-pressured spill-return nozzle) coupled with an actuator with flat frequency response (a low-mass voice coil). The design and development of the actuator (and its control system) are described, and a combination of phase-Doppler interferometry and imaging are used to establish its performance. Results show that the system is capable of producing sprays which have little variation in cone angle or spray distribution function despite variations in mass flow rate (number density) of greater than 50% over a range of frequencies of interest for control of combustion instability (10 Hz to 1 kHz).
[DOI: 10.1115/1.1496118]

Introduction

Pressure oscillations in gas turbine combustors can cause serious problems such as flame out and mechanical damage. Because combustor instability is often discovered only during full-scale development and testing, expensive redesigns can result. With the advent of modern sensor and actuator technology, fast, active control strategies can be applied, resulting in significant improvements in combustor stability. Previous work in this area has shown that modulating the mass flow rate of fuel injected into the combustor can be an effective method for reducing pressure oscillations.

Most modulated spray injectors reported to date use piezoelectric materials as their actuation element (Dressler [1], Takahashi et al. [2], Ganji and Dunn-Rankin [3], Chung et al. [4], Wang et al. [5,6], and Sipperley et al. [7,8]). However, as a consequence of its strong frequency-dependent characteristic, piezoelectric-based devices are only effective in certain frequency bands. As a result, actuator frequency response is complex, and dealing with the dynamics of the actuator itself becomes a key implementation issue. Piezoelectric devices also have the disadvantage that the normal range of operating frequencies ($\sim$3–30 kHz) is a poor match to the fundamental frequency of the instability to be controlled ($<$3 kHz).

Figures 1 and 2 illustrate the situation, showing data from a study in which a piezoelectric crystal was used to modulate the pressure (and thereby flow rate) of fuel delivered to a commercial pressure-swirl atomizer (Edwards and Sipperley [9]). Figure 1(*a*) shows a poorly developed, low-pressure operating condition for the nozzle. Figure 1(*b*) shows the nozzle operating with the same average fuel flow rate but with the use of piezoelectric modulation upstream of the nozzle at a frequency of 6 kHz. Comparing the two images it is apparent that modulation has resulted in a significant improvement in fuel dispersion at this underdeveloped flow condition.

What is less apparent is that the droplet size/velocity distribution has also been affected by the modulation. Figure 2 illustrates this, showing the effect of modulation on the Sauter mean diameter (D_{32}) and mean axial velocity (V_z) for this same configuration but operating where the spray is fully developed and reasonably well atomized. Even under well-developed spray conditions,

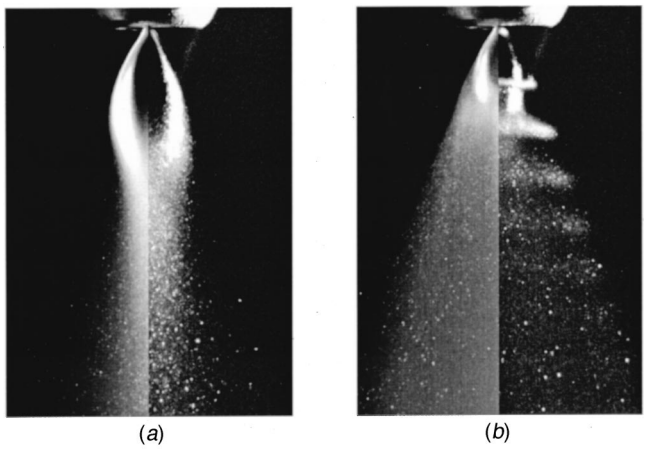

Fig. 1 Spray modulation using a piezoelectric actuator upstream of a pressure-swirl atomizer. The image to the left (*a*) is of an underdeveloped water spray. The image to the right (*b*) is taken with the same average flow rate but using 6 kHz modulation. The left side of each image is a time-averaged exposure while the right is phase-locked to the modulation.

[1]To whom correspondence should be addressed.

Contributed by the International Gas Turbine Institute (IGTI) of THE AMERICAN SOCIETY OF MECHANICAL ENGINEERS for publication in the ASME JOURNAL OF ENGINEERING FOR GAS TURBINES AND POWER. Paper presented at the International Gas Turbine and Aeroengine Congress and Exhibition, New Orleans, LA, June 4–7, 2001; Paper 2001-GT-454. Manuscript received by IGTI, Dec. 2000, final revision, Mar. 2001. Associate Editor: R. Natole.

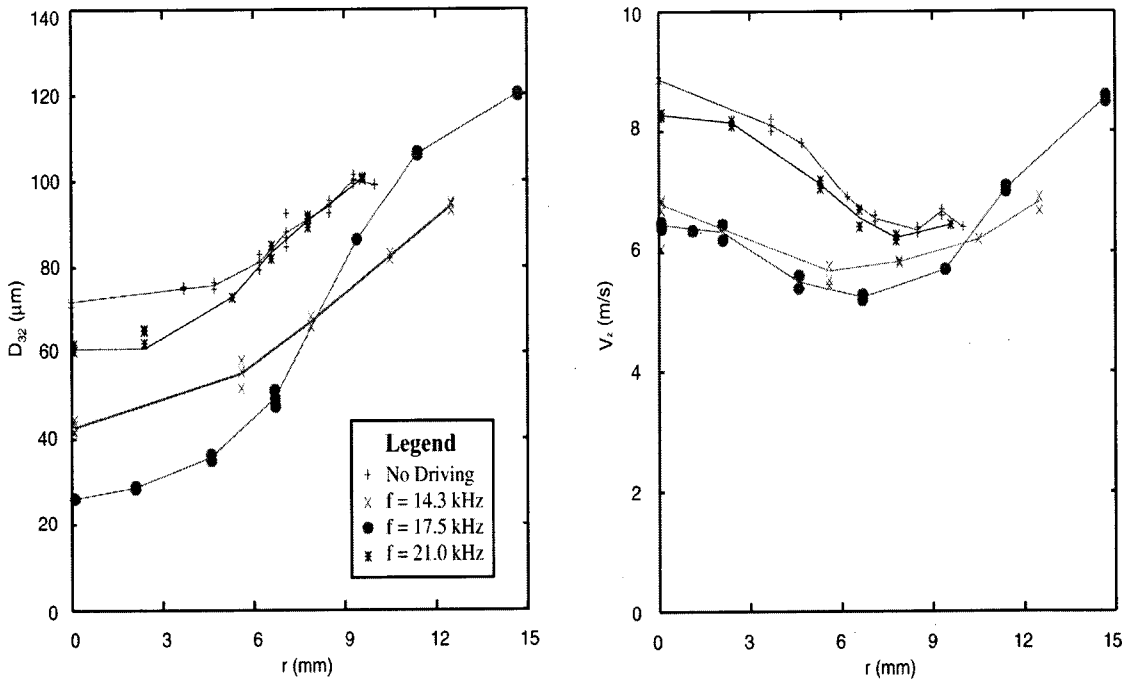

Fig. 2 Effect of piezoelectric modulation on Sauter mean diameter and mean drop velocity. Note the dependence of the drop size, speed, and trajectory on modulation frequency.

modulation can alter the droplet size and velocity distributions; using piezoelectric actuation this effect is a strong function of frequency.

While these results illustrate that the potential exists to significantly alter the spray delivered to the combustor, they also illustrate two problems. The first is a lack of a well-behaved frequency response. Setting aside the fact that the modulation frequency is significantly higher than the frequency of the instability (making direct control via fuel flow rate modulation problematic), the additional issue exists that the response of the atomization is too complex a function of frequency to be used in any but the simplest ways (e.g., on/off control with a fixed modulation frequency). The second problem is that the changes induced by modulation are highly coupled. If modulation is applied with the intent to alter droplet size (and hence evaporation), the fact that drop velocity (and therefore cone angle) is also changed causes difficulties. If modulation is applied with the intent to alter fuel flow rate, the fact that droplet size cannot be decoupled from the modulation causes difficulties. This coupling becomes particularly apparent when a modulated injector is used to control combustion instability. Although combustor acoustic response can certainly be affected by fuel modulation, one has no way of knowing whether the effect is due to evaporation time (drop size and slip velocity), spatial distribution of the fuel (cone angle), or temporal modulation (overall fuel delivery rate). An approach that permits decoupling of fuel flow rate from the spray size/velocity distribution is needed to obtain unambiguous results. Development of such an injector is the objective of this work.

Towards a Modulated Injector With Controlled Spray Dynamics

Achieving modulated injection without affecting spray dynamics requires two elements: an atomization strategy which is independent of flow rate and an actuation strategy that allows flow rate to be modulated with well-behaved, high-bandwidth response. Since a primary interest in developing this actuator is its application to study of combustion instability in a model can combustor, target flow parameters were defined which include a time-average mass flow rate in the range of 1–2 g/s, a modulation frequency range of 10–1000 Hz, and a mass flow rate modulation amplitude of no less than 10% of the mean flow (with an upper target of 50%).

Several candidate atomization strategies were considered for this injector. These included air-assist and air-blast, pressure-swirl, spill-return, ultrasonic, and rotary. The key concept in screening candidate strategies was their ability to provide flow-independent atomization. By this we mean the ability to deliver a spray with a fixed joint size/velocity distribution (and therefore mean diameter, cone angle, etc.) independent of the liquid flow rate (assuming quasi-steady flow). A second constraint was that the method used for atomization should not be affected by the existence of strong acoustics in the combustor. In this way the modulation can be imposed on the combustion process in a way that is independent of combustor state. A third constraint was practicality of implementation—the approach chosen must be easily integrable into an overall combustor control system and potentially applicable to full-scale systems.

These three constraints eliminated the majority of atomization strategies. Pressure-swirl atomization was deemed unsuitable due to the strong dependence of both drop size and cone angle on pressure drop (and therefore flow rate). Air-blast atomization, while extremely attractive from the point of view that air momentum can be used to provide flow-independent atomization, was rejected on the basis that the air pressure drop across the nozzle is

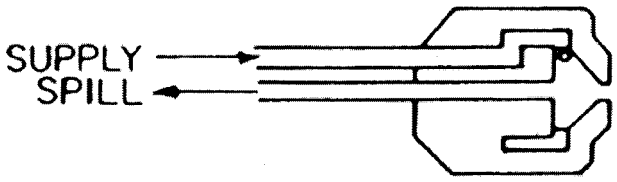

Fig. 3 Schematic of a spill-return nozzle (Lefebvre [10]). While similar to a pressure-swirl atomizer, it includes a return flow path from the swirl chamber which permits the flow rate delivered to the combustor to be decoupled from the pressure drop across the atomizer.

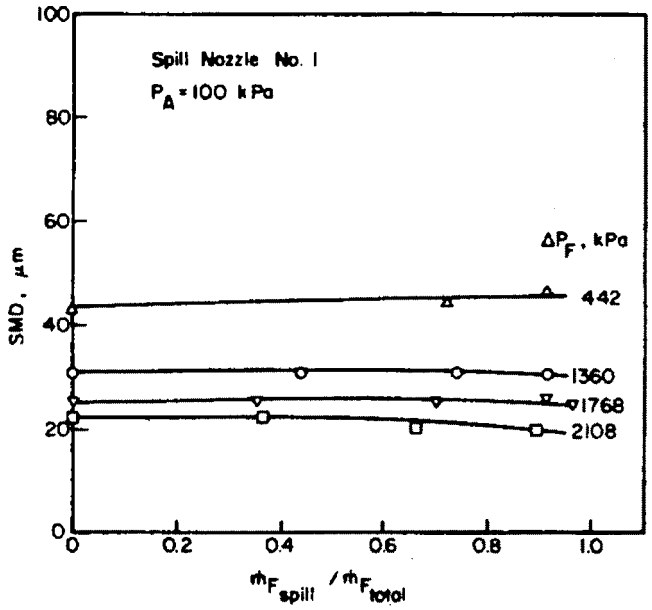

Fig. 4 Sauter mean diameter (SMD) as a function of spilled fraction at fixed overall pressure drop (ΔP_F) injecting into ambient pressure (P_A) (Rizk and Lefebvre [10]). Little effect is observed over a range of conditions approaching 90% turn down in fuel delivery.

of the same order as pressure fluctuations during combustion instability. As such, the primary means for atomization would be coupled to the instantaneous combustor state and controlled spray delivery would not be possible. Use of air-assist atomization (with external air injection at high pressure) was also considered. It has the positive features that both flow-independent atomization and a system with relatively little compliance with combustor acoustics can be achieved (for sufficiently large air pressure drops). But this was rejected as being impractical at large scale and high combustor pressures due to the volume of air that would need to be generated at pressures significantly higher than that of the combustor. Ultrasonic and rotary atomization were rejected on the basis of system complexity, modulation bandwidth, and lack of flow-independent atomization.

The candidate which emerged from these preliminary studies was the spill-return atomizer. Figure 3 shows a simplified schematic from the text of Lefebvre [10]. Similar to the pressure-swirl (simplex) atomizer in many ways, the spill-return atomizer forms a thin sheet of liquid at the inner lip of an orifice by using tangential fuel injection to achieve high internal swirl velocities. This, in turn, allows the development of an internal air core which permits use of a relatively large exit orifice with a substantially smaller liquid film thickness. In the case of the conventional pressure-swirl atomizer, the fact that the liquid flow rate is coupled to the pressure drop (and hence the angular momentum in the swirl cavity and thereby the film thickness) leads to a strong dependence of drop size on flow rate. If an elongated intact liquid sheet exists downstream of the exit orifice, cone angle is also strongly affected.

The spill-return nozzle alleviates some of these problems by allowing a fixed pressure drop to be maintained across the tangential injection ports regardless of delivered flow rate. This is accomplished by always supplying the same flow rate of liquid to the atomizer but then drawing a portion off through the back of the swirl chamber to alter the quantity delivered from the exit orifice.

Figure 4 (Rizk and Lefebvre [11]) shows the effect of spill fraction (the fraction returned to the tank) on Sauter mean diameter at various overall pressure drops (corresponding to $\dot{m}_{F,\text{total}}$). It is apparent that, at least under steady-flow conditions, the Sauter mean diameter can be decoupled from the delivered flow rate. This same observation holds for the size distribution itself (not just its moments), as shown by Rizk and Lefebvre [12].

A potential limitation of the spill-return atomizer is a small dependence of cone angle (and therefore drop velocity vector) on delivered flow rate. Figure 5 shows that some angular redistribution of the spray occurs as the spill fraction is varied. This redistribution is attributable to changes in the intact liquid sheet emerging from the atomizer. As the delivered fraction is increased, the sheet velocity appears to increase (in lieu of its thickness) and the

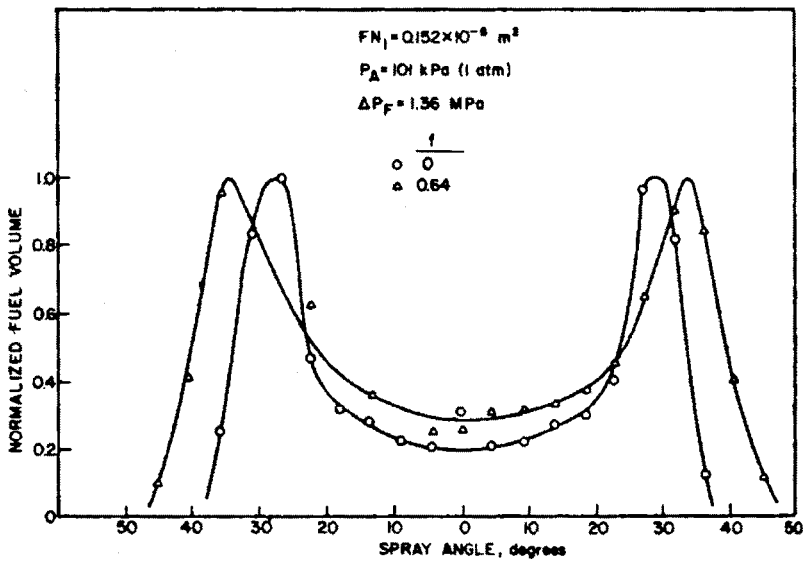

Fig. 5 Spray patternation at full fuel delivery (zero spilled fraction) and with a turn down to 36% delivery (0.64 spilled fraction) (Rizk and Lefebvre [12]). F_N is the flow number of the nozzle.

cone narrows. Note that this can be alleviated to some degree by forcing the breakup to occur close to the filming surface where geometric constraints dominate (i.e., by operating at a high overall pressure drop).

In addition to a flow-independent atomization strategy, an actuation strategy capable of modulating the liquid flow rate in a well-behaved manner at any frequency from a few Hertz to ~1 kHz is needed. Candidate strategies for this task included piezoelectric, voice coil, and solenoid actuators. Piezoelectric actuation was eliminated due to the limited range of motion, mismatch in operating frequency range, and lack of flat frequency response. Solenoids valves have been used in conjunction with pressure-swirl or air-assist atomizers in previous (and current) studies of combustion control (e.g., Yu et al. [13]). While these have been shown to be capable of providing suitable frequency response (~1 kHz), they are digital (on/off) in nature and therefore incapable of providing the sort of arbitrary, smoothly modulated liquid delivery required for achieving control of the spray distribution. Voice coils are capable of operating in a well-behaved, bidirectional, analog fashion over a wide range of displacements and frequencies up to and beyond 1 kHz. As such they are particularly well suited to the present application. A permanent-magnet, linear-motor configuration using a commercial pulse-width-modulated amplifier was chosen for this work.

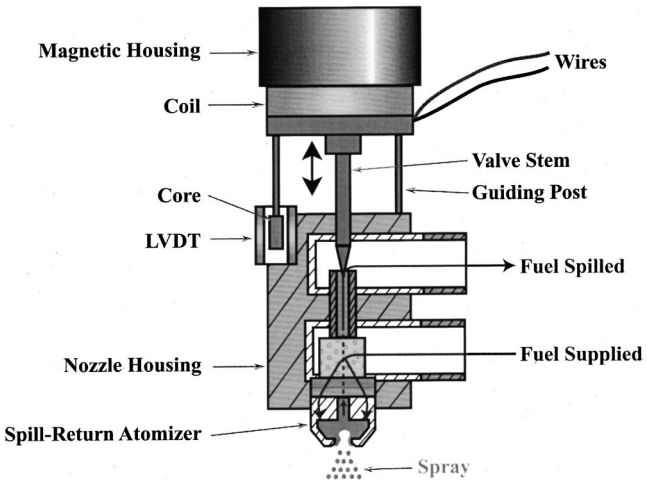

Fig. 6 Integrated actuator/atomizer assembly. The voice coil is used to modulate the spill return flow rate by varying the position of the valve stem. An LVDT is used to provide a position feedback signal to the control system.

Actuator Design and Performance

Figure 6 is a schematic of the integrated atomizer/actuator system. A commercial spill-return nozzle (Delavan Variflo series) was chosen for ease of adaptation and range of available flow numbers and cone angles. This is coupled to a commercial voice coil (BEI LA15) which modulates the position of a tapered valve stem aligned with a seat in the spill port of the atomizer. A linear variable differential transformer (LVDT) is used to provide valve stem position feedback from the modulator. In the current implementation, a peak lift of 0.2 mm is used to achieve a flow rate modulation of approximately 50%.

After developing a dynamic model of the actuator assembly, it was found that a second-order LEAD compensator (Franklin et al. [14]) should be adopted to meet the 1 kHz bandwidth limit. The whole system was tested over the range of 100–900 Hz and its results are shown with a MATLAB simulation plot in Fig. 7.

The test range was inevitably limited up to 900 Hz due to the heat dissipation problem near 1 kHz but the actuator showed stable performance over the frequency range, even though there were some amplitude variations. The test almost covered the required bandwidth. The difference observed in the phase diagram

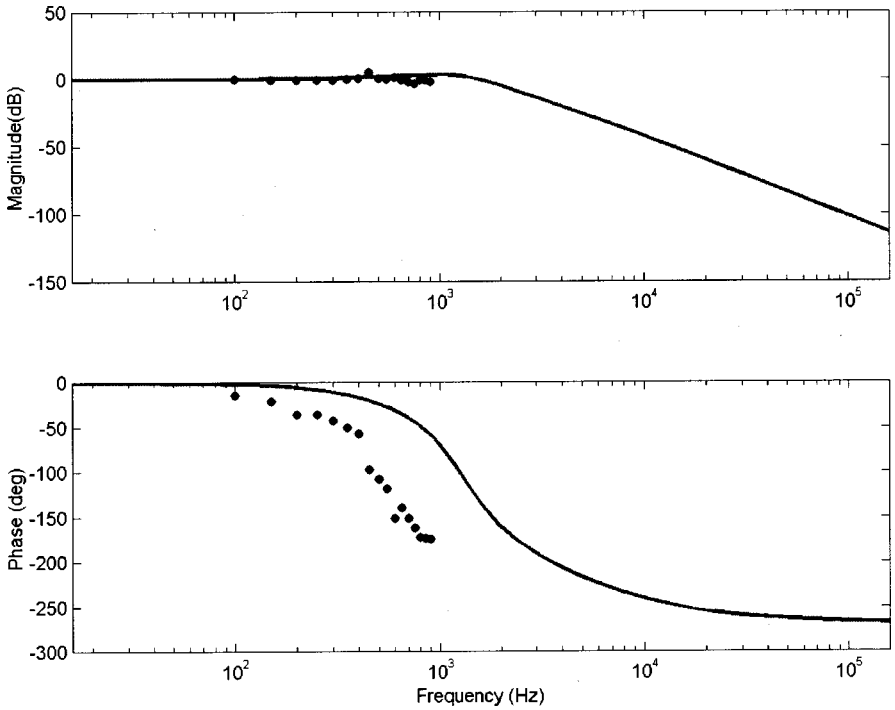

Fig. 7 Closed-loop response of the LEAD-compensated actuator system as a function of modulation frequency. Amplitude response remains flat to ~1 kHz while stable performance is expected up to ~2 kHz. (Dots: real experimental data/Solid line: simulations)

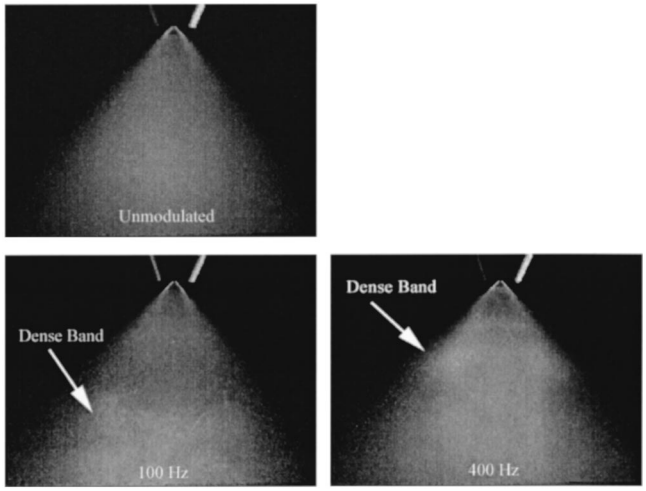

Fig. 8 Strobe-lighted images of overall spray structure with and without modulation. Without modulation a uniform spray field is evident. With modulation, light and dark bands appear, synchronized with the modulation frequency. These bands are advected downstream at the induced flow velocity.

still remains to be explained. Currently it is considered to be caused by a minor modeling error or a classic delay problem caused by the power unit driving the voice coil.

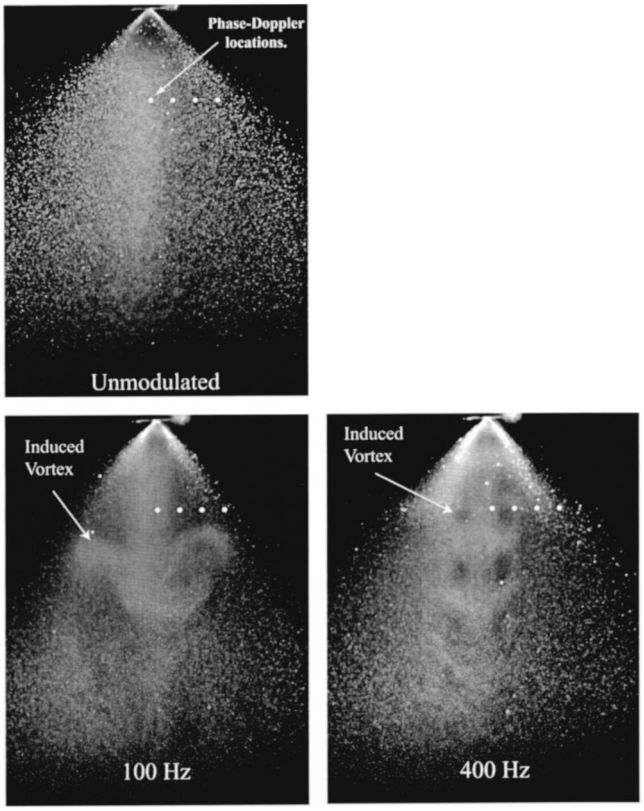

Fig. 9 Laser-sheet images of the internal structure of the spray with and without modulation. Without modulation little internal structure is evident. With modulation, gas-phase vortical structures appear, made evident by preferential droplet transport. These cause the dense bands observed in the overall spray images of Fig. 8. As modulation frequency is increased, the scale of these structures decreases and their spatial frequency rises.

As mentioned above, a considerable amount of heat was generated in exercising the system at high frequencies. It was found that the thermal resistance of the voice coil (~5°C/W) was sufficient to cause the windings to exceed the maximum allowable temperature (155°C) at frequencies above ~450 Hz. For this reason, a provision was made for forced convective cooling inside the actuator. Compressed air (or nitrogen) at room temperature is injected along the central axis of the housing, impinges on the armature, flows through the magnet/winding clearance gap, and exits through the housing/winding gap to the environment. Analysis of the forces introduced by the addition of this cooling flow indicate that they are negligible compared to those required to accelerate the moving assembly.

Spray Performance

Figure 8 shows still images taken using forward scattering from a fast strobe light. While the unmodulated image shows a uniform droplet field, the modulated images show bright bands corresponding to higher-than-surrounding light scattering. These bands appear at the fundamental frequency of the flow modulation, and correspond to regions of enhanced droplet number density.

The detailed structure of these regions is shown more clearly in Fig. 9 where laser-sheet scattering has been used to visualize a slice (~1 mm thickness) through the spray. These images show that modulation of the liquid induces ring vortices in the gas phase which, in turn, are made visible by the droplet clustering they promote. Note the absence of large-scale coherent structures in the unmodulated image. This is consistent with the fact that in none of the cases is there any imposed gas motion—the spray is injected into quiescent surroundings. In the two modulated cases, however, strong, periodic vortices are generated in the gas. In the case of the lower modulation frequency, the scale of the vortices is larger and it appears that they help to advect drops downstream at an

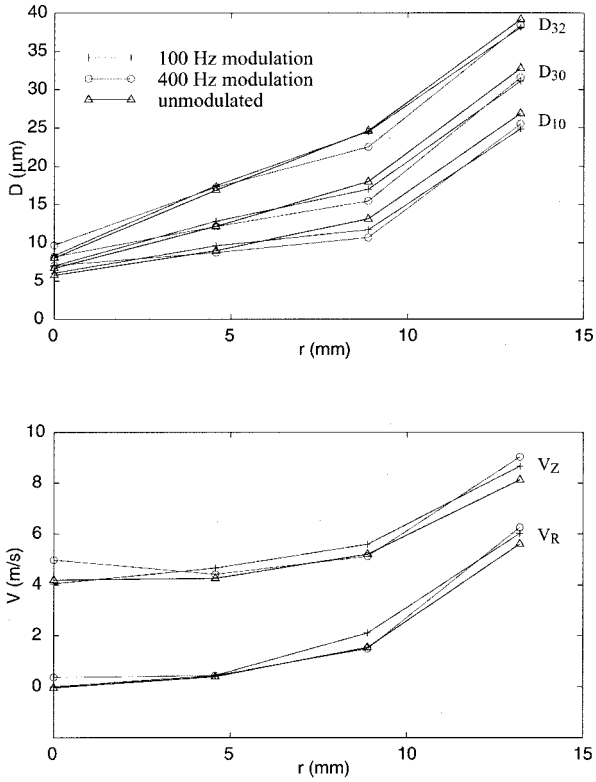

Fig. 10 Time-averaged phase Doppler data taken along a radius 19 mm downstream of the nozzle exit. Neither the mean droplet diameters nor the mean drop velocities are significantly altered by modulation.

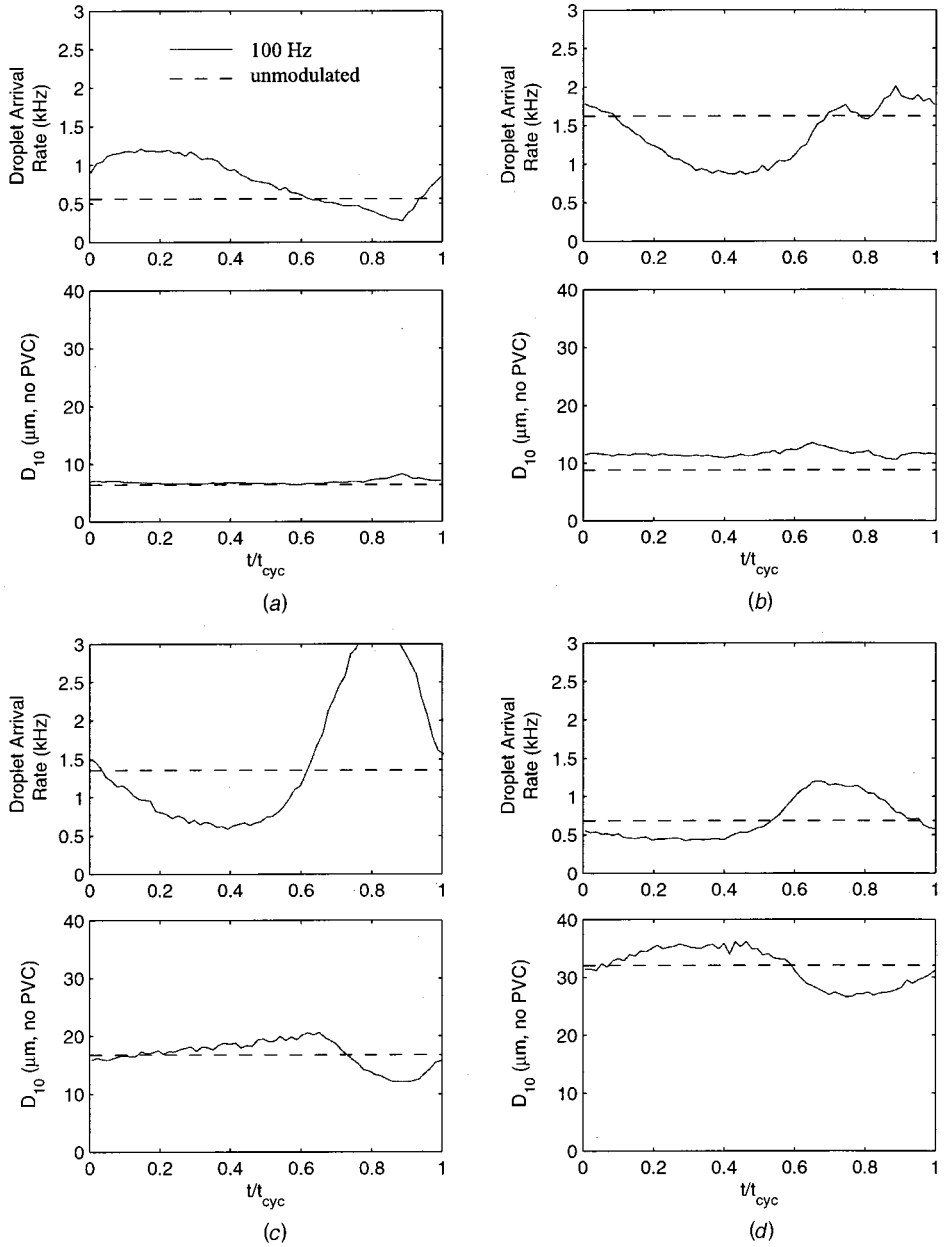

Fig. 11 Phase-averaged droplet arrival rates and droplet mean diameters for 100 Hz modulation spray. Data taken at $z=19$ mm and (*a*) $r=0$ mm, (*b*) $r=4.5$ mm, (*c*) $r=9$ mm, (*d*) $r=13$ mm.

enhanced rate along the axis of the spray. In the case of the higher modulation frequency, the scale is correspondingly reduced, but again enhanced droplet advection along the centerline appears to occur.

Phase Doppler interferometry (PDI) was used to obtain quantitative data about the distribution function of the spray. Data were taken at the four locations depicted in the images of Fig. 9. Figure 10 shows the results of time-averaged measurements of the spray properties. In contrast to the results with piezoelectric modulation (Fig. 2) here little effect of the modulation is evident. This result holds for all three of the commonly used mean diameters—Sauter (D_{32}), volume (D_{30}), and arithmetic (D_{10})—as well as for the ensemble-average (over all droplets) spray velocity components. Taken in conjunction with the images which show moving bands of enhanced light scattering, we conclude that the primary result of the modulation is not to change the spray size/velocity distribution but to modify the number density of drops sourced by the atomizer.

This view—that the primary effect of modulation is to alter the drop number density—is partially confirmed by the phase-resolved PDI data shown in Figs. 11 and 12. Each of these plots shows the overall droplet arrival rate (proportional to flux rate) and the arithmetic mean diameter as a function of command signal phase. These data were calculated by binning the droplet data according to its time of arrival in the modulation cycle and then ensemble averaging over many modulation cycles to obtain converged statistics. Since the unmodulated data have no preferred arrival phase, they appear as the (constant) dashed lines across each plot. Note that the two middle measurement locations correspond to points within the high-flux-rate portion of the spray cone

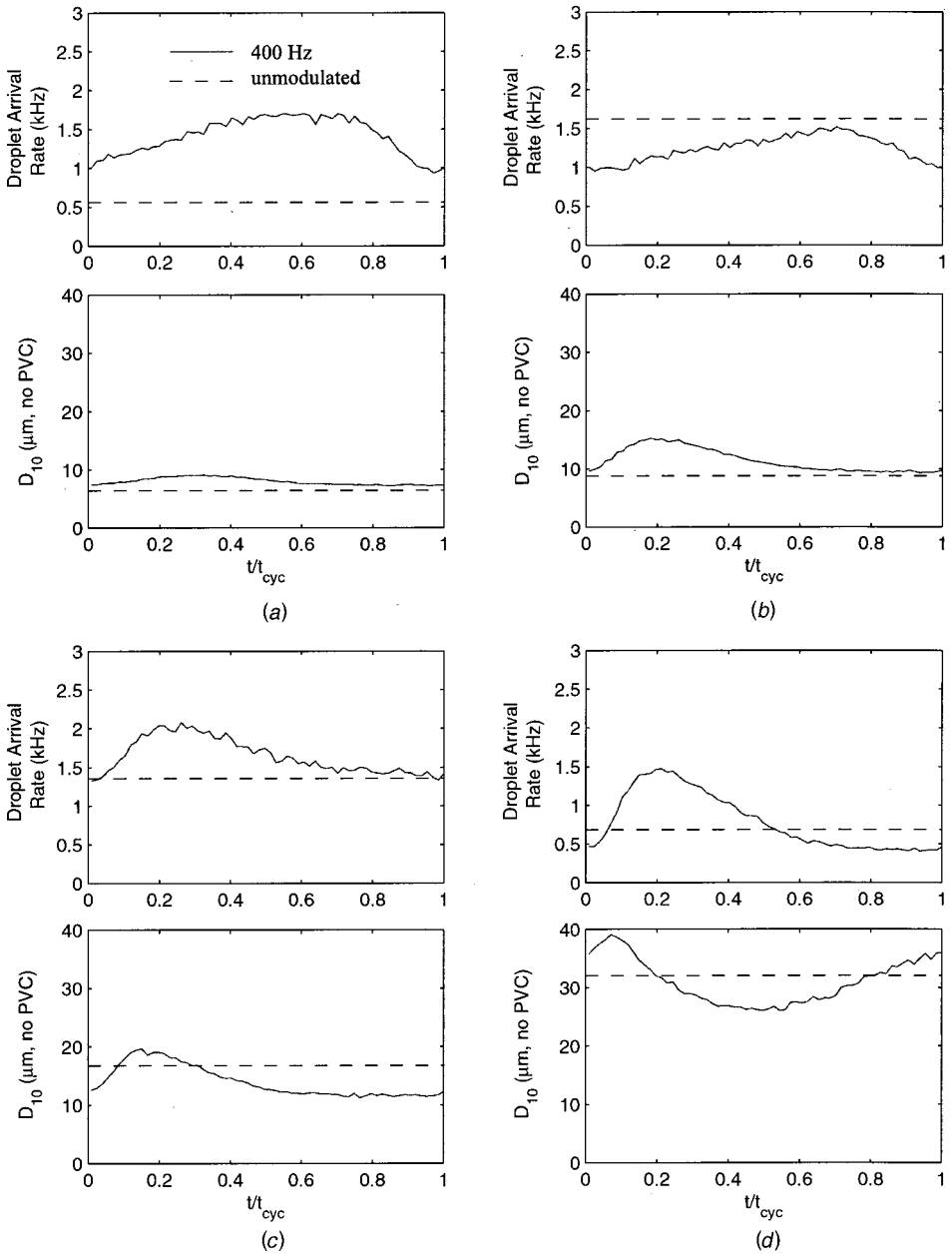

Fig. 12 Phase-averaged droplet arrival rates and droplet mean diameters for 400 Hz modulation spray. Data taken at $z=19$ mm and (*a*) $r=0$ mm, (*b*) $r=4.5$ mm, (*c*) $r=9$ mm, (*d*) $r=13$ mm.

while the two extreme locations (centerline and outer edge) have a considerable influence of gas-phase advection. In each case it is also worth noting that these data do not correspond to what is issuing from the atomizer—or even the end of the breakup region—redistribution effects caused by gas-phase interactions are always present to some extent in spray characterization data.

Despite this caveat, the data show that droplet flux is affected such that variations in arrival rate of about a factor of two are achieved. Considering the 100 Hz case first, it is also apparent that the mean droplet size is only slightly impacted by the modulation. For example, at the 4.5-mm radial location D_{10} is seen to increase slightly at all cycle times in keeping with the time-averaged data of Fig. 10. At the other locations, however, the mean drop size is almost completely unchanged despite the fact that some redistribution of drop size occurs as a function of cycle time. This redistribution is consistent with the kind of gas-phase structure evident in the laser-sheet images of Fig. 9. Small drops that are capable of following the flow are redistributed locally by the vortical structures induced by modulation.

Slightly different results are observed with 400 Hz modulation. Again the droplet flux rate is changed by close to a factor of two, but here the redistribution effect of the vortical structures is even stronger. Note that throughout the cycle time the arrival rate is suppressed at the location corresponding to the inner edge of the spray cone. Inspection of the laser sheet images shows that this is the region that corresponds to where the vortical structures first pick up droplets. These droplets are then transported by the structures toward the centerline where an arrival rate more than double the unmodulated case results. As with the 100 Hz data some evidence of size class correlation with modulation phase is also evident.

Taken together with the time-averaged spray data, the mean

cone angle data, and the imaging data, these data indicate that our original assumption—that flow-independent atomization might be achieved by modulating the spill port of a spill return atomizer—appears to be confirmed. Note too, that while interesting droplet redistribution effects are observed downstream of the atomizer, these are not due to changes in the spray injected but to the way the injected spray is subsequently distributed. Stated another way, we believe that the true (but unmeasurable) time-averaged distribution function of the spray is largely unchanged by the modulation. It is the interaction with the gas phase that induces the structural differences evident in the downstream phase-Doppler data. These differences are unavoidable in well-atomized sprays where the droplet response time is sufficiently small that rapid kinematic equilibration with the ambient gas results. Note too that in a strong convective environment (such as the swirl-induced recirculation zone of a combustor) it is unlikely that these weak vortex structures will persist long enough to significantly affect droplet dispersion. However, since primary atomization is largely unaffected by the downstream convective environment, the modulation will still produce a time-varying spray.

Summary

A temporally modulated fuel injector with controlled spray dynamics has been developed for use in studies of liquid-fueled gas turbine combustion. The primary motivation for developing the injector was to provide a tool which allowed changes in fueling rate to be decoupled from changes in spray structure. Previous systems—particularly piezoelectrically modulated simplex atomizers—have not been able to fulfill this requirement.

Two components were identified as critical to success: use of a flow-independent atomization strategy and use of a flat-frequency-response actuator. A number of atomization strategies were considered. Of these only air-assist and spill-return atomization were found to be suitable. Air-assist was subsequently rejected due to the air-generation requirements at large scale. (Air blast atomization was rejected due to compliance of the atomizing air flow with combustor acoustics.) Use of a spill-return strategy was therefore selected. An additional element in this decision was that modulation of the return flow was thought to be less likely to induce disturbances in the liquid film than upstream (supply-side) modulation. This was critical since there was an implicit assumption in the screening studies that the modulated atomizer performance could be viewed as though the atomizer were passing through a succession of steady states. This idea of quasi-steady modulation is incompatible with strategies that take advantage of dynamic resonances (either in the actuator or the liquid).

The actuator chosen was a high-acceleration, permanent-magnet, voice coil. A commercial unit capable of >200g accelerations and, in our configuration, modulation of spill flow rate up to 50% at frequencies up to 1 kHz, was selected. A suitable feedback sensor and a closed-loop control system were developed and implemented with the required cooling. Combining and testing all the units successfully, the actuator has been operated at frequencies up to 900 Hz, with spray characterizations being performed at lower frequencies (up to 400 Hz). Modifications to provide the required cooling near its frequency limit (1 kHz), and studies up to dynamics-limited performance will occur shortly including the explanation for the differences observed in the phase diagram.

Spray characterization studies indicate that the overall spray structure (joint size/velocity PDF) is not strongly affected by modulation. Time-averaged mean diameters and velocities vary little with operating frequency. Cycle-resolved studies show that droplet flux rates can be changed by more than a factor of two. Since mean velocities are essentially unchanged, these differences can be directly ascribed to a change in the number density of the spray.

An unanticipated side effect of the modulation is generation of a stream of gas-phase vortices that travel downstream along the axis of the injector. While not impacting the atomization process, they do affect post-atomization droplet transport—at least in the present case where no co-flow was used. In application to the gas turbine control problem, where the injector will be mounted in the center of a strongly swirled, turbulent air stream, we anticipate that these vortices will be of little consequence. We note their occurrence with some interest, however, since in another application it may be possible to use them to advantage.

Acknowledgments

Research was sponsored by NASA-Ames Research Center, under the Ultra-Efficient Engine Technologies program, grant NAG2-1219.

References

[1] Dressler, J. L., 1993, ''Liquid Droplet Generator,'' U.S. Patent No. 5,248,087.
[2] Takahashi, F., Schmoll, W. J., and Dressler, J. L., 1995, ''Characteristics of a Velocity-Modulated Pressure-Swirl Atomizing Spray,'' J. Propul. Power, **11**, pp. 955–963.
[3] Ganji, A. R., and Dunn-Rankin, D. 1996, ''Spray Modulation With Potential Application in Gas Turbine Combustors,'' 32nd AIAA/ASME/SAE/ASEE Joint Propulsion Conference, Lake Buena Vista, FL, Paper No. AIAA 96-2625.
[4] Chung, I. P., Dunn-Rankin, D., and Ganji, A. R., 1997, ''Characteristics of a Spray from an Ultrasonically Modulated Nozzle,'' Atomization Sprays, **7**, pp. 295–315.
[5] Wang, D., Ganji, A. R., Sipperley, C. M., and Edwards, C. F., 1997, ''Spray Modulation Characteristics of Simplex Nozzles,'' 9th Annual Conference on Liquid Atomization and Spray Systems, Ottawa, Canada.
[6] Wang, D., Ganji, A. R., Sipperley, C. M., and Edwards, C. F., 1998, ''Characteristics of a Modulated Spray Under High Ambient Pressure,'' 10th Annual Conference on Liquid Atomization and Spray Systems, Sacramento, CA.
[7] Sipperley, C. M., Edwards, C. F., Wang, D., and Ganji, A. R., 1997, ''Effect of Actuation Frequency on RMS Pressure Amplitude and Atomization Quality of Piezoelectrically Modulated Simplex Atomizers,'' 9th Annual Conference on Liquid Atomization and Spray Systems, Ottawa, Canada.
[8] Sipperley, C. M., Edwards, C. F., Wang, D., and Ganji, A. R., 1998, ''Piezoelectrically Driven Simplex Atomizers at Atmospheric Pressure,'' 10th Annual Conference on Liquid Atomization and Spray Systems, Sacramento, CA.
[9] Edwards, C. F., and Sipperley, C. M., 1999, ''Spray Studies of a Modulated Gas Turbine Atomizer,'' final report for Berkeley Applied Science and Engineering, NASA Subcontract No: 96-181-01.
[10] Lefebvre, A. H., 1989, *Atomization and Sprays*, Hemisphere, Washington, DC.
[11] Rizk, N. K., and Lefebvre, A. H. 1985, ''Spray Characteristics of Spill-Return Atomizers,'' J. Propul. Power, **1**, pp. 200–204.
[12] Rizk, N. K., and Lefebvre A. H. 1985, ''Drop-Size Distribution Characteristics of Spill-Return Atomizers,'' J. Propul. Power, **1**, pp. 16–22.
[13] Yu, K. H., Parr, T. P., Wilson, K. J., Schadow, K. C., and Gutmark, E. J., 1996, ''Active Control of Liquid-Fueled Combustion Using Periodic Vortex-Droplet Interaction,'' Twenty-Sixth Symposium (Intl.) on Combustion, The Combustion Institute, Pittsburgh, PA, pp. 2843–2850.
[14] Franklin, G. F., Powell, J. D., and Emami-Naeini, A., 1994, *Feedback Control of Dynamic Systems*, 3rd Ed., Addison-Wesley, Reading, MA.

Investigation of Flow in a Steam Turbine Exhaust Hood With/Without Turbine Exit Conditions Simulated

J. J. Liu

Y. Q. Cui

H. D. Jiang

Institute of Engineering Thermophysics,
Chinese Academy of Sciences,
P. O. Box 2706,
Beijing 100080, P. R. China

Experimental and numerical investigations for the flow in an exhaust hood model of large steam turbines have been carried out in order to understand the complex three-dimensional flow pattern existing in the hood and also to validate the CFD solver. The model is a typical design for 300/600 MW steam turbines currently in operation. Static pressure at the diffuser tip and hub endwalls and at the hood outer casing is measured and nonuniform circumferential distributions of static pressure are noticed. The velocity field at the model exit is measured and compared with the numerical prediction. The multigrid multiblock three-dimensional Navier-Stokes solver used for the simulations is based upon the TVD Lax-Wendroff scheme and the Baldwin-Lomax turbulence model. Good agreement between numerical results and experimental data is demonstrated. It is found that the flow pattern and hood performance are very different with or without the turbine exit flow conditions simulated. [DOI: 10.1115/1.1499726]

Introduction

In a condensing steam turbine, the low-pressure exhaust hood, consisting of a diffuser and a collector (or volute), connects the last stage turbine and the condenser. The function of the hood is to transfer the turbine leaving kinetic energy to potential energy while guiding the flow from the turbine exit plane to the condenser. Most of exhaust hoods discharge towards the downward condenser. Flow inside the hood therefore must turn about 90 deg from the axial direction to the radial direction before exhausting into the condenser. The 90-deg turning results in vortical flow in the upper half part of the collector and also high losses. The exhaust hood is one of the few steam turbine components that has the potential to be improved considerably in the aerodynamic sense. It is a challenge for engineers to design a hood with high-pressure recovery and low total pressure loss in a compact axial length.

Traditional approaches for the design of steam turbine exhaust systems are based upon the experimental data obtained from axial-radial diffuser models and/or exhaust hood models. In those experiments (e.g., Zaryankin et al. [1] and Owczarek et al. [2]), the inflow conditions are usually clean, i.e., without flow swirling and total pressure profile distortion. A well-designed hood under clean inflow conditions does not guarantee satisfactory aerodynamic performance at operational conditions because strong interactions between the last stage turbine and the exhaust hood generate distorted inflow to the hood and hence influence the flow behavior in the hood.

It has been realized that the design of steam turbine exhaust systems should be an interactive process in which the aerodynamic interactions among the last stage turbine, mixed flow diffuser and collector should be considered. In the full-scale tests reported by Gray et al. [3], the hood pressure recovery coefficient can be increased for the same exhaust hood by redesigning the last row of blades, although the pressure recovery coefficient after modifying the blades is only slightly above zero. Full-scale tests can only be done after the steam turbine components have been manufactured and further modifications for either the blades or the hood are usually impracticable. CFD plays a very important role in the design and optimization of turbomachinery blade rows and is being applied to the simulations of flow in steam turbine exhaust hoods (Tindell et al. [4], Deckers and Doerwald [5]) and turbine-exhaust interactions (Benim et al. [6]). Liu [7] developed an approach in which the turbine blade rows are represented by actuator disks and turbine-diffuser-collector interactions are fully considered. Numerical simulation using this approach showed that the hood pressure recovery coefficient of 50 percent is achievable by sensibly controlling the collector cross sections.

The present research combines experimental study and numerical simulations. Measurements aim at providing required data for CFD code validation, whereas simulations provide flow details and help to understand the flow behavior inside the hood. The importance of inlet conditions to hood aerodynamic performance is emphasized.

This paper is organized as follows: after the Introduction, the test facility and test plan are described. The numerical method used for the simulations is then outlined. Experimental results together with numerical ones are presented and compared with each other. The paper ends with conclusions.

Test Facility

The test rig is an open-loop low-speed continuously operating facility with air as the working fluid. General arrangement of the rig is shown in Fig. 1. It consists of a blower, control valve, parallel-convergent inlet, and test section. The test section includes an annular screen, guide vane, and 1/15 hood model, as shown in Fig. 2. The geometry of the diffuser and collector is virtually the same as that of 300/600 MW steam turbines designed by Westinghouse (transferred to China in the 1980s). The nonuniform annular screen was used to generate required total pressure radial distributions and the guide vane to produce required swirling.

Static pressure distributions at the diffuser hub and tip endwalls and at the collector outer casing were measured. There are 5×12 pressure taps at the diffuser hub, 3×12 taps at the diffuser tip, and 6×9 taps at the outer casing. The axial locations of the taps are indicated in Fig. 2, i.e., H1 to H5 for the hub, T1 to T3 for the tip,

Contributed by the International Gas Turbine Institute (IGTI) of THE AMERICAN SOCIETY OF MECHANICAL ENGINEERS for publication in the ASME JOURNAL OF ENGINEERING FOR GAS TURBINES AND POWER. Paper presented at the International Gas Turbine and Aeroengine Congress and Exhibition, New Orleans, LA, June 4–7, 2001; Paper 2001-GT-488. Manuscript received by IGTI, Dec. 2000, final revision, Mar. 2001. Associate Editor: R. Natole.

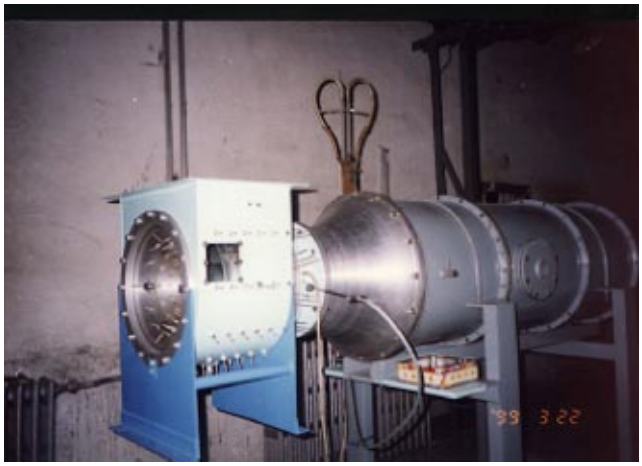

Fig. 1 General arrangement of the rig

and C1 to C6 for the casing. At diffuser hub and tip endwalls, the 12 circumferential locations of the taps are equally distributed (every 30 deg) around the annulus. And so are the circumferential locations for the taps at the collector outer casing, except at the model outlet where three locations are not applicable (see Fig. 3).

Traverses were made by using a five-hole probe at the model inlet, outlet, and diffuser outlet. The model outlet plane is equally divided into 10×20 subareas. Velocity at each subarea center was measured to form the model outlet velocity field. Velocity radial distributions at the model (also diffuser) inlet and diffuser outlet were measured at four circumferential locations corresponding to vertical and horizontal planes. At far upstream, the uniformity of total pressure radial distributions was monitored using a total pressure probe. Mean velocity at far upstream is estimated using the total pressure at midspan and the static pressure at the outer wall in the horizontal plane.

Pressure values from the probes and static pressure taps were obtained by using transducers. The data uncertainties are: the five-hole probe positioning error is ±0.2 mm, flow angle error is ±0.3 deg and transducer error is ±1.5 mm H_2O.

The annular screen and guide vane used in the present research are removable. Two test cases corresponding to clean and distorted inflow conditions are considered. At the clean inflow condition, both annular screen and guide vane are absent. At far upstream, the averaged air speed is 62 m/s, the Reynolds number based on the annulus height (68.03 mm) is 2.8×10^5. At distorted inflow condition, both the annular screen and guide vane are present. The screen is nonuniform in the radial direction, i.e., dense near the endwalls and sparse near the midspan. The resulted total pressure and swirl angle radial distributions at the hood inlet correspond to the turbine exit flow at the design condition. The averaged air speed in this case at far upstream is 47 m/s and the corresponding Reynolds number is 2.1×10^5.

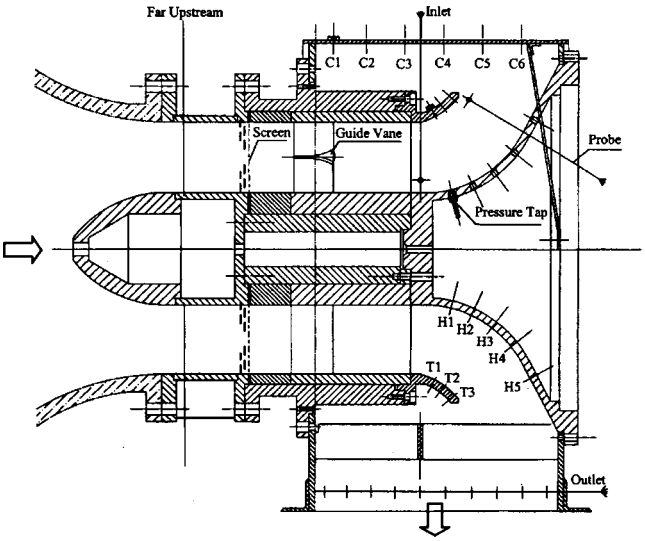

Fig. 2 Schematic of the test section

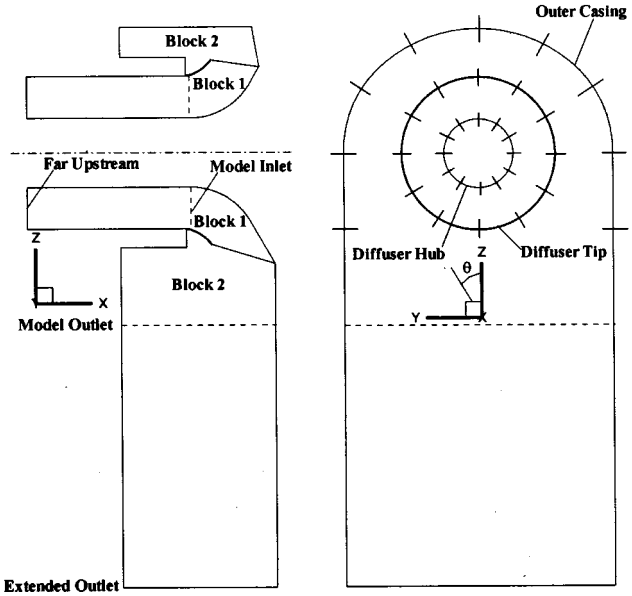

Fig. 3 Diagram of computational domain

Numerical Approach

Solution Method. The three-dimensional flow solver used for the present calculation, named DiscRow, is developed to simulate the asymmetric flow in the turbine exhaust systems and flow in multiple blade-rows. The Reynolds-averaged Navier-Stokes equations are solved by using the cell-vertex finite volume TVD Lax-Wendroff scheme incorporating Roe's approximate Riemann solver (Roe [8]). It is generally recognized that numerical dissipation introduced in a TVD scheme (in order to stabilize the calculations) is minimal, and that Roe's Riemann solver resolves both shear layer and flow discontinuity very well (Van Leer et al. [9]).

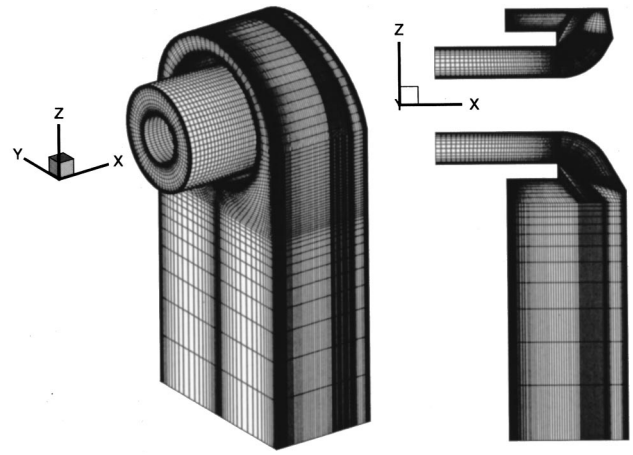

Fig. 4 Three-dimensional hood mesh and a two-dimensional cut

Table 1 Mesh dimensions applied at clean inflows

Notation	Block 1	Block 2	Total Nodes
Mesh 1	113×65×21	85×113×21	355,950
Mesh 2	113×65×25	89×113×25	435,050
Mesh 3	113×65×33	97×113×33	604,098
Mesh 4	113×65×41	105×113×41	787,610

Numerical experiment showed that the application of the TVD scheme is essential for the present flow solver to resolve the vortices in the exhaust hood by using a relatively coarse mesh (compared to the central scheme plus a blend of second-order and fourth-order smoothing).

The turbulent eddy viscosity is estimated by using the Baldwin-Lomax model. In this model a turbulence boundary layer is divided into an inner and an outer region. In the inner region, the eddy viscosity is determined by

$$(\mu_t)_{\text{inner}} = \rho l^2 |\omega| \tag{1}$$

where ρ is the fluid density, l is a length scale proportional to the distance from the wall (scaled by a damping factor D), and ω is the vorticity. In the outer region, the eddy viscosity is given by

$$(\mu_t)_{\text{outer}} = C_{\text{outer}} \rho F_{\text{wake}} F_{\text{kleb}} \tag{2}$$

where C_{outer} is a constant, F_{kleb} is the intermittency factor, F_{wake} is a function of $d_{\max}$, $F_{\max}$, and V_{dif} (difference between maximum and minimum velocity in the profile). $F_{\max}$ is the maximum value of the function $F = d|\omega|D$, and $d_{\max}$ is the distance d (from the wall or wake center) at which this maximum occurs. For a complicated flow field, F may exhibit multiple local maxima. The maximum closest to the wall is chosen in the present implementation. Standard coefficients due to Baldwin and Lomax [10] are used.

In practice, both inner-layer viscosity and outer-layer viscosity are computed for the entire boundary layer and the smaller one is taken as the actual eddy viscosity.

For a complicated flow domain, two solid walls (e.g., A and B) may intersect. The eddy viscosity in this case is first computed according to each of the two walls and then weighted by the distance from the wall to form the effective eddy viscosity,

$$\mu_t = \frac{d_B^2 (\mu_t)_A + d_A^2 (\mu_t)_B}{d_A^2 + d_B^2} \tag{3}$$

where d_A is the distance from wall A, and d_B from the wall B.

The multigrid algorithm (Ni [11]) is applied in the present flow solver to speed up the convergence to a steady state. The multiblock method is also incorporated to handle complicated flow domains. The solution details and applications can be found in Liu and Hynes [12] and Liu [13].

The solver took 0.0385 ms per node per multigrid cycle on a single processor of a Pentium II 400MHz computer. For low-speed test cases presented in this paper, the mass flow rate and the static pressure recovery coefficient (together with residuals) were monitored during the calculation. A converged solution was obtained when the monitored flow quantities stopped changing and it took about 5000 multigrid cycles, or 20 to 40 CPU hours (depending on the total nodes applied) on the single processor computer.

Computational Mesh. Structured hexahedral mesh is used for the present numerical simulation. The computational domain, as shown in Fig. 3, is divided into two blocks, one for the diffuser and upstream extension, and the other for the collector and downstream extension. Meshes for the two blocks are generated using an algebraic method and a Poisson mesh-smoother. The meshes for the individual blocks are patched together to form a multiblock three-dimensional mesh for the whole domain. Boundary nodes are sorted and grouped according to the boundary types so that the boundary conditions can be applied integratively.

The computational domain shown in Fig. 3 has been extended towards the upstream and downstream. The flow near the model outlet appears complicated. It was noticed in the experiments that flow goes inward (or reverse flow) in some regions at the model outlet plane. As a result, calculations cannot converge if static pressure is specified at the model outlet. Specifying measured static pressure distributions instead of uniform back pressure at the model outlet cannot resolve this problem of convergence. It was found that extending the outlet to further downstream so that the reverse flow region is contained in the computational domain can stabilize the calculations. The domain, including upstream extension, is used for one of the calculations at clean inflow conditions.

Figure 4 shows the three-dimensional hood mesh (with upstream extension) and a two-dimensional cut at the central vertical plane. The mesh dimensions of $I \times J \times K$ for block 1 and block 2 are 113×65×25 and 89×113×25, respectively. I, J, and K are the mesh indices corresponding to the coordinate directions of x, θ, and r.

Boundary Conditions. Four types of numerical boundaries exist in the computational domain, namely inlet, outlet, solid wall, and block interface. For the present test cases, both inflow and outflow are subsonic. Distributions of total pressure, total temperature, pitch angle, and swirl angle are specified at the domain inlet, and the averaged static pressure is specified at the domain outlet. Flow is assumed adiabatic at the solid wall. To avoid using an extremely fine mesh near the solid wall, the wall-function due

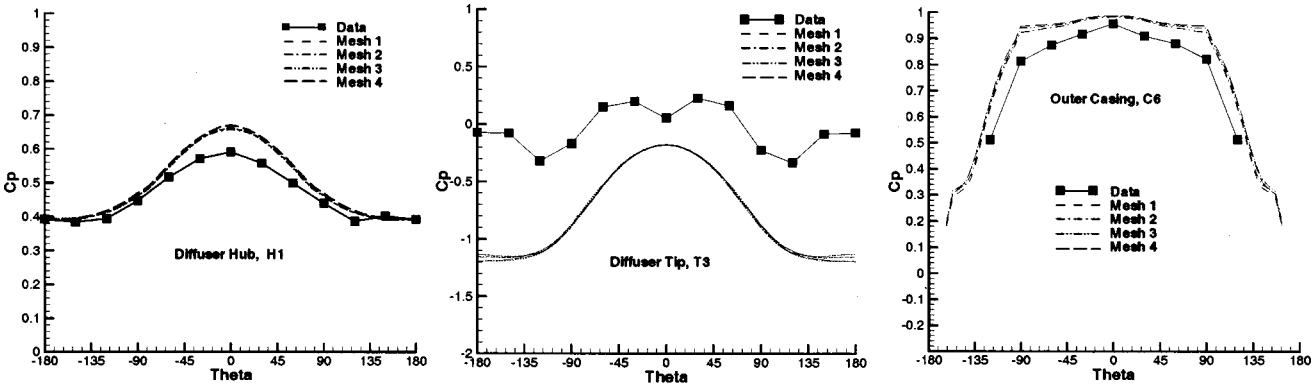

Fig. 5 Static pressure coefficient distributions

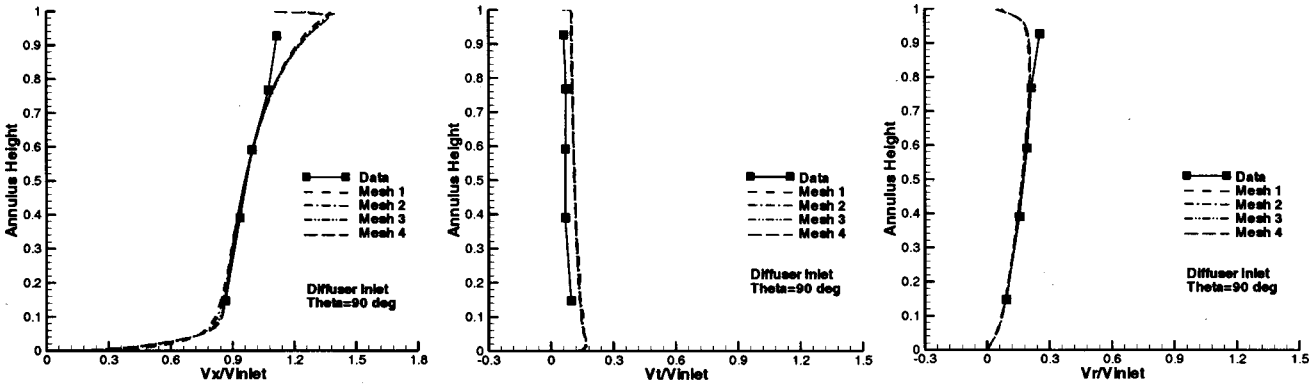

Fig. 6 Velocity distributions at diffuser inlet, θ=90 deg

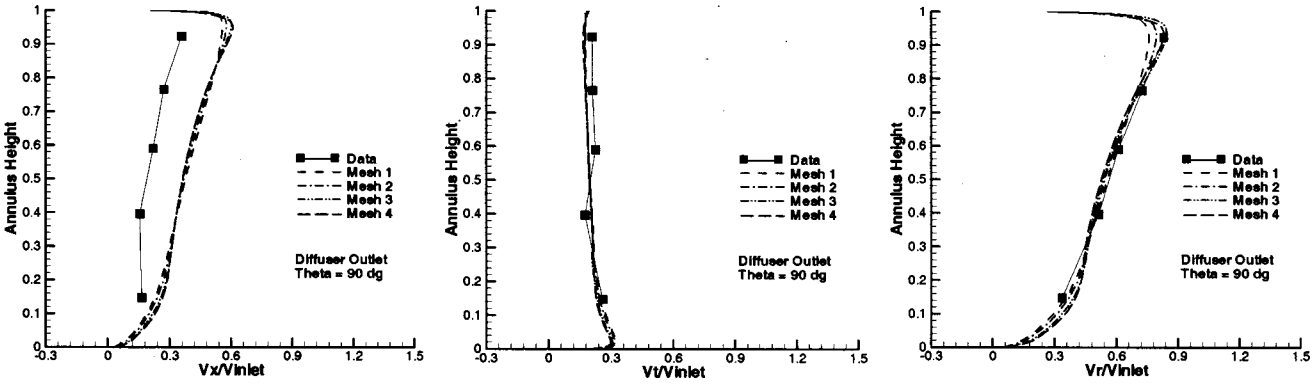

Fig. 7 Velocity distributions at diffuser outlet, θ=90 deg

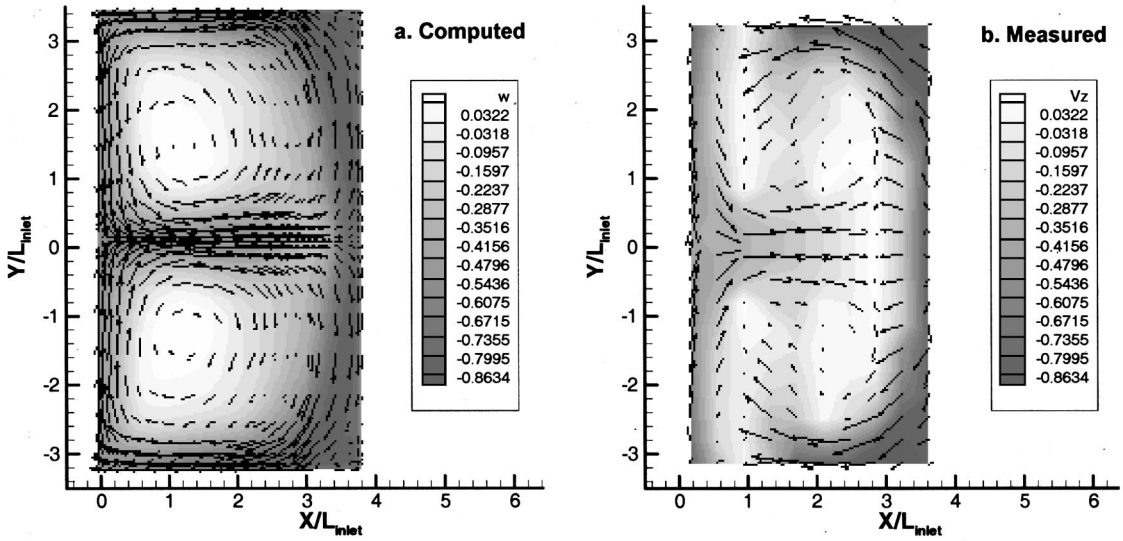

Fig. 8 Comparisons of velocity field at model outlet

to Spalding is applied. Nodal storage of flow variables and one-to-one abutment simplify the boundary treatment at the block interface. Flows of two adjacent blocks are connected by averaging the conservative flow variables corresponding to each side of the interface. A numerical experiment showed that the above treatment gives smooth transit through the interface without using an overlapped mesh.

At far upstream, total pressure, total temperature, swirl angle, and pitch angle are about uniform. Due to the asymmetric hood, the flow at the model inlet is circumferentially nonuniform even at clean inflow conditions (i.e., without the screen and guide vane). Two types of inlet treatments are attempted for the simulations at clean inflow conditions. First, with upstream extension, uniform total pressure and total temperature together with zero pitch angle and zero swirl angle are specified at far upstream. Second, without upstream extension, the measured distributions of total pressure, swirl angle, pitch angle, and uniform total temperature are specified at the model inlet. The second inlet treatment is also used for the simulation at distorted inflow conditions, i.e., specifying the measured distributions of total pressure, swirl angle, pitch angle, and uniform total temperature at the model inlet (without upstream extension).

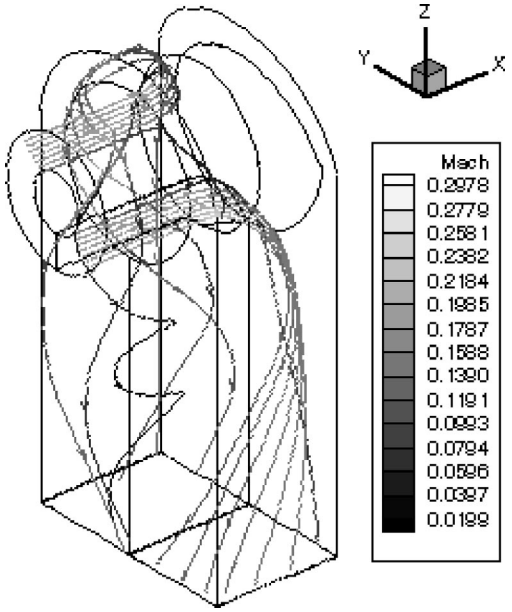

Fig. 9 Streamlines in the hood

Results and Discussions

Clean Inflow Cases. The numerical and experimental results at clean inflow conditions are presented in this subsection. The computational domain for the following simulations is with upstream extension. Total pressure $p_0 = 103{,}140$ Pa, total temperature $T_0 = 293$ K, swirl angle $\alpha = 0$ deg and pitch angle $\gamma = 0$ deg are specified at the far upstream. The freestream Reynolds number based on the annulus height is 2.8×10^5. Uniform static pressure $p_2 = 101{,}100$ Pa is specified at the extended outlet. Four meshes applied in the simulation were illustrated in Table 1. Mesh density is mainly varied in the *K*-direction.

Computed pressure coefficients at the diffuser hub endwall and tip endwall and at the hood outer casing are compared with the experimental data. Numerical and experimental results at location H1 of the diffuser hub, location T3 of the diffuser tip, and location C6 of the outer casing are presented in Fig. 5, where the theta is defined as $\theta = \arctan(y/z)$. It can be seen that the static pressure is circumferentially nonuniform, i.e., pressure is high near the hood top ($\theta = 0$ deg) and low near the hood bottom ($\theta = \pm 180$ deg). The nonuniform pressure distributions are caused by the one-side discharge hood. Good comparisons between numerical and experimental results are noticed at location H1 and C6, variations are observed at location T3. In the experiment, flow separation was noticed at the diffuser tip endwall near $\theta = \pm 180$ deg (location T3 was in the separation region). In the calculation, however, the flow was accelerated along the diffuser tip endwall and the flow separation was not predicted. The present calculation may indicate that the Baldwin-Lomax model is inadequate to predict this flow separation. Calculations including the cross-type struts at the model outlet showed that the struts had negligible influence on the static pressure distributions. The fact of good agreement between the calculation and experiment at location H1 and C6 but discrepancy at location T3 suggested that the effect due to the flow separation was restricted to the diffuser tip region.

Computed velocity radial distributions at four traverse locations of diffuser inlet (also model inlet) are compared with the experiment. Numerical and experimental results at the horizontal plane ($\theta = 90$ deg) are presented in Fig. 6. The distributions of computed three velocity components v_x, v_t, and v_r are well compared with the experimental data, except near the tip endwall the predicted axial velocity is slightly higher than the measurement. It has been

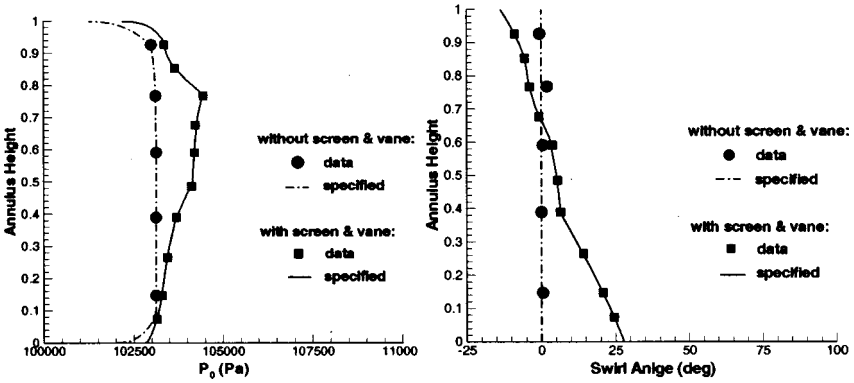

Fig. 10 P_0 and α distributions at model inlet, $\theta = 0$ deg

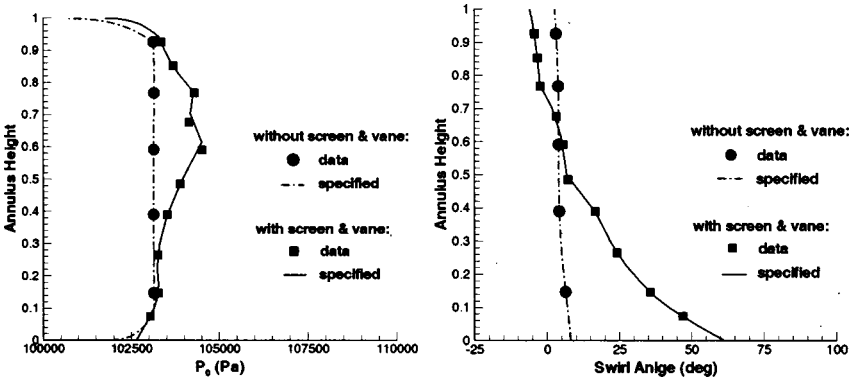

Fig. 11 P_0 and α distributions at model inlet, $\theta = 90$ deg

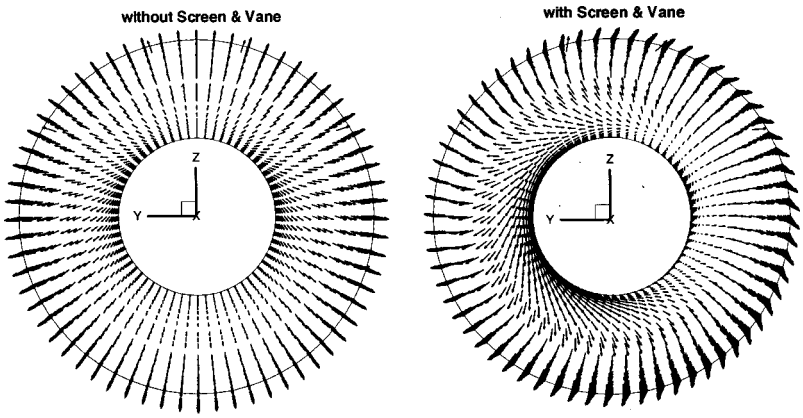

Fig. 12 Velocity vectors at model inlet

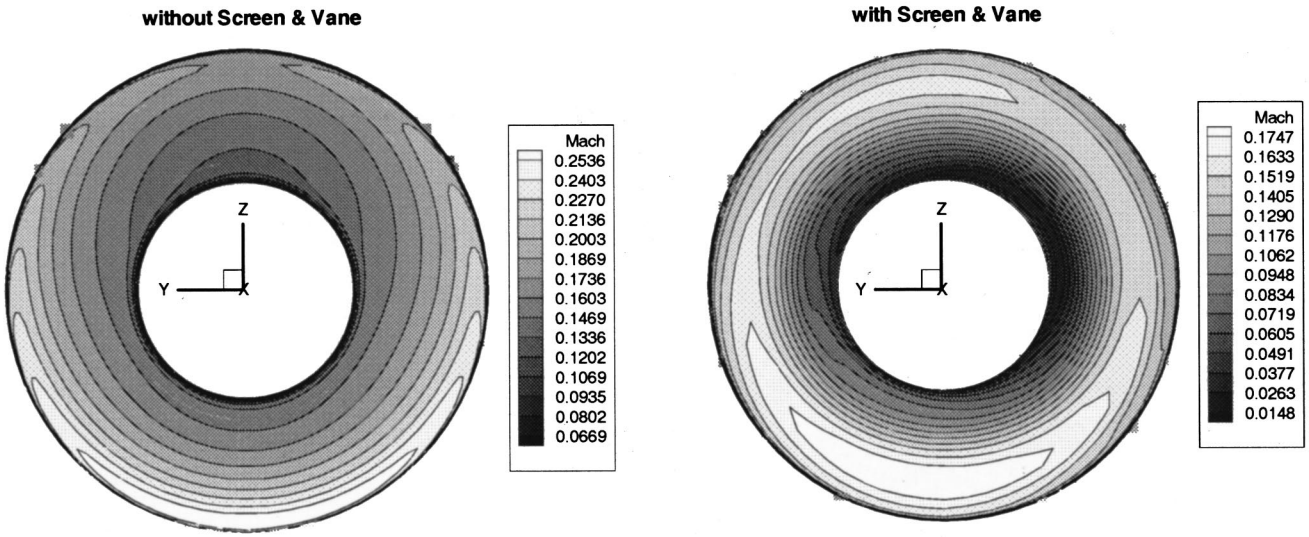

Fig. 13 Mach contours at model inlet

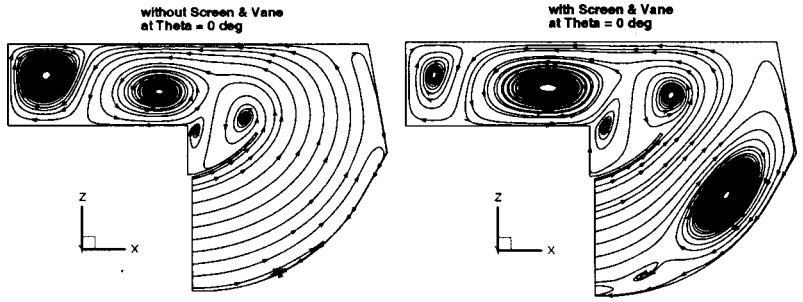

Fig. 14 Stream traces at section of θ=0 deg

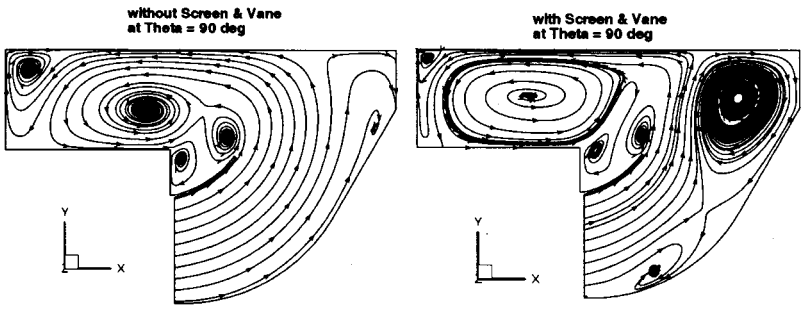

Fig. 15 Stream traces at section of θ=90 deg

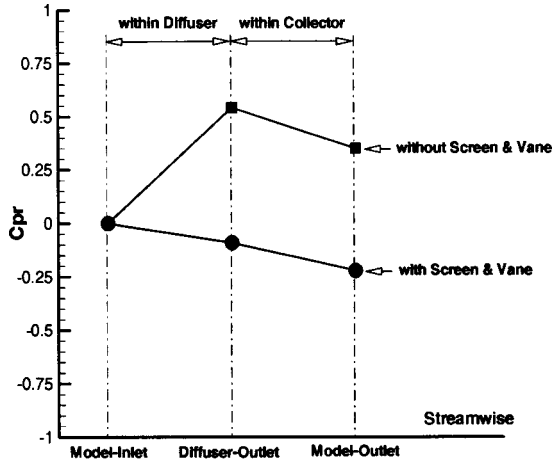

Fig. 16 Computed *Cpr* within the diffuser and collector

mentioned earlier that the swirl angle at far upstream is set to zero. Figure 6 showed that the tangential velocity at the model inlet differs from zero at the annular location of $\theta=90$ deg, which indicated that the swirl angle at the model inlet is nonuniform around the annulus.

Computed velocity radial distributions at four traverse locations of the diffuser outlet are also compared with the experiment. Figure 7 presents the comparisons at $\theta=90$ deg. The computed v_t and v_r coincide with the measurement. The predicted v_x is higher than the measured data, though the trend is the same.

Due to the high-resolution TVD scheme applied in the solver, the numerical solutions are not particularly sensitive to the mesh density of Mesh 1 to 4. Numerical results showed that Mesh 2 is a good compromise between accuracy and computational efficiency and is adequate to capture the main flow patterns inside the hood, although using more nodes can resolve the boundary layer more accurately and can provide more flow details.

The computed (using Mesh 2) and measured velocity fields at the model outlet are given in Fig. 8, in which contours represent the velocity component (i.e., w or v_z) perpendicular to the x-y plane. Negative w or v_z means flow going out of the hood. In this section, flow discharges mainly along the endwalls. The numerical simulation predicted a pair of passage vortex and a pair of corner vortex, which are consistent with the measurement.

The computed streamlines (using Mesh 2) starting from two radial lines at far upstream are given in Fig. 9. In the upper half part of the hood, the flow turns into the hood collector (or volute) before discharging downwards to the hood exit. In the lower half part, in contrast, the flow directly discharges downwards along the hood endwalls. Vertices formed in the volute are the origins of the passage vortex shown in Fig. 8.

Clean/Distorted Inflow Cases. To understand the influence of inflows to the hood performance, simulations at clean and distorted inlet conditions were carried out. The computational domain used for the two simulations is without upstream extension in order to allow for straightforward comparisons. The two simulations utilize the same mesh, $65\times65\times25$ for block 1 and $89\times113\times25$ for block 2.

Boundary conditions applied at the numerical inlet (identical to the model inlet) are the flow variables measured at four circumferential locations of $\theta=\pm180$ deg, -90 deg, 0 deg, $+90$ deg. At the inlet, the measured and specified total pressure P_0 and swirl angle α distributions for the circumferential locations of $\theta=0$ deg, $+90$ deg at the clean (without screen and vane) and distorted (with screen and vane) inflow conditions are shown in Fig. 10 and Fig. 11. The specified P_0 and α were interpolated from the measured values, except near the endwalls where the total pressure was modified to fit in with the turbulent boundary layer.

Without the screen and vane, the total pressure is uniform in the main stream; the swirl angle is zero at $\theta=0$ deg and slightly differs from zero at $\theta=+90$ deg. With the screen and vane, the required total pressure profile is produced; the swirl angle near the hub endwall at $\theta=+90$ deg is quite large.

Figures 12 and 13 present inlet velocity vectors and Mach contours at the clean and distorted inflow conditions. The flow is indeed nonaxisymmetric. It is clearly seen that the swirl angle is not zero even without the guide vane. The guide vane was designed to generate a swirling flow with $+15$ deg swirl angle at the hub and -15 deg at the tip (linearly distributed from the hub to tip). The actual swirl angle distribution with the guide vane (see also Fig. 10 and Fig. 11) is close to the trend of design in the tip region and very different with the trend of design in the hub region. The velocity is usually low near the top and high near the bottom. At distorted inflows, a low-speed region is noticed around the hub.

Stream traces have been plotted at a number of sections in order to investigate the impacts of inlet conditions on the flow patterns inside the hood. Figures 14 and 15 showed the stream traces at two sections of $\theta=0$ deg and $\theta=+90$ deg. At clean inflow conditions, no large separation or vortex is observed within the diffuser. At distorted inflow conditions, however, large vortex is noticed in the diffuser at section of $\theta=0$ deg and the vortex moves backwards to the diffuser exit at the section of $\theta=90$ deg. This vortex markedly reduces the effective area of the diffuser and therefore reduces the diffuser pressure recovery capability (see Fig. 16). In the collector, two pairs of vortices are noticed at both sections for the clean and distorted inflows.

The computed capabilities of static pressure recovery for the diffuser and collector at the clean and distorted inflows are summarized in Fig. 16. Pressure recovery within the collector is negative and at about the same level for the two inflow conditions. The pressure recovery within the diffuser is over 50 percent at the clean inflow and -10 percent at the distorted inflow due to the reduction of the effective diffuser area. Significant difference in overall hood pressure recovery was confirmed by the varying of inlet conditions. As mentioned earlier, radial traverses were performed at only four circumferential locations at the diffuser inlet and outlet. The measured data were not adequate to get reliable mass-flow-averaged total pressure and static pressure. The comparisons between the predicted static pressure recovery coefficients and the measured ones are not applicable.

Conclusions

Numerical and experimental investigations for the flow in a laboratory hood model at clean and distorted inlet conditions were presented. The influence of inlet conditions on the flow pattern inside the hood and on the diffuser and/or hood performance was discussed. Hood overall pressure recovery is determined by the performance of the diffuser and collector. Pressure recovery is unlikely acquired by the collector but is by the diffuser. The diffuser performance is strongly influenced by the inflow conditions, as well as the conditions of outflow. To obtain satisfactory hood pressure recovery, it is suggested to design a diffuser that can work effectively in the actual environment.

Acknowledgments

The authors gratefully acknowledge the support provided by the Knowledge Innovation Program of the Chinese Academy of Sciences and the National 973 Program of China.

Nomenclature

Cp = pressure coefficient, $(p-\overline{p}_1)/(\overline{p}_{01}-\overline{p}_1)$
Cpr = pressure recovery coefficient, $(\overline{p}-\overline{p}_1)/(\overline{p}_{01}-\overline{p}_1)$
I,J,K = mesh indices
d = distance from the wall

p = static pressure
p_0 = total pressure
T_0 = total temperature
v_x = axial velocity
v_t = tangential velocity
v_r = radial velocity
x,y,z = Cartesian coordinates
x,θ,r = cylindrical coordinates
α = swirl angle, $\arctan(v_t/v_x)$
γ = pitch angle, $\arctan(v_r/v_x)$
μ_t = eddy viscosity
$\underline{\ }$ = mass-flow-averaged quantity
$_1$ = inlet

References

[1] Zaryankin, A. E., Zatsepin, M. F., and Shakh, R. K. D., 1966, ''Effect of the Geometrical Parameters on the Operation of Annular Mixed Flow Diffusers,'' Therm. Eng., **13**, pp. 39–43.

[2] Owczarek, J. A., Warnock, A. S., and Malik, P., 1989, ''A Low Pressure Turbine Exhaust End Flow Model Study,'' *Latest Advances in Steam Turbine Design, Blading, Repairs, Condition, Assessment, and Condenser Interactions*, D. M. Rasmussen, ed., ASME, New York, **7**, pp. 77–88.

[3] Gray, L., Sandhu, S. S., Davids, J., and Southal, L. R., 1989, ''Technical Considerations in Optimizing Blade-Exhaust Hood Performance for Low Pressure Steam Turbines,'' *Latest Advances in Steam Turbine Design, Blading, Repairs, Condition, Assessment, and Condenser Interactions*, D. M. Rasmussen, ed., ASME, New York, **7**, pp. 89–97.

[4] Tindell, R. H., Alston, T. M., Sarro, C. A., Stegmann, G. C., Gray, L., and Davids, J., 1996, ''Computational Fluid Dynamics Analysis of a Steam Power Plant Low Pressure Turbine Downward Exhaust Hood,'' ASME J. Eng. Gas Turbines Power, **118**, pp. 214–224.

[5] Deckers, M., and Doerwald, D., 1997, ''Steam Turbine Flow Path Optimizations for Improved Efficiency,'' Power-Gen Asia'97, Singapore, Sept. 9–11.

[6] Benim, A. C., Geiger, M., Doehler, S., Schoenenberger, M., and Roemer, H., 1995, ''Modeling the Flow in the Exhaust Hood of Steam Turbines Under Consideration of Turbine-Exhaust Hood Interaction,'' First European Congress on Turbomachinery Fluid Dynamics and Thermodynamics Aspects, Mar. 1–3.

[7] Liu, J. J., 1998, ''The Calculation of Asymmetric Flow in Turbine Exhaust Systems,'' Ph.D thesis, Cambridge University Engineering Department, Cambridge, United Kingdom.

[8] Roe, P. L., 1981, ''Approximate Riemann Solvers, Parameter Vectors and Difference Scheme,'' J. Comput. Phys., **43**, pp. 357–372.

[9] Van Leer, B., Thomas, J. L., Roe, P. L., and Newsome, R. W., 1987, ''A Comparison of Numerical Flux Formulas for Euler and Navier-Stokes Equations,'' AIAA Paper No. 87-1104.

[10] Baldwin, B. S., and Lomax, H., 1978, ''Thin Layer Approximation and Algebraic Model for Separated Turbulent Flows,'' AIAA Paper No. 78-257.

[11] Ni, R. H., 1989, ''Prediction of 3D Multi-Stage Turbine Flow Field Using a Multiple-Grid Euler Solver,'' AIAA Paper No. 89-0203.

[12] Liu, J. J., and Hynes, T. P., 2000, ''A Navier-Stokes Solver Using Edge-Based Smoothing,'' *Proceedings of First International Conference on Computational Fluid Dynamics*, July 2000, Kyoto, Japan, Springer, Berlin, pp. 313–318.

[13] Liu, J. J., 2000, ''Numerical Simulation of 3D Viscous Flows using Multigrid Multiblock Method,'' J. Eng. Thermophys., **23**(1) (in Chinese).

Inlet Fogging of Gas Turbine Engines Detailed Climatic Analysis of Gas Turbine Evaporation Cooling Potential in the USA

M. Chaker
C. B. Meher-Homji
T. Mee III
A. Nicholson

Gas Turbine Division,
Mee Industries, Inc.,
204 West Pomona Avenue
Monrovia, CA 91016

Inlet fogging of gas turbine engines has attained considerable popularity due to the ease of installation and the relatively low first cost compared to other inlet cooling methods. With increasing demand for power and with shortage envisioned especially during the peak load times during the summers, there is a need to boost gas turbine power. There is a sizable evaporative cooling potential throughout the world when the climatic data is evaluated based on an analysis of coincident wet bulb and dry bulk information. These data are not readily available to plant users. In this paper, a detailed climatic analysis is made of 122 locations in the U.S. to provide the hours of cooling that can be obtained by direct evaporative cooling. These data will allow gas turbine operators to easily make an assessment of the economics of evaporative cooling. The paper also covers an introduction to direct evaporative cooling and the methodology and data analysis used to derive the cooling potential in different regions of the U.S. Simulation runs have been made for gas turbine simple cycles using a reference plant based on a GE Frame 7111EA gas turbine at the 122 locations studied in the U.S. to provide a feel for the sensitivity of operation with inlet fogging. [DOI: 10.1115/1.1519266]

1 Introduction

Gas turbine output is a strong function of the ambient air temperature with power output dropping by 0.3–0.5% for every 1°F (0.5–0.9% for every 1°C) rise in ambient temperature. On several heavy frame gas turbines, power output drops of around 20% can be experienced when ambients reach 95°F (35°C), coupled with a heat rate increase of about 5%. Aeroderivative gas turbines exhibit even a greater sensitivity to ambient conditions. Figure 1 derived by examining several turbines provides a representation of the power boost capability for different types of gas turbines. This was derived using GTPRO[1] software over a range of turbines. This loss in output presents a significant problem to utilities, cogenerators, and IPPs when electric demands are high during the hot summer months. In the petrochemical and process industries, the reduction in output of mechanical drive gas turbines often curtails plant output. For example, at some LNG plants, production may have to be curtailed during the hot afternoons when the refrigeration capacity is limited by gas turbine driver power. One way to counter this drop is to cool the inlet air. While there are several cooling technologies available, fogging has seen large-scale application because of the advantage of low first cost when compared to other techniques including media evaporative cooling and refrigeration technologies[2].

One obstacle faced by gas turbine users in analyzing the potential for fog evaporative cooling is that there is sparse climatic data available in a form that users can make a decision on the benefits of evaporative cooling. The obstacle may be broken into two factors:

1 Operators cannot easily locate the appropriate weather data for their site. Much of the data are available at a plant site may be based on *average* data points with no representation of the values of *coincident* dry and wet bulb temperatures. These data are invaluable when evaluating any evaporative cooling solution.

2 Even when some appropriate data are available through web sites or other sources, the data tables and information are not in a format to enable an operator to rapidly access the potential of evaporative cooling. The data have often to be considerably massaged and collated before any meaningful estimate can be made of cooling potential at the site.

This paper will provide a detailed analysis of multiple locations in the U.S. providing useful climatic data which allows users to evaluate the power augmentation potential available. To our

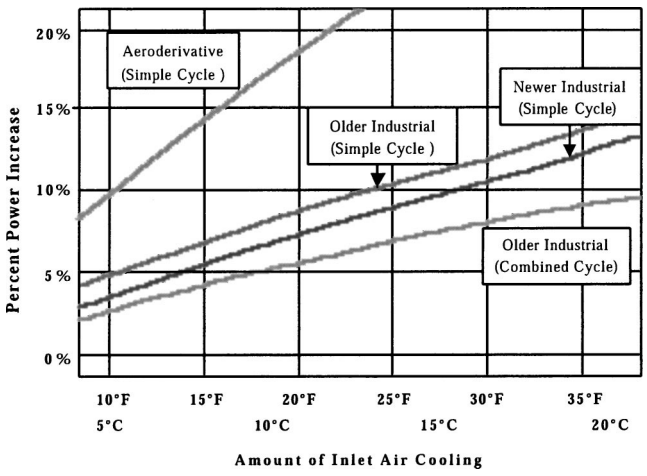

Fig. 1 Representation of power boost possible by inlet cooling

Contributed by the International Gas Turbine Institute (IGTD) of THE AMERICAN SOCIETY OF MECHANICAL ENGINEERS for publication in the ASME JOURNAL OF ENGINEERING FOR GAS TURBINES AND POWER. Paper presented at the International Gas Turbine and Aeroengine Congress and Exhibition, New Orleans, LA, June 4–7, 2001; Paper 2001-GT-526. Manuscript received by IGTI, Dec. 2000, final revision, Mar. 2001. Associate Editor: R. Natole.

[1]Program by Thermoflow, Inc.

[2]Cost ratios are about 5:1 but can vary based on project specifics.

knowledge, this is the first attempt to consolidate these data in a form that users can use easily. It is planned to extend this analysis in a later paper, to sites located at several locations in the world.

McNeilly [1] has provided an excellent study on the importance of accurate climatic data when evaluating gas turbine inlet cooling projects. The relative potential of different gas turbines to capacity increase due to inlet cooling has been evaluated by Kitchen et al. [2].

Gas turbine inlet air-cooling has been treated by Meher-Homji and Mee [3], Girouf [4], and Giunn [5].

2 Overview of Evaporative Cooling Technology

2.1 Traditional Evaporative Cooling. Traditional media-based evaporative coolers have been widely used in the gas turbine industry especially in hot arid areas. The basic principle of evaporative cooling is that as water evaporates, it consumes around 1100 BTU/b_m (~2600 KJ/Kg) of heat (latent heat of vaporization) and in doing so reduces the ambient air temperature.

Traditional evaporative coolers are described in detail by Johnson [6].

Evaporative cooler effectiveness is given by

$$E = \frac{T_{1DB} - T_{2DB}}{T_{1DB} - T_{2WB}} \tag{1}$$

where
T_1=inlet temperature
T_2=exit temperature of evaporative cooler
DB=dry bulk
WB=wet bulb.
A typical value for effectiveness is 85–90%, which means that the wet bulb temperatures can never be attained.

The temperature drop is given by

$$\Delta T_{DB} = 09(T_{1DB} - T_{2WB}) \tag{2}$$

A pschometric chart can be used to obtain the values. The exact power increase depends on the particular machine type, site altitude, and ambient conditions.

The presence of a media-type evaporative cooler inherently creates a pressure drop which results in a drop in turbine output. As a rough rule of thumb, a 1 (25.4 mm) WB increase in inlet duct losses will result in a 0.3 to 0.48% drop in power and a 0.12% increase in heat rate. These numbers would be somewhat higher for an aeroderivative machine. Increases in inlet duct differential pressure will cause a reduction of compressor mass flow and engine operating pressure. Increase in inlet differential pressure results in a reduction of the turbine expansion ratio.

The inherent loss of efficiency and increased inlet pressure loss in a traditional evaporative cooling system never allows for the maximum cooling effect to be attained. Water quality requirements are, however, less stringent than those required for direct fog cooling systems and this may be an important factor in some site locations when demineralized water is not easily available or is expensive.

2.2 Inlet Fogging. Direct inlet fogging is a method of cooling where demineralized water is converted into a fog by means of special atomizing nozzles operating at 2000 psig (138 barg). This fog provides cooling when it evaporates in the air inlet duct of the gas turbine. This technique allows 100% effectiveness in terms of attaining 100% relative humidity at the gas turbine inlet and thereby gives the lowest temperature possible without refrigeration (the wet bulb temperature). Direct high pressure inlet fogging can also be used to create a compressor intercooling effect by allowing excess fog into the compressor, thus boosting the power output considerably. In this paper, consideration is only made of *evaporative* fogging alone, with no discussion of fog intercooling being considered. A photograph showing a typical high-pressure fogging skid is shown in Fig. 2. This consists of a series of high pressure reciprocating pumps providing demineralized water to an array of high pressure fogging nozzles located after the air filter elements. The nozzles create a large number of micron size droplets which evaporate cooling the inlet air to wet bulb conditions. A photo of a nozzle array fogging an inlet duct for a large frame machine is shown in Fig. 3.

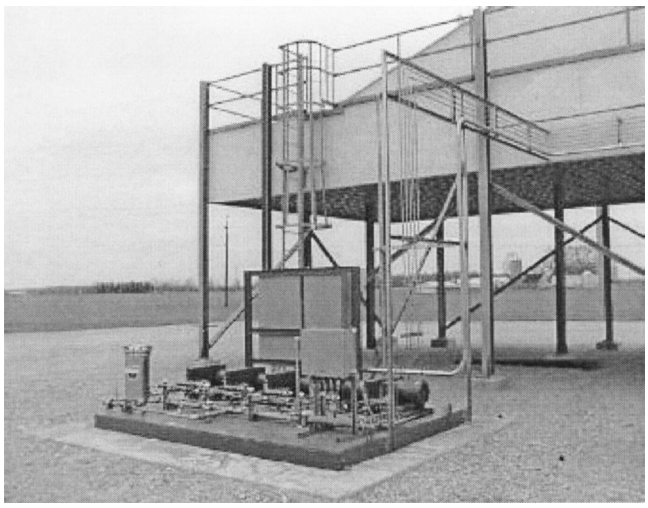

Fig. 2 Typical high-pressure fogging skid. The feed lines from the high-pressure pumps to the inlet system can be seen here.

2.2.1 Control of Inlet Fogging Systems and the Importance of Climatic Data. The control system incorporates a programmable logic controller (PLC), which is mounted on the high-pressure pump skid. Sensors are provided to measure relative humidity and dry bulb temperature. Programming algorithms within the PLC use these measured parameters to compute the ambient wet bulb temperature and the wet bulb depression (i.e., the difference between the dry bulb and wet bulb temperature) to quantify and control the amount of evaporative cooling that is possible at the prevailing ambient conditions. The system turns on (or off) fog cooling stages to match the ability of the ambient air conditions to absorb water vapor. The software would then be configured to adjust the amount of fog injected in proportion to the inlet air mass flow.

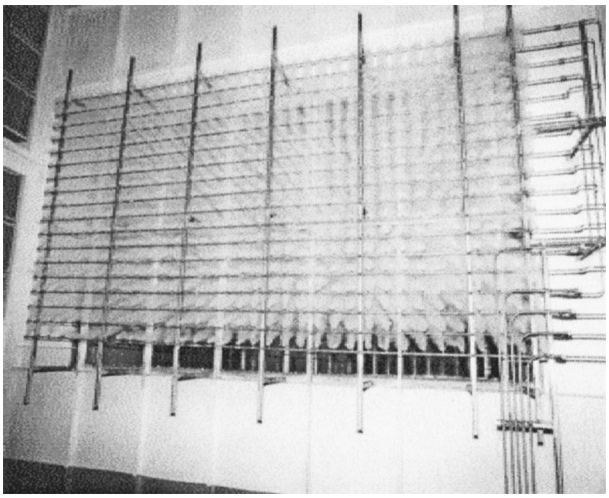

Fig. 3 High-pressure fogging skid operation for a heavy-duty gas turbine

By choosing pump displacements (i.e., flow in gpm) it is possible to derive multiple cooling stages with the utilization of different pump combinations.

Obviously, the control of the skid is based on climatic conditions and so the overall utilization of the fogging system at any location, is a strong function of the climatic conditions. *It is this reason that makes an accurate understanding of the variations in climatic conditions an imperative.*

3 Climatic and Psychrometric Aspects of Inlet Fogging

3.1 Modeling of Climatic Data. There are numerous problems and traps when modeling climatic data—several of which derive the concept of ''averaging'' of data. One example of this is using data such as shown in Fig. 4. This figure provides a correlation of dry bulb and wet bulb averages at a certain site. The graph shows that the linear behavior may lead one to conclude that at a dry bulb temperature of 2.5°C, the expected wet bulb is 20°C allowing a wet bulb depression of 5°C. (i.e., a measure of evaporative cooling potential). This is totally erroneous as the data was derived by taking the *average* WB temperature and the *average* DB temperature and plotting the curve. Consequently, the graph does *not* reflect *coincident* WB and DB conditions and will therefore indicate a much reduced cooling potential. This sort of error is very common. There is also a tendency of engineers to specify operating conditions that represent the ''worst case'' in terms of temperature and humidity. This is done in an attempt to derive an installation that will provide required capacity under the most stringent conditions, but in most cases, these extreme conditions can never exist in nature. The result is that plants may end up more expensive than they need to be[3]. This philosophy also pervades the definition of site conditions for power generation and mechanical drive applications. More than often the capacity conditions are defined at a very high temperature in combination with a high or average relative humidity. This often leads to more expensive plant construction than is needed, [1].

It is advisable that the site's temperature profile for a full year of hourly data with the 20–30 year average wet and dry bulb coincident temperatures be considered in the analysis. These data can be used to generate ''evaporative cooling degree hour'' (ECDH) numbers for each hour of the year and allow a turbine operator to make a detailed and accurate analysis of potential power gain from inlet fogging.

[3]The problem is compounded as the EPC contractor for the plant who is held to a guarantee, enforces the extreme climatic conditions on the turbine manufacture, possible resulting in an oversized turbine.

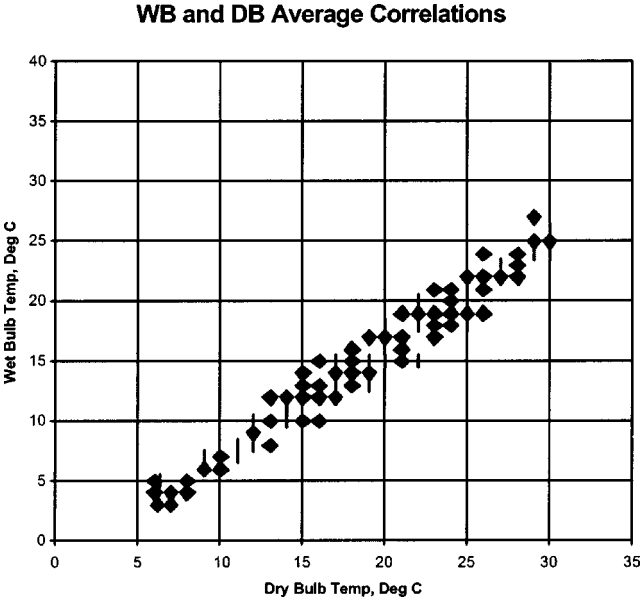

Fig. 4 Correlation of wet bulb (WB) and dry bulb (DB) temperatures—averaged data

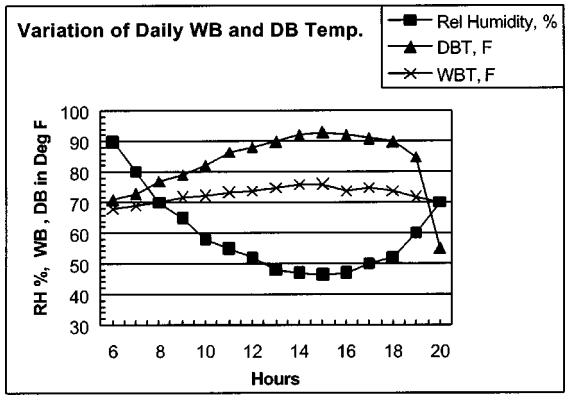

Fig. 5 Daily variation of dry bulb (DB) and wet bulb (WB) temperatures

High relative humidity conditions do not occur with high dry bulb temperatures. A typical pattern of variation of dry bulb and wet bulb temperature over a day is depicted in Fig. 5. As can be seen, during the afternoon hours, there is a considerable difference between the wet bulb and dry bulb temperatures. It is this spread that allows the use of fog evaporative cooling.

A common mistake made by potential users is to take the reported high relative humidity and temperature for a given month and base the design on these. The problem is that the high relative humidity generally occurs time-coincident with the lowest temperature and the lowest relative humidity occurs with the highest temperature. This mistake results in the erroneous conclusions that very little evaporative cooling can be accomplished and has historically been the underlying cause of the maxim that evaporative cooling is not possible in ''high humidity regions.''

Table 1 shows a sample calculation that computes °F (°C) of evaporative cooling potential for a site based on DOE climatic data. This table provides one months worth of data and a summary for the year's operation. The total indicated is the total annual °C-hours of cooling potential by the use of fog. A bar chart showing composite data considering all the months of the year from another site (Orlando, FL) is depicted in Fig. 6.

3.2 Fog Evaporative Cooling in High Humidity Regions. Even the most humid environments allow for up to 15°F (9.4°C) of evaporative cooling during the hotter part of the day. The term ''relative humidity'' refers to the moisture content in the air ''relative'' to what the air could hold at that temperature. In contrast ''absolute humidity,'' is the absolute amount of water vapor in the air (normally expressed in unit mass of water vapor per unit mass of air).

The moisture-holding capacity of air depends on its temperature. Warmer air can hold more moisture than cooler air. Consequently, relative humidity is highest during the cool morning and evening hours and lowest in the hot afternoon hours. Since inlet air fogging systems cause a very small pressure drop in the inlet air stream, and are relatively inexpensive to install, they have been successfully applied in areas with very high summer time humidity such as the Texas Gulf Coast region in the U.S.A.

4 Methodology and Analysis to Create the U.S. Database for Evaporative Cooling Degree Hours

Data were obtained from a DOE climatic database. The climatic data was primarily obtained from both National Climatic Data Center and the California Energy Commission.

The database consists of two types of files:

Table 1 Data taken for a typical month

DB (°C)	Hrs	Avg Coincident WB (°C)	WB Depression (°C)	Evap Cool Potential (°C-hrs)
43-30	0			
29	1	22	8	8
29	1	21	8	8
28	0			
28	2	22	6	12
27	7	23	4	28
27	9	23	4	36
26	9	23	3	27
26	13	22	3	39
25	10	22	3	30
24	22	21	4	88
24	29	21	3	87
23	37	21	2	74
23	41	20	3	123
22	38	19	3	114
22	62	19	3	186
21	76	19	2	152
			TOTAL:	**1012**

1 TMY Files—These are typical meteorological year data generated by selecting long-term data gathered over approximately 20 years. The typical year is a combination of 12 typical months chosen from the entire long-term database. Consequently, the typical year can be composed of 12 months from up to 12 different years. This data includes DB and WB temperature, barometric pressure, and other climatic data. TMY files were used for the analysis in this paper as they represent the most typical conditions and would provide the best estimate of future trends.

2 TRY Files—This is a test reference year by selecting data from a long-term database by a process of elimination wherein years that have months with extreme temperatures are eliminated until only one year remains. The final remaining year becomes the test reference year.

After data were collated from the above data files, a cross check was performed with ASHRE data. Finally, the data were placed in a spreadsheet and then a tabulation provided in the Appendix was derived. The ECDH was chosen with a lower limit of 45°F (7.2°C). This was considered a prudent number to avoid any possibility of inlet icing.

A detailed list of 122 cities covering all the states of the U.S.A. has been provided in Appendix A with a month-by-month calculation of the cooling hours (ECDH) in °F-hrs available[4]. The goal of the analysis was to determine the equivalent cooling degree hours (ECDH) for a variety of locations in the U.S.A. The ECDH is defined as a number that provides the total amount of cooling that can be derived for a given time period. The total ECDH is arrived at by summing the ECDHs derived for the 12 months at a location. For example, in the tabulation in Appendix A, the total ECDH for Atlanta GA, is derived by summing the numbers in that row, from January to December.

A Map of the U.S.A. provided in Appendix B, provides a pictorial depiction of the available cooling degree hours in major U.S. cities.

4.1 Use of the Equivalent Cooling Degree Hours (ECDH) Table. Any gas turbine operator can immediately see the potential for evaporative cooling per month in his or her location based on a long-term historical database. The results can be directly read off the tabulation and it is relatively easy to compute the MW-hours of capacity available by the use of evaporative fogging. In order to do this the ECDH number would be multiplied by the

[4]ECDH in °C-hrs may be obtained from Appendix A by multiplying by 1.8.

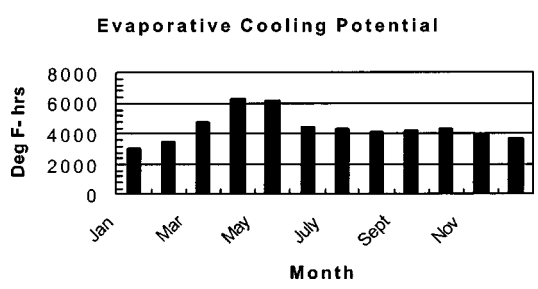

Fig. 6 Evaporative cooling potential for a year

Table 2 Salient features of gas turbine engine used for simulation

ENGINE MODEL	GE 7111EA
RPM	3600
Power	84920 kWe
Pressure Ratio	12.4:1
TIT	1104 °C
EGT	527 °C
Mass flow rate of air	293 kg/sec
Heat Rate	10,774 kJ/kWhr
Thermal Eff	32%

turbine specific MW/°F (MW/°C) cooling number. This can be obtained from the gas turbine OEMs curves. If the ECDH number is used to compute MW-hr boost over the year, it is important to note that this would imply that fogging is employed whenever there is even a 1°F (0.6°C) depression[5]. In reality there may be a delay set in the control system to trigger the first stage of cooling and also the cooling degrees per stage, would have to be larger than the depression. Typical stage cooling is 2–3°F (1.1–1.7°C). An economic evaluation can then be developed on a month-by-month basis knowing the site-specific economic criteria.

ECDH data can also be looked at more closely to account for differences in energy market values at different times of the year. For example, examination of data could provide an estimate of the revenue stream during the hot summer months alone.

5 Gas Turbine Simulation

In order to put the entire situation into perspective, A GTPRO simulation was made using a Frame 7111EA gas turbine in simple cycle configuration (fueled by natural gas) as a reference plant. Salient particulars of this gas turbine are provided in Table 2. A schematic showing the thermodynamic parameters is shown in Fig. 6.

The procedure used followed the following steps:

1 GTPRO was used to define the MW versus temperature relationship for the particular engine. This was done by assuming three different wet bulb depressions of approx 35°F, 21°F, and 6°F, (19.4, 11.7, and 3.3°C) and then by simulating the engine output for the different wet bulb conditions using GTPRO. From this the MW/°F (MW°C) sensitivity for the engine could be determined for the different extents of cooling (as opposed to just taking a linear relationship or utilizing a rule of thumb). In the case of the Frame 7111EA the relationship was found to be linear and so a value of 0.28MW/°F (0.5MW/°C) was used.

2 Using the tabulated ECDH data, the MW-hrs that can be augmented on a Frame 7 EA gas turbine is provided in the last column of the table of Appendix A.

6 Economic Criteria for Inlet Cooling

The specific decision to utilize inlet evaporative fogging technology is an economic one and the total project cost must be evaluated over the life cycle. Because of the varying economic situation in different parts of the country, no economic analysis is presented here. Dominating factors which should be taken into account in doing a study are

- climatic profile (discussed above).
- installed cost of the cooling system in terms of $/incremental power increase.
- amount of power gained by means of inlet air-cooling. This should take into account parasitic power used, and the effect of increased inlet pressure drop. With fogging systems, the maximum parasitic power is in 50–80 kW for larger turbines when the maximum wet bulb depression has to be derived. The inlet pressure drop is almost nil due to the configuration and design of the nozzle array.
- fuel and demin water costs, and costs of incremental power, i.e., what benefit is attained by the power boost.
- projected O&M costs for the system.
- environmental impact.
- for cogeneration applications, the time of use electric rates and the PPA have to be carefully considered.
- potential impact on existing emission licenses.
- Economic analysis for inlet cooling systems may be found in Utamuta et al. [7], Ondryas [8], van Der Linden, and Guinn [9].
- In this paper, the emphasis is more on the climatological aspects as opposed to the economic analysis due to the fact that the economic conditions are very site specific in terms of a deregulating market that exists at this time in the U.S. market.

7 Closure

The paper has provided a tool to easily enable operators in the U.S.A. to determine the degree of evaporative cooling potential in terms of evaporative cooling degree hours. The tabulation provides a tool that any gas turbine operator can use to determine feasibility of the application of evaporative cooling to specific applications. Further, the data provided would reduce the effort that is needed to make an economic analysis of the potential of evaporative cooling.

Nomenclature

ECDH = equivalent cooling degree hours
GPM = Gallons/minute
DB = dry bulb temp
WB = wet bulb temp
WG = water gauge

[5]For this and other reasons, it may be prudent to multiply the ECDH numbers by approximately 10%.

Appendix A

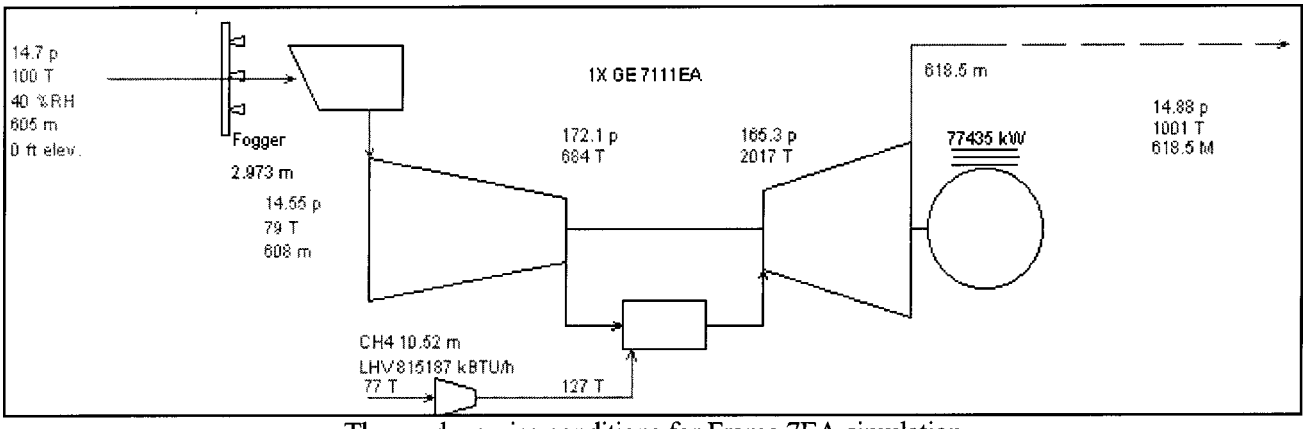

Thermodynamics conditions for Frame 7EA simulation

Appendix B

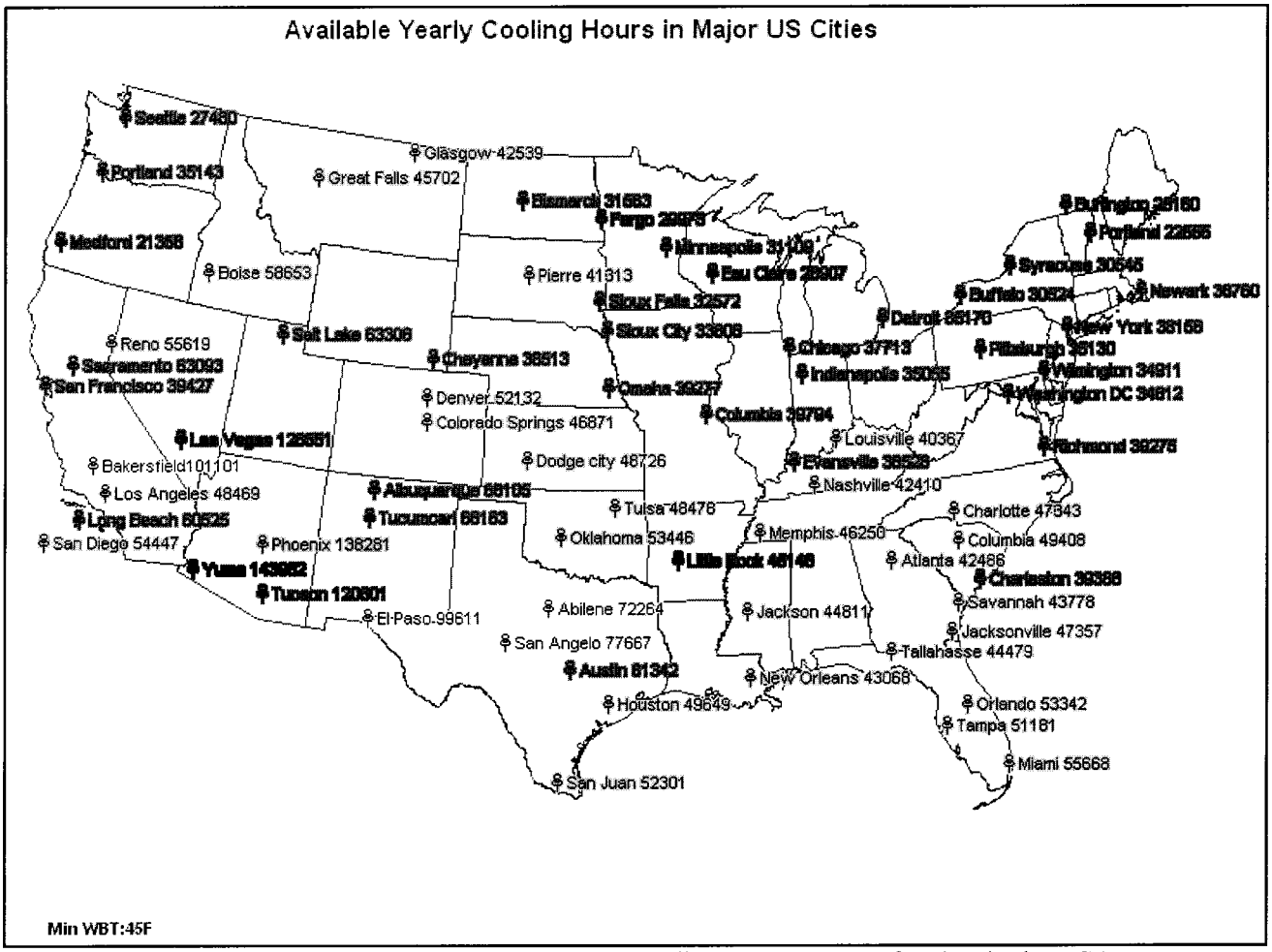

Map showing representative Evaporative Cooling Degree Hours for sites in the USA
Available Yearly and Monthly Cooling hours in USA Cities.

Appendix C

ECDH in °C- hr. based on Data From: National Climatic Data Center
Gas Turbine: 7111EA , Min WBT=7.2°C
(MW/°C): 0.49, Power boost for Frame 7EA (MWh) shown in last column

City	Year	Jan	Feb	Mar	Apr	May	Jun	Jul	Aug	Sep	Oct	Nov	Dec	MWh
Abilene, TX	40147	871	1184	2488	3461	5536	5044	5297	5858	4119	2879	2315	1096	19676
Albany, NY	17869	0	0	151.7	1369	2818	3258	3207	2863	2408	1462	318	15	8758
Albuquerque, NM	37836	0	30	544.4	1972	5804	7819	6501	6122	4928	3625	477	13.3	18544
Allentown, PA	16143	32.8	0	399.4	1384	2096	2911	2832	2263	1937	1562	614	112	7912
Alpena, MI	13529	0	0	88.33	447.2	2107	2684	3216	2176	1524	1121	166	0	6631
Amarillo, TX	32606	266	302	1356	3663	5273	4195	4561	4617	3717	3374	1131	153	15980
Apalachicola, FL	25444	1079	1216	1774	2155	2648	2442	2146	2272	3391	2766	1654	1903	12470
Asheville, NC	15172	619	280	890	1960	2516	1777	1843	1539	1217	1281	880	371	7436
Atlanta, GA	23603	655	567	1371	3056	2997	2766	2532	2748	2082	2740	1371	718	11568
Austin, TX	34079	1424	1561	2889	3040	3637	3686	4293	4379	3098	2707	2146	1219	16702
Bakersfield, CA	56167	864	1913	3173	4496	5872	7820	8409	8072	6305	5222	2783	1238	27528
Baltimore, MD	20889	83.9	229	762.2	1529	3136	3398	3037	2834	3012	2141	657	69.4	10238
Bangor, ME	13580	2.22	0	0.556	334.4	1918	2749	2801	2770	1673	1182	150	0	6656
Barbers Point, HI	32367	2019	2398	2538	2652	3047	2946	3023	3082	2868	2869	2301	2625	15863
Baton Rouge, LA	25812	1199	1588	2413	2731	3125	2568	2151	2681	1562	2681	1704	1409	12650
Bismarck, ND	17535	0	0	70.56	671.7	2714	2805	3554	4302	2495	922.8	0	0	8594
Boise, ID	32585	0	129	167.2	670.6	4043	5011	7714	7156	4908	2377	409	0	15970
Boston, MA	18667	76.7	121	70	811.1	2729	3102	3504	3352	2670	1676	532	23.3	9149
Buffalo, NY	16958	24.4	42.8	183.9	1087	2166	3063	3326	2833	2333	1386	466	47.8	8311
Burlington, IA	18377	15	1.67	409.4	1697	3169	2103	3353	2804	2471	1747	607	0	9007
Burlington, VT	13978	0	0.56	65.56	160.6	2274	2693	2871	3075	1632	1043	82.8	80.6	6851
Cedar City, UT	32587	23.3	66.7	192.8	646.7	3821	6574	6792	6839	5021	2342	269	0	15971
Charleston, SC	21881	962	1069	1991	2093	2917	1929	2099	2272	1777	2117	1639	1016	10724
Charleston, WV	22582	381	206	1175	2481	3088	3190	3559	2266	1965	2306	1297	669	11068
Charlotte, NC	26302	499	824	1660	2861	3068	3383	3131	3294	3068	2452	1373	688	12891
Cheyenne, WY	21396	0	0	84.44	507.2	2448	3743	4806	4740	3580	1477	10.6	0	10486
Chicago, IL	20952	0.56	15	157.2	1303	2561	3863	4036	3348	2888	2069	673	37.8	10268
Cincinnati, OH	22024	61.1	77.8	601.1	1811	3220	3894	3333	3409	2573	2105	599	339	10794
Colorado Springs, CO	26023	0	42.2	0	943.3	3344	5483	4876	4302	4772	2134	127	0	12754
Columbia, MO	22108	297	213	550.6	2117	3148	2877	3367	3171	3073	2037	1098	161	10835
Columbia, SC	27282	648	649	2031	3789	3093	3549	3333	2606	2812	2272	1514	986	13371
Columbus, OH	19618	58.3	81.1	445	1528	3060	2843	3542	2778	2522	1766	808	187	9615
Concord, NH	15260	3.33	63.9	42.22	777.2	2921	2713	2878	2511	1710	1387	206	47.8	7479
Corpus Christi, TX	26164	1542	1764	1734	1741	1969	2228	3299	2724	3357	2582	1951	1272	12823
Daggett, CA	67699	1367	1824	3795	4711	7976	8823	10469	9818	8438	5844	3292	1342	33180
Denver, CO	28962	0	0	391.1	1492	3612	4764	6522	4992	4861	1921	323	84.4	14195
Detroit, MI	19539	0	25	231.7	1115	2734	3314	3987	2939	2705	1903	492	92.2	9576
Dodge City, KS	27070	81.7	75.6	814.4	2136	3604	4317	4631	5067	2940	2411	887	106	13267

City	Year	Jan	Feb	Mar	Apr	May	Jun	Jul	Aug	Sep	Oct	Nov	Dec	MWh
Eagle, CO	20508	0	0	0	465.6	2542	4107	4548	4407	3166	1216	57.8	0	10051
Eau Claire, WI	16059	0	0	0	1158	2743	3232	2736	2733	1822	1531	103	2.22	7871
Elko, NV	28269	0	0	221.1	230	3528	4597	7304	6589	4218	1349	233	0	13855
El Paso, TX	55339	869	955	3249	5324	7982	8673	7402	6772	6061	5368	2146	537	27122
Evansville, IN	21404	148	138	915	2083	2679	3256	3240	3243	2624	2118	760	201	10490
Fairbanks, AK	11874	0	0	0	0	1957	3239	3302	2426	942.8	7.778	0	0	5820
Fargo, ND	16652	0	0	0	530	2619	2869	3166	3529	2186	1725	27.8	0	8161
Glasgow, MT	23633	0	0	277.2	685.6	3366	4536	5140	5019	3748	853.9	6.67	0	11583
Goodland, KS	24579	172	83.3	371.7	1642	2880	3786	4934	4825	3363	2262	260	0	12046
Grand Rapids, MI	16586	0	0	164.4	939.4	2676	2881	3673	2616	1737	1614	285	0	8129
Great Falls, MT	25390	47.2	59.4	0	629.4	2929	4413	6311	5812	3298	1601	283	7.78	12444
Hartford, CT	18373	1.67	2.22	167.8	1320	2722	3309	3910	2539	2241	1816	253	91.7	9005
Hilo, HI	24192	2497	2150	2354	1893	2161	2018	1911	1629	1891	1947	1836	1904	11856
Honolulu, HI	38389	2196	3015	2656	2840	3594	3479	3733	3660	3683	3438	3106	2989	18815
Houston, TX	27583	1484	1494	2319	2617	2761	2702	3048	2796	2561	2394	2337	1069	13518
Indianapolis, IN	19475	39.4	104	452.8	1589	2611	3224	3103	2929	3029	1889	443	61.1	9545
Jackson, MS	24895	623	1047	1957	2419	3022	2460	2732	2994	2281	2826	1660	873	12201
Jacksonville, FL	26309	1141	1692	2643	3232	3477	2786	2371	2494	1748	2268	1394	1064	12894
Juneau, AK	6467.2	0	0	0	0	1074	1776	1569	1254	635	157.8	0	0	3170
Las Vegas, NV	70306	632	933	3127	4012	9261	11106	11051	10824	9657	7137	2472	94.4	34457
Lewistown, MT	18315	11.1	0	33.89	280.6	2094	2858	4404	4155	2683	1592	181	21.1	8976
Lihue, HI	29143	1952	2537	2552	2393	2286	2446	2814	2877	2612	2350	2536	1788	14283
Little Rock, AK	25082	437	656	1949	2198	3071	3098	3377	3552	2406	2352	1303	683	12293
Long Beach, CA	33625	2122	2356	2783	3027	2716	2479	3436	2563	3528	3407	2693	2514	16480
Los Angeles, CA	26927	2226	1789	1966	2634	2074	1602	2176	2348	2079	2409	2796	2828	13197
Louisville, KY	22426	152	179	830.6	2009	3381	2922	3383	2882	3197	2128	807	556	10991
Lovelock, NV	36797	142	182	640.6	778.3	4112	5858	8998	8117	5116	2319	505	28.9	18034
Lufkin, NV	25142	1236	1493	2249	2354	2629	2574	2766	3089	2178	1979	1577	1020	12322
Madison, WI	16871	0	0	35	1221	2723	2739	2978	2708	2582	1629	256	0	8268
Medford, OR	11866	142	252	195.6	932.8	1557	1303	1392	1910	1836	1173	665	508	5815
Memphis, TN	25694	337	667	1727	2963	2958	3369	3804	2909	2297	2441	1448	774	12593
Miami, FL	30927	2178	2894	2793	3101	2838	2447	2251	2564	2016	2368	2683	2794	15157
Minneapolis, MN	17283	0	0	0	1253	2866	3592	3150	2903	2154	1246	116	3.33	8470
Nashville, TN	23561	463	709	1541	2453	2803	3249	2863	2835	2479	2284	1387	494	11547
Newark, NJ	21533	15	73.9	157.8	1896	3183	3622	4008	3200	2659	1879	594	246	10554
New Orleans, LA	23927	1127	1636	2088	2317	2611	2583	2103	2808	1818	2394	1501	941	11727
New York Cent. Park, NY	17892	8.33	0	198.3	1484	2388	2436	3214	3077	2632	1807	558	91.1	8769
New York La Guardia, NY	21198	78.3	0	256.1	1420	2483	3355	3856	3591	2871	2182	1034	72.2	10389
Norfolk, VA	21745	419	23.3	1007	2701	2576	3226	2887	2508	2486	1804	1846	261	10657
Oakland, CA	20801	831	1339	1833	1808	1876	1853	1771	2088	2421	2288	1762	933	10195
Oklahoma, OK	29692	368	528	1897	3183	3373	3446	4659	4328	3521	2737	1278	373	14552
Omaha, NE	21821	0	0	515	2481	3942	3601	3635	2782	2362	1838	488	177	10694

City	Year	Jan	Feb	Mar	Apr	May	Jun	Jul	Aug	Sep	Oct	Nov	Dec	MWh
Orlando, FL	29634	1718	1929	2666	3523	3450	2504	2393	2292	2379	2431	2253	2096	14524
Philadelphia, PA	19982	80	43.9	605	1192	3371	2938	3138	3274	2596	1928	662	153	9793
Phoenix, AZ	76823	2633	2613	4918	6371	9531	10397	9671	9163	8487	6893	3962	2184	37651
Pierre, SD	22952	8.89	0	45.56	1622	3045	2654	4471	5168	3522	2283	132	0	11249
Pittsburgh, PA	19517	63.3	138	491.7	1544	3456	3072	3284	2910	2218	1535	571	234	9565
Pocatello, ID	28628	0	0	128.3	331.1	3549	4472	7206	6501	4640	1801	0	0	14031
Portland, ME	12531	2.78	0	173.9	427.2	1926	2293	2572	2180	1465	1291	200	0	6141
Portland, OR	19524	141	337	1012	1220	2558	3046	3658	2431	2838	1357	744	183	9569
Providence, RI	17293	47.2	40.6	106.7	922.8	2654	2621	3361	2848	2207	1891	444	150	8475
Pueblo, CO	37236	71.7	538	1143	1778	5093	6210	6524	6007	5237	3729	674	231	18249
Raleigh, NC	21499	684	777	1508	2442	2499	3057	2168	2413	2671	1669	1257	354	10537
Reno, NV	30899	0	263	813.9	1127	3128	5569	6278	6603	4448	1952	717	0	15144
Richmond, VA	21819	245	904	1139	2893	2770	2457	2475	3209	2025	1576	1487	639	10694
Rochester, MN	14511	0	0	32.78	1035	2480	2858	2279	2477	1653	1502	187	6.67	7112
Sacramento, CA	35052	377	1193	1801	2548	3820	4608	5088	4995	4441	3459	2099	623	17179
Salt Lake City, UT	35170	0	52.8	114.4	1296	4059	5265	8477	7768	5273	2276	589	0	17237
San Angelo, TX	43148	1322	1978	3034	3903	5298	5168	6232	5178	4248	2653	2256	1879	21147
San Diego, CA	30248	2756	2281	2422	2271	3069	2190	1772	2471	2479	3514	2756	2269	14825
San Francisco, CA	21904	946	1229	1652	1945	2109	2021	2000	2151	2637	2653	1445	1116	10735
San Juan, PR	29056	2543	2666	2590	3336	3119	2182	2228	2292	1857	2068	1898	2279	14241
Savannah, GA	24321	1249	1226	2078	2826	2931	3099	2145	2214	1701	2474	1421	959	11920
Scotts Bluff, NE	24819	27.2	119	295	1550	3301	4423	4933	4598	3638	1721	213	0	12164
Seattle, WA	15267	66.1	258	550	508.3	1953	2262	2884	3083	1878	1064	595	164	7482
Sheridan, WY	21402	0	41.1	118.3	662.8	2733	2783	4779	5393	3327	1511	42.2	11.7	10489
Sioux City, IA	18781	0	26.1	300.6	1738	3424	2815	2912	2633	2105	2364	258	204	9205
Sioux Falls, SD	18096	0	26.1	218.3	926.7	2868	3609	3318	3054	1699	2172	204	0	8869
Spokane, WA	24558	0	21.7	0	575	3147	3637	5691	6309	3946	1223	8.89	0	12036
St. Louis, MO	21815	261	356	996.7	2396	3209	2848	3179	2576	2571	2596	669	158	10692
Sunnyvale, CA	24292	1208	1455	2098	2398	2020	2473	2111	2546	2432	2303	1911	1337	11905
Syracuse, NY	16969	12.8	13.3	210	1430	2104	2976	3168	2717	2217	1519	463	141	8317
Tallahassee, FL	24711	1164	1467	1984	2779	2816	3052	2279	1968	2109	2452	1732	907	12111
Tampa, FL	28434	1669	1843	2407	3192	3220	2049	2529	2564	2001	2652	2382	1926	13936
Tonopah, NV	33987	106	0	326.1	1318	3218	6777	7375	7378	5254	2113	122	0	16657
Truth or Consequences, NM	44041	103	212	1787	3166	6799	8469	6883	5473	6083	4068	997	0	21585
Tucson, AZ	67001	2312	1766	4066	5896	8697	10397	7682	6457	6999	6568	3947	2212	32837
Tucumcari, NM	36757	177	866	1472	3318	5537	5366	5518	5433	3989	3268	1404	411	18015
Tulsa, OK	26932	413	551	1886	2932	2661	2948	4043	4428	2550	2818	1229	474	13200
Waco, TX	35472	1005	1508	2686	3371	3662	3959	5373	4718	2845	3337	1933	1076	17385
Washington, DC	19340	110	146	630	2152	3215	2328	2749	3124	2157	1631	1010	87.8	9479
Wilmington, DE	19395	31.1	36.1	510	1503	2664	3039	3611	2988	2596	1774	472	170	9506
Winslow, AZ	38693	0	74.4	930	1526	5222	7977	6916	6632	5342	3277	778	20.6	18964
Yucca Flats, NV	44877	40	312	293.3	2271	5111	7925	9296	8476	6276	3584	1231	62.8	21995
Yuma, AZ	79973	3084	3939	5994	7722	9170	10024	8845	8213	7669	6982	5527	2802	39195

References

[1] Mc Neilly, D., 2000, ''Application of Evaporative Coolers for Gas Turbine Power Plants,'' ASME Paper No. 2000-GT-303.

[2] Kitchen, B. J. and Ebeling, J. A., 1995, ''QUALIFYING Combustion Turbines for Inlet Air Cooling Capacity Enhancement,'' ASME Paper No. 95-GT-26.

[3] Meher-Honiji, C. B., and Mee, T. R., 2000, ''Inlet Fogging of Gas Turbine Engines-Part A: Theory Psychrometrics and Fog Generation and Part B: Practical Considerations, Control and O&M Aspects,'' ASME Paper Nos. 2000-GT-307 and 200-GT-308.

[4] Giourof, A., 1995, ''Gas, Turbine Inlet Air Cooling: You Can Almost Pick Your Payback,'' Power, May.

[5] Guinn, G. R., 1993, ''Evaluation of Combustion Gas Turbine Inlet Air Precooling for Time Varying Annual Climatic Conditions,'' ASME Cogen-Turbo 1993, Bournmouth, UK, Sept. 21–23, 1993, IGTI-Vol. 8, ASME, New York.

[6] Johnson, R. S., 1988, ''The Theory and Operation of Evaporative Coolers for Industrial Gas Turbine Installations,'' ASME Paper No. 83-GT-41.

[7] Utamura, M., Ishikawa, A., Nishimura, Y., and Ando, N. 1996, ''Economics of Gas Turbine Inlet Air Cooling System for Power Enhancement,'' ASME Paper No. 96-GT-515.

[8] Ondryas, I. S., ''Options in Gas Turbine Power Augmentation Using Inlet Air Chilling,'' ASME Paper 90-GT-250.

[9] Van Der Linden, S., and Searles, D. E., 1996, ''Inlet Conditioning Enhances Performance of Modern Combined Cycle Plants for Cost—Effective Power Generation,'' ASME Paper No. 96-GT-298.

Selecting and Developing Advanced Alloys for Creep-Resistance for Microturbine Recuperator Applications[1]

P. J. Maziasz
e-mail: maziaszpj@ornl.gov

R. W. Swindeman

Metals and Ceramics Division,
Oak Ridge National Laboratory,
1 Bethel Valley Road,
Oak Ridge, TN 37831-6115

Recuperators are considered essential hardware to achieve the efficiencies desired for advanced microturbines. Compact recuperator technologies, including primary surface, plate and fin, and spiral, all require thin section materials that have high-temperature strength and corrosion resistance up to 750°C or above, and yet remain as low cost as possible. The effects of processing and microstructure on creep-rupture resistance at 750°C and 100 MPa were determined for a range of austenitic stainless alloys made into 0.1-mm foils. Two groups of alloys were identified with regard to improved creep resistance relative to type 347 stainless steel. Alloys with better creep-rupture resistance included alloys 120, 230, modified 803 and alloy 740 (formerly thermie-alloy), while alloy 214 and 625 exhibited much better creep strength. Alloys 120 and modified 803 appeared to have the most cost-effective improvements in creep strength relative to type 347 stainless steel, and should be attractive for advanced microturbine recuperator applications.
[DOI: 10.1115/1.1499729]

Introduction

Microturbines are a new and increasingly exciting subset of combustion gas turbines being used and improved for stationary power generation. Microturbines have generally evolved from automotive or aerospace small turbine applications, or from efforts to make industrial turbines smaller, and tend to fall in the 5 to 500 kW size range ([1]). They are an important part of the evolving distributed power generation picture, which includes stand-alone generation, combined cycle applications with fuel cells, and combined heat and power (CHP) application ([2]).

Microturbines have several design features that are unique relative to larger industrial engines. Microturbines operate at higher speeds and lower pressure ratios than larger gas turbines, and they need recuperation of exhaust heat to achieve desired efficiencies ([1,2]). Low-cost materials are also a must for mass-producing microturbines. Compact recuperators are heat exchangers that boost the thermal efficiency of current microturbines to about 30% (about 20% without recuperation), and are essential for advanced microturbines to achieve the desired efficiencies of up to 40%. Recuperators also significantly muffle the noise from turbines ([2–4]), which is important in many potential applications. Recuperators represent 25–30% of the overall microturbine cost, so it is extremely important to balance the need for high performance and durable materials with the need to make them as cost effective as possible.

There are several different kinds of compact metallic recuperator technologies available for microturbines, including primary surface, plate and fin, and spiral recuperators, each with a variety of final configurations designed for specific engine applications ([1–6]). While some envision ceramic recuperators in the future ([1]), most current compact recuperators are manufactured from austenitic stainless steels like type 347 or from heat-resistant Ni-based alloys like 625 ([1,4]). Two years ago, the Department of Energy initiated a new advanced microturbine program ([7]) and awarded contracts to turbine manufacturers (Capstone, Honeywell, General Electric, United Technologies Research Center, and Ingersoll-Rand) to design and build microturbines with efficiencies of 40% or more. The only way to achieve that efficiency is higher operating temperatures. Such advanced microturbines will push the metallic recuperator maximum temperatures to 750°C or higher and demand service lifetimes of 45,000 h or more ([7]). Although critical or life-limiting properties vary for each of the different compact recuperator technologies, they all require thin-section alloys with good resistance to oxidation in moist air or exhaust, and good resistance to creep, fatigue, or fracture, at 750°C or above. They also need sufficient ductility at room temperature for various component manufacturing processes and probably need to be as close to the cost of type 347 stainless steel as possible. There is a range of commercial heat-resistant and corrosion-resistant alloys available that fall between type 347 stainless steel and alloy 625, and there are comprehensive data bases, selection rules, and design guidelines for such high-temperature alloys for thick-section pressure vessels and piping applications ([8–10]). However, there are few such data on most of these alloys processed into thin sections or foils specifically for use in selecting materials for or designing recuperators. Processing variations can dramatically affect and improve the creep resistance of type 347 stainless steel foils at 700°C ([11]). Therefore, the purpose of this work is to provide a preliminary but systematic database on a range of heat and corrosion-resistant alloys between type 347 stainless steel and alloy 625 processed appropriately into foils and creep tested at 750°C and above. These data should be useful to aid materials selection for microturbine recuperator applications. This work is also intended to provide a sound physical metallurgical basis (processing, properties, microstructure correlations) for further modifying or developing alloys with improved performance that are most cost-effective relative to type 347 stainless steel for advanced microturbine recuperator applications. This work is a portion of the new DOE Advanced Microturbines Program ([7]).

[1]2001, Best Paper Award, also given by ASME/IGTI Vehicular and Small Turbomachinery Committee.

Contributed by the International Gas Turbine Institute (IGTI) of THE AMERICAN SOCIETY OF MECHANICAL ENGINEERS for publication in the ASME JOURNAL OF ENGINEERING FOR GAS TURBINES AND POWER. Paper presented at the International Gas Turbine and Aeroengine Congress and Exhibition, New Orleans, LA, June 4–7, 2001; Paper 2001-GT-541. Manuscript received by IGTI, Dec. 2000, final revision, Mar. 2001. Associate Editor: R. Natole.

Table 1 Compositions of heat-resistant austenitic stainless alloys processed into foils (wt.%)

Alloy/vendor	Fe	Cr	Ni	Mo	Nb	C	Si	Ti	Al	Others
347 steel (Allegheny-Ludlum)	68.7	18.3	11.2	0.3	0.64	0.03	0.6	0.001	0.003	0.2 Co
Modified 803 (Special Metals, developmental)	40	25	35	n.a.	n.a.	0.05	n.a.	n.a.	n.a.	n.a.
Thermie-alloy (now alloy 740) (Special Metals)	2.0	24	48	0.5	2.0	0.1	0.5	2.0	0.8	20 Co
Alloy 120 (Haynes International)	33	25	32.3	2.5 max	0.7	0.05	0.6	0.1	0.1	3 Co max, 3 W max, 0.2 N
Alloy 230 (Haynes International)	3 max	22	52.7	2	-	0.1	0.4	-	0.3	5 Co max, 14 W, + trace La
Alloy 214 (Haynes International)	3.0	16	76.5	-	-	-	-	-	4.5	+ minor Y
Alloy 625 (Special Metals)	3.2	22.2	61.2	9.1	3.6	0.02	0.2	0.23	0.16	

n.a.—not available

Experimental

All of the austenitic stainless steels and alloys were commercial grades obtained from production-scale plate stock that was 1.5–6.5 mm thick. Type 347 stainless steel was obtained from Allegheny-Ludlum, modified 803 developmental alloys, alloy 740 (formerly thermie-alloy), and alloy 625 were obtained from Special Metals, Inc., and alloys 120, 214, and 230 were provided by Haynes International, Inc. Alloy compositions are given in Table 1.

Pieces of each alloy were processed into 0.1-mm thick foils using laboratory-scale processing equipment at ORNL. The general processing steps were similar for most of the alloys, but specific processing parameters, particularly the final steps, were tailored for each individual alloy, based on processing information for thicker products given by the materials producers, and on experience in alloy processing at ORNL. Generally, the goal was to produce foils with about five to ten grains across the thickness. Alloys were reduced to 1.3-mm thickness by hot rolling at 1150°C or above, and then further reduced by a series of cold-rolling and solution-annealing steps into foils. Annealing times and temperatures varied from several minutes to over 30 minutes at 1050 to 1200°C depending on the particular alloy, with final annealing temperatures being slightly lower and times much shorter to control the final grain size. Anneals of thicker materials were performed in an argon muffle in a large box (air) furnace, whereas the final anneals of thin foils were done in a special radiant-heating furnace (high-intensity tungsten-halogen lamps for very rapid heating and cooling), with precise measurement and control of time and temperature and an argon-4%hydrogen atmosphere to produce a bright finish.

Creep specimens were laser cut from as-processed foil with 25.4-mm long and 6.4-mm wide gages. The specimens were creep tested in special pin-hold grips designed for foils, in dead-load machines with LVDT strain sensors and computerized data acquisition systems. All specimens were evaluated by creep-rupture testing at 750°C and 100 MPa, with a few tests also being done at 800°C and lower stress. Several of the alloys were tested to evaluate differences in processing conditions.

Optical metallography was performed on all the as-processed alloys to determine the final grain size and observe the amount of undissolved precipitates or other phases. More detailed analytical electron microscopy (AEM) was done on a few of the alloys to

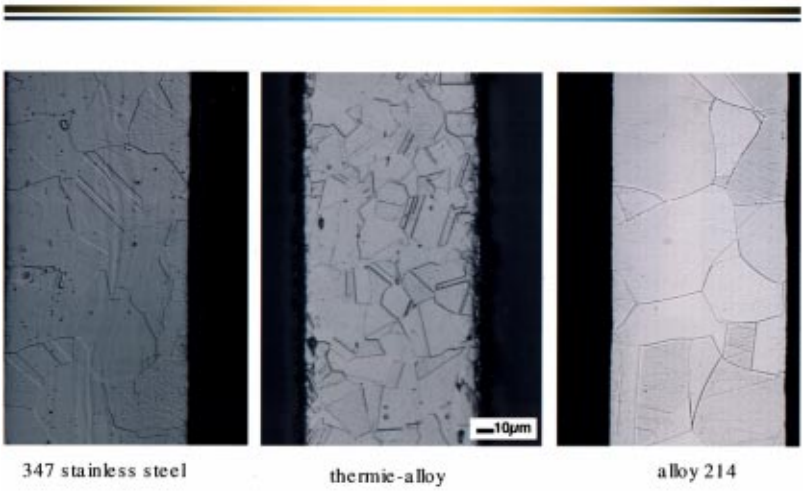

Fig. 1 Optical metallography of polished and etched specimens of as-processed 0.1-mm thick foils to show grain sizes of (*a*) type 347 stainless steel, (*b*) alloy 740 (formerly thermie-alloy), and (*c*) alloy 214

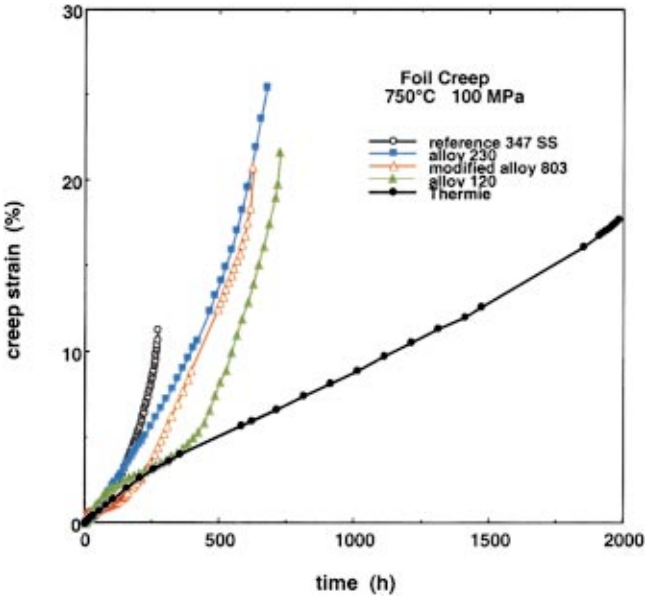

Fig. 2 Plots of creep strain versus time for creep-rupture testing of foils ranging from type 347 stainless steel to alloy 740 (formerly thermie alloy) at 750°C and 100 MPa

observe and identify finer precipitates in the matrix and along grain boundaries, using a Philips CM30 (300KV, LaB_6 gun), a Philips CM200 (200KV, field emission gun), or a Philips Tecnai 20 (200KV, LaB_6 gun).

Results

Figure 1 shows the typical range of grain sizes obtained for the more heat-resistant and corrosion-resistant alloys relative to type 347 stainless steel. Both the type 347 stainless steel and alloy 214 had coarser grain sizes than desired (>20 μm), while the grain size in the alloy 740 (formerly thermie alloy) was finer and similar to the other alloys processed at ORNL. Processing of alloys 214 and 625 was varied to refine the grain size, but only the alloy 625 had a much finer grain size (>5 μm).

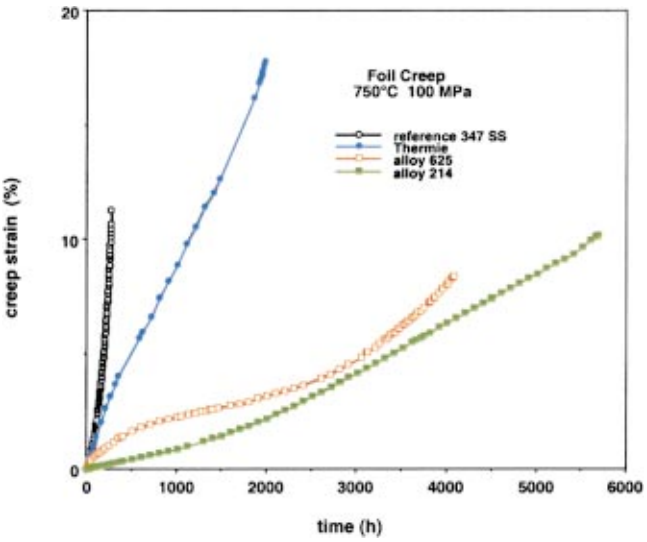

Fig. 3 Plots of creep strain versus time for creep-rupture testing of foils ranging from type 347 stainless steel to alloys 625 and 214 at 750°C and 100 MPa

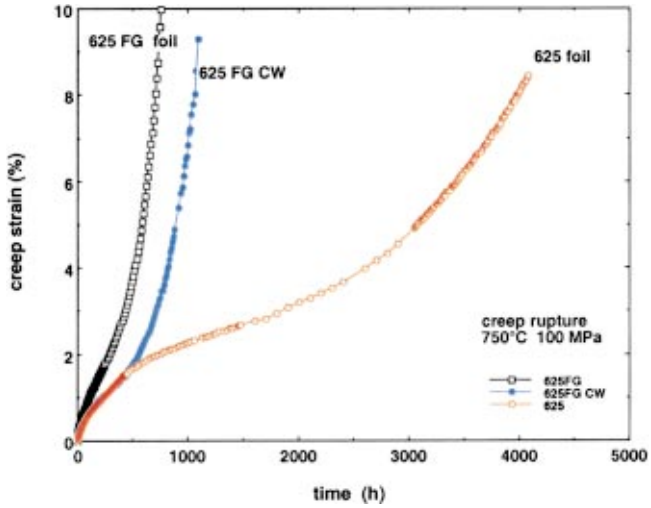

Fig. 4 Plots of creep strain versus time for creep-rupture testing at 750°C and 100 MPa of foils of alloy 625 processed at different conditions (FG = fine grained) or with 2.5% cold prestrain

The plots of creep strain versus time of the various alloys after creep-rupture testing at 750°C and 100 MPa are shown in Figs. 2 and 3. The creep response can be separated into two groups, with the alloy 740 (formerly thermie alloy) being the dividing line common to both groups. The first group is the alloys that are somewhat better than type 347 stainless steel, with alloy 120 and modified alloy 803 lasting two to three times longer and also having more than double the rupture elongation. Alloy 230 is a little weaker than the modified 803 (Fig. 2), but has about 5% more rupture elongation. Clearly, alloy 740 (formerly thermie alloy) has much more creep resistance than this first group of alloys, lasting 2000 h instead of 600–750 h, and still having close to 20% rupture elongation. The second group includes alloys 214 and 625, which are considerably stronger and last much longer than alloy 740 (formerly thermie alloy) (Fig. 3). Alloy 214 is the best at these conditions, lasting almost 6000 h and still having close to 10% rupture elongation.

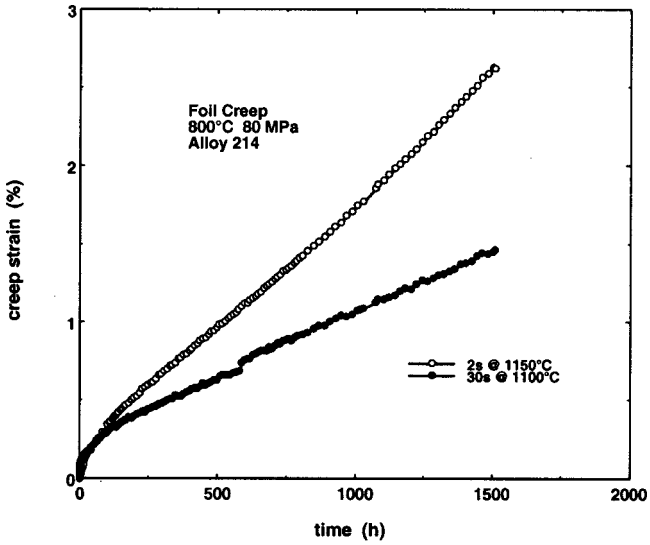

Fig. 5 Plots of creep strain versus time for creep-rupture testing at 800°C and 80 MPa of foils of alloy 214 processed at different conditions that slightly vary final grain size, with 2s at 1150°C being finer

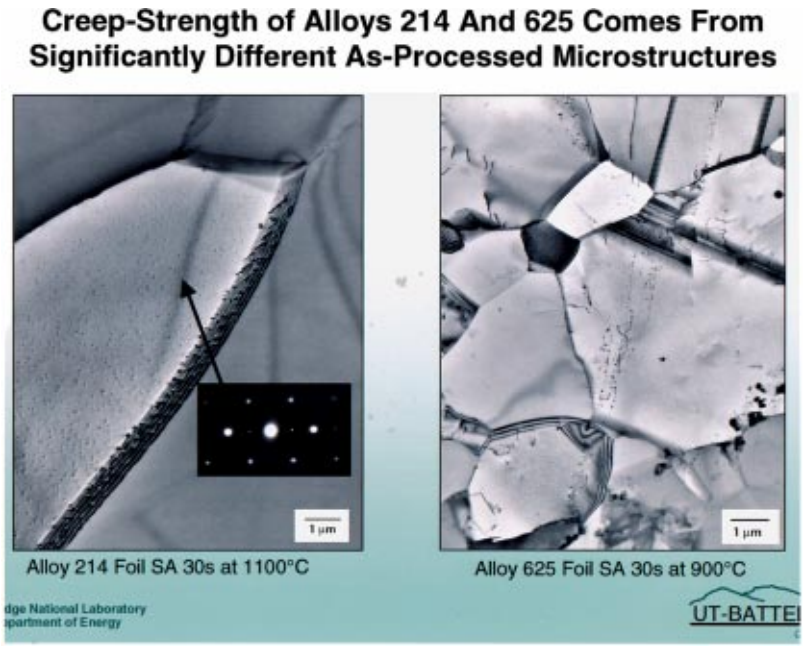

Fig. 6 TEM images showing the microstructures within grains and along grain boundaries for as-processed foils of (*a*) alloy 214 with a final solution anneal (SA) of 30s at 1100°C, and (*b*) alloy 625 (FG) with a final recrystallization anneal of 30s at 900°C. The superimposed diffraction pattern shows the characteristic extra spots from the γ' (Ni_3Al) coherent precipitates shown as black spots in the image. The alloy 625 had coarser precipitate particles of Ti and Nb-rich MC carbides and finer η phase silicides.

Two processing variations were included for alloy 625, one with a much finer grain size and the second with a finer grain size and a small amount of additional cold tensile prestrain (2.5%) (Fig. 4). The fine-grained foil is significantly less creep resistant relative to the coarser-grain foil, which is expected, while the small amount of added prestrain actually improves the creep-resistance slightly. Two processing variations were also included for alloy 214, with the shorter anneal producing a slightly finer grain size than the longer anneal (Fig. 5). Both show good creep resistance at 800°C and 80 MPa, with the material having slightly coarser grains also being slightly better.

AEM analysis was performed on the 347 stainless steel, and alloys 625 and 214, with the latter two being shown in Fig. 6. The stabilized 347 steel has only some coarser NbC particles in austenite grains that are otherwise free of any other types of carbides. The alloy 625 has some patches of very fine particles and sparce clusters of much coarser particles in otherwise austenite grains. High special resolution X-ray energy dispersive spectroscopy (XEDS) microcompositional analysis revealed that the coarse particles are all Ti and Nb-rich MC carbides (about 80% Ti, 20% Nb), while the fine precipitates are Nb-rich eta silicides (roughly equal parts of Nb, Cr, Si and Ni). AEM analysis of alloy 214 shows that there is a very fine and uniform dispersion of coherent Ni_3Al (γ') precipitates in the austenite grains and along grain boundaries, clearly identified by electron diffraction. AEM analysis of all the other as-processed alloys is in progress and some of the creep-tested specimens will also be analyzed to determine the nature of their creep resistance. The fine γ' precipitation prior to creep in alloy 214 is clearly a difference relative to the other primarily solid-solution alloys, and is consistent with the robust creep resistance this alloy exhibits. Knowing and understanding the high-temperature strengthening mechanisms in each of these different alloys provides important feedback as to whether or not further processing modifications or alloy development are likely to improve the observed creep resistance.

Discussion

Creep-rupture testing provides just one measure of performance for ranking or selecting materials at elevated temperatures, but above 600– 650°C where creep can limit the lifetime of Fe-Cr-Ni stainless steels and alloys, it can be a better indicator than tensile properties alone. Ultimate tensile strength and total elongation of the various alloys considered in this work are given in Table 2, and are taken from either alloy data sheets available from the various materials producers (Allegheny Ludlum, Special Metals, or Haynes International) or the literature ([12]). For thin-section compact recuperators for microturbines, both creep and oxidation resistance, particularly with water vapor effects included, are important life-determining parameters that must be considered for materials selection ([4,13–15]). However, for the different kinds of compact recuperators, other properties, including cyclic and thermal fatigue, and thermal expansion are also important, and relative cost is an essential consideration. With regard to oxidation resistance, studies in 4–15% water vapor at 700–800°C indicate that above 700°C, stainless steels and alloys with over 20 wt.% Cr will perform better than stainless steels with lower Cr ([14,15]), and that alloys like 625 (22 wt. Cr) and 214 (16 wt.% Cr + 4.5 % Al) show very good behavior under such conditions ([16]). With the exception of alloy 214, which contains both Cr and Al, all of the heat-resistant alloys included in this study have 22–25 wt.% Cr and Ni levels of 35% or more (Table 1).

Ranking the alloys according to creep-rupture resistance at 750°C as foils is generally consistent with the relative differences in their ultimate tensile strengths (UTS) as thicker wrought products, but there are several important exceptions. While alloy 740 has the highest UTS at 750°C, its creep-rupture resistance is significantly lower that alloys 625 and 214, with 214 being clearly the best of the alloys tested. Alloy 230 has UTS similar to alloy 625, but the creep resistance is only somewhat better than type 347 stainless steel, and a little less than the creep resistance of the

Table 2 Typical tensile properties of heat-resistant austenitic stainless alloys wrought plate or tube at 750°C

Alloy	Ultimate Tensile Strength (MPa)	Total Elongation (%)
347 stainless steel	240	45
Modified alloy 803	310	63
Alloy 120	485	45
Alloy 230	590	45
Alloy 740	795	30
Alloy 214	690	15
Alloy 625	620	70

(data from the literature or data sheet from materials suppliers)

modified alloy 803, which has about half the UTS of alloy 230. Clearly, alloy 230 ranks lower in relative creep resistance as a foil product than alloy 120 or modified alloy 803. Both total tensile elongation and creep-rupture elongation at 750°C are also important factors to consider in trying to assess reliability and durability during long-term service, particular regarding resistance to cracking in an aggressive, corrosive environment. In terms of tensile elongation for thick-section products, the modified alloy 803 and alloy 625 have the highest ductility, which gives alloy 625 the highest combination of UTS and total elongation of the alloys considered. The other alloys all show >40% elongation, with alloy 740 having 30% and alloy 214 having only 15%. As finer grained foil products, type 347 steel and alloys 214 and 625 have creep-rupture ductilities of about 10% or less. Alloy 214 maintains its ductility after creep, despite being a relatively coarser grained foil. Alloy 625 shows much lower creep-rupture ductility relative to its total tensile elongation, and even very fine grained foil has about the same rupture ductility. The other austenitic alloys all show >20% creep-rupture ductility (about twice that of type 347 steel), with alloy 230 having the best (about 25%).

When considering rough relative cost estimates of these stainless alloys compared to type 347 stainless steel, the modified 803 and alloy 120 appear to be about three times more expensive than type 347 ([13]), which is significantly less than alloy 625 which is about five times more expensive. Since alloy 230 and alloy 740 would fall closer in cost to alloy 625 (based mainly on alloy composition without regard to processing), and alloy 214 is even more expensive, the most cost-effective alloys with improved performance for microturbine recuperator applications in the temperature range of 700–750°C appear to be alloy 120 and the new modified alloy 803. Since both alloys have about 25% Cr supported by higher alloy Ni contents, they should also have much better oxidation/corrosion resistance than type 347 stainless steel, even in a moist exhaust environment.

Clearly these data are very preliminary, and there is a need for long creep-tests at lower stresses as well as appropriate corrosion testing in water vapor, but both of these alloys warrant further investigation, particularly with regard to specific recuperator component fabrication issues such as formability, welding or brazing. In terms of even higher metallic foil performance, both alloys 625 and 214 should be able to withstand temperatures of 800°C or above, but the same component fabrication issues must also be addressed.

Finally, another consideration for selection of these alloys in various compact recuperator applications is thermal expansion ([4,13]). Type 347 stainless steel has relatively higher thermal expansion than the other austenitic alloys considered here, with the relative expansion decreasing with increasing Ni content. Alloy 625 has 20–25% less expansion than type 347 stainless steel in the temperature range of 600–800°C, with alloy 120 and modified alloy 803 falling about half way in between. Although the specific effects of thermal expansion are different in each of the various microturbine recuperator technologies, there is a definite benefit to lower thermal expansion, which provides an added benefit when considering replacement of type 347 stainless steel with alloy 120 or modified alloy 803.

Microturbine recuperator design and performance should be enhanced by continued development of a systematic data base of alloy properties derived for appropriately processed thin section or foil, and including a range of stainless alloys and superalloys. Moreover, metallurgical insight into the microstructure/processing relationships and the effects of such microstructures on creep and aging mechanisms of thin section alloys should at least allow performance optimization for given alloys like alloy 120 or modified 803. Such data may also enable significant modifications to develop new, more cost-effective alloys in between these standard alloys and type 347 stainless steel. Such data will also be applicable to the other thin section hardware that supports the compact recuperator cores, including containment, ducting, and flexible connectors.

Conclusions

A group of heat-resistant and oxidation/corrosion resistant austenitic stainless alloys have been processed into 1.3-mm foils and creep-rupture tested at 750°C and 100 MPa. Alloys 230, 120, and modified 803 lasted several times longer than type 347 stainless steel, while alloy 740 was almost ten times better. Alloys 625 and 214 showed much better creep-rupture resistance than thermiealloy, with alloy 214 showing the best behavior observed for this entire group. Alloy 740, and alloys 625 and 214 probably have the potential for use at low stresses at 800°C and above. These alloys are also sensitive to variations in processing parameters. Because alloys 214 and 625 are considerably more expensive than type 347 steel, alloy 120 and modified alloy 803 may be the most cost-effective alternatives to type 347 steel for microturbine recuperator applications, particularly if they demonstrate good resistance to oxidation in moist exhaust gas. Minor alloying or processing modifications may also further improve the creep resistance of both of these alloys.

Acknowledgments

We want to thank Allegheny-Ludlum (an Allegheny-Teledyne Company) for providing type 347 stainless steel, Special Metals, Inc. for providing modified 803 alloys and alloy 740, and Haynes International, Inc. for providing alloys 120, 230, and 214. We also thank K.S. Blakely and others at ORNL for expert processing of the various alloys into foils, H. Longmire for metallographic analysis, and J.W. Jones for TEM specimen preparation. Research was sponsored by the U.S. Department of Energy, Assistant Secretary for Energy Efficiency and Renewable Energy, Office of Power Technologies as part of the Microturbines Materials Program, and by Office of Fossil Energy, Advanced Research Materials Program as part of a CRADA (ORNL98-0529) between ORNL and Special Metals, Inc., under contract DE-AC05-00R22725 with UT-Battelle, LLC.

References

[1] McDonald, C. F., 1996, ''Heat Recovery Exchanger Technology for Very Small Gas Turbines,'' International Journal of Turbo and Jet Engines, **13**, pp. 239–261.
[2] Massardo, A. F., Mcdonald, C. F., and Korakianitis, T., 2000, ''Microturbine/Fuel-Cell Coupling for High-Efficiency Electrical-Power Generation,'' ASME Paper No. 20000-GT-0175.
[3] McDonald, C. F., 2000, ''Low Cost Recuperator Concept for Microturbine Applications,'' ASME Paper No. 2000-GT-0167.
[4] Ward, M. E., 1995, ''Primary Surface Recuperator Durability and Applications,'' Turbomachinery Technology Seminar Paper No. TTS006/395, Solar Turbines, San Diego, CA.
[5] Oswald, J. I., Dawson, D. A., and Clawley, L. A., 1999, ''A New Durable Gas Turbine Recuperator,'' ASME Paper No. 99-GT-369.
[6] Child, S. C., Kesseli, J. B., and Nash, J. S., 1999, ''Unit Construction Plate-Fin Heat Exchanger,'' U.S. Patent No. 5,983,992, Nov. 16.
[7] *Advanced Microturbine Systems—Program Plan for fiscal Years 2000–2006*, Office of Power Technologies, Office of Energy Efficiency and Renewable

Energy, U.S. Department of Energy, Washington, D.C., Mar.
[8] Swindeman, R. W., and Marriott, D. L., 1994, ''Criteria for Design with Structural Materials in Combined-Cycle Applications Above 815°C,'' Trans. ASME, **116**, pp. 352–359.
[9] Kane, R. H., 1991, ''The Evolution of High Temperature Alloys: A Designer's Perspective,'' *Heat-Resistant Materials*, K. Natesan and D. J. Tillack, eds., ASM-International, Materials Park, OH, pp. 1–8.
[10] Stringer, J., 1995, ''Applications of High-Temperature Materials,'' *Heat-Resistant Materials II*, K. Natesan, P. Ganesan, and G. Lai, eds., ASM-International, Materials Park, OH, pp. 19–29.
[11] Maziasz, P. J., et al., 1999, ''Improved Creep-Resistance of Austenitic Stainless Steel for Compact Gas Turbine Recuperators,'' Mat. High Temp., **16**, pp. 207–212.
[12] Stoloff, N. S., 1990, ''Wrought and P/M Superalloys,'' *Properties and Selection: Irons, Steels, and High-Performance Alloys*, **1**, *Metals Handbook*, 10th Ed. ASM-International, Materials Park, OH, pp. 950–980.
[13] Harper, M. A., Smith, G. D., Maziasz, P. J., and Swindeman, R. W., 2001, ''Materials Selection for High-Temperature Metal Recuperators,'' paper to be presented at ASME Turbo Expo 2001 Conference.
[14] Pint, B. A., and Rakowski, J. M., 2000, ''Effects of Water Vapor on the Oxidation Resistance of Stainless Steels,'' Corrosion 2000 Paper No. 00259, NACE International, Houston, TX.
[15] Rakowski, J. M., and Pint, B. A., 2000, ''Observations of the Effects of Water Vapor on the Elevated Temperature Oxidation of Austenitic Stainless Steel Foil,'' Corrosion 2000 Paper No. 00517, NACE International, Houston, TX.
[16] Pint, B. A., Swindeman, R. W., More, K. L., and Tortorelli, P. F., 2001, ''Materials Selection for High Temperature (750–1000°C) Metallic Recuperators for Improved Efficiency Microturbines,'' paper to be presented at ASME Turbo Expo 2001 Conference.

Predicted Effects of Bearing Sump and Injection Pressures on Oil Labyrinth Leakage

S.-Y. Park

D. L. Rhode

Mechanical Engineering Department,
Texas A&M University,
College Station, TX 77843

New information and an enhanced understanding concerning the oil vapor contaminant leaking through nonflooded oil labyrinth seals are provided. The results were obtained using a finite volume Navier-Stokes computer code that was extended to include the concentration transport equation. The minimum (i.e., critical) pressure and flow rate at which uncontaminated buffer gas must be injected to prevent oil vapor from leaking to the process gas was determined for a range of seal geometries and operating conditions. It was found that the variation of the critical buffer-gas injection pressure with bearing gas and process gas pressures, for example, was surprisingly small for the cases considered. In addition, the bearing gas and oil vapor flow rates for a wide range of bearing and injection (where present) pressures and geometries were determined for both buffered as well as nonbuffered seals. [DOI: 10.1115/1.1520161]

Introduction

Labyrinth seals are noncontacting flow-restriction devices as shown in Fig. 1. They are widely used in turbomachinery to minimize the leakage flow, or to maintain a desired coolant flow for example. Labyrinths with, as well as without buffer-gas injection are used to isolate the process gas from the oil-contaminated bearing gas. For buffer-gas seals noncontaminated buffer gas enters through injection holes located on the stator wall. A buffer-gas labyrinth seal is located between the process gas and the oil sump. The oil sump gas has a high (typically saturated) oil vapor concentration containing tiny oil mist particles.

There are two primary sources of oil vapor in such oil labyrinths. First, oil vapor is diffused from the bearing side of the seal to the process side, the rate depending on the seal leakage flow. For both the nonbuffered labyrinth (Fig. 1(*a*)) and for the buffered labyrinth at low injection pressure (Fig. 1(*b*)), where the bearing gas leaks to the process gas side, the vapor diffusion from the bearing is in the direction of the seal leakage velocity and is called ''forward diffusion.'' Further, when buffer gas is injected into the seal at or above the injection pressure required to prevent the bearing gas from reaching the process side, backward diffusion occurs. Backward diffusion is the phenomenon where the vapor diffusion from the bearing to the process gas is in the direction opposite to that of the buffer gas flowing toward the bearing. The total amount of vapor diffusion reaching the process side depends strongly on the direction and magnitude of the leakage velocity.

Secondly, when a liquid oil film is present inside the seal, the evaporation of the film is a source that is subsequently convected by the gas within the seal. The seal surface can be easily contaminated with a thin oil film during an undesirable machine start-up or shutdown situation for example. The presence of a liquid film within the entire seal is referred to as a ''flooded condition.'' In flooded cases, increasing the injection pressure well above the critical value to prevent process gas contamination actually increases the contamination. This increased oil vapor reaching the process gas side is due to the increased evaporation (and subsequent convection) rate from the film existing between the injection holes and the process side. The amount of oil contaminant flow strongly depends on the turbulence intensity and the seal geometry where the oil film exists.

There is a continuing void of understanding and design information available concerning the amount of oil vapor escaping from oil labyrinths. For buffer oil seals this void is especially acute, and it results in two problems: (a) unnecessarily high oil vapor migration against the buffer-gas leakage and into the process gas and (b) an excessively high buffer-gas pressure requirement that gives massive process gas contamination whenever the buffer gas pressure is not sufficiently high or the seal clearance is not sufficiently tight.

Objective

For flooded conditions, it appears to be impossible to prevent oil contaminant from reaching the process side. However, for nonflooded conditions, it is possible to find the minimum (i.e., critical) injection pressure that will prevent oil vapor contaminant from reaching the process gas side of the seal. Because no investigation has reported such important design information, no useful design curves or standards are available. The objective of the present study is to obtain an enhanced understanding and design information for nonflooded conditions. Specifically, the critical injection pressure required to prevent oil contaminant from reaching the process side will be obtained for numerous conditions. Also, the performance of particular labyrinth configurations with and without buffer-gas injection will be compared and analyzed.

Previous Work

The oil contaminant flow through nonbuffered or buffered labyrinths has rarely been studied. However, there are a few studies related to contaminant back diffusion due to the concentration gradient and the evaporated contaminant transport due to a thin film on a surface.

Boyman and Suter [1] provided an interesting theoretical and experimental identification of the contaminant transport mechanisms in a labyrinth seal. However, complete information of their experiments was not provided, and no design information was given. They measured the contaminant concentration in labyrinth cavities and visualized the overall flow behavior in a teeth-on-rotor labyrinth seal. Further, flow visualization was performed using a dye-injection method.

Park and Rhode [2] investigated the effects of geometry on oil vapor flow in flooded buffer-gas labyrinth seals. They found that

Contributed by the International Gas Turbine Institute (IGTI) of THE AMERICAN SOCIETY OF MECHANICAL ENGINEERS for publication in the ASME JOURNAL OF ENGINEERING FOR GAS TURBINES AND POWER. Paper presented at the International Gas Turbine and Aeroengine Congress and Exhibition, New Orleans, LA, June 4–7, 2001; Paper 2001-GT-118. Manuscript received by IGTI, December 2000, final revision, March 2001. Associate Editor: R. Natole.

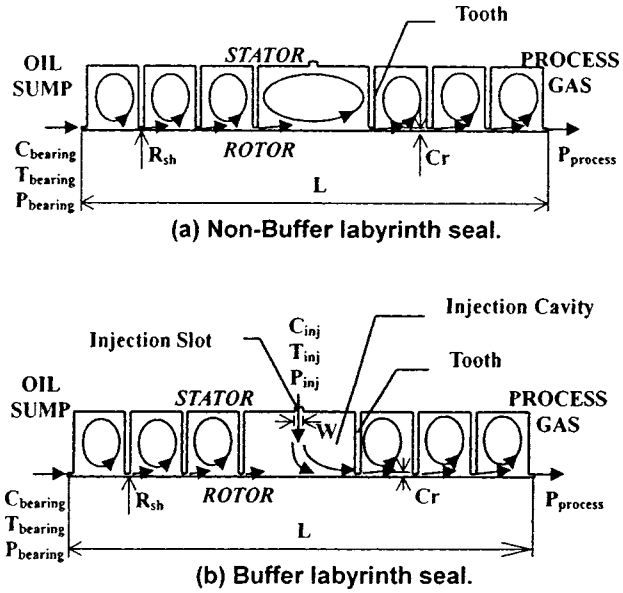

Fig. 1 Schematic diagram of the two types of labyrinth seals considered

no noticeable back diffusion occurs for their range of turbulent flow conditions, and that a thin oil film existing on the surface of the seal was the sole source of the oil transported. Assuming that only the stator seal surfaces are covered with a thin oil film, they obtained and analyzed oil vapor mass flow rates and the oil vapor concentration distribution. They considered the effects of geometry, such as clearance, injection slot width, cavity depth, and tooth pitch. Also, they suggested the best geometry for minimizing the contaminant inflow to the process gas.

Verma et al. [3] investigated the back diffusion of oxygen with surface evaporation in a ventilation pipe flow for a clean room chamber. Minimum purge gas flow rates that completely eliminate contaminant penetration were numerically obtained. The impurity desorption and adsorption between the contaminated pipe wall surface and the contaminated fluid, as well as back diffusion, were numerically investigated.

Method

The mass transfer model was developed under the following main assumptions: (a) no chemical reaction is involved; (b) the density variation due to that of the oil vapor concentration is so small that the concentration equation is uncoupled from the momentum equations; (c) the seal surfaces have no liquid oil film. Assumption (b) is based on the finding that the typical mass fraction of oil vapor for the cases considered here is 0.0011 kg of oil vapor per kg of mixture. Regarding assumption (c), based on discussions with several designers there appears to be no definitive information from industry. However, it seemed reasonable to assume that there are several different flow regimes for the bearing fluid entering an oil labyrinth. The nonmist regime considered in the current investigation is assumed to be applicable for: (a) a nonmist type of bearing lubrication, (b) fairly low peripheral speeds, (c) the presence of an effective centrifugal slinger to protect the seal inlet from significant oil particles and (d) the absence of an oil splash ring, for example. For the regime involving significant oil particles (i.e., oil mist), there is a major uncertainty concerning the size and number of such particles for the wide range of operating conditions. Boyman and Suter [1] considered oil transport, both with and without oil droplets. The present investigation focuses on nonmist oil transport.

The oil concentration problem as well as the injection flow capability, for example, were added to a Navier-Stokes, finite volume computer code that was previously developed at Texas A & M University. The code employs the SIMPLEC (SIMPLE Consistent) algorithm modified by Van Doormaal and Raithby [4]. The standard high Reynolds number version of the two-equation k-ε turbulence model is utilized. The three-point QUICK (quadratic upstream interpolation for convective kinematics) differencing scheme of Leonard [5] for the momentum equation convection terms is applied to reduce the false diffusion numerical error.

Table 1 Concentration equation terms

	ϕ	Γ_ϕ	S_ϕ
Concentration	C_{oil}	$\frac{\mu_t}{Sc_t}\left[=\rho(D_{AB})_t\right]$	**0**

The continuity, momentum, energy, and concentration transport equations can be written in the following general form with cylindrical, axisymmetric coordinates:

$$\frac{1}{r}\left[\frac{\partial}{\partial x}(\rho u r\phi)+\frac{\partial}{\partial r}(\rho v r\phi)-\frac{\partial}{\partial x}\left(r\Gamma_\phi\frac{\partial\phi}{\partial x}\right)-\frac{\partial}{\partial r}\left(r\Gamma_\phi\frac{\partial\phi}{\partial r}\right)\right]=S_\phi \tag{1}$$

where ϕ and S_ϕ represent the dependent variable and the source term according to each governing equation, [6]. For example, the dependent variable, the diffusion coefficient, and the source term for the concentration equation are given in Table 1. The binary diffusion coefficient ($D_{AB}=2.37\times10^{-6}\,m^2/s$) of the oil vapor diffusing into air was calculated by following the procedure of Rohsenow and Hartnett [7] and Özisik [8].

Since the velocity at the bearing inlet and the injection inlet are not known, the pressure as well as the temperature and oil vapor concentration in the bearing chamber and in the injection chamber are specified. Further, at the seal exit (i.e., process side) the usual practice of specifying zero normal gradient for all quantities (velocities, pressure correction, enthalpy, concentration, k, and ε) was followed. On each of the walls, the no-slip boundary condition was applied via wall functions for the two wall shear stresses acting on each wall segment. In addition, zero normal gradient was used for the concentration on each wall segment.

The nondimensional mass flux parameter was determined from the CFD solutions as

$$\Phi_{inj}=\frac{\dot m_{inj}\sqrt{R_{inj}T_{inj}}}{P_{inj}A_{inj}}$$

$$\Phi_{bearing}=\frac{\dot m_{bearing}\sqrt{R_{bearing}T_{bearing}}}{P_{bearing}A_{Cr}} \tag{2}$$

$$\Phi_{oil}=\frac{\dot m_{bearing}\sqrt{R_{bearing}T_{bearing}}}{P_{bearing}A_{Cr}}\frac{C_{oil}M_{oil}}{\rho_{mix}}.$$

Here $\rho_{mix}=P_{bearing}/(R_{bearing}T_{bearing})$ and $M_{oil}=550$ kg/kmol is used in accordance with a typical lubrication oil. Further, the approximation $A_{Cr}=\pi D$ Cr was used along with $A_{inj}=\pi DW$.

Results

Figure 1(a) shows the nonbuffer labyrinth seal case wherein the leakage flows from the bearing side (oil sump) of the seal to the process gas side. The oil concentration at the bearing side is convected to the process gas side by the leakage flow. The middle labyrinth tooth is removed as shown in Fig. 1(*a*) to allow a more valid comparison between nonbuffered and buffered labyrinths. Figure 1(*b*) shows the buffer-gas labyrinth seal considered for which the buffer gas is injected through a large number of very closely spaced (circumferentially) holes that have been approximated by a circumferential slot of the same total injection area. This approximation is quite reasonable for the present operating

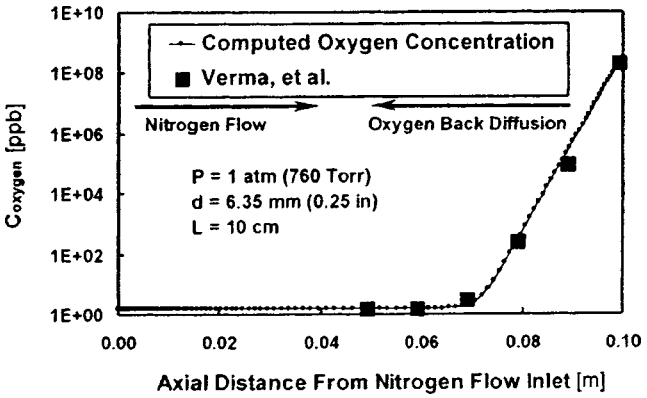

Fig. 2 Comparison of the computed oxygen concentration with the results from Verma et al. [3]

conditions. Specifically, intense turbulence energy and high swirl velocity (very high rpm) within the injection cavity cause the large number of circumferentially closely spaced, highly turbulent jets to mix together immediately upon entering the seal. The flow structure in the injection cavity is very complicated. When the circumferential injection sheet of circumferentially mixed jets reaches the shaft surface, it forms a circumferentially distributed stagnation point flow region. The stagnation point flow is skewed toward the process side when the bearing pressure is greater than the process pressure (see Fig. 1(b)). The injected flow is mixed with the oil-contaminated flow from the bearing side. In the injection cavity the turbulent mixing is intense along the boundary of the injection flow, along the wall jet region near the shaft, and near the recirculation zones. The buffer gas has zero oil vapor concentration, and the bearing side is considered to be saturated with a concentration value of $C_{\text{bearing}}=3.20\times10^{-6}$ kmol/m^3 for the given oil sump temperature ($T_{\text{bearing}}=344$ K). Also the fixed injection temperature $T_{\text{inj}}=298$ K is used in the present study.

In order to verify the model for such problems, Fig. 2 shows a comparison of the computed concentration values with that of Verma et al. [3] for a test case involving oxygen back diffusion in a pipe flow. The oxygen is diffusing against the nitrogen gas flow of 1.91×10^{-7} kg/s (10 cm^3/min) with a pressure of 1 atm (760 Torr). Notice that the nitrogen gas flow is sufficient to essentially stop the oxygen back diffusion if the pipe is longer than 0.04 m for these conditions.

Nonbuffered Labyrinth Seal

Grid Independence. The results of grid independence testing for the nonbuffered seal are shown in Table 2. Three different grid systems were tested. All grid systems have highly nonuniform expansion and contraction rates in the x and r-directions. The nondimensional oil vapor mass flux parameter (Φ_{oil}) values are compared. The 146×38 grid system was selected for the production computer runs.

Table 2 Grid Independence for nonbuffered labyrinth seal [Cr =0.36 mm (0.014 in.), H=5.08 mm (0.2 in.), S=3.81 mm (0.15 in.), R_{sh}=100.13 mm (3.942 in.), L=30.86 mm (1.215 in)]

Grid Lines	Φ_{oil}	$\frac{\Phi_{\text{finer}}-\Phi_{\text{coarser}}}{\Phi_{\text{finer}}}$ [%]
123×28	2.956×10^{-4}	1.56
146×38	2.911×10^{-4}	0.95
168×55	2.883×10^{-4}	-

Table 3 Parameters for the nonbuffered seal

(a) Baseline Operating Conditions

Quantity	Value
RPM	18,000
W_{in}	0.3 $R_{sh}\omega$ (56.556 m/s)
$P_{process}$	100 kPa
$T_{bearing}$	344 K
$C_{bearing}$	3.20×10^{-6} kmol/m^3

(b) Geometry of The Non-Buffered Seal Cases [$P_{process}$=100 kPa, RPM=18000, W_{in}=0.3$R_{sh}\omega$]

Non-Buffer Cases	Cr [mm]	L [mm]	R_{sh} [mm]	W_{in} [m/s]
Baseline	0.25	30.86	100.13	56.56
Case A	0.36	30.86	100.13	56.56
Case B	0.25	15.62	100.13	56.56
Case C	0.25	30.86	200.25	113.24
Case D	0.25	30.86	50.06	28.31
Case E	0.36	15.62	100.13	56.56

Cases Considered. As it is assumed that no oil film exists on the surface, the oil contaminant transport is by convection and forward diffusion from the oil sump. As expected, a small labyrinth tooth clearance gives a small leakage, but this small clearance causes numerical iteration convergence difficulties. Therefore, the primary focus is on Cr=0.25 mm (0.01 in.) and Cr=0.36 mm (0.014 in.), which are referred to as ''medium'' and ''large'' clearances. For nonbuffered labyrinth seals, the baseline geometry has a medium clearance, and further details are given in Table 3.

To explore the geometry effects, the seal clearance, length, and rotor radius are varied for various pressure boundary conditions. Specifically additional values including Cr=0.36 mm (0.014 in.), L=15.62 mm (0.615 in.), R_{sh}=50.06 mm (1.971 in.), and R_{sh} =200.25 mm (7.884 in.) are considered. The inlet swirl velocity was set to 30 percent of the rotor peripheral velocity.

Overall Flow Field. Figure 3(*b*) shows the velocity field for the region indicated in Fig. 3(*a*) of the baseline case. There are two distinct flow regions within each cavity. One is the through-flow region near the rotor surface, and the other contains the large recirculation zone. Since the middle tooth is removed for equitable comparison with the buffer-gas labyrinth seal, a large recirculation zone exists in the large injection cavity. The air flows from the bearing side to the process side convecting the oil vapor contaminant.

Discussion. Figure 4 shows the variation of the nondimensional oil vapor mass flux parameter (Φ_{oil}) with bearing

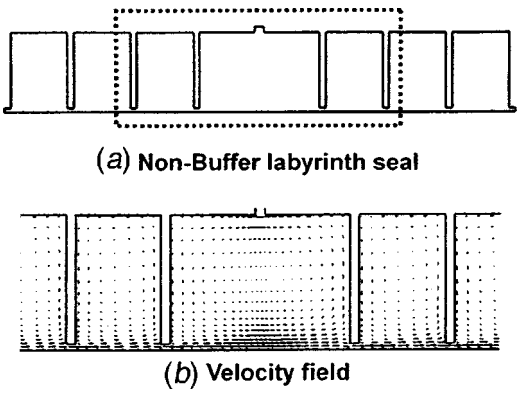

Fig. 3 Flowfield for the nonbuffer labyrinth seal

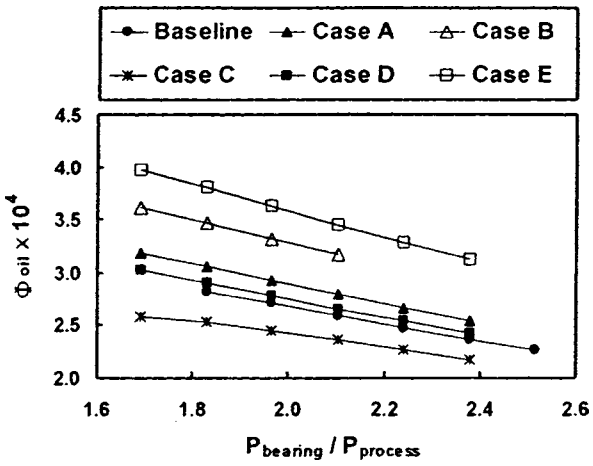

Fig. 4 Variation of nondimensional oil vapor mass flux parameter with bearing pressure ratio for nonbuffered labyrinth seals (see Table 3(*b*))

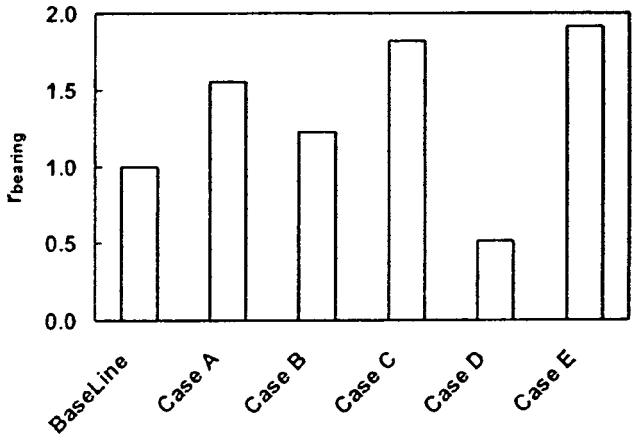

Fig. 5 Variation of the bearing mass flow ratio ($r_{bearing} = \dot{m}_{oil}/\dot{m}_{oil}|_{baseline}$) for $P_{bearing}/P_{process} = 2.1$ for nonbuffered labyrinth seal cases (see Table 3(*b*))

pressure ratio ($P_{bearing}/P_{process}$). A simple, but slightly approximate expression for $\dot{m}_{oil}$ is $\dot{m}_{oil} = \Phi_{oil} P_{bearing} A_{Cr}/\sqrt{R_{bearing} T_{bearing}}$. As one expects, the bearing mass flux ($\Phi_{bearing}$) increases steadily as $P_{bearing}/P_{process}$ increases. Since Φ_{oil} is carried along by the leakage from the bearing side, an increase of $\Phi_{bearing}$ increases Φ_{oil}. However, because of the presence of $P^2_{bearing}$ in the Φ_{oil} expression (Eq. (2)), the curves for Φ_{oil} are linearly decreasing as the pressure ratio $P_{bearing}/P_{process}$ increases.

The clearance Cr is generally the dominant factor determining the leakage flow rate. The effect of tooth clearance on the oil flow is seen by comparing the oil vapor flux [multiplied by its tooth tip flow area (πD Cr)] of Case A for Cr=0.36 mm (0.014 in.) with that of the baseline for Cr=0.25 mm (0.01 in.). As expected, from the change of flow area, the increased clearance increases $\dot{m}_{oil}$ more than it increases Φ_{oil}. For $P_{bearing}/P_{process} = 2.1$, for example, $\dot{m}_{oil}$ increases 56 percent as the clearance of Case A is increased 40 percent from that of the baseline.

The seal length reduction by 50 percent shows that for $P_{bearing}/P_{process} = 2.1$, Φ_{oil} of Case B is 22 percent higher than that of the baseline case. Case E shows the combined effect of reduced clearance and reduced seal length, which gives a 33 percent increase of mass flux from the baseline at $P_{bearing}/P_{process} = 2.1$.

Cases C and D give the results for a 100 percent increased and a 50 percent decreased shaft radius, respectively. Comparing Cases C and D with the baseline case gives the effect of shaft radius on Φ_{oil}. Because the domain inlet swirl velocity was consistently taken as 30 percent of the rotor peripheral velocity, a 100 percent increase of the radius (from the baseline) in Case C gives a 100 percent increase of the inlet swirl velocity. This increase of swirl velocity appears to decrease Φ_{oil} by increasing the $P^2_{bearing}$ quantity (see Eq. (2)). Also, the tooth clearance flow area for Cases C and D is increased and decreased from the baseline by 100 percent and 50 percent respectively. Because of the combined effect of doubled flow area and increased inlet swirl velocity for Case C, for $P_{bearing}/P_{process} = 2.1$, Φ_{oil} is decreased 9 percent from the baseline case. Also, because of the combined effect of the halved flow area and decreased inlet swirl velocity for Case D, for $P_{bearing}/P_{process} = 2.1$, Φ_{oil} is increased 2 percent from that of the baseline case.

For the case of $P_{bearing}/P_{process} = 2.1$, Figure 5 shows the oil vapor mass flow ratio ($r_{bearing} = \dot{m}_{oil}/\dot{m}_{oil}|_{baseline}$). The oil vapor mass flow ratio shows a different trend from that of the oil vapor mass flux parameter Φ_{oil} in Fig. 4. The clearance change and the shaft radius change mainly affect the oil vapor mass flow rate. For example, the 40 percent increase of the clearance in Case A increases the oil vapor mass flow rate in Fig. 5 by 55 percent while increasing the mass flux by only 8 percent. Further, the clearance change of Case A has a larger effect on the mass flow than does the seal length change of Case B. Specifically, the oil vapor mass flows of Cases A and B are increased 56 percent and 22 percent, respectively. In addition, because of the flow area change due to the shaft radius change, the oil vapor mass flow of Cases C and D increases and decreases by 82 percent and 49 percent from the baseline, respectively. Note also that Case C shows a 9 percent decrease of the mass flux in Fig. 4. Finally, Case E shows the combined effect of the clearance increase and the reduced seal length, and the oil vapor mass flow increases 92 percent from that of the baseline case.

Buffered Labyrinth Seal

Grid Independence. The grid independence test results for the buffered labyrinth seal shown in Fig. 1(*b*) are shown in Table 4. The baseline geometry was computed using three different, highly nonuniform grid systems. The non-dimensional injected buffer-gas mass flux (Φ_{inj}) and the nondimensional oil vapor mass flux (Φ_{oil}) reaching the process side of the seal are compared. The 146×37 grid system was selected for the production computer runs because of the small relative difference of Φ_{oil} between a given grid system and its finer grid system.

Cases Considered. As explained earlier, for nonbuffer labyrinth seal cases, the oil contaminant is primarily by convection from the bearing side of the seal to the process gas side. However, for buffer-gas labyrinth seal cases, the injected buffer-gas pressure attempts to prevent the flow from the bearing carrying the oil vapor contaminant. By controlling the injection pressure (or the injection mass flow rate), it is possible to prevent oil contaminant from reaching the process gas in nonflooded cases. Important values for the baseline case for the buffer-gas labyrinth are given in Table 5.

Table 4 Grid independence results [Cr=0.25 mm (0.010 in.), W=0.38 mm (0.015 in.), H=5.08 mm (0.2 in.), S=3.81 mm (0.15 in.), R_{sh}=100.13 mm (3.942 in.), L=30.86 mm (1.215 in.)]

Grid Lines	Φ_{inj}	Φ_{oil}	$\frac{\Phi_{finer} - \Phi_{coarser}}{\Phi_{finer}}$ [%]	
			Φ_{inj}	Φ_{oil}
123×28	1.425×10^{-1}	1.408×10^{-4}	1.30	2.83
146×37	1.407×10^{-1}	1.369×10^{-4}	0.63	2.04
168×54	1.398×10^{-1}	1.342×10^{-4}	-	-

Table 5 Parameters for the buffered seal

(a) Baseline Operating Conditions

Quantity	Value
RPM	18,000
W_{in}	0.3 R_{sh} ω (56.556 m/s)
$P_{process}$	100 kPa
$T_{bearing}$	344 K
T_{inj}	298 K
$C_{bearing}$	3.20×10^{-6} kmol/m^3
C_{inj}	0 kmol/m^3

(b) Geometry of The Buffered Seal Cases
[$P_{process}$=100 kPa, RPM=18000, W_{in}=0.3R_{sh}ω]

Buffer Cases	Cr [mm]	W [mm]	L [mm]	R_{sh} [mm]	W_{in} [m/s]
Baseline	0.25	0.38	30.86	100.13	56.56
Case 1	0.36	0.38	30.86	100.13	56.56
Case 2	0.25	0.38	15.62	100.13	56.56
Case 3	0.25	0.38	46.10	100.13	56.56
Case 4	0.25	0.38	30.86	200.25	113.24
Case 5	0.36	0.38	15.62	100.13	56.56

For the baseline case, the effect of tooth clearance, seal length, and shaft radius are explored for various pressure boundary conditions. For a given process side pressure, the injection pressure and the bearing pressure determine $\dot{m}_{oil}$ and $\dot{m}_{inj}$. These mass flow rates are investigated for various pressure boundary conditions.

Overall Flow Field. Figure 6(*b*) shows the velocity field for the buffered baseline case within the three middle cavities identified in Fig. 6(*a*). The buffer gas enters the seal through the injection "slot". Observe in Fig. 6(*b*) that the buffer-gas flowing from the injection slot is deflected toward the process gas side because the bearing side pressure exceeds that of the buffer gas. In the injection cavity, the flow structure is complicated and has two inflows. Except for the injection cavity, there is a single large recirculation region within each cavity. Because of the addition of the buffer gas, the fluid velocities abruptly increase immediately downstream from the injection cavity.

Discussion. Figure 7(*a*) shows the nondimensional oil vapor mass flux parameter (Φ_{oil}) variation with the injection pressure ratio for the buffered baseline geometry. The oil mass flow rate is easily obtained from Φ_{oil} as $\dot{m}_{oil}=\Phi_{oil}P_{bearing}A_{Cr}/\sqrt{R_{bearing}T_{bearing}}$ (see Eq. (2)). To further restrict oil vapor from reaching the process gas, one can reduce $P_{bearing}$ for a given P_{inj}, or increase P_{inj} for a given $P_{bearing}$. Observe in the figure that the Φ_{oil} curves become steeper as $P_{inj}/P_{bearing}$ increases for a fixed $P_{bearing}$. Figures such as this can be used as a design tool to estimate the minimum, i.e., critical injection pressure P^C_{inj} that prevents oil vapor from entering the process gas. However, it is very difficult to obtain a numerical solution for conditions giving approximately $\dot{m}_{oil}=0$. Thus the required P_{inj} value for $\dot{m}_{oil}=0$ is easily estimated using extrapolation of the curves shown in Fig. 7(*a*). Such a P^C_{inj} value can be used in seal design by including a safety factor to account for typical uncertainties which include that of labyrinth wear degradation. An arbitrary reference case for comparison of $P_{bearing}=210\,\text{kPa}=P_{process}+110\,\text{kPa}$ (16 psi) gives $P^C_{inj}/P_{bearing}=1.02$ for $\Phi_{oil}=0$ from Fig. 7(*a*). This corresponds to $P^C_{inj}=214\,\text{kPa}$. For all the cases considered in Fig. 7(*a*), there is no oil vapor mass flow for $P_{inj}/P_{bearing}>1.02$. Observe further that these

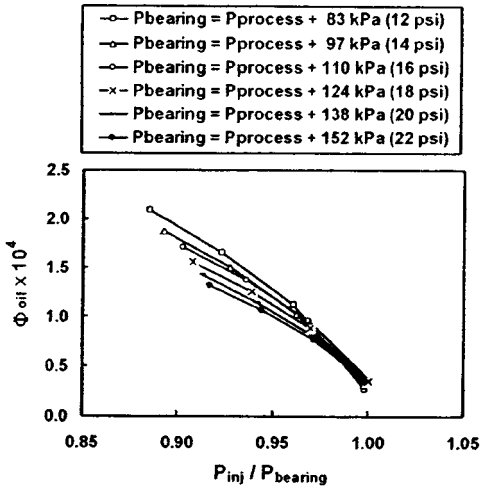

(*a*) Oil Vapor Mass Flux

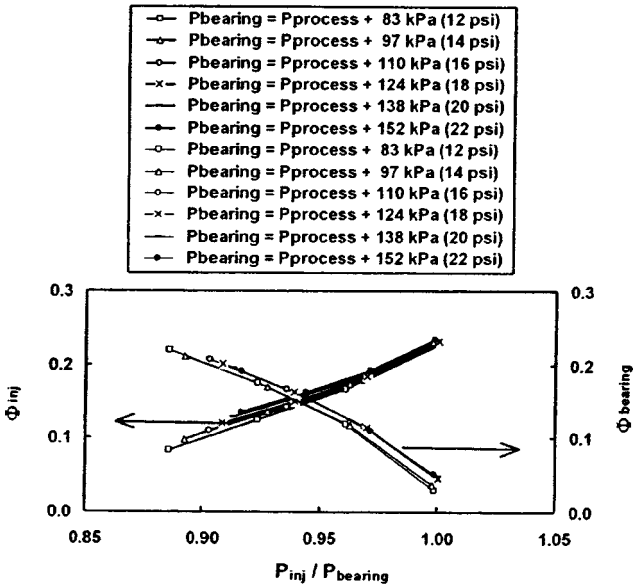

(*b*) Injection and Bearing Gas Mass Flux

Fig. 7 Variation with injection pressure of (*a*) oil vapor mass flux and (*b*) injection gas and bearing gas mass flux reaching the process gas side of the seal. [$P_{process}$=100 kPa (14.5 psi), Cr=0.25 mm (0.01 in), W=0.38 mm (0.015 in.), L=30.86 mm (1.215 in.), R_{sh}=100.13 mm (3.942 in.), rpm=18,000, W_{in} =0.3$R_{sh\omega}$=56.556 m/s].

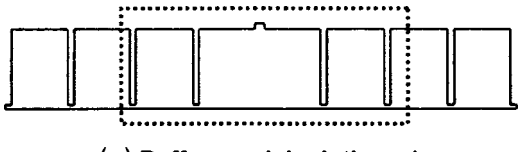

(*a*) Buffer-gas labyrinth seal

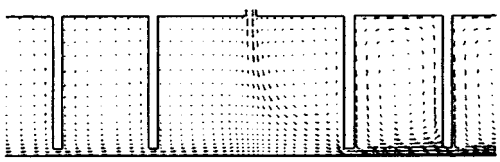

(*b*) Velocity field

Fig. 6 Flowfield for the buffer-gas labyrinth seal

curves are somewhat steeper for decreased P_{bearing}, which indicates that Φ_{oil} is more sensitive to $P_{\text{inj}}/P_{\text{bearing}}$ as P_{bearing} decreases.

The nondimensional injection and bearing gas mass fluxes corresponding to the Φ_{oil} values of Fig. 7(*a*) for the baseline case are given in Fig. 7(*b*). Observe from the two figures that, for a given bearing pressure, an increase of the injection pressure increases the injection cavity pressure, which in turn opposes the bearing gas flow that carries the oil vapor flow to the process side of the seal. Thus Fig. 7(*a*) and 7(*b*) give the entire set of pressure and mass flow information for use in specifying the buffer gas supply for such a seal. Further, the amount of oil vapor flow prevented by sufficient buffer gas pressure and flow is easily estimated by comparing the values from Fig. 7(*a*) and 7(*b*) with those for the corresponding nonbuffer case of Fig. 4. An example of the use of Fig. 7(*b*) is that, for the condition of $P_{\text{bearing}}=P_{\text{process}}+110$ kPa (16 psi), the critical injection mass flow $\dot{m}^C_{\text{inj}}$ is extrapolated as 4.75×10^{-2} kg/s at $P^C_{\text{inj}}=214$ kPa. That is, the oil vapor mass flow rate reaching the process side (2.73×10^{-5} kg/s in Fig. 4 for the corresponding nonbuffer case) can be prevented by using buffer air with $P_{\text{inj}}>214$ kPa and $\dot{m}_{\text{inj}}>4.75\times10^{-2}$ kg/s.

The case shown in Fig. 8 has identical parameters to that of the baseline case except for the clearance. Here the medium clearance of the baseline case has been increased to a large clearance of Cr=0.036 mm (0.014 in.). The Φ_{oil} curves of Fig. 8(*a*) have a similar character to that of the baseline in Fig. 7(*a*). However, the increase of the Cr has a minor effect on P^C_{inj}. For example, for $P_{\text{bearing}}=P_{\text{process}}+110$ kPa (16 psi), $P^C_{\text{inj}}=221$ kPa, which is increased about 3.3 percent over that of the medium clearance case in Fig. 7(*a*). The Φ_{inj} and Φ_{bearing} for the large clearance case in Fig. 8(*b*) show a similar trend to the corresponding curves for the medium clearance. As expected, for the large Cr in Fig. 8(*b*), there is a higher buffer-gas mass flow rate for a given P_{bearing} than for the medium Cr. Even though P^C_{inj} shows a small increase, the extrapolated $\dot{m}^C_{\text{inj}}$ is 7.2×10^{-2} kg/s at $P^C_{\text{inj}}=221$ kPa, which is a 52 percent increase due to the increased Cr of 40 percent. The oil contaminant for the corresponding nonbuffered seal, $\dot{m}_{\text{oil}}=4.24\times10^{-5}$ kg/s in Fig. 4, can be avoided by using buffer gas at $P_{\text{inj}}>221$ kPa and $\dot{m}_{\text{inj}}>7.2\times10^{-2}$ kg/s.

Figures 9(*a*) and 9(*b*) show the solutions for the shortened version ($L=15.62$ mm (0.615 in.)) of the buffered baseline case. For all the conditions considered in Fig. 9(*a*), all the P^C_{inj} values exhibit less than a 1 percent increase over that of the corresponding baseline case. For the $P_{\text{bearing}}=P_{\text{process}}+110$ kPa (16 psi) condition in Fig. 9(*b*), the extrapolated $\dot{m}^C_{\text{inj}}$ is 5.15×10^{-2} kg/s at $P^C_{\text{inj}}=216$ kPa, which is an 8.6 percent increase over that of the baseline case. Also, the oil contaminant of the corresponding shortened nonbuffer seal in Fig. 4, which has $\dot{m}_{\text{oil}}=3.34\times10^{-5}$ kg/s, can be eliminated by using buffer air with $P_{\text{inj}}>216$ kPa and $\dot{m}_{\text{inj}}>5.15\times10^{-2}$ g/s. As expected, reducing the seal length has a smaller effect on the P^C_{inj} and $\dot{m}^C_{\text{inj}}$ than does increasing the clearance.

Figures 10(*a*) and 10(*b*) show the mass fluxes of the lengthened version $L=46.1$ mm (1.82 in.) of the buffered baseline case. For the $P_{\text{bearing}}=P_{\text{process}}+110$ kPa (16 psi) condition in Fig. 10(*a*), the P^C_{inj} value is only about 0.8 percent increased over that of the baseline case. Thus lengthening as well as shortening the seal has only a minor effect on P^C_{inj}. Further, in Fig. 10(*b*), the extrapolated $\dot{m}^C_{\text{inj}}$ is 4.25×10^{-2} kg/s at $P^C_{\text{inj}}=215$ kPa, which is only about a 10 percent decrease from that of the baseline case. Thus lengthening the seal has a negligible effect on P^C_{inj} and a small effect on $\dot{m}^C_{\text{inj}}$.

Figures 11(*a*) and 11(*b*) show the increased radius version $R_{\text{sh}}=200$ mm (7.88 in.) of the buffered baseline case. The increased radius increases the throughflow area by 100 percent and the injection slot flow area by 95 percent. Because the bearing (i.e., domain inlet) swirl velocity was taken as 30 percent of the rotor peripheral velocity, note that a 100 percent increase of the radius has a 100 percent increase of the inlet swirl velocity from the baseline case. Because the 100 percent increase of the domain inlet swirl velocity contributes to P_{bearing} (stagnation pressure and not to P_{inj}), the extrapolated critical injection pressure P^C_{inj} is smaller than P_{bearing}, i.e., $P_{\text{inj}}/P_{\text{bearing}}<1.0$. In Fig. 11(*a*), for the condition of $P_{\text{bearing}}=P_{\text{process}}+110$ kPa (16 psi), $P^C_{\text{inj}}=198$ kPa which is a 7.5 percent decrease from that of the baseline case. In Fig. 11(*b*), the extrapolated $\dot{m}^C_{\text{inj}}$ is 8.43×10^{-2} kg/s at $P^C_{\text{inj}}=198$ kPa, giving a 78 percent increase over that of the baseline case.

Further, for the corresponding nonbuffered case with $P_{\text{bearing}}=P_{\text{process}}+110$ kPa (16 psi) in Fig. 4, $\dot{m}_{\text{oil}}=4.97\times10^{-5}$ kg/s can be prevented by using buffer air with $P_{\text{inj}}>198$ kPa and $\dot{m}_{\text{inj}}>8.43\times10^{-2}$ kg/s.

Figures 12(*a*) and 12(*b*) are for the case with increased clearance and shortened length, Cr=0.036 mm (0.014 in.) and L

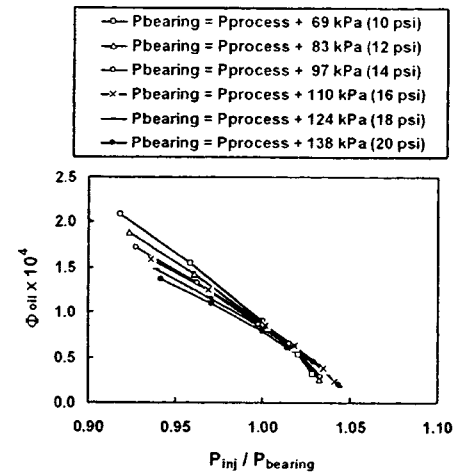

(*a*) Oil Vapor Mass Flux

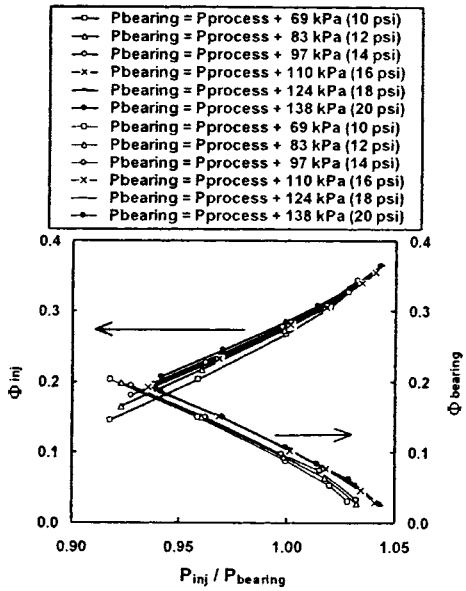

(*b*) Injection and Bearing Gas Mass Flux

Fig. 8 Variation with injection pressure of (*a*) oil vapor mass flux and (*b*) injection gas and bearing gas mass flux reaching the process gas side of the seal. [$P_{\text{process}}=100$ kPa (14.5 psi), Cr=0.36 mm (0.014 in.), $W=0.38$ mm (0.015 in.), $L=30.86$ mm (1.215 in.), $R_{sh}=100.13$ mm (3.942 in.), rpm=18,000, $W_{in}=0.3\,R_{sh\omega}=56.556$ m/s].

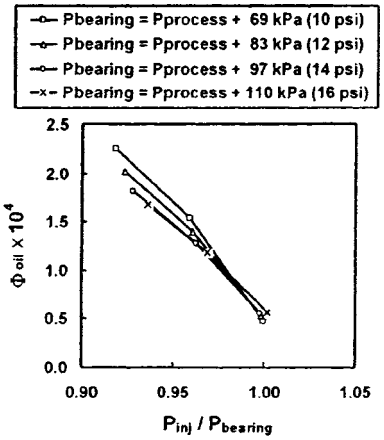

(a) Oil Vapor Mass Flux

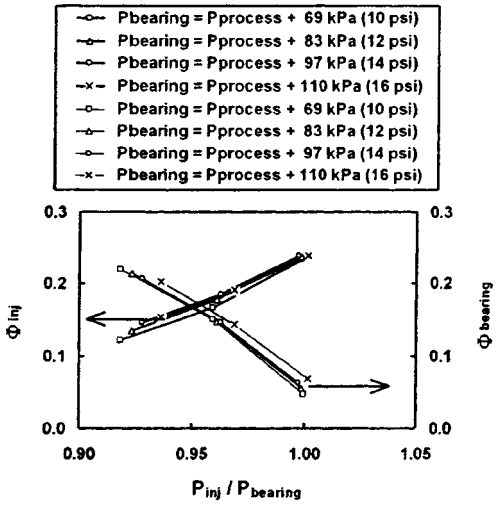

(b) Injection and Bearing Gas Mass Flux

Fig. 9 Variation with injection pressure of (*a*) oil vapor mass flux and (*b*) injection gas and bearing gas mass flux reaching the process gas side of the seal. [$P_{process}$=100 kPa (14.5 psi), Cr=0.25 mm (0.01 in.), W=0.38 mm (0.015 in.), L=15.62 mm (0.615 in.), R_{sh}=100.13 mm (3.942 in.), rpm=18,000, W_{in} =0.3$R_{sh\omega}$=56.556 m/s].

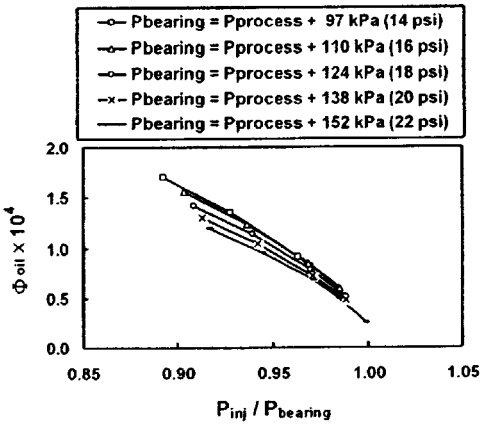

(a) Oil Vapor Mass Flux

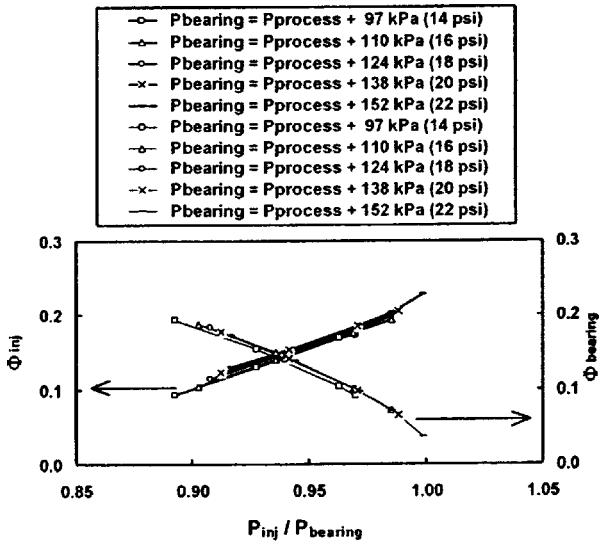

(b) Injection and Bearing Gas Mass Flux

Fig. 10 Variation with injection pressure of (*a*) oil vapor mass flux and (*b*) injection gas and bearing gas mass flux reaching the process gas side of the seal. [$P_{process}$=100 kPa (14.5 psi), Cr=0.25 mm (0.01 in.), W=0.38 mm (0.015 in.), L=46.10 mm (1.815 in.), R_{sh}=100.13 mm (3.942 in.), rpm=18,000, W_{in} =0.3$R_{sh\omega}$=56.556 m/s].

=15.62 mm (0.615 in.). For $P_{bearing}=P_{process}+110$ kPa (16 psi) in Fig. 12(*a*), $P^C_{inj}=221$ kPa which is a 3.3 percent increase over that of the baseline case. In Fig. 12(*b*), the extrapolated $\dot{m}^C_{inj}$ is 7.57 $\times10^{-2}$ kg/s at $P^C_{inj}=221$ kPa which is a 60 percent increase compared to that of the baseline case. In addition, $\dot{m}_{oil}=5.23\times10^{-5}$ kg/s in Fig. 4 can be eliminated by using buffer air with $P_{inj}>221$ kPa and $\dot{m}_{inj}>7.57\times10^{-2}$ kg/s.

Figures 13(*a*) and 13(*b*) show the combined case of increased clearance and increased slot width, Cr=0.36 mm (0.014 in.) and W=0.51 mm (0.02 in.). For $P_{bearing}=P_{process}+110$ kPa (16 psi) in Fig. 13(*a*), the P^C_{inj} value of 216 kPa is only a 0.94 percent increase over that of the baseline case. Compared to the increased Cr case in Fig. 8, P^C_{inj} here shows only a 2.3 percent decrease. In Fig. 13(*b*), the extrapolated $\dot{m}^C_{inj}$ is 7.81×10^{-2} kg/s at P^C_{inj} =216 kPa, giving a 65 percent increase over that of the baseline case.

Figure 14 shows the variation of $P^C_{inj}/P_{bearing}$ with $P_{bearing}/P_{process}$. All the cases show that $P^C_{inj}/P_{bearing}$ is slightly larger than unity except for Case 4. This exception is apparently due to the fact that Case 4 has a bearing inlet swirl velocity which is twice that of the baseline case. Note that a 40 percent increase of the clearance has more effect than a 50 percent increase or decrease of the seal length on the pressure ratio $P^C_{inj}/P_{bearing}$.

Figure 15 shows the variation of the critical injection mass flow ratio ($r_m=\dot{m}^C_{inj}/\dot{m}^C_{inj|baseline}$) and critical injection pressure ratio ($r_p=P^C_{inj}/P^C_{inj|baseline}$) relative to the baseline value for $P_{bearing}/P_{process}=2.1$. Note that the critical injection pressure ratio varies only slightly, i.e., within ±8 percent. However, the critical injection mass flow rate is sensitive to the clearance increase (Cases 1 and 5) and the shaft radius increase (Case 4). These clearance and radius effects are mainly related to the tooth clearance area variations. The 50 percent increase and decrease of the seal length (Cases 2 and 3) shows only about a 10 percent increase and decrease of the critical injection mass flow rate, respectively.

Summary

The oil vapor (i.e., contaminant) transport in ''nonflooded'' labyrinth seals is investigated. An important new cause-and-effect

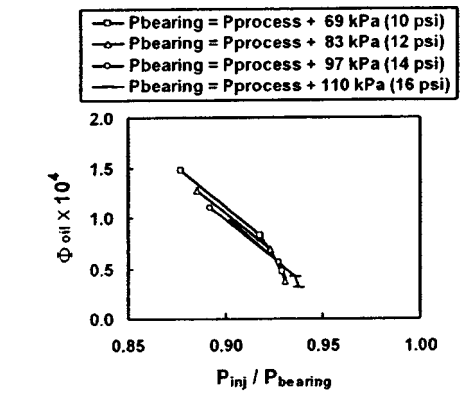

(*a*) Oil Vapor Mass Flux

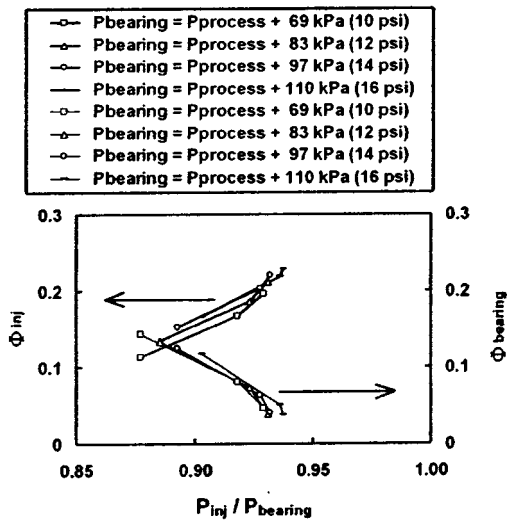

(*b*) Injection and Bearing Gas Mass Flux

Fig. 11 Variation with injection pressure of (*a*) oil vapor mass flux and (*b*) injection gas and bearing gas mass flux reaching the process gas side of the seal. [$P_{process}$=100 kPa (14.5 psi), Cr=0.25 mm (0.01 in.), W=0.38 mm (0.015 in.), L=30.86 mm (1.215 in.), R_{sh}=200.25 mm (7.884 in.), rpm=18,000, W_{in} =0.3$R_{sh\omega}$=113.24 m/s].

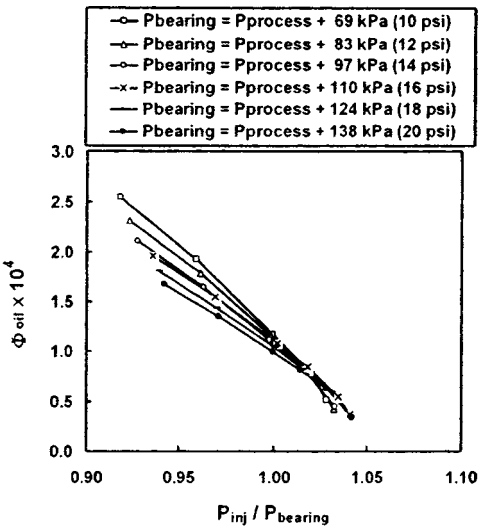

(*a*) Oil Vapor Mass Flux

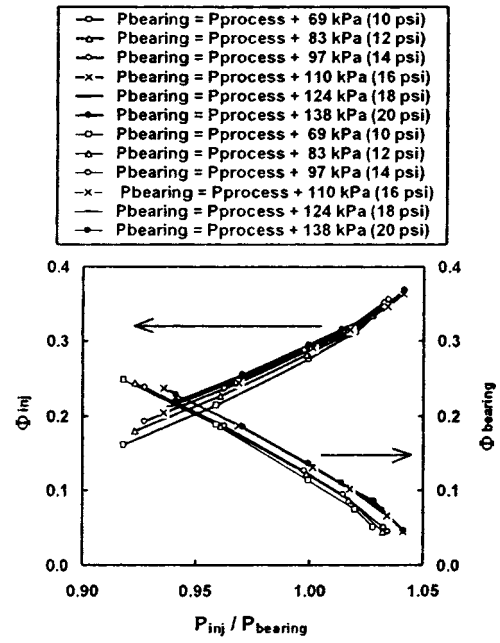

(*b*) Injection and Bearing Gas Mass Flux

Fig. 12 Variation with injection pressure of (*a*) oil vapor mass flux and (*b*) injection gas and bearing gas mass flux reaching the process gas side of the seal. [$P_{process}$=100 kPa (14.5 psi), Cr=0.36 mm (0.014 in.), W=0.38 mm (0.015 in.), L=15.62 mm (0.615 in.), R_{sh}=100.13 mm (3.942 in.), rpm=18,000, W_{in} =0.3$R_{sh\omega}$=56.556 m/s].

understanding is analyzed and presented. Specifically, the reader can evaluate a ''critical injection pressure'' by extrapolating from the new leakage-pressure-drop data to determine the injection pressure sufficient to prevent oil contaminant from entering the process gas for a given set of pressures. The dependence of the oil vapor mass flow rate on the injection gas pressure (if present), as well as on the bearing gas and process gas pressures, is examined. Also, the injection and bearing gas mass flow rates are determined and discussed for various pressure boundary conditions. For the cases considered:

1 The critical injection pressure P_{inj}^{C} and critical mass flux Φ_{inj} required to prevent oil vapor from reaching the process gas were determined and plotted for numerous bearing gas pressures for each of numerous seal geometries. In addition, the oil vapor contaminant flow resulting from the absence of buffer gas injection was determined.

2 The largest deviation of P_{inj}^{C} from the buffered baseline case (Fig. 7(*a*)) was only 7.5 percent for $P_{\text{bearing}}=P_{\text{process}}+110$ kPa, for example. This deviation was found for the case where the shaft radius was increased by 100 percent.

3 For numerous geometries as well as bearing, process and injection (where present) pressures, the leakage values of oil vapor, bearing gas, and injected buffer gas are presented and discussed for convenient application.

4 For the nonbuffered labyrinth seal with $P_{\text{bearing}}=P_{\text{process}}+110$ kPa, for example, the oil vapor leakage varied from its baseline value by up to 92 percent. Specifically, the nonbuffered labyrinth oil vapor leakage increase from its baseline value (Fig. 4) was: (*a*) 55 percent if the seal clearance is increased by 40 percent (*b*) 22 percent if the seal length is reduced by 50 percent, (*c*) 82 percent if the shaft radius is increased by 100 percent and (*d*) 92 percent if the clearance and length are increased and decreased by 40 percent and 50 percent, respectively. However, for

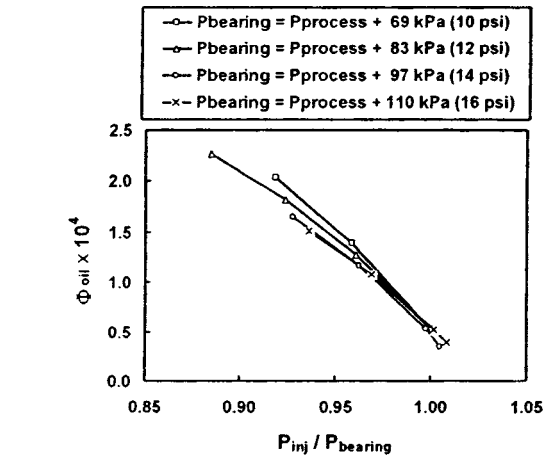

(*a*) **Oil Vapor Mass Flux**

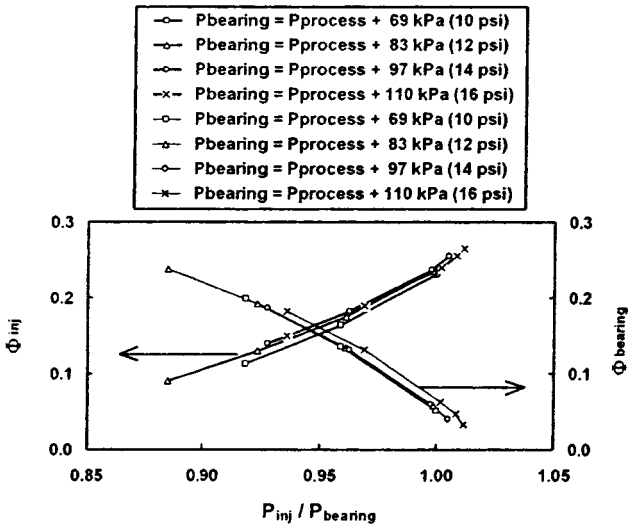

(*b*) **Injection and Bearing Gas Mass Flux**

Fig. 13 Variation with injection pressure of (*a*) oil vapor mass flux and (*b*) injection gas and bearing gas mass flux reaching the process gas side of the seal. [$P_{process}$=100 kPa (14.5 psi), Cr=0.36 mm (0.014 in.), W=0.51 mm (0.02 in.), L=30.86 mm (1.215 in.), R_{sh}=100.13 mm (3.942 in.), rpm=18,000, W_{in} =0.3$R_{sh\omega}$=56.556 m/s].

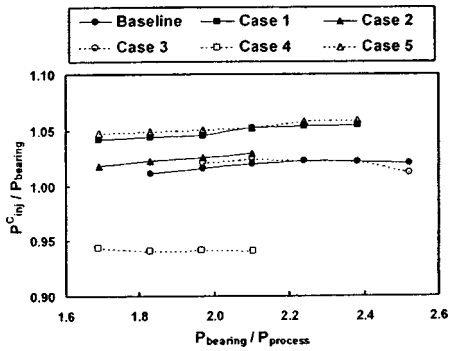

Fig. 14 Variation of the ratio of critical injection pressure ratio ($P^C_{inj}/P_{bearing}$) with bearing pressure ratio ($P_{bearing}/P_{process}$) for buffered labyrinth seal. (See Table 5(*b*)).

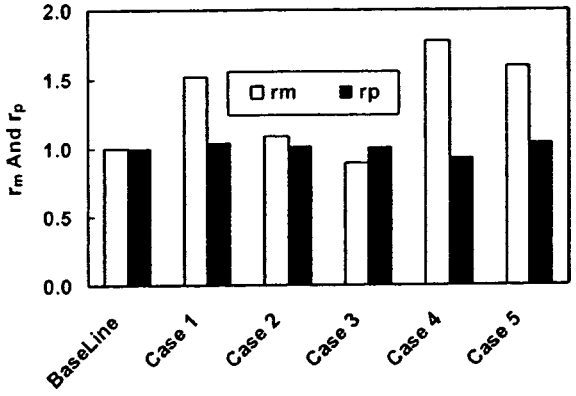

Fig. 15 Variation of the critical injection mass flow ratio ($r_m = \dot{m}^C_{inj}/\dot{m}^C_{inj}|_{baseline}$) and critical injection pressure ratio ($r_p = P^C_{inj}/P^C_{inj}|_{baseline}$) for $P_{bearing}/P_{process}$=2.1 for buffered labyrinth seal cases. (See Table 5(*b*)).

all of the buffer labyrinth seal cases considered, the oil vapor leakage can be completely prevented if the buffer-gas injection pressure is at least 6 percent higher than that of the bearing gas pressure.

Acknowledgments

The authors are grateful for the financial support of the Texas Advanced Technology Program and also of the Texas A&M University Supercomputer Center.

Nomenclature

A = area (m^2)
C = concentration (kmol/m^3)
Cr = clearance of the seal (mm)
D = diameter (mm)
D_{AB} = binary diffusion coefficient (m^2/s)
H = cavity depth (mm)
L = seal length (mm)
M = molecular weight (kg/kmol)
$\dot{m}$ = mass flow rate (kg/s)
P = pressure (Pa)
ppb = Parts per billion
R = gas constant (Nm/(kgK))
R_{sh} = rotor radius (mm)
$r_{bearing}$ = bearing mass flow ratio
r_m = critical injection mass flow ratio
r_p = critical injection pressure ratio
S = tooth pitch (mm)
Sc = Schmidt number
S_ϕ = source term
T = temperature (K)
u,v,w = velocities in (x,r,θ) coordinate system
W = injection slot width (mm)
W_{in} = swirl velocity at bearing side inlet (m/s)

Greek Symbols

Γ_ϕ = diffusion coefficient (kg/(ms))
Φ = Nondimensional mass flux parameter
ϕ = dependent variable
μ = viscosity (kg/(m·s))
ρ = density (kg/m^3)
ω = shaft speed (rad/s)

Subscripts

baseline = baseline case
bearing = bearing side
Cr = clearance
coarser = coarser grid

finer = finer grid
inj = injection
mix = mixture (oil vapor and air)
oil = oil vapor
process = process side
t = turbulent

Superscript

C = critical value

References

[1] Boyman, T., and Suter, P., 1978, ''Transport Phenomena in Labyrinth-Seals of Turbomachines,'' AGARD CP-237, pp. 8-1–8-10.

[2] Park, S., and Rhode, D. L., 2000, ''Predicted Geometry Effects on Oil Vapor Flow Through Buffer-Gas Labyrinth Seals,'' *Proceedings of the 8th International Symposium on Transport Phenomena and Dynamics of Rotating Machinery*, ISROMAC-8, **II**, pp. 1032–1040.

[3] Verma, N. K., Haider, A. M., and Shadman, F., 1993, ''Contamination of Ultrapure Systems by Back-Diffusion of Gaseous Impurities,'' J. Electrochem. Soc., **140**, pp. 1459–1463.

[4] Van Doormaal, J. P., and Raithby, G. D., 1984, ''Enhancements of the Simple Method for Predicting Incompressible Fluid Flows,'' Numer. Heat Transfer, **7**, pp. 147–163.

[5] Leonard, B. P., 1979, ''A Stable and Accurate Convective Modeling Procedure Based on Quadratic Upstream Interpolation,'' Comput. Methods Appl. Mech. Eng., **19**, pp. 59–98.

[6] Patankar, S. V., 1980, *Numerical Heat Transfer and Fluid Flow*, McGraw-Hill, New York.

[7] Rohsenow, W. M., and Hartnett, J. P., 1973, *Handbook of Heat Transfer*, McGraw-Hill, New York.

[8] Özisik, M. N., 1985, *Heat Transfer—A Basic Approach*, McGraw-Hill, New York.

K. Kitagawa
Research Center for Advanced Energy Conversion,
Nagoya University,
Furo-cho, Cikusa-ku,
Nagoya 464-8603, Japan
e-mail: kuni@apchem.nagoya-u.ac.up

N. Konishi
Department of Molecular Design and Engineering,
Graduate School of Engineering,
Nagoya University,
Furo-cho, Chikusa-ku,
Nagoya 464-8063, Japan

N. Arai
Research Center for Advanced Energy Conversion,
Nagoya University,
Furo-cho, Chikusa-ku,
Nagoya 464-8603, Japan

A. K. Gupta[1]
The Combustion Laboratory,
Department of Mechanical Engineering,
University of Maryland,
College Park, MD 20742
e-mail: akgupta@eng.umd.edu

Temporally Resolved Two-Dimensional Spectroscopic Study on the Effect of Highly Preheated and Low Oxygen Concentration Air on Combustion

Spontaneous emission spectroscopy has been applied to measure the time-resolved temperature profiles of gaseous fuel flames using high temperature and low oxygen concentration combustion air. Two emission peaks of C_2 radical species have been observed at visible wavelengths from propane-air flames. The ratio of these two peaks depends on the flame temperature. The relationship between the ratios of these peaks was correlated with the thermocouple output using a premixed flat flame burner and a multichannel CCD spectrometer. Using this relationship, the flame temperature was determined from the ratio of the C_2 peaks. Time-resolved emission intensity profiles of the two C_2 bands (two-wavelength image) were observed simultaneously with a high sensitivity video camera fitted with an optical system. The time-resolved temperature profiles were constructed from these intensity profiles by utilizing the previously determined relationship at each pixel. To evaluate fluctuations of flame temperatures, the standard deviation profiles for the temperature profiles have been constructed. This spectroscopic diagnostic technique has been used to measure the profiles of mean flame temperature and temperature fluctuation produced from a concentric diffusion flame using propane as the fuel and high temperature and low oxygen concentration combustion air. In this study, the effect of air-preheat and low oxygen concentration in the combustion air on the subsequent flame temperature and temperature fluctuations has been determined by analyzing the spectra of spontaneous emission from the C_2 radicals. [DOI: 10.1115/1.1520155]

Introduction

Recently, a variety of diagnostic techniques have been used to analyze the thermal behavior of flames. These diagnostic techniques include LIF (laser-induced fluorescence) spectroscopy and CARS (coherent antistokes Raman spectroscopy), [1–3]. Gas or radical species concentration as well as temperature can be measured using these laser diagnostic techniques. LIF spectroscopy allows measurements of two-dimensional profiles of flame temperature and concentration of combustion generated radicals. In contrast, CARS provides relatively precise information on the flame temperatures. However, there is difficulty in applying these laser diagnostic techniques to systems operating under harsh and severe conditions. Spontaneous emission analysis is a relatively simple diagnostic method for flames as compared to the more sophisticated and more expensive laser diagnostics techniques. The spontaneous emission spectrometry provides a very simple tool for flame diagnostics with only one detector or camera to examine practical flames.

Analysis of spontaneous emission from the combustion radicals in a flame can provide information on the temperature and relative concentration of the radical species. Furthermore, this analysis is nonintrusive and in-situ without using a laser. In this study, the spatially and temporally resolved flame temperature has been measured using the spontaneous emission from selected combustion species. The data was also analyzed for determining the flame fluctuation. Determination of these properties is critical for the study of NO_x emission from flames, emission of other pollutants, and combustion efficiency and intensity.

The use of highly preheated and low oxygen concentration air as an oxidizer in regenerative combustion systems is of significant interest in all sectors of industrial and power systems, [1–15]. The use of high temperature and low oxygen concentration combustion air has been shown to provide significant (a) energy savings of the order of about 30%, (b) pollution reduction, including NO_x, of the order of about 25%, and (c) reduction of the physical size of the combustion equipment of the order of about 25%, [6,10–15]. Reduced energy consumption also means reduced CO_2 emission to the environment. In some cases energy savings in excess of 60% has been shown from practical furnaces. It is now well known that the flame temperature increases with increase in temperature of the combustion air, and decreases with diluted (low) oxygen concentration in the air. In addition, the flame fluctuation at high temperature becomes lower with diluted (or low) oxygen concentration in the combustion air, [4–6,15]. Information on the fluctuations of flame and temperature, besides the mean flame temperature, are amongst the important factors for process quality and product control. Instantaneous high temperature fluctuations from large flame fluctuations contribute to high NO_x emission. In this study the flame thermal properties have been examined by the spontaneous emission of C_2 species from flames, which was then used to determine the two-dimensional profiles of flame temperature and its fluctuation, in terms of standard deviation.

Temperature Calibration

Figure 1 shows typical spectrum of C_2 emission bands (Swan band), observed from a propane-air flame. In this figure, two

[1]To whom correspondence should be addressed.

Contributed by the Fuels and Combustion Division of THE AMERICAN SOCIETY OF MECHANICAL ENGINEERS for publication in the ASME JOURNAL OF ENGINEERING FOR GAS TURBINES AND POWER. Manuscript received by the F&C Division August 2001; final revision received by the ASME Headquarters May 2002. Associate Editor: S. R. Gollahalli.

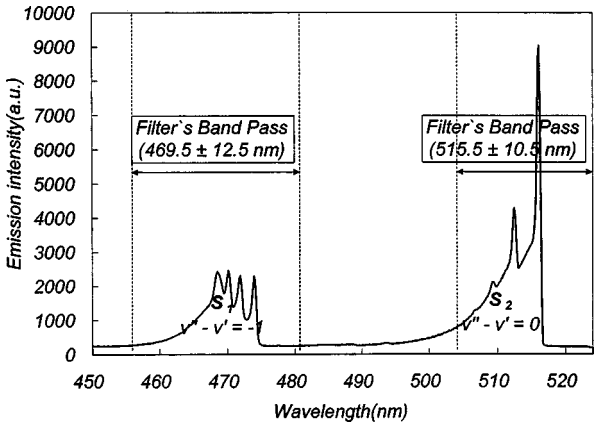

Fig. 1 Spectra of C_2 emission bands

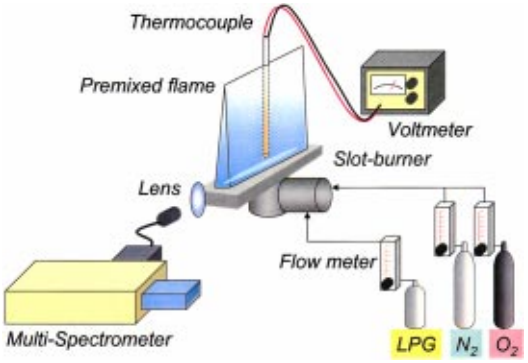

Fig. 2 Experimental apparatus for temperature calibration

major peaks centered around 469.5 nm and 515.5 nm can be observed. The integrated intensity at these two bands is denoted as S_1 and S_2, respectively. The ratio of the peak intensity at these two wavelengths is a function of the gas temperature. This can easily be derived theoretically. The only assumption made here is that the two wavelengths are close together so that the emissivity of the gas does not differ significantly at these two wavelengths. In the present study the two selected wavelengths are relatively close together. It is to be noted that the difference in wavelength between the peak at S_1 and S_2 results from the difference in transitions between the vibrational levels. In general, the emission intensity I of a component line is given by

$$I = h\nu AN^* \tag{1}$$

where h is the Planck's constant, ν is the frequency, A is the Einstein's coefficient for spontaneous emission, and N^* is population in the exited state. In this study, band-pass filters were used which isolate the band emission, see Fig. 1. The band emission intensity, S, measured with these filters can be described by the expression

$$S = \sum_i h\nu_i A_i N_i^* . \tag{2}$$

Based on the Boltzmann distribution law, the population in an excited state, N^*, is expressed as

$$N^* = N_{\text{total}} g \exp(-E^*/kT)/Q(T) \tag{3}$$

where g is the degeneracy in the excited state, E^* is the excitation energy, k is the Boltzmann's constant, N_{total} is the total number of species, T is the excitation temperature, and $Q(T)$ is the partition function. The ratio of emission intensity from the different transitions (i and j) depends only on the temperature, since h, g, A, and k are constant, and N_{total} and $Q(T)$ are omitted as seen from the following equation:

$$\frac{S_i}{S_j} = \frac{\sum_i A_i \nu_i \exp(-E_i^*/kT)}{\sum_j A_j \nu_j \exp(-E_j^*/kT)} . \tag{4}$$

The temperature calculated from Eq. (4) using the ratio of C_2 peaks indicates the vibrational temperature and is not consistent with the thermocouple temperature. Likely causes include the overpopulation of the higher vibrational levels on the excited electronic state due to the excess energy generated through chemical reactions, as well as the long vibrational relaxation time. Therefore, the relationship, or calibration is necessary that provides a relationship between the temperatures measured from the thermocouple and that determined from the ratio of the C_2 peaks. This was accomplished using the apparatus shown in Fig. 2.

A premixed flat flame produced by a slot burner has the property of a uniform temperature distribution in the flame. A multi-spectrometer is used to measure precisely the ratio of the two C_2 peak intensities. The spectra shown in Fig. 1 were measured with the spectrometer (Monochromator: Spectra Pro®-500, Detector: Insta Spac™ V), and this was then used to obtain exact information on the ratio of the C_2 peak intensity. The observation was made in the longitudinal direction for two seconds at any given location and the measurements were repeated three times. A 0.1-mm-diameter R-type thermocouple was placed at the center of the flame in the longitudinal (vertical) direction. Correction for the radiation loss was applied to the temperature measured with the thermocouple. The position of the thermocouple bead was the same as that measured with the spectrometer. The flame temperature was adjusted by changing the flow rates of N_2, O_2, and LPG (mostly propane) fuel. The C_2 spectra and temperatures were measured with this apparatus under several different conditions.

Figure 3 shows a plot of the relationship between measured temperature from the thermocouple and the ratio of peak intensities from C_2 species. The error bars in this figure indicate the standard deviation for the three different measurements made at a given location. The results clearly show that the flame temperature increases with the increase in ratio of the two C_2 peak intensity signals. This relationship is linear in the range of 1200 to 2000 K. In contrast, the curve in Fig. 3 is calculated by using Eq. (4) from the measured ratio of the C_2 peaks for the experimental range. The calculated temperatures of 3700 to 5500 K shown in the Fig. 3 are

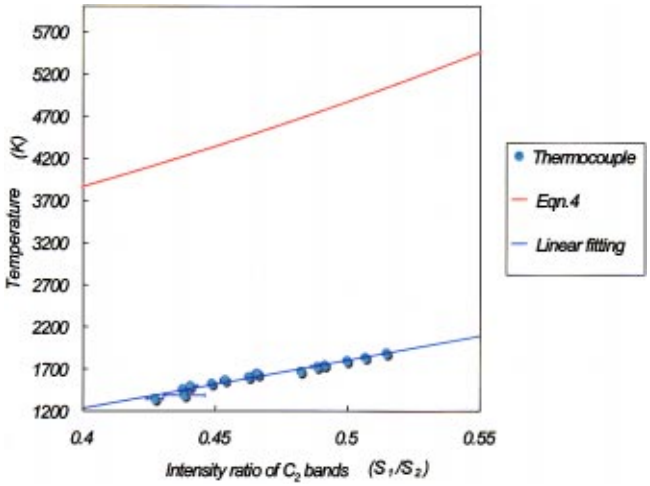

Fig. 3 Relationship between the ratio of C_2 intensities and temperature measured with a thermocouple

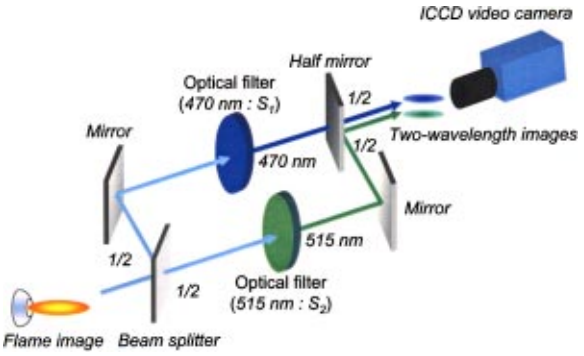

Fig. 4 A schematic diagram of the optical system used to obtain the two-dimensional temperature profiles

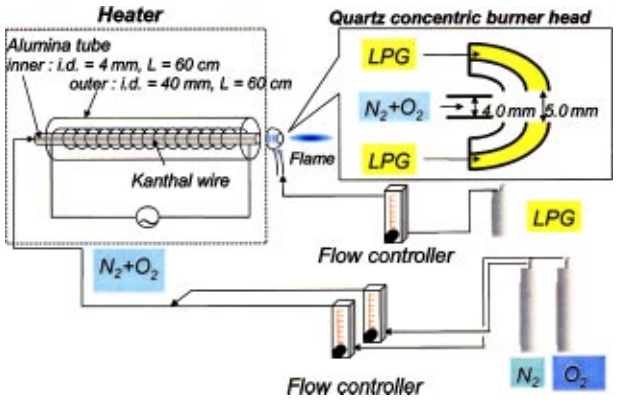

Fig. 5 A schematic diagram of the experimental apparatus, including the air preheat system for normal and diluted low oxygen concentration air, and the burner head

much higher than those obtained experimentally. This suggests that no local thermal equilibrium (LTE) exists between the vibrational systems of C_2 molecules and the thermocouple crystal lattice. A possible and likely cause for the higher C_2 temperature may be the overpopulation of the excited vibrational levels caused by an excess energy transfer through chemical reactions that produce this radical specie. The results in Fig. 3 show that even with this uncertainty there is a clear relationship between the two temperatures. Using this calibration curve, one can convert the two-dimensional spectroscopic temperature into the conventional temperature obtained using a thermocouple. This gas temperature, or an average temperature of the translational, vibrational and rotational temperature of gases involved induces this temperature during combustion.

For a strict discussion on non-LTE conditions we should use these temperatures separately. The temperature obtained from a thermocouple is particularly important for radiative heat transfer calculations using models. The temperature difference between the gas and soot are among other examples. A detailed discussion on such a phenomenon will be reported later elsewhere.

Time-Resolved Temperature Profile

In order to measure two-dimensional temperature profile at a given location and time, emission intensity profiles at two wavelengths must be observed simultaneously. In this study, this is achieved by using the optical system shown in Fig. 4. The image formed from the flame emission is split into two images of equal intensity using a beam splitter. One image passes through straight while the other image reflects at 90 deg (normal) to the first image. These two images pass through the optical filters (centered at 515 and 470 nm, respectively) to give monochromatic radiation at the two desired wavelengths. The two images are combined after passing through the half mirror and observed with the ICCD video camera. The shutter speed and frame speed of this video camera were 0.114 and 0.2 sec., respectively.

Figure 5 shows a schematic diagram of the experimental facility, which included a concentric diffusion flame burner system and an electrically heated air-preheat system. The air could be preheated to temperatures in excess of 1000°C with this system. The air was prepared using a mixture of oxygen and nitrogen so that any concentration of oxygen in air could be obtained. The electrical heater consisted of Kanthal wire and alumina tube to preheat the gas mixture of air and nitrogen. Kanthal wire of 1-mm diameter is wound around the inner alumina tube of 4 mm ID, 5 mm OD, and 60 mm in length. This tube is placed inside another alumina tube of 37 mm ID, 40 mm OD, and 60 mm in length. Alumina/silica wool is packed between these tubes to provide good thermal insulation so that maximum electrical energy is utilized to preheat the air. For the flow conditions used here, 400 Watt electric power was required to preheat the air to a temperature of 1000°C. The voltage required was 80 Volts for the 16 ohms total resistance of the wire.

A quartz concentric burner head produces a partial premixed flame. Three different conditions of the oxidizer mixture have been used to examine the flame features. For all the conditions, liquefied petroleum gas (LPG, mostly propane) was used as the fuel at a flow rate of 50 mL/min at normal temperature and pressure (NTP). The flow rate of the oxidizer (O_2+N_2) was held constant at 5 L/min at NTP. Three different conditions for the nitrogen and oxygen gas mixture examined here are: (1) room temperature (300 K) oxidizer mixture at normal oxygen concentration of 21%, (2) diluted oxidizer having 4% oxygen concentration in air at room temperature (300 K), and (3) diluted oxidizer having 4% O_2 concentration in air preheated to 900 K. The equivalence ratios for the three conditions were 0.25, 1.25, and 1.25, respectively. The temperature of oxidizer (mixture of nitrogen and oxygen) was measured with a thermocouple located immediately downstream of the burner exit.

The flame photographs taken for the three different conditions given above are shown in Fig. 6. They show that the flames are lengthened with the low oxygen concentration of 4%. For Case 2 with the room temperature oxidizer, the flame was visually very unstable. In contrast, using highly preheated air for Case 3, the flame stability was greatly increased. The flame obtained with preheated and nondiluted oxidizer (normal O_2 in air) is omitted, as the flame was very luminous for this condition. In addition the C_2 bands were not detected clearly due to continuum emission from soot particles and recombination of CO molecule with O atom in the flames under these conditions. The time-resolved two-wavelength images were therefore only measured for three condi-

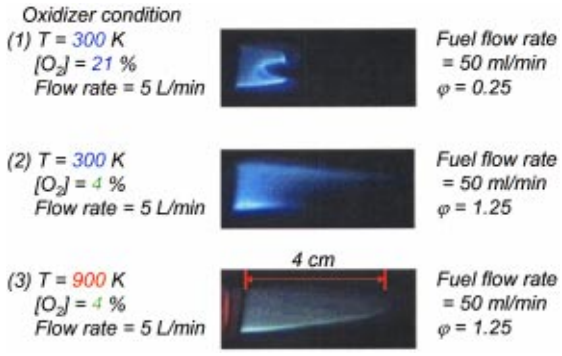

Fig. 6 Flame photographs obtained for three different conditions of air

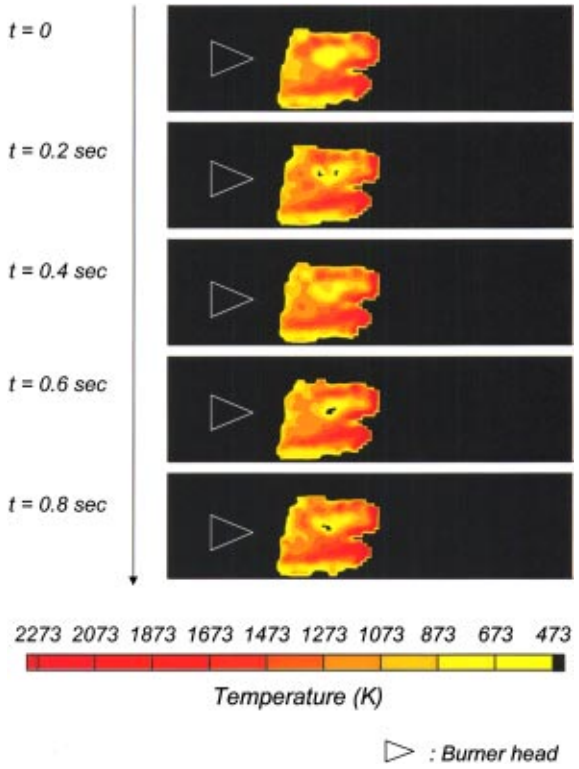

Fig. 7 Time-resolved temperature profiles with normal oxygen concentration air at 300 K, corresponding to condition (1)

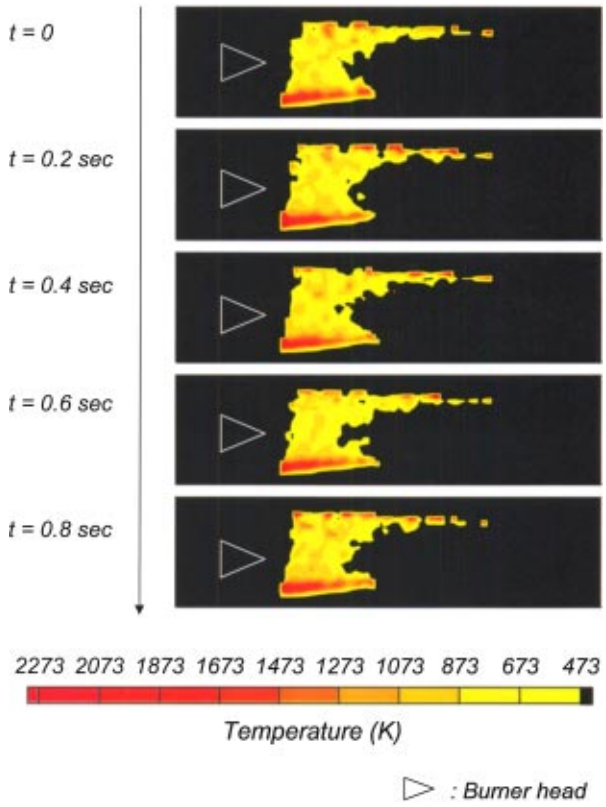

Fig. 8 Time-resolved temperature profiles with diluted air (4% O_2 in air) at 300 K, corresponding to condition (2)

tions using the video system shown schematically in Fig. 4. The time-resolved temperature profiles were determined on the basis of the relationship shown in Fig. 3.

The continuum emission levels have also been measured in a separate measurement at a wavelength of about 450 nm using the video system. This ''background'' image was measured at an exposure time of 1.14 sec for all the three flames examined. The background image was subtracted from time-resolved two-wavelength images. The difference in optical loss due to the two different optical paths in the experimental setup was calibrated with nonfiltered images of the flame emission. This procedure allowed determination of images with net emission level from the C_2 radicals. Time-resolved temperature profiles were calculated from these time-resolved net images of C_2 emission measured at the two wavelengths of 515 and 470 nm for the three significantly different flame conditions.

Figures 7, 8, and 9 show the temporal evolution of temperature profiles for the three different flames (Cases 1, 2, and 3), respectively. The temperature profiles for a flame are presented at a constant time interval of 0.2 seconds (i.e., at 0, 0.2, 0.4, 0.6, and 0.8 seconds) between each plot. These figures indicate both the spatial and temporal differences under these conditions. A comparison between Figs. 7 and 8 shows the effect of normal air and diluted air (low oxygen concentration air) with no air preheat. The results show that room temperature air having low oxygen concentration (as compared to the normal oxygen concentration air) decreases the flame temperature, reduces the uniformity of temperature distribution in the combustion zone, and reduces the volumetric expansion of the flame. A comparison between Figs. 8 and 9 shows the effect of preheating the oxidant using the diluted air (4% oxygen in air). The effect of preheating the oxidizer having diluted oxygen concentration is to increase the flame temperature as that found for case1. The uniformity of temperature distribution as well as the volumetric expansion of the flame region becomes more significant for Case 3, having preheated oxidizer

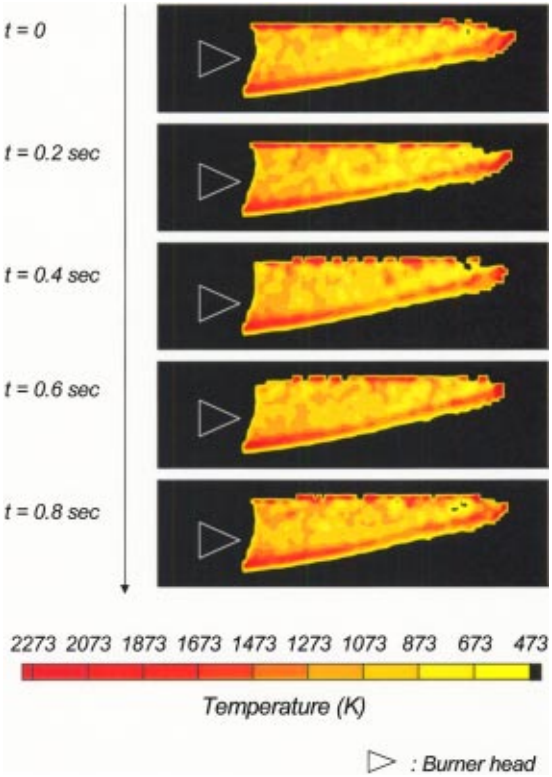

Fig. 9 Time-resolved temperature profiles with diluted air (4% O_2 in air) at 900 K, corresponding to condition (3)

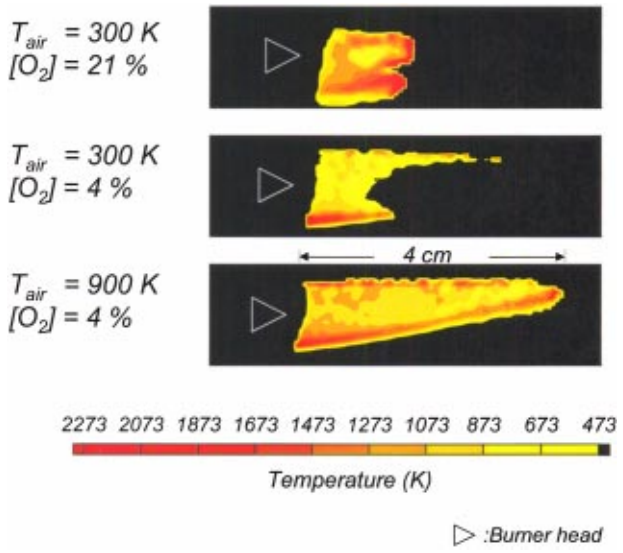

Fig. 10 Temperature profiles averaged over five flames for the three different flames

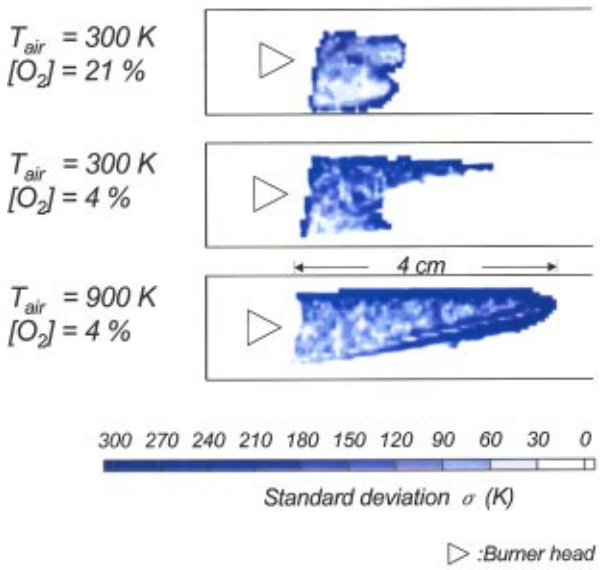

Fig. 11 Profiles of flame temperature fluctuations for the three different flames

with low O_2 concentration. All the profiles have high temperature zones around the flame. These zones can be considered as a direct result of the reaction between the fuel and air.

The time-averaged temperature profiles obtained for five frames are shown in Fig. 10. The abovementioned effects of diluting the oxygen concentration in the oxidizer and preheating the oxidizer on the subsequent flames produced can also be recognized from other studies conducted by the authors, [6–13]. Data obtained with the thermocouple measurement as well as the numerical simulation showed similar trends of increased flame volume and higher temperature using diluted air at high degree of air preheat. In this study, we have provided an analysis of spontaneous emission from flames. Furthermore we have successfully measured the thermal field uniformity in flames formed with diluted air at high temperature using nonintrusive, in-situ diagnostics (without the use of laser) that also provides high spatial and temporal resolution.

For more precise determination of the flame temperature, a correlation between the spectroscopic and thermocouple temperatures should be made for other diluted air combustion conditions. Another problem is the time resolution of 0.1 sec used. Although this shutter speed is not so slow for the transverse direction of the flame, streaking can be significant along the longitudinal direction, resulting in partially time-averaged images. Use of an ICCD camera with higher sensitivity and time resolution is the key to overcome this problem. Further insights to these issues will be examined at a later stage.

The profiles of the flame temperature fluctuation were estimated from the time-resolved temperature profiles. In this study, the standard deviation at each pixel location in the frame was calculated from the five flame temperature profiles. We recognize that by considering only five frames is not adequate to give a statistical representation. But this procedure captures the key features associated with the flame fluctuations.

The profiles of flame fluctuations were calculated for the three flames. For the room temperature oxidizer the effect of oxygen dilution on the flame fluctuation can be seen from a direct comparison of the temperature fluctuation profiles shown in the top two flames in Fig. 11. The flame fluctuation becomes greater with reduced oxygen concentration in the oxidizer. A comparison of the middle and bottom profiles of temperature fluctuation, shown in Fig. 11, reveals that the flame fluctuation decreases in the central area of the flame by preheating the oxidizer. These three profiles indicate that the flame fluctuation is higher in magnitude around the peripheral part of the flames. Since the fuel reacts with the surrounding oxidizer, the temperature becomes unstable mainly due to the convection effects. The time-resolved temperature profiles provide a clear indication on the flame fluctuations in normal and high temperature air combustion conditions. Less flame fluctuations and good thermal field uniformity suggests uniform heat flux distribution from the flame under diluted and high temperature air combustion conditions.

Conclusions

The relationship between the flame temperatures measured with a thermocouple and ratio of two emission bands from C_2 radicals (S_1/S_2) using a spectrometer has been determined experimentally. The results show that the flame temperature increases with the ratio of the two C_2 radicals as shown from the theoretical Eq. (4), assuming the Boltzmann distribution law. The temperatures calculated with Eq. (4), however, are much higher than those measured with the thermocouple. This discrepancy suggests that the Boltzmann distribution law does not govern the population level of the C_2 radicals. In both cases a linear relationship was found between the thermocouple temperature and the ratio of C_2 emission bands over the measured range. This linear relationship was used as the calibration curve to calculate the flame temperature from the ratio of the C_2 emission bands.

In order to calculate the time-resolved temperature profiles, the time-resolved emission intensity profiles from C_2 radicals were simultaneously measured at two different wavelengths. An intensified CCD video camera and the optical system developed for this study allowed this measurement. The background emission level and optical loss associated with the two different paths were taken into consideration for measuring the profiles of temperature and temperature fluctuation.

Time-resolved temperature profiles have been measured with the calibration curve and the video camera system for three different flames using different oxygen concentration in air and air preheat temperature. The effect of diluting oxygen concentration in the oxidizer and preheating the oxidizer on the flame temperature were experimentally confirmed through the image analysis of spontaneous emission from C_2 radicals. The technique is nonintrusive, in-situ and does not require the use of a laser. Furthermore the technique provides high spatial and temporal resolution.

The flame fluctuations were estimated from the measured standard deviation of the time-resolved temperature. The profiles of

flame fluctuation were compared amongst the flames for the three different flames examined. This comparison also indicated the effect of diluting oxygen concentration in the oxidizer and preheating the oxidizer on the flame temperature and flame fluctuation.

The information on the flame temperature and flame fluctuation has been obtained with the image analysis of the spontaneous emission from C_2 radicals. The developed method is much simpler than the more expensive laser diagnostic techniques and is, therefore, usable for nonintrusive and in-situ analysis of practical combustion systems, such as, combustors in industrial furnaces and boilers, with high spatial and temporal resolution.

Acknowledgments

The research support provided by NEDO is gratefully acknowledged. One of the authors (AKG) would also like to acknowledge the support provided by NSF and NASA microgravity combustion program for this research.

References

[1] Hancock, R. D., Bertagnolli, K. E., and Lucht, R. P., 1997, ''Nitrogen and Hydrogen CARS Temperature Measurements in a Hydrogen/Air Flame Using a Near-Adiabatic Flat-Flame Burner,'' Combust. Flame, **109**(3), pp. 323–331.

[2] Haudiquert, M., Cessou, A., Stepowski, D., and Coppalle, A., 1997, ''OH and Soot Concentration Measurements in a High-Temperature Laminar Flame,'' Combust. Flame, **111**(4), pp. 338–349.

[3] Bengtsson, P., Martinsson, L., and Aldén, M., 1995, ''Combined Vibrational and Rotational CARS for Simultaneous Measurements of Temperature and Concentrations of Fuel, Oxygen, and Nitrogen,'' Appl. Spectrosc., **49**(2), pp. 188–192.

[4] Kishimoto, K., Watanabe, Y., and Kasahara, M., 1997, ''Observational Study of Chemiluminescence from Flames with Preheated and Low Oxygen Air,'' *Proc. The First Asia-Pacific Conference on Combustion*, Osaka, Japan, May 12–15, pp. 468–471.

[5] Hasegawa, T., Tanaka, R., and Niioka, T., 1997, ''Combustion with High Temperature Low Oxygen Air in Regenerative Burners,'' *Proc. The First Asia-Pacific Conference on Combustion*, Osaka, Japan, May 12–15, pp. 290–293.

[6] Gupta, A. K., and Li, Z., 1997, ''Effect of Fuel Property on the Structure of Highly Preheated Air Flames,'' *Proc. Joint Power Generation Conference (IJPGC)*, **1**, Denver, CO, Nov. 2–5, pp. 247–258.

[7] Kitagawa, K., Kubota, M., Arai, N., and Gupta, A. K., 2002, ''Profiling of REDOX Index During Combustion by Chemical Seeding and Application to Monitoring of Degradation of C/C Composite in a Flame,'' J. Propul. Power, **18**(2), accepted for publication.

[8] Konishi, N., Kitagawa, K., Arai, N., and Gupta, A. K., 2002, ''Two-Dimensional Spectroscopic Analysis of Spontaneous Emission from a Flame During Highly Preheated Air Combustion,'' J. Propul. Power, **18**(1), pp. 199–204.

[9] Ishiguro, T., Tsuge, S., Furuhata, T., Kitagawa, K., Arai, N., Hasegawa, T., Tanaka, R., and Gupta, A. K., 1998, ''Homogenization and Stabilization During Combustion of Hydrocarbons With Preheated Air,'' *Proc. 27th Symposium (International) on Combustion*, The Combustion Institute, Pittsburgh, PA, pp. 3205–3213.

[10] Gupta, A. K., Bolz, S., and Hasegawa, T., 1999, ''Effect of Air Preheat and Oxygen Concentration on Flame Structure and Emission,'' ASME J. Energy Resour. Technol., **121**, pp. 209–216.

[11] Gupta, A. K., 2000, ''Thermal Characteristics of Gaseous Fuels Flames Using High Temperature Air,'' *Proc. of the 3rd International Symposium on High Temperature Air Combustion and Gasification*, Yokohama, Japan, Mar. 6–9.

[12] Hasegawa, T., Mochida, S., and Gupta, A. K., 2002, ''Development of Advanced Industrial Furnace Using Highly Preheated Air Combustion,'' J. Propul. Power, **18**(2), pp. 10–18.

[13] Gupta, A. K., 2001, ''High Temperature Air Combustion: Experiences From the USA-Japan Joint Energy Project,'' *Proc. of the 4th High Temperature Air Combustion and Gasification Symposium*, Rome, Italy, Nov. 27–30.

[14] Katsuki, K., and Hasegawa, T., 1998, ''The Science and Technology of Combustion in Highly Preheated Air,'' *27th Symposium (Intl.) on Combustion*, The Combustion Institute, Pittsburgh, PA, pp. 3135–3146.

[15] Tsuji, H., Gupta, A. K., Hasegawa, T., Katsuki, M., Kishimoto, K., and Morita, M., 2003, *High Temperature Air Combustion: From Energy Conservation to Pollution Reduction,* CRC Press, Boca Raton, FL.

Enhancement of Methane-Air Mixing Using Shock and Expansion Waves

D. Brasoveanu

A. K. Gupta
Professor and Director
e-mail: akgupta@eng.umd.edu

The Combustion Laboratory,
Department of Mechanical Engineering,
University of Maryland,
College Park, MD 20742

A unified model of gaseous fuel and air mixing is applied here to study the use of shock waves for enhancement of mixing between methane and air. The model uses fuel mass fraction within infinitesimal fluid elements and the total derivative of this fraction with respect to time to measure the degree and rate of mixing, respectively. The model is accurate only for low-pressure combustors since it is based on the ideal gas law. The model is also limited to gaseous fuels that contain single chemical specie, or those that behave like single specie. The model presented here can be applied to any combustor geometry or operational conditions. Results show that mixing can be completed within the narrow region of the shock wave and therefore in a negligibly short time, if pressure, temperature, and velocity distributions within this region are optimized. Furthermore, the combined effects of air preheat and shock waves can enhance both mixing mechanisms with air penetration into the fuel and with fuel dispersion into the surrounding air. These results provide important guidelines for the mixing in supersonic combustors that are required to provide high efficiency and high intensity, while maintaining low levels of pollutants emission. [DOI: 10.1115/1.1519274]

Introduction

Combustion cannot begin until the fuel and air are mixed to the molecular level, i.e., the distance between fuel and air molecules becomes smaller than the free molecular path, [1]. In addition, the fuel to air ratio has to be maintained between the rich and lean flammability limit, in order to avoid flame extinction, [2]. In other words, increased combustor efficiency as well as lower pollutants emission requires enhanced fuel-air mixing, [3], and tight control of equivalence ratio within the flame (levels of both unburned hydrocarbons and NO_x can be kept below the acceptable thresholds by using fuel-lean flames or staged combustion). Therefore, the mixing between fuel and air requires better understanding, especially the determination of conditions that reduce mixing times.

Modern combustors need to operate over a wide variety of operational conditions. Shock or expansion waves can occur within the mixing region of fuel and air. Shock waves are regions of step transition or discontinuity within fluid that are characterized by virtually instantaneous pressure and temperature variations, [4,5]. Regions of more gradual pressure reduction that are called rarefaction waves may accompany shock waves. The occurrence of shock or rarefaction waves increases the complexity of combustor design problems. In contrast the shock and rarefaction waves may be used to enhance the performance of combustors.

At atmospheric pressure the thickness of a shock wave is about 10^{-7} m. Fuel or airflow would pass through a shock wave in only a few nanoseconds. The mixing between fuel and air within a shock wave would be completed virtually instantaneously. Mixing within a rarefaction wave would also be fast. This paper analyzes conditions that provide conditions for good and complete mixing within shock and rarefaction waves.

Theoretical Approach

The unified mixing model that was presented by the authors in previous papers, [6–9], is applied here together with the mass, momentum and energy conservation law, [4,5], to determine the pressure and temperature jumps that provide complete mixing within shock or expansion waves. Consider an infinitesimal fluid element that contains fuel, air and trace amounts of combustion products (no more than 5% by mass). The fuel has to be gaseous and contains a single chemical specie. It is further assumed that the ideal gas law is applicable, i.e., the operating pressure is less than ~ 5 atm. The degree of mixing is measured using the local equivalence ratio (i.e., within the infinitesimal fluid element) or the local mass fraction of fuel, y_f. The rate of mixing is given by the total derivative with respect to time of the degree of mixing. Mapping the fuel-air boundary with such elements would provide a global picture on mixing.

Mixing may occur with air penetration into the fuel flow, or with fuel dispersion into the surrounding air, [6]. When the first of the above mixing mechanisms is involved, producing a flammable mixture requires lowering the local equivalence ratio from infinity to the upper flammability limit, i.e., 1.68^2. Mixing using the second mechanism requires increasing the local equivalence ratio from 0 to 0.5, which is the lower flammability limit. The control of fuel and air ratio in a flame itself has been presented in a previous paper by the authors, [6–10].

The equation of diffusion is not necessary to study fuel-air mixing. A far more simple method of analyzing fuel-air mixing is presented in detail in a previous paper by the authors, [6]. Assuming ideal gas and a fuel that contains a single chemical specie, only pressure, temperature and velocity gradients (caused by vorticity for example) promote mixing. It is true that rates of mixing, [6–9], also depend on initial pressure, temperature, velocity of fuel and airflow, and fuel molecular weight. However, mixing is not possible in the absence of the above-mentioned gradients. Shock and expansion waves are regions of abrupt variations of pressure, temperature and velocity that are difficult to model in detail. However, it is not necessary to do so in order to determine conditions that provide complete mixing within these waves. Here, the rate of mixing is quantified by the total derivative with respect to time of fuel mass fraction, dy_f/dt, [7,8]; i.e., it can be calculated as follows:

$$\frac{dy_f}{dt} \approx \frac{(y_{f,2} - y_{f,1})}{t_{\text{pass}}}$$

Contributed by the Fuels and Combustion Division of THE AMERICAN SOCIETY OF MECHANICAL ENGINEERS for publication in the ASME JOURNAL OF ENGINEERING FOR GAS TURBINES AND POWER. Manuscript received by the F&C Division, February 2000; final revision received by the ASME Headquarters April 2002. Associate Editor: S. R. Gollahalli.

where t_{pass} is time required to pass through the wave, $y_{f,2}$ is the final mass fraction of fuel, and $y_{f,1}$ is the initial mass fraction of fuel. These final and initial mass fractions are ~0.03 and 0, respectively, for mixing with fuel dispersion into the surrounding air. For mixing with air penetration into fuel, the final and initial mass fractions of fuel are ~0.09 and 1, respectively. The time required to pass through the shock or expansion waves being $\sim 10^{-9}$ s, the rate of mixing is of the order of $1/10^{-9} = 10^{9}$ (s^{-1}) for mixing with air penetration into fuel and of the order of $0.03/10^{-9} = 3 \times 10^{11}$ (s^{-1}) for mixing with fuel dispersion into the surrounding air. From the ideal gas law

$$\frac{P_2}{P_1} = \frac{M_1}{M_2}\frac{T_2}{T_1}\frac{\rho_2}{\rho_1} \tag{1}$$

where indices 1 and 2 indicate conditions before and after passing through the shock or expansion wave, respectively. The molecular weight and therefore mass fractions change due to mixing. The initial molecular weight, M_1, is equal to 0.016 kg/mole and 0.0289 kg/mole within the fuel and airflow, respectively. The final molecular weight of mixture is 0.0269 kg/mole and 0.0283 kg/mole, for mixing with air penetration into fuel and mixing with fuel dispersion into the surrounding air, respectively. For mixing with air penetration into fuel, the initial $y_{f,1}$ and final $y_{f,2}$ mass fraction of fuel are 1 and 0.089, respectively. For mixing with fuel dispersion into the surrounding air, the initial and final mass fraction of fuel is 0 and 0.02825, respectively.

Consider an infinitesimal fluid element that is split by the shock or expansion wave. Using a coordinate system that moves with the shock wavefront, the law of mass conservation shows that, [4,5],

$$\rho_1 u_1 = \rho_2 u_2 \tag{2}$$

where, u is the component of flow velocity that is normal to the front of the shock or expansion wave, while the other velocity components, i.e., v and w, provide mixing within the fluid element.

The law of momentum conservation applied to shock and expansion waves can be written as, [4,5],

$$P_1 + \rho_1 u_1^2 = P_2 + \rho_2 u_2^2. \tag{3}$$

Neglecting heat transfer, the conservation of energy law shows that, [4],

$$e_1 + \frac{u_1^2}{2} + \frac{P_1}{\rho_1} = e_2 + \frac{u_2^2}{2} + \frac{P_2}{\rho_2}. \tag{4}$$

Assuming constant specific heat capacity at constant pressure, the specific enthalpy of mixture before and after passing through the wave, h_1 and h_2, respectively, are

$$h_1 \approx c_{pm,1} T_1 \tag{5}$$

and

$$h_2 \approx c_{pm,2} T_2. \tag{6}$$

The specific heat at constant pressure depends on temperature and species mass fractions of fuel and air (note that conservation equations need to be written for a two-component system). Therefore, the initial and final specific heat at constant pressure of mixture, $c_{pm,1}$ and $c_{pm,2}$, respectively, are given by

$$c_{pm,1} = c_{pa}(1 - y_{f,1}) + c_{pf} y_{f,1} \tag{7}$$

$$c_{pm,2} = c_{pa}(1 - y_{f,2}) + c_{pf} y_{f,2} \tag{8}$$

where, $y_{f,1}$ and $y_{f,2}$ are the initial and final mass fraction of fuel, respectively. Based on Eq. (1) through (8), mixing is completed within the shock or expansion wave, whenever

$$\frac{\rho_1}{\rho_2} = \frac{u_2}{u_1} = \frac{-b \pm \sqrt{b^2 - 4ac}}{2a} \tag{9}$$

where

$$a = u_1^2 \left(\frac{1}{2c_{pm,2}} - \frac{M_2}{R} \right) \tag{10}$$

$$b = \frac{M_2}{M_1} T_1 + \frac{M_2}{R} u_1^2 \tag{11}$$

$$c = -\frac{c_{pm,1}}{c_{pm,2}} T_1 - \frac{u_1^2}{2c_{pm,1}}. \tag{12}$$

The temperature, T_2/T_1, and pressure jump (or ratio), P_2/P_1 should be

$$\frac{T_2}{T_1} = \left[\frac{M_2}{M_1} + \frac{M_2}{RT_1} u_1^2 \cdot \left(1 - \frac{-b \pm \sqrt{b^2 - 4ac}}{2a} \right) \right] \left(\frac{-b \pm \sqrt{b^2 - 4ac}}{2a} \right) \tag{13}$$

$$\frac{P_2}{P_1} = 1 - \frac{M_1}{RT_1} u_1^2 \left(\frac{-b \pm \sqrt{b^2 - 4ac}}{2a} - 1 \right). \tag{14}$$

Because Eqs. (9), (13), and (14) are quadratic, complete mixing within a shock or expansion wave is possible only for limited ranges of initial temperature, pressure, and axial velocity.

Before the wave, the fluid elements of the mixture are nonhomogenous. During transition through wave, fuel is carried into the airflow or air into the fuel flow due to the nonaxial components of velocity, i.e., v and w. Velocity gradients are correlated as seen from the equation of continuity:

$$\frac{d\rho}{dt} = -\rho \cdot \mathrm{div}(\mathbf{U}).$$

Therefore, after choosing the distribution of one nonaxial component of velocity, v for example, the gradient of w is given by (the gradient of axial component being calculated using a finite difference scheme)

$$\frac{dw}{dz} \approx \frac{u_1 - u_2}{\delta} - \frac{dv}{dy} + \frac{\rho_1 - \rho_2}{\rho_1 \cdot t_{pass}} \tag{15}$$

The above conditions are based on well-established laws and therefore are expected to provide near-instantaneous fuel-air mixing.

Numerical Approach

Mixing with both fuel dispersion into the surrounding air and air penetration into fuel is analyzed based on Eqs. (7) through (14). The overall range of initial axial velocity and temperature that is considered here is 180 m/s to 800 m/s and 270 K to 360 K, respectively. Calculations were performed using MATHCAD 8.0.

Results and Discussion

Results are presented here to include the pressure and temperature jump across the discontinuity for assuring complete methane-air mixing within both shock and expansion waves. Figure 1 shows initial axial velocity and temperature values that allow mixing with air penetration into the fuel within a shock wave. The axial velocity is listed on the horizontal axis; the temperature on the vertical axis and the resulting pressure jump is shown on the contours. For initial axial velocity and temperature of 575 m/s and 360 K, respectively, the value of the pressure jump is 1.22. The associated temperature jump is 1.8. The pressure and temperature ratios increase for higher and lower initial axial velocity and temperature, respectively. These ratios attain the maximum values of 4.00 and 2.31, respectively, for initial velocity of 800 m/s and temperature of 270 K. Therefore, methane and air are easier to mix within shock waves if initial axial velocity is low and initial temperature is high. Mixing with air penetration into fuel flow within shock waves is restricted to supersonic combustors.

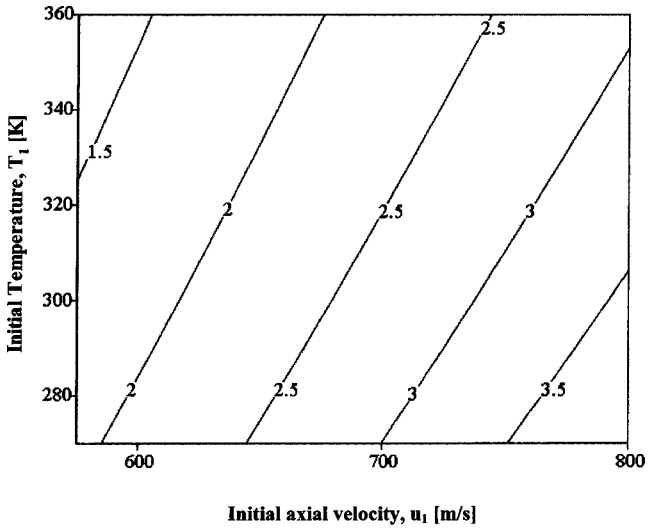

Fig. 1 Pressure jump, P_2/P_1, for complete methane-air mixing with air penetration into the fuel within shock waves

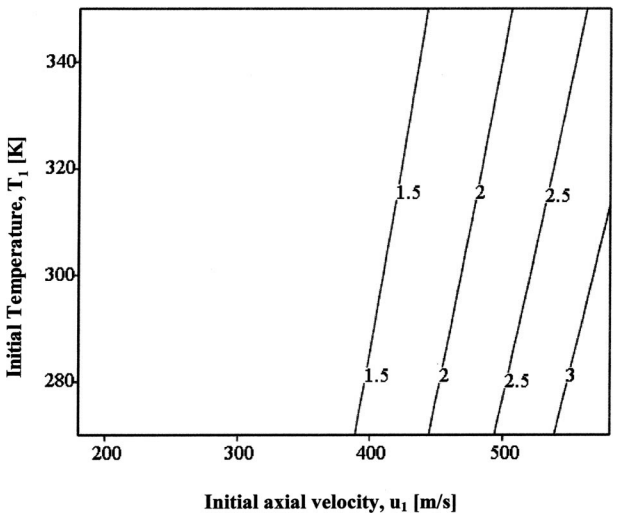

Fig. 3 Pressure jump, P_2/P_1, for complete methane-air mixing with fuel dispersion into the surrounding air within shock waves

The pressure jumps required for complete mixing within expansion waves using air penetration into fuel are shown in Fig. 2. The range of initial temperature is about the same as for mixing within shock waves, but the initial axial velocity is restricted to a narrow range, i.e., 200 m/s to 320 m/s. For initial axial velocity and temperature of 200 m/s and 350 K, respectively, the pressure ratio, should be only 0.024. This value is very low for practical purposes. The associated temperature jump is 0.59. Higher and lower initial axial velocity and temperature, respectively, reduce the severity of the pressure jump. The maximum pressure and temperature ratio is 0.667 and 1.64, respectively. These ratios require an initial axial velocity and temperature of 320 m/s and 270 K, respectively.

Mixing with air penetration into fuel increases the molecular weight of the mixture. The pressure ratio, P_2/P_1, has to be less than 1, whenever mixing occurs with air penetration into fuel at constant temperature and density, since pressure is inversely proportional to molecular weight, see Eq. (1). Shock waves increase pressure. Therefore either the temperature has to decrease, or the axial velocity has to increase, see Eq. (2), to allow mixing with air penetration into the fuel. In contrast, expansion waves reduce pressure. Therefore both the initial axial velocity and the temperature jump are lower than required for mixing within a shock wave. As a consequence mixing with air penetration into the fuel flow is better suited for expansion waves.

Figure 3 shows jump conditions for mixing with fuel dispersion into the surrounding air within a shock wave. The range of initial temperature and axial velocity is 270 to 350 K and 180 m/s to 580 m/s, respectively. Complete methane-air mixing could be achieved using a mild transition (pressure and temperature ratios of 1.003 and 0.972, respectively) for an initial axial velocity of 180 m/s and a temperature of 350 K. The jumps severely increase for higher and lower initial axial velocity and temperature, respectively. The maximum pressure and temperature ratio is 3.5 and 1.45, respectively. In general, mixing with fuel dispersion into the surrounding air requires a less severe shock wave and a lower initial axial velocity than mixing with air penetration into fuel, compare Figs. 1 and 3. In addition shock waves are thinner than expansion waves and are expected to provide the shortest mixing

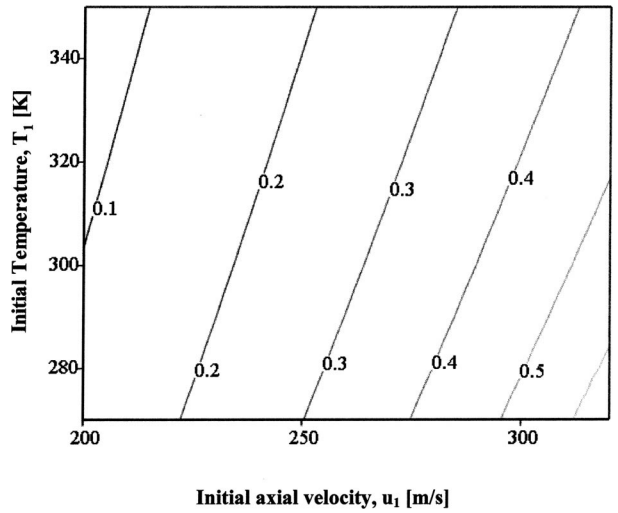

Fig. 2 Pressure jump, P_2/P_1, for complete methane-air mixing with air penetration into fuel within expansion waves

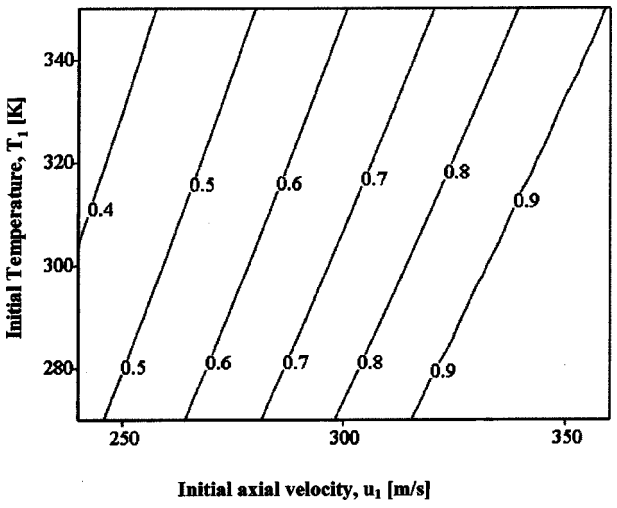

Fig. 4 Pressure jump, P_2/P_1, for complete methane-air mixing with fuel dispersion into the surrounding air within expansion waves

times. Therefore, in agreement with previous studies, [6,9], the recommended mixing mechanism is fuel dispersion into the surrounding air within a shock wave.

Mixing with fuel dispersion into the surrounding air is also possible, as shown in Fig. 4. Because this mixing mechanism reduces the molecular weight of the mixture, the pressure would increase unless the temperature and/or axial velocity jump are higher as compared to mixing within shock waves. As a consequence, the range of initial axial velocity is only 240 m/s to 360 m/s, if the range of initial temperature remains unchanged (i.e., 270 K to 350 K). The minimum and maximum pressure ratio is 0.327 and 0.996, respectively. The temperature ratio associated with the former is 0.696. The maximum temperature ratio is 0.976. The higher and lower the initial temperature and axial velocity, respectively, the stronger the wave should be.

Conclusions

Within shock waves methane and air mixing times can be reduced to a few nanoseconds. To a lesser degree, expansion waves may also provide enhanced mixing. Two mixing mechanisms that can be distinguished are air penetration into fuel and fuel dispersion into the surrounding air. The former is better associated with expansion waves, the latter works best within shock waves. Smaller pressure and temperature jumps are required to complete mixing within both shock and expansion waves when using fuel dispersion into air as compared to air penetration into fuel. Best results are expected with fuel dispersion into the surrounding air within a shock wave.

Future prospects in the area include examination of pressure and temperature ratios using more accurate equations of state and values of specific heat at constant pressure. Detailed combustor geometry and shock or expansion wave characteristics should also be determined. The use of such waves to enhance mixing of other fuels and air should also be analyzed. Mixing at higher initial temperatures is also of interest and should be examined.

Acknowledgments

This research was partially supported by NASA Glenn Research Center and the University of Maryland. This support is gratefully acknowledged.

Nomenclature

c_{pa} = specific heat capacity of air at constant pressure (J/kg K)

c_{pf} = specific heat capacity of methane at constant pressure (J/kg K)

$c_{pm,1}$ = specific heat capacity of mixture at constant pressure before passing through the shock or expansion wave (J/kg K)

$c_{pm,2}$ = specific heat capacity of mixture at constant pressure after passing through the shock or expansion wave (J/kg K)

h_1 = specific enthalpy of mixture before passing through the shock or expansion wave (J/kg)

h_2 = specific enthalpy of mixture after passing through the shock or expansion wave (J/kg)

M_1 = molecular weight of mixture before passing through the shock or expansion wave (kg/mole)

M_2 = molecular weight of mixture after passing through the shock or expansion wave (kg/mole)

p_1 = pressure before the shock or expansion wave (Pa)

p_2 = pressure after the shock or expansion wave (Pa)

R = universal gas constant (J/K mole)

T_1 = mixture temperature before the shock or expansion wave (K)

T_2 = mixture temperature after the shock or expansion wave (K)

t_{pass} = time for passing through the shock or expansion wave (s)

$\mathbf{U}$ = overall velocity (m/s)

u_1 = axial velocity of mixture element before passing through the shock or expansion wave (m/s)

u_2 = axial velocity of mixture element after passing through the shock or expansion wave (m/s)

v_1, w_1 = nonaxial components of velocity of mixture element before passing through the shock or expansion wave (m/s)

v_2, w_2 = nonaxial components of velocity of mixture element after passing through the shock or expansion wave (m/s)

$y_{f,1}$ = mass fraction of fuel within the mixture element before passing through the shock or expansion wave (dimensionless)

$y_{f,2}$ = mass fraction of fuel within the mixture element after passing through the shock or expansion wave (dimensionless)

Greek

ϕ = desired equivalence ratio (dimensionless)

ρ_1 = mixture density before passing through the shock or expansion wave (kg/m^3)

ρ_2 = mixture density after passing through the shock or expansion wave (kg/m^3)

δ = thickness of the shock or expansion wave (m)

References

[1] Khavkin, Y. I., 1996, *Combustion System and Design*, Pennwell Books, Tulsa, OK, pp. xiii, xixi.

[2] Strehlow, R. A., 1984, *Combustion Fundamentals*, McGraw-Hill, New York, pp. 28, 370–375.

[3] Gupta, A. K., and Lilley, D. G., 1994, "Combustion and Environmental Challenges for Gas Turbines in the 1990s," J. Propul. Power, **10(2)**, pp. 137–147.

[4] Barnard, J. A., and Bradley, J. N., 1985, *Flame and Combustion*, 2nd Ed., Chapman and Hall, New York, pp. 91–107.

[5] Drumheller, D. S., 1998, *Introduction to Wave Propagation in Nonlinear Fluids and Solids*, Cambridge University Press, Cambridge UK, pp. 2–4, 73–85, 171–183.

[6] Brasoveanu, D., and Gupta, A. K., 1999, "Analysis of Gaseous Fuel and Air Mixing," Combust. Sci. Technol., **141**, pp. 111–121.

[7] Brasoveanu, D., and Gupta, A. K., 1999, "Analysis of Propane-Air Mixing Under Reacting and Non-Reacting Conditions," 35th AIAA/ASME/SAE/ASEE Joint Propulsion Conference and Exhibit, Los Angeles, CA, June 20–24, Paper No. 99-2873.

[8] Brasoveanu, D., and Gupta, A. K., 2000, "Maximum Mixing Times of Methane and Air," J. Propul. Power, Vol. **16**(6), pp. 956–963.

[9] Brasoveanu, D., and Gupta, A. K., 2001, "Determination of Propane and Air Maximum Mixing Times," ASME J. Eng. Gas Turbines Power, **123**(1), pp. 226–230.

[10] Brasoveanu, D., and Gupta, A. K., 2000, "Analysis of Gaseous Fuel and Air Mixing in Flames and flame Quenching," J. Propul. Power, **16**(5), pp. 829–836.

Schlieren Observation of Spark-Ignited Premixed Charge Combustion Phenomena Using a Transparent Collimating Cylinder Engine

K. Kozuka
Senior Researcher

T. Ozasa
Senior Researcher

T. Fujikawa
Senior Researcher

A. Saito
Fellow

Toyota Central R&D Labs, Inc.,
Nagakute-cho, Aichi-ken 480-1192
Japan

The schlieren photographs of in-cylinder processes in a spark-ignited premixed charge gasoline engine were observed via a transparent collimating cylinder and were presented in comparison with a pressure analysis. The schlieren photographs of the spark, the initial flame and the unburned gas ejection from the piston crevice, which is unable to be observed by direct photography, were clearly taken. It shows that the small difference in the initial combustion process among cycles is intensified by the movement of the piston during the expansion stroke. Finally, this difference appears as the cycle by cycle variation in the pressure and the rate of heat release. The observed flame size increased faster and was larger than the burned gas estimated from the pressure. The difference between them is large enough and can not be explained without considering the mixing of burned and unburned gases inside the flame front. [DOI: 10.1115/1.1496774]

1 Introduction

The schlieren visualization method, which is a way to observe the change in the density of gas, is one of the most effective ways to understand the phenomena concerning ignition, combustion, and unburned gas. Therefore, the schlieren method has been applied to visualize the in-cylinder processes of experimental engines viewed from the top of a cylinder (Sinnamon et al. [1]) and viewed from the side of a pre-chamber (Solomon [2]).

The schlieren visualization of in-cylinder processes from the side of an engine is also useful to understand the phenomena which change along the cylinder axis. Many studies have been carried out using rectangular combustion chamber (Zhu et al. [3]) or square piston engines (Namazian et al. [4], Namazian and Heywood [5], Heywood and Vilchis [6], Edwards et al. [7], and Weaver and Santavicca [8]). However, the cylinder shape of the square piston engine is quite different from practical engines, so a transparent cylinder, which permits schlieren observation, had been desired. The authors developed such a transparent cylinder named the transparent collimating cylinder (TCC) (Fujikawa et al. [9]).

In gasoline engines, the schlieren observation of in-cylinder phenomena is important concerning flame development and the behavior of unburned gas. Especially, the relation between flame development and the rate of heat release seems to be very interesting. Furthermore, a comparison of the combustion phenomena between different cycles is important. This is because gasoline engines have a larger cycle-by-cycle variation in combustion than diesel engines. Therefore, spark-ignited premixed charge combustion phenomena should be observed by taking notice of the items mentioned above.

In the present report, the high speed schlieren photographs of the combustion in a premixed charge (Electronic Fuel Injection (EFI)) gasoline engine taken with the TCC are presented coupled with the in-cylinder pressure analysis and discussed by taking notice of the items mentioned above.

2 Experimental Apparatus

2.1 Principle of Transparent Collimating Cylinder (TCC) and Schlieren System. Figure 1 shows the principle of the TCC, namely the cross sectional view of the TCC and the path of light rays incident to the cylinder. The inner surface of the TCC is a cylindrical shape. To retain parallel light rays both inside and outside of the TCC, the form of the outer surface is determined by a special function (Fujikawa et al. [9]). The TCC used in this study was made of acrylic plastic having the same dimensional accuracy as reported in a previous study (Fujikawa et al. [9]). Since then, the manufacturing precision of the TCC has been improved. The optical property in the present state was already reported (Fujikawa et al. [10]).

The schlieren system is shown in Fig. 2. It consists of an Ar-ion laser as the light source, a convex lens (focal length: 20 mm), two plane mirrors, two spherical mirrors (focal length: 1500 mm) and a knife edge. In the present experiment, a circular edge was selected as the knife edge. It consists of transparent glass with a metal circle having diameter of 9×10^{-3} m (9 mm). The reasons why the circular edge and its diameter were selected were already described in a previous report (Fujikawa et al. [9]). A high-speed camera, NAC E-10 having frame speed of 4800 fps, was used for the image recording. Crank angle numerals written on the flywheel were also simultaneously taken in each schlieren photograph to mark the time of each photograph.

2.2 Visualization Engine and Operating Conditions. The construction and specification of the visualization engine are shown in Fig. 3 and Table 1, respectively. The visualization engine was based on an experimental single-cylinder 4-stroke cycle engine. The TCC with a 4.2×10^{-2} m (42 mm) height was mounted between a cylinder block and a cylinder head with two asbestos gaskets. To avoid the interference between the piston rings and the TCC, an elongated piston having a top land height of 3.5×10^{-2} m (35 mm) was used. The cylinder head has a helical

Contributed by the Internal Combustion Engine Division of THE AMERICAN SOCIETY OF MECHANICAL ENGINEERS for publication in the ASME JOURNAL OF ENGINEERING FOR GAS TURBINES AND POWER. Manuscript received by the ICE Division, Dec. 2000; final revision received by the ASME Headquarters, Feb. 2002. Editor: D. N. Assanis.

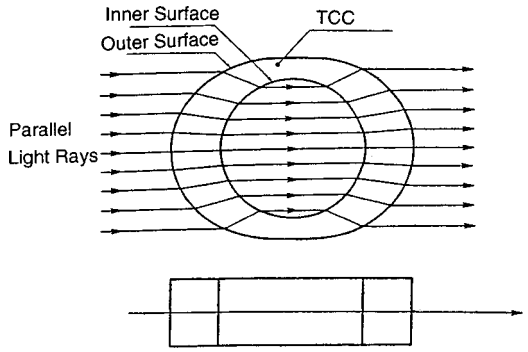

Fig. 1 Cross-sectional view of the transparent collimating cylinder (TCC) and the path of light rays incident to the cylinder

intake port whose steady swirl ratio measured with a static test rig is 2.6. It generates a swirl flow in the cylinder in the clockwise direction seen from top of the cylinder head.

The front view in Fig. 3, which corresponds to photographs in the cylinder, is the cross section of the visualization engine with the TCC seen from the high-speed camera. A spark plug with an electrode 1.4×10^{-2} m (14 mm) in length was used for ignition. Gasoline was used as the fuel.

To observe the combustion in the EFI engine, gasoline was injected in an electrically heated intake port with an injection nozzle located 0.35 m (350 mm) up stream from the intake valve. The injection pressure was 0.2 MPa. The operating conditions are shown in Table 2.

Table 1 Specifications of the visualization engine

Bore	0.083 m (83 mm)
Stroke	0.085 m (85 mm)
Displacement volume	4.599×10^{-4} m^3 (459.9 cm^3)
Compression ratio	9.5
Combustion chamber	Disk Shape
Fuel system	Electronic fuel injection (EFI)
Heating	Hot water and electric heater
Fuel	Gasoline
Ignition	Spark ignition
Swirl ratio	2.6
TCC	Acrylic plastic
Inner radius	0.0415 m (41.5 mm)
Maximum thickness	0.025 m (25 mm)
Height	0.042 m (42 mm)

Table 2 Engine operating conditions

Speed	13.33 rad/s (800 rpm)
Air/fuel ratio	17
Volumetric efficiency	56%
Spark timing	−0.349 rad ATDC (−20 deg ATDC)

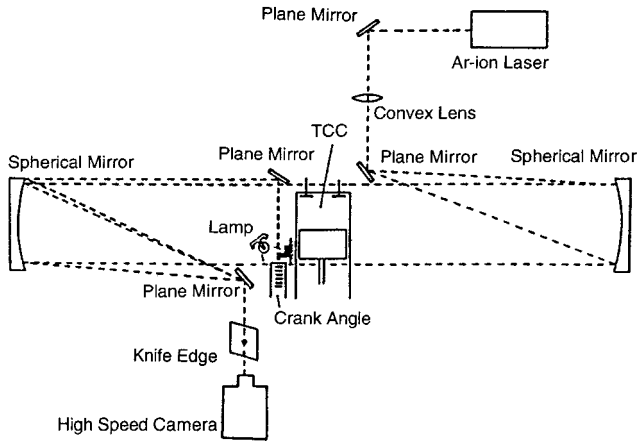

Fig. 2 Schlieren system

2.3 Measurement of In-Cylinder Pressure and Its Analysis. The in-cylinder pressure was measured using a piezo-electric transducer, AVL Type 8QP500C, plugged in the cylinder head toward the cylinder. The piezoelectric transducer was connected to a charge amplifier, Vibro Meter SA TA-3/D, that was calibrated before the experiments. The pressure signal of the charge amplifier and an event signal from the high speed camera were simultaneously acquired by a data acquisition system, VAX11 750 computer, to make the correspondence between the in-cylinder pressure and the frames of the high-speed film. A pulse-generating

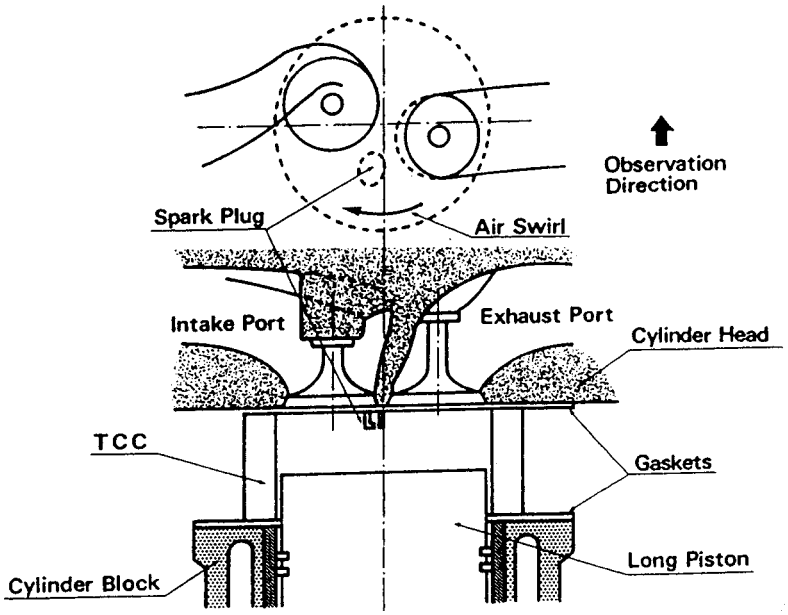

Fig. 3 Schematic diagram of the visualization engine

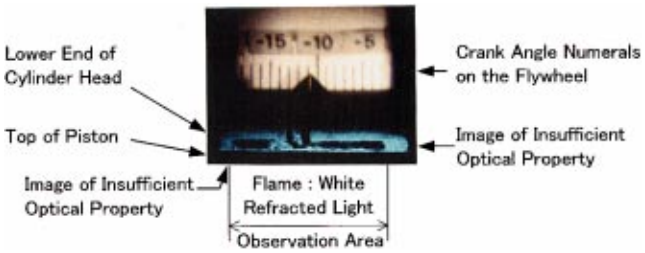

Fig. 4 Representative photograph of the image recording at −11 deg after top dead center (ATDC) in cycle (b)

device was mounted on the front end of the crankshaft and was used as a clock for the data acquisition system. The pressure data were used to calculate the burned and unburned gas temperatures in the cylinder and the rate of heat release, $dQ/d\theta$, using the VAX11 750 computer. Here, the temperatures in the cylinder and the rate of heat release were estimated based on the equation of state and the first law of thermodynamics, respectively, assuming zero-dimensional two zones in the cylinder. The details are shown in Appendix A.

3 Observation Results

3.1 A Sample Photograph. Figure 4 shows a representative photograph of the image obtained in the present experiment. The schlieren photograph was taken with the crank angle numerals written on the flywheel of the visualization engine, so that the crank angle numerals were recorded in the upper area of the photograph and an in-cylinder image was taken in the lower area of the photograph. In the photograph of the in-cylinder image, the top and bottom ends of the image correspond to the lower end surface of the cylinder head and the top surface of the piston, respectively. The white zones near the left and right ends of the in-cylinder image indicate schlieren images of the cylinder itself due to its insufficient optical property. Therefore, the phenomena in the cylinder can be observed inside the above white zones. The ignition, flame, and unburned gas emerge as white images by refraction of the parallel light caused by the density change in the gas. In the following sections, the representative photographs are presented with the corresponding pressure analyzed results. The time of the events is expressed by the crank angle, θ, in degrees after top dead center (ATDC) in the expansion stroke.

3.2 Combustion of Electronic Fuel Injection (EFI) Engine. Figure 5 shows the schlieren photographs of the in-cylinder phenomena over two consecutive cycles of the EFI engine with the

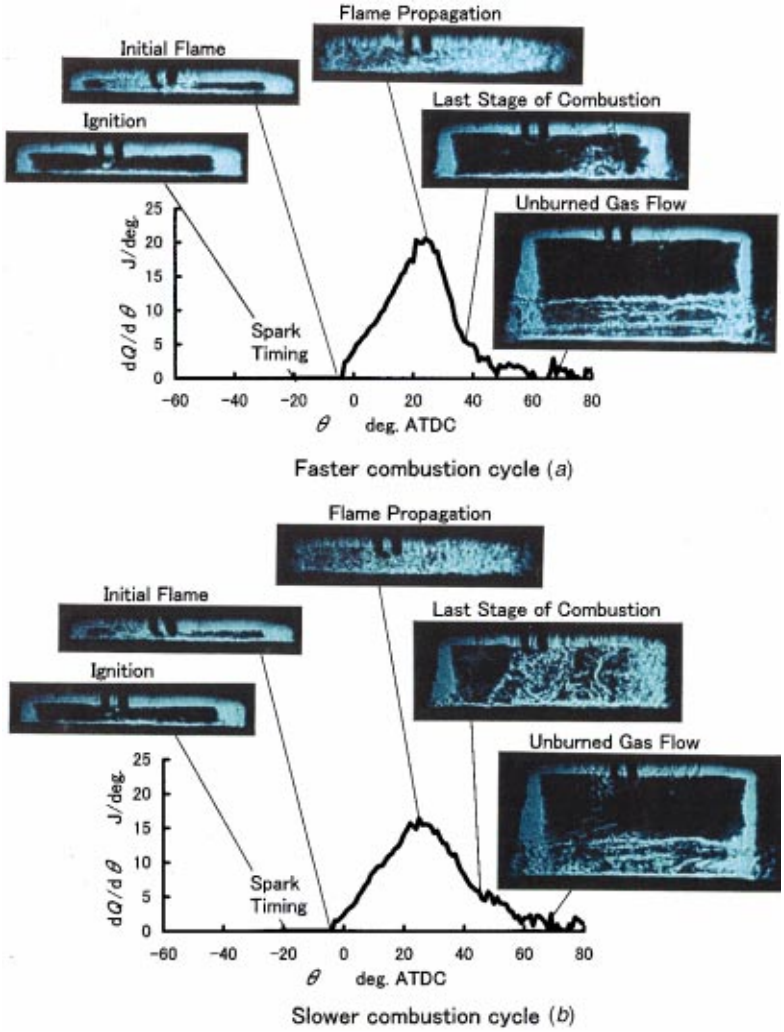

Fig. 5 Schlieren photographs of the in-cylinder phenomena over two consecutive cycles with the rate of heat release $dQ/d\theta$

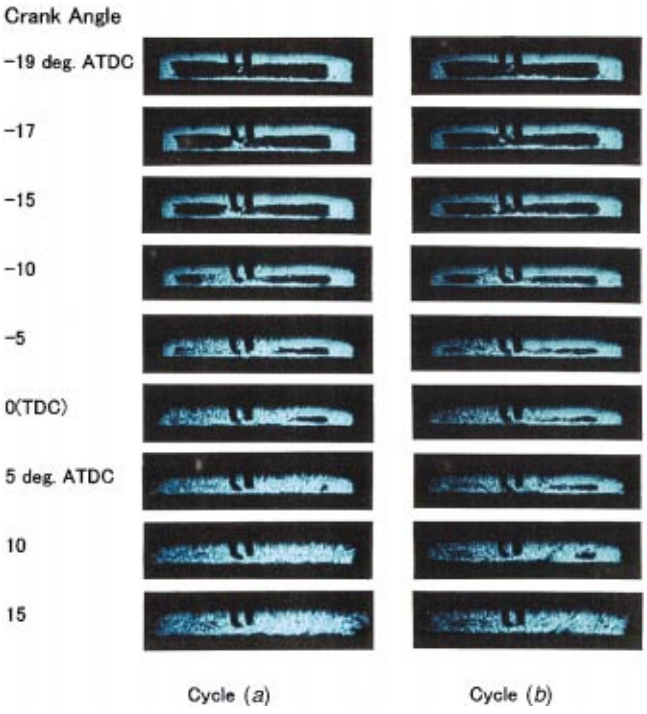

Fig. 6 Schlieren photographs of the ignition and initial combustion of two consecutive cycles, (a) and (b)

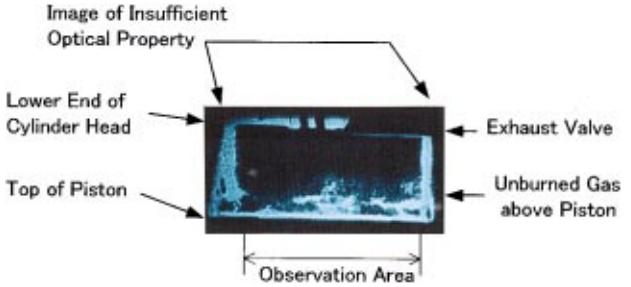

Fig. 7 Schlieren photograph of the in-cylinder phenomena at −62 deg ATDC during exhaust stroke in cycle (a)

rate of heat release, $dQ/d\theta$, estimated from the pressure analysis. The maximum $dQ/d\theta$ of cycle (a) is about 20 percent higher than that of cycle (b), though the total heat releases in cycle (a) and cycle (b) are almost the same.

The following phenomena can be seen in the photographs. At −18 deg ATDC, a spark is seen in the gap between the two electrodes. At −6 deg ATDC, initial development of the flame is observed in the photographs, though there is almost no heat release. The white schlieren image increases till 15 deg ATDC (see Fig. 6). The white schlieren image then decreases as seen in the photographs at the peak of the heat release. The burned gas zone with the same density diminishes the white schlieren image. Therefore, it may be thought that combustion within the flame tends to be completed. At about 40 deg ATDC, that is near the end of the combustion due to the heat release, white refracted light can be seen in cycle (b), but there is almost no white refracted light in cycle (a). The unburned gas ejections from the piston crevice are observed after 47 deg ATDC in cycle (a) and 53 deg ATDC in cycle (b). The representative schlieren photographs at 62 deg ATDC are shown with the indication of unburned gas flow. Namazian and Heywood [5] already showed unburned gas ejected from the piston crevice and jet from the top ring gap using a production piston inserted into the square cross-section piston of their visualization engine. In their results, there is no influence by the moving wall of the piston having a relative velocity on the gas ejected from the piston crevice. In the present study, the unburned gas ejections from the piston crevice were more realistic than those of Namazian and Heywood by means of TCC but it was intensified and the jet from the top ring gap could not be observed due to the long top land height.

The representative schlieren photograph of the in-cylinder phenomena during the exhaust stroke is shown in Fig. 7. The white schlieren image, which is considered to be unburned gas, is observed above the top of the piston. Tabaczynski et al. [11] took vortex flows at a moving corner using an experimental test rig. Namazian et al. [4] took vortex flows clearly during the exhaust stroke using their square piston engine. The white schlieren image in the present study, which is considered to be vortex flows, is taken in the engine cylinder but the vortex image did not clearly appear due to the insufficient optical property near the left and right ends of the TCC. The relation between the vortex flows and the exhaust hydrocarbon emission was already explained by Tabaczynski et al. [12].

Weaver and Santavicca [8] have studied the relation between cyclic fluctuation in the flame kernel growth and cylinder pressure using their two-stroke cycle square piston engine. In the present study, the difference between the maximum $dQ/d\theta s$ in the two consecutive cycles is investigated using the schlieren photographs of the ignition and initial combustion. The schlieren photographs of the two consecutive cycles are shown in Fig. 6. At −19 deg ATDC, that is a 1 deg after spark timing, the spark between the two electrodes of the spark plug can be seen. At −17 and −15 degs ATDC, the formation of the initial flame around the electrode can be seen. At −10 deg ATDC, the initial flames grow to the left side with the swirl flow in both cycles. Swirl flow in the compression stroke was measured using a similar combustion chamber and intake port as those used in the present experiment (Okubo et al. [13]). It can be seen from these photographs that the initial flame grows faster in cycle (a) than in cycle (b). The ignition and initial flame can not be observed by the direct observation method. Therefore, the schlieren observation from the side of an engine is necessary. So far, schlieren observations using the square piston engine (Namazian et al. [4]) were carried out. However, in the case of the cylindrical piston engine, it was the first time to be able to observe the ignition and initial flame by the schlieren method using the TCC. At −5 deg ATDC, flame propagates right side of the spark plug in cycle (a), but there is no flame in the right side of the spark plug in cycle (b). At TDC, 5 deg ATDC and 10 deg ATDC, these differences clearly appear. For instance, at 5 deg ATDC, the space of the photograph is almost covered by the flame in cycle (a), but there is some space with no flame in the left side of the spark plug and the flame slowly progresses to the right side in cycle (b). Thus the small difference in the initial flame expands as a large difference in the subsequent combustion stages.

The schlieren photographs in Fig. 6 were analyzed by the image analysis technique. The white image in the photograph was picked out, the ends of white image were measured and converted into locations of the flame ends in the cylinder according to the principle of the TCC. Witze [14] took shadowgraph photographs of flame propagations from the top of the engine of about the same size in the present study. In his results, the circular image of the flame propagation is observed under low swirl, a swirl ratio of 3.2 and spark plug on the cylinder wall location. In the present study, the swirl ratio is 2.6 and the spark plug offset is 18 mm from the cylinder axis. The present study has a lower swirl and spark plug location closer to the cylinder axis than the Witze's low swirl case. Furthermore, the authors took direct photographs of the combustion using the bottom view engine in which the flame propagated near the circular image as shown in Fig. 8. From the above reasons, the spherical flame propagation, namely the cylindrical flame propagation in this high compression engine, could be as-

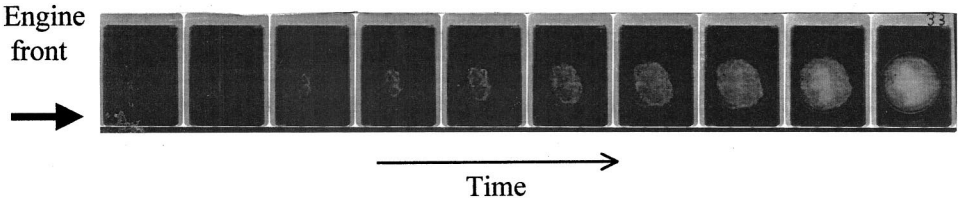

Fig. 8 Direct photographs of combustion with same cylinder head and bottom view engine

sumed. The areas of the white image in the photograph, A_{flame}, could be converted to the cross-sectional flame areas in the cylinder. The cross-sectional flame area in the cylinder was then normalized by the cross-sectional area of the combustion chamber. That is the cross-sectional area ratio of the flame, the white image, to the cylinder of the combustion chamber, $A_{\text{flame}}/A_{\text{cylinder}}$. The details of the equations are shown in Appendix B.

On the other hand, the volume of burned gas was calculated by the pressure analysis by considering the temperatures of the burned and unburned gas zones. The cross-sectional area of the burned gas, A_{pb}, was calculated assuming a cylindrical volume. After that, the cross-sectional area of the burned gas was normalized by the cross-sectional area of the combustion chamber. That is the cross-sectional area ratio of the burned gas to cylinder of the combustion chamber, $A_{pb}/A_{\text{cylinder}}$. The A_{pb} is considered as the two-dimensional expression of the burned gas with thermal expansion and can be compared to the two dimensional visualization of a three-dimensional flame, A_{flame}. The explanation and the equations are described in Appendices A and B.

Figure 9 shows the comparison of the cross sectional area ratio of the flame to cylinder, $A_{\text{flame}}/A_{\text{cylinder}}$, and the cross-sectional area ratio of the burned gas to cylinder, $A_{pb}/A_{\text{cylinder}}$ in both cycles. The curve of $A_{pb}/A_{\text{cylinder}}$ began to rise at the time of 60% in cycle (a) and 40% in cycle (b) in $A_{\text{flame}}/A_{\text{cylinder}}$. The $A_{\text{flame}}/A_{\text{cylinder}}$ increased faster and higher than the $A_{pb}/A_{\text{cylinder}}$ in both cycles (a) and (b). The difference between them is large enough and can not be explained without considering the mixing of the burned and unburned gases inside the flame front. A comparison between the flame image and mass fraction burned, which is derived from the pressure analysis, has already been carried out by Namazian et al. [4] and Gatowski et al. [15]. Namazian et al. [4] calculated the mass derived from the density of the gas and the assumption of spherical flame propagation. In these results, though they used a square piston engine with low compression ratio, the flame propagation based on the observations was faster than that expected from the pressure analysis. Heywood [16] explains in his textbook that the difference between the flame image and the mass fraction burned is derived from the thermal expansion and corner volume of the square piston engine. However, in the present study, the difference between the image analysis and the pressure analysis is shown even with considering thermal expansion and using a cylindrical combustion chamber.

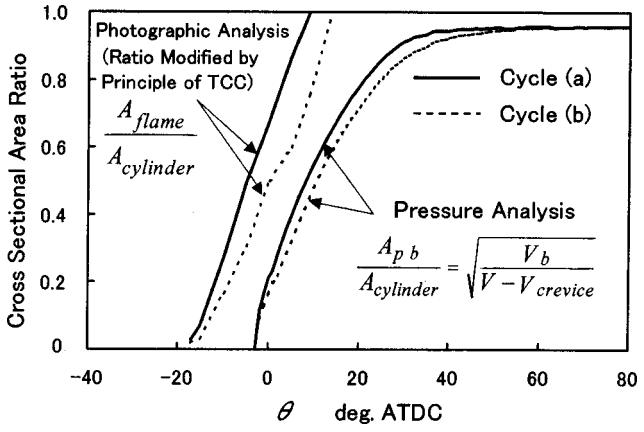

Fig. 9 Cross-sectional area ratio of flame to cylinder by photographic analysis versus cross-sectional area ratio of burned gas to cylinder by pressure analysis

Namazian et al. [4] described that the difference between the image analysis and the pressure analysis is consistent with the turbulent entrainment model reported by Tabaczynski et al. [17] and Hires et al. [18], which considers the entrainment of unburned gas into the flame zone and defined it as the turbulent flame reaction zone between the burned and unburned zones. The authors also think that the white schlieren image, light refraction from the flame area, is the change in density not only with the heat release caused by the combustion but also by the mixing of the burned and unburned gases inside the flame front. The authors think that the relation between $A_{\text{flame}}/A_{\text{cylinder}}$ and $A_{pb}/A_{\text{cylinder}}$ is consistent with the turbulent entrainment model even for the high-compression cylinder engine.

In the observation engines, it is difficult to take images for a long duration. Therefore, the cycle-by-cycle variation must be discussed using the observed phenomena in only a few cycles. In the present study, the differences in the flame images and pressure traces between two consecutive cycles are used for discussion. As described in Section 2.3, the flame images and pressure are in the same cycle and strictly correspond for each other. It is obvious in the photograph that the flame speed of cycle (a) is faster than that of cycle (b). Therefore, the $A_{\text{flame}}/A_{\text{cylinder}}$ of cycle (a) is larger than that of cycle (b). The reason for the cycle-by-cycle variation is considered as follows. The flame spreads widely before the rise in $A_{pb}/A_{\text{cylinder}}$, which is related to the mass fraction burned. Therefore, the rate of the combustion is decided before the beginning of the heat release. The difference in the initial combustion processes between the cycles is intensified by the increase in the cylinder volume during the expansion stroke. The flame of cycle (b) must propagate into a larger space with a 0 to 30 K lower temperature than that of cycle (a). Therefore, it can be said that the small difference in the initial combustion processes among the cycles is intensified by the movement of a piston and finally appears as the cycle-by-cycle variation in the pressure and the rate of heat release.

4 Summary of the Observations

The schlieren photographs of the in-cylinder processes in an EFI engine were observed by the TCC and were presented in comparison with the pressure analysis to discuss the phenomena. The summaries of the schlieren observations are described as follows.

(1) Schlieren photographs of the spark between the electrodes of the spark plug and initial flame were clearly taken. These phenomena cannot be clearly observed by conventional direct photography because of their weak radiation. The TCC allows the schlieren observation of these phenomena using a cylindrical piston.

(2) The combustion can be detected by the pressure analysis after a large portion of the combustion chamber is occupied by the flame with the schlieren observation. The observed flame size increased faster and was larger than the burned gas estimated from

the pressure analysis. The difference between them is large enough and can not be explained without considering the mixing of burned and unburned gases inside the flame front. The relation between the schlieren photographs and pressure analysis is consistent with the turbulent entrainment model.

(3) The flame spreads widely before the combustion is detected by the pressure analysis. The difference in the flame development between cycles was also observed by the schlieren images. Therefore, the rate of combustion is decided in the early stage of the combustion. The small difference in the initial combustion processes among cycles is intensified by the movement of a piston and finally appears as the cycle-by-cycle variation in the pressure and rate of heat release.

(4) The schlieren images of unburned gases ejected from the piston crevice during the expansion stroke and above the top of a piston during the exhaust stroke in a cylinder engine, which can not be observed by a direct photography, can be observed using the TCC.

Finally, the authors confirmed based on these results that the schlieren observation method by the TCC is very useful to understand the in-cylinder phenomena of a practical engine.

Nomenclature

A = area (m^2)
h = height of combustion chamber in cylinder (m)
n_λ = refractive index of transparent material
r = radius (m)
r_0 = inner radius of cylinder (m)
t = thickness of transparent material at β radian from X-axis (m)
t_0 = thickness of transparent material along X-axis (m)
V = volume (m^3)
X = location of light ray from Y-axis (m)
Y = location of light ray from X-axis (m)
β = angle in cylinder (rad)
γ = angle in TCC (rad)

Subscripts

b = burned gas
c,d = ends of flame b burned gas
flame = flame
crevice = top land crevice between cylinder and piston
cylinder = combustion chamber in cylinder
in = inside of the inner circle of TCC
out = outside of TCC
p = pressure analysis

Appendix A

A.1 Pressure Analysis.

A1.1 Fundamentals. Pressure analysis of the combustion process is based on a two-zone model. The concept of the model is shown in Heywood's textbook ([19]). The authors would like to show the present analysis in detail. One zone is unburned gas, which is a mixture composed of air, fuel, and residual combustion gas in the cylinder. Here, it is assumed that the property of the fuel is based on iso-octane and residual gas is in chemical equilibrium at 1500 K. The other zone is burned gas, which is a mixture under chemical equilibrium condition at the burned gas temperature. The chemical equilibrium calculation is based on eleven components which are N_2, O_2, CO, CO_2, H_2O, H, H_2, OH, O, N, and NO. The enthalpy including the chemical energy and chemical equilibrium constants of each component are values from the JANAF thermochemical tables (Chase et al. [20]).

The molecular weights and thermal properties of the burned and unburned gases are based on the mol fractions of the components in each zone. The two-zone model is based on the equations of states assuming an ideal gas in each zone and energy equations according to the first law of thermodynamics for unburned and burned gases. The temperature and volume of each zone, mass fraction burned and rate of heat release are determined by the measured pressure and flow rates of air and fuel. The mass of the residual gas is assumed to be that calculated from the volume and the condition at suction TDC. The energy equations contain heat losses to the cylinder wall in each zone.

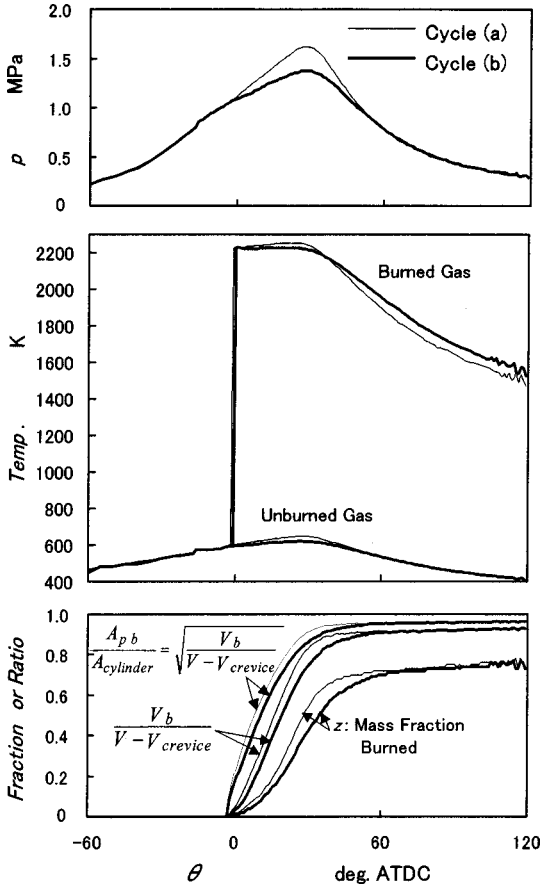

Fig. 10 Measured pressure and its analysis

A1.2 Calculation.

A1.2.1 Initial combustion. Before combustion starts, the temperature of the unburned gas in the cylinder is calculated by the equation of state. At initial combustion, the initial condition is determined with the assumption that unburned gas burns under constant pressure with heat losses to the cylinder wall and then the burned gas is adiabatically compressed to the pressure for the initial condition of the combustion process. The unburned gas condition is also calculated with the energy equation and the equation of state. The initial combustion is calculated between the spark timing and the crank angle at the initial condition of the combustion process. The calculations are iterated by changing the crank angle at which the initial condition of the combustion process is converged with more than 0.8% of the mass fraction burned.

A1.2.2 Combustion process. The energy equations in the form of differential equations were applied for the burned and unburned zones. The energy equations of the unburned and burned gases were simultaneously calculated to determine the changes of the mass fraction burned, volumes, and temperatures. The heat losses of the burned and unburned zones to the cylinder wall were calculated with the assumption that the areas of the cylinder walls covered by the unburned and burned gases are proportional to their volumes. Woschni's equation ([21]) is used for the heat transfer coefficients. The calculation was performed using the Runge-Kutta method with chemical equilibrium calculations

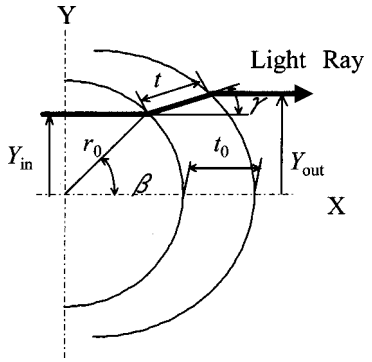

Fig. 11 Principle of TCC

in each step to determine the property of the burned gas. The measured pressure and the results of the temperatures and mass fraction burned by the pressure analysis are shown in Fig. 10 and the results of the rate of heat release by the pressure analysis are shown in Fig. 5 along with the corresponding photographs.

Appendix B

Comparison Between Photographs and Pressure Analysis Observed flame in the photographs must be modified to the shape of the flame in the cylinder based on the principle of TCC. From Fig. 11, the location of the light ray outside the TCC is described by Fujikawa et al. [9].

$$X = r_0 \cos \beta + t \cos \gamma$$
$$Y = r_0 \sin \beta + t \sin \gamma. \tag{1}$$

Thickness of TCC is

$$t = t_0 \frac{(n_\lambda - 1)}{(n_\lambda - \cos \gamma)} \tag{2}$$

where

$$\gamma = \beta - \sin^{-1}\left(\frac{\sin \beta}{n_\lambda}\right). \tag{3}$$

In this acrylic plastic case, $n_\lambda = 1.49$. Relations between light rays inside and outside of TCC are

$$Y_{in} = r_0 \sin \beta \tag{4}$$

$$Y_{out} = r_0 \sin \beta + t \sin \gamma. \tag{5}$$

The locations of the flame ends in the cylinder are

$$Y_{ina} = r_0 \sin \beta_a = Y_{outa} - t_a \sin \gamma_a \tag{6}$$

$$Y_{inb} = r_0 \sin \beta_b = Y_{outb} - t_b \sin \gamma_b. \tag{7}$$

Assuming cylindrical flame propagation, the diameter of the flame is

$$2r = Y_{ina} - Y_{inb}. \tag{8}$$

Finally, the cross-sectional area ratio of flame to the cylinder is

$$\frac{A_{\text{flame}}}{A_{\text{cylinder}}} = \frac{2rh}{2r_0 h} = \frac{Y_{ina} - Y_{inb}}{2r_0}. \tag{9}$$

The cross-sectional area ratio of the flame to the cylinder, $A_{\text{flame}}/A_{\text{cylinder}}$, was compared with that directly calculated from the photograph without modification in Fig. 12.

On the other hand, the volume of burned gas V_b is analyzed by the cylinder pressure as shown in Appendix A. The authors already took direct photographs of the combustion using the bottom view engine, which has a quartz window on the top of a long piston and the same cylinder head. The bottom view engine is the

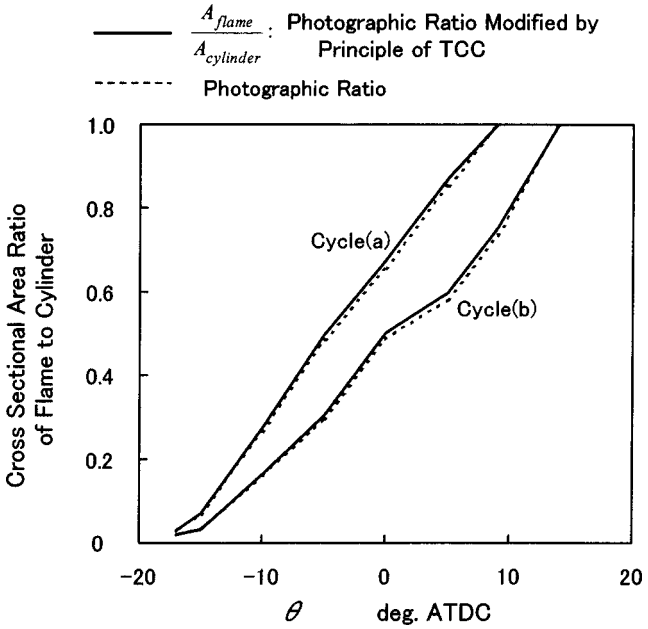

Fig. 12 Effect of inside and outside light rays of TCC on photographic analysis

same as that used for combustion o bservations with a television system (Kozuka et al. [22]) except for the cylinder head. The dimensions and operating conditions are 83 mm in bore, 85 mm in stroke, 8.9 in compression ratio, −21 deg ATDC in spark timing, 18 in A/F, 1200 rpm in engine speed and 68% in volumetric efficiency. As shown in Fig. 8, the flame propagated near the circular image. Assuming a cylindrical flame propagation, the relation between radius of burned gas, r_p, and V_b is

$$V_b = \pi r_p^2 h. \tag{10}$$

Total volume of the cylinder is the summation of the disc combustion chamber and crevice between cylinder and piston. That is

$$V = \pi r_0^2 h + V_{\text{crevice}}. \tag{11}$$

Therefore, the ratio of the cross-sectional area of burned gas, A_{pb}, to that of the cylinder, A_{cylinder}, is

$$\frac{A_{pb}}{A_{\text{cylinder}}} = \frac{2r_p h}{2r_0 h} = \sqrt{\frac{V_b}{V - V_{\text{crevice}}}} \tag{12}$$

where V_{crevice} is 4.53×10^{-6} m^3 (4.53 cm^3). V_{crevice} is large because of the long top land height of the piston.

Thus, a comparison between $A_{\text{flame}}/A_{\text{cylinder}}$ and $A_{pb}/A_{\text{cylinder}}$, namely $A_{\text{flame}}/A_{\text{cylinder}}$ and $\sqrt{V_b/V - V_{\text{crevice}}}$, shows the relation between the flame and burned gas. The results are shown in Fig. 9.

References

[1] Sinnamon, J. F., Lancaster, D. R., and Steiner, J. C., 1980, "An Experimental and Analytical Study of Engine Fuel Spray Trajectories," SAE Trans., **89**, Sec. 1, pp. 765–785, Paper No. 800135.

[2] Solomon, A. S. P., 1986, "A Photographic Study of Fuel Spray Ignition in a Rapid Compression Machine," SAE Trans., **95**, Sec. 1, pp. 1.406–1.422, Paper No. 860065.

[3] Zhu, Y., Hu, G., Wei, X., and Yu, J., 1988, "A Study on a New Combustion System for D.I. Diesel-CSCS System," SAE Trans., **97**, Sec. 6, pp. 6.768–6.781, Paper No. 880429.

[4] Namazian, M., Hansen, S., Lyford-Pike, E., Sanchez-Barsse, J., Heywood, J. B., and Rife, J., 1980, "Schlieren Visualization of the Flow and Density Fields in the Cylinder of a Spark-Ignition Engine," SAE Trans., **89**, Sec. 1, pp. 276–303, Paper No. 800044.

[5] Namazian, M., and Heywood, J. B., 1982, "Flow in the Piston-Cylinder-Ring Crevices of a Spark-Ignition Engine: Effect on Hydrocarbon Emissions, Efficiency and Power," SAE Trans., **91**, Sec. 1, pp. 261–288, Paper No. 20088.

[6] Heywood, J. B., and Vilchis, F. R., 1984, "Comparison of Flame Development

in a Spark-Ignition Engine Fueled With Propane and Hydrogen,'' Combust. Sci. Technol., **38**(5), pp. 313–324.
[7] Edwards, C. F., Stewart, H. E., and Oppenheim, A. K., 1985, ''A Photographic Study of Plasma Ignition Systems,'' SAE Paper No. 850077.
[8] Weaver, C. E., and Santavicca, D. A., 1992, ''Correlation of Cycle-Resolved Flame Kernel Growth and Cylinder Pressure in an Optically-Accessible Engine,'' SAE Paper No. 922171.
[9] Fujikawa, T., Ozasa, T., and Kozuka, K., 1988, ''Development of Transparent Cylinder Engines for Schlieren Observation,'' SAE Trans., **97**, Sec. 6, pp. 6.1714–6.1723, Paper No. 881632.
[10] Fujikawa, T., Kataoka, M., and Katsumi, N., 1994, ''Schlieren Observation of In-Cylinder Processes With a Transparent Collimating Cylinder,'' Trans. Jpn. Soc. Mech. Eng., Ser. B, **60**(580), pp. 4309–4315 (in Japanese).
[11] Tabaczynski, R. J., Hoult, D. P., and Keck, J. C., 1970, ''High Reynolds Number Flow in a Moving Corner,'' J. Fluid Mech., **42**, Part 2, pp. 249–255.
[12] Tabaczynski, R. J., Heywood, J. B., and Keck, J. C., 1972, ''Time-Resolved Measurements of Hydrocarbon Mass Flowrate in the Exhaust of a Spark-Ignition Engine,'' SAE Trans., **81**, Sec. 1, pp. 379–391, Paper No. 720112.
[13] Okubo, Y., Otsuka, M., Kato, J., Kozuka, K., and Sugiyama, K., 1986, ''The Back Scattered LDV Measurements of Swirl Flow in an Internal Combustion Engine,'' Trans. Jpn. Soc. Mech. Eng., Ser. B, **52**(480), pp. 3121–3126 (in Japanese).
[14] Witze, P. O., 1982, ''The Effect of Spark Location on Combustion in a Variable-Swirl Engine,'' SAE Trans., **91**, Sec. 1, pp. 165–175, Paper No. 820044.
[15] Gatowski, J. A., Heywood, J. B., and Deleplace, C., 1984, ''Flame Photographs in a Spark-Ignition Engine,'' Combust. Flame, **56**(1), pp. 71–81.
[16] Heywood, J. B., 1989, *Internal Combustion Engine Fundamentals*, McGraw-Hill, New York, pp. 360–402.
[17] Tabaczynski, R. J., Ferguson, C. R., and Radharkrishnan, K., 1977, ''A Turbulent Entrainment Model for Spark-Ignition Engine Combustion,'' SAE Trans., **86**, Sec. 3, pp. 2414–2433, Paper No. 770647.
[18] Hires, S. D., Tabaczynski, R. J., and Novak, J. M., 1978, ''The Prediction of Ignition Delay and Combustion Intervals for a Homogeneous Charge, Spark Ignition Engine,'' SAE Trans., **87**, Sec. 2, pp. 1053–1067, Paper No. 780232.
[19] Heywood, J. B., 1989, *Internal Combustion Engine Fundamentals*, McGraw-Hill New York, pp. 376–383.
[20] Chase, N. W., Jr., Davies, C. A., Downey, J. R., Jr., Frurip, D. J., McDonald, R. A., and Syverud, A. N., 1985, ''Journal of Physical and Chemical Reference Data,'' *JANAF Thermochemical Tables*, 3rd Ed., **14**, the American Chemical Society and the American Institute of Physics.
[21] Woschni, G., 1967, ''A Universally Applicable Equation for the Instantaneous Heat Transfer Coefficient in the Internal Combustion Engine,'' SAE Trans., **76**, Sec. 4, pp. 3065–3083, Paper No. 670931.
[22] Kozuka, K., Saito, A., Otsuka, M., and Kawamura, K., 1981, ''Television System for Viewing Engine Combustion Processes and the Image Analysis,'' SAE Trans., **90**, Sec. 3, pp. 2299–2309, Paper No. 810753.

S. G. Poulopoulos

C. J. Philippopoulos[1]

Department of Chemical Engineering,
Chemical Process Engineering Laboratory,
National Technical University of Athens,
Heroon Politechneiou 9,
Zographou Campus, GR,
157 80 Athens, Greece

The Effect of Adding Oxygenated Compounds to Gasoline on Automotive Exhaust Emissions

In the present work, the effect of adding ethanol or methyl tertiary butyl ether (MTBE) to gasoline on the regulated and unregulated emissions from an internal combustion engine with a typical three-way catalyst was studied. The addition of ethanol to fuel (10% w/w) increased both the research octane number and the Reid vapor pressure of the fuel, whereas adding 11% w/w MTBE caused an increase only in the research octane number of the fuel. When the fuel contained MTBE, less hydrocarbons, carbon monoxide, and acetaldehyde were emitted in the tailpipe. The increased emissions of acetaldehyde and ethanol were the main disadvantages of using ethanol. [DOI: 10.1115/1.1501076]

Introduction

Several oxygenated compounds have been used as gasoline additives since 1970. These compounds are used as octane enhancers of gasoline in place of lead and to reduce hazardous emissions, mainly carbon monoxide. Methyl tertiary butyl ether (MTBE) and ethanol are the dominant compounds in the market of oxygenates. Specifically, MTBE is almost exclusively used in Europe, whereas in the U.S.A. ethanol is also present in gasoline. It has to be noted that ethanol is also used as fuel in some countries such as Brazil.

Many studies have investigated the effect of ethanol addition into gasoline on the automotive exhaust emissions [1–4]. It has been reported that lower hydrocarbon and carbon monoxide exhaust emissions were observed for ethanol-containing fuels compared to unleaded gasoline, whereas acetaldehyde exhaust emissions and the total evaporative emissions were significantly increased.

The impact of MTBE addition to gasoline on the exhaust emissions has been also examined by many authors [5–10]. It is not clarified whether the use of MTBE as gasoline additive results in a decrease in exhaust emissions or not. In most studies, it is reported that carbon monoxide emissions decreased when MTBE was added to the fuel. The main disadvantage of using MTBE seems to be its potential for carcinogenicity and its high solubility in water. It has been detected in vast portions of ground and surface water reservoirs, and leaking underground storage tank systems as well as faulty pipeline systems and accidental spills are thought to be the sources. In response to the growing concerns regarding MTBE in water, the U.S. Environmental Protection Agency appointed an independent blue ribbon panel of leading experts to investigate the air quality benefits and water quality concerns associated with oxygenates in gasoline. The panel recommended that the use of MTBE should be substantially reduced nationwide.

Fewer studies are dedicated to the comparison between ethanol and MTBE blend fuels [11,12]. The variations of the engine type, base fuel composition, and of the operating conditions make such comparison from different studies rather uncertain.

In the present work, MTBE and ethanol, the most common oxygenates in use, were compared to each other in terms of their influence on the exhaust emissions from an internal combustion engine equipped with a three-way catalytic converter. Beyond the regulated emissions, i.e. total hydrocarbons (HC) and carbon monoxide (CO), some important unregulated compounds such as methane, hexane, ethylene, acetone, acetaldehyde, toluene, acetic acid, benzene, 1,3-butadiene, MTBE, and ethanol were measured at the engine exhaust and after the catalytic treatment. Especially, the concentrations of acetaldehyde, benzene, 1,3-butadiene, MTBE, and ethanol are of great importance. Acetaldehyde, benzene, and 1,3-butadiene are toxic compounds, whereas acetaldehyde is also very effective in the formation of photochemical smog. Ethanol and MTBE are in the middle in the list of the compounds involved in the process of photochemical smog creation [13], whereas MTBE has been also accused of lung and eye irritation [14]. Moreover, the concentrations of ethanol and MTBE in exhaust emissions had to be measured in order to be associated with the presence of MTBE and ethanol in the fuel. The efficiency of the catalytic converter on the conversion of each compound was also studied.

Table 1 Fuel properties

% w/w	Base Fuel	Eth10%	MTBE11%
Oxygen	0.16	3.58	2.15
Aromatics	43.7	42.9	39.9
Saturated	49.7	38.1	42.5
Alkenes	5.7	5.8	5.8
Benzene	2.52	2.25	2.29
Xylene	10.7	9.9	9.8
Toluene	11.1	10.7	10.4
RON	95.5	98.9	98.2
MON	86.0	87.0	87.4
RVP (100° F) kPa	61.4	65.9	60.1

Table 2 Analysis details

	GC-MS	GC-FID
Apparatus	Hewlett Packard GC 6890–MSD 5973	Sigma 3B Perkin-Elmer
Column	HP-Plot Q	Porapak Q
Length	30 m	3 m
Internal diameter	$0.032 \cdot 10^{-3}$ m	$0.32 \cdot 10^{-2}$ m
Carrier gas	Helium	Nitrogen
Total flow	25 mL min^{-1}	20 mL min^{-1}
Mode	Splitless–Scan (range: 10–300)	Splitless
Injector temperature	250°C	150°C
Detector temperature	MS Quad: 150°C Ms Source: 230°C	250°C
Oven temperature	Initial: 60°C for 4 min 60°C→190°C with 25°C min^{-1} Final: 190°C for 7 min	160°C

[1]To whom correspondence should be addressed. e-mail: kphilip@chemeng.ntua.gr

Contributed by the Internal Combustion Engine Division of THE AMERICAN SOCIETY OF MECHANICAL ENGINEERS for publication in the ASME JOURNAL OF ENGINEERING FOR GAS TURBINES AND POWER. Manuscript received by the ICE Division, July 13, 2000; final revision received by the ASME Headquarters, Dec. 5, 2001. Editor: D. N. Assanis.

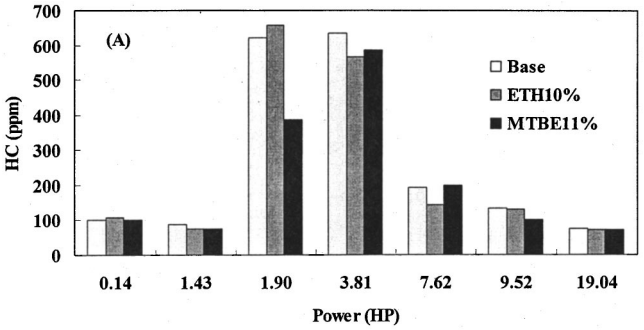

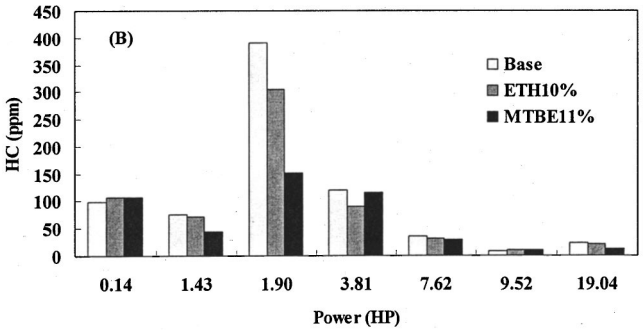

Fig. 1 HC emissions at (A) engine and (B) tailpipe exhaust

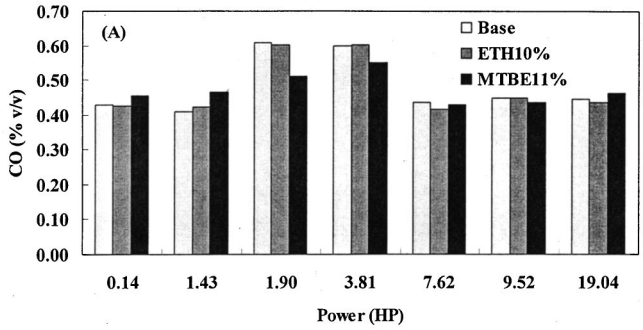

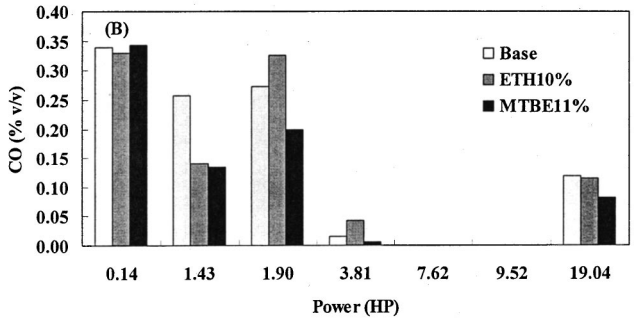

Fig. 2 CO emissions at (A) engine and (B) tailpipe exhaust

Experimental Section

Test Fuels. Three test fuels were used in this study. The first one was unleaded gasoline without any oxygenate additives, with octane number of 95.5, which was used as base fuel for the preparation of gasoline/oxygenate blends and it is called hereinafter as ''base.'' The second and the third fuels were gasoline-oxygenate mixtures containing 10% ethanol (Eth10%) and 11% MTBE (MTBE11%) w/w, respectively. The properties of the fuels used are presented in Table 1.

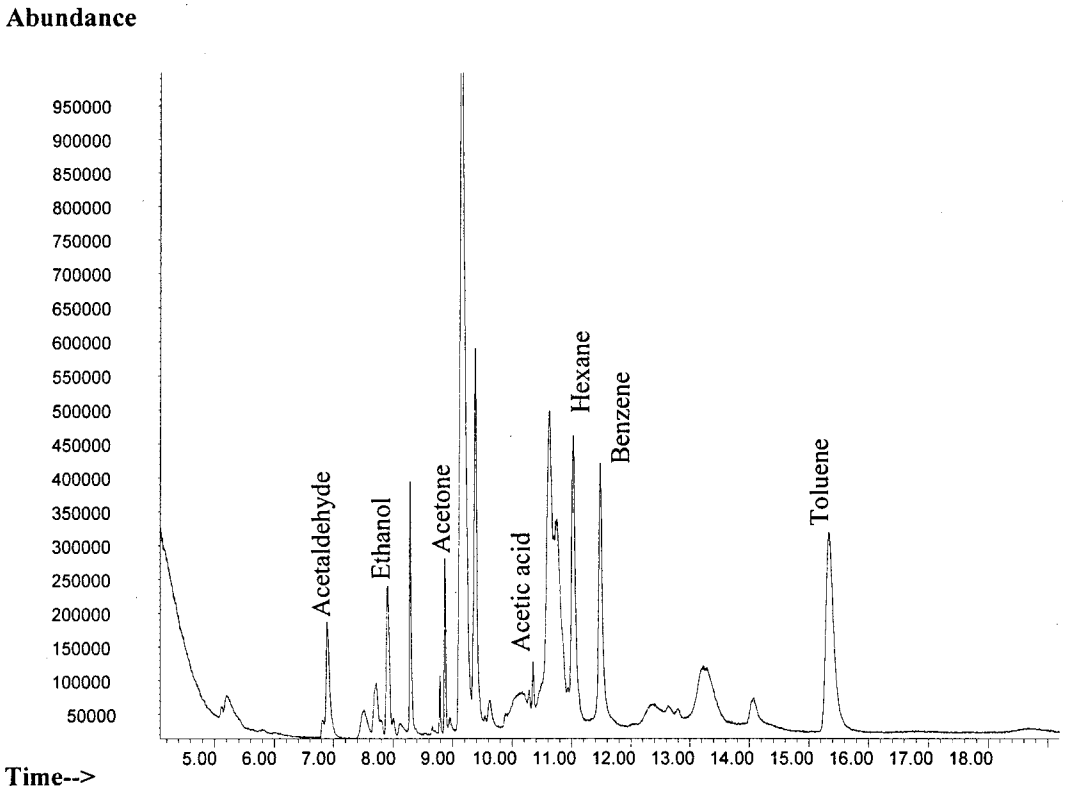

Fig. 3 A typical chromatogram from GC-MS

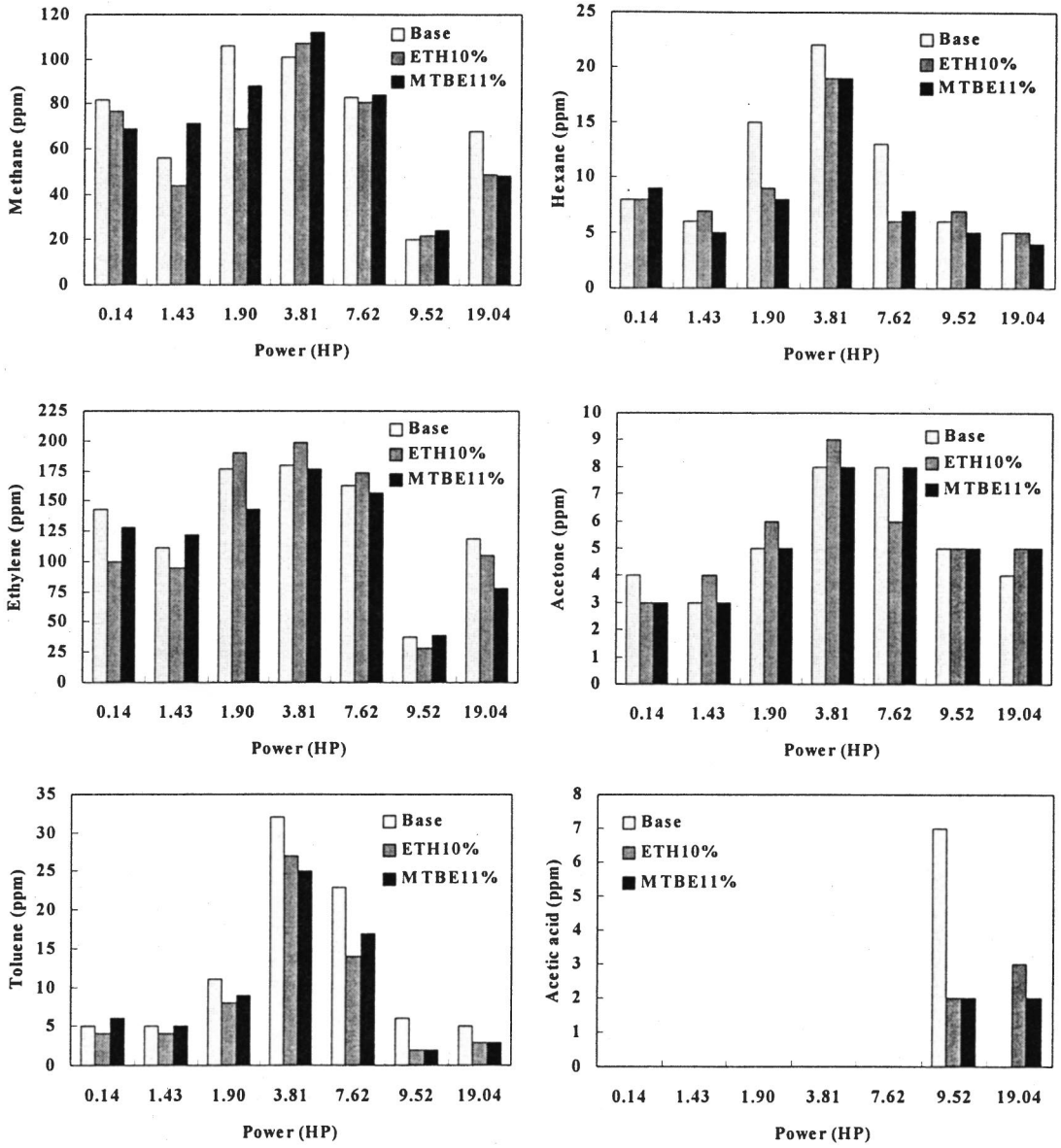

Fig. 4 The concentrations of various compounds in engine-out exhaust emissions

Test Engine and Procedure. A four-cylinder OPEL 1.6 L (compression rate: 9.2:1, fuel point: single point injection, exhaust control: oxygen sensor) engine, equipped with a hydraulic brake dynamometer (Clayton, CAM-250E) for changing the engine load, was used. The engine torque was measured using a hydraulic load cell. A typical commercial three-way catalytic converter (Pt/Rh: 5/1) with ceramic monolithic support was used. The power of the engine was increased in the range of 0–20 HP according to a specific time program by imposing selected pairs of engine speed (1000–2500 rpm) and torque (0.1–40 lb_f ft). The experimental setup and procedure are described in more detail in a previous work [9].

Analysis. A SUN MGA-1200 analyzer was used to measure continuously the concentrations of HC (total unburned hydrocarbons, ppm propane equivalent, v/v), CO (% vol), CO_2 (% vol), and the air-to-fuel ratio (λ). Specifically, total hydrocarbons, carbon monoxide, and carbon dioxide were analyzed by nondispersive infrared and oxygen by chemiluminescence. The analyzer provided a CO measurement range of 0 to 10% with a resolution of 0.01%, CO_2 range of 0 to 20% with a resolution of 0.01% and HC range from 0 to 9999 ppm with a resolution of 1 ppm.

Samples from the engine (engine-out exhaust emissions) and the catalytic converter (tailpipe exhaust emissions) exhaust gases at each engine power, were analyzed by gas chromatography with flame ionization detection (GC-FID) and by gas chromatography with mass spectrometry detection (GC-MS). Methane and ethylene were detected with GC-FID while the rest hydrocarbons were analyzed with GC-MS. The column (HP-PLOT Q) used in GC-MS permitted the detection of polar and nonpolar compounds simultaneously. The chromatographs were calibrated using gas mixtures of known composition in the range of actual engine exhaust samples (10-200 ppm for methane and ethylene, 1-60 ppm for the compounds detected with GC-MS). All the concentrations of the various compounds are expressed as ppm (v/v). Analysis details are presented in Table 2.

Four tests for each fuel and three measurements for each compound concentration at each engine power were made to evaluate the repeatability of the engine and the analytical methods used.

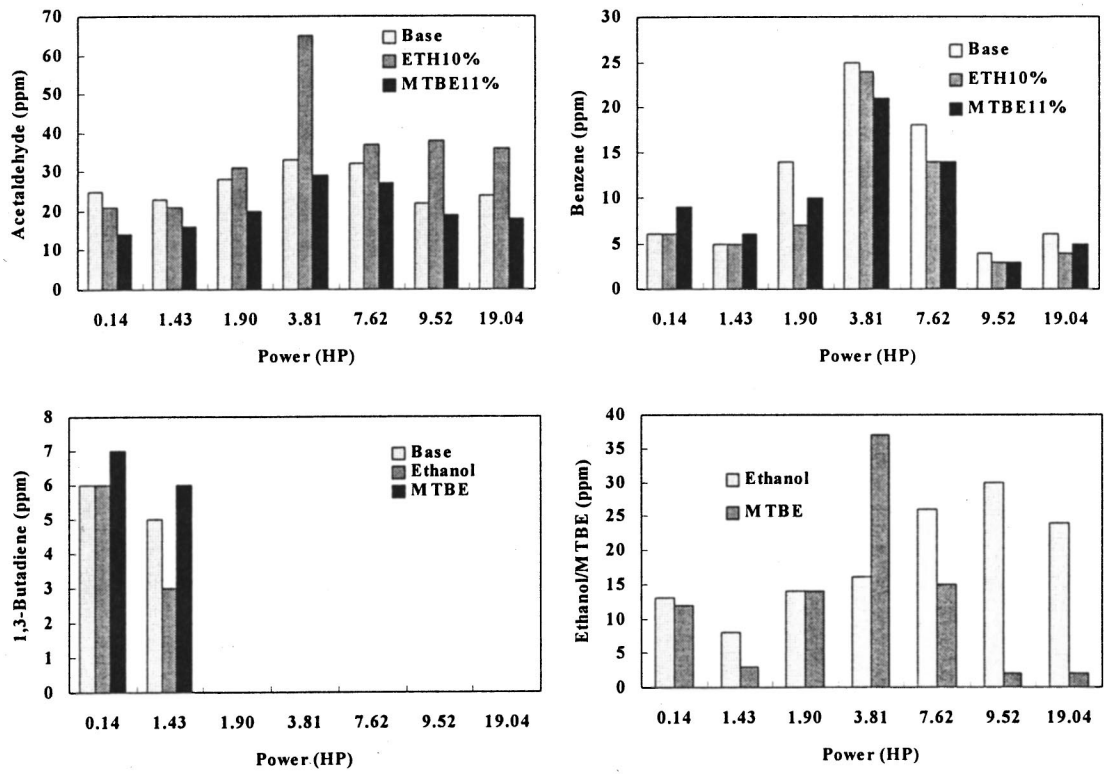

Fig. 5 The concentrations of toxic compounds in engine-out exhaust emissions

The standard error of the mean value of HC and CO concentration (as % of the mean) was 5–10% in the most cases. The standard error of the mean value of each compound concentration was 10–15% in the majority of the measurements, although higher standard errors were observed in some cases for concentrations below 10 ppm.

Results

Hydrocarbon and Carbon Monoxide Emissions. Ethanol addition into gasoline resulted in a 3.6% increase in the research octane number (RON) and in a 7.3% increase in the Reid vapor pressure (RVP) of the fuel. MTBE addition into gasoline resulted in a 2.8% increase in the research octane number and a 2.1% decrease in the Reid vapor pressure of the fuel. The increase in the Reid vapor pressure of the fuel in the case of ethanol addition is an indication of increased evaporative emissions, although such measurements were not conducted in this study. In addition, more oxygen was transferred to gasoline by ethanol addition than by MTBE addition.

At the start of the engine operation (ambient temperature 20–25°C), hydrocarbon concentration ranged in 80–110 ppm at the engine exhaust for all the test fuels (Fig. 1). The most hydrocarbons were emitted at 1.90 and 3.81 HP, and they decreased significantly when MTBE was added to the fuel. At higher engine powers, the concentration of the hydrocarbons decreased due to higher engine operating temperatures and the differences from one fuel to another were insignificant, that means below the experimental error. At tailpipe exhaust, the concentration of the hydrocarbons ranged in 10–400 ppm. In most cases, less hydrocarbon emissions were observed when MTBE11% was used as fuel.

Carbon monoxide in the engine-out emissions ranged in 0.40–0.60% v/v and the observed differences from fuel to fuel were below the experimental error (Fig. 2). In contrast, at tailpipe exhaust, the addition of MTBE into gasoline resulted in a great decrease in CO emissions, especially at 1.43 HP where carbon monoxide emissions for MTBE11% were almost half that for the base fuel.

Hydrocarbon Speciation in Engine Exhaust Gases. A typical chromatogram (total ion) from GC-MS is presented in Fig. 3. Among the various compounds detected in exhaust emissions, the following ones were measured: methane, hexane, ethylene, acetone, toluene, acetic acid, acetaldehyde, benzene, 1,3-butadiene, and ethanol for ethanol-containing gasoline or MTBE for MTBE/gasoline blends. MTBE is known to increase the concentration of formaldehyde (toxic compound) from simple oxidation experiments ([15,16]), but such measurements were not conducted in this work due to analysis limitations.

Methane constituted a great amount of emitted hydrocarbons at engine exhaust. Its concentration ranged in 20–115 ppm and no specific pattern due to the change of fuel was observed. Hexane emissions were generally lower for oxygenated fuels, especially when MTBE was used as additive. Ethylene emissions were lower for ETH10% up to 1.43 HP, whereas at higher engine powers lower emissions were observed in the case of MTBE11%. Toluene emissions decreased when an oxygenated compound was added into gasoline. Among the oxygenated fuels that were used, lower emissions were observed for ETH10%. Acetic acid was observed in a few cases at engine exhaust and no conclusion can be extracted from its measurements. The concentration of each compound mentioned above is presented in Fig. 4.

Acetaldehyde emissions increased after 1.90 HP for ETH10% fuel, especially at 3.81 HP, where they were the double that for gasoline. In contrast, acetaldehyde emissions were less for MTBE11% than for base fuel in the whole engine operating range. Benzene emissions decreased for the oxygenated gasolines, especially when ethanol was used as additive. 1,3-Butadiene was emitted only at low engine temperatures, at 0.14 and 1.43 HP. They decreased only for ETH10% compared to the base fuel. Ethanol emissions were higher than MTBE emissions, with the exception

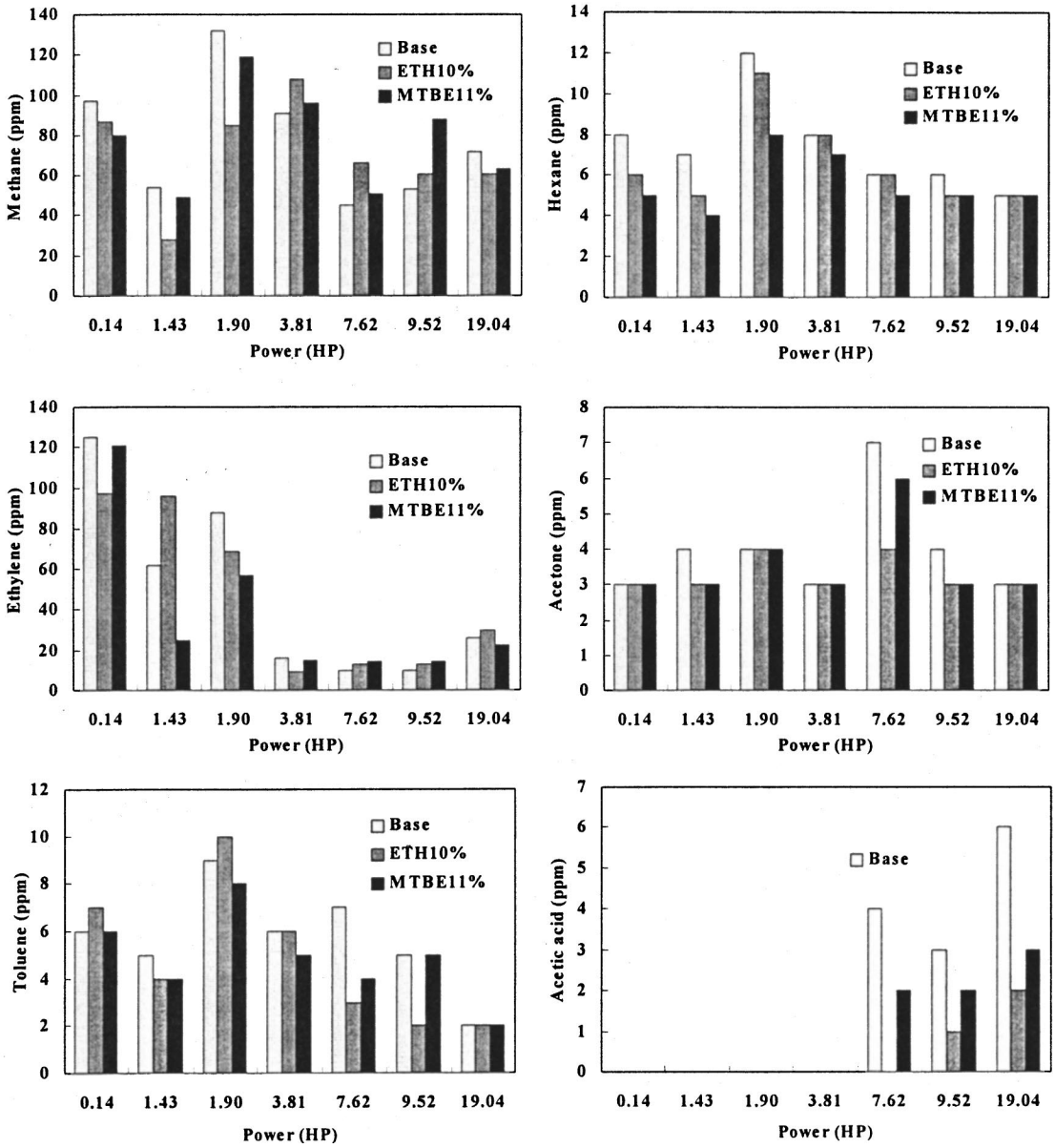

Fig. 6 The concentrations of various compounds in tailpipe exhaust emissions

of 3.81 HP. Especially at 9.52 and 19.04 HP, ethanol emissions were ten times higher than MTBE emissions. The concentrations of acetaldehyde, benzene, 1,3-butadiene, and ethanol or MTBE are presented in Fig. 5.

Considering these results, it is obvious that 3.81 HP was the worst engine operating condition with respect to the exhaust gas emissions.

Hydrocarbon Speciation in Tailpipe Exhaust Gases. At tailpipe exhaust, that means after the catalytic converter, methane concentration ranged in 30–130 ppm. There was not any specific trend for its concentration related to the change of the test fuel. Hexane concentration ranged in 4–12 ppm and decreased when MTBE was added to gasoline. Lower acetone emissions were observed for ETH10% at engine powers up to 1.43 HP, whereas at higher power MTBE addition was more favorable. Acetone emissions were lower for oxygenated fuels, especially for ETH10%, although the observed differences were rather insignificant. Toluene concentration ranged in 2–10 ppm. From one operating condition to another, the fuel that resulted in a decrease in toluene emissions was different. Acetic acid was detected at tailpipe exhaust only above 7.62 HP and its concentration was the half that for oxygenated fuels. The use of ethanol was more beneficial than the use of MTBE in terms of acetic acid elimination. The concentrations of the compounds mentioned above are presented in Fig. 6.

Acetaldehyde concentration increased for ethanol-containing fuel at tailpipe exhaust taking the whole experimental cycle into account, whereas the use of MTBE resulted in decreased acetaldehyde emissions in almost the whole engine operating range compared to these for the base fuel. The operation of the catalytic converter diminished at tailpipe exhaust the differences in benzene concentration due to the change of the fuel. 1,3-Butadiene was detected only at the first two operating conditions, where the catalyst activity was very low because of low temperature. The addition of oxygenated compounds did not result in any significant decrease in 1,3-butadiene concentration. Finally, MTBE emissions from MTBE11% fuel were two to ten times lower than ethanol emissions from ETH10%. Especially, at the highest engine power, 20 ppm of ethanol was emitted in the exhaust gases,

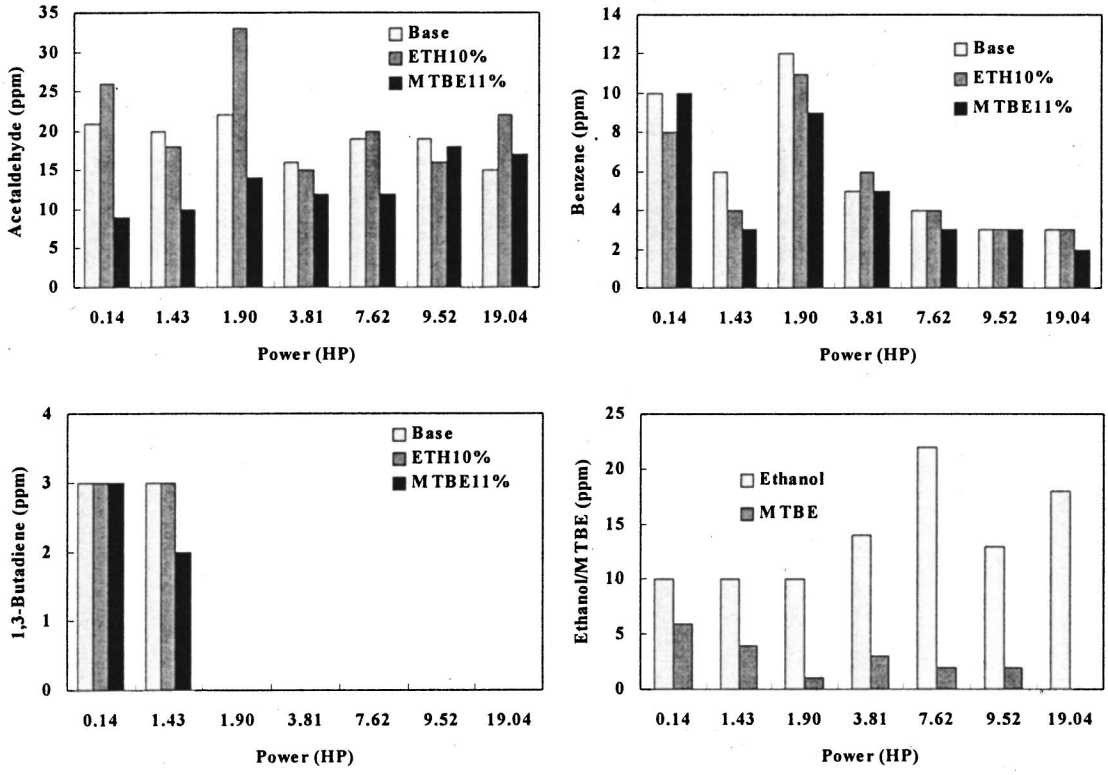

Fig. 7 The concentrations of toxic compounds in tailpipe exhaust emissions

while MTBE was not even detected. The concentrations of acetaldehyde, benzene, 1,3-butadiene, and ethanol or MTBE at tailpipe exhaust are presented in Fig. 7.

The worst engine operating condition concerning the tailpipe exhaust emissions was 1.90 HP, where both engine and catalyst operating temperatures were low.

Catalytic Converter Efficiency. It is obvious that the catalytic converter was more effective in the oxidation of carbon monoxide than in the elimination of hydrocarbons. MTBE addition into gasoline had as a result higher achieved conversions of both HC and CO than ethanol in the whole engine power range and especially at 1.43–3.81 HP, where the catalyst operation started.

Among the individual compounds examined, benzene, toluene, ethylene and MTBE were readily oxidized. On the other hand, acetaldehyde and ethanol were quite resistant to oxidation. Methane was not only the most resistant compound, but also it was formed over the catalyst in some cases owing to the decomposition of other hydrocarbons. 1,3-Butadiene was identified in the exhaust gases only at the first two operating conditions, where engine and catalyst operated at low temperatures. Finally, acetic acid was formed on the catalyst at the two highest engine powers. Between the two oxygenated compounds, higher conversions were achieved for the individual compounds studied in most cases for MTBE.

Conclusions

In the present work, the effect of the addition of two different oxygenated compounds (MTBE and ethanol) into gasoline on the regulated and the unregulated exhaust emissions, was studied. Summarizing the results obtained:

(a) less hydrocarbon (35%) and carbon monoxide (43%) emissions were observed at tailpipe exhaust when MTBE11% was used as test fuel compared to those for the base fuel, taking into account the whole experimental cycle.

(b) increased acetaldehyde concentrations in engine exhaust gases were measured when ETH10% was used as fuel, almost the double that for gasoline in some cases. On the other hand, the addition of ethanol to gasoline resulted in a decrease in benzene emissions (4–50%) at engine exhaust. Above 7 HP, ethanol emissions were two to ten times higher than those of MTBE.

(c) the catalytic converter operation eliminated the observed differences due to fuel change at tailpipe exhaust. However, increased acetaldehyde concentrations were observed for ETH10% in most cases. Moreover, the ethanol emitted at tailpipe exhaust from ethanol-containing gasoline was 1.5–11 times higher than the MTBE emitted from MTBE-containing fuel.

(d) higher conversions of both hydrocarbons and carbon monoxide were observed for MTBE blend fuel, especially at the start of catalyst operation.

Taking into account all the observations in this study, it seems that MTBE should be preferably used instead ethanol as gasoline additive, although more research is needed.

Acknowledgments

We thank the Hellenic Refinery of Aspropirgos for gasoline donation.

References

[1] Bata, R. M., and Roan, V. P., 1989, ''Effects of Ethanol and/or Methanol in Alcohol-Gasoline Blends on Exhaust Emissions,'' ASME J. Eng. Gas Turbines Power **111**, pp. 432–438.

[2] Rice, R. W., Sanyal, A. K., Elrod, A. C., and Bata, R. M., 1991, ''Exhaust Gas Emissions of Butanol, Ethanol, and Methanol Gasoline Blends,'' ASME J. Eng. Gas Turbines Power **113**, pp. 377–381.

[3] Stump, F., Knapp, K., Ray, W., Siudak, P., and Snow, R., 1996, ''Influence of Ethanol-Blended Fuels on the Emissions From Three Pre-1985 Light-Duty Passenger Vehicles,'' ASME J. Eng. Gas Turbines Power J. Air Waste Manage. Assoc. **46**, pp. 1149–1161.

[4] Mulawa, P. A., Cadle, S. H., Knapp, K., Zweidinger, R., Snow, R., Lucas, R., and Goldbach, J., 1997, ''Effect of Ambient Temperature and E-10 Fuel on Primary Exhaust Particulate Matter Emissions from Light-Duty Vehicles,'' Environ. Sci. Technol. **31**, pp. 1302–1307.
[5] Hamai, K., Mitsumoto, H., Iwakiri, Y., Ishihara, K., and Ishii, M., 1992, ''Effects of Clean Fuels (Reformulated Gasolines, M85, and CNG) on Automotive Emissions,'' SAE Technical Paper 922380, pp. 1–10.
[6] Jeffrey, J. G., and Elliot, N. G., 1993, ''Gasoline Composition Effects in a Range of European Vehicle Technologies,'' SAE Technical Paper No. 932680, pp. 1–28.
[7] Kivi, J., Niemi, A., Nylund, N., Kyto, M., and Orre, K., 1992, ''Use of MTBE and ETBE as Gasoline Reformulation Components,'' SAE Technical Paper No. 922379, pp. 1–17.
[8] Osman, M. M., Matar, M. S., and Koreish, S., 1993, ''Effect of Methyl Tertiary Butyl Ether (MTBE) as a Gasoline Additive on Engine Performance and Exhaust Emissions,'' Fuel Sci. Technol. Int. **11**, pp. 1331–1343.
[9] Poulopoulos, S., and Philippopoulos, C., 2000, ''Influence of MTBE Addition into Gasoline on Automotive Exhaust Emissions,'' Atmos. Environ. **34**, pp. 4781–4786.
[10] Stump, F., Knapp, K., Ray, W., Siudak, P., and Snow, R., 1994, ''Influence of Oxygenated Fuels on the Emissions From Three Pre-1985 Light-Duty Passenger Vehicles,'' Atmos. Environ. J. Air Waste Manage. Assoc. **44**, pp. 81–786.
[11] Furey, R. L., and King, J. B., 1981, ''Evaporative and Exhaust Emissions From Cars Fuelled With Gasoline Containing Ethanol or Methyl Tert-Butyl Ether,'' SAE Technical Paper No. 800261, pp. 1200–1216.
[12] Reuter, R. M., Benson, J. D., Burns, V. R., Gorse, R. A., Hochhauser, A. M., Koehl, W. J., Painter, L. J., Rippon, B. H., and Rutherford, J. A., 1992, ''Effects of Oxygenated Fuels and RVP on Automotive Emissions — Auto/Oil Quality Improvement Program,'' SAE Technical Paper No. 920326, pp. 391–412.
[13] Grosjean, E., Rasmussen, R. A., and Grosjean, D., 1998, ''Ambient Levels of Gas Pollutants in Porto Alegre, Brazil,'' Atmos. Environ. **32**(20), pp. 3371–3379.
[14] Bodenstein, Y., and Duffy, L. K., 1998, ''Expression of Hsp60, a Stress Protein, in Human Nasal Septa Cells After Exposure to MTBE,'' Atmos. Environ. Environ. Toxicology Pharmacology **5**, pp. 79–83.
[15] Ciajolo, A., D'Anna, A., and Kurz, M., 1997, ''The Relationship Between Chemical Reaction and Anti-Knock Effect of MTBE,'' in *Proceedings of ECCE-1*, Italy, May 4–7, pp. 2909–2912.
[16] Fields, D. L., Lim, P. K., and Roberts, G. W., 1998, ''Catalytic Destruction of Methyl Tertiary Butyl Ether (MTBE) With a Pt/Rh Monolithic Automotive Exhaust Catalyst,'' Appl. Catal., B **15**, pp. 93–105.

Experimental and Theoretical Optimization of Combustion Chamber and Fuel Distribution for the Low Emission Direct-Injection Diesel Engine

Y. Kidoguchi
M. Sanda
K. Miwa

Ecosystem Engineering,
Graduate School of Engineering,
The University of Tokushima,
2-1 Minamijosanjima,
Tokushima 770-8506, Japan

Effects of combustion chamber geometry and initial mixture distribution on the combustion process were investigated in a direct-injection diesel engine. In the engine experiment, a high squish combustion chamber with a squish lip could reduce both NO_x and particulate emissions with retarded injection timing. According to the results of CFD computation and phenomenological modeling, the high squish combustion chamber with a central pip is effective to keep the combusting mixture under the squish lip until the end of combustion and the combustion region forms rich and highly turbulent atmosphere. This kind of mixture distribution tends to reduce initial burning, resulting in restraint of NO_x emission while keeping low particulate emission. [DOI: 10.1115/1.1501077]

Introduction

Direct-injection diesel engines have been used not only in heavy duty applications but also in light duty ones because of their high thermal efficiency and low CO_2 emissions. However, reduction of exhaust emissions is an urgent necessity from the standpoint of preserving the environment. It is important to improve the combustion process in order to reduce exhaust emissions. Many efforts, such as high-pressure injection ([1–4]) and modification of combustion chamber geometry ([5–8]) have been made to reduce particulate emissions. EGR ([9]) is also employed to reduce NO_x emissions. However, these measures have the problem of a tradeoff relationship between NO_x and particulate emissions. In order to overcome the tradeoff problem, two-stage combustion ([10]) and premixed lean combustion ([11–14]) have been introduced. Authors ([15]) have also reported that a high squish combustion chamber with a squish lip has the possibility to reduce NO_x and particulate emissions simultaneously at retarded injection timing. This chamber tried to realize two-stage combustion, namely, fuel-rich combustion at initial burning to reduce NO_x and high turbulence combustion at diffusion burning to reduce particulate.

In this study, the effect of the high squish combustion chamber geometry was investigated in detail with the engine experiment and CFD calculation. This study also investigated the effect of initial fuel distribution in the high squish combustion chamber on the history of heat release rates because the fuel distribution greatly affects the fuel-air mixing and formation of exhaust emissions. This study tries to find the optimum mixture distribution for the low-emission DI diesel engine and introduce measures in order to realize this distribution.

Experimental setup

The test engine was a four-stroke single-cylinder naturally aspirated direct-injection diesel engine (Yanmar NFD170). Engine specifications were 102 mm bore, 105 mm stroke, and compression ratio of 17. A Bosch PFR-IAW injection pump was mounted, and a four-hole injection nozzle with a 0.29 mm hole-diameter and spray angle of 150 deg was used. JIS #2 diesel fuel (density of 841 kg/m^3, lower heating value of 45690 kJ/kg) was used. Combustion chamber geometries are shown in Fig. 1. The standard combustion chamber (STD) was the original toroidal combustion chamber. Chambers R35 and R35S were high squish combustion chambers. In order to obtain a high squish flow, the throat diameter of the high squish combustion chambers was reduced while keeping the compression ratio and top clearance the same as the STD chamber. The throat diameter to bore diameter ratio d/D was 55.6% for the STD chamber and 35% for the R35 and R35S chambers. To form a fuel-rich mixture inside the piston cavity, the R35S chamber had the central pip almost the same as STD chamber. Figure 2 shows the schematic diagram of the experimental apparatus. Engine performance and emissions data were obtained under steady operating conditions at an engine speed of 1800 rpm with high load of mean effective pressure Pe=0.7 MPa. A coolant temperature was kept at 80°C and exhaust pressure was 30 mm Hg without EGR. A mini-dilution tunnel with a 70 mm inner

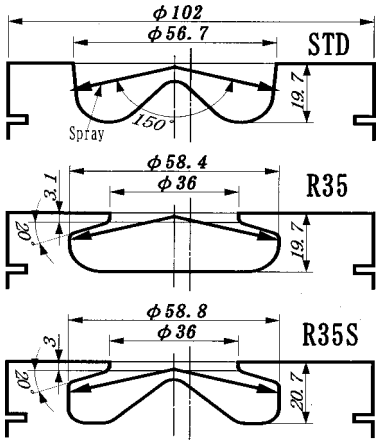

Fig. 1 Combustion chamber

Contributed by the Internal Combustion Engine Division of THE AMERICAN SOCIETY OF MECHANICAL ENGINEERS for publication in the ASME JOURNAL OF ENGINEERING FOR GAS TURBINES AND POWER. Manuscript received by the ICE Division, Oct. 2001; final revision received by the ASME Headquarters, Mar. 2002. Editor: D. N. Assanis.

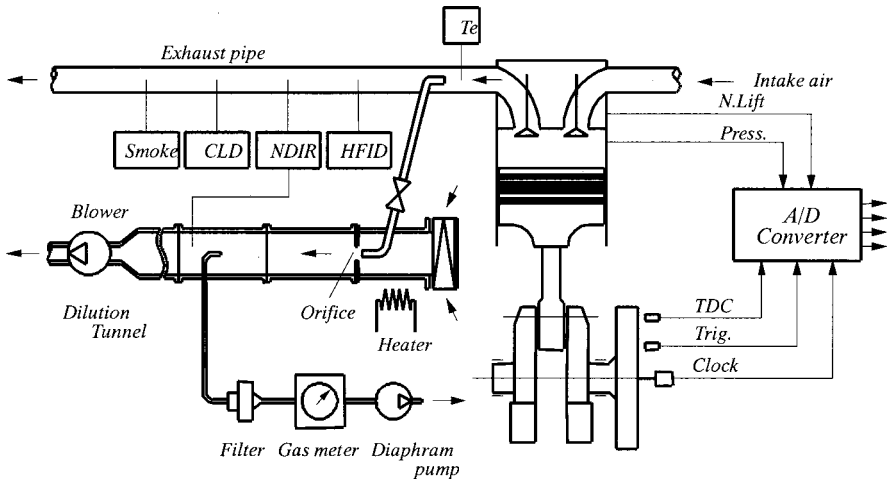

Fig. 2 Schematic diagram of experimental setup

diameter and 680 mm length was employed for sampling particulate emissions. A portion of the exhaust gas was introduced to the mini-tunnel 1.6 m downstream from the exhaust valve and diluted at dilution ratio of 10 ([16]). Particulate concentrations were determined by measuring filter weight before and after the sampling. Soluble organic fraction (SOF) was extracted from the particulate sampling filter by the Soxhlet extraction method using dichloromethane as solvent. Total hydrocarbons (THC) were sampled using a hot sampling line held at 210°C and analyzed by a gas chromatograph with a heated flame-ionization detector (Yanaco G2800). NO_x concentration was measured with a chemiluminescence analyzer (Yanaco ECL-77A), and smoke density was measured with a Bosch smoke meter. Cylinder pressure was measured with a piezoelectric pressure transducer (Kistler 601A). Pressure diagrams were obtained as a function of crank angle by averaging 128 successive cycle data.

Outline of the Calculation

The engine CFD code FREC ([17,18]) is employed in this study to analyze the combustion process. The governing equations are conservation equations for mass, momentum, enthalpy, and concentrations of chemical species. Turbulent kinetic energy k and its dissipation rate ε are described by the standard k-ε two-equation model. It is assumed that initial turbulent kinetic energy at the timing of intake valve closure is 74% of the square of the mean piston speed, whereas the initial turbulence length scale is 7% of the cylinder bore ([19]).

It is assumed in the combustion model that the pre-mixture of fuel and oxygen is first formed then consumed after ignition delay. The mass of pre-mixture formed per unit time in unit volume is given by

$$R_m=(1+S_{ox})A_m\frac{\rho\varepsilon}{k}\min\left(m_{fu},\frac{m_{ox}}{S_{ox}}\right) \tag{1}$$

where m_{fu} and m_{ox} are the mass fractions of fuel and oxygen, respectively, ρ is the mixture density, S_{ox} is the stoichiometric oxygen requirement per unit mass of fuel, and $A_m=4$ ([20]). This form is similar to the eddy breakup model ([20]). After ignition, the pre-mixture is consumed by a single-step chemical reaction in Arrhenius form as follows,

$$R_f=\frac{S_{ox}}{1+S_{ox}}\frac{\rho^2 m_{mi}^2}{M_{O2}}F_f\exp(-D_f/T) \tag{2}$$

where m_{mi} is the mass fraction of the pre-mixture, M_{O2} is the molecular weight of oxygen, F_f is the frequency factor, and D_f is the activation temperature. F_f and D_f are set to 10^{10} and 12,000 K, respectively ([21]). The net rate of the pre-mixture formation is equal to R_m-R_f. During the ignition delay period, the pre-mixture accumulates because R_f is low due to low temperature. However, when combustion commences, temperature rises and R_f increases. As a result, the combustion rate is determined by the mixture formation rate R_m. In this study, it is defined that ignition occurs when the concentration of some activated species in the pre-mixture exceeds a certain limit due to the increase of temperature. When spontaneous ignition occurs at the initial stage of diesel combustion, pressure and temperature rise rapidly. Based on the variable ignition delay mechanism ([22]), the rising of temperature shortens ignition delays at other positions in the combustion chamber. According to Ikegami et al. ([23]), this process can be calculated in the following way. The formation rate of the activated species s is calculated using the fuel concentration $[F]$, oxygen concentration $[O]$, and mean temperature T of each cell as follows:

$$s=A[F]^B[O]^C\exp(-D/T) \tag{3}$$

where $A=1.1$ for STD, 2.75 for R35, and 3.2 for R35S, which have to be decided so that predicted heat release rates agree with the measured data, and $B=0.3$, $C=1.2$, and $D=9300$ ([23]). It is assumed that ignition will occur if integrated s exceeds unity.

The spray is treated as a quasi-steady gas jet. This model is based on the experimental results that the injected fuel gasifies quickly ([24]). When fuel is injected into the cavity, surrounding air is entrained into the spray. This model calculates the amount of air entrainment based on the momentum theory ([25]), and the mixture of the injected fuel and entrained air, momentum, and other quantities such as turbulence intensity and enthalpy are assumed to outflow near the spray tip. A sink zone is placed at the halfway of the spray path where air entrainment into the jet is calculated. A source region is placed near the spray tip, where ignition first occurs according to the photography in the engine cylinder ([26]). In the source region, momentum, turbulent kinetic energy and enthalpy of the mixture flow out. In this way, this model can avoid denser computational grids in the spray region. In addition, changing the source region corresponds to changing the initial mixture distribution. Regarding emissions, NO_x formation is calculated based on the extended Zeldovich mechanism.

Results and Discussion

Effect of Combustion Chamber Geometry. The effect of combustion chamber geometry on combustion and emission characteristics was investigated by the experiment. Figure 3 shows the histories of cylinder pressure (p), heat release rate (dQ/dt) and nozzle needle lift (N.L.) against crank angle (θ) at various injection timing (θ_i) at a high load with a mean effective pressure of

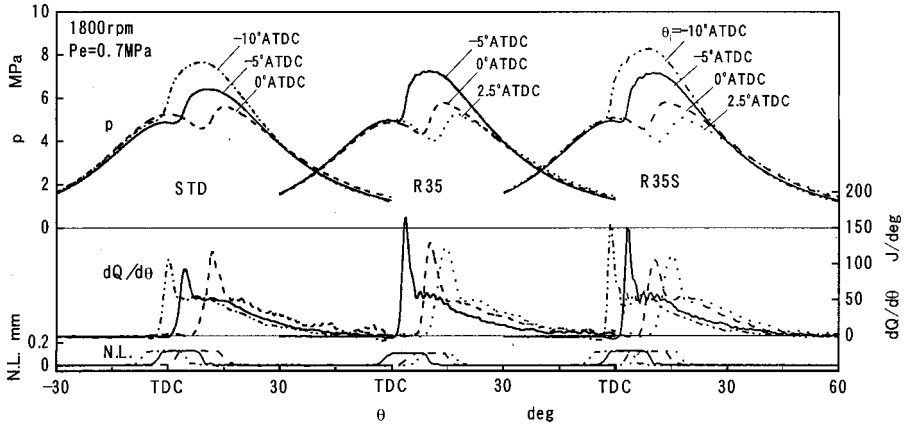

Fig. 3 Time histories of combustion pressure and heat release rate

Pe=0.7 MPa and engine speed of $n=1800$ rpm. The swirl ratio changed by a swirl plate is 2.2 for the STD and R35 chambers, and 3.6 for the R35S chamber, which is the optimum swirl ratio decided experimentally by engine performance and emissions for every chamber. It is seen from the figure that the high squish chambers R35 and R35S show higher cylinder pressures and initial heat release rates compared with the STD chamber. In particular, the R35 chamber shows the highest initial heat release rate. Thus, the R35 chamber cannot be operated at earlier injection timing because of heavy engine knocking caused by the rapid rise of cylinder pressure. The initial heat release rate for the R35S chamber is lower than that of the R35 chamber. Therefore, the R35S chamber can be operated at an earlier injection timing than the R35 chamber. Both the R35 and R35S chambers can be operated at later injection timings, while the STD chamber cannot be operated at a later injection timing than $\theta_i=2.5$ deg ATDC due to higher smoke and fuel consumption. The R35S chamber can use a wider range of injection timings in comparison with the STD and R35 chambers. Figure 4 compares emission characteristics, such as NO_x concentration, total hydrocarbons (THC), smoke density (S), particulate emissions (PART), and fuel consumption rate (b_e). Particulate emissions are classified into the solid fraction (SOLID) and soluble organic fraction (SOF). Experimental conditions are the same as in Fig. 3. As seen from the figure, NO_x emissions decrease with retarded injection timings for every chamber. At the same time, smoke and particulate emissions increase for the STD chamber; however, both NO_x and particulate emissions decrease for the R35 and R35S chambers. Accordingly, it is shown that the simultaneous reduction of NO_x and particulate emissions is obtained for the R35 and R35S chambers when injection timing is retarded. In particular, the R35S chamber produces less smoke and particulate emissions in comparison with the R35 chamber.

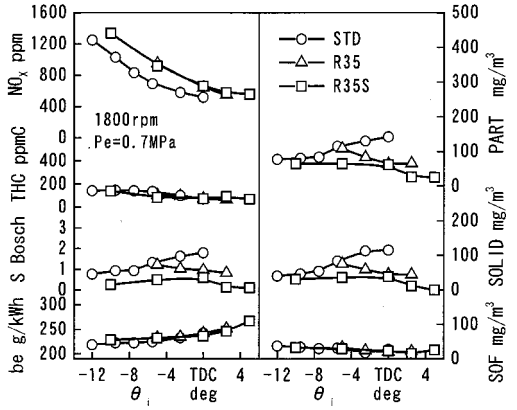

Fig. 4 Effect of combustion chamber geometry

The effect of high squish combustion chamber geometry on combustion and emissions was investigated by CFD computation in order to analyze the experimental results. Figure 5 compares cylinder pressures and heat release rates between measured and calculated results for the three chambers at an injection timing of $\theta_i=0$ deg ATDC condition. The figure indicates that computational results can predict the heat release rate for every chamber, although the cylinder pressure for the R35 chamber is a little lower than that predicted. Figure 6 shows the mass averaged turbulent kinetic energy $\bar{k}$ normalized by its initial value of k_0 at intake valve closure under the same conditions as Fig. 5. Turbulent kinetic energy of R35 and R35S is much higher than that of STD. High turbulence is produced during the compression stroke in the high squish chambers due to intensified squish and swirl caused by the squish lip. The turbulence intensity decreases once with the reduction of piston speed near TDC. When combustion commences, turbulence is strengthened again. In particular, the R35 chamber produces higher turbulence intensity than the R35S

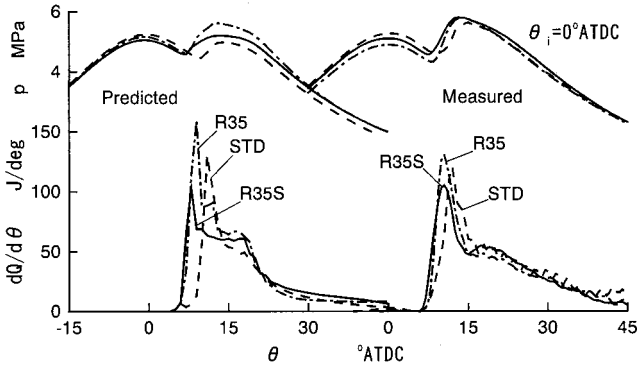

Fig. 5 Comparison of combustion pressure and heat release rate

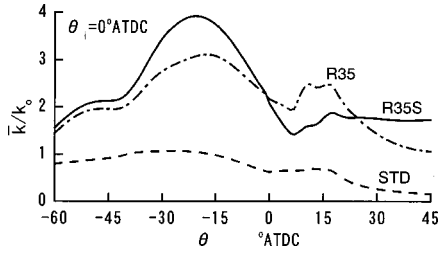

Fig. 6 Effect of combustion chamber geometry on time histories of turbulent kinetic energy

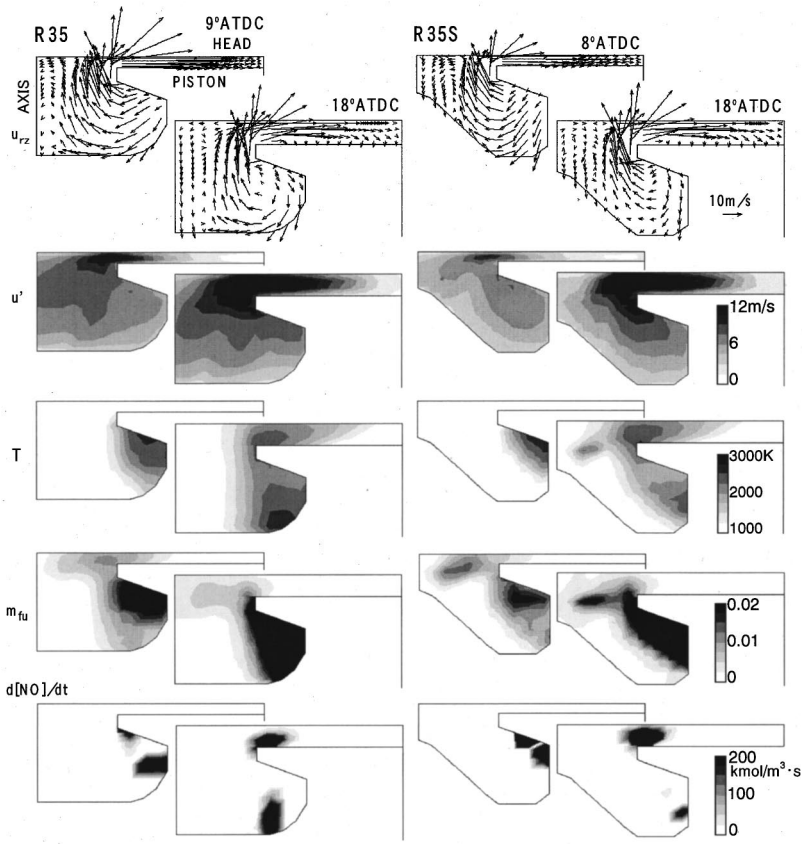

Fig. 7 Comparison of gas velocity, turbulence kinetic energy, temperature, fuel mass fraction, and NO formation rate

chamber because the initial heat release rate is higher due to air motion as will be mentioned later. However, for the R35 chamber, turbulence intensity decreases after the crank angle of θ=15 deg ATDC, whereas the R35S chamber keeps high turbulence intensity for a long time. This result shows that the R35S chamber is more effective for promoting diffusion combustion due to high swirl and high squish, which is one of the reasons that lower particulate emission is produced for the R35S chamber in the experiment.

Figure 7 compares axial section gas velocity u_{rz}, turbulence intensity u', temperature T, fuel mass fraction m_{fu}, and NO formation rate d[NO]/dt at the peak initial combustion stage of crank angle θ=9 or 8 deg ATDC and diffusion combustion stage of θ=18 deg ATDC. As seen from the air motion in the R35 chamber, burned gas flows from the outer edge of the cavity to the center along the bottom wall of the chamber. However, for the R35S chamber, burned gas flows from beneath the squish lip to the cavity bottom along the outer wall of the cavity. The air motion then turns upward along the central pip in the chamber. A high turbulence region is located under the squish lip of the R35S chamber, while the R35 chamber distributes a larger region of high turbulence than the R35S chamber. The central pip of the R35S chamber seems to make the air motion rolled up, and the gas velocity near the bottom wall is slower than that of the R35 chamber. More burned gas may roll back to the rich and high turbulence region of the R35S chamber. The burning gas keeps rotating inside the cavity of the chamber and forms a doughnut-like rich mixture before flowing out the clearance region. These air motions affect fuel and temperature distributions. The high temperature and high fuel density region tends to be distributed from the outer wall to the bottom of the cavity of the R35 chamber. The R35S chamber tends to keep the high temperature and rich mixture under the squish lip for a long time. NO_x is produced near the high heat release region. It is indicated that combustion gas tends to spread through the whole cavity of the R35 chamber. This is one of the reasons that the R35 chamber produces a high initial heat release rate in the engine experiment. In other words, in order to control initial combustion, it is necessary to keep a small region with high heat release. The central pip of the R35S chamber plays an important role in restraining initial combustion. Moreover, it can be said that the R35S chamber keeps locally rich and high turbulence combustion under the squish lip during the combustion period. This kind of combustion process for the R35S chamber seems not only to reduce particulate emissions but also to restrain NO_x formation in spite of high turbulence combustion. The discussion mentioned above shows that CFD and phenomenological modeling could be applied to analyze the combustion process in a high squish combustion chamber.

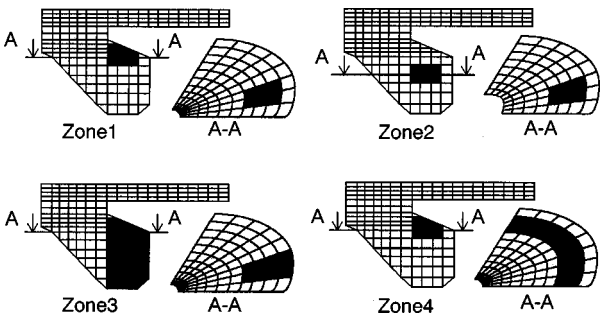

Fig. 8 Initial mixture distribution

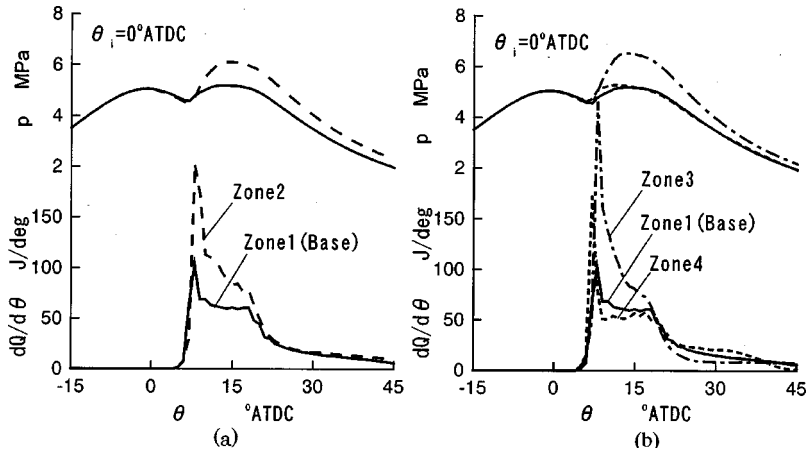

Fig. 9 Effect of initial mixture distribution on combustion process

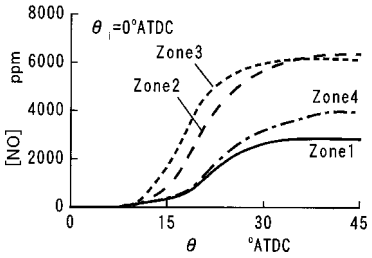

Fig. 10 Time histories of NO concentration

Effect of Initial Mixture Distribution. In order to clarify the experimental results, the effect of initial mixture distribution in the combustion chamber on initial heat release rate is investigated next. The CFD code used in this study has the compact spray model mentioned above. Changing the mixture source region corresponds to the initial fuel distribution because the injected fuel is modeled to flow out of this region. Figure 8 shows the initial mixture distributions calculated in this study. The computations are carried out with the R35S chamber under the same conditions as in Fig. 5. There are four distribution zones as initial mixture sources in the chamber. Zone 1 is the base distribution. The mixture at zone 2 moves the distribution to a lower position than zone 1, which corresponds to using an injector with a smaller spray angle. Zone 3 gives a large axial distribution, which corresponds to the high-pressure injection. These three zones have the same

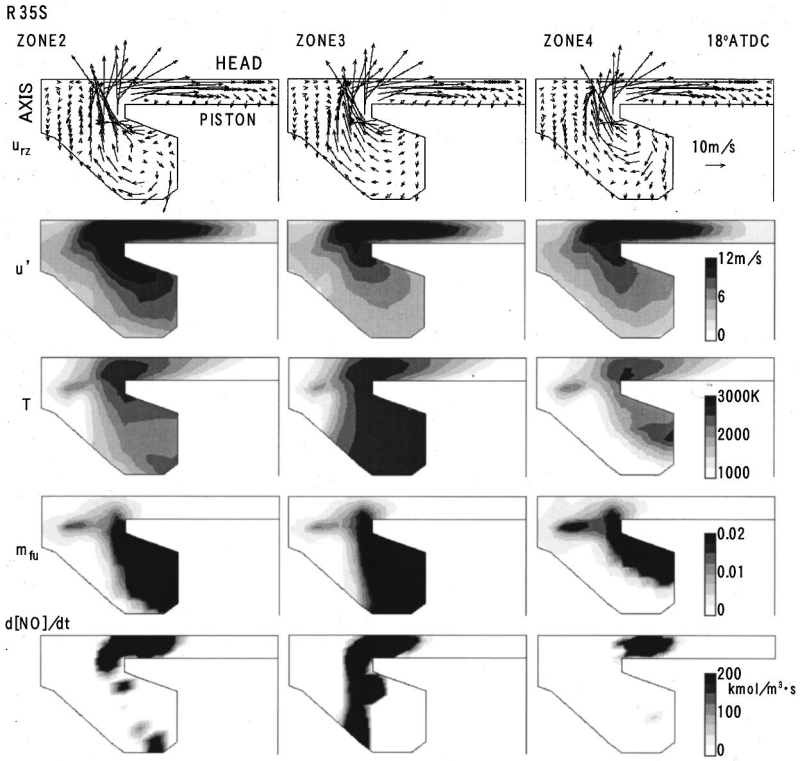

Fig. 11 Effect of mixture distribution on gas velocity, turbulence intensity, temperature, fuel mass fraction, and NO formation rate

circular distribution. Zone 4 gives a large circular distribution while keeping the same axial distribution as zone 1. Zone 4 simulates a high swirl condition.

Figure 9 shows the computational results of cylinder pressure p and heat release rate $dQ/d\theta$ against crank angle θ. Figure 9(*a*) compares zone 2 with zone 1, and Fig. 9(*b*) compares zone 3 and zone 4 with zone 1. In Fig. 9(*a*), when the position of the mixture distribution is lowered (zone 2), the initial combustion is promoted, resulting in a heat release curve similar to that of the R35 chamber shown in Fig. 5. In Fig. 9(*b*), a large mixture distribution (zone 3) also increases the initial heat release rate. The distribution of zone 3 resembles the case of the high-pressure injection that is known to produce a high initial heat release. It is shown that a large mixture distribution tends to produce a high initial heat release rate, while zone 4, in which the mixture is distributed widely in the circular direction, shows a heat release rate history similar to that of zone 1. Figure 10 shows the histories of NO_x concentration. It is found from the figure that zone 2 and zone 3 form high NO_x emissions. It can be said that a high initial heat release rate results in high NO_x emission. Zone 1 and zone 4 have the possibility of lower NO_x emissions. Although NO_x prediction is based on Zeldovich mechanism in this study, it may be necessary to introduce NO_x reduction mechanism caused by decomposed hydrocarbons in the rich combustion ([27]) in order to analyze NO_x restriction of the R35S chamber.

Based on the results in Figs. 9 and 10, the combustion process for lower initial heat release rate and lower NO_x condition was examined. Figure 11 shows the distributions of gas velocity, turbulence intensity, temperature, the fuel mass fraction and the NO formation rates for the distributions of zones 2, 3, and 4 under the conditions corresponding to Fig. 7. Zones 2 and 3, which produce a high initial heat release rate, show a large gas velocity along the central pip in the chamber. This is the same result as in the R35 chamber without a central pip. This air motion seems to carry the mixture to the cavity center. The rich and high-temperature region tends to spread from the bottom to the cavity center, resulting in a high heat release rate at initial combustion. However, zone 4 shows the similar air motion and distributions as zone 1, as shown in Fig. 7, namely, a strong clockwise flow is formed in the outer region of the cavity. Combustion continues under the squish lip, resulting in a local rich and high-temperature region that remains under the squish lip throughout the combustion process. It is inferred that local rich and high turbulence combustion can restrain initial combustion. A squish lip is effective for producing high turbulence. Considering that zone 4 corresponds to a high swirl condition, the high swirl condition of the R35S chamber may both restrain initial combustion and promote diffusion combustion.

Conclusions

This study investigated the effect of combustion chamber geometry and initial mixture distribution on combustion process in a direct-injection diesel engine by means of experiment and computation using CFD and phenomenological modeling. It was concluded that

(1) the high squish combustion chamber with a squish lip produces simultaneous reduction of NO_x and particulate emissions at retarded injection timing. According to the calculation, local rich and high-turbulence combustion occurs in the high squish combustion chamber.

(2) as the high squish combustion chamber with a central pip keeps high turbulence intensity under the squish lip for a long time, the chamber is effective for promoting diffusion combustion, resulting in lower particulate emissions.

(3) combustion continues under the squish lip until the end of combustion for the high squish combustion chamber with a central pip, and the combustion region forms a rich mixture and high turbulence atmosphere, which reduces the initial heat release and restrain NO_x formation. However, the high squish combustion chamber without a central pip produces a high initial heat release rate and a pressure increase because burned gas flows to the cavity center.

(4) in order to reduce the initial heat release and NO_x emission, the initial mixture should be distributed in the small region of the cavity, and high turbulence should be produced in the region. The high squish combustion chamber with a central pip can effectively realize this kind of combustion process.

(5) when the mixture is distributed in the bottom or large region in the high squish combustion chamber, burned gas tends to spread to the cavity center and the initial heat release rate increases even in the high squish combustion chamber with a central pip.

(6) for the high squish combustion chamber with a central pip, diffusion burning is promoted by high swirl while keeping a lower initial heat release rate.

Acknowledgments

The authors would like to thank YANMAR DIESEL Co. for supporting this work. The authors also wish to express their appreciation to Dr. C. Yang and Mr. R. Kato for their contribution to this study.

References

[1] Shundoh, S., Kakegawa, T., Tsujimura, K., and Kobayashi, S., 1991, ''The Effect of Injection Parameters and Swirl on Diesel Combustion with High Pressure Fuel Injection,'' SAE Paper No. 910489.
[2] Pierpont, D. A., and Reitz, R. D., 1995, ''Effects of Injection Pressure and Nozzle Geometry on D.I. Diesel Emissions and Performance,'' SAE Paper No. 950604.
[3] Nakakita, K., et al., 1994, ''Optimization of Pilot Injection Pattern and Its Effect on Diesel Combustion with High-Pressure Injection,'' JSME Int. J. Ser. B. **37**, pp. 966–973.
[4] Middlemiss, I. D., 1978, ''Characteristics of the Perkins 'Squish Lip' Direct Injection Combustion System,'' SAE Paper No. 780113.
[5] Daisho, Y., et al., 1986, ''Effects of Combustion Chamber Geometry in a Direct-Injection Diesel Engine,'' Trans. Jpn. Soc. Mech. Eng., Ser. B **52**(479), pp. 2768–2773.
[6] Konno, M., et al., 1991, ''Reduction of Smoke and NO_x Emissions by Active Turbulence Generated in the Late Combustion Stage in Diesel Engines — 2nd Report,'' Trans. Jpn. Soc. Mech. Eng., Ser. B **57**(534), pp. 773–777.
[7] Zhang, L., et al., 1996, ''Effect of Chamber Geometry on Flame Behavior in a DI Diesel Engine,'' Trans. Jpn. Soc. Mech. Eng., Ser. B **62**(600), pp. 3213–3219.
[8] Sakata, K., et al., 1990, ''Development of Toyota Reflex Burn (TRB) System in DI Diesel Engine,'' SAE Paper No. 900658.
[9] Baert, R. S. G., Beckman, D. E., and Verbeek, R. P., 1996, ''New EGR Technology Retains HD Diesel Economy with 21st Century Emissions,'' SAE Paper No. 960848.
[10] Konno, M., Chikahisa, T., and Murayama, T., 1993, ''An Investigation on the Simultaneous Reduction of Particulate and NO_x by Controlling Both the Turbulence and the Mixture Formation in DI Diesel Engines,'' SAE Paper No. 932797.
[11] Shimazaki, N., et al., 1998, ''Combustion and Emission Characteristics of Premixed Lean Diesel Combustion — Attempts to Control Ignition Timing of PREDIC with Several Kinds of Gas Added into Intake,'' Trans. JSAE. **29**(3), pp. 61–65.
[12] Matsui, Y., et al., 1997, ''A New Combustion Concept for Small DI Diesel Engines — 1st Report: Introduction of the Basic Technology, Trans. JSAE **28**(1), pp. 41–46.
[13] Yanagihara, H., et al., 1997, ''A Study of DI Diesel Combustion under Uniformly-Highly Dispersed Mixture Formation,'' Trans. JSAE **28**(4), pp. 17–22.
[14] Hashizume, T., et al., 1998. ''Combustion and Emission Characteristics of Multiple Stage Diesel Combustion,'' SAE Paper No. 980505.
[15] Kidoguchi, Y., Yang, C., and Miwa, K., 1999, ''Effect of High Squish Combustion Chamber on Simultaneous Reduction of NO_x and Particulate From a Direct-Injection Diesel Engine,'' SAE Paper No. 1999-01-1502.
[16] Miwa, K., Ueta, T., and Ishiyama, T., 1991, ''Effect of Swirl on Particulate Emissions from Direct- Injection Diesel Engines,'' Trans. Jpn. Soc. Mech. Eng. **57**(538), pp. 2159–2165.
[17] Ishiguro, J., Kidoguchi, Y., and Ikegami, M., 1998, ''Three-Dimensional Simulation of the Diesel Combustion Process,'' JSME Int. J., Ser. II **31**(1), pp. 158–165.
[18] Ikegami, M., Hida, M., and Ishiguro, J., 1989, ''Simulation of Flow and Combustion in Engine Combustion Chambers with Arbitrary Geometries,'' Tans. JSAE **42**, pp. 33–37.
[19] Ikegami, M., Kidoguchi, Y., and Nishiwaki, K., 1986, ''A Multidimensional Model Prediction of Heat Transfer in Non-Fired Engines,'' SAE Paper No. 860467.

[20] Magunussen, B. F., and Hjertager, B. H., 1976, ''On Mathematical Modeling of Turbulent Combustion with Special Emphasis on Soot Formation and Combustion,'' *16th Symp. (Int.) on Combust.*, The Combustion Insitute, pp. 719–727.
[21] Edelman, R. B., and Harsha, P. T., 1975, ''Laminar and Turbulent Gas Dynamics in Combustors – Current Status,'' Prog. Energy Combust. Sci. **4**, pp. 1–62.
[22] Ikegami, M., Miwa, K., and Ikeda, H., 1974, ''Analysis of the Diesel Combustion Process Based on Varying Delay Mechanism,'' Bull. JSME **17**(114), pp. 1619–1628.
[23] Ikegami, M., Nakatani, K., and Shioji, M., 1996, ''Stochastic Model for Ignition of a Diesel Spray,'' *The 34th Symp. on Combust.*, Combustion Society of Japan, pp. 286–288.
[24] Ikegami, M., Miwa, K., and Li, X., 1986, ''Spray Process and Pyrolysis in the Initial Stage of Diesel Combustion,'' Bull. JSME **29**(253), pp. 2189–2195.
[25] Wakuri, Y., et al., 1959, ''Studies on the Penetration of Fuel Spray of Diesel Engine,'' Trans. Jpn. Soc. Mech. Eng. **25**(156), pp. 820–826.
[26] Yang, C., Kidoguchi, Y., and Miwa, K., 1999, ''Effect of Rich and High Turbulence Combustion on Emissions and Flame Behavior in a Direct-Injection Diesel Engine,'' Trans. Jpn. Soc. Mech. Eng. **65**(637), pp. 3203–3208.
[27] Myerson, A. L., 1975, ''The Reduction of Nitric Oxide in Simulated Combustion Effluents by Hydrocarbon-Oxygen Mixture,'' *Combust. 15th Symp. (Int.) on Combust.*, Combust. Inst., pp. 1085–1092.

D. Caceres

J. R. Reisel[1]
e-mail: reisel@uwm.edu

Mechanical Engineering Department,
University of Wisconsin-Milwaukee,
Milwaukee, WI 53201-0784

A. Sklyarov
Advanced Analysis Facility,
University of Wisconsin-Milwaukee,
3209 N. Maryland Avenue,
Milwaukee, WI 53211

A. Poehlman
Briggs and Stratton Corporation,
Milwaukee, WI 53201-0702

Exhaust Emission Deterioration and Combustion Chamber Deposit Composition Over the Life Cycle of Small Utility Engines

In this study, a laboratory test procedure to mimic the life cycle of the small air-cooled engines in field operation is developed. A characterization of exhaust emissions over the life cycle of the engines is achieved with special focus given to the hydrocarbon emissions. Both Briggs and Stratton four-stroke (four-cycle) overhead-valve and side-valve engines with a nominal power output of 3.7 kW (5 hp) are used in this study. Different levels of emissions are observed for each type of engine configuration, and it is noted that the hydrocarbon emissions changed more than CO or NO_x *emissions. These data support the idea that combustion chamber deposits (CCD) are a significant cause of deteriorating emissions. Chemical analysis techniques are applied to the CCD, and it is found that the deposits consist primarily of polynuclear aromatic compounds and unsaturated hydrocarbons.* [DOI: 10.1115/1.1496773]

Introduction

The utility, lawn, and garden engine (ULGE) family is a category of small spark-ignition, air-cooled, internal combustion engines with power under 20 kW. Applications for these engines include lawnmowers, garden tractors, and snow blowers. Usually, the emissions from these engines are tested in laboratory facilities shortly after a break-in period and then again at the end of the engine's lifetime. When used as lawnmower engines, the engines operate through a series of transient loads where the engine load varies as a function of grass condition and lawnmower type ([1]). There has been little quantification of how these small engines degrade over time.

As engines age, combustion chamber deposits (CCD) form on piston tops and cylinder heads and can contribute to a significant hydrocarbon (HC) emissions increase ([2]). However, there is some uncertainty as to the exact effect of CCD on emissions ([3–5]). In some cases ([3]), the HC emissions increase dramatically due to high CCD accumulation, while in other cases ([4,5]), the CCD formation has no effect on HC emissions. This uncertainty stems from the fact that CCD can act either as a HC-increasing agent by absorbing and desorbing unburned fuel or as a HC-reducing agent by plugging crevices in the cylinder and piston top ([2]). The effects of the CCD on the HC emissions are dependent on which of these mechanisms is dominant for a given engine and operating condition.

In order to study the deterioration of the exhaust emissions over time, a set of Model 11 (overhead-valve) and Model 12 (side-valve) four-stroke engines from Briggs and Stratton are tested for 200 hours. Several engines are tested using an in-laboratory test procedure, and several are tested under normal field operation; this is done to facilitate the development of an acceptable in-laboratory life cycle test for use in future studies. To characterize the deterioration of the emissions, the hydrocarbon, nitrogen oxides (NO_x), and carbon monoxide (CO) emissions are measured at various intervals. The results of these measurements are presented below.

In addition, the results from a chemical analysis of the deposits formed in the engine are presented. The characterization procedure is performed on the deposits at the end of the life cycle testing. While not a complete picture of the chemistry of the deposits over the lifetimes of the engines, these results can still serve as a baseline for future studies involving the deposit formation in these types of engines.

Experimental Procedure

Emission Characterization Procedure. The engines are operated for 200 hours, which is the expected useful lifetime of the Model 11 and Model 12 engines. During the emissions tests, all engines are tested on a vertical/horizontal shaft eddy-current small engine dynamometer (manufactured by Froude Consine) using the standard SAE J1088 test procedure ([6]). Exhaust emissions are taken from a probe that meets the specifications given in 40 CFR 86.310-79 ([7]). Measurements of the CO_2, CO, NO_x, and HC emissions are obtained with an AMA 2000 Pierburg emissions bench, with the hydrocarbons being reported as C_1. A Nicolet FTIR spectrometer is also used to measure the emissions at the end of the lifetime period for the in-laboratory engines. During all the tests, the speed, brake torque, brake power, fuel flow rate, intake air temperature, oil temperature, spark plug seat temperature, and exhaust gas temperature are measured together with the emissions.

During the emission tests, the engines are operated at 85% of the rated speed (3060 rpm). As the engines were not designed for operation at idle conditions, only five modes of operation in the J1088 test are considered. Elimination of the idle mode from the J1088 test requires the redistribution of the percentage weights over the rest of the modes. Raw sampling is performed for three minutes until all the parameters stabilize. Concentrations are converted to mass emission rates using the J1088 fuel flow method ([6]).

The in-laboratory life cycle testing procedure consists of operating the engines at a fixed load for set periods of time, and then testing the emissions every 50 hours. Four engines of each type are mounted in stationary mower decks and equipped with fixed

[1]To whom correspondence should be addressed.

Contributed by the Combustion and Fuels Division of THE AMERICAN SOCIETY OF MECHANICAL ENGINEERS for publication in the ASME JOURNAL OF ENGINEERING FOR GAS TURBINES AND POWER. Manuscript received by the CF Division Aug. 23, 2000. final revision received by the ASME Headquarters Jan. 28, 2002. Associate Editor: P. Malte.

paddles that are designed to provide 25% of the full load at continual operation. The engines are operated for four hours on one day, followed the next day by four hours of operation, a 30-minute cool-off period, and then two additional hours of operation. After these ten hours of operation the oil level is measured. During general engine operation, the engines use 87-octane pump gasoline and SAE 30HD oil. For emissions tests, CARB Phase II fuel is used.

Maintenance on the in-laboratory engines was performed before each of the emission tests, except for the 50-hour test point. At the 50-hour intervals, the maintenance procedure involved replacement of the spark plug and the replacement of the air filter. In addition, at the 100-hour intervals (100 hours and 200 hours), the carburetor was cleaned, checked for leaks and the outside surface around the cooling fins was cleaned of oil and dirt.

Four field-test engines of each type are operated under normal commercial cutting applications. The maintenance described above is performed before each emissions test. The emissions for the field-test engines are tested at 0, 66, 125, and 200 hours following the SAE J1088 procedure.

Deposit Characterization Procedure. The techniques of nuclear magnetic resonance (NMR), Fourier transform infrared analysis (FTIR), scanning electron microscopy with energy dispersive X-ray analyzer (SEM/EDX) and thermogravimetric/differential thermal analysis (TGA/DTA) are used to characterize the deposits. The main concerns in this study are the general composition and sources of the deposits. As described below, the deposits form in two zones. When possible, the two zones are kept separate for characterization.

Nuclear magnetic resonance is performed using the technique of cross polarization/magic angle spinning (CP/MAS). Because different types of carbon resonate at different spectral positions, this technique makes possible the distinction between aliphatic and aromatic molecules. The apparatus used is a Bruker PRX-500 ^{1}H, C13 CP/MAS unit running at 8.5 kHz.

Fourier transform infrared microscopy data are obtained with a quantum microscope and a Mattson 3000 spectrometer. The samples are pressed between two diamond windows to allow partial separation of the solid and liquid phases present in the deposits. Focusing the beam in the FTIR microscope on different parts of a sample allows the characterization of the two phases separately.

Thermogravimetric analysis (TGA) ([8]) is a dual-gas method that is applied to determine the fraction of volatiles, synthetic polymers, soot, and ash in the deposits. Tests are done first in an inert atmosphere (argon), and then in an oxidizing atmosphere (air) after the sample is cooled. In TGA, the weight of the sample is recorded as the temperature increases at a fixed rate. As the weight decreases, volatilization of compounds is evident and the existence of different thermal events can be distinguished in the weight loss versus temperature curve. In order to exclude oxidation that could be caused by a presence of trace amounts of oxygen, differential thermal analysis curves are also recorded.

Results

Life Cycle Emissions. The changes in the emissions as the engines age are determined for the Briggs and Stratton Model 11 and Model 12 engines. The normalized $HC+NO_x$ emissions data for the in-laboratory Model 11 engines are shown in Fig. 1. The results for the Model 12 engines are similar, although the rate of increase in the emissions is considerably larger. Figure 2 presents the fractions of HC and NO_x in the total $HC+NO_x$ measurement for the in-laboratory engines. The results in Fig. 2 are the average contribution from HC and NO_x at each test point for the four Model 11 and four Model 12 engines. The HC fraction of the total $HC+NO_x$ measurement increases over time, and typically is approximately 80% of the total, while the NO_x fraction decreases over time, and is around 20% of the total. It should be noted that

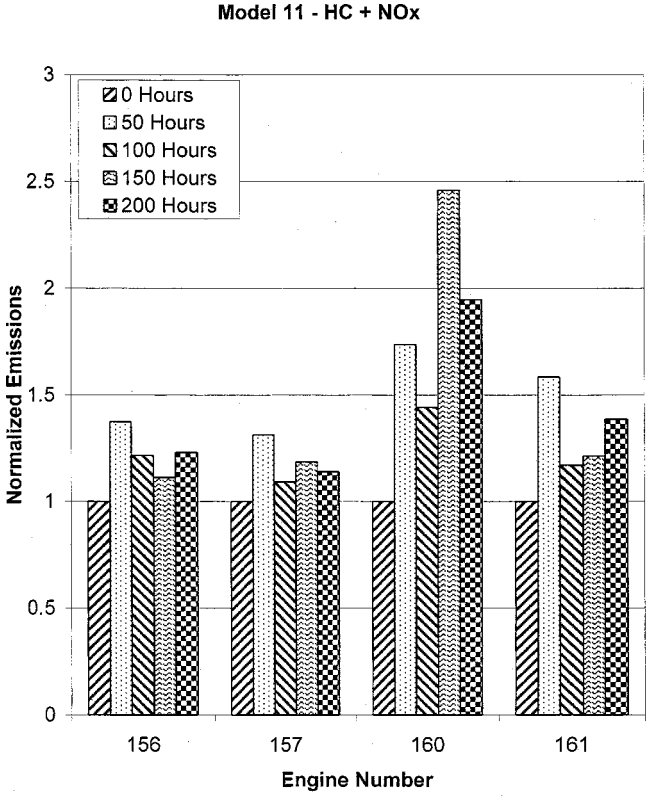

Fig. 1 Normalized measurements of $HC+NO_x$ emissions from the in-laboratory Model 11 (overhead-valve) engines

the zero-hour point absolute measurements of HC emissions are on the order of 7 g/kW·hr and the NO_x emissions are on the order of 2 g/kW·hr.

The average values for the $HC+NO_x$ emissions for both the in-laboratory test and field-test engines for the Model 11 and Model 12 engines are shown in Figs. 3 and 4, respectively. Figure 5 presents the normalized data for the CO emissions from the in-laboratory Model 11 engines; again, the data are similar for the Model 12 engines. The zero-hour point absolute measurements of CO concentrations are on the order of 370 g/kW·hr. The normalization of the data is conducted by dividing each data point by the zero-hour baseline emissions measured for each engine.

Figures 1, 3, and 4 show that the $HC+NO_x$ emissions increase consistently with time, except for the in-laboratory test engine data at 50-hour test point. Note that there was no routine maintenance performed on the in-laboratory engines before the 50-hour emissions test. As a result, the $HC+NO_x$ emissions measurements are higher than would be expected from the rest of the data. For the subsequent emissions tests the routine maintenance is performed and the data begin to closely resemble the levels achieved by the field-test engines.

A comparison of averaged normalized $HC+NO_x$ emissions data between the laboratory and field engines is performed, and is shown in Figs. 3 and 4. These figures present averaged normalized data from the engines while the uncertainty bars represent the standard deviation of the measurement. The standard deviation is presented to give an indication of outlying engine tests. An unusual engine test can significantly affect the average for the small sample size used. Engine #160 of the Model 11 engines at the 150-hour point is an example of this. From 100 to 150 hours, engine #160 operated poorly, and this carried over to the emissions test. The large uncertainty bar indicates that one of the measurements is significantly different from the other tests (as can be noted from Fig. 1). If that data point is excluded, the data would fall close to the expected trend. From Figs. 3 and 4 it can be seen

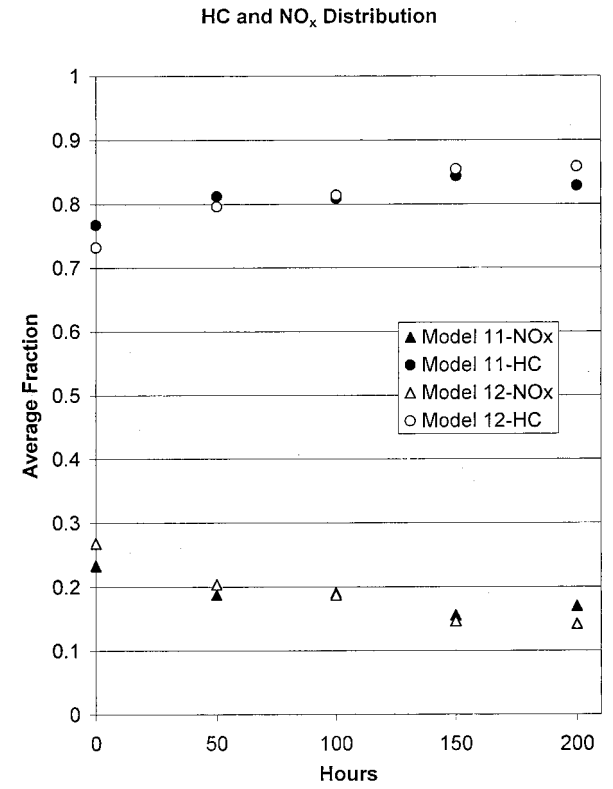

Fig. 2 Average fraction of the HC and NO_x in the total HC $+NO_x$ emissions measurements for the laboratory-test Model 11 and Model 12 engines

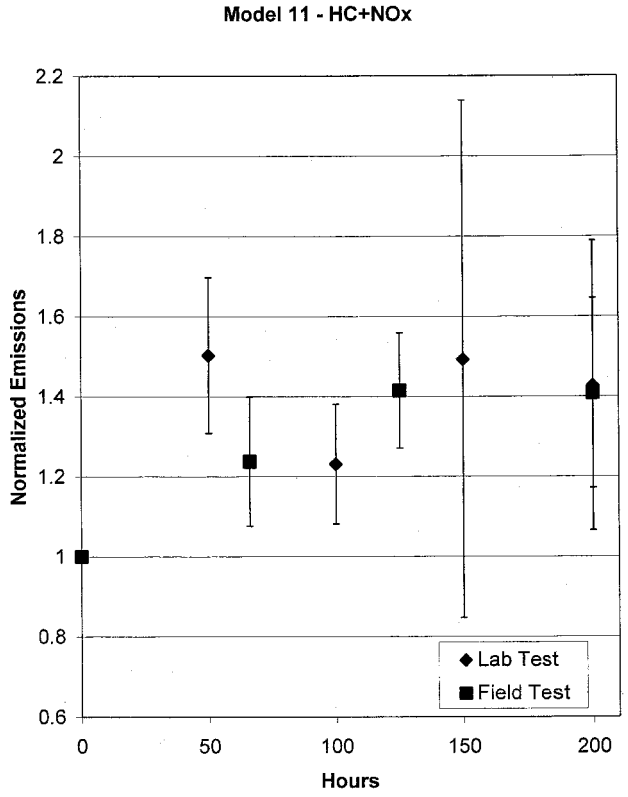

Fig. 3 Averaged normalized $HC+NO_x$ emissions measurements for both the laboratory-test and field-test Model 11 engines

that the in-laboratory test adequately replicates the trend of emissions deterioration for $HC+NO_x$ seen in the field.

Figure 5 shows that the CO emissions remain nearly constant over time for the Model 11 engines; this is also seen in the Model 12 engines. Some small fluctuations exist in the data but there is no indication of consistent significant changes in the emissions. While not shown here, the field-test engines exhibit similar behavior. In some cases, the CO emissions measurements in the field-test engines increase, and in other cases decrease. However, most of the fluctuations are within 20% of the baseline (zero-hour) measurement, similar to the in-laboratory test data. Therefore, the laboratory test procedure appears to be sufficient at replicating the field operation from a CO standpoint as well.

As the engines age, engine components wear and deteriorate causing more oil introduction into the combustion chambers. As a consequence of this phenomena, more deposits due to oil and oil additives can form. One characteristic about CCD is their ability to absorb and desorb unburned fuel during the compression and exhaust stroke, respectively, of the engine cycle ([9]). This can lead to increased hydrocarbon emissions. Confirming the idea that HC emissions increase as the engine deteriorates, when the HC and NO_x are analyzed separately, it is noted that the NO_x emissions are nearly constant over time and that the hydrocarbon emissions increase represents the vast majority of the total $HC+NO_x$ increase.

An alternative explanation for the increase in HC emissions over time is that as the engine ages, the air-fuel mixture may become richer, resulting in more incomplete combustion of the fuel. However, if the air-fuel mixture is becoming richer, the CO emissions would be expected to increase while the NO_x emissions would be expected to decrease. As can be seen in Fig. 5 the CO emissions are showing little change and, as mentioned above, the NO_x emissions are also nearly constant. Therefore, the substantial increase in HC emissions over time does not appear to be due to an increasingly richer air-fuel mixture, and it appears probable that the increase is due primarily to the influence of the CCD.

Before proceeding to an analysis of the CCD, a few observations on the operational differences between the side-valve and overhead-valve engines can be made. First, it should be noted that the side-valve engines run approximately 30°C hotter than the overhead-valve engines (as determined by measuring the oil temperature and the cylinder temperature near the spark plug). The side-valve engines also tend to run at a lower air-fuel ratio. Both of these conditions may affect the amount and type of CCD formed. Both types of engines also experience similar deposit patterns, with CCD being present on the piston tops and the cylinder heads.

Figure 6 presents the averaged results of the FTIR measurements of the emissions from the laboratory-test engines at the 200-hour test point. The distribution for the small hydrocarbons is very similar to the observations in previous small engine work ([10]). For both engine models, the small hydrocarbon emissions are primarily in the form of CH_4, C_2H_2, C_2H_4, and C_3H_6. There is also a significant C_4H_8 concentration in these tests. Meanwhile, 39% of the hydrocarbon emissions in the overhead-valve engines and 46% of the hydrocarbon emissions in the side-valves engines are in the form of higher molecular-mass hydrocarbons. Based on the trends seen in the relative concentrations of the smaller hydrocarbons, these larger hydrocarbons are likely unburned fuel (rather than products of partial oxidation or fuel pyrolysis). As a result, the much higher hydrocarbon emissions seen for the side-valve engines at the 200-hour test point, in comparison to the overhead-valve engines, are likely the result of more unburned fuel passing through the side-valve engines during the combustion process.

Figure 7 shows the averaged normalized power over time for the in-laboratory engines for both engine types. From this it is apparent that power from the Model 12 engines is decreasing at a faster rate than from the Model 11 engines. In addition, the oil

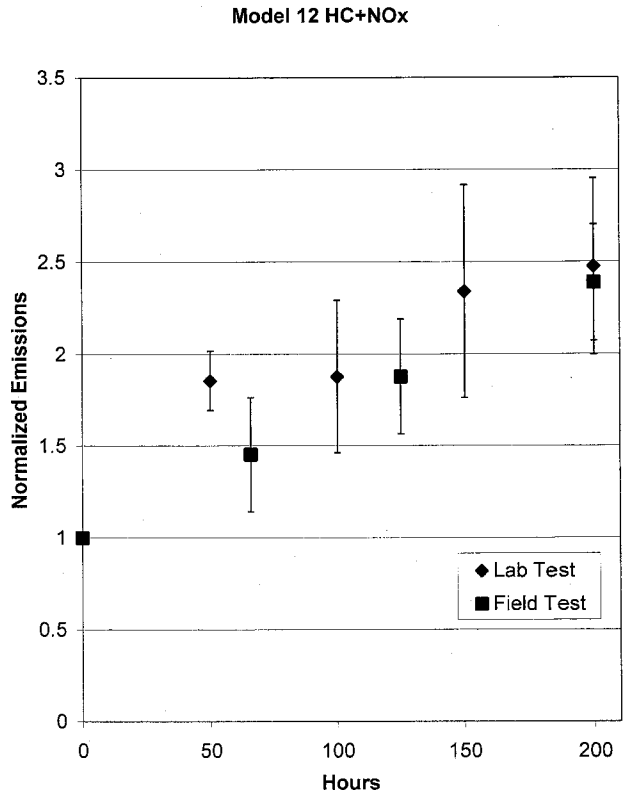

Fig. 4 Average normalized HC+NO_x emissions measurements for both laboratory-test and field-test Model 12 engines

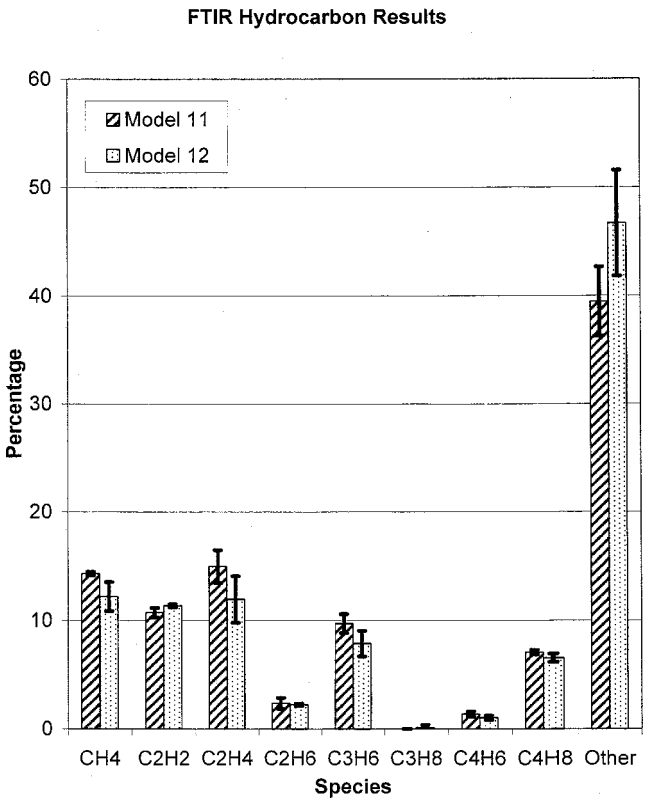

Fig. 6 Average percentages of various hydrocarbon species in the exhaust of the Model 11 and Model 12 engines at 200 hours, as measured by FTIR

consumption data indicate that while the oil consumption increases as all of the engines age, there is more oil consumption in Model 12 engines than the Model 11 engines (excluding engine #160). Therefore, it appears that the side-valve engines deteriorate more rapidly than the overhead-valve engines.

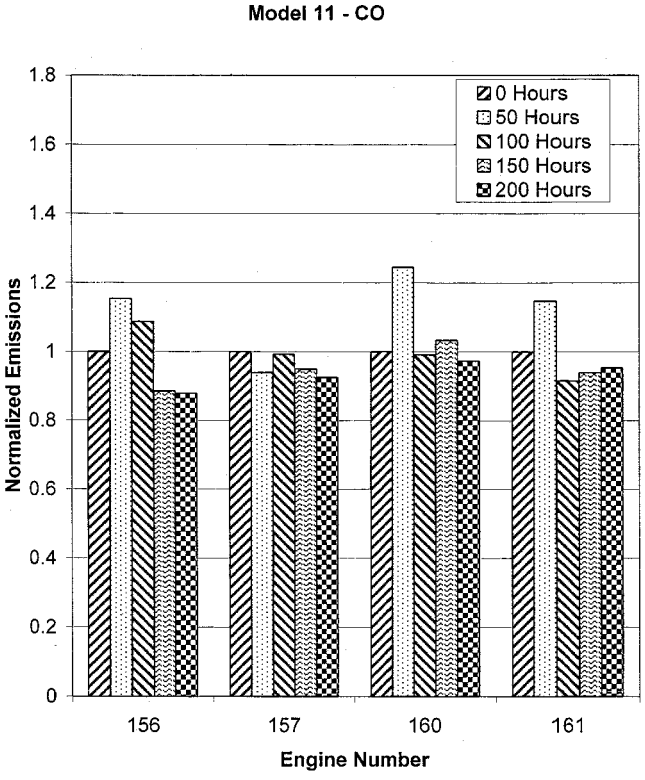

Fig. 5 Normalized measurements of CO emissions from the in-laboratory Model 11 (overhead-valve) engines

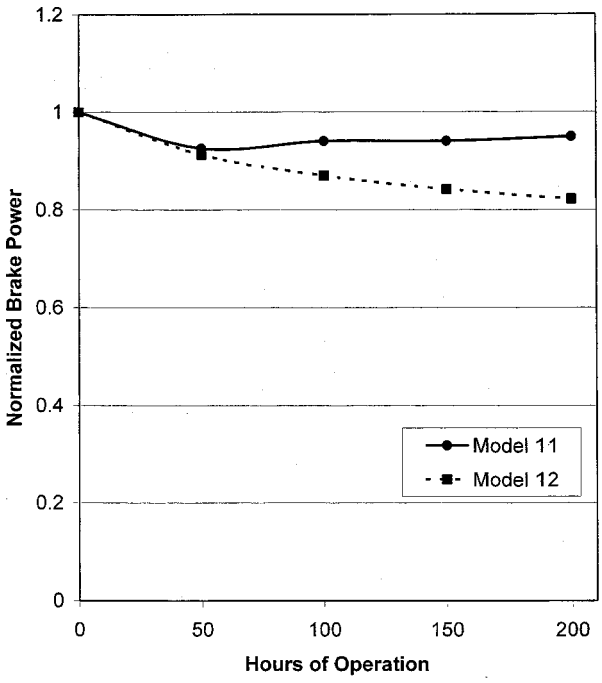

Fig. 7 Normalized power at the emissions test points during the life cycle of the in-laboratory engines

Table 1 ^{13}C NMR integrated area ratios for aliphatic to aromatic content in the CCD for Zone 1 and Zone 2 for the Model 11 and Model 12 engines

Engine Type	Engine Number (Zone)	Integrated Area Ratio Aliphatic: Aromatic
Model 11	156 (Zone 1)	0.57
	156 (Zone 2)	0.70
	161 (Zone 1)	0.62
	161 (Zone 2)	0.43
Model 12	279 (Zone 1)	0.33
	279 (Zone 2)	0.50
	281 (Zone 1)	0.29
	281 (Zone 2)	0.57

Table 2 Summary of the TGA analysis of the CCD in the in-laboratory engines. The values represent an average for Zone 1 and Zone 2 for each engine.

Engine Type	Engine Number	% Weight Loss in Argon	% Weight Loss in Air	% Ash Residues
Model 11	156	48.5	32.8	18.7
	161	44.2	40.9	15.0
Model 12	279	41.8	36.2	22.0
	281	34.9	39.0	26.8

Combustion Chamber Deposits Analysis. Most of the studies involving the problems originating from CCD have been performed in larger gasoline and diesel engines, while little work has been reported for small spark-ignition engines. As a result, the small engine industry has little information upon which to base modifications to the engines to control CCD formation. By modifying the design of an engine, deposit problems can be controlled. However, redesign can lead to new deposit characteristics and therefore new studies have to be performed. The results presented below can serve as a baseline for analysis of the changes resulting from future engine modifications.

Based on visual inspection of the combustion chamber and piston deposits, the CCD exist in two layers. Previous studies ([11–13]) have indicated the existence of two major zones of deposit formation. Zone 2, the zone closer to the metal surface, is a region in which the condensation of highly volatile compounds from the fuel and oil takes place. As observed during removal of this zone, the CCD has a ''lacquer-type'' structure and is very difficult to remove. The second layer, Zone 1, is composed of molecules with less bonding tendency and which can be more easily removed. This zone is carbonaceous in character and has a soot-like chemical structure.

To provide baseline information on these small spark-ignition engines, a chemical characterization of the CCD in the engines is performed at the end of the life cycle testing. The results of this characterization are as follows.

The deposits from four engines are studied using the ^{13}C CP/MAS NMR technique. This technique produces intensity spectra for each sample, and each peak can be assigned to a specific class of compounds ([14–15]). By integrating the areas over the spectra corresponding to the different classes, the NMR technique is used to obtain a ratio of the aliphatic hydrocarbons to the aromatic compounds and condensed phases in both deposit zones. The results are summarized in Table 1.

The results of the NMR analysis show that the CCD are primarily composed of aromatic compounds and condensed phases. In addition, in three of the four engines, there is a higher aliphatic fraction in Zone 2 than in Zone 1, which is consistent with the findings of Daly et al. [12]. It is also noticeable that the Model 12 engines present a larger aromatic fraction than the Model 11 engines in Zone 1.

The FTIR analysis provides a molecular characterization of both the liquid and solid phases of the deposits. It is found that the liquid phase has characteristic IR bands at 2800–3000 cm^{-1} and 1350–1450 cm^{-1}. These bands can be assigned to absorption by saturated hydrocarbons. The source of those hydrocarbons may be either oil or high molecular-mass components of the fuel.

A measured FTIR spectra of the oil used in the engines is found to be very similar to the FTIR spectrum of the liquid phase. This oil spectrum shows all the small details of the liquid phase spectrum with the exception of two broad bands around 1100 and 750 cm^{-1}. These bands may be attributable to additives accumulated during the tests. For example, the broad peak at 1100 cm^{-1} may be assigned to SiO_2.

The spectrum of the solid phase allows for the assignment of different bands that are present in that phase. First, a broad band around 3400 cm^{-1} may be attributed to OH groups and bands around 1600–1700 cm^{-1} to C—O and C═O groups correspondingly. Therefore, these bands suggest a high degree of oxidation. The broad absorption band around 1100 cm^{-1} can be attributed to ester and ether groups. A shoulder at 3100 cm^{-1} indicates the presence of aromatic compounds in the sample.

Previous spectra of CCD ([16]) have shown the same absorption bands as the spectra which would result from combining the liquid phase and solid phase spectra in this study. This suggests that Kim et al. [16] measured both the liquid and solid phases simultaneously. By using FTIR microscopy, the phases are analyzed separately. This separate phase analysis makes FTIR microscopy a very useful tool, because it is believed that due to the porous structure of CCD, the solid phase would always include oil compounds that would cause difficulty in the analysis.

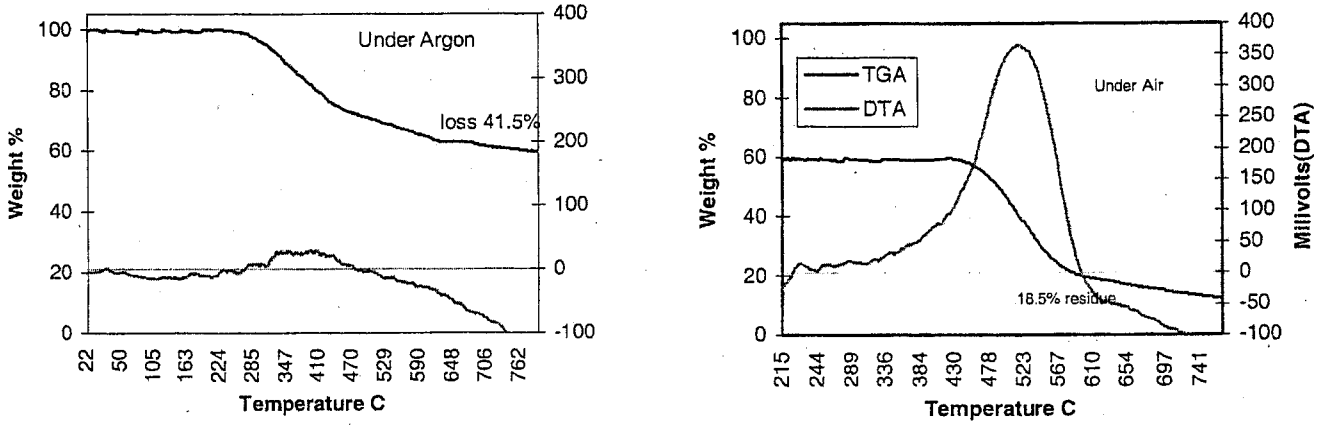

Fig. 8 Typical dual-gas TGA/DTA of a Model 11 engine CCD under argon and air

Table 3 Summary of the concentrations of the most common inorganic elements in CCD of the in-laboratory engines. The values represent average atomic percent concentrations for Zone 1 and Zone 2.

Engine Model	Engine Number (location)	Mg	Al	P	S	Ca	Fe	Zn	Si	Cu
Model 11	156 (head)	14	6	19	18	25	2	24		
	161 (head)	16	6	15	16	17	5	25		
	154 (piston top)	9	1.8	28	14	24	5	32		
Model 12	279 (head)	13	7	20	13	20	2	25		
	281 (head)	12	6.4	20	14	19	2	27	1.4	
	67 (piston top)	9	6	12	14	24	5	25		7

The dual gas TGA/DTA approach is used to identify several distinct components based on volatilities or thermal stabilities. Figure 8 presents typical curves resulting from the application of the dual method and the results are summarized in Table 2. Significant weight loss is seen under argon between the temperatures of 200°C and 600°C, which is due to volatilization of several different compounds such as polymeric components and highly oxidized hydrocarbons ([8]). The residue under argon tentatively consists of amorphous carbonaceous compounds and inorganic salts since these are thermally stable under argon. Further reheat under air rapidly oxidizes the remnants above 300°C.

The tests show higher weight loss under argon for Model 11 engines than Model 12 engines which may be attributed to the presence of higher molecular-mass hydrocarbons in the sample. The residue after burning all the carbon-containing compounds in air is larger for Model 12 compared with Model 11. The higher content of ash (suggestive of oil additives) in the residue indicates that oil sources for deposit formation are greater for the side-valve engines.

The elemental analysis on the deposits listed in Table 3 is conducted with an energy dispersive X-ray analyzer. Concentrations of inorganic compounds such as Cu, Si, and Zn are determined. The weight percentage of carbon in the deposits ranged from 35–55% and for hydrogen about 3–5% (Table 4) resulting in close agreement with Adams and Baker [17].

As seen in Table 3, the deposits from the piston tops and the deposits from the engine heads have a similar composition in terms of inorganic materials. The only significant difference is the presence of copper on the piston tops. The likely sources of the materials are as follows. Iron and aluminum are from wear and corrosion of the heads and pistons. Copper is known to be a fuel impurity and silicon originates mostly from dust in air. Zinc, phosphorus and calcium are likely from oil additives.

A lower H/C ratio for a deposit indicates that the deposit is more carbonaceous and less oxidized. In the case of a higher ratio, less carbon would be consumed during combustion and slightly lower concentrations of lubricant inorganics would be expected ([17]). The results show a ratio of 0.85–0.95 in the samples for both engine types. However, slightly higher ratios are noticeable in the Model 12 engines, agreeing with the higher oil consumption and higher HC emissions discussed earlier.

Very low atomic H/C ratios (<1) indicate the presence of highly unsaturated organic compounds such as polynuclear aromatic compounds. Recall that the NMR study indicates predominantly aromatic compounds in the CCD. The H/C ratios seen here are higher than expected from these compounds. The higher values of H/C obtained for these particular engines are likely caused by a presence of oil residues with H/C close to 2, which increases the low H/C ratios that would be found for polynuclear aromatic compounds.

Deposits from the combustion chamber are observed with a SEM micrograph using a magnification of 200X. Figures 9 and 10 show different structures from Zone 2 and Zone 1, respectively. As seen from the SEM image of Zone 2 the deposits are more homogeneous and maintain their cohesiveness. Zone 1 deposits present more loose particles of different shapes with dull edges, more disperse in structure and covered with very viscous liquid or polymers such as from oil. In Zone 1, the particles are likely

Table 4 Summary of the atomic H/C ratio analysis of the CCD in the in-laboratory engines. The values represent averages for Zone 1 and Zone 2.

Engine Model	Engine Number	%C	%H	%N	Atomic H/C Ratio
Model 11	156	46.51	2.98	1.04	0.77
	161	55.54	4.24	1.34	0.91
Model 12	279	45.24	3.57	1.08	0.94
	281	45.11	3.41	1.11	0.91

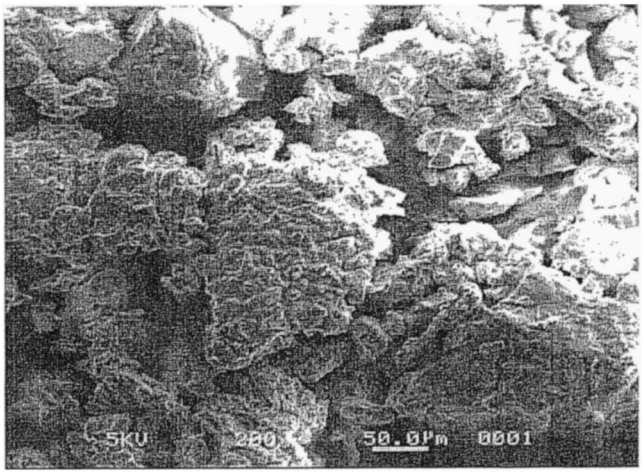

Fig. 9 SEM micrograph of Zone 2 of a CCD

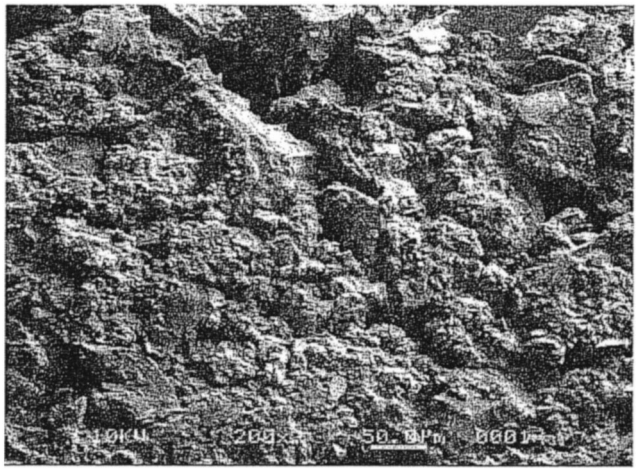

Fig. 10 SEM micrograph of Zone 1 of a CCD

formed by the carbonization of highly oxidized and very polar hydrocarbon liquid droplets condensed on the surface ([16]).

While it is difficult to reach definitive conclusions on the deposits based on these limited results, a few general observations can be made. First, while deposits are formed from fuel, oil, and engine wear, these deposits appear to be formed primarily from oil and oil additives. Second, the oil contributes more to deposit formation in the side-valve (Model 12) engines than the overhead-valve engines. Third, a relatively small amount of the deposits appear to originate from worn engine parts.

Conclusions

In this study, a life cycle laboratory test procedure is developed that agrees well with field test behavior with regards to emissions degradation. This test procedure can allow for more controlled life cycle testing of the engines in the future. The procedure is used to measure the change of the emissions from the engines over their life cycle. An appreciable increase in $HC+NO_x$ emissions (mostly in HC) is observed in these engines while the CO concentration remains fairly constant.

Based on the behavior of the emissions with time, the most significant mechanism leading to the change is the formation of combustion chamber deposits. Chemical analysis of the deposits is performed, and some conclusions can be drawn from it. While fuel, oil, and engine wear all can contribute to CCD formation, the presence of the ash residues, the fractions of inorganic materials, and the type of hydrocarbons found are suggestive that oil sources are the primary contributor to CCD. The oil appears to be an even greater source in the side-valve engines. In addition, CCD analysis provides evidence of more aromatic content in the CCD from the side-valve engines, correlating with the greater degradation of emissions seen in these engines.

Based on these results, the greatest challenge facing small engine manufacturers with regards to improving emissions over the lifetime of their engines involves minimizing the increase in HC emissions. An important component of this is to reduce the CCD formation in the engines. In turn, it appears necessary to increase the durability of the engine components so as to reduce the oil introduction into the engine cylinder in order to minimize the CCD formation.

Acknowledgments

The authors would like to thank the Wisconsin Small Engine Consortium, the Wisconsin Department of Administration, and the Wisconsin Department of Commerce for funding this project. The authors would also like to acknowledge the contributions of the following to this project: K. Neusen, D. Gill, D. Janisch, and D. Pieper from the Alternative Fuels Program at UWM, A. Blumenfeld from the Department of Chemistry at UWM, and S. Hardcastle from the Advance Analysis Facility at UWM.

References

[1] Gabele, P., 1997, ''Emissions From 4-Cycle Walk-Behind-Mover Engines: Test Cycle Effects,'' SAE Paper No. 972793.

[2] Haidar, H. A., and Heywood, J. B., 1997, ''Combustion Chamber Deposits Effects on Hydrocarbon Emissions From a Spark-Ignition Engine,'' SAE Paper No. 972887.

[3] Valdatoros, T. H., Wong, V. W., and Heywood, J. B., 1991, ''Fuel Additive Effects on Deposit Build-up and Engine Operating Characteristics,'' *Symposium on Fuel Composition/Deposit Tendencies*, American Chemical Society, **36**(1).

[4] Wagner, R. W., 1993, ''The Effects of Fuel Composition and Deposit Control Additives on Combustion Chamber Deposits,'' *Proceedings of the CRC Workshop on Combustion Chamber Deposits*, Nov.

[5] Bower, S. L., Litzinger, L. A., and Frottier, V., 1993, ''The Effect of Fuel Composition and Engine Deposits on Emissions from a Spark Ignition Engine,'' SAE Paper No. 932707.

[6] SAE J1088 Recommended Practice, 1993, test procedure for the measurement of gaseous exhaust emissions from small utility engines.

[7] Federal Register, 1995, ''Control of Air Pollution; Emission Standards for New Non-road Spark-Ignited Engines at or Below 19 Kilowatts,'' Fed. Reg. 40 CFR Parts 9 and 90, Final Rule, **60**(127), July 3.

[8] Siegl, W. O., and Zinbo, M., 1985, ''On The Chemical Composition and Origin of Engine Deposits'' *Chemistry of Engine Deposits*, Plenum Press, New York.

[9] Harpster, M. O., Jr., Matas, S. E., Fry, J. H., and Litzinger, T. A., 1995, ''An Experimental Study of Fuel Composition and Combustion Chamber Deposit Effects on Emissions From a Spark Ignition Engine,'' SAE Paper No. 950740.

[10] Reisel, J. R., Kellner, T. A., and Neusen, K. F., 2000, ''Speciated Hydrocarbon Emissions in Small Utility Engines,'' J. Air Waste Manag Assoc., **50**, pp. 522–528.

[11] Kalghatgi, G., 1990, ''Deposits in Gasoline Engines—A Literature Review,'' SAE Paper No. 902105.

[12] Daly, D. T., Bannon, S., Fog, D., and Harold, S., 1994, ''Mechanisms of Combustion Chamber Deposit Formation,'' SAE Paper No. 941889.

[13] Lepperhoff, G., and Houben, M., 1993, ''Mechanisms of Deposit Formation in Internal Combustion Engines and Heat Exchangers,'' SAE Paper No. 931032.

[14] Solum, M., Pugmire, R. J., and Grant, D. M., 1989, ''^{13}C Solid State NMR of Argonne Premium Coals,'' Energy Fuels, **3**, pp. 187–193.

[15] Edwards, J., and Choate, P., 1993, ''Average Molecular Structure of Gasoline Engine Combustion Chamber Deposits Obtained by Solid-State 13C, 31P, and 1H Nuclear Magnetic Resonance Spectroscopy,'' SAE Paper No. 932811.

[16] Kim, P., Cheng, S., and Majorski, S., 1991, ''Engine Combustion Chamber Deposits: Fuel Effects and Mechanisms of Formation,'' SAE Paper No. 912379.

[17] Adams, K. M., and Baker, R. E., 1985 ''Effects of Combustion Chamber Deposit Location and Composition,'' *Chemistry of Engine Deposits*, Plenum Press, New York.

CO_2 Emission Abatement From Fossil Fuel Power Plants by Exhaust Gas Treatment

M. Gambini
e-mail: gambini@ing.uniroma2.it

M. Vellini
e-mail: vellini@ing.uniroma2.it

Department of Energetic Sciences
and Technologies,
University of Rome "Tor Vergata,"
Via del Politecnico, No. 1,
00133 Roma, Italy

In this paper thermodynamical and economic analyses of fossil-fuel-fired power plants, equipped with systems for CO_2 recovery, are presented. The investigation has been developed with reference to power plants representative both of consolidated technology (i.e., steam cycle and combined cycle power plants), and of emerging or innovative technology (integrated coal gasification combined cycle, IGCC, and advanced mixed cycle, AMC). There are two main methods to reduce CO_2 from power plant flue gas: physical and chemical absorption. In this work chemical absorption and liquefaction of CO_2 removed have been considered. With reference to thermodynamical and economic performance, significant comparisons have been made between the above introduced reference plants. An efficiency decrease and an increase in the cost of electricity has been obtained when power plants are equipped with CO_2 removal systems and units for liquefaction of the removed carbon dioxide. The main results of the performed investigation are quite variable among the different power plants here considered: their efficiency decreases in a range of 6 percentage points to nearly 13, while the electricity production cost increases in a range of 25% until 72%. The AMC stands out among the other power plants here analyzed because, after CO_2 recovery, it exhibits the lowest net work output decrease, the highest net efficiency and the lowest final specific CO_2 emission. In addition to this, its economic impact is favorable when the AMC is equipped with systems for CO_2 recovery. As a result it achieves a net electric efficiency of about 50% with a carbon dioxide emission of about 0.04 kg/kWh, and the electricity production cost rises to about 25% in comparison with an AMC without CO_2 removal and liquefaction systems.
[DOI: 10.1115/1.1519270]

1 Introduction

Continuous development of the world economy involves a substantial increase of the emission of carbon dioxide resulting from the combustion of fossil fuels. This increase in the concentration of carbon dioxide and other greenhouse gases in the atmosphere may enhance the green house effect. As a consequence the climate on earth may change considerably, causing environmental degradation. In order to limit the risks of climatic change, the manmade carbon dioxide emissions have to be reduced.

In this paper a process of separation from exhaust gas to reduce the emissions of CO_2 in power plants of different typology has been considered. At present there are two main feasible methods for the removal of CO_2 from power plant flue gas: chemical or physical absorption. The latter method, [1,2], briefly consists of dissolving the CO_2 in a physical solvent; as the solubility of CO_2 in physical solvent increases with higher pressure and lower temperature, this method has to be operated at a low temperature and high pressure. After physical absorption, the carbon dioxide is released from the solvent by reducing the pressure step by step. This process needs a low temperature and high pressure: so, if exhaust gases are at atmospheric pressure, they must be compressed to an appropriate pressure value, before CO_2 recovery is possible, with the consequential high energy requirement. For these reasons this method is not so suitable for exhaust gas treatment, but it may be convenient for the treatment of particular fuels like in an integrated coal gasification combined cycle (IGCC) where the recovery of CO_2 may be carried out on syngas before combustion, [3]. A coal gasifier, in fact, converts coal to a synthesis gas, where hydrogen and carbon monoxide are the main components. Before combustion, it's possible to introduce a shift reactor where CO and steam are converted to CO_2 and H_2. The shifted syngas stream contains a relatively high concentration of CO_2: i.e., about 40% at high pressure. For such a condition a process of physical absorption can be suitably applied.

In this paper a chemical absorption technique for CO_2 removal has been considered which allows a drastic CO_2 emission abatement (about 90%) and presents relevant performance as well as technical feasibility.

In a previous work the authors investigated the thermodynamical performance of a new advanced mixed cycle (AMC) in comparison with that attainable by an up-to-date combined cycle power plant (CC), [4]. The AMC plant layout consists of a reheat gas turbine with steam injection in the first combustion chamber, a steam turbine for steam expansion before its injection, a heat recovery boiler for superheated and resuperheated steam generation, and an atmospheric separator for water recovery from exhaust gas mixture. Steam recirculation in this cycle allows the reduction of the excess air, used to limit the turbine inlet temperature and thus the enrichment of the exhaust gas by CO_2. Due to this lower stack flow rate, the exhaust gas treatment for CO_2 removal may be more suitably applied.

In this paper our analysis is extended to other power plants, different both in typology and in fuel feeding. A proper thermodynamical analysis will show the implications of the CO_2 recovery on the plant performances.

But to make CO_2 recovery an attractive option for reducing CO_2 emissions, the associated costs must be as low as possible: a proper economic calculation has therefore been developed to evaluate the electricity production cost increase. The various

Contributed by the Power Division of THE AMERICAN SOCIETY OF MECHANICAL ENGINEERS for publication in the ASME JOURNAL OF ENGINEERING FOR GAS TURBINES AND POWER. Manuscript received by the Power Division Sept. 2001; final revision received by the ASME Headquarters May 2002. Associate Editor: D. Lou.

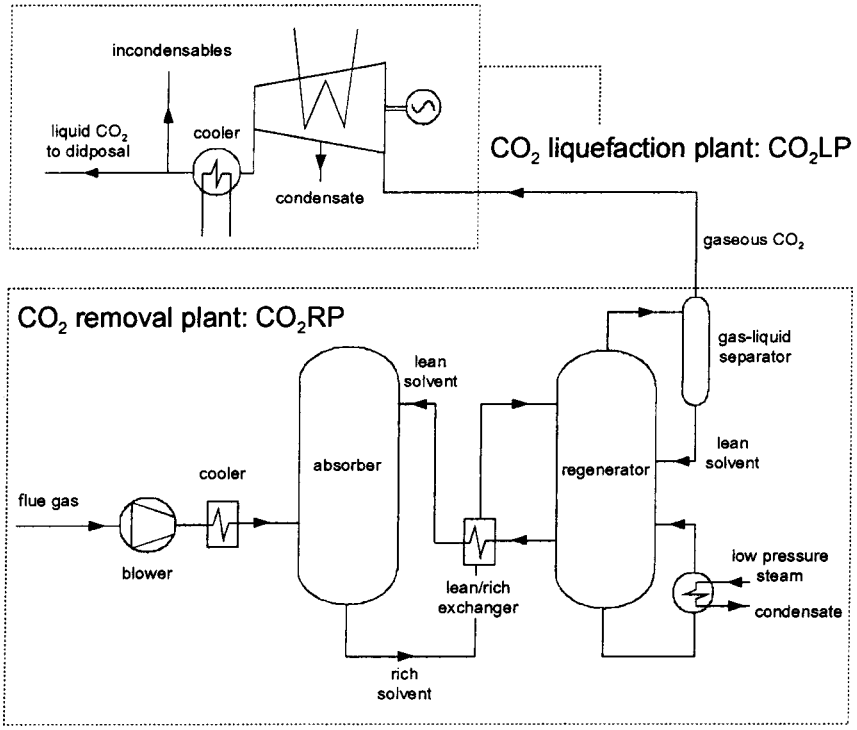

Fig. 1 CO_2 removal and liquefaction systems

schemes have been examined thermodynamically and economically so in this way it is possible to determine the option with the best potential performance.

It is important to recognize the limitations of the economic calculations presented here. The assumptions about costs have been made to enable comparisons of different technologies; but obviously the more established the technology the more accurate the costs. Moreover the cost of a given power plant will vary according to the localization. For the purpose of this paper, the convention assumed was that the plants would be in Europe. Three power plants (OSC, CSC, and CC) have been taken to represent their present status, while IGCC and AMC represent emerging and innovative technology, respectively.

2 CO_2 Separation and Liquefaction

Chemical absorption is the most suitable method for the separation of CO_2 from exhaust gases, when carbon dioxide has a low concentration (5–15% by volume) in a gaseous stream at atmospheric pressure. The CO_2 separation process, analyzed in this paper, is based on a commercially available process which uses aqueous solution of amines as solvents. Using this process, a recovery factor of 90% of CO_2 in feed flue gas is possible.

The separation process of carbon dioxide by chemical absorption consists of two steps:

1. the absorption of CO_2 by chemical solvents at a low temperature (40–65°C) and
2. the recovery of CO_2 from chemical solvents by using low grade heat (a temperature in the range of 100–150°C), usually extracted from power plants.

A flow diagram of the chemical absorption method, here considered, is shown in Fig. 1; here, the adopted liquefaction section is also shown. Regarding the separation section, it can be seen that the exhaust gases enter into the removal plant at a pressure slightly above the ambient pressure and at a temperature depending on the power plant upstream. First, they are compressed to about 1.3 bars, to overcome pressure drops within the system, and cooled to nearly 50°C. Then, the gases go to the absorption column where the carbon dioxide binds to the solvent chemically. The reach solution (i.e., the solution containing the absorbed CO_2) flows to a lean/rich heat exchanger: Here the hot lean solution, coming from the stripper column (regenerator), cools itself giving out its heat to the rich solution, which then goes to the regenerator. Here the solvent is regenerated by heat where the chemical bonds are decomposed thermally.

There are two energy requirements for this process:

1. heat for the regeneration of the solvent: we have considered that the required heat is 4 MJ per kg of recovered carbon dioxide, according to the literature, [5–7]. We have considered that this heat is provided by the low pressure steam from the power plant. We have assumed that the temperature for the regeneration of the solvent should be about 150°C so that the extraction of the steam takes place at about five bars. The steam gives out its latent heat of condensation and returns into the power plant as satured liquid at the same pressure as its extraction. The amount of steam for the regeneration is therefore determined by the quantity of recovered CO_2 and by the characteristics (temperature and pressure) of the extracted steam.
2. Energy for the compression of the flue gases and for the pumping of the amine solution through the removal plant: we have considered that the required energy is 0.11 MJ per kg of recovered carbon dioxide, according to the literature, [8]. This amount of energy is subtracted from the total plant work to obtain the net work.

After the separation of CO_2 from the exhaust gases, we have also considered liquefaction and dehydration of the removed carbon dioxide. We have assumed that the compression, dehydration and liquefaction are necessary so that the carbon dioxide can be transported, utilized, or stored elsewhere, without further energy expense. Usually the compression is carried out in various steps by alternately compressing and cooling the gaseous stream. During this intercooling, part of the steam condenses as the continuous increasing of the total pressure and the decreasing of the temperature produces a steam reduction in the gaseous mixture. After

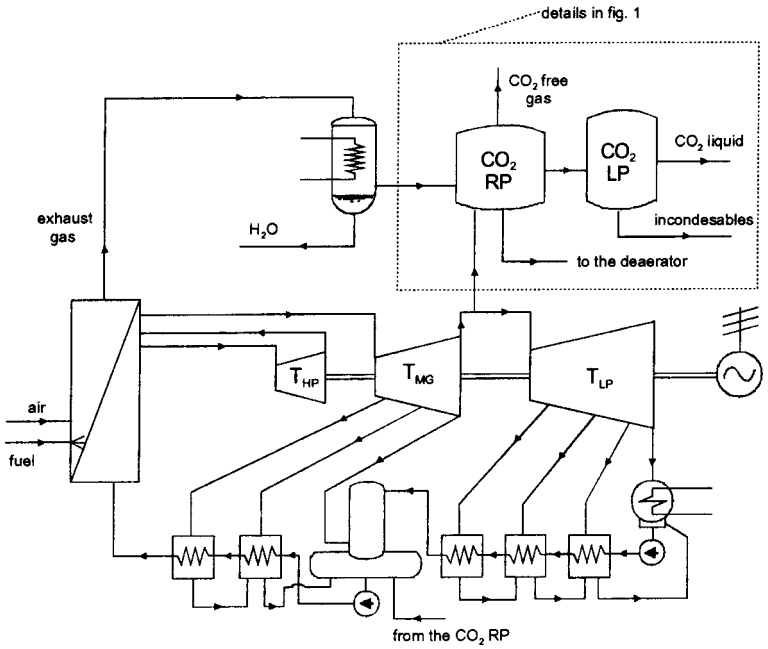

Fig. 2 The CSC and OSC scheme

each intercooling the condensate is removed. A final drying of carbon dioxide is required because the combination of water and carbon dioxide makes a corrosive solution. For this process a certain amount of energy for the compression is necessary: We have assumed an intercooled compression in six steps with equal partial compression ratio, until a final pressure of 150 bars is reached. Every step is characterized by a polytropic efficiency of 0.85, while the mechanical efficiency is assumed as 0.98. Under these conditions we have determined an energy consumption equal to 0.44 MJ per kg of recovered carbon dioxide; no consideration has been made regarding heat for intercooling because it is supposed that an adequate refrigerant fluid is easily available.

3 Analysis of Reference Power Plants

In this paper the comparison of the performance decrease and the electricity cost increase of some power plants fed by fossil fuels when equipped with CO_2 removal and liquefaction systems is treated. The reference power plants, analyzed here, are as follows:

- CSC: steam power plant fed by pulverized coal
- OSC: steam power plant fed by oil
- CC: combined cycle power plant, fed by natural gas
- IGCC: integrated coal gasification combined cycle
- AMC: advanced mixed cycle, fed by natural gas.

In Fig. 2–5 the plant layouts, here considered, are shown.

The first scheme, Fig. 2, represents CSC and OSC, as they vary only according to their power plant fuel supply.

The CSC is a seawater-cooled, conventional pulverized coal-fired steam plant with flue gas desulphurization. This layout and its working parameters have been chosen as representative of normal medium-large size steam power plants: a subcritical steam unit with SH/RH temperature of 540°C and p_{max} of 140 bars. A boiler module provides superheated steam for a first high-pressure turbine; then a resuperheated steam expands in a second turbine and finally there is a condensing turbine, characterized by a final pressure of 0.06 bars. Seawater is used for cooling in the condenser. There are six steam extractions for regenerative feed-water preheating; the pressure in the deaerator is at about 6 bars. The boiler is of a conventional drum-type, utilizing natural circulation. The flue gas from the boiler module, after particulate separation in electrostatic precipitators, is cooled and scrubbed in a gas desulphurization unit and then is sent to the CO_2 removal and liquefaction plants.

The OSC has the same thermodynamical cycle as the CSC, but, as the boiler is now fed by oil, the boiler module of this power plant is not provided with a flue gas desulphurization unit.

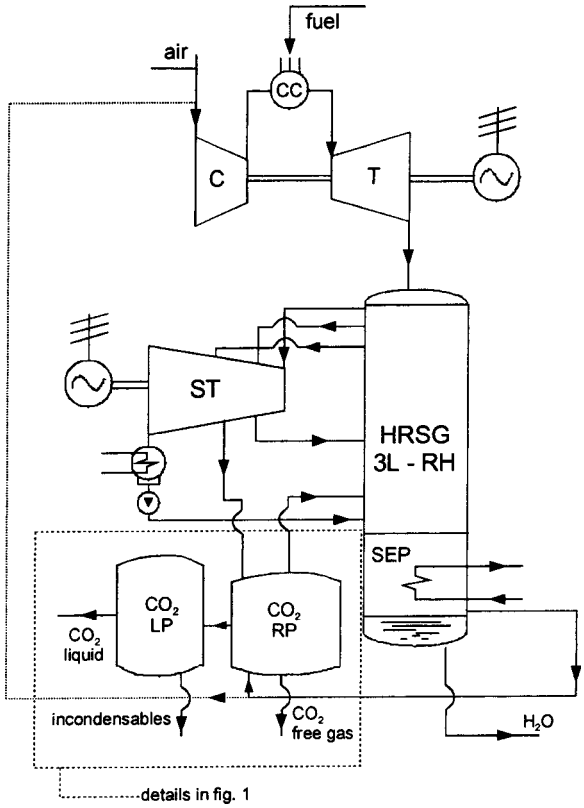

Fig. 3 The CC scheme

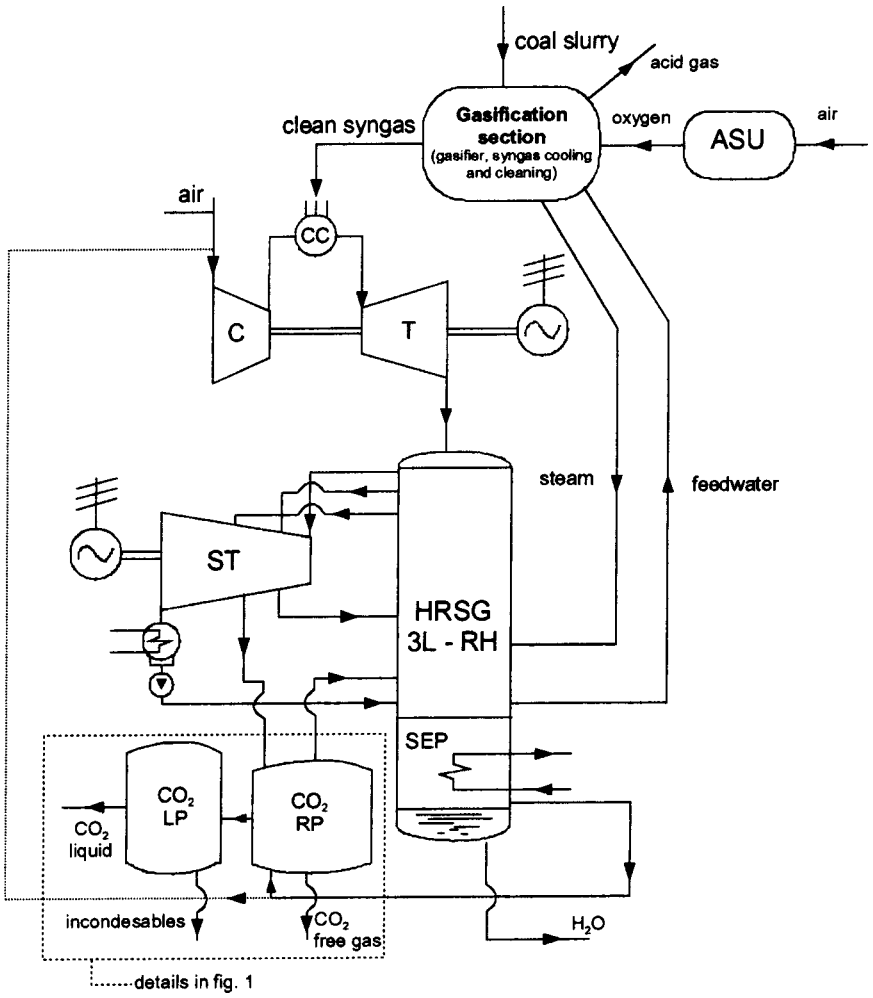

Fig. 4 The IGCC scheme

Figure 3 shows an up-to-date combined cycle (CC), equipped with CO_2 removal and liquefaction systems.

There is a heavy-duty gas turbine, as topping cycle, and a three-pressure-level, reheat steam cycle, as bottoming cycle. The dashed line to the compressor inlet represents the recirculation of part of the exhaust gas to the gas turbine compressor. In this way it is possible to reduce the flow rate of the exhaust gases to be treated and to increase the CO_2 concentration. Not only are thermal and electric requirements lower, the systems are smaller and thus cheaper. With respect to a conventional gas turbine, the working fluid is rich in CO_2 and low in O_2, but the consequences on the gas turbine operating conditions are minor, [9].

These former three power plants are selected as being representative of consolidated technology, but our attention has also been given to solutions that can be considered representative of either emerging technology, such as an IGCC, or of innovative technology, such as the AMC.

Figure 4 shows the scheme of an IGCC built around a Texaco gasifier which is equipped with CO_2 removal and liquefaction systems.

In the coal gasification section, clean syngas is produced from coal: in the block shown in Fig. 4 (gasification section), the coal treatment plant, gasifier, syngas cooling and cleaning are included. A conventional air separation unit (ASU) produces the oxygen necessary to gasification. The syngas is then burned in the gas turbine combustor, using air as an oxidizer and part of the exhaust gases when recirculation is planned for. After turbine expansion, a heat recovery steam generator uses the hot combustion gases to

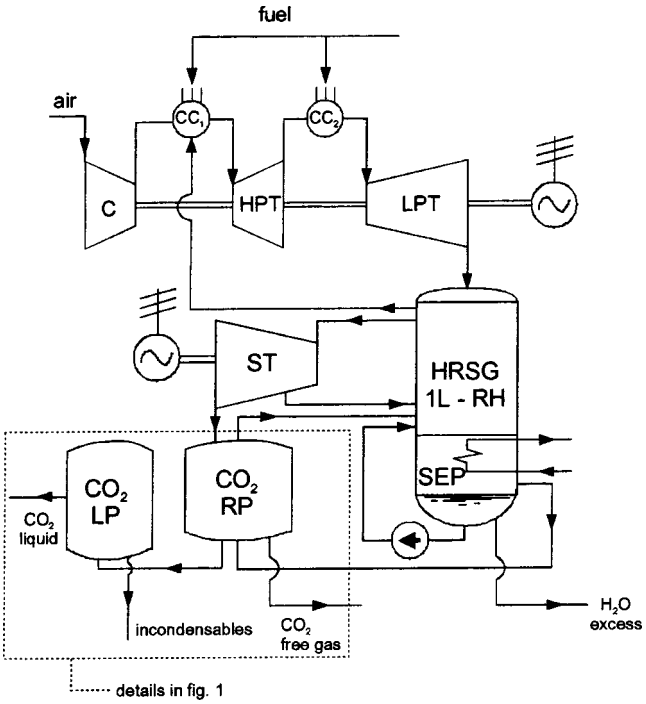

Fig. 5 AMC scheme

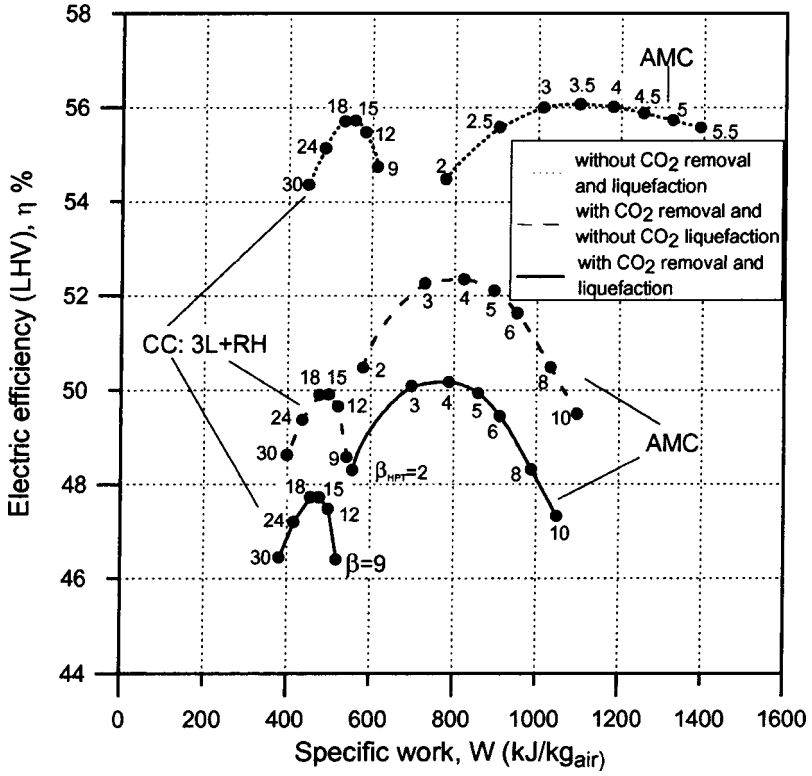

Fig. 6 Performance of the AMC and the CC with and without CO_2 recovery

feed a bottoming steam cycle, featured by three levels of pressure and reheat. At the exit of the HRSG, exhaust gases go into the CO_2 removal and liquefaction plants. As in the case of the CC, it is possible for the IGCC to have a partial recirculation of flue gas with the advantages previously noted.

Finally, Fig. 5 shows the scheme of a new advanced mixed cycle (AMC), recently proposed by the authors, [10–12]: It is a plant scheme with a full natural gas supply which attains very significant performance.

As can be seen in the plant scheme of Fig. 5, the AMC is a mixed gas-steam cycle in which steam works in a closed cycle. There is an initial steam heating, carried out in a regenerative way, and then steam heating (SH and RH) is carried out partly in a regenerative way, in the component named SEP, and partly by mixing steam with exhaust gases from the internal combustion of natural gas and compressed air in the two combustion chambers (cc_1 and cc_2). In the AMC cycle, water separation and recovery are necessary to operate in a closed steam cycle mode. In fact in this plant solution there is a special water separation unit, consisting of a heat exchanger arrangement where the mixture (incondesable gases and steam) is cooled below the condensation temperature of steam. Waste heat flow is profitably recovered: in this plant layout there is a full regenerative steam generation. It is also necessary to point out that the steam recirculation in this cycle allows the reduction of the excess air used to limit the turbine inlet temperature; it is therefore possible to attain a ratio between the stack gas flow rate and the generated electric power which is much lower than that related to conventional combined cycles. This is very advantageous with regard to the installation of a CO_2 scrubber at the exhaust gases exit. In Fig. 5 the scheme of the AMC integrated with the CO_2 separation and liquefaction units is shown. A steam extraction from the turbine of the power plant provides the thermal energy requirement. The return condensate from the stripper goes to the feedwater tank of the HRSG. The cooling of exhaust gases from the HRSG before the treatment in the separation unit is carried out by the separator for water recovery.

Figure 6 shows the overall performance of the AMC compared with that attainable with the up-to-date CC, as introduced above, with and without the CO_2 removal and liquefaction, [4].

The results for the two power plants with the CO_2 recovery are referred to $\beta=15$ and $r=0.4$ for the CC and to $\beta=30$ and $\beta_{HPT}=5$ for the AMC. For all calculations a value of TIT of 1200°C has been assumed (the other assumptions are listed in the Appendix).

There is a very interesting result in Fig. 6: while the two plants without CO_2 removal systems attain similar efficiency levels, the AMC plant attains an efficiency (about 50%) of over two points higher than the CC (47.7%), when equipped with CO_2 removal and liquefaction plants. The total efficiency drop due to the CO_2 removal and liquefaction is of about eight points for the CC and of about six points for the AMC. The causes must be investigated in the energy interaction between the two power plants and the CO_2 removal system, because the penalty due to the liquefaction system is of the same value. In fact, the steam bled involves a higher efficiency penalty in the CC than in the AMC because this bled steam involves a relevant work decrease of the low pressure steam turbine of CC, which virtually becomes a back pressure steam turbine. In the AMC plant, on the other hand, the steam bled reduces the work of the gas turbines (reduction of the injected steam), but this work reduction is partly recuperated because the back pressure of the steam turbine is reduced (from 30 bars related to the injection pressure in the AMC without the CO_2 removal to five bars related to the pressure of the steam feeding the stripper reboiler in the AMC plant with CO_2 removal).

To show these results, a numerical investigation has been realised, using a proper numerical model developed by the authors. This model is based on calculation procedures for conventional

Table 1 The performance without CO_2 recovery

	W kJ/kg	η %	CO_2 % vol.	CO_2 kg/kWh
OSC	1250	40,6	11,7	0,646
CSC	1250	39,6	13,7	0,823
CC	558	55,7	3,48	0,355
IGCC	674	46,0	7,90	0,709
AMC	1100	56,0	6,60	0,353

components (turbines, compressors, pumps, heat exchangers, etc.) and for an unconventional component, i.e., the water separator. The calculation procedure of this latter component is explained in a previous work, [13]. The main numerical assumptions and the evaluation criteria are reported in the Appendix. Regarding the comparison with CCs, the performance of these plants has been evaluated by using the same numerical model for gas turbine units (obviously without steam injection), to ensure the same calculation conditions for the two plants, and by using the GateCycle (AA.VV., 1996) to evaluate the up to date HRSG (three pressure level and reheat) for the CC plant.

For the two steam cycle power plants, the numerical investigation has been realised completely by the GateCycle, while the results of the IGCC, here adopted, have been elaborated by other authors in previous papers, [14], the IGCC efficiency and power output has been estimated by a proper computer code designed by these authors to evaluate heat and mass balances of complex gas-turbine-based power plants, [15–18].

4 Technical and Economic Performance

Table 1 reports the most important performance parameters (specific work and efficiency), CO_2 content in the flue gases and specific emission rate of carbon dioxide for the five power plants here analyzed.

These data refer to the performance without the CO_2 removal and liquefaction. It is interesting to note that shifting from low-hydrogen fuel (coal) to high-hydrogen fuel (oil or natural gas) is already an alternative for reducing the power plant CO_2 emissions: For example, the CO_2 rate emission of the steam cycle fed by oil is over 20% lower than that of the steam cycle fed by coal, with an efficiency level almost similar. Moreover, when the same fuel supply is considered, increasing the efficiency of power generation allows the limitation of the CO_2 emissions: in fact the IGCC has a carbon dioxide emission rate almost 14% lower than that related to the steam cycle fed by coal.

After the CO_2 removal, all the power plants showed a relevant reduction of net specific work output and a substantial penalty of net electric efficiency: these data are reported in Table 2 with the specific rate of CO_2 removed and the final CO_2 emission.

The CSC is the most penalized scheme: the net work output decreases by about 32% and the efficiency is over 12 percentage points lower; moreover the CSC is again the power plant with major CO_2 emission. In fact a removal efficiency of 90% is assumed for all schemes, except for the IGCC where the CO_2 removal efficiency is adjusted to isolate 91.5% of the carbon in the

Table 2 The performance with CO_2 recovery

	W kJ/kg	η %	$CO_{2\ removed}$ kg/kWh	$CO_{2\ emission}$ kg/kWh
OSC	924	30,4	0,87	0,086
CSC	851	27,0	1,09	0,121
CC	799	47,8	0,37	0,041
IGCC	580	38,4	0,78	0,072
AMC	860	49,9	0,36	0,040

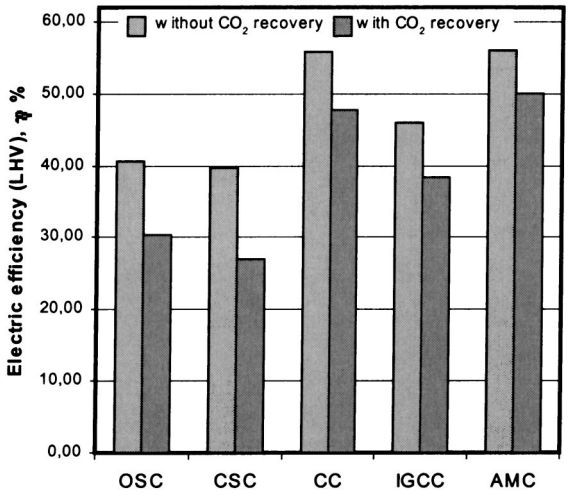

Fig. 7 The net electric efficiency

coal fuel. The CSC exhibits a substantial decrease in its performance because it produces a relevant quantity of carbon dioxide and thus needs a large amount of steam to regenerate the chemical solvent used. As the OSC is fed by a higher hydrogen fuel, its performance is slightly better than the CSC: The net work output decreases by about 26% and the efficiency is about ten percentage points lower.

For the latter three schemes, the penalties are less relevant: the CO_2 recovery reduces the net work output by 11 to 14% and efficiency between six to eight percentage points. In fact, without CO_2 recovery, they are characterized by higher power plant efficiency; so gas emissions are reduced and, when they are equipped with systems for CO_2 recovery, energetic requirements penalize their performance in a minor way because the specific CO_2 reduction is lower.

On the whole, the AMC stands out because it exhibits the lowest net work output decrease, the highest net efficiency and the lowest final specific CO_2 emission. This performance is possible because this scheme can be suitably integrated with CO_2 recovery systems, as explained above.

Finally, Figs. 7 and 8 show the penalty in the efficiency level and the corresponding reduction of the CO_2 in all the power plants, here analyzed, before and after the CO_2 recovery.

To complete the evaluation of these power plants a preliminary economic analysis has been carried out. Investment costs have been estimated following the indications and trends reported in

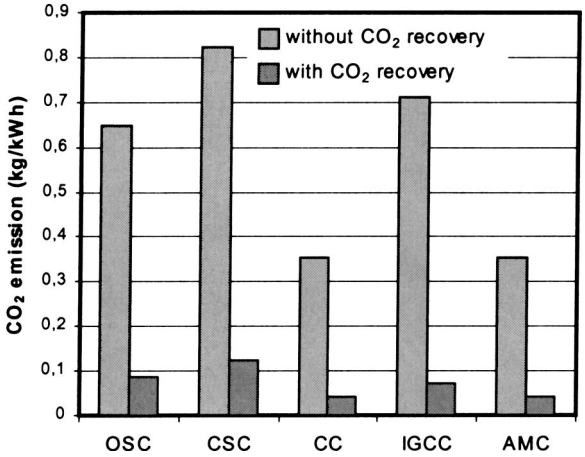

Fig. 8 The CO_2 specific emission rate

Table 3 Overview of the costs for the power plants with and without CO_2 recovery

	OSC	CSC	CC	IGCC	AMC
Capital costs ($/kW)					
power plant	1100	1250	600	1550	800
CO_2 removal plant	210	270	190	190	150
CO_2 liquefaction plant	60	70	30	40	50
Total capital costs	1370	1590	820	1780	1000
Annualized costs ($/kW·yr)					
capital charges power plant	129	147	70	182	94
capital charges CO_2 recovery plants	32	40	26	27	23
fuel feedstock	148	108	152	93	151
O&M costs power plant	40	45	22	56	29
O&M costs CO_2 recovery plants	10	12	8	8	7
Total annualized costs	359	352	278	366	304
Output					
Pw/Pwo	0,738	0,681	0,861	0,859	0,890
Electricity production costs (mills/kWh)					
reference plant	45,30	42,78	34,86	47,23	39,11
plant with CO_2-recovery	69,39	73,74	46,09	60,82	49,02

literature, [14,19]. These data have been used to evaluate the investment costs of the latter three power plants, which are of medium-large size.

More precisely, the IGCC investment cost had already been elaborated in previous papers by the authors mentioned, while the CC investment cost has been elaborated following those indications. Also the AMC investment cost has been elaborated in accordance with the same data, but with some hypotheses; in the AMC we have a reheat gas turbine and its cost is assumed to be 30% higher than the cost of a standard gas turbine because there are two other components: a second combustion chamber and a second expander. The ''steam cycle'' (i.e. a high pressure steam turbine and a simple HRSG at one pressure level and RH) has also been considered as a conventional bottoming steam cycle: in fact in this plant steam condensation from a gas/steam mixture is absolutely necessary, but involves plant lay out implications. Therefore the steam cycle in the AMC is simpler than the one in the CC, but the same investment costs have been taken in to consideration because of the presence of an unconventional component (the separator). Moreover, all component costs have been ulteriorly increased by 30% because all components can be seen as unconventional ones: in fact the AMC isn't technological reality as yet, as combined cycles are.

Regarding steam cycles, investment costs found in literature have been used because they are now a consolidated technological reality.

Total investment costs were then obtained by a 50-fold increase in the component costs; this percentage considers the following aliquots: the balance of the plant 12%, engineering costs 18%, contingencies 20%, respectively.

After defining investment costs, it is possible to estimate the cost of the electricity produced. In this cost, three aliquots have been envisaged:

- depreciation,
- fuel, and
- operation and maintenance.

For our calculations some assumptions have been made: a discount rate of 10% was taken and depreciation over 20 years to quantify capital charges of the power plants and the recovery systems. With regards to fuel, an assumed coal price of $ 42 per ton, oil price of $ 105 per ton and natural gas price of $ 0.12 per Nm^3 was used. These costs are meant to represent the average trends on the European market. The operation and maintenance (O&M) costs were set at a fixed percentage of the investment cost (exactly 3.6%). Finally, all the power plants analyzed were assumed to operate for 7000 hours per year. The ratio Pwo/Pw, in Table 3, represents the power output decrease when the power plants are equipped with CO_2 recovery plants: this value is important for evaluating electricity production costs when CO_2 recovery is considered.

Table 3 shows the results of the economic analysis, but it is necessary to remember that the absolute values do not inspire much confidence, considering the uncertainties of our analysis. It is important, however, to realize the significant comparisons between the power plants and to evaluate the increase in the cost of electricity, considering that all the systems respect the same economic assumptions.

Figure 9 shows the cost of kWh in each scheme, before and

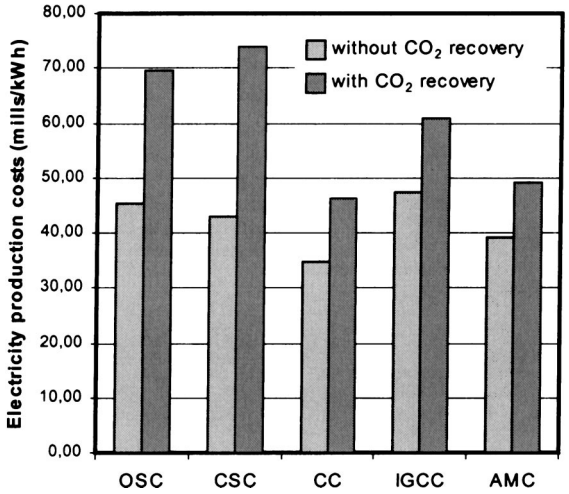

Fig. 9 Electricity production costs

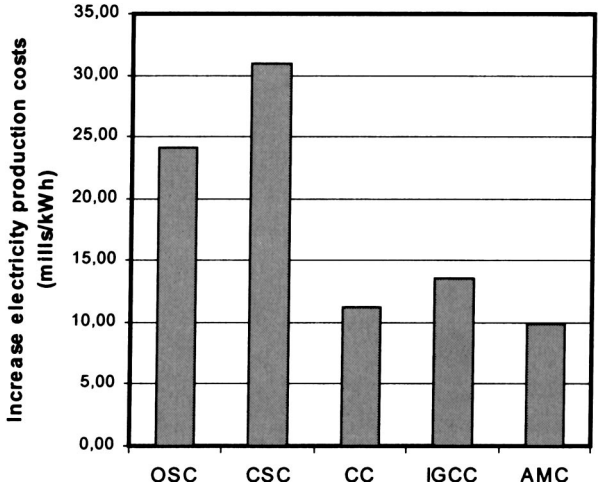

Fig. 10 The electricity production cost increase

after the carbon dioxide recovery; while Fig. 10 reports the increase in the electricity production costs.

Without the CO_2 recovery there is a fairly large difference in the cost of the electricity between the power plants here analyzed. Among the power plants, representative of consolidated technology, results show that the maximum cost, obtained in the OSC, is higher than the minimum cost, in the CC, by about 30%. The OSC shows the highest cost because it has a rather low net electric efficiency and a rather high total specific investment cost, and it was also seen that oil fuel is not the cheapest (2.4 $/GJ against 1.7$/GJ for coal). The CC, on the other hand, shows the lowest cost because it has a very high net electric efficiency, the lowest total specific investment cost, although natural gas is the most expensive fuel (3.3 $/GJ).

With the CO_2 recovery, there are major differences. In this case the maximum cost, in the CSC, is higher than the minimum cost, in the CC, by about 60%. The most penalized power plant is the CSC: not only has it a drastic decrease in its thermodynamical performance, but it must also abate a large amount of CO_2. The size and thus the costs of the recovery systems are higher than those of the other power plants. In Fig. 9 the CSC cost bar, after CO_2 recovery, stands out although this power plant does not have the highest cost of electricity without carbon dioxide recovery.

Finally, Fig. 10 shows the increase in kWh cost for all the power plants here analyzed; two different cases must be considered:

i. Power plants with low electric efficiency (CSC and OSC) increase their electricity cost by approximately 53 to about 72%.
ii. Power plants with high electric efficiency (CC, IGCC and AMC) increase their electricity cost less drastically: by approximately 25 to about 32%.

Thus, it is evident that the power plants based on gas turbines (CC, IGCC and AMC) attain an economic performance higher than that of the conventional steam power plants with respect to the CO_2 emission abatement.

Although our economic calculations contain many uncertainties, the AMC seems to be the best solution both in thermodynamical performance and in economic aspects. The good energetic integration between power plant and CO_2 recovery systems allows the lowest efficiency decrease and the lowest electricity cost increase. It is also important to point out that the AMC steam recirculation permits a reduction in the excess air used to limit the turbine inlet temperature and to enrich the exhaust gas by CO_2, thus enabling a stack flow rate much lower and thus recovery systems smaller and cheaper.

5 Conclusions

This paper has analyzed the thermodynamical performance and the economic aspects of five power generation schemes and compared the results in terms of energy efficiency, emission of CO_2 and electricity production cost. Among the power plants here analyzed, there is a new advanced mixed cycle (AMC), proposed by the authors: It has shown relevant performance also with respect to the CO_2 emission abatement and to the electricity production cost.

The main result is that the AMC stands out both thermodynamically and economically, when equipped with systems to abate carbon dioxide emissions; it is able to achieve very limited CO_2 emissions (0.04 kg/kWh), converting thermal power from fuel to electrical power at an efficiency level of about 50% and increasing its electricity production cost by about 25%.

With regard to the other power plants, it has been seen that, with a CO_2 emission reduction of about 90%, the efficiency penalty is variable: from 10 to 13 percentage points for the steam cycle power plants, about 8 points for the CC and the IGCC, and only six points for the AMC. The thermodynamical reason for this result is amply discussed in the paper.

Regarding economic aspects, although the calculations may contain many uncertainties, all the plants respect the same assumptions and hypotheses so the comparisons performed are significant. Results show that the increase of electricity production cost is variable: The steam power plants show the highest increase (72% and 53% when fed by coal and oil, respectively), while the power plants based on gas turbine units (CC, IGCC, and AMC) show a more homogeneous increase (from 25 to 32%).

These results confirm that power plants based on gas turbines have great potential with both high performance and low atmospheric impact.

Finally, we can conclude that all power plants here analyzed can be coupled to a chemical absorption system to reduce the specific CO_2 emissions drastically. The conventional steam cycle power plants are the most penalized, while the AMC shows the best thermodynamical and economic performance. The CC and IGCC are placed in an intermediate position. Thus even if the AMC is not a technological reality compared with the other conventional solutions (OSC, CSC and CC), its high performance makes this power plant, in our opinion, noteworthy when it is necessary to reduce CO_2 emissions with high conversion efficiency levels and low economic impact on the electricity production cost.

Nomenclature

r = recirculation ratio in combined cycle: mass fraction of the exhaust gas at the separator exit, recirculated to the gas turbine compressor inlet
T = temperature (°C)
W = specific work (kJ/kg)
β = pressure ratio
η = efficiency
%vol = molar fraction

Subscripts

HP = high pressure
MP = medium pressure
LP = low pressure
HPT = high pressure gas turbine
1,2 = referred to the first and the second cc

Acronyms

1L, 3L = one, three pressure level
AMC = advanced mixed cycle
ASU = air separation unit
C = compressor
CC = combined cycle
cc = combustion chamber

CSC = steam power plant fed by coal
HPT = high pressure turbine
HRSG = heat recovery steam generator
IGCC = integrated coal gasification combined cycle
LHV = fuel lower heating value
LP = liquefaction plant
LPT = low pressure turbine
OSC = steam power plant fed by oil
RH = reheater
RP = removal plant
SEP = separator
SH = superheater
ST = steam turbine
T_{IT} = turbine inlet temperature

Appendix

Numerical Assumptions. The results of the performed investigations have been attained by employing a proper numerical model and by numerical assumptions.

The numerical model has developed by the authors and it has been briefly explained in the paper. In this section we like to point out the main numerical assumptions for AMC and CC cycle calculations. They are listed in Table 4.

The supercritical steam conditions for the HRSG of AMC have been chosen according to the results achieved in previous works, [10–12]. The steam pressures for the HRSG of CC are virtually at optimal conditions for a three pressure level and reheat HRSG (exhaust gas temperature about 80°C).

Obviously the main numerical assumptions for the calculations regard the TIT and the polytropic efficiency of the gas turbines. In order to reduce calculation efforts we have assumed a TIT by ISO definition (i.e., the resulting temperature from mixing outlet combustion chamber gas flow rate and all cooling flow rates from compressor) and a uncooled expansion in the turbine with a reduced value of polytropic efficiency to take into account the losses related to the blade coolings. This is fully in agreement with other calculation models, [20], and the results are very close to those related to cooled stage calculations and with manufacturer's data. In particular, with reference to an advanced combined cycle (reheat, three pressure steam cycle) based on GE Frame 9FA, the model has provided results in full agreement with literature, [21], and GE data, [22], Regarding reheat gas turbines also (as GT26 of ABB) the comparison between ABB data, [22], and the results of the numerical model have confirmed the reliability of the above assumptions.

Table 4 Numerical assumptions

Gas Turbine Inlet Temperature TIT (ISO definition)	1200	°C
Compressor efficiency (polytropic)	89	%
High pressure gas turbine efficiency (polytropic)	86	%
Medium pressure mixed flow turbine efficiency (polytropic)	86	%
High pressure steam turbine efficiency (adiabatic)	87	%
Low pressure steam turbine efficiency (adiabatic)	85	%
Pump efficiency	80	%
Organic-mechanical losses of every single turbomachine	1	%
Combustor heat loss (referred to fuel heat input)	0.4	%
Generator electric-mechanical losses	1.5	%
Combustor pressure loss (air)	3	%
Combustor pressure loss (steam)	10	%
HRSG pressure loss (gas-side)	5	%
HRSG pressure loss (RH steam)	8	%
HRSG pressure loss (SH steam, water)	15	%
Pinch point in HRSG	10	°C
Approach point in HRSG	30	°C
Steam pressure (AMC)	300	bar
Steam temperature (AMC)	565	°C
Steam pressures (HP/MP/LP - CC)	140/20/5	bar
Steam temperature (SH/RH - CC)	540	°C
Condenser pressure (CC)	0.05	bar
Ambient air temperature	15	°C
LHV of fuel (natural gas)	50	MJ/kg

References

[1] Schütz, M., Daun, M., Weinspach, P. M., Krumbeck, M., and Hein, K. R. G., 1992, "Study on the CO_2 Recovery From an IGCC Plant," *Proceedings of the First International Conference on CO_2 Removal*, Amsterdam, Pergamon Press, New York.

[2] Allam, R. J., and Spilsbury, C. G., 1992 "A Study of the Extraction of CO_2 From the Fossil Fuel Gas of a 500 MW Pulverised Coal Fired Boiler," *Proceedings of the First Int. Conf. on CO_2 Removal*, Amsterdam, Pergamon Press, New York.

[3] Chiesa, P., and Consonni, S., 1998, "Shift Reactors and Physical Absorption for Low-CO_2 Emission IGCCs," International Gas Turbine & Aeroengine Congress & Exhibition, Stockholm.

[4] Gambini, M., Guizzi, G. L., and Vellini, M., 1999, "New High Efficiency Mixed Cycles With Air-Blown Combustion for CO_2 Emission Abatement," *Proceedings of the International Joint Power Generation Conference*, San Francisco, ASME, New York.

[5] Hendriks, C. A., Blok, K., and Turkenburg, W. C., 1989, "The Recovery of Carbon Dioxide From Power Plants," *Climate and Energy*, P. A. Okken, R. J. Swart, and S. Zwerver, eds., Kluwer, Dordrecht, The Netherlands.

[6] Yagi, K., Shibuya, H., and Sasaki, T., 1992, "Application of Chemical Absorption Process to CO_2 Recovery From Flue Gas Generated in Power Plants," *Proceedings of the First International Conference on CO_2 Removal*, Amsterdam, Pergamon Press, New York.

[7] Suda, T., Fujii, M., Yoshida, K., Iijima, M., Seto, T., and Mitsuoka, S., 1992, "Development of Flue Gas Carbon Dioxide Recovery Technology," *Proceedings of the First International Conference on CO_2 Removal*, Amsterdam, Pergamon Press, New York.

[8] Bolland, O., and Mathieu, P., 1997, "Comparison of Two CO_2 Removal Options in Combined Cycle Power Plants," *Proc. of FLOWERS'97*, Florence World Energy Research Symposium, Firenze, SGE Editoriali.

[9] Chiesa, P., and Lozza G., 1998, "CO_2 Emission Abatement in IGCC Power Plants by Semiclosed Cycles. Part A: With Oxygen-Blown Combustion," International Gas Turbine & Aeroengine Congress & Exhibition, Stockholm.

[10] Gambini, M., and Guizzi, G. L., 1997, "Parametric Analysis on a New Hybrid Power Plant Based on Internal Combustion Steam Cycle (GIST Cycle)," *Proc of Flowers'97*, Florence World Energy Research Symposium, Firenze, SGE Editoriali.

[11] Caputo, C., Gambini, M., and Guizzi, G. L., 1997, "Internal Combustion Steam Cycle (G.I.S.T. Cycle): Thermodynamical Feasibility and Plant Lay-Out Proposals," ASME Paper No. 97-AA-134.

[12] Caputo, C., Gambini, M., and Guizzi, G. L., 1997, "New Hybrid Power Plants Based on Internal Combustion Steam Cycles (GIST Cycles)," *Proc. of 9th National Conference "Tecnologie e Sistemi Energetici Complessi—Sergio Stecco,"* Milano, SGE Editoriali (in Italian).

[13] Gambini, M., Guizzi, G. L., and Vellini, M., 1997, "Calculation Model for Unconventional Components of GIST Cycles," *Proc. of 9th National Conference "Tecnologie e Sistemi Energetici Complessi,"* Milano, Italy, SGE Editoriali (in Italian).

[14] Chiesa, P., Consonni, S., and Lozza, G., 1998, "A Comparative Analysis of IGCCs With CO_2 Sequestration," 4th International Conference on Greenhouse Gas Control Technologies, Interlaken, Switzerland.

[15] Lozza, G., 1990, "Bottoming Steam Cycles for Combined Gas-Steam Power Plants: A Theoretical Estimation of Steam Turbine Performance and Cycle Analysis," ASME Cogen-Turbo, New Orleans, LA.

[16] Consonni, S., 1992, " Performance Prediction of Gas/Steam Cycles for Power Generation," Ph.D. thesis No. 1893-T, Mechanical and Aerospace Engineering Department, Princeton University, Princeton, NJ.

[17] Chiesa, P., Consonni, S., Lozza, G., and Macchi, E., 1993, "Predicting the Ultimate Performance of Advanced Power Cycles Based on Very High Temperature Gas Turbine Engines," ASME Paper 93-GT-384.

[18] Macchi, E., Consonni, S., Lozza, G., and Chiesa, P., 1995 "An Assessment of the Thermodynamic Performance of Mixed Gas-Steam Cycles: Part A—Intercooled and Steam Injected Cycles," ASME Journal of Engineering for Gas Turbine and Power, **117**.

[19] Chiesa, P., and Consonni, S., 1999, "Natural Gas Fired Combined Cycle With Low CO_2 Emissions," 44th ASME Gas Turbine and Aeroengine Congress, Indianapolis, IN.

[20] Hofstäder, A., Frutschi H. U., and Haselbacher H., 1998, "Effects of Steam Reheat in Advanced Steam Injected Gas Turbine Cycles," ASME Paper No. 98-GT-584.

[21] Lozza, G., 1993, "Steam Cycles for Large Size High Gas Temperature Combined Cycles," Proc 7th ASME Cogen-Turbo, Bournemuth, UK.

[22] Gas Turbine World, 1996, "Basic Specifications of Combined Cycles," GTW.

Thermodynamic Property Models for Moist Air and Combustion Gases

D. Bücker

R. Span

W. Wagner[1]

Lehrstuhl für Thermodynamik,
Ruhr-Universität Bochum,
D-44780 Bochum, Germany

A new model for the prediction of caloric properties of moist air and combustion gases has been developed. The model very accurately predicts ideal gas caloric properties of undissociated gas mixtures at temperatures from 200 K to 3300 K. In addition, a simple model has been developed to account for caloric effects of dissociation at temperatures up to 2000 K. As a part of the project, scientific equations for the ideal gas isobaric heat capacity of the individual combustion gas components have been established. Based on this reference, an assessment and comparison of the new model with the most common technical models have been carried out. Results of the simplified dissociation model are compared to the results of complex chemical equilibrium programs. To mark out the limits of the ideal gas hypothesis, some sample calculations are given, which compare results of the new ideal gas model to results from sophisticated real gas models.
[DOI: 10.1115/1.1520154]

1 Introduction

Nowadays, a number of different sets of equations is used to calculate the ideal gas caloric properties of combustion gases. Although some of these models, such as [1–3], are accepted standards in different industrial branches, their mutual consistency is rather poor. This fact leads to contradictory results and to conflicts especially in acceptance tests on the relevant machinery. As a result of these discrepancies a project was initiated in 1997 by the Verein Deutscher Ingenieure (VDI; Association of German Engineers) to evaluate the performance of the common models and to establish a standard which can be used for contractual commitments as well as for design and application procedures.

As a part of this project, so-called scientific equations were developed which represent the ideal gas isobaric heat capacity of the main components of combustion gases with the highest possible accuracy. The following substances are considered the main components of typical exhaust gases:

- nitrogen,
- oxygen,
- argon,
- neon,
- water,
- carbon dioxide,
- carbon monoxide, and
- sulfur dioxide.

Based on this scientific standard, the common technical models were evaluated with regard to accuracy, simplicity, computing time, and entirety concerning the considered components. Since it was found that none of the existing models meets all the requirements to a satisfactory degree, a new set of technical equations was developed based on values calculated with the new scientific equations. Furthermore, a simplified model was set up to account for the effects of dissociation on the caloric properties of the combustion gas. Although dissociation reactions considerably affect combustion gas properties at temperatures relevant in gas turbine processes, only two of the common models, [3,4], address this problem.

This paper gives details on the development of the scientific equations and on the new set of equations for technical use. An assessment of the common technical models is given on the basis of the scientific standard. A simplified dissociation model is introduced which enables a simple but still sufficiently accurate consideration of dissociation in typical gas turbine applications. To mark out the limits of the ideal gas hypothesis, some results of sample calculations are illustrated comparing values computed by the new model to results obtained from an accurate equation of state for dry air, [5], and a model for the prediction of thermodynamic properties of real gas mixtures, [6].

2 New Scientific Equations for the Ideal Gas Isobaric Heat Capacity of the Components

New scientific equations for the heat capacity of the components were developed to establish a reference for the assessment and comparison of the available technical models and to provide consistent sets of data for the development of new technical equations. These scientific equations have to meet several requirements:

- They should be developed independently from common technical models, based only on the most reliable data available for the ideal gas heat capacity of the considered pure fluids.
- The entire temperature range of interest should be covered, i.e., $200\ \mathrm{K} \leqslant T \leqslant 3300\ \mathrm{K}$.
- Even though the equations are basically empirical, their functional form should be based on results from statistical thermodynamics to allow for reliable inter and extrapolation.

Two methods are widely used to determine the ideal gas isobaric heat capacity. One method uses experimental speed of sound data extrapolated to the limit of zero density. Uncertainties arise mainly from the measurements themselves, the extrapolation of real fluid data to ideal gas values, and for some fluids from the effect of vibrational relaxation time on the heat capacity. Detailed information on the determination of caloric properties from acoustic measurements is given in [7]. However, the temperature range where such data are available is restricted to the temperature range which can be covered with accurate experimental setups. Thus, the most common method to determine the heat capacity of ideal gases uses theoretical models that depend on molecular constants measured by spectroscopy. These models generally consider contributions to the heat capacity from molecular translation, rotation,

[1]To whom correspondence should be addressed.

Contributed by the Power Division of THE AMERICAN SOCIETY OF MECHANICAL ENGINEERS for publication in the ASME JOURNAL OF ENGINEERING FOR GAS TURBINES AND POWER. Manuscript received by the Power Division Dec. 2000; final revision received by the ASME Headquarters May 2002. Associate Editor: D. Lou.

Table 1 Values of the substance specific parameters of the equations constituting the new scientific reference, Eq. (4)

Substance	N_{pol}	N	i	n_i	d_i	r_i
N_2	4	5	1	3.50000000×10^{0}	0	1 K
			2	3.06646900×10^{-6}	1	1 K
			3	4.70124000×10^{-9}	2	1 K
			4	$-3.98798400\times10^{-13}$	3	1 K
			5	1.01294100×10^{0}	-	3364.011 K
O_2	1	4	1	3.50159974×10^{0}	0	1 K
			2	1.02675113×10^{0}	-	2243.13655 K
			3	7.96461522×10^{-2}	-	6175.74152 K
			4	9.03195011×10^{-1}	-	12078.1664 K
Ar	1	1	1	2.50000000×10^{0}	0	1 K
Ne	1	1	1	2.50000000×10^{0}	0	1 K
H_2O	1	6	1	3.98693380×10^{0}	0	1 K
			2	9.48353379×10^{-1}	-	2251.45019 K
			3	3.82497101×10^{-1}	-	27115.4033 K
			4	1.87776616×10^{0}	-	5085.05635 K
			5	2.51990445×10^{-2}	-	230.778387 K
			6	7.27149861×10^{-1}	-	7786.57472 K
CO_2	1	6	1	3.50000000×10^{0}	0	1 K
			2	1.94443033×10^{0}	-	955.678512 K
			3	1.88980660×10^{-1}	-	1354.87878 K
			4	1.07579428×10^{0}	-	2123.33967 K
			5	8.99817300×10^{-1}	-	3709.45515 K
			6	2.22108660×10^{-1}	-	14758.0336 K
CO	1	3	1	3.50000000×10^{0}	0	1 K
			2	1.02749426×10^{0}	-	3084.18124 K
			3	8.77597600×10^{-2}	-	10644.3633 K
SO_2	2	5	1	4.00000132×10^{0}	0	1 K
			2	1.26016569×10^{-8}	2	1 K
			3	1.98295758×10^{0}	-	1823.44146 K
			4	5.23933554×10^{-2}	-	4670.09595 K
			5	1.03949573×10^{0}	-	753.61342 K

and vibration, and, where necessary, from excited electronic states. For more complex polyatomic molecules internal rotation has to be considered as well. In simple models, each mode has its own distinguished energy scale, denoted by a characteristic temperature. For higher accuracy, especially at high temperatures, contributions from mutual interactions between different modes have to be considered. See [8] for further information.

Assuming constant contributions from molecular transition and rotation and neglecting excited electronic states and interactions between different modes leads to the very simple model of rigid rotation and harmonic oscillation (RRHO). The only temperature-dependent contribution then is provided by the vibrational modes and the isobaric heat capacity reads

$$c_p^o = \frac{5}{2}R + c_{p,\mathrm{rot}}^o + R\sum_{i=1}^{N_{\mathrm{vib}}}\left(\frac{\theta_{\mathrm{vib},i}}{T}\right)^2 \frac{\exp(\theta_{\mathrm{vib},i}/T)}{[\exp(\theta_{\mathrm{vib},i}/T)-1]^2}. \quad (1)$$

The contribution from rotation is

$$c_{p,\mathrm{rot}}^o = R \quad (2)$$

for linear molecules and

$$c_{p,\mathrm{rot}}^o = \tfrac{3}{2}R \quad (3)$$

for nonlinear molecules. N_{vib} and $\theta_{\mathrm{vib},i}$ denote the number of vibrational modes and the characteristic temperature of the ith vibrational mode, respectively.

Equation (1) yields reasonably accurate values at moderate temperatures. For higher accuracy of the calculated values, especially at high temperatures, corrections to the RRHO model have to be applied that take into account the effects of centrifugal stretching, anharmonic vibration and mutual interactions between different modes, especially rotational-vibrational coupling. At very high temperatures, contributions of excited electronic states may also become profound and have to be considered. At very low temperatures the rotational modes may not be fully excited leading to temperature dependent contributions. Although the contributions of all these effects are relatively small, their calculation becomes very complex. However, numerous authors have published values for the ideal gas properties of fluids based on statistical mechanical models which consider all of the necessary corrections, see [9–17]. Thus, data of sufficient accuracy are available for all the components considered in this paper.

These data can be represented accurately using an equation of the general form

$$\frac{c_p^o}{R} = \sum_{i=1}^{N_{\mathrm{pol}}} n_i\left(\frac{T}{r_i}\right)^{d_i} + \sum_{i=N_{\mathrm{pol}}+1}^{N} n_i\left(\frac{r_i}{T}\right)^2 \frac{\exp(r_i/T)}{[\exp(r_i/T)-1]^2} \quad (4)$$

and fitting the empirical parameters n_i and r_i to the published data. In this way, numerically difficult terms which result from small corrections are avoided and still the empirical equation yields reasonable inter and extrapolations since its functional form corresponds basically to the theoretically expected one. The number of polynomial terms, N_{pol} and the number of Planck-Einstein type terms ($N-N_{\mathrm{pol}}$) may be varied to reach the desired accuracy. Accurate equations of state usually use a functional form according to Eq. (4) as a basis for the description of caloric properties (see, for instance, [5,15,18,19]).

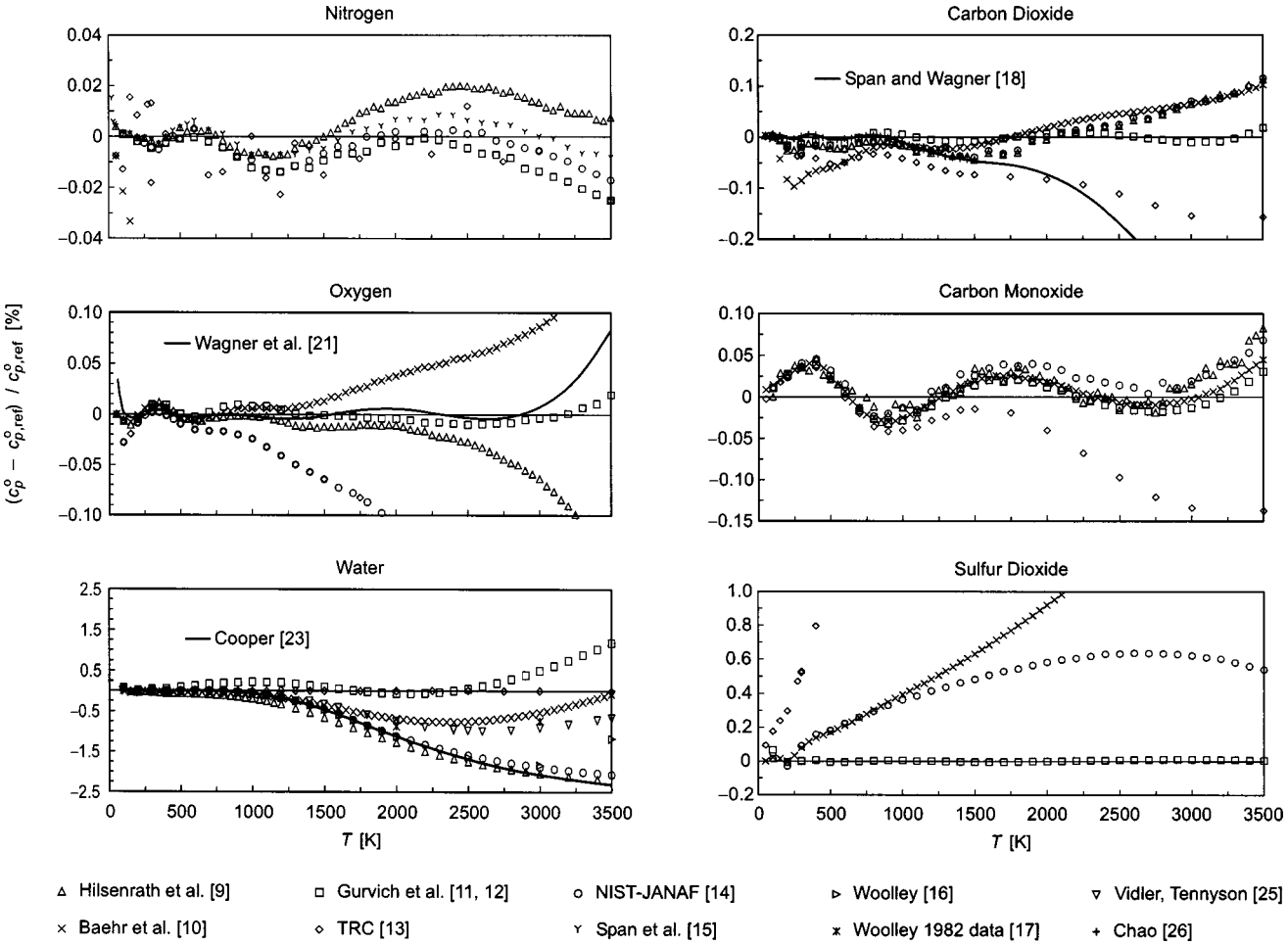

Fig. 1 Percentage deviations of different tabulated values c_p^o for the ideal gas isobaric heat capacity from values $c_{p,ref}^o$ calculated with Eq. (4) for the non-noble gas components

Prior to setting up new equations for the individual substances, a thorough review of the relevant literature was carried out. Appropriate equations using the functional form of Eq. (4) were included either without modification or—if the range of validity of the published formulations is insufficient—after refitting the parameters to data covering the required temperature range.

The general structure of all equations used to set up the new scientific reference corresponds to Eq. (4). The substance specific parameters N_{pol}, N, n_i, d_i, and r_i are given in Table 1. Figure 1 shows deviations between the data published in the literature and values calculated from the equations of the new scientific reference, Eq. (4). Characteristics of the equations for the individual substances are briefly outlined below.

Nitrogen. Span et al. [15] developed a reference quality equation of state for nitrogen using a functional form according to Eq. (4) to describe the ideal gas heat capacity. The parameters were fitted to data calculated by themselves at temperatures up to 5000 K. Their own data are represented within $\Delta c_p^o \leqslant \pm 0.01\%$. Figure 1 shows that the data by other authors agree well with these new results, usually within $\Delta c_p^o \leqslant \pm 0.02\%$. Only the values calculated by Baehr et al. [10] show large deviations from the results of the other authors as well as from values calculated with the correlation equation. Thus, the equation by Span et al. [15] can be used as reference for nitrogen without any modifications.

Oxygen. The International Union of Pure and Applied Chemistry (IUPAC) established a scientific reference equation of state for the thermodynamic properties of molecular oxygen in 1987, [20]. The equation for the ideal gas heat capacity has the functional form of Eq. (4) but it includes an additional term to represent contributions from excited electronic states at higher temperatures (see [21] for details). The range of validity is 30 K to 3000 K. The authors used data by Baehr et al. [10] to fit the parameters at temperatures from 30 K to 1100 K and data by Gurvich et al. [22] at temperatures from 100 K to 3000 K. To maintain a uniform functional structure of the scientific equations and to extend the range of validity a new equation was developed in this work. The parameters of the equation were fitted to the very data used for the IUPAC equation with the only exception that a more recent edition of the Gurvich data was used [11] and that the considered temperature range was extended to 3500 K. As illustrated in Fig. 1 the considered data are represented by Eq. (4) with deviations of $\Delta c_p^o \leqslant \pm 0.015\%$. Data from the current NIST-JANAF Tables, [14], and from the TRC Tables, [13]—both calculated with inferior methods—show greater deviations while the data by Hilsenrath et al. [9] remain within $\Delta c_p^o \leqslant \pm 0.015\%$ at temperatures up to 2000 K.

Water. An equation which uses the general functional form given in Eq. (4) was published by Cooper [23]. Even today it is still considered the scientific reference for the ideal gas heat capacity of water at moderate temperatures, [19]. Cooper used data by Woolley [16] at temperatures from 100 K to 2000 K to fit the parameters of his equation. However, Woolley later modified his statistical mechanical model (e.g., inclusion of centrifugal effects, modifications of rotational and vibrational cutoff effects). De-

Table 2 Estimated uncertainties of values of the ideal gas isobaric heat capacity calculated with the scientific equations, Eq. (4)

Substance	Temperature Range	Δc_p^o [%]
N_2	200–3300 K	±0.02
O_2	200–1500 K	±0.015
	1500–3300 K	±0.1
H_2O	200–1300 K	±0.25
	1300–1700 K	±0.5
	1700–3300 K	±1
CO_2	200–2000 K	±0.08
	2000–3300 K	±0.15
CO	200–2000 K	±0.05
	2000–3300 K	±0.15
SO_2	200–1000 K	±0.4
	1000–3300 K	±0.7

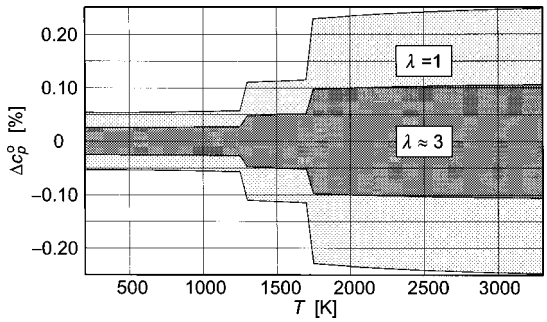

Fig. 2 Expected uncertainties of ideal gas isobaric heat capacities of a typical combustion gas calculated with the new scientific reference, Eq. (4), for the stoichiometric case (λ=1) and for an air equivalence ratio of λ≈3; effects of dissociation are not considered

pending on the kind of modification, Woolley [17] published two different c_p^o data sets called "1982 version" and "1984 version." The Thermodynamic Research Center (TRC) published additional interim values based on the 1984 series of Woolley's data, [13]. Therefore, the parameters of the equation were refitted using the TRC data at temperatures from 100 K to 3500 K. Figure 1 shows that deviations between values calculated with the refitted equation and the TRC data remain within $\Delta c_p^o \leqslant \pm 0.05\%$. Deviations of data by Gurvich et al. [11] and Baehr et al. [10] from values calculated with the new equation remain within $\Delta c_p^o \leqslant \pm 0.25\%$ at temperatures below 1300 K and within $\Delta c_p^o \leqslant \pm 1\%$ at higher temperatures. The 1980 Woolley data, [16], and the data by Hilsenrath et al. [9], however, show considerably higher deviations from values calculated with the new equation. The data from the current NIST-JANAF tables, [14], are based on the older Woolley data, [16], and on data by Friedmann and Haar [24]. More recently, new data based on a calculation of the partition function of water have been published, [25]. These data were not available when the equations presented in this work were established. They are also shown in Fig. 1.

Carbon Dioxide. The current reference equation of state for carbon dioxide, [18], was developed using data by Chao [26] for the ideal gas isobaric heat capacity. These data are considered as the most reliable data available today but they only cover temperatures up to 1500 K. To extend the temperature range, the equation for the ideal gas isobaric heat capacity introduced in [18] was refitted additionally using data by Gurvich et al. [12]. At temperatures around 900 K the considered data sets agree with each other well while the deviations increase at higher temperatures. Thus, the Chao data were considered only at temperatures up to 1000 K while the Gurvich data were used only at temperatures above 900 K. Both data sets are represented by the refitted equation with maximum deviations of $\Delta c_p^o \leqslant \pm 0.05\%$, see Fig. 1. Data by other authors agree within $\Delta c_p^o \leqslant \pm 0.15\%$ over the entire temperature range.

Argon/Neon. Monoatomic molecules do not have vibrational or rotational contributions to their internal energy. Besides this, contributions from excited electronic states become relevant only at temperatures far beyond 3500 K for argon and neon. Thus, the equation for the ideal gas isobaric heat capacity for both substances reads

$$c_p^o = \tfrac{5}{2} R. \tag{5}$$

Carbon Monoxide. For carbon monoxide, a new equation for the ideal gas heat capacity had to be developed. The parameters were fitted to data published by Baehr et al. [10] at temperatures from 70 K to 500 K and to data by Gurvich et al. [12] at temperatures from 100 K to 3500 K. The deviations between the considered data and values calculated with the new equation remain within $\Delta c_p^o \leqslant \pm 0.05\%$, see Fig. 1. Data by other authors agree with the calculated values within $\Delta c_p^o \leqslant \pm 0.05\%$ at temperatures up to 2000 K and within $\Delta c_p^o \leqslant \pm 0.15\%$ at higher temperatures.

Sulfur Dioxide. The new equation for sulfur dioxide was fitted to data by Gurvich et al. [11] at temperatures from 200 K to 6000 K. Data by Baehr et al. [10] were additionally used at very low temperatures, namely from 20 K to 200 K. Values calculated with the resulting equation deviate from the data used in the fit by $\Delta c_p^o \leqslant \pm 0.035\%$, see Fig. 1. Data by Baehr et al. [10] at temperatures up to 1500 K and the values from the NIST-JANAF tables, [14], deviate from the new results by $\Delta c_p^o \leqslant \pm 0.7\%$. Data from the TRC tables, [13], however, show significantly higher deviations from values calculated with the new equation.

Uncertainties. The estimated uncertainties of values calculated with the scientific equations are given in Table 2 for the individual substances. For any given mixture, the uncertainty of calculated properties can be estimated using the law of error propagation. Due to the rather high uncertaintiy of the isobaric heat capacity of water, the uncertainty of calculated mixture properties depends strongly on the concentration of this component. Therefore, the highest uncertainties are expected for gases resulting from stoichiometric combustion. Figure 2 shows estimated uncertainties of calculated isobaric heat capacities of a typical combustion gas for the stoichiometric case ($\lambda = 1$) and for an air equivalence ratio (air number) of $\lambda \approx 3$.

3 Commonly Used Technical Models

Some of the technical models discussed in this paragraph are accepted standards in different industrial branches. The intention here is not to give a complete review of the existing technical models but rather to point out advantages and shortcomings of some of the most commonly used models.

The ANSI/ASME Performance Test Codes 4.4, [1], are widely used in the design of gas turbine cycles. Equations consisting of up to five terms are given for the enthalpy of the typical combustion gas components. No explicit information is given on the range of validity, but comparisons to values calculated with the scientific equations introduced in Section 2 and by other technical models suggest that the functions have been fitted to data in a temperature range from approximately 300 K to 1350 K. The consistency of the equations introduced by the performance test codes to other technical models and to the scientific equations described in Section 2 is poor with maximum deviations of more than $\Delta c_p^o = \pm 0.5\%$ for typical combustion gases (see Fig. 3) and more than $\Delta c_p^o = \pm 1\%$ for single components. Outside the very restricted fitting range the observed deviations become even larger. At temperatures above 1500 K deviations of several per-

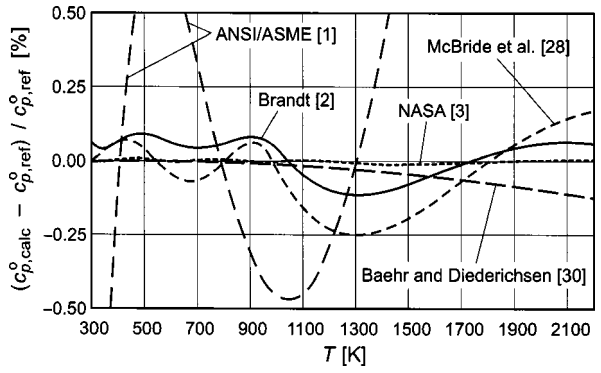

Fig. 3 Percentage deviations of values for the ideal gas isobaric heat capacity of a typical combustion gas ($\lambda \approx 3$) calculated by commonly used technical models from values calculated with the new scientific reference, Eq. (4)

cent are observed. Despite these severe deficiencies the ANSI/ASME Performance Test Codes 4.4 are still used as a standard by many companies in the gas turbine industry.

Thermodynamic properties of moist air and combustion gases to be used in gas turbine calculations in the aerospace industry are outlined in the SAE Aerospace Standard AS681, [27]. This guideline refers to the current NIST-JANAF tables, [14]. In practice, since these tabulated data are not suitable for computer-based applications, thermodynamic properties are calculated with the Chemical Equilibrium Program with Applications (CEA, formerly Chemical Equilibrium Program, CEP) provided by the NASA, [3]. CEA enables the calculation of the chemical equilibrium composition of multicomponent ideal gas systems by means of iterative algorithms. Thermodynamic functions of several hundreds of species are included in the program. The functions describing the isobaric heat capacity of the components consist of seven terms each. The range of validity of the equations is split into the three intervals $200\ \mathrm{K} \leqslant T \leqslant 1000\ \mathrm{K}$, $1000\ \mathrm{K} \leqslant T \leqslant 6000\ \mathrm{K}$, and $6000\ \mathrm{K} \leqslant T \leqslant 20000\ \mathrm{K}$. Each interval requires a different set of coefficients for every component.

The agreement between caloric properties of undissociated combustion gases calculated with CEA and with the reference equations presented in Section 2 is very good with maximum deviations of $\Delta c_p^o \leqslant \pm 0.05\%$. Among the existing technical models, CEA is the only one that describes the caloric properties of combustion gases with satisfactory accuracy over the entire temperature range. However, the splitting of the range of validity at 1000 K unduly complicates calculations and the use of iterative algorithms to predict properties of dissociated combustion gases distinctly increases computing time (see Section 5). Furthermore, the very general objective and the large scope of possible applications of the program obstruct its use as an easily manageable standard for industrial practice.

Until 1994, CEA used fourth-order polynomials to calculate isobaric heat capacities of the individual components, see for instance, [28]. Naturally, the agreement between the fourth-order polynomials and the new scientific equations is not as good as it is for the recent seven-term functions. Since the older polynomial functions are still commonly used today they are included in Fig. 3.

The German Fachverband Dampfkessel- Behälter- und Rohrleitungsbau e.V. (Association of Steam Boiler, Pressure Vessel and Piping Manufacturers) recommends a model introduced by Brandt [2,4] to calculate combustion processes. This model refers to a 1963 version of the NASA polynomials, [29], for the calculation of caloric properties. The accuracy of these polynomials is comparable to the one of the functions used until 1994. An introduction to the calculation of properties of a dissociated combustion gas by means of iterative algorithms is included in the second volume, [4]. A common feature of all mentioned NASA formulations, [3,28,29], is that different functions are used for temperatures below and above 1000 K.

Another set of equations which is widely used in industry was published by Baehr and Diederichsen [30]. The equations for the isobaric heat capacity of the components consist of twelve terms. Their parameters were fitted to data which are based on theoretical models and which were taken from Baehr et al. [10] for the most part. In the high temperature range above 1500 K, these data deviate systematically from data published by other authors. Selover and Sychev [31] assumed deficiencies in the underlying models leading to systematic errors increasing with temperature. At lower temperatures, however, the equations by Baehr and Diederichsen [30] are very consistent to the new scientific standard.

Aside from these models, a number of other formulations is used to calculate caloric properties of combustion gases. A complete discussion would go beyond the scope of this paper. However, either with respect to their range of validity, their accuracy, or the entirety of the set of considered components, the other investigated models are inferior to the ones discussed above.

4 A New Set of Equations for Technical Use

To overcome the above mentioned shortcomings of the available models, a new set of simple equations for the isobaric heat capacity of the components of combustion gases has been developed. These equations are the core of the new model for technical applications. The aim was to develop a set of simple empirical functions which cover the whole temperature range from 200 K to 3300 K with a single set of parameters for each component. The uncertainty of these technical equations should be of the same order of magnitude as the one of the scientific standard.

In a first step, consistent data sets for the ideal gas heat capacity were calculated for all components with the equations presented in Section 2. To avoid undetected oscillations of the numerically very instable equations a narrow grid of calculated data was used (about 160 data points for each substance). The general form of the new technical equations for the isobaric heat capacity of the components reads

$$c^o_{p,k} = \sum_{i=1}^{10} a_{k,i} \left(\frac{T}{T_0} \right)^{b_i}, \tag{6}$$

with index k denoting the component and $T_0 = 273.15$ K. The exponents b_i were established using a simplified version of the simultaneous optimization algorithm by Span et al. [32]. Their values are not substance specific and are given in Table 3. The substance specific coefficients $a_{k,i}$ were determined in a linear fit and are given in Table 4. Integrating Eq. (6) with respect to temperature yields the enthalpy of the components

$$h^o_k = a_{k,\mathrm{I}} + \sum_{i=1}^{10} a_{k,i} \frac{T_0}{b_i + 1} \left(\frac{T}{T_0} \right)^{b_i + 1}. \tag{7}$$

Table 3 Values of the exponents b_i of the new technical equations, Eqs. (6), (7), and (9)

i	b_i
1	0.00
2	−1.50
3	−1.25
4	−0.75
5	−0.50
6	−0.25
7	0.25
8	0.50
9	0.75
10	1.00

Table 4 Values of the substance specific coefficients $a_{k,i}$ [J mol^{-1} K^{-1}] of the new technical equations, Eqs. (6), (7), (9)

i	Nitrogen	Oxygen	Argon	Neon
I	4.305300363×10^{8}	5.295253592×10^{7}	-5.677745067×10^{3}	-5.677745067×10^{3}
II	-4.085709350×10^{6}	-7.353805669×10^{5}		
1	2.475830346×10^{6}	6.408242565×10^{5}	2.078618000×10^{1}	2.078618000×10^{1}
2	-2.815239891×10^{4}	-1.599937045×10^{3}		
3	1.116401165×10^{5}	9.984801256×10^{3}		
4	-8.147644187×10^{5}	-1.280873444×10^{5}		
5	2.185120405×10^{6}	4.186599156×10^{5}		
6	-2.978031305×10^{6}	-6.720142804×10^{5}		
7	-1.308008001×10^{6}	-3.799977202×10^{5}		
8	4.305948510×10^{5}	1.378691801×10^{5}		
9	-8.082302563×10^{4}	-2.806954185×10^{4}		
10	6.622545214×10^{3}	2.459943097×10^{3}		
i	Water	Carbon Dioxide	Carbon Monoxide	Sulfur Dioxide
I	-7.574888563×10^{8}	2.042361458×10^{8}	4.306836224×10^{8}	-3.845730250×10^{8}
II	7.373724814×10^{6}	-1.912121053×10^{6}	-4.203685809×10^{6}	3.543224735×10^{6}
1	-4.747782033×10^{6}	1.103695150×10^{6}	2.670755728×10^{6}	-2.076653674×10^{6}
2	4.799919289×10^{4}	-1.365096910×10^{4}	-2.715629936×10^{4}	2.589571253×10^{4}
3	-1.931588954×10^{5}	5.357704944×10^{4}	1.096509012×10^{5}	-1.012523438×10^{5}
4	1.460728340×10^{6}	-3.816063864×10^{5}	-8.303525865×10^{5}	7.161863952×10^{5}
5	-4.000075762×10^{6}	1.008950325×10^{6}	2.269213594×10^{6}	-1.889754780×10^{6}
6	5.576209858×10^{6}	-1.352938737×10^{6}	-3.151865706×10^{6}	2.535020356×10^{6}
7	2.570488297×10^{6}	-5.701809626×10^{5}	-1.438126165×10^{6}	1.082842148×10^{6}
8	-8.670521019×10^{5}	1.828513133×10^{5}	4.824833432×10^{5}	-3.524395911×10^{5}
9	1.666429390×10^{5}	-3.329618224×10^{4}	-9.227524508×10^{4}	6.552035769×10^{4}
10	-1.396634620×10^{4}	2.635366727×10^{3}	7.701550175×10^{3}	-5.325634796×10^{3}

The constants of integration, $a_{k,\mathrm{I}}$, were chosen to set h_k^o equal to zero at $T=T_0=273.15$ K.

The entropy is calculated as

$$s^o=\int\frac{c_p^o}{T}\mathrm{d}T-\int\left(\frac{\partial v^o}{\partial T}\right)_p\mathrm{d}p_T. \tag{8}$$

Carrying out this integration yields

$$s_k^o=a_{k,\mathrm{II}}-R_m\ln\left(\frac{p}{p_0}\right)+a_{k,1}\ln\left(\frac{T}{T_0}\right)+\sum_{i=2}^{10}\frac{a_{k,i}}{b_i}\left(\frac{T}{T_0}\right)^{b_i}. \tag{9}$$

Here, the constants of integration, $a_{k,II}$, were chosen to set s_k^o equal to zero at $T=T_0=273.15$ K and $p=p_0=0.101325$ MPa.

Caloric properties of any given mixture of the components can be calculated either by summation of the according properties of the components

$$c_{p,\mathrm{mix}}^o=\sum_{k=1}^{8}x_k c_{p,k}^o, \tag{10}$$

$$h_{\mathrm{mix}}^o=\sum_{k=1}^{8}x_k h_k^o, \tag{11}$$

$$s_{\mathrm{mix}}^o=\sum_{k=1}^{8}x_k s_k^o+\Delta^{\mathrm{mix}}s^o, \tag{12}$$

with the entropy of mixing

$$\Delta^{\mathrm{mix}}s^o=-R_m\sum_{k=1}^{8}x_k\ln(x_k), \tag{13}$$

or by calculating the coefficients for the mixture according to

$$a_{\mathrm{mix},i}=\sum_{k=1}^{8}x_k a_{k,i}, \quad i=\mathrm{I,II},1,2,\ldots,10 \tag{14}$$

and then directly calculating the required property of the mixture

$$c_{p,\mathrm{mix}}^o=\sum_{i=1}^{10}a_{\mathrm{mix},i}\left(\frac{T}{T_0}\right)^{b_i}, \tag{15}$$

$$h_{\mathrm{mix}}^o=a_{\mathrm{mix,I}}+\sum_{i=1}^{10}a_{\mathrm{mix},i}\frac{T_0}{b_i+1}\left(\frac{T}{T_0}\right)^{b_i+1}, \tag{16}$$

$$s_{\mathrm{mix}}^o=a_{\mathrm{mix,II}}-R_m\ln\left(\frac{p}{p_0}\right)+\Delta^{\mathrm{mix}}s^o+a_{\mathrm{mix},1}\ln\left(\frac{T}{T_0}\right)+\sum_{i=2}^{10}\frac{a_{\mathrm{mix},i}}{b_i}\left(\frac{T}{T_0}\right)^{b_i}. \tag{17}$$

Equations (14)–(17) are particularly convenient if properties of a mixture with constant composition have to be calculated at various temperatures and pressures.

For the considered non noble gas components, Fig. 4 shows

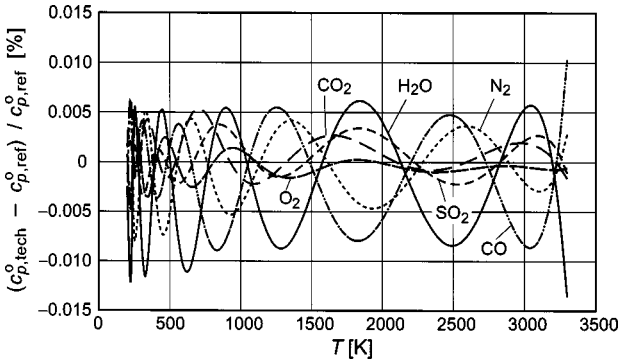

Fig. 4 Percentage deviations of values for the ideal gas isobaric heat capacity calculated with the technical equations, Eq. (6), from values calculated with the scientific reference, Eq. (4)

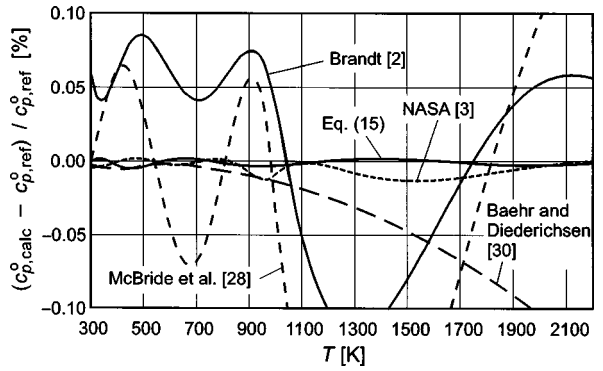

Fig. 5 Percentage deviations of values for the ideal gas heat capacity calculated with the new technical equations, Eq. (15), and some commonly used technical models from values calculated with the new scientific reference, Eq. (4)

deviations between values of the ideal gas isobaric heat capacity calculated with the technical equations, Eq. (6), and values calculated with the scientific reference, Eq. (4). For all components the observed deviations remain within $\Delta c_p^o \leqslant \pm 0.015\%$ in the temperature range $200\ \mathrm{K} \leqslant T \leqslant 3300\ \mathrm{K}$. For a typical combustion gas Fig. 5 shows deviations between values for the isobaric heat capacity calculated with different technical models and values calculated with the scientific standard introduced in Section 2. Only the latest version of the NASA formulations, [3], represents values calculated with the scientific standard with an accuracy comparable to the one of Eq. (15).

5 A Simplified Model of Dissociation

The equations for the caloric properties of combustion gas mixtures given in Section 4 do not account for effects of dissociation. Depending on the desired level of accuracy, these effects become relevant at temperatures above about 1200 K. Figure 6 illustrates the increase of the effective isobaric heat capacity due to dissociation for a typical flue gas resulting from the combustion of a common natural gas with an air equivalence ratio of $\lambda \approx 3$.

To correctly account for the caloric effects of dissociation, the chemical reaction equilibrium of the gas mixture has to be calculated. This requires solving of a system of nonlinear equations and thus the use of iterative algorithms. However, for a good approximation of the caloric effects it is not necessary to know the exact equilibrium composition of the dissociated gas, especially since

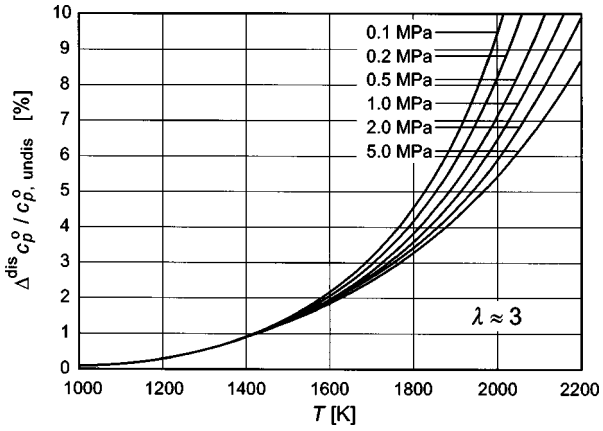

Fig. 6 Increase of the effective isobaric heat capacity due to dissociation for a typical combustion gas resulting from the combustion of a common natural gas with an air equivalence ratio of $\lambda \approx 3$

the degree of dissociation is very small for the systems and temperatures of interest. Thus, a simplified dissociation model has been developed which avoids iterative algorithms and which enables straightforward calculation of the required properties using only few additional equations.

The first simplification is a reduction of the number of considered species and stoichiometric equations. For temperatures up to 2000 K, the caloric effect of dissociation is dominated by the formation of only a few species. Without substantial loss of accuracy, the system can be described by the following stoichiometric equations:

$$\mathrm{CO_2} \rightleftarrows \mathrm{CO} + \tfrac{1}{2}\mathrm{O_2}, \tag{18}$$

$$\mathrm{H_2O} \rightleftarrows \mathrm{H_2} + \tfrac{1}{2}\mathrm{O_2}, \tag{19}$$

$$\tfrac{1}{2}\mathrm{H_2O} + \tfrac{1}{4}\mathrm{O_2} \rightleftarrows \mathrm{OH}, \tag{20}$$

$$\tfrac{1}{2}\mathrm{H_2} \rightleftarrows \mathrm{H}, \tag{21}$$

$$\tfrac{1}{2}\mathrm{O_2} \rightleftarrows \mathrm{O}, \tag{22}$$

$$\tfrac{1}{2}\mathrm{N_2} + \tfrac{1}{2}\mathrm{O_2} \rightleftarrows \mathrm{NO}. \tag{23}$$

Introducing equilibrium constants to describe the chemical equilibrium yields

$$x^*_{\mathrm{CO}} = k_1 \frac{x^*_{\mathrm{CO_2}}}{\sqrt{x^*_{\mathrm{O_2}}}} \left(\frac{p}{p_0}\right)^{-0.5}, \tag{24}$$

$$x^*_{\mathrm{H2}} = k_2 \frac{x^*_{\mathrm{H_2O}}}{\sqrt{x^*_{\mathrm{O_2}}}} \left(\frac{p}{p_0}\right)^{-0.5}, \tag{25}$$

$$x^*_{\mathrm{OH}} = k_3 \sqrt{x^*_{\mathrm{H_2O}}}\ \sqrt[4]{x^*_{\mathrm{O_2}}} \left(\frac{p}{p_0}\right)^{-0.25}, \tag{26}$$

$$x^*_{\mathrm{H}} = k_4 \sqrt{x^*_{\mathrm{H_2}}} \left(\frac{p}{p_0}\right)^{-0.5}, \tag{27}$$

$$x^*_{\mathrm{O}} = k_5 \sqrt{x^*_{\mathrm{O_2}}} \left(\frac{p}{p_0}\right)^{-0.5}, \tag{28}$$

$$x^*_{\mathrm{NO}} = k_6 \sqrt{x^*_{\mathrm{N_2}}} \sqrt{x^*_{\mathrm{O_2}}}, \tag{29}$$

where x^* denotes the concentration of a component of the dissociated combustion gas. The equilibrium constants k_j may be taken from literature. In this work, empirical functions were established for the k_j which read

$$k_j = A_j \exp(B_j / T). \tag{30}$$

The parameters of Eq. (30) were fitted to results calculated with CEA, [3]. The resulting values of A_j and B_j are given in Table 5.

The second simplification has more substantial implications. In the simplified model, the species are strictly divided into educts which make up the composition of the undissociated gas and products which are formed in the process of dissociation. CO is considered as a product of dissociation. It is assumed that the change in mole number of the educts due to dissociation is negligible, hence

$$x^*_{\mathrm{educt}} \approx x_{\mathrm{educt}}. \tag{31}$$

To avoid iterative algorithms, new variables U_j, called ''reaction numbers'' are introduced to substitute for the actual concentrations of the species resulting from dissociation. With Eq. (31) the Eqs. (24)–(29) can be rewritten using the concentrations of the educts in the undissociated combustion gas

Table 5 Values of the parameters of the correlation functions for the equilibrium constants, Eq. (30), and for the characteristic energetic contributions, Eq. (41)

j	Formation of	A_j [–]	B_j [K]	C_j [J mol^{-1} K^{-1}]	D_j [J mol^{-1}]	E_j [J K mol^{-1}]
1	CO	20413.2	−33086.5	−19.5	-1.15×10^5	9.483×10^9
2	H_2	1075.5	−30283.3	−65.2	3.03×10^5	7.277×10^9
3	OH	165.95	−19526.8	−18.7	5.72×10^4	3.136×10^9
4	H	1491.75	−27488.0	−3.60	3.93×10^5	5.826×10^9
5	O	3235.34	−30807.8	−21.8	1.50×10^5	7.659×10^9
6	NO	4.55420	−10973.6	−5.60	1.62×10^4	9.940×10^8

$$U_1=A_1\frac{x_{CO_2}}{\sqrt{x_{O_2}}}\left(\frac{p}{p_0}\right)^{-0.5}\exp(B_1/T), \tag{32}$$

$$U_2=A_2\frac{x_{H_2O}}{\sqrt{x_{O_2}}}\left(\frac{p}{p_0}\right)^{-0.5}\exp(B_2/T), \tag{33}$$

$$U_3=A_3\sqrt{x_{H_2O}}\sqrt[4]{x_{O_2}}\left(\frac{p}{p_0}\right)^{-0.25}\exp(B_3/T), \tag{34}$$

$$U_4=A_4\sqrt{U_2}\left(\frac{p}{p_0}\right)^{-0.5}\exp(B_4/T), \tag{35}$$

$$U_5=A_5\sqrt{x_{O_2}}\left(\frac{p}{p_0}\right)^{-0.5}\exp(B_5/T), \tag{36}$$

$$U_6=A_6\sqrt{x_{N_2}}\sqrt{x_{O_2}}\exp(B_6/T). \tag{37}$$

Equations (32)–(37) are independent and can be evaluated directly. The change of enthalpy in the system which is caused by dissociation can be calculated from the contributions of all considered reactions. When using the reaction extent numbers according to Eqs. (32)–(37) the total change in enthalpy due to dissociation becomes

$$\Delta^{dis}h^o\approx\sum_{j=1}^{6}U_j(\Delta_j^{dis}h^o)_T \tag{38}$$

with

$$(\Delta_j^{dis}h^o)_T=\sum_{n=1}^{N_{spec,j}}\nu_{nj}\left[\int_{T_0}^{T}c_{p,nj}^o dT+\Delta_0^f h_{nj}\right]. \tag{39}$$

Index nj denotes the nth species in the jth stoichiometric equation, see Eqs. (18)–(23), and $N_{spec,j}$ is the total number of species in that equation. Note that the stoichiometric coefficients, ν_{nj}, have to be considered with a positive sign for the products and with a negative sign for the educts. $\Delta_0^f h_{nj}$ is the enthalpy of formation of species nj at the standard temperature T_0. Differentiation of Eq. (39) with respect to temperature yields "characteristic contributions," V_j, for the change in isobaric heat capacity due to dissociation for each considered reaction

$$V_j=\frac{d}{dT}(\Delta_j^{dis}h^0)_T=\frac{d}{dT}\sum_{i=1}^{N_{spec}}\nu_i\left[\int_{T_0}^{T}c_{p,i}^o dT+\Delta_0^f h_i\right]. \tag{40}$$

Values for these characteristic contributions were calculated at temperatures ranging from 1000 K to 2500 K using CEA, [3], to calculate the heat capacities of the products and the enthalpies of formation. Empirical functions

$$V_j=C_j+\frac{D_j}{T}+\frac{E_j}{T^2} \tag{41}$$

were fitted to these values in a linear least-squares fit. Values for the parameters C_j, D_j, and E_j are given in Table 5.

The reaction numbers U_j were introduced as substitutes for the concentrations of the dissociation products $x^*_{product}$. Neglecting the consumption of the educts—see Eq. (31)—leads to

$$\sum x^*=\sum_{educts}x^*_{educt}+\sum_{products}x^*_{product}$$

$$\approx\sum_{educts}x_{educt}+\sum_{j=1}^{6}U_j=1+\sum_{j=1}^{6}U_j>1. \tag{42}$$

I.e., the determined reaction numbers are too high and the effect of dissociation is slightly overestimated. To minimize this error, a "total reaction number," U_{tot}, is introduced

$$U_{tot}=1+\sum_{j=1}^{6}U_j \tag{43}$$

and the caloric effect due to the considered dissociation reactions is divided by this number. The total effect of dissociation on the isobaric heat capacity can finally be calculated as

$$\Delta^{dis}c_p^o=\frac{1}{U_{tot}}\sum_{j=1}^{6}U_jV_j. \tag{44}$$

Integration of Eq. (44) yields the contribution of dissociation to enthalpy. The functional structure of the resulting integral is quite complex, but most of the terms result only in very small contributions to the numerical result. Therefore, the formally correct integral can be replaced by the simple approximation

$$\Delta^{dis}h^o=-\frac{T^2}{U_{tot}}\sum_{j=1}^{6}\frac{U_jV_j}{B_j}. \tag{45}$$

Compared to results from the correct integration, the relative error of $\Delta^{dis}h^o$ calculated according to Eq. (45) is less than ±1% for all tested combustion gas compositions. The contribution of dissociation to the entropy of the gas is calculated as

$$\Delta^{dis}s^o=\frac{\Delta^{dis}h^o}{T}=-\frac{T}{U_{tot}}\sum_{j=1}^{6}\frac{U_jV_j}{B_j}. \tag{46}$$

To obtain the caloric properties of the dissociated gas, the contributions of dissociation can simply be added to the corresponding properties of the undissociated gas as calculated with Eqs. (15)–(17):

$$c_{p,dis}^o=c_{p,mix}^o+\Delta^{dis}c_p^o, \tag{47}$$

$$h_{dis}^o=h_{mix}^o+\Delta^{dis}h^o, \tag{48}$$

$$s_{dis}^o=s_{mix}^o+\Delta^{dis}s^o. \tag{49}$$

The simplified dissociation model given by Eqs. (32)–(37), (41), (43)–(49) provides a simple but effective way to calculate caloric properties of dissociated combustion gases. Figure 7 shows deviations between isobaric heat capacities calculated with this simplified model and values calculated with a sophisticated

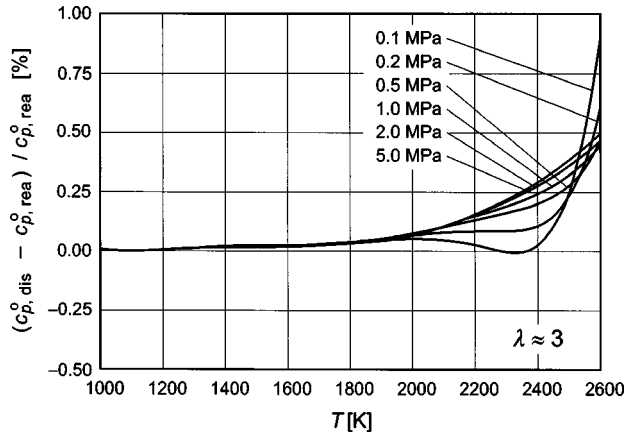

Fig. 7 Deviations of isobaric heat capacities $c^o_{p,\mathrm{dis}}$ calculated with the new simplified dissociation model, Eq. (47), from values $c^o_{p,\mathrm{rea}}$ calculated with an iterative chemical equilibrium algorithm, [3], for a typical combustion gas resulting from the combustion of a common natural gas with an air equivalence ratio of $\lambda \approx 3$

iterative algorithm, [3], for a typical flue gas resulting from the combustion of a natural gas with an air equivalence ratio of $\lambda \approx 3$.

The assumption that the change in the mole numbers of the educts is negligible implies that $x_{\mathrm{educt}} \gg U_j$ for all educts participating in the dissociation reaction j. This surely holds for N_2, CO_2, and H_2O for typical combustion processes. The concentration of O_2 in the undissociated exhaust gas, however, depends on the air equivalence ratio λ. For $x_{O_2} < 1\%$ (corresponding to $\lambda < \approx 1.05$) the assumption that the concentration of oxygen remains constant becomes questionable. Substantially different dissociation processes have to be considered in this case. Figure 8 shows deviations between values for the ideal gas isobaric heat capacity at 0.1 MPa calculated with Eq. (47) for gases resulting from combustions of a typical natural gas at different air equivalence ratios λ from values calculated according to Ref. [3]. For temperatures significantly exceeding 2000 K, reactions and components other than the ones considered in Eqs. (18)–(23) become relevant for the caloric properties of the exhaust gas. Therefore, the application of the simplified dissociation model should be restricted to gases resulting from complete combustion with $\lambda \geqslant 1.05$ and to temperatures $T \leqslant 2000$ K.

If calculations are based on a gas analysis which contains a relevant amount of CO (i.e., the composition is not the equilibrium composition), the composition has to be traced back stoichiometrically to $x_{\mathrm{CO}} = 0$ by considering Eq. (18). The "theoretical concentrations" determined in this way have to be used as input values. The caloric properties of the undissociated nonequilibrium gas may then be estimated from the theoretical equilibrium composition using Eqs. (15)–(17) by adding the contribution from Eqs. (44)–(46) setting $U_j = 0$ for $j \neq 1$ and $U_1 / U_{\mathrm{tot}} = x_{\mathrm{CO}}$.

6 Limits of the Ideal Gas Hypothesis

In Sections 2 to 5 all fluids are treated as ideal gases. Particularly at low temperatures and high pressures intermolecular forces and the finite extent of the molecules affect the thermodynamic properties of the system leading to considerable deviations from the assumed ideal gas behavior. However, no thermodynamic property models are available which accurately describe the real gas properties of moist air and combustion gases at temperatures down to the beginning of condensation. Comparisons to estimations from existing models, [6], indicate that deviations from the ideal gas behavior do not have major effects on the calculation of polytropic and isentropic efficiencies. Nonetheless, these results may not be generalized if accurate values of caloric properties are needed for other applications.

For dry air reliable values of thermodynamic properties can be calculated using an accurate equation of state, [5]. Figure 9 shows percentage deviations between isobaric heat capacities of dry air and those calculated using Eq. (15) for the corresponding ideal gas mixture. Neglecting real gas effects results in significant inaccuracies of the calculated values especially in the low temperature range. Differences between the enthalpy of real dry air and the corresponding ideal gas mixture are shown in Fig. 10. The deviations in enthalpy are small compared to the total value but they may have a major impact if enthalpy differences are calculated between two states at comparable temperature and distinctly different pressure.

Real gas effects will rise considerably for moist air and combustion gases due to the presence of water and, if applicable, carbon dioxide. The actual effect depends on the concentrations of these components. Figure 11 shows differences between enthalpies of a real gas resulting from combustion of a typical natural gas at an air equivalence ratio of $\lambda \approx 3$ and enthalpies calculated with Eq. (16) for the corresponding ideal gas mixture. The estimation of the real gas values has been carried out using the generalized property model by Lemmon and Jacobsen [6]. The model was slightly modified to account for water as an additional component.

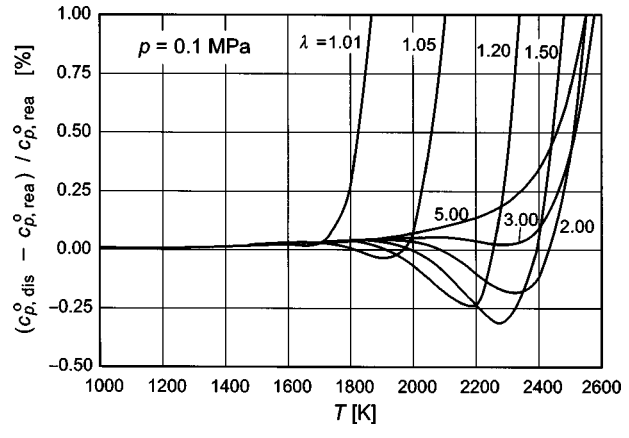

Fig. 8 Deviations of ideal gas isobaric heat capacities at 0.1 MPa calculated with Eq. (47) for combustion gases resulting from combustions of a common natural gas at different air equivalence ratios λ from values calculated with an iterative chemical equilibrium algorithm, [3]

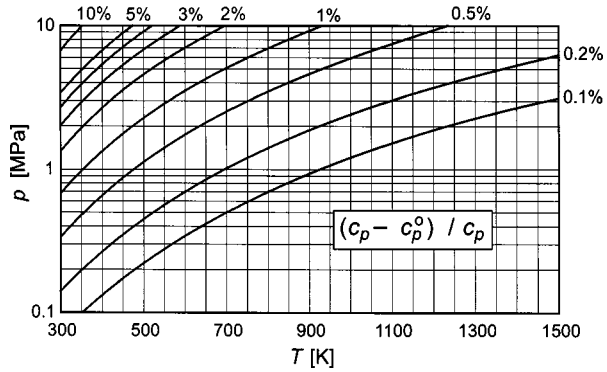

Fig. 9 Percentage deviations of isobaric heat capacities of dry air calculated with [5] (i.e., considering real gas behavior) from those calculated using Eq. (15) for the corresponding ideal gas mixture

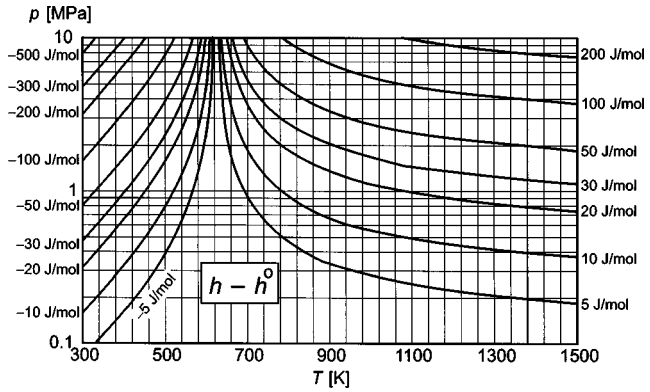

Fig. 10 Absolute deviations of enthalpies of dry air calculated with [5] (i.e., considering real gas behavior) from those calculated using Eq. (16) for the corresponding ideal gas mixture

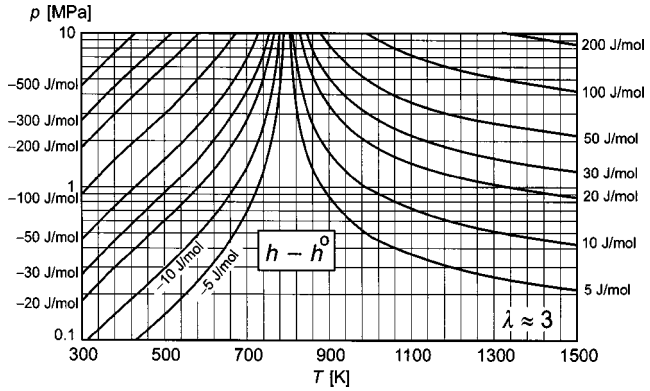

Fig. 11 Absolute deviations of enthalpies of typical combustion gases calculated with [6] (i.e., considering real gas behavior) from those calculated using Eq. (16) for the corresponding ideal gas mixture

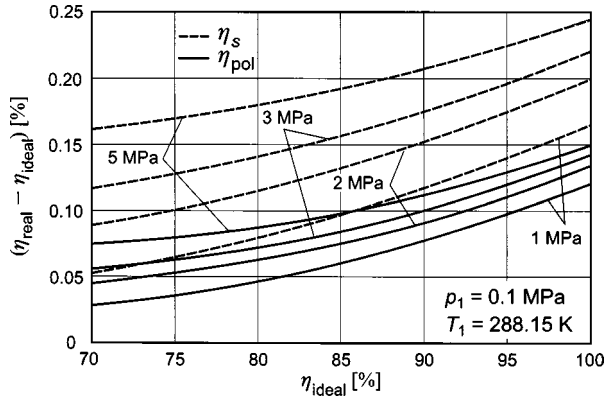

Fig. 12 Deviations of isentropic and polytropic efficiencies for the compression of dry air (for different outlet pressures p_2) calculated considering real gas effects, [5], from efficiencies calculated using Eqs. (16), (17) for the corresponding ideal gas mixture

Figure 11 clearly indicates that the effect of real gas behavior is not negligible at high pressures and low temperatures particularly when approaching the dew point of water.

When calculating efficiencies of turbines and compressors, the neglection of real gas effects causes systematic errors both in enthalpy and entropy. These errors partially compensate each other, leading to significantly smaller deviations in the efficiencies

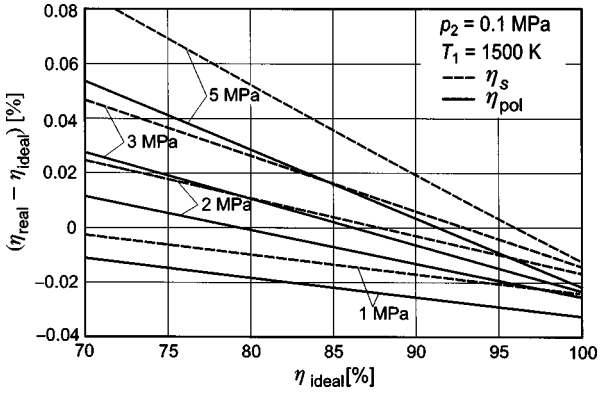

Fig. 13 Deviations of isentropic and polytropic efficiencies for the expansion in a gas turbine (for different inlet pressures p_1) calculated considering real gas effects, [6], from efficiencies calculated using Eqs. (16), (17) for the corresponding ideal gas mixture (all values calculated for a combustion gas resulting from the combustion of a common natural gas at $\lambda \approx 3$)

than expected from the deviations of the caloric properties. For polytropic and isentropic compressor efficiencies, Fig. 12 shows deviations resulting from neglecting the real gas behavior of dry air. However, calculation of processes such as the compression of very cold ambient air or the high-pressure stage of a compressor with intercooler would lead to substantially higher deviations. For typical gas turbine expansions, which take place at high temperatures, the influence of the real gas behavior remains distinctly smaller. Figure 13 shows deviations between real and ideal polytropic and isentropic efficiencies of a typical gas turbine.

Conclusions

The new thermodynamic property model for technical applications reliably predicts caloric properties of moist air and undissociated combustion gases with the highest possible accuracy. None of the common technical models available today reaches the same level of accuracy using only one set of coefficients per component for the entire temperature range of practical interest. The new simple dissociation model enables a straight forward calculation of caloric properties of dissociated combustion gases at temperatures up to 2000 K, complete combustion with $\lambda \geqslant 1.05$ provided.

Application of the new model is restricted by two effects. At low temperatures and high pressures, especially when approaching the dew point of water, the influence of real gas behavior on the thermodynamic properties becomes substantial. Extensive experimental work and further work on empirical real gas models will be required to set up a model that accurately accounts for these effects. Also, at temperatures exceeding 2000 K, the simple dissociation model introduced above will fail. To calculate compositions and caloric properties of combustion gases at higher temperatures, iterative algorithms have to be applied.

Nomenclature

a = coefficient
A = coefficient
b = exponent
B = empirical parameter
c = heat capacity
C = empirical parameter
d = exponent
D = empirical parameter
E = empirical parameter
h = enthalpy
k = equilibrium constant
n = coefficient
N = number of terms/species/modes

p = pressure
r = empirical parameter
R_m = 8.314472 [J mol^{-1} K^{-1}]
= molar gas constant
s = entropy
T = thermodynamic temperature
U = reaction number
V = characteristic contribution
v = molar volume
x = mole fraction (molar concentration)

Greek Letters

Δ = deviation, uncertainty
Δ^{dis} = change of a thermodynamic property due to dissociation
$\Delta_0^f h$ = enthalpy of formation
$\Delta^{\mathrm{mix}} s^o$ = entropy of mixing (ideal gas)
η = efficiency
λ = air equivalence ratio (air number)
ν = stoichiometric coefficient
θ = characteristic temperature

Subscripts

0 = standard state ($T_0 = 273.15$ K; $p_0 = 0.101325$ MPa)
calc = calculated
dis = dissociated gas
educt = component of the undissociated gas
i = index
ideal = calculated neglecting real gas effects
j = index of the reactions
k = index of the components
mix = mixture
n = index of the species in a stoichiometric equation
p = isobaric
pol = polynomial term, polytropic
product = product of dissociation reaction
rea = calculated considering the exact reaction equilibrium
real = calculated considering real gas effects
ref = calculated with the new scientific reference
rot = contribution from rotation
s = isentropic
spec = species in a stoichiometric equation
T = at constant temperature
tech = calculated with the new technical equations
tot = total
undis = undissociated
vib = contribution from vibration

Superscripts

* = in the dissociated gas
o = ideal gas state

References

[1] ANSI/ASME PTC 4.4—1981, *Gas Turbine Heat Recovery Steam Generators*, Performance Test Codes, ASME, New York.
[2] Brandt, F., 1991, *Brennstoffe und Verbrennungsrechnung*, FDBR-Fachbuchreihe, **1**, Second Ed., Vulkan-Verlag, Essen.
[3] Gordon, S., and McBride, B. J., 1994, ''Computer Program for Calculation of Complex Chemical Equilibrium Composition and Applications,'' NASA RP-1311, National Aeronautics and Space Administration, Washington, DC.
[4] Brandt, F., 1995, *Wärmeübertragung in Dampferzeugern und Wärmetauschern*, FDBR-Fachbuchreihe, **2**, Second Ed., Vulkan-Verlag, Essen.
[5] Jacobsen, R. T., Clarke, W. P., Penocello, S. G., and McCarty, R. D., 1990, ''A Thermodynamic Property Formulation for Air. I. Single-Phase Equation of State from 60 to 873 K at Pressures to 70 MPa,'' Int. J. Thermophys., **11**, pp. 169–177.
[6] Lemmon, E. W., and Jacobsen, R. T., 1999, ''A Generalized Model for the Thermodynamic Properties of Mixtures,'' Int. J. Thermophys., **20**, pp. 825–835.
[7] Trusler, J. P. M., 1991, *Physical Acoustics and Metrology of Fluids* (The Adam-Hilger Series on Measurement Science and Technology), IOP Publishing Ltd., Bristol, UK.
[8] Kestin, J., and Dorfman, J. R., 1971, *A Course in Statistical Thermodynamics*, Academic Press, New York.
[9] Hilsenrath, J., Beckett, C. W., Benedict, W. S., Fano, L., Hoge, H. J., Masi, J. F., Nuttal, R. L., Touloukian, Y. S., and Woolley, H. W., 1955, *Tables of Thermal Properties of Gases*, Circ. 564, U.S. National Bureau of Standards.
[10] Baehr, H. D., Hartmann, H., Pohl, H.-C., and Schomäcker, H., 1968, *Thermodynamische Funktionen Idealer Gase für Temperaturen bis 6000°K*, Springer-Verlag, Berlin.
[11] Gurvich, L. V., Veyts, I. V., and Alcock, C. B., 1989, *Thermodynamic Properties of Individual Substances*, Fourth Ed., **1**, Part 2, Hemisphere, Washington, DC (Originally published as [22]. Revised and updated from the Third Russian Ed.).
[12] Gurvich, L. V., Veyts, I. V., and Alcock, C. B., 1991, *Thermodynamic Properties of Individual Substances*, Fourth Ed., **2**, Part 2, Hemisphere, Washington, DC (Revised and updated from the Third Russian Ed.)
[13] *TRC Thermodynamic Tables—Non-Hydrocarbons*, 1999, Thermodynamic Research Center: The Texas A&M University System, College Station, Texas (loose-leaf data sheets, extant, 1999).
[14] Chase, M. W., Jr., 1998, ''NIST-JANAF Thermochemical Tables,'' Fourth Ed., *Journal of Physical and Chemical Reference Data*, Monograph No. 9.
[15] Span, R., Lemmon, E. W., Jacobsen, R. T., Wagner, W., and Yokozeki, A., 2000, ''A Reference Equation of State for the Thermodynamic Properties of Nitrogen for Temperatures from 63.151 to 1000 K and Pressures up to 2200 MPa,'' J. Phys. Chem. Ref. Data, accepted for publication **29**, pp. 1361–1433.
[16] Woolley, H. W., 1980, ''Thermodynamic Properties for H_2O in the Ideal Gas State,'' *Water and Steam: Their Properties and Current Industrial Applications, Proceedings of the 9th International Conference on the Properties of Water and Steam*, J. Straub and K. Scheffler, eds., Pergamon Press, New York, pp. 166–175.
[17] Woolley, H. W., 1987, ''Ideal Gas Thermodynamic Functions for Water,'' J. Res. Natl. Bur. Stand., **92**, pp. 35–51.
[18] Span, R., and Wagner, W., 1996, ''A New Equation of State for Carbon Dioxide Covering the Fluid Region from the Triple-Point Temperature to 1100 K at Pressures up to 800 MPa,'' J. Phys. Chem. Ref. Data, **25**, pp. 1509–1596.
[19] Wagner, W., and Pruß, A., 2002, ''The IAPWS Formulation 1995 for the Thermodynamic Properties of Ordinary Water Substance for General and Scientific Use,'' J. Phys. Chem. Ref. Data, **31**, pp. 387–535.
[20] Wagner, W., and de Reuck, K. M., 1987, *Oxygen—International Thermodynamic Tables of the Fluid State—9*, IUPAC Thermodynamic Tables Project, Blackwell Scientific Publications, Oxford, UK.
[21] Wagner, W., Ewers, J., and Schmidt, R., 1982, ''An Equation for the Ideal-Gas Heat Capacity of Molecular Oxygen for Temperatures from 30 K to 3000 K,'' Ber. Bunsenges. Phys. Chem., **86**, pp. 538–540.
[22] Gurvich, L. V., Veyts, I. V., and Medvedev, V. V., 1978, *Thermodinamicheskie svoystva individual'nykh veshchestv*, Third Ed., **1**, Nauka, Moscow (in Russian).
[23] Cooper, J. R., 1982, ''Representation of the Ideal-Gas Thermodynamic Properties of Water,'' Int. J. Thermophys., **3**, pp. 35–43.
[24] Friedmann, A. S., and Haar, L., 1954, ''High-Speed Machine Computing of Ideal Gas Thermodynamic Functions—I. Isotopic Water Molecules,'' J. Chem. Phys., **22**, pp. 2051–2058.
[25] Vidler, M., and Tennyson, J., 2000, ''Accurate Partition Function and Thermodynamic Data for Water,'' J. Chem. Phys., **113**, pp. 9766–9771.
[26] Chao, J., 1986, private communication, Lehrstuhl für Thermodynamik, Ruhr-Universität Bochum.
[27] Society of Automotive Engineers, 1999, *Gas Turbine Engine Steady-State and Transient Performance Presentation for Digital Computer Programs*, SAE AS681 Rev. H, Warrendale, PA.
[28] McBride, B. J., Gordon, S., and Reno, M. A., 1993, ''Coefficients for calculating thermodynamic and transport properties of individual species,'' NASA Technical Memorandum 4513.
[29] McBride, B. J., Heimel, S., Ehlers, J. G., and Gordon, S., 1963, *Thermodynamic Properties to 6000 K for 210 Substances Involving the First 18 Elements*, NASA Special Publication 3001, Office of Technical Services, US Department of Commerce, Washington, DC.
[30] Baehr, H. D., and Diederichsen, C., 1988, ''Berechnungsgleichungen für Enthalpie und Entropie der Komponenten von Luft und Verbrennungsgasen,'' Brennst.-Wärme-Kraft, **40**, pp. 30–33.
[31] Selover, T. B., and Sychev, V. V., 1987, *Thermodynamic Properties of Nitrogen*, Hemisphere, Washington, DC.
[32] Span, R., Collmann, H.-J., and Wagner, W., 1998, ''Simultaneous Optimization as a Method to Establish Generalized Functional Forms for Empirical Equations of State,'' Int. J. Thermophys., **19**, pp. 491–500.

Direct Constrained Computational Fluid Dynamics Based Optimization of Three-Dimensional Blading for the Exit Stage of a Large Power Steam Turbine

P. Lampart
Institute of Fluid Flow Machinery,
Polish Academy of Sciences,
Gdansk, Poland
e-mail: lampart@imp.gda.pl

S. Yershov
Institute of Mechanical Engineering Problems,
Ukrainian Academy of Sciences,
Kharkov, Ukraine
e-mail: yershov@ipmach.kharkov.ua

The paper describes results of direct constrained optimization using Nelder-Mead's method of deformed polyhedron and a Reynolds-averaged Navier-Stokes (RANS) solver to optimize the shape of three-dimensional blading for the exit stage of a large power steam turbine. The computations of the flowfield in the stator and rotor are compressible, viscous, and three-dimensional. Turbulence effects are taken into account using the modified model of Baldwin-Lomax. The objective function is the stage efficiency, with the exit energy considered a loss, and with constraints imposed on the mass flow rate in the form of a penalty function if the mass flow rate falls beyond the required range. The blade sections (profiles) are assumed not to change during the optimization. Two optimization tasks are reported in this paper, first—optimizing the stator straight and compound circumferential lean, and also stator and rotor stagger angles to keep the flow rate unchanged, giving a total number of optimized parameters equal to 5; second—optimizing the stator straight and compound axial sweep, also with stator and rotor stagger angles, also giving five optimized parameters. The process of optimization is carried out for a nominal load; however, due to the fact that exit stages of steam turbines operate over a wide range of flow rates away from the nominal conditions, the original and final geometries are also checked for low and high loads. The process of optimization gives new designs with new three-dimensional stacking lines of stator blades, and with significantly increased efficiencies, compared to the original design, at least for a larger part of the assumed range of load. [DOI: 10.1115/1.1520157]

Introduction

Principal effects of three-dimensional blade stacking for turbine blading systems of axial turbomachinery are known (see Harrison [1], Singh et al. [2], Denton and Xu [3], Wang [4], Lampart and Gardzilewicz [5], and Lampart et al. [6]). There are many possible ways of blade stacking, for example lean, sweep, twist—straight or compound, or combinations of the above. Due to a large number of shape parameters arising from the application of three-dimensional blade stacking that can effect flow patterns and efficiencies, it is highly required that automatic optimization techniques and automatic changing of flow geometry corresponding to the shape parameters obtained in the process of optimization are used so as to find the optimum design. Therefore, works on optimization of turbomachinery blading based on three-dimensional codes are in progress. Results of three-dimensional inverse design using Euler or Navier-Stokes codes are reported by Demeulenaere and Van Den Braembussche [7], and Damle et al. [8]. A concept of two-dimensional/three-dimensional optimization with the help of an artificial neural network trained over a data base of RANS solutions is presented by Pierret and Van Den Braembussche [9] and Pierret [10]. A brief literature review of shape optimization of turbomachinery blades and aerodynamic shapes, as well as a comparative study of optimization methods including genetic algorithms, simulated annealing and sequential quadratic programming, can be found in a paper of Shahpar [11].

This paper pursues the idea of direct optimization where the final shape of the blading is obtained from minimizing/maximizing an objective function, for example, the total energy loss or efficiency, total pressure loss of the stage, etc., and where the current values of the objective function are found from three-dimensional RANS computations of geometries changed during the process of optimization. An example of direct efficiency-based optimization of three-dimensional stacking lines for compressor blading without changing the blade section can be found in a paper of Lee and Kim [12]. In the present paper, efforts are also concentrated on optimizing the three-dimensional stacking line for the stator blade, trying the use of stator blade lean and sweep, both straight and compound, while keeping the blade section unchanged. The optimization is carried out using Nelder-Mead's method of deformed polyhedron, which enables efficient optimization of five to eight or even ten geometrical parameters of the considered stage. This method is relatively easy to work with constraints imposed on the mass flow rate, reaction, and exit angle.

Direct three-dimensional optimization is considered highly time-consuming. To save CPU times, three-dimensional computational grids used during optimization are relatively coarse. Therefore, at least the original and final geometries must be checked on refined grids, and the possible changes in flow patterns and efficiency gains must be implied based on the comparison of post-

Contributed by the Power Division of THE AMERICAN SOCIETY OF MECHANICAL ENGINEERS for publication in the ASME JOURNAL OF ENGINEERING FOR GAS TURBINES AND POWER. Manuscript received by the Power Division Apr. 26, 2001; final revision received by the ASME Headquarters May 22, 2002. Associate Editor: D. Lou.

optimization computations of the original and final geometries on refined grids. Certainly, computational fluid dynamics (CFD) results are to some extent grid-dependent. Nevertheless, the authors are inclined to agree that major tendencies in changing flow patterns with changing geometry of the turbine/stage can be discovered on coarse grids.

Three-Dimensional Reynolds-Averaged Navier-Stokes (RANS) Solver

CFD computations are performed with the help of the code FlowER—solver of viscous compressible flows through multistage turbomachinery developed by Yershov and Rusanov [13,14] (see also Yershov et al. [15]). The solver draws on the set of thin-layer Reynolds-averaged Navier-Stokes (RANS) equations for perfect gas. The effects of turbulence are taken into account with the help of a modified algebraic model of Baldwin-Lomax. The governing equations are solved numerically based on the Godunov-type upwind differencing and high-resolution ENO scheme for the calculation of convective derivatives, assuring second-order accuracy everywhere in space and time, and third-order accuracy locally. The computational domain also extends on the radial gap above the unshrouded rotor blade tips. The following boundary conditions are incorporated: no-slip and no heat flux at the walls; spanwise distribution of the total pressure, total temperature, and flow angles at the inlet to the stage; at the exit a midspan value of the static pressure with the radial equilibrium equation assumed there. The computations carried out in one blade-to-blade passage of the stator and rotor converge to a steady state, with the condition of spatial periodicity, and a mixing plane approach assumed that makes use of a concept of pitchwise averaging of flow parameters in the axial gap between the stator and rotor. The assumed inlet/exit boundary conditions impose the pressure drop and let the mass flow rate be resultant.

Optimizer

The shape optimization of the exit turbine stage is carried out with the help of the code Optimus (see Yershov et al. [16]). Mathematically, the process of optimization is an iterative procedure that seeks for an extremum of the objective function f

$$\min_g f(\mathbf{r}(\mathbf{g}),\mathbf{g}) \quad \text{or} \quad \max_g f(\mathbf{r}(\mathbf{g}),\mathbf{g})$$

assuming that $\mathbf{r}\in[\mathbf{r}_{\min};\mathbf{r}_{\max}]$; $\mathbf{g}\in[\mathbf{g}_{\min};\mathbf{g}_{\max}]$, where f is an objective function, $\mathbf{r}$—vector of assumed flow parameters; $\mathbf{g}$—vector of assumed geometrical parameters. As objective functions in the code Optimus, the following functions can be optimised: moment of force at the rotor blades or stage power, efficiency or energy losses of the stage, both with or without the exit energy. The following parameters of blade shape can be considered during the optimization for each blade row: blade number, stagger angle, blade height, linear twist angle, linear lean angle, and linear sweep angle, four parameters of compound lean (two at hub, two at tip), four parameters of compound sweep, and four parameters of compound twist. Each parameter is allowed to vary in a prescribed range of variation.

The current value of the objective function is found from postprocessing of three-dimensional RANS computations. In order to secure global flow conditions, there are also constraints imposed on the mass flow rate, exit swirl angle, average reaction, and reaction at tip and root. The exit swirl angle and reactions are not allowed to assume values beyond certain ranges of variation, meaning that if they fall beyond these ranges, an infinity is prescribed as a current value of the objective function. The penalty function is imposed on the mass flow rate if it falls beyond the assumed, usually very narrow, range of variation, with a penalty weight coefficient prescribed in a way that the objective function sharply rises to infinity with increasing distance from the lower or upper limits of the assumed range of variation.

A very important question in optimization tasks is the proper choice of optimization methods. As in general it is difficult to make an a priori assumption concerning the smoothness of the objective function, nongradient methods of optimization are used in the code Optimus. The results presented in the paper are obtained using the method of deformed polyhedron proposed by Nelder and Mead [17], based on a simplex method initially worked out by Spendley et al. [18] for regular simplexes.

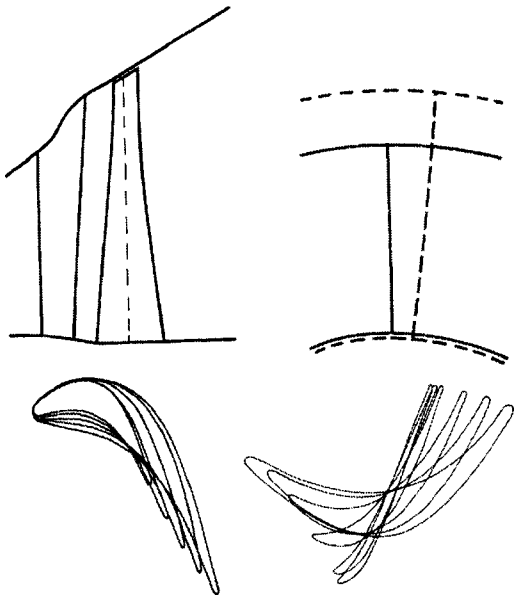

Fig. 1 Original geometry of the LP exit stage: meridional view (top left), circumferential view of stator leading and trailing edges (top right), and stator and rotor profiles (bottom)

An essential feature of the method of deformed polyhedron is that, unlike its simplex prototype, the deformed polyhedron adapts to changing topography of the objective function by means of the following operations: symmetrical reflection, stretching, compression, or reduction. Of great importance for effective operation of the algorithm is proper selection of the reflection ratio α, compression ratio β, stretching ratio γ, and reduction ratio δ. The recommendation of Nelder and Mead and also the experience of the authors suggest that the following values be used: $\alpha=1$, $\beta=\delta=0.5$, and $\gamma=2$.

The method of deformed polyhedron becomes more and more popular. What is characteristic for the method is that its efficiency, measured by the number of calculations of the objective function during one iteration, does not depend on the number of optimized parameters and for the majority of cases is limited to two to three calculations per iteration. It should be mentioned, however, that attempts to prove the convergence of the method for wide classes of functions have failed, (Torczon [19]). Some numerical experiments also show that the method is not always convergent, especially when the number of parameters exceeds 7. However, even in this case it can still produce solutions whose objective function is better than that of the initial design.

Optimized Exit Stage of a Steam Turbine

The optimized LP stage of a steam turbine has the aspect ratio—span/diameter changing throughout between 0.25–0.35. The original geometry of the LP exit stage is presented in Fig. 1 in meridional view, circumferential view showing the stator leading and trailing edges (as if looking downstream, and the moving blades rotate clockwise), stator, and rotor profiles. The stage operates under the conditions of pressure ratio (p_2/p_{0T}) between 0.2–0.5, inlet temperature 340–350 K, mass flow rate 35–85 kg/s, exit dryness fraction $x=0.92-0.98$. The calculations were carried out for ''perfect steam'' assuming the specific heat ratio γ

$=1.08-1.09$ and gas constant $R=440-450$, on an H-type grid refined at the endwalls, blade walls, and at the leading and trailing edges of the blades.

The objective function was the level of kinetic energy losses in the stage, with the exit energy considered a loss. The mean exit angle was assumed not to change more than by 5 deg compared to the original design. The reaction at the root was assumed not to decrease below, the reaction at the tip—not to increase above that of the original design. The penalty function was imposed on the mass flow rate if it changed by more than $\pm 0.5\%$, compared to the original design. The optimization was carried out in the proximity of nominal operating conditions (mass flow rate of 56 kg/s, pressure ratio of 0.34); however the results were also checked for a low load (mass flow rate of 38 kg/s, pressure ratio of 0.51), and a high load (mass flow rate of 75 kg/s, pressure ratio of 0.25). Due to time restrictions, RANS computations in the course of optimization were carried out on coarse grids of 100,000 cells (stator + rotor). After optimization, the original and optimised geometries were recalculated on more refined grids—600,000 cells (stator+ rotor). The comparative results for the reaction and losses in the original and optimised geometries presented in the paper are those of refined grids.

Two optimization tasks were performed. Task 1 was devoted to optimization of the stator straight circumferential lean and compound lean at the root, with the stator and rotor stagger angles also optimized to keep the flow rate unchanged. The compound lean was assumed in the parabolic form. There were five shape parameters—stator straight lean angle, two parameters of the stator compound lean, the stator, and rotor stagger angles (but without introducing extra blade twist). In Task 2, the stator straight axial sweep and compound axial sweep at the tip were optimized, also with the stator and rotor stagger angles. The compound sweep was also assumed in the parabolic form, giving also five shape parameters—stator straight sweep angle, two parameters of the stator compound sweep, the stator, and rotor stagger angles. For both tasks the blade sections (profiles) were assumed not to change during the optimization.

Outcome of Task 1

The optimizer chose the following changes of the original geometry of the considered exit stage:

- stator straight lean angle—13.6 deg; the stator blade tip is leaned with rotation of the moving blades;
- stator compound lean rate—0.1; compound lean begins 0.1 of the blade span from the root;
- stator compound lean angle—34.5 deg; this shows the angle at which the compound leaned blade meets the cylindrical root endwall in the circumferential plane; compound lean blade is protruded at the root against the rotation of the rotor;
- stator stagger angle increment—0.2 deg; slightly closing throats in the stator; and
- rotor stagger angle increment—1.1 deg; also closing throats in the rotor.

The optimized geometry of the exit stage with leans is presented in Fig. 2. Interesting! The optimizer chose circumferential lean mainly in the form of straight lean with little contribution of compound lean at the root. About 80 iterations were performed amounting to 140 RANS computations of different geometries. The objective function (stage loss with the exit energy) was decreased by 1.0% (on coarse grids for nominal operating conditions).

Outcome of Task 2

The optimiser chose the following geometrical changes:

- stator straight sweep angle—6.3 deg; the stator blade tip is swept forward (downstream);

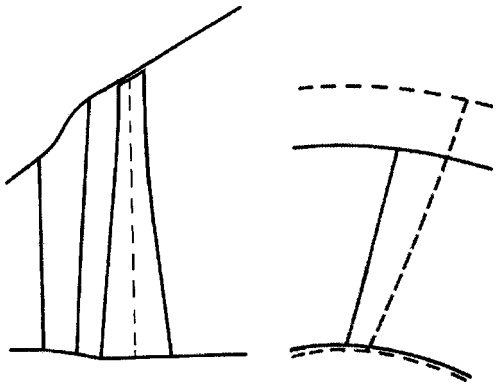

Fig. 2 Final geometry with optimized straight and compound circumferential leans: meridional view (left), circumferential view of stator leading and trailing edges (right)

- stator compound sweep rate—0.4; compound sweep begins 0.4 of the blade span from the tip;
- stator compound sweep angle—27.7 deg; this shows the angle at which the compound swept blade meets the cylindrical tip endwall in the meridional plane; compound swept blade is protruded backward (upstream);
- stator stagger angle increment—0.6 deg; slightly closing throats in the stator; and
- rotor stagger angle increment—0.3 deg; also slightly closing throats in the rotor.

The optimized geometry of the exit stage with sweeps is presented in Fig. 3. Unlike for leans, there is a great contribution of compound sweep at the tip in the new configuration. About 50 iterations were performed amounting to 90 RANS computations of different geometries. This time the objective function (stage loss with the exit energy) was decreased by 1.6% (on coarse grids for nominal operating conditions).

Recalculation of Original and Optimized Geometries on Refined Grids

The original geometry and new designs found in the course of optimization were recalculated on refined grids so as to, first, validate the results that were obtained on coarse grids, and second, find how the new designs would perform away from the nominal load, that is in the conditions for which they were not optimized.

Circumferential leans and axial sweeps change flow patterns which is explained in Appendix A. These changes result in redistribution of blade load, mass flow rate, and loss spanwise. The redistribution of stage reaction, stator loss, rotor loss, and stage

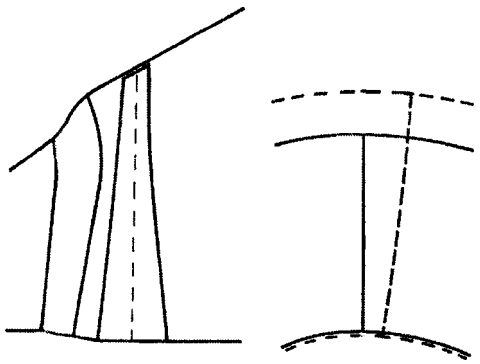

Fig. 3 Final geometry with optimized straight and compound axial sweeps: meridional view (left), circumferential view of stator leading and trailing edges (right)

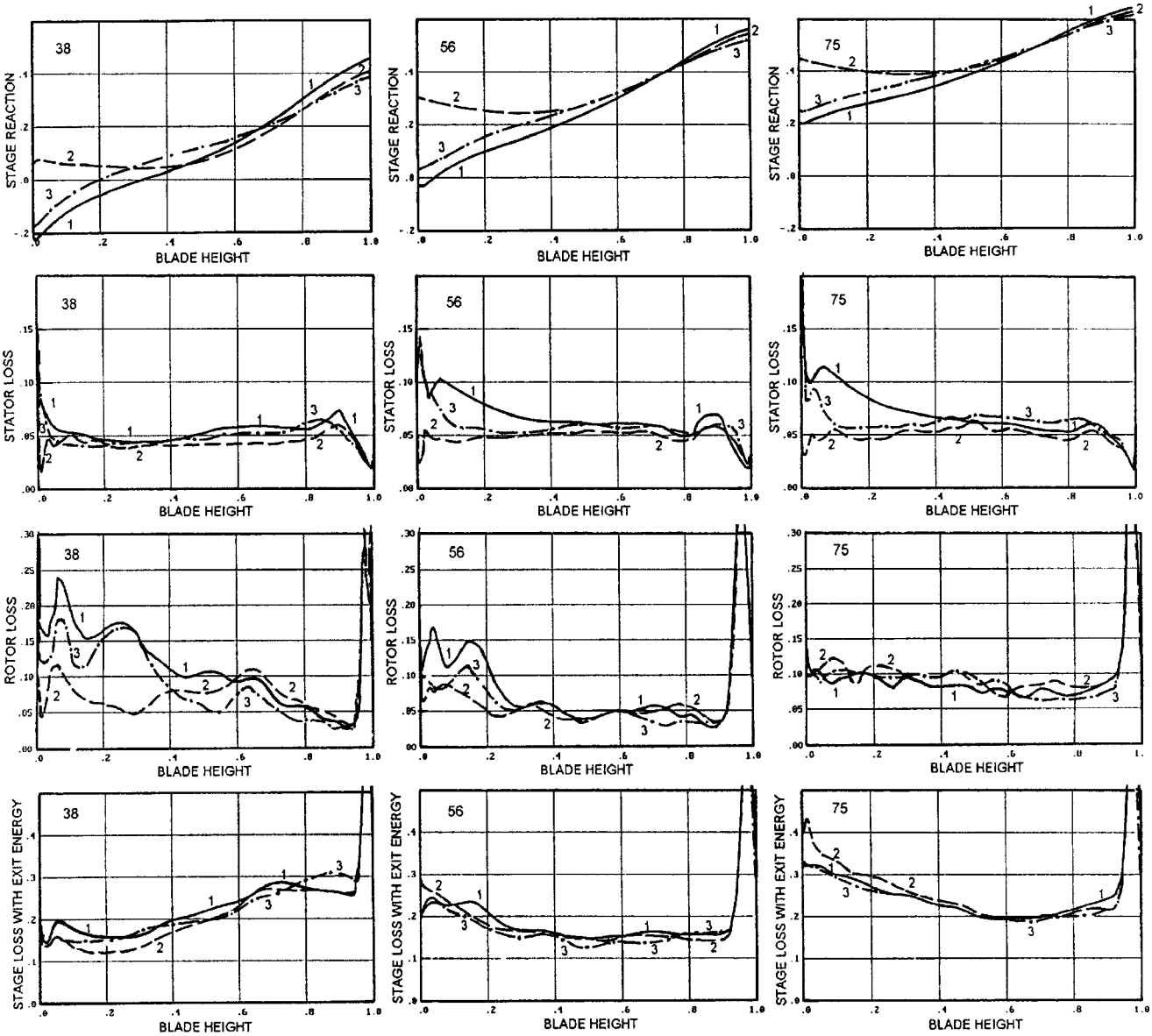

Fig. 4 Spanwise circumferentially averaged distribution of stage reaction, stator loss, rotor loss, and stage loss with the exit energy in the exit stage for three mass flow rates: 38 kg/s (left), 56 kg/s (center), 75 kg/s (right) for the original stage (1), stage with circumferential leans (2), and stage with axial sweeps (3)

loss with the exit energy between the original stage, stage with circumferential leans, and stage with axial sweeps for three mass flow rates: 38, 56, and 75 kg/s is presented in Fig. 4 (definitions of stage reaction and kinetic energy losses are given in Appendix B). The spanwise gradient of reaction is reduced both with leans and sweeps. The most spectacular increase of reaction at the root occurs for the designs with leans. The new designs give efficiency gains both in the stator and rotor. The stator loss is considerably decreased, especially at the root sections for higher loads, and especially for the design with circumferential leans. This is due to the fact that transonic stator blades become unloaded at the root. Efficiency gains are also significant in the rotor, especially at the root sections for lower loads, and again especially for the design with circumferential leans, as the underloaded rotor blades operating under conditions of negative or low reaction become reloaded at the root. Rotor blades are also unloaded at the tip reducing the tip leakage loss. However, for high loads, especially circumferential leans give more loss in the rotor at the root. Gains in the design with axial sweeps are more moderate, but more evenly distributed spanwise.

The combination of stator loss and rotor loss provides that stage losses without the exit energy are unanimously decreased both for axial sweeps and circumferential leans, compared to the original design, along the entire blade span and for the entire range of load. The stage losses with the exit energy also decrease, with one exception, that is for circumferential leans at high loads (Fig. 4). This is the effect of exit swirl angle and exit energy. The exit energy forms a great share of the overall kinetic energy loss of the exit stage, and apart from low loads, the exit swirl angle is usually less favorable for the optimized designs, especially for the design with circumferential leans, resulting in increased exit energy in the optimized designs.

The efficiency gains, that is differences in pitch/span averaged values of the kinetic energy losses (with the exit energy) between

the optimized and original designs, found from recalculation of the geometries on refined grids, are as follows:

- For circumferential leans
  - nominal load (56 kg/s)—+0.8%;
  - low load (38 kg/s)—+2.6%! (very large improvement); and
  - high load (75 kg/s)—−0.3%! (efficiency loss).
- For axial sweeps
  - nominal load (56 kg/s)—+1.5%;
  - low load (38 kg/s)—+0.6%; and
  - high load (75 kg/s)—+0.8%.

The distributions of losses in the rotor and stage as well as the distributions of the exit velocity and swirl angle behind the stage are captured 45% of the rotor axial chord downstream of the rotor trailing edge, and still some pressure recovery can take place, and not all exit energy should necessarily be considered a loss.

The exit stage was optimized on coarse grids; however, the computations made on more refined grids confirm the tendencies discovered on coarse grids. The predictions of efficiency gains from coarse grids, for the nominal load for which the exit stage was optimized, were corrected on refined grids by 0.1–0.2%. For circumferential leans, the objective function (the stage losses with the exit energy) decreased on coarse grids by 1.0%, whereas on refined grids by 0.8%, compared to the original design; for axial sweeps—1.6% on coarse grids and 1.5% on refined grids. All restrictions imposed on coarse grids on reactions at the root and tip, exit swirl angle, and mass flow rate still hold on refined grids. This refers both to the nominal and non-nominal conditions. The fact of holding restrictions for the reactions can easily be verified in Fig. 4. The prescribed restrictions for variations of the exit angle and mass flow rate, that is 5 deg and 0.5%, are easily held on refined grids for the design with axial sweeps in the entire range of load, and just held, but also in the entire range of load, for the design with circumferential leans. Differences in computational results on coarse and refined grids are relatively consistent, which seems to further back up the idea of direct optimization on coarse grids.

Conclusions

Two optimization tasks were performed on an exit stage of a large power steam turbine based on direct constrained optimization using Nelder-Mead's method of deformed polyhedron and a three-dimensional RANS solver. The optimization of the objective function was carried out on coarse grids. Nevertheless, it enabled us to reveal major tendencies in changing flow patterns with changing geometry, and these tendencies were later confirmed by computations of the original and final geometries on refined grids. As a result of optimization of the exit stage, the stator blading acquired new three-dimensional stacking lines, first with circumferential straight lean and compound lean at the root, second with axial straight sweep and compound sweep at the tip. The efficiency of the new designs significantly increased, compared to the original reference design, for the nominal load for which the stage was optimized. Recalculation of the design with axial sweeps shows also efficiency improvements both for low and high loads, the design with circumferential leans only for low loads.

Acknowledgments

The authors would like to thank Prof. Andrzej Gardzilewicz from Institute of Fluid Flow Machinery, and Dr. Andrey Rusanov from Institute of Mechanical Engineering Problems, Kharkov, Ukraine, for their helpful comments and discussions.

Appendix A

Figures 5 and 6 are enclosed in this paper to help us understand the previously described changes in efficiency characteristics of the exit stage that take place with changing geometry. As already mentioned, the new designs reduce the spanwise gradient of stage reaction. The reaction is increased at the root and decreased at the tip. There are changes in flow patterns both in the stator and rotor. The stator blades become reloaded at the tip (for a wide range of load in the subsonic region) and unloaded at the root (in the transonic region). The comparison of Mach number contours in the stator at the root for the original stage and stage with optimized circumferential leans for nominal operating conditions presented in Fig. 5 shows that in the optimized design velocities are decreased in stator throats at the root, resulting in less endwall loss and reduced intensity of trailing edge shocks. The rotor blades are unloaded at the tip and reloaded at the root, which means less tip

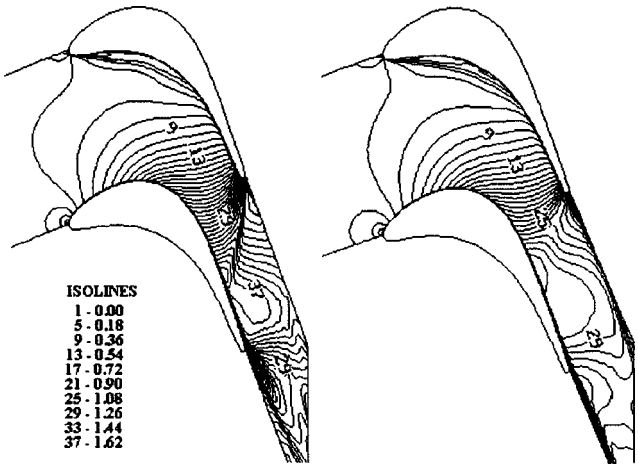

Fig. 5 Mach number contours in the stator 10% of the blade span from the root for the mass flow rate of 56 kg/s for the original stage (left) and stage with circumferential leans (right)

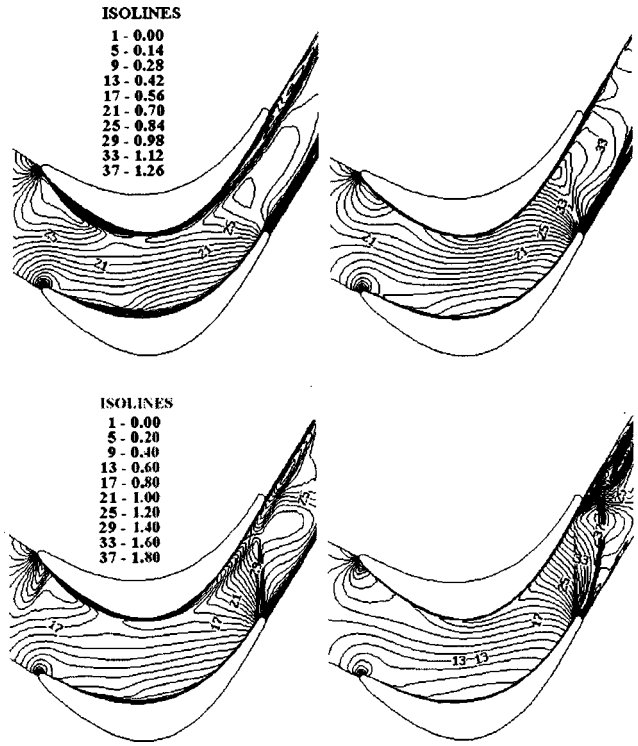

Fig. 6 Mach number contours in the rotor 10% of the blade span from the root for the mass flow rates of 56 kg/s (top) and 75 kg/s (bottom) for the original stage (left) and stage with circumferential leans (right)

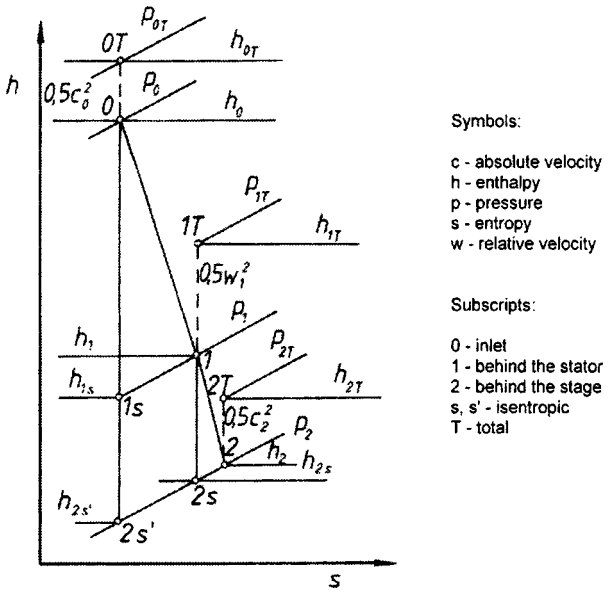

Fig. 7 Enthalpy-entropy diagram for a turbine stage

leakage loss and better expansion in the rotor at the root. More mass is passed in the rotor at the root, and for the nominal load and below it, the size of the separation zone at the rotor blade suction surface at the root is considerably reduced, as can be seen from the comparison of Mach number contours presented in Fig. 6 (upper pictures). For very low loads, usually below typical operating conditions, massive separation at the rotor root results in blockage of a considerable spanwise part of the channel (see Lampart [20]). The optimized designs, especially stator blade lean, are nice designs to correct this failure and extend the operational range on lower loads. For large loads the new designs also reduce the risk of appearance of inlet shock waves at the rotor root. This is due to the fact that the stator blades are unloaded at the root and no supersonic velocities occur at the leading edge of the rotor blade, which is clear from the comparison of Mach number contours in Fig. 6 (lower pictures). However, for large loads the rotor blades of new designs are further reloaded at the trailing edge, which is especially unfavorable for circumferential leans, giving rise to strong interaction between the configuration of intensive shocks, boundary layers and wakes. The absolute exit velocity also increases, which explains the calculated efficiency losses for circumferential leans at large loads. The effect of geometrical changes in the exit turbine stage on blade losses is also described in Lampart [20]. A detailed explanation of loss mechanisms in turbomachinery can be found in Denton [21].

Table 1 Stage reaction and kinetic energy losses in stator, rotor, and stage

Reaction	$\rho=(h_1-h_{2s})/(h_{0T}-h_{2s'})$
Stator loss	$\xi_1=(h_1-h_{1s})/(h_{0T}-h_{1s})$
Rotor loss	$\xi_2=(h_2-h_{2s})/(h_{1T}-h_{2s})$
Stage loss (without exit energy = stator + rotor loss)	$\xi_{12}=(h_2-h_{2s'})/(h_{0T}-h_{2s'})$
Stage loss (with exit energy = stator + rotor loss + exit energy)	$\xi_{12c}=(h_{2T}-h_{2s'})/(h_{0T}-h_{2s'})$

Appendix B

In this chapter, the stage reaction and kinetic energy losses in the stator, rotor, and stage are defined. Figure 7, illustrating the process of expansion in a turbine stage in the form of an enthalpy-entropy diagram, will help to explain definitions gathered in Table 1.

References

[1] Harrison, S., 1992, The Influence of Blade Lean on Turbine Losses, ASME J. Turbomach., **114**, pp. 184–190.

[2] Singh, G., Walker, P. J., and Haller, B. R, 1995, "Development of Three-Dimensional Stage Viscous Time Marching Method for Optimization of Short Height Stages," Europ. Conf. on Turbomachinery, Fluid Dynamics and Thermodynamic Aspects, Erlangen, Germany, Mar. 1–3.

[3] Denton, J. D., and Xu, L., 1999, "The Exploitation of 3D Flow in Turbomachinery Design," VKI LS 1999-02.

[4] Wang, Z., 1999, "Three-Dimensional Theory and Design Method of Bowed-Twisted Blade and Its Application to Turbomachines," VKI LS 1999-02.

[5] Lampart, P., and Gardzilewicz, A., 1999, "Numerical Study of 3D Blading in HP Impulse Turbines," *Int. Symp. SYMKOM'99*, Arturówek-Łódź, Poland, Oct. 5–8, Cieplne Maszyny Przepływowe, **115**, pp. 297–310.

[6] Lampart, P., Gardzilewicz, A., Rusanov, A., and Yershov, S., 1999, "The Effect of Stator Blade Compound Lean and Twist on Flow Characteristics of a Turbine Stage—Numerical Study Based on 3D NS Simulations," *2nd Symp. on Comp. Technologies for Fluid/Thermal/Chemical Systems With Industrial Applications*, ASME, New York, PVP-Vol. 397.2, pp. 195–204.

[7] Demeulenaere, A., and Van Den Braembussche, R., 1998, "Three-Dimensional Inverse Method for Turbomachinery Blading Design," ASME J. Turbomach., **120**, pp. 247–254.

[8] Damle, S., Dang, T., Stringham, J., and Razinsky, E., 1998, "Practical Use of 3D Inverse Method for Compressor Blade Design," ASME Paper No. 98-GT-115.

[9] Pierret, S., and Van Den Braembussche, R., 1998, "Turbomachinery Blade Design Using a Navier-Stokes Solver and Artificial Neural Network," ASME Paper No. 98-GT-4.

[10] Pierret, S., 1999, "Three-Dimensional Blade Design by Means of an Artificial Neural Network and Navier-Stokes Solver," VKI LS 1999-02.

[11] Shahpar, S., 2000, "A Comparative Study of Optimization Methods for Aerodynamic Design of Turbomachinery Blades," ASME Paper No. 2000-GT-523.

[12] Lee, S. Y., and Kim K. Y., 2000, "Design Optimization of Axial Flow Compressor Blades With Three-Dimensional Navier-Stokes Solver," AMSE Paper No. 2000-GT-0488.

[13] Yershov, S., and Rusanov, A., 1996, "The High Resolution Method of Godunov's Type for 3D Viscous Flow Calculations," *Proc. 3 Colloq. Proc. Simulation*, A. Jokilaakso, ed., Espoo, Finland, June 13–16, pp. 69–85.

[14] Yershov, S., and Rusanov, A., 1996, "The Application Package FlowER for Calculation of 3D Viscous Flows Through Multi-stage Turbomachinery," Certificate of Ukrainian state agency of copyright and related rights, Kiev, Ukraine, Feb. 19.

[15] Yershov, S., Rusanov, A., Gardzilewicz, A., and Lampart, P., 1999, "Calculations of 3D Viscous Compressible Turbomachinery Flows," *2nd Symp. on Comp. Technologies for Fluid/Thermal/Chemical Systems With Industrial Applications*, ASME, New York, PVP-Vol. 397.2, pp. 143–154.

[16] Yershov, S., Shapochka, A., and Rusanov, A., 2000, "Code Optimus," Rep. Sci. Group FlowER, No. 2/2000.

[17] Nelder, J. A., and Mead, R., 1965, "A Simplex Method for Function Minimisation," Computer Journal, **7**(1), pp. 308–313.

[18] Spendley, W., Hext, G. R., and Himsworth, F. R., 1962, Technometrics, No. 4/441.

[19] Torczon, V. J., 1989, "Multi-directional Search:A Direct Search Algorithm for Parallel Machines," Ph.D. thesis, Rice University, Houston, TX.

[20] Lampart, P., 2000, "The Application of Stator Blade Compound Lean at Root to Increase the Efficiency of LP Turbine Stages From Low to Nominal Load," ASME Paper No. IJPGC-15015.

[21] Denton, J. D., 1993, "Loss Mechanisms in Turbomachines," ASME J. Turbomach., **115**, pp. 621–656.

T. Nakagaki
e-mail: takao.nakagaki@Toshiba.co.up

T. Ogawa

H. Hirata

K. Kawamoto

Y. Ohashi

K. Tanaka

Toshiba Corporation,
Power and Industrial Systems Research
and Development Center,
2-4 Suehiro-cho,
Turumi-ku, Yokohama 230-0045, Japan

Development of Chemically Recuperated Micro Gas Turbine

Micro gas turbines (MGTs) are subject to certain problems, notably low thermal efficiency of the system and high emission including NO_x. The chemically recuperated gas turbine (CRGT) system introduced in this paper is one of the most promising solutions to these problems. The CRGT system we propose uses an endothermic reaction of methane steam reforming for heat recovery. It is usually thought that the reaction of methane steam reforming does not occur sufficiently to recover heat at the temperature of turbine exhaust, but we confirmed sufficient reaction occurred at such low temperature and that applications of the chemical recuperation system to some commercial MGTs are effective for increasing the efficiency. [DOI: 10.1115/1.1520158]

Introduction

As a consequence of deregulation of energy markets in recent years, distributed power sources have become widespread in some parts of the world. Micro gas turbines (MGTs) are small-scale power sources which have attracted attention due to their good cost performance and easy operation. With a view to competing in markets, many manufacturers are developing MGTs, which have certain common specifications: (1) the power output is 30–300 kW, (2) radial compressors and turbines with comparatively low pressure ratio are used, (3) natural gas, LP gas or kerosene are available as gas turbine fuel. However, certain problems have been identified under practical operating conditions, namely machine reliability, low thermal efficiency of the system, and high emission including NO_x.

Methane, the principal component of natural gas, is converted into hydrogen-rich gas with steam. This steam-reforming reaction of methane is well known in the case of hydrogen refineries, which are generally operated at about 800°C with Ni-based catalyst, but 20–50% conversion could be realized under the equilibrium conditions using turbine exhaust at 600°C. The chemical heat recovery from turbine exhaust using an endothermic reaction of steam reforming increases generating power and efficiency beyond what is possible with direct combustion. Also, NO_x emission is reduced because the good combustibility of hydrogen-rich gas and the existence of much steam in the gas decrease adiabatic combustion temperature.

Concerning CRGT systems, there are some reports on the use of methanol, but few on the use of methane. Carapellucci et al. [1,2] have reported feasibility studies of a CRGT system using methanol as fuel. Kuroda et al. [3] and Nagaya et al. [4] have reported on the practical tests that were conducted at 1.5 MPa. Methanol is almost completely converted to hydrogen-rich gas at 300°C using Cu-Zn catalyst, which is a lower conversion temperature than is attainable for methane. Therefore, it is easier to design a methanol reformer than it is to design a methane one. However, methanol is a less widely used fuel than methane. Also, change in enthalpy in the case of methanol steam-reforming reaction is 49.5 kJ/mol, which is smaller than that for methane (165.1 kJ/mol), and so improvement of the efficiency is inferior to that in the case of methane.

A number of studies on methane steam reforming have been reported. For example, Xu and Froment have presented a useful formula of reaction rate in their reports, [5]. Simulations of a methane reformer have been an object of study for several decades (Hyman [6]). Murray et al. [7] have estimated methane conversion, considering energy balance only when configuration of the reformer is changed. Alatiqi et al. [8] have presented a design of a methane steam reformer, for which purpose they used a reaction rate equation from the literature. There are many papers that report on heat and mass transfer in a methane reformer. Fukusako et al. [9] have described a reformer in a fuel cell system, and Altman and Wise [10] and Wijngaarden and Westerterp [11] have studied the effect of chemical reactions on heat transfer.

In this report, we describe the feasibility of applying chemical recuperation to a commercial MGT system. At first, the mass and heat balance of the CRGT system was analyzed in order to estimate outline of the heat recovery reformer. Next, the basic performance of some commercial catalysts was tested to select suitable catalysts for the reformer, and the heat transfer and the conversion rate to hydrogen-rich gas were examined using a tube 300 mm in length packed with a catalyst. Based on the results of these examinations, a simulation code was developed in order to evaluate the transportation phenomena in the reformer. Using this code, a shell-and-tube reformer unit was designed and the total performance of this reformer unit was evaluated. Finally, the adequacy of this reformer design was confirmed by the comprehensive reforming test using a U-shape tube, a furnace, and a blower.

Outline of the Chemically Recuperated Gas Turbine (CRGT) System

Figure 1 shows a block diagram of a CRGT system. In an MGT system, turbine exhaust temperature is about 600°C, and the power generation efficiency is increased by heat recovery of air recuperator, but in the CRGT system, the reformer recovers the turbine exhaust heat first. As shown in Fig. 1, the equipment after the reformer is the air recuperator, and next is the evaporator, but the system works if sequence of the equipment after the reformer is arranged in accordance with layout of the engine system of micro gas turbines. The amount of heat recovered by the reformer is determined by enthalpy change of chemical reaction which converts fuel and steam into hydrogen-rich gas. The principal reactions in a reformer are expressed as follows:

$$CH_4 + H_2O \Leftrightarrow CO + 3H_2 \qquad \text{(steam reforming)}$$

$$CO + H_2O \Leftrightarrow CO_2 + H_2 \qquad \text{(water gas shift)}$$

Contributed by the Advanced Energy Division of THE AMERICAN SOCIETY OF MECHANICAL ENGINEERS for publication in the ASME JOURNAL OF ENGINEERING FOR GAS TURBINES AND POWER. Manuscript received by the AE Division August 20, 2001; final revision received by the ASME Headquarters June 9, 2002. Associate Editor: G. Reistad.

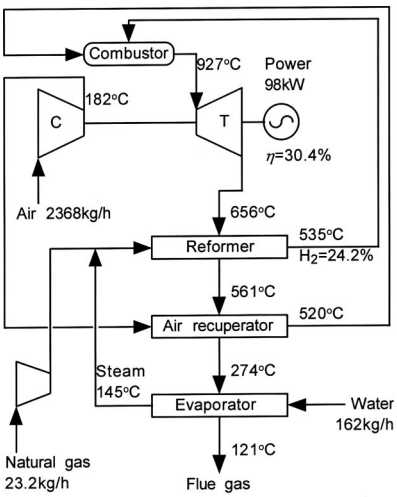

Fig. 1 The principal stream conditions of CRGT system

The reaction rate of water gas shift is larger than that of steam reforming, and it is regarded as equilibrium. Thus, the molar stoichiometric ratio between methane and steam (i.e., steam carbon ratio, S/C) in the above reactions is 2.0, but S/C is operated from 3 to 4 in order to avoid deposition of carbon by Boudouard's reaction expressed as follows:

$$2CO \Leftrightarrow CO_2 + C \qquad \text{(Boudouard's)}$$

The steam-reforming reaction occurs partially below 600°C, methane of 100% is not converted into hydrogen-rich gas. The maximum conversion of methane is limited thermodynamically, which is influenced by physical conditions: temperature T, total pressure P, and S/C. For example, equilibrium conversion is about 35% under the conditions of $T=500°C$, $P=0.4$ MPa, and S/C $=4.0$. The reaction pressure P in the reformer is higher than that in the combustor, and it ranges between 0.3 and 0.5 MPa. The more temperature or S/C increases, the more equilibrium conversion increases. Therefore, it is preferable that temperature and S/C in the reformer are set high to enlarge heat recovery. However, configurations of the gas turbine and the evaporator restrict the amount of steam, and S/C has an upper limit. In the gas turbine, surge limit of the compressor determines the maximum flow rate including steam through the turbine. In the evaporator, the upper limit of steam generation is determined because the pinch point temperature difference becomes critical. Hence, the maximum S/C is set to approximately 7. Besides, the temperature in the reformer is influenced by the configuration of the reformer because the reaction occurs in the reformer exchanging heat with turbine exhaust. Hence, the design of the reformer is very important.

Table 1 Summary of assumptions in evaluation of mass and heat balance

Category	Device	Processing
Pressure drop of air or exhaust	Burner nozzle	Ignored
	Air Recuperator	3% each for P(abs)
	Reformer	2% for P(abs)
	Evaporator	2% for P(abs)
Pressure drop of fuel or water	Burner nozzle	30% for P(abs)
	Reformer	Included in burner nozzle
	Evaporator	Ignored
	Fuel gas compressor	Ignored
Power	Fuel gas compressor	Subtracted from output
Heat loss	All devices	Ignored

Figure 1 shows the principal stream conditions of a chemically recuperated MGT based on a commercial 75 kW MGT system using natural gas as fuel. Figure 2 shows a schematic illustration of heat balance in the system shown in Fig. 1. Figure 2 also shows each energy percentage of natural gas LHV (lower heating value). Table 1 shows the summary of assumptions in evaluation of mass and heat balance. In the system shown in Fig. 1, as much steam as possible is generated to enlarge heat recovery by large conversion and S/C is set to 6.3. The heat duty of the reformer is estimated, considering reactions as equilibrium, and the reformer uses exhaust heat from 656°C to 561°C. The mole fraction of hydrogen in the reformer output is 24%, and the conversion rises to 51%. The heat recovery at the reformer is 82.4 kW, which recovers 25.6% of fuel LHV. The air recuperator is placed after reformer and it heats compressed air until 520°C using exhaust heat from 561°C to 274°C, which recovers 40.5 kW. The evaporator uses the bottom of exhaust heat from 274°C to 121°C. According to this system analysis, the output and the efficiency were expected to improve up to 98 kW and 30.4%, respectively, comparing with 75 kW and 28% of the original MGT.

Another advantage of the CRGT system is reduction of NO_x emission. NO_x is created in combustion, and it is roughly classified as prompt NO_x and thermal NO_x according to reaction mechanisms. In the CRGT system, addition of steam lowers combustion temperature and decreases thermal NO_x. Figure 3 shows the effect of S/C on adiabatic combustion temperature, and horizontal axis expresses equivalence ratio (air fuel ratio/stoichiometric air fuel ratio). In the evaluation of adiabatic combustion temperature, the temperature of combustion air was applied as the outlet temperature of the air recuperator shown in Fig. 1. The fuel temperatures were 535°C in the CRGT shown in

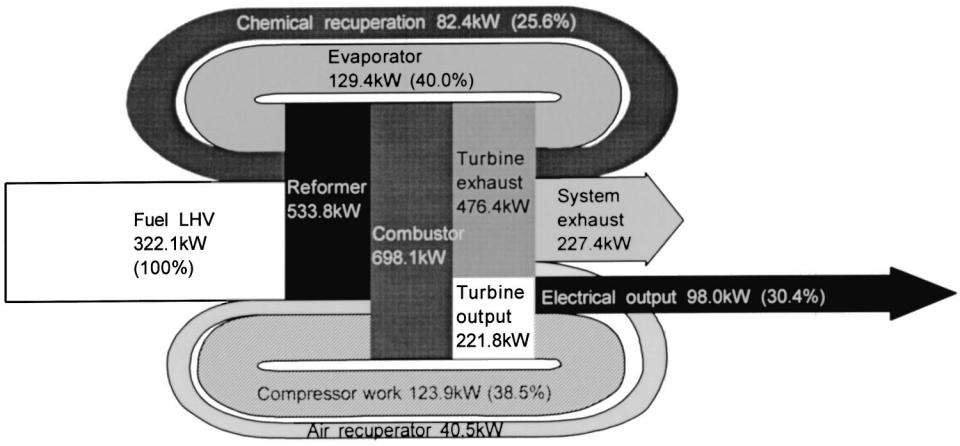

Fig. 2 Heat balance in the CRGT system. ( ) is expressed as percentage of natural gas LHV.

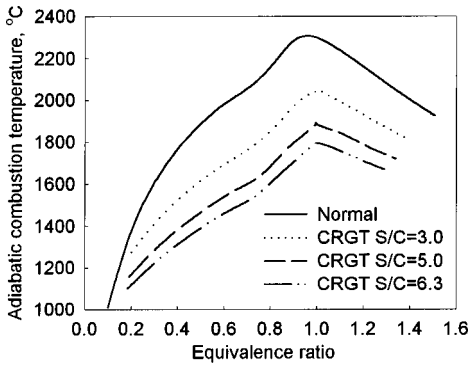

Fig. 3 Effect of S/C on adiabatic combustion temperature

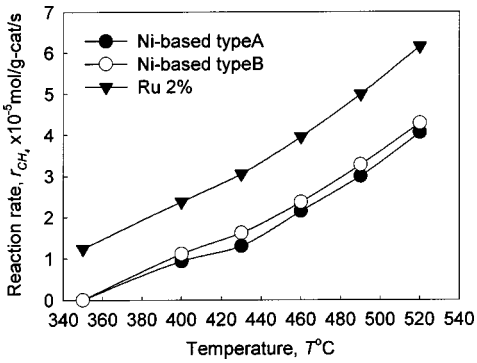

Fig. 5 Experimental results for catalyst performance

Fig. 1, but in the norm, it is the outlet temperature of the fuel compressor. It is clearly shown in Fig. 3 that the CRGT system lowers adiabatic combustion temperature, and the lowering becomes more marked with larger S/C.

Approach to Development

Catalyst Examination. In the next step of development of a chemical recuperation system and the selection of catalysts for steam reforming is necessary and their performances should be examined. For the catalyst, the following specifications are required: difficulty of carbon deposit or easy desorption by steaming, high activity at low temperature below 500°C, chemical and mechanical robustness for DSS (daily start and stop), long life, no necessity of reduction treatment, ability of preservation purging with steam or air at cool down, large thermal conductivity, and small pressure drop. We sought to identify commercially available catalysts whose basic performances largely satisfy the above specifications.

The experimental apparatus is shown in Fig. 4. The materials of steam reforming were methane controlled by mass flow controller (MFC) and steam generated by vaporization of demineralized water sent by constant flow pump, and they were mixed in the required S/C. The mixture gas was heated and adjusted to the required temperature and passed to the packed bed of catalyst with a small volume kept at the required pressure by the regulating valve. Components of output gas were analyzed by a TCD-type gas chromatograph (GC) and the flow rate was measured by a gas meter.

Figure 5 shows an example of results with some kinds of catalysts, which are expressed as the relation between reaction rate and temperature, and the summary of the examination parameters is shown in Table 2. The catalyst containing ruthenium of 2% shows higher activity at low temperature than does a nickel-based catalyst. It was confirmed by an additional experiment that Ru catalyst satisfied almost all of the required specifications mentioned above. The reaction ratio is influenced by diverse parameters, which are temperature, total pressure, partial pressure of each component, velocity in a tube, and so on. However, the parameters of a target reformer are not so broad. Total pressure or exhaust heat at the rated conditions is specified by the target MGT system. When the temperature is under 350°C, the reaction rate is fairly small and negligible. Even S/C, which takes comparatively broad range, is from 3.0 to 7.0 at most. The steam reforming in a catalyst bed is a heterogeneous surface reaction and several models explained the reaction kinetics as represented by Langmuir-Hinshelwood kinetics. Within such limited ranges, the reaction rate can be expressed in a formula of simple power law. As a result of examination under almost all the conditions required to design the reformer, characteristic data could be arranged in the modified Grover equation, [12]. The reaction rates of catalysts r_{CH_4} are expressed in the following equation:

$$r_{CH_4} = A \cdot f(u) \cdot e^{-E/RT} \cdot P^b \cdot \left(p_{CH_4} - \frac{p_{H_2}^3 p_{CO}}{p_{H_2O} K} \right)$$

where A, $f(u)$, E, and b depend on catalyst. The shift reaction can be regarded as equilibrium, which is mentioned above.

Design of Reformer. For the CRGT system shown in Fig. 1, a shell-and-tube type reformer was designed because of advantage in cost. Figure 6 shows a photograph of the trial reformer. The reformer has two bundles of staggered tube banks, each bank consisting of 48 tubes whose inner diameter is 22 mm and length is 430 mm. The mixture of fuel gas and steam is sent into the inlet manifold and distributed into the 48 tubes of the first bundle. A catalyst is packed in each tube and the mixture gas takes a U-turn into the second bundle at the lower manifold. The mixture gas

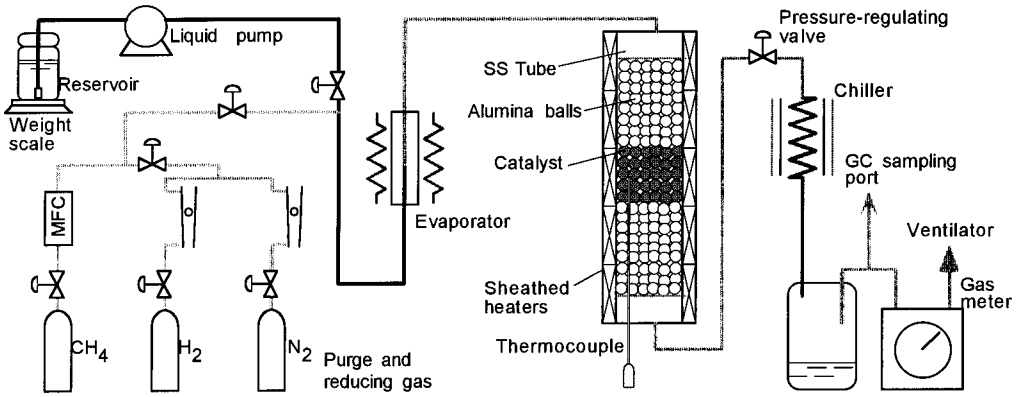

Fig. 4 Experimental apparatus of catalyst examination

Table 2 Summary of parameters in catalyst examination

Parameter	Description
Total pressure, MPa	0.1, 0.4, 0.6, 1.0
Catalyst temperature, °C	350, 400, 430, 460, 490, 520
S/C	2.5, 3.5, 4.5, 5.5
Approach velocity, m/s	0.3 – 5.0
Effect of partial pressure	H_2 (Product), Dilution with N_2

flows through toward the outlet manifold, converting into hydrogen-rich gas. The first and second bundles are placed so that the mixture gas may flow counter from downstream of turbine exhaust to upstream. Turbine exhaust flows through the tube bank and exchanges heat with internal catalyst or hydrogen-rich gas through the tube walls. Figure 7 shows a photograph of the detail of manifold. The stainless steel meshes are attached at top and bottom of each tube to hold the catalyst bed and avoid blowing away.

The following configuration parameters are considered for designing the reformer shown in Fig. 6: pitch of tube bank, diameter and length of tube, number of tubes in a bundle, and number of bundles. In order to determine these parameters, influence on pressure drop and heat transfer inside and outside of the tube should be surveyed, which is similar to the case of designing heat exchangers. For instance, since tightening the pitch of the tube bank makes the pressure drop of the turbine exhaust increase, the backpressure of the turbine increases and the generation of electricity decreases. Simultaneously, since it makes velocity of turbine exhaust though the tube bank increase, the heat transfer coefficient of the external tube wall enlarges and heat recovery increases. Thus, configuration parameters affect pressure drops and heat transfers positively or negatively, and they affect the efficiency, too. The reformer shown in Fig. 6 is one of the optimized solutions, which balances pressure drops and heat transfers so as to maximize the efficiency.

Numerical Analysis. In the reformer shown in Fig. 7, 12 tubes are lined up across the exhaust stream and 8 rows are parallel with the stream. Concerning these 8 tube rows, a numerical analysis was conducted to evaluate substance and heat flow inside and outside of the tubes. The analysis solved the following equations simultaneously and two dimensionally using the control volume method: continuous, momentum expressed as modified Darcian, energy, each chemical component expressed as forced convection and diffusion and ideal gas state, [13]. The reaction rate of the Ru catalyst was included in source term of the chemical component equation. Temperature drop of the exhaust gas was also solved to estimate heat flux through the tube wall, and all equations were made to converge until the approaching temperature of the exhaust gas was equal to the required value. The analyzed area was surrounded by a given inlet: a boundary, symmetric boundary along the center axis of tube, a free outlet boundary and a known boundary of velocity, and heat flux at internal tube wall. In the energy equation, Gnielinski equation, [14], was used as heat transfer coefficient of forced convection in the tube banks, and Yagi-Kunii equation, [15], was used as heat transfer in packed bed. Figure 8 shows contour at intervals of 10°C in 8 tubes under the conditions of $T_g = 655°C$, $P = 0.4$ MPa and S/C = 6.3, which are required for the system shown in Fig. 1. The mixture gas of methane and steam flows from the right side of the figure to the left in a U-shape, and the exhaust gas flows inversely from left to right. Temperature profile of exhaust gas is also shown in the figure. In the first bundle, intervals of contour are narrow and an ascent of the temperature is large. In the second bundle, the contour is vertical and the radial gradient of temperature is larger than in the first bundle. It is considered that since reaction rate at nearly 500°C increases exponentially, increase of heat flux enlarges the temperature gradient. Besides, the pressure drop of tube bank is approximately 1 kPa, [16], which is equal to or less than pressure drop of a conventional air recuperator. Also, the pressure drop in a packed bed is evaluated by the Ergun equation, [17], which is expressed in the following equation. It is approximately 22 kPa, which is relatively large, but it is substantially within the allowable range of the gas compressor.

$$\frac{\Delta p}{L} = \frac{150\mu u(1-\varepsilon)^2}{d^2\varepsilon^3} + \frac{1.75\rho u^2(1-\varepsilon)}{d\varepsilon^3}$$

Confirmatory Tests. In order to confirm adequacy of the design and analysis, the comprehensive reforming test is conducted. Figure 9 shows the photograph of the experimental apparatus. In this test, a furnace and a blower were used to simulate the turbine exhaust flow. The inlet temperature of the blower is cooled with air mixing at the end of test section so that it may not exceed acceptable temperature of the blower. The flow rate of the hot air over 500°C was controlled by three dampers, which are attached

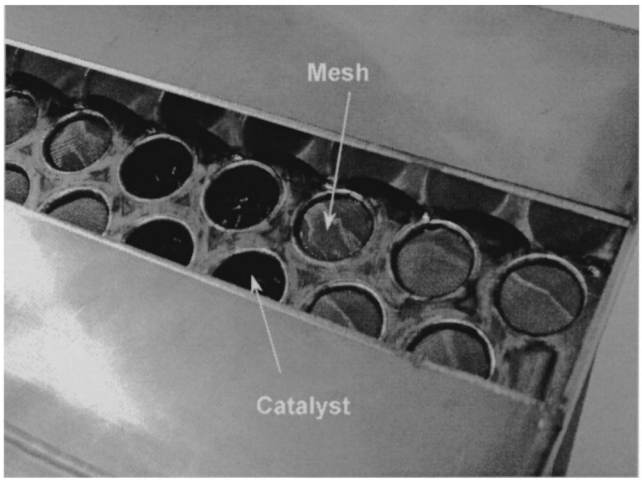

Fig. 7 The detail of manifold

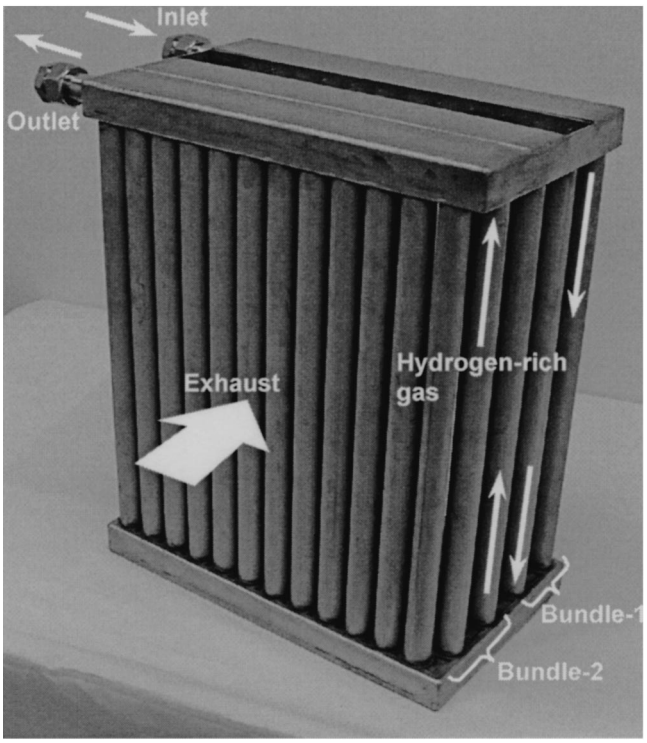

Fig. 6 The trial reformer for 75 kW MGT

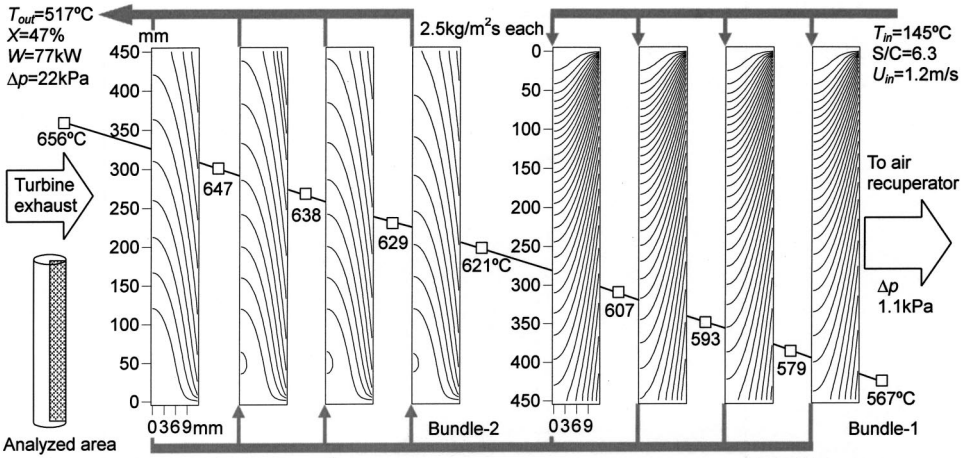

Fig. 8 Analytical result of temperature profile in reformer (contour at intervals of 10°C)

on the furnace, cooling air tube and inlet of the blower, respectively. Also, it was evaluated as the difference between the flow rates of the cooing air and cooled hot air under 200°C measured by each orifice plates because it is difficult to measure the flow rate of the hot air directly. Besides, a U-shape tube was mounted in the duct as the test section, which is packed with the Ru catalyst in a length of 430 mm. A mass flow controller and a plunger pump controlled methane and steam generated in the evaporator mounted in the duct, respectively, were mixed and flowed into the catalyst bed. A pressure regulator controlled pressure of the reformer outlet and the GC analyzed the composition of the hydrogen-rich gas. Several thermocouples were attached on the test section to measure temperatures of outer tube wall, inlet, and outlet temperature of gas in the tube, distribution on the center axis of the catalyst bed, and perpendicular distribution of the hot air temperature.

Figure 10 shows a result of the test under the conditions of $T_g = 655°C$, $T_{in} = 158°C$, $P = 0.4$ MPa, and S/C = 6.3, which are almost equal to the analysis showed in Fig. 8. The flow rate of hot air was adjusted to 320 Nm^3/h, considering that convective heat transfer coefficient at the outer tube wall (α_w) might equate to 150 W/m^2K, which was that of the designed reformer showed in Fig. 6 under the rated condition. Figure 10 also shows the prediction in the analysis shown in Fig. 9, which is the average of four tubes in each bank. Comparisons of the heat recovery and the methane conversion are shown in Table 3. Tube 1 and Tube 2 correspond to Bundle 1 and Bundle 2, respectively. This test could not exactly simulate gradual temperature drop of the exhaust gas in the duct due to heat exchange with reformer, and it is assumed that the tube wall was heated only in the length of packed bed in the analysis, but the U bent portion of the test section was also heated in the test. Despite the above differences, the two temperature profiles do not differ significantly. Also, the recovery heats and the methane conversions are comparable. Considering this result, it is confirmed that the designed reformer can convert the natural gas to hydrogen-rich gas and recover the expected amount of heat.

Finally, combustibility of hydrogen-rich gas was examined. The

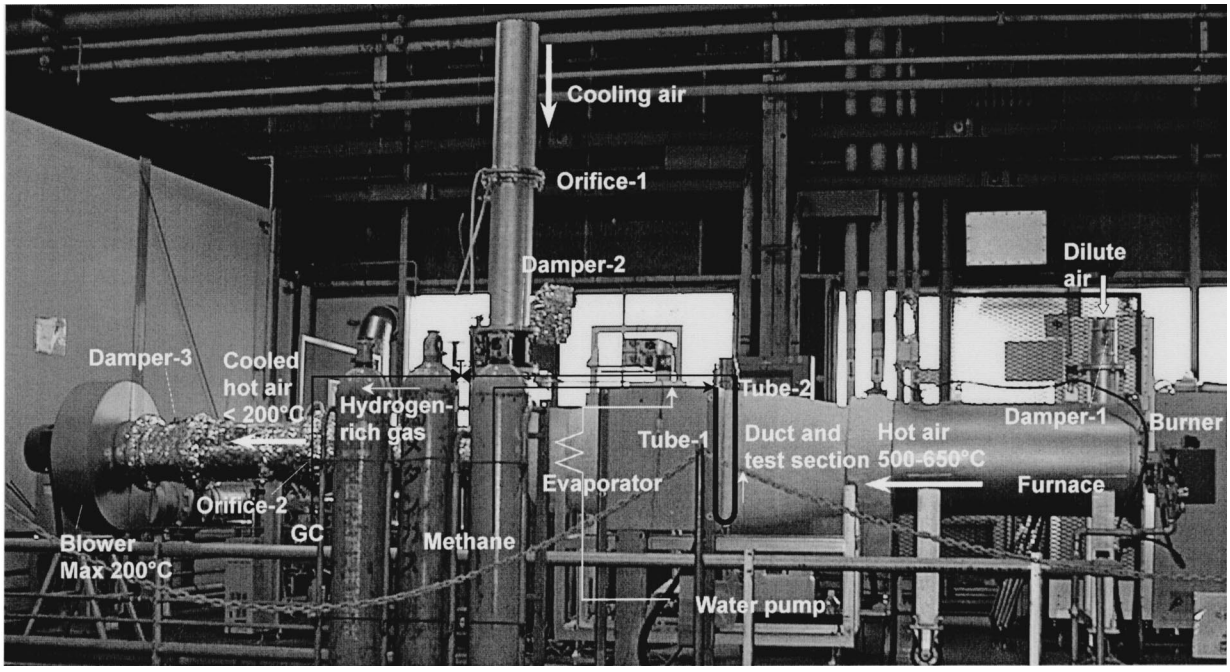

Fig. 9 Experimental apparatus of the comprehensive reforming test

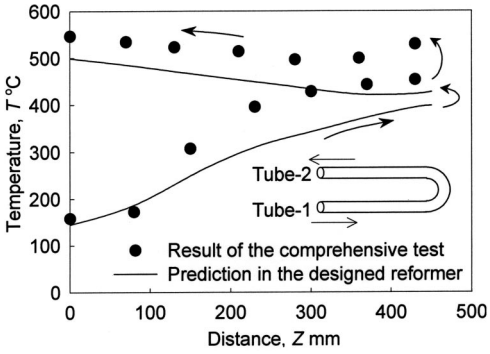

Fig. 10 Result of the reforming test (T_g=655°C, T_{in}=158°C, P=0.4 MPa, S/C=6.3 and α_w=150 W/m^{2}K)

hydrogen-rich gas mainly contains H_2, H_2O, CH_4, and CO_2. It also contains a small amount of CO and other alkanes. The heating value of hydrogen-rich gas is different from that of natural gas so that different characteristics of combustion are expected. The cylinders of simulated gas were provided, which contained H_2 of 26%, CH_4 of 18%, CO_2 of 6%, and the balance gas of N_2 was substituted for H_2O, and the gas was discharged from a burner with heated air and burned at atmospheric pressure. The burner has dual concentric nozzles, which discharge the natural gas for the pilot and the hydrogen-rich gas, respectively. Figures 11(*a*) and 11(*b*) show photographs of flames, which are the combustion of the natural gas and the hydrogen-rich gas, respectively. The hydrogen-rich gas shows stability and good combustibility in Fig. 11(*b*), and also shows light color in comparison with the natural gas because of hydrogen combustion. On the assumption of the start up of an actual operation of CRGT system, an attempt was made to gradually switch from natural gas to hydrogen-rich gas, and it was confirmed that these gases could be switched without flame-out. Also, combustion of the hydrogen-rich gas showed lower NO_x concentration than that of the natural gas.

Table 3 Comparisons of the heat recovery and the methane conversion

Parameter	No.	Test result	Prediction
Heat recovery, W	1	1119	1021
	2	655	582
Methane conversion, %	1	18.7	21.6
	2	54.4	47.0

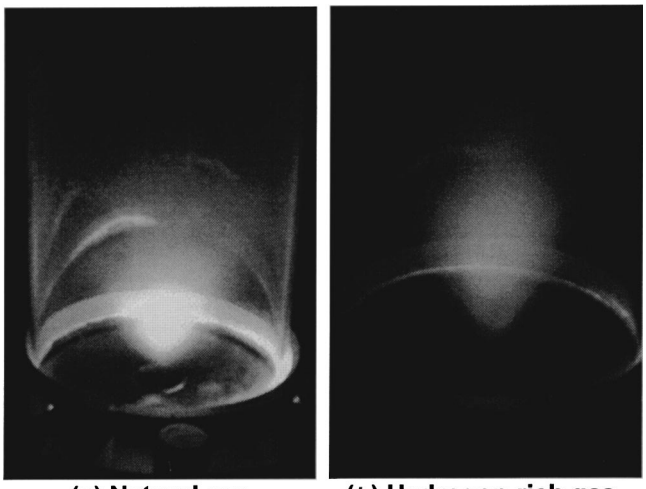

Fig. 11 Photographs of flames

Conclusion

The results of this study indicate that the CRGT system may be effective for improving the power generation efficiency and lowering the NO_x emission. The performances of some catalysts were examined and a Ru catalyst was selected for application to DSS use of MGTs. The trial reformer was designed considering all transportation phenomena, and adequacy of the design and prediction was confirmed by the comprehensive reforming test. Furthermore, combustibility of the hydrogen-rich gas was examined.

The results of this study indicate the practicability of the CRGT system. CRGT systems can be attached to existing systems and they are applicable to small and medium-size GTs ranging from micro GT to MW class GT. In the next step of this work, we intend to perform a combination test using an actual GT engine.

Nomenclature

A = frequency factor
d = diameter of catalyst particle, m
E = activation energy, J/mol
K = equilibrium constant, MPa^2
L = length of catalyst bed, m
P = total pressure, Pa
p_i = partial pressure of component i, MPa
R = gas constant, J/mol/K
r = reaction rate, mol/g-cat/s
T = temperature, °C
u = velocity, m/s
W = heat recovery, W
X = methane conversion
z = distance from inlet of packed bed, mm
α = Convective heat transfer coefficient
Δp = pressure drop, Pa
ε = porosity of catalyst bed
μ = viscosity, Pas
ρ = density, kg/m^3

Subscripts

g = turbine exhaust
in = inlet
out = outlet
w = wall

References

[1] Carapellucci, R., Risalvato, V., and Cau, G., 1994, "Characteristics of the Heat Recovery Methanol Reforming in CRGT Power Generation Systems," *Proc., ASME COGEN-TURBO*, IGTI-Vol. 9, ASME, New York, pp. 257–264.
[2] Carapellucci, R., Risalvato, V., Bruno C., and Cau, G., 1996, "Performance and Emissions of CRGT Power Generation Systems With Reformed Methanol," *Proc., IECEC 96*, ASME, New York, **2**, pp. 707–712.
[3] Kuroda, K., Imai, T., and Yanagi, M., 1989, "Development of Methanol Reformer," Mitsubishi Jukou Gihou, **26**(5), pp. 408–412.
[4] Nagaya, K., Oshiro, H., Ito, H., and Yoshino, N., 1993, "Demonstration Test of Reformed Methanol Gas-Turbine Power Generation," Hitachi Zousen Gihou, **54**(3), pp. 180–184.
[5] Xu, J., and Froment, G. F., 1989, "Methane Steam Reforming, Methanation and Water-Gas Shift: I. Intrinsic Kinetics," AIChE J., **35**(1), pp. 88–96.
[6] Hyman, M. H., 1968, "Simulate Methane Reformer Reactions," Hydrocarbon Process., **47**(7), pp. 131–137.
[7] Murray, A. P., and Snyder, T. S., 1985, "Steam-Methane Reformer Kinetic Computer Model with Heat Transfer and Geometry Options," Ind. Eng. Chem. Process Des. Dev., **24**, pp. 286–294.
[8] Alatiqui, I. M., Meziou, A. M., and Gasmelseed, G. A., 1989, "Modeling, Simulation and Sensitivity Analysis of Steam-Methane Reformers," Int. J. Hydrogen Energy, **14**(4), pp. 241–256.
[9] Fukusako, S., Yamada, M., and Usami, Y., 1997, "Heat and Mass Transfer Characteristics in a Reforming Catalyst Bed," J. HTSJ, **36**(140), pp. 18–26.
[10] Altman, D., and Wise, H., 1956, "Effect of Chemical Reactions in the Boundary Layer on Convective Heat Transfer," Jet Propul., (4), pp. 256–269.
[11] Wijngaarden, R. J., and Westerterp, K. R., 1989, "Do the Effective Heat Conductivity and the Heat Transfer Coefficient at the Wall Inside a Packed Bed Depend on a Chemical Reaction? Weakness and Applicability of Current Models," Chem. Eng. Sci., **44**(8), pp. 1653–1663.
[12] Grover, S. S., 1970, Hydrocarbon Process., **49**(4), pp. 109.

[13] Nakagaki, T., Ogawa, T., Murata, K., and Nakata, Y., 2001, ''Development of Methanol Steam Reformer for Chemical Recuperation,'' ASME J. Eng. Gas Turbines Power, **123**, pp. 727–733.
[14] Gnielinski, V., 1978, ''Gleichungen zur Berechnung des Wärmeübergangs in querdurchströmten einzelnen Rohrreihen und Rohrbündeln,'' Forsch. Ingenieurwes., **44**, pp. 15–25.
[15] Yagi, S., and Kunii, D., 1962, ''Studies on Heat Transfer in Packed Beds,'' *Int, Devel. Heat Transfer, Part IV*, pp. 750–759.
[16] Zukauskas, A. A., Makarevičisu, V. J., and Slančiauskas, V. J., 1968, ''Heat Transfer in Banks of Tubes in Crossflow of Fluid,'' Thermophy., **1**, pp. 47–68.
[17] Ergun, S., 1952, ''Fluid Flow Through Packed Columns,'' Chem. Eng. Prog., **48**, pp. 89–94.